Proceedings of:

Precision Grinding of Brittle Materials

1996 Spring Topical Meeting

June 3-6, 1996
St. John's College
Annapolis, Maryland

The American Society for Precision Engineering (ASPE) is a multidisciplinary professional and technical society concerned with research and development, design, manufacture and measurement of high accuracy components and systems. ASPE activities encompass relevant aspects of mechanical, electronic, optical and production engineering, physics, chemistry, and computer and materials science. Membership is open to anyone interested in any aspect of precision engineering.

Founded in 1986, ASPE provides a new focus for a diverse but important community. Other professional organizations have covered aspects of precision engineering, always as a sideline to their principal goals. ASPE is based on the core of generic concepts necessary to achieve precision in any application; independent of discipline, ASPE intends to be the focus for precision technology — and to represent all facets from research to application.

ASPE — The American Society for Precision Engineering
401 Oberlin Road, Suite 108
P.O. Box 10826
Raleigh, NC 27605-0826
Phone (919) 839-8444 Fax (919) 839-8039

Preface

This book comprises the proceedings of the 1996 Spring Topical Meeting. The contributions reflect the authors' opinions and are published as presented to ASPE, without change. Their inclusion in this publication does not necessarily constitute endorsement by the ASPE, or its editorial staff.

Individual readers of this book and nonprofit libraries acting for them are permitted to make fair use of the material contained in this book to be used in teaching or research; provided they copy said paper in total, as written by the author. Permission is granted to quote excerpts from the scientific or technical works in this book with proper acknowledgment of the source to include: the author's name, the book name, and the ASPE tag line. Reproduction of figures and tables is likewise permitted from the contents of this book, provided that the same acknowledgment of the same source and content is printed.

Any other type reproduction, systematic copying or multiple reproduction of any material in this book is expressly prohibited except with the written permission of the ASPE editorial staff, addressed to the Society's headquarters.

ISBN 1-887706-15-1

1996

American Society for Precision Engineering
401 Oberlin Road, Suite 108
Raleigh, NC 27605-0826

Printed in the United States of America

1996 Spring Topical Meeting

Contents

Preface . . . . . *ii*

Contents . . . . . *iii*

Program . . . . . *iv*

Foreword . . . . . *v*

Technical Paper Index . . . . . *vi-vii*

Technical Papers *3-126*

Author Index *127*

1996 Spring Topical Meeting

Meeting Schedule

Monday, June 3		Tuesday, June 4	Wednesday, June 5	Thursday, June 6
	7:30	REGISTRATION	CONTINENTAL BREAKFAST	
	8:30 10:00	APPLICATIONS & ECONOMICS	CHIP GEOMETRY	COOLANTS
		BREAK	BREAK	
	10:30 12:00	PRECISION GRINDING MACHINE DESIGN	MATERIAL REMOVAL MECHANISMS	SUMMARY
		LUNCH		CLOSE OF CONFERENCE
	1:00	OPEN FOR DISCUSSIONS	OPEN FOR DISCUSSIONS	
ON-SITE REGISTRATION	5:00			
	6:30	DINNER		
	7:30 9:30	WORKPIECE MATERIAL PROPERTIES	GRINDING WHEELS	

Foreword

Because of their optical properties, high strength, and low weight, brittle materials are attractive for a variety of applications from ceramic bearings to glass optics. However, fabrication of these materials is difficult and can account for up to 70% of the cost of the finished component. The typical fabrication procedure involves rough grinding to produce the desired shape and loose abrasive polishing to remove the damage created by the grinding process. Damage remaining from this process in the form of surface and subsurface fractures can reduce the strength of a mechanical component and the quality of an optic. In addition, the polishing process is pressure sensitive rather than motion sensitive and cannot take advantage of a rigid, accurate machine tool. About ten years ago, a new fabrication process — ductile regime or precision grinding — was proposed that involved fixed abrasive grinding at low feed rates with little if any post polishing. This process makes use of the accuracy and repeatability of a precision machine tool to improve the speed of fabrication as well as the quality of the finished surface.

The 1996 ASPE Spring Topical Meeting was organized to bring together specialists from industry, national labs and academia for an open discussion of the state-of-the-art in precision grinding. The format of the meeting was designed to emphasize discussion among the participants and was organized by selecting from the contributed papers, as well as inviting speakers in areas that were deemed important by the organizing committee but not covered in the submitted papers. Each of the authors was asked to present both a status report of their subject and a good indication of the real problems that they are currently facing in their work. The organizers hope that the outcome of the meeting will be the identification of important areas of agreement related to precision machining of brittle materials as well as those areas needing further research.

The Organizing Committee
of the 1996 Spring Topical Meeting

Co-Chairs:
Thomas G. Bifano, Boston University
Thomas A. Dow, North Carolina State University
Ronald O. Scattergood, North Carolina State University

Members:
Kenneth L. Blaedel, Lawrence Livermore National Lab.
Jeffrey W. Carr, IBM Corporation
Donald Golini, University of Rochester
Michele H. Miller, Michigan Technological University
David H. Youden, Rank Pneumo, Inc.

Technical Paper Index

Session I
Applications and Economics
Tuesday, June 4, 8:00 a.m. - 9:30 a.m.

Session Chair: Thomas A. Dow (North Carolina State University)

1. ***Development of Massproductive Ultraprecision Grinding Technology for Brittle Material Devices***
   A. Kanai, M. Miyashita (Ashikaga Institute of Technology), and M. Daito (Nissin Machine Works Ltd.) . . . . . page 3
2. ***Precision Grinding of Ceramic Diesel Engine Components (Invited Paper)***
   A. J. Shih, D. J. Gust, M. B. Grant (Cummins Engine Company, Inc.) . . . . . page 8

Session II
Precision Grinding Machine Design
Tuesday, June 4, 9:45 a.m. - 12:00 p.m.

Session Chair: David H. Youden (Rank Pneumo)

1. ***An Investigation Into High Stiffness Adjustable Natural Frequency Hydrostatic Slide Units***
   D. Devitt (New Way Machine Components, Inc.), and E. R. Marsh (The Pennsylvania State University) . . . . . page 12
2. ***Grinding Machine Technology Required to Achieve Ductile Regime Ceramic Grinding****
   J. D. Flinchbaugh (Weldon Machine Tool, Inc.), and E. R. Marsh (The Pennsylvania State University)
3. ***The Role of Loop Stiffness on Grinding***
   E. R. Marsh, D. S. Yantek (The Pennsylvania State University) . . . . . page 16
4. ***Normal Force Sensors Increase Internal Grinding Precision***
   R. S. Hahn (Hahn Engineering, Inc.) . . . . . page 22
5. ***Development of Sequential Grinding-Polishing Process***
   N. Yasunaga, A. Yamanouchi, M. Takashina (Tokai University) . . . . . page 29
6. ***Design of a New Generation CNC Grinding Machine for the Deterministic Micro Grinding of Glass Optical Lenses***
   M. Walter (Rank Pneumo/Rank Taylor Hobson) . . . . . page 34

Session III
Workpiece Material Properties
Tuesday, June 4, 7:30 p.m. - 9:30 p.m.

Session Chair: Ronald O. Scattergood (North Carolina State University)

1. ***Fracture & Flow Processes in Grinding and Microgrinding of Optical Glasses***
   J. C. Lambropoulos (University of Rochester) . . . . . page 39
2. ***Influence of Dicing Parameters on the Strength of Silicon****
   R. Ebbutt, S. Danyluk (Georgia Institute of Technology), and I. Weisshaus (Kulicke & Soffa [Israel] Ltd.)
3. ***Controlled Microcutting Tests on Single Crystal Silicon***
   B. V. Tanikella, R. O. Scattergood (North Carolina State University) . . . . . page 45
4. ***Effects of Workpiece Properties on Material Removal Process and Damage Tolerance in Ceramic Grinding (Invited Paper)***
   H. H. K. Xu, S. Jahanmir, L. K. Ives (National Institute of Standards and Technology) . . . . . page 52

Session IV
Chip Geometry
Wednesday, June 5, 8:30 a.m. - 10:00 a.m.

Session Chair: Michele H. Miller (Michigan Technological University)

1. ***Geometric Optimization of Process Parameters for Contour Grinding***
   G. E. Storz II, T. A. Dow (North Carolina State University) . . . . . page 58

2. **Edge Chipping and Grinding Damage**
S. Liang (Manufacturing Technology, Inc.), and I. D. Marinescu (Kansas State University) . . . . . page 64
3. **The Effect of Workpiece Modulation on Grinding Kinematics**
M. H. Miller, K. S. Moon (Michigan Technological University) . . . . . page 70

Session V
Material Removal Mechanisms
Wednesday, June 5, 10:30 a.m. - 12:00 p.m.
Session Chair: Thomas G. Bifano (Boston University)

1. **Surface Integrity in Grinding of Ceramics**
B. Zhang (University of Connecticut) . . . . . page 76
2. **Subsurface Microstructure in Nanoground and Nanoturned Silicon (Invited Paper)**
K. E. Puttick, L. C. Whitmore, C. Jeynes (University of Surrey), and A. E. Gee (Cranfield University) . . . . . page 82
3. **Double Fracture Model in Lapping of Ceramics**
I. D. Marinescu (Kansas State University) . . . . . page 88

Session VI
Grinding Wheels
Wednesday, June 5, 7:30 p.m. - 9:30 p.m.
Session Chair: Don Golini (University of Rochester)

1. **Working with the Superabrasives Industry to Optimize Tooling for Grinding Brittle Materials (Invited Paper)**
J. S. Taylor, M. A. Piscotty, K. L. Blaedel (Lawrence Livermore National Laboratory), and F. A. Gray (Industrial Diamond Association) . . . . . page 95
2. **Influence of Workpiece Properties on Tool Performance in Deterministic Microgrinding of Optical Materials**
Y. Zhou, P. D. Funkenbusch (University of Rochester) . . . . . page 103
3. **Diamond Wheel Wear Sensing with Acoustic Emission — Wheel Wear Mechanisms and the Effects of Process Variables**
J. Tang, D. Dornfeld (University of California at Berkeley) and K. Syoji (Tohoku University) . . . . . page 109
4. **Trueing and Dressing of Fine Grit Super-Abrasive Products (Invited Paper)**
M. Tricard and K. Subramanian (Norton Company) . . . . . page 115

Session VII
Coolants
Thursday, June 6, 8:30 - 10:00 a.m.
Session Chair: Jeffrey W. Carr (IBM Corporation)

1. **Chemical Mechanical Finishing of Brittle Materials (Invited Paper)***
L. M. Cook (Rodel)
2. **Fabrication of Lapped Surfaces in the Magnetic Storage Industry***
J. W. Carr (IBM Corporation)
3. **The Effect of the Coolant on the Glass Work and the Diamond Tool in Deterministic Microgrinding**
S. D. Jacobs, B. E. Gillman, J. C. Lambropoulos, T. Fang, Y. Zhou, D. Golini, M. Atwood (University of Rochester) . . . page 121

Summary
Thursday, June 6, 10:30 a.m. - 12:00 p.m.
Session Chair: Kenneth L. Blaedel (Lawrence Livermore National Laboratory)

* *Extended abstract not available at press time*

Technical Papers

Development of Massproductive Ultraprecision Grinding Technology for Brittle Material Devices

A. Kanai*, M. Miyashita* and M. Daito**
* Ashikaga Institute of Technology, 268 Omae, Ashikaga 326, Japan
** Nissin Machine Works, 300 Aritamanisimachi, Hamamatsu 431-31, Japan

1. Introduction

Ultraprecision grinding of brittle material devices can be realized by assuming ductile mode material removal mechanism. That is, every grain depth of cut of all active abrasive grains on grinding wheel has to be no more than ductile-brittle transition in depth of cut of the workmaterial. Therefore, a truing technology to keep grain protrusion heights of abrasive grains to be very precisely uniform, and ultraprecision, high stiffness grinding machine to control every grain depth of cut within the above limitation are inevitably required. And for applying this ductile mode grinding technology to massproduction processes, the following items have to be additionally satisfied simultaneously :

(1) High repeatability of relative motion between grinding wheel and workpiece :
under uncertain factors such as backlash, stick-slip, variation of frictional and grinding loads, environmental disturbances of vibration and temperature and so on, high repeatability and reliability of motion characteristics of grinding machine achieving relative motion between wheel and workpiece with sufficient accuracy for generating specified profile on workmaterial are required,

(2) application of sensors for detecting precisely relative displacement between wheel and workpiece, and design of optimum metrology loop:
application of sensors differentially detecting relative motion between wheel and workpiece, and minimization of elastic deformation of metrology loop,

(3) high reliability and stability of displacement sensors under environment of workshop :
application of sensors with higher reliability and stability in workshop than He-Ne laser interferometer, and

(4) stability of distribution of active abrasive grains :
high stability and repeatability of distribution of active abrasive grains under ductile mode grinding conditions as of after truing and dressing operation and during grinding operation.

In this paper, experimental results on ultraprecision centerless grinding system satisfying both of conditions realizing ductile mode grinding of brittle material devices and massproduction are reported. Postprocess work diameter measuring stand is newly equipped to the ultraprecision, high stiffness grinding machine with feedback system of relative motion between grinding and regulating wheels by use of linear encoder. And a new grinding system is constructed with NC command including correcting pulses of work diameter errors obtained from the measuring stand.

Continuous grinding of ferrule - $\phi 2.5 \times 10$, Z_rO_2 - per lot of about 2000 pieces is carried, and the averaged diameter error of less than 0.03 μm and the diameter distribution of $3\sigma \cong 0.4$ μm are typically resulted.

2. Construction of ultraprecision and high stiffness centerless grinding machine and the motion characteristics[1],[2]

Fig. 1 shows the sectional construction of plain bearing guideways. The force-operated positioning servo system has no Abbe's offset approximately at the driving point, but the linear encoder of displacement feedback sensor has it at the detecting point. As shown in Fig. 2, the scale of linear encoder is fixed on the grinding wheel head and pickup is fixed on regulating wheel head respectively. Experimental results on the yawing and the feed resolution of grinding wheel head are shown respectively in Fig. 3 which also includes a record of stepwise feed in 10 nm / step.

Plain bearing guideways are applied expecting their damping effect over wide frequency range. Fig. 4 shows

simplified presentation of frictional load characteristics in nanometer travel range, which is composed of transient and stationary domains. The former ranges up to 300 nm approximately. It is difficult to expect high damping effect from this spring-like behavior.

Fig. 5 shows the shaking test on the feed system and test results, which means the share ratio against the applied load to the slide between the frictional resistance and the driving force of actuator. The expected high damping force is achieved.

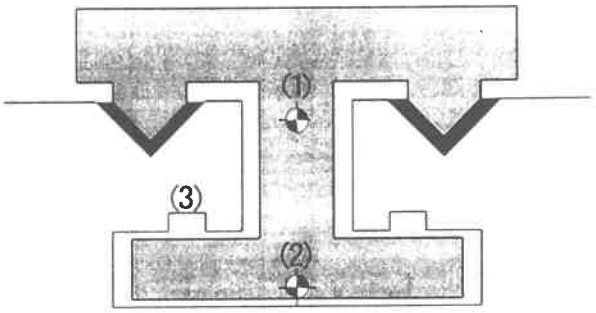

(1) Center of wheel . guideways and feed actuator

(2) Linear scale

(3) Hydrostatic pads

Plain bearing guideways

Fig. 1[1] Guideway mechanism

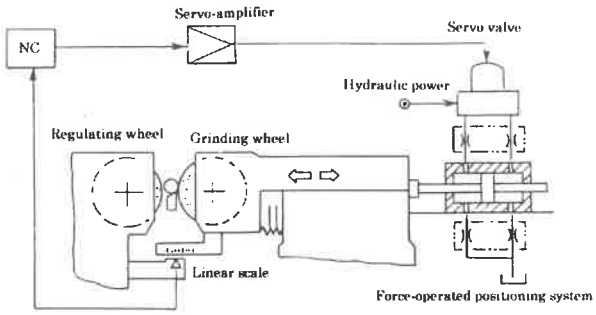

Fig. 2[1] Feed system of grinding wheel

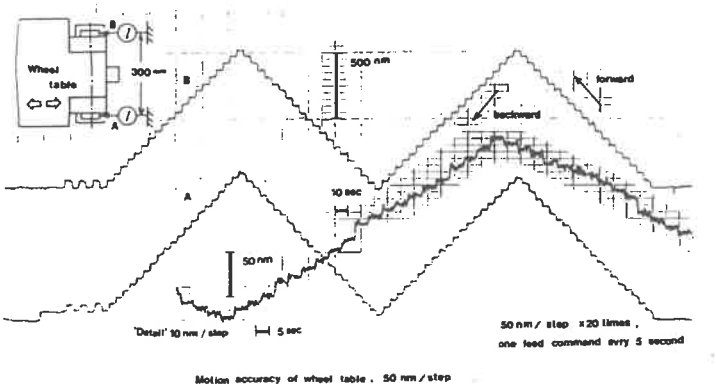

Fig. 3[1] Motion accuracy of grinding wheel slide

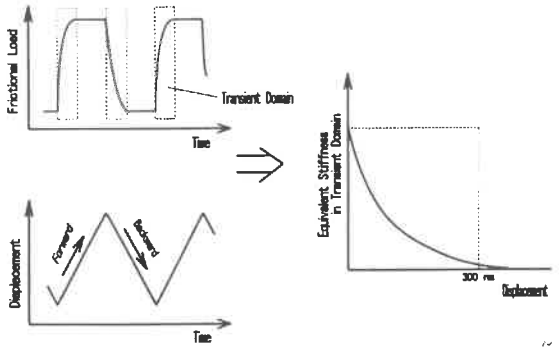

Fig. 4[2] Frictional load characteristics of plain bearing guideway

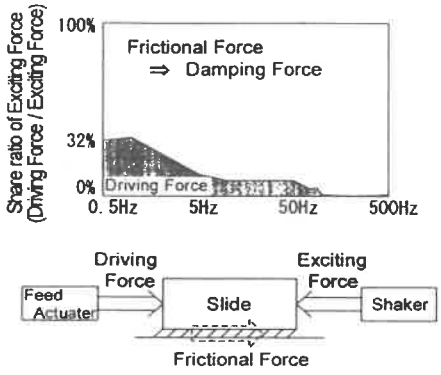

Fig. 5[2] Force share ratio of plain bearing guideway against exciting force

3. Grinding accuracy in terms of the principles of motion copying for ferrules

3.1 Grinding accuracy of ferrules - comparison with lapped ferrules

Fig. 6 is the comparison of ground and lapped ferrules for arbitrarily picked up samples from massproduction processes. Fig. 7 is the comparison in surface finish.

3.2 Feed characteristics of grinding wheel head and copying resolution to work diameter

Fig. 8 shows the copied accuracy to work diameter corresponding to every step of the stepwise grinding wheel head feeds of 0.2 μm/step forward and backward. The copying error is 3σ of 0.05 μm.

3.3 Variation of room temperature and the effect on work diameter

Fig. 9 shows a varying history of the work diameter in thrufeed centerless grinding at the room temperature of 23 ± 2 °C. The dimensional variation of no more than 0.5 μm for 5 hours is achieved except one hour just after starting.

3.4 Bond materials and stability of ground work diameter

Fig. 10 shows a varying history of the work diameter for resin bonded and vitrified diamond wheels.

4. NC centerless grinding system with size error correction equipped with postprocess work diameter measuring stand

4.1 Fig. 11 is the layout of thru-feed centerless grinding, the postprocess diameter measuring stand and the error correction NC command system. A resolution of linear encoder is 10 nm and NC pulse is 0.05 μm/step.

4.2 Grinding accuracy in massproduction

Fig. 12 shows distribution of the work diameters in massproductive thru-feed centerless grinding of ferrules for lot size of 1870. The following grinding errors are obtained :

mean dimensional error in diameter : 0.00 μm, 3σ : 0.38 μm.

Fig. 13 is examples of roundness errors of arbitrary picked up samples. Table 1 shows the grinding and the truing conditions.

5. Conclusion

Ultraprecision grinding of ferrules by use of NC centerless grinding system with size error correction is shown to be practically applicable as a massproductive ultraprecision grinding technology. This is realized by application of the following key items corresponding to the requirements for massproductive ultraprecision grinding :

(1) force-operated positioning servo system of slide on plain bearing guideways,
(2) measurement of relative motion between grinding and regulating wheels with differential linear encoder,
(3) application of linear encoder being stable even in workshop and
(4) application of microtruing technology[3] to wheels.

References

(1) M. Daito, A. Kanai M. Miyashita and J. Yoshioka, Design strategies for ultraprecision, high stiffness feed system of slide on plain bearing guideways, Proc. of ASPE 1996 Annual Meeting

(2) A.Kanai, M. Miyashita and Y. Kishimoto, Experimental analysis of grinding wheel head feed mechanism on plain bearing guideways with Force-operated linear actuator, Proc. of ASPE 1994 Spring Topical Meeting

(3) M. Miyashita, New concept of grinding technology for predictability of manufacturing operation, SME/CIRP 2nd Int. Grinding Conf. in Philadelphia, 1986

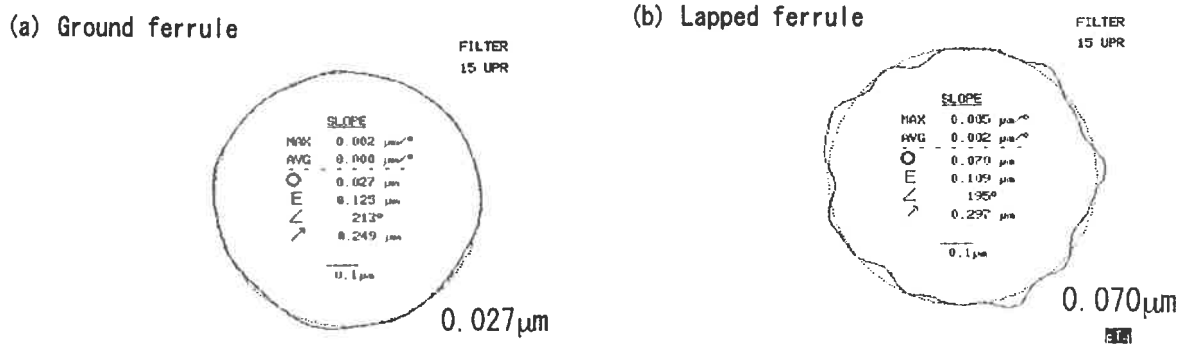

Fig. 6 Roundness of ground and lapped ferrules

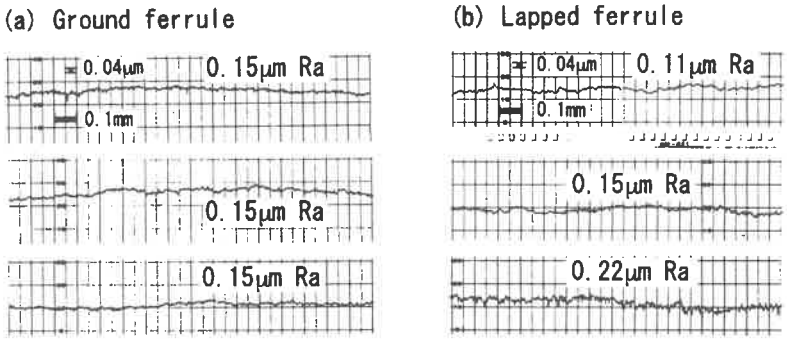

Fig. 7 Surface finish of ground and lapped ferrules

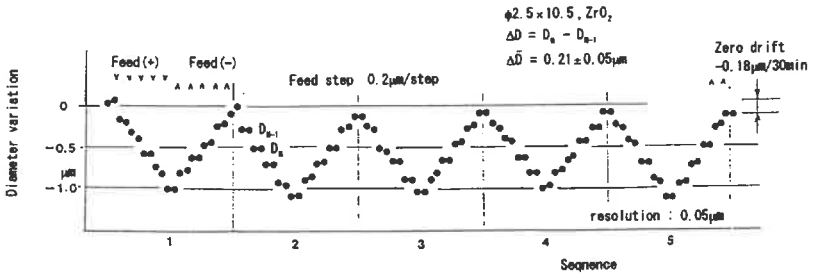

Fig. 8 Copied acuuracy to ground workpiece diameter corresponding to wheel head feed

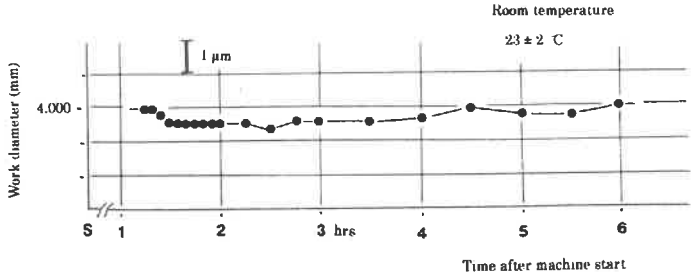

Fig. 9 Variation of ground workpiece diameter

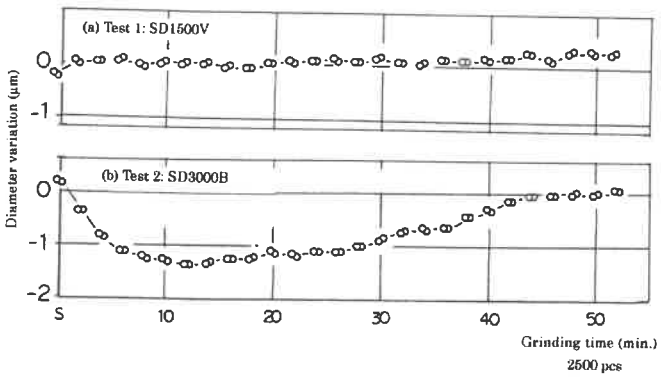

Fig. 10 Comparison of variation of ground workpiece diameter due to bond materials of grinding wheel

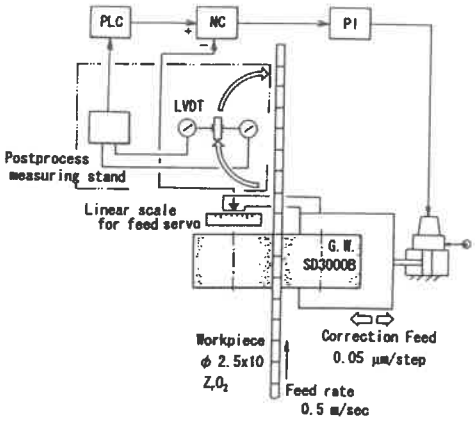

Fig. 11 Lay-out of centerless grinding machine with size error compensation

Table 1 Test conditions

(a) Grinding conditions

Grinding wheel	: SD3000B, ϕ175 x 50
Thru-feed	: 0.5 m/min
Material removal	: 3 μm in diameter
Coolant	: soluble

(b) Truing / Dressing conditions

Truer	: SD200B, ϕ100 x 5
Depth of cut	: 1 μm / pass
Coolant	: soluble

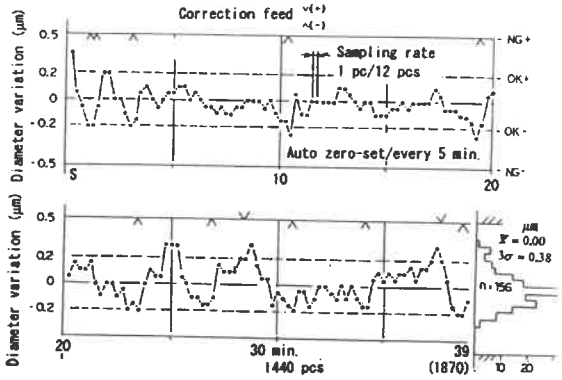

Fig. 12 Variation of workpiece diameter ground with centerless grinding machine with size error compensation

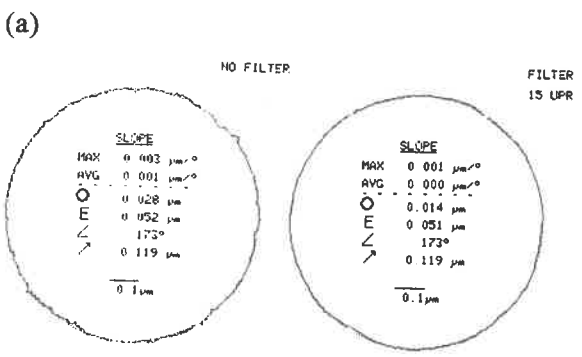

Fig. 13 Roundness error of workpiece ground with centerless grinding machine with size error compensation

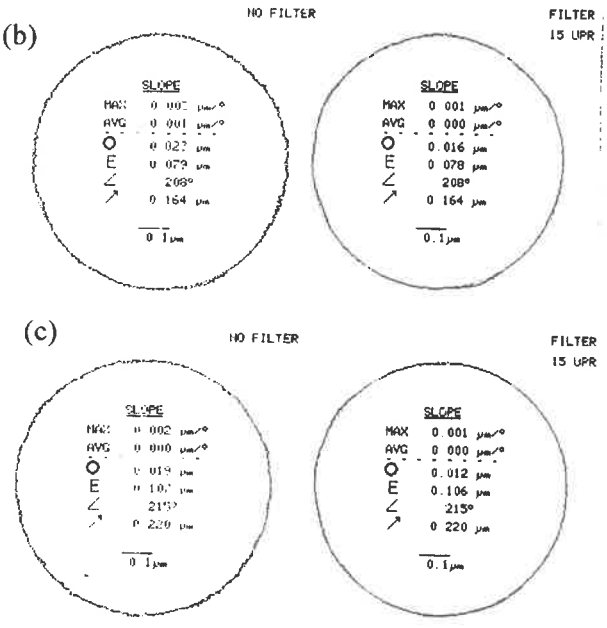

Precision Grinding of Ceramic Diesel Engine Components

Albert J. Shih, Darryl J. Gust, and Marion B. Grant
Cummins Engine Company, Inc.
Columbus, Indiana 47201

Abstract

The successful introduction of a ceramic plunger in the fuel system of Cummins' heavy-duty diesel engines is recognized as the first application of a sub-micron precision ground ceramic component in high-volume production. Process development was accomplished by using simulation on scaled-down thru-feed centerless grinding equipment and by using a systems approach to determine key variables for a production diamond grinding system. Various other applications for ceramics in diesel engines are also discussed. The customers for diesel engines request a very reliable product to minimize down time. They are willing to pay higher price for a reliable product. The overall cost, including the savings gained by a more reliable engine with ceramic plunger, actually promotes the implementation of ceramics.

Introduction

In the late 70s and early 80s, several ceramic materials were made into internal combustion engine components to evaluate the usefulness of ceramics in these type of applications. Extensive test results have shown some ceramic components can enhance engine thermal efficiency, improve wear and durability, and reduce exhaust emissions. Since the earlier successful laboratory demonstrations, ceramics have not been widely used in today's production engines due to high material and high process costs. Mass-production is understood as an effective way for reducing material and process costs for many products. In order for ceramic material to be more competitive in the market, suitable applications have to be found in engines to increase the ceramic production and lower its cost.

In recent years, we have started to see the trend of lowering cost for both ceramic material and industrial diamond, the prime abrasive for ceramic grinding and lapping. This and the continuous improvement and innovation of new ceramic material have given a bright future for ceramic applications and the development of ceramic manufacturing technology. This paper intends to summarize the applications of ceramic material in diesel engines and to describe one successful example of the sub-micron precision grinding of ceramic plunger at the Fuel Systems Division of Cummins Engine Company.

Application of Ceramic Components in Diesel Engine

In recent years, much attention has been focused on vehicle exhaust emissions. The Clean Air Act in the U.S. and similar environmental regulations in Europe, Japan, and developing countries have given diesel engine manufacturers tremendous technical challenges and opportunities. Along with the development of engines with alternative

fuels, the most practical and environmentally least damaging system is a diesel engine optimized to offer low exhaust emissions. Unlike gasoline engines, the carbon monoxide (CO) and hydrocarbon (HC) emissions do not constitute problems in diesel engines due to the higher combustion temperature in the direct fuel injection engines. The challenges in the diesel engine emissions are the nitrogen oxide (NOx) and particulate emissions. The following figures illustrate the past, present, and future of on-highway diesel engine emission standards in U.S., Europe, and Japan.

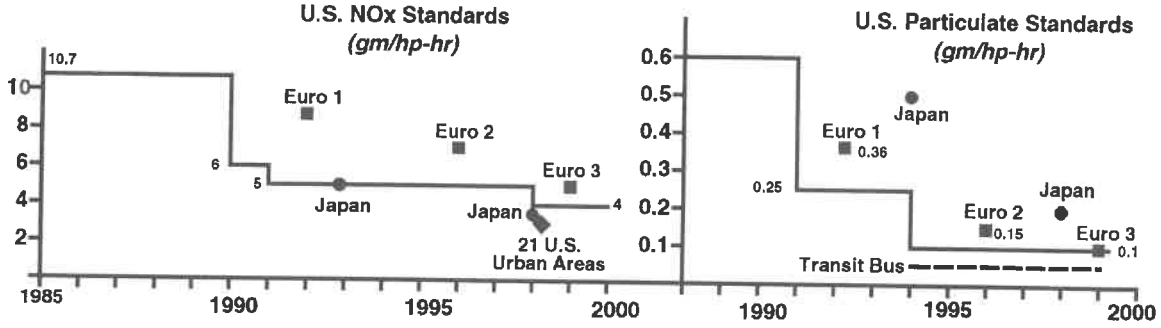

The development of low-emission diesel engines relies on:

1. *Clean Diesel Fuel*: The sulfur and aromatics contents in the diesel fuel have been reduced from 0.2% to 0.001% and 30% to 5%, respectively, in recent years. Clean diesel fuels have helped to reduce exhaust emissions. The reduction in sulfur content has lowered the lubricity of diesel fuel and created seizure problems in the tightly matched fuel system metal components.
2. *Electronic Controlled Fuel Injection*: The electronically controlled fuel systems are able to deliver the correct amount of fuel into the combustion chamber at the exact timing based on feedback signals from sensors mounted in the engine.
3. *High Injection Pressure*: The diesel fuel is injected into the combustion chamber by an injector, atomized into small particles, and then started the combustion process. Higher injection pressures can improve the atomization of fuel and results in smaller fuel droplets which are easier to incinerate. Fuel injection pressure has increased from 10 kpsi in the 70s, to 20 kpsi in the 80s, and the design in the 90s is over 30 kpsi.

Ceramic components play a critical role in all three development areas. Ceramics have definite advantages of low friction, low density, and good wear resistance over steels. All these have made ceramic plungers especially suitable for different diesel fuels, either the clean, low-lubricity diesel fuel or the contaminated fuel with derbies and/or additives. Field test results have shown ceramic plungers can function under harsh conditions and still maintain closely matched clearance in electronic controlled injectors and pumps to generate high injection pressure.

Besides the ceramic plungers for diesel fuel systems, ceramic material can also be found in some production diesel engines for durability and performance improvement. These include:

- Ceramic valve for high temperature strength and better engine performance
- Ceramic cam roller for high stiffness, good wear resistance, and low friction
- Ceramic check ball for lower inertia, better response, and less beat-in
- Ceramic turbocharger rotor for light weight and low friction
- Ceramic push link in injector-rocker chain for wear resistance

Prior to introduce these ceramic components in the production engine, a thorough cost analysis has to be done for each and every application to justify the financial benefits. Cost effective is also the key for other ceramic applications in the future. Our experience has shown the cost calculation for ceramic application has to be done in a broad sense. If we only compare the cost of a ceramic component against similar steel part, the ceramic component will very likely be more expensive. The benefits gained from improvements in engine durability and reliability must be considered in the overall cost.

Development of Grinding Process for Ceramic Plungers

The development of new diesel fuel systems has resulted in a trend of tightening tolerance specifications in the past and foreseeable future for engine components. Achieving a cost effective, statistically capable sub-micron precision grinding operation in the production shop floor environment presents significant technical challenges. In the Spring of 1995, Cummins implemented a ceramic plunger for injector timing control in heavy-duty diesel engines. It is recognized as the first high-volume application of sub-micron precision ground ceramic component in the automotive industry. Two key factors in the success of this project were: (1) Team work with suppliers and (2) System approach for process development and production implementation.

Cummins Fuel System has developed a sound supplier base for production support, which treats suppliers as partners and maintains an excellent working relationship with them. Suppliers are expected to be experts in their respective technical fields. Not all of the suppliers on this project had experience in superabrasive grinding, even fewer suppliers had worked with the ceramic material before. The team included the following suppliers: ceramic material, machine tool, grinding wheel, rotary dressing device, in-process sizing gage, acoustic sensor, coolant, coolant filtration, and material handling. This team approach from concept thru to production, insured the success of the Cummins project.

A system approach (Subramanian and Lindsay, 1992) was used for the development of a production grinding process for the ceramic plunger. The successful application of diamond grinding wheel required careful attention to all aspects of this "grinding system" -- an approach that addresses four key inputs to the grinding process: machine tool, wheel selection, work material properties, and operational factors. Test grinding of Magnesium Oxide Transform Toughen Zirconia ceramic plunger using vitrified bond diamond grinding wheels on modified thru-feed centerless grinding equipment was first conducted (Gust, *et al.*, 1996) to identify the variables influencing the diamond grinding system. These variables were used to design and build the

production grinding system, and were further validated in the high-volume production at the shop floor. The study also showed that thru-feed centerless grinding of ceramics, an expensive production process using a large diamond grinding wheels and high cost machine tools, can be successfully simulated on a scaled-down configuration prior to full size production. The production process further demonstrated the capability of vitrified bond micro-grit diamond grinding wheels to achieving a surface finish of 50 to 100 nm Ra range, which previously could only be done by resin bond diamond wheels. During the test, a notable difference in grindability for different ceramic vendors providing the same type of Zirconia ceramic component was seen.

Concluding Remarks

In this paper, the rationale for application of various ceramic components in diesel engine and the importance of application of ceramics in automotive industry were presented. An example of the precision grinding of ceramic plunger in high-volume production, recognized as the first application of sub-micron engineering ceramics in automotive industry, was introduced. A system approach was implemented for the process development and production implementation.

In recent years, ceramic components have gradually been applied in diesel engines. Cost continues to be an decisive factor in the future application of ceramics. Due to the lack of near-net shape capability for ceramic blanks, the cost of prototyping ceramic components for early development will be considerably high. Diamond grinding wheels, as the most efficient means of ceramic machining, will be a significant initial cost barrier. Cost effective manufacturing of ceramics will continue to be the number one hurdle needing to be overcome.

The overall cost, including the savings gained by a more reliable product with ceramic component, has to be used to justify the application of ceramics. The customers for diesel engines request a very reliable product. They are willing to pay higher price for a reliable engine, an engine with ceramic components. This cost premium can be easily justified with less down time of the truck or equipment. In the end, the cost actually promotes the implementation of ceramics. This is one of the reasons why application of ceramics in diesel engine is leading the automotive industry.

References

Gust, D. J., Shih, A. J., Tricard, M., and Subramanian, K., (1996) "An Approach for Thru-Feed Grinding of Ceramic," *Symposium on Advanced Machining and Finishing Processes for Ceramics, Composites, and High Temperature Alloys*, ASME World Congress & Expo., Atlanta, Georgia.

Subramanian, K., and Lindsay, R. P., (1992), "A Systems Approach for the Use of Vitrified Bonded Superabrasive Wheels for Precision Production Grinding," ASME Transactions, Journal of Engineering for Industry, Vol. 114, pp. 41-52.

AN INVESTIGATION INTO HIGH STIFFNESS ADJUSTABLE NATURAL FREQUENCY HYDROSTATIC SLIDE UNITS

Drew Devitt
New Way Machine Components, Inc.
Aston, PA

Eric Marsh
The Pennsylvania State University
University Park, PA

Grinding process optimization traditionally entails adjustments of grinding wheel-type and speed, depth of cut, coolant, etc. to achieve the highest productivity. A limiting factor has been machine dynamics because it is not readily adjustable. This research attempted to demonstrate that machine dynamic characteristics can be adjusted by varying the stiffness of hydrostatic slide units. This would be significant because through an intelligent adjustment at setup or through an active feedback system, the structural dynamics could be optimized creating the proverbial chatterless grinder or at least increase machine productivity and capability.

This research was suggested by the experience of some machine tool builders and users. This experience indicates that intentionally using weaker components in the structural loop can reduce chatter in some applications. Apparently the correct stiffness for dynamic purposes can be better for process optimization than maximum stiffness. This adjustability in stiffness by simply varying oil input pressure would make for a convenient mechanism for tuning the natural frequency of a machine.

THE SLIDE UNIT

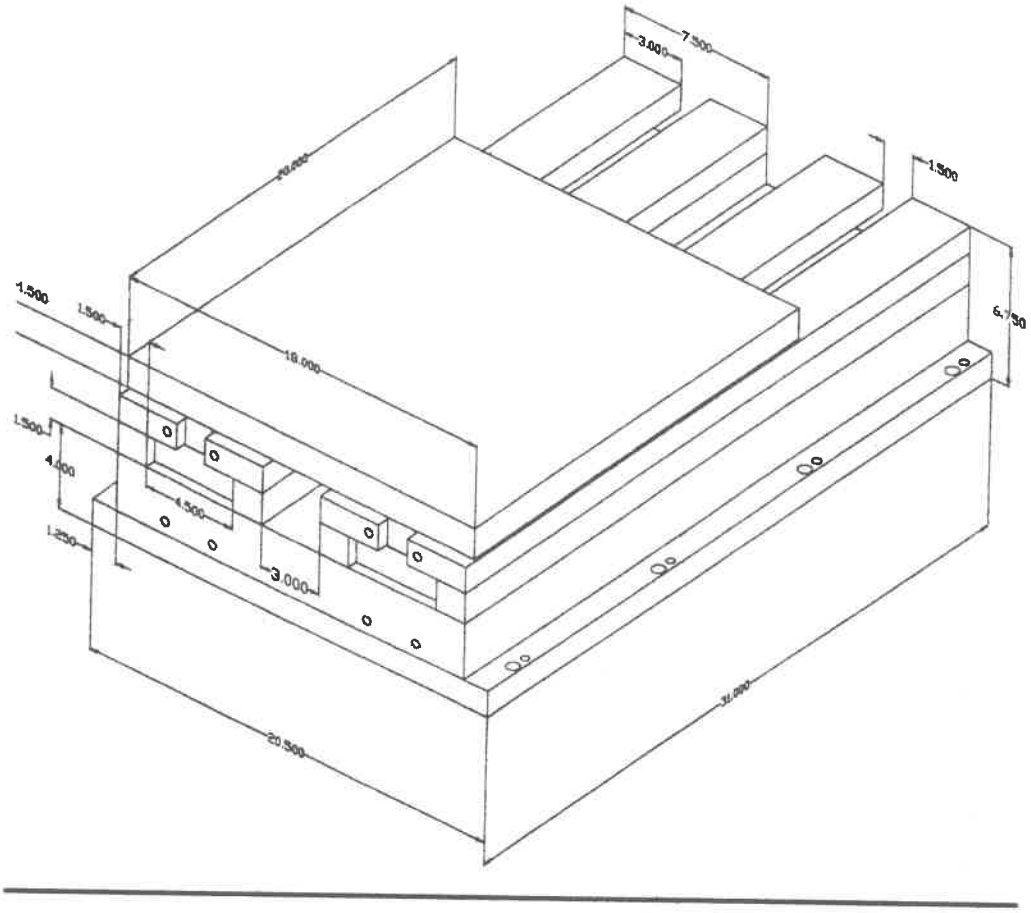

Illustration 1

The slide unit employs a self-compensating system consistant with Prof. Slocum's gap compensation technology which has been described in the Fall '95 issue of the ASPE Quarterly Journal. This slide unit differs from previous slides in that the guide ways wrap around the bearing elements rather than the bearing elements wrapping around a guide way. Notice that in illustration 1, the profile of the guide is similar to an inverted "T" slot. One bearing block runs in the bottom of each "T" slot. Each bearing block has 12 individual hydrostatic pockets, 12 compensators and all the necessary internal porting so that only one supply line runs to each block. No restrictors are used. The slide is over constrained in that both bearing blocks give vertical and horizontal guidance.

STATIC STIFFNESS

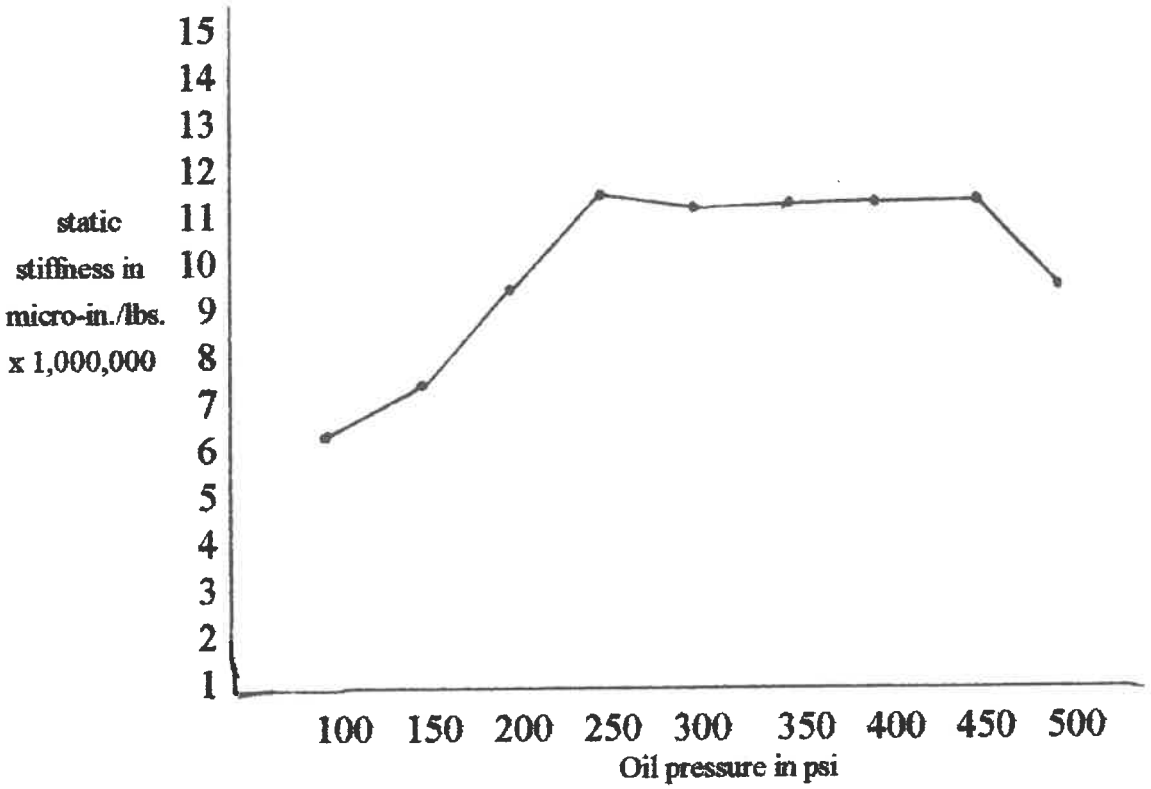

Illustration 2

Because of the relatively high stiffness capable of this system, we were able to vary the static stiffness significantly through a broad working range (see illustration 2). This stiffness data is the average of three trials measured in three locations using Lion capacitance probes and a change in load of 200 lbs. We believe this graph flattens out and even drops off because of deflection of the base retaining way. At 500 psi this deflection was in excess of 50% of the original hydrostatic gap and could explain the drop in stiffness. The original hydrostatic gaps were .0005" - .0007" on all sides. An ISO 10 oil was used as a hydrostatic fluid. The fluid temperature stabilized at 80° F after running for 2 hours at 300 psi. Significantly higher stiffness was found using ISO 25 oil.

DYNAMIC COMPLIANCE

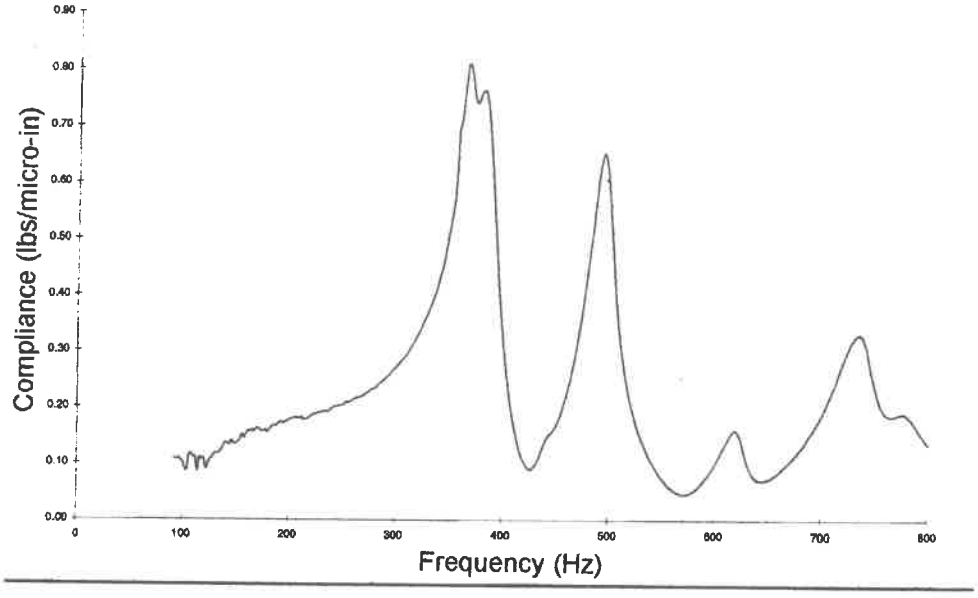

Illustration 3

Unfortunately we found that we could make no significant changes to the Compliance Chart (illustration 3) by adjusting supply pressure. In retrospect it seems obvious that the top plate itself would be the major source of compliance. In fact, there was so much compliance in the top plate (illustration 4) that little could be learned about the actual oil film dynamics. We are presently producing a much stiffer top plate in an effort to simulate more closely actual conditions when large castings are likely to be bolted to the plate. Hopefully under these conditions we will be able to detect differences caused by stiffness variances in the oil bearing. The chart is impressive though in that even at resonance, the dynamic stiffness is better than 1,000,000 lbs/micro-in.

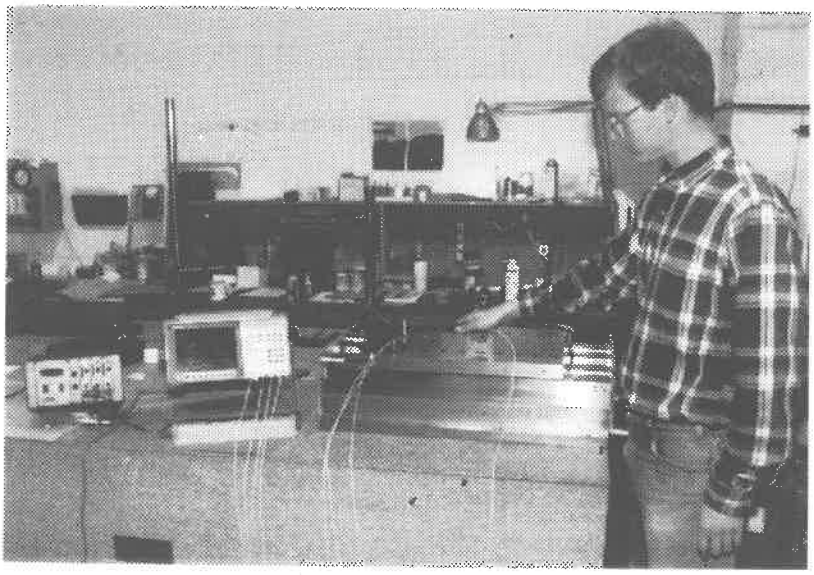

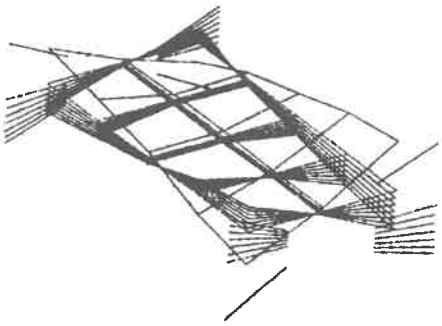

Illustration 4

The Role of Loop Stiffness on Grinding

Eric R. Marsh, David S. Yantek
The Pennsylvania State University
University Park, PA 16802

This paper seeks to address aspects of machine performance and structural design that can be used to meet the challenge of today's increasingly difficult grinding materials. The paper briefly reviews the interpretation of frequency response functions - a powerful tool for characterizing the dynamic performance of a grinding machine. Then, frequency response functions for two grinding machines are presented, with a discussion of how the design features of each structure manifest themselves in the dynamic performance. These results indicate the importance of grinding machine design.

Review of Frequency Response Functions - Single Degree of Freedom

A single degree of freedom system idealizes a single mode of vibration. Machine components with high aspect ratios such as boring bars or CMM rams have compliance that may be readily modeled with a single degree of freedom. The behavior of more complicated (linear) structures can be treated as the superposition of many SDOF systems. For these reasons, a study of single degree of freedom system dynamics is important. The traditional SDOF model includes a mass, spring, and dashpot as shown in Figure 1.

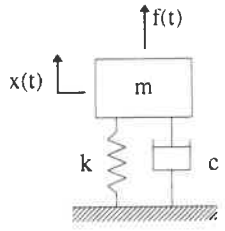

Figure 1 Single degree of freedom mass-spring-dashpot model.

The equation of motion of this SDOF system may be obtained by a force balance acting on the mass. The spring force and the damping force oppose the applied force $f(t)$ to yield the classic equation of motion.

$$m\ddot{x} + c\dot{x} + kx = f(t) \tag{1}$$

The free vibration response of this system may be obtained by setting the excitation force equal to zero and determining the response of the mass to initial conditions on x and $\dot{x}$. Although the solution is dependent on the mass, spring rate, and damping constant, we usually substitute in two new parameters, the damping factor ζ and the undamped natural frequency ω_n. The quality factor Q is another traditional measure of the damping in a SDOF system and relates to the damping factor as shown.

$$x(t) = e^{-\frac{c}{2m}t}\left(A\sin\sqrt{\frac{c^2}{m^2}-\frac{4k}{m}}t + B\cos\sqrt{\frac{c^2}{m^2}-\frac{4k}{m}}t\right) = e^{-\zeta\omega_n t}\left(A\sin\omega_d t + B\cos\omega_d t\right) \tag{2}$$

where:

$$\zeta = \text{damping factor} = \frac{c}{2\sqrt{km}} \approx \frac{1}{2Q}$$

$$\omega_n = \text{natural frequency} = \sqrt{\frac{k}{m}}$$

$$\omega_d = \text{damped natural frequency} = \omega_n\sqrt{1-\zeta^2} \approx \omega_n \text{ (for lightly damped systems)}$$

The smaller the damping factor ζ, the longer the settling time. Figure 2 shows a typical under-damped response of the single degree of freedom system. Virtually all mechanical systems exhibit damping factors much less than 1, resulting in the sinusoidal decay shown in the figure. A typical welded structure may have damping factors as low as $\zeta = 0.005$. A bolted structure may have damping factors closer to $\zeta = 0.01$ to 0.05.

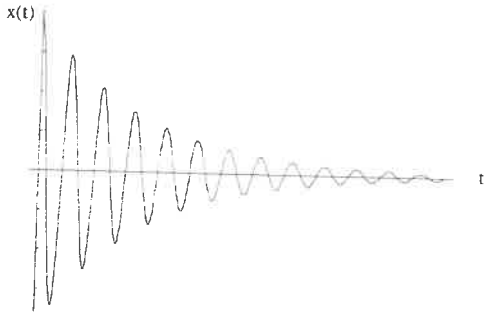

Figure 2 Free vibration response of a single degree of freedom system.

The vibration response of the system, when driven by a sinusoidal forcing function of amplitude F can also be determined for the SDOF system. The resulting vibratory motion will also be a sinusoid, but there will generally be a phase difference between the applied force and the response. The sinusoidal response is traditionally normalized by the excitation force, and contains an amplitude and phase dependent on m, c, k, and the driving frequency ω. This normalized response has units of displacement per unit force and is commonly referred to as dynamic compliance.

$$\frac{x}{F} = H(r)\sin(\omega t + \varphi(r)) \tag{3}$$

where:

$$H(r) = \frac{1}{k\sqrt{(1-r^2)^2 + (2\zeta r)^2}} \quad \text{magnitude of dynamic compliance}$$

$$\varphi(r) = \arctan\frac{2\zeta r}{1-r^2} \quad \text{phase of dynamic compliance}$$

$$r = \omega/\omega_n$$

The magnitude of the response, $H(r)$, can be broken down into three regimes. The first is the stiffness controlled region. When r is low, in other words when the driving frequency is much lower than the natural frequency of the oscillator, the vibration amplitude is controlled by the stiffness k. Similarly when r is high, the response amplitude is controlled by the amount of mass m in the system. At resonance, the response is controlled by the amount of damping c in the structure. Figure 3 shows $H(r)$ and the three regions.

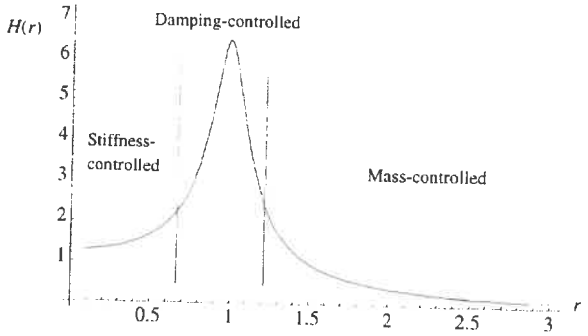

Figure 3 Frequency response function $H(r)$ of a SDOF system. The low frequency response is controlled by stiffness, the high frequency by mass, and the response at resonance is controlled by damping.

Design for Dynamic Response of a Second Order System

Examination of the single degree of freedom system response offers valuable insight into the dynamic behavior of mechanical systems. An understanding of the behavior is crucial because the trends observed in changing the mass, stiffness, and damping of a second order system are valid for more complex structures. Plots of the frequency response function will be presented as the system parameters are varied to provide insight into their effects on the system.

Effects of Changing Stiffness on the System

Figure 4 shows the trends in single degree of freedom system response as the stiffness is increased. Raising the stiffness increases the natural frequency and reduces vibration displacements for a given force input. The figure shows dramatic differences in the three curves below the resonant peaks. The behavior at high frequencies shows little change because high frequency behavior is dictated by the mass, not the stiffness of the system.

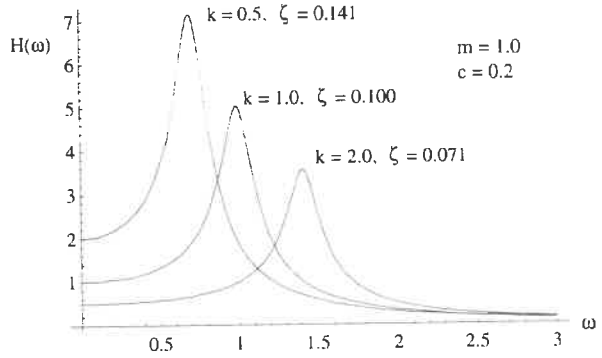

Figure 4 SDOF response as a function of frequency and stiffness.

Figure 4 suggests that raising the stiffness of a system is desirable, but acoustical noise and vibration may be worsened by adding stiffness without adding damping (because increasing the stiffness tends to reduce the damping factor). Acoustical radiation can therefore become significant in the panels that enclose a machine. In general, machine tool bases are built as stiffly as possible, whereas non-structural components likely to radiate noise can intentionally be made less stiff (e.g., thin covers and panels).

Effects of Changing Damping on the System

Increasing the system damping makes a dramatic improvement in the system response near its natural frequency (the damping controlled region). Figure 5 shows how increasing the damping lowers the amplification at resonance of the system. Although a damping factor of 0.2 is difficult to obtain in practice, the plot shows the dramatic improvement available by doubling the damping.

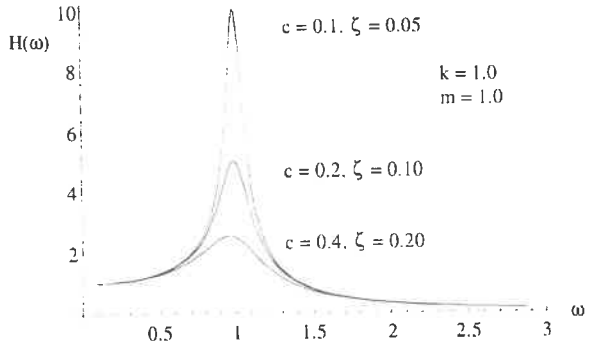

Figure 5 Second order response as a function of frequency and damping.

As mentioned before, the damping factors in typical machine tool structures are typically between 0.01 and 0.05. A damping factor of 0.10 would be considered excellent.

Effects of Changing Mass on the System

Intuitively, decreasing the mass of the system will enhance the ability of the system to respond quickly to command signals. The tradeoff is that the system will lose the ability to attenuate high frequency noise and vibration. This trend is shown in Figure 6.

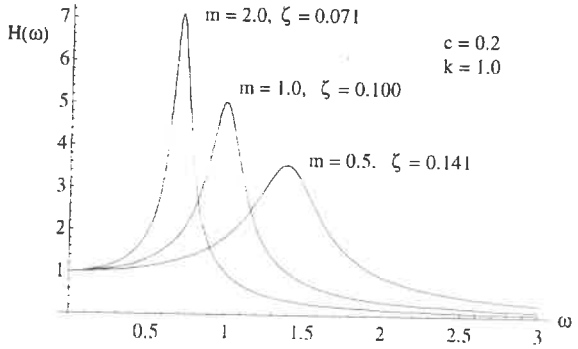

Figure 6 Second order response as a function of frequency and mass.

As shown in the figure, the system with less mass offers a higher natural frequency and damping factor. This means that higher frequency controller signals can be used without increasing the power requirements of the actuators. However, the low mass system has the greatest amplitude at frequencies above the peak frequency (the mass controlled region). As a result, the system attenuates less high frequency noise and vibration. In machine design, high frequency vibration attenuation may be a negotiable design feature, but sound quality of the design is often governed by the same high frequency modes.

In summary, the stiffness of most structures should be maximized and the mass should be minimized in components requiring substantial controller effort. Elsewhere, mass may be desirable to attenuate noise and vibration.. Damping must be present to attenuate vibration and compensate for high machine stiffness. Intuitively, the importance of high damping is reasonable and its importance can be seen in machine components predisposed to vibration or chatter.

Review of Frequency Response Functions - Multiple Degree of Freedom

Like the single degree of freedom representation, a multiple degree of freedom system is used as a mathematical idealization of a complex system. The techniques used to analyze a single degree of freedom system can still be used in the MDOF case; however, the scalar masses, damping values, and stiffnesses in the equation of motion become matrices. A sample MDOF system is shown in Figure 7. The frequency response of this system is shown in Figure 8, along with an illustration of how the individual modes are superimposed to create the total frequency response.

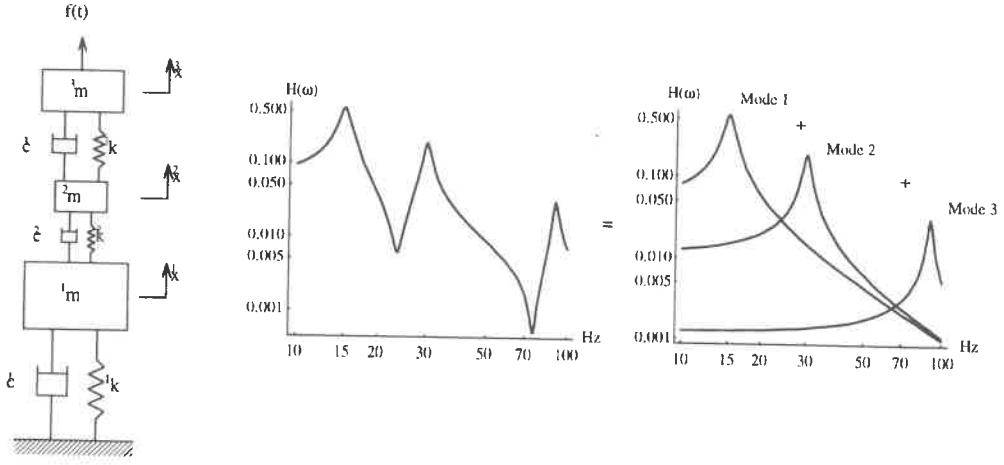

Figure 7 A three degree of freedom system and its dynamic compliance as a superposition of three vibration modes.

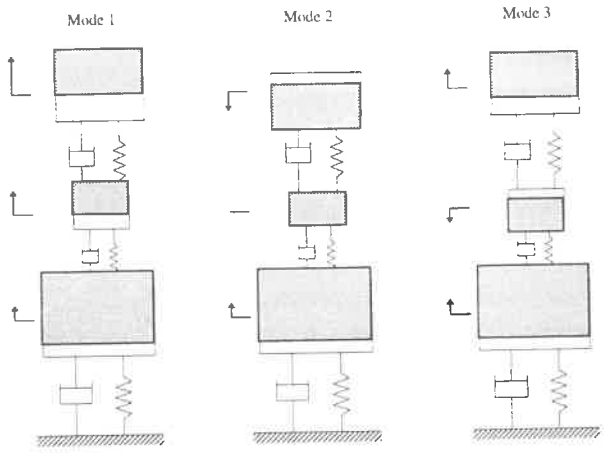

Figure 8 Mode shapes of the three degree of freedom system.

Dynamic Compliance of Two Centerless Grinding Machines

The dynamic compliance of a machine tool can be measured using modern vibrations testing equipment. Measurement of the input and output to a machine tool structure with an instrumented hammer and an accelerometer allows the calculation of the compliance plots introduced above. Then, the peaks in compliance can be understood by performing a modal analysis on the structure.

The resulting compliance plots are extremely useful in characterizing the dynamic performance of the machine. An experimental modal analysis will correlate the peaks in the compliance plots (which correspond to structural resonances) to the motion of various components in the structure. Figure 9 shows the loop compliance measurement of two different centerless grinding machines. These grinders both show several peaks in the compliance plots that correspond to relative motion between the grinding wheel and the regulator wheel. If any of these modes are excited during operation of the grinder, the workpieces may suffer inaccuracies.

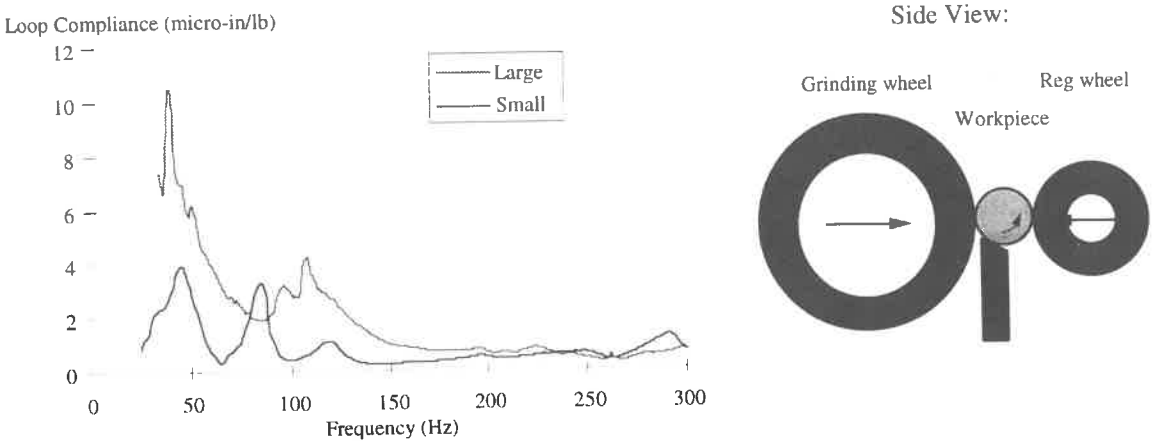

Figure 9 Loop compliances from two centerless grinding machines.

Figure 10 shows the deflection pattern in the small centerless grinding machine. The view is taken from the left side of the machine. The components to the left house the grinding wheel and the right hand side components contain the regulator wheel. The pictured mode shape captures a single instant of the oscillatory path of the two out of phase components.

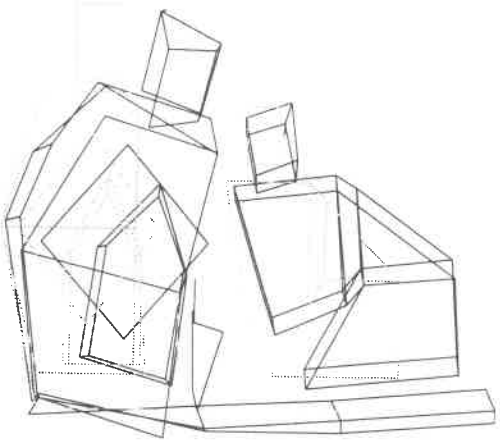

Figure 10 Centerless grinding machine vibration leading to poorly shaped parts.

As seen in the plot, the tendency of the machine to vibrate in this preferred pattern can lead to workpieces with surface profile errors.

Conclusion

This paper seeks to re-introduce the use of machine tool loop stiffness (or compliance) plots in the trouble shooting of precision machine designs. Any machine tool has countless structural modes of vibration, some of which involve compliance in the structural loop between the workpiece and tool. Excitation of these modes can occur during the cutting process, resulting in workpiece inaccuracies.

Use of loop stiffness measurements and experimental modal analysis is a convenient way of visualizing the structural performance of a machine tool design. The results can be used to identify weak points in the structural design and identify sources of excitation that should be eliminated.

NORMAL FORCE SENSORS INCREASE INTERNAL GRINDING PRECISION

Robert S. Hahn, Pres.
HAHN ENGINEERING INC.
Auburn, MA.

INTRODUCTION

Computer controls with open architecture, coupled with sensors embedded in the grinding machine provide the means to improve output quality, reduce cycle time and grinding costs.

Modern grinding machines can position slides to microinch accuracies but fail to produce workpiece accuracies of the same order. Internal grinding machines contain a series of compliances consisting of ball screws, thrust bearings, wheelhead spindles, wheel-supporting quills or arbors, the workpiece and its supporting structure, and the grinding wheel itself. The sum of those compliances produce the system stiffness. As the wheel engages the workpiece, grinding force develops at the wheel-work interface. The normal component of that force deflects the system and causes an error between the actual slide position and the position of the cutting surface of the grinding wheel. Even after a "sparkout" (feed is stopped) the force decays, not to zero, but to a finite value called the threshold force. Size errors frequently result from variations in deflection of the grinding system at the size out point.

Production-type internal grinding machines use the dressing tool as a reference for automatically sizing the workpiece, the dressing tool being located at a fixed distance from the workpiece centerline. When the wheel is dressed, the controller captures and saves the cross-slide position. The slide position at "size" is referenced to the dress position, so that, for any wheel diameter, the controller must feed the slide by the referenced amount to achieve "size". That procedure assumes there will be negligible wheelwear during the grinding operation. Variations in wheelwear will cause size errors. A system for compensating for wheelwear as well as deflection errors is described below.

Production grinding cycles are expected to hold close size and surface finish tolerances regardless of variations in incoming stock, workpiece metallurgy, wheel sharpness, and changes in wheel size, and, moreover, to do so in the least possible time.

DEFLECTION-COMPENSATED SIZING

In order to eliminate size errors caused by force variations, normal force sensors have been added to a Service Network Inc.(SNI) (Auburn, MA.) machine grinding a bore 2.636 in. x 1.25 in. long and interfaced to an HEI PC control (See Table 1). The control can

TABLE 1
Typical grinding conditions

MATERIAL	AISI 4340 60-62 Rockwell
BORE:	2.636 in. x 1.25 in long
STOCK:	0.024 in on diameter
WHEEL:	2.25 in. x 1 in.wide x 1 in bore
	32A80 JVBE
WHEELSPEED:	12000 RPM
WORKSPEED:	435 RPM
COOLANT:	CIMPERIAL 20 5% sol.

BIBLIOGAPHY

1. Allenson D.R.,Kelly S.,Terry S.,Moruzzi J.L.,Rowe W.B., "Coping with Compliance in the Control of Grinding Processes", Annals of the CIRP vol 38/1/1989

2. Kaliszer H., "Adaptive Control in Grinding Processes", Proc. International Conference on Production Engineering, Tokyo 1980

3. Toenshoff H.K.,Zinngrebe M., Kemmerling M., "Optimization of Internal Grinding by Micro-Computer-Based Force Control", Annals of the CIRP, vol 35/1 1986

4. Tlusty J.,Andrews G.C., "A Critical Review of Sensors for Unmanned Machining", Annals of the CIRP, vol 32/2/1983

5. Hahn R.S., "Improving Grinding Performance with Force-Adaptive Monitoring of Wheel Sharpness/Workpiece Metallurgy Variations", SME Paper MR88-612

6. Vaillette B.D., "CBN - Adaptive Grinding", SME Paper MR91-160

7. Smith R., "Energy-Adaptive Grinding", Abrasive Engineering Society Magazine, Jan-Feb 1981

8. Lindsay R.P., "On the Metal Removal and Wheel Removal Parameters, Surface Finish, Geometry, and Thermal Damage in Precision Grinding", PhD Thesis, Worcester Polytechnic Inst. 1971.

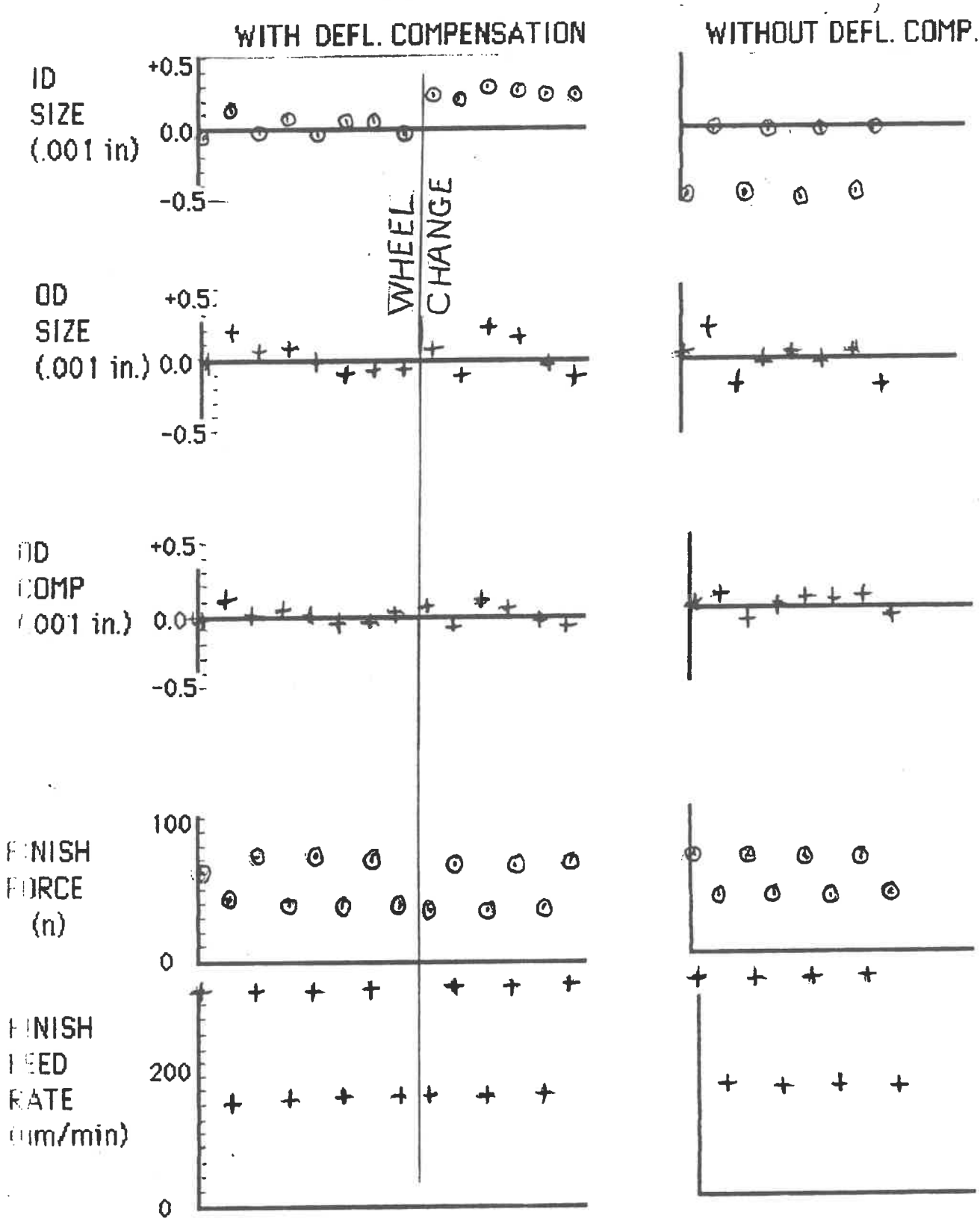

Figure 4 Bore Grinds showing ID size plot with and without deflection-compensated sizing for alternating finish feedrates of 300 and 150 um/min.
System stiffness= 4200 n/mm (24027 lb/in)

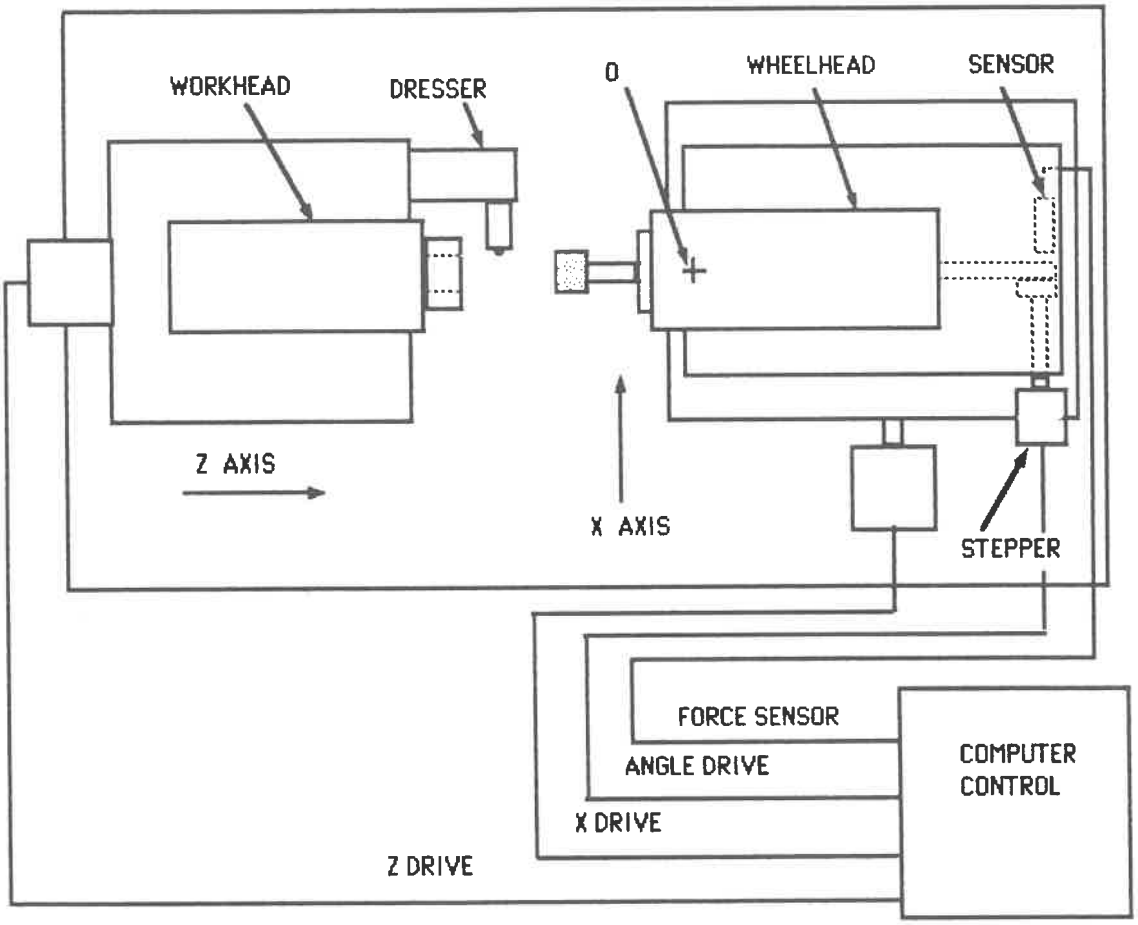
WORKHEAD
DRESSER
0
WHEELHEAD
SENSOR
Z AXIS
X AXIS
STEPPER
FORCE SENSOR
ANGLE DRIVE
X DRIVE
Z DRIVE
COMPUTER
CONTROL

FIGURE 2

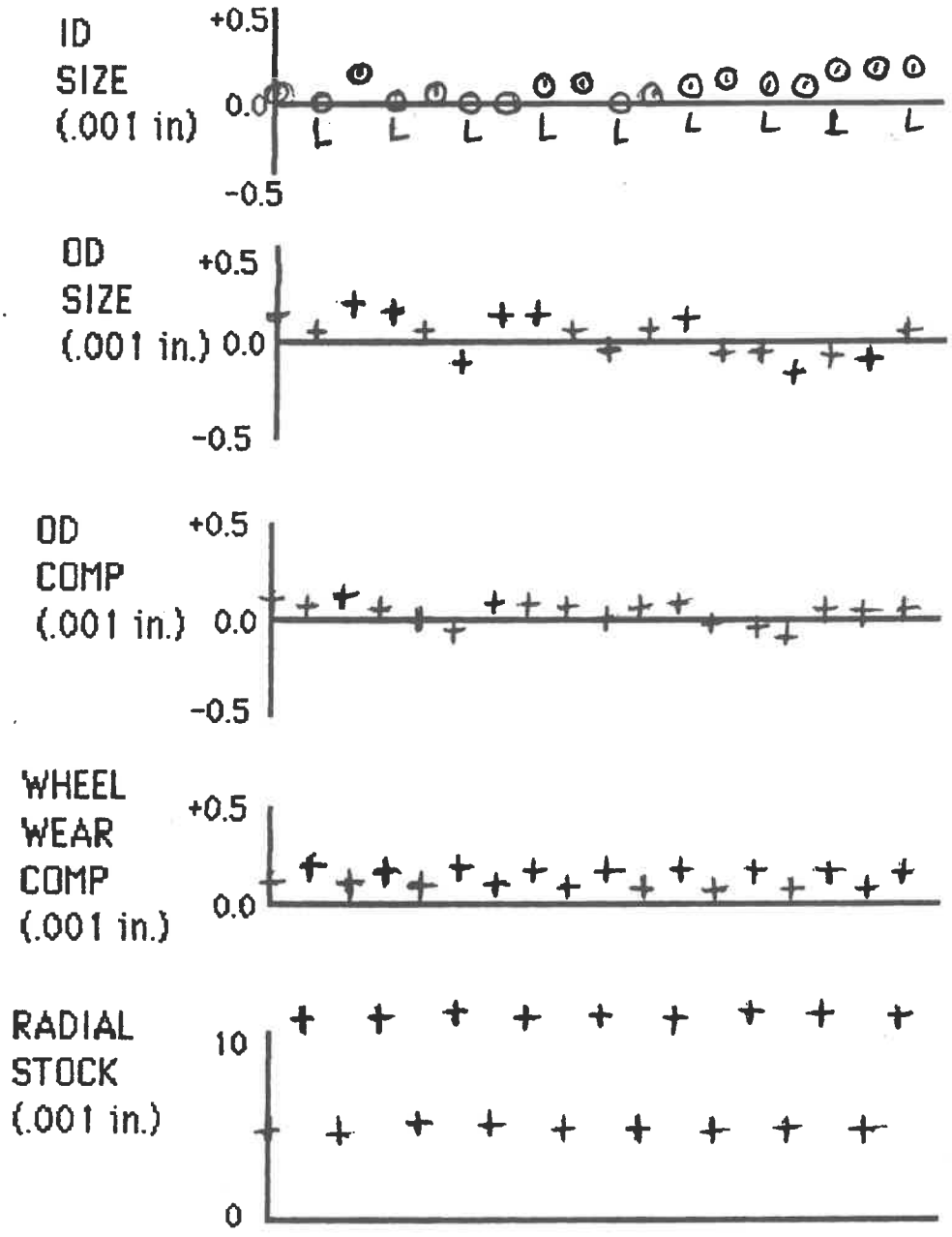

Figure 3 Bore grinds showing ID size plot for dress-at-load cycle with alternating incoming stock, no sparkout "new" and "used" wheelwear velocities .45 and .27 um/sec
Points marked "L" correspond to large stock.
Second trace: OD size error.
Third trace: Computer-generated OD error compensation
Fourth trace: Computer-generated wheelwear compensation
Fifth trace: Alternating incoming radial stock.

Development of Sequential Grinding-Polishing Process

Nobuo YASUNAGA, Atsushi YAMANOUCHI and Mamoru TAKASHINA
Tokai University, 1117 Kitakaname, Hiratsuka, Japan

1 Introduction

Higher flatness and smoothness will be required for higher quality next generation Si wafers with the sizes larger than 8 inchs. It will become hard to fabricate these large-size wafers with very high flatness in the currently most popular lapping and polishing process. New procedures including the ultra-fine grinding and the sequential final polishing will be necessary in the future processes.

Grinding is a typical motion-control-type machining process. In order to operate ductile-mode fine grinding of brittle materials, a grinding machine is needed which has very high stiffness and high motion accuracy with a fine depth of cut. Polishing is, on the other hand, a typical pressure-control-type process, where obtainable shape accuracy depends on the form accuracy of the polishing plate and uniformity of the contact between the workpiece and the polishing plate. Because of the difference of the fundamental motion mechanisms, separate machines must have been prepared in grinding and polishing operation, respectively.

The authors have developed a new vertical-spindle-type grinding /polishing machine with a rotary-wheel-head and a rotary-table, by which both the motion-control-type grinding and the pressure-control-type polishing can be sequentially performed using a single-spindle-head and without demounting and moving the workpiece. Experimental results have revealed that this new process is very effective for improvement of machining accuracy of the Si wafers.

2 Outline of the sequential grinding-polishing machine developed

A schematic diagram of the vertical-spindle-type grinding-polishing machine developed is shown in Fig.1. The wafer to be worked is set at the center of the rotary-table. Grinding procedure is performed by step-infeeding of a cup-wheel coupled to the spindle-head which is driven by the ball-screw and slides down along a linear ball-guide just behind the spindle-head. Polishing procedure is operated by direct pressing of the same spindle-head by air sylinder after separating the step-infeeding mechanism from the head and exchanging the grinding wheel for a polishing disk, which is also coupled to the spindle-head directly and not through a universal joint essentially used in usual polishing operation. In this machining system, grinding and polishing operations can be sequentially conducted without demounting the workpieces from the rotary-table. Fundamental specifications of this prototype machine are shown in Table I. This machine enables to conduct new types of machining processes such as

pressure-control-type grinding and motion-control-type polishing. Available process variations are shown in TableⅡ.

3 Experimental procedure

As the primary experiment, the sequential process of path ① in TableⅡ was tried, where motion-control-type grinding was first conducted and pressure-control-type polishing was then followed.

Si wafer specimen (125mmϕ, 2mm$t$) was mounted at the center of the rotary-table and a diamond cup-wheel of the outer diameter of 100mm was set so that the working surface of the wheel would pass over the rotational center of the Si wafer. The wafer was first roughly ground by a #140 diamond cup-wheel and next by a #800 diamond wheel with step-infeeding operation. Mechanical-chemical loose-abrasive polishing was then carried out after exchanging the grinding wheel for a polishing disk of the same diameter of 100mm on which a polishing pad was attached.

4 Experimental results

4.1 Step-infeed grinding with a diamond cup-wheel

Fine grinding using #800 diamond cup-wheel was carried out under the conditions of TableⅢ. Truing and dressing of the wheel was done with a #400 silicon-carbide stone-stick. Surface roughness measurement on the wafers ground at different wheel speeds (roughness meter : Kosaka Laboratory's SE-30K, max. 2×10^5) has revealed that a smoother surface was obtained when the wheel rotation speed is higher. Figure 2 shows surface roughness change

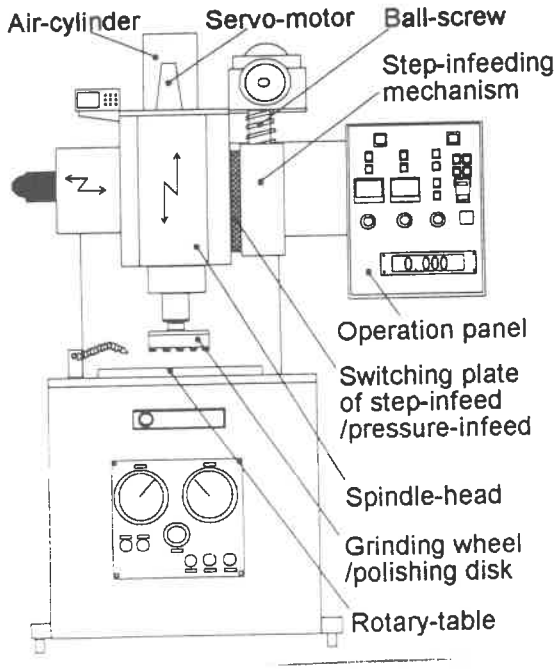

Fig.1 Schematic diagram of the prototype sequential grinding -polishing machine

TableⅠ Fundamental specifications of the developed machine

Wheel revolution Wheel speed	0～4000 rpm 0～1256 m/min
Table revolution	0～100 rpm
Loop stiffness between spindle and table	About 10 N/μm
Minimum depth of cut	1 μm
Pressure range	49～980 N

TableⅡ Process variations available in the developed machine

Control / Machining	Motion-control	Pressure-control
Grinding		② ③
Polishing	⑤ ④	①

related to spark-out times at 5 μm infeeding and indicates that the surface roughness becomes settled after spark-out once. Here " spark-out times of 0" means first one revolution of the rotary table just after a 5 μm infeeding, and "spark-out once" means next one revolution at the same vertical position of the wheel-head, namely under no further infeeding of the wheel-head. Taking these results into account, the grinding conditions in this study were fixed to the wheel speed of 1256m/min (4000rpm), the rotary-table rotation of 10 rpm, and the spark-out times of 1.

4.2 Definite-pressure polishing after step-infeed grinding

After #800 diamond cup-wheel grinding, definite-pressure polishing was carried out by exchanging the cup-wheel for a polishing disk of the same diameter. Here the polishing disk is mounted on a holder having the same structure as that for the cup-wheel and so directly coupled to the spindle head

Table Ⅲ grinding conditions

Grinding method	Step-infeed
Diamond-cup-wheel	#140, #800 Concentration 100 Vitrified bonded Breadth : 5 mm ϕ100 mm 12 segments
Grinding fluid	City-water 6 l/min
Total depth of cut	20 μm (5 μm×4)
Table revolution	10 rpm
Wheel speed	314, 1256 m/min
Number of spark-out	0~5 times

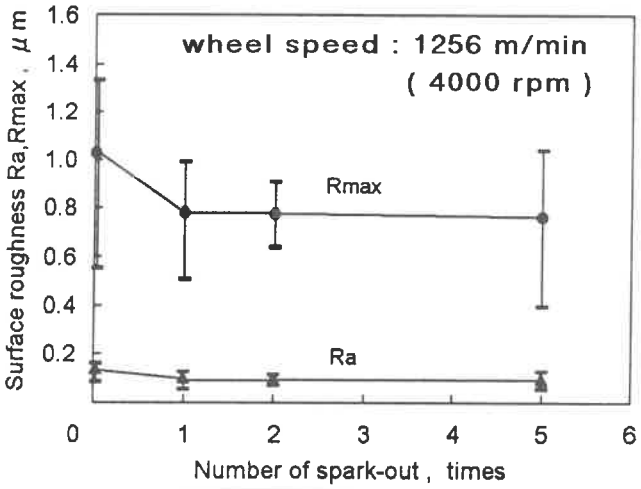

Fig.2 Surface roughness change related to spark-out times

Table Ⅳ polishing conditions

Polishing method	Pressure-infeed	
Polishing pad	Pad-A	Asker-c hardness : 95 Thickness : 0.8 mm
	Pad-B	Asker-c hardness : 80 Thickness : 1.27 mm
Polishing disk	ϕ100 mm, aluminum	
Disk revolution	1000 rpm	
Table revolution	60 rpm	
Working pressure	19.6 kPa	
Slurry	SiO_2+KOH solution (pH:10.62 at 23℃) 350 ml/min	

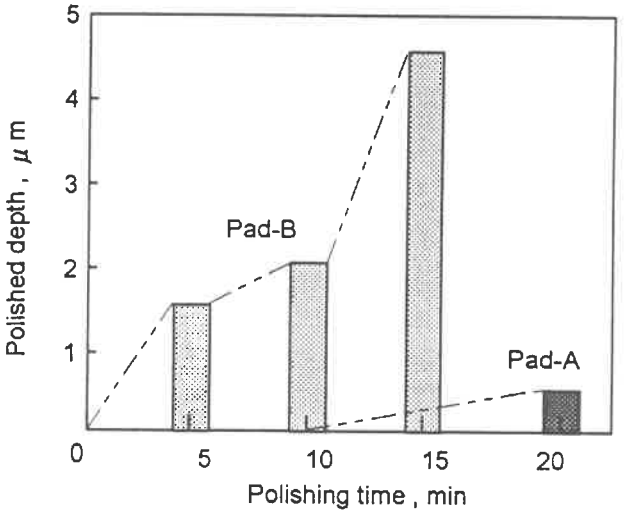

Fig.3 Polished depth related to polishing time

without any universal joint which is used in a usual polishing process. The disk surface should be first cut flat on machine to minimize it's run-out during rotation. Two different types of polishing pads were then attached on the disk surface, namely very hard and smooth-faced pad-A mainly used in CMP process for global planarization and comparatively soft and fibrous-faced pad-B suitably used for primary polishing (both made by Rodel Nitta Co.). The slurry of KOH solution mixed with ultra-fine SiO_2 powder was supplied. TableⅣ shows the specifications of the polishing disk and the polishing conditions.

Figure 3 shows a relationship between the polished depth of the wafer and polishing time. In case of polishing by pad-A, the stock removal of the wafer was no more than 0.5 μm even after 20min operation. Figure 4 shows roughness profiles of different 3 points on the surface ground by #800 wheel (upper) and sequentially 5min polished by the pad-A (lower). It is clearly seen that the top of the surface asperities is almost uniformly polished over the whole wafer surface. This indicates that uniform contact of the pad onto the ground surface could be firmly kept even at the start of polishing. This easy contact-uniformity would be derived from the use of a single tool-spindle and the same coupling mechanism of the grinding wheel with that of the polishing disk.

On the other hand, in case of polishing by pad-B relatively large stock removal of 4.5 μm depth was obtained after 15min operation as seen in Fig.3 and the surface roughness reached the values less than Ra 0.8nm. Figure 5(a) compares cross-sectional profiles through the center of the wafers measured by a straightness measuring system after grinding with #800 diamond wheel and after 15min polishing with pad-B, revealing that a surface shape nearly identical with that of the as-ground surface is kept even after 4.5 μm polishing. The

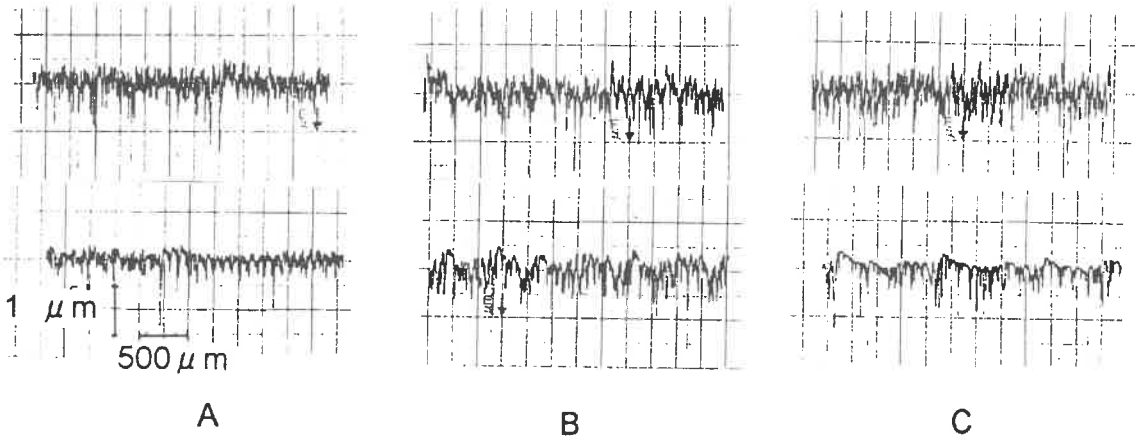

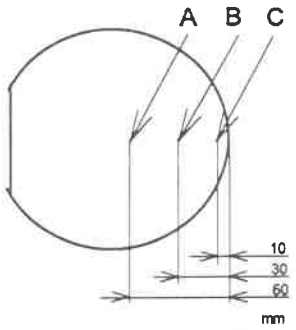

Upper profiles : after #800 grinding
Lower profiles : after subsequent 5 min polishing

Fig.4 Comparisons of surface profiles after #800 grinding and after subsequent 5min polishing by pad-A

convex shape seen in these figures would be mainly caused by tilting of the spindle axis against the rotary-table axis. Figure 5(b) shows a comparison of the surface profiles near wafer-edges measured with a surface roughness meter, observing excellent followability of the surface shapes and small round-off at the edge area less than 3mm in horizontal length and 1 μm in vertical heights. These results indicate that this sequential grinding-polishing process is much suitable and efficient for improving shape accuracy.

5 Conclusions

A new vertical-spindle-type machine has been developed, with which motion-control-type grinding and pressure-control-type polishing is sequentially carried out by easy exchange of spindle-head step-infeeding mechanism guided by a ball screw with pressure-infeeding one by an air-cylinder. Five-inch size Si wafer machining has comfirmed that

1) Sequential operation of step-infeed grinding and pressure-infeed polishing is possible without demounting the workpiece from the rotary-table.
2) Uniform contact of the polishing disk surface with the whole as-ground surface is easily realized during operation by direct coupling of the polishing disk to the spindle-head through no universal joint.
3) The surface shape formed by diamond wheel grinding can be kept unchanged over the whole wafer surface after subsequent pad-polishing.

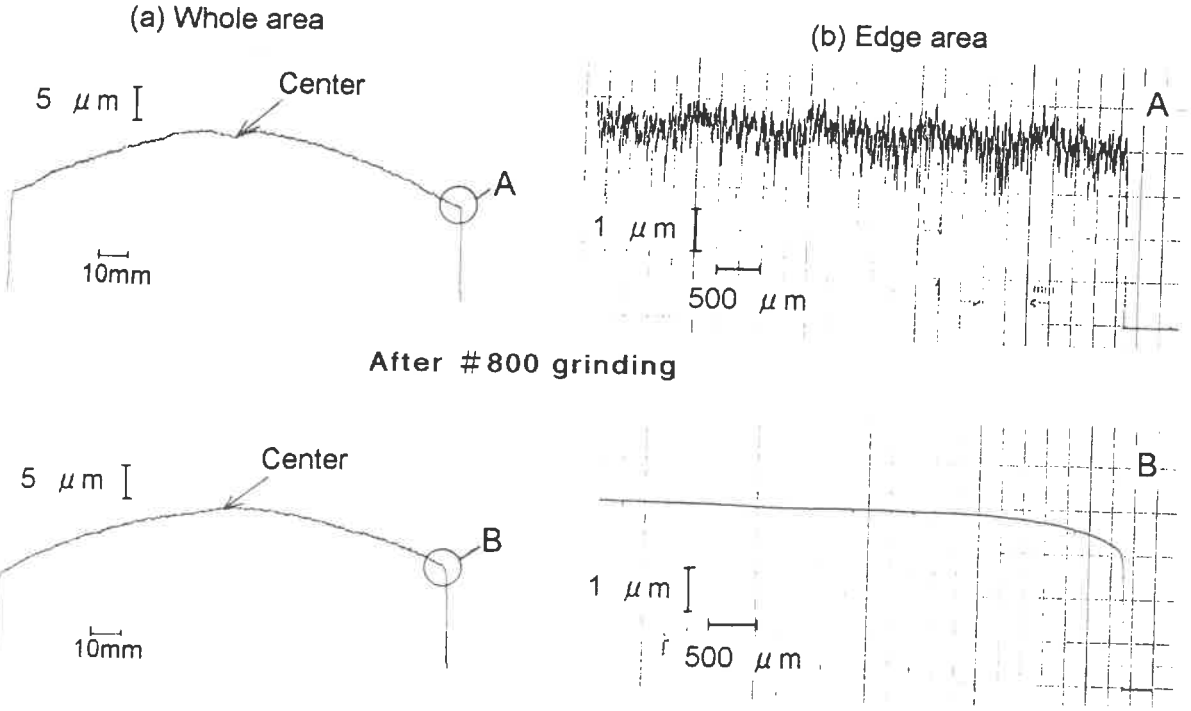

Fig.5 Comparisons of surface shapes and edge profiles

DESIGN OF A NEW GENERATION CNC GRINDING MACHINE FOR THE DETERMINISTIC MICRO GRINDING OF GLASS OPTICAL LENSES

Mark Walter
Rank Pneumo / Rank Taylor Hobson
Keene, NH

In the early 1990s, the Opticam SM lens grinding machine was designed and built by Rank Pneumo to specifications set forth by the Center for Optics Manufacturing (COM) in Rochester, NY. Rank Pneumo has since undertaken the design of a second generation, production oriented, lens grinding machine, the Microform® SM. This new machine is smaller and less expensive than the original, but grinds glass surfaces to the same specifications as the original machine.

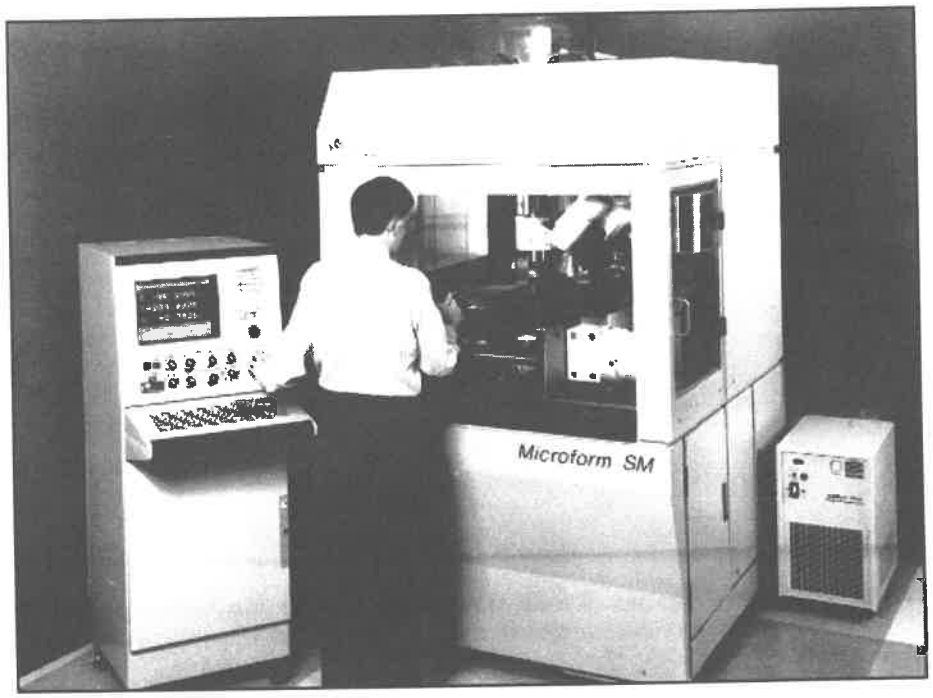

The Microform SM spherical/aspheric CNC deterministic micro grinding machine

The Microform SM machine was newly designed from the ground up and bears no resemblance to the earlier design Opticam SM machine. Its design incorporates constructive inputs from Opticam operators, customers, and technicians at the COM. The work spindle orientation was changed to be vertical, to permit easy access to view or inspect the part. The wheel spindle is then positioned above the work piece for grinding. Three CNC axes (X, Z, and B) are required to move the spindles into the correct orientation for grinding a sphere by chordal generation techniques.

Machine Configuration:

We initially looked at tilting the wheel spindle to make the machine 'look' similar to existing lens generators, and by doing so increase customer acceptance. However, this left the work spindle on the X and Z stacked axes, in a part of the machine heavily splashed by coolant. This was not an acceptable solution. To seal the CNC axes from coolant splash, we had a choice of designing all three axes in a stacked configuration, where the work spindle is mounted directly to the base, and the wheel spindle moves in X, Z, and B; or tilting the work spindle in B (which can be sealed using conventional rubber lip type seals) and stacking the wheel spindle on X and Z, outside the heavy splash zone. We chose the latter design, both for serviceability and to maximize the structural loop stiffness (from wheel to work) of the machine. This presents a different difficulty, that of feeding the wheel into the work. To feed in the direction of the depth of cut requires a coordinated motion of both X and Z along a virtual axis, that rotates with the B angle position.. This is provided by the controller and is invisible to the operator in normal usage of the machine.

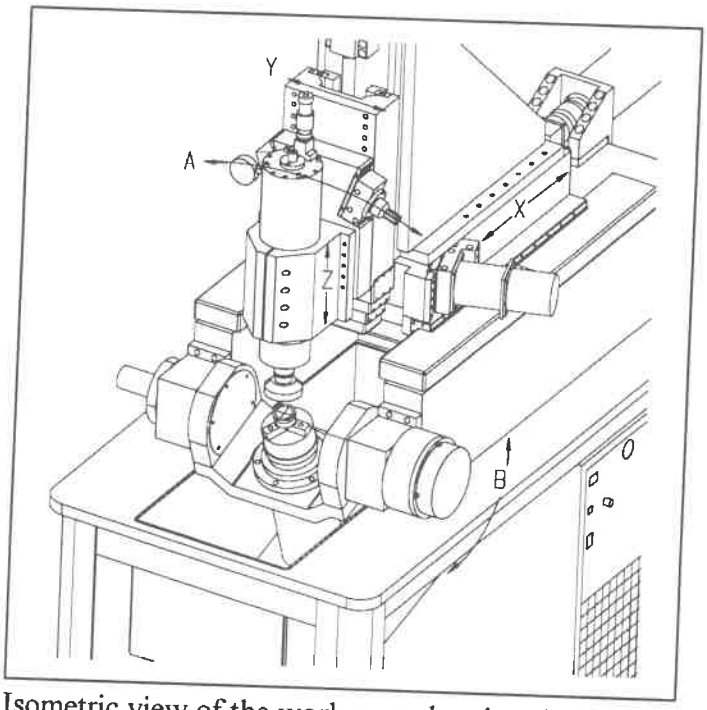

Isometric view of the work area showing the X, Z, and B CNC axes, and the Y and A manual adjustment axes.

Reduced Size:

The Microform SM only requires one half of the floor space of an Opticam SM, while retaining the same maximum work piece capacity of 150 mm diameter. It was designed deliberately and intentionally to have a small machine 'footprint'. The base for the older Opticam SM machine weighs an estimated 5000 kg (11,000 lbs) and is supported on five air isolators. The Microform SM base weighs an estimated 645 kg (1420 lbs) and is supported on passive isolators on a steel frame to raise the working height to an appropriate level. It took a concerted effort, especially in the early days of the design, to keep the machine size minimized.

Machine Alignment:

On the Opticam SM, it is difficult to align the two spindles to exactly intersect. This alignment is required to grind a true sphere. We added flexible elements to the new Microform SM machine, to allow the spindles to be moved into intersection without the added cost of a slide way. This motion is driven with a preloaded differential screw that moves the spindle .05 mm (0.002 inch) per revolution of the screw. The flexing elements were designed using Finite Element Analysis to ensure that the motion is provided without over stressing the flexures, while maintaining the desired vertical stiffness of 180 N/micron (1,000,000 lbs/inch).

The previous Opticam machine also suffered from thermal drifting problems during warm up and use. These errors were most detrimental when the drift moved the spindles out of intersecting alignment. The Microform SM has been designed with symmetry about this intersecting alignment plane to minimize the thermal drift in this direction. Temperature changes now expand or contract the machine to both the right and left. The grinding zone, which is in the middle, is left unchanged.

Another source of drift for the Opticam machine is the water cooled high speed wheel spindle. When it is turned off, the spindle chiller still operates, cooling the spindle (which it is supposed to do) but causing the wheel position to drift. However, on the Microform SM we added a coolant bypass valve to reduce the cooling rate, and drift, when the spindle is off.

Work piece and Wheel Fixturing:

The grinding wheels on the Opticam SM are mounted in a collet integral with an SK-30 taper spindle adapter. We changed the design to bolt the wheels directly to a HSK-32 taper spindle adapter. This significantly improved balance quality and increased stiffness, by having fewer joints, and avoiding the neck down to the collet holding diameter in the previous holders.

We also changed the work piece clamping mechanism to a three jaw chuck. This allows part fixtures to be easily made on a lathe. The chuck has a clamping repeatability of 0.0001 inch, to ensure surface alignment accuracy (minimum wedge) in the ground part.

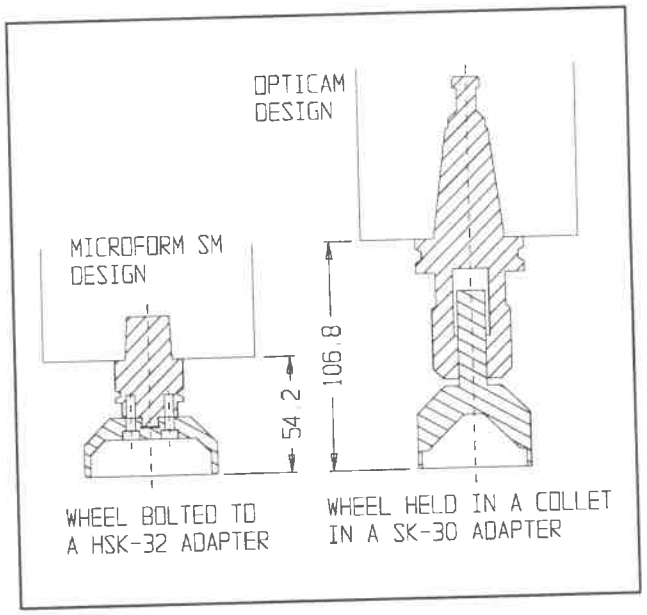

Coolant:

The Opticam SM, due to clearance with the tool changer, requires the coolant nozzles to be positioned about a foot away from the work and wheel. This also requires a large box around the grinding zone to contain the coolant splash. On the Microform SM, the wheel spindle is backed away from the coolant box for tool changing. As a result, the coolant splash box is much smaller and nozzles can be placed without these restrictions. The box is made of stainless steel for corrosion protection. Easy access is provided to the part by sliding back two covers.

A dual canister filter system allows the operator to easily change whichever filter is in use by operating a manual valve. While one filter is being used, the other is closed from the circuit, allowing a contaminated filter element to be changed while the machine is using the other filter.

Controller:

- Grinding programs (software) have been a limitation on previous machinery, forcing the grinding cycle to have one rough, one medium, and one finish pass, for example. Now grinding sequences can easily be rearranged or added as required. Part programs can now accommodate

virtually any number of edging, beveling, sagging, concave, and convex surface grinds in one mounting of the lens.

• Coordination of rough, medium, and fine stock removal are simplified. The operator can request the medium grind to start where the roughing grind ended, or to end the medium grind where the fine grind is to start, etc.

• The spherical radius is also adjusted for each grind so an equal depth of cut is taken from the entire surface with each wheel.

• Obviously, grinding wheels wear away during use. Another limiting factor in existing equipment is that stored wheel data consists of a single length and diameter. This requires the wheel to have a sharp cutting edge, so that the wheel grit zone is in the same position for any head angle. Our new Nanopath® CNC Control software keeps track of the wheel wear in a map of the wheel grit area for each wheel. This eliminates wheel dressing to restore a sharp edge. The control software also corrects for any workpiece error resulting from wheel wear. The operator enters the data for a surface ground incorrectly. The controller then updates the wheel grit map to compensate for the error. In this manner, the next part to be ground is correctly surfaced and the wheel grit area map is kept up to date.

Aspherics:

Aspheres are much more difficult to generate and polish than spherical optics. However, the CNC controlled axes on the Microform SM machine also allow an aspheric surface to be ground using a peripheral style grinding wheel with continuous path contouring of the X, Z, and B axes simultaneously. This provides an aspheric surface much closer to the final form than found using the best fit sphere.

A work piece can initially be rapidly rough ground to a best fit sphere by conventional chordal generation techniques, then a peripheral style grinding wheel can be selected by the automatic wheel changer and used for the continuous path contour grinding of the aspheric surface. Additional operations such as edging, beveling, and sagging can still be incorporated on aspheric lenses, which will drastically simplify the alignment of the optical axis during the final assembly of the lens into the system.

Process:

Traditionally, lenses are blocked to fixturing using pitch or wax. These compounds are ideal for conforming to and adhering to the lens surface while remaining flexible, to prevent distortion of the lens. They also require solvents for cleaning. Both the pitch and solvents are coming under increasing scrutiny with regard to workplace health and safety, and could be banned from use in the future due to the hazards involved. Lenses to be ground on the Microform SM can be blocked using a UV curing compound that is easily removed with water. This is environmentally cleaner than bonding with pitch or wax, and cleaning afterward with solvents. Any glass types that can not be exposed to water, or are stained by the UV compound, can be blocked by conventional methods.

Since lenses can be produced in a "semi-polished" state, the loose abrasive lapping or grinding process that traditionally follows the spherical generation is eliminated. This also eliminates the expense associated with the manufacture of cast iron tools that were required for each different radius processed by this interim lapping procedure.

Optional features of the machine:

- An optional coolant system is supplied with a centrifuge for swarf removal from the waste coolant stream. The Opticam SM machine had coolant pump seal failures that we feel were due to the residual levels of contaminants after the coolant had been cleaned using vortex type cyclonic filters. The cyclonic filters only work well down to particle sizes of 10 microns diameter or below. The centrifuge used on the Microform SM continually cleans the coolant each time the coolant passes through it, and a wash nozzle in the machine keeps coolant flowing through the centrifuge at all times.

- A toolchanger is available for the automatic exchange of grinding wheels with an eight station magazine. This allows production parts to be produced with a minimum of operator involvement.

- A mist extractor is used for the removal of grinding coolant mist. Use of the mist extractor extends the life of the machine, as mist is purged before it can condense on surfaces and cause corrosion of components otherwise not exposed to coolant. Mist removal also improves the health and safety conditions in the operator's working environment.

Spherical Grinding Results:

Typical finish ground surfaces are smooth enough to be inspected directly on an interferometer for surface form errors. Rank Pneumo installed the first Microform SM at a customer's facility in March, 1996. In proving the machine capability, a test part lens of BK-7 was ground on all sides. The lens has a 48 mm OD, 100 mm convex and 28 mm concave sides. The part was edged, sagged, and beveled on the SM.

The following accuracies were achieved (after delivery of the machine):

- Surface roughness of 120 Angstroms Rq (RTH Talysurf) and 75 Angstroms Ra (Wyco),
- P-V form error (irregularity) of 0.14 microns (0.5 fringe) (Zygo),
- Radius size error of .003 mm (Electronic spherometer),
- Surface wedge after grinding was measured to be 0.004 mm +/- .001 mm.

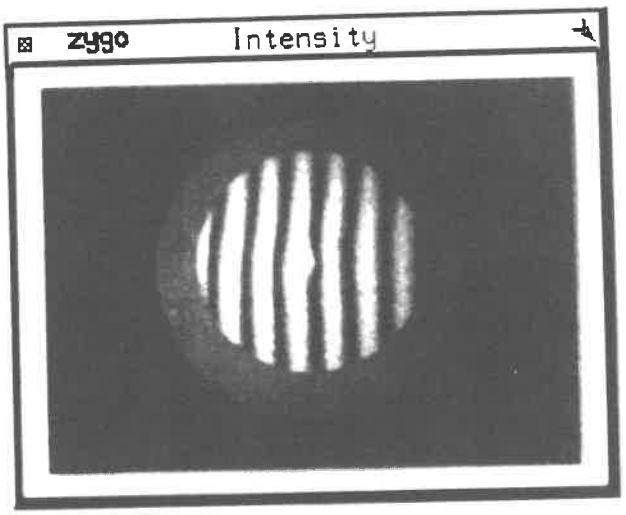

FRACTURE & FLOW PROCESSES IN GRINDING AND MICROGRINDING OF OPTICAL GLASSES

John C. Lambropoulos

Department of Mechanical Engineering & Center for Optics Manufacturing
University of Rochester, Rochester, NY 14627

ABSTRACT We review the applicability of glass mechanical properties to various optics manufacturing methods [Karow, 1993]. The cold working of commercially available optical glasses consists of grinding, microgrinding and polishing. We discuss these processes by using three fundamental mechanical properties for brittle glasses: Young's modulus E, hardness H, and fracture toughness K_c. Various combinations of these properties may be used to correlate the surface quality (surface roughness, subsurface damage, residual stresses) resulting from optics manufacturing with glass mechanical properties.

GLASS MECHANICAL PROPERTIES Glasses, like other brittle materials, are characterized by their hardness and fracture toughness [Cook and Pharr, 1990; McColm, 1990]. Fig. 1 shows data for these material properties, with the fracture toughness determined by microindentation via the model of Evans [1979], which is in good agreement with the measurement of fracture toughness via bulk methods. Evans [1979] used dimensional analysis and curve fitting over a range of c/(D/2) from 1.5 to 7, and proposed

$$K_c = H\sqrt{D/2}\left(\frac{E}{H}\right)^{0.4} 10^{f(x)} \quad , \quad x = \log_{10}\left(\frac{c}{D/2}\right)$$

$$f(x) = -1.59 - 0.34\,x - 2.02\,x^2 + 11.23\,x^3 - 24.97\,x^4 + 16.32\,x^5 \qquad (1)$$

where K_c is the fracture toughness, H the hardness (Vickers), D the indentation diagonal, E the Young's modulus, and c the half-crack size. Note that microindentation of densifying glasses, such as fused silica, can not be analyzed in this manner [Arora et al., 1979; Li and Bradt, 1992].

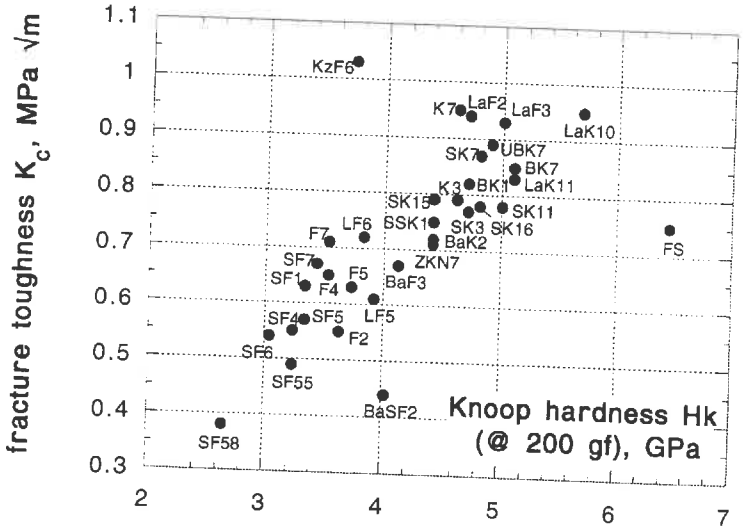

FIG. 1 Correlation of fracture toughness and Knoop hardness for some optical glasses. Data are from Lambropoulos et al. [1995a]. Typical error in fracture toughness is ±10%.

The measured Vickers hardness can be converted to a glass yield (flow) stress, for example using the model of Hill (1950; plastic growth of a spherical cavity in an infinite solid under internal pressure). Identification of the cavity pressure with Vickers hardness yields

$$\frac{\left(E/H_v\right)}{3\,(1-\nu)}\,\frac{1}{\left(\sigma_Y/H_v\right)} = \exp\left[-1+\frac{3/2}{\left(\sigma_Y/H_v\right)}\right] \qquad (2)$$

from where the uniaxial yield stress σ_Y can be found (ν is the Poisson ratio). Fig. 2 shows the correlation of hardness and yield stress.

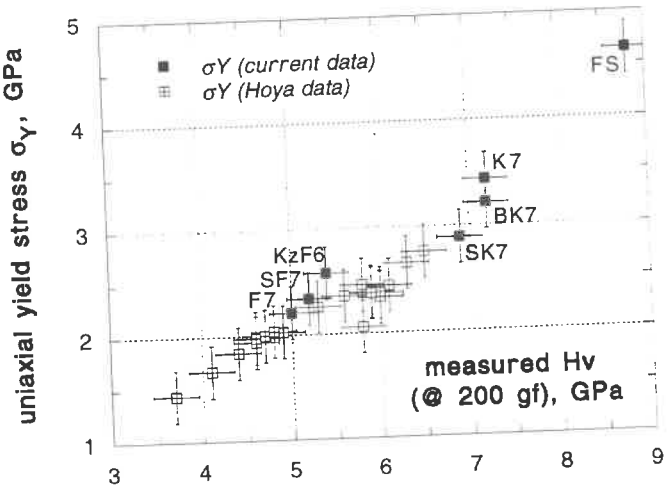

FIG. 2 The correlation of the measured Vickers hardness (the open squares are from Izumitani [1971, 1973, 1986]) with the uniaxial yield stress as calculated from the Hill analysis [1950].

LAPPING In loose abrasive grinding (also known as lapping, at fixed nominal pressure), the surface roughness increases with $1/\sqrt{H}$, see Fig. 3, indicating that formation of surface roughness is similar to indentation. Furthermore, a model of brittle material removal by the initiation and growth of subsurface lateral cracks (which eventually intersect the free surface and thus create a removed chip) allows the correlation of the volume removal rate with the glass mechanical properties [Evans and Marshall, 1981; Marshall et al., 1982; Lambropoulos et al., 1992; Buijs et al., 1993], see Fig. 4. Note that the subsurface damage is linearly correlated with the surface roughness, see Fig. 5. See also Preston [1921-1922], and Edwards and Hed [1987].

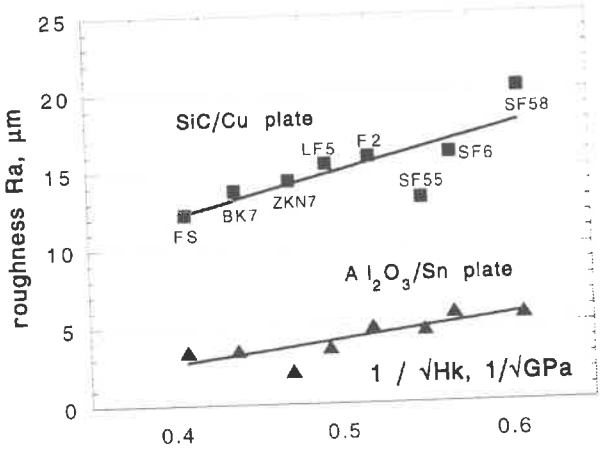

FIG. 3 Correlation of the surface roughness Ra measured by Buijs and Korpel-Van Houten [1993] with glass Knoop hardness.

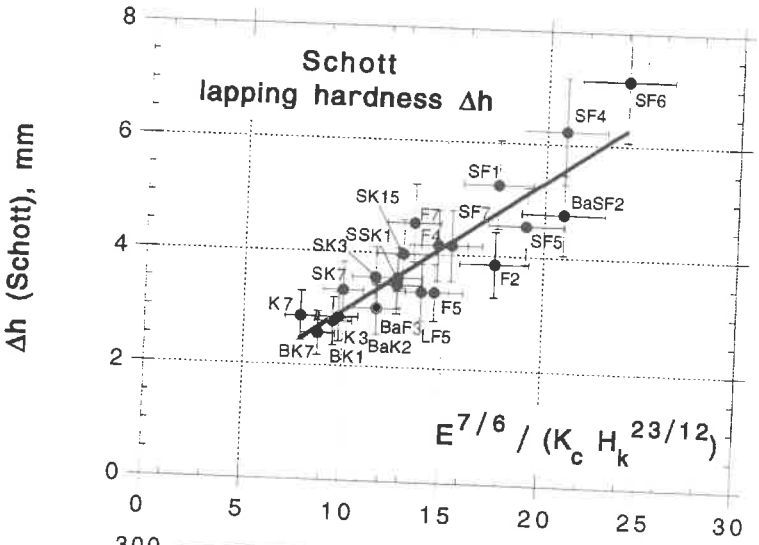

FIG. 4 Correlation of the height reduction Δh in lapping measured by Schott (1992; 115 μm alumina abrasives, pressure of 60 kPa, relative speed of 0.7 m/s) [32] with model predictions for material removal by lateral cracking (E in units of GPa, K_c in MPa$\sqrt{m}$, H_k in GPa).

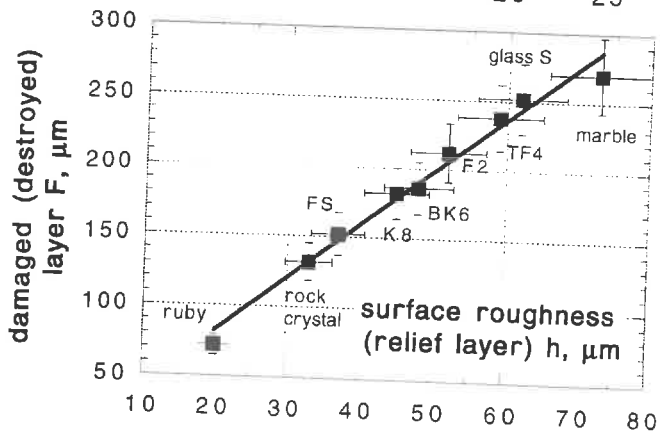

FIG. 5 Correlation of surface roughness (relief layer) and surface damage (relief layer), as measured by Aleinikov [1957]. See Glebov and Tolstoi [1995] for Russian glass designations.

TWYMAN EFFECT When an originally polished thin glass plate has one side ground, the plate bends as if the ground side is in a compressive state of stress over a thin surface layer [originally observed by Twyman in 1905; See Twyman, 1952]. The bending force P_0 per unit length in various glasses is well correlated with the microindentation behavior of the glasses, see Fig. 6 [Lambropoulos et al., 1995b]. The bending force ($P_0 = \sigma_0 d_s$) increases with abrasive size, although the grinding stress σ_0 increases and the compressive layer d_s decreases with decreasing abrasive size. In the limit of micron-size abrasives (Fig. 7), the surface compressive stress attains values equal to the yield stress of the glass, implying that ductile grinding is occurring [Bifano et al., 1991; Golini and Jacobs, 1991; Namba and Abe, 1993]. This result is corroborated by finite element [Lambropoulos et al., 1995b] or other simulations of indentation [Chiang et al., 1982a, b].

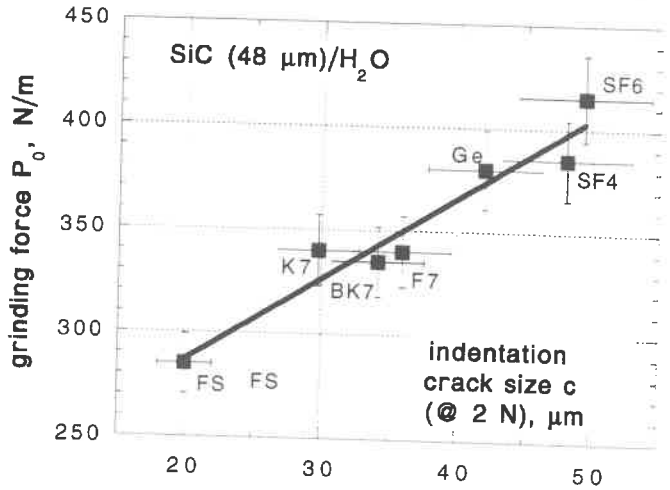

FIG. 6 Dependence of the surface compressive force P_0 on indentation crack size. P_0 due to lapping was measured by Podzimek [1986] via interferometry.

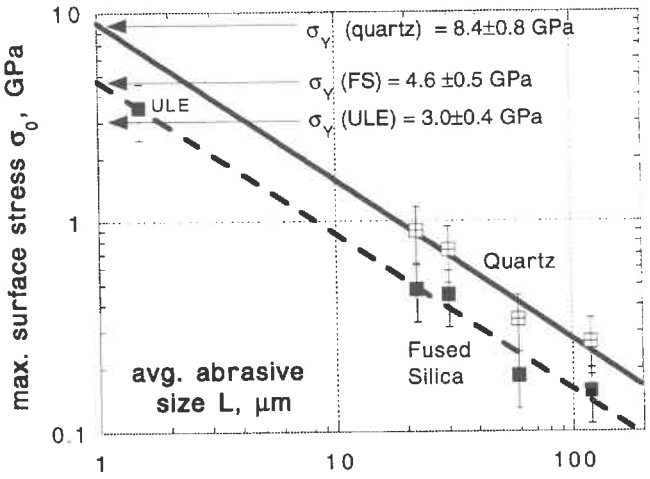

FIG. 7 Extrapolation of surface compressive stress due to grinding (abrasives > 3 μm) and microgrinding (abrasives < 3 μm) to ultra-low abrasive size shows that the surface compressive stress is commensurate with the uniaxial yield stress of the glass, which is approximately proportional to the glass hardness.

DETERMINISTIC MICROGRINDING In this manufacturing operation, the infeed rate of the bound abrasive tool is constant [Pollicove and Moore, 1992]. The resulting surface roughness correlates poorly with glass hardness across different glass families, but the correlation improves when the fracture toughness and the hardness of the glasses are combined into the ductility index $(K_c/H_k)^2$, which has the units of length, see Fig. 8 [Lambropoulos et al., 1995a]. The ductility index is in reverse analogy to the brittleness discussed originally by Aleinikov [1957] and later by Lawn et al. [1975].

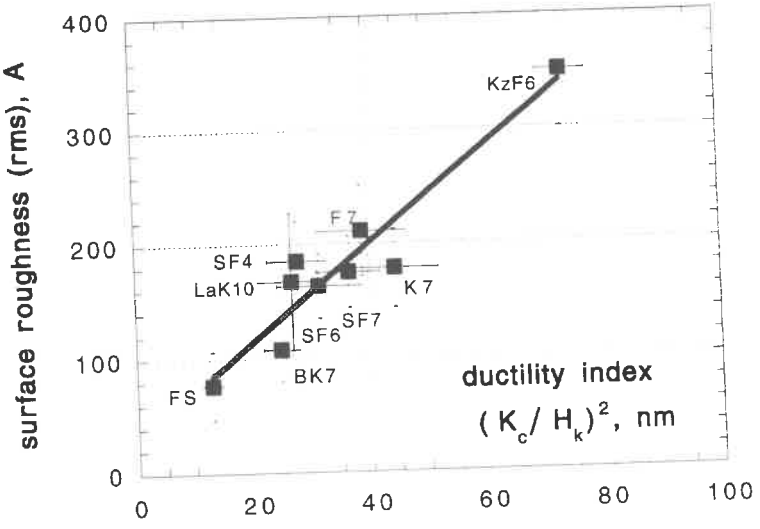

FIG. 8 Correlation of surface roughness in deterministic microgrinding with glass ductility index.

MECHANICAL EFFECTS IN POLISHING Conventional polishing data by Izumitani (1982; polyurethane pads with CeO_2 abrasives, pressure of 20 kPa, relative speed of 0.5 m/s), also show the effects of mechanical properties during polishing, see Fig. 9. These effects are parallel to the well known chemical effects [Cook, 1992], and show the chemo-mechanical issues involved in polishing. The inclusion of the fracture toughness is not surprising as the fracture toughness essentially measures the work required to produce new surface area.

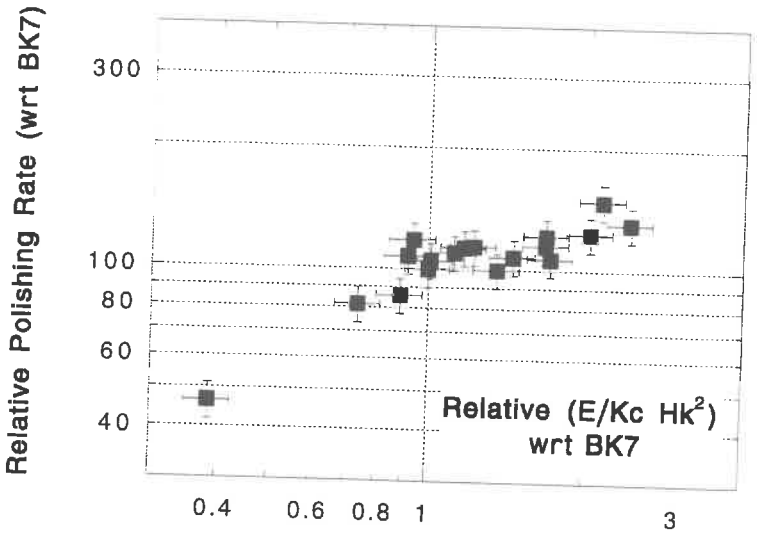

FIG. 9 Correlation of polishing rate with glass mechanical properties.

Similar conclusions may be drawn for the case of magnetorheological finishing (MRF) of optical glasses, whereby the lap is replaced by a stiff magnetic fluid within which the abrasives are mixed, and whose stiffness can be controlled by appropriate magnetic fields [Jacobs et al., 1995. Lambropoulos et al., 1996].

CONCLUSIONS The conclusions drawn from these examples are that elastic, plastic, and fracture properties of glasses must all be involved in correlating the surface quality resulting from cold working optics manufacturing with the glass properties.

REFERENCES

F. K. Aleinikov, 1957, The effect of certain physical and mechanical properties on the grinding of brittle materials, Sov. Phys. Tech. Phys. 27 (10), 2529-2538.

A. Arora, D. B. Marshall, and B. R. Lawn, 1979, Indentation deformation/fracture of normal and anomalous glasses, J. Non-Crystall. Solids 31, 415-428.

T. G. Bifano, T. A. Dow, and R. O. Scattergood, 1991, Ductile-regime grinding: A new technology for machining brittle materials, J. Engineering for Industry (Trans. ASME) 113, 184-189.

M. Buijs and K. Korpel-Van Houten, 1993, A model for lapping of glass, J. Mater. Sci. 28, 3014-3020.

S. S. Chiang, D. B. Marshall, and A. G. Evans, 1982a, The response of solids to elastic/plastic indentation, I. Stresses and residual stresses, J. Appl. Phys. 53, 298-311.

S. S. Chiang, D. B. Marshall, and A. G. Evans, 1982b, The response of solids to elastic/plastic indentation, II. Fracture initiation, J. Appl. Phys. 53, 312-317.

L. M. Cook, 1990, Chemical processes in glass polishing, J. Non-Crystall. Sol. 120, 152-171.

R. F. Cook and G. M. Pharr, 1990, Direct observation and analysis of indentation cracking in glasses and ceramics, J. Am. Ceram. Soc. 73, 787-817.

D. F. Edwards and P. P. Hed, 1987, Optical glass fabrication technology. 2: Relationship between surface roughness and subsurface damage, Applied Optics 26, 4677-4680.

A. G. Evans, 1979, Fracture toughness: the role of indentation techniques, in *Fracture Mechanics Applied to Brittle Materials*, ASTM STP 678, S. W. Freiman, ed., American Society for Testing and Materials, 112-135.

A. G. Evans and D. B. Marshall, 1981, Wear mechanisms in ceramics, in *Fundamentals of friction and wear of materials*, ed. D. A. Rigney, 441-452, ASM.

L. B. Glebov and M. N. Tolstoi, 1995, Designation of Russian optical glasses, in *CRC Handbook of Laser Science and Technology*, pp. 823-826, CRC Press.

D. Golini and S. D. Jacobs, 1991, Physics of loose abrasive microgrinding, Applied Optics 30, 2761-2777.

R. Hill, 1950, *The mathematical theory of plasticity*, Oxford University Press.

T. S. Izumitani, 1971, Lapping hardness of optical glass, Hoya technical report HGW-O-7E, Hoya Glass Works, Ltd (20 Feb. 1971).

T. S. Izumitani and I. Suzuki, 1973, Indentation hardness and lapping hardness of optical glass, Glass Technology 14, 35-41.

T. S. Izumitani, 1982, Polishing rate of optical glass, Workshop on Optical Fabrication and Testing, paper MA1, pp. 1-4, OSA, December 13-15, Palo Alto.

T. S. Izumitani, 1986, *Optical glass*, American Institute of Physics.

S. D. Jacobs, D. Golini, Y. Hsu, B. E. Puchebner, and D. Strafford, 1995, Magnetorheological finishing: A deterministic process for optics manufacturing, SPIE Proceedings vol. 2576, pp. 372-382.

H. H. Karow, 1993, *Fabrication methods for precision optics*, Wiley, New York.

J. C. Lambropoulos, M. Cumbo and S. D. Jacobs, 1992, The effects of materials properties and process parameters on surface quality during microgrinding of glass, in *Optical Fabrication & Testing Workshop Technical Digest,* 1992 (Optical Society of America, Washington, D.C., 1992) Vol. 24, pp. 50-53.

J. C. Lambropoulos, Tong Fang, P. D. Funkenbusch, S. D. Jacobs, and D. Golini, 1995a, Surface roughness of optical glasses under deterministic microgrinding, to appear in Applied Optics.

J. C. Lambropoulos, Su Xu, Tong Fang, and D. Golini, 1995b, Twyman effect mechanics in grinding and microgrinding, to appear in Applied Optics.

J. C. Lambropoulos, Fuqian Yang, and S. D. Jacobs, 1996, Toward a mechanical mechanism for material removal in magnetorheological finishing, Proceedings of Optical Society of America Topical Meeting, Optical Fabrication and Testing (Boston, 29 April-3 May 1996).

B. R. Lawn, T. Jensen, and A. Arora, 1975, Brittleness as an indentation size effect, J. Mater. Sci. 11, 573-575.

H. Li and R. C. Bradt, 1992, The indentation load/size effect and the measurement of the hardness of vitreous silica, J. Non-Crystal. Solids, 146, 197-212.

D. B. Marshall, B. R. Lawn, and A. G. Evans, 1982, Elastic/plastic indentation damage in ceramics: The lateral crack system, J. Amer. Ceram. Soc. 65, 561-566.

I. J. McColm, 1990, *Ceramic Hardness*, Plenum Press.

Y. Namba and M. Abe, 1993, Ultraprecision grinding of optical glasses to produce super-smooth surfaces, Annals of the CIRP 42(1), 417-420.

O. Podzimek, 1986, Residual stress and deformation energy under ground surfaces of brittle solids, Technical report WB-85-16, 112 pages, 23 April 1986, Twente University of Technology.

H. H. Pollicove and D. T. Moore, 1992, Center for Optics Manufacturing Overview, in Optical Fabrication and Testing Workshop, Vol. 24, 1992 OSA Technical Digest Series, 44-47.

F. W. Preston, 1921-22, The structure of abraded glass surfaces, Trans. Optical Soc. 23, 141-164.

Schott Glass Catalog, 1992, Publication 10000, Schott Glass Technologies Inc., Duryea, PA 18642.

F. Twyman, 1952, *Prism and lens making*, p. 318, Hilger & Watts, London.

Controlled Microcutting Tests on Single Crystal Silicon

B.V. Tanikella and R.O. Scattergood

Precision Engineering Center
Department of Materials Science and Engineering
North Carolina State University, Raleigh, NC 27695-7918

INTRODUCTION

Precision grinding [1] is accomplished by the cutting action of many sharp diamonds embedded in the wheel binder material. The fracture damage in the resulting part is dependent on the material properties and operating conditions. Considering grinding as a multi-scratch process, the response of a single cutting grain and the damage transitions produced by the cutting action as the load on the grain is varied, will be of primary interest. The microcutting action of a single cutter is important because it plays a key role in determining the subsurface fracture damage produced in processes such as polishing and grinding [1,2]. In recent studies with glass and amorphous SiC thin films, Tanikella and Scattergood [3,4,5] demonstrated a one-to-one correspondence between crack-initiation and depth-of-cut during microcutting. Extension of the results using statistical averaging effects will facilitate the prediction of the surface finish and subsurface fracture damage. The effect of crystallography is important for developing these models for crystalline materials. The purpose of the present work is to investigate the cracking thresholds, crystallography, and tool geometry effects for single crystal silicon. An understanding of the micromechanics of silicon would also enhance its utility as a high-precision, high-strength, high-reliability mechanical material, especially applicable in micro mechanical devices and components in conjunction with integrated electronics.

EXPERIMENTAL DETAILS

The material used in the present study was device grade single crystal p-type silicon with (100) and (111) surfaces. A freshly sharpened Vickers diamond pyramid indentor was used as the cutting tool for a series of tests and its condition was monitored frequently. All of the tests were conducted in controlled laboratory air at 20 ± 0.05^{o} C and $40 \pm 10\%$ relative humidity. A field emission JOEL 6400 scanning electron microscope (SEM) was used for micrographic observations. Two different test systems [4,5,6] were used for conducting the microcutting tests and they adopt either force control or depth control.

In the force controlled setup [4], a 140 μm range piezo translator (PZT) was mounted to the moveable crosshead of an ATS benchtop load frame and the PZT amplifier was interfaced to a PC for closed-loop load control profiles during microcutting tests. A 10 N load cell and fixture to hold a Vickers diamond indentor were attached to the PZT. An x-y stage was mounted to the base of the load frame for sample positioning. One axis of the stage was driven by a motorized micrometer screw using an analog encoder-controller for speed control. An acoustic emission sensor with a frequency-detection window set between 100 KHz to 900 KHz (200 KHz resonance frequency) was used for the acoustic measurements. A nominal cutting speed of 5 μm/sec was used for all of the microcutting tests. The microcutting grooves for different maximum loads appear as shown in Figure 1a. The length of the entrance, exit and hold portion of each groove is constant because of the fixed cutting speed, but the groove widths change with maximum load as indicated. During a loading profile the acoustic pulses detected by the oscilloscope were transferred and stored in the PC (using Labview® software) for comparison with the load values.

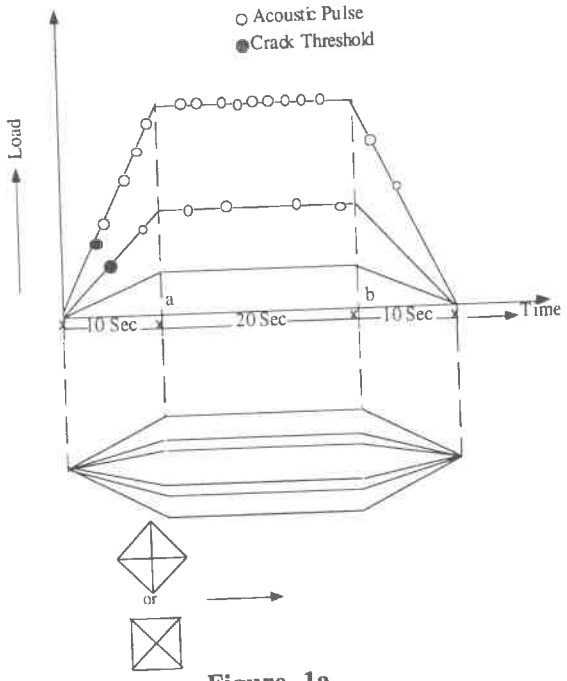

Figure 1a.
Test scheme during force control Tests

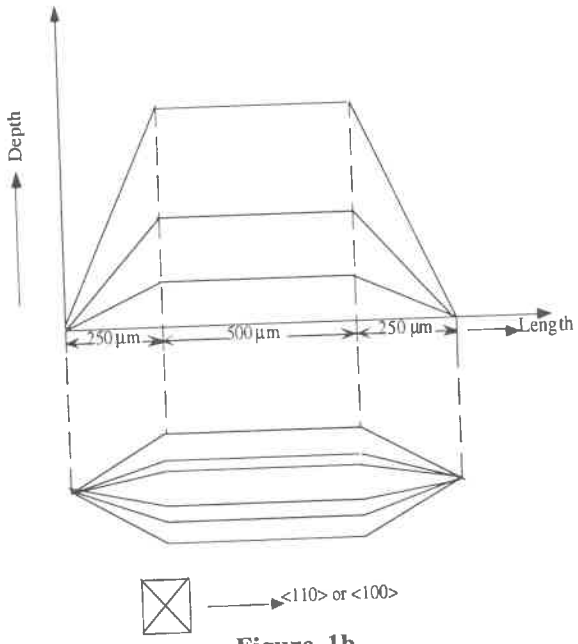

Figure 1b
Test scheme during depth control Tests

In the depth controlled setup [6], a Rank Pneumo ASG 2500 diamond turning machine (DTM) was used for conducting microcutting tests. This DTM features T-base configured hydrostatic bearing slides, an aerostatic bearing workpiece spindle, and laser interferometer feed back. The spindle of the diamond turning machine was locked mechanically and the vacuum chuck mounted on it was used to hold the sample. The sample was a 4 inch wafer and was mounted on the vacuum chuck of the DTM in as-received condition. <110> and <100> crystallographic directions of the wafer were adopted as two different cutting directions, and the direction was fixed before locking the spindle. A three-axis PZT load cell was used for recording the force data. The load cell and a specially fabricated fixture were mounted on a custom built dynamometer. Viscous grease was used between the interfaces and the assembly was held together with a torque of 11.3 N-m, to achieve a stiff setup. The slides of the DTM were programmed to perform the microcutting tests. A schematic of the test scheme is shown in Figure 1b. The x-slide of the DTM was programmed to give a nominal speed of 10 mm/min during all the microcutting tests. The side of the Vickers diamond is along the cutting direction. In earlier studies using the force controlled setup, it was found out that cutting along the side of the indentor produces less fracture damage compared to cutting along the diagonal for silicon. Performing constant depth-of-cut tests on single crystal silicon is complicated due to the nonflatness in silicon wafers due to residual stresses. A capacitance gage was used to determine the slope before conducting each microcutting test and the data thus obtained was applied in the part program assuming a linear slope. Thus, the resulting microcutting grooves would have the desired depth at a given position along the microcutting groove. The force data was acquired into a PC using Labview® software.

RESULTS AND DISCUSSION

Force Control

Microcutting tests as shown in Figure 1a were conducted in the load range of 0.03 to 3 N. The variables during microcutting were load, indentor orientation, cutting direction in relation to the crystal direction, and the normal to the crystal surface (i.e. (100) or (111)). The crack-initiation threshold, as manifest by the detection of an acoustic pulse during the load cycle in Figure 1a, was 0.04 to 0.4 N, depending upon test conditions. The threshold observed during the loading part of

orientation in Figure 1a. The indentor oriented with its diagonal along the cutting direction produced more damage compared to the cutting grooves made with the indentor side along the cutting direction. This is in contrast to the observations with glassy amorphous materials such as borosilicate glass [4,5], wherein the extent of damage produced is less while cutting along the diagonal of the tool. Thus, in the case of single crystal silicon, a wedge-shaped tool produces more fracture damage compared to a flat-faced tool.

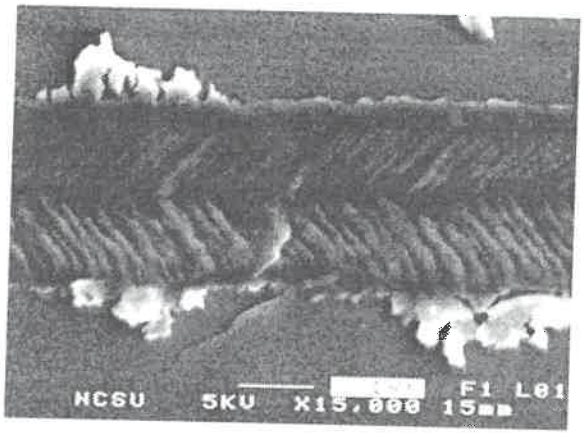

Figure 4
A close-up look at a 0.05 N microcutting groove

The effect of crystallography along with the indentor orientation provides an optimal direction for cutting. There were four different configurations when working with a (100) wafer. These constitute cutting along <110> and <100> directions, with two different indentor orientations. Cutting along <100> direction with the side of the indentor along the cutting direction is the optimal combination for minimal fracture damage in the microcutting grooves. Figures 5a and 5b show comparison of two microcutting grooves (with crystal surface (100)) at a load of 0.5 N, with differences in the indentor and crystallographic orientations. Figure 5a had the cutting direction along <100> with the indentor side oriented along the cutting direction, while Figure 5b had the cutting direction along <110> with the indentor diagonal oriented along the cutting direction. Figure 5a shows significant portions of ductile areas, while the groove in Figures 5b shows severe chipping damage. The crystallographic relations are in agreement with the observations in literature [7]. Similar crystallographic effects were observed in the case of (111) wafers [8].

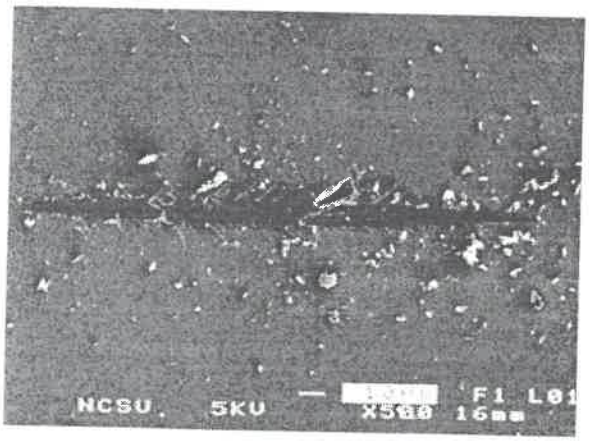

Figure 5a
Microcutting groove at 0.5 N along <100>
cut with the side of the Vickers indentor.

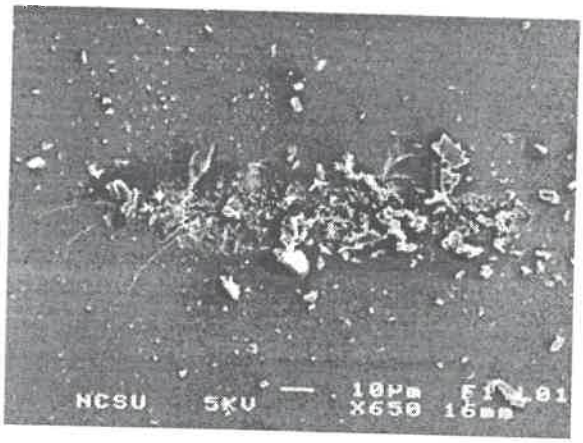

Figure 5b
Microcutting groove at 0.5 N along <110>
cut with the diagonal of the Vickers indentor.

Depth Control

Figure 6a shows a plot of normal force vs time for a microcutting groove at a depth-of-cut of 200 nm. Figure 6b shows an SEM micrograph corresponding to a portion of the groove in Figure 4, at the maximum cutting depth. Closer examination showed that the whole groove is crack-free and ductile. Also, the force is constant (above the noise level) at the maximum depth, indicating a uniform depth-of-cut. If the correction for the surface tilt of the wafer was inappropriate, the force profile would show a tilt of the force trace at the maximum depth-of-cut, indicating the deviation from a constant depth-of-cut.

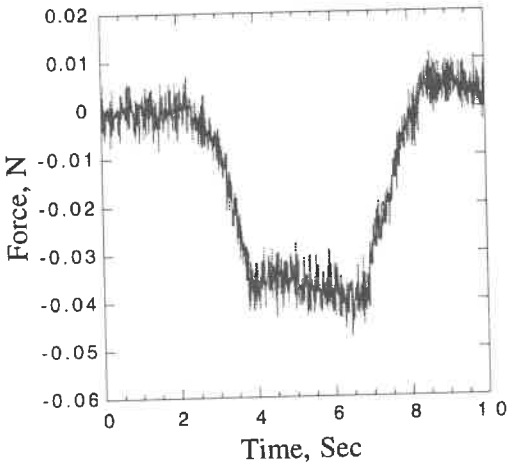

Figure 6a
Normal Force vs Time for a 200 nm depth-of-cut microcutting groove

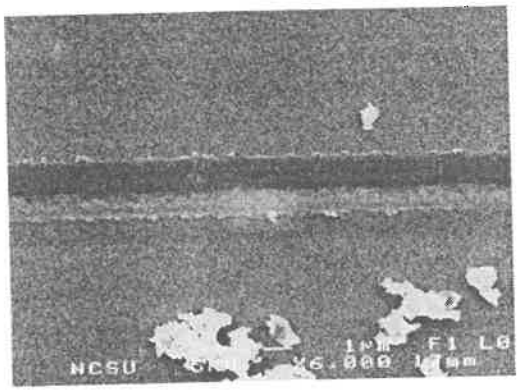

Figure 6b
SEM micrograph of the microcutting groove corresponding to Figure 6a at maximum depth

Above the cracking threshold, the force plots show significant deviation from Figure 6. Cracking thresholds are manifest as (unloading) pulses in the force traces. The threshold can be expressed in terms of a critical force or a critical depth-of-cut, since the tool geometry is known. As one would expect, results obtained from the depth-control tests match very well with the cracking thresholds obtained using the force control system. Figure 7a shows the force profile corresponding to a microcutting groove just above the threshold, at a depth-of-cut of 250 nm. In Figure 6a, the maximum normal force could be observed to be below the threshold, and the groove was of ductile nature. The maximum force in Figure 7a is about 0.06 N, and this is clearly above the threshold.

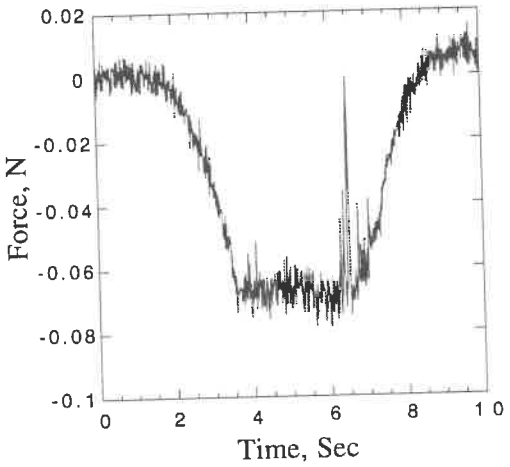

Figure 7a
Normal Force Profile for a 250 nm depth-of-cut micocutting groove

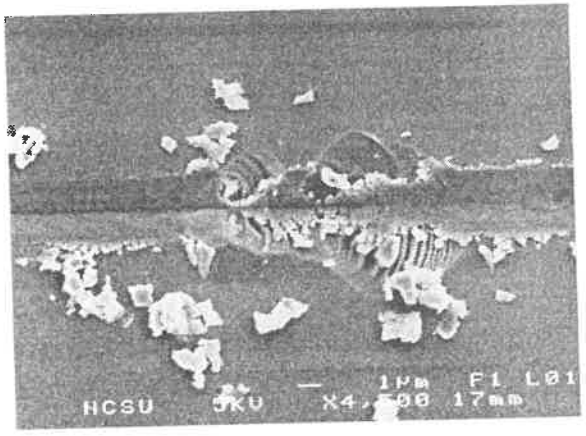

Figure 7b
SEM micrograph showing the fracture event associated with the large force pulse in Figure 7a

Detailed SEM observations showed a one-to-one correspondence between these force pulses in Figure 7a and a fracture event within the groove. The lateral chip in a portion of the microcutting groove shown in Figure 7b was associated with the largest force pulse in Figure 7a. This large force pulse indicates that the tool is unloaded to a large extent due to this large chip (or missing material ahead of the tool tip), and the force comes back to the normal position upon subsequent cutting to maintain the programmed depth. Similarly, the smaller force pulses corresponded to radial cracking and smaller scale chipping damage.

Figure 8a shows the normal and cutting force vs time respectively, for a microcutting groove at a programmed depth-of-cut of 1000 nm. It is evident that the depth-of-cut for this groove is well above the critical depth-of-cut. The initial force pulse during the load cycle occurs well above 0.045 N, indicating an increase in the cracking threshold as the loading rate goes up (loading rate increases with the depth-of-cut because the ramp distance in Figure 1b is fixed and the cutting speed is fixed). The initial pulse in Figure 8a occurs at a load close to 0.12 N. SEM observations showed no evidence of fracture in the microcutting groove before this initiation point. The loading rate effect clearly supports the results in Figure 2. The number of force pulses in Figure 8a far exceeds the number in Figure 7a. The cutting force profiles also showed a force pulse corresponding to each large pulse on the normal force profile. This indicates that there is also a significant force change in the cutting direction due to the chipping action. Detailed SEM observations of the microcutting groove corresponding to Figure 8a showed a one-to-one correspondence between the fracture events and the force pulses. Qualitatively, the magnitude of the force pulses were proportional to the extent of fracture. No attempts were made to provide quantitative measure of the extent of fracture. Figure 8a clearly shows that the tool is completely unloaded at the largest force pulse and this corresponded to the SEM micrograph shown in Figure 8b. There is a lateral chip ahead of the tool, and the tool is in a completely unloaded state for a short period due to the missing material, as indicated by the force information.

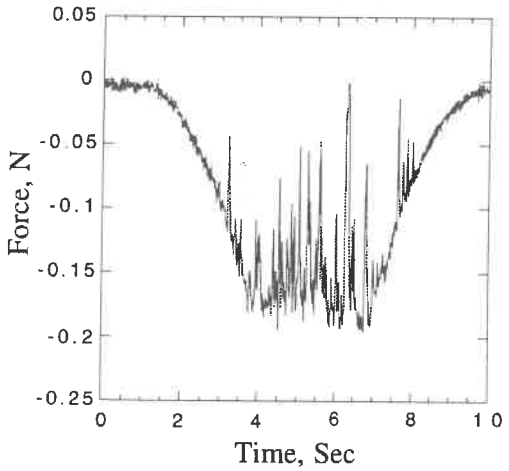

Figure 8a
Normal Force vs Time for a 1000 nm depth-of-cut microcutting groove

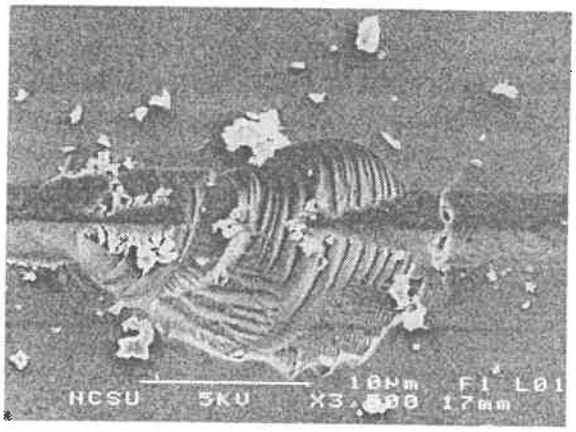

Figure 8b
SEM micrograph showing the fracture event associated with the large force pulse in Figure 8a

All the above results were obtained for cutting along the <110> direction on the (100) silicon wafers. Changing the cutting direction to <100> (by rotating the spindle by 45°), showed significant differences in the fracture morphologies of the microcutting grooves. Figure 9a shows the normal force corresponding to microcutting groove at a depth-of-cut of 1200 nm. This force curve doesn't show any force pulses similar to those in Figure 8a. The maximum normal force in this case is about 0.2 N, and is higher than that in Figure 8a. Even at such high force levels, there was no indication of large scale fracture associated with the present cutting groove. Detailed SEM

observations showed no lateral chips along the whole groove. However, the groove was observed to have radial cracks along both sides of the groove as shown in Figure 9b. This can be explained from consideration of the tool geometry, cleavage planes and directions. Indentation fracture [9] shows that the radial cracks originate from the corners of a Vickers indentor. When the cutting direction is along <100>, the radial cracks on {111} cleavage planes would initiate in the <110> directions. Since the <110> directions are the favorable directions for crack propagation, the radial cracks extend and show up along the edges of the cutting grooves. While cutting along <110>, the radial cracks could not propagate along the <100> directions and thus causing significant residual stress build-up. The residual stresses thus cause large scale chipping rather than radial cracking, for this geometry.

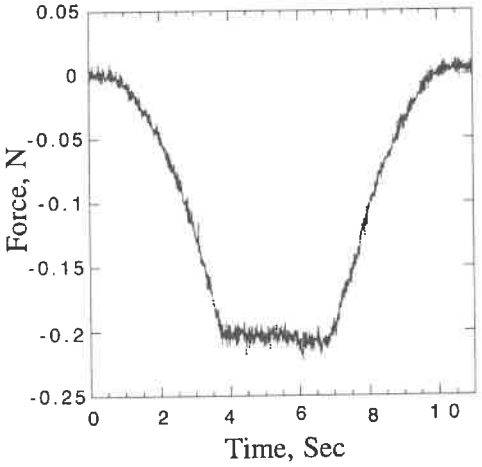

Figure 9a
Normal Force vs Time for a 1200 nm depth-of-cut microcutting groove, while cutting along <100>

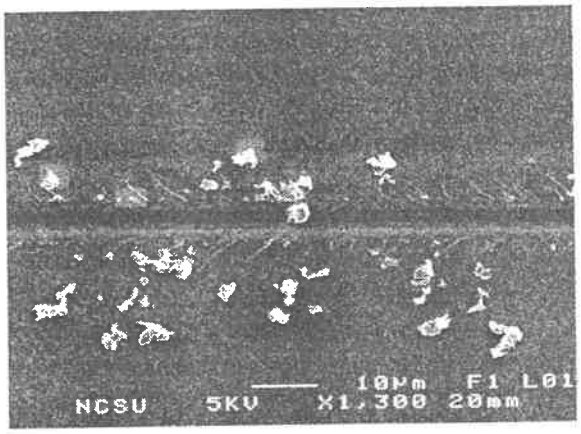

Figure 9b
SEM micrograph showing typical fracture morphology while cutting along <100> direction

Microplasticity

The features in the grooves and the debris around the microcutting grooves suggested pressure induced phase transformation during microcutting [10]. MicroRaman analysis confirmed the presence of amorphous Si phase within microcutting grooves and particle debris removed from the grooves. This can be attributed to the formation of the ß-tin metallic Si phase during the cutting process. Periodic features observed within the grooves (Figures 3b and 4) are consistent with an intemittent shear-type of chip formation process that will be facilitated by the formation of a ductile metallic phase. The MicroRaman scans also indicate the presence of large tensile residual stresses that are attributed to a mixture of amorphous and crystalline phases produced by microcutting. In situ recrystallization of the amorphous phase during microcutting has been suggested as a mechanism [10].

SUMMARY

Crack-initiation studies were conducted using two different test systems using force control and depth control respectively. Acoustic emission and force sensing were used as the tools for determining the cracking thresholds. An increase in the cracking threshold with loading rate was observed, and this would have important ramifications with respect to diamond turning and grinding. Cutting along the side of the Vickers indentor and <100> directions of the wafer were found to produce minimal fracture damage. Pressure induced phase transformation of silicon was understood to be the reason for periodic features in the grooves.

REFERENCES

1. T. Bifano, T. A. Dow, and R. O. Scattergood, "Ductile-Regime Grinding: A New Technology for Machining Brittle Materials", J. of Engr. for Ind., **113**, pp 184-189, 1991.

2. P. Blake et al., "Precision Machining of Brittle Materials", Ceramic Bulletin, **67** [6], (1988).

3. B.V. Tanikella and R.O. Scattergood, "Acoustic Emission during Indentation Fracture",J. Am. Ceram. Soc., **78** [6] pp 1698-702, 1995.

4. B.V. Tanikella and R.O. Scattergood, "Fracture damage in Borosilcate Glass During Microcutting Tests" Scripta Met., **34** [2], pp 207-213, 1996.

5. B.V. Tanikella, K.A. Gruss, R.F. Davis, and R.O. Scattergood, "Indentation and Microcutting Fracture Damage in a SiC coating on an Incoloy Substrate" surf. coat. tech., in press.

6. B.V. Tanikella and R.O. Scattergood, "Controlled Microcutting Tests on Semiconductor Silicon Crystals using a Diamond Turning Machine", Prec. Engg., to be submitted.

7. W.S. Blackley and R.O. Scattergood, "Crystal Orientation Dependence of Machining Damage-A Stress Model", J. Am. Ceram. Soc., **73** [10], pp 3113-15, 1990.

8. B.V. Tanikella, PhD thesis, North Carolina State University, in progress, 1996.

9. B.R. Lawn, "Fracture of Brittle Solids - second edition", Cambridge University Press, 1993.

10. B.V. Tanikella, A.H. Somasekhar, A.T. Sowers, R.J. Nemanich, and R.O. Scattergood, "Phase Transformation During Microcutting Tests on Silicon", Appl. Phys. Let., to be submitted.

EFFECTS OF WORKPIECE PROPERTIES ON MATERIAL REMOVAL PROCESS AND DAMAGE TOLERANCE IN CERAMIC GRINDING

Hockin H. K. Xu, Said Jahanmir, and Lewis K. Ives

National Institute of Standards and Technology
Gaithersburg, MD 20899

Structural ceramics are being increasingly used in engineering applications for the production of valves, rotors, nozzles, and bearings. Manufacture of these components generally requires diamond grinding. Due to the high hardness and brittleness, grinding of structural ceramics is difficult and costly[1]. An understanding of the relationship between grinding response and workpiece properties is needed to improve the machining process for structural ceramics.

The forces generated between the grinding wheel and the workpiece during grinding are often used as an indication of grinding response of the workpiece (*i.e.*, the larger the forces, the more difficult it is to grind the workpiece). Based on the assumption of material removal by the extension of lateral cracks that are parallel to the surface, the grinding forces are related to the toughness and hardness of the workpiece materials in the Evans-Marshall model[2]:

$$F_n \sim K_c^{4/9} H^{5/9} \qquad (1)$$

where F_n is the specific normal grinding force, K_c is the toughness, and H is the hardness.

For structural ceramics such as in-situ toughened silicon nitrides, the toughness is not a constant but increases with crack extension (*i.e.*, rising toughness-curve)[3-5]. Therefore, in using the Evans-Marshall model for predicting and analyzing machining behavior, the question arises as to what toughness value should be used. Although a few studies have suggested a possible effect of rising toughness-curves on machining[6,7], in most studies a single value of toughness measured with specimens containing cracks ranging from several hundreds of micrometers to millimeters have been used to analyze the machining of ceramics[1,8-10].

However, recent studies in our laboratory[11-13] have demonstrated that the material removal process in machining of polycrystalline ceramics involves local microscopic fracture (*i.e.*, microfracture) with cracks of a few micrometers to a few tens of micrometers. These studies, therefore, suggest that the toughness corresponding to small cracks associated with the microfracture process must be used for the analysis of the machining process. In this paper, "short-crack toughness"[14] (or T_{short}) is used to refer to the toughness corresponding

to cracks of about 30 μm. In contrast, "long-crack toughness" (or T_{long}) is used when the corresponding cracks are much larger than this value.

Nineteen ceramic materials with different microstructures and compositions were included in the investigation on the correlation between grinding forces and the toughness and hardness of the workpiece materials. The hardness values were measured with a standard Vickers hardness test using an indentation load of 10 N. The toughness-curves of these materials were characterized using an indentation-strength technique and a fracture mechanics analysis[14].

Grinding forces were measured using a surface grinder with a resin bonded 320 grit peripheral diamond wheel. The wheel width was 12.5 mm and the wheel diameter was 203 mm. A soluble-oil emulsion grinding fluid was used. The grinding wheel was trued and dressed prior to the grinding tests. Rectangular specimens were ground along the 4 mm x 25 mm surface at a table speed of 0.12 m s^{-1} and a wheel surface speed of 37 m s^{-1}. The full specimen width (4 mm) was ground on each pass without cross-feed. The depth of cut per pass (down feed) was 30 μm. Six passes were made to establish steady-state conditions before force measurements were undertaken. Normal and tangential grinding forces were measured with a 3-component piezoelectric dynamometer and normalized by the specimen width to give force per unit specimen width (N/mm).

In order to determine which value of toughness is most appropriate for grinding, predictions of equation (1) are compared with experimental results using toughness values corresponding to "short" and "long" cracks. In Fig. 1A, the long-crack toughness T_{long} corresponding to a crack length of about 300 μm is used for K_c in equation (1). The line is the linear least square best fit to the data resulting in a correlation coefficient of $R^2 = 0.09$. Such a low R^2 value is an indication of a poor correlation, suggesting that the long-crack toughness should not be used for the prediction of grinding forces in machining of ceramics.

In contrast, Fig. 1B shows a much better correlation when the short-crack toughness T_{short} corresponding to a crack size of about 30 μm is used for K_c in equation (1). The straight line is the linear least square best fit to the data resulting in a correlation coefficient of $R^2 = 0.58$. This R^2 value is significantly larger than that obtained with the long-crack toughness. Therefore, these results suggest that the material removal process in grinding ceramics follows primarily from the formation of "short" cracks, rather than long cracks. This is consistent with observations of material removal via microfracture and grain-scale material dislodgement process[11-13].

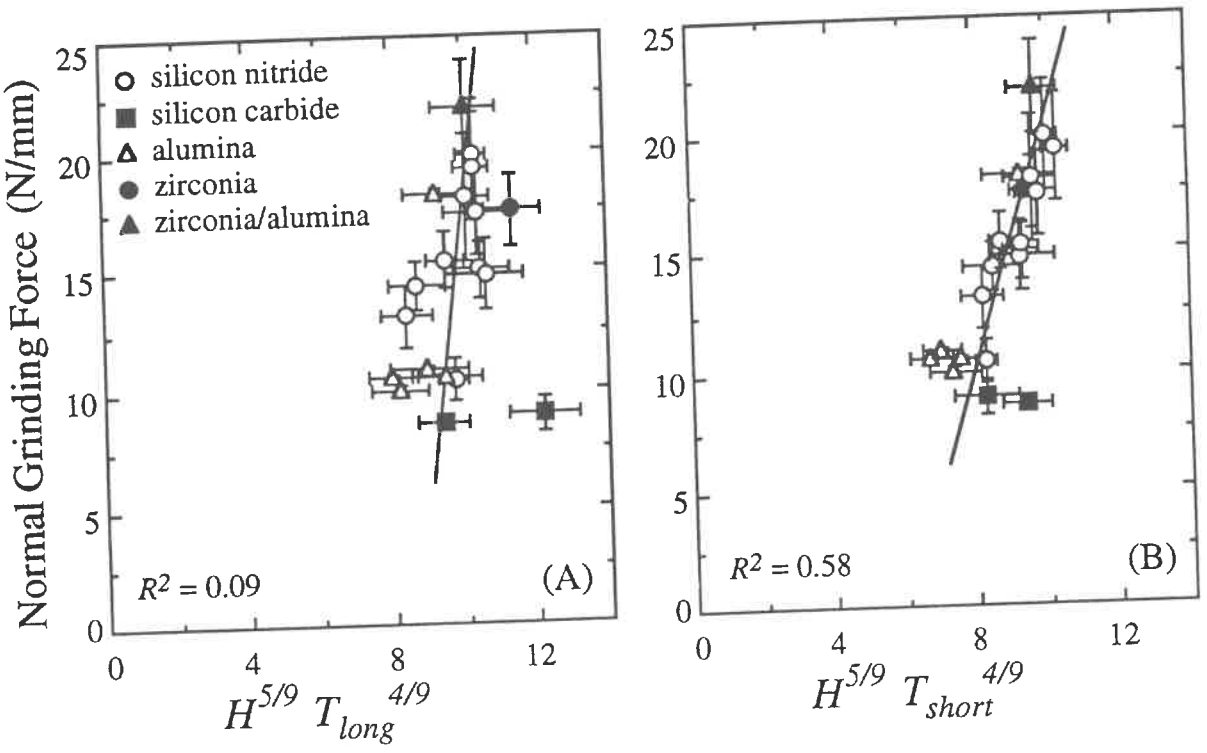

Fig. 1 Specific normal grinding force against (A) $H^{5/9}\ T_{long}^{4/9}$, and (B) $H^{5/9}\ T_{short}^{4/9}$. The unit for H is GPa and for T is MPa·m$^{1/2}$.

In order to examine the effect of workpiece properties on damage tolerance, specimens were transverse-ground with an 80 grit diamond wheel and then fractured in four-point bending to measure the strength. The toughness-curves of two of the materials tested in this type of experiment are shown in Fig. 2. Material I is a silicon nitride with relatively coarse and elongated grains and an associated steeply rising toughness-curve[15]. Material II is a fine grain silicon nitride with a mildly rising toughness-curve[15]. The strengths of the ground specimens of these two materials are plotted against depth of cut in Fig. 3. The data points represent the average strength values from four specimens; the error bars denote ± one standard deviation for the measurements. The rectangular data points at the left axis represent the strength for the polished specimens (i.e., the base-line strength). A significant difference in the strength response of the two materials is evident. The base-line strength of material II is about 200 MPa larger than that for material I. However, material I exhibits a much smaller loss in strength as a result of grinding. For example, the strength of material I ground at a depth of cut of 2.5 μm was reduced by only 25% compared to the polished specimens, while the strength of material II was reduced by 60%. Similar strength behavior was observed in grinding of silicon carbide[13] and glass-ceramics[16].

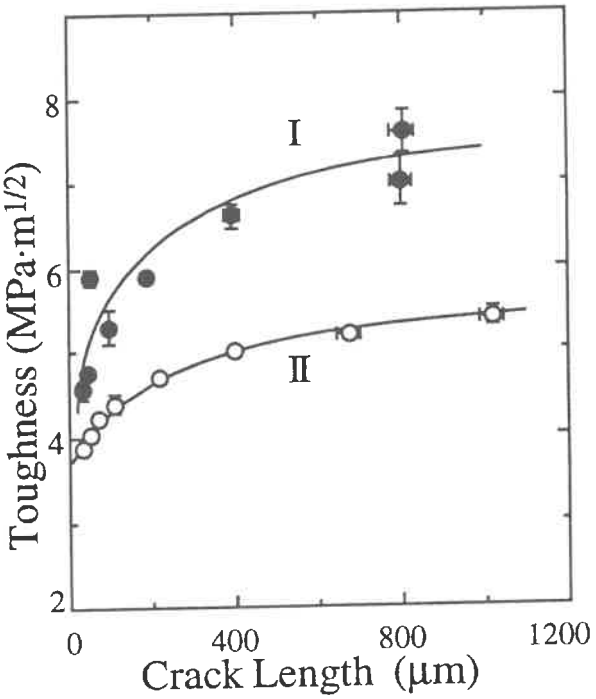

Fig. 2 Toughness against crack length (i.e., toughness-curves) for silicon nitride I and II.

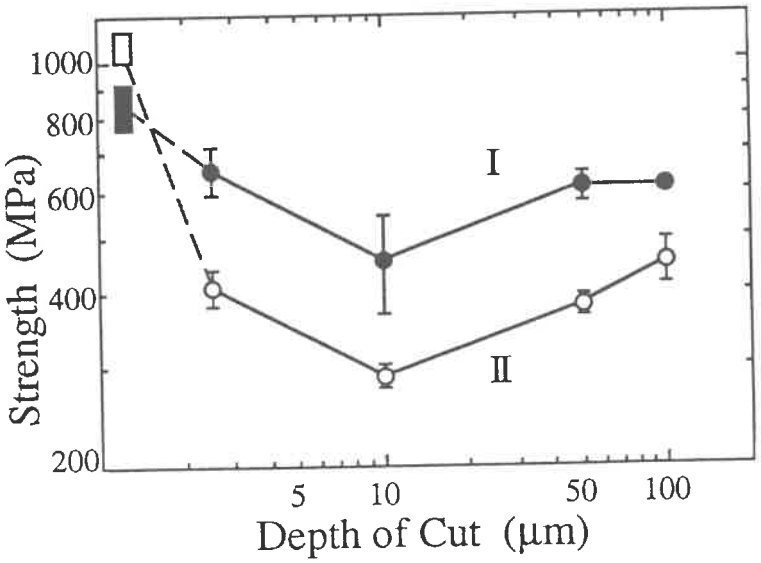

Fig. 3 Strength against depth of cut in grinding for silicon nitride materials I and II.

In conclusion, this study has investigated the correlation between grinding forces and the workpiece properties for nineteen different structural ceramics. The major results of this study are summarized as follows:

(1) Grinding forces correlate more closely with $H^{5/9} T_{short}^{4/9}$, where H is the hardness and T_{short} is the short-crack toughness, as compared with the long-crack toughness.

(2) For materials whose toughness increases with crack size, the short-crack toughness provides a better indication of machining response since the material removal process follows formation of short cracks resulting in grain-scale material dislodgement in abrasive machining.

(3) Structural ceramics with steeply rising toughness-curves show superior damage tolerance and relatively little strength loss even under very aggressive grinding conditions compared to ceramics with flat toughness-curves.

REFERENCES

1. S. Jahanmir, L.K. Ives, A.W. Ruff, and M.B. Peterson, *Ceramic Machining: Assessment of Current Practice and Research Needs in the United States (*NIST Special Publication **834**, U.S. Government Printing Office, Washington DC, 1993).
2. A. G. Evans and D. B. Marshall, "Wear Mechanisms in Ceramics," pp. 439-452 in *Fundamentals of Friction and Wear of Materials*, edited by D. A. Rigney, ASM Metals Park, OH, 1981.
3. B. R. Lawn, *Fracture of Brittle Solids*, Chapters 7-9, Cambridge University Press, Cambridge, U. K., 1993.
4. C. W. Li and J. Yamanis, "Super-Tough Silicon Nitride with R-Curve Behavior," *Ceram. Eng. Sci. Proc.*, **10** [7-8] 632-45 (1989).
5. H. H. K. Xu, *Crack-Bridging Toughening in Ceramics and Ceramic Composites at Ambient and Elevated Temperatures*, Ph.D. Thesis, University of Maryland, College Park, MD, 1993.
6. R. O. Scattergood, S. Srinivasan, T. G. Bifano, and T. A. Dow, "R-Curve Effects for Machining and Wear of Ceramics," *Ceramica Acta*, **3** [4-5] 53-64 (1991).
7. S. Srinivasan and R. O. Scattergood, "R-Curve Effects in Solid Particle Erosion of Ceramics," *Wear*, **142** 115-33 (1991).
8. M. N. Gardos and R. G. Hardisty, "Fracture Toughness- and Hardness-Dependent Wear of Silicon Nitride Ceramics," *Tribo. Trans.*, **36** [4] 652-60 (1993).
9. P. Roth and H. K. Tonshoff, "Influence of Microstructure on Grindability of Alumina Ceramics," pp. 247-60 in *Machining of Advanced Materials*, edited by S. Jahanmir, U.S. Government Printing Office, Washington DC, NIST SP 847, 1993.
10. D. S. Baik, K. S. No, J. S. S. Chun, and Y. J. Yoon, "Mechanical Properties of Mica Glass-Ceramics," *J. Am. Ceram. Soc.*, **78** [5] 1217-22 (1995).
11. H. H. K. Xu and S. Jahanmir, "Scratching and Grinding of a Machinable Glass-Ceramic with Weak Interfaces and Rising *T*-Curve," *J. Am. Ceram. Soc.*, **78** [2] 497-500 (1995).
12. H. H. K. Xu, L. Wei, and S. Jahanmir, "Grinding Force and Microcrack Density in Abrasive Machining of Silicon Nitride," *J. Mater. Res.*, **10** [12] 3204-09 (1995).
13. H. H. K. Xu, N. P. Padture, and S. Jahanmir, "Effect of Microstructure on Material Removal-Mechanisms and Damage Tolerance in Abrasive Machining of Silicon Carbide," *J. Am. Ceram. Soc.*, **78** [9] 2443-48 (1995).
14. L.M. Braun, S.J. Bennison and B.R. Lawn, "Objective Evaluation of Short-Crack Toughness-Curves Using Indentation Flaws: Case Study on Alumina-Based Ceramics," *J. Am. Ceram. Soc.* **75** [11] 3049-57 (1992).
15. H. H. K. Xu, S. Jahanmir, and L. K. Ives, "Material Removal and Damage Formation Mechanisms in Machining of Silicon Nitride," *J. Mater. Res.*, accepted for publication.
16. H. H. K. Xu and S. Jahanmir, "Effect of Microstructure on Abrasive Machining of Ceramics," *Ceram. Eng. Sci. Proc.*, **16** [1] 295-314 (1995).

GEOMETRIC OPTIMIZATION OF PROCESS PARAMETERS FOR CONTOUR GRINDING

Gene E. Storz, Thomas A. Dow
Precision Engineering Center
North Carolina State University
Raleigh, NC

INTRODUCTION

To understand the mechanisms of contour grinding, it is necessary to understand the geometry of the chips that produce both surface roughness and surface damage. Over the past few years, the effects of the geometry have been studied and led to the development of the Virtual Contour Grinding Model [1]. The model combines the effects of wheel speed (Nw), part speed (Np), wheel radius (R), nose radius (A), crossfeed rate (cf), and part diameter (D) to create a theoretical grinding chip and surface. Additional parameters can be included such as critical chip thickness and subsurface damage penetration depth so that the amount fracture can be determined given a predefined set of grinding conditions. Several values can then be calculated from the theoretical chip and surface such as surface roughness, chip thickness, damage generated, etc. The model is limited to geometric effects of grinding (Boolean geometry) using the assumption that a single region of the wheel performs the majority of cutting once per revolution. Although the model is limited in this aspect, it does show the interaction of the base geometry and provide predictions for grinding conditions to obtain better surface characteristics. The Virtual Contour Grinding Model was also used to generate data for surface roughness and chip thickness values. The current focus of research is to verify the Contour Grinding Model and determine how it can be used in application.

VERIFICATION OF CONTOUR GRINDING MODEL

Method Of Model Verification

To verify the Contour Grinding Model, a direct method of comparison between the grinding model and experiments is required. The method used is to examine the chip signature created by each pass of the grinding wheel using an interrupted cutting test, or ICT, developed by Fawcett [2]. The chip signature is the feature left behind on the surface of the material after each revolution of the grinding wheel has been completed. This feature is not the result of one diamond, but the summation of diamonds which come into contact with the workpiece over one revolution of the grinding wheel. The chip signature is compared to a theoretical chip by comparing the outline, dimensions, and shape. If the once per revolution assumption is accurate and the model is correctly predicting the chip shape, then the chip signature and theoretical chips should compare favorably.

Setup For Interrupted Cutting Test

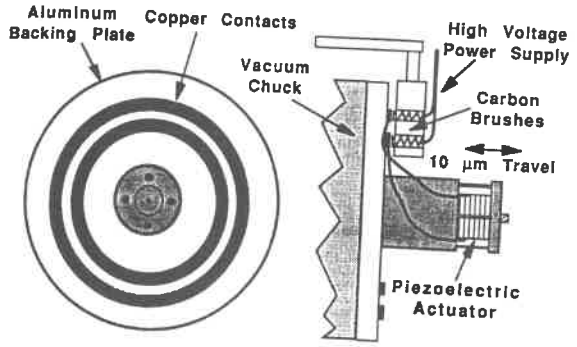

Figure 1: Experimental setup for interrupted cutting tests

An interrupted cutting test is performed by mounting the workpiece on a charged Piezoelectric actuator which is mounted on the vacuum chuck of the diamond turning machine. Once cutting begins and the grinding wheel has moved several feeds into the surface, the voltage supplied to the actuator is turned off. This pulls the workpiece away from the grinding wheel a distance of 10 µm (a 5 µm depth of cut is used for the experiment) in less than 10 µs, or one hundredth of a revolution of the wheel. A diagram of the experimental setup is shown in Figure 1. For further explanation of the setup, refer to *Development and Implementation of a Grinding Technique for Precision Finishing of Brittle Materials* by Fawcett [2].

Experiments Using Full Grinding Wheel

Several experiments were conducted using the interrupted cutting tests. One example of these tests is shown. The grinding conditions used for this test are shown in Table 1.

Figure 2 displays the results of the interrupted cutting test using the grinding conditions shown in Table 1. Figure 2(a) shows the theoretical grinding chip from the Contour Grinding Model. The theoretical chip has an arrow-like shape due to the small nose radius of the grinding wheel with a knife edge on the lower edge of the chip. Figure 2(b) shows the chip signature produced by the interrupted cutting test. The chip signature is oriented in both the vertical and horizontal directions so that the width and height of the chip could be measured with the scalar on the

microscope. The theoretical chip length in the upfeed direction is 515 μm while the experimental chip length was measured at 502 μm. In the crossfeed direction, both the theoretical and experimental chips were measured at 100 μm in width. As shown in Figure 2, the size and shape of the theoretical and experimental chips match almost identically. Even the knife edge on the lower region of the chip is reproduced in the chip signature.

Interrupted Cutting Test
Wheel Speed = 7150 rpm
Part Speed = 22 rpm
Part Diameter = 16 mm
Crossfeed Rate = 0596 mm/min
Wheel Radius = 36 mm
Nose Radius = 0.75 mm

Table 1: Grinding conditions for interrupted cutting tests on Germanium, depth of cut = 5 μm

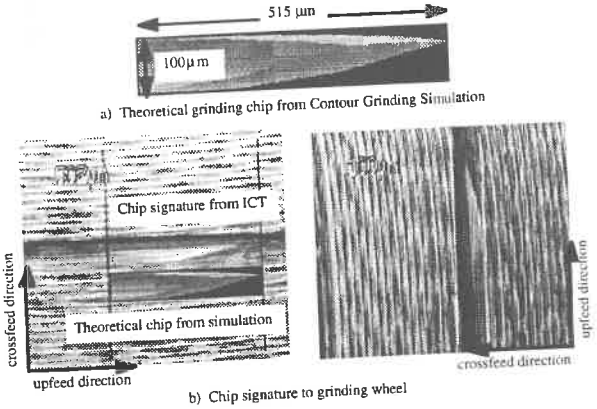

Figure 2: Interrupted cutting test performed on Germanium with Np = 22 rpm and A= 0.75 mm

Conclusions Of Interrupted Cutting Tests

In all the experiments performed using the interrupted cutting tests, the chip dimensions produced by the Contour Grinding Simulation matched the chip dimensions produced in the experiments to within 1%. Also, the shape of the chips and surfaces were remarkably alike. The same type of curvature and changes in geometry displayed in the theoretical chips were seen in the chip signatures. These experiments showed that the Contour Grinding Model produces close approximations to the chips features formed during grinding.

These tests also give strong evidence that features formed on the surface of the material are caused by a once per rev cutting action of the grinding wheel. For all tests, the radial error of the grinding wheel was between 3 to 10 μm, approximately equal to the 5 μm depth of cut. These tests also indicated that the trailing edge of the chip is raised relative to the lowest cutting point of the grinding wheel during one revolution. This produces cusps in the surface of the material. These are seen as the alternating light and dark areas in the upfeed direction and could only be caused by a once per rev cutting motion.

PART SPEED EFFECTS ON SURFACE ROUGHNESS

With the Contour Grinding Model established for predicting chip geometry, further tests were required to determine if predictions could be made for surface roughness. It has been established that part speed plays a critical role in obtaining minimum surface roughness and minimizing phase effects. What follows is a discussion of the role of part speed in surface roughness generation and a comparison between theoretical and experimental results.

Surface Roughness And Pattern Index

Using the Virtual Contour Grinding Model, a set of theoretical surface roughness curves were developed using the theoretical maximum surface roughness and the pattern index. The pattern index is an analytical expression developed from relationships in the surface roughness data calculated from the Virtual Grinding Model for a range of grinding conditions. The maximum surface roughness, $RMSmax$, is a theoretical equation derived by Fawcett [2] using the geometry of contour grinding. The pattern index is defined as C in Equation (1) and the maximum surface roughness is defined in Equation (2). Changing the value of the pattern index changes the shape of the surface roughness versus phase curve as shown in Figure 3. The maximum surface roughness can be multiplied by the point on the characteristic curve at the appropriate phase to yield an estimate of the geometric surface roughness. The phase (ph) is determined by the ratio of wheel speed to part speed given by Equation (3). The INT specifies the integer portion of the calculated value. The upfeed (uf) and crossfeed (xf) are given by Equations (4) and (5).

$$C = \log\frac{R}{A} - 2 * \log\frac{uf}{xf} \qquad (1)$$

$$RMS_{max} = \sqrt{\frac{uf^4}{720 * R^2} + \frac{xf^4}{720 * A^2}} \; ; mm \qquad (2)$$

$$ph = \frac{N_w}{N_p} - INT\,\frac{N_w}{N_p} \; ; \; radians \qquad (3)$$

$$uf = \frac{\pi * N_p * D}{N_w} ; mm \qquad (4)$$

$$xf = \frac{cf}{Np} ; mm \qquad (5)$$

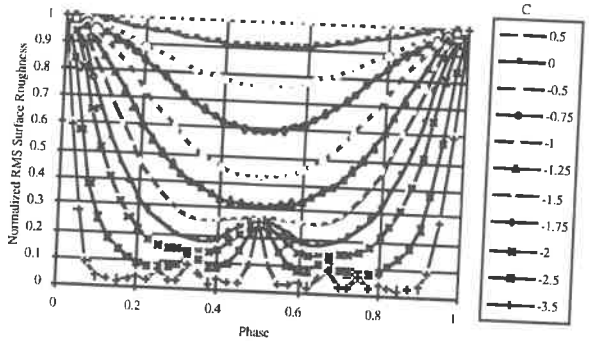

Figure 3: Theoretical surface roughness curves for contour grinding

The concept of the pattern index and maximum surface roughness were developed independently and without any apparent relationship. However, careful examination of the maximum surface roughness over a range of part speeds revealed that a minimum occurs at a pattern index value of 0. Maximum surface roughness and the pattern index have now been explored more closely to determine if a direct relationship exists.

If a minimum *RMSmax* value occurs over a range of part speeds at a pattern index value of 0, then a relationship must exist between the pattern index and the derivative of the maximum surface roughness. First, the upfeed and crossfeed are substituted into Equations (1) and (2) so that both equations are a function of part speed. Next, the pattern index (Equation (1)) and the derivative of Equation (2) with respect to part speed are set equal to 0. Solving both equations independently for part speed yields Equation (6) showing that the maximum surface roughness and the pattern index are directly related through this equation.

$$Np = \left(\frac{cf * Nw}{\pi * D}\right)^{\frac{1}{2}} * \left(\frac{R}{A}\right)^{\frac{1}{4}} ; rpm \qquad (6)$$

Not only does Equation (6) predict at what part speed the theoretical minimum *RMSmax* value will occur, it also predicts when variations in the surface roughness will begin to occur due to phase. Figure 3 shows that a pattern index value greater than 0 will maintain the maximum surface roughness independent of the wheel and part speeds. As the pattern index approaches 0, the surface roughness curves begin to vary with phase. As the pattern index drops below 0, the variation of surface roughness with phase continues to increase indicating that large variations will occur on a surface with a negative pattern index value. To predict a lower bound for the surface roughness, the normalized minimums in Figure 3 were examined as a function of the pattern index, C, resulting in Equation (7).

$$RMS_{min} = 10^{(-0.0348+0.17855*C-0.165*C^2-0.02374*C^3)} * RMSmax \qquad (7)$$

Experimental Verification Of Surface Finish

To verify the theoretical results, experiments were conducted using the Small and Large Form Grinders at the PEC. The Large Form Grinder uses grinding wheels 38 mm in radius with a top speed of 7200 rpm. The Small Form Grinder uses grinding wheels 9 mm in radius with top speeds of 65000 rpm. The results obtained from the Small Form Grinder are shown in Figure 4. The theoretical maximum and minimum surface roughness values determined by Equations (2) and (7) are plotted as a function of the part speed. The minimum surface roughness starts at a part speed of approximately 50 rpm as calculated from Equation (6) where phase variations begins to occur. As the part speed increases beyond 50 rpm, the theoretical maximum and minimum diverge. This indicates that both the pattern index is becoming more negative and the surface roughness as measured on a ground surface will have larger variations due to variations in phase.

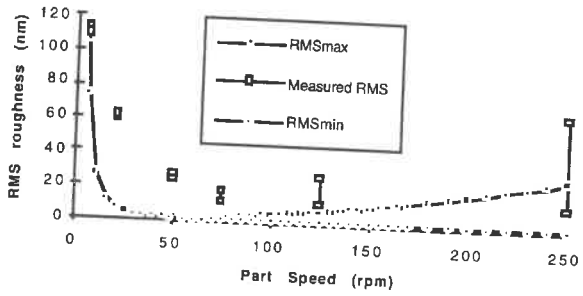

Figure 4: Theoretical and experimental RMS surface roughness for R = 7 mm, A = 5 mm, D = 6 mm, cf = 0.596 mm/min, Nw = 63000 rpm. Material = CVD Silicon Carbide

Experimental tests were conducted at part speeds of 5, 20, 50, 75, 125, and 250 rpm. Surface roughness measurements were then performed on a Maxim Interferometer at a fixed radial distance around the workpiece. At low part speeds, the variation in

surface roughness at different locations on the ground surface was small. At 50 rpm, a variation in surface roughness was detected. These variations continued to increase as the part speed was increased as shown in Figure 4. Experiments on the Large Form Grinder show similar results.

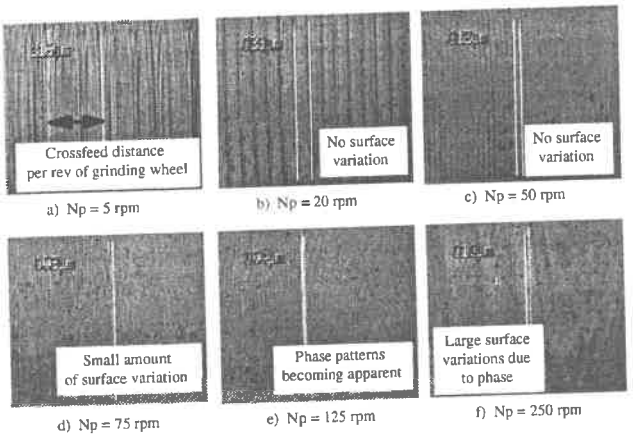
Crossfeed distance per rev of grinding wheel
a) Np = 5 rpm
No surface variation
b) Np = 20 rpm
No surface variation
c) Np = 50 rpm
Small amount of surface variation
d) Np = 75 rpm
Phase patterns becoming apparent
e) Np = 125 rpm
Large surface variations due to phase
f) Np = 250 rpm

Figure 5: Experimental surfaces of CVD Silicon Carbide using grinding conditions of R = 7 mm, A = 5 mm, D = 6 mm, cf = 0.596 mm/min, Nw = 63000 rpm

Figure 5 shows the experimental surfaces from which the surface roughness measurements were made for Figure 4. Below each picture is the corresponding part speed used for that experiment. The crossfeed distance (distance between the plane of white internal lines) is also shown and corresponds correctly to the calculated spatial crossfeed distance given by Equation (5). In Figure 5(a) through (c), there is no variation in roughness and the feed marks are easily observed. In Figure 5(d), the part speed is 75 rpm and a small amount of spatial variation in surface roughness can be seen. Figure 5(e) shows even larger spatial variations. At a part speed of 250 rpm, shown in Figure 5(f), the phase is constantly changing, thus causing dramatic surface variations over small areas. This produced the largest measured variations in the surface roughness.

Conclusions Of Part Speed Analysis

These experiments demonstrate that phase variations are always occurring as a result of speed variations, but that under the appropriate conditions, the geometry does not show these effects either in the surface or the surface roughness. Grinding wheel speed control is not an option at this point due to the accuracy required to maintain constant speed to less than 1 out of 60000 rpm. The objective then is to minimize phase variation effects and thereby minimize surface roughness and surface variations using the geometry of contour grinding.

Both the model and the experimental measurements indicate that an optimum part speed can be chosen to obtain a minimum surface roughness for given grinding conditions. The experiments also show that a minimum surface roughness is reached soon after phase variations begin to take place and the variation in the surface roughness increases with increased part speed. Therefore, it is desirable to use part speeds slightly above those calculated by Equation (6) to obtain a minimum surface roughness with minimum surface variations.

NOSE RADIUS EFFECTS ON SURFACE DAMAGE

The nose radius of the grinding wheel plays a deterministic role in the amount of damage generated in a workpiece during grinding. Damage to the workpiece is generated when the localized chip thickness exceeds some critical value that depends on the geometry, wheel characteristics, machine characteristics, and material properties. The nose radius has a direct impact on chip area and therefore localized chip thickness. When the area removed per cut of the grinding wheel is increased, a larger number of grits come into contact with the workpiece. This causes the volume removed per grit to decrease which also causes less damage. This section examines the effects of the nose radius on damage generation both theoretically and experimentally.

Theoretical Nose Radius Effects On Chip Geometry

An example of the effect of the nose radius on chip geometry generated by the Contour Grinding Model is shown in Figure 6. This figure shows a top down view of a grinding simulation. The surface generated during grinding is at the bottom of the figure indicted by the small rectangular areas.

The grinding conditions for the two chips shown are identical except for the nose radii. The nose radius on Figure 6(a) is 50 mm while the nose radius on Figure 6(b) is 5 mm. Although the nose radii are different, the chip volumes removed in one revolution of the grinding wheel are the same and therefore the area and thickness of the two chips must be different. When calculated, the area of the chip with the 50 mm nose radius was found to be more than twice as large as the area of the chip with the 5 mm nose radius. This indicates that the 50 mm nose radius chip must have a smaller chip thickness. This is obvious when Figure 6 is examined. The chip in Figure 6(a) is approximately three times as long as the chip in Figure 6(b) in the crossfeed direction,

but the shape of the surfaces are similar. Therefore, the wheel with the 50 mm nose radius must pass over a single point on the surface many more times removing smaller amounts of material than the 5 mm nose radius chip. Because smaller amounts of material are removed by each pass of the grinding wheel with the 50 mm nose radius, the chip thickness of the material removed is smaller, leading to less fracture.

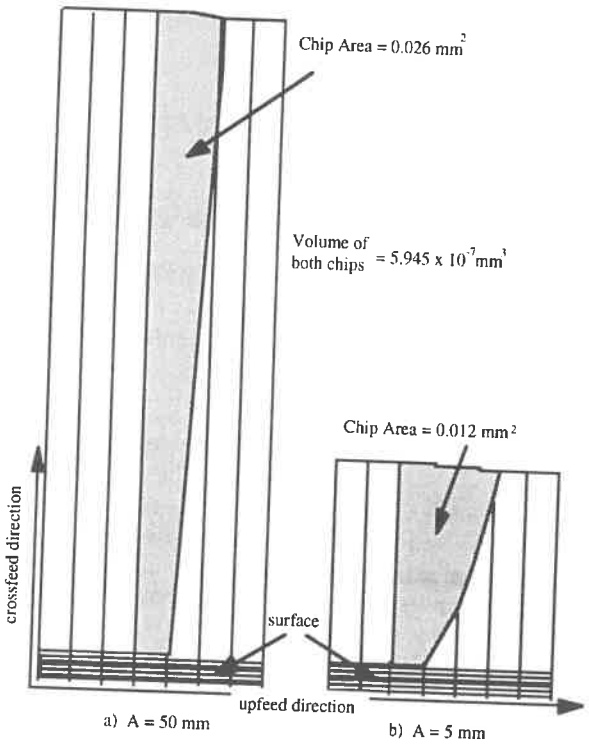
Chip Area = 0.026 mm²
Volume of both chips = 5.945 x 10⁻⁷mm³
Chip Area = 0.012 mm²
crossfeed direction
surface
upfeed direction
a) A = 50 mm
b) A = 5 mm

Figure 6: Top down view of grinding simulation. Grinding Conditions: R = 8.8 mm, D = 16 mm, Nw = 63000 rpm, Np = 30 rpm, cf = 0.149 mm/min, depth of cut = 5 μm

Experimental Verification of Nose Radius Effect on Damage Generation

Grinding experiments were used to verify the assumption of less fracture with a large nose radius. Two sets of grinding conditions were sought that differed only in wheel nose radius with one creating damage in the finished surface. Using the Contour Grinding Model, several grinding conditions were examined to find a suitable set of testing parameters. For the model to predict damage generation in the surface, a critical chip thickness and critical crack length were required. The workpiece material selected was BK-7 due to its well characterized properties and small critical chip thickness. From experiments performed by Miller [3], the critical chip thickness for a resin bonded wheel with 4 to 8 micron diamond grits and 100% concentration used on BK-7 is approximately 5 nm. A critical crack length of 4 times the critical chip thickness was used in the simulation. The results of these theoretical simulations are shown in Figure 7. The chip shape is shown on the left with the corresponding surface generated on the right. The size of the surface is three upfeeds by three crossfeeds and has been magnified for viewing purposes. The dark areas indicate fracture on that portion of the chip or surface. The grinding conditions used for the simulations are given in the figure caption. Small and large nose radii of 5 mm and 50 mm were used with varying part speeds of 5, 10, and 30 rpm in the simulations. In each case, the 5 mm nose radius chip is short and wide while the 50 mm nose radius chip is long and thin. This is a direct result of the different nose radii.

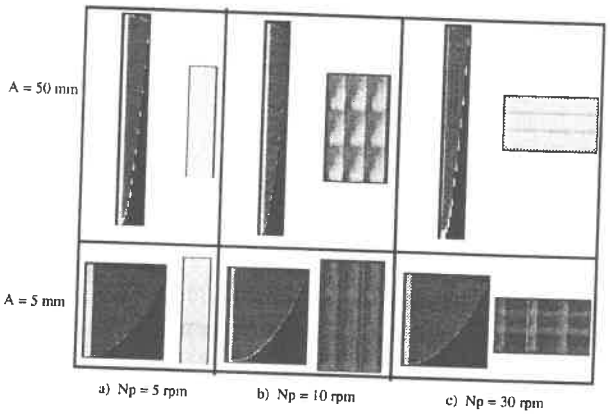

Figure 7: Damage generation simulations for BK-7. Grinding conditions: R = 8.8 mm, D = 16 mm, cf = 0.149 mm/min, Nw = 63000 rpm, depth of cut = 5 μm.

As seen in Figure 7, a large percentage of each chip is damaged. This indicates that the chip thickness in that region of the chip is greater than the critical chip thickness of BK-7. However, some of the surfaces created are damage free such as Figure 7(a). This is because the fracture was removed from the surface before the final cut. In Figure 7(b), the chips look approximately the same as in Figure 7(a), but in this case both surfaces produced in the simulation are fractured. In Figure 7(c), the chips are again similar to those for the previous part speeds, but the surfaces are very different. The surface generated with the 5 mm nose radius was completely fractured. The surface generated with the 50 mm nose radius was fracture free.

The theoretical surface roughness was also examined for this case to determine if any large variations were present. The theoretical surface roughness for the 5 mm nose radius was 2.433 nm and the 2.426 nm for the 50 mm nose radius. Since the theoretical surface

roughness measurements were similar, the surface roughness measured from the experiments should also be similar over small areas where large amounts of fracture are not present. These conditions provided an ideal test to determine if the model is accurate in its damage prediction for the different nose radii.

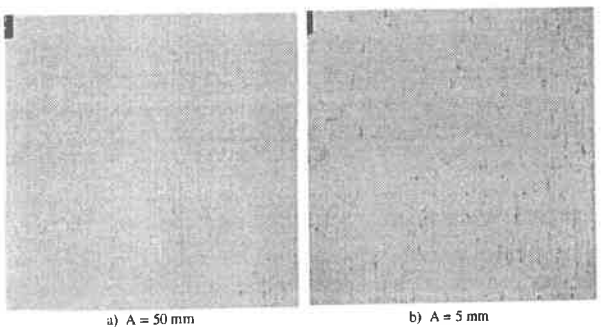

Figure 8: Damage generation experiments on BK-7. Grinding conditions: R = 8.8 mm, D = 16 mm, cf = 0.149 mm/min, Nw = 63000 rpm, Np = 30 rpm, depth of cut = 5 μm.

Using the grinding conditions specified in Figure 7 with a part speed of 30 rpm, two tests were performed on BK-7 with nose radii of 5 mm and 50 mm. The grinding wheel used in both cases was resin bonded with 4 to 8 micron diamond grits at 100% concentration. Before each test, the wheel was trued and dressed using a diamond nub and a dressing stick. Micro graphs of the two ground surfaces are shown in Figure 8. Figure 8(a) shows the surface developed from the 50 mm nose radius. Figure 8(b) shows the surface developed from the 5 mm nose radius. The surface roughness was measured for both surfaces to determine if any significant variation was present. The measured RMS surface roughness for the 50 mm nose radius was 8.8 nm. For the 5 mm nose radius, the RMS surface roughness was 10.1 nm. There was no significant difference in the surface roughness measurements, but a large difference in the amount of fracture on the surface of the material. Figure 8(a) has no apparent fracture, while Figure 8(b) shows several areas of surface fracture. These surfaces are significantly different considering that the nose radius was the only parameter changed.

CONCLUSION

Experiments have been conducted to verify the predictions of the Contour Grinding Model. Interrupted cutting tests were performed on Germanium to verify predictions of chip geometry. The results from these experiments show that the model does predict chip geometry in size, shape, and dimension using the once per revolution assumption. Further tests were then conducted on CVD Silicon Carbide to determine applicability of the Contour Grinding Model for surface roughness predictions. The model proved to be a valuable method for predicting surface roughness. A new method for predicting the part speed at which phase variations will effect the surface roughness was also developed. A final set of experiments were performed to determine if surface damage could be reduced using the Contour Grinding Model. The model was first used to find a set of conditions which produced similar surface roughness results but different surface fracture results by only changing the grinding wheel nose radius. Experiments were then performed on BK-7 using those grinding conditions. The results clearly show an improved surface with less damage using the optimized grinding conditions. These experiments have both verified the results of the Contour Grinding Model and shown its applicability to optimizing grinding conditions.

REFERENCES

[1] Storz, G.E., "Theoretical Modeling of Contour Grinding", MS Thesis, North Carolina State University (1994).

[2] Fawcett, S.C., "Development and Implementation of a Grinding Technique for Precision Finishing of Brittle Materials," Ph.D. Dissertation, North Carolina State University, 1991.

[3] Miller, M.H., "A Model for the Grinding of Brittle Materials," Ph.D. Dissertation, North Carolina State University, 1994.

EDGE CHIPPING AND GRINDING DAMAGE

S. Liang
Manufacturing Technology Inc., Ventura, CA
I. Marinescu
Kansas State University
Manhattan, KS

Introduction

Grinding is an important process, contributing a considerable percentage of machining cost in manufacturing industry. In row-slicing operation of thin-film magnetic head wafer industry, strict wafer cutting is realized with precise, rigid machines using thin diamond wheels. In Manufacturing Technology Inc., advanced machines with CNC and automatic vision alignment systems, such as the MSS-816 and NSS-612, are made and used to cut and to grind magnetic head wafers, various ceramics and glass. A variety of MTI/Norton wheels are employed to meet grinding operations with special requirements.

Grinding process removes material and creates surface finish and dimensional tolerance, however, grinding also generates damage in the workpiece, such as cracks and residual stress [1]. During grinding the physical interaction between the abrasive grits and the work material creates large, instantaneous mechanical stress and heat at the grinding zone. The material being ground will experience plastic deformation and localized failure in a scale dominated by the grinding parameters and the material properties. Grinding damage in the form of cracks is more often seen in brittle materials such as ceramics. In the thin film magnetic head wafer industry the quality of wafer-dicing process is carefully evaluated for edge chippage and cutting straightness. This is because large chipping increases the amount of material stock to be removed in the subsequent finish operations including lapping and finishing, resulting in a corresponding increase in cycle time and cost, and a reduction in yield. The chipping damage becomes a factor restricting the use of high feed rate for high production rate. Therefore, for a higher material rate, better finish and good product integrity, mechanism of grinding damage associated with the process parameters has to be fully understood. In this paper, edge chipping in grinding of silicon nitride has been investigated and the correlation between edge chip size and the grinding process parameters was studied and further, mechanism of grinding damage was explored.

Grinding Damage and Edge Chipping

Grinding process inevitably introduces damage to the workpieces. especially for ceramic materials.

Surface defects and edge chipping are the common damage in the ground workpieces. Fig. 1 shows schematically the formation of edge chipping during grinding and its relation to grinding process. Edge chipping is considered to be related with tensile stress and the associated crack nucleation and propagation. For ceramic materials grinding is predominantly a brittle fracture process associated with localized plastic deformation. The localized tensile stress, caused by mechanical interaction between the wheel grits and the material, and the grinding heat will cause crack nucleation and propagation around the grinding zone. In Fig. 1, edge chipping occurs when the crack growth reaches the side-face of the workpiece. In the dicing operation of magnetic head wafer edge chipping is also the results of excessive grinding stresses. The size of edge chipping is expected to be closely related to grinding intensity. When grinding intensity is high, large cracks can be generated due to high level of tensile stress, and the edge chipping will be severe. Therefore, the degree of edge chipping can represent the degree of grinding damage, i.e., the level of residual tensile stress and the extent of cracking [2]. To further understand the relationship between edge chipping and the grinding process experimental study was conducted and results are presented below.

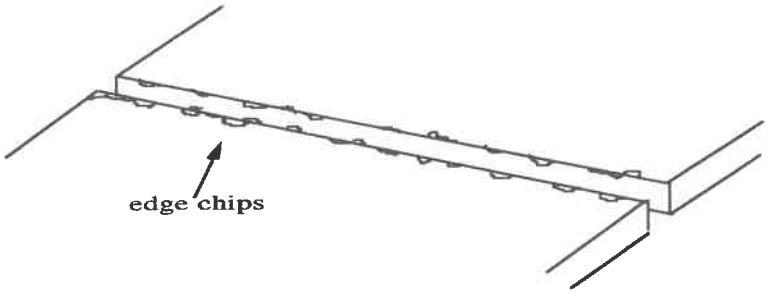

a) Edge chipping in row-slicing of magnetic head wafer.

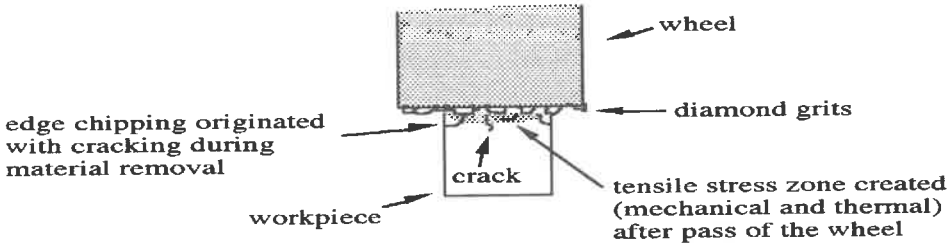
wheel
diamond grits
edge chipping originated with cracking during material removal
crack
tensile stress zone created (mechanical and thermal) after pass of the wheel
workpiece

b) Edge chipping and damage in surface grinding.

Fig. 1 Edge chipping and workpiece damage during grinding

Correlation of Edge Chipping with Grinding Parameters

Experimental investigation on the relation of grinding parameters to edge chipping was conducted. The degree of edge chipping is defined as the average chip length of the workpiece. Grinding tests were conducted on a MTI grinding machine. A resinoid bond diamond wheel was used with a wheel peripheral speed of 25.5 m/s. Reaction-bonded silicon nitride was used with a water soluble oil for coolant.

In Fig. 2 the effect of depth of cut on edge chip length (ECL) is shown. Within the range of depth of cut tested, it can be seen that ECL has the smallest value at the depth of cut of 3 mil. When the depth of cut decreases from this point ECL increases; if depth of cut increases, the ECL increases at first and then it decreases slowly. The relation of depth of cut to ECL seems to be contrary to expectation because increasing the depth of cut always causes large grinding forces as indicated in Fig. 3. The effect of table feed rate on edge chip length is shown in Fig. 4. Edge chip length increases in proportion to table feed rate. The variation of grinding forces with table feed rate is shown in Fig. 5. In Fig. 6 different grinding operations including creep feed grinding were also compared in terms of edge chipping. Grinding tests were conducted at the same material removal rate (Q_w'=0.47 in^3/in·min.) and ECL versus grit depth of cut for four different grinding conditions is shown. It is obvious that creep feed grinding generates the smallest edge chipping.

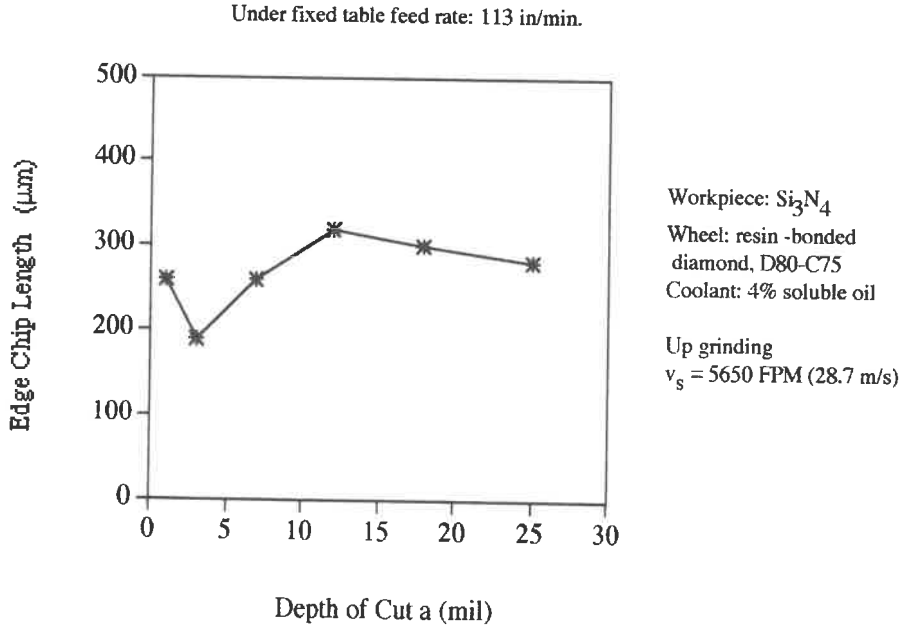

Fig. 2 Effect of depth of cut on the severity of edge chipping.

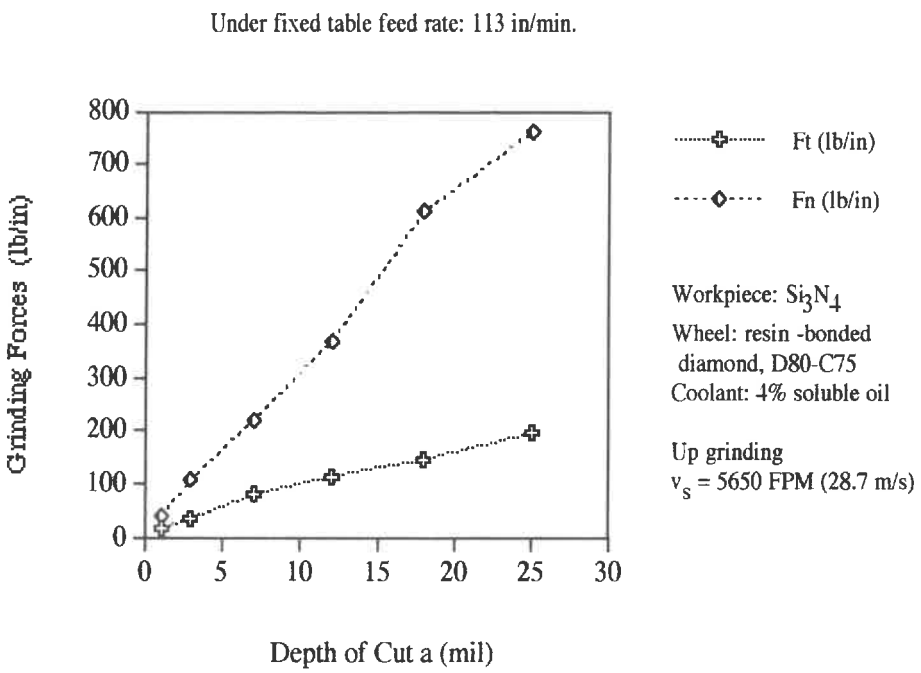

Fig. 3 Relationship between depth of cut and grinding forces.

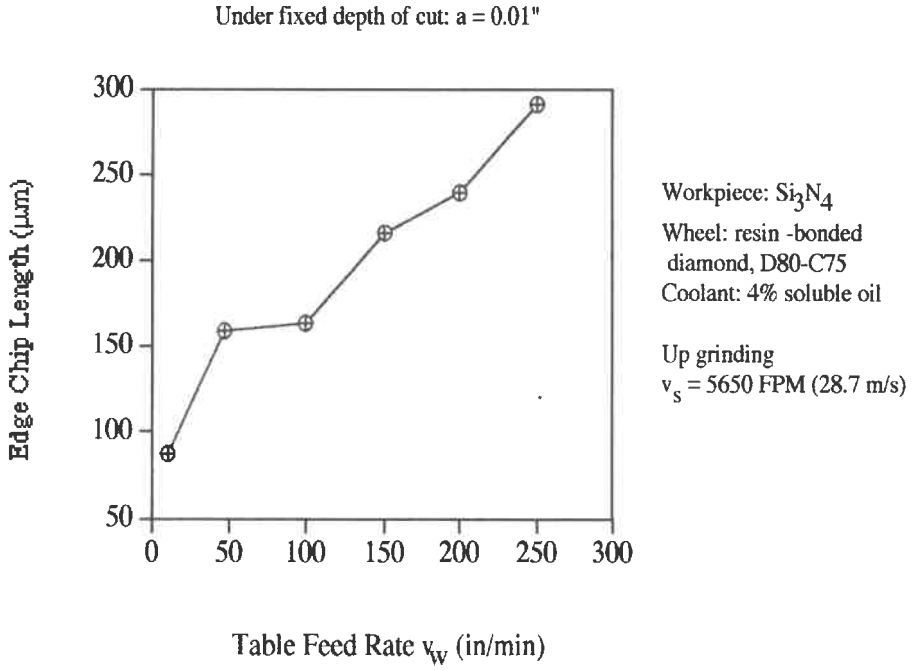

Fig. 4 Relationship between table feed rate and edge chipping.

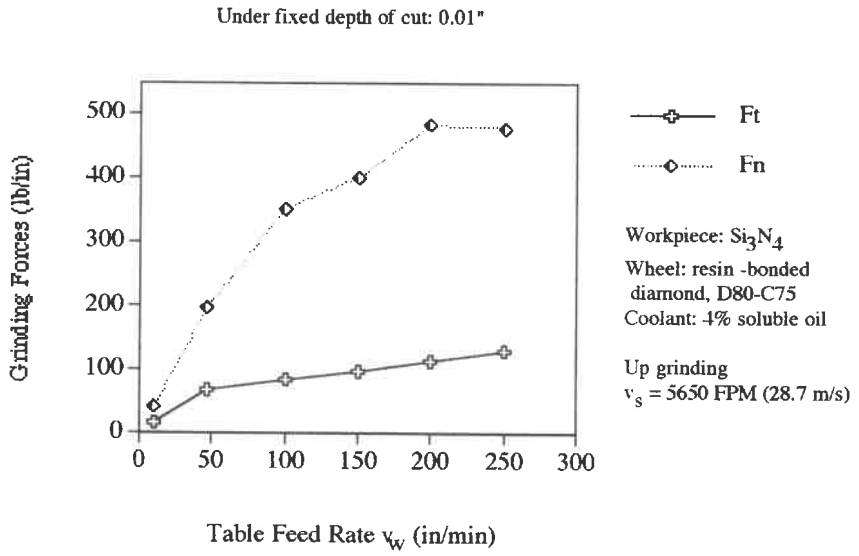

Fig. 5 Variation of grinding forces with table feed rate.

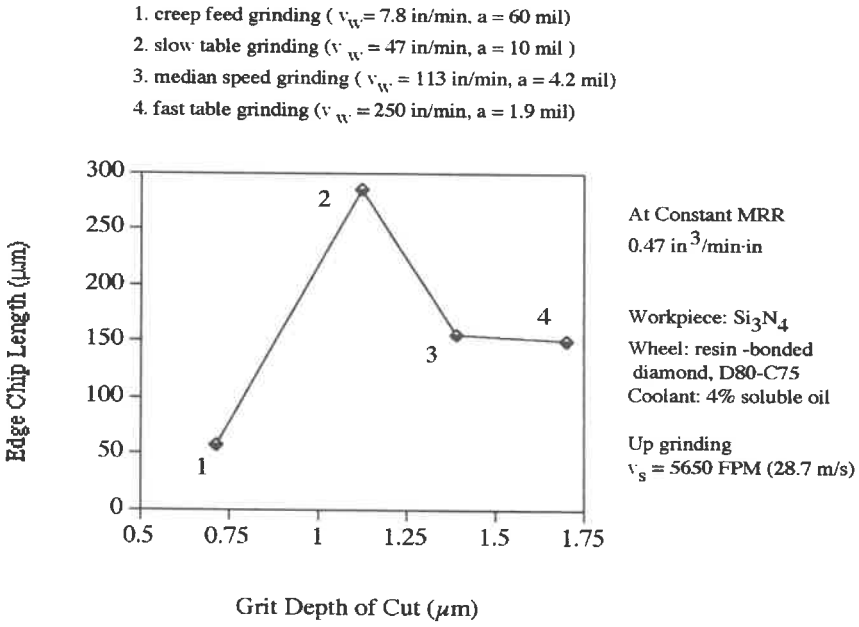

Fig. 6 Effect of grinding parameters on edge chipping.

Discussion and Conclusions

The preliminary study of the correlation of edge chipping with grinding process parameters has led to an important proposal of the relationship between grinding damage and grinding process parameters. As indicated in Fig. 2, large depth of cut implies high grinding intensity and generally leads to

rough grinding, but not necessarily to severe damage because grinding damage is the damage *induced in the ground workpiece*, not the damage that occurs along the grinding arc. Large depth of cut leads to large grit depth of cut, i.e., a large un-deformed chip thickness at the top of grinding arc. However, the intensity of grinding will vary along the grinding arc; the damage introduced by grinding is not simply related to the depth of cut, i.e., the intensity of grinding around the top of grinding arc. Thus, if the depth of cut is large, severe fracture or chipping may occur far above the finished surface, therefore, the effect of grinding on the ground surface could be less than with a small depth of cut. We believe that the proportion of brittle fracture to plastic deformation varies along the grinding arc, with the most brittle fracture occurring at the top of the arc. When the depth of cut is small, however, the effect of brittle fracture process on the ground surface will become prominent because of the very short grinding arc, i.e., it will occur close to the finished surface. Therefore, at constant table feed rate the depth of cut that may cause the least damage to a workpiece may be a value near the size of grinding-initiated macrocracks, as shown in Fig. 2. Compared Fig. 2 with Fig. 3 it can be seen that grinding forces would not simply reflect amount of damage introduced to the workpiece. In Fig. 4 edge chip length increases in proportion to table feed rate. This is expected because under fixed depth of cut, a higher table speed leads to a larger grit depth of cut, the grinding intensity at a fixed point along the grinding arc will increase correspondingly and, therefore, the damage in the ground workpiece will increase proportionally. Different grinding operations may cause different degree of grinding damage even under the same material removal rate, as the results shown in Fig. 6. Based on our analysis on the relationship of grinding damage with process parameters, it is reasonable that creep feed grinding has the smallest ECL because of the large depth of cut and small grit depth of cut. Comparing grinding cases 2, 3 and 4 in Fig. 6, under the same material removal rate the large edge chip length at a slower table feed rate may be linked to a higher temperature and thermal stress generated.

It may be concluded that

1. Grinding damage is determined by the mechanical and thermal influences in the ground surface and near-surface region, rather than simply by the grinding intensity.
2. The magnitude of grinding forces cannot represent the degree of grinding damage.
3. Edge chip size is a simple parameter which can be used to aid understanding the damage mechanism in ceramic grinding.

References

1. S. Malkin and J. E. Ritter, " Grinding Mechanisms and Strength Degradation for Ceramics," Winter Annual Meeting of ASME, Chicago, 1988, pp.57 - 72.

2. S. Liang, " Damage Assessment in Ceramic Grinding " Ph.D. Dissertation, University of Connecticut, 1995.

The Effect of Workpiece Modulation on Grinding Kinematics

M. H. Miller, K. S. Moon
Michigan Technological University

Introduction

Ductile regime grinding is an enabling technology in the manufacture of ceramic components because it produces accurate shapes deterministically and without fracture. However, the process requires very small chip thicknesses which limit material removal rates (MRR) and consequently economic viability. Many factors affect chip size including feedrate, wheel speed, and wheel characteristics. A purely geometric or kinematic view of the process (which neglects important effects like strain rate, temperature, grit sharpness) suggests that to improve material removal rates, more grits must remove a given volume of material at a faster rate. Optimizing feedrate, wheel speed, and wheel characteristics can provide only incremental improvements in MRR. New techniques that can provide order of magnitude improvements are needed.

This paper investigates a new approach for engaging more grits in the cutting process and thereby improving MRR: workpiece modulation. Experiments and simulations at Michigan Tech have shown that high frequency modulation transverse to the cutting direction reduces roughness in the surface grinding of metals. That work has recently been expanded to look at the effect of modulation on grit chip size. A reduction in chip size for a given feedrate and depth of cut would improve the grinding of ceramics.

The wheel/work interface for the surface grinding geometry shown in Figure 1 was modeled from a kinematic perspective [1,2]. The purpose of the modeling process is to identify a range of amplitudes and frequencies which provide significant chip size reduction. Based on the required amplitudes and frequencies, the feasibility of implementation could be evaluated.

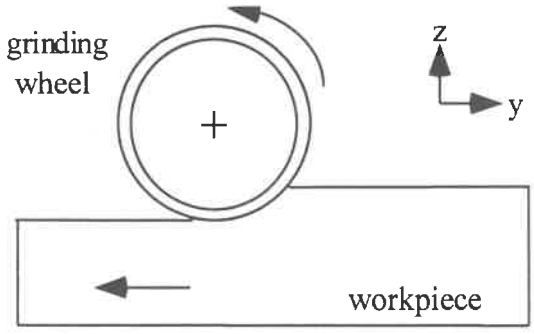

Figure 1: Surface grinding geometry; modulation is applied in the X direction

Simulation Description

In the simulation the workpiece is represented by a grid in the X-Y plane. Before grinding begins, the Z coordinate of each grid point is 0. Spherical grits are randomly distributed in three dimensions about the periphery of the grinding wheel. As the wheel rotates and workpiece feeds, each grit is checked for interference with the workpiece grid. When interference occurs, the Z coordinate of the affected grid point is modified. The thickness and area for a particular X-Z plane slice of a chip are as shown in Figure 2. The volume of the chip is calculated as the sum of the cross-sectional areas times the Y direction grid spacing. Of all the X-Z plane slices that compose one chip, the maximum slice area is saved as the chip area. The maximum thickness is saved as the chip thickness.

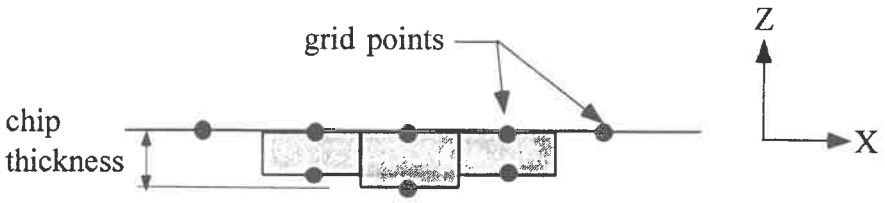

Figure 2: Thickness and area of an X-Z plane slice of a chip; the shaded area approximates the chip area

Simulation results

Figure 3 shows an example of a surface created with the simulation. In this test the wheel rotated at 500 rad/sec (4775 rpm) and the workpiece fed at 1 mm/sec. The 5 μm depth of cut is evident from the figure. The signature of the individual cutting grits can be clearly seen. Figure 4 shows a surface generated under the same conditions except with the addition of workpiece modulation in the X direction at an amplitude of 10 μm and frequency of 25,000 rad/sec. For this example the workpiece modulates 25000/500 or 50 times per wheel revolution. However, each cutting grit is in contact with the work for only about 2.6 degrees of its circular arc. Therefore, within the contact zone each grit modulates only a fraction of a cycle (50x2.6/360=0.36).

A series of simulations across a range of modulation amplitudes and frequencies were conducted. Figure 5 shows that the number of cutting grits increases with modulation frequency--a positive result. However, as shown in Figure 6, the chip thickness from the same simulation trials does not decrease with frequency as hoped. In fact, it increases slightly.

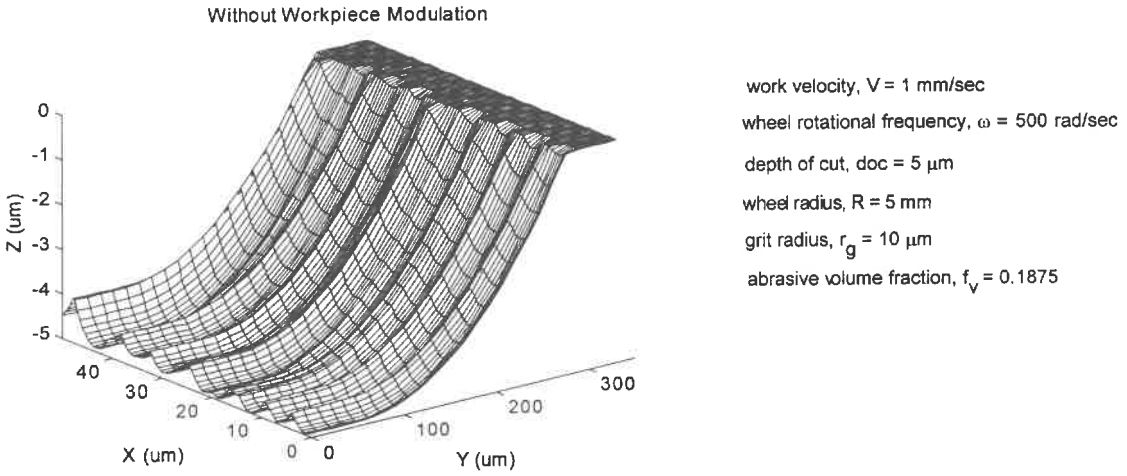

Figure 3: Simulated surface without workpiece modulation after five wheel revolutions

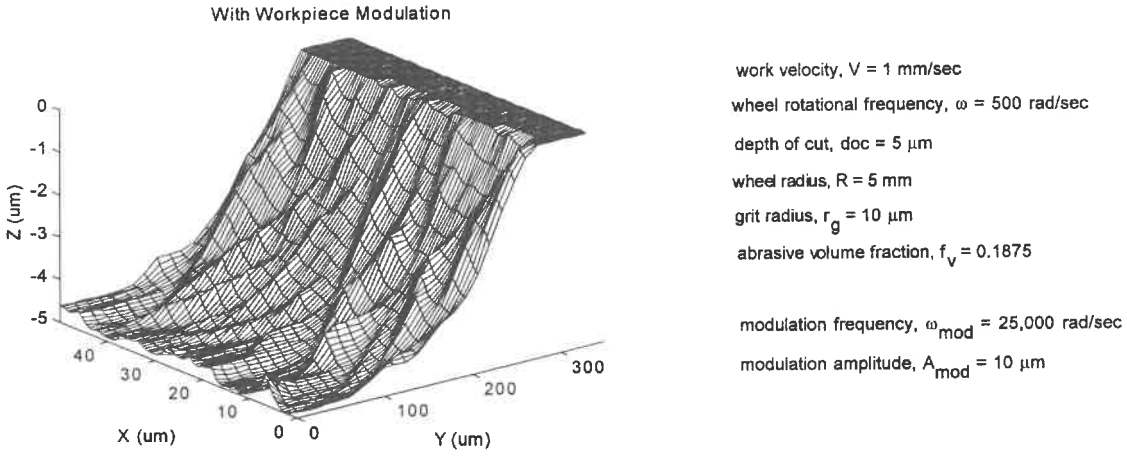

Figure 4: Simulated surface with workpiece modulation in the X direction

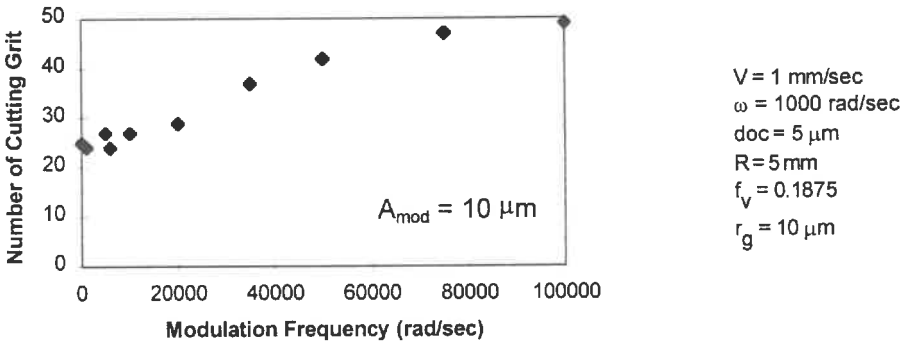

Figure 5: Number of cutting grits per wheel revolution for integer ω_{mod}/ω

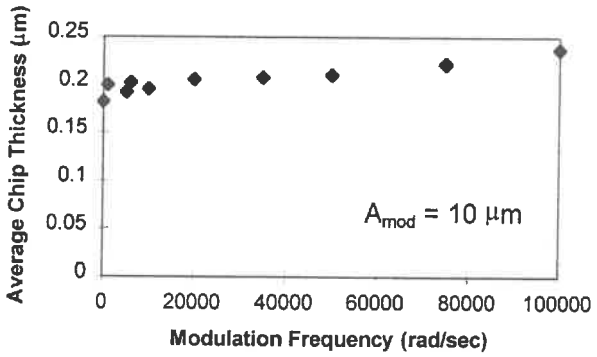

Figure 6: Average maximum chip thickness for integer ω_{mod}/ω

Figures 7 and 8 show two other measures of chip size--average maximum cross-sectional area and average volume. The average chip area remains fairly constant while the volume decreases with increasing frequency. The decrease in volume makes sense as the volume per chip should be approximately inversely proportional to the number of cutting grits.

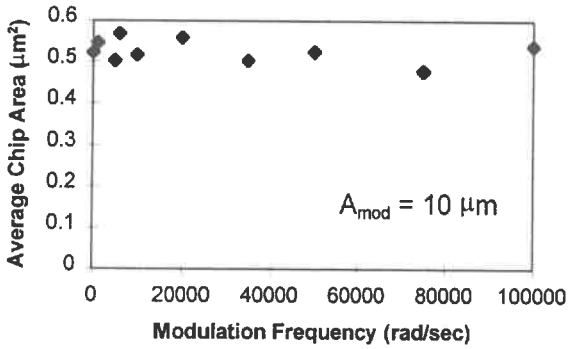

Figure 7: Average maximum chip area for integer ω_{mod}/ω

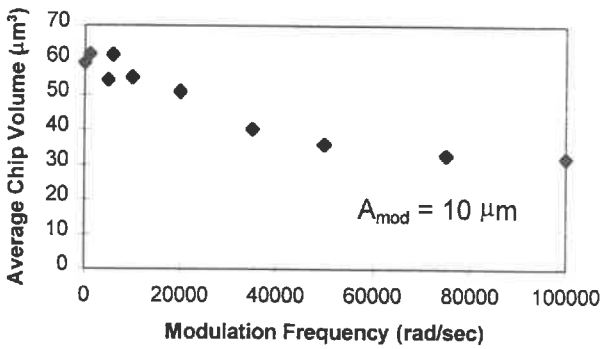

Figure 8: Average chip volume integer ω_{mod}/ω

Figures 5 through 8 present results for trials in which the modulation frequency is an integer multiple of the wheel rotation frequency. Under that condition the path of an individual cutting grit repeats itself in the successive revolutions. When the modulation frequency is not an integer multiple of the wheel frequency, the direction of a grit's cutting path changes with each revolution. The multiple path directions have a positive effect on surface roughness but a negative effect on chip thickness. Figure 9 is a plot of root mean square roughness for modulation frequencies ranging from 50,000 to 51,000 rad/sec and for a wheel speed of 1000 rad/sec. Figure 10 is the corresponding plot for

average chip thickness. The in-phase cutter paths at 50,000 and 51,000 rad/sec produce a high roughness but a small chip thickness. Out-of-phase paths (for all the frequencies in-between) produce lower roughness but larger chip thickness. The effect of phase on chip thickness and roughness is similar to that exhibited in contour grinding (in which the ratio of wheel and work rotational frequencies determine the phase) [3,4].

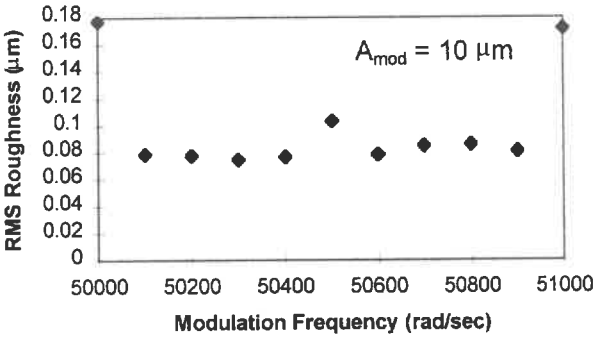

Figure 9: Surface roughness for ω_{mod}/ω ranging from 50 to 51

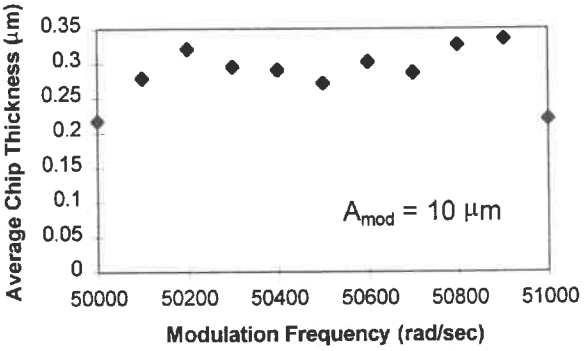

Figure 10: Average chip thickness for ω_{mod}/ω ranging from 50 to 51

The effect of modulation amplitude was also examined. Figure 11 indicates that the modulation amplitude does not have a significant effect on chip thickness. The area and volume results are similar.

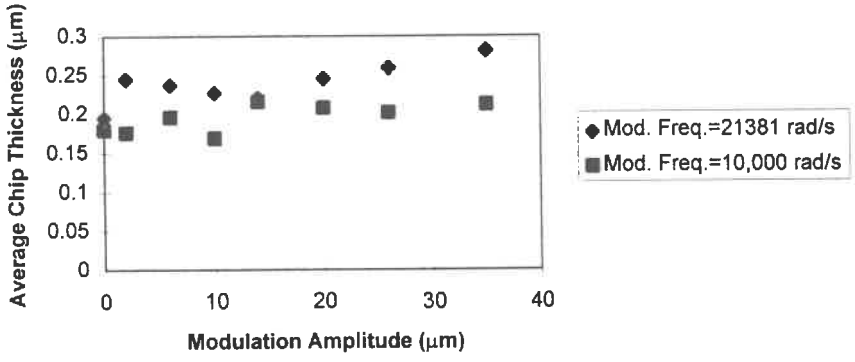

Figure 11: Effect of modulation amplitude on chip thickness for the same conditions as listed in Figure 5

Conclusions

The introduction of modulation does not have the hoped for effect of reducing chip thickness. Under certain conditions (ω_{mod}/ω = integer), it does reduce chip volume. It is unknown if chip volume reduction without chip thickness reduction would promote

ductile grinding. The results presented here support earlier findings that modulation decreases surface roughness. The importance of phase and ω_{mod}/ω ratio to the roughness reduction is a new finding that requires further study.

References

[1] Miller, M. H., "A Model for the Grinding of Brittle Materials," *PhD Dissertation*, N. C. State University, 1994.

[2] Domala, K. V., E. J. Salisbury, K. S. Moon and J. W. Sutherland, "A Three-Dimensional Geometric Model for the Surface Texture Generated by a Single Pass of the Wheel in a Surface Grinding Process, *Proceedings of the Symposium on Material Removal and Surface Modification Issues in Machining Processes*, ASME IMECE, 1995.

[3] Fawcett, S. C. and T. A. Dow, "Influence of wheel speed on surface finish and chip geometry in precision contour grinding," *Precision Engineering*, Vol. 14, No. 3, pp. 160-167, 1994.

[4] Storz, G. E. and T. A. Dow, "A Practical Guide to Theoretical Modeling of Contour Grinding," *Proceedings of the 1994 ASPE Annual Meeting*, pp. 420-423.

SURFACE INTEGRITY IN GRINDING OF CERAMICS

Bi Zhang
Department of Mechanical Engineering
Precision Manufacturing Center
University of Connecticut
Storrs, CT 06269, USA

ABSTRACT

Grinding experiments are conducted on advanced ceramics using the diamond wheels with different grit sizes. Surface integrity of ground samples is assessed using damage inspection techniques incorporating scanning electron microscopy. Subsurface damage is identified as material pulverization in the superficial layers forming a powder regime and crack/void generation in the subsurface layers. Both powder regime layer and crack/void layer are characterized with respect to the types of ceramic materials, and the grit sizes of the wheels. The mechanism of crack/void nucleation and development is discussed.

INTRODUCTION

Grinding using a diamond wheel is an inherently damaging process to ceramics since an abrasive grain is forced into the surface of ceramics. It is not surprising that a grinding operation causes a strength decrease to a machined component, an effect frequently reported in the literature. In the grinding of ceramics, material-removal can take place based on such mechanisms as crushing, chipping or fracture, pulverization, and plastic deformation. In dealing with a precision grinding process, where the depth of cut is normally in a submicron range, crushing and chipping mechanisms can be excluded from this list. Material pulverization occurs when ceramic grains sized in micrometers are pulverized during grinding into finer grains in submicron range or even smaller. Pulverization can occur along the cleavage planes and slip systems of a ceramic grain, leading to the formation of a large number of finer grains. More surfaces and a larger specific surface area are thereby generated. The residual surface and subsurface damage of a ground component may seriously alter its surface properties, and cause a strength degradation or even a catastrophic failure. The exact nature, the manner and the penetration depth of grinding induced damage are, however, still not clear, leaving many uncertainties and sometimes danger in using ceramics as structural materials.

Due to the lack of an established damage inspection technique, grinding induced damage is very often assessed by the surface inspection techniques such as SEM and surface profilometry. These techniques have been proven to be good and simple in certain applications. However, they may sometimes lead to an erroneous assessment on a ground component. Zhang [1988] demonstrated that a ceramic sample ground to a smooth surface could be left with subsurface damage such as crack/voids. Pfeiffer and Hollstein [1993] also reported that a silicon nitride sample ground with a surface roughness of $R_z = 11.5\,\mu m$ had

a residual bending strength of 587 MPa, while another with $R_z = 7.9\ \mu m$ had 552 MPa. This implies that subsurface damage and residual strength are not always reflected only by the outside appearance as to whether a ground surface is rough or smooth. Instead, they should be reflected by both surface and subsurface conditions.

Damage inspection techniques are used in this experimental study to assess subsurface damage in grinding of ceramics. This paper presents results of assessment and measurements of subsurface damage of the ceramics ground by metal bond diamond wheels. Furthermore, mechanisms of damage nucleation and development are discussed.

EXPERIMENTAL PROCEDURES

Polycrystalline silicon nitride, alumina, zirconia, and silicon carbide were used as sample materials for this investigation. Silicon nitride and alumina were prepared using a hot-press, while zirconia and silicon carbide were commercial products prepared by the slip-cast and the pressureless sintering techniques, respectively. The zirconia was partially stabilized containing a certain amount of the metastable tetragonal modification that could transform into the monoclinic form at an elevated temperature or under a high level stress field. Ceramic specimens were sliced into bars with dimensions of 5×5×30 mm. Three rectangular surfaces of each specimen were polished with a diamond paste of 15 μm to remove possible damage induced by the previous procedures. The non-polished rectangular surface was bonded to the surface of a steel holder with the araldite adhesive.

Grinding experiments were performed on a grinding machine having an aerostatic spindle and slideway. A Heidenhain linear encoder was used to control the wheel depth of cut at a resolution level of 0.5 μm. Metal bond diamond wheels with blocky grits (#80, #140, and #400 of MBG-II type made by GE) were used in the investigation. The diamond wheels had an outside diameter of 125 mm, a bore diameter of 50.8 mm, a width of 10 mm and a grit layer thickness of 2 mm. Grinding was performed at a wheel surface speed of 1,600 m/min, a table speed of 1.4 m/min, a wheel depth of cut of 15 μm, and a grinding width of 5 mm. Water-based grinding coolant was used. No cross feed was given, and no spark-out or further surface treatment was conducted.

Truing of the wheels was performed by a cup type diamond wheel SD140-P100M-30, and dressing by an alumina stick WA150G10V. The truing was conducted at a grinding wheel speed of 400 m/min, a truer speed of 60 m/min, a table cross feed of 0.1 mm per truer revolution, and truing feedrates of 3 μm/stroke and 1 μm/stroke. The dressing was done at a grinding wheel speed of 400 m/min with a cumulative amount of dresser removal of 2 mm each time. In order to stabilize the wheel surface grits after truing and dressing, each wheel performed grinding on a zirconia block (5×11.5×80 mm) at a wheel depth of cut of 10 μm to a cumulative removal of 6 mm in thickness. After grinding, each sample was inspected in both its cross-section and its subsurface parallel to the ground surface by the etching, taper polishing and fracture techniques for subsurface damage information [Zhang, 1988]. Lapping with diamond pastes of 6, 1, and 0.25 μm was employed to expose the subsurface of each sample.

RESULTS

Pulverization was observed on the superficial surface layers of the ground samples. Pulverization is a consequence of intergranular and/or transgranular micro-cracking due to a localized stress field of shear stresses superimposed by hydrostatic compressive stresses induced by abrasive grits in grinding. Ceramic grains are fractured into finer ones by a pulverization process. Pulverization was observed using transmission electron microscopy and SEM on ground

samples. The thickness of a powder regime layer had a non-uniform distribution across the ground surface of a sample. The etching technique was used in aid of the investigation of the thickness variations of powder regime layers with respect to the wheel grit sizes. The investigation was performed by measuring the changes of a ground surface subjected to etching in reference to that before being etched. Due to the non-uniform thickness distribution of a powder regime layer across a ground surface, the measurement was conducted along a cross-section of 500 μm in width. The 500 μm measurement region was then divided into 10 identical parts, each having a width of 50 μm. The maximum thickness, the minimum thickness, and the ten-point average of the powder regime layer were obtained from the measurement and are plotted in Fig. 1. For silicon nitride and alumina, the thicknesses of powder regime layers were the largest in using the SD80-N50M wheel, and followed by that in using the SD140-N75M wheel. The SD400-N75M wheel generated the least powder regime as compared to those by other diamond wheels. The SD80-N50M wheel produced a powder regime layer on a material such as alumina of an average thickness over 6 μm while the SD400-N75M wheel produced that of less than 2 μm. The experimental results suggested that a grinding wheel of a larger grit size generates more amount of powder regime than does that of a smaller grit size. The powder regime generated by the diamond wheel with an average grit size of 230 μm was more than three times of that by the wheel with an average grit size of 40 μm. Accordingly, the number of the active cutting points per unit area of the SD400-N75M wheel was 5-6 times that of the SD80-N50M wheel, resulting in a large difference in the grit depth of cut. The grit depth of cut for the SD400-N75M wheel was less one-third of that for the SD80-N50M wheel. The larger the grit depth of cut a wheel has, the more is the powder regime, and vice versa.

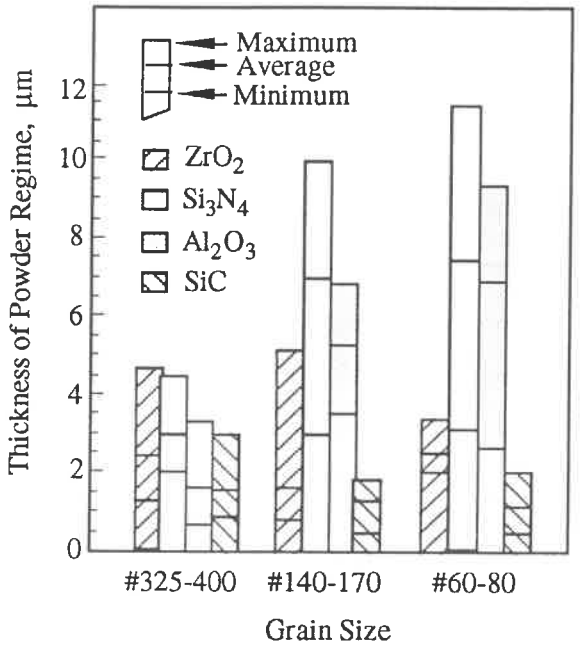

Fig. 1 Thickness variations of powder regime layers of various ceramics with grit size of the wheels.

When a diamond wheel was used on different ceramic samples, the amount of powder regime generated on the silicon nitride sample was the largest which was followed by the alumina and zirconia samples. Silicon carbide generated the least amount of powder regime. This result suggests that hardness and fracture toughness should play a significant role on pulverization of ceramics, and retention of the pulverized grains. Due to its high hardness and low toughness, silicon carbide, among other materials tested, exhibited severe chippings on its ground surfaces. The chipping level increased with the grit size of the wheels used. It was chipping that carried away most part of the powder regime layers. In contrast, silicon nitride and alumina had a lower hardness, and a higher toughness. The chipping levels on these materials were not as high as that in grinding silicon carbide. The powder regime layers, if generated, were mostly retained on the ground surface.

The grit size of the diamond wheels did not give a large effect on the thickness of powder regime layer on the silicon carbide and zirconia

samples. The average thickness of powder regime layer was around 1.5-2.0 μm for silicon carbide, and 2.0 μm for zirconia. Although the zirconia sample had the lowest hardness and the largest toughness among these ceramics, no large amount of powder regime was generated on the ground surface of this material. This might be due to the fact that zirconia was a partially stabilized material, it contained a certain amount of the metastable tetragonal modification which could transform into the monoclinic form. The phase transformation would result in a high fracture toughness, and bestows an excellent resistance to pulverization and crack initiation.

To quantitatively evaluate the effect of grit size on the subsurface crack/void formation, the ground surfaces of all the ceramic samples were inspected using SEM in aid of the etching technique. Both clustered and scattered crack/voids were identified in the subsurfaces of silicon nitride, alumina, and zirconia samples while mainly scattered crack/voids in silicon carbide. These clustered crack/voids aligned themselves in the grinding direction. The crack/void density decreases with an increase of the depth of subsurface layer, with the densest distribution close to the powder regime layer of the ground surface. The size of the crack/voids were about 1 μm in diameter. The SEM observations indicated that whether clustered crack/voids or scattered crack/voids form depends on the properties of ceramics, specifically, hardness and fracture toughness. A material with a large hardness and a low toughness, e.g., silicon carbide, tends to have more amount of scattered crack/voids than clustered ones, while on the other hand, a material having a low hardness and a large toughness, e.g., silicon nitride, tends to have more amount of clustered crack/voids than scattered ones. With a diamond wheel with a fine grit size, only scattered crack/voids were observed in the subsurfaces of the ceramics. The scattered crack/voids had a fairly uniform distribution across the subsurfaces of all the samples. As the grit size decreases, the number of active cutting points per unit area on a grinding wheel surface increases, which in turn results in a uniform distribution of the active cutting points, and a decrease in spacing between these active cutting points. In consequence, it is more difficult for cluster crack/voids to be generated.

The maximum depth of crack/voids was quantitatively measured with respect to the grit size of the diamond wheels used. Fig. 2 provides the measurement results on the depth of crack/voids across an area of 500×500 μm of lapped samples. In using the SD80-N50M wheel, silicon nitride showed the largest depth of crack/voids which was around 40 μm. This was then followed by alumina, zirconia and silicon carbide. The same trend was observed in using the SD140-N75M wheel. However, silicon carbide had a larger depth than zirconia did in using the SD400-N75M wheel. On the other hand, as the grit size decreased, the maximum crack/void depth decreased, but the rate of decrease was different among the ceramics. There were two categories of materials in terms of crack/void penetration depth, with silicon nitride and alumina being the first category, zirconia and silicon carbide the second category. The maximum crack/void depth of the ceramics in the first category showed a larger rate of decrease than that showed by the ones in the second category. There was a little decrease of the maximum crack/void depth for the ceramics in the second category as the grit size decreased. This was especially true for silicon carbide. It can be addressed to the reason that hardness and fracture toughness are the major factors governing the penetration depth of crack/voids. The results shown in Fig. 2 suggest that a relatively coarse wheel should induce almost the same level of subsurface damage as a fine wheel does in a material with a relatively large value of brittleness, whereas, a relatively coarse wheel should induce a higher level of

subsurface damage than a fine wheel does on a material with a relatively low value of brittleness. In other words, it does not make a difference in a sample surface integrity whether a rough or a fine grinding conditions are used on a relatively brittle material; however, it does make a difference on a relatively less brittle material.

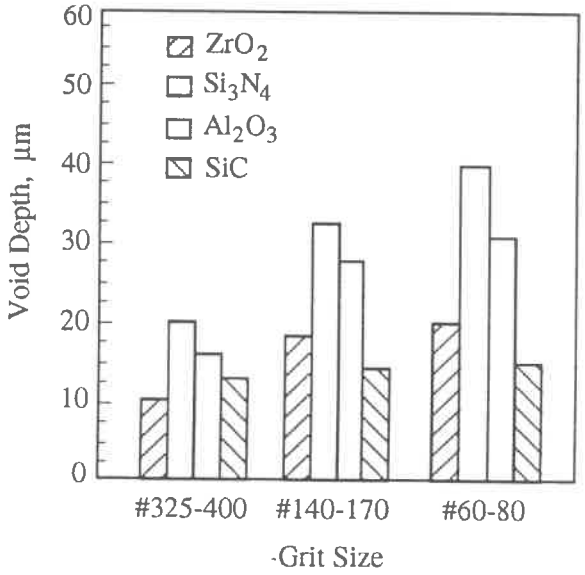

Fig. 2 Variations of the maximum depth of crack/voids with grit size of the wheels in grinding of various ceramics.

DISCUSSION

It is likely that crack/voids, specifically clustered crack/voids, give an influence on the residual strength of a ground component. However, the nature of crack/void formation needs to be discussed. Hagan [1979] claimed that voids are formed by grain boundary slippage in an indentation process. Shear stresses, rather than tensile stresses, are responsible for the dislocation movement. In dealing with the nucleation mechanisms of cracks induced by indentation, Lawn extended the original dislocation pile-up models developed by Zener, Stroh, Cottrell, *et al.* principally in the context of metals to both the ionic and the covalent ceramics [Lawn, 1993]. An assumption was given that stress is concentrated at the edge of a shear-activated dislocation array due to the primary slip systems. The dislocation array is constrained for further progress to form dislocation pile-up by a certain internal microstructural barrier, such as a second-phase particle, grain boundary, microtwin, etc. The dislocation pile-up then initiates a crack/void at the internal microstructural barrier. A crack nucleation model was then proposed by Lawn based on dislocation pile-up and barrier parameters. It is considered to be an appropriate model for the description of nucleation of crack/voids. Referring to Fig. 3, from a dislocation source S, edge dislocation loops are generated by the resolved shear stress on a slip plane. These dislocations pile up against the barriers B and B' with a distance d apart. The dislocation pile-up exerts a driving force on the barriers B and B' and causes nucleation of a crack/void at the barrier B.

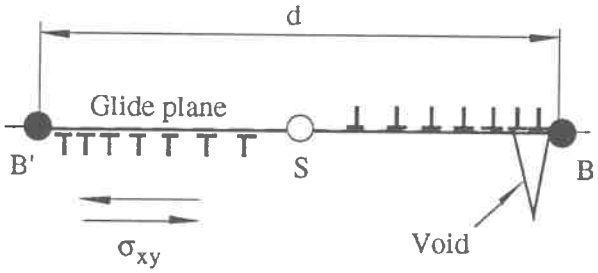

Fig. 3 Nucleation of a crack/void by dislocation pile-up. Under shear stress σ_{xy}, the dislocation source S generates dislocation loops which pile-up at barriers B, B' in glide plane. Stress concentration at barrier B nucleates the crack/void. [Lawn, 1993]

It is understood that the resolved shear stress varies with the distance from the sample surface. The shear stress decreases as the distance increases. When the value of the shear stress becomes smaller than the yield shear strength of the ceramic sample, the distance reaches a limit where a dislocation array of the primary slip systems is no longer able to form a dislocation pile-up large enough to initiate a crack/void. It was observed in Fig.

3 that the value of the distance varied with material properties, specifically hardness and fracture toughness of a ceramic sample. On the other hand, as the value of the shear stress increases, the secondary slip systems may be activated by the shear stress. The increased numbers of active slip systems would result in a larger density of dislocation pile-ups, and thus a larger density of crack/voids. This explains that experimental facts that the crack/voids had a high density near the sample surface, but a low density away from the surface.

It appears that the hardness and fracture toughness of a sample are the dominant factors determining whether a fracture is in the form of a small number of relatively large crack/voids (in the case of silicon nitride and alumina) or a large number of small crack/voids (in the case of silicon carbide). The former case may be interpreted as that the energy given by an abrasive grit into a sample is dissipated in a concentrated manner, while the latter case in a distributed manner. In the latter case, crack/voids may be nucleated at a low level of dislocation pile-ups due to the brittle nature of the material. As a consequence, this would relax the shear stress at a relatively short range, resulting in microcracks in a small dimension but a large number. In the latter case, the lower brittleness nature of the materials would bring a dislocation pile-up to a higher level before a crack/void could be nucleated. The shear stress would not be released until a certain level of stress concentration could be reached, which results in a stress relaxation at a relatively long range. This process would result in microcracks in a large size but a small number.

CONCLUSIONS

Based on the subsurface assessment of ground ceramics, the following points can be declared:

- Two types of subsurface damage are identified: powder regime in the superficial layer, and crack/voids in the subsurface of a ground sample.
- The penetration depth of crack/voids is related to the hardness and fracture toughness of a sample . A smaller depth is found on a sample with a lower hardness and a larger toughness, while a larger depth on those with a higher hardness and lower toughness.
- The penetration depth of crack/voids varies with the grit size of the wheels. A larger depth is found in a sample ground with a wheel of a larger grit size, and vice versa.
- Two types of grinding induced crack/voids are identified, clustered and scattered. The diamond wheel with the smallest grit size does not generate any clustered crack/voids in any of the samples.
- A sample having both clustered and scattered voids has a larger crack/void penetration than does the one only having scattered crack/voids.

REFERENCES

Zhang, B., "Study on Surface Integrity of Advanced Ceramics Ground by Diamonds," Ph.D. dissertation, Tokyo Institute of Technology, Japan, March 1988.

Pfeiffer, W., T. Hollstein, "Damage Determination and Strength Prediction of Machined Ceramics by X-Ray Diffraction Techniques," from "Machining of Advanced Materials," edited by S. Jahanmir, National Institute of Standards and Technology SP 847, (Government Printing Office, Washington, D.C., 1993), pp.235-245.

Hagan, J.T., "Nucleation of Median and Lateral Cracks around Vickers Indentation in Soda-Lime Glass," from "The Science of Ceramic Machining and Surface Finishing II," edited by B.J. Hockey and R.W. Rice, National Bureau of Standards SP 562, (Government Printing Office, Washington, D.C., 1979), pp.15-21.

Lawn, B.R., "Fracture of Brittle Solids - Second Edition," Cambridge University Press, 1993, pp. 249-319.

SUBSURFACE MICROSTRUCTURE IN NANOGROUND AND NANOTURNED SILICON

K. E. Puttick, L. C. Whitmore, C. Jeynes
University of Surrey, Guildford, Surrey GU2 5XH, UK
and A. E. Gee
Cranfield University, Cranfield, Bedford MK43 0AL, UK

1. Introduction

The results of an initial study of the subsurface damage induced in silicon single crystals by ductile machining were included in a paper presented to the Spring Topical Meeting in Tucson three years ago (Puttick 1993) and elaborated in Puttick et al (1994). It was concluded from observations by electron microscopy (TEM) and Rutherford ion backscattering (RBS) that the damage consisted principally of a dislocated layer a few hundred nanometres deep, together with occasional submicron cracks and amorphous patches in the ground specimens. This paper describes more detailed microphysical and microchemical studies of the upper layers of damage.

2. Experimental

Materials and machining procedure were as described in Puttick et al (1994): silicon substrates were machined by grinding on the Cranfield seven-axis grinder using the minimal nominal cut depth of 0.5 μm and deionized water as the coolant. Ductile turning was achieved on the dedicated single point diamond turning (SPDT) facility developed by Puttick et al and by Gee et al (1988, 1989) without coolant. Machined surfaces were examined by atomic force microscopy (AFM), by X-ray photoelectron spectroscopy, and by TEM and RBS.

3. Results

3.1 AFM profiles

Profiles were taken by a Nanoscope II atomic force microscope. Details are given by Puttick et al (1995): the main topographical parameters are summarized in Table I.

Table I Roughness of nanomachined silicon (nm)

	SPDT	Resin bonded wheel ground	Metal bonded wheel ground
R_a	0.7	7.4	21
R_{max}	5.8	64	148

We believe that these represent much more accurate and reliable values of roughness than those previously measured by conventional profilometry, though it must be remembered that the scan length in AFM is inevitably much shorter than those attainable with instruments such as the Talysurf.

3.2 XPS survey

Fig 1(a) illustrates the energy spectrum obtained by XPS from the surface of an as-received wafer. The number of counts detected by the electron spectrometer are plotted against the binding energy calculated from the measured kinetic energy of the emitted electron, so that sharply defined peaks are seen at values corresponding to particular quantum states of inner shell electrons of any atoms present. This spectrum shows the expected cleanness of the surface, with the only peaks apart from silicon denoting the presence of the usual thin oxide film and a small amount of carbon deposited from hydrocarbons present in the specimen chamber.

Fig 1(b) represents the spectrum from the surface ground with a metal bonded wheel, showing a significant increase in the oxygen and carbon 1s peak and a small nitrogen line. Fig 1(c), from the surface ground with a resin bonded wheel, on the other hand, displays significant evidence of contamination by sodium and fluorine in addition to carbon and oxygen.

Finally, Fig 1(d) is a comparable spectrum from a SPDT surface, where the salient peaks correspond to enhanced levels of oxygen and carbon only.

It is possible to deduce from these results a value for the thickness of the oxide overlayer, as set out in Table II.

Table II Oxide layer thickness (nm)

Metal Bond Wheel	Resin Bond Wheel	SPDT
0.93	1.28	1.4

There is, however, some evidence from the RBS data (see below) that these values may be dependent on machining conditions, especially (for SPDT) on the shape of the diamond tool.

3.3 Electron microscopy

The XTEM observations reported in 1993 (see also Puttick et al 1994) recognized dislocations as the main defects induced by nanomachining, together with (in the case of grinding) occasional subsurface cracks and patches of amorphous silicon. More recent work, however, has demonstrated that amorphous material is present on all types of machined or polished surfaces, and may have important practical consequences, particularly in optical components. (Whitmore et al 1994, Puttick et al 1995). The main conclusions are:

(i) Polished surfaces possess an amorphized (Beilby) layer 10-50 nm thick.

(ii) Nanoturned surfaces show amorphous material typically 100 nm deep. For specimens with a depth of cut of about the critical value of 0.5 μm, however, the layer may be up to 500 nm in depth.

(iii) On ground specimens the amorphous layer is very variable in depth, tending to fill the deeper grooves. Cracks and delaminations are occasionally observed within the layer (Whitmore 1995).

3.4 Rutherford Backscattering

Preliminary work (Puttick et al 1992) indicated that RBS spectra from machined surfaces were invariably characterized by a marked peak in the numbers of ions scattered from the first few hundred nanometres of the specimen subsurface. At the time it seemed possible to associate this only with the dislocated region. Nevertheless, it seemed difficult to believe that the observed density of dislocations in turned material could produce so many displaced atoms as were indicated by RBS data. In addition, the high level of scattering from deeper levels remained unexplained.

During the past year we have taken spectra from a second series of workpieces machined by SPDT, using a new microbeam facility (Jeynes et al 1995) giving greater lateral resolution. Typical results are presented in Fig 2 for two sites. The region denoted r has an exceptionally wide peak with a width corresponding to a depth of about 350 nm, while region "u" yields a peak from a depth of 200 nm.* Also shown is the spectrum corresponding to a non-aligned or "dechannelled" beam: this is essentially the level expected from amorphous material. Both surface peaks attain this level, providing strong evidence that they originate in amorphous silicon.

Corroboration is furnished by a simulation known as DICADA (Dechannelling in Crystals and Defect Analysis), developed by Dr K. Gärtner of Jena to interpret channelled ion beam spectra. This calculates the number of defects of a specified type as a function of depth causing the observed dechannelling: in the present case it was assumed that the defects consisted of displaced interstitial atoms and dislocations. For example, for region "u" the surface peak is shown to correspond to silicon with a concentration of displaced atoms between 30% and 80%, which is consistent only with an amorphous state. Below this the scattering levels are consistent with the observed density of dislocations.

We conclude that RBS constitutes a sensitve non-destructive test of the surface state of machined crystals, with particular reference to the amorphized layer.

Discussion

The surface spectroscopy indicates first, that the machined surfaces are in all cases free of marked chemical contamination, and second, that amorphous silicon is everywhere present. The XPS results confirm that, as intuition would suggest, some

---

*Site "u" also provides some evidence, in the form of a minor scattering peak for the presence of oxide.

transfer of material occurs from the diamond tool or abrasive, probably in the form of graphite to which the diamond material has transformed by frictional heating. In addition, some transfer has taken place from the bonding material in the case of the resin bonded grinding wheel, In all cases the XPS results yield a value of oxide layer thickness in the region of 1 nm.

The AFM profiles, on the other hand, show that resin bonded wheels appear to provide a somewhat lower value of surface roughness than those bonded with metal. Both types of ground surface, however, are markedly inferior to the wafers machined by SPDT, the quality of which meets the requirements for all types of optical surface. Further research is needed into the effects of subsurface damage on optical properties.

The RBS results taken together with the direct observations by electron microscopy emphasize the potential importance of surface amorphization during machining. Amorphous silicon has been found in residual indentations in silicon crystals (e.g. Clark et al 1989) where it is uncertain whether the phase transformation occurs by a solid-solid mechanism or by pressure-induced melting. During machining, however, it seems likely that the latter process operates, since the interfacial temperature at the tool tip is believed to exceed 1200°C, the level to which the local pressure reduces the melting point of silicon. Accordingly one must regard the amorphous layer as representing the irreducible minimum of sub-surface damage inflicted by machining.

References

Ball,M.J., Murphy,M.A., and Shore,P. 1991: Proc SPIE 1573, 30

Clark,D.R., Kroll,M.C., Kirchner,P.D. and Cook,R.F. 1988 Phys Rev Letters 60, 2156

Gee,A.E., McCandlish,S.G. & Puttick,K.E.1988 Proc SPIE 1015, 74

Jeynes,C., Puttick,K.E., Whitmore,L.C., Gaertner,K., Gee,A.E., Millen,D.K., Webb,R.P., Peel,R.M.A. and Sealy,B.J. 1995: "Laterally Resolved Crystalline Damage in SPDT Silicon". Presented at 12th Meeting on Ion Beam Applications (IBA-12, Phoenix Az)

Puttick,K.E., Rudman,M.R., Smith,K.J. and Franks,A. 1989 Proc Roy Soc A426, 19

Puttick,K.E., Jeynes,C., Rudman,M.R., Gee,A.E. and Chao,C.L. 1992: Semicond. Sci Technol. 7 255

Puttick,K.E. 1993 Proc ASPE Spring Topical Meeting p. 14

Puttick,K.E., Whitmore,L.C., Zhdan,P., Gee,A.E. and Chao,C.L.1995: Tribology Int. 28 349

Whitmore,L.C., Puttick,K.E.and Watts,J.F.1994 ICEM-13-PARIS p 799

Whitmore,L.C. 1994 Ph.D. Thesis, University of Surrey

Acknowledgement We acknowledge with thanks permission to reproduce Figs 2(a) and (d) from Tribology International Vol 28 p. 354, and Fig 2 from the Proceedings of the 12th Ion Beam Applications Meeting(IBA-12, Phoenix,Az.) to be published in Nuclear Instrumentation and Methods.

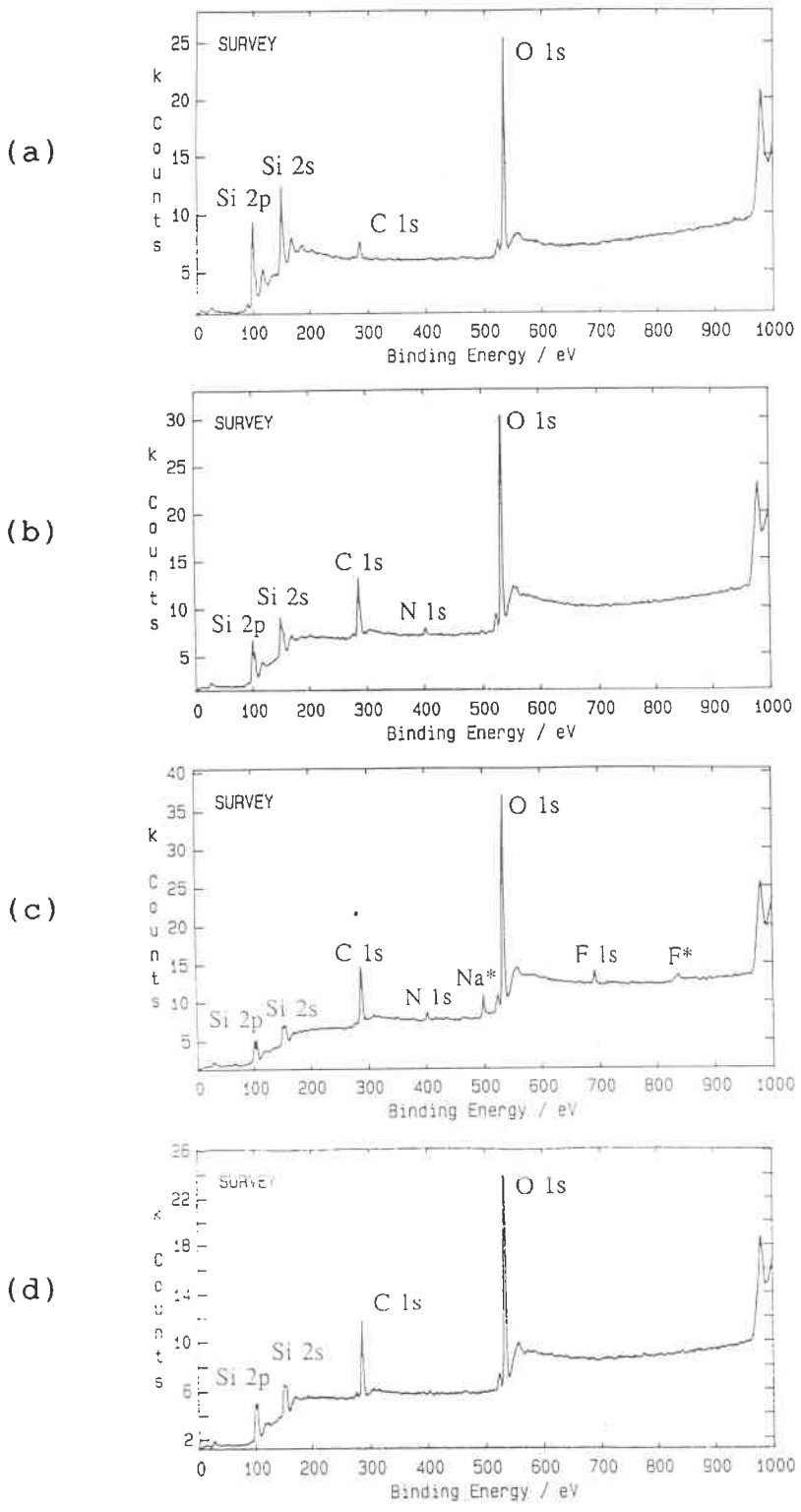

Fig 1 X-ray photoelectron spectra (XPS) of silicon wafers
(a) as received (b) ground with metal bonded wheel
(c) ground with resin bonded wheel (d) SPDT

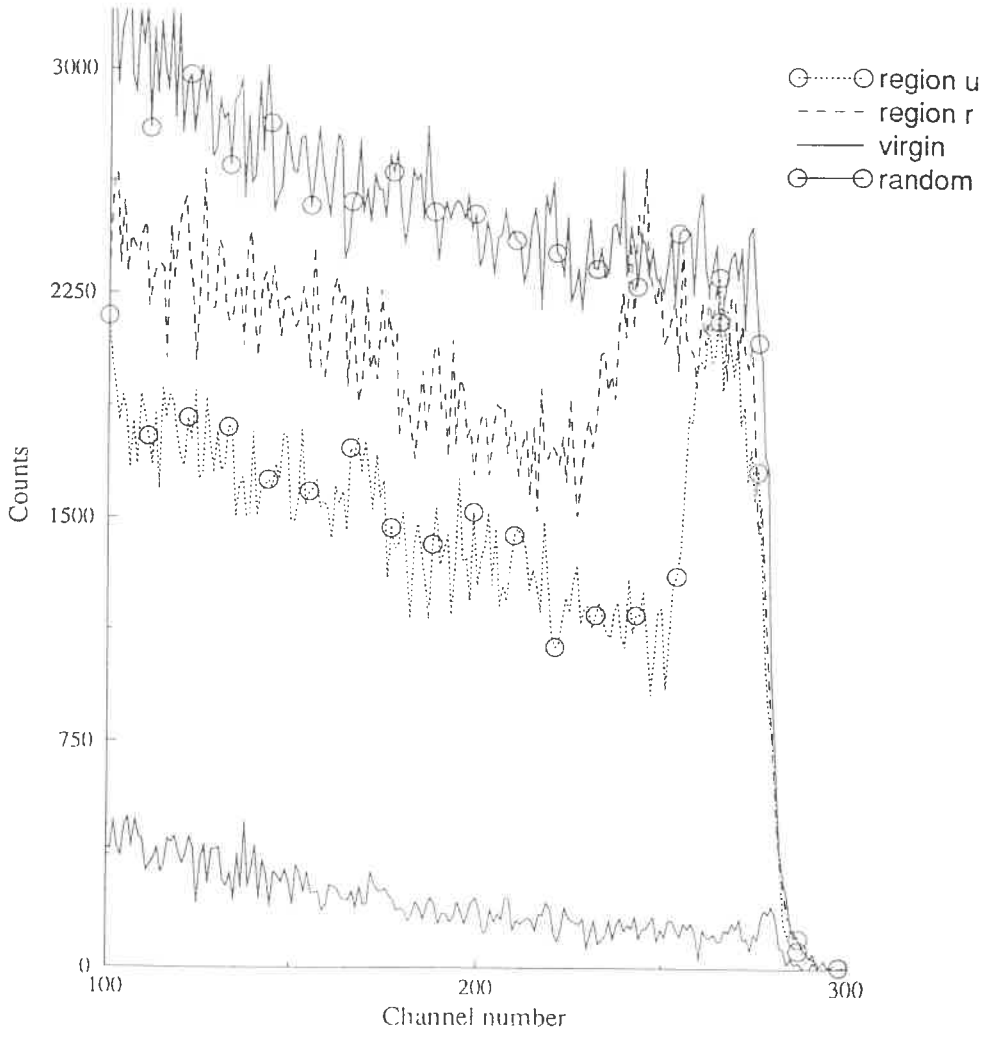

Fig 2 Rutherford backscattering spectra (RBS) from SPDT silicon crystal, showing surface peaks from two regions intersecting the dechannelled spectrum representing amorphous material

DOUBLE FRACTURE MODEL IN LAPPING OF CERAMICS

Ioan D. Marinescu
Abrasive Micro-Machining Center
Kansas State University
Manhattan, KS 66506-5101

1. Introduction

Advanced ceramic materials offer superior temperature, tribological and strength characteristics to metals, although the replacement of metal parts with ceramic parts, in many instances, has been hindered by the high cost associated with conversion. Ceramic parts are expensive because of the difficulties of fabrication (20% - 30%) and machining (70% - 80%). Much of the effort to reduce cost has been applied to fabrication methods to obtain techniques for near-net shape processing. This goal is becoming harder to achieve because required tolerances are tightening every year. Thus, effective and adapted machining methods are required.

The task of machining ceramics differs greatly from metal machining. Metals are much more ductile than ceramics, so material removal is primarily by plastic deformation, which enables good surface quality and finish with high dimensional accuracy to be obtained with relative ease. However, ceramic material is usually removed through brittle fracture [1]. This mechanism makes it difficult to machine ceramics and good surface quality and integrity. Surface grinding with diamond wheels has been practically applied, but the surface integrity (primarily surface stresses and cracking damage) suffer because initiation of cracks occur during grinding, and the resulting surface quality is not sufficient for many applications [2,5].

To improve the surface integrity of ceramic materials, as well as achieving good surface quality, micro-machining techniques are used. Lapping, fine-grinding, polishing, honing and abrasive belt grinding are some of the micro-machining methods that are utilized for achieving this. Material removal is accomplished less aggressively, i.e. smaller material removal rates, than machining processes and in a more "ductile" fashion. Among the processes mentioned, lapping and polishing differ from machining and other micro-machining methods in that the abrasive is loose and not bonded to any surface. Lapping and polishing are commonly used to improve the surface of ceramics materials.

2. Experimental Procedures

A) Materials

Zirconia-toughened alumina is an aluminum oxide (Al_2O_3) ceramic material in which stabilized zirconia (ZrO_2) is present as a secondary dispersed phase. It is composed of 80% Al_2O_3 and 20% yttria-stabilized zirconia (15.4% ZrO_2 , 4.6% YtO_3). The method of fabrication is hot isostatic pressing (HIP) then sintering to almost 100% density. The properties are listed in the Table 1. This material has advantages over single-oxide alumina ceramics because the addition of stabilized zirconia to alumina increases the toughness, strength, and wear resistance, while retaining good chemical and heat resistance [3]. The material's tetragonal (metastable) phase to monoclinic (stable) phase transformation provides these enhanced characteristic. This material is used for cutting tools and for applications where high abrasion is required.

Table 1. Properties of Zirconia - Toughened Alumina

Density	g/cm^3	4.45
Hardness	MPa	900 - 1000
Fraction Toughness, K_{ic}	MPa $m^{1/2}$	~ 7.5
Young Modulus	MPa	2000
Porosity	%	0.1

Material was cut by using a diamond saw to obtain dimensions of 1.35cm (0.53in) x 1.35cm. Surfaces to be lapped were surface-ground prior to lapping. Grinding simulated a machining step that a ceramic part might see prior to lapping. The surface finish was 1.78μm Ra ±0.89μm (7.0μin Ra ±0.5μin). GE Man Made standard series diamond powders of sizes 30-40, 10-20, and 2-4 microns were used. Concentration of diamond was kept constant at 7 carats (1.4g) per 500ml of carrier.

B) Apparatus

A Lapmaster "12C", single side, flat lapping machine was used for experiments. Figure 1 illustrates the set-up. The twelve-inch, radially-grooved lap plates and conditioning rings are cast iron. Speed of the lap plate was constant at 56 RPM. Normal force was kept constant at 2.07 Kg (4.6 LB). The carrier used is Amplex Corp. type WS/BC (a generic polypropylene glycol carrier). A special carrier type W805 (a new proprietary carrier) was used in a separate test. A peristatic pump delivered the diamond-carried slurry at a flow rate of 1.5ml/min. Lapping power was measured by using a power cell connected to the lap plate drive motor. Surface finish was determined by using a stylus-type surface analyzer and was quantified using the roughness average parameter (Ra). Volume of material removal was calculated by using average thickness values and verified through weight measurements.

C) Methodology

Lapping experiments were conducted by using three abrasives of different sizes. ZTA workpieces were lapped with all three abrasives in descending order: 30-40μm, 10-20μm, and 2-4μm. Three workpieces were lapped simultaneously. Lap time was 60 minutes, divided into 4 segments of 15 minutes each. Surface finish and material removal was measured after each lap segment. Further tests used 10-20μm and 2-4μm abrasive, respectively, to highlight the surface finish performance with respect to time.

3. Stock Removal Mechanism

During the lapping process it is possible to have two types of stock removal mechanism. One of them we named: double fracture mechanism. The fracture is a macro-fracture and is the effect of a grain which is working like an indentor, Fig. 2.

Coinciding time with the fracture, a quantity of energy will be transformed into local heat because of the friction and deformation. In the unloading phase of the lapping, because of a small thermal shock, a micro-fracture will appear on the particles which just were separated by the macro-fracture, Fig 3a-b.

This mechanism will give us an explanation of what is happening in grinding wherein the phenomena is more intense because of the dynamics of the process. Even in ductile grinding where the removed material is in a plastic deformed mode because of the thermal shock, the plastic chips will suffer a thermal fracture and some of them will be transformed into a powder.

The SEM picture of the collected chips from ductile grinding of alumina oxide, Fig. 4 shows a spiraled deformed shape like a turning chip. Because of this thermal shock, even the ground surface can be affected and some cracks can be observed. To avoid this, some Japanese researchers used a low power laser to close the cracks after grinding.

These are some hypotheses combined with some pieces of evidence. More detailed research is necessary to elucidate the stock removal mechanism of brittle materials and especially for different types of ceramics.

4. Results and Discussion

As previously mentioned, the material removal mechanism in the case of brittle materials is either brittle fracture or plastic deformation. Our analysis of the lapping experiments performed attempts to

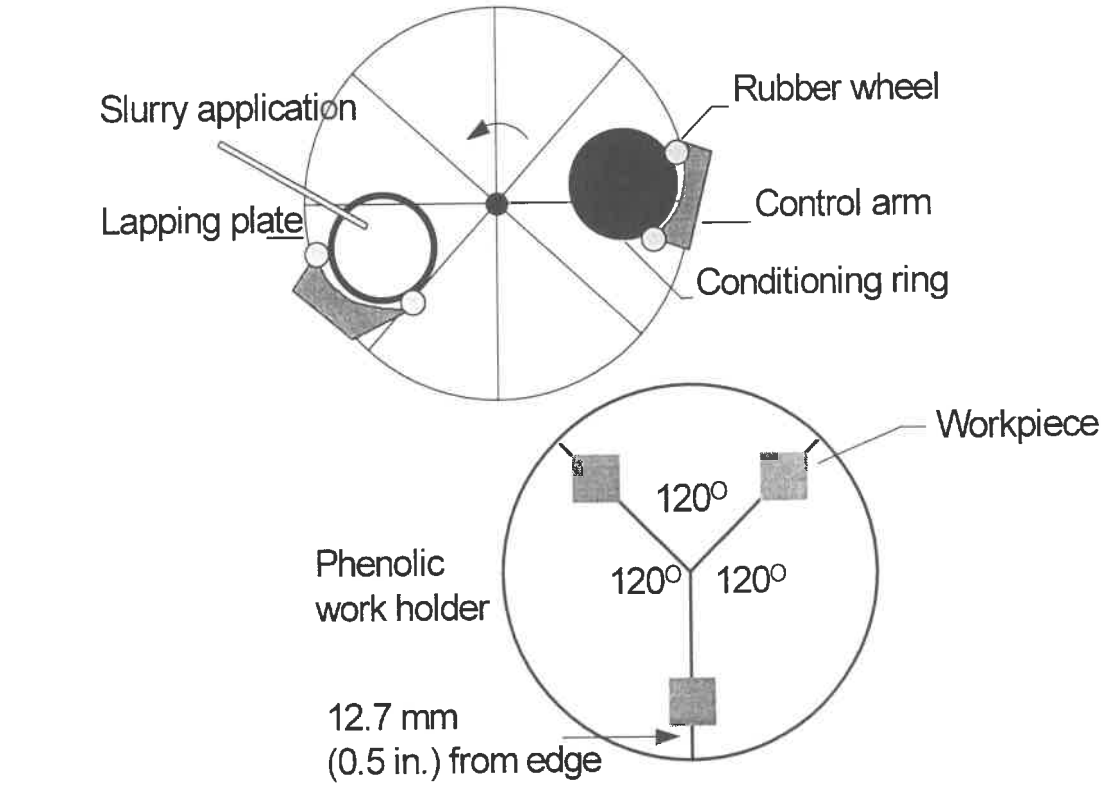

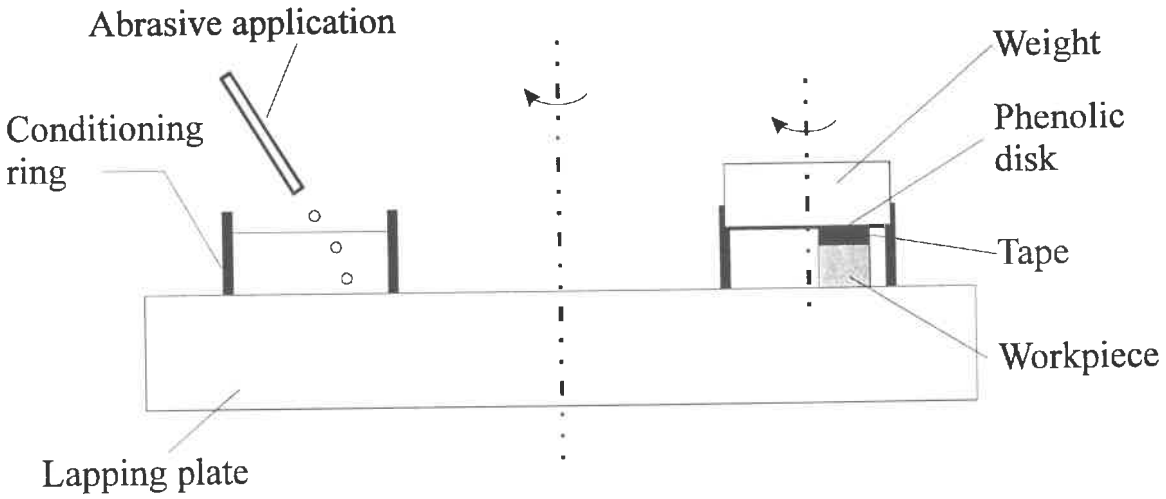

Fig. 1. Experimental set-up

illustrate the different modes. The result indicates that two different trends occur. It appears that, during lapping with the 30-40 μm and 10-20 μm abrasive size, material removal is through the brittle fracture mode. The process is very stable from the viewpoint of surface finish, stock removal rate (Q_W), and specific energy (E_{SP}), as seen in Figure 5a-b. Specific energy values are higher for the 10-20 μm abrasive size than the 30-40 μm. This is due to the greater number of diamond grains associated with the smaller size. There is approximately eight times greater the number of grains with the 10-20 μm abrasive than in the same amount of 30-40 μm abrasive. Corresponding with this trend, the abrasive coefficient, μ_a , or force ratio, has the same relationship. The stock removal rates (Q_W) are practically equal for both sizes.

Another observation with the 30-40 μm and 10-20 μm grit size is that a 15 minute lapping cycle is long enough to obtain the best surface finish with the respective grit size. Lapping for longer times does not improve the surface finish [6].

From Figure 5a-b, it is observed that the behavior of the 2-4 μm abrasive differs from the other two abrasives used. The behavior of this grit size is due primarily to the fact that these grains are much smaller, thus the number of grains is much larger than in the previous cases. For the same concentration of diamond powder, the 2-4 μm powder has 1000 times more grains than the 30-40 μm powder. From the graphs, we can see that specific energy was at minimum values after 45 minutes of lapping. Specific energy then increases with a larger lap time. Based on ceramic grinding experience, the increase of the specific energy usually is an indication of the transition of material removal mechanism from brittle mode to ductile mode. This appears to have occurred with this abrasive size. The abrasion coefficient follows the same trend. We concluded from this test data that, with lapping longer than 45 minutes, material removal is primarily through plastic deformation and not brittle fracture. More intense research focusing on brittle fracture/ plastic deformation in lapping needs to be performed.

Further observation on 2-4 μm abrasive results shows that surface finish values improve continuously for the entire 60 minutes, which is not the case for the other abrasives. It appears that the best surface finish obtainable with this abrasive size was not achieved in the 60 minutes of lap time. A longer lap time would likely improve the finish further. A separate test was performed in which time was increased to try and reach the best surface finish (Figure 6). The best surface finish was obtained with 90 minutes of lapping. Further lapping didn't improve the finish. With 90 minutes of lapping, the surface finish improved to an R_a of approximately 0.02 μm (0.8 μin).

Discussion so far has been on experiments using a generic carrier, WS/BC. These experiments were repeated with a proprietary carrier, W805. The surface finish results of both WS/BC and W805 tests are presented in Figure 7a-b. Better final surface quality was obtained by using the WS/BC carrier (0.0254 μm vs. 0.0347 μm R_a). It appears this is due to the different lubricating properties of each carrier. The aim of the carrier is not only to carry the abrasive, but also to lubricate the surface. A lower diamond concentration to ensure the minimum lubrication is obtained in the abrasion process. The W805 carrier performed comparatively well with the 10-20 μm abrasive but not as well with the 30-40 μm and, more importantly, with the 2-4 μm abrasive. It appears that the W805 carrier does not have quite the lubricating strength as the WS/BC carrier with this particular lapping operation (ZTA ceramic, cast iron lap plate, and diamond powder). The carrier flow rate used was adequate for the WS/BC carrier, but might not have been adequate for the W805 carrier. Besides the lower surface quality with the W805 carrier, the lap plate appeared very dry compared to the WS/BC carrier.

Taking a global view of the results obtained, it can be seen that lapping with 30-40 μm abrasive size does not improve sufficiently the surface finish, so this size can be eliminated in a production system. (It can be seen in Figure 5a and more closely in Figure 7a, the roughness for 30-40 μm is practically constant with time and no improvement of the surface is observed). However, lapping with the 10-20 μm abrasive size has a substantial influence on the surface quality within the first 15 minutes of lapping. However, no significant improvement in surface finish was obtained with longer lap times. A separate test was performed to verify this trend. Figure 8 shows the results of lapping un-machined workpieces with the 10-20 μm abrasive. The as-fabricated surface finish of the ZTA workpiece was 1.02 μm $R_a \pm 0.18$ μm (41 μin $R_a \pm 7.0$ μin). Within the first 15 minutes the surface finish was brought down to 0.089 μm (3.3 μin) R_a. Thirty more minutes of lap time reduced the surface finish a little more to 0.084 μm (3.3 μin) R_a, and plateau was reached. Lapping time longer than 15 minutes is not required with the 10-20 μm abrasive. A recommendation is to design a rough lapping process with this abrasive with a 15-minute lap time.

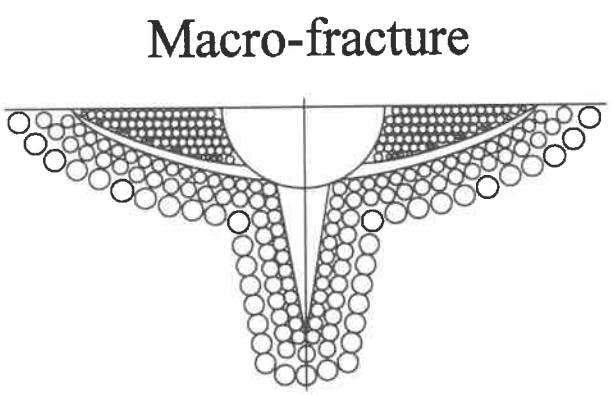

Fig. 2. Macro-fracture of ceramics

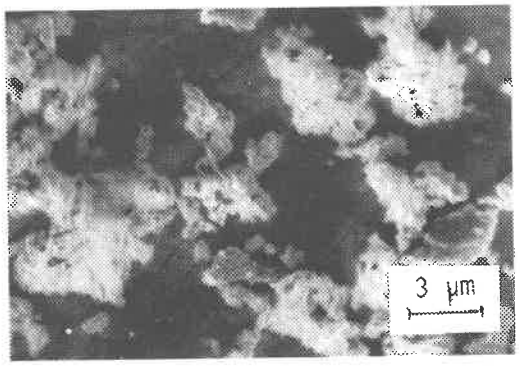

Fig. 4. Ductile ceramic chips

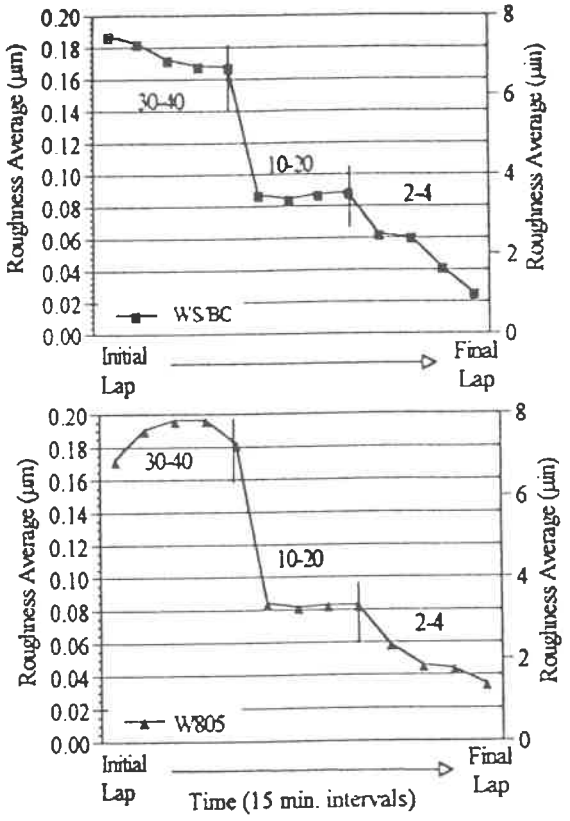

Fig.7. Comparison of surface finish results between material lapped with (a) WS/BC and (b) W805 carriers.

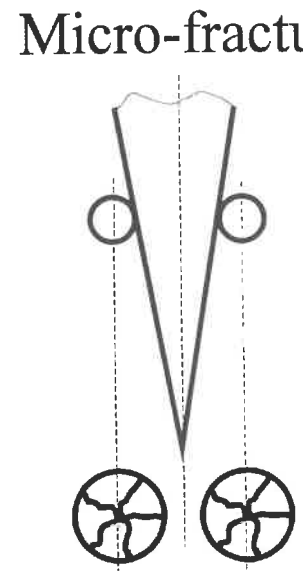

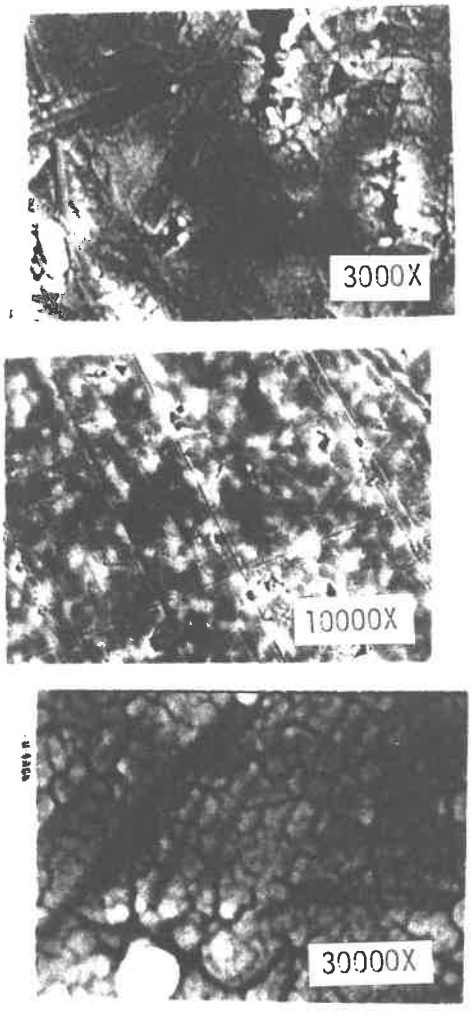

Fig. 3. Micro-fracture of ceramics

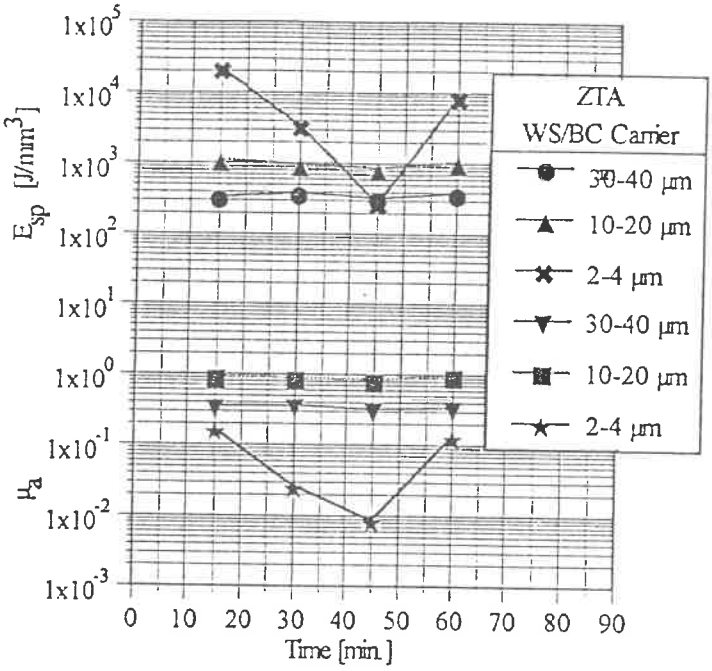

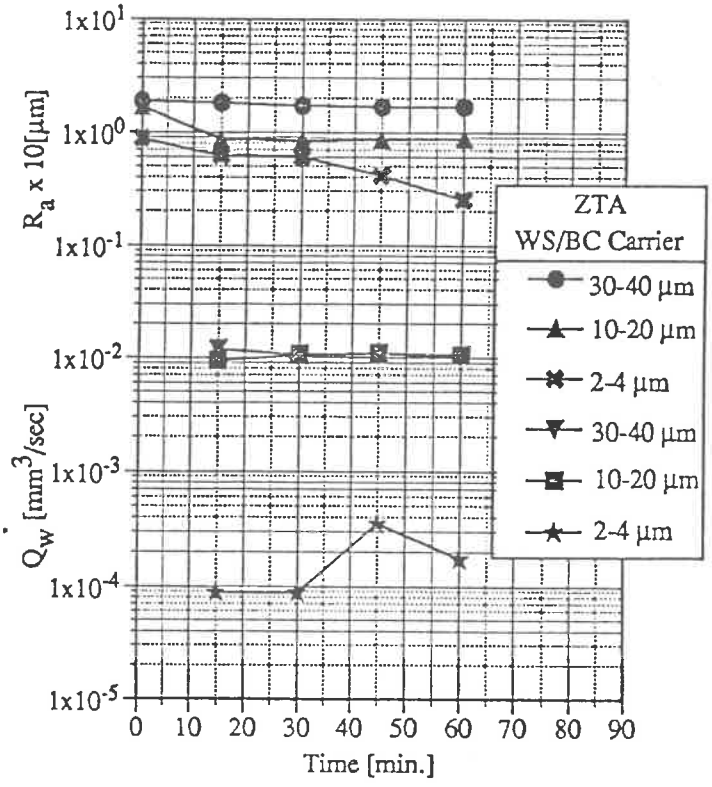

Fig. 5. Results for tests using all three abrasives. Each symbol represents an average of three parts. Plotted versus time (a) specific energy E_{SP} and abrasive coefficient (force ratio) μ_a ; (b) Roughness average R_a and stock removal rate Q_W.

5. Conclusions

The following conclusions can be drawn from these lapping experiments:

1) Zirconia-toughened alumina can be lapped to surface finishes having an R_a better than 0.0254 μm (1.0 μin).

2) Lapping with 10-20 μm abrasive can reduce the surface R_a by a factor of 10, i.e. from as high as 1.041 μm (41 μin) down to less than 0.102 μm (4.0 μin) in only 15 minutes.

3) Lapping with 30-40 μm abrasive does not improve surface finish and the stock removal rate is almost identical to the 10-20 μm abrasive. And since the 10-20 μm abrasive is effective for surfaces with a relatively high R_a , the 30-40 μm abrasive is not recommended for use with this material.

4) The lubricity of the carrier plays an important factor in the performance of a lap.

5) Material removal is mostly through plastic deformation when lapping with the 2-4 μm size abrasive, as evidenced by the SEM micro-graphs and the test data.

References

1. Buijs, M. and K. Korpel-van Houten, "Three-body Abrasion of Brittle Materials as Studied by Lapping". *Wear*, 166, pp. 237-45, (1993).
2. Chen, C. S. Sakai and I. Inasaki, "Lapping of Advanced Ceramics". *Materials & Manufacturing Processes*", 6(2), 211-226 (1991).
3. Matsumoto, Y. et. al., "Mechanical Properties of Hot Isostatically Pressed Zirconia-Toughened Alumina Ceramics from Coprecipitated Powders", *J. Am. Ceram. Soc.*, 76(10) 2677-80 (1993).
4. Chanadrasekar, S. K. Kokini and B. Bhushan, "Influence of Abrasive Properties on Residual Stresses in Lapped Ferite and Alumina", *J. Am. Ceram. Soc.*, 73(7) 1907-11 (1990).
5. Szuder, Andrei, I. Marinescu and M. Popescu, "Study of the Influences on Flat Lapping", *SME*, Michigan, MR86-633.
6. Turco, M., "Flat Lapping of Zirconia - Toughened Alumina with Diamond Powders", *Master of Science Thesis*, University of Connecticut, 1995.

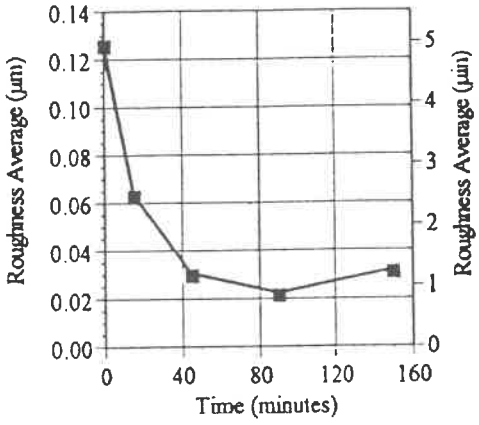

Fig. 6. Results from a separate test where material was lapped with 2-4 μm abrasive for 150 minutes to determine approx. time needed to obtain the best finish.

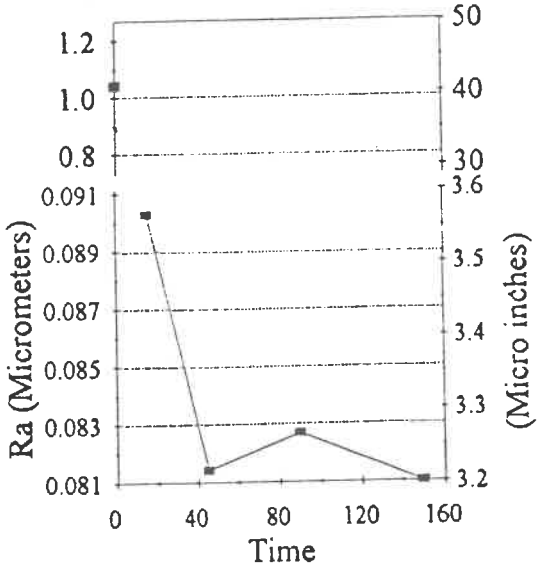

Fig. 8. Results from a separate test using 10-20μm abrasive to lap un-machined workpieces.

Working with the Superabrasives Industry to Optimize Tooling for Grinding Brittle Materials*

John S. Taylor, Mark A. Piscotty, Kenneth L. Blaedel
Lawrence Livermore National Laboratory

Fred A. Gray
Industrial Diamond Association

Introduction

The optics manufacturing industry is undertaking a significant modernization, as computer-numeric-controlled (CNC) equipment is joining or replacing open-loop equipment and hand lapping/polishing on the shop floor.[1] Several prototype CNC lens grinding platforms employing ring tools are undergoing development and demonstration at the Center for Optics Manufacturing in Rochester, NY, and several machine tool companies have CNC product lines aimed at the optics industry.[2] Benefits to using CNC ring tool grinding equipment include: essentially unlimited flexibility in selecting radii of curvature without special radiused tooling,[3] the potential for CIM linkages to CAD workstations, and the cultural shift from craftsmen with undocumented procedures to CNC machine operators employing computerized routines for process control. In recent years, these developments have inspired a number of US optics companies to invest in CNC equipment and participate in process development activities involving bound diamond tooling.[4] This modernization process extends beyond large optics companies that have historically embraced advanced equipment, to also include smaller optical shops where a shift to CNC equipment requires a significant company commitment.

An essential element that must accompany the development of any new CNC grinding equipment is a corresponding material removal process that meets customer requirements for workpiece quality, throughput, and labor cost. The elements that contribute to the grinding material removal process are diagrammed in Figure 1, and include the machine tool, grinding wheel, workpiece, environmental variables such as temperature and vibration, and specific process choices, such as the speeds, feeds, and dressing/truing methodologies. Among these elements, the grinding wheel appears to be the least characterized element and has undergone the least optimization, particularly for the grinding of brittle materials such as glass.

This paper addresses our efforts to optimize fine grinding wheels to support the new generation of CNC equipment. We begin with a discussion of how fine grinding fits into the optical production process, and then describe an initiative for improving the linkage between the optics industry and the grinding wheel industry. For the purposes of this paper, we define fine wheels to have diamond sizes below 20 μm, which includes wheels used for what is sometimes called medium grinding (e.g. 10-20 μm diamond) and for fine grinding (e.g. 2-4 μm diamond).

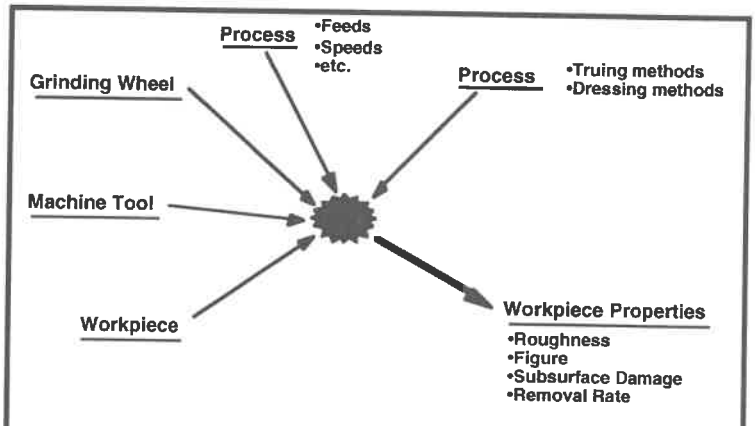

Figure 1. The system view of grinding encompasses all input variables that affect workpiece properties and cost.

* This work was performed under the auspices of the U. S. Department of Energy by Lawrence Livermore National Laboratory under contract No. W-7405-Eng-48.

Ring Tool Grinding in Optics Manufacturing

The key metrics for assessing the benefits of a finishing processes include the quality, cost, and throughput of the *completed* workpiece. Thus the benefit of incorporating a new CNC grinding process will be judged not only by the speed and quality of grinding, but also on how grinding affects the entire finishing process, particularly the cost of the subsequent polishing operation. It is important to note that production costs depend not only on machine time, but also embody all labor requirements, such as handling, washing, blocking/deblocking, machine set-up, truing, and dressing.

Two typical production scenarios,[5] where CNC ring tool grinding is employed for precision optics, are shown in Figure 2. The upper diagram shows a "2-wheel" process where the final grinding operation employs a 10-20 micron diamond wheel, which produces a high quality matte finish of about 2000 Å rms. The workpieces are then polished, using either high-speed polyurethane pads or standard pitch polishing. The lower production chart shows a "3-wheel" process where a fine grinding operation uses a 2-4 micron diamond wheel. Here the fine ground surface might have a finish of 80-150 Å rms and be characterized by a morphology of small fractures on a relatively smooth (ductile ground) background.

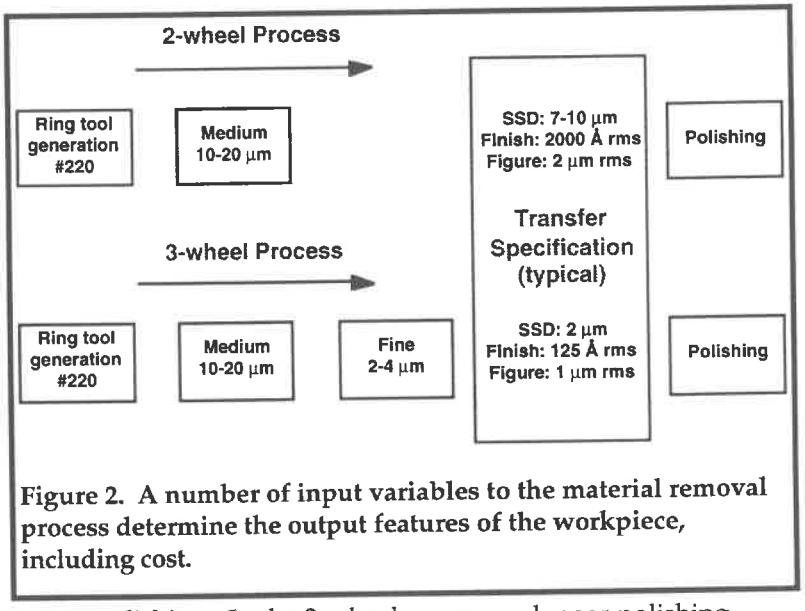

Figure 2. A number of input variables to the material removal process determine the output features of the workpiece, including cost.

For both scenarios, the key is to minimize the total labor time to repeatably produce a part. Most companies employ the 2-wheel process where the requirement of the medium grinding step is to repeatably produce high quality matte finishes at very high in-feed rates. Alternatively, the 3-wheel process employs a finer diamond wheel to significantly lower the roughness and subsurface damage, while benefiting from a higher removal rate and better figure control than in polishing. In the 2-wheel process, a longer polishing cycle substitutes for the fine wheel used in the 3-wheel process.

The complete analysis of the relative merits of the two processes involves the details of the machining platform(s), the level of skill of the polishing technicians, grinding process choices, etc. and is well-beyond the scope of this talk. However, a key issue in assessing the relative benefits of a 3-wheel vs. a 2-wheel process lies in the trade-off between subsurface damage and figure error as the part moves from grinding to polishing. The subsurface damage from the medium grinding operation might be several times higher than the figure error. Thus when the part is being polished, the optician must maintain or improve the figure tolerance while the subsurface damage is being removed. For the fine ground part, the figure errors and the subsurface damage are on the same order of magnitude, offering the optician the potential for converging to the figure and finish specifications with similar required amounts of material removal.

From this analysis, two goals of grinding process development can be formulated, where wheel optimization is an essential element. For the 2-wheel process, it would be beneficial to improve the subsurface damage to a depth of a few micrometers, to more closely approximate the figure error. For the 3-wheel process, an ultimate goal is to completely eliminate the need for post-polishing. However, a more likely near-term goal is to sufficiently converge on the combined specifications of figure, finish, and subsurface damage so that only a very brief polishing operation is required, primarily to reduce scatter and improve cosmetics. Because polishing is typically the rate limiting step, improving the

grinding operation in order to shorten the polishing operation to the same order of time as the grinding steps, will improve the production flow so that all of the adjoining operations have approximately the same rate of throughput.

The Wheel Industry

Table 1 shows the relatively small number of companies that we have identified as manufacturers of fine diamond wheels. We estimate that fine diamond wheels are 1-5 percent of the diamond wheel industry. Most of the industrial diamonds going into fixed abrasives are used for concrete cutting/grooving, quarrying, deep drilling, and carbide grinding.[6] Because fine wheels are such a small market segment, there is little motivation for wheel makers to devote significant resources for optimizing or developing wheels for optics applications. Exceptions to this rule include a few companies that are closely coupled with optics manufacturers and companies that support the ceramics industry, where there is a substantial technical overlap with glass grinding.

Survey that Identifies Grinding Problems with Wheels

Our group at LLNL was invited to report on a casual survey of optics companies at the 1995 Annual Meeting of the Industrial Diamond Association (IDA).[7] The survey asked optics companies about their satisfaction with their wheels and their wheel suppliers. Most survey responses were anecdotal (and unscientifically analyzed), but there was a clear thread of concern about the repeatability of wheels from their current sources, as well as a frustration of not being able to buy wheels from additional sources, without a lengthy trial and error period.[8] At this meeting, there was also an optics company representative who very strongly suggested that the communication between wheel makers and users was sufficiently poor that it precluded the effective specification of wheel

Table 1. Manufacturers of bound diamond tooling with diamond sizes ≤ 20 μm.

Company Name	Contact	State	Phone	Fax
Abrasive Technology, Inc.	Loyal M Peterman, Jr.	OH	614-548-4100	614-548-7617
Action Superabrasive Products, Inc.	Joe Haag	OH	216-688-8505	216-688-8518
Alpex Wheel Company	Steve Michel	NJ	201-871-1700	201-871-1521
Applied Superabrasives, Inc.	James Godin	CT	203-654-1780	203-654-1782
Braemar	Chuck Fillipone	AZ	602-966-9311	602-966-2273
Diagrind, Inc.	Donald P. Sommer	IL	708-460-4333	708-460-8842
Diamond Devices, Inc.	Mike Wire	CA	916-823-3333	916-823-7618
Diamond Fabricators, Inc.	Mark Greathouse	OH	216-942-7400	216-942-3183
Fuji Die	Mr. Vasuchika Fukaya	Japan	81-3-3579-7181	81-3-3756-7381
Fujimi	Charles Tiedman	CA	510-460-0601	510-460-0419
General Industrial Diamond Co., Inc.	Ronald M. Schwarz	NJ	201-884-2500	201-884-0392
Greenlee Diamond Tool Co.	Glen P. Rosier	IL	708-803-7366	708-803-9761
Inland Diamond Products	Dennis R. Raffaelli	MI	313-858-2330	313-589-0499
LOH	Mike Krueger	WI	414-255-6001	414-255-6002
Lunzer Industrial Diamonds, Inc.	J. Peter Lunzer	NJ	201-794-2800	201-794-2338
National Diamond Laboratory	Peter Skorewicz	NY	914-737-3774	914-737-1774
Noritaki	Joseph Michaelic	OH	800-688-8234	513-771-4006
Norton Co. Diamond Tool Div.	Dick Sioui	MA	508-795-2364	508-795-5507
Scomac	Larry Scott	NY	716-494-2200	716-494-2300
Superabrasives, Inc.	Charles A. Halprin	MI	313-348-7670	313-348-8037
The Wickman Corporation	Ben Stormes, II	MI	1-800-367-9398	810-548-3831
Universal Superabrasive		IL	708-238-3300	708-238-3315
Web Industries	Bud Begone	NJ	201-335-1200	201-335-7054
Wendt Dunnington Co.	Daniel Herzog	PA	610-458-5181	610-458-8903
Wickman's Diamond & CBN Products	Fred Lindblad	MI	313-548-3822	313-548-3822
Ernst Winter & Son, Inc.	Jerry L. Martin	SC	803-834-4145	803-834-3730

performance requirements.[9] The IDA members were quite receptive to the survey input and were open to ways to improve the dialogue with wheel users.

LLNL and the IDA are currently updating this survey, with input from both wheel users and wheel makers. From the wheel makers' point-of-view, we hope to learn how important fine wheels are to their overall business, their satisfaction in meeting the needs of the fine wheel users, and what considerations might lead to better tool optimization. From the users' point-of-view, we hope to learn how satisfied they are with their wheels and wheel suppliers, and do they think that improved tooling would improve their productivity (in the presence of other limitations in their process). All wheel makers and wheel users who would like to participate in this survey should contact one of the authors for a copy of the survey. This is an ideal opportunity for the fine grinding community to formulate a message for the wheel manufacturers in terms how they might better service their customers. The Industrial Diamond Association has invited the results of this survey to be published in their quarterly magazine *Finer Points*. Some survey results will presented as part of this paper, but the complete results as well as any actions initiated by the results will be presented at *SuperTech 1996* (Superabrasives Technology), a workshop that will be held at LLNL on November 7-8, 1996.[10]

Assessing Wheel Performance from the Users' Point-of-View

In responding to industry concerns that fine diamond wheels (particularly 2-4 μm wheels) are not sufficiently optimized, we are assessing the performance of wheels in terms of repeatability and overall quality. Our first effort was to formalize the standard cutting test that most users employ: examine the roughness, subsurface damage, and figure errors produced during a grinding test.[11] The formalization comprises running the same tests for all evaluations to allow apples-to-apples comparisons of wheel performance, and the control of various independent variables, such as *standardized truing/dressing procedures* and the use of *identical sequences for breaking in a tool.* Typical data from this type of evaluation are presented in Figure 3, where the relative performances of metal-bonded wheels are compared to Cu-resin-bonded wheels.

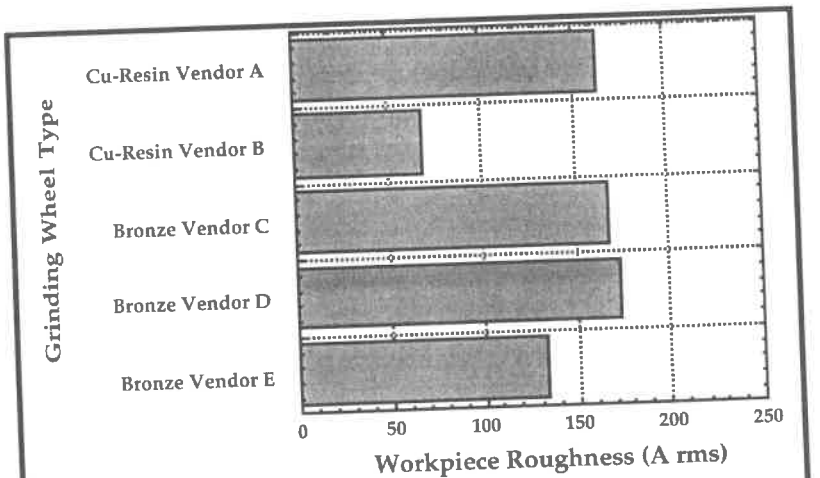

Figure 3. Comparison of roughness values (Zygo NewView 20x) achieved with commercial wheels; 2-4 μm wheels.

The metric that an optics company ultimately uses in judging tool performance is how well it meets requirements for part quality and cost per workpiece (labor plus materials). Thus, a user's evaluation of *grindability* for a particular tool, includes a weighted judgment of how well the tool met all of the desired performance specifications. This type of assessment might be viewed as either a qualitative or quantitative evaluation such as that diagrammed in Figure 4a. The weighting coefficients would reflect the user's specific application, and his method to optimize the production process. Although it is doubtful that users would carry out this evaluation in a rigorous sense, clearly some assessment like this must take place when a specific tool is selected among a field of several candidates. In this diagram, the composite grindabilty G represents a figure-of-merit for the selection of grinding wheels.

Assessing Wheel Performance from the Wheel Makers' Point-of-View

The metric used by the wheel maker in selecting a wheel design for meeting a customer's requirement will be cast in terms of the variables involved in making the wheel, such as those enumerated in Figure 4b. In general, the selection of wheel ingredients and wheel style for meeting a performance requirement are proprietary information. It is interesting to note that the *cost* figures-of-merit for the user and the wheel maker may have very different connotations.

(a)

$$G^2_{user} = a_1 (rms)^2 + a_2 (SSD)^2 + a_3 (figure)^2 + a_4 (g-ratio)^2 + a_5 (feedrate)^2 + a_6 (effort)^2 + a_7 (cost)^2$$

(b)

$$G^2_{maker} = b_1 (diamond)^2 + b_2 (bond)^2 + b_3 (filler)^2 + b_4 (porosity)^2 + b_5 (concentration)^2 + b_6 (procedure)^2 + b_7 (cost)^2$$

Figure 4. Figures of merit (FOM) for grinding wheels. (a) qualitative FOM used in selecting a wheel for grinding lenses – users' point-of-view; (b) qualitative FOM used in selecting wheel ingredients to meet an application – wheel makers' point-of-view.

Lack of Common Language

In considering the two thought schemes for evaluating a wheel as depicted in Figure 4, there is clearly a lack of common language between the user and wheel maker. The user defines grindability in terms of the performance of the wheel for a specific application, while the wheel maker considers wheel performance from a consideration of what types of ingredients are used. This view is clearly exaggerated and of course both groups generally make an attempt to incorporate the others' point-of-view. However, there typically is not an open dialogue between the two groups that would enable the correlation between wheel ingredients and the user's performance indicators. This lack of correlation between G^2_{maker} and G^2_{user} is especially a problem for fine wheels because there is minimal market incentive for most wheel companies to invest in a program of optimization.

A Proposed Solution to a Better Dialogue

A potential bridge between the somewhat disparate languages of the wheel user and the wheel maker may lie in the form of a set of intermediate performance indicators for the wheel, which are sensitive to wheel ingredients, but can also be correlated with wheel performance in the user's application. We are proposing a set of well-defined wheel evaluation tests, each of which is sensitive to a key performance property of the wheel. This is a very different approach from the performance evaluation test mentioned earlier, where specific workpieces are ground and then examined for figure, finish, etc. These proposed tests might include wheel hardness, thermal conductivity, friability, etc. A preliminary collection of performance figures-of-merit are given in Figure 5, where they are all summed (sum of squares) to form a composite FOM to enable a selection of one wheel over another. The weighting coefficients are determined by identifying relative importance of the performance specifiers for a given application. Both the user and wheel maker internally translate the format of Figure 4 into the familiar descriptors of Figure 2, and which largely involve proprietary information.

Composite Figure - of - Merit

$$G^2 = \sum_i a_i (FOM_i)^2$$

FOM_i = elemental performance metrics

a_i = application specific weighting coefficients

$$G^2 = a_1 (hardness)^2 + a_2 (friability)^2 + a_3 (clearance)^2 + a_4 (protrusion)^2 + a_5 (temp\ stability)^2 + a_6 (dressabilty)^2 + a_7 (self\ sharpening)^2 + a_8 (heat\ transfer)^2 + a_9 (grit\ shape)^2 + a_{10} (chem\ stabilty)^2$$

Figure 5. Proposed performance figures-of-merit can bridge between user requirements and proprietary wheel information.

A Voluntary Product Standard

During the next several months LLNL and the IDA will be investigating whether such a list of performance specifiers constitutes a useful approach for reconciling user requirements and wheel preparation methods. In the event that there is a clear message from the optics industry that this type of system is beneficial, and that wheel makers can relate these performance specifiers to composition, then it may be appropriate to adopt these performance specifiers as a voluntary product standard. Clearly, not all wheel companies and optics companies would need to participate, but if several agreed to a trial of the system, then the value of such a system could be assessed.

Hardness as a Performance Indicator

Hardness or resistance to indentation is one example of a performance indicator that relates to both the wheel ingredients and performance as observed by a user. Hardness has been used by many wheel manufacturers as a performance indicator. It typically refers to resistance to abrasion, but clearly is related to the mechanical properties of the bond and the bond-grit system. There is only a loose connection among the common letter hardness grades among wheel companies, although an "N-bond" is usually considered to be "medium".

We are promising a testing procedure for one aspect of hardness: resistance to indentation. This concept has a rich history in the mechanics literature,[12] but standardized testing procedures focus on plastic deformation, and usually require a polished surface for sizing of indentation marks. Because the wheel is a composite material with a high diamond concentration, polishing the wheel surface for inspection of micro-hardness indentation marks is problematic. Thus there is a need for an alternate instrumentation approach for measuring hardness.

Another experimental methodology for characterizing hardness is measuring the increase in force as an indenter is pressed into the surface.[13] The indentation force is plotted versus indentation depth for both the loading and unloading operations. By analyzing the curves, it is possible to assess both elastic and permanent deformation. The area under the curve can be integrated to assess deformation energy.

The indentation properties of the wheel that relate to its performance may encompass plastic, elastic, and fracture mode behavior. These, in turn, may relate to the performance of fine grinding wheels by reflecting the ability of the wheel to accommodate various disturbances or errors that may lead to large grit-to-glass forces and commensurately high subsurface damage. It may not be important which of the three above deformation modes occur, as long as the wheel provides sufficient accommodation for limiting single-grit force excursions.

Figure 6 shows plots of force versus indentation, where a 1 mm radius indentor was indented to a maximum of 2 μm into a bronze bond wheel and a Cu-resin wheel. Clearly, the bronze bond tool exhibits higher force levels for the same indentation. Examining the unloading curves shows that there is permanent deformation, as illustrated by the force going to zero, prior to the indentation returning to zero. These measurements were taken using a stiff T-base machine tool as the feeding mechanism, an LVDT located very close to the indentor, and Kistler piezoelectric force dynamometer.

Finally, the resistance of the wheel to indentation might be expected to vary as a function of the size of the indenter. This would relate to the performance of the tool, as disturbances might span a wide range of spatial sizes. For example, the ability of the wheel to accommodate a solitary diamond that protrudes further from the bond than neighboring diamonds might ideally be tested using a very small-radius indentor. The ability of the wheel to accommodate waviness on the wheel due to truing errors, might ideally be tested by using a large-radius indentor.

Figure 7 shows how a hardness evaluation could comprise multiple tests that span a range of spatial scales. The three examples correspond to long, mid, and short spatial wavelengths (λ_{sp}). These correspond to wheel compliance as manifested by different spatial features on the wheel. A hardness test might target these different spatial scales using indenters with different radii-of-curvature (ROC). Finally, examples are given of the physical sources of disturbance corresponding to each spatial scale. A hardness characterization might encompass numerical values corresponding to each spatial scale.

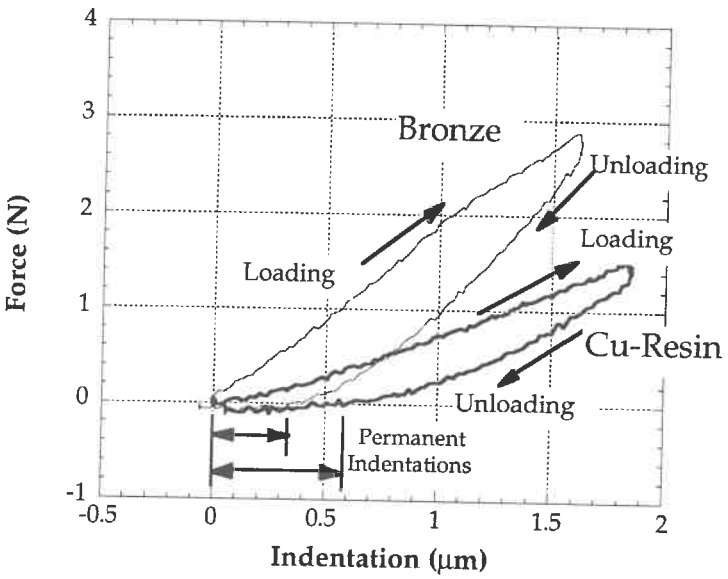

Figure 6. An example of a 'hardness' test that compares resistance to indentation between a Cu-resin-bond wheel and a bronze-bond wheel.

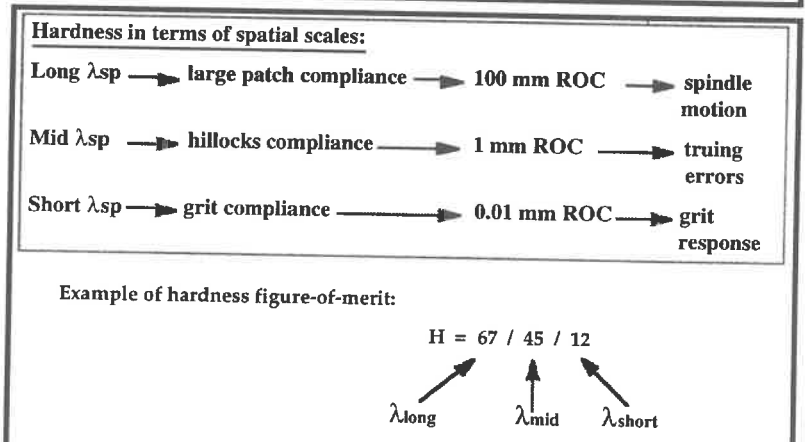
Hardness in terms of spatial scales:
Long λsp → large patch compliance → 100 mm ROC → spindle motion
Mid λsp → hillocks compliance → 1 mm ROC → truing errors
Short λsp → grit compliance → 0.01 mm ROC → grit response
Example of hardness figure-of-merit:
H = 67 / 45 / 12
λlong
λmid
λshort

Figure 7. Several scale lengths may be necessary to represent a grinding wheel's resistance to indentation.

Enabling Technologies

The optimization of grinding wheels, and their insertion into production practice may be coupled with the development of enabling technologies. For example, we have observed the performance of metal-bonded wheels to degrade more than resin-bonded wheels in the presence of machine vibrations. This observation may relate to the hardness concepts mentioned in terms of accommodating wheel motion errors. Thus, for some wheels to produce smooth surfaces, it may be necessary to employ stiff, well-damped machine tools. Therefore, the further development and availability of high quality machine tools may enable more success stories for fine grinding in US industry.

Although resin-bonded wheels may provide better levels of surface finish, their wear rates tend to be much higher than for metal-bonded wheels. During a production run, this increased wear quickly leads to an uncertainty in knowing the position of the tool relative to machine coordinates, and often the tool spends a significant duration performing 'air grinding.' A reliable, non-contact, tool-to-workpiece proximity sensor that functions under grinding conditions (i.e. fluid flowing and spindles running) would enable the position of the tool relative to the workpiece to be determined in real-time, for each workpiece. We have successfully demonstrated such a non-contact acoustic emission (AE) sensing scheme at LLNL,[14] and will soon be installing a prototype in the production equipment at the Center for Optics Manufacturing. One of our goals is to use this AE sensing scheme to enable the production use of resin-bonded tools in the presence of extensive tool wear.[15]

Conclusions

The goal of this paper is to present an approach for improving the linkage between the users and makers of fine diamond grinding wheels. A promising avenue for accomplishing this is to formulate a voluntary product standard that comprises performance indicators that bridge the gap between specific user requirements and the details of wheel formulations. We propose a set of performance specifiers or figures-of-merit, that might be assessed by straightforward and traceable testing methods, but do not compromise proprietary information of the wheel user or wheel maker. One such performance indicator might be wheel hardness as measured by the resistance to indentation. Resistance to indentation may indicate the wheel's ability to accommodate geometric errors over several different scale lengths, while maintaining the grinding force below the level required for high quality grinding. In addition, we considered technologies that might be required to realize the benefits of optimized grinding wheels. A non-contact wheel-to-workpiece proximity sensor may provide a means of monitoring wheel wear and thus wheel position, for wheels that exhibit high wear rates in exchange for improved surface finish.

Acknowledgments

The authors would like to thank Blaine Beith for performing wheel evaluation tests mentioned in this paper, and Don Golini (COM) for interesting discussions regarding fine grinding.

Notes

[1] Pollicove, H. M., "The Center for Optics Manufacturing", **1994 Technical Digest for the Optical Fabrication and Testing Workshop**, paper OWD1 (1994); Leshne, R. H., "Support for the US precision optics manufacturing base: The Center for Optics Manufacturing", **Proc. SPIE**, vol. 1168, 2-8 (1989).
[2] For example: CNC Systems, Ontario, NY; Loh Optical Machinery, Inc., Milwaukee, WI; Rank Pneumo, Keene, NH.
[3] The extent to which these benefits can be realized depends upon the specific choices for which platforms are employed.
[4] Ray Lacroix, President, American Precision Optics Manufacturers Association (APOMA), personal communication.
[5] Some optical shops may employ a 1-wheel process for meeting some production requirements.
[6] Gray, F., "A Look at the Superabrasives Industry Today," **Finer Points**, vol. 7, no. 4, 1995, pp. 8-10.
[7] Taylor, J. S. and Piscotty, M. A., "Survey of Wheel Users and Review of Precision Machining at LLNL", Invited paper at IDA Annual Meeting, Tucson, AZ, April 1-5, 1995.
[8] It should be noted that not all companies contacted had complaints about their wheel supplier, nor were all companies fully committed to transitioning away from loose abrasive lapping.
[9] Vakiner, J., "What Tool Users Need to Know," Invited speaker at IDA Annual Meeting, Tucson, AZ, April 1-5, 1995.
[10] *SuperTech 1996: Grinding and Machining Brittle Materials with Superabrasives* is being hosted by Lawrence Livermore National Laboratory and the Industrial Diamond Association, to be held at LLNL on November 7-8, 1996, just prior to the 1996 ASPE Annual Meeting in Monterey; for more information, please contact one of the authors.
[11] Piscotty, M. A., Taylor, J. S., Blaedel, K. L., "Performance Evaluation of Bound Diamond Ring Tools," **Optical Manufacturing and Testing**, Proceedings SPIE, vol. 2536, pp. 231-246 (1995).
[12] Johnson, K. L., **Contact Mechanics**, Cambridge University Press, New York (1987).
[13] Polvani, R. S. and Evans, C., "Micro-indentation assessment of near surface material properties and subsurface damage in precision machining," in **Ultraprecision in Manufacturing Engineering**, Proc. of the International Congress for Ultraprecision Technology, May 1988, Aachen, pp. 271-286.
[14] Taylor, J. S., Piscotty, M. A., Blaedel, K. L., Weaver, L. F., and Dornfeld, D. A., "Investigation of Acoustic Emission for Use as a Wheel-to-Workpiece Proximity Sensor in Fixed-Abrasive Grinding," **Proc. of the ASPE 1995 Annual Meeting, American Society for Precision Engineering**, 159-162 (1995).
[15] Other issues, such as extreme non-trueness, may also limit the use of some wheels in the presence of extensive wear.

Influence of Workpiece Properties on Tool Performance in Deterministic Microgrinding of Optical Materials

Yiyang Zhou[1], and Paul D. Funkenbusch[1, 2]

[1]Center for Optics Manufacturing and [2]Department of Mechanical engineering
The University of Rochester, Rochester, NY 14623

Abstract

The influence of workpiece properties on tool performance in deterministic microgrinding includes issues such as macroscopic and microscopic tool performance, influence of workpiece properties on tool behavior, micro-chip formation and its influence on tool behavior. A general review is presented for the research pursued in the past years. Ideas and hypothesis are also included for discussion and reference.

Introduction

Deterministic microgrinding with bound abrasives is a complex process involving both mechanical and chemical interactions among the workpiece, the grinding abrasive, and the matrix material. It is important to understand the dependence of tool performance on workpiece properties in microgrinding of optical materials, because it controls not only grinding efficiency, tool life, and process cost, but also the component quality such as surface and subsurface damage.[1, 2]

Workpiece properties can strongly affect tool performance, which is commonly characterized by tool wear or grinding ratio.[3] The properties of optical materials vary over a wide range. Tooling and grinding conditions acceptable for one material are likely to be inadequate for another. To understand the influence of workpiece properties requires knowledge of both macroscopic tool wear and microscopic tool surface topography.

In addition, the workpiece surface features (e.g. roughness) and the characteristics of the swarf produced in the grinding process need to be examined in order to acquire an adequate picture of the dynamic tool-workpiece interaction.

The Influence of Workpiece Properties on Macroscopic Tool Performance

An example of the strong influence of workpiece mechanical properties on tool behavior was found in the microgrinding of a series of glass ceramics. Figure 1 shows the accumulated tool wear data for these materials, which had similar overall chemistries but different percentages of the

glass and ceramic phases. Flat surfaces were ground. The figure in the Appendix shows the tool setup for all flat surface generation used in this study.

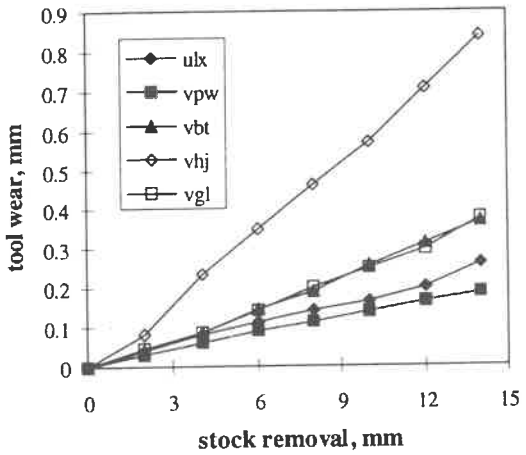

Figure 1 Accumulated tool wear vs. stock removal for five glass ceramics. A thin wall (1 mm thickness) 10/20 um N75 metal-bond wheel was used. The spindle speed was 2000 rpm, and the feed rate was 0.2 mm/min. Tool wear was measured with a probing device built on the grinding machine every 2 mm of stock removal.

An important recent discovery in the microgrinding field is the utility of a combination of mechanical properties, known as the ductility index in correlating the roughness of ground or polished surfaces.[4] The ductility index is defined as

$$\Xi = (K_c/H)^2$$

where, K_c is the fracture toughness and H is the hardness.

Figure 2 shows the correlation of the roughness of the glass ceramics following grinding with the ductility index. One hypothesis for the correlation is that the surface roughness is determined by the size of the micro-chips; and the chip size correlates with ductility index.[5]

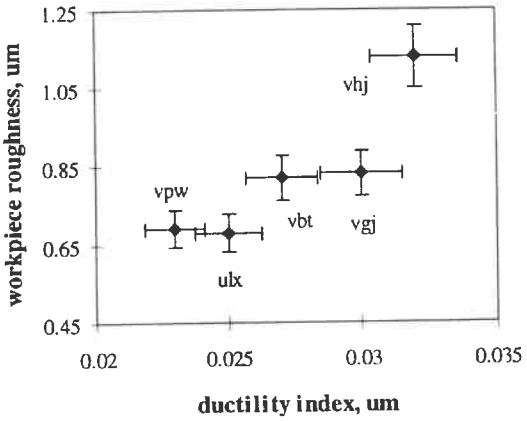

Figure 2 Surface roughness vs. ductility index for glass ceramics.

Figure 3 shows that the tool wear rate also exhibits a correlation with the ductility index for these materials, where the tool wear rate is obtained by linear regression on the accumulated tool wear data (Figure 1). This is believed to also reflect the influence of chip size.

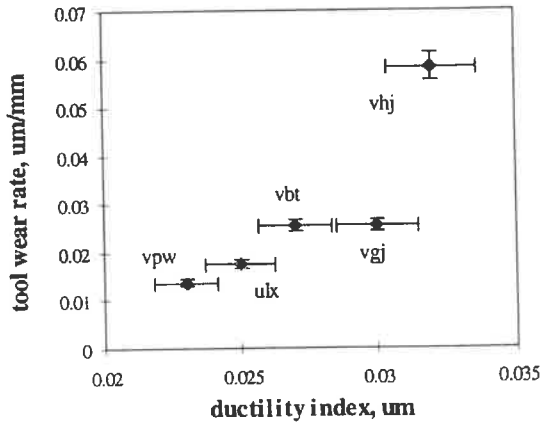

Figure 3 Tool wear rate vs. ductility index of glass ceramics.

A similar tool wear rate experiment was also performed for a wide range of optical glasses, and the results are shown in Figure 4. The selection of glasses used in the test spans the range of mechanical properties

generally observed for optical glasses and also includes a wide range of chemistries.

The influence of workpiece properties on tool behavior is clearly seen. However a simple correlation of the type observed for the glass ceramics has not yet been found. This indicates that workpiece mechanical properties may not be entirely explicable to tool wear behavior. Since the glasses also differ in their chemistry, it is speculated that the workpiece chemistry also affects tool wear.

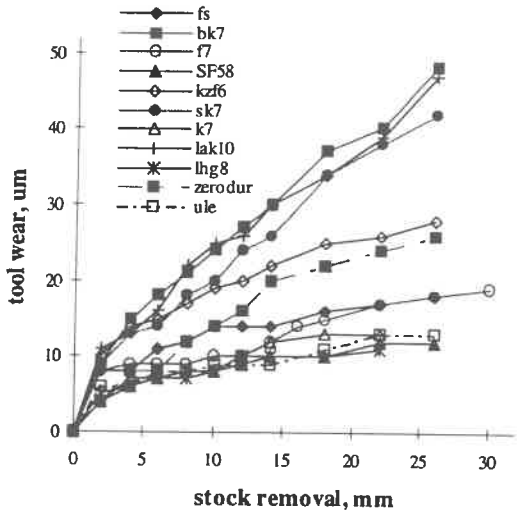

Figure 4 Accumulated tool wear vs. stock removal for eleven optical materials. Diameter of the glass blankes was 40 mm. A 10/20 um metal-bond N75 wheel was used. The spindle speed was 5000 rpm. The feed rate was 0.1 mm/minute.

The Influence of Workpiece Properties on Microscopic Tool Performance

Microscopic tool performance is characterized by measuring the protrusion height and the wear flat size of individual diamond particles on the tool surface.[6,7] An average value of protrusion and wear flat size was obtained by measuring a number of particles on the tool surface.

Figure 5 and 6 show the average protrusion height and wear flat size vs. workpiece hardness for some of the optical materials tested above. Protrusion height decreases with workpiece hardness, indicating that the capability of abrasive particle penetration into the workpiece becomes smaller as the workpiece gets harder. Wear flat size increases with workpiece hardness, indicating that more particles with larger wear flat size stay on the tool surface as the workpiece hardness gets higher. This increases the total load on the grinding wheel under a constant feed rate condition.

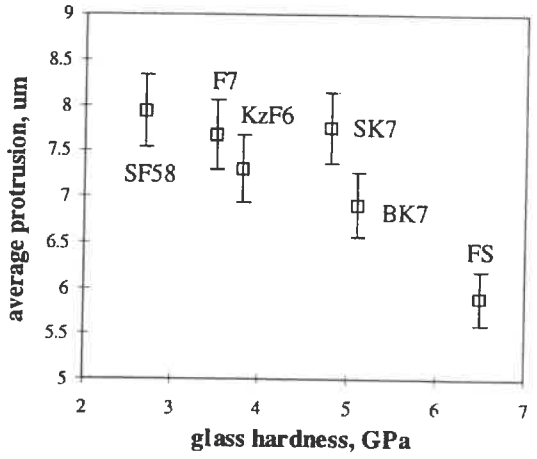

Figure 5 Average protrusion vs. hardness.

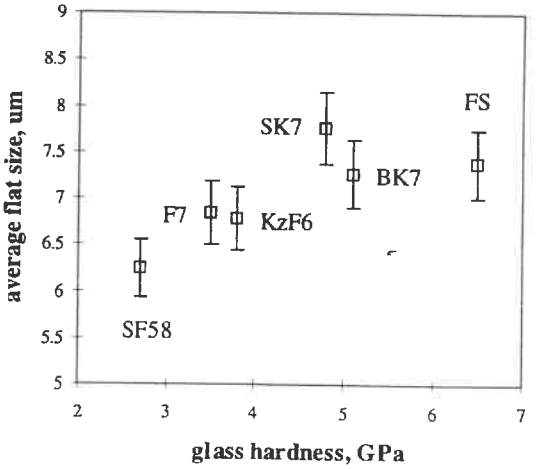

Figure 6 Average wear flat size vs. hardness.

The ratio of protrusion and wear flat size is also used as a single parameter to characterize microscopic tool behavior. Figure 7 shows the correlation between the p/f ratio and workpiece hardness. Correlation of the ratio with other mechanical properties is weak. So, workpiece hardness is the control factor to microscopic tool behavior. The p/f ratio can also be used to rank material grindability. A material with high p/f ratio is easy to grind, therefore has high grindability.

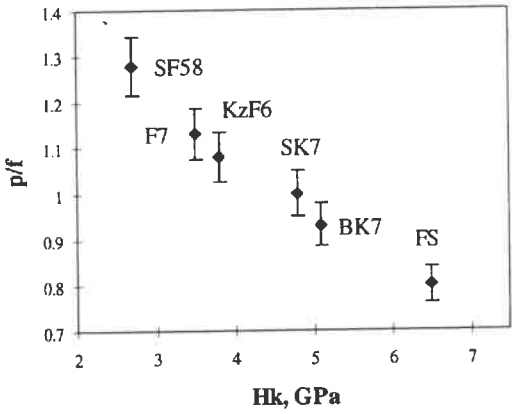

Figure 7 The p/f ratio vs. workpiece hardness.

Sapphire Grinding

Microgrinding of sapphire is difficult because tool performance usually deteriorates after small amounts of workpiece removal. To meet the requirement of CNC grinding systems, new wheels that can retain their sharpness during grinding should be developed. We have been testing vitrified-bond wheels, which tend to have higher wear rates than the metal-bond wheels. Two interesting initial observations are reported here.

Figure 8 shows the tool spindle deflection during grinding for a 220 grit vitrified-bond diamond wheel in grinding a 52 mm diameter single crystal sapphire. The deflection is proportional to the force applied to the wheel. Larger deflection implies larger force on the wheel.

There are three drops in spindle deflection. After 12 mm of stock removal, the deflection stayed at a relative high level. The test was terminated because the sapphire blank was exhausted. The grinding wheel wear is about 100 μm over about 18 mm of stock removal. The variation of spindle deflection indicates an associated change in grinding force. The possible reason for the force decrease is that the wheel self-sharpened, and its grinding efficiency increased. This was the first time in our study that tool self-sharpening was observed in grinding sapphire.

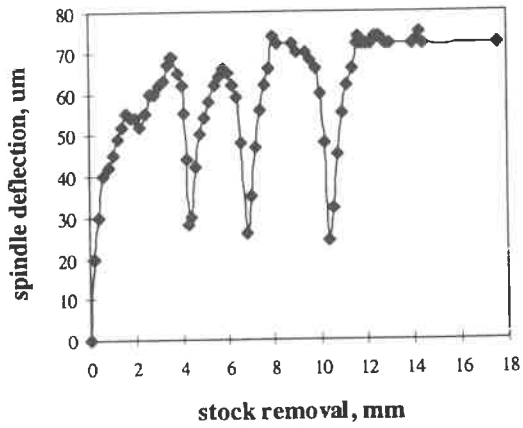

Figure 8 Spindle deflection vs. stock removal. The grinding condition was 1500 rpm spindle speed and 0.2 mm/min. feed rate.

The effect of diamond type was also examined in grinding sapphire for possible improvement on component quality. Figure 9 shows the surface roughness generated by a conventional 400 grit vitrified bond diamond wheel and a 400 grit vitrified bond poly-crystalline diamond wheel. The poly diamond wheel gives a much smoother surface than the conventional wheel. The

phenomena is currently being investigated in more detail.

Investigation of Micro-chips (Swarf)

The function of swarf in microgrinding of optical materials is not clear. Preliminary experiments have been conducted to asses the size of swarf produced from different workpiece materials, and its dependence on the grinding parameters/diamond size.

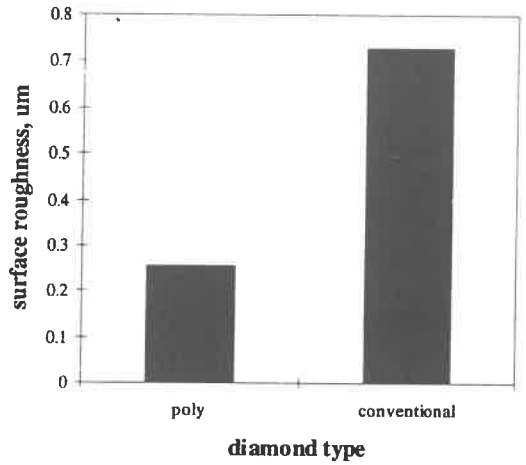

Figure 9 Effect of diamond type on surface finish.

Two types of optical glass, Fused Silica (FS), and BK7 were tested. Figure 10 shows the average chip size vs. glass type and grinding condition. The wheel used and the grinding conditions were listed in the figure caption. The tool speed and workpiece speed were same in the test. Note that the two different diamond sizes also had different infeed rates, so the size effects observed include infeed differences as well.

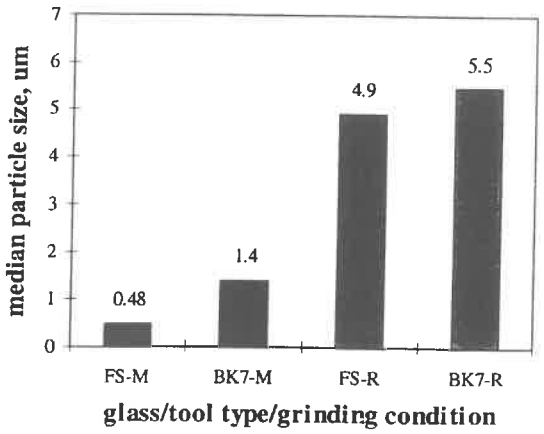

Figure 10 Average chip size vs. glass type, tool type, and grinding condition, where "M" represents the 10/20 μm diamond wheel with 0.1 mm/min. feed rate, and "R" represents the 220 grit diamond wheel with 0.5 mm/min. feed rate. The spindle and workpiece rotation are same in the test.

From Figure 10, diamond size, combined with grinding condition, has a great influence on chip size, as shown by the difference between the "R" cases and the "M" cases. The difference in chip size for the 220 grit wheel is not very large, but that for the 10/20 μm wheel is considerable (about a factor of three). The fine diamond wheel is more sensitive to glass properties. More test is underway.

Conclusion

1. Tool performance is strongly affected by workpiece properties in microgrinding of optical and other materials.

2. In grinding a series of chemically similar glass-ceramics, a correlation between the tool wear and workpiece ductility index was observed.

3. Tool topography during microgrinding of optical glasses was found to correlate strongly with workpiece hardness.

4. Vitrified bond wheels, with a relatively high rate of tool wear, offer great promise in the microgrinding of hard materials such as sapphire.

5. Diamond size and workpiece properties have a strong influence on the size of swarf. Swarf formation appears to be more sensitive to workpiece properties for tools with finer diamond size.

Appendix

Flat surface was generated by plunging the wheel downward, as shown in Figure A-1 below.

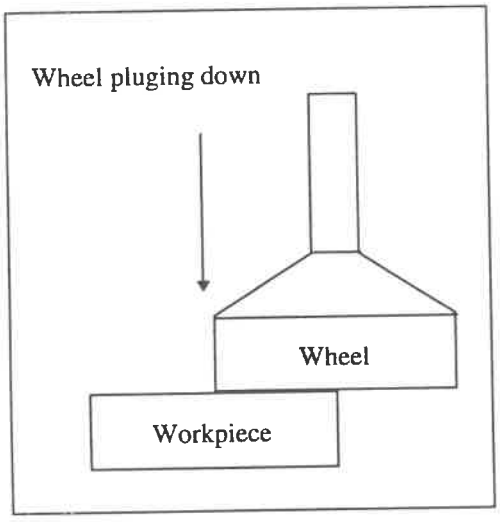

Figure A-1 Grinding geometry

Acknowledgment

The authors thank Donald Golini and Mark Atwood for their advice and technical support. We are grateful for Stephen D. Jacobs and John C. Lambropoulos for their advice and material support. Maynard Smith from Crystal Systems and Ben Stormes from the Wickman Corporation own our special appreciation for their active participation, creative ideas, and innovative technical support. Crystal Systems provides finantial support for this project. Our thanks also go to Harrie Stevens of Corning Incorporated for partially funding this work, and for providing the glass ceramics. Finally, we thank the Army Material Command for funding support.

Reference

[1] D. Golini and W. Czajkowski, Laser Focus World, July edition, 1992

[2] Y. Zhou, D. J. Quesnel, P. D. Funkenbusch, D. Golini and A. Linquist, J. Am. Ceramics, 77, 1994, p. 3277

[3] S. Malkin and N. H. Cook, Trans. ASME, Nov., 1971, p. 1120

[4] J. C. Lambropoulos, T. Fang, P. D. Funkenbusch, M. J. Cumbo, and D. Golini, to be published on Applied Optics

[5] A. G. Evans and D. B. Marshall, Fundamentals of Friction and Wear of Materials, ASME, 1981, p.439

[6] H. Tsuwa, J. Eng. Ind., 1964, p. 371

[7] J. Verkerk and J. Perters, Annals of CIRP, 26/2, 1977, p. 385

Diamond Wheel Wear Sensing with Acoustic Emission
--wheel wear mechanisms and the effects of process variables

Jianshe Tang*, Katsuo Syoji** and David Dornfeld*
*Department of Mechanical Engineering
University of California at Berkeley, Berkeley, CA 94720, USA
**Department of Mechatronics and Precision Engineering
Tohoku University, Sendai 980, JAPAN

Abstract-The wear of diamond wheels has significant influence on the surface finish of ground ceramics and the resulting subsurface fracture damage. For optimization and control of the grinding process it is necessary to monitor the wear states of the grinding wheels. A project on diamond wheel wear sensing with acoustic emission was started recently in the Laboratory of Manufacturing Automation at the University of California at Berkeley. The main aims of the project are: (a) to identify the possible wheel wear patterns at different combinations of bond materials, grits, and grinding conditions. (b) to develop suitable AE signal processing methods to extract the AE features to represent the wheel wear characteristics, and establish a strategy for using AE for in-process monitoring of diamond wheel wear in grinding of ceramics. This paper presents the results of part of the project. It mainly focuses on the diamond wheel wear mechanisms, the effects of process variables including basic wheel elements and grinding parameters, and the relationship with AErms and AE frequency content.

1. Introduction

Acoustic emission can be used for many applications in the grinding process. In the past ten years several studies have already been done, mainly focused on: wheel loading and contact detection [Dornfeld, 1984], dressing control [Inasaki, 1985], chatter [Inasaki, 1991], ductile/brittle model transition [Bifano, 1992], burn detection [Koenig, 1993], surface integrity [Webster, 1994], and dimensional characterization of the wheel [Oliveira and Dornfeld, 1994]. The objective of this research is to establish a relationship between AE signals and diamond wheel wear in grinding of brittle ceramics.

To correlate AE features to diamond wheel wear, the first step is to identify the specific wheel wear patterns in grinding of ceramics. In grinding with conventional wheels, it is generally recognized that there are three main mechanisms of wheel wear, each of which dominates in a different range of the material removal rate (MRR): abrasive grit wear at low MRR, fracture of the grits at medium MRR, and bond fracture at high MRR. However in grinding with diamond wheels, most of which are manufactured with a matrix type bond, the wheel wear mechanisms are not well identified. In this paper, the influence of several variables on the diamond wheel wear process was first investigated. Then pin-on-disk tests were conducted to help relate grit wear patterns to the AE signal features.

2. Diamond wheel wear mechanisms in grinding of ceramics

In this research, two types of grits with quite different friability G2 and G5, are chosen. The bond materials are the most practically used metal and resin. Table 1 gives the specifications of the 4 types of diamond wheels used. The wheels were made in a ring shape with a removable part. In this way, the grit morphology on a wheel surface can be easily observed with a scanning electron microscopy if necessary. Table 2 gives the truing and grinding conditions. A GC cup truer was employed for the diamond wheel truing and dressing. To keep the initial surface of different diamond wheels after truing as same as possible, GC400I7V and GC200I7V were separately used for truing of resinoid and metal bonded wheels [Syoji, 1991]. Two sets of grinding conditions, moderate with material removal rate Z'=0.17mm^3/mm×s and aggressive with Z'=3.3mm^3/mm×s, were chosen.

Table 1 The specifications of diamond wheels

	Resinoid, N Grade	Metal, R Grade
G2N	SDC(G2N)270N75BE2 (Type2)	SD(G2)270R75ME (Type3)
G5	SD(G5)270N75BE2 (Type1)	SD(G5)270R75ME (Type4)

Table 2 Truing and grinding conditions

Machine	Surface grinding machine
Coolant	Chemical solution type
Workpiece	Si3N4, 60mm(L)×4mm(W)
Truing conditions	GC cup truer, GC400I7V, GC200I7V
Grinding conditions Wheel speed (1) Moderate (2) Aggressive	 1900m/min υ=1m/min, Δ=10μm υ=10m/min, Δ=20μm

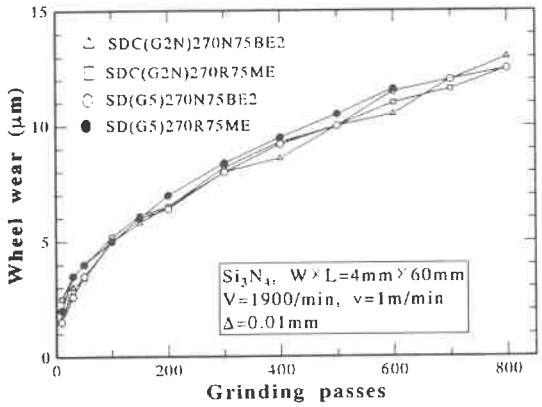

Fig. 1 Wheel wear vs. grinding passes

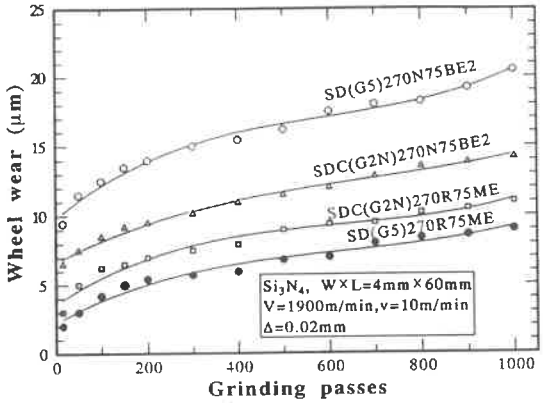

Fig. 2 Wheel wear vs. grinding passes

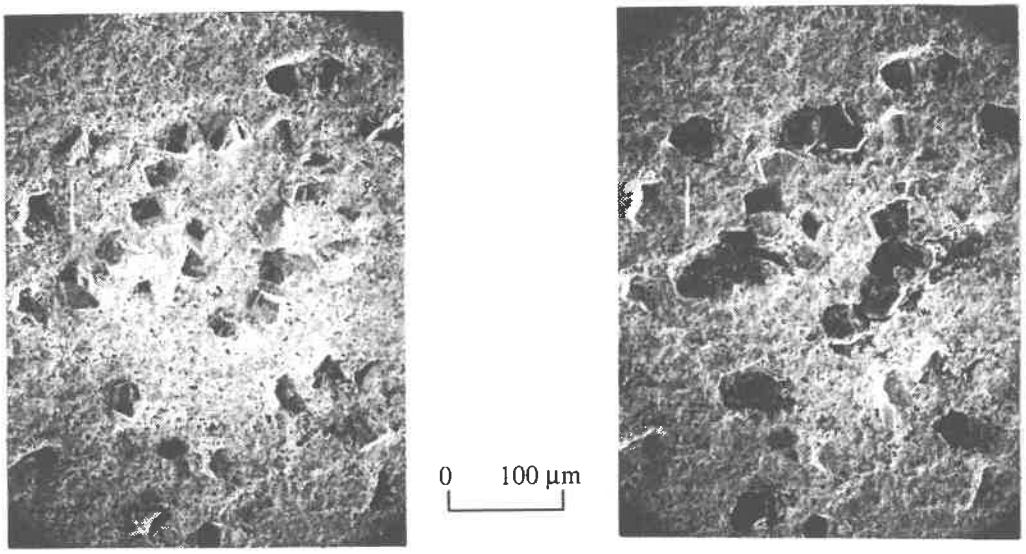

(a) After dressing

(b) After 100 passes grinding

Fig. 3 Blocky grit wheel surfaces

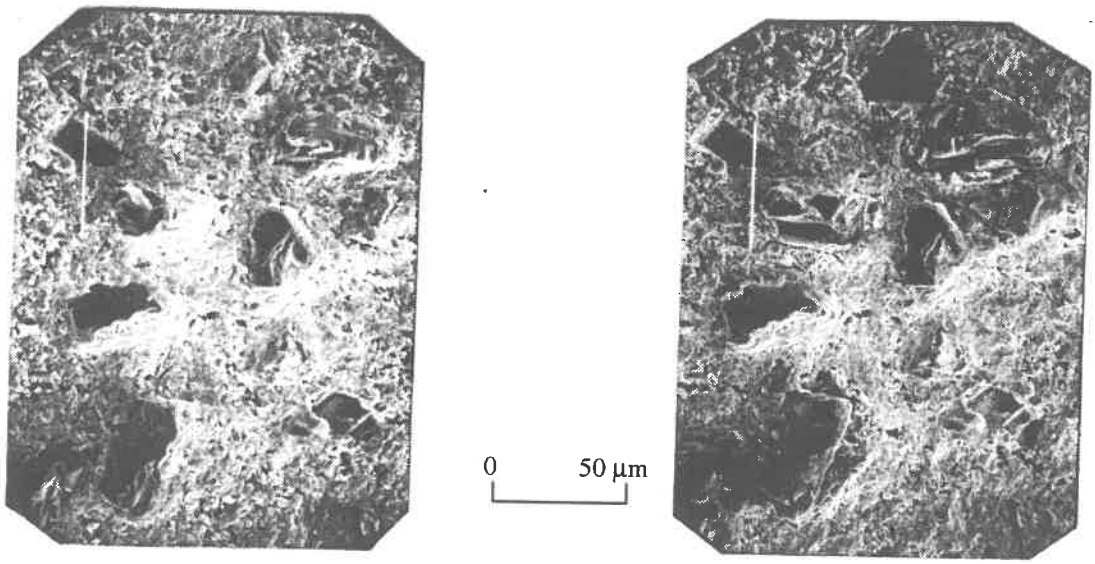

(a) After dressing

(b) After 200 passes grinding

Fig. 4 Friable grit wheel surfaces

Under moderate grinding conditions, as shown in Fig. 1, the radial wheel wear does not appear to be any different for the 4 kinds of wheels. This is simply because grit wear takes place in the form of abrasion regardless of the bond and grit types.

Under aggressive grinding conditions, the radial wheel wear amount is quite different for different wheels, see Fig. 2. This implies that the wheel wear pattern should not be the same for different wheels. Fig. 3 shows the surfaces of a blocky grit resin bonded wheel. It is obvious that grit pull-out and grit sinking are the dominant wear patterns for this kind of wheel and result in the largest radial wheel wear. Fig. 4 gives the surfaces of a friable grit resin bonded wheel. Grit cracking, which some times extends inside the bond material, represents the prevailing wear mechanism. On the other hand, for metal bonded wheels, which hold the grit more firmly than resin bond, attritious wear is the main wear pattern for blocky grit wheels. A micro-chipping wear pattern was seen for the friable grit wheels. The wheel wear patterns in different combinations of grits and bond materials is summarized in figure 5.

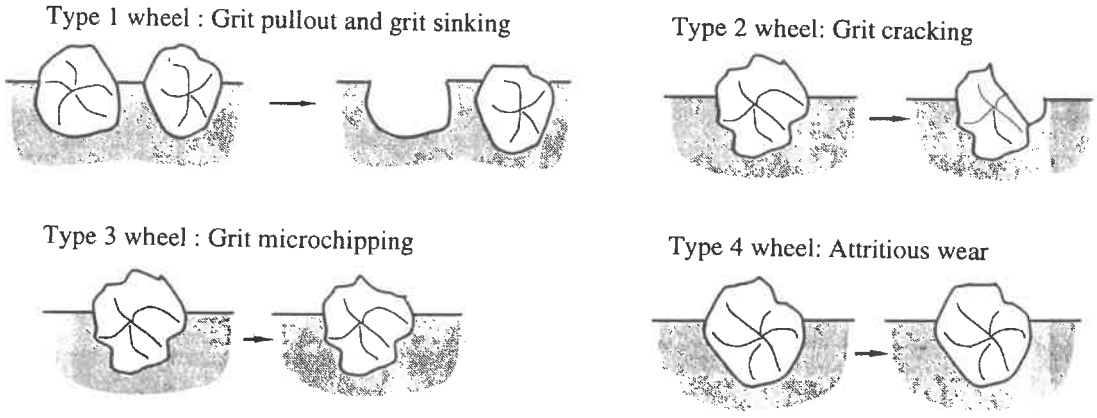
Type 1 wheel : Grit pullout and grit sinking
Type 2 wheel: Grit cracking
Type 3 wheel : Grit microchipping
Type 4 wheel: Attritious wear

Fig. 5 Wheel wear patterns under aggressive grinding conditions

3. Pin-on-disk wear test and its correlation with AE

In addition to the AE generated by different grit wear patterns and chip formation, several other AE source types occur in grinding, such as coolant supply and chip wheel interaction. To understand how AE is generated by grit wear, it makes sense to isolate these sources and study their signal features. For this purpose we use a pin-on-disk sliding test to simulate the grit-work interaction of a single diamond grit in grinding process.

Jiaa and Dornfeld [Jiaa, 1990] have used AE to investigate sliding and wear of metal-metal pairs in pin-on-disk tests. As shown in figure 6, for a long-sliding distance test of AISI 1018-OFHC copper pairs, three different regions, running-in, steady state and self-acceleration, corresponding to the coefficient of friction variation, can be distinguished from the results of AE rms signal. The AE signal is very sensitive to changes in the pin-disk interface during grinding.

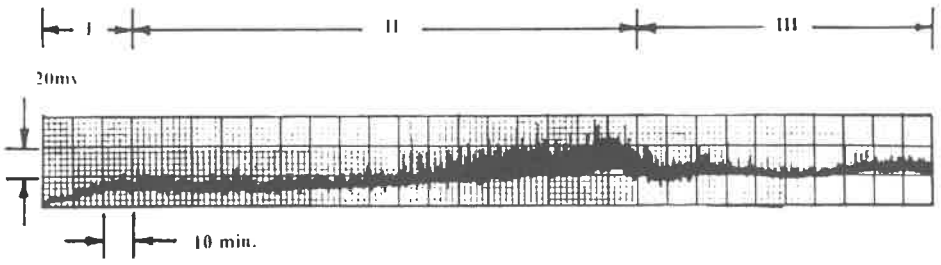

Fig. 6 Experimental records of AE rms signals vs. time in long-distance sliding tests
I, running-in region; II, steady state region; III, self-acceleration region.

This research will focus on diamond-Si3N4, that is, brittle materials pairs. Experimental tests were conducted on a pin-on-disk machine developed by Misra [Misra, 1979], the same used by Jiaa and Dornfeld. Figure 7 is a schematic of the data acquisition set up. A PAC model S9208 wide band acoustic emission sensor attached to the pin holder was used to measure the AE signal from the sliding process. AE signals from the transducer passed through a preamplifier and a main amplifier which provided a total gain of 60 dB, then band-pass filtered with the pass band between 50~1000 kHz. The signals were then fed into a HP digital oscilloscope for visual inspection and to a GageScope data acquisition board, where the analog signals were sampled at 5 MHz and stored in an IBM PC for further signal processing.

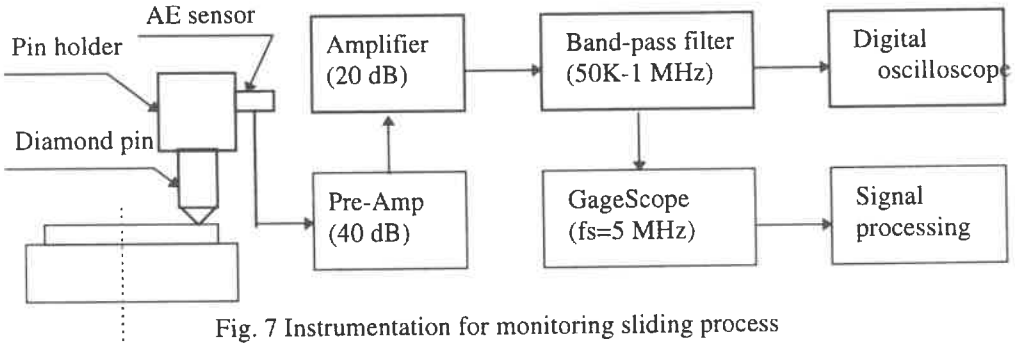

Fig. 7 Instrumentation for monitoring sliding process

Figure 8 shows the variation of the mean value of AE rms voltage with sliding distance when using a diamond cone as a pin in dry sliding. The diamond cone has an included angle of about 90°and a tip radius of about 10 μm. Two distinct AE rms stages can be identified. The high initial AE rms was probably due to the plowing and microcutting actions of the diamond cone tip. As sliding progressed, the AE rms decreased from 67 mv to 38 mv when steady state sliding was reached. The fast decrease in AE rms in the first 200 m of sliding also suggests that quick pin wear occurred on the tip of the diamond in the earliest sliding and the tip became dull thereafter. These observations are consistent with the results published by other investigators from the viewpoint of coefficient of friction of diamond-Si3N4 pairs [Miyoshi, 1992, Lai, 1994, Hayward,1991, Gangopadhyay, 1993].

Figure 9 gives the frequency domain of the recorded raw signals over the two regions. The magnitude in the frequency band of 350~650 kHz decreased about 20 dB after 300 m sliding from the start of the test. This was also due to the transition from plowing and microcutting to sliding, or the transition of the diamond tool from sharp to dull.

The same trends are also observed when using other shaped diamond pins, such as round edge and rough edge diamond cutting tools.

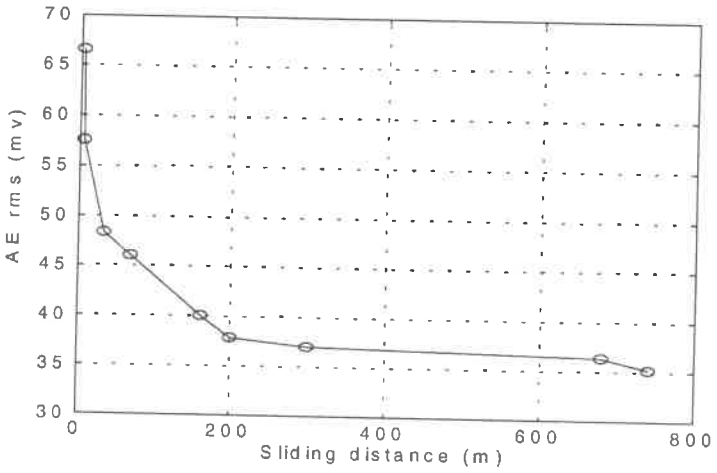

Fig. 8 Mean AE rms vs. sliding distance

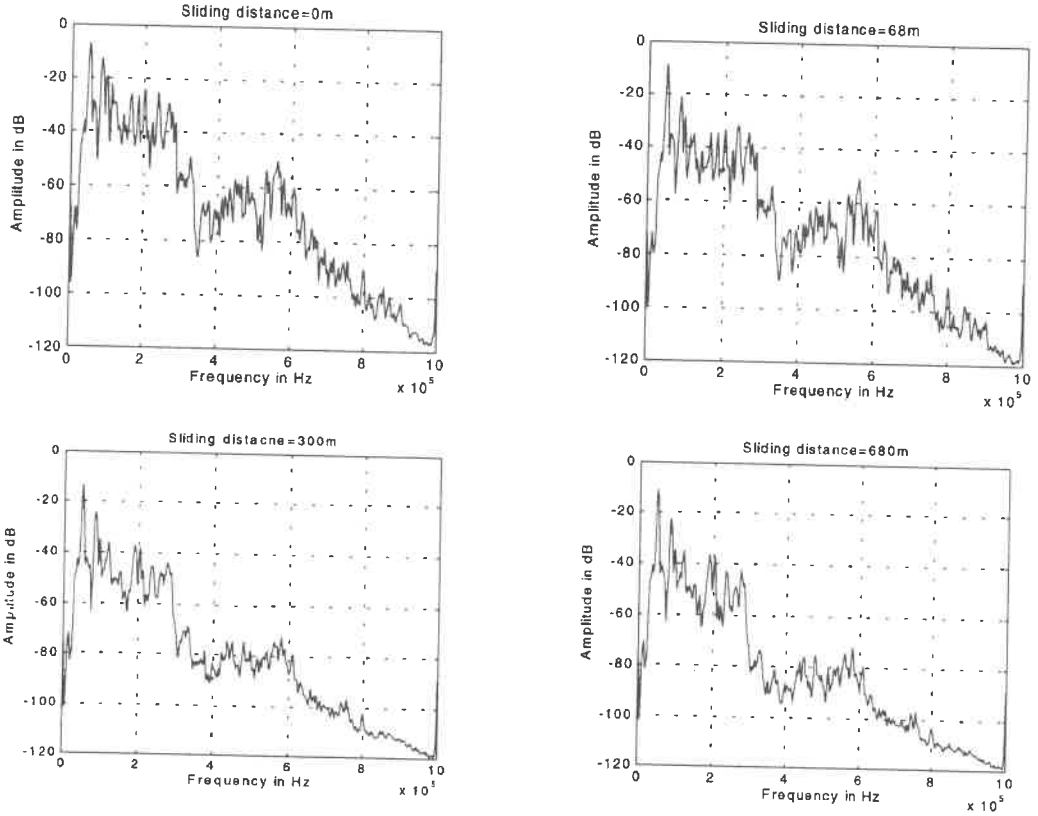

Frequency resolution Be=25kHz, number of averages n=200

Fig. 9 Frequency characteristic of the AE when sliding with a cone shaped tool

4. Conclusions

1. Under moderate grinding conditions, the attritious wear of grits is the dominant wear pattern for all of the wheels manufactured with different bonds and grits. This causes the wheel radius wear amount to be the same regardless of the combination of bonds and grits.
2. Under aggressive grinding conditions, four typical wear patterns are observed, with each corresponding to a specific combination of bond materials and diamond grit types. For resinoid bonded wheels, which have weak grit retention and poor thermal conductivity, pull-out and macro-cracking are the dominant wear mechanisms of blocky and friable type grit wheels, respectively; for metal bonded wheels, which hold the grit more firmly than resin bond, attritious wear is the main wear pattern of blocky grit wheels and micro-chipping wear pattern was seen in the friable grit wheels.
3. pin-on-disk tests show that different sliding regions, plowing-microcutting state and steady sliding state, can be distinguished by AE rms variation and signal amplitude in the frequency band of 350-650 kHz. In these two regions, the sharpness of the pin is quite different, therefore these AE features were also concluded to be related to the sharpness loss of a diamond tool.

Work in progress is evaluating the feasibility of using pin-on-disk test results to describe the wear phenomena in diamond wheels.

References

Bifano, T., et al. "Acoustic Emission as an Indicator of Material Removal Regime in Glass Micromachining", Journal of Precision Engineering , Vol. 14, No. 4, pp. 219-228, 1992.

Dornfeld, D., et al., "An Investigation of Grinding and Wheel Loading Using Acoustic Emission", Trans. ASME, Journal of Engineering for Industry, Vol. 106, No. 1, pp. 28-33, 1984.

Gangopadhyay, A., et al., "Friction and wear behavior of diamond films against steel and ceramics", Wear, Vol. 169, pp. 221-229, 1993.

Hayward, I., "Friction and wear properties of diamond and diamond coatings", Surface and coatings technology, Vol. 49, pp. 554-559, 1991.

Koenig, W., et al., "Monitoring and Sensor Concepts for Higher Process Reliability", SME 5th Grinding Conference, Ohio, 1993.

Inasaki, I., "Monitoring of Dressing and Grinding Process with Acoustic Emission Signals", Annals of the CIRP, Vol. 34, No. 1, pp. 277-280, 1985.

Inasaki, I., "Monitoring and Optimization of Internal Grinding Process", Annals of the CIRP, Vol. 40, No. 1, pp. 359-362, 1991.

Jiaa, C., et al., "Experimental studies of sliding friction and wear via acoustic emission signal analysis", Wear, Vol. 139, pp. 403-424, 1990.

Lai, C., et al., "Relation of friction and wear to processing parameters of polycrystalline diamond films grown on silicon and silica substrates by the hot filament method", Materials Science and Engineering, A183, pp. 257-265, 1994.

Miyoshi, K., et al., "Friction and wear of diamond and diamond-like carbon coatings", Surface and coatings technology, Vol. 54/55, pp. 428-434, 1992.

Oliveira, J., et al., "Dimensional Characterization of Grinding Wheel Surface through Acoustic Emission", Annals of the CIRP, Vol. 43, No. 1, pp. 291-294, 1994.

Syoji, K., et al., "Studies on truing of diamond vitrified wheels", Int. J. Japan Soc. Prec. Eng., Vol. 25, No. 4, pp. 21-26, 1991.

Webster, J., et al., "Acoustic Emission for Process Control and Monitoring of Surface Integrity during Grinding", Annals of the CIRP, Vol. 43, No. 1, pp. 299-304, 1994.

Zhang, B., "Wear characteristics of diamond tools in machining ceramics", Tribology transactions, Vol. 38, No. 2, 466-472, 1995.

Truing and Dressing of Fine Grit Super-Abrasive Products

by Marc Tricard and K. Subramanian
World Grinding Technology Center – Norton Co.

Typically overlooked in process development the truing and dressing are some of the key factors contributing to the technical and economic success of any superabrasives grinding operation. This paper will describes the grinding, truing and dressing operations as three "Systems", each relying on a few microscopic interactions. A good understanding of the nature and sources of those microscopic interactions, through careful analysis and/or macroscopic measurements, can in turn lead to quantum improvements in the Truing and Dressing systems, thereby significantly enhancing the output of the grinding systems.

As referenced in numerous papers the systems approach has been successfully applied to grinding processes using super-abrasives, either CBN or diamond, in a variety of applications (1-6). The following flow chart provides the Systems description for grinding processes:

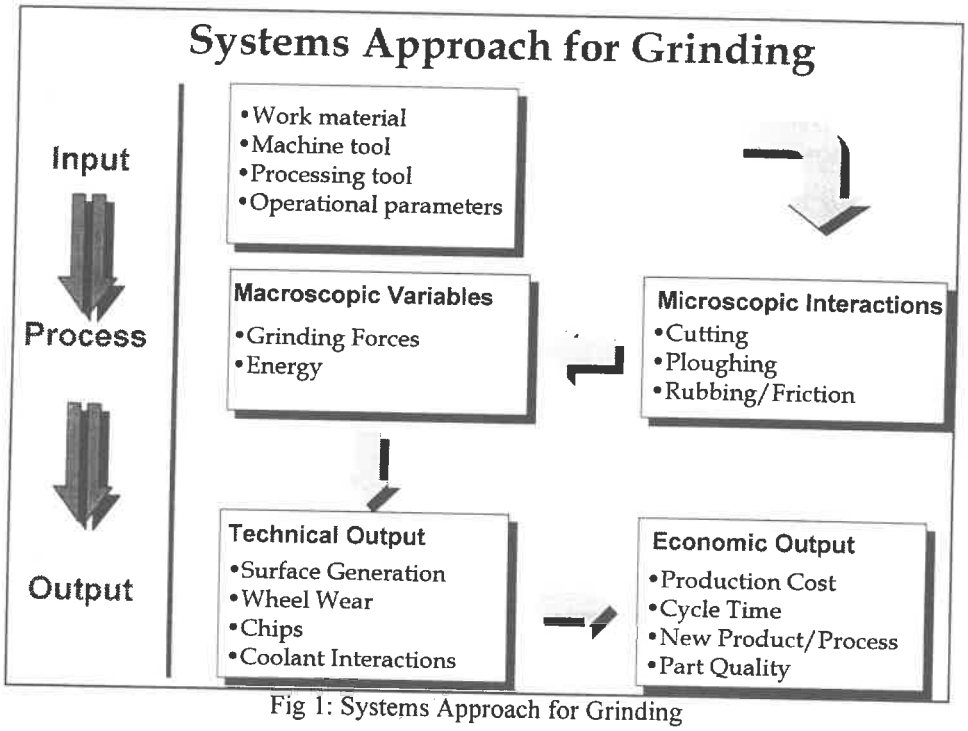

Fig 1: Systems Approach for Grinding

In summary, while grinding processes are influenced by hundreds of variables, they can be grouped under four input categories. These in turn lead to a few microscopic interactions which in turn can be quantified or monitored using certain measures or macroscopic variables. The result of these interactions are outputs which can be delineated between technical and economic aspects. The microscopic interactions can be further broken down into (see Fig 2):

- abrasive/workpiece interactions (encompassing cutting, plowing and sliding)
- chip/bond interactions
- chip/workpiece interactions
- bond/workpiece interactions

Of which the abrasive/work interaction typically plays the critical role for the two requirements of a grinding process: the surface generation and the characteristics of the generated surface .

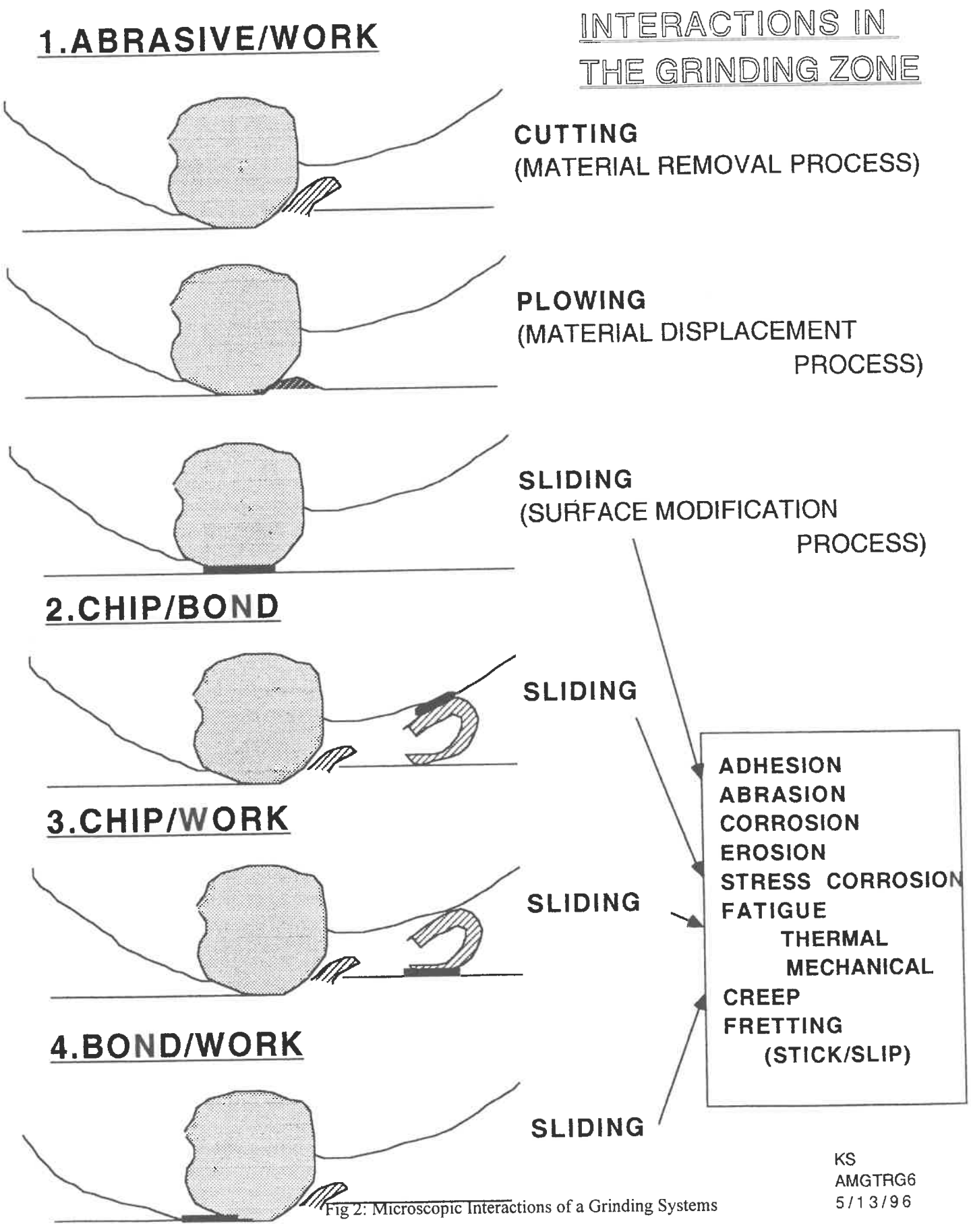

Fig 2: Microscopic Interactions of a Grinding Systems

Any grinding system consists of several subsystems. Two of them are the truing and dressing operations which can be described using Fig 3 and 4, with their microscopic interactions shown in Fig 5 and 6.

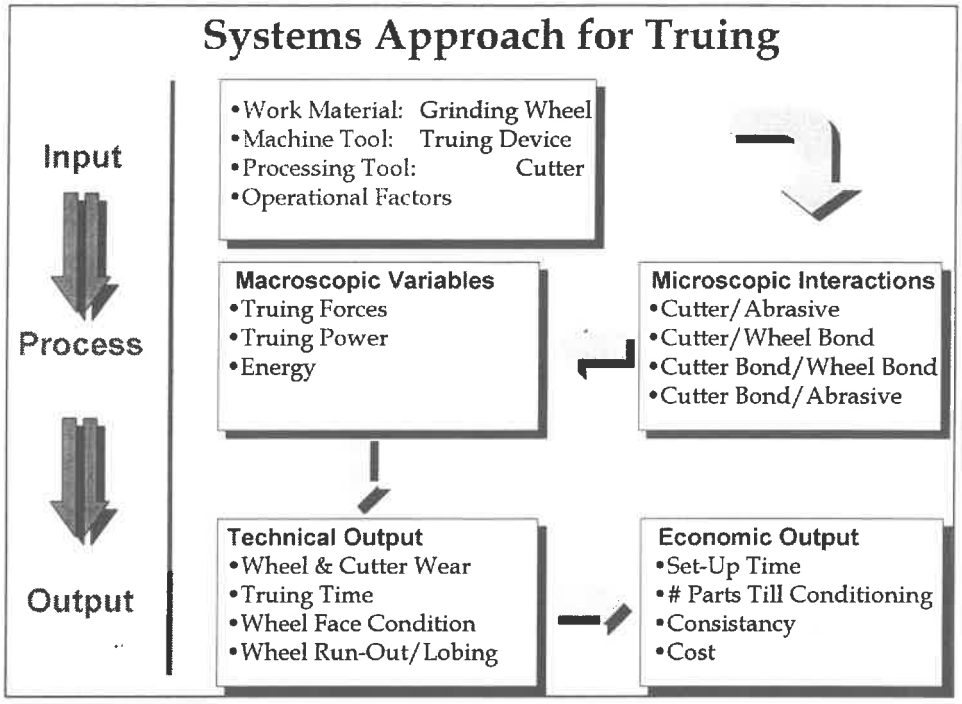

Fig 3: Systems Approach for Truing

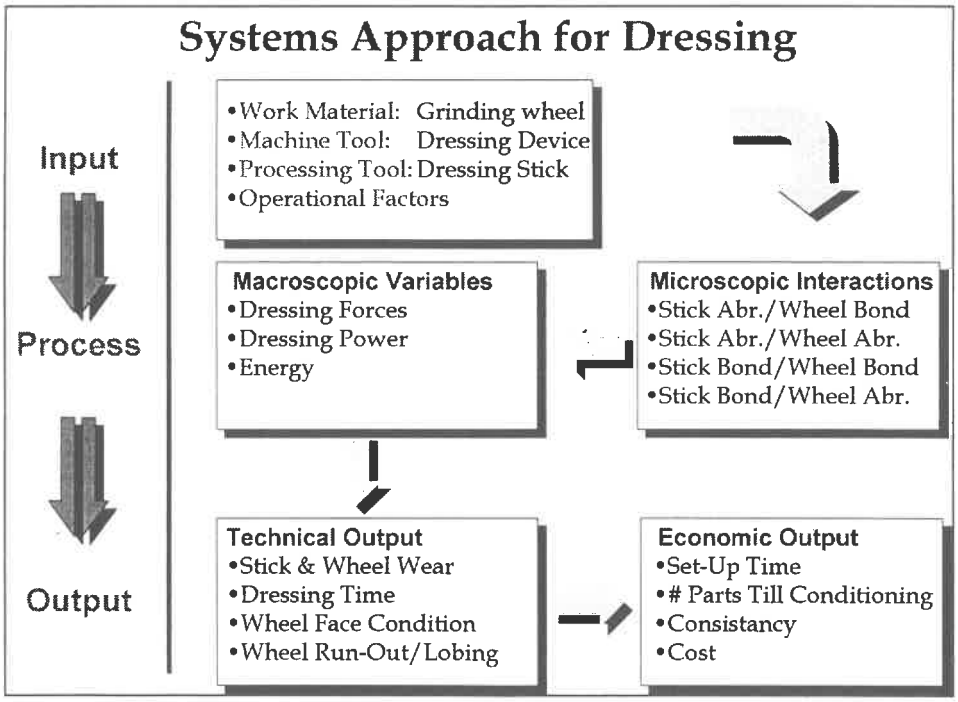

Fig 4: Systems Approach for Dressing

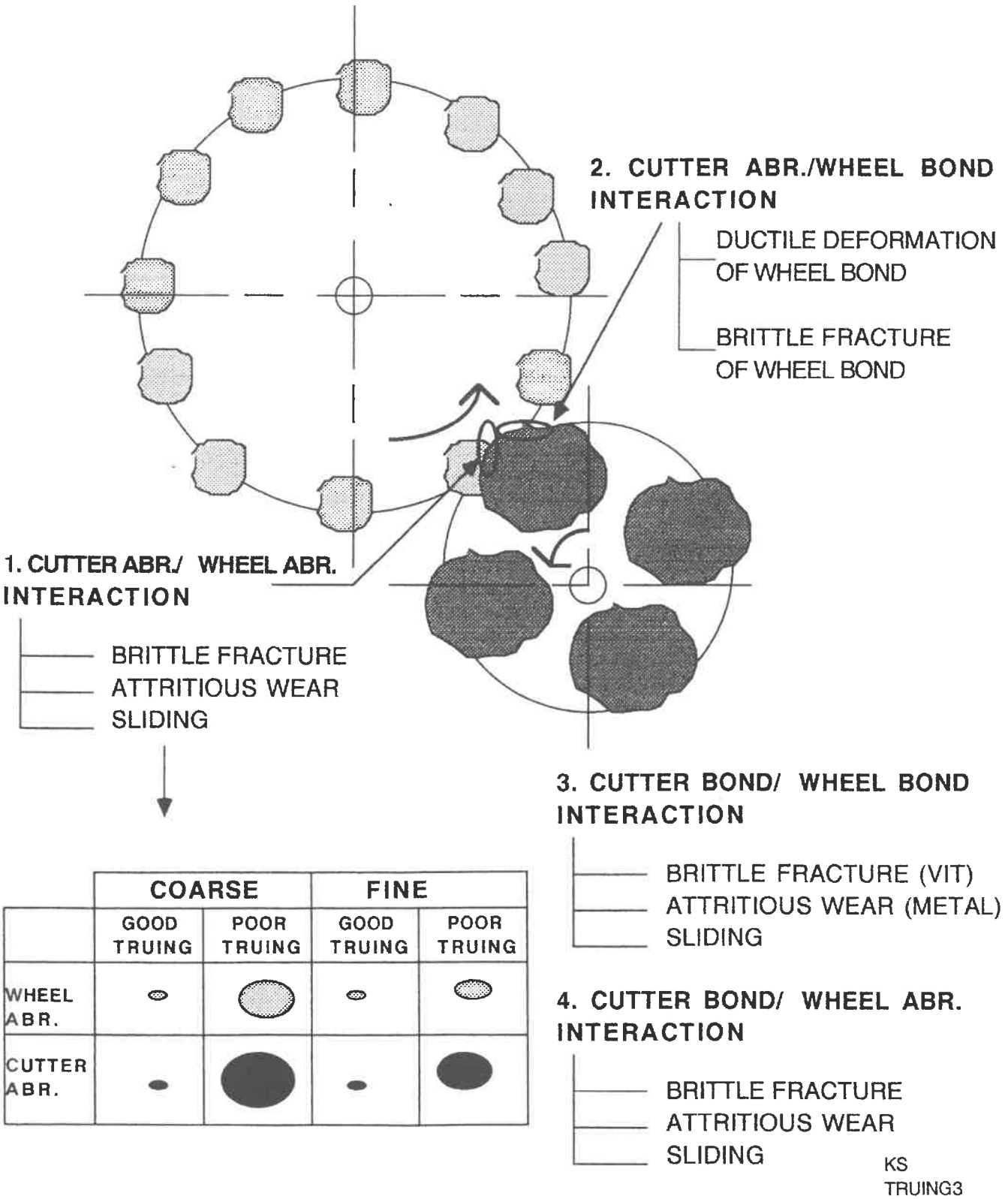

Fig 5: Microscopic Interactions of a Truing Systems

DRESSING OF S/A WHEEL WITH ABRASIVE STICK

(MICROSCOPIC INTERACTIONS)

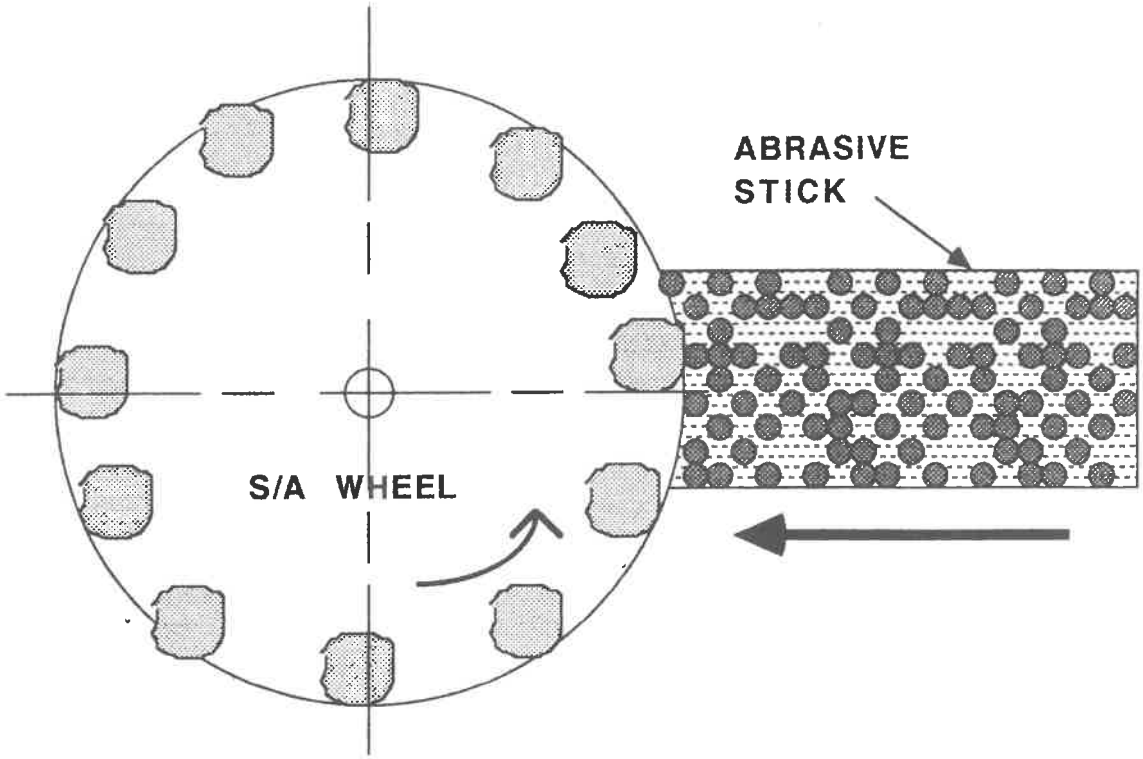

2. STICK ABR./WHEEL ABR. INTERACTION

- BRITTLE FRACTURE
- ATTRITIOUS WEAR
- SLIDING

	WHEEL ABRASIVE			
	COARSE		FINE	
	GOOD TRUING	POOR TRUING	GOOD TRUING	POOR TRUING
AFTER TRUING	●	⬮	●	⬮
AFTER DRES-SING	●	⬮	●	⬮

1. STICK ABR./WHEEL BOND INTERACTION

- ATTRITIOUS WEAR
- SLIDING
- EROSION
- "MACHINING" OF ABR. STICK (AT STEADY STATE)

3. STICK BOND/WHEEL BOND INTERACTION

- SLIDING
- EROSION OF WHEEL BOND

4. STICK BOND/WHEEL ABR. INTERACTION

- BRITTLE FRACTURE
- ATTRITIOUS WEAR

KS
TRUING4
5/12/96

Fig 6: Microscopic Interactions of a Dressing Systems

References

1. Bright, E.; J.F. Eckalbar; B.J. Mc Entire, V.K. Pujari and M. Advanced Ceramic Manufacturing of SiALON Exhaust Valves", SAE Technical Papers # 960051, International Congress and Exposition, February 26-29, 1996, 11 pages.

2. Subramanian, K. "Make the best use of CBN grinding wheels through proper truing, dressing and conditioning", SME Technical Paper MR85-302, 12 pages.

3. Subramanian, K. and Lindsay, R. P. "A System Approach for the Use of Vitrified Bonded Superabrasives Wheels for Precision Production Grinding", Journal for Engineering for Industry, February 1992, Vol. 114, pp. 41-52.

4. Subramanian, K.; Redington, P. D., and Ramanath, S. "A Systems Approach for Grinding of Ceramics", Bulletin of the American Ceramic Society, March 1994 Mar, Vol. 73, No. 3, pp. 61-66.

5. Tricard, M. "Truing And Dressing Superabrasives - Matching Methods to Needs", Modern Machine Shop, June 1995.

6. Tricard, Marc; John Hagan; Patrick Redington; K. Subramanian and Mike Haselkorn "Development of Plasma Spray Coated Cylinder Liners", SAE Technical Papers # 960048, International Congress and Exposition, February 26-29, 1996, 7 pages.

The Effect of the Coolant on the Glass Work and the Diamond Tool in Deterministic Microgrinding

by
S. D. Jacobs[1,2], B. E. Gillman[1,2], J. C. Lambropoulos[2,3], Tong Fang[2,3], Yiyang Zhou[2], D. Golini[2] and M. Atwood[2]

(1)Laboratory for Laser Energetics (2)Center for Optics Manufacturing (3)Department of Mechanical Engineering
University of Rochester Rochester, NY 14623

We are studying the effect of various coolants on the grinding of optical glasses with metal bonded, diamond abrasive ring tools. These tools are used in deterministic generating of spheres and aspheres on the Opticam® machines at the Center for Optics Manufacturing (COM). We find that there is a strong correlation between decreasing surface tension of the coolant and increased microroughness of the glass surface when grinding with a 10-20 μm bronze bonded tool. This results in improved cutting efficiency of the tool at constant infeed. This paper gives a brief overview of our findings and offers several possible explanations for the observed results. One explanation concerns the coolant's ability to lubricate the work zone, and the second explanation involves coolant-induced changes to the near-surface mechanical properties of the glass.

Commercial Coolant Survey

Coolants used in modern optics manufacturing are greater than 90% water, with the remainder consisting of commercial additives to prevent rusting, foaming, and bacterial growth. Table 1 gives the properties of 18 commercial coolant concentrates which are sold specifically for use in machining brittle materials. When mixed to the recommended dilution, the resulting coolant is basic and has a unique color. A given formulation may contain some mineral oil which leaves a protective coating on machine parts, and it may have a unique fragrance. Most other properties of the diluted mixture, like electrical resistivity, total dissolved solids, viscosity, and specific gravity are dominated by the water. The quality of water is important[1], and it varies by geographic region within the United States. The tap water used in the Opticam® machines at COM and in the experiments reported here is considered "good" by industry standards, and it has the following characteristics:

Property	Analysis Results
pH	6.9
hardness	91 ppm $CaCO_3$
chlorides	23 ppm

Property	Analysis Results
sulfates	18 ppm
lead	<1 ppb
conductivity	250 μmhos

Coolant Surface Tension and Microroughness[2]

Surface tension is the one coolant property which varies significantly, depending on the type and amount of concentrated additive[3]. An initial experiment was conducted with a Rogers & Clarke G-150 generating machine using 11 coolant formulations diluted according to manufacturer recommendations. The surface roughness, R_a, of K7 optical glass was evaluated for a given coolant after 3 minutes of grinding to remove 100 μm of material[4]. Twelve repetitions were done for a given coolant, and the tool was trued before switching coolants. Experimental conditions are summarized below, and the results are shown in Fig. 1. The coolants break up into two groups, one above and one below ~55 dynes/cm. It is observed that lower surface tension coolants give rougher surfaces than higher surface tension coolants. This experiment was repeated for optical glasses BK7, SF7, SK7, and KzF6 with similar results.

Table 1. Properties of commercial aqueous coolants

	1	2	3	4	5	6	7	8	9	10	11	12	13	14	15	16	17	18
	Amitron Prod.	Master Chemical	Interrsface Dynamics	Interrsface Dynamics	NCH Corp	Blaser Swisslube	LOH Optical	DeBois	Rhodes	Milacron	Milacron	Rhodes	Salem	Sarbond	Texas Ntal	Noritake	Castrol Industrial	Dexcon
	Buff-O-Mint	Trim HM	Challenge 60SHT	Challenge 300HT	Long-Life 20/20	Blasecut 883	K-40	ICF-31NF	Diamond Kool	CX-417	GL 2015	H-D	Spectra-Cool	Surcool K-11	Tool Kool	AFG-T	Safety-Cool 130	Rustlick
Color	green	yellow/green	blue	blue	yellow/green	red	yellow	lt yellow	yellow	lt yellow	pink	orange	blue	orange	amber	yellow	amber	clear
pH	9.8	9.5	9.1	9.5	8.5-9.5	8.79	10.14	10.25	9.7	9.7	10.1	10.1	9.3	10.2	10.16	12.5	9.4	10.4
Boiling point (Celcius)	100	106	NA	NA	100	286	134	> 95	102	100	100	102	NA	105	NA	NA	99.9	101
Specific gravity	1.06	1.09	1.05	1.05	1.06	0.957	0.90	1.01	1.05	1.030	1.095	1.05	1.048	1.07	1.04	1.14	1	1.07
Surface Tension (dynes/cm)	29.7	34.9	36.1	59.9	31.6	34.1	26.2	25.6	37.7	36.7	31.3	30.7	28	28.8		44.5	28.1	35.1
Conductivity (µmohs)	0.31	0.38	0.056	0.033	0.4	0.22	0.011	0.80	0.02	0.022	0.06	0.02	0.00297	0.03	0.09	>7.5	3	0.029
Total dissolved solids (PPB)	205	255	37	23	270	149	7.5	520	13.5	14.5	40	12	20	198	13.5	21.3	195	19.7
Viscosity (cps)	3.89	7.38	2.49	2.52	15.92	152	1800	3.32	5.8	2.86	5.3	5.9	1.6	8.9	3.46	1.7	7.8	3.1
% Volatiles	80%	60.34%	60%	60%	50%	nil	NA	> 80%	NA	NA	NA	NA	60%	NA	85%	NA	60-80 %	NA
Incompatibilities	nitrites	nitrites,oxidizers	nitrites	nitrites,oxidizers	nitrites	strong oxidizers	NA	oxidizers,acid	strong acids	strong acids	strong acids	strong acids	nitrites	strong acids			oxidizers	
Dilution *	10:1-75:1	10:1-75:1	10:1-75:1	10:1-75:1	10:1-75:1	30:1	40:1	20:1-40:1	20:1-100:1	10:1-20:1	20:1-50:1	30:1-80:1	25:1-80:1	20:1-40:1	50:1	50 :1	35:1	40:1
Chemicals Components																		
water	45 -65%	44-75%	45-65%	45-65%	45-65%	none	yes	yes	yes	yes	yes	yes	yes	yes	yes	54-65%		
propylene glycol	<10%	1-10%			<10%											3-5%		
mineral oil						40-70%	yes											
(substituted amine)					<20%													
amine borate		10-20%														8-10%		
boric acid																		<10%
amine carboxylates		10-20%							yes									
monoethanolamine										yes	20% max	yes	1-10%	0-5%		20-25%		<10%
diethanolamine	0.90%													0-5%				<10%
triethanolamine			<30%	<30%					yes	yes	20% max						5-10%	<20%
fragrance	mint	<1%	yes	yes	yes	almond	yes	yes	no									
pine oil		<1%																
substituted indole		<1%																
substituted amide derivative		<1%																
thioamine salt		<1%																
hexahydro-1,3,5-triethyl-s-triazine	0.30%																	
pelargonic acid										yes								
neodecanoic acid										yes								
sodium 2-mercaptobenzothiazole	0.50%																	
anionic emulsifiers						30-50%												
polar additives						2-5%												
corrosion/fungi inhibitors	yes	yes	yes	yes	yes	0.5-1%										0.1-0.5%		
soap/surfactant	yes	yes	yes	yes	yes	yes	major component	yes	yes	yes	yes							
stabilizers	yes	yes	yes	yes	yes	0.1-0.5%				yes	yes							
isopropanolamine mixture												yes						
triethylenediamine tetraacetic acid												yes						
propylene glycol methyl ether												yes						
benzotriazole												yes						
sodium 2-pyridinethiol-1-oxide												yes						
hexylene glycol														3%				
mineral spirits																	10-15%	

*Depends on user

12/6/94

•coolant

quantity:	16 liters
flow rate:	4.3 liters/min
temp. control:	none
mode of use:	recirculate, no filtration

•ring tool

bond type:	bronze N bond
diamond type:	synthetic sc
diamond size:	10-20 µm
diamond concentration:	75

•machine set-up

tool speed:	8000 rpm
tool in-feed rate:	30 µm/min
cutting time:	3 min
cuts per piece:	1
spindle speed:	82 rpm

•workpiece

glass type/quantity:	K7/12 pcs.
shape:	convex
radius of curvature:	116 mm
diameter:	40 mm

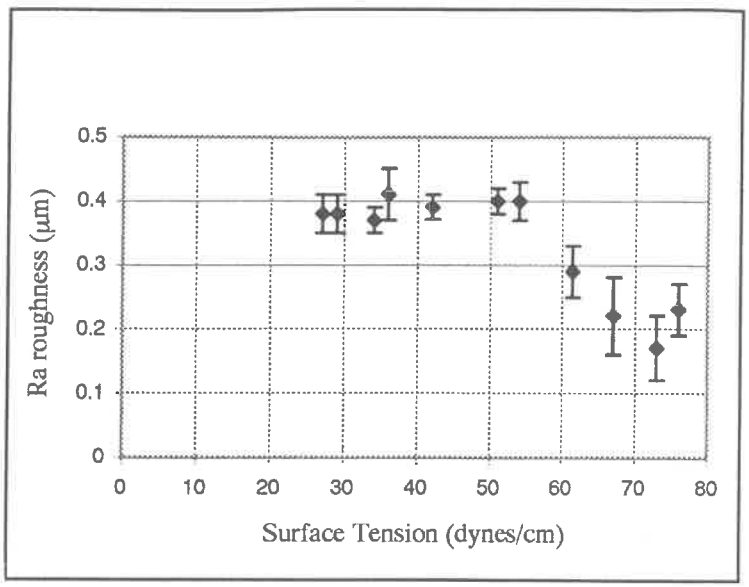

Fig. 1 Surface roughness for K7 glass ground with 11 coolants.

Explanation of Results: Diamond Wear Hypothesis

One hypothesis to explain the observed grinding results is that the diamonds wear less rapidly in an aqueous coolant with low surface tension. The sharp diamond facets are preserved, and this results in rougher ground surfaces. Indirect confirmation of this comes from an experiment recently performed with SK7 glass on the Opticam® SX. Cutting efficiency was evaluated using a 10-20 µm ring tool with first a high surface tension (70 dynes/cm), and then a low surface tension (33 dynes/cm) coolant. All other conditions were kept constant. The maximum achievable infeed rate was observed to increase by 60% to over 1.5 mm/min with the lower surface tension coolant.

In a 1979 review article on diamond drilling in rock, G. A. Cooper reported similar results to the above[5]. He proposed that, in aqueous coolants with small quantities of additives to promote wetting, three mechanisms occur: 1)There is less heat generated, possibly due to improved lubricity and reduced friction; 2)There is more efficient heat transfer from the diamond grains to the coolant by nucleate boiling, rather than film boiling; 3)There is a chemical effect on the diamonds, relating to oxidation or graphitization. A recent article by C. Y. Wang et al.[6] reaffirms and emphasizes the important roles of mechanisms 1) and 2), stating that, "When coolant has a low surface tension, the rate of thermal conduction and penetration into the cutting field to form lubricating films and to accelerate the development of cracks will increase, thus reducing cutting temperature and cutting forces."

Introduction of Propylene Glycol

Because of possible confounding effects from company proprietary additives present in the commercial coolant concentrates, two additional experiments were conducted with the Rogers & Clarke G-150 generating machine on BK7 glass using mixtures of reagent grade propylene glycol and tap water. [These experiments were conducted under conditions identical to those already described, except that they were performed three years apart by two different machine operators.] Propylene glycol was selected, because it has a low toxicity and is a commonly employed additive (see Table 1). The surface tension values for the propylene glycol/water mixtures cover the range of interest, from 38.8 dynes/cm (100% propylene glycol) to 73.0 dynes/cm (100% water).

Results are given in Fig. 2 (absolute roughness values) and Fig. 3 (roughness values normalized to the maximum measured @75 wt. % propylene glycol). The same trend is observed here for BK7 as that shown for K7 in Fig. 1. Lower surface tension coolants give rougher surfaces.

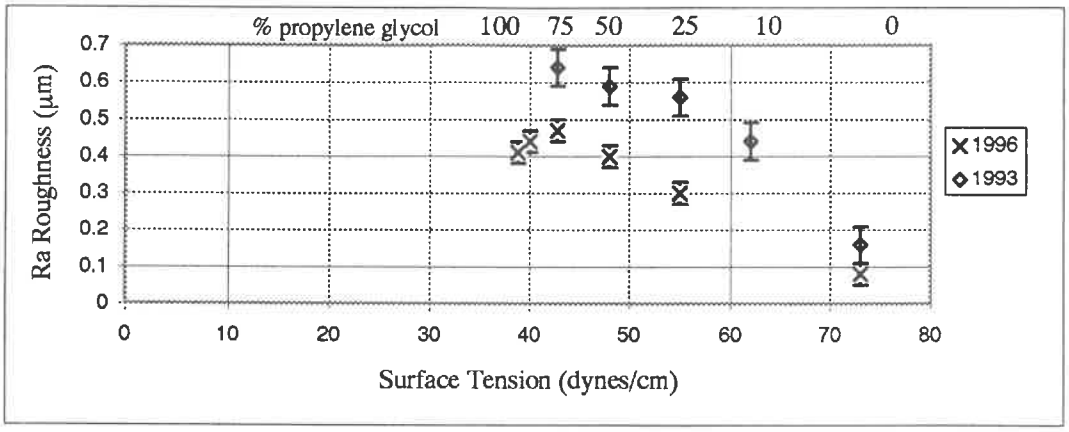

Fig. 2. Surface roughness for BK7 ground with propylene glycol/water mixtures.

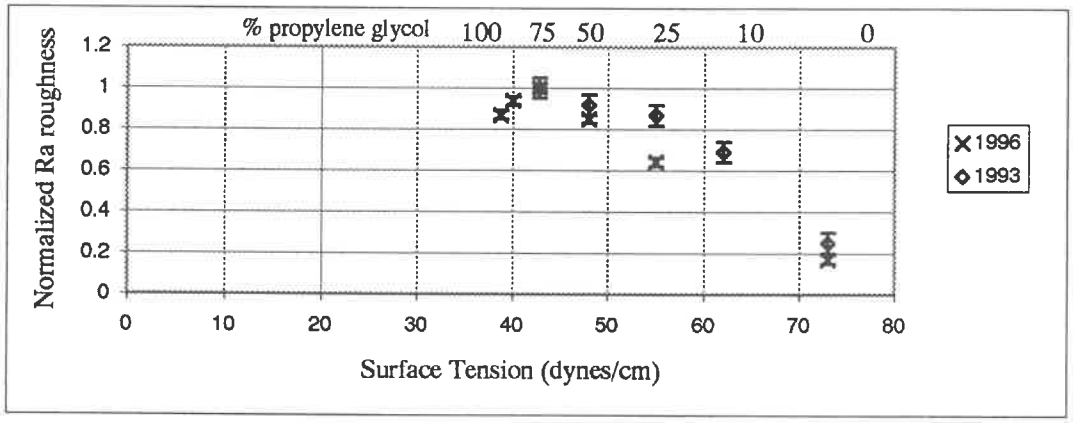

Fig. 3. Normalized surface roughness for BK7 ground with propylene glycol/water mixtures (see text).

Explanation of Results: Modified Near Surface Mechanical Properties [7]

As the nonaqueous content of the coolant rises, it is expected that the efficacy of water at promoting crack growth will be reduced[8, references therein]. Microindentation measurements were carried out for BK7 glass while immersed in propylene glycol/water mixtures (5 min immersion, 5 indents @500gf). Vicker's hardness, H_v, Knoop hardness, H_k, and fracture toughness, K_c, were calculated from measurements of indentation diagonal, indentation length, and crack length (model of Evans[9]), respectively. The results, given in Table 2, show a 17% to 23% increase in glass

Table 2. BK7 glass physical properties measured in propylene gylcol/water mixtures

Propylene glycol, wt. %	0	10	25	50	75	100	standard deviation, %
Surface tension, dynes/cm	73.0	62.0	55.0	48.0	43.0	38.8	1
Knoop hardness, H_k, GPa	5.37	na	5.60	6.12	6.17	6.30	2
Vicker's hardness, H_v, GPa	6.30	na	7.00	7.10	7.50	7.70	5
Fracture toughness, K_c, MPa $m^{1/2}$	0.61	na	0.69	0.79	0.84	0.91	~30
Ductility index, $(K_c/H_k)^2$, nm	12.9	na	15.18	16.66	18.53	20.8	--

hardness and approximately a 50% increase in glass fracture toughness when the coolant changes from 100% water to 100% propylene glycol.

The experimental results for grinding BK7 in propylene glycol/water mixtures may be plotted against the ductility index, $(K_c/H_k)^2$ (units of length) which was recently introduced by Lambropoulos et al.[10]. This parameter is useful for predicting the roughness of glass in grinding, since it accounts for the competition between fracture and flow processes. High ductility implies high roughness from grinding, because of high material fracture toughness or low hardness.

The plots are given in two forms. Fig. 4 is plotted with a fixed value of H_k (5.37 GPa @500gf). If it is assumed that there is insufficient time for glass hardness to be affected by coolant fluid properties, then Fig. 4 shows that the increase in ductility (read fracture toughness) of the glass surface could partly explain increased surface roughness from grinding with high surface tension coolants. Alternatively, if it is assumed that there is sufficient time for the hardness of the glass surface to respond to the coolant fluid properties, then Fig. 5 shows that there could be an even higher degree of sensitivity of surface roughness to glass surface ductility.

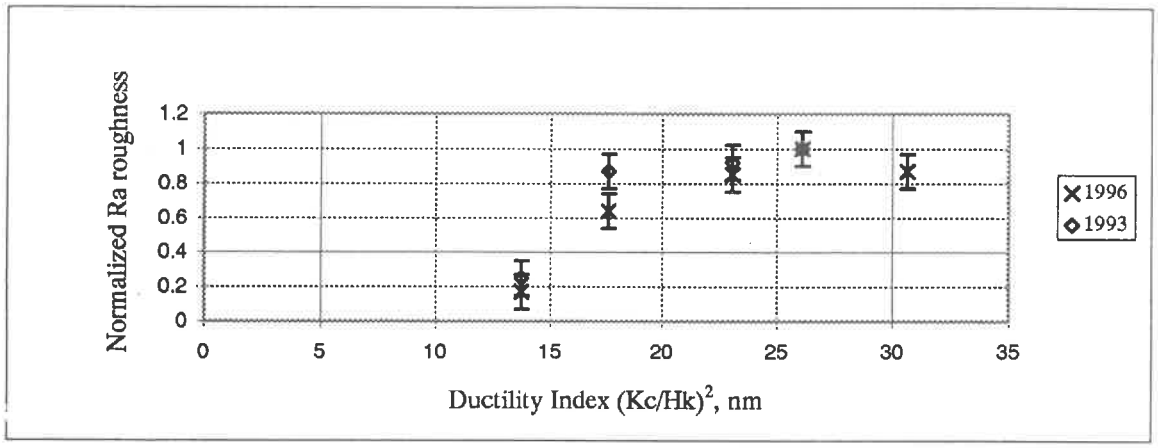

Fig. 4. Normalized surface roughness for BK7 as a function of glass ductility index for a constant glass hardness.

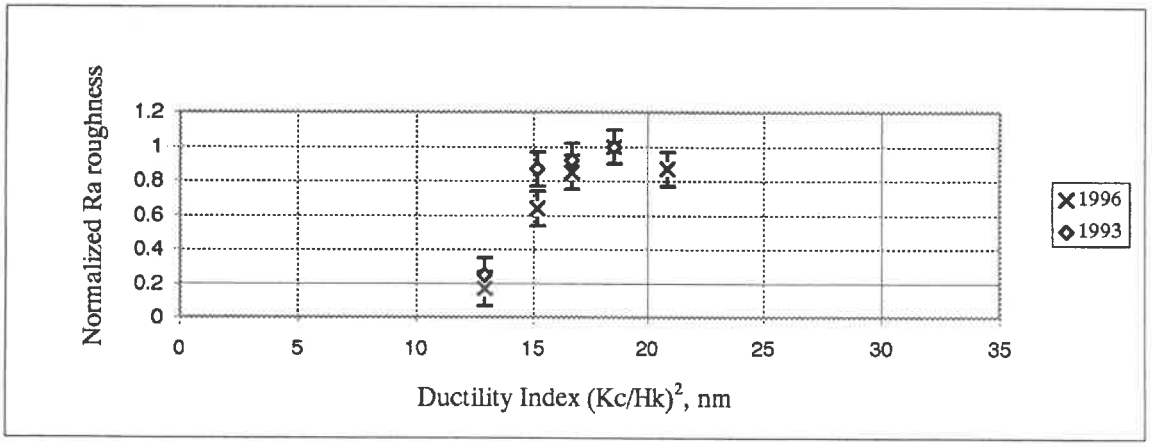

Fig. 5. Normalized surface roughness for BK7 as a function of glass ductility index for a varying glass hardness.

Concluding Remarks

This study must be continued, possibly with nanoindentation techniques, to evaluate the significance of surface mechanical property modifications. Testing is required for various surface tension conditions in coolant environments whose water concentrations are at or above 90 vol. % , in keeping with the actual conditions used on Opticam® deterministic generating machines. It may then be possible to understand whether it is the tool or the workpiece that responds to increases in coolant surface tension to improve cutting efficiency at the expense of surface roughness.

References:

[1] B. Puchebner, "Your Water Supply", *COM Communications Newsletter*, (Dec., 1994);
B. Puchebner, "Common Coolant Problems", *COM Convergence Newsletter*, (Feb., 1995);
B. Puchebner, "Fluid Management", *COM Convergence Newsletter*, (Mar., 1995).

[2] B. E. Puchebner, A. Feltz, W. Ng, and S. D. Jacobs, "Coolant Performance in Bound Diamond Ring Tool Grinding of K7 Optical Glass", *OSA Optical Fabrication and Testing Workshop* 13, pp. 40-43(June, 1994).

[3] Surface tension was measured at T = 23° C with a Fisher Surface Tensiomat, according to ASTM Method D-1331-Surface and Interfacial Tensions of Solutions.

[4] Ra, is the arithmetic average height of surface irregularities measured from a mean line, with an evaluation scan length of 4 mm, using a Federal Products Pocket Surf III® [instrument range: 0.03 - 6.35 μm]. Three scans were made on a given ground surface.

[5] G. A. Cooper, "Some Observations on Environmental Effects When Diamond Drilling", *The Science of Ceramic Machining and Surface Finishing II*, B. J. Hockey and W. R. Rice, ed., National Bureau of Standards Special Publication 562 , pp. 115-125 (U. S. Gov. Printing Office, Wash., D. C., 1979).

[6] C. Y. Wang, X. Wei, Z. L. Tang, and Z. C. Pan, "The Role of Coolant in Granite Sawing", *Industrial Diamond Review*, 55, pp. 156-160 (April, 1995).

[7] J. C. Lambropoulos, Tong Fang, B. Puchebner, and S. D. Jacobs, "The Effect of Coolant Surface Tension in Microgrinding of Glass", paper #1-SIP-95F, presented at the International Symposium on Manufacturing Practices and Technologies, Joint Fall Meeting of the American Ceramic Society, New Orleans, LA, (Nov., 1995).

[8] D. Golini and S. D. Jacobs, "Physics of Loose Abrasive Microgrinding", *Appl. Opt.* 30, pp. 2761-2777 (July, 1991).

[9] A. G. Evans, "Fracture toughness: the role of indentation techniques", *Fracture Mechanics Applied to Brittle Materials*, ASTM STP 678, S. W. Freiman, ed., pp. 112-135 (American Society for Testing and Materials, 1979).

[10] J. C. Lambropoulos, Tong Fang, P. D. Funkenbusch, S. D. Jacobs, M. J. Cumbo, and D. Golini, "Surface Microroughness of Optical Glasses under Deterministic Microgrinding", to be published in *Applied Opt.*

Author Index

Atwood, Mark 121
Blaedel, Kenneth L. 95
Carr, Jeffrey W. . . . . *
Cook, Lee M. . . . . *
Daito, Masamichi. 3
Danyluk, Steven. . . . . *
Devitt, Drew. 12
Dornfeld, David A. 109
Dow, Thomas A. 58
Ebbutt, Ralph . . . . . *
Fang, Tong 121
Flinchbaugh, James D. . . . . *
Funkenbusch, Paul D. 103
Gee, Anthony E. 82
Gillman, B. E. 121
Golini, Donald 121
Grant, Marion 8
Gray, Fred A. 95
Gust, Darryl 8
Hahn, Robert S. 22
Ives, Lewis K. 52
Jacobs, Stephen D. 121
Jahanmir, Said 52
Jeynes, C. 82
Kanai, Akira 3
Lambropoulos, John C. 39, 121
Liang, Shawn. 64
Marinescu, Ioan. 64, 88
Marsh, Eric R.* 12, 16
Miller, Michele H. 70
Miyashita, Masakazu. 3
Moon, K. S. 70
Piscotty, Mark A. 95
Puttick, Keith E. 82
Scattergood, Ronald O. 45
Shih, Albert 8
Storz II, Gene E. 58
Subramanian, K. 115
Syoji, Katsuo 109
Takashina, Mamoru 29
Tang, Jianshe 109
Tanikella, B. V. 45
Taylor, John S. 95
Tricard, Marc 115
Walter, Mark 34
Weisshaus, Ilan . . . . . *
Whitmore, L. C. 82
Xu, Hockin H. K. 52
Yamanouchi, Atsushi 29
Yantek, David S. 16
Yasunaga, Nobuo 29
Zhang, Bi. 76
Zhou, Yiyang 103, 121

* Extended abstract not available at press time

Groove depth d (mm)	0	2.5	7.5
Flatness of mirror (nm p-v)	98.8	76.0	70.4
Surface roughness (Rmax)	0.04 μ m		
Material	Oxygen free copper		

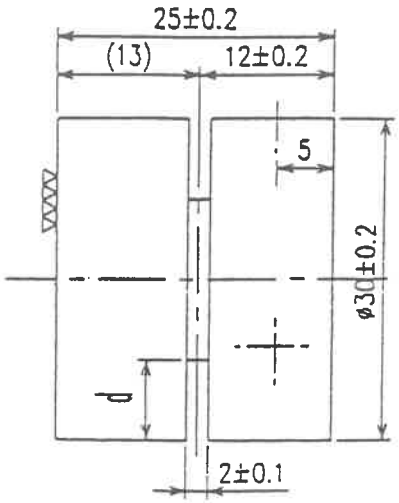

Figure 2. Metal mirrors

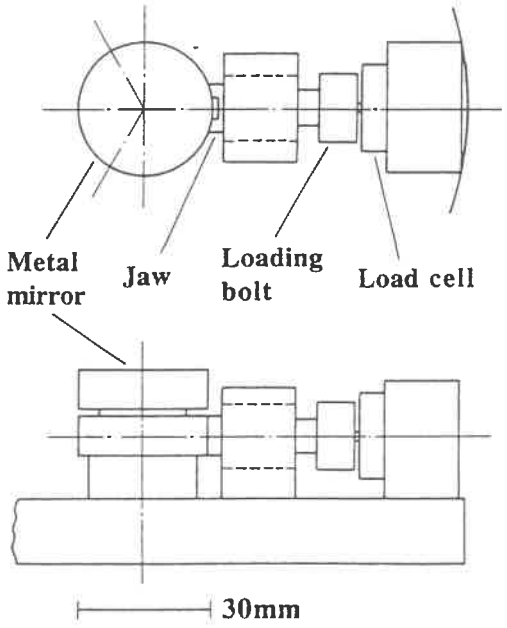

Figure 3. Three jaw chuck

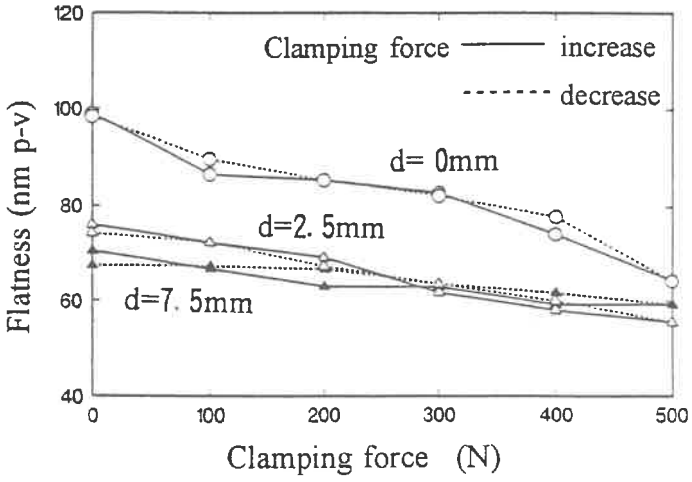

Figure 4. Relationship between clamping force and flatness of the mirror

Groove depth (mm)	0	2.5	7.5	Boundary conditions
Number of node	832	888	888	Constrained nodes: 4 nodes of bottom Loading condition: 500 (N), normal and uniform load
Number of element	567	585	585	

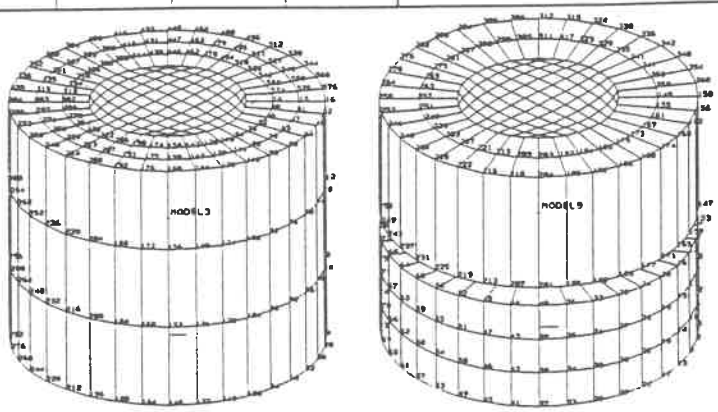

Table 1. Condition of FEM analysis

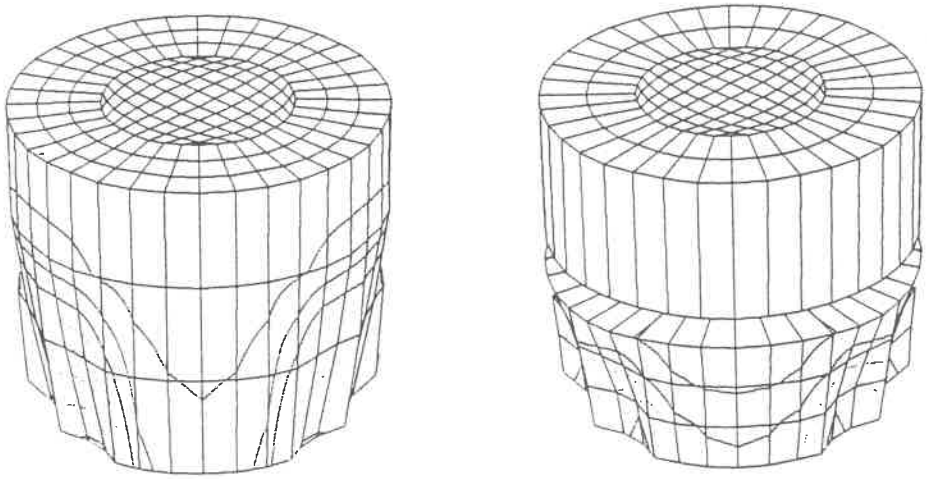

Figure 5. Example of FEM analysis(Left: d=0mm, Right: d=7.5mm)

Groove depth (mm)	0	2.5	7.5
Experimental results (nm)	34.3	19.5	9.6
FEM analysis (nm)	32.9	27.9	8.8

Table 2. Comparison of experimental results and FEM analysis(0-500N)

Sampling Plan for Point-To-Point Performance Test of Touch Trigger Probes on Coordinate Measuring Machines

Yin-Lin Shen and Sungho Moon
Department of Civil, Mechanical, and Environmental Engineering
George Washington University
Washington, DC 20052

INTRODUCTION

Touch trigger probes are devices through which coordinate measuring machines (CMMs) collect dimensional measurement data in modern manufacturing environments. The vast majority of probes used on CMMs are touch trigger probes, and most of these probes employ a kinematic seating mechanism for the probe stylus (Reid, 1993). Point-to-point probing test is typically used to evaluate touch trigger probe performance. The test method specified in the ANSI (American National Standards Institute) B89 standard consists of measuring 49 points on a highly spherical reference ball and the 49 points are distributed by following a sampling plan or test pattern (ANSI, 1991). The user is allowed to specify desired sampling plan which contains 49 points. Standards of other countries usually require that a number of points are taken over one hemisphere of a reference ball roughly uniformly distributed. (For example, fifty points are used in VDI/VDE 2617 standard.) A best-fit sphere is then computed using the manufacturer's recommended algorithms (usually least squares) and the set of radii to each probing point (from the best-fit center) is calculated. The range of the 49 radii is defined as the point-to-point performance index.

In this research, we investigated the 49-point sampling plan specified in the ANSI B89 standard when touch trigger probes are used on CMMs. The sampling plan was tested by using experimental data of a touch trigger probe on a computer-controlled CMM and research findings indicate that the probe performance is overestimated due to a systematic bias in the Z coordinate of the best-fit reference ball center in the probing test. In this paper we propose a two-latitude sampling plan synthesis method based on a pretravel model for touch trigger probes. It is shown that the proposed method can be used to synthesize sampling plans resulting in a near-unbiased reference ball center.

ANSI B89 49-POINT SAMPLING PLAN IN POINT-TO-POINT PROBING TEST

The B89 probe performance test method consists of measuring 49 points on a high-quality reference sphere by following a sampling plan. The user is can specify desired sampling plan which contains 49 points. In the B89 default sampling plan, 49 points are probed on the reference ball (test ball) at five different heights on the ball: 12 equally spaced points per latitude are taken on four specified latitudes (approximately 100°, 90°, 60°, and 30°) and one point on the north pole. In addition, there is a 10° rotation of the 12 points on one latitude after the 12 points on the previous latitude are taken. The B89 default sampling plan spreads 49 measurements over the reference ball. It is designed to test three-dimensional (3D) probe performances associated with different probe approach directions.

EVALUATION OF B89 49-POINT SAMPLING PLANS

Experimental probing data were collected on a computer-controlled CMM, and a commonly-used 5-way 3D touch trigger probe with a 50 mm straight stylus extension was used. The probe and the stylus were oriented vertically. In each experiment, 1561 points of probe data, which represent 1561 probe approach directions, were measured. These points are distributed in thirteen (13) latitudes of the reference ball and one point at the north pole. The polar angles of the thirteen latitudes are: 130°, 120°, 110°, ..., 20°, and 10°. One hundred and twenty (120) equally spaced points are measured in each latitude. The point index of the 1561 probe data is arranged as follows: the first 120 points (point 1 to 120) are on the 130° polar latitude, the second 120 points (point 121 to 240) on the 120° polar latitude,..., and the last point is on the north pole (point 1561). A probe approach speed of 7.5 mm/sec was used. The experiment was repeated ten (10) times. From the experimental data, we extract 100 sets of 49-point data by following the B89 sampling plan: 10 sets of different 49-point data can be extracted from each 1561-point

experiment; and 10 repetitions of the 1561-points experiment provide 100 sets of 49-points data. For each 49-point data set we calculate the best-fit center and radius of the reference ball by using the 49-point data and a least-squares sphere fitting software developed by the National Institute of Standards and Technology (NIST) (Hopp, 1993). We then calculate 49 radii from the measurement points to the best-fit center. We can find the range of the 49 radii, which is the probe performance index, for each of the 100 49-point data sets.

To ensure that we obtain a good estimate of the true center of the reference ball from the 49-point data, we use a dense-data approach to calculate the reference ball center. The dense data are defined as the probing data around the equator of reference ball in the 1561-point experiment, i.e., all data from the 130° latitude up to the 50° latitude (9 latitudes, 1080 points). For each 1561-point experiment, we can calculate a best-fit reference ball center (1080-point center) by using the NIST sphere fitting software. We compare it with the centers of the 10 49-point data sets extract from this experiment. We then follow the same procedures to calculate 49 radii for each 49-point data by using the 1080-point center. The values of the 1080-point reference ball radius are extremely stable (between 7.9881 mm and 7.9883 mm), while those of the 49-point cases fluctuate in a small range of approximately 1 μm (7.9868 mm to 7.9878 mm). As for the best-fit reference ball centers, the X and Y coordinates of the 49-point center are very close to those of the 1080-point center; however, there is a bias in the Z coordinates between the best-fit reference ball centers obtained by using the two methods (see Figure 1).

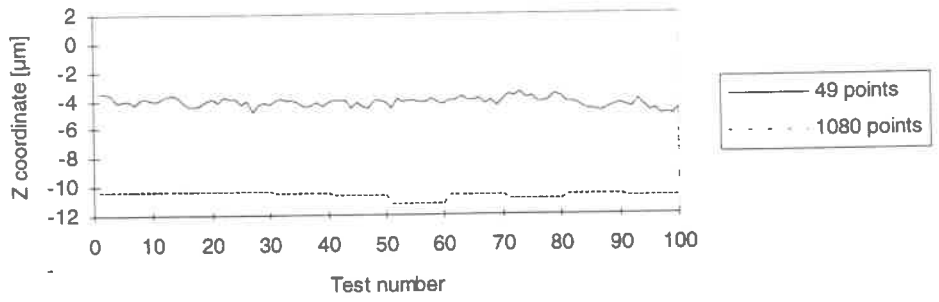

Figure 1. *Z coordinate of the reference ball center using the B89 49 point method and the 1080 point method*

The impact of the quality of the best-fit reference ball center on probe performance is then evaluated. Figures 2 and 3 show the range of the 49 radii (probe performance index) of the 100 test cases by using (1) the 49-point best-fit center and (2) the 1080-point best-fit center. When the 49-point centers are used, the probe performance index (the range of 49 radii) of the 100 test cases has a mean of 10.847 μm and a standard deviation of 1.106 μm. When the 1080-point center are used, the probe performance index (the range of 49 radii) of the 100 test cases has a mean of 16.775 μm and a standard deviation of 1.001 μm. The probe performance is overestimated when B89 49-point sampling plan is used.

TWO-LATITUDE SAMPLING PLAN SYNTHESIS METHOD FOR PROBING TEST

We use a pretravel model for touch trigger probes to develop a sampling plan synthesis method for point-to-point probing tests. Pretravel is the travel distance of the CMM between the instant the probe touches the workpiece and the instant the probe generates a trigger signal. It is highly repeatable but can be adversely influenced by force variations encountered in different probe approach directions in dimensional measurements. Pretravel, mainly caused by bending deflection of the probe stylus shaft, accounts for the majority of touch trigger probes (Jarman and Traylor, 1990; Reid, 1993). Shen and Zhang have developed a pretravel model for vertically-oriented touch trigger probes with straight styli (1996), and the model accounts for bending deflection of the stylus shaft at the trigger instant. The pretravel behavior above and below the equator of the reference ball is approximately symmetrical according to the pretravel model. Based on this near-symmetry characteristic of probe pretravel, we propose a two-latitude sampling plan synthesis method for point-to-point probing test by using the pretravel model.

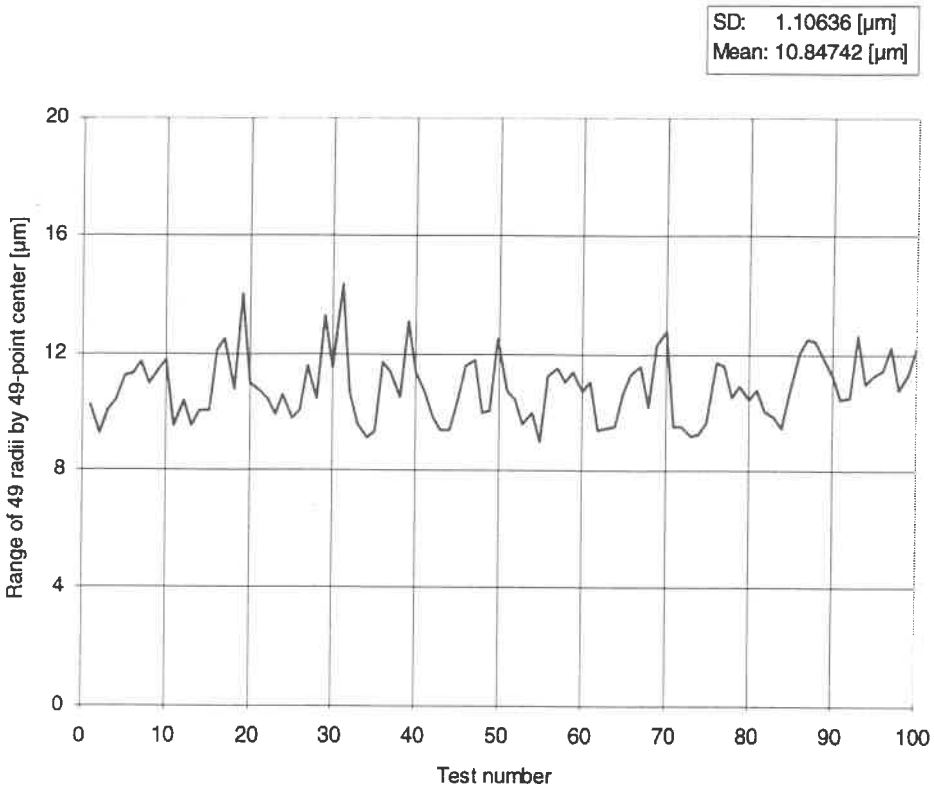

Figure 2. *Range of the 49 radii obtained by using the B89 49-point center*

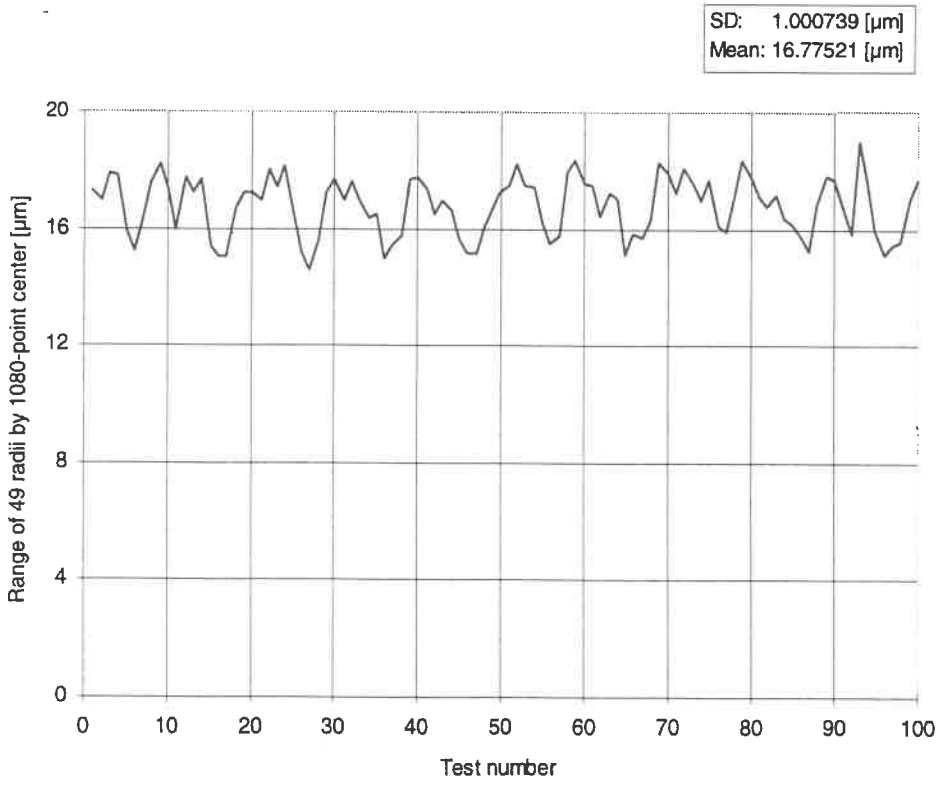

Figure 3. *Range of the 49 radii obtained by using the 1080-point center*

The two latitudes include one latitude above the equator and another latitude below the equator of the reference ball. We choose one latitude first (e.g., 100° latitude), then use the pretravel model to identify the corresponding latitude which would result in an unbiased reference center. We choose 24 equally spaced points on each latitude, so each sampling plan consists of 48 points on two latitudes. There is no rotation between the two 24-point patterns. Furthermore, due to the direction-dependent characteristic of probe lobing of touch trigger probes, we use 15 different starting angles to generate 15 24-point data sets on each latitude. As a result, we obtain 15 different 48-point data sets for a specific two-latitude sampling plan. We then calculate 15 best-fit centers and radii of the reference ball for each sampling plan. From the dispersion of the 15 best-fit centers, we evaluate the quality of the best-fit reference ball center. We choose 100° latitude first because it is the lowest latitude in the B89 method.

TESTS OF TWO-LATITUDE SAMPLING PLANS WITHOUT NOISE IN THE DATA

Figure 4 shows the least squares fit center (mean and standard deviation) when the 100° latitude is fixed in implementing the two-latitude sampling plan synthesis method. The 86°-100° pair gives a near-unbiased Z coordinate; the mean is 0.004 μm, the standard deviation (s.d.) is 0.020 μm. The X and Y coordinates of the center are very close to the true center; mean is 0.0004 μm and s.d. is 0.0006 μm for X; and mean is 0.0001 μm and s.d. is 0.0005 μm for Y. The calculated radius of the reference ball has a mean value of 7.987924 mm, and the s.d. is 0.068 μm.

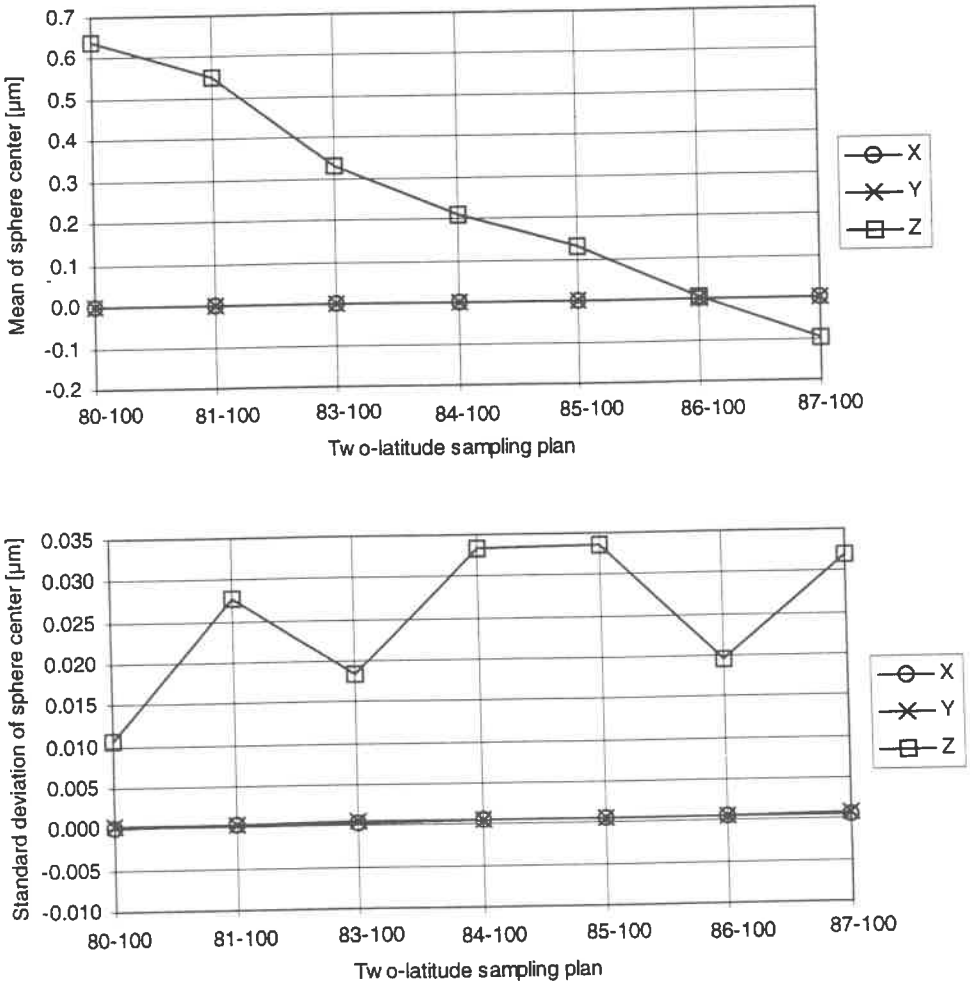

Figure 4. *Center of the reference ball by using the 80°-based two-latitude 48-point sampling plan: (a) mean and (b) standard deviation of X, Y, and Z coordinates*

The center of the calculated reference ball is very close to the true center location (0,0,0) when the 86°-100° two-latitude sampling plan is used in the probing test. There is no noise in the synthesized measurement data. Tables 1 and 2 summarize the results of other tests: when 110°, 120°, and 130° latitudes are selected in implementing the two-latitude sampling plan; 76°-110° pair, 66°-120° pair, and 56°-130° pair give near-unbiased reference ball center.

Table 1. *Mean of the center and radius of the reference ball of the tested two-latitude sampling plans*

Two-latitude sampling plan	X [μm]	Y [μm]	Z [μm]	R [mm]
56°-130°	0.000004	0.000005	0.006536	7.990268
66°-120°	0.000007	-0.000002	0.003930	7.989152
76°-110°	0.000065	-0.000020	0.000182	7.988362
80°-106°	-0.000197	0.000026	0.000399	7.988144
86°-100°	0.000397	0.000109	0.004260	7.987924

Table 2. *Standard deviation of the center and radius of the reference ball of the tested two-latitude sampling plans*

Two-latitude sampling plan	X [μm]	Y [μm]	Z [μm]	R [mm]
56°-130°	0.000036	0.000031	0.006417	0.000055
66°-120°	0.000057	0.000072	0.006260	0.000062
76°-110°	0.000292	0.000268	0.011197	0.000066
80°-106°	0.000729	0.000844	0.009250	0.000067
86°-100°	0.000578	0.000464	0.019569	0.000068

TESTS OF TWO-LATITUDE SAMPLING PLANS WITH NOISE IN THE DATA

To test the robustness of the proposed sampling plan synthesis method, we add Gaussian noise (normally distributed noise) to the 48-point data synthesized by using the pretravel model, and generate 1500 sets of 48-point data containing noise. We use noise data from a normal distribution with mean zero and s.d. of 1 μm in the data generating process; i.e., 99% of the noise falls within ±3 μm. The 86°-100° pair gives a mean Z coordinate close to zero (mean is -0.016 μm), however, the s.d. is 1.178 μm (as compared to 0.020 μm in the no-noise case). Furthermore, the Z coordinate oscillates between -3.981 μm and +3.770 μm from the simulation results. The mean values of the X and Y coordinates of the center are is still very close to the true center; 0.0049 μm for X and 0.0113 μm for Y; however, the s.d. values increase: 0.201 μm for X, and 0.211 μm for Y. The calculated radius of the reference ball still very stable: mean is 7.987920 mm, and s.d. is 0.170 μm.

DISCUSSION AND CONCLUSION

The center of the calculated reference ball center is a critical parameter in the evaluation of probe performance. It is shown that the ANSI B89 49-point sampling plan results in a biased Z coordinate when the 49 points are used to find the best-fit center and radius of the reference ball. The same problem exists in standards of other countries because the specified sampling plans cover only one hemisphere of the reference ball. This finding suggests that the probe performance (the range of the 49 radii) can be overestimated significantly due to the shift of the reference ball in the Z axis.

A two-latitude sampling plan synthesis method, based on a pretravel model for kinematic touch trigger probes, is proposed. The method can be implemented to synthesize two-latitude sampling plans which result in a near-unbiased reference ball center in the probing test. We present the statistics of the calculated reference center to support the suggestion. Furthermore, we use simulations to check the effect of noise to the proposed method by adding Gaussian noise (mean = 0, and s.d. = 1 μm) to each sampled point of the 48-point data. The noise-embedded data reflect real-world situations in which touch trigger probes are used, and the research finding suggests that the uncertainty in the reference ball center contributes to the overall uncertainty of the measurement process. The

uncertainty in identifying the reference ball center should be included in the assessment of the total uncertainty of measurement processes. Moreover, the center shift range increases significantly when noise is added to the synthesized probe data. As a result, we suggest repeated measurements and averaging be used to reduce the range of reference ball center shift in probe performance test and probe calibration, particularly when precision measurement results are required.

The proposed two-latitude sampling plan synthesis method can be used to assess the center of the reference ball in probing tests. However, the method is not designed to replace the 49-point method specified in ANSI B89 standard in that the 49-point test is needed to test probe performances in various approach directions for touch trigger probes in three dimensional (3D) probe tests. In addition, more points (than 48 points used in the tests) and repeated measurements may be useful in ensuring the quality of the probe performance tests.

ACKNOWLEDGEMENT

This work was supported in part by the NIST Computational Metrology Program under Grant No. 70NAB4H1681 and the National Science Foundation under Grant No. DMII-9308648. We thank the Computational Metrology Group of the National Institute of Standards and Technology (NIST) for useful discussions. We also thank Bruce Borchardt of NIST for providing experimental data, and Kusol Prommul, Xianping Zhang, and Marlow E. Springer of the George Washington University for useful discussions.

REFERENCES

ANSI/ASME B89.1.12M-1990, Methods for Performance Evaluation of Coordinate Measuring Machines, ASME, New York (1990).

Jarman, T., and Traylor, A., Performance Characteristics of Touch Trigger Probes, *Proceedings of Precision Metrology with Coordinate Measurement Systems* (SME, Troy, Michigan, 1990).

Reid, C., Probe Technology - Beyond Accuracy, *Proceedings of Applying Imaging and Sensoring Technology to CMM Applications* (SME, Nashville, Tennessee, 1993).

Bosch, J., Evolution of Measurement, in *Coordinate Measuring Machine and Systems*, J. Bosch, Ed., Marcel Dekker Inc., New York (1995).

Butler, C., An Investigation Into the Performance of Probes on Coordinate Measuring Machines, *Industrial Metrology* (v2, 1991) pp. 59-70.

Hopp, T., Computational Metrology, *Proceedings of the International Forum on Dimensional Tolerancing and Metrology*, pp. 97-111 (1993).

Shen, Y., Zhang, X., A Pretravel Model for Touch Trigger Probes with Straight Styli, Part I: Vertical Probes, *Proceedings of the North American Manufacturing Research Conference*, pp. 127-132, Ann Arbor, MI, May, 1996.

Estler, W.T., Phillips, S.D., Borchardt, B., Hopp, T., Witzgall, C., Levenson, M., Eberhardt, K., McClain, M., Shen, Y., and Zhang, X., Error Compensation for CMM Touch Trigger Probes, *Proceedings of ASPE Annual Meeting* (Austin, Texas, 1995), pp. 428-431.

A Robust Pretravel Model for Touch Trigger Probes in Coordinate Metrology

Yin-Lin Shen and Marlow E. Springer
Department of Civil, Mechanical, and Environmental Engineering
George Washington University
Washington, DC 20052

INTRODUCTION

This paper describes a pretravel model for kinematic touch trigger probes widely used on coordinate measuring machines (CMMs). A trigger signal is generated when the probe stylus touches the workpiece in the measurement process and the signal enables the recording of an x-y-z coordinate point on the workpiece surface where the probe stylus touches. In fact, the trigger signal is not generated at the touch instant, and the probe continues to travel in the probe approach direction and the stylus continues to be deflected until a probing force (on the probe stylus) is large enough to set off the trigger signal at the trigger instant. The travel distance between the touch instant and the trigger instant is known as probe pretravel. Pretravel is a well-known type of error, and accounts for the majority of touch trigger probe errors (Jarman and Traylor, 1990; Reid, 1993). It is a large source of measurement uncertainty in touch-trigger-probe CMMs (Butler, 1991; Bosch, 1995; NIST, 1996). Pretravel errors are highly repeatable but can be adversely influenced by force variations encountered in different probe approach directions (Reid, 1993). This can lead to measurement errors caused by variations in stylus shaft bending prior to triggering. Pretravel errors are referred to as probe-lobing errors because the probe yields a three-lobed error pattern when inspecting a ring gauge.

Estler et al. (1995 and 1996) have developed a multi-parameter pretravel model accounting for the combined effects of rotational displacement, bending displacement, and frictional effects. Shen and Zhang (1996a and 1996b) have developed pretravel models accounting for bending of the stylus shaft for vertically- and horizontally-oriented touch trigger probes. In this paper, a trigger force model for vertical probes was first derived and used to model the trigger force, i.e., the probing force at the trigger instant. A basis for this work was the assumption that the probe behaves statically as a cantilever beam. The trigger force model was used to model the bending deflection of the stylus shaft at the trigger instant in order to verify the cantilever beam assumption. Experimental data of trigger forces and x-y-z coordinates were used to validate the pretravel model. It is shown that 24 points of equatorial data measured in the probe calibration process can be used to accurately identify the only model parameter. Also, 12 points of equatorial data provides reasonably good results.

PRETRAVEL MODEL

When the probe tip is in contact with the workpiece during the measurement process, a probing force is developed. This probing force causes the stylus shaft to deflect, resulting in the probe pretravel. Calculation of the deflection is dependent upon the magnitude and direction of the trigger force. The trigger force is defined as the probing force at the trigger instant. The free body diagram of the probe tripod-stylus is shown in Figure 1. The spring force, F_S, and the weight of the tripod-stylus structure, W, act downward (negative Z direction) to keep the tripod in its rest position. Each tripod leg (A,B,C) of length R is supported by two of six contact forces (F_{A1}, F_{A2}, F_{B1}, F_{B2}, F_{C1}, F_{C2}) between the tripod and the kinematic seating arrangement. A kinematic support angle, α, can be used to describe the direction of the contact forces. The probing force, F_p, increases from zero before the probe tip contacts the workpiece, to a maximum value at the trigger instant. The direction of F_p is opposite to the probe approach direction, described by the polar angle (θ) measured from the positive z-axis to the probing force, and the azimuthal angle (ϕ) measured from the positive x-axis to the component of the probing force in the x-y plane (positive from the positive x-axis to the positive y-axis).

During the duration of the probing, from the contact instant to the trigger instant, the following forces are involved: F_S, W, F_{A1}, F_{A2}, F_{B1}, F_{B2}, F_{C1}, F_{C2} and F_p. Based on kinematic principles six equilibrium equations can be used to describe the relationships among these forces until the trigger instant. Manipulation of these equations leads to solutions for the six contact forces as functions of spring force F_S, weight of the tripod-stylus structure W, kinematic support angle α, probing force F_p, stylus length L, tripod leg length R, polar angle θ, azimuthal angle ϕ, and tripod phase angle ϕ_o (Shen and Zhang, 1996a). As F_p increases during the measurement process, the six contact forces increase or decrease in magnitude, but remain constant in direction due to the

kinematic seating arrangement. There are six azimuthal regions of 60 degrees each in which the contact forces are calculated. Within each of the six azimuthal regions, there is one contact force which reaches a threshold contact force, F_t, first.

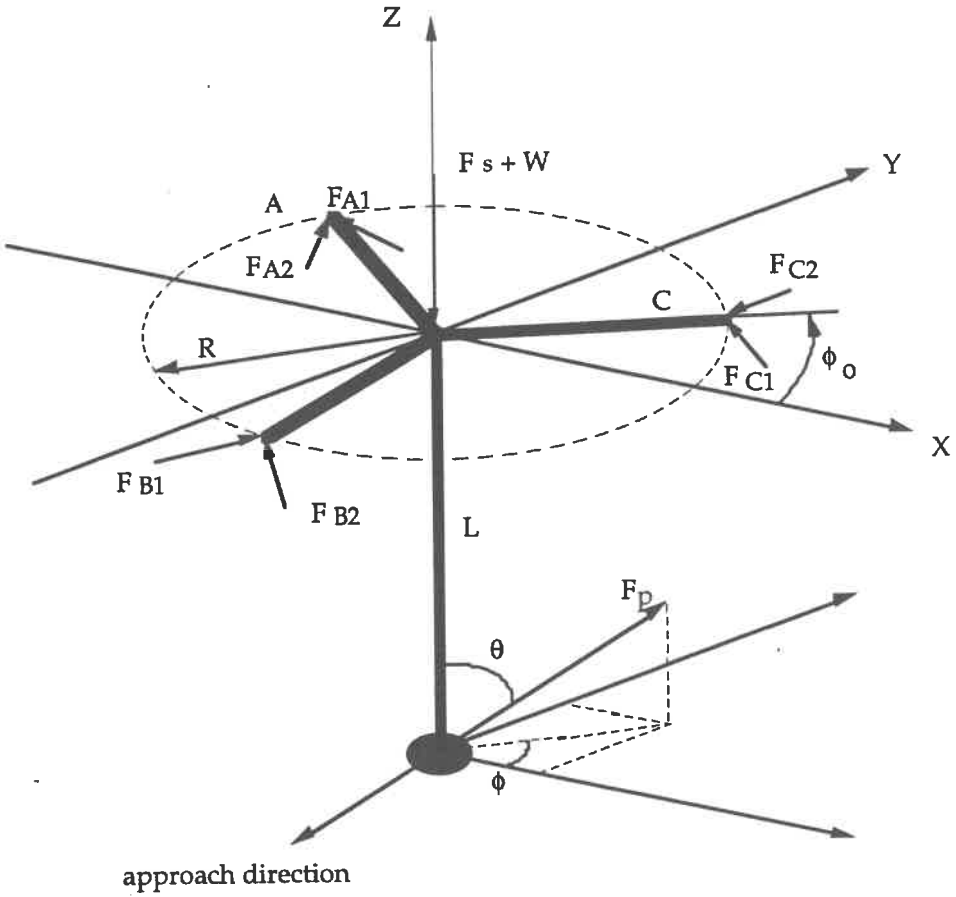

Figure 1. *Free body diagram of the tripod-stylus structure in a vertically-oriented probe*

At the junctions between two regions, two contact forces will reach the threshold. The probe trigger condition is assumed as follows: when one of the six contact forces reaches F_t, the trigger signal is generated. The trigger force can be expressed as:

$$F_p=\frac{F_s+W-6\sin\alpha F_t}{[\cos\theta+2\frac{L}{R}\sin\theta\cos(\phi-\phi_o)]+2\sin\theta\sin(\phi-\phi_o)\tan\alpha} \qquad (0°\le\phi-\phi o\le 60°),\ (1)$$

$$F_p=\frac{6\sin\alpha F_t-(F_s+W)}{\frac{L}{R}\sin\theta[\cos(\phi-\phi_o)-\sqrt{3}\sin(\phi-\phi_o)]-\cos\theta-\sin\theta\tan\alpha[\sin(\phi-\phi_o)+\sqrt{3}\cos(\phi-\phi_o)]} \qquad (60°\le\phi-\phi o\le 120°),\ (2)$$

$$F_p=\frac{6\sin\alpha F_t-(F_s+W)}{\frac{L}{R}\sin\theta[\cos(\phi-\phi_o)-\sqrt{3}\sin(\phi-\phi_o)]-\cos\theta+\sin\theta\tan\alpha[\sin(\phi-\phi_o)+\sqrt{3}\cos(\phi-\phi_o)]} \qquad (120°\le\phi-\phi o\le 180°),\ (3)$$

$$F_p=\frac{6\sin\alpha F_t-(F_s+W)}{\frac{L}{R}\sin\theta[\cos(\phi-\phi_o)+\sqrt{3}\sin(\phi-\phi_o)]-\cos\theta-\sin\theta\tan\alpha[\sin(\phi-\phi_o)-\sqrt{3}\cos(\phi-\phi_o)]} \qquad (180°\le\phi-\phi o\le 240°),\ (4)$$

$$F_p=\frac{6\sin\alpha F_t-(F_s+W)}{\frac{L}{R}\sin\theta[\cos(\phi-\phi_o)+\sqrt{3}\sin(\phi-\phi_o)]-\cos\theta+\sin\theta\tan\alpha[\sin(\phi-\phi_o)-\sqrt{3}\cos(\phi-\phi_o)]} \quad (240°\le\phi-\phi o\le 300°), \quad (5)$$

$$F_p=\frac{F_s+W-6\sin\alpha F_t}{[\cos\theta+2\frac{L}{R}\sin\theta\cos(\phi-\phi_o)]-2\sin\theta\sin(\phi-\phi_o)\tan\alpha} \quad (300°\le\phi-\phi o\le 360°). \quad (6)$$

The deflection of the stylus shaft at the probe tip is caused by bending and compression or tension due to the increasing probing force. The deflection model can be simplified by treating only the dominant bending deflection caused by the horizontal component of the trigger force (Jarman and Traylor, 1991; Shen and Zhang, 1996a) specified by

$$F_H=F_p\sin\theta, \quad (7)$$

where F_H is the horizontal trigger force component. Thus, treating the stylus as a cantilevered beam, the magnitude of the projection of the 3D pretravel vector along the probing force direction is described as

$$\delta_{pt}=\frac{F_H L^3}{3EI}\sin\theta=\frac{F_p(\sin\theta)^2 L^3}{3EI}, \quad (8)$$

where δ_{pt} is the model predicted pretravel, E is the modulus of elasticity of the stylus shaft material, and I is the moment of inertia of the stylus shaft.

EXPERIMENTAL DATA

Experimental probing data were used to determine the magnitude of the threshold contact force (F_t) needed to generate the trigger signal. Using the model of the trigger force (Eqs. 1 to 6), various values of F_t were tested in an attempt to match the shape and magnitudes of the experimental probing force data. Using a value of 3.8 grams, the predicted forces are fairly close to the data, so it is concluded that the threshold force is somewhere close to 3.8 grams. This value yielded acceptable results in the model.

Data were collected using a direct computer controlled (DCC) CMM, and a commonly-used 5 way 3D probe with a 50 mm straight stylus extension. The stylus material is steel and the 50 mm stylus extension has the following geometric configuration: 3 mm diameter (20 mm length), tapered to 2 mm diameter (10 mm length), and 2 mm diameter (20 mm length). The probe and stylus were oriented vertically. The probe approach speed was 7.5 mm per second. In each experiment 1561 coordinate points representing 1561 probe approach directions to a reference sphere were measured. The points were obtained using the following scheme: one hundred twenty (120) points uniformly spaced at each of thirteen polar latitudes of the reference ball (130°, 120°, 110°, ..., 20°, and 10°), plus one point at the north pole. The points were taken beginning at the 130 degree polar latitude and ending at the north pole. The 1561 point experiment was repeated ten (10) times, so we have 10 single runs of 1561 point experimental data. The experimental pretravel data (1561 points) of each single run were calculated using the x-y-z coordinate probing data. Define r_i, i=1,2, ..., 1561, as the distance from each measured point to the reference ball center. Let R_o (7.99$\bar{9}$3 mm) be the sum of radii of the reference ball (4.9996 mm) and the probe tip (2.9997 mm). Pretravel associated with each probe approach direction is then the difference of the measured point distance (r_i) and the reference radius (R_o).

$$\delta_i=R_o-r_i, \quad (9)$$

where δ_i is the experimental pretravel.

RESULTS

The moment of inertia (I) is needed to predict the pretravel deflections (see Equation 8). Due to the structure of the stylus shaft (varying cross-section, threads, through holes) it is not feasible simply to calculate the moment of inertia. Thus, it is the only unknown parameter of the pretravel model, and the effective radius of the stylus shaft

(r_e) is used to represent that parameter. The least-squares method is used to minimize the error between the experiment pretravel and the model-predicted pretravel. With only one parameter to be determined, there is a closed-form solution.

The baseline model by which to judge the results of the succeeding models was developed using 1080 points of averaged pretravel (from 130 degree latitude to 50 degree latitude, inclusive) to find the model parameter. To reiterate, the other parameters used were: F_s = 156.6 gm, α = 41.0°, L = 59.0 mm, R = 5.0 mm, R_o = 7.9993 mm, F_t = 3.8 gm, and E = 200.0 GPa. Using this model, r_e was found to be 1.302 mm. Figure 2 shows the averaged experiment pretravels, the model predicted pretravels, and the prediction errors (model - experiment) for all 1561 approach directions. The mean of the 1561 prediction errors is 0.15 μm, and the standard deviation (std) of the 1561 errors is 0.56 μm.

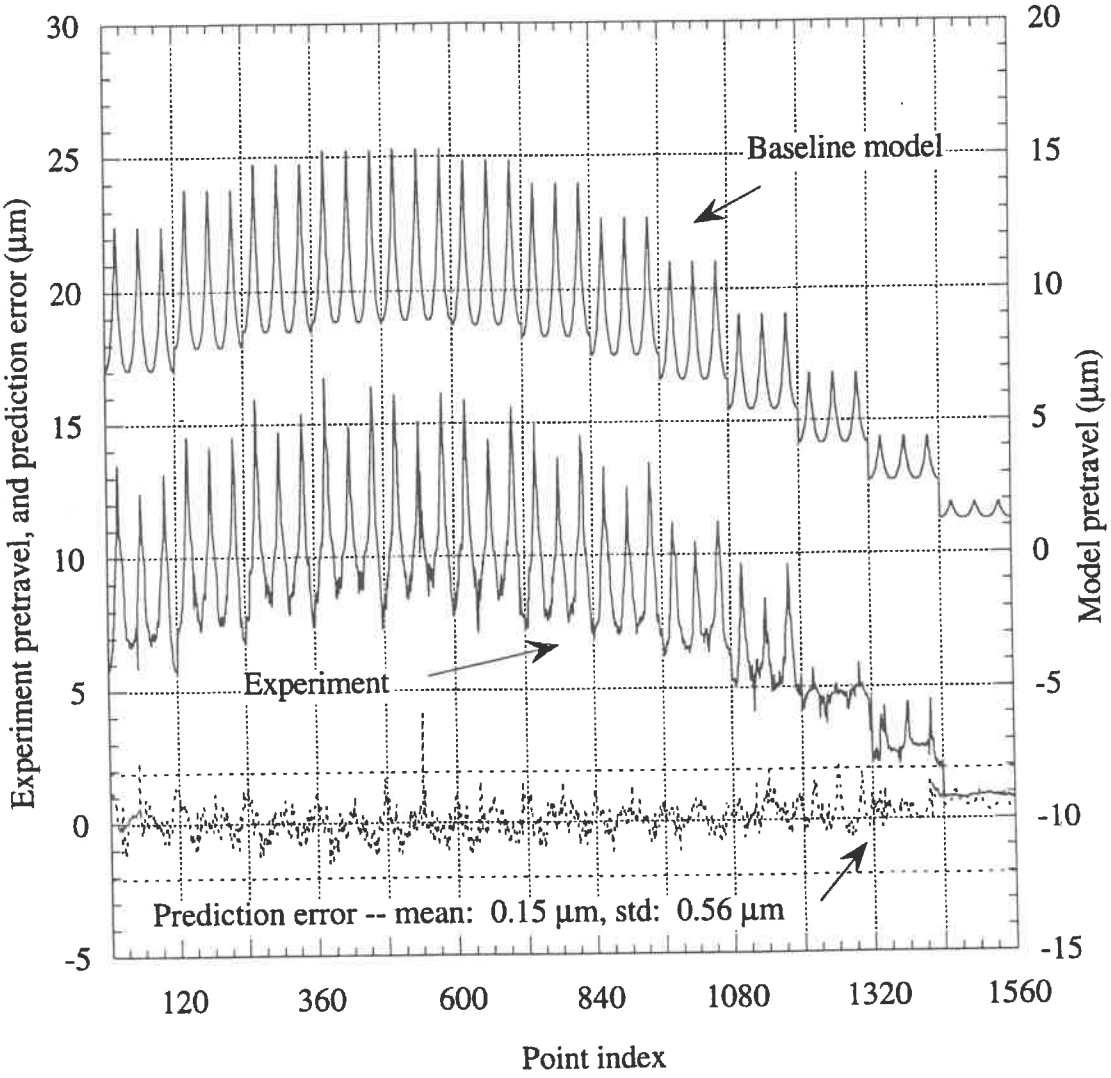

Figure 2. *Experiment and baseline model predicted pretravels and prediction error in 1561 approach directions*

The model was tested with fewer points, as it is desirable to use the smallest number of points possible to identify the model parameter. The results obtained for these sampling patterns are shown in Table 1. The most

promising testing scheme is that using 24 points equally spaced around the equator. This yields five sample sets from each of the ten 1561 point experimental data sets, making a total of fifty (50) test cases. The model parameter is fairly stable, with a mean of 1.299 mm, and the standard deviation being 0.006 mm. The standard deviations of 1561 prediction errors of the fifty 24 point cases range from 0.52 μm to 0.72 μm. As a check of the robustness of the model, 12 points from the equator were sampled for use in the model parameter calculation. The twelve points were equally spaced, and resulted in ten sample sets from each of the ten data sets, yielding a total of one hundred (100) test cases. There is a gain using these cases, as fewer points must be measured, but there is a cost in the accuracy of the pretravel prediction. The standard deviations of 1561 prediction errors of the 100 point cases range from 0.67 μm to 1.06 μm. The effective radius still has a mean of 1.304 mm, but the standard deviation has increased to 0.009 mm (as compared to 0.006 mm in 24 point cases).

Table 1. *Results of model tests from sparse data cases*

No. of points used in model	Statistic	Phase angle (°)	Effective Radius (mm)	Mean of 1561 errors (μm)	Std of 1561 errors (μm)	No. of runs
24 (equator)	Mean	1.411	1.299	-0.23	0.57	50
	Std	1.165	0.006	0.14	0.03	
	Min	-2.166	1.285	-0.56	0.52	
	Max	3.932	1.315	0.17	0.72	
12 (equator)	Mean	1.324	1.304	-0.10	0.67	100
	Std	3.202	0.009	0.21	0.11	
	Min	-5.358	1.283	-0.63	0.52	
	Max	9.975	1.339	0.68	1.06	

DISCUSSION AND CONCLUSION

By way of this research an analytical model for the probe triggering process has been built, which has deepened the understanding of a key technology in modern dimensional metrology and automation. The threshold contact force level (F_t) is one of the key issues in developing the pretravel model, and experimental probing force data were used to determine the value of this threshold. Use of a correct threshold force level results in more accurate prediction of the probing forces. The model presented herein makes use of data from the equator to determine the model parameter and the phase angle. The beauty of the model is that the probing pretravel behavior is effectively captured by the model without the need to use pretravel data from latitudes other than the equator. Moreover, the model parameter (r_e) is accurately and consistently identified using only twenty-four (24) points from one level. As measurements from only one level are needed, the model can be fit using a 2D artifact, such as a ring gauge, rather than a 3D artifact.

The tripod phase angle must be used in the model, and can be determined using the same equatorial data at no extra cost to the user. However, we have shown that a more accurate value of the phase angle can improve the prediction effectiveness and reduce probing error in CMM measurements. As a result, we suggest that probe vendors provide the phase angle information in ways such as markings on the probe or a signal to the machine system. The model is practical in its simplicity and that it can be implemented by using a computer program, which can be incorporated into the machine's probe calibration process. This provides for real time pretravel compensation for CMMs and machine tools.

ACKNOWLEDGEMENT

This work was supported in part by the National Science Foundation under Grant No. DMII-9308648 and the National Institute of Standards and Technology (NIST) Computational Metrology Program under Grant No. 70NAB4H1681. We thank Professor James D. Lee of the George Washington University (GWU) for useful suggestions, and the Computational Metrology Group of NIST for valuable discussions. We also thank Bruce Borchardt of NIST for providing experimental data, and Xianping Zhang of GWU for discussion.

REFERENCES

Bosch, J., 1995, *Evolution of Measurement, in Coordinate Measuring Machine and Systems*, J. Bosch, Ed., Marcel Dekker Inc., New York.

Butler, C., 1991, "An Investigation Into the Performance of Probes on Coordinate Measuring Machines", *Industrial Metrology*, Vol. 2, pp. 59-70.

Estler, W.T., S.D. Phillips, B. Borchardt, T. Hopp, C. Witzgall, M. Levenson, K. Eberhardt, M. McClain, Y. Shen and X. Zhang, 1995, "Error Compensation for CMM Touch Trigger Probes", *Proceedings of ASPE Annual Meeting*, Austin, Texas, pp. 428-431.

Estler, W.T., S.D. Phillips, B. Borchardt, T. Hopp, C. Witzgall, M. Levenson, K. Eberhardt, M. McClain, Y. Shen and X. Zhang, 1996, "Error Compensation for CMM Touch Trigger Probes", accepted for publication in *Journal of Precision Engineering*.

Jarman, T., and Traylor, A., 1990, "Performance Characteristics of Touch Trigger Probes", *Proceedings of Precision Metrology with Coordinate Measurement Systems*, SME, Troy, Michigan.

NIST, 1996, "Superfit Greatly Reduces Major Source of CMM Errors", Press Release 96-06, National Institute of Standards and Technology (NIST), Gaitherburg, MD.

Reid, C., 1993, "Probe Technology - Beyond Accuracy", *Proceedings of Applying Imaging and Sensoring Technology to CMM Applications*, SME, Nashville, Tennessee.

Shen, Y., and Zhang, X., 1996a, "A Pretravel Model for Touch Trigger Probes with Straight Styli, Part I: Vertical Probes", *Proceedings, North American Manufacturing Research Conference*, Vol. 24, SME, Ann Arbor, Michigan, pp. 127-132.

Shen, Y., and Zhang, X., 1996b, "A Pretravel Model for Touch Trigger Probes with Straight Styli, Part II: Horizontal Probes", *Proceedings, North American Manufacturing Research Conference*, Vol. 24, SME, Ann Arbor, Michigan, pp. 133-138.

CALIBRATION METHODS FOR DUAL PROBE CMMs

B. P. Vishwas and R. G. Wilhelm
Precision Engineering Laboratory
Department of Mechanical Engineering and Engineering Science
University of North Carolina at Charlotte NC 28223

A low cost method for 2-D software compensation of a dual probe coordinate measuring machine is described and the results are compared with results from a compensation technique using a laser interferometer.The measuring machine (WERTH Inspector) is equipped with both contact and non contact probes; the contact type being a touch trigger probe (TTP) and the non contact type being a CCD camera fitted with lenses of magnification 0.2x to 100x. To make use of the dual probe nature of the measuring machine, two types of calibrated artifacts are planned for calibration; one being a hole plate with ring gages as the holes and the other being a grid plate.The TTP probe and the CCD camera are used to measure the hole plate and the grid plate respectively in different orientations and the measured data is used for 2-D calibration of the measuring machine by two methods.

Early work in the area of calibration of coordinate measuring machines was done at NIST by Hocken and Borchardt[1].They presented a simple method for the determination of scale and squareness errors in two dimensional measurements.A method for applying software compensation to a commercial three axis coordinate measuring machine was presented by Zhang and Veale[2]. They presented a technique of compensation for geometric positioning errors and some thermal effects. Also, in the area of vision based systems, calibration methods have been developed by Raugh[3] who developed a method for calibration of an e-beam lithography machine (with a high precision X-Y stage) using a movable grid plate and Ananda[4] who presented a method for 2-D calibration of a vision CMM using a 1-D calibrated grid plate. A method for 3-D calibration of a three axis CMM by measuring 2-D reference objects in four positions has been developed at PTB by Kunzmann[5].

As a first step a mathematical model is developed to describe all the parametric error terms associated with the motion of the machine.The 21 geometric errors associated with the CMM are measured using a laser interferometer.The measured data is analyzed and a polynomial is approximated to each type of error data using the least squares method. Direct error compensation is done by linear interpolation all along the measuring volume. In the second step, a set of holes on a calibrated hole plate are to be measured in four different orientations using the TTP probe. The measurements are then repeated for a series of cross patterns on a grid plate using the CCD probe.

In each orientation, the machine coordinate system must be made to coincide with the artifact coordinate system. Using the data in each orientation, a set of equations is formed to relate positions expressed in the machine coordinate system to positions expressed in the hole plate coordinate system by the transformation matrix containing the coefficients of error polynomials. These coefficients are obtained using least squares elimination by minimizing the chi-square.

The measuring machine (WERTH Inspector) belongs to XYFZ type (notation introduced by Charleton) where the XY table positions the part, the TTP and vision probe being mounted on the Z-rail.The error model of the CMM is developed by following the method presented by Zhang[2]. The main assumptions made are that the machine components (base,carriages, etc.) nearly behave as rigid bodies and the error terms of a carriage depend only on the position of that carriage, not on the position of any other carriages.The matrix equation describing the true position of the probe with respect to the part is

$$\vec{XYZ} = R_x[R_y(R_z^{-1} \cdot \vec{P} + \vec{Z} - \vec{Y}) - \vec{X}]$$

After performing the above operations the equations for the compensated coordinates of the CMM are obtained which is of the form

$$X_{Actual} = X_{CMM} + X_p + \Delta X$$

with similar equations for the Y and Z axes.However the Z axis equation is not considered in the model since 2-D calibration is the criterion.

Measurements are carried out with the probe in the vertical position (probe axis perpendicular to XY plane) and hence the probe offsets Xp &Yp are equal to zero and only Zp exists.Therefore the error terms for this calibration include all terms except the errors that are function of Z.

Individual parametric errors are expressed in the form of polynomials,from the knowledge of error data. The error data is analyzed and a polynomial is approximated for each type of error. For example the scale error in X axis is expressed as a first order polynomial in X $\delta x(X) = A+BX$.

Figures 1 through 4 show the configurations of the hole/grid plate The axes of the machine coordinate system are indicated as (xm,ym) and (xg,yg) represent the axes of the hole/grid plate coordinate system. Positions labeled 1 through 9 are hole/grid points.

As a first step, the machine coordinate system is made coincident with the hole/grid plate coordinate system with the axes of both coordinate system being aligned. The next position is a clockwise rotation of the grid plate through 90 degrees and the third position is the rotation of the grid plate through 180 degrees clockwise from the first position.The fourth position is obtained by translating the grid plate in the X direction by a known distance.

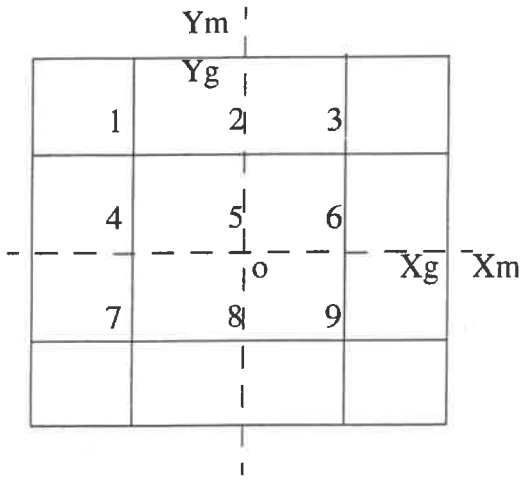

Figure 1. First position.

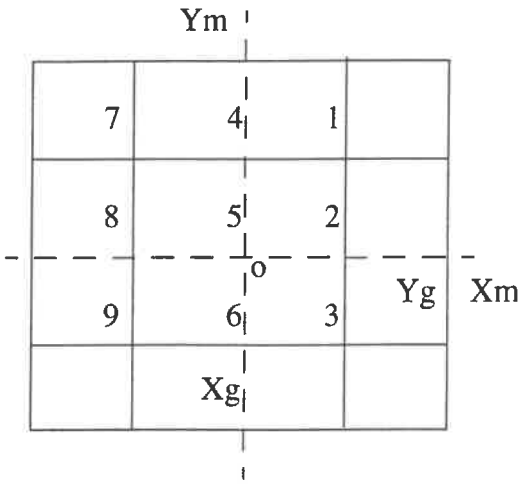

Figure 2. Second position. Rotation in clockwise direction through 90 degrees from the first position.

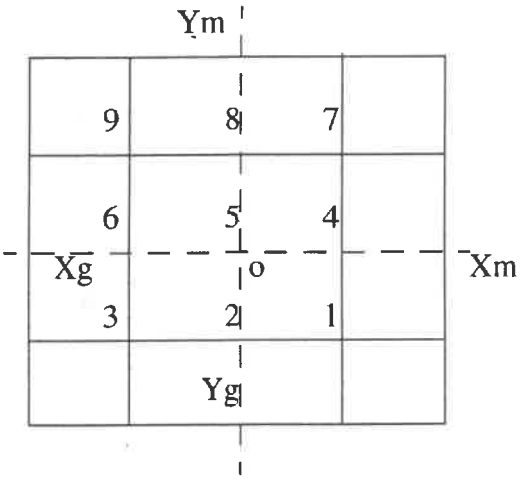

Figure 3. Third position. Rotation in clockwise direction through 180 degrees from the first position.

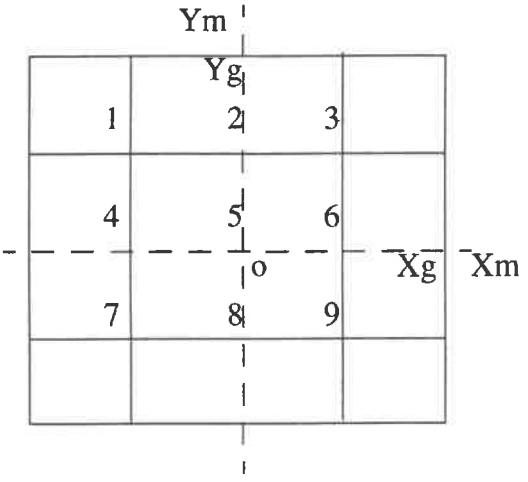

Figure 4. Fourth position. Translation through a known distance along X axis from the first position.

The calibration parameters are developed by relating positions in the hole/grid plate and machine coordinate systems while accounting for the parametric errors of the machine. A typical equation for the relationship between the hole/grid point at position one and position two is shown below.

$$M_{1j}\begin{bmatrix} xm_{1j} \\ xm_{1j} \end{bmatrix} = R_1^{-1} M_{2j}\begin{bmatrix} xm_{2j} \\ ym_{2j} \end{bmatrix}$$

The M matrices refer to the machine errors found at two different positions. The x parameters are the hole/grid points and the R matrix describes the rotations for the various calibration positions. Additional equations are developed by equating the coordinates in the first position to the third and fourth positions respectively. Since the plate is calibrated the distance between any two hole centers is known.

The system of equations is then solved to determine the coefficient of the polynomials by using the least squares method to minimize the chi-square.The main criteria is to minimize the number of features, holes/grid points, and also meet the accuracy requirements.

Experiments are now in progress to determine the minimum feature requirements and to compare the calibration results obtained by hole plate and grid plate with that of software correction by the laser interferometer method. By this method a 2-D calibration using measured artifacts in different orientations will be possible. It is expected that the artifact method will be both faster and less expensive than interferometer method.

Acknowledgments

This work has benefited greatly from the exceptional research environment provided by the UNCC Precision Engineering Laboratory and the Cameron Center for Applied Research. This material is based upon work supported by the National Science Foundation under Grant No. DMI-9457168.

References

1. R. J. Hocken and B. Borchardt, "On Characterizing the Measuring Machine Geometry", NBSIR, 79-1752.
2. G. Zhang and R. Veale, "Error Compensation of Coordinate Measuring Machines", Annals of the CIRP, Vol.34/1, 1985.
3. M. Raugh, "Absolute two-dimensional sub-micron metrology for electron beam lithography", Integrated Circuit Metrology 2, SPIE,Vol 480,1984.
4. M. V. Ananda, "Residual Error Compensation of A Vision Based Coordinate Measuring Machine", Master's Thesis, UNC Charlotte, 1992.
5. H. Kunzmann, "A uniform concept for Calibration, Acceptance Test, and Periodic Inspection of Coordinate Measuring Machines using Reference Objects", PTB, 1990.

EVALUATION OF ELLIPTICAL PROFILES AND ITS APPLICATION IN CYLINDER MEASUREMENT BY CMMS

Yiding Wang, Kee S. Moon and John W. Sutherland

Department of Mechanical Engineering-Engineering Mechanics
Michigan Technological University
Houghton, MI 49931

ABSTRACT

This paper presents improved algorithms for the evaluation of elliptical profiles measured by coordinate measuring machines. The value *D/R*, which *D* is the distance between the center of the ellipse and the origin and *R* is the half major axis, is identified as a critical value to make the commonly used least square algorithm not robust. The improved algorithm can reduce the computation error caused by singularity of the coefficients matrix when using the least square method. The method can be further applied in the evaluation of the data for cylinder measurement by CMMs when the axis of the cylinder is not parallel to the *Z* axis of the CMMs. The evaluation errors relating to the distribution of the sampling points and the deviation of the axial direction of the cylinder from the *Z* direction are investigated by simulation.

Keywords: metrology, CMM, algorithm.

INTRODUCTION

Coordinate measuring machines (CMMs) assess the parameters of mechanical parts on a point-by-point basis. The acquired data are analyzed to produce a "substitute geometry" to be compared with the design intent. However, CMMs based dimensional inspection has some drawbacks. Besides the hardware error of the machine, the most significant ones are the effects of sampling strategies and the fitting algorithms on the reported results. These errors are caused by estimating the measured features according to a particular number and distribution of the measurement points instead of all the points on the surface. Therefore, the reported results may contain large errors. With the development of software technique, the errors caused by the software of CMMs aroused great concerns in coordinate metrology area. As reported by Waldele (Waldele, 1993), certain algorithms are capable of stating that the measurement is worse than the actual data gathered up to an error of 37%. The software errors are usually caused by the fitting objectives of a problem, optimization methods used, and computing environment (word length, rounding method), etc., (Hopp, 1993) to make the evaluation software far from robust.

This paper describes the analysis of the evaluation errors for measuring a cylinder subjecting to different sampling conditions in the case that its axis is unparalleled to the Z axis of the CMM. The evaluation of elliptical profiles is suggested to be used in the evaluation of a cylinder measurement in this case. The drawbacks of the commonly used least-square fitting algorithms (especially for the singularity problem) are investigated. Improved algorithms for the evaluation of elliptical profiles are presented. The methods can be used in the evaluation of the data acquired by CMM for the workpiece with elliptical profiles.

ANALYSIS OF THE ERRORS IN CYLINDER MEASUREMENT

The most common way of measuring a cylinder is to measure a number of circular traces to be taken at different horizontal sections of the cylinder. For the simplest measurement, three measurement points on each section are needed to fit a circle. The measurement points are usually uniformly distributed. However, in the case that the axis of the cylinder is not parallel to the *Z* axis, the horizontal sections of the cylinder are not circular but elliptical. Using circles as fitting objectives will cause significant errors. Phillips (Phillips, 1993) illustrated the distribution of distances between the best fit center location and the true center position for a randomly oriented circular feature having a 10 μm elliptical form error. The results show that the correct center is never found using three measurement points (120^0 spaced) to fit for a circle.

In order to demonstrate the error caused by the effect of the unparallelness between the axis of the cylinder and the Z axis as well as the starting angle of the measurement on the fitting results, a simulation procedure was developed. Three uniformly spaced points in a horizontal section of a cylinder are sampled each time and used to fit for a circle. The angle between the axis of the cylinder and the *Z* axis is denoted ϕ and the starting angle for each sampling process is denoted θ (Fig. 1). The relative errors of the calculated results compared with the real values for the center coordinates and the radius are illustrated in Fig. 2 to Fig. 4.

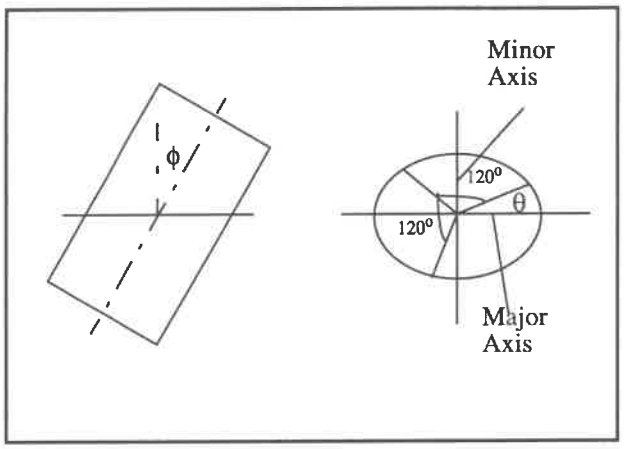

FIG.1 MEASUREMENT OF A CYLINDER

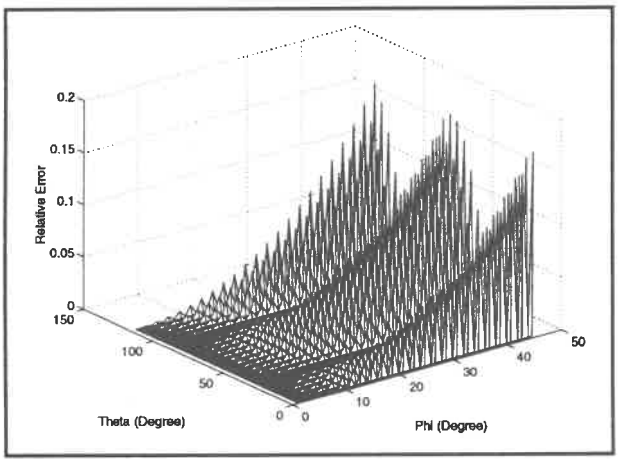

FIG.2 RELATIVE ERRORS OF THE CALCULATED X CENTER COORDINATE

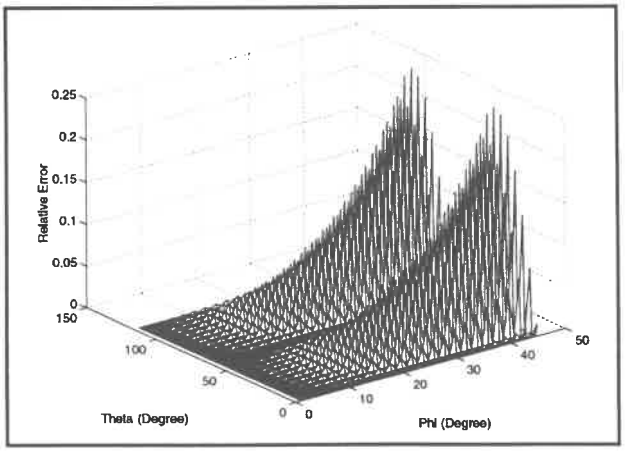

FIG.2. RELATIVE ERRORS OF THE CALCULATED Y CENTER COORDINATE

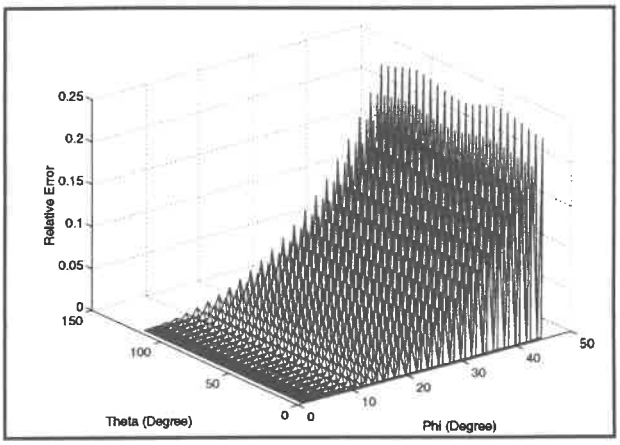

FIG. 3. RELATIVE ERRORS OF THE CALCULATED RADIUS

These significant errors are caused by the fitting algorithms only. In order to improve the calculating accuracy in this case, it is suggested that the fitting objective in each plane should be an ellipse instead of a circle. The centers of each ellipse are fitted to form the axis of the cylinder. The form error can be derived using least square method or min-max method.

ANALYSIS OF THE METHOD FOR EVALUATION OF THE ELLIPTICAL PROFILES

A commonly used method for evaluating the elliptical profile is based on the least-square method (Murthy, 1983). The general equation for an ellipse is:

$$x^2 + ay^2 + bxy + cx + dy + e = 0 \qquad (1)$$

Theoretically, the center position, the major axis and the minor axis can be uniquely defined by any five points on the ellipse. In the case of multi-point measurement, the fitting objective is defined as:

$$\varepsilon = \sum_{i=1}^{N} \left(x_i^2 + a y_i^2 + b x_i y_i + c x_i + d y_i + e \right)^2 \qquad (2)$$

where: x_i, y_i:coordinates of the measurement points,

N: number of measurement points.

Differentiate eqn. (2) with respect to a, b, c, d and e:

$$\frac{\partial \varepsilon}{\partial a} = 0, \frac{\partial \varepsilon}{\partial b} = 0, \frac{\partial \varepsilon}{\partial c} = 0, \frac{\partial \varepsilon}{\partial d} = 0, \frac{\partial \varepsilon}{\partial e} = 0 \qquad (3)$$

From these five equations, *a, b, c, d* and *e* can be calculated and the center coordinates, major axis and minor axis can also be obtained.

Simulations were done to verify this algorithm. We define the distance between the center of the ellipse and the origin as D, the length of the half major axis as R. Ellipses with different values of D/R were simulated and fitted using the least square method. The results show that: when $D/R<1.4142$, the relative error of the calculated results is less than 0.1%; when $D/R=4$, the relative error is 1.797%; when

D/R< 9.428, the relative error is 9.337%; when D/R=14.142, the relative error is 51.130%. Therefore, when D/R is greater than 9.428, the calculated results can not be accepted in engineering applications.

The reason for this phenomena is that, as D/R increases, the differences among coefficients of the eqn. (2) usually increase. Therefore, the condition number of the coefficient matrix in eqn. (3) is very high. The condition number is a measure of how close the matrix is to a singular matrix. The solutions are usually biased for a coefficient matrix which is near singular with a high condition number.

One way of improving the accuracy is to perform normalization transformation for the measured data. For the equations with the form of $AL=B$ such as eqn. (3), do the following transformation to obtain normalized equations $WQ=Y$, where:

$$\|a_i\|^2 = \sum_{j=1}^{N} a_{ji}^2 \tag{4}$$

$$M = \begin{bmatrix} \|a_1\| & & & \\ & \|a_1\| & & \\ & & \cdots & \\ & & & \|a_1\| \end{bmatrix} \tag{5}$$

$$W = AM^{-1} \tag{6}$$

$$Y = \|B\|^{-1}B \tag{7}$$

The solutions of the normalized equation $WQ=Y$ can be used to obtain the solutions of the original equations by transformation:

$$L = \|B\|M^{-1}Q \tag{8}$$

This method is usually too involved and will reduce the speed of the software.

IMPROVED METHOD BASED ON LINEARIZATION

Linearization technique is employed to derive the improved algorithm. For the multi-point measurement process, in order to fit all the measurement points to eqn. (2), first, we select the data of five points from the measured points to plug into eqn.(2) and get the initial solution (a_0,b_0,c_0,d_0,e_0). This result is usually very close to the results obtained when using all the points on the profile. Then, the right side of eqn. (2) can be expressed by the Taylor series (the terms whose power is bigger than 2 are omitted) as:

$$\begin{aligned} \varepsilon(a,b,c,d,e) &= \varepsilon(a_0,b_0,c_0,d_0,e_0) \\ &+ \left[\left(\frac{\partial\varepsilon}{\partial a}\right)_0,\left(\frac{\partial\varepsilon}{\partial b}\right)_0,\left(\frac{\partial\varepsilon}{\partial c}\right)_0,\left(\frac{\partial\varepsilon}{\partial d}\right)_0,\left(\frac{\partial\varepsilon}{\partial e}\right)_0\right]\cdot\Delta^T \\ &+ \frac{1}{2}\Delta\cdot H\cdot\Delta^T \end{aligned} \tag{9}$$

where: $\Delta=[\Delta a, \Delta b, \Delta c, \Delta d, \Delta e]$, and $\Delta a=a-a_0$, $\Delta b=b-b_0$, $\Delta c=c-c_0$, $\Delta d=d-d_0$, $\Delta e=e-e_0$, and

$$H = \begin{bmatrix} \left(\frac{\partial^2\varepsilon}{\partial a^2}\right)_0 & \left(\frac{\partial^2\varepsilon}{\partial a\partial b}\right)_0 & \left(\frac{\partial^2\varepsilon}{\partial a\partial c}\right)_0 & \left(\frac{\partial^2\varepsilon}{\partial a\partial d}\right)_0 & \left(\frac{\partial^2\varepsilon}{\partial a\partial e}\right)_0 \\ \left(\frac{\partial^2\varepsilon}{\partial b\partial a}\right)_0 & \left(\frac{\partial^2\varepsilon}{\partial b^2}\right)_0 & \left(\frac{\partial^2\varepsilon}{\partial b\partial c}\right)_0 & \left(\frac{\partial^2\varepsilon}{\partial b\partial d}\right)_0 & \left(\frac{\partial^2\varepsilon}{\partial b\partial e}\right)_0 \\ \left(\frac{\partial^2\varepsilon}{\partial c\partial a}\right)_0 & \left(\frac{\partial^2\varepsilon}{\partial c\partial b}\right)_0 & \left(\frac{\partial^2\varepsilon}{\partial c^2}\right)_0 & \left(\frac{\partial^2\varepsilon}{\partial c\partial d}\right)_0 & \left(\frac{\partial^2\varepsilon}{\partial c\partial e}\right)_0 \\ \left(\frac{\partial^2\varepsilon}{\partial d\partial a}\right)_0 & \left(\frac{\partial^2\varepsilon}{\partial d\partial b}\right)_0 & \left(\frac{\partial^2\varepsilon}{\partial d\partial c}\right)_0 & \left(\frac{\partial^2\varepsilon}{\partial d^2}\right)_0 & \left(\frac{\partial^2\varepsilon}{\partial d\partial e}\right)_0 \\ \left(\frac{\partial^2\varepsilon}{\partial e\partial a}\right)_0 & \left(\frac{\partial^2\varepsilon}{\partial e\partial b}\right)_0 & \left(\frac{\partial^2\varepsilon}{\partial e\partial c}\right)_0 & \left(\frac{\partial^2\varepsilon}{\partial e\partial d}\right)_0 & \left(\frac{\partial^2\varepsilon}{\partial e^2}\right)_0 \end{bmatrix} \tag{10}$$

Differentiate eqn. (9) with respect to a, b, c, d and e, we can get:

$$H\Delta = D \tag{11}$$

where: $D = -\left[\left(\frac{\partial\varepsilon}{\partial a}\right)_0,\left(\frac{\partial\varepsilon}{\partial b}\right)_0,\left(\frac{\partial\varepsilon}{\partial c}\right)_0,\left(\frac{\partial\varepsilon}{\partial d}\right)_0,\left(\frac{\partial\varepsilon}{\partial e}\right)_0\right]^T$

eqn. (11) can be solved to yield Δa, Δb, Δc, Δd and Δe. Then $a=a_0+\Delta a$, $b=b_0+\Delta b$, $c=c_0+\Delta c$, $d=d_0+\Delta d$, $e=e_0+\Delta e$. In order to further improve the accuracy, the obtained a, b, c, d and e can be used as the initial values and use this method to calculate again and update the most recently obtained value until the results satisfy a pre-assigned termination condition. The center coordinate of the ellipse (m, n), half major axis R and half minor axis r can be calculated by:

$$m = \frac{2ac-bd}{b^2-4a} \tag{12}$$

$$n = \frac{2d-bd}{b^2-4a} \tag{13}$$

$$R = \sqrt{\frac{2\left(bcd-ac^2-d^2+4ae-eb^2\right)}{\left(b^2-4a\right)\left(1+a-\sqrt{b^2+(1-a)^2}\right)}} \tag{14}$$

$$r = \sqrt{\frac{2\left(bcd-ac^2-d^2+4ae-eb^2\right)}{\left(b^2-4a\right)\left(1+a+\sqrt{b^2+(1-a)^2}\right)}} \tag{15}$$

In order to test this algorithm, ellipses with different D/R values are simulated and evaluated using the improved method. The results showed that when D/R<9.428, the relative error is less than 0.930%; when D/R=14.142, the relative error is 9.030%; when D/R=18.562, the relative error is 23.310%. The comparison of the relative calculation error of the commonly used least square method and the improved method is shown in fig.5. It is evident that the improved method can accurately get the results in a wider range of D/R values than the commonly used least square method.

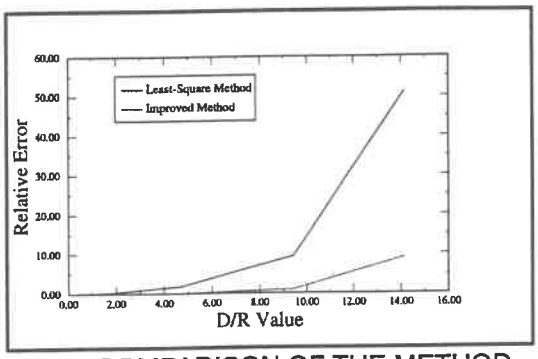

FIG. 4 COMPARISON OF THE METHOD

ROBUST ALGORITHM IN THE EVALUATION OF AN ELLIPSE

Although the improved method has good accuracy for a wide range of *D/R* values, it still can not guarantee that the results are always accurate. An iterative method is proposed.

Eqns. (3) can be represented as:

$$AL = B \tag{16}$$

where: $L=[a, b, c, d, e]^T$,

$$A = \begin{bmatrix} \sum_{i=1}^{N} y_i^4 & \sum_{i=1}^{N} x_i y_i^3 & \sum_{i=1}^{N} x_i y_i^2 & \sum_{i=1}^{N} y_i^3 & \sum_{i=1}^{N} y_i^2 \\ \sum_{i=1}^{N} x_i y_i^3 & \sum_{i=1}^{N} x_i^2 y_i^2 & \sum_{i=1}^{N} x_i^2 y_i & \sum_{i=1}^{N} x_i y_i^2 & \sum_{i=1}^{N} x_i y_i \\ \sum_{i=1}^{N} x_i y_i^2 & \sum_{i=1}^{N} x_i^2 y_i & \sum_{i=1}^{N} x_i^2 & \sum_{i=1}^{N} x_i y_i & \sum_{i=1}^{N} x_i \\ \sum_{i=1}^{N} y_i^3 & \sum_{i=1}^{N} x_i^2 y_i^2 & \sum_{i=1}^{N} x_i y_i & \sum_{i=1}^{N} y_i^2 & \sum_{i=1}^{N} y_i \\ \sum_{i=1}^{N} y_i^2 & \sum_{i=1}^{N} x_i y_i & \sum_{i=1}^{N} x_i & \sum_{i=1}^{N} y_i & N \end{bmatrix}$$

$$B = -\begin{bmatrix} \sum_{i=1}^{N} x_i^2 y_i^2 & \sum_{i=1}^{N} x_i^3 y_i & \sum_{i=1}^{N} x_i^3 & \sum_{i=1}^{N} x_i^2 y_i & \sum_{i=1}^{N} x_i^2 \end{bmatrix}$$

N is the number of measurement points.

Eqn. (16) can be solved and yield a, b, c, d and e. These values can be plugged in eqns. (12) ~(15) to get the center coordinate (m_0, n_0), half major axis R_0 and half minor axis r_0. Then, perform transformation to the measurement data using: $x_i=x_i-m_0$, $y_i=y_i-n_0$, ($i=1$~N). Put the transformed data into eqn. (16) to calculate the new center coordinate, half major axis and half minor axis. The process proceeds until a pre-assigned termination condition is satisfied. The simulation results showed that this method can always yield the accurate results for arbitrary *D/R* value. To make the process simple, the first run of calculation can be done by using the coordinates of only five measurement points. Experiences show that generally 1~2 iterations are needed for the calculation to terminate.

The algorithm proposed can be used in the evaluation of the cylinder measured by CMMs when the axis of the cylinder is not parallel to the Z axis of the machine.

CONCLUSION

The software of the CMMs might have significant errors to make the reported results biased. The errors involved in the measurement of a cylinder by CMMs using the conventional method are demonstrated by simulation. It is argued that fitting an ellipse to the measurement data for one layer instead of a circle will yield more accurate results. The ratio *D/R*, which *D* is the distance between the center of the ellipse and the origin and *R* is the half major axis of the ellipse, is identified as a critical value to make the algorithm not robust. An improved algorithm based on the linearization is proposed. This algorithm shows advantages over the commonly used least square method. Furthermore, a robust algorithm is proposed which is based on iteration. These algorithms can easily be applied in the software of the CMMs.

REFERENCES

Hockon, R. J., Raja, J. and Babu, U. (1993), Sampling Issues in Coordinate Metrology. International Forum on Dimensional Tolerancing and Metrology. CRTD-Vol. 27, 97-111. ASME.

Hopp, T. H., (1993), Computational Metrology. International Forum on Dimensional Tolerancing and Metrology. CRTD-Vol. 27, 207-217. ASME.

Lotze, W. (1994), General Solution for Tsebyshev Approximation of Form Elements in Coordinate Measurement. Measurement. Vol. 12, 337-344.

Murthy, T. S. R., Reddy, G. C., and Radhakrishnan, V., (1983), A Method for Evaluation of Elliptical Profiles. Precision Engineering. Vol. 5, No. 2., 77-81.

Murthy, T. S. R., (1982), A Comparison of Different Algorithms for Cylindricity Evaluation. Int J. Mach. Tool Des. Res. Vol. 22, No.4, 283-292.

Murthy, T. S. R., (1980), Minimum Zone Evaluation of Surfaces. Int J. Mach. Tool Des. Res. Vol. 20, 123-136.

Phillips, S. D., et al., (1993), Measurement Uncertainty Considerations for Coordinate Measuring Machines. NISTIR 5170.

Shunmugam, M. S., (1987), Comparison of Linear and Normal Deviations of Forms of Engineering Surfaces. Precision Engineering. Vol. 9, No.2, 96-102.

Shunmugam, M. S., (1991), Criteria for Computer-Aided Form Evaluation. Transactions of the ASME, Journal of Engineering for Industry. Vol. 113. 233-238.

Waldele, et al., (1993), Testing of Coordinate Measuring Machine Software. Precision Engineering. Vol. 15, 121-123.

INVESTIGATION OF ERROR MOTIONS OF AEROSTATIC SPINDLES

M. Weck, M. F. Soltani
Fraunhofer Institut für Produktionstechnologie, IPT
Aachen, Germany

1 Introduction

The perfect function of an air bearing is among other aspects secured through the form accuracy of the bearing. Should high guidance accuracy and stiffness be achieved, the bearing gap height and the form deviation must be kept very small. High requirements on measurement and form accuracy of the bearing parts are the main cause of high manufacturing costs of aerostatic spindle systems. To minimise manufacturing costs it is very important to know which influence the form error of rotor and stator has on the error motion of the spindle. This report describes influences on the error motion of an aerostatic spindle and gives some experimental results.

2 Theoretical model of influences on the error motion of aerostatic spindles

Error motions of aerostatic spindles are affected by the bearing configuration chosen and the manufacturing tolerances. The bearing gap is formed by the machined surfaces of the rotor and the stator of the spindle. Any inaccuracies in form and position of these surfaces lead to local pressure variations in the bearing gap. When the pressure distribution changes while the spindle is rotating, error motion occure. In addition to the manufacturing and assembling errors, the bearing specifications, gravitational, centrifugal and other forces in a fixed direction (e.g. cutting force) as well as the spindle speed may influence the error motion of an aerostatic spindle [1]. For a better understanding of the influences mentioned above a simple model (spring model) has been developed (fig. 1). An equation for the simplified calculation of the error motion of an aerostatic journal bearing with orifice restrictors has been performed. Every pressure pad has been simplifed by a spring with a constant stiffness.
The error motion in radial x and y can be written as:

$$\Delta X(\varphi_z) = \frac{1}{\sum_{i=1}^{I}(K_i*\cos^2\theta_i)}*[\sum_{i=1}^{I}[K_i*\cos\theta_i*(\sum_{n=1}^{N}(B_n*\cos(n*\theta_i-\Delta\theta_n) - \sum_{j=1}^{J}(A_j*\cos(j*\theta_i-j*\varphi_z-\Delta\phi_j)))]+F_{z_x}+F_{ce_x}+F_{g_x}]$$

$$\Delta Y(\varphi_z) = \frac{1}{\sum_{i=1}^{I}(K_i*\sin^2\theta_i)}*[\sum_{i=1}^{I}[K_i*\sin\theta_i*(\sum_{n=1}^{N}(B_n*\cos(n*\theta_i-\Delta\theta_n)) - \sum_{j=1}^{J}(A_j*\cos(j*\theta_i-j*\varphi_z-\Delta\phi_j)))]+F_{z_y}+F_{ce_y}+F_{g_y}]$$

The variables are given in the nomenclature.

This model is an easy to handle tool which gives users the possibility to determine the radial error motion of an aerostatic spindle. Because of the approximation which are made in this model the results have to be understood also as approximations. With the help of this model statements about runout characteristics of a rotor supported by an externally pressurized gas journal bearing with special attention to the relationship between runout and manufacturing errors such as out-of-roundness of rotor and stator can be performed.

The most important statements are:

- if the rotor roundness is perfect there will be no error motion
- the stator roundness has no influence on the error motion
- the effect of a combination of a given number of supply holes (orifices) and a number of lobes on the rotor is either a "zero error" or the complete rotor error is reproduced as an error motion of the spindle [1]. For a given number of orifices I the only lobes U to contribute to an error motion are:

  $$U = K*I \pm 1, \text{ where } K = 1,2,3....$$

- the frequency of the error motion is the same as the frequency of the roundness error of the rotor

3 Experimental investigation of the error motion of an aerostatic spindle

The aim of this experiment is to study the influence of inlet pressure, number of orifices and form error of the rotor on the error motion of the spindle. Two rotors with different form errors were used. The first rotor will be used as a reference. From there its form accuracy during finish machining was not deliberately affected. To study the additonal influence of form errors of the rotor on the motion accuracy of the rotating axis the second rotor was manufactured with a defined roundness deviation.
Figure 2 shows a cross section of the test spindle. Up to 12 pocketed orifices can be used for the radial guidance of the rotor. Every orifice is separately supplied with pressurized air. The axial guidance of the rotor is taken over by 3 axial orifices, which are equally distributed over the circumference of the lower part of the stator. The radial error measurements were carried out with two ADE capacitance sensors, which measured against a cylindrical master. The error is calculated using the "difference method" (A-B)/2. This method reduces the influence of noise on the total error and eliminates the even numbered form deviations of the master. To increase the measurement accuracy evaluation of the measured values is carried out over 16 revolutions.

3.1 Experimental results by using a "perfect" rotor

The following measurements are carried out at low speed (average 50 rpm) and free run of the spindle to prevent influences from drive and unbalance on the error motion. Several measurements were performed with different supply pressure values (3, 5 and 7 bar) and number of orifices (3, 4, 6 and 12).
Figure 3 shows that the total error was more dependent on the number of orifices than on the supply pressure. There is an averaging effect only with 4, 6 and 12 orifices. The averaging effect means that the rotating accuracy is much better than the magnitude of machining errors at rotor and bearing, which were measured to about 0.23 µm and 0.31 µm respectively.
The synchronous error is a repeatable error and gives more information about the effects of systematic error sources - such as shaft form - on the error motion of the spindle. Therefore only this error type will be considered in the investigation of the influence of shaft form on rotation accuracy of the spindle.
The spectrum of the synchronous error (fig. 4) confirms the $k*I\pm1$ expectations from the spring model for I=3, 4 and 6 orifices. For 12 orifices the second harmonic is the largest, but the 11^{th} and 13^{th} are larger than the 12^{th} harmonic. The relation between the number of orifices and the frequency of the form deviation of the rotor will be further investigated in the next chapter.

3.2 Experimental results by using a rotor with a defined roundness deviation

The rotor used in this experiment has 11 lobes at the circumference with an amplitude of 0.5 µm (fig. 3.4). According to the spring model this shaft shape should lead to an error motion with a frequency of 11 per revolution independent from the number of orifices and the inlet pressure. The radial rotor shape was manufactured using a Fast Tool Servo System as described in [1].

The frequency analysis of the synchronous error with different number of orifices and different values for inlet pressure are shown in figure 6. At 7 and 5 bar inlet pressure the frequency 11/R (Revolution) could be found. With 3 orifices the 2/R and the 4/R are the dominant error frequencies. With 4 orifices the 3/R and 5/R and with 6 orifices the 5/R and the 7/R are the dominant error frequencies.

At 3 bar inlet pressure the amplitude of the 11/R increases and at 1 bar pressure the error with 11/R frequency is the dominant one and its amplitude was measured to about 0.5 µm. As the air supply pressure decreases, the correlation between theory and experimental results increases.
One reason for this behaviour can be found in the influence of gap variation and eccentricity between rotor and stator. The theory of the spring model neglects stiffness variations at each orifice. The influence of gap variation on the stiffness can be studied in figure 7, which shows the theoretical stiffness of an orifice bearing plotted against gap height at different values of inlet pressure [2]. The real gap in this case was measured to about 16 µm. At 7 and 5 bar inlet pressure a deviation of the gap height leads to high changes of stiffness from orifice to orifice. In this case the main condition of stiffness stability at each orifice in the spring modell is not true. As the inlet pressure decreases, the stiffness variation because of gap height deviation decreases too. At 1 bar inlet pressure the stiffness at each orifice remains constant over a large interval of gap height. In this case the influence of the gap variation on the stiffness is neglectable and the spring model is valid.

4 Conclusion

The first step in the error motion study was to develop an approximation theory for the dependence of error motions on different influences, especially the manufacturing tolerances. Because of the very high number of parameters which influence error motions, the research work was focused on a journal bearing with pocketed orifice restrictors. With the help of the developed "spring model" it is possible to predict error motions. Several error motion measurements were performed using a rotor with "perfect form" and a second one with well known form deviations (11 UPR). The error motion was detected to be more dependent on the number of orifices than on the inlet pressure.
With the "perfect rotor" it was found out that there is a clear relationship between synchronous error frequency and number of orifices, which confirms the K*I±1 expectation from the spring model. The validity of the spring model using the rotor with 11 UPR was only prooved at low values of inlet pressure (≤ 3 bar). The reason for this behaviour could be found in the fact that stiffness variations due to gap variations are disregarded in the spring model. In this case a constant stiffness over large gap variation is only true for low inlet pressure.

5 Nomenclature

I	: number of orifices	i	: orifice number
J	: maximum number of rotor lobes/2π	N	: maximum number of stator lobes/2π
K_i	: stiffness of pressure pad i	θ_i	: angle position of orifice i
φ_z	: angle of rotation		
F_z	: force; fixed direction	F_{ce}	: centrifugal force
F_g	: gravitational force	Fi	: inner force at orifice i
h	: theroetical gap hight	hi	: gap hight at orifice i
(x,y)	: fixed coordinate system	(ξ,η)	: rotating coordinate system
B_n	: amplitude of the roundness profile of the stator with n lobes/2π		
A_j	: amplitude of the roundness profile of the rotor with j lobes/2π		
$\Delta\theta_n$	: phase of the roundness profile with n lobes/2π (stator)		
$\Delta\phi_j$	: phase of the roundness profile with j lobes/2π (rotor)		

6 References

[1] Final Report on BRITE-EURAM Project BE-519
"High Precision High-Speed Spindle System", 1/1996

[2] M. Weck
Werkzeugmaschinen, Fertigungssysteme, Band 2, VDI-Verlag, Düsseldorf 1991

7 Figures

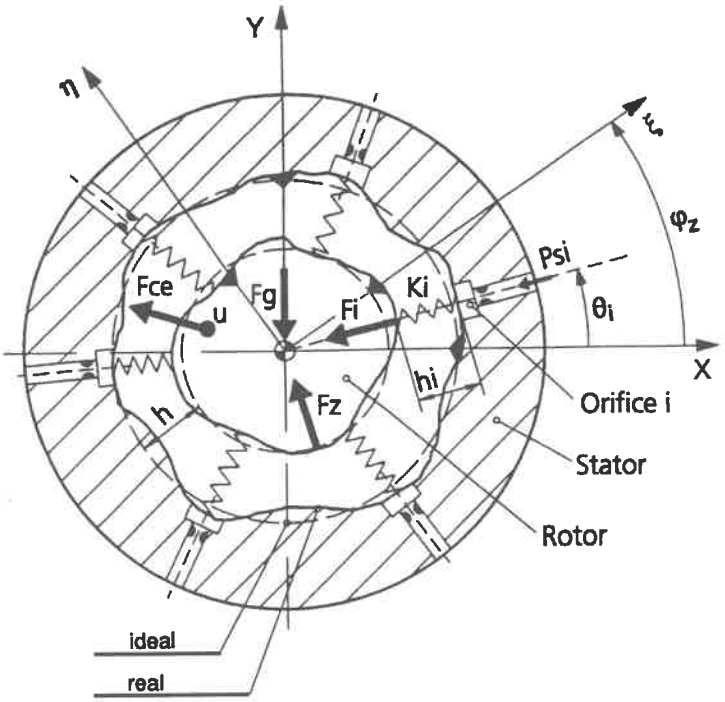

Fig. 1 Theoretical model

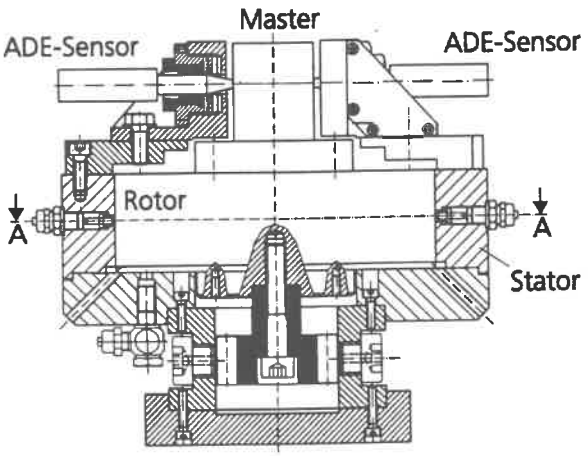

Fig. 2 Experimental set up

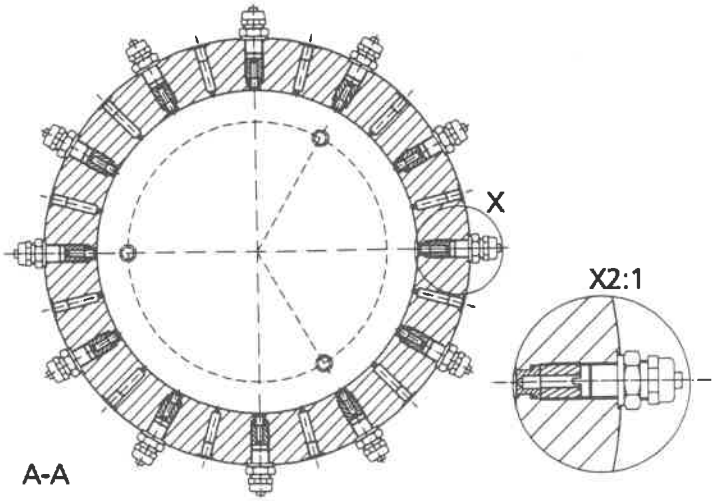

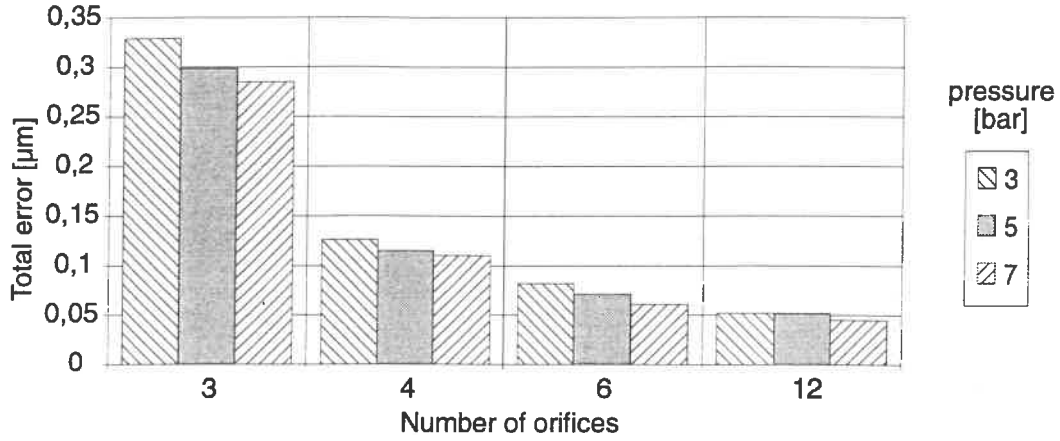

Fig. 3 Total error depending on number of orifices and inlet pressure

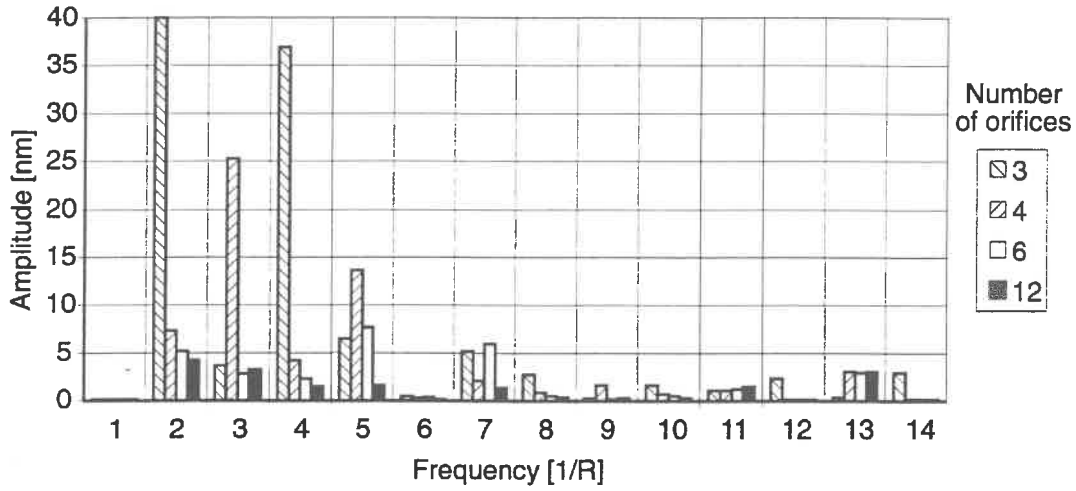

Fig. 4 Influence of the number of orifices on the amplitude of the synchronous error

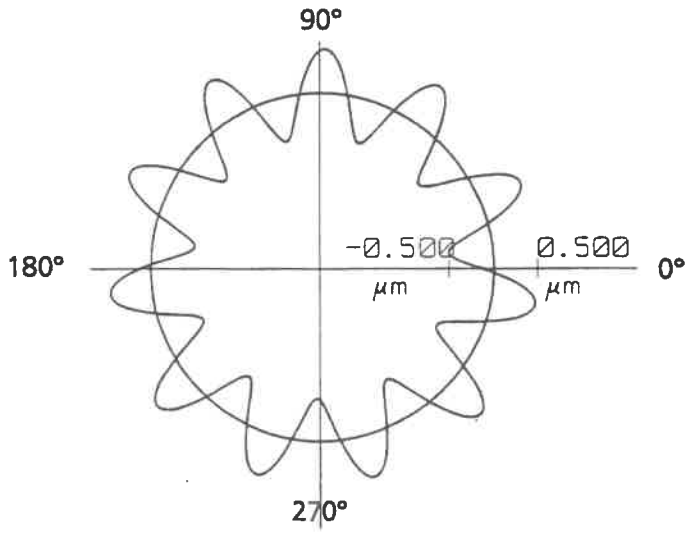

Fig. 5 Rotor with 11 undulations per revolution (UPR)

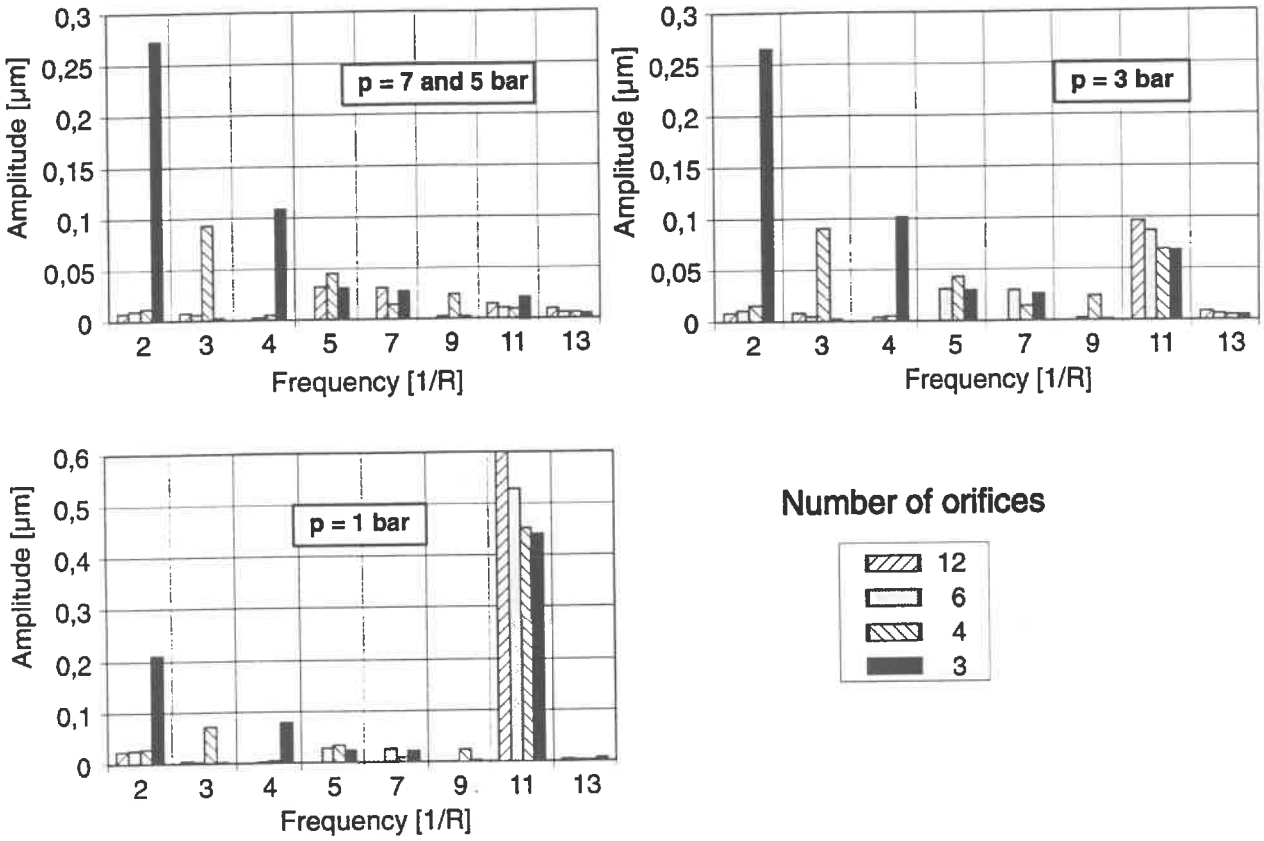

Fig. 6 Frequency analysis of the synchronous error at different number of orifices and inlet pressures (rotor with 11 UPR)

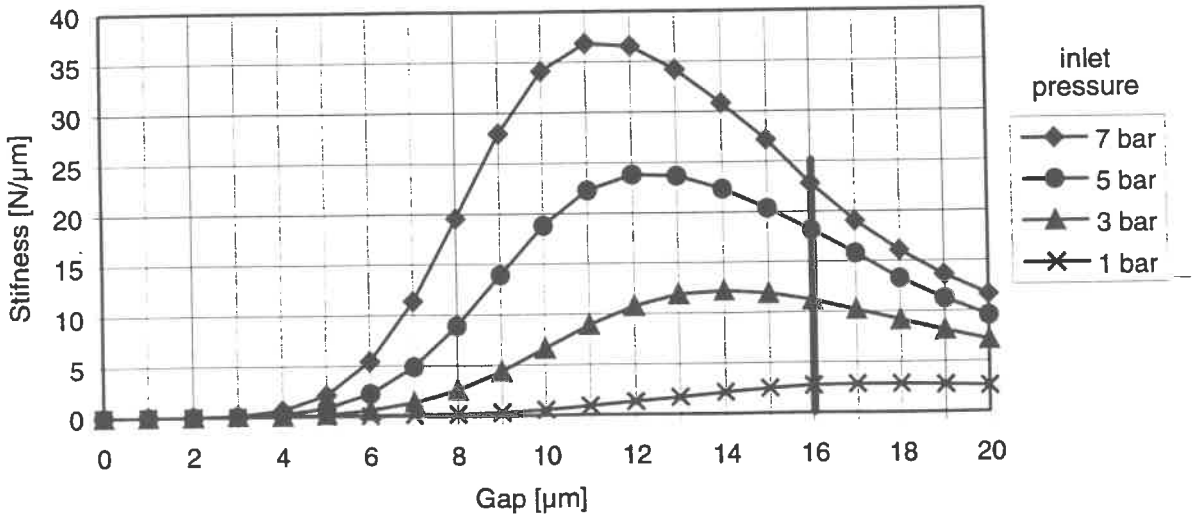

Fig. 7 Influence of inlet pressure and gap height on the Stiffness of an orifice bearing

SURFACE APPROXIMATION AND GENERATION OF COMPLEX GEOMETRIC MODEL FROM LASER SCAN DATA

Hong-Tzong Yau and Jenq-Shyong Chen
Department of Mechanical Engineering
National Chung Cheng University
Chia-Yi, Taiwan

Introduction

With the integration of computer controlled measuring machines and CAD/CAM systems, reverse engineering has emerged as an important design and manufacturing tool in recent years. Traditionally a design drawing or CAD model is created prior to the manufactured part. However, in some cases where the existing parts are modified due to poor performance or manufacturing limits, or in other cases where the design model simply does not exist, reverse engineering would then become indispensable. The goal of reverse engineering is to capture or recreate part geometry directly from measurement. Therefore, reverse engineering is an important technology aiming at closing the loop from measurement to design and manufacturing.

This paper describes the development of an intelligent reverse engineering system for automatic generation of complex geometry from laser scan data. The system consists of three major modules: (1) intelligent surface boundary detection, (2) NURBS surface approximation of scattered point data, and (3) automatic surface connection and B-Rep solid creation. The first module deals with the automatic detection and division of individual surface regions based on surface continuity considerations. Edges with curvature discontinuity will be automatically detected from the dense point data. With the grouping of various closed surface regions, planning is made to segment the entire point data map to individual surface patches. The second module then takes over by fitting a NURBS surface to each individual segmented region. First, the scattered data in the region is filtered and gridded if necessary. Then, NURBS surface approximation is made possible by minimizing the sum of squared deviations from the points to the surface. The third module matches the surface boundaries according to the position or tangency conditions based on the edge detection. The result is a complex B-Rep solid model that can be output by IGES translation to various CAD/CAM systems. The developed technology has been successfully applied to the modeling of dies and molds from automotive industry.

Feature Extraction and Edge Detection

Feature extraction here is referred to the detection and separation of geometric features from the scanned data. It consists of extraction of geometric features such as circle, plane, cylinder, etc., and detection of boundary edges that separate different surface regions. In this paper, the

emphasis has been placed on the automatic detection of surface boundaries so that various surface regions can be patched and connected for the creation of the entire complex model.

By laser scanning, objects are usually scanned by parallel scan lines. The distribution of the scanned data points typically do not follow the geometric pattern of the objects. Therefore, to segment the scanned data based on the geometric pattern, surface boundaries or edges need to be detected from the original parallel scan lines. To achieve this purpose, it is defined that points which are discontinuous in curvature be connected as "characteristic curves" and used as boundaries to separate surface regions. Any curve in a 3D space parameterized by the arc length s can be represented as

$$\vec{r}(s) = x(s)\vec{i} + y(s)\vec{j} + z(s)\vec{k} \qquad (1)$$

The curvature value can be obtained by differentiating the vector against the arc length s twice: $k = |\vec{r}''(s)|$. Given three continuous points P_{i-1}, P_i, P_{i+1}, the curvature value can be approximated by

$$k = |r_i''| = \sqrt{\frac{2|r_{i+1} - r_i|}{(h_i + h_{i+1})}} \qquad (2)$$

where $r_i = \left(\frac{x_i - x_{i-1}}{h_i}, \frac{y_i - y_{i-1}}{h_i}, \frac{z_i - z_{i-1}}{h_i} \right)$ and h_i is the distance between P_i and P_{i+1}.

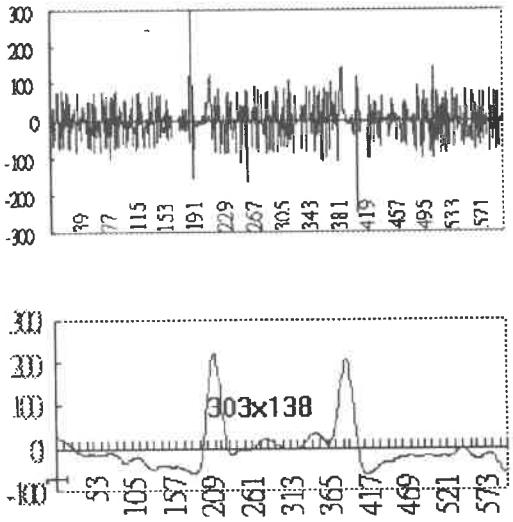

Figure1. Applying Gaussian filter to curvature data.

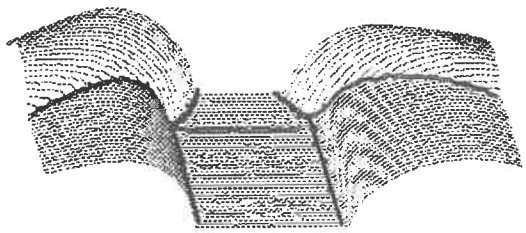

Figure2. Automatic edge detection of laser scanned data.

However, the laser scanned data is typically contaminated with substantial measurement noises. Results from direct computation of curvatures by the scanned data is often difficult to

judge and use. Therefore, Gaussian filtering is applied to the curvature data to remove high frequency noises (see Figure 1). Thus, the detection of surface boundaries can be more accurate. Figure 2 shows a successful example of finding the surface edges from a set of scanned data.

Surface Approximation

Point-to-surface conversion is the core process in reverse engineering. Since from a hierarchical planning point of view, lower level entities (points) should first be grouped into higher level entities (curves or surfaces) to make the task (creating a complex geometric model) more manageable. NURBS (Non-Uniform Rational B-Splines) has recently become the standard for surface representation in most CAD/CAM systems. NURBS is appealing in that it can represent both analytic geometry (such as conics) and free-form surfaces. In addition, NURBS has more flexibility than B-splines because it has more manipulation tools such as weights. In this work, a new approach to the fitting of NURBS is adopted [1]. Given a set of scanned data, $Q_i, i = 1,..., m$, and objective function to be minimized is formulated as

$$F = \sum_{i=1}^{m} e_i^2 \tag{3}$$

where the error

$$e_j = Q_j - \frac{\sum_{i=1}^{n} w_i P_i N_i(u)}{\sum_{i=1}^{n} w_i N_i(u)} \tag{4}$$

and w_i, P_i, and $N_i(u)$ are weights, control points, and blending functions respectively. The fitting algorithm can be summarized as [1]

1. Initialization:

   Set k = 1

   $f_k = 0$

   Let w_i = 1, i = 1,..., n

   $u_1 = 0.$

   $$u_j = \frac{\sum_{i=2}^{j} |Q_i - Q_{i-1}|}{\sum_{i=2}^{m} |Q_i - Q_{i-1}|} \quad , j = 2 ..... m$$

2. Update [WP]:

   $$[WP] = ([N]^T[N])^{-1}[N]^T[QNW]$$

3. Update [W]:

$$[W] = ([Q^x N]^T[Q^x N]+[Q^y N]^T[Q^y N]+[Q^z N]^T[Q^z N])^{-1} \cdot$$
$$([Q^x N)^T[NWP]^x + [Q^y N)^T[NWP]^y + [Q^z N)^T[NWP]^z)$$

4. Update [U] by solving

$$\frac{d}{du_j}|Q_j - C(u_j)|^2 = 0 \qquad j = 1,\ldots,m$$

5. k = k + 1

Let $f_k = \left(\sum_{j=1}^{m} c_j^2 / m\right)^{1/2}$

if ($f_k - f_{k+1} < \delta$ or k > max_k) go to 7

6. Go to 2

7. $P_i = (wP)_i / w_i \qquad i = 1,\ldots,n$

8. Stop

The above curve fitting algorithm can be extended to the surface case. Or the popular skinning process [2] can be used to loft the curves to the desired surface. Figure 3 shows the resulting surfaces from the data in Figure 2.

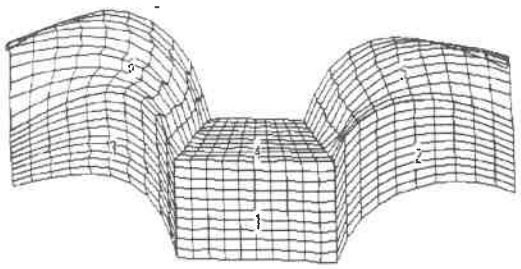

Figure3. NURBS surface approximation.

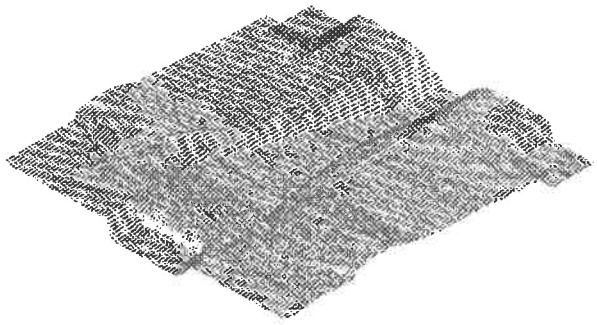

Figqure4. Diditized data of a complex die Geometry.

Surface Merging and Creation of Complex Model

In the segmentation of scanned data, cases may occur that gaps or overlaps exist between surfaces. Since our objective is to create an enclosed volume for a solid model, the boundary continuity has to be maintained. Therefore, boundary merging is needed after individual surfaces

are created. In this work, merging is applied to boundaries between two surfaces to obtain C^0 and C^1 continuity.

If surfaces $S1$ and $S2$ are adjacent to each other, to merge $S2$ to $S1$ the following operations can be carried out.

C^0: $(\overline{P}^w_{i,1})_{S2} = (\overline{P}^w_{i,1})_{S1} \quad (i = 1,\ldots,n)$ (5)

C^1: $(\overline{P}^w_{i,2})_{S2} = 2(\overline{P}^w_{i,1})_{S1} - (\overline{P}^w_{i,1-1})_{S1} \quad (i = 1,\ldots,n)$ (6)

Figure 4 shows a set of digitized data for a die . Using the procedures proposed in this paper, a complex geometric model consisting of 32 NURBS surfaces was created (Figure 5). Note that the surface boundaries are automatically detected by the curvature analysis, and the surface parametric distribution are generally following the geometric pattern. Figure 6 shows the shaded image.

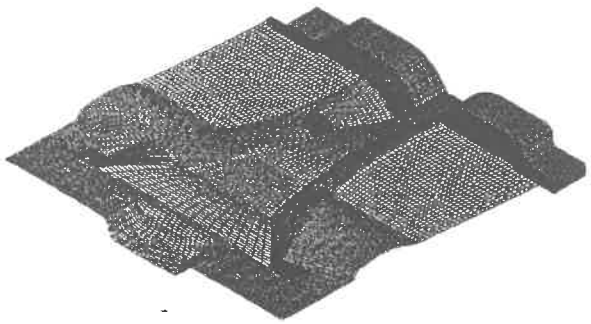

Figure5. Creation of complex surface model.

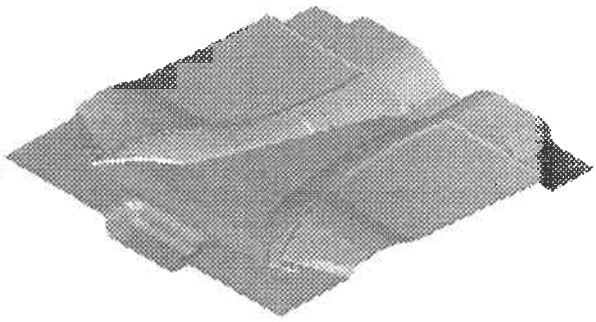

Figure6. Shaded image of the complex die surface.

References

[1] H.T. Yau, 1996, "Reverse Engineering of Engine Intake Ports by Digitization and Surface Approximation", Int. J. of Machine Tools and Manufacture, in press.

[2] C.D. Woodward, 1987, "Cross-Sectional Design of B-Spline Surfaces", Computers and Graphics, Vol. 11, No. 2.

MACHINE TOOL ACCURACY CHARACTERIZATION USING TELESCOPIC BALLBAR

A. Chukwujekwu Okafor and Yalcin M. Ertekin
Labaratory for Industrial Automation and Flexible Manufacturing
Department of Mechanical and Aerospace Engineering and Engineering Mechanics
University of Missouri-Rolla
Rolla, MO 65409-0050

ABSTRACT

The increasing global market competition has focused the attention of manufacturers on how to manufacture products at the least cost and in the shortest time with the highest precision to increase manufacturing efficiency, productivity, and improved quality [1]. Increasing demand for both higher machine tool accuracy and machining tolerances has resulted in a great need to measure and characterize the accuracy of NC machine tools and minimize machine tool induced errors on machined components before cutting parts, instead of inferring it from parts already machined. Statistical process control (SPC) provides no more than after-the-fact deduction of process capability.

This paper presents our on-going research on machine tool accuracy characterization and error compensation using telescopic magnetic ballbar. The results of the accuracy/repeatibility assessment of an old Bridgeport Series I CNC 2 1/2 axes vertical machining center are presented. The effects of speeds and feeds are also presented.

INTRODUCTION

Most of the accuracy characteristics of machine tools deteriorate as a function of running time due to wear of tool and machine components [2]. Accuracy also decreases after any job involving unusually high cutting forces, whenever the machine tool is moved, after any spindle crash into the workpiece and also due to environmental influence. Any machine tool which is out of alignment operates under less than optimum conditions, resulting in higher maintenance, part and labor costs, scrap and re-work rates. Out of alignment cutting tools will wear out faster under increased stresses and break down more often, thus both productivity and operational profits will be reduced [3].

There are three main sources of errors in machine tools that determine machine tool accuracy. 1) Errors due to geometric inaccuracies which are caused by the mechanical imperfections of the machine tool structure and the misalignment of machine tool elements. They all change gradually due to wear of the components. The effect of the geometrical inaccuracies is to produce errors in the squareness and parallelism between the machine's moving elements. 2) Thermally induced errors are generated by environmental temperature and local sources of heat from drive motors, gear trains and other transmission devices, thus causing expansion, contraction and deformation of the machine tool structure and resulting in positional errors between the cutting tool and workpiece. The machine tool elements particularly effected by self generated thermal distortion are spindles and leadscrews. 3) Load induced error which are produced by varying mechanical loads applied to the machine tools, therefore, causing elastic strain of the machine tool structure [4].

There are various methods for assessing and correcting undesired errors in the accuracy of machine tools. These procedures are categorized mainly in two sections where the machine tools are measured and to those where machined part is measured. The methods are given as: 1) Conventional geometric measurement of machine tools using mechanical devices such as step gages, squares, levels. 2) Monitoring of test pieces. 3) SPC monitoring of the machined workpieces. 4) Measuring the machine by modern test artifacts such as telescopic Double BallBar (DBB) or laser/optical calibration. Although laser calibration procedures may be time consuming , they are complete and absolute in their error mapping test procedures. This allows the overall volumetric envelope of the machine tool to be re-calibrated by adjusting/correcting software of CNC through error table in the memory. Complementary to such absolute techniques are artifact based assessment procedures ranging from telescopic/fixed length DBB s [5, 6] to circularity tests using a circular masterpiece [7].

EXPERIMENTAL PROCEDURES

A Renishaw serial BallBar was used for data collection with a nominal length of 150 mm (including extension bar). The BallBar system had a resolution of 0.1 μm and accuracy of ±1.0 μm (at 20 °C) and calibrated prior to data acquisition with a zerodur calibrator.

A schematic diagram of the experimental set-up for data collection using BallBar is given in Figure 1. For dynamic data capturing, the Bridgeport CNC milling machine was programmed to move in the xy plane using a 100 mm circular contouring radius in both Clockwise (CW) and Counter Clockwise (CCW) directions. Angular overshoot was 180 ° before and after data capture and 360 ° data capture arc was utilized. Three different feed rates of 127, 254, and 508 mm/min and three cutting speeds of 60, 100, and 130 RPM were used to study the effects of feed rate and cutting speed. Sampling rate of the dynamic data capture software was 7.81 samples/s except for the feedrate of 127 mm/min where 1.95 samples/s was used. For static data capturing the same set-up was used. The CNC milling machine was programmed to move into 8 target points in circular interpolation both CW (G2) and CCW (G3) directions and dwelled for static data capturing in the xy plane using 100 mm radius. Feedrates were the same as for dynamic data capture but only 60 RPM was utilized. Target points are given in Figure 2.

Renishaw calibration software system was used to generate circular plots and calculate error diagnostics as well as statistical repeatibility.

RESULTS AND DISCUSSION

Samples of captured dynamic circularity error plots using ISO 230-1 are shown in Figure 3 for two different feedrates of 254 and 508 mm/min and two spindle speeds of 60 and 130 RPM. ISO 230-1 circularity error value is the difference between maximum outward deviation and maximum inward deviation from the best circle through the captured data. Using different cutting speeds of 60, 100, and 130 RPM and feedrates of 254 mm/min and 508 mm/min, the resulting circularity error plots shown in Figure 4a indicates that the error is not very sensitive to spindle speed changes in both CW and CCW directions. Also this graph indicates that circularity error increases when feedrate is increased from 254 to 508 mm/min in CW direction whereas in CCW direction, there is no significant change in circularity error. Figure 4b shows similar result when circularity error is plotted as a function of feed at fixed cutting speed (60 RPM).

In another attempt to investigate feedrate effects on the circularity error of the CNC milling machine, the machine was programmed to run four runs (2 CW, 2 CCW @ 60 RPM) at feedrates of 254 and 508 mm/min and bi-directional circularity error data were captured. The circular diagnostic plots are given in Figure 5. For a feedrate of 254 mm/min, negative backlash error in the Y axis direction is the highest error with a magnitude of -19.1μm (+Y axis), -18.2 μm (-Y axis) which constitutes 13% of the independent circularity errors. Reversal spikes and backlash errors in the X axis are second and third highest ranked errors. A Renishaw Ballbar diagnostic printouts for feedrates of 254 and 508 mm/min are given in Figure 6a and 6b respectively.

Servo mismatch is the biggest error component at the higher feedrate of 508 mm/min and followed by negative backlash errors in Y and X axes respectively (Figure 6b). High negative backlash errors are probably caused by play in the guideways of the machine causing a dwell in motion when the direction in which the machine is being driven changes. Another possible cause may be that the CNC milling machine is affected by encoder hysteresis. Servo mismatch value is the time in milliseconds by which one of the machines axis servos leads other. From the plots in Figure 5 servo mismatch is clearly seen where the plots have an oval shape along the 45° (CW) and 135° (CCW). The magnitudes of servo mismatch errors are -3.75 ms and -3.60 ms for feedrates of 254 and 508 mm/min respectively. Negative sign indicates that X axis leads Y axis in XY plane. Servo mismatch error can be corrected by balancing the loop gains of the axes servos by adjusting the machine controller. In this case X axis gain should be lowered.

Bi-directional statistical repeatibility of the Bridgeport CNC milling machine is calculated according to ISO 230-2 by the diagnostic software. Using 8 target positions, static data were captured at different feedrates (127, 254, and 508 mm/min @60 RPM) with runs of 5 (3 CCW, 2CW), 8 (4CCW, 4CW), and 8 (4CCW, 4CW) respectively. Statistical and maximum repeatibility values are plotted in Figure 7. The figure shows that repeatibility values are higher at a feedrate of 254 mm/min and lower at 127 and 508 mm/min. All values are lower than factory specification of ±0.0076 mm. Circular plots of captured static data are given in Figure 8, which also indicates larger errors for the feedrate of 254 mm/min.

Captured static data was also used to calculate squareness and scale mismatch errors which are plotted in Figure 9a and 9b respectively. Squareness error is the angle between x and y axes in the xy plane. A negative squareness error indicates that the angle between the two axes is less than 90°. The plot shows that squareness error is highest at a feedrate of 254 mm/min. The squareness error may be caused by worn machine guideways causing a certain amount of play in the axes or may be the axes are bent locally or there may be an overall axis misalignment in the machine. Figure of merit is the scale mismatch error normalized to units of μm/m to give a scale mismatch error which is independent of the ballbar's length. It indicates that one of the machine's axes is either over traveling or under traveling. The graph given in Figure 9b shows that the higher the feedrate the better the scale mismatch error (figure of merit).

CONCLUSIONS AND FUTURE WORK

The results obtained from the experiments conducted with ballbar show that circular contouring errors are highly dependent on the feedrate used and not so sensitive to spindle speeds used in this research. Generally a medium feedrate of 254 mm/min consistently gave higher errors. This shows the importance of machine tool characterization in a real manufacturing environment, where one can identify less favorable cutting conditions of the machine tool and avoid using them during production. The Bridgeport CNC milling machine was diagnosed with large backlash and servomismatch errors indicating that the machine is over due for maintenance. In the future same tests will be conducted after proper maintenance.

REFERENCES:

1. Sydenham, P. H., Thorn, R., " Handbook of Measurement Science", John Wiley & Sons, 1992.
2. Torvinen, S., Andersson, P. H., Vihinen, J., Holsa, J., "An Off-line Condition Monitoring System for Machine Tools", Proceedings of LANDAMAP 95, Southhampton, UK, July 1995, pp. 237-250.
3. Hamar, M., Moreyn, C., "Flat, Straight, Square, Parallel", Cutting Tool Engineering, Oct. 1993, pp. 62-69.
4. Ford, D. G., Proceedings of LANDAMAP 95, Southhampton, UK, July 1995, pp. 277-286.
5. Kakino, Y., Ihara Y., Nakatsu, Y. J., Okamura, K., "Measurement of Motion Errors of NC Machine Tools & Diagnosis of Their Origins by Using Telescopic Magnetic BallBar Method", Annals of CIRP, Vol. 36, 1, 1987.
6 Knapp, W., "Test of the 3-D Uncertainty of Machine Tools & Measuring Machines and its Relation to Machined Errors", Annals of CIRP, Vol. 32, 1983, pp. 459-464.
7 Bryan, J. B., "A simple Method for Testing Measuring Machines & Machine Tools", Precision Engineering, 1982, Part1 (Vol. 4, pp. 61-69), part 2 (Vol 4, pp125-138)
8. Renishaw calibration software manual.

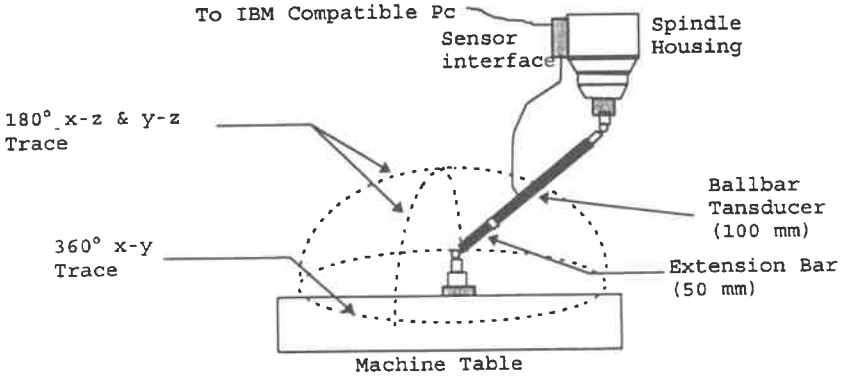

Figure1. Experimental set-up.

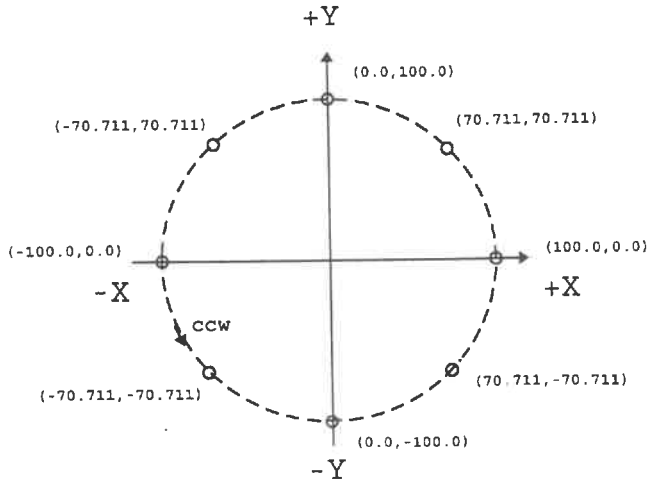

Figure 2. Static data capture target locations.

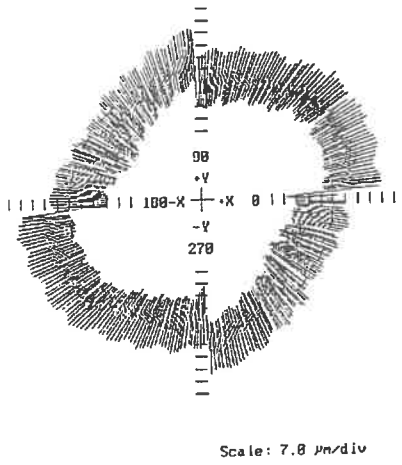

a) F=254 mm/min , 60RPM, CW

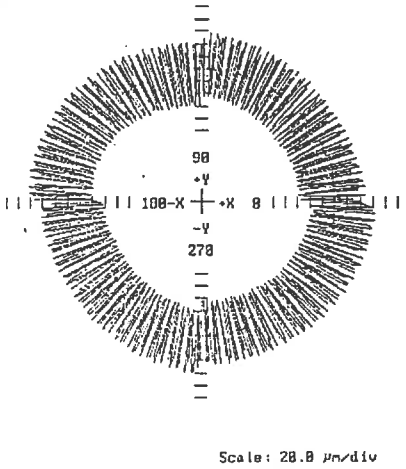

b) F=254 mm/min, 130RPM, CCW

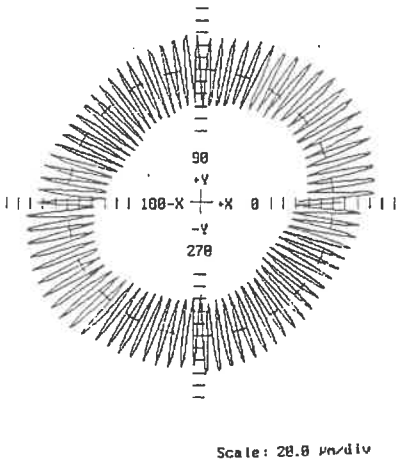

c) F=508 mm/min, 60 RPM, CW

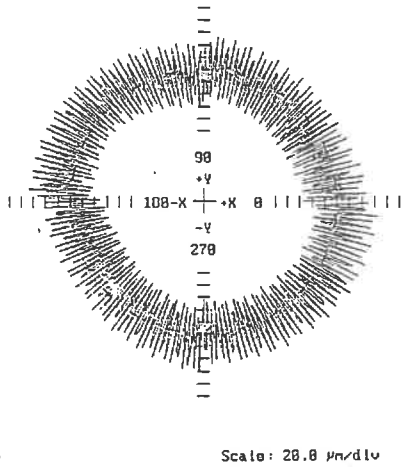

d) F=508 mm/min, 130 RPM, CCW

Figure 3. Dynamic Circularity error plots.

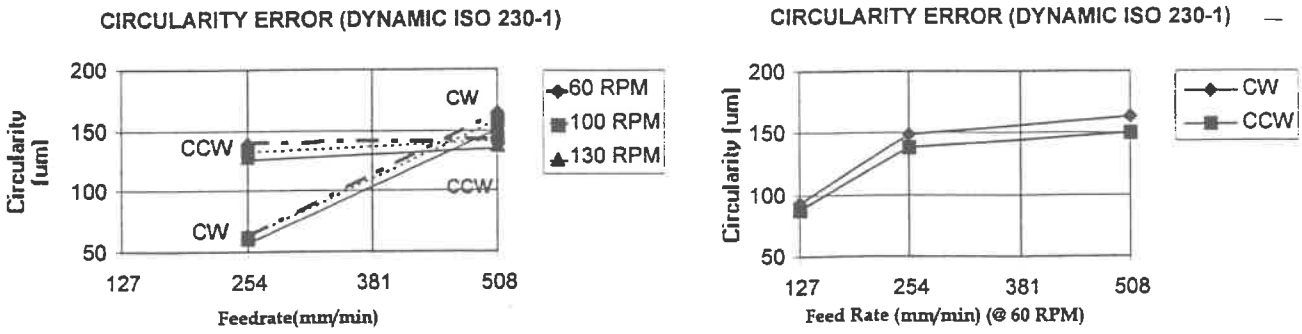

Figure 4. Circularity error.

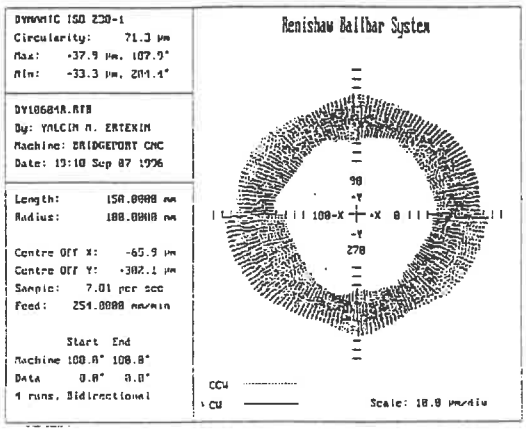

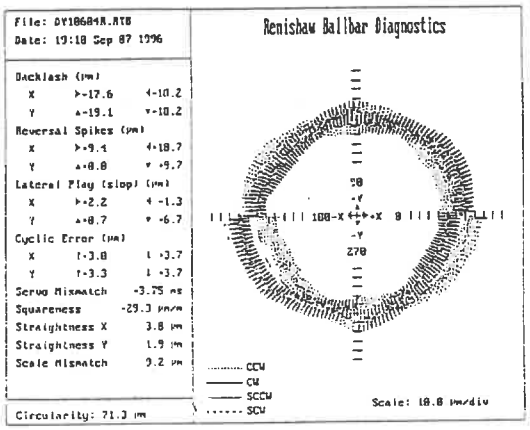

a) F=254 mm/min, 60 RPM, 4 runs (2CW, 2CCW)

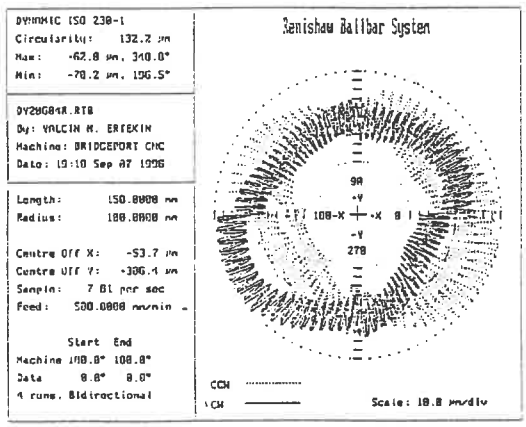

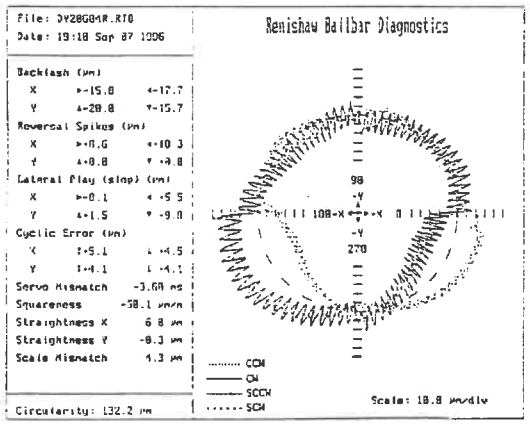

b) F=508 mm/min, 60 RPM, 4 runs (2CW, 2CCW)

Figure 5. Circular diagnostic plots.

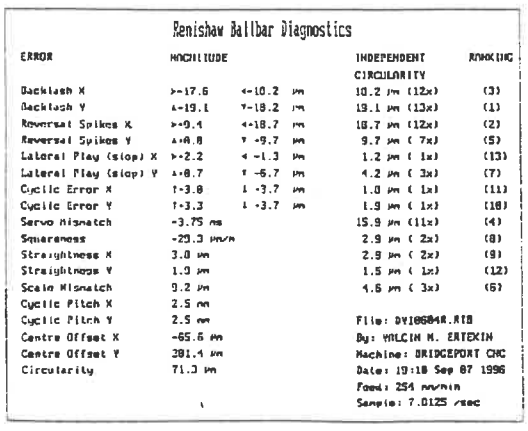

Renishaw Ballbar Diagnostics

ERROR	MAGNITUDE		INDEPENDENT CIRCULARITY	RANKING
Backlash X	+17.6	+10.2 µm	10.2 µm (12x)	(3)
Backlash Y	+19.1	+18.2 µm	19.1 µm (13x)	(1)
Reversal Spikes X	+9.4	+18.7 µm	18.7 µm (12x)	(2)
Reversal Spikes Y	+8.8	+9.7 µm	9.7 µm (7x)	(5)
Lateral Play (slop) X	+2.2	+1.3 µm	1.2 µm (1x)	(13)
Lateral Play (slop) Y	+8.7	+6.7 µm	4.2 µm (3x)	(7)
Cyclic Error X	+3.8	+3.7 µm	1.0 µm (1x)	(11)
Cyclic Error Y	+3.3	+3.7 µm	1.9 µm (1x)	(10)
Servo Mismatch	-3.75 ms		15.9 µm (11x)	(4)
Squareness	-29.3 µm/m		2.9 µm (2x)	(8)
Straightness X	3.8 µm		2.9 µm (2x)	(9)
Straightness Y	1.9 µm		1.5 µm (1x)	(12)
Scale Mismatch	9.2 µm		4.6 µm (3x)	(6)
Cyclic Pitch X	2.5 mm			
Cyclic Pitch Y	2.5 mm		File: DY10684R.RTB	
Centre Offset X	-65.6 µm		By: YALCIN M. ERTEKIN	
Centre Offset Y	301.4 µm		Machine: BRIDGEPORT CNC	
Circularity	71.3 µm		Date: 19:10 Sep 07 1996	
			Feed: 254 mm/min	
			Sample: 7.0125 /sec	

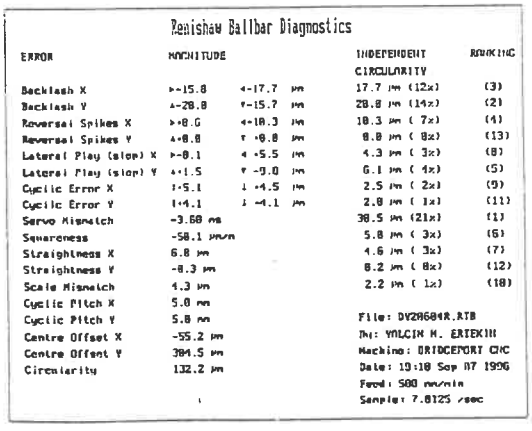

Renishaw Ballbar Diagnostics

ERROR	MAGNITUDE		INDEPENDENT CIRCULARITY	RANKING
Backlash X	+15.8	+17.7 µm	17.7 µm (12x)	(3)
Backlash Y	+28.8	+15.7 µm	28.8 µm (14x)	(2)
Reversal Spikes X	+8.6	+18.3 µm	18.3 µm (7x)	(4)
Reversal Spikes Y	+8.8	+8.8 µm	8.8 µm (8x)	(13)
Lateral Play (slop) X	+8.1	+5.5 µm	4.3 µm (3x)	(8)
Lateral Play (slop) Y	+1.5	+9.0 µm	6.1 µm (4x)	(5)
Cyclic Error X	+5.1	+4.5 µm	2.5 µm (2x)	(9)
Cyclic Error Y	+4.1	+4.1 µm	2.8 µm (1x)	(11)
Servo Mismatch	-3.68 ms		30.5 µm (21x)	(1)
Squareness	-58.1 µm/m		5.8 µm (3x)	(6)
Straightness X	6.8 µm		4.6 µm (3x)	(7)
Straightness Y	-8.3 µm		8.2 µm (8x)	(12)
Scale Mismatch	4.3 µm		2.2 µm (1x)	(10)
Cyclic Pitch X	5.0 mm			
Cyclic Pitch Y	5.8 mm		File: DY20604R.RTB	
Centre Offset X	-55.2 µm		By: YALCIN M. ERTEKIN	
Centre Offset Y	304.5 µm		Machine: BRIDGEPORT CNC	
Circularity	132.2 µm		Date: 19:10 Sep 07 1996	
			Feed: 500 mm/min	
			Sample: 7.8125 /sec	

a) F=254 mm/min, 60 RPM, 4 runs (2CW, 2CCW)

b) F=508 mm/min, 60 RPM, 4 runs(2CW, 2CCW)

Figure 6. Renishaw ballbar diagnostic printout.

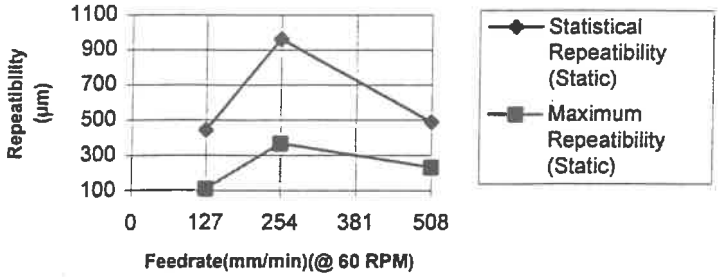

Figure 7. Statistical and maximum repeatibility.

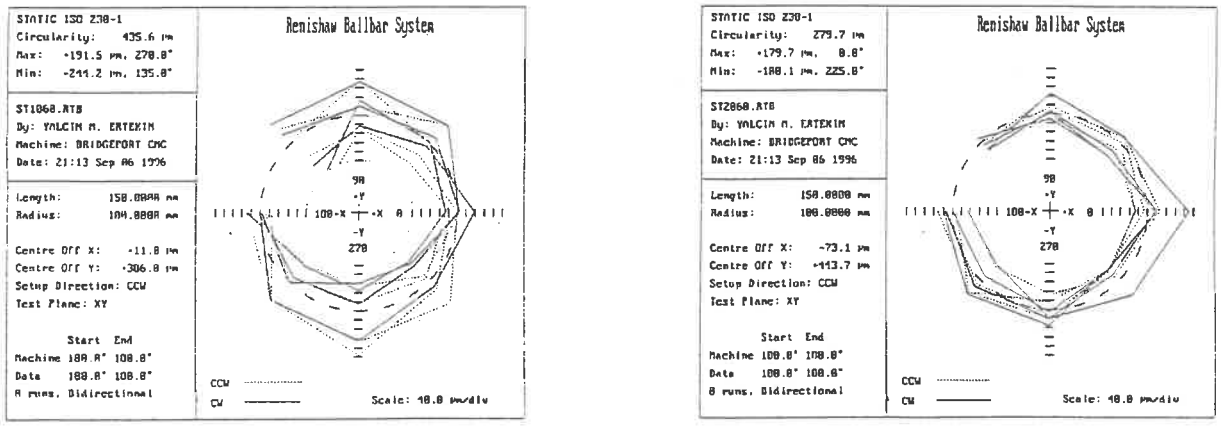

a) F=254 mm/min, 60 RPM, 8 runs (4 CW, 4 CCW)

b) F=508 mm/min, 60 RPM, 8 runs (4 CW, 4 CCW)

Figure 8. Static captured circular plots.

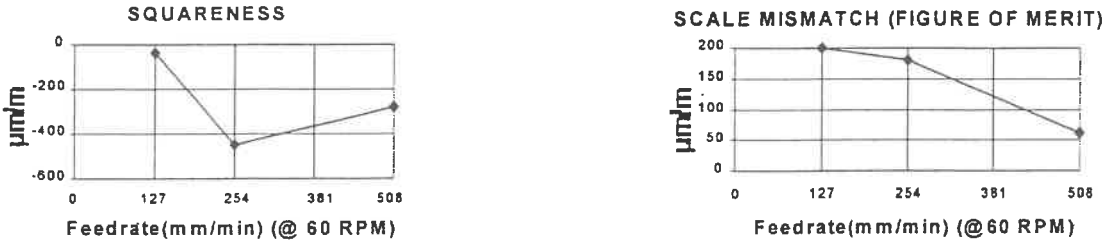

(a)

(b)

Figure 9. Squareness and scale mismatch errors.

A NEW TECHNIQUE FOR VOLUMETRIC ERROR ASSESSMENT OF CNC MACHINE TOOLS INCORPORATING THE BALL-BAR MEASUREMENT AND THE 3D VOLUMETRIC ERROR MODEL

Heui Jae Pahk , Young Sam Kim, Joon Hee Moon
Dept. of Mechanical Design and Production Eng.
Seoul National University
Seoul, Korea

ABSTRACT

This paper presents an useful technique for assessing the volumetric errors in multiaxis machine tools using the kinematic double ball bar. This system has been developed based on the volumetric error model which describes the 3 dimensional errors of machine tools. The developed system inputs the measured radial data performed on the 3 orthogonal planes, analyzing the parametric errors such as positional, straightness, angular, squareness, and backlash errors. The developed system also can assess dynamic performance of machine tools such as errors due to the servo gain mismatch. The developed system has been tested in a practical machine tool, and showed high potential for error assessment of multi-axis machine tools.

1. INTRODUCTION

Development of efficient techniques for performance verification of machine tools has been considered as a important task for accuracy enhauncement and quality assurance for users and manufacturers of machine tools and coordinate measuring machines.

In order to assess the performance checking of machine tools, the double ball bar or kinematic ball bar has been frequently used. There are several previous research[1,2,5,3,4] on the kinematic ball bar measurement for checking accuracy of machine tools. This paper presents a new technique for analyzing the 3 dimensional parametric errors of CNC machine tools in the volumetric sense using the ball bar measurement.

2. ERROR MEASUREMENT USING THE KINEMATIC BALL BAR

Fig.1 shows a typical setup of a commercially available ball bar, where one ball is fixed on the table of machine tool and the other ball is attached to the spindle of the machine tool.

In the Fig.1, let O(0,0,0) be the centre point of the ball on the table, and P(X,Y,Z) be nominal coordinates of the ball centre attached to the spindle. When the machine is commanded to move to P(X,Y,Z) position, the actual position of the machine is assumed P'(X',Y',Z'). Thus the machine geometric error can be defined as the difference between the two coordinates. That is,

$$\Delta X = X' - X, \quad \Delta Y = Y' - Y, \quad \Delta Z = Z' - Z \tag{1}$$

where $\Delta X, \Delta Y, \Delta Z$ are the X, Y, Z error components at the nominal position P(X,Y,Z) position with respect to the O(0,0,0) point. When the error components $\Delta X, \Delta Y, \Delta Z$ are present, the error in the distance between the two points, ΔR, can be evaluated as,

$$(R+\Delta R)^2 = X'^2+Y'^2+Z'^2 = (X+\Delta X)^2+(Y+\Delta Y)^2+(Z+\Delta Z)^2 \tag{2}$$

where R is the nominal distance between the two points.

When ignoring the second order terms of error components, and remembering $R^2 = X^2 + Y^2 + Z^2$

$$\Delta R = (X\Delta X + Y\Delta Y + Z\Delta Z) / R \tag{3}$$

Eq(3) gives the error in the length direction of the ball bar when the error components (ΔX, ΔY, ΔZ) are present during the machine movement from O to P, and it can be used for the error diagnosis of the machine tools.

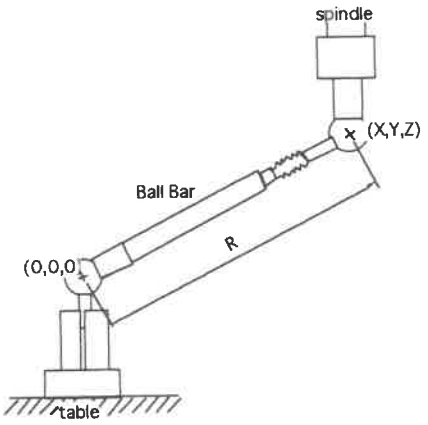

Fig.1 ERROR MEASUREMENT USING KINEMATIC BALL BAR

3. PARAMETRIC ERROR MODELING FOR MACHINE TOOLS

It is widely acknowledged that there are 6 geometric error components when a machine element moves along the guideway, and they are 3 translational

errors(positional error, horizontal/vertical straightness error) and 3 rotational errors (pitch, yaw, and roll errors). When multiaxis movement is considered, each axis has the above 6 geometric error components, and 3 squareness errors between X-Y axis, Y-Z axis, and Z-X axis. There are also dynamic errors due to servo gain mismatch between X-Y axis, Y-Z axis, and Z-X axis. In this paper, a polynomial based error modeling has been performed for the above geometric/parametric error components of machine tools, prior to the error analysis.

3.1 POSITIONAL ERROR COMPONENTS

Positional error components, $\delta x(X)$, $\delta y(Y)$, $\delta z(Z)$ along X,Y,Z axis, which are mainly due to scale errors, lead screw pitch errors, are usually defined as the difference between the actual coordinates and the nominal coordinates along the X,Y,Z axis. Thus it is possible to model the positional error as a polynomial function of position along each axis. Therefore the X positional error components are,

$$\delta x(X)=dxx_1*(X/R)+dxx_2*(X/R)^2+\ldots = \sum_{i=1}^{N} dxx_i*(X/R)^i \quad (4)$$

where X/R is the dimensionless coordinates of position along X axis, and dxx_i is the coefficients of the polynomial. The Y, Z positional errors can be similarly modeled.

3.2 STRAIGHTNESS ERROR COMPONENTS

Straightness error is mainly due to non-straightness of guideway and due to the bearing interfaces in machine tools. As the straightness error is defined as the perpendicular deviation along each axis, it can be modeled as the polynomial functions beginning with second order terms, while the first order polynomial function is considered for modeling the squareness error between the neighboring axis. That is,

$$\delta y(X)= dyx_2*(X/R)^2+dyx_3*(X/R)^3+\ldots = \sum_{i=2}^{N} dyx_i*(X/R)^i \quad (5)$$

$$\delta z(X)=dzx_2*(X/R)^2+dzx_3*(X/R)^3+\ldots = \sum_{i=2}^{N} dzx_i*(X/R)^i \quad (6)$$

where dyx_i, dzx_i are the coefficients of the polynomial function to be determined.The rest of straightness error components along Y, Z axis can be similarly modeled.

3.3 ANGULAR ERROR COMPONENTS

PITCH AND YAW ERROR

Pitch and yaw errors are the angular error components in the perpendicular direction along each axis, and they are influenced by the guideway geometry and bearing interfaces of machine tools, thus can be related to the straightness profile along each axis. For example, pitch error, Ex(Y), along Y axis can be derived as the derivative of the vertical straightness error along the y axis. That is,

$$Ex(Y)=\partial(\delta z(Y))/\partial y=\sum_{i=2}^{N} i*dzy_i*(Y/R)^{i-1}/R \quad (7)$$

Yaw error component, Ez(Y), along Y axis can be derived as the derivative of the horizontal straightness error along the Y axis, that is,

$$Ez(Y)= -\partial(\delta x(Y))/\partial y = -\sum_{i=2}^{N} i*dxy_i*(Y/R)^{i-1}/R \quad (8)$$

where the minus sign is considered for the sign convention of the angular error components. Similarly, the rest of pitch and yaw errors are modeled as the derivatives of the respective straightness error profiles.

3.4 BACKLASH ERROR COMPONENTS

Backlash error, or reversal error, is mainly caused by the backlash in the screw/gear assembly during the motion reversal.

When the amount of backlash in the X axis is Bx, the error in the X axis due to the backlash, ΔX, can be modeled as follows.

$$\Delta X = -Bx/2 * sign(dX/dt) \quad (9)$$

where sign( ) is sign function returning the sign of the term inside the bracket, and dX/dt is the time derivative of position, which is velocity. The minus sign in eq(9) is to give the positive backlash when the motion is changed from the forward direction to the reverse direction.

Similarly, the backlash errors in the Y, Z axis can be modeled.

3.5 SQUARENESS ERROR

Squareness error is defined as the out of squareness between the two nominally orthogonal axis, and it is mainly due to the misalignment, or misassembly in the orthogonal axes.

Let a be the amount of nonsquareness of X axis from the nominal X axis (in XY plane) at the the position of distance R from the origin point. Then the Y_ positional error at X position, ΔY, due to the nonsquareness of X axis is as follows,

$$\Delta Y = -\alpha * X/R \quad (10)$$

Similarly, the rest of squareness error components can be modeled.

3.6 ERRORS DUE TO SERVO GAIN MISMATCH

When the amplifier gains of the servo drives for the axis motion are not properly matched, there exists a kind of steady state following errors. The steady state

following error, ΔR, between the actual position and the command position in the radial direction can be derived from the control theory (e.g.[7])

$$\Delta R = Mxy\ (X/R)\ (Y/R) \quad \text{for CCW rotation}$$
$$= -Mxy\ (X/R)\ (Y/R) \text{ for CW rotation} \qquad (11)$$

where Mxy is the coefficient for the gain mismatch between X-Y axis. Eq(8) represents the circular error which is influenced by the gain mismatch. Similarly, the circular errors due to the gain mismatch between the Y-Z axis and Z-X axis can be modeled.

4. VOLUMETRIC ERROR MODEL AND THE BALL BAR MEASUREMENT OF MACHINE TOOLS

4.1 VOLUMETRIC ERROR EQUATIONS

Three dimensional error behavior, that is, volumetric error consideration is vital for error assessment of machine tools in 3D working space. In this paper, the influence of volumetric error model on the ball bar measurement has been assessed, and appropriate error diagnosis has also been performed for a practical machine tool.

Volumetric error equations generally can be derived by the kinematic chain of each machine element when the parametric error components are calibrated (e.g.[6]), and they are dependent on the kinematic configuration of machine tools.

For the column type milling machine, the volumetric error equations[6] are,

$$\begin{aligned}\Delta X=&\delta x(X)-\delta x(Y)+\delta x(Z)\\ &+Z[-Ey(Y)-b1-Ey(X)]+Y[Ez(Y)+Ez(X)]\\ &+Yp[Ez(X)+Ez(Y)-Ez(Z)]\\ &+Zp[-Ey(X)-Ey(Y)+Ey(Z)]\end{aligned}$$

$$\begin{aligned}\Delta Y=&-\delta y(X)+\delta y(Y)+\delta y(Z)\\ &+X[-Ez(X)+a]+Z[Ex(X)+Ex(Y)-b2]\\ &+Xp[-Ez(X)-Ez(Y)+Ez(Z)]\\ &+Zp[Ex(X)+Ex(Y)-Ex(Z)]\end{aligned}$$

$$\begin{aligned}\Delta Z=&-\delta z(X)-\delta z(Y)+\delta z(Z)+XEy(X)\\ &+Y[-Ex(X)-Ex(Y)]\\ &+Xp[Ey(X)+Ey(Y)-Ey(Z)]\\ &+Yp[-Ex(X)-Ex(Y)+Ex(Z)]\end{aligned} \qquad (12)$$

4.2 INTEGRATION OF THE VOLUMETRIC ERROR EQUATIONS AND THE BALL BAR MEASUREMENT

The influence of the volumetric error behaviour of machine tools on the circular error pattern of the ball bar measurement can be considered when eq(12) are applied to the circular error equation (eq.1). Thus when the volumetric error behaviour is involved for the the column type milling machine, the circular error of ball bar measurement is,

$$\begin{aligned}\Delta R=&(X*\Delta X + Y*\Delta Y + Z*\Delta Z)/R\\ =&\Delta X*(X/R) + \Delta Y*(Y/R) + \Delta Z*(Z/R)\\ =&\ dxx_1*(X/R)^2 + dyy_1*(Y/R)^2\\ &+ dzz_1*(Z/R)^2 - 3dxy_1*(X/R)*(Y/R)^2\\ &+dxz_2*(X/R)*(Z/R)^2 -dyx_2*(Y/R)*(X/R)^2\\ &+dyz_2*(Y/R)*(Z/R)^2+dzx_2*(Z/R)*(X/R)^2\\ &+dzy_2*(Z/R)*(Y/R)^2\\ &-dxb/2*(X/R)*sign(dX/dt)\\ &- dyb/2*(Y/R)*sign(dY/dt)\\ &- dzb/2*(Z/R)*sign(dZ/dt)\\ &- \beta_1*(Z/R)*(X/R) + \alpha*(X/R)*(Y/R)\\ &- \beta_2*(Y/R)*(Z/R)+Mxy*(X/R)*(Y/R)*Dir\\ &+Myz*(Y/R)*(Z/R)*Dir\\ &+ Mzx*(Z/R)*(X/R)*Dir\end{aligned} \qquad (13)$$

where the first terms of polynomial functions are considered for each parametric error components for the efficiency of calculation, and Dir is a function returning plus(Clockwise) or minus(Counterclockwise) depending on the rotation of kinematic ball bar. For the volumetric error equations, the roll error components and the effect of tool offsets are not considered here for simplicity of modeling.

4.3 LEAST SQUARES TECHNIQUE FOR THE ERROR DIAGNOSIS

When the ball bar measurement data, ΔR, are provided, there are several error components involved as in eqs(13). In order to analyse the error components from the ball bar measurement data, the least squares technique has been effectively applied in this paper.

When ΔRm is the circular error to be modeled, eqs(13) can be expressed as the linear combination of polynomial functions.

$$\Delta Rm = \Sigma\ A_i*F_i \qquad (14)$$

where F_i is the ith polynomial function, and A_i is the coefficient of the ith polynomial function.

Let E as the sum of squares of deviation between ΔR and ΔRm, then

$$E = \Sigma\ (\Delta R - \Delta Rm)^2 \qquad (15)$$

Applying the variational principle to eq(15) for minimizing E,

$$\partial E/\partial A_i = 2\ \Sigma\ (\Delta Rm - \Delta R)\ \partial(\Delta Rm)/\partial A_i = 0 \qquad (16)$$

From eq(14), $\partial(\Delta Rm)/\partial A_i = F_i$, thus eq(16) becomes

$$\Sigma\ \Delta Rm\ F_i = \Sigma\ \Delta R\ F_i \qquad (17)$$

If we set $f=[F_1, F_2.., F_n]^T$, $a=[A_1, A_2.., A_n]^T$, then eq(17) becomes

$$(f\ f^T)\ a = (\Delta R\ f) \qquad (18)$$

Eq(18) is a typical linear equation for unknown matrix, and therefore it can be solved by applying numerical methods such as Gauss elimination method, etc.

5.PRACTICAL APPLICATION

The developed error analysis technique has been practically applied to a column type machining center , which was installed on the shop floor in the Seoul National University.

A commercially available kinematic ball bar of 150mm nominal length has been used for the circular error measurement, and Fig.2 shows a typical setup for the ball bar measurement. The ball bar has been precalibrated with respect to a calibration fixture made of Zerodour, prior to performing measurement. After the measurement path has been planned, the appropriate CNC code has been generated for the circular contouring, then it has been downloaded on the CNC machine tool. The measured data are then analysed and the error diagnosis has been performed.

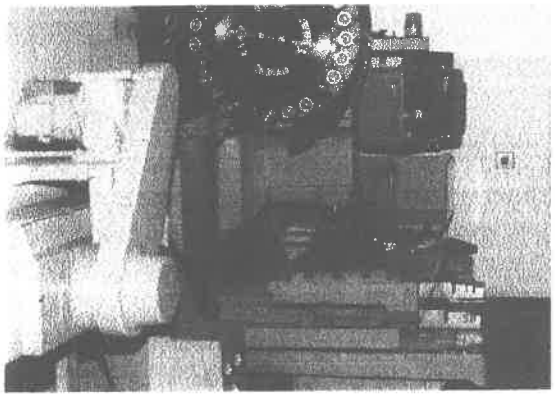

Fig.2 SETUP FOR THE BALL BAR MEASUREMENT

Fig.3 shows the raw data plot for the circular error measurement in XY,YX, and ZX planes, respectively, where the dotted line indicates the counter clockwise contour and the solid line does the clockwise contour. The raw data were analysed by the developed system and the error components were evaluated. The analysed error components were removed from the raw data of the circular measurement, and the residual circular errors were calculated then plotted. Fig.4 shows the residual circular errors after removing the error components, giving remarkably reduced error pattern.

Therefore the developed error analysis system was found as an efficient tool for the error diagnosis of machine tools based on the kinematic ball bar measurement.

6. CONCLUSION

(1) A computer aided analysis system has been developed for the parametric error components, based on the circular error measurement using the kinematic ball bar.

(2) In this paper, a new approach has been proposed and tested such that the 3D volumetric error model is effectively integrated for the ball bar measurement, thus the 3D volumetric errors has been efficiently assessed with the ball bar measurement data.

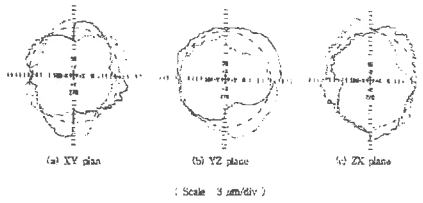

Fig.3 RAW DATA PLOT FOR THE BALL-BAR MEASUREMENT (COLUMN TYPE MACHINING CENTER)

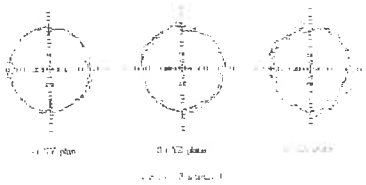

Fig.4 RESIDUAL ERROR PLOT AFTER ANALYSING ERROR COMPONENTS (COLUMN TYPE MACHINING CENTER)

REFERENCE

1.Bryan,J.,A simple method for testing measuring machines and machine tools, Precision Engineering, Vol.4(2), 1982

2. Knapp,W.,Test of three dimensional uncertainty of machine tools and measuring machines and its relation to machine errors, Annals of CIRP, Vol.32(1), 459-464, 1983

3.Kakino,Y., etal, The measurement of motion errors of NC machine tools and diagnosis of their origins by using telecoping magnetic ball bar method, Annals of CIRP, Vol36(1), 377-380, 1987

4.Burdekin,M., Park,J. A computer aided system for assessing the contouring accuracy of NC machine tools, Proceeding of the 28th MATADOR conference, Manchester, 1988

5.Kunzmann,H., etal. On testing coordinate measuring machines with kinematic reference standards, Annals of CIRP, Vol32(1), 465-468,1983

6.Pahk,H., Development of computer software for volumetric error map integrating the machine geometric error and the probe error in pursuit of a numerical virtual CMM, J. of KSME, Vol.20(3),945-959,1996 (in Korean)

7.Y.Koren, Computer Control of Manufacturing Systems, McGraw-Hill Co., 1983

8.Renishaw Ballbar Diagnostic Manual, Renishaw Co.1992

ACKNOWLEDGEMENT

The authors are grateful to the NSDM-ERC of Pusan National University for the partial funding to the research.

Analysis of Tool Trajectories (2D Tool Paths) in Machine Tools

Prof. Dr. F. Rehsteiner, S. Weikert
Institute of Machine Tools and Manufacturing (IWF)
Swiss Federal Institute of Technology (ETH)
Zürich, Switzerland

Abstract

At the Institute of Machine Tools and Manufacturing (IWF) methods have been developed to investigate the performance of machine tools particularly with regard to high feed rates by means of the newly introduced cross grid system distributed by Heidenhain.

The measuring grid is well suited for observing the relative motion of two bodies in planar motion within a circular range of 160 mm. It is based on the same measuring principle as the well-known glass scales, and thus it features the same high resolution and accuracy. In its application to machine tools the two components, i.e., the grid plate and the optical scanning head, are fixed to the tool holder (in case of milling machines: the spindle head) and to the workpiece table, respectively. This enables them to observe geometric and dynamic effects of machine tool performance on the tool path. In the present paper a number of such effects are analyzed.

Keywords:

Dynamic Measurements, Machine Tool Metrology, Measuring Grid, Axis Cross-Talk

Introduction

With the growing use of high speed cutting methods the importance of the dynamic performance of machine tools ist increasing steadily. While at low feed rates the tool path errors are caused prmarily by geometric inaccuracies of the machine tool due to inaccuracies in part geometry, assembly, and thermal effects, at high feed rates structural deformations due to high accelerations and path deviations due to inadequate control and feed drive performance become increasingly important.

This new situation calls for new, adequate methods for monituring the tool path in real time in order to allow a complete assessment of machine tool performance. In the past the most widely used method to do this was to machine suitable parts and use the results of measuring their geometry, dimension, and surface quality to interpret machine tool performance and to improve it. This method is not only time consuming but the results are also influenced by the machining process which tends to introduce additional errors. The method based on the cross grid system, however, does away with these problems and permits a much faster improvement cycle by making the results of modifications to the machine tool and to the controls observable in real time and unobstructed by secondary effects. Additionally, static features like the true straightness of „straight" paths, angle deviations of rectangular movements, or positioning errors, can also be investigated. The combined information about machine parameters, motion parameters (like, e.g., feed rate and acceleration) and their result in terms of position coordinates as a function of time allow quite a complete assessment of systems performance.

Measuring system

At the heart of the system there is the grid plate measuring 160 mm in diameter which carries two line grids orthogonal to each other, see Fig. 1. A scanning head which is also equipped with an orthogonal line grid simultaneously lights the grid and observes the reflected light. The intensity of the latter varies sinusoidally as the two grids move relative to each other.

The signal picked up is interpolated in 1024 intervals by the measuring circuit which, together with the grid constant of 8 µm, results in a resolution of about 5 nm. A personal computer (PC) is then used for storing and further processing the recorded data. Peak monitoring frequency in the system used at the IWF laboratories is 8 kHz allowing 200'000 points (x-y coordinates) to be picked up in a single measurement. In the standard version (ACCOM®-software) up to 8000 points can be stored and processed further by a number of suitable algorithms (ISO 230-4 standard)[1].

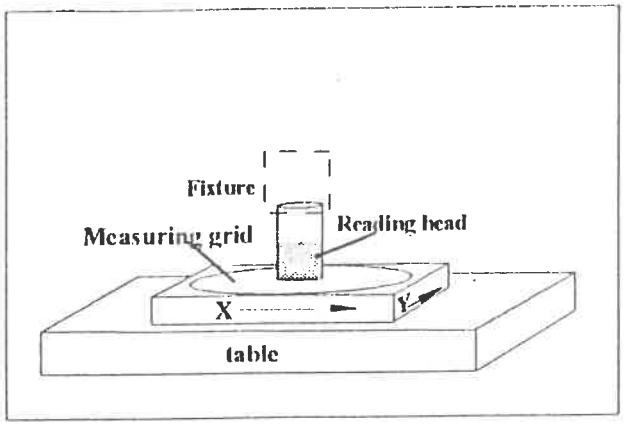

Fig.1: Components of Measuring System

To perform a measurement, first the measuring grid is placed on the machine table with grid lines arranged parallel to the guideways. Second, the scanning head is mounted to the tool fixture at a vertical distance of 0.5 mm from the grid. If the head is mounted in the tool spindle then care must be taken to clamp the latter such that the head can not change its orientation. The angle between the head and the grid is fine-tuned by observing the signal output, whereupon the actual measurements may begin. This whole procedure typically takes about 10 to 15 minutes.

Multiple Measuring Options

A variety of measurements can now be made with the system described above, see Fig. 2.

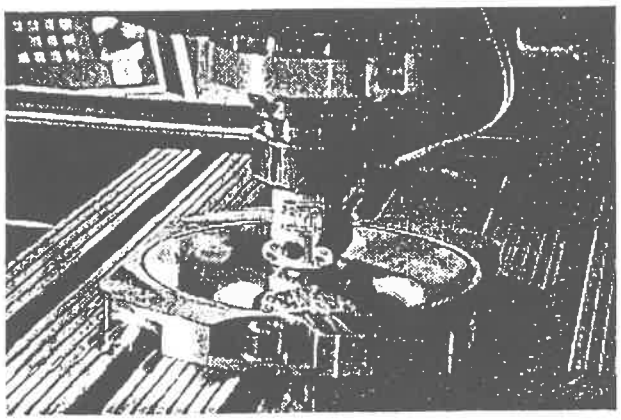
Fig. 2: The measuring system mounted to a machine tool (measuring grid on machine table, measuring head in tool fixture)

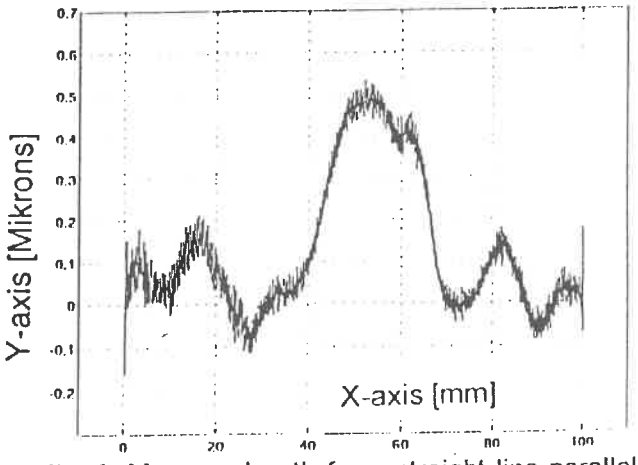

Fig. 3: Measured path for a straight line parallel to the X-axis at a feed rate of 4m/min.

Straightness

A very simple test path, i.e., a straight line parallel to one of the machine axes which is to be run at a given constant feed rate is shown in Fig. 3. The high resolution and fast read-out of the measuring system not only allow to monitor path deviations in the direction of feed as could be done also by laser interferometry, but also transverse ones. These are direct indications about the quality of the mechanical machine elements like the straightness of the feed spindle and of the guideways.

Cross-talk in reversing motion

Moving along a path in one direction and then reversing it will yield deviations in the axial as well as the lateral direction that are specific to this reversal. Results of such a test are shown in Fig. 4: Movement starts at point 1 in the positive direction; at point 2 it stops for 2 seconds. Then it goes on to position 3 and, without stopping, back to position 2 where there is again a stop of 1 second. Next, point 1 is again approached in the original (positive) direction and a stop of 1 second is put in. Finally it moves to point 1 via point 5 (no stop) and a new cycle starts. The lateral displacement between paths obtained by movement in opposite directions is clearly visible.

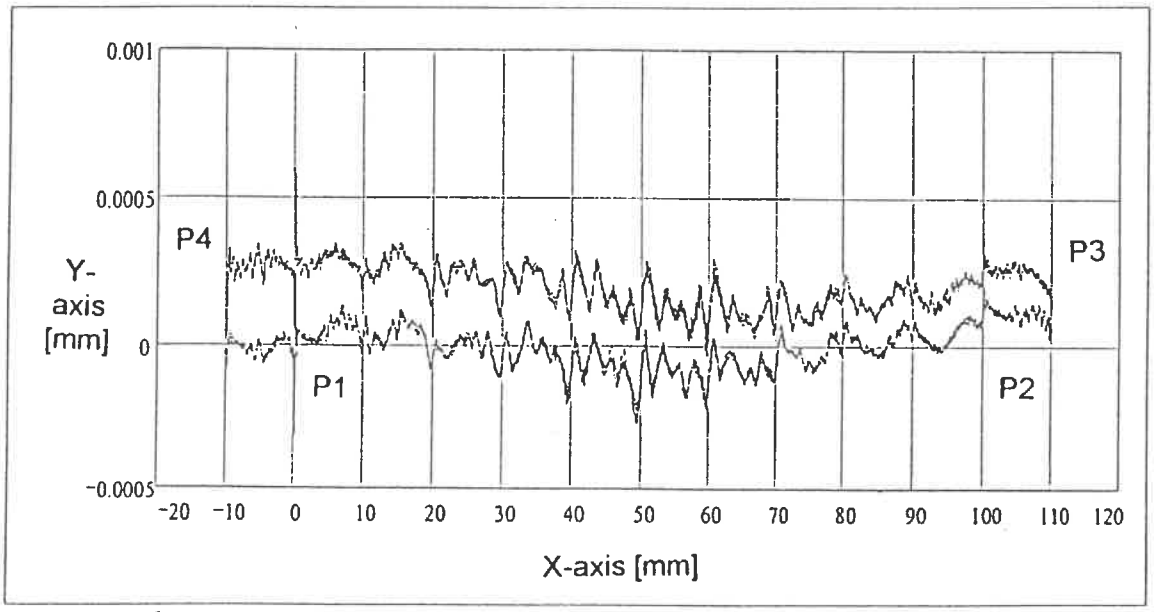

Fig. 4: Back-and-forth motion along a straight axis with short stops at various positions (v_f = 3000 mm/min)

In addition there is a strong lateral deviation occurring at the rate of spindle pitch which, here, is 10 mm. Contrary to *axial* deviations caused by spindle pitch errors which can be detected easily by laser interferometry and which do not show up in the machined surface this error enters surface quality full size.

Displacement due to thermal effects

If the scheme described in the previous section is continued during a prolonged time there is an additional displacement of the whole motion due to non-uniform heating of the structural elements. This is shown in Fig. 5 for the y direction. Displacement reaches a maximum after about one hour but gets reduced somewhat later on. However, the short term displacements remain practically identical during the whole experiment. By observing the displacement occurring even if no axis movement takes place one can observe also the thermal effect of temperatur variations in the surroundings of the machine.

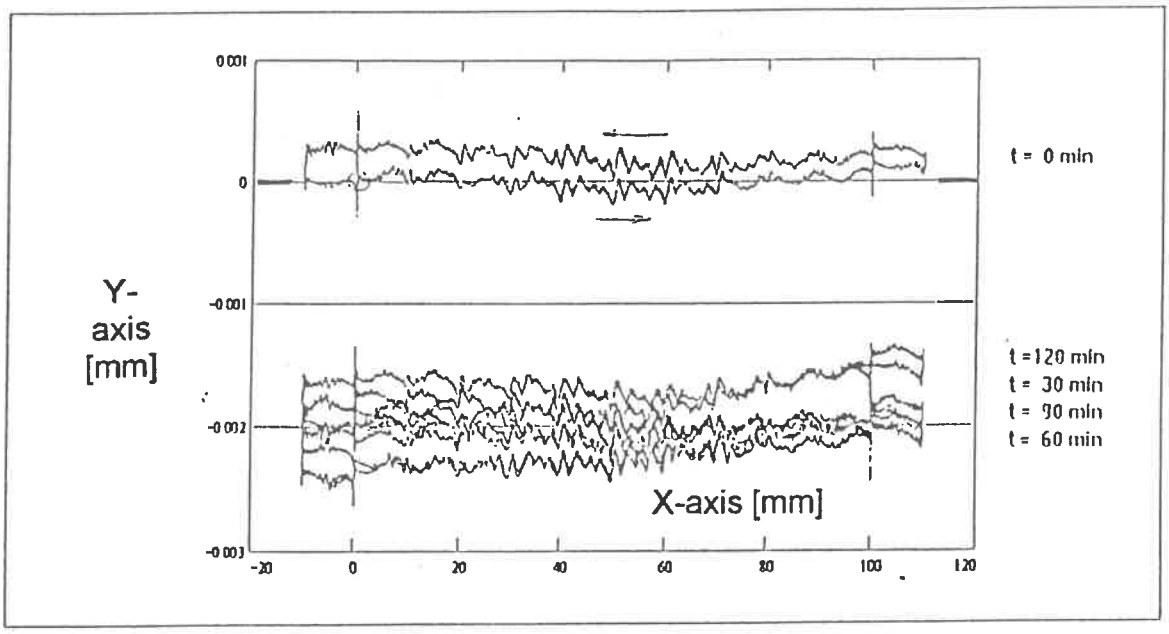

Fig.5: Back-and-forth motion along a straight axis with longer stops at various positions (v_f = 3000 mm/min) over two hours (shown graphs measured at the start, after 30, 60 90 and 120 minutes)

Another application referring directly to machine dynamics is „cornering" (moving along a path with a pointed, rectangular corner) where the amount of overrun at various parameter settings is of particular interest. This is shown in Fig. 6 for running around a sharp corner at a programmed speed of 6000 mm/min. Some overrun is clearly visible. The shape of the path can also be interpreted in terms of speed and acceleration and thus yields a lot of information about the quality of machine tool dynamics.

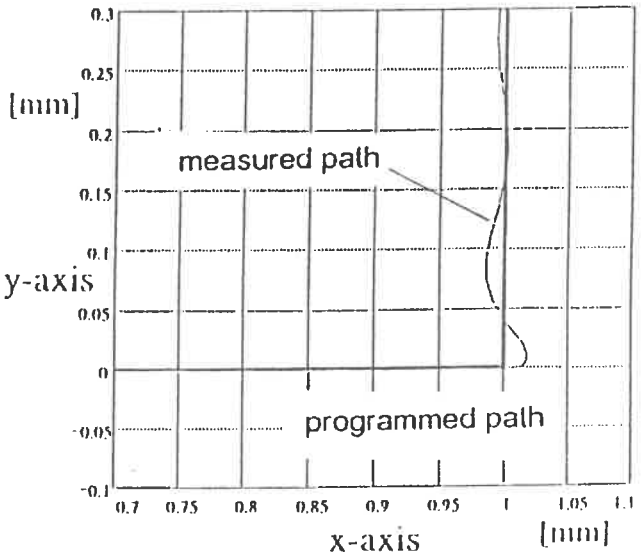

Fig. 6: Cornering an edge at v_f = 6000 mm/min.

Circular test

In the classical „circular test" (using a ball bar or tracing a master) a circular test piece of high quality is traced by a mechanical tracer and the deviation of the recorded path from a true circle is then used to interpret machine quality [2]. Tracer friction respectively inertia limit this method to fairly low speeds. In contrast the optical tracing method permits much higher tracing speeds; the system used here could be used up to a feed rate of v_f = 24 m/min with 5 nm resolution. Figs. 7 and 8 show results obtained on two different machines for identical motion inputs (circle with 10 mm diameter to be followed at v_f = 6 m/min). Fig. 7 was obtained on a highly dynamic machine: Good average accuracy but strong radial oscillations, whereas Fig 8 shows corresponding results for a less dynamic but „good-natured" machine. There is a substantial error all along the path but little oscillations.

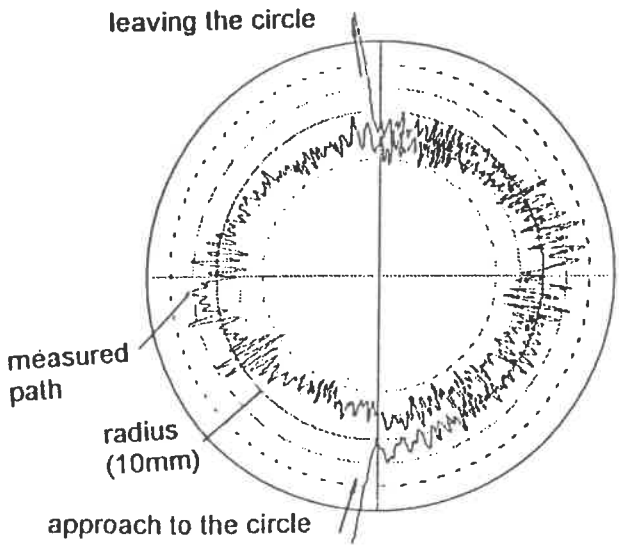

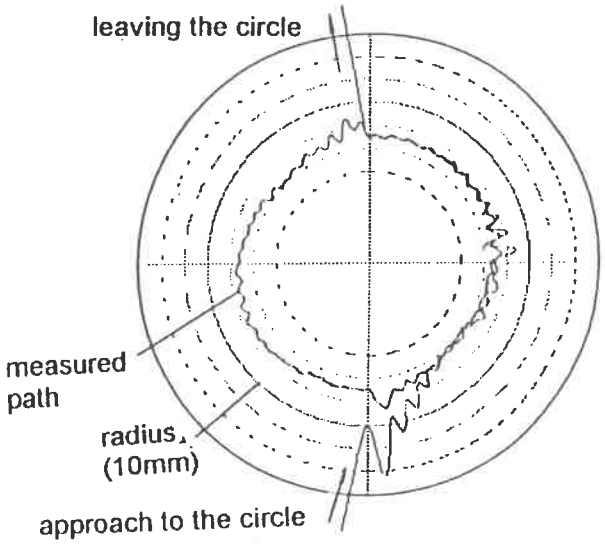

Figs 7, 8 Results of measurements performed at a feed rate of 6 m/min on two different machine tools. The theoretical path is a circle of 10 mm radius. Line separation is 10 µm.

Axis cross talk

By the displacement of machine parts relative to each other due to machine tool motion its mass distribution changes constantly. Thus, accelerations create different, configuration dependent displacements which may point in directions other than the feed direction (cross talk). These are, however, often poorly recognizable by the standard (linear) measuring systems on machine tools since they occur outside the measuring/control loop.

Fig. 9 shows the path that was observed on a large machining center the axis configuration of which is shown in Fig. 10 when a straight line parallel to one machine axis was to be run. Lateral displacements proportional to the acceleration in the feed direction can be seen clearly. The reason is the large distance between the point of feed force input at the feed spindle and the center of gravity of the moving column. As the lower curve shows the programmed peak acceleration of 2 m/sec^2 in the z direction was realized correctly.

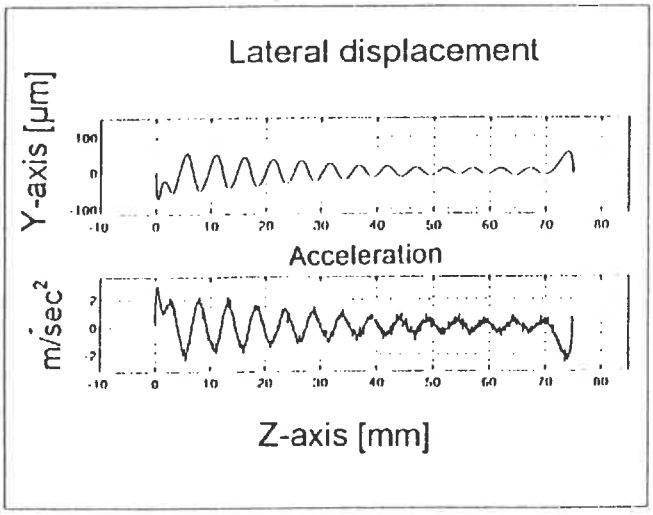

Fig.9: Acceleration and path-deviation along a straight line 100 mm long. Top: x-y plot of measured data, Bottom: acceleration over z-axis

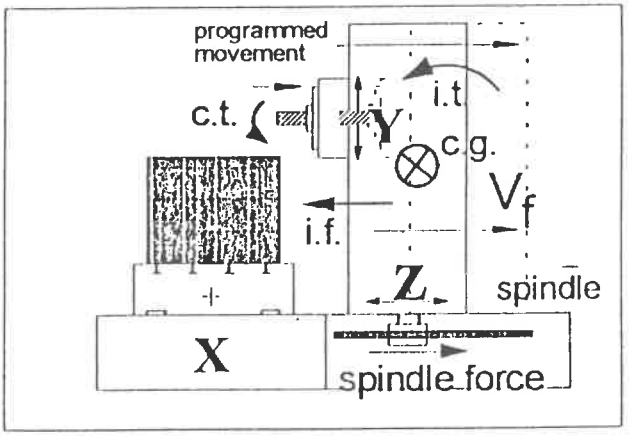

Fig.10: Axis configuration of a large machining center and programmed path for the measurements of Fig. 9 (c.g.=center of gravity; i.f.= inertia force; i.t.=inertia torque; c.t.= crosstalk motion of tool)

Comparison of results by the cross grid system and surface measurements

Consider a surface created by face milling. A comparison of the surface contour as measured by conventional methods (stylus tracing) and the one obtained from grid measurements by incorporating cutter geometry shows good agreement between the two. Such a comparison is shown in Fig. 11. Features with a long wave length agree well while those with a short wave length differ substantially. Apparently the reason for this is the poor roundness of the two flute cutter used in this test. Although the cutting conditions were quite conventional (cutter diameter 10 mm, feed 5 mm, cutting speed 720 m/min) their influence on the resulting part geometry was small. However, both measuring methods show well the influence of spindle pitch, see Fig. 11.

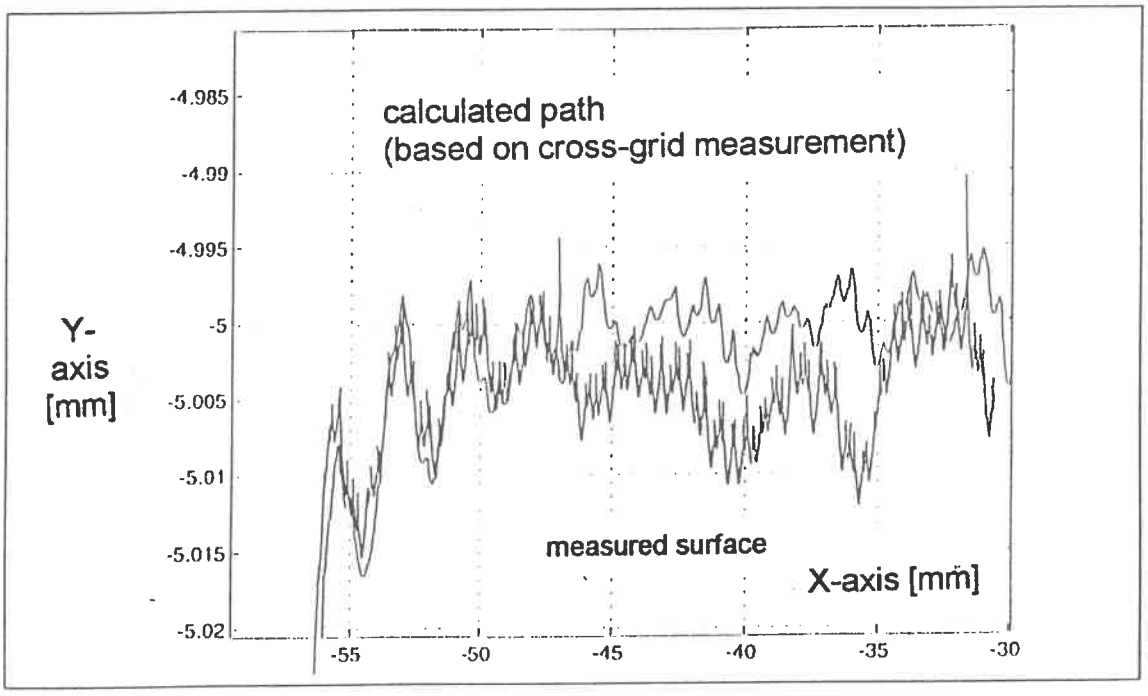

Fig. 11: Comparison of a measured surface, alt the theoretical contour, that was calculated, based on a cross-grid measurement

Conclusion

As a new tool for investigating machine tools both with respect to static and dynamic performance the cross grid system offers a large number of possibilities.

Particularly in high speed machining where the cutting force is small the actual surface contour of the workpiece can be deduced to a high degree of validity from grid measurements. Thus, the actual tool path which has been influenced by the controls and control algorithms, by the drive and structural characteristics of the machine tool can be observed readily without resorting to cutting tests. This reduces strongly the effort needed to optimize machine performance - e.g., by adapting control parameter settings.

References

[1] HEIDENHAIN-Information, „Messgeräte zur Abnahme und Kontrolle von Werkzeugmaschinen" 5/95

[2] Knapp W.,Hrovat S. Der Kreisformtest zur Prüfung von NC-Werkzeugmaschinen Eigenverlag S. Hrovat, 1986

[3] ISO 230-2: Acceptance code for machine-tools - Part 2;: Determination of accuracy and repeatability of positioning of numerically controlled machine tools. International Organisation of Standardisation, 1988

Comparison of Control Strategies for Piezoelectric and Magnetostrictive Micropositioning Devices for Ultra-Precision Machining

J. C. Campos Rubio[1], J. G. Duduch[1], A. E. Gee[2],
A. J.Vieira Porto[1] and H.Lêdo[1]

[1] Escola de Engenharia de São Carlos (EESC) - Universidade de São Paulo (USP)
Departamento de Enganharia Mecânica (SEM) - LAMAFE / Ultra-Precisão
P.O. Box 359 CEP 13560-254 - São Carlos - SP- Brazil

[2] School of Industrial and Manufacturing Science
Cranfield University - Cranfield, Bedfordshire MK43 0AL -England

Abstract

Ultra-precision machining to sub-micrometre depths is shown to be a threshold area of work requiring a combination of the best of materials, sensors, positioning devices (actuators) and control strategies. In ultra-precision design, it is extremely likely that there will be few design options for selection. In the case of ultra fine tool feed, the piezoelectric actuator is a potential choice. Currently, European and Japanese tool manufacturers are investigating magnetostrictive actuators for this purpose. Both piezoelectric and magnetostrictive materials suffer from hysteresis type non-linearity, so that the output of such systems depends upon the previous input, and absolute positioning is only achievable with the aid of feedback control. This work compares some modern control techniques for the positioning of a tool post for ultra-precision machining of brittle materials (in the nanometric range), eg, lead-lag Filter, PID with feedforward and fuzzy logic. The performance of the micropositioning device (tool post) using both piezoelectric and magnetostrictive actuators is assessed by means of simulation techniques. The predicteis performance is compared with results obtained by other authors.

Key words: Micropositioning Devices, Piezoelectric Actuators, Magnetostrictive Actuator, Control Strategies.

1. Introdution

In recent years, ultra precision machining to submicrometre range has gained increasing importance. The fabrication of components with high form accuracy (of the order of 0.1 μm) and surface roughness of the order of 10 nm Ra (eg scanner mirrors, infrared optics, lens molds, computer memory disks etc) has demanded the use of machines with higher positioning precision of the order of nanometres (**Dow** et al, 1991).

Currently, efforts have been made to machine ceramics and vitreous materials using single point diamond tools where the material is removed under certain restricted conditions which permit plastic removal, resulting in surfaces free of sub-surface damage. This ductile mode regime is obtained by controlled depths of cut and feedrates.

Together with the necessity of controlling the parameters involved, there is also the need to correct systematic errors and to attenuate disturbances in the cutting process. This can be done by correcting the movement of the cutting edge through real time control of the position of the tool via a position feedback signal from a sensor which controls directly a tool holder, before or during the process.

It is therefore necessary to use a servo-controlled micropositioning system (micro tool servo drive) which permits low amplitude movements and low following error to high frequencies. One of the basic components of these systems is the actuator which changes an electrical signal into movement and is based on solid state technology.

To reach the requirements quoted above, the next generation of machine tools will have to possess better accuracy and repeatibility characteristcs added

to adequate dynamic performance to make possible the ecomomic production of highly complex components with superior metrological characteristics and made of several difficult-to-machine materials.
This work proposes the use of modular micropositioning systems which can be encorporated to exixtent machines as well as to new designs. Two types of solid state actuators will be considered: piezoelectric and magnetostrictive. The dynamic performance of these actuators will be compared using different closed loop digital control strategies through numerical simulation.

2. Micropositioning device and prototype

Most commercial precision machines do not have repeatibility and accuracy capabilities to machine brittle materials. The development of positioning/correction systems of the tool is important as it is ultimately responsible for the form, finish and subsurface integrity of a workpiece.
Several devices have been proposed and developed. Figure 1 shows a modular type of tool holder which uses a flexure support system. (**Kohno** et al, 1989)

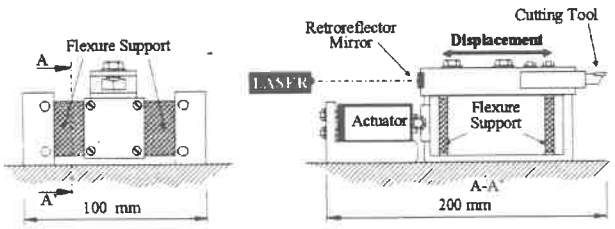

Fig. 1 - Modular Toolholder for Micropositioning

3. Solid State Actuators

Solid state actuators are a special group of linear positioners whose principle is based on strain phenomena. This type of actuator is recommended for high precision positioning. Other types of linear actuator could be presented in this work (eg, eletromagnetic, hydraulic, pneumatic), but they are hardly used to solve problems of positioning in the submicrometre range (**Campos** et al, 1996 a).
Piezoelectric and magnetostrictive actuators are presented below.

3.1 Piezoelectric Actuators

Piezoelectric actuators are based upon the properties that certain crystalline materials possess to expand or contract when a voltage is applied to them. The opposite mode exists: when a mechanical pressure is applied to the crystal a voltage is produced on its surface. Crystalline materials normally used are sinterized ceramics such as barium titanate, lead titanate-lead zirconate (**PZT**).
One common type of piezoelectric actuator is the PZT stack. In this arrangement, a number of plates and electrodes are stacked together. The number of plates determines the stiffness and stability of the actuator.
The advantages of piezoelectric actuators are:

- Nanometric positioning resolutions
- No backlash
- High efficiency
- High load carrying capacity
- Large bandwidth (limited by the sound speed in the crystalline material (**Physik Instrumente**, 1992)

Piezoelectric actuators, however, do not support loads out of centre and cannot be loaded in tension (some are pre-loaded), They are sensitive to temperature variations and present up to about 15% hysteresis and non-linearities. Feedback control is used to overcome the problems of non-linearities and hysteresis (**Slocum**, 1992).

3.2 Magnetostrictive Actuators

Originally developed as part of a US Navy project to find new sonar materials, magnetostrictive materials transduce low voltage electrical energy into mechanical movement (**Edge Technologies**, 1995).
The term Magnetostriction refers to the physical phenomenon of dimensional variation that occurs in a magnetic material when a magnetic field is applied (Guillemen effect).
Magnetostrictive translator (**MST**) are built from an alloys of metals, terbium, dysprosium and iron.
Among the characteristics that make this kind of actuator one of the best solutions, one can mention:

- High repeatibility
- Reliability
- High load carrying capacity
- Large bandwidth
- scarcely affected by environmental changes

Its high performance makes this type of actuator an excellent alternative for micropositioners, vibration control, seismic sources, noise control. However it suffers from thermal drift.
Both MST and PZT materials work in a way to transform an electric signal into linear motion in the

range of a few micrometres. The load carrying capacity can easily reach the order of kN and frequencies can range from zero to several kHz. Due to their excellent positioning precision and speed stability, these actuators can be utilized in the positioning of ultra-precision machine tools (**Schäfer** and **Janocha**,1995).

4. Modeling of Micropositioning Device

Each element of the dynamic system will be described by its respective mathematical model. The block diagram of Figure 2 shows the structure of the dynamic system.

This system may be divided into two parts: the digital controller and the plant which comprizes the other elements (eletromechanical components) .

On the plant, two parts can be clearly distinguished, one is the actuator (PZT or MST) and the other is the moving mechanical elements.

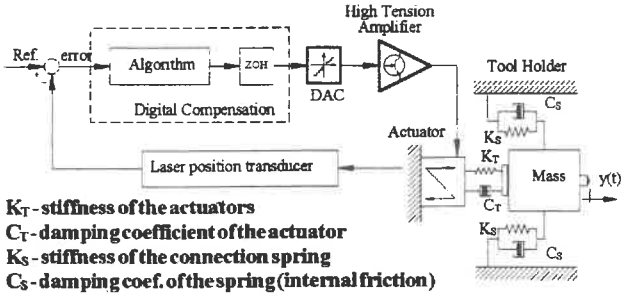

K_T - stiffness of the actuators
C_T - damping coefficient of the actuator
K_S - stiffness of the connection spring
C_S - damping coef. of the spring (internal friction)
M - mass of the moving mechanical elements

Fig. 2 - Structures of Dynamic Sistem

Mechanical Elements (Tool holder)

The mathematical model of the moving mechanical elements of the tool holder is shown in Equation 1 where ζ is the damping ratio (0.08) and ω is the resonant frequency of the system (200 Hz) for a mass of 650 g. (**Miron**, 1989 / **Sato** et al, 1994).

$$\frac{Y(s)}{X(s)} = \frac{2\cdot\zeta\cdot\omega_c \cdot \left(s + \frac{\omega_c}{2\cdot\zeta}\right)}{s^2 + 2\cdot\zeta\cdot s + \omega_c^2} \qquad [01]$$

Actuators

These devices convert an electrical input into a displacement. In this model, it is assumed that the actuator displacement is proportional to voltage/current input. The actuator may, therefore, be described as a second-order system where ζ is the damping ratio and ω_n is the resonant frequency ($\omega_n = 2\pi f_r$) (**Sanchez** et al, 1992 / **Okazaki**, 1988 / **Tanaka** et al, 1994).

• **PZT** - In this work is considered a Physik Instrumente P-239-10 piezoelectric actuator , with 10 μm expansion at -1000 volts.

$$\frac{X(s)}{V(s)} = \frac{K_{PZT}\cdot\omega_n^2}{s^2 + 2\cdot\zeta\cdot\omega_n + \omega_n^2} \qquad [02]$$

• **MST** - An MP 50/6 Etrema Terfenold-D^R magnetostrictive actuator is considered with -+25 μm expansion at -+ 1.5 ampere.

$$\frac{X(s)}{I(s)} = \frac{K_{MST}\cdot\omega_n^2}{s^2 + 2\cdot\zeta\cdot\omega_n + \omega_n^2} \qquad [03]$$

Both piezoelectric and magnetostrictive materials suffer from hysteresis type non-linearity, so that the output of such systems depends upon the previous input, and absolute positioning is only achievable with the aid of feedback control. There appear to be two regimes of operation, one for several micrometre range where the effect is strictly 'amplitude dependent' and that below this level where the effect diminishes with reducing amplitude. The former can be modelled as a (fixed) attenuation and phase lag; the latter indicates that for ultra-precision control systems this effect is negligible (**Duduch** and **Gee**, 1990)

Table 1 - System parameters

	Tool holder	PZT	MST
freq. resp. (f_r)	450 Hz	10 kHz	5 kHz
stiffness (k)	$5.25\cdot10^6$ N/m	$140\cdot10^6$ N/m	$7\cdot10^6$ N/m
damping ratio	0.080	0.700	0.097
gain factor(K_{iii})	452.39	$7.66\cdot10^{-7}$ m/V	1.66·10-5 m/A

5. Measurement System

As shown earlier, solid state actuators have limited repitibility due to non-linearities which makes necessary the use of position feedback control to improve performance.

Comercial micropositioning devices normally have a built-in position sensor such as capacitance micrometer or strain gauges.

In this work, a Laser Diode (GaAlAs) Michelson Interferometer was chosen. This choice gives high resolution (1.5 nm, $\lambda/512$ with λ = 780 nm) and

complies with Abbé principle as well as permitting mounting on an independent metrological frame (Gee et al. 1989).

6. DSP-Based Board Controller

The board used for the digital control of movement is based upon DSP TMS320C26 of Texas Instruments. It provides easy communication with the host comuter (PC-AT 386), permitting real time analyses of system performance, digital/analog input/output with 14 bits resolution and direct connection with power amplifiers.
It is possible to implement various compensation algorithm.

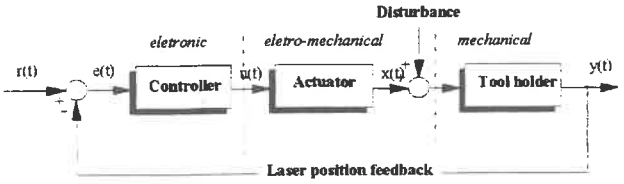

Fig. 3 - Block diagram of closed-loop control system

7. Displacement Control System

The next step is to propose a closed-loop position control system adequate for the system described above and able to meet all (ultra-precision) required specification. Lead-Lag Filter, PID, PID - feedforward and Fuzzy Logic will be considered.

• .Lead-Lag Filter

A direct digital controller will first be considered, based upon the knowledge of its analog equivalent (Lead-Lag filter).

• .PID

In the PID filter, the proportional term contributes to improve the frequency response, the derivative term improves stability and the integral term diminishes the following error

• .PID - feedforward

The integral term of a PID control system reduces the following error on the one hand, but decreases stability on the other. Using a "feedfordwar" loop, it is possible to reduce steady-state error without, however, reducing stability (damping).

• .Fuzzy Logic

A Fuzzy Logic-based controller is proposed in this study. A Fuzzy Logic controller basically has the following characteristics: it uses linguistic variables instead of or in addition to numerical ones; it is determined by simple relationships between variables stablishing "fuzzy" conditionh; and complex relationships between variables are represented by "fuzzy" algorithms.
This fuzzy controller is based on classical models where the main part is a "lock up" table, previously determined. This table corresponds to a matrix where the inputs are position errors and position-error variation. Thus, pair of input elements corresponds to an element of the matrix, whose value gives a quantitative measure of how is the system compared with the behaviour desired (Li and Lau, 1989).

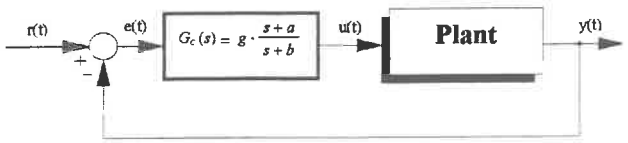

(a) Lead-Lag Filter

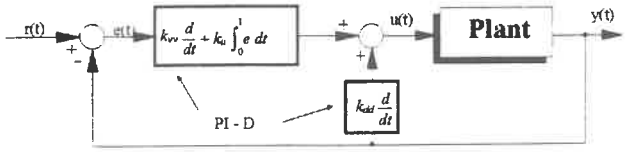

(b) PID

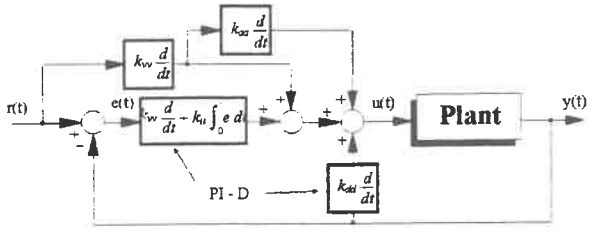

(c) PID - feedforward

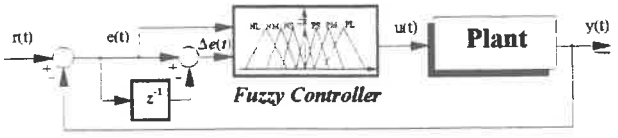

(d) Fuzzy Logic

Fig. 4 - Digital Filters

8. Numerical Simulation

Three parameters will be used to assess the servo-controllers' behaviour: (a) transient response (as quick as possible, without overshoot), (b) rejection

ability of disturbance to attenuate noises occurring (e.g. due to cutting process), and (c) dimensional accuracy of complex contours - ability to follow variable (with time) contours with little or no error.
The model proposed (in section 4) is a preliminary approximation and was obtained analytically. There are no expermental results as yet. For this reason, control techniques where chosen to satisfy the control requirements set out above, without taking into consideration optimization, self tuning, etc.
The parameters of the digital filters were selected through a sensitivity study of the loop and the sampling time value was set as 300 μsec. for all cases. The effect of the digital/analog convertion was considered as it limits the limits the resolution
Figures 4, 5 and 6 show the closed-loopresponse obtained for different types of exitation. The graphs were plotted through simulation of the dynamic system and controller via MATLAB^R simulation software.

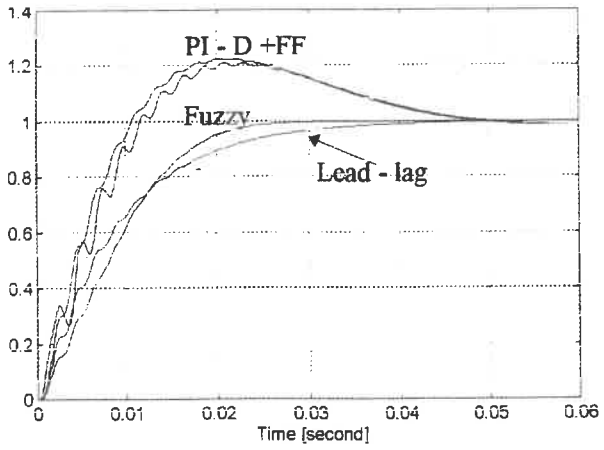

Fig. 4 - Transient response (unit step)

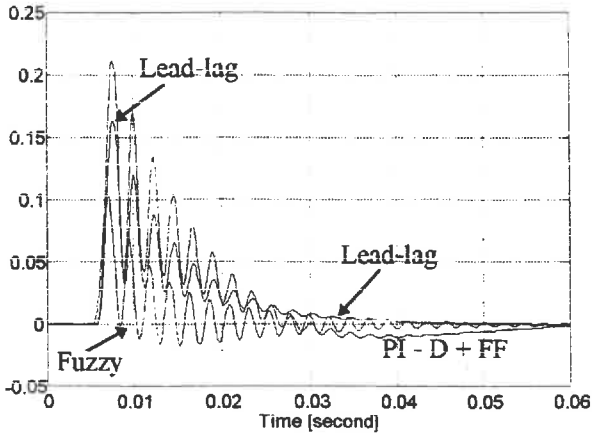

Fig. 5. - Disturbance rejection ability

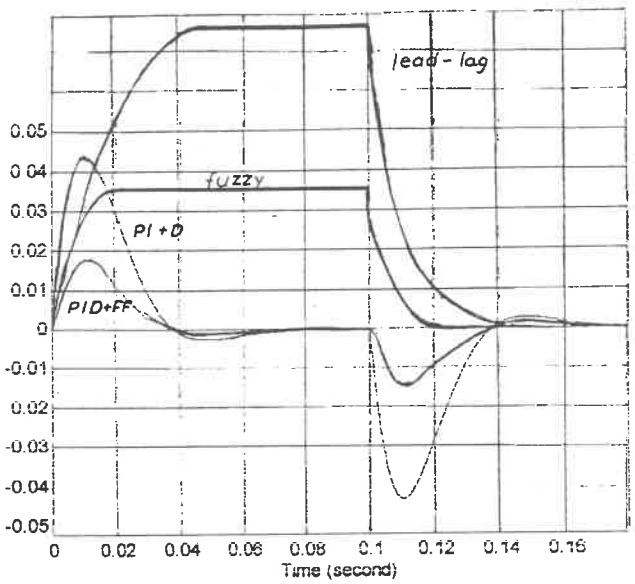

Fig. 6. - Trajectory tracking

9. Summary and Conclusions

This work is intended to show the development of a micropositioning system to be used in ultra-precision single-point diamond turning. The system utilizes the micro-displacement characteristics of solid state actuators. Generally, it can be said that this type of actuator greatly facilitates the design of a micro-tool holder. The mathematical model proposed, although neglecting non- linearities such as static friction, variable stiffness and damping, represents fairly well the dynamic behaviour of the electro-mechanical dynamic system.
The dynamic system obtained permits changing the actuator to suit the desired characteristics and needs, making the system modular and easily re-configurable.
The comparison of the various control strategies shown here allows us a better insight of the system behaviour and judgement of which modifications can be performed for the correct performance.
Finally, the results obtained in this study point to the possibily of knowledge-based techniques, such as Fuzzy Logic and Neural Networks to control magnetoestrictive actuators, as these techniques do not require detalied mathematical models to formulate the algorithms, and have more adaptive capability to the variations intrinsic to the process.

10. References

Campos Rubio, J. C., **Duduch**, J. and **Porto**, A.; Acionamento Direto de Ferramentas de Corte em Máquinas de Ultra-Precisão. Anales CIM, Valdivia (Chile), pp 220-223, 1996.

Dow, T., **Miller**, M. and **Falter**, P.;Application of Fast Tool Servo for Diamond Turning of Nonrotationally Symetric Surfaces, Precision Engineering, Vol. 13, N°4, pp 243-250, 1991.

Duduch, G. and **Gee**, A; Proc. ASPE, Vol. 2, Rochester, NY. pp 170-173, 1990.

Edge Technologies, Inc., Etrema Terfenold-D Magnetoestrictive Actuators (catalog), Ames, IA, 1995.

Gee, A. **McCandlish**, S. and **Puttick**, K.; On-axis Interferometric Measurement for Tool Positioning in Ultra-Precision Single-Point Machining. Proc. SPIE. Vol. 1121, pp 74-80, 1989.

Kohno, T., **Okazaki**, Y., **Ozawa**, N., **Mitui**, K.and **Omoda**, M.; In-Process Measurement and a Work-Piece -Referred Form Accuracy Control System (WORFAC): concept of the method and preliminary experiment, Precision Engineering, Vol. 11, pp 9-14, 1989.

Li, Y. and **Lau**, C.; Development of Fuzzy Algorithms for Servo Systems, IEEE Control Systems Magazine, April, pp 65-71, 1989.

Miron, D., Design of Feedback Control Systems, HBS Publishers, 1989.

Okazaki, Y.; A Micro Positioning Tool Post a Piezoelectric Actuator for Diamond Turning Machimes (in Japanese), JSPE, Vol. 54, N°7, pp 163-168, 1988.

Physik Instrumente; Products for Micropositioning (cataloge) edition E, 1992.

Sanchez, LJ. **Albertazzi**, A. and **Barczak**, C.; Sistema de Ativo de Estabilização Aplicado a Holografia Eletrônica, Anales CIM, Santiago (Chile), pp 513-518, 1994.

Sato, K., **Obata**, F., **Matsubara**, T. and **MIzumoto**, A.; Active Chatter Suppression of Slender Boring Bar Using Piezoelectric Actuators. JSME International Journal, Series C, Vol. 38, N°1, pp 36-41, 1995.

Schafer, J.. and **Janocha**, H.; Compensation of Hystere-sis in Solid-State Actuators, Sensors and Actuators, A 49, pp 97-102, 1995.

Slocum, A; Precision Machine Design. Prentice-Hall, Englewood Cliffs, NJ, 1992.

Tanaka, H., **Murayama**, Y., **Imada**, S. and **Shimokhobe**, A.; Control and Elimination of Lead Screw Backlash for Ultra-Precision Positioning. JSME International Journal, Series C, Vol. 37, N°3, pp 601-606, 1994.

A Study on Feeding Control Mechanism Analysis of Industrial Lock Stitch Sewing Machine

Keyoung Jin Chun, Dae Young Shin
Korea Academy of Industrial Technology
371-36, Kasan-Dong, Kumchon-Gu, Seoul, Korea

1. Introduction

This paper deals with a kinematic analysis of the feeding control mechanism (FCM) and design variable's effects for rotational angles of the feed regulator link in an industrial lock stitch sewing machine. Relations of the feeding distance of the feed regulator dial shaft and the rotational angle of the feed regulator link are studied. The sensitivity data of each design variable used for tolerances are obtained. The mutual relations of the design variables are discussed from these sensitivity data.

2. Kinematic analysis of the FCM

The FCM has a sliding contact mechanism (SCM) and a four bar linkage (FBL) as shown in Fig. 1.

The origin of a stationary Cartesian X-Y reference frame is on the rotational axis of the feed regulator, which is the absolute origin.

2.1. Kinematic awnalysis of the SCM

The SCM is shown in Fig. 2. When the feed regulator dial shaft is most close to the absolute origin, D is the distance between the absolute origin and the center of $C3_u$ or $C3_b$. While the feed regulator dial shaft is moving, d represents the motion of $C3_u$'s or $C3_b$'s center.

The SCM has the two characteristics in the motion as follows. The one is that the feed regulator dial shaft and the feed regulator is contacted by force F and tangent. Here, F has two force directions F_1 or F_2. The other is that a tangent point is moved by d. While F_1 is being on the feed regulator and d is increasing gradually from 0.0, $C3_u$ contacts with $C1_u$, and then with $L1_u$ after passing arcs. Thus, the kinematic analysis of the SCM could be done at four cases when tangent point is between ①$C3_u$ and $C1_u$, ②$C3_u$ and $L1_u$, ③$C3_b$ and $C1_b$, ④$C3_b$ and $L1_b$.

To simplify the analysis of the SCM, two assumptions may be introduced here.

ASSUMPTION 1: Geometries of contacting surfaces of the feed regulator are symmetric.

ASSUMPTION 2: Geometries of contacting surfaces of the feed regulator dial shaft are symmetric.

From ASSUMPTIONs 1 and 2, two

rotational angles (θ_s, θ_s') of the feed regulator's symmetric axis made by $F_1(\uparrow)$ or $F_2(\downarrow)$ have the same magnitude and the opposite direction each other as shown in Fig. 2. Thus, the kinematic study could be focused on the rotational angle θ_s only while F_1 is acting on.

2.1.1. Analysis of the rotational angle θ_s

2.1.1.1. Kinematic analysis when tangent point is between $C3_u$ and $C1_u$

When F_1 acts on, $C3_u$ and $C1_u$ are tangent each other as shown in Fig. 3. Two constraint equations are given as

$$\begin{aligned} f_1 &\equiv l_1\cos(\theta_{c1}) - (r_1+r_3)\cos(\psi_{c1}) \\ &\quad - l_2\cos(\theta_2) = 0 \\ f_2 &\equiv l_1\sin(\theta_{c1}) - (r_1+r_3)\sin(\psi_{c1}) \\ &\quad - l_2\sin(\theta_2) = 0 \end{aligned} \tag{1}$$

where $l_2 = \sqrt{(D+d)^2 + d_y^2}$, $\theta_2 = tan^{-1}\left(\frac{d_y}{D+d}\right)$.

From the equation (1), The equations of two dependent variables θ_{c1} and φ_{c1} are derived as

$$\theta_{c1} = \theta_2 + \cos^{-1}\left(\frac{l_1^2 + l_2^2 - (r_1+r_3)^2}{2l_1l_2}\right) \tag{2}$$

$$\psi_{c1} = \cos^{-1}\left(\frac{l_1\cos(\theta_{c1}) - l_2\cos(\theta_2)}{r_1+r_3}\right) \tag{3}$$

Thus, θ_s is derived as

$$\theta_s = \theta_{c1} - \eta_1 \tag{4}$$

2.1.1.2. Kinematic analysis when tangent point is between $C3_u$ and $L1_u$

While F_1 acts on, $C3_u$ and $L1_u$ are tangent as shown in Fig. 4. Two constraint equations are given as

$$\begin{aligned} g_1 &\equiv (r_2+r_3)\cos(\theta_{c2}) - t_1\sin(\theta_{c2}) \\ &\quad - l_2\cos(\theta_2) = 0 \\ g_2 &\equiv (r_2+r_3)\sin(\theta_{c2}) + t_1\cos(\theta_{c2}) \\ &\quad - l_2\sin(\theta_2) = 0 \end{aligned} \tag{5}$$

From the equation (5), The equations of two dependent variables θ_{c2} and t_1 is derived as

$$\theta_{c2} = \theta_2 - \cos^{-1}\left(\frac{r_2+r_3}{l_2}\right) \tag{6}$$

$$t_1 = \frac{(r_2+r_3)\cos(\theta_{c2}) - l_2\cos(\theta_2)}{\sin(\theta_{c2})} \tag{7}$$

Thus, θ_s is derived as

$$\theta_s = \theta_{c2} - \eta_2 \tag{8}$$

2.1.2. Analysis of the feed regulator's the rotational angle θ_i

θ_i is shown in Fig. 2 and derived as

$$\theta_i = \lambda + (-1)^n \cdot \theta_s \tag{9}$$

where n=2 when F_1 is acting, n=1 when F_2 is acting on, and λ is an angle relative to the symmetric axis.

2.2. Kinematic analysis of the FBL

Fig. 5 shows the initial state of the FBL. Two constraint equations are given as

$$\begin{aligned} f_3 &\equiv k_1\cos(\theta_i) + k_2\cos(\xi_1) - k_3\cos(\xi_2) \\ &\quad - k_4\cos(\theta_f) = 0 \\ f_4 &\equiv k_1\sin(\theta_i) + k_2\sin(\xi_1) - k_3\sin(\xi_2) \\ &\quad - k_4\sin(\theta_f) = 0 \end{aligned} \tag{10}$$

From the equation (10), the equations of two dependent variables θ_f and ξ_1 are derived as

$$\theta_f = cos^{-1}\left(\frac{k_1^2 - k_2^2 + k_3^2 + k_4^2 - 2k_1k_3\cos(\theta_i - \xi_2)}{2k_4\sqrt{k_1^2 + k_3^2 - 2k_1k_3\cos(\theta_i - \xi_2)}}\right) + \chi \tag{11}$$

where $\chi = \tan^{-1}\left(\frac{k_1 \sin(\theta_i) - k_3 \sin(\xi_2)}{k_1 \cos(\theta_i) - k_3 \cos(\xi_2)}\right)$

when $k_1 \cos(\theta_i) \geq k_3 \cos(\xi_2)$, or

$\chi = \pi + \tan^{-1}\left(\frac{k_1 \sin(\theta_i) - k_3 \sin(\xi_2)}{k_1 \cos(\theta_i) - k_3 \cos(\xi_2)}\right)$

when $k_3 \cos(\xi_2) > k_1 \cos(\theta_i)$.

$$\xi_1 = \left(\frac{k_3 \cos(\xi_2) + k_4 \cos(\theta_f) - k_1 \cos(\theta_i)}{k_2}\right) \quad (12)$$

In the equation (12), there are two possible values of ξ_1 within domain $0 \leq \xi_1 \leq 2\pi$. Thus, the exact value of ξ_1 has to be selected from satisfing with the equation (10).

3. Sensitivity analysis of the FCM

Variations of dependent variables $\underline{\Omega}: R^m \rightarrow R^n$ by design variables $\underline{\Psi}$ can be expressed as

$$\delta\Omega_i = z_{ij}(0)\ \delta\Psi_j \quad (13)$$

where z_{ij} is a sensitivity coefficient matrix expressing the sensitivity of dependent variables to small changes in design variables.

From ASSUMPTIONs 1 and 2, the analyzing process of z_{ij} is devided into two cases. The one is when $C3_u$ and $C1_u$ are tangent and the other is when $C3_u$ and $L1_u$ are tangent

3.1. Sensitivity coefficient matrix when $C3_u$ and $C1_u$ are tangent

In this case, there are nine design variables $\underline{\zeta} = [l_1, r_1, r_3, D, d_y, k_1, k_2, k_3, k_4]^T$ which are independent each other, four dependent variables $\underline{w}(\underline{\zeta}) = [\theta_{c1}, \varphi_{c1}, \theta_f, \xi_1]^T$ and four constraint equations $\underline{f}(\underline{\zeta}, \underline{w}) = [f_1, f_2, f_3, f_4]^T$.

Four constraint equations can be differentiated with the design variables $\underline{\zeta}$ by using the chain rule as

$$[\ u_{mn}]\ [\ a_{pq}] + [\ b_{kl}] = 0 \quad (14)$$

where $u_{mn} = \partial f_m / \partial w_n$ $(1 \leq m \leq 4\ ;\ 1 \leq n \leq 4)$,

$a_{pq} = \partial w_p / \partial \zeta_q$ $(1 \leq p \leq 4\ ;\ 1 \leq q \leq 9)$,

$b_{kl} = \partial f_k / \partial \zeta_l$ $(1 \leq k \leq 4\ ;\ 1 \leq l \leq 9)$, and $[u_{mn}]$ is a nonsingular matrix.

3.2. Sensitivity coefficient matrix when $C3_u$ and $L1_u$ are tangent

In this case, there are eight design variables $\underline{\rho} = [r_2, r_3, D, d_y, k_1, k_2, k_3, k_4]^T$ which are independent each other, four dependent variables $\underline{e}(\underline{\rho}) = [\theta_{c2}, t_1, \theta_f, \xi_1]^T$ and four constraint equations $\underline{g}(\underline{\rho}, \underline{e}) = [g_1, g_2, g_3, g_4]^T$. Here, $g_3 = f_3$ and $g_4 = f_4$.

Four constraint equations can be differentiated with the design variables $\underline{\rho}$ by using the chain rule as

$$[\ v_{\alpha\beta}]\ [\ s_{\gamma\varepsilon}] + [\ h_{\tau\mu}] = 0 \quad (15)$$

where $v_{\alpha\beta} = \partial g_\alpha / \partial e_\beta$ $(1 \leq \alpha \leq 4\ ;\ 1 \leq \beta \leq 4)$,

$s_{\gamma\varepsilon} = \partial e_\gamma / \partial \rho_\varepsilon$ $(1 \leq \gamma \leq 4\ ;\ 1 \leq \varepsilon \leq 8)$,

$h_{\tau\mu} = \partial g_\tau / \partial \rho_\mu$ $(1 \leq \tau \leq 4\ ;\ 1 \leq \mu \leq 8)$, and $[v_{\alpha\beta}]$ is a nonsingular matrix.

4. Results

4.1. Kinematic analysis of the SCM

While F_1 is acting on the feed regulator, θ_f has the linear relation to d as shown in Fig. 6 and the equation (16). In the case of F_2, the result is similar to the case of F_1.

$$\theta_f = (-1)^n A\ d + \theta_{f,0} \qquad (16)$$

where $A = 0.137\ rad\ /\ mm$, $\theta_{f,0} = 2.98 rad$, which is the rotational angle of feed regulator link when $d = 0.0[mm]$, n=1 when F_1 is acting on, and n=2 when F_2 is acting on.

4.2. Sensitivity analysis

In the sensitivity analysis of the dependent variable, the sensitivity coefficient matrix is normalized to show the mutual relation in design variables as

$$s_{ij} = \frac{z_{ij}}{\max(z_{ij})} \qquad (17)$$

Because θ_f is the final output of the feed control mechanism (FCM), θ_f is the most important of all dependent variables. Thus, we focuses only on the sensitivity of θ_f.

While d is increasing from 0.0 mm to 3.0 mm by 0.5 mm each, components of normalized sensitivity coefficient matrix (NSCM) are shown in Fig. 7 and Fig. 8, and its statistical data are shown in Table 1. Here, $\overline{m}$ is the mean value and σ is the standard deviation.

5. Conclusions

① θ_f has the linear relation to d. Here, d is the feeding distance of the feed regulator dial shaft and θ_f is the rotational angle of the feed regulator link.

② d have an little effect on the sensitivity of a design value because σ is very small.

③ In NSCM, mean values of the design variables r_1, r_2, r_3 and D are two or three times as large as those of the design variables l_1, d_y, k_2 and k_3, and are nine or ten times as large as those of the design variables k_1 and k_4. Therefore the allowable tolerances of the design variables r_1, r_2, r_3, and D have to be applied three times as tight as those of the design variables l_1, d_y, k_2 and k_3, and nine times as tight as those of the design variables k_1 and k_4.

④ In generally, because the design variables of the SCM is two or three times as sensitive as the design variables of the FBL. Therefore, The SCM should be designed more carefully than the FBL.

Acknowledgement

This research was financially supported by Korea Sewing Machine Co., Ltd. and the authors thank President I. C. Park.

References

1. George H. Martin, "Kinematics and Dynamics of Machines", 2nd edition
2. Donald T. Greenwood, "Principles of Dynamics", 2nd edition, Prentice Hall
3. Walter Ledermann, "Handbook of Applicable Mathematics, Volume Ⅳ :

Analysis", John Wiley & Sons
4. C. H. Edwards, JR., "Advaced Calculus of Several Variables", Accademic Press

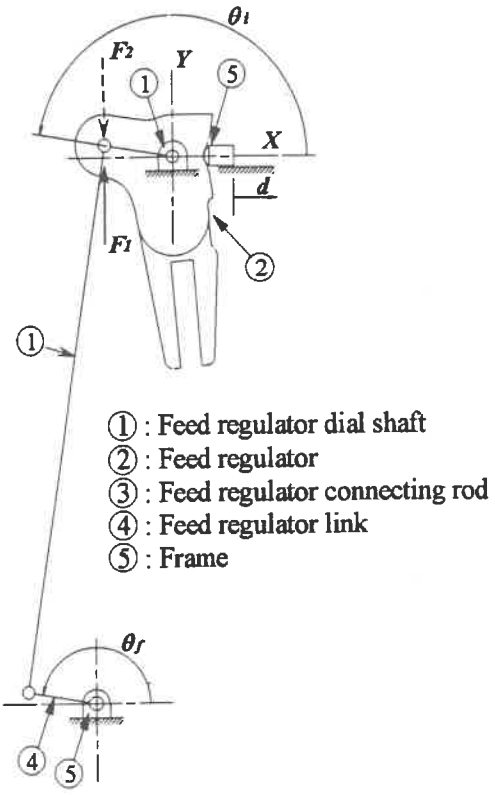

Fig. 1. Feeding Control Mechanism

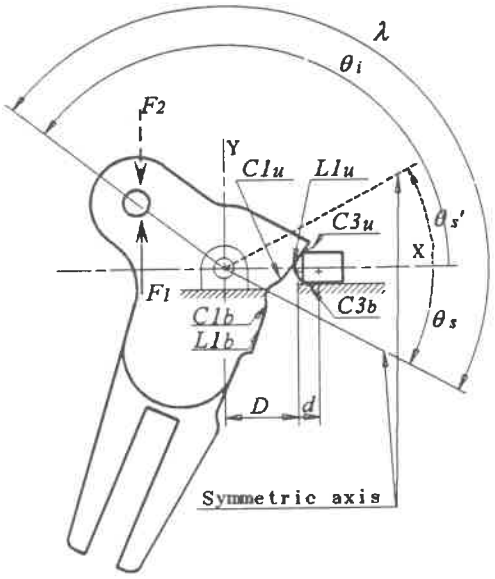

Fig. 2. Sliding contact mechanism when F_1 acts on the feed regualtor

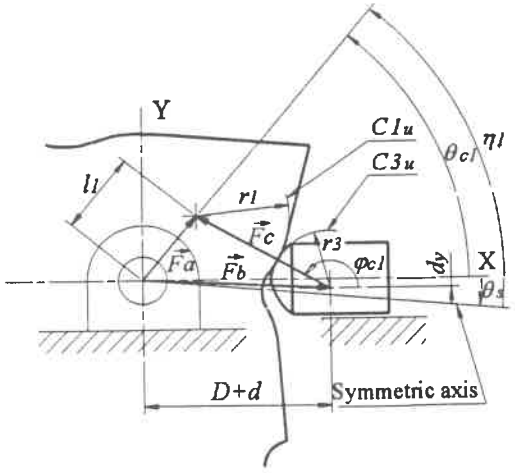

Fig. 3. Kinematic analysis when tangent point is between $C3_u$ and $C1_u$

Acting force	Statistical data	Design variable									
		l_1	r_1	r_2	r_3	D	d_y	k_1	k_2	k_3	k_4
F_1	$\overline{m}$	0.24	1.00	1.00	1.00	-0.87	0.48	-0.09	0.35	-0.35	0.09
	σ	0.098	0.000	0.000	0.000	0.022	0.039	0.060	0.059	0.059	0.060
F_2	$\overline{m}$	-0.29	-1.00	-1.00	-1.00	0.88	-0.48	0.10	0.35	-0.35	-0.10
	σ	0.098	0.000	0.000	0.000	0.022	0.039	0.058	0.057	0.057	0.058

Table 1. statistical data for θ_f

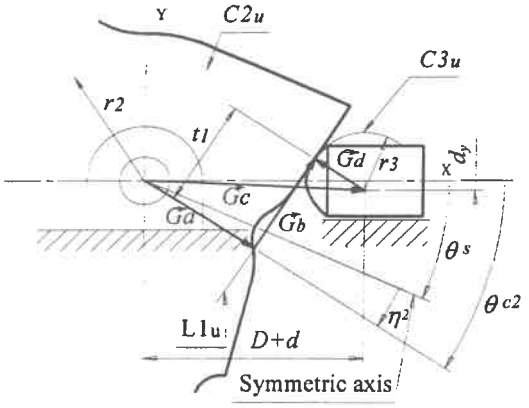

Fig. 4. Kinematic analysis when tangent point is between $C3_u$ and $L1_u$

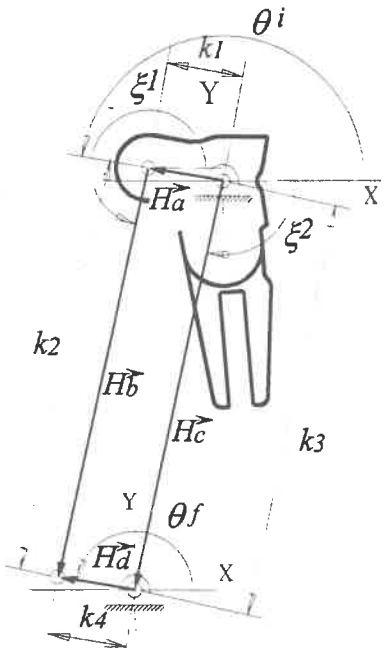

Fig. 5. Four bar linkage

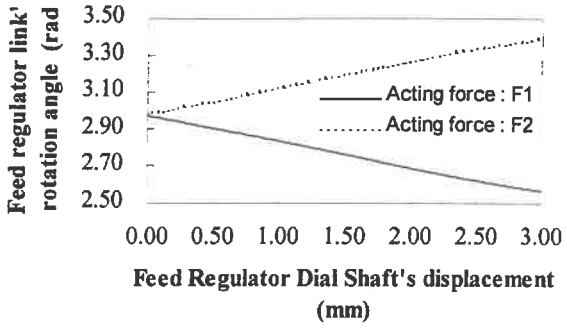

Fig. 6. Relation between d and θ_f

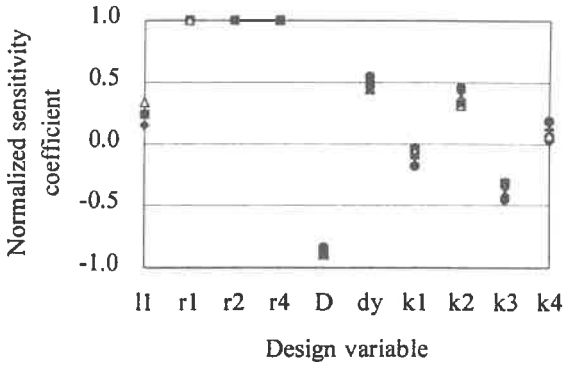

Fig. 7. Component of NSCM when F_1 is acting on

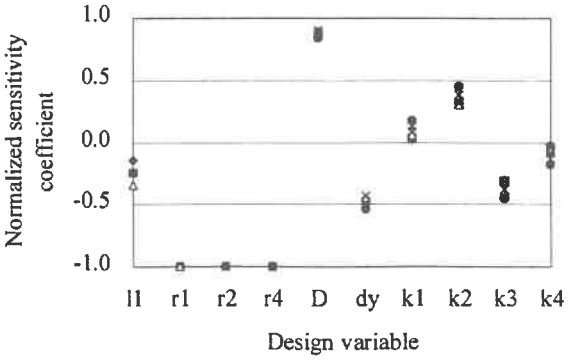

Fig. 8. Component of NSCM when F_2 is acting on

Piezoelectric Microactuator Including Compliant Mechanism

Daniel Enke
Technical University of Ilmenau, Faculty of Mechanical Engineering
Department of Microsystem Technology
PO-Box 0565, 98684 Ilmenau / Germany

Abstract

For the application in optical telecommunications a two dimensional microactuator is developed, which can adjust two optical waveguides to each other. Fibres, integrated optical chips and optical elements like lenses can be positioned. The piezoelectric bending actuator is a planar structure. It can be used for several tasks, e.g. for manipulators, adjusting actuators and microgrippers. The following paper describes the dimensioning, optimization, manufacturing and technical details of the manipulator, with its functional components for movement generation, transmission and its link to the mechanical environment. In the introduction aspects for miniaturizing of bending actuators will be discussed.

Introduction

The core diameter of monomode fibres requires very low mechanical tolerances for coupling. Precise manufacturing essentially determines the costs of connectors (see [1]). The microactuator is one part of an active flexible connector, that means a microsystem, which adjusts two optical waveguides itself. The damping of the coupler will be below 1 dB [2, 3]. Figure 1 shows the 6 axes of misalignment. The x- and y-direction have the biggest influence on the damping of a connector. These are the two axes we adjust. The maximum of movement range (100µm), and the accuracy of the actuator (<100nm) follow from the maximum of misalignment and the core diameter. Piezoelectric actuators (like PZT-Ceramics) are often used in mechanical and optical appliances for movements in the micrometer range. You can buy macroscopic appliances for microscopic movements. They are big and heavy.

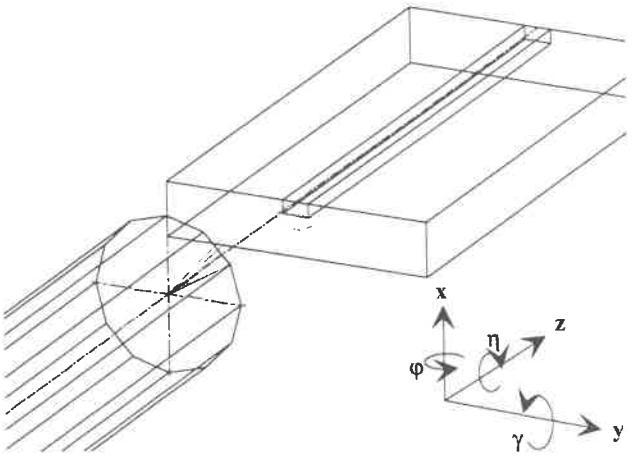

Fig. 1: Adjusting movements in a fibre-chip-coupler

But piezoelectric actuators are easy to combine with microtechnologies, because of their

- planar structure,
- high energy density,
- very low energy consumption in static running (< 1 mW).

The disadvantages are the high driving voltages and the very small deflections with a contraction of less than 0,05% in their length. For micropositioning a bigger motion range and smaller forces are needed. Therefore we use a hinge gear for the movement transmission. Two-axes in motion are realized serially. For the x-direction (out of the wafer) a bimorph is used, the y-direction has elastic hinges in a compliant mechanism.

How to dimension the microactuator

The microactuator has to be investigated with its connection to the surrounding microsystem. The limits of miniaturizing result from:

- feasible energy density,
- feasible deflection and force (stiffness adaption),
- getting losses away from the chip,
- optical limits,
- technological limits.

feasible energy density: The volume of a piezoelectric microactuator which is necessary to get out the mechanical energy is calculated from the power balance. As the movement is slow, only the static running is taken into consideration.

$$V_{\min} = \frac{2 \cdot W_{mech}}{k^2 \varepsilon_0 \varepsilon_r E_{\max}{}^2} \qquad (1)$$

W_{mech} ... necessary energy
k ... el.-mech. coupling factor
E_{max} ... max of piezo field strength

The actuating volume sufficient for the maximum bending of the fibre is: $V_{\min} = 0{,}089\ mm^3$. That is equivalent to a sheet of piezoelectric ceramics: the size of 1 mm by 1 mm, 100 microns thick.

feasible deflection and force: The forces (F) and displacements (s) are, if the voltage remains constant, in a linear connection with a rise of F_a/s_a, its spring stiffness (fig. 2). In operation with a flexible load F=f(s) (fibre) the operating point OP appears as the intersection of both characteristics. Adaption of stiffness (c) is fulfilled if:

$$c = \frac{F_0}{s_0} = \frac{F_a}{s_a}$$

Thus the maximum deflection and forces are dimensioned to:

$$s_a = 2 \cdot s_0 \text{ und } F_a = 2 \cdot F_0$$

The dimensioning of both gears will be discussed later in this article.

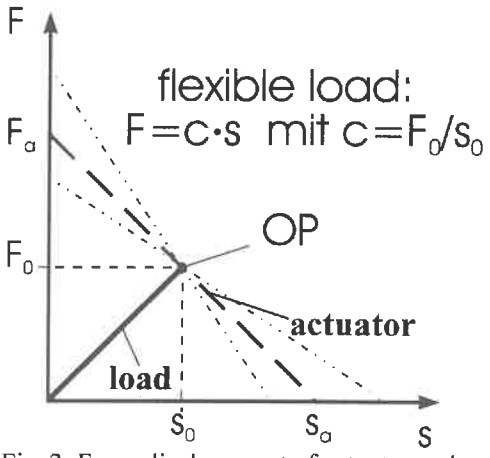

Fig. 2: Force displacement of actuator and load

getting losses away from the chip: In the quasistatic running losses are generated only by a leakage current. These losses can be neglected.

optical limits: Because the piezoactuator is polarized, the movement is only a contraction in one direction. The transmitted movement is a rotation, an angular deflection. The maximum angles φ_{max} , $\gamma_{max} = 1°$ (see fig. 1) may be tolerated by the required damping (see introduction). Thus the minimum radius of the rotation and the minimum bending length are calculated as limits of miniaturizing.

technological limits: There are two kinds of limits caused by manufacturing: fixed and movable. Fixed limits in the processes of silicon micromachining are the minimum ditch widths as a function of the wafer thickness. They fix the minimum hinge distance to 300 microns. Some limits are movable such as the smallest size of structure (mask and etching technology: 10 to 30 microns). Due to manual assembly we also get a minimum working size.

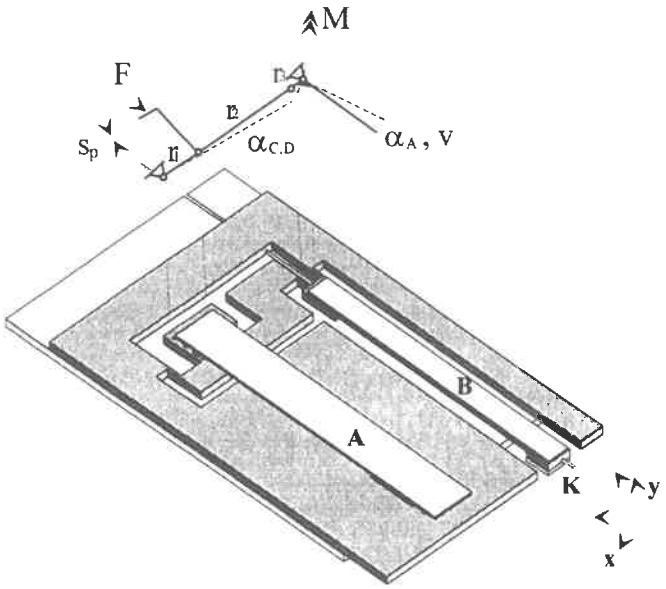

Fig. 3: Schematic display of the piezoelectric microactuator

The compliant mechanism works by the bending of silicon hinges. The piezoceramics plate A contracts (Monomorph) and bows the mechanism in two gear steps, which results in a movement in the plane of the structure (y-direction). The movement straight up from this plane (x-direction) results from a completely glued piezoceramics together with the silicon tongue B (Bimorph). The position of the elastic hinges you can see in the layout in figure 3. In dashed lines you can see the maximum shape of the compliant mechanism. The coupling point K moves into the two adjusting directions.

At first we describe the bimorph system (**x-direction**). The movement from an active layer (piezoceramics plate) is brought into a passive layer (silicon tongue) through a complete connection of the surfaces. The deflection (without load) can be calculated:

$$v(L) = \frac{3}{4} \cdot f_v \cdot d_{31} E \cdot \frac{L^2}{h_{pi}} \qquad \text{(2) from [4]}$$

d_{31} ... piezomodule
E ... field strength
h_{pi} ... thickness of piezolayer
f_v ... constant

The deflection depends on the length L and the thickness of the bimorph tongue. The constant f_v involves the proportions of thickness in the bimorph layers and their Joung´s moduli. For this actuator $f_v = 0{,}625$. The thickness of the piezolayer has technological reasons, at this time a minimum of 100 microns. Thus the minimum length L=10 mm for the required deflection range. The force in the bimorph tongue depends on:

$$F = \frac{3}{2} \cdot f_m \cdot \frac{d_{31} E}{S_{11}} \cdot \frac{{h_{pi}}^2 \cdot b}{L} \qquad \text{(3) from [4]}$$

b ... width of the tongue
S_{11} ... stiffness of the piezoceramics
f_m ... constant

The usable force of the tongue depends on the momentum deflection. The constant f_m involves the proportions of layer thickness and their Joung´s moduli. The block force is F_a=7,5mN. From maximum deflection and block force the stiffness of the whole actuator can be calculated, which has to be adapted to the stiffness of the fibre:

$$\frac{F_a}{v_a} = c_{act} = c_{fibre} = \frac{F_{fibre}}{v_{fibre}}$$

The dimensional equation for the adapted bimorph tongue can be written. The left side shows the variable parameters:

$$\frac{f_m}{f_v} \cdot {h_{pi}}^3 \cdot b = \frac{3\pi}{128} \cdot \frac{S_{pi}}{S_{fibre}} \cdot {d_{fibre}}^4 \qquad (4)$$

For the miniaturizing limits it is important to know that the length of the bimorph tongue (if its equal to the bending length of the fibre) does not take any influence in the stiffness adaption of the x-direction (see equation 4).

The second movement direction in the wafer plane (**y-direction**) uses the bending of microhinges summarized to a flexible mechanism. Two gear steps enlarge the deflection of the piezotranslator and the total transmission rate is:

$$\ddot{u}_{tot} = \ddot{u}_1 \cdot \ddot{u}_2 = \frac{L}{r_1}\left(1 + \frac{r_2}{r_3}\right) \qquad (5)$$

The elastic hinges take up energy for their bending (W_M), and the usable energy (W_L) becomes smaller:

$$W_{mech} = W_L + W_M$$

If you take the same transmission ratio in both gear steps the total transmission is on a maximum. But if you take a higher transmission rate in the last gear step, the bending and its energy is smaller. These two arguments have to be adapted to the special task.
The basic equations (deflection, force) express, what the influence of the turning stiffness γ_i and the lengths of levers r_i is like. In equation 6 you can see the case of stiffness adaption, if c_{act}=c_{fibre}. In this direction the width of the piezoceramics has an influence on the deflection.

$$\frac{1}{r_1}\left[\gamma_A \cdot \ddot{u}_\alpha + \gamma_B \cdot (\ddot{u}_\alpha + r_1 + 2(r_2 + r_3)) + \frac{\gamma_C + \gamma_D}{\ddot{u}_\alpha}\right] = 3 \cdot \frac{(EI)_{fibre}}{L^2} \text{ with } \ddot{u}_\alpha = \frac{r_2 + r_3}{r_1} \qquad (6)$$

The optimization of the hinges in the last gear step (with biggest deflection) is the most important, the turning stiffness of hinges A and B have the strongest influence on the stiffness of the microactuator.

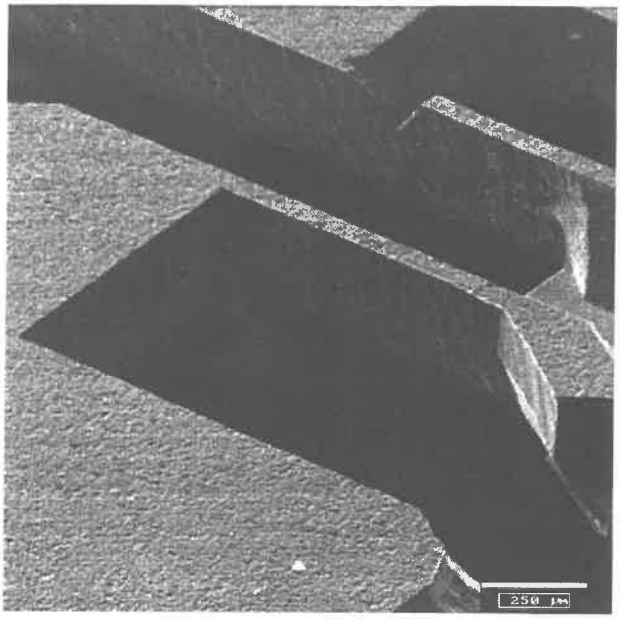

Fig. 5: SEM of a hinge structure

Manufacturing and Measuring

All hinge structures are made in (100)-silicon by wet anisotropic etching on both sides in one etch step. In the cross-section they are nearly rectangular (see fig. 5) with an aspect ratio bigger than 1:5. The fibre will be guided through the actuator between a V-groove on the side below of the chip and a grounding substrate. Thus a z-movement is possible and an adjusting possibility for fibres, keeping the polarization direction, is given in the fibre axis (η). The piezoceramics plates are mounted on the surface of the wafer.

The following table gives technical details:

parameter:	
length, width, height:	15 mm, 10 mm, 1 mm
mass:	100 mg
deflection range:	per axis 100 µm
input voltage range:	0 - 100 V
positioning time:	2 ms
block force:	10 mN
	no energy consumption in static running; hold position at galvanic separation

Further Development

Further optimization of the micropositioner is directed towards miniaturizing and the use of new technologies in connecting the silicon and the piezoelectric layer. The goals are smaller driving voltages and higher resonance frequencies, because of a smaller mass. Much more uses are possible for this actuator, e.g. microgrippers, fibre-switches and multiplexer, in sensor technology, surface metrology and precision positioning.

Acknowledgement

The work presented is supported by the German Federal Government (contract number: 13MV0316) and the Thuringian State Government (contract number: W6-918/3-183).

References:

[1] Lutzke, D.: *Lichtwellenleitertechnik : Bauelemente, Systeme, Meßtechnik.* (eng.: Fibretechnics) München: Pflaum. 1986.

[2] Enke, D.; Frank T.; Gerlach T.: *Mikropositionierantriebe für Lichtwellenleiter* (eng: Micropositioner for optical waveguides) In: Tagungsband des 41. Int. Wiss. Kolloquium Ilmenau, 23.-26.9.96, Technical University of Ilmenau

[3] Gerlach, T.; Enke, D.; Frank, T.; Hutschenreuther, L.; Schacht, H.-J.; Schüler, R.: *Towards an integrated microsystem for the automatic adjustment of monomode optical waveguides.* In: Proceedings of the Workshop „MicroMechanics Europe MME'96". Barcelona 21-22 October 1996

[4] Pfeifer, G.: *Piezoelektrische lineare Stellantriebe.* (eng.: Piezoelectric linear actuators) Wiss. Schriftenreihe der TH Karl-Marx-Stadt (TU Chemnitz), 6/1982

A SEMI-TOROIDAL FLEXURE SYSTEM FOR EXTENDED LINEAR MOTION

C. Jeffrey Finlayson and James F. Cuttino
The Department of Mechanical Engineering
The University of Alabama

Introduction

A number of linear motion precision devices rely on flexures to allow small displacements with atomic level accuracies. Flat, annular flexural bearings are often used in applications involving axial motion between concentric cylinders. However, a significant disadvantage to these flexures is the limited range of motion imposed by the necessity to keep stresses below the fatigue limit.

A preliminary study of a new flexure geometry has been conducted with the goal of increasing the range of axial displacement of two cylinders while maintaining concentricity. To improve the flexure's limited range, a new cross sectional profile has been developed and analyzed. As shown in Figure 1, the main feature of the flexure is that it resembles a bottom portion of the shell of a toroid.

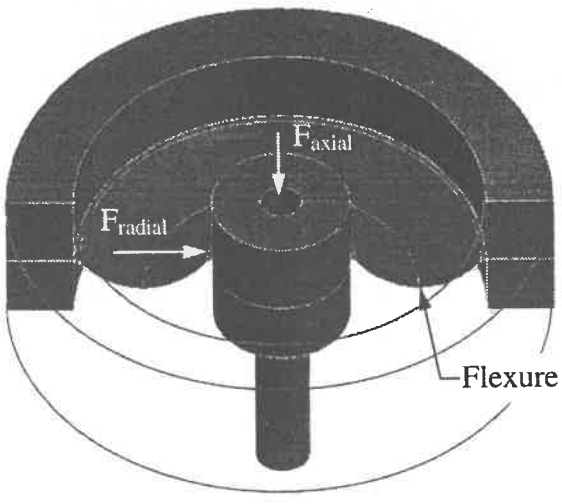

Figure 1: Flexure Configuration

The motivation behind the new geometry was twofold. First, the cross-sectional shape of the flexure allows the flexure to "roll" as the inner cylinder (hereafter referred to as a "shuttle") translates. This rolling action reduces the stresses from bending that are found in the flat flexure. Second, due to its curved shape, the flexure is ideal for conditions where the annular region between the cylinders is pressurized. Since the flexure is curved, it acts as a pressure vessel, reducing bending moments and stresses in the material.

Modeling and Analysis of Flexures

A finite element model of the curved flexure was constructed to analyze advantages and disadvantages of the new design. The study assumed the flexure would be loaded only in the axial and radial directions as shown in Figure 1. Due to symmetry in radial loading, only 1/2 of the flexure was modeled. The flexure's surface was meshed with 6-node, triangular, plate-bending elements. The axial and radial loads were applied separately to examine the two respective stiffnesses. These loads were uniformly distributed over the clamped section in the shuttle. In both loading configurations, the nodes along the outer boundary were constrained in all translations and rotations and the clamped portion in the shuttle was constrained in all rotations. Symmetric boundary conditions were applied along the line of symmetry. Convergence studies were conducted for the models to ensure validity of the data.

Results of Parameter Study

The parameter study was begun by first identifying all physical parameters that characterize the curved flexure bearing. The five principal parameters are the outer radius, r_o, the inner radius, r_i, the radius of curvature, r_c, the fillet radius, r_f, and the thickness, t. These parameters are shown in Figure 2. The distance to the bottom of the flexure is described by a *depth ratio* defined as $(r_o-r_i)/r_c$. This ratio provides a nondimensional parameter that characterizes the depth and curvature of the flexure. This parameter allows the comparison of curved and flat flexures, since $r_c=\infty$ for a flat flexure.

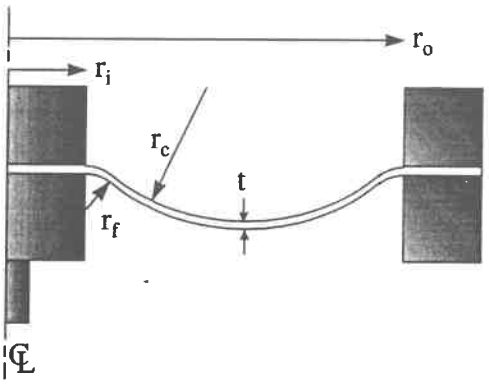

Figure 2: Flexure Parameters

Figure 3 relates stiffness and stress to the principal curvature of the flexure. Figure 3 shows that the highest stress values and lowest stiffness occur at a depth ratio of zero, corresponding to that of the flat flexure. The stress appears to have a "transition" region, dropping off rapidly as the depth ratio is increased to 1 and finally decreasing by a factor of 4 as the depth ratio reaches 2.25. More tests are planned to study this transition region.

The stiffness curve is smoother as the depth ratio is increased. At a ratio of 2.5, the axial stiffness has increased over that in the flat flexure by a factor of 4.5. While the results are not yet conclusive, these preliminary curves show that stress decreases and axial stiffness increases as the principal curve becomes deeper (decreasing r_c).

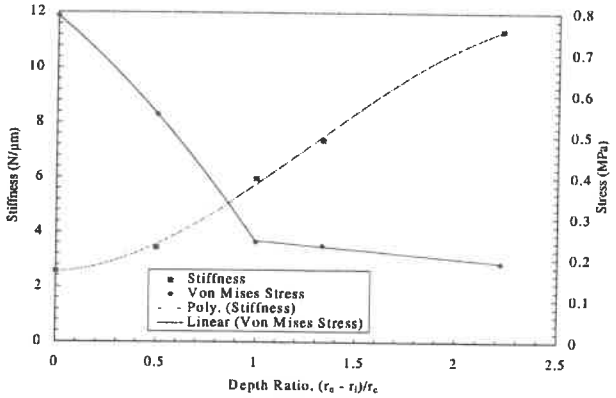

Figure 3: Flexures of Varying Depth Ratios in Axial Loading

Figure 4 plots stress and stiffness versus depth ratio for radial loading. Figure 3 and Figure 4 use the same scales for stress for comparison. In this case, the resulting stress and stiffness curves oppose those in axial loading since the stiffness decreases with increasing depth ratio while stress increases. The results appear to simulate the analogous case of a curved beam under axial loading. Both stiffness and stress show exponential behavior as a function of depth ratio. The stress value for radial loading is only 3% of that for axial loading of the flat flexure, but it increases to 90% for the maximum depth ratio. This demonstrates that stresses from radial loads can be as significant as stresses from axial loads for the larger values of depth ratio or can be negligible for small depth ratios.

Figure 5 presents a plot of stiffness and stress versus the ratio of r_o/r_i for flexures in axial loading. Stress and stiffness decrease with increasing r_o/r_i ratios. Stress decreases by 17% as r_o/r_i is increased from 3 to 6. However, stiffness decreases by a factor of almost 2.5 over the same range of r_o/r_i.

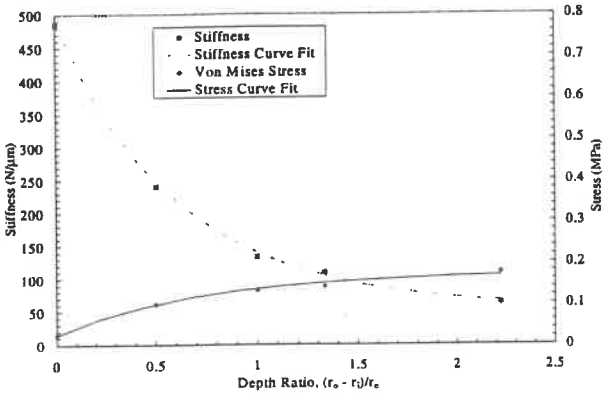

Figure 4: Flexures of Varying Depth Ratios in Radial Loading

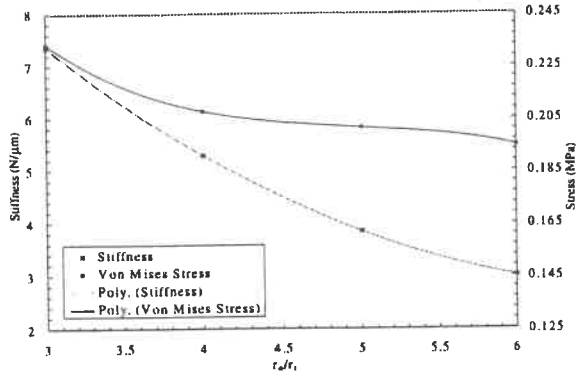

Figure 5: Flexures of Varying r_o/r_i Ratios in Axial Loading

Figure 6 shows stiffness and stress plotted against r_o/r_i ratios for radial loading. Radial stiffness decreases and stress increases with larger r_o/r_i ratios. Stiffness decreases by a factor of 2.7 for an increase of r_o/r_i from 3 to 6. Radial stiffness follows a power relation proportional to $(r_o/r_i)^{1.5}$. Stress increases by a factor of over 1.5 over the same range of r_o/r_i. Figure 5 and Figure 6 have the same stress scale to allow easy comparison. For a r_o/r_i ratio of 3, stresses from axial loading are over 1.6 times larger than stresses from radial loading. However, for a r_o/r_i ratio of 6, stresses from radial loading are slightly larger than the stresses from axial loading.

Figure 7 shows stress and stiffness plotted against flexure thickness under axial loading. Stiffness increases and stress decreases as thickness is increased. Stiffness appears to be proportional to thickness squared.

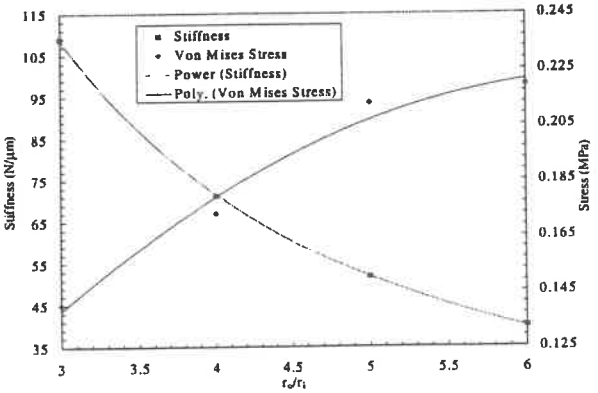

Figure 6: Flexures of Varying r_o/r_i Ratios in Radial Loading

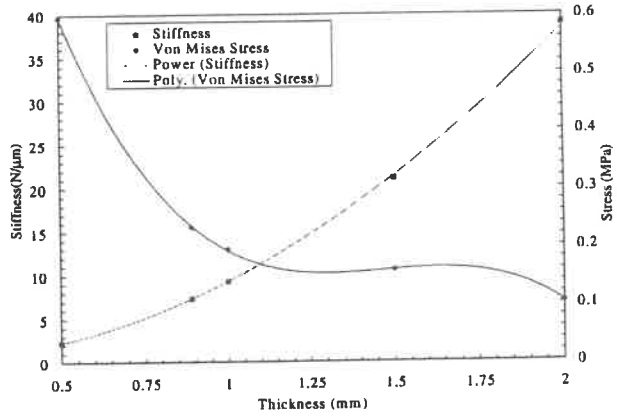

Figure 7: Flexures of Varying Thickness in Axial Loading

In Figure 8 stiffness and stress are plotted against flexure thickness for radial loading. Stiffness is shown to increase and stress decrease with increasing thickness. Stress and stiffness are both a function of thickness raised to a power similar to the axial loading case.

Figure 9 displays stiffness and stress plotted against fillet radius for axial loading. The graph shows maximum stress values decreasing linearly with increasing fillet radii. Stress decreases by 18% over the range of fillet radius of 1 mm to 4 mm. Since the purpose of the fillet is to reduce stresses, this result is expected.

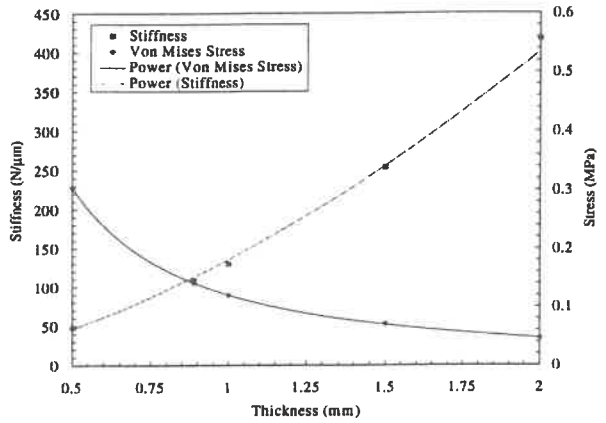

Figure 8: Curved Flexures of Varying Thickness in Radial Loading

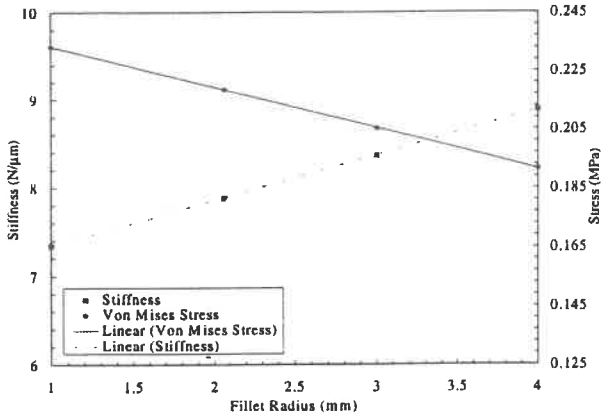

Figure 9: Curved Flexures of Varying Fillet Radii in Axial Loading

The axial stiffness increases linearly by 21% as fillet radius is increased from 1 mm to 4 mm. Whereas the axial stiffness increased for a decreasing radius for the principal curve, it increases for *increasing* fillet radius. Although this effect may be due to the shortening of the principal curve, further study is planned to isolate the cause. It can be concluded, however, that median values of fillet radii offer a compromise between low axial stiffness and low stress levels. For actuators with high force to displacement ratios, the larger fillet radii are optimal.

Figure 10 shows that the stress values for radial loading are less pronounced than for axial loading, changing by 9%. As expected, the radial stiffness increases as the fillet radius is increased. The stiffness also varies by 9% over the range of fillet radii.

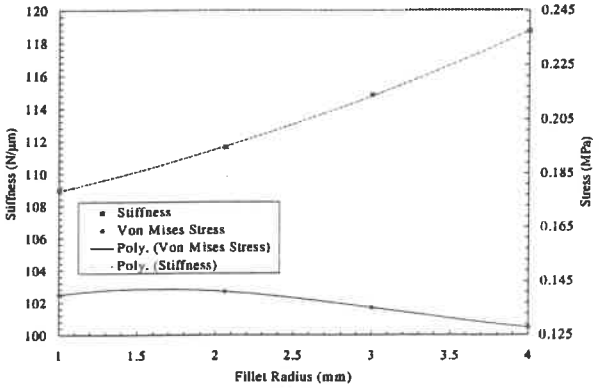

Figure 10: Curved Flexures of Varying Fillet Radii in Radial Loading

Conclusions

Based on the new geometry, a curved flexure stressed to the same stress level as a flat flexure provides over 4 times more deflection. However, radial stiffness decreases by a factor of 5. For cases where the radial direction is the non-sensitive direction, the gain in axial displacement may justify the reduction in radial stiffness.

The results show that for axial loading, stiffness increases and stress decreases with increasing depth ratios, flexure thickness, and fillet radius. Stress and stiffness decrease with larger r_o/r_i ratios. For radial loading, stiffness increases with increasing fillet radii and thickness, but decreases with increasing depth ratios and r_o/r_i ratios. Stress decreases with increasing fillet radius and thickness, but increases with larger depth ratios and r_o/r_i ratios.

Preliminary work has begun on a dimensional analysis to identify functional relationships between stiffness, stress and the geometric parameters presented in this study. Based on this work, a design methodology for toroidal flexures will be developed.

MICROSCOPIC BEHAVIOR OF LEADSCREW-NUT SYSTEM AND ITS IMPROVEMENT

Shigeo Fukada
Department of Mechanical Systems Engineering
Shinshu University
500 Wakasato, Nagano 380 JAPAN

1. Introduction

The positioning accuracy of a precision stage driven by a leadscrew-nut system depends mostly on the characteristics of the leadscrew in microscopic range. Recently it has been suggested that preloaded ball screws have some nonlinear elastic characteristics between the small torque input and the nut displacement within microscopic range, and that these characteristics are readily available in the nanometer positioning control [1) 2) 3)]. This paper presents the experimental results on this microscopic behavior of a ball screw and a conventional sliding leadscrew. It also proposes a method of improving the positioning performance of the sliding leadscrew.

2. Microscopic behavior of ball screw

2.1 Experimental method

The experimental apparatus is shown in Fig. 1. The outer diameter of the screw shaft is 32mm and the lead is 5mm/rev. The circuit of the ball circulation is 2.5×2. The ball screw is double nut type, and the preload is set between the nuts by a specially designed device which consists of adjusting screws and load cells inserted between the nuts. The screw shaft is fixed horizontally, and a small circumferential torque is applied to the nut by solenoids.

The axial displacement and the rotational angle of the nut are measured by capacitive gap sensors. The nut in the setup does not touch the sensors or actuators, and it keeps contact only with the screw shaft through the circulating balls.

2.2 Results and consideration

Fig. 2 shows the quasi-statical response of the displacement and the rotational angle of the nut to the applied torque in clockwise (cw) direction when the preload is 900 N. First, the displacement and the rotational angle increase according to the increase of the torque, and next they decrease following the decrease of the torque. This means that the response shows nothing but the elastic characteristics within microscopic range. Fig. 3 shows the relation between the displacement and the rotational angle. The broken line in the figure represents the theoretical line estimated from the lead of the screw. In this microscopic range, the relation between the displacement and the rotational angle is also subject to the lead of the screw as it is in the macroscopic range.

Fig. 4 shows the relation between the applied torque and the displacement, i.e. stiffness curve, arranged from data similar to Fig. 2 in the case of 600 N preload. The curve shows nonlinear elastic characteristics with hysteretic effect in the cw direc-

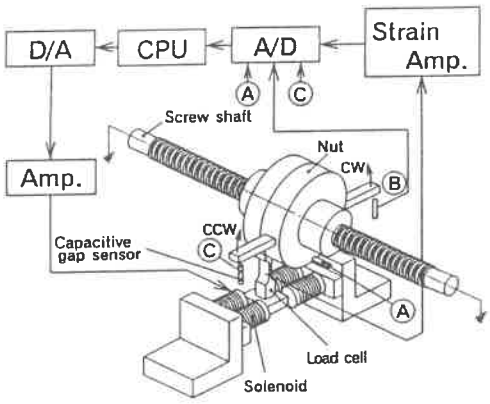

Fig. 1 Experimental apparatus for ball screw

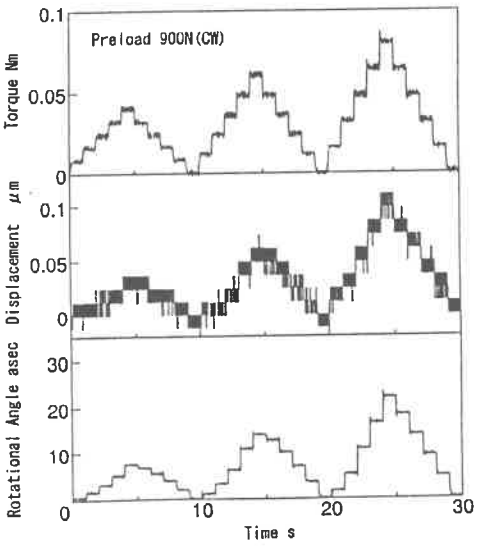

Fig. 2 Response of displacement and rotational angle

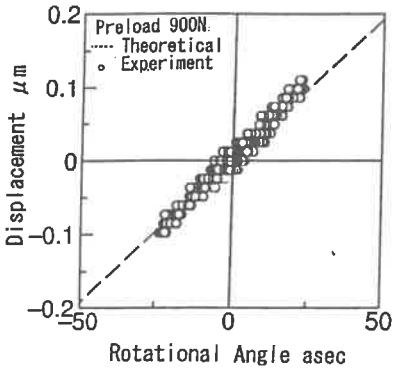

Fig.3 Displacement vs. rotational angle

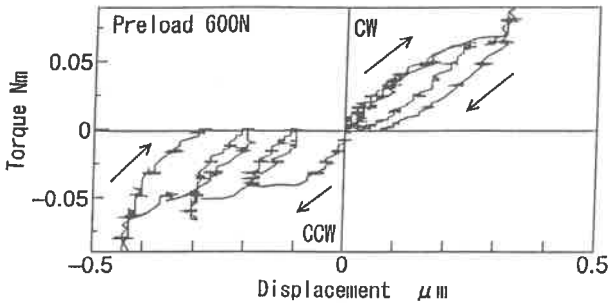

Fig.4 Torque vs. displacement

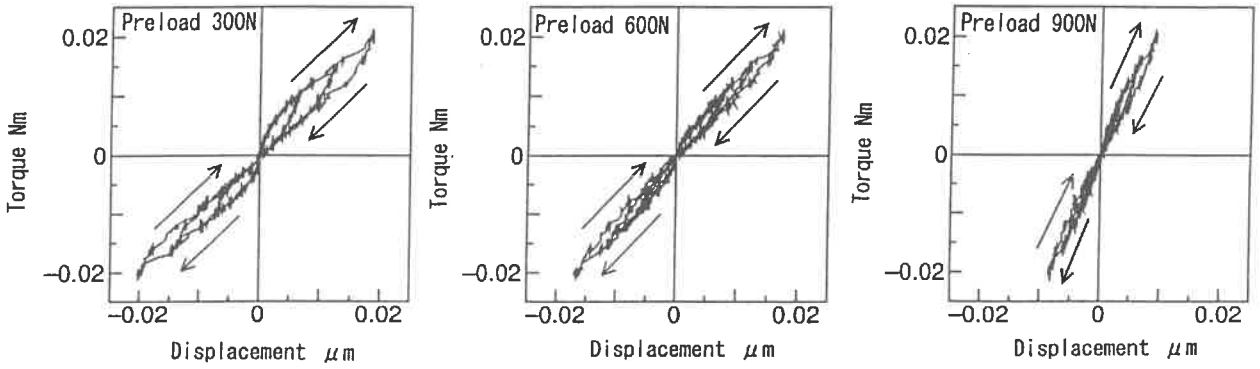

(a) Preload 300 N (b) Preload 600 N (c) Preload 900 N

Fig.5 Stiffness curves

tion. In the counter-clockwise (ccw) direction, the torque exceeds the limit of elastic range at -0.05 Nm, and the nut rotates macroscopically.

Further experiments are performed in more microscopic range with higher resolution. Fig. 5 shows the stiffness curves when the preload is changed into three values. The elastic characteristics becomes stiffer and more linear according to the increase of the preload.

3. Characteristics of positioning table driven by sliding leadscrew

3.1 Experimental method

To consider the characteristics of sliding leadscrew, some experiments are performed on a positioning table driven by a sliding leadscrew as shown in Fig. 6. The table is guided by a cross-roller guide, and the stroke of the table is 100 mm. The sliding leadscrew has a trapezoidal screw thread of Tr14×2. A small preload is given between double nuts to eliminate backlash. The leadscrew is coupled to a DC servo motor of 80 W through coupling. The motor is driven by a linear current amplifier. The table position is detected by a optical linear encoder of 10 nm resolution, and can be controlled by software servo system with full closed feedback loop.

3.2 Results and consideration

As with the experiments on the ball screw, the response of the table displacement to the torque input is investigated. Fig. 7 shows changes of the torque and the table displacement and their relationship. Unlike the case of ball screw, the table displacement stays in a state of complete rest until the motor torque exceeds a certain amplitude. The preload of the leadscrew was adjusted before assembling so that the start torque is 0.1 Nm, and the figure shows the table starts with the start torque of the leadscrew.

Fig. 7 has the same dimensions as Fig. 4. The figure shows no elastic characteristics, and the table is stationary until it moves macroscopically. This means that the microscopic behaviour of the sliding leadscrew is ruled by Coulomb's friction: this friction spoils the positioning performance of the sliding leadscrew. The positioning accuracy of the table controlled by simple proportional controller is no more than 30 μm dispersion.

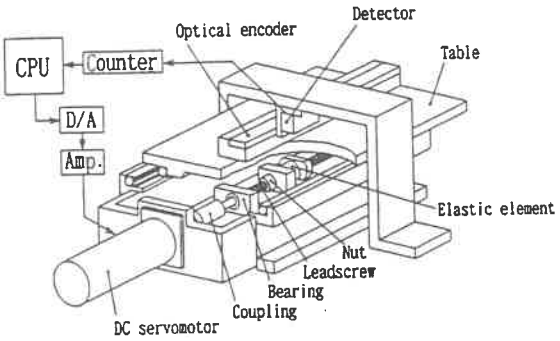

Fig.6 Experimental setup of positioning system using sliding leadscrew

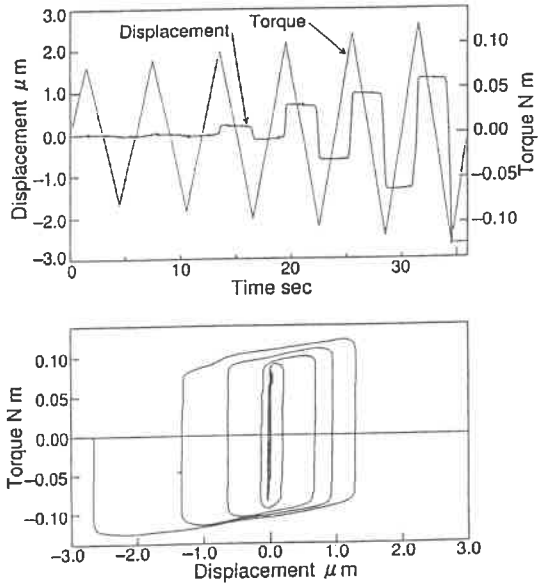

Fig.7 Torque vs. displacement

4. Improvement of positioning performance of sliding leadscrew

4.1 Principle and design of mechanism

Ball screws have elastic characteristics in the relation between torque input and nut displacement though hysteretic. It has been indicated that this property is very available to the positioning control because the displacement shows no stick and responds to the torque input however small [1]. If such elastic characteristics can be given to a sliding leadscrew, its positioning performance will be improved. Considering this, a simple method is proposed.

Fig.8 shows the principle of the proposed method. When the nut is fixed to the screw shaft so that the friction does not exceed the maximum static friction, any torque input to the screw shaft is transmitted to the nut direct. Therefore, if the elastic element which converts the torsional moment into the axial

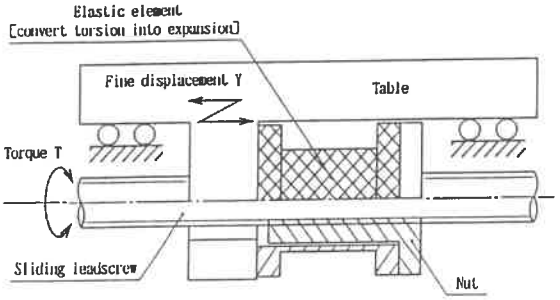

Fig.8 Principle of proposed method

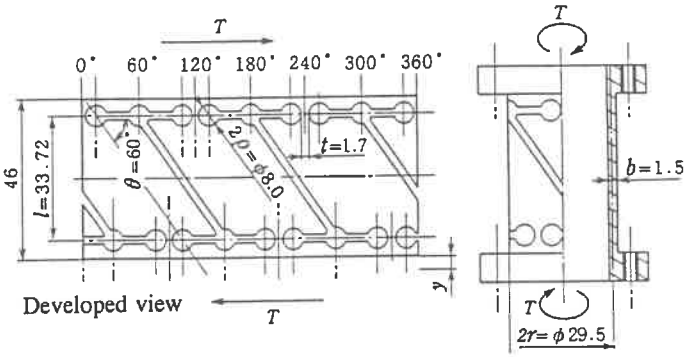

Fig.9 Configuration of elastic element

expansion elastically is inserted between the nut and the table, the table displacement is easily controlled in microscopic range by operating the torque input.

For the elastic element, a cylinder with some flexure hinges formed by notching, as shown in Fig. 9, was devised. When the torsional torque is applied to both ends, the hinges deform elastically, and both end surfaces expand relatively. The relation between the torque T and the expansion y is summarized in the following equation [4].

$$T = K \cdot y = \frac{4 E b t^{5/2} r \tan\theta}{3 \pi \rho^{1/2} l^{2}} y \qquad (1)$$

where E is Young's modulus and b, ρ, t, l, θ, r are geometrical parameters as shown in Fig. 9. On the basis of the experimental results in the preceding chapter, the stiffness K in eq.(1) can be calculated as 0.1Nm/30μm. The dimensions are designed as shown in Fig. 9.

4.2 Experiments and evaluation

The designed elastic element is manufactured using phosphor bronze, and attached to the leadscrew in the system of Fig. 6. Fig. 10 shows the relation between torque input and table displacement. It is confirmed that the torque is converted into the displacement elastically.

The PTP positioning for the step length of 10 mm is performed with PI controller. The control action is

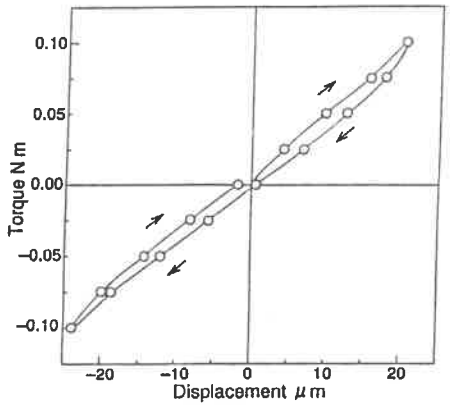

Fig. 10 Torque vs. displacement

switched for the ranges of deviation divided into three regions — coarse, fine and ultra-fine; and the PI parameters are determined for each region by trial-error method. Fig. 11 shows the transition of displacement and motor current during the positioning. The control parameters are switched from coarse to fine at 0.3 mm deviation, and from fine to ultra-fine at 3 μm deviation. The motor current corresponds to the displacement simply and converges smoothly. Fig. 11(c) shows the histogram of the positioning error attempted 100 times. Each error is less than 10 nm which is the resolution of the linear encoder.

Fig. 12 shows the response of the positioning system to 10 nm step input. Fig. 12(a) shows the feedback signal from the linear encoder, and (b) shows the measured data by another capacitive gap sensor independent of the control system. It is confirmed that the positioning system actually responds to an input of 10 nm resolution.

5. Conclusions

The conclusions are summarized as follows.

(1) The experiments on the ball screw show the elastic characteristics in the relation between torque input and nut displacement within microscopic range. The linearity of the elastic property improves when the preload is increased.

(2) It is shown by another experiment that the sliding leadscrew does not have any elastic characteristics at all.

(3) A simple mechanism using an elastic element to convert torsional moment into expansion is proposed. It is then verified experimentally that the device is readily available to vastly improve the positioning performance of the sliding leadscrew.

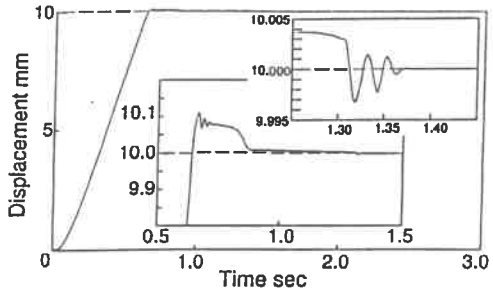

(a) Displacement

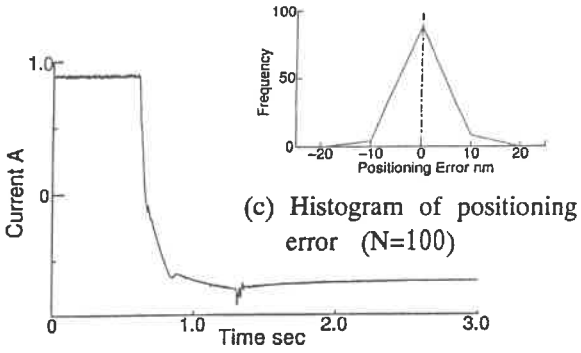

(c) Histogram of positioning error (N=100)

(b) Motor current

Fig. 11 Response to 10 mm step input

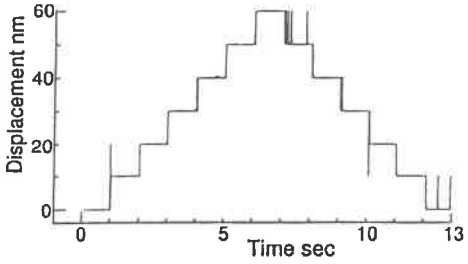

(a) Output of linear encoder

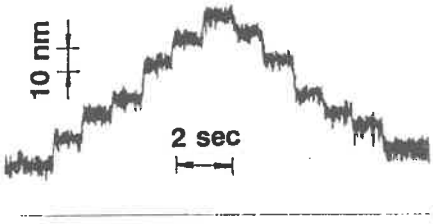

(b) Measurement by capacitive gap sensor

Fig. 12 Response to 10 nm step input

References

1) Jiro Otsuka, Shigeo Fukada et al.: Ultraprecision positioning Using Lead Screw Drive, Int. J. JSPE, 27,2 (1993) 142.
2) Jiro Otsuka: Nanometer Positioning Using Three Kinds of Leadscrews, Nanotechnology, 2, 3 (1992) 29.
3) James F. Cuttino and Thomas A. Dow: The Preloaded Ball Screw As A Nanometer Actuator,
4) J. M. Paros: How to Design Flexure Hinges, Machine Design, Nov. 25 (1965) 151.

Recent Advancements In Piezoelectric Stepping Motors

David Henderson, Dana Jensen and Peter Piccirilli
Burleigh Instruments, Burleigh Park, Fishers, NY 14453

Piezoelectric (PZT) stepping motors such as the Inchworm® combine the high resolution and stiffness of piezoelectric stacks with the long travel of more conventional electromagnetic motors and leadscrews. Recent advances in co-fired PZT materials make it possible to produce a high performance Inchworm that operates at only 60 volts (1). We call this new "inside-out" and spring loaded design the Inchworm II™. This linear motor concept has been further improved to operate at "constant velocity" (2) with minimal "glitch" and achieve continuous rotary motion.

Constant velocity and minimum glitch performance are achieved using a modified Inchworm II design. Previous PZT stepping motors produce discrete motion steps with a finite dwell period while the clamps are changing as shown in Figure 1. The dwell period occurs during each clamp change when both clamps are activated (i.e. both clamps are supporting the moving structure but are stationary). This period of stationary clamp overlap is needed to prevent slippage and loss of actuation force. A constant velocity motor independently moves each clamp-extension assembly and allows the clamps to be moving during the clamp change. This effectively eliminates the stationary dwell period as shown in Figure 2.

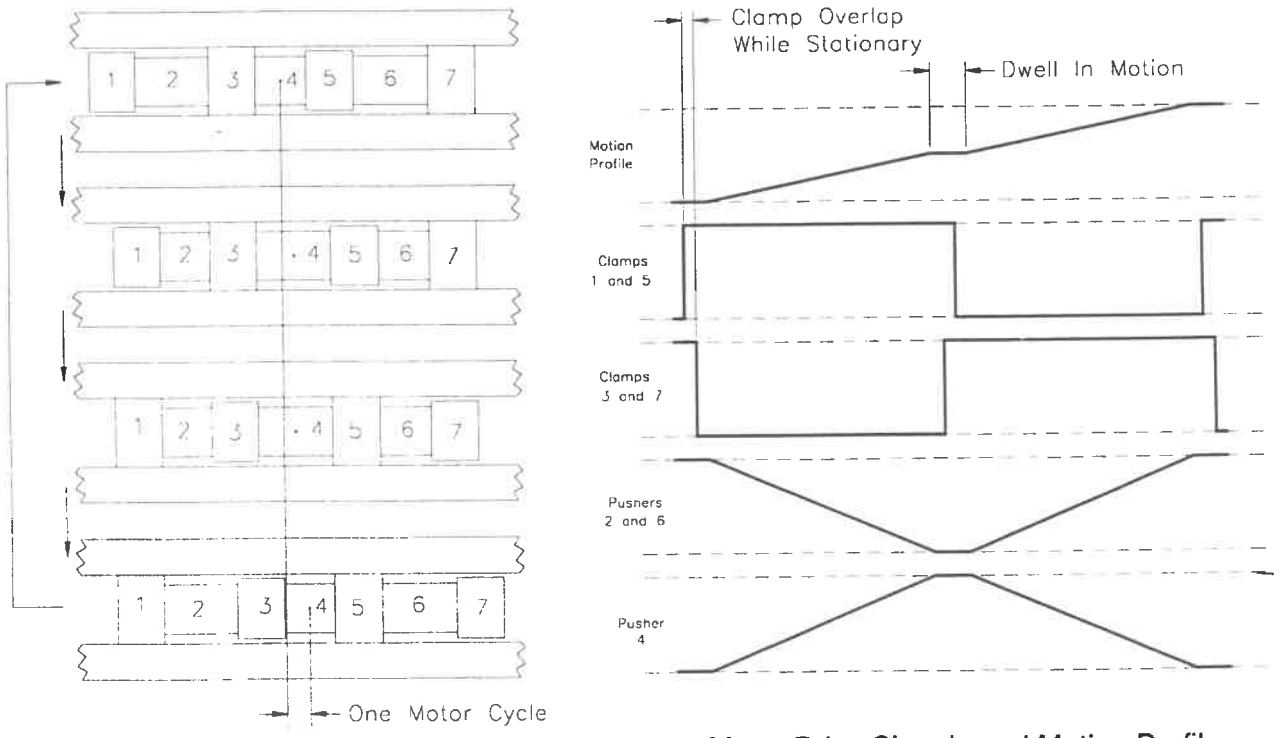

Motor Sequence

Motor Drive Signals and Motion Profile

Figure 1 - Clamps Overlap While Stationary And Produce A Dwell In The Motion Profile In Current Inchworm Motors

"Glitch" during clamp changes is minimized by using only the D_{33} motion of the PZT stacks and not the D_{31} motion. The clamping mechanism must produce minimum axial motion

(i.e. motion parallel to the motor's output axis) when a clamp is activated or deactivated. Designs that ignore cross coupling effects produce glitches that are one third of the clamping stroke. (For example a three micrometer clamping stroke produces a glitch of one micrometer.) The Inchworm II glitch is reduced to less than 30 nm using line contacts on the clamp pads and a symmetric configuration as shown in Figure 3.

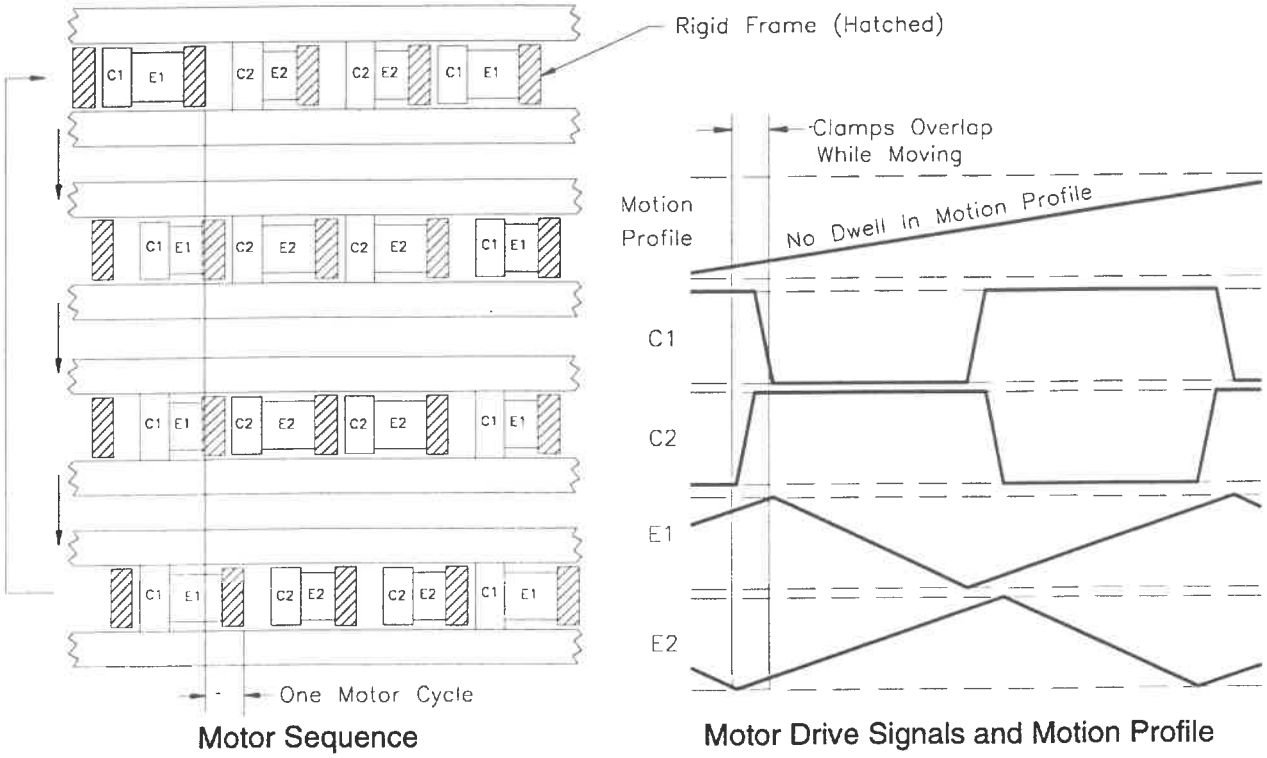

Figure 2 - Clamps Overlap While Moving And Produce No Dwell Using Constant Velocity Approach

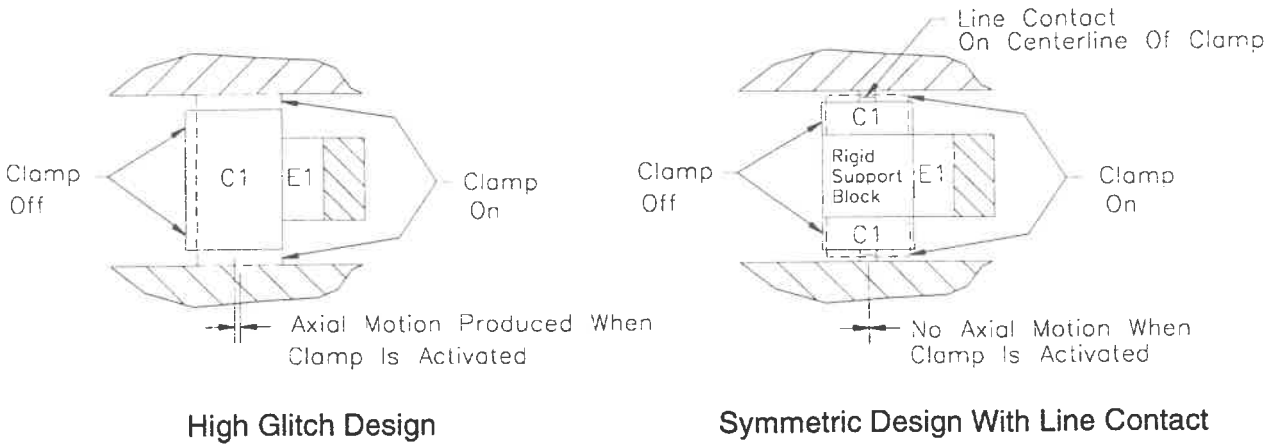

Figure 3 - Proper Clamp Design To Minimize Glitch

The constant velocity and low glitch innovations have been demonstrated with a small stage shown in Figure 4. This stage uses a moving carriage to preload the rails against the

motor assembly. A separate set of rolling element bearings guide the top and bottom plates of the stage.

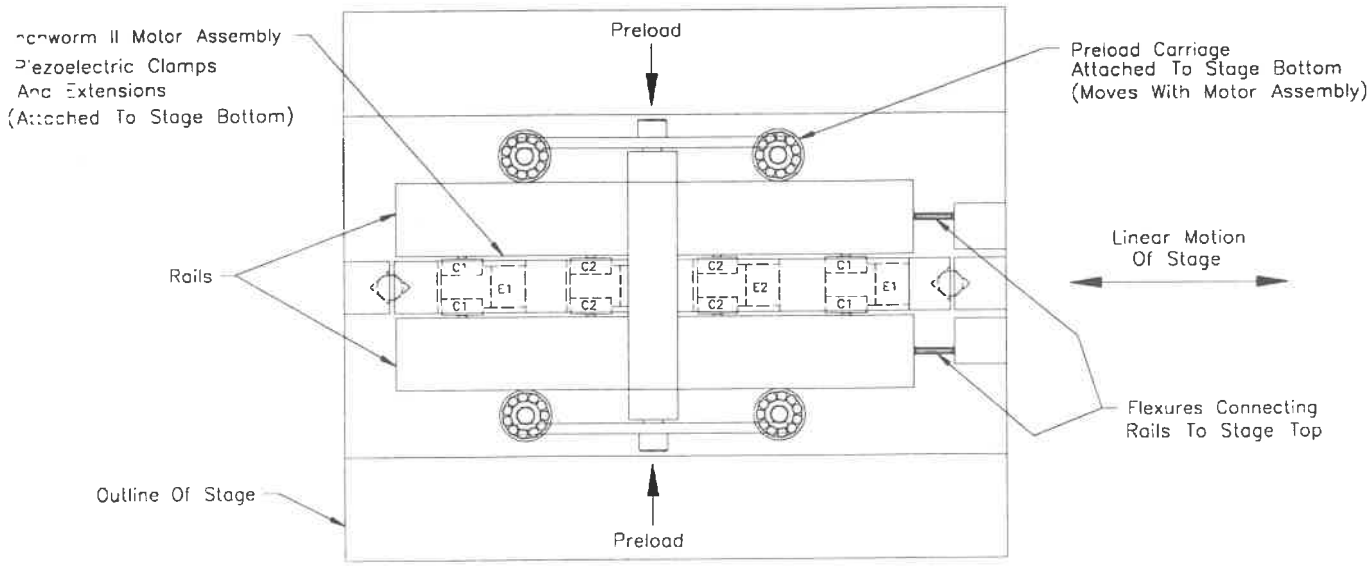

Figure 4 - Prototype Constant Velocity Inchworm II Linear Stage

Demonstrated Prototype Performance

Preload	25 pounds
Output Force	3 pounds
Static Holding Force	10 pounds
Maximum Speed	1 mm/second
Glitch During Clamp Changes	Less than 30 nm (At the resolution limit of test equipment.)

Future Work

- Evaluate the motion profile of this prototype with a higher resolution position encoder to measure the glitch more precisely.
- Simplify the prototype design so that fewer parts are required and manufacturing costs are reduced.
- Optimize the stiffness of the motor assembly frame to reduce stored energy and the corresponding glitch. As the clamps change the load paths in the frame change the energy stored in the frame is released to produce glitch. At the nanometer level this is a significant effect that must be minimized.

A rotary stepping motor has also been designed that uses the constant velocity concept as a tangential drive. Lapped rails are replaced with lapped rings. Six clamp-extension assemblies are used (instead of four) and are sandwiched between two drive rings with designations C1, C2, E1, and E2.. The drive rings rotate and the clamp-extension assemblies are fixed to the housing. The drive rings are pressed against the clamp pads using symmetric opposing forces that are internally supported by the shaft. See Figure 2 for the operating sequence. This new rotary motor design is simple and inexpensive to manufacture. This

concept is also small, stiff, lightweight easily scaled to accommodate larger diameters and hollow shafts.

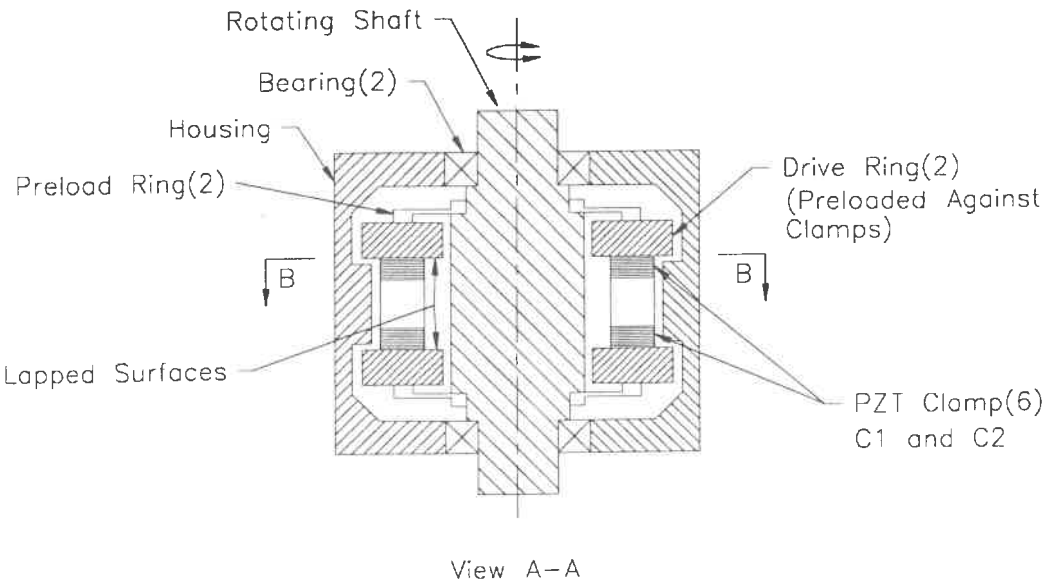

Figure 5 - Cross Section Of Rotary Motor

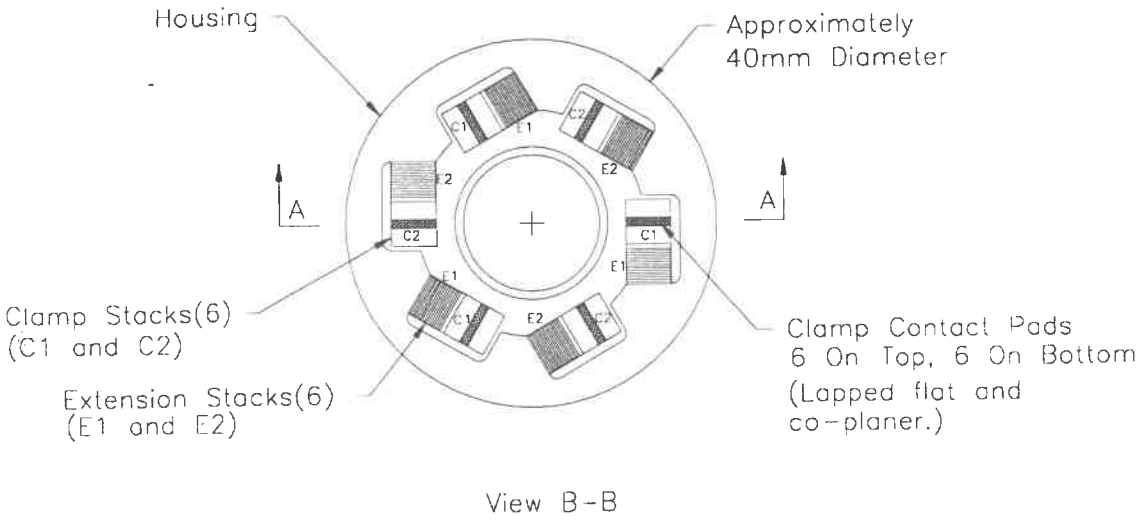

Figure 6
Plan View Of Rotary Motor

References:

1. David Henderson, "A New Inchworm® Motor For Industrial Nanopositioning Applications", ASPE Annual Meeting, 1995.

2. Dan E. Luttrell, Thomas A. Dow, "Design of a Constant Velocity Micro-Stepping Actuator", Precision Engineering Center Annual Report, 1987.

A Long-Range Scanning Stage Design (The LORS Project)

Mike Holmes, Robert Hocken
Precision Engineering Group, University of North Carolina,
Charlotte, NC, USA

David Trumper
Mechanical Engineering Department, Massachusetts Institute of Technology,
Cambridge, MA, USA

This extended abstract describes a magnetically-suspended six-degree-of-freedom precision motion control stage which is presently being built in the Precision Engineering Laboratory at the University of North Carolina at Charlotte. This Long-Range Scanning (LORS) stage will have travel in the horizontal plane of 25 mm^2 along with 100 μm of vertical travel. Vertical position feedback will be provided by three capacitance probe sensors while heterodyne laser interferometry will be used for lateral position feedback. The stage is to have a positioning resolution of 0.1 nm, positioning repeatability of 1 nm, and a positioning accuracy of 10 nm. These performance objectives have been chosen to match the measurement requirements associated with present and future production needs for devices such as integrated circuits, photo-masks, and micromechanical actuators.

Keywords: magnetically suspended; precision motion control

Introduction

The objective of this research is to analyze, design, construct, and test a precision motion control stage with performance objectives of 0.1 nm positioning resolution, 1 nm repeatability, and 10 nm accuracy inside the 25 x 25 x 0.1 mm^3 range of travel. The LORS stage will be used for the positioning of samples in scanned probe microscopy. Scanned probe microscopy will ultimately be used to characterize the performance of the LORS stage. The LORS stage is scheduled to come on-line in February of 1997 with a project completion date of August 1997. This extended abstract presents a summary of the final design along with some performance predictions.

Mechanical Design

The LORS stage, shown in Figures 1 and 2, consists of a moving element (**platen**), a **machine frame**, and a **metrology head**. The bottom of the platen holds four permanent magnet arrays. A **reference block** is mounted to the top of the platen via three flexures[1,2]. As in previous work[3,4], the platen is light-weighted and floated in oil to reduce bias currents in the motors and to provide viscous damping and high-frequency coupling. The stator windings are mounted in the machine frame opposite the magnet arrays. The reference block contains the reference surfaces for the position feedback sensors, namely, target mirrors for the interferometers and a conductor plane which acts as the targets for the capacitance probes. The sample to be imaged is supported by a sample holder

which is kinematically mounted to the reference block. The metrology head is kinematically mounted to the top of the machine frame. The metrology head contains the feedback sensors, three interferometers for lateral position feedback and three capacitance probes for vertical position feedback. The metrology head also provides support for the scanned probe microscope head. To reduce the effects of thermal drift, the metrology head and the reference block are made of Zerodur, with a coefficient of thermal expansion of[5] 0.05 μm/m/°C. The idea is to control the currents in the motors, thereby controlling the forces exerted on the platen, based on the position feedback from the interferometers and the capacitance probes. We will be able to image various samples which will be placed on the sample holder. The scanned probe interface mount is designed to support various types of scanned probe microscope heads (i.e., Atomic Force Microscopes (AFM) and Scanning Tunneling Microscopes (STM)).

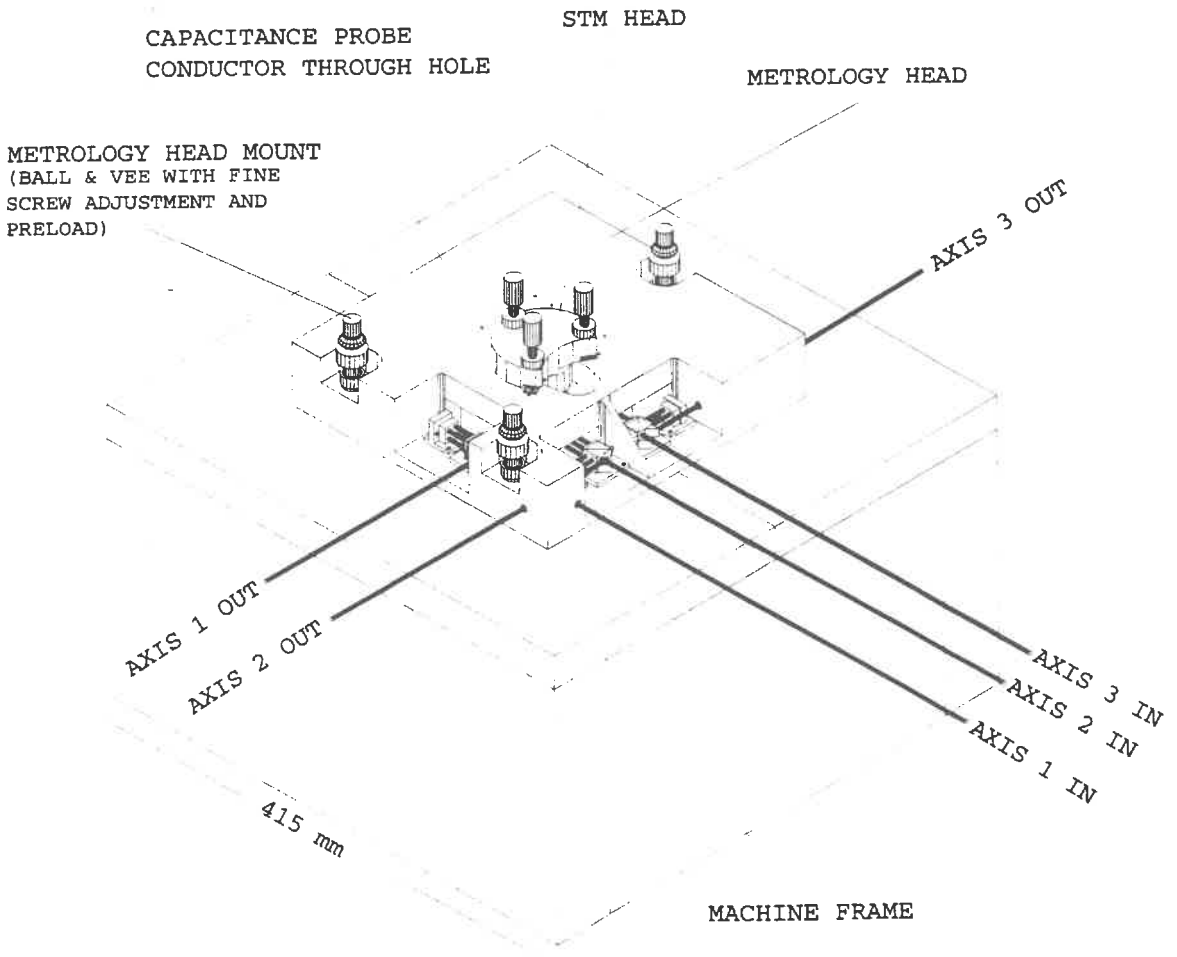

Figure 1: The LORS Stage (External View)

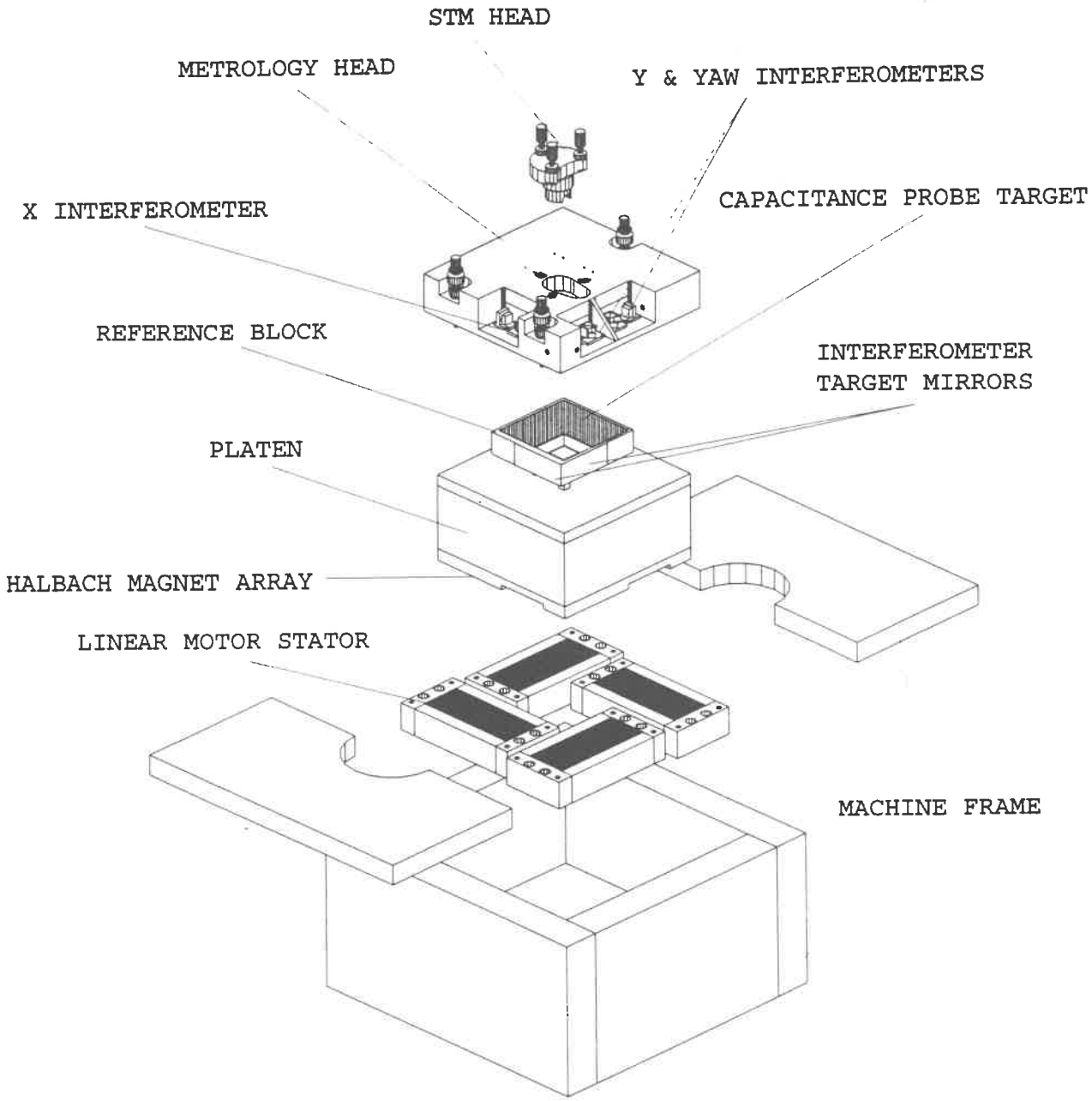

Figure 2: The LORS Stage (Exploded View)

Linear Motor Design

Four linear motors[6], of the type shown in Figure 3, are used to suspend and servo the moving element (platen). The design procedure is outlined by Trumper et al[7] where the design of a two phase linear motor is presented. For the sake of brevity, only the key features of the LORS Stage linear motors are presented here, the reader is referred to the reference for a detailed treatment of linear motor design.

Each of the linear motors consist of a stator and a permanent magnet array. The permanent magnet array consists of 16 NdFeB permanent magnets arranged in the Halbach configuration[7]. Positioned 500 μm directly beneath the magnet array is the stator (in

Figure 3 the gap between the magnet array and the stator is exaggerated for clarity). The stator consists of 66 coils each of which contains 10-turns of 18 gauge wire. Every sixth coil is connected in anti-series to make a six-phase linear motor. The motor phase resistance is 0.4Ω and the phase inductance is calculated to be approximately 30 μH[8]. The linear motor shown is capable of exerting bidirectional vertical and horizontal forces Fv and Fh as indicated. This motor is designed for a gain of approximately 6 N/A with nominal operational forces of less than 1 N. The combined power dissipation of the four motors when the platen is suspended and driven with a lateral velocity of 1 mm/sec is calculated to be approximately 30 mW. A fixture has been built which will allow us to characterize the force-current-gap relationships for each of the linear motors. This fixture will also be used to measure unmodelled forces resulting from imperfect motor fabrication and assembly.

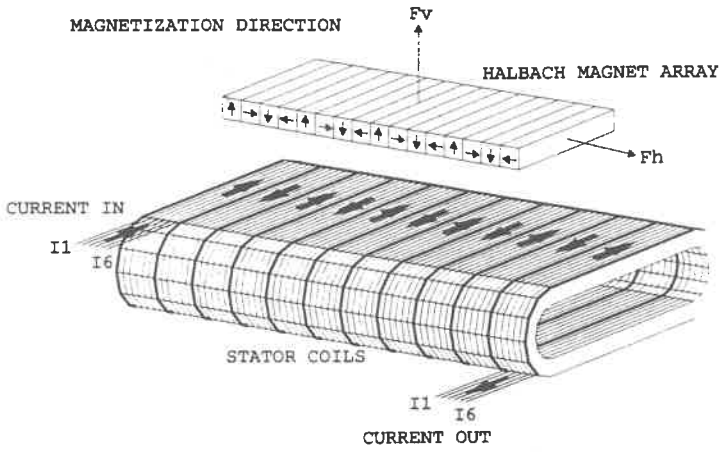

Figure 3: LORS Stage Linear Motor Configuration

Metrology

The LORS Stage metrology scheme is shown in Figure 4. The vertical position of the reference block is measured by the 3 capacitance probes. The capacitance probes are an integral part of the metrology head and are fabricated by depositing aluminum on the polished Zerodur surface. In Figure 4, the probe electrodes are shown in position over the reference block, although these electrodes are part of the metrology head. The overall probe diameter is 35 mm with a sensor diameter of 25 mm. The capacitance gage electronics are being provided by ADE Technologies[9]. The capacitance probes will be calibrated for a range of 100 μm in air with a goal of 0.1 nm resolution inside a bandwidth of 10 Hz.

The lateral position of the reference block is measured by the 3 heterodyne interferometers. The 8 pass interferometer configuration was designed in collaboration with Zygo Corporation[10]. A Time-Interval-Analyzer (TIA) will be used to measure the relative phase of each of the measurement arm signals with respect to the reference arm signals. From this the lateral position and orientation of the reference block will be calculated with a resolution of 0.1 nm inside a bandwidth of 4 kHz.

Some Performance Predictions

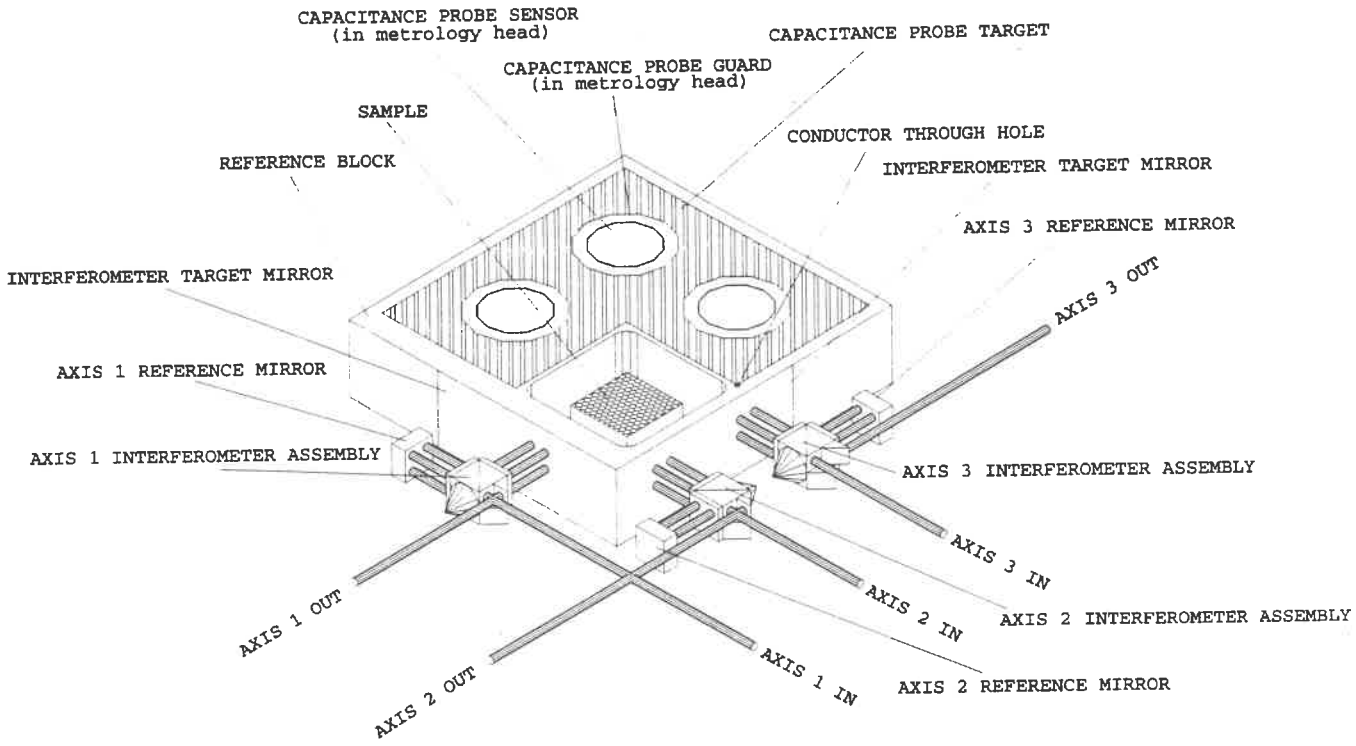

Figure 4: LORS Stage Metrology

The performance of the LORS stage will depend on sensor noise, disturbance forces, environmental influences, and systematic errors resulting from form errors of the reference block. Extensive modelling has been done in an effort to build a set of design tools which were utilized in the design phase of this project in an effort to achieve the performance criterion as stated in the introduction. These tools include a random noise model following the results of Ludwick et al[11,12], a heterodyne interferometer simulator[13,14,15,16,17], and a systematic error budget[5,17,18]. Due to limited space in this extended abstract, only the results of these models are given herein.

The random noise model predicts a vertical position standard deviation of 0.024 nm and a horizontal standard deviation of 0.056 nm. The heterodyne interferometer simulator predicts, for the LORS stage interferometers, a temperature sensitivity of 1.2×10^{-8}m/°C in air and a pressure sensitivity of 2.5×10^{-7}m/psi. The simulator also predicts a 2.5 nm nonlinearity due to beam mixing. Note that the temperature and pressure errors where calculated for a maximum beam air-path imbalance of 12.5 mm. The systematic error budget predicts maximum lateral position errors of 4 nm and 7 nm and a maximum vertical position error of 10 nm.

The random noise predictions are conservative and we expect better performance than predicted. The temperature and pressure sensitivity will become less significant if we run the interferometers in a Helium filled constant pressure vessel which is currently planned. The systematic errors will be mapped in an effort to compensate for them and thereby lessen their influence.

Acknowledgments

This research is being funded by the National Science Foundation. The ADE Corporation

is providing the capacitive gaging electronics and Zygo Corporation is assisting with the metrology head and reference block fabrication.

References

[1] Smith, S.T., and Chetwynd, D.G., *FOUNDATIONS OF ULTRAPRECISION MECHANISM DESIGN*, Gordon and Breach Science Publishers, Yverdon, Switzerland, 1994.

[2] Personal communication with Dr. Stuart Smith.

[3] Holmes, M.L, Trumper, D.L., and Hocken, R. J., "Atomic-scale precision motion control stage (The Angstrom Stage)," *CIRP Ann.*, vol. 44, no. 1, pp.455-460, 1995.

[4] Holmes, M.L., and Trumper, D.L., "Magnetic/fluid-bearing stage for atomic-scale motion control (the Angstrom stage)," *Precision Eng.*, vol. 18, no. 1, pp. 38-49, Jan. 1996.

[5] Slocum, A., *Precision Machine Design*, Prentice Hall, Englewoods Cliffs, NJ, 1992.

[6] Trumper, D.L., "Magnetic Suspension Techniques for Precision Motion Control," Ph.D. Thesis, Dept. of Elec. Eng. and Comp. Sci., M.I.T., Camb., Mass., Sept., 1990.

[7] Trumper, D.L., Williams, M.E., and Nguyen, T.H., "Magnet Arrays for Synchronous Machines," in *Proc. IEEE IAS 28th Annu. Meet.*, Oct. 1993, pp.9-18.

[8] Trumper, D.L., Kim, W.J., and Williams, M.E., "Design and Analysis Framework for Linear Permanent-Magnet Machines," in press, *IEEE Trans. Ind. Applic.*, vol. 32, no. 2, Mar/Apr 1996.

[9] ADE Technologies, 77 Rowe Street, Newton, Mass. 02166.

[10] Zygo Corporation, Laurel Brook Road, Middlefield, Conn. 06455.

[11] Ludwick, S.J., and Trumper, D.L., "Noise Optimal Control in a Fluid-Floated Magnetic Positioner," in *ASME International Mechanical Engineering Congress and Exposition*, Atlanta, GA., Nov. 96.

[12] Ludwick, S.J., Trumper, D.L., and Holmes, M.L., "Modeling and Control of a Six Degree of Freedom Magnetic/Fluidic Motion Control Stage," *IEEE Transactions on Control Systems Technology*, vol. 4, no. 5, Sept. 1996.

[13] Howard, L.P., and Stone, J.A., "Computer modeling of interferometer errors using matrix methods," Proceedings ASPE Annual Meeting, pp. 143-146, 1995.

[14] Personal communication with Dr. Lowell Howard at NIST.

[15] Estler, W.T., "High-accuracy displacement interferometry in air," Applied Optics, Vol. 24, No. 6, 15, March 1985.

[16] Bobroff, N., "Recent advances in displacement measuring interferometry," Meas. Sci. Technol., **4**, 907-926, 1993.

[17] Personal communication with Dr. Robert Hocken.

[18] Evans, C., Hocken, R., and Estler, T., "Self-Calibration: reversal, redundancy, error separation, and "absolute testing."," *CIRP Ann.*, vol. 45, no. 2, 1996.

A Study on a High-Precision Linear Motion Table with Magnetic Bearing Suspension

Yoon Joung, Hyeong-Joon Ahn*, Oui-Serg Kim*, In-Bae Chang** and Dong-Chul Han***

Ultraprecision group, Production Engineering Center, Samsung Electronics Co., Suwon, Korea

*Graduate Student, Dept. of Mech. Design and Production Eng., Seoul National Univ.

** Dept. of Precision Mechanical Eng., Kangwon National Univ., Chuncheon, Korea

***Dept. of Mech. Design and Production Eng., Seoul National Univ., Seoul, Korea

Abstract

This paper describes a design, analyses and performances of a new type linear motion table with magnetic bearing suspension. Linear motion table with 250mm stroke in X axis is drived by linear motor and 5 d.o.f in other axes are actuated by magnetic bearing at arbitrary X position. The motor drives the table through its center of mass so that the driving forces may not cause any moment on the table which lead to Abbe errors on the table surface. The table consists of a platen and four magnetic bearing units and Each unit which consists of 3 electromagnets and 3 capacitance sensors affords control of forces by detecting the air gap between the table and guideway. Modeling of the 5 d.o.f system is carried out and compared with the experimental results in this paper. The performance test including positioning accuracy and resolution of the table system shows the feasibility of utilizing magnetic bearing suspension in high precision semiconductor manufacturing equipments.

1. Introduction

Magnetically levitated table system has lots of advantages when it is used in high precision machines like wafer steppers, IC measurement systems and scanned probe microscopy. A fully levitated stage requires no lubricants, which generates wear particles, and is well suited in high clean or vacuum environment. Also it has perfectly no friction and shows no stick-slip motion so that relatively high resolution can be obtained in comparison with other mechanical bearings. Many researches in this field are under way recently, and show good performances.[1-4]

This paper describes the design, analysis and performance of a new type 5 d.o.f linear motion table with magnetic bearing suspension. The table of 250mm stroke is driven by a linear motor and its position is detected by a linear scale. The table consists of platen and four magnetic bearing units which are composed of electromagnets and capacitance sensors. Each magnetic bearing is controlled by displacement feedback signal from each capacitance sensor placed in line with electromagnets. One main axis of the table is driven by a linear motor in 250mm stroke, and other 5 axes are actuated by 6 magnetic bearings by controlling bias current in each electromagnet. The positioning accuracy and resolution of the table depends not on bearings but only on linear scale.

2. System Design

Table system. The typical system of interest here consists of guideways, supporting bed, linear motor with linear scale, and moving table with built-in gap sensors and electromagnets. Figure 1 shows the schematics of the linear motion table system.

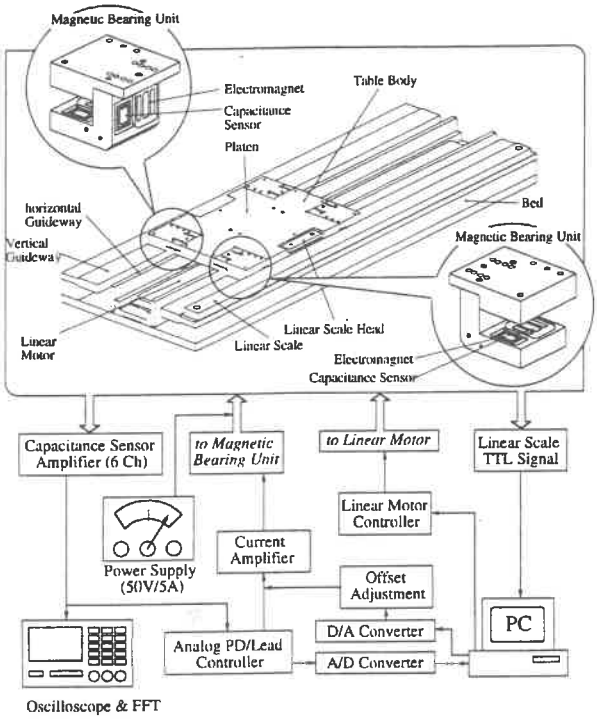

Fig. 1 Schematics of the linear motion system

The table consists of platen and four magnetic bearing units which can act as a suspension and 5 d.o.f actuators. Linear motor drives the table along the horizontal guideway through its center of mass according to its position feedback signal of the linear scale. In consequence, one d.o.f (long stroke) of the table is driven by linear motor and the other 5 d.o.f are actuated by each magnetic bearing.

Magnetic Bearing unit. Each magnetic bearing unit in figure 1 is composed of 3 electromagnets and 3 sensor plates. Two electromagnets placed opposite to each other in vertical axis act as a vertical bearing which support the platen by controlling the electromagnetic forces. Also one electromagnet placed in the side of this unit act as a horizontal bearing together with one in the other unit. Capacitance sensor plates are placed in line with each electromagnet to feedback the displacement signal of the table to the controller immediately.

Controller & Gap sensor. 6 Ch capacitance gap sensors are used to feedback the displacement signal to the controller. The plates of the sensor with amplifiers are made in our laboratory, performance of which was proven in an early report[2]. To improve a linearization characteristic of the sensors, the signal of each sensor plate was differentially amplified so that two sensor plates become one gap sensor.

As shown in figure 1, each sensor signal is amplified and transmitted to the analog P/D controller which has offset adjustment, P/D, lead & phase compensation and filter circuits. The sensors placed close to each magnetic bearing allow us to use simple analog controller so that the table system can be made very simple and reliable.

Table. 1 Specifications of the table system

Table system	Table size	250×250mm
	Stroke	250mm(X axis) 0.1mm(Y,Z axis)
	Resolution	0.25㎛
	Accuracy	< ±1㎛
Electro magnet	Clearance	0.6 mm
	Core	0.35mm thickness Si steel 72 sheets
	Coil	ϕ 0.35 330 turns
	Pole area	320 mm^2
Gap sensor	Bandwidth	1.2 kHz
	Linearity	1%
	Linear range	±0.05mm
	Resolution	0.1㎛
Linear motor	Stroke	250mm
	Peak force	30 lbs
	Acceleration	1 g
Linear Scale	Resolution	0.25 ㎛
	Accuracy	±1㎛

Linear motor & Linear scale. To get 250mm stroke of the table, linear brushless D.C. motor is used which has simple structure and has no contact nature. Normag BLC04-32 motor with 30 lbs of peak force, has no attraction force in any other axis than driving axis so that the motor gives no disturbance force to the magnetic bearings. Heidenhein LS405 linear scale with 10㎛ of grating period shows good performance to use in position feedback system of less than 1㎛ order accuracy.

3. System Modeling

Figure 2 shows the coordinate system for 5 d.o.f modeling of the table.

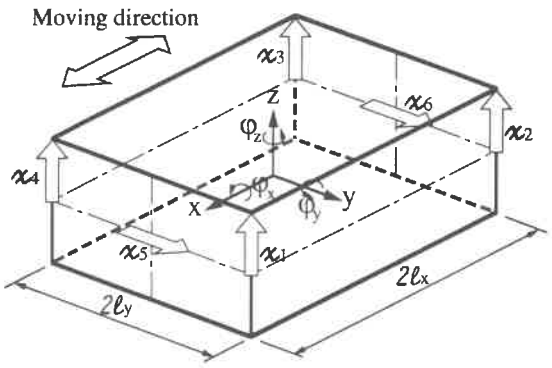

Fig.2 Coordinate system for 5 d.o.f modeling

The displacement of actuating point in Cartesian coordinate is $\vec{x} = [y\ z\ \varphi_x\ \varphi_y\ \varphi_z]^T$ and local displacements, which consist of four vertical and two horizontal direction, are $x_1 \sim x_6$, where electromagnets are placed. Once a position vector $\vec{R}_i$ and a direction vector $\vec{N}_i$ of each actuator are defined, local force, (f), generated by each bearing and external force, $\vec{F}$, on Cartesian coordinate are related as follows;

$$\vec{N}_a \cdot (f) = \vec{F} \tag{1}$$

where actuator characteristic matrix $\vec{N}_a$ is defined as,

$$\vec{N}_a = (\vec{Q}_1, \vec{Q}_2, \cdots\cdots, \vec{Q}_n) \tag{2}$$

$$\vec{Q}_i = \left[\vec{N}_i^T, (\vec{N}_i \times \vec{R}_i)^T\right]^T$$

The sensor signal s_i can be defined with sensor characteristic matrix $\vec{N}_s^T$ as follows,

$$(s) = (s_1, s_2, \cdots, s_n)^T = \vec{N}_s^T \cdot \vec{x} \tag{3}$$

$$\vec{N}_s^T = (\vec{N}_1^T, (\vec{N}_1 \times \vec{R}_1)^T) \tag{4}$$

$\vec{N}_a, \vec{N}_s^T$ are function of the distance of electromagnets l_x, l_y.

Governing equation of the system is as follows;

$$M\ddot{\vec{x}} + K\vec{x} = \vec{F} \tag{5}$$

$$M = diag[m\ \ m\ \ J_x\ \ J_y\ \ J_z]$$

$$K = diag[2k_{yy}\ \ 4k_{zz}\ \ 4k_{zz}l_y^2\ \ 4k_{zz}l_x^2\ \ 4k_{yy}l_x^2]$$

where m is mass of the table, J_x, J_y, J_z are mass moment of inertia with respect to axes x,y and z. The position stiffness at each direction, k_{yy} and k_{zz} ,is the force variation due to the table displacement at nominal table position.

Finally figure 3 shows the block diagram for system modeling.

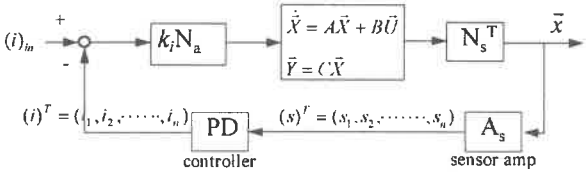

Fig.3 Block diagram for system modeling

where the state variables are

$$\vec{X} = [y\ \ z\ \ \varphi_x\ \ \varphi_y\ \ \varphi_z\ \ \dot{y}\ \ \dot{z}\ \ \dot{\varphi}_x\ \ \dot{\varphi}_y\ \ \dot{\varphi}_z]^T$$

and k_i is an actuator gain which is a function of bias current.

4. Experimental Results

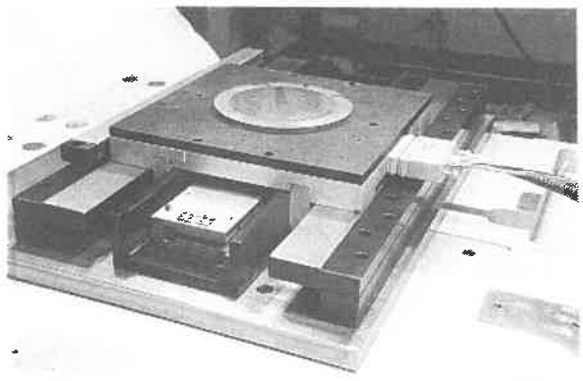

Fig. 4 General view of the table system

Figure 4 shows the general view of the linear motion table system.

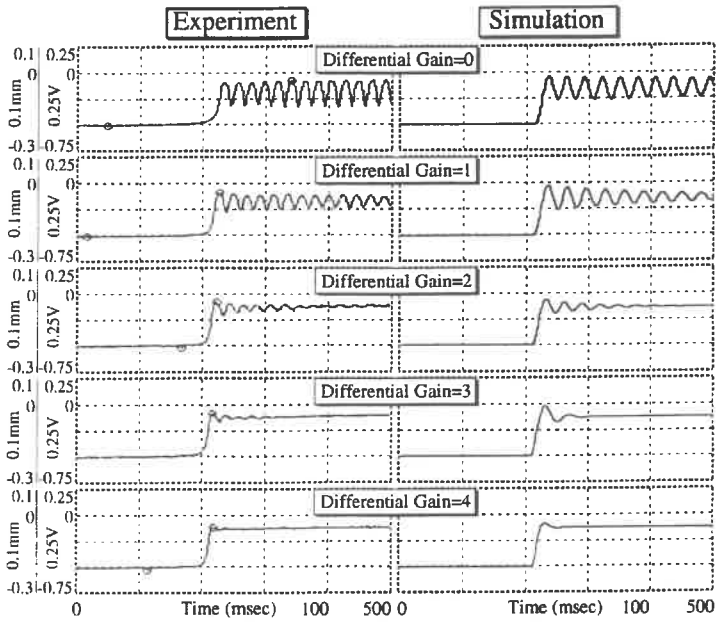

Fig. 5 Step response of the table system

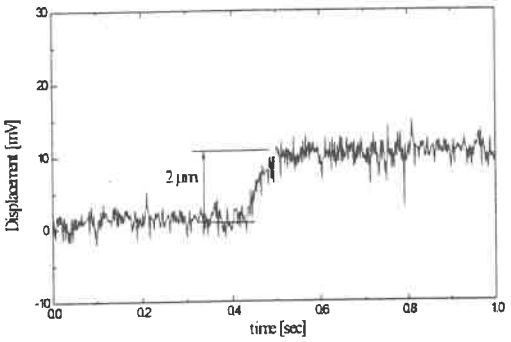

Fig. 6 2μm step in Z-axis

The result of step response of the system by experiment and simulation is shown in figure 5. The validity of analytical results are confirmed by comparison with experimental results. The damping characteristics could be improved by increasing the differential gain of the controller, however, the system becomes unstable when the gain is more larger than 5. Figure 6 shows 2 μm step in Z-axis, perpendicular to the main axis, by actuating electromagnet with DAC of 12 bits resolution. Noise component in figure 6 is ground noise which limits the position resolution of the bearings.

5. Conclusions

Linear motion table with magnetic bearing suspension and built-in capacitance gap sensor has been developed. Linear motor and linear scale of 0.25μm resolution are adopted to get 250 mm stroke in X-axis and other 5 axes are controlled by each magnetic bearing in 0.1mm stroke. Analytical results of 5 d.o.f modeling and experimental result show good agreement.

Acknowledgements

This work was funded by Samsung Electronics Co. and supported in part by Turbo & Power Machinery Research Center and Institute of Advanced Machinery & Design in Seoul National University.

References

[1] M.E.Williams, D.L.Trumper. "Precision magnetic bearing six degree of freedom stage", *3'rd Int'l Symp. on Magnetic Suspension Tech.*, July, 1995, pp.453.

[2] Y.Joung, S.C.Jung, I.B.Chang, D.C.Han, "An experimental study on the high-precision linear motion table with magnetic bearing suspension", *Proceedings of ASPE 10'th Annual Meeting*, Oct., 1995, pp.328.

[3] D.Eisenhaure, A.Slocum, A.R.Hockney, "Magnetic Bearings for Precision Linear Slides", *1'st Int. Symposium on Magnetic Bearings*, 1988, pp. 67.

[4] S.Shingu, "Design Method of Magnetically Suspended Positioning Mechanism", *Journal of JSME*(in Japanese), Vol.55, No.518, 1989, pp.2559.

[5] I.B.Chang, "A study on the performance improvement of a magnetic bearing system using built-in capacitive type transducer", Ph.D. diss., Seoul Nat'l Univ., 1994, Seoul, Korea

FABRICATION AND THERMAL ANALYSIS OF A GAS-LIQUID PHASE-CHANGE MICRO-ACTUATOR

Shigeo KATO
Nippon Institute of Technology,
Miyashiro, Saitama 345, Japan

1. Introduction

When a liquid is vaporized, the volume of the phase-changed gas is more than 200 times that of the liquid. Gas-liquid phase-change actuators are thermal engines that utilize the large change in volume that occurs during a phase-change. These actuators are expected to be applied as the micro-actuators used in micro-robots operating in very small pipings or the human-body, because conventional electric power, laser beams or microwaves can be used as the source of vaporizing energy. So far, these actuators have been applied as micro-pumps for very small flow rates. Mizoguchi et al. fabricated a micro-pump whose flow rate was 30 nl per cycle [1]. We have fabricated a prototype of a gas-liquid phase-change micro-actuator that supplies an actuating force of 3 N to micro-robots sufficient to operate in the human-body. This paper presents a fabrication and thermal analysis of the gas-liquid phase-change micro-actuator.

2. Characteristics of the fabricated actuator

A cross section of the fabricated micro-actuator is shown in Fig. 1. The casing including the flange is made of aluminum. It has a liquid pool with a volume of 79 μl. The volume of 79 μl is almost the same as that of two or three drops from an eye-dropper. The operating fluid is R-113, because its vaporizing temperature, though higher than the human body, is still only 47.56 °C and its latent heat for vaporization is only 1/16 that of water. Consequently, the energy needed for vaporization is very low. The operating liquid is heated by a heater 0.2-mm thick and 136-mm long made of coiled constantan wire with an electrical resistance of 2.1 W. The force of volume-change is received by a 0.2-mm thick artificial rubber-membrane, then transferred to the stroke of a small piston.

An electrical power of 2.1 W is supplied with in 1 second to the heater and it is cut after 3 seconds. This operation is repeated. The maximum displacement of the piston gradually increases. After 60 seconds, the maximum displacement reaches 1 mm and the minimum displacement reaches 0.44 mm. This motion is shown in Fig. 2 by the solid line.

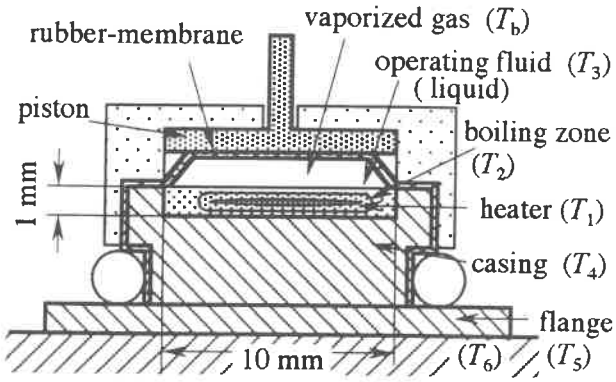

Fig. 1 A gas-liquid phase-change micro-actuator

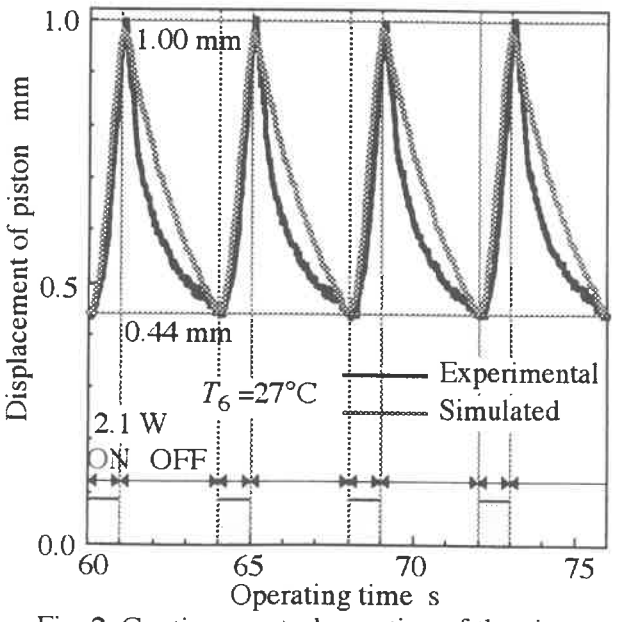

Fig. 2 Continuous stroke motion of the piston

Thus, this actuator is confirmed to have a reciprocating motion with a 0.5-mm stroke at an average power of 0.525 W. In order to make a mathematical thermal model of the actuator, 1-stroke motion was examined in an experiment. If the heater is heated by 2.1 W of electricity, the piston starts to move up 0.41 seconds after power is supplied at an ambient temperature of 26°C and its displacement reaches 1 mm 2.2 seconds after power is supplied.

By switching off the power, the piston begins to move downward after 0.2 seconds delay. Its displacement is 0.4 mm after 5 seconds, and 0.15 mm 10 seconds after the power switched on. This motion is indicated by the solid line in Fig. 3.

If the power decreases to 0.5 W from 2.1 W, the stroke of the piston freezes. The performance of the actuator is considered to be thermally critical. In this case, the ambient temperature (T_6) is 25 °C, the temperature of the flange is 26.35 °C, and the temperature of the operating liquid is 37 °C.

3. Mathematical model of the actuator

In order to simulate the actuator, we needed to create a mathematical thermal model of the actuator. A model of the actuator is shown in Fig. 4. The temperature distribution is very complicated. However, we simply considered five thermal elements receiving the heat and their temperature changes. These are (1) the heater, (2) the operating liquid near the heater (boiling zone), (3) the operating liquid near the casing, (4) the actuator-casing, and (5) the flange for dissipating the heat. If we select only one liquid for the operating fluid, we cannot explain why vaporization starts 0.41 seconds after power is supplied. The heat capacity, the temperature, and the heat transfer area of the element-i are C_i(J/°C), T_i(°C), and A_i(m^2), respectively. The heat flow rate and the heat transfer coefficient from element-i to element-(i+1) are q_i(W), and h_i(W/m^2°C), respectively. The heat flow rate to the heater is q_H(=2.1 W). The heat flow rate for vaporizing is q_V(W). The heat flow rate when the vaporized gas is re-liquefied and the liquefying area are q_L(W) and A_L(m^2), respectively. Simultaneous differential equations of the thermal model are solved by the Runge-Kutta method.

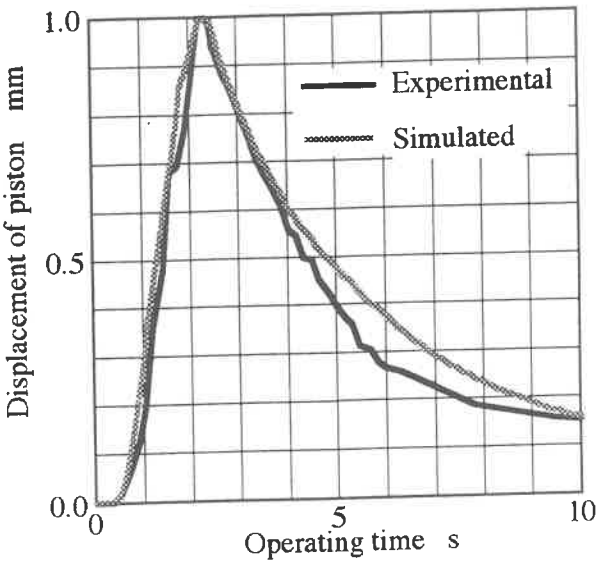

Fig. 3 Displacement of piston versus the operating time

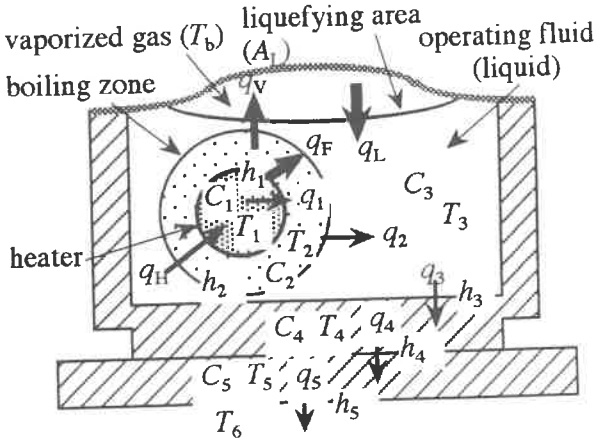

Fig. 4 Thermal model of the actuator

3.1 Under power supply (from start to vaporization)

When power is supplied to the heater, the operating liquid near the heater quickly vaporizes. For the period from the start till vaporization occurs, the heat balances of the five thermal elements are represented by next five differential equations. t represents the operating time.

$$C_1 \frac{dT_1}{dt} = q_H - q_1 = q_H - A_1 h_1 (T_1 - T_2) \quad (1)$$

$$C_2 \frac{dT_2}{dt} = q_1 - q_2 = A_1 h_1 (T_1 - T_2) - A_2 h_2 (T_2 - T_3) \quad (2)$$

$$C_3 \frac{dT_3}{dt} = q_2 - q_3 = A_2 h_2 (T_2 - T_3) - A_3 h_3 (T_3 - T_4) \quad (3)$$

$$C_4 \frac{dT_4}{dt} = q_3 - q_4 = A_3h_3(T_3 - T_4) - A_4h_4(T_4 - T_5) \quad (4)$$

$$C_5 \frac{dT_5}{dt} = q_4 - q_5 = A_4h_4(T_4 - T_5) - A_5h_5(T_5 - T_6) \quad (5)$$

3.2 Under power supply (boiling zone is partial in the pool)

When the temperature of the operating liquid near the heater reaches the boiling temperature (T_b=47.56 °C), vaporization starts. When vaporization starts, the relating heat transfer coefficients h_1 and h_2 are assumed to change to h_{1V} and h_{2V}, respectively.

$$C_1 \frac{dT_1}{dt} = q_H - q_1 = q_H - A_1h_{1V}(T_1 - T_b) \quad (6)$$

$$C_2 \frac{dT_2}{dt} = 0 \quad (7)$$

$$C_3 \frac{dT_3}{dt} = q_2 - q_3 + q_L = (A_2h_{2V} + A_Lh_L)(T_b - T_3) - A_3h_3(T_3 - T_4) \quad (8)$$

$$C_4 \frac{dT_4}{dt} = q_3 - q_4 = A_3h_3(T_3 - T_4) - A_4h_4(T_4 - T_5) \quad (9)$$

$$C_5 \frac{dT_5}{dt} = q_4 - q_5 = A_4h_4(T_4 - T_5) - A_5h_5(T_5 - T_6) \quad (10)$$

$$q_1 - q_2 = A_1h_{1V}(T_1 - T_2) - A_2h_{2V}(T_2 - T_3) = q_V + q_F \quad (11)$$

The zero in Eq. (7) shows that temperature T_2 maintains the boiling temperature, and $(q_1 - q_2)$ is obviously not equal to zero. The term q_F in Eq. (11) is the heat flow rate that is used to spread the vaporizing zone (the operating liquid near the heater). Supposing that β is a constant less than 1, it is assumed that terms q_V and q_F can be represented as follows.

$$q_V = \beta (q_1 - q_2) \quad (12)$$

$$q_F = (1 - \beta)(q_1 - q_2) \quad (13)$$

Increasing of the vaporizing zone is represented as

$$(T_b - T_3) \frac{dC_2}{dt} = q_F = (1 - \beta)\ (q_1 - q_2) \quad (14)$$

The mass per unit of time of the vaporizing fluid (kg/s) is represented as

$$m_V = \frac{q_V - q_L}{H_b} \quad (15)$$

where H_b is the latent heat for vaporization (kJ/kg °C) of the operating fluid.

Table 1 Simulation data

Heat Transfer Area	A_1=85.4 A_2=85.4 – A_3=109.9 A_4=95 A_5=530 A_{L1}=78.5	×10⁻⁶ m²
Heat Capacity	C_1=0.0156 C_2=0.000128 – C_3= – 0.111 C_4=1.252 C_5=2.582	J/°C
Heat Transfer Coefficient	h_1 =560 h_{1V} =1120 h_2 =549 h_{2V} =1098 h_3 =432 h_{3V} =880 h_4 =30000 h_5 =699 h_L =80	W/m² °C
Ratio of Heat Flow Rate for Vaporization	β=0.103	

3.3 Terminated power supply (no boiling zone)

$$C_1 \frac{dT_1}{dt} = -q_1 = -A_1h_1 (T_1 - T_3) \quad (16)$$

$$C_2 \frac{dT_2}{dt} = 0 \quad (17)$$

$$C_3 \frac{dT_3}{dt} = q_1 - q_3 + q_L = A_1h_1(T_1 - T_3) - A_3h_3(T_3 - T_4) + A_Lh_L(T_b - T_3) \quad (18)$$

$$C_4 \frac{dT_4}{dt} = q_3 - q_4 = A_3h_3(T_3 - T_4) - A_4h_4(T_4 - T_5) \quad (19)$$

$$C_5 \frac{dT_5}{dt} = q_4 - q_5 = A_4h_4(T_4 - T_5) - A_5h_5(T_5 - T_6) \quad (20)$$

$$q_L = A_Lh_L(T_b - T_3) \quad (21)$$

$$m_V = -\frac{q_L}{H_b} \quad (22)$$

Eq. (17) shows that C_2 is equal to 0.

4. Supposition of the heat transfer coefficients

Using the heat transfer areas shown in Table 1 and critical power of 0.5 W, some heat transfer coefficients have been supposed. We consider that T_2 is at a boiling temperature of 47.56 °C. Under these conditions, h_2 is 549, h_3 is 432, h_4 is 3×10^4, and h_5 is 699 (W/m² °C).

The heat transfer coefficient h_1 is estimated from the start-up time of the piston. The initial

thickness of the fluid near the heater is considered to be 1, 5 or 10 μm. The relationship between the heat transfer coefficient h_1 and the start-up time of the piston is simulated. Since we know h_1=572 (W/m^2°C) from the calculation and the start-up time of the piston is 0.41 s, the initial thickness of the fluid near the heater may be about 1 μm. We decided to use h_1=560 (W/m^2°C) and 1 μm for the initial thickness of the fluid near the heater for simplicity.

If the heat transfer coefficient h_3 increases, heat transfer to the casing increases and vaporization decreases. Since the displacement of the piston reaches 1 mm at t= 2.2 s, we know that the heat transfer coefficient h_{3V} is equal to 880 (W/m^2 °C) by simulation. This value is about two times h_3=432 (W/m^2 °C) which is the heat transfer coefficient prior to boiling. Consequently, we supposed that h_{1V} and h_{2V} which are heat transfer coefficients may be two times the heat transfer coefficients prior to boiling, i.e., h_{1V} = 1120, h_{2V} = 1098 (W/m^2 °C), respectively.

The heat transfer area for liquefying A_L is an area of 10-mm diameter (A_{L1}=78.5x10^{-6}m^2) if the displacement is as large as H= 1 mm. However, if the displacement of the piston decreases, the area where the gas and liquid come in contact with each other may decrease due to the capillary phenomenon. If the displacement is zero, then area A_L may be zero. Consequently, we assume that area A_L is related to displacement H and is represented as

$$A_L=A_{L1}\left(\frac{H}{H_1}\right)^2 \tag{23}$$

where H_1 shows a displacement of 1-mm.

The heat transfer coefficient for liquefying h_L is assumed to be h_L= 80 (W/m^2 °C), because this value enables the displacement of the piston to reach H=0.15 mm 10 s after power supply is supplied.

5. Simulation of the displacement of the piston

We simulated the displacement of the actuator using the values shown in Table 1. We used a value of β=0.103, because this value enables the displacement of the piston to reach H=1 mm 2.2 s after energy is supplied.

The relationship between volume V (μl) of the vaporized gas and displacement H (mm) is represented as

$$V=69\,H \tag{24}$$

The relationship between the pressure in the rubber membrane P (MPa) and the displacement H (mm) is represented as

$$P=0.101+0.04H \tag{25}$$

The pressure and the volume are represented by the equation of state for the ideal gas as

$$PV=M_V\,R\,T_b \tag{26}$$

where M_V and R are the mass of the gas in the rubber membrane and the gas constant of the operating fluid, respectively.

Because the molecular weight of R-113 is 187.376, from Eqs. (24), (25), and (26), the relationship between the displacement H and the mass of the gas M_V(kg) is represented as

$$H\,(0.101+0.04\,H) = 149050\,M_V \tag{27}$$

If we know the mass of the gas, we obtain the displacement of the piston by Eq. (27).

The results of the simulation for one stroke of the piston are shown in Fig. 3 by the dotted line. We see a difference of about 0.1 mm at t=6 s. However, we know that although the simulation coincides with the experiment there is a small difference. The simulation of the continuous reciprocating movement of the piston is shown in Fig. 2 by the dotted line. It is confirmed that continuous reciprocating movement of the piston with a 0.5-mm stroke can be simulated.

6. Conclusions

(1) We fabricated a gas-liquid phase-change micro-actuator that is 16 mm in diameter and 10 mm thick, and that has a liquid pool with a volume of 79 μl. The operating fluid was R-113. This actuator generated a force of 3N.

(2) By dividing the operating fluid into two thermal elements, we could make a simple mathematical model for the gas-liquid phase-change micro-actuator.

(3) By experiment and simulation, the actuator was confirmed to reciprocate continuously with a 0.5-mm stroke at an average input power of 0.525 W.

Reference

[1] H. Mizoguchi, M. Ando, T. Mizuno, T. Takagi, and N. Nakajima: Proc. of Micro Electro Mechanical Systems '92 pp. 31-36.

LOAD-DEPENDENT BEHAVIOUR IN PTFE-GLASS SLIDEWAYS

A. F. Monteiro and D. G. Chetwynd

Centre for Nanotechnology and Microengineering
Department of Engineering,
University of Warwick, Coventry CV4 7AL UK

Introduction. There has been much recent interest in using slideways for nanometre-precision linear translation [1,2]. Typically, these are constructed with an optically polished glass prismatic surface carrying thin-film PTFE bearing pads. Compared to elastic deformation mechanisms these offer the possibility of much larger ranges and lower parasitic tilts in yaw, roll and pitch. However, one characteristic of sliding motion, particularly significant at the nanometre level, is a hysteretic (lost motion) behaviour, documented in theoretical modelling and laboratory tests [3,4]. This sliding hysteresis (typically of the order of 100 nm) is a result of the stresses and strains present at the contact points between the moving carriage feet and the flat slideway surface and theory suggests that its magnitude is strongly dependent on the normal load at the contact points.

Reducing the hysteresis is important if there is a need to work open-loop to high levels of accuracy, but even when feedback is used a much flatter hysteresis cycle helps make the control system reliable and easier to design. Thus an experimental investigation has been carried out into how in practice reducing the normal force at the bearing pads of an ultra-precision slideway carriage will alter the sliding hysteretical curve.

Modelling. Each bearing pad of the slideway behaves as a Hertzian contact with a thin film entrapped between harder sphere and flat. Theoretical models of Hertzian contacts under transverse load were developed as early as 1953 by Mindlin and Deresiewicz [3], by making some plausible assumptions about the distribution of regions of microslip and of elastic contact, relaxing the solutions to the ensuing stress distributions in order to smooth discontinuities and then assuming that in the microslip regions the horizontal traction is given by the conventional limiting friction condition of the local normal load. They considered only the contact of spheres of identical material in the initial model, but given the nature of the other approximations, extending it to our more complex interface does not appear an extreme step.

Hertzian analysis shows that pressing a smooth sphere of radius R onto a smooth flat surface by a stationary perpendicular force P, causes a circular contact zone of radius a, given by

$$a = \left(\frac{3PR}{4E^*}\right)^{1/3} \qquad (1)$$

where

$$\frac{1}{E^*} = \frac{1-\upsilon_1^2}{E_1} + \frac{1-\upsilon_2^2}{E_2} \qquad (2)$$

and ν and E are the Poisson's ratio and elastic modulus of the two materials respectively. Applying a tangential force T to the sphere, would cause an infinite stress around the edge of the circular contact region unless microslip started there and as T increases, an annular region of slip grows towards the centre of the contact area with an inner radius of slip, c, given by

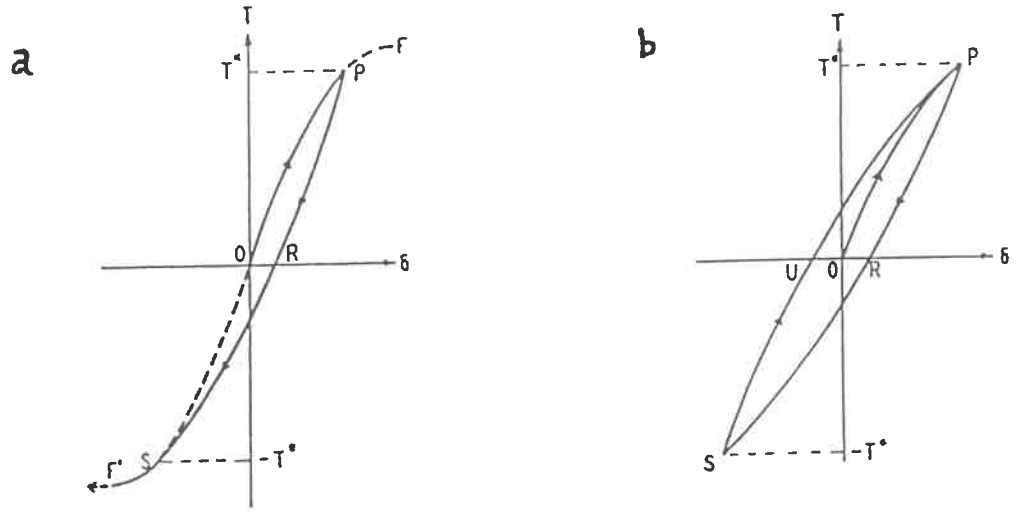

Figure 1: Hysteretic transverse displacement of sphere under microslip under (a) initial load and unload and (b) continued cyclical loading.

$$c = a\left(1 - \frac{T}{\mu P}\right)^{1/3} \qquad (3)$$

where μ is the coefficient of friction. When T reaches μP, the inner radius reduces to a point and sliding occurs. For $T < \mu P$, Mindlin and Deresiewicz estimate the lateral displacement from elastic deflections of the non-slip region as

$$\delta_t = \frac{3(2-u)\mu P}{8Ga}\left(1 - \frac{c^2}{a^2}\right) = \frac{3(2-\upsilon)\mu P}{8Ga}\left[1 - \left(1 - \frac{T}{\mu P}\right)^{2/3}\right] \qquad (4)$$

where G is the shear modulus (taken by us to be that of the interface material).

If we load initially to some value T^* and then decrease the load towards zero and into the opposite direction, similar analysis shows that there will be an offset in the displacement, figure 1a, that leads to a classic hysteresis curve if the cycle is repeated, figure 1b. We define the hysteresis (H) of this cycle as the maximum difference in the respective positions of the bearing at the same nominal point for the two directions of travel (twice the length OR in figure 1a) given by

$$H = 2 \times \frac{3(2-\upsilon)\mu P}{8Ga}\left[2\left(1 - \frac{T^*}{2\mu P}\right)^{2/3} - \left(1 - \frac{T^*}{\mu P}\right)^{2/3} - 1\right] \qquad (5)$$

The cyclic lost motion from these elastic effects if gross sliding is allowed is found by setting T^* to μP, the limiting condition. As the radius of the bearing remains basically fixed for a given system, it can be absorbed, along with elastic properties, into a constant K, so

$$H = K\mu P^{2/3} \qquad (6)$$

Experimental Method. Tests of sliding-direction hysteresis were carried out on a mechanism specially designed and built to study kinematic techniques for straight line motion with sub-nanometre and sub-milli-arc-second error motions [4], figure 2. It is made almost completely of Zerodur ultra-low-expansion glass ceramic, with sintered PTFE-bronze-lead bearing pads, spherically radiused and carrying a thin (generally sub-micrometre) film of PTFE across their surface. A 45° half angle optically flat prism is connected to a base plate forming the slideway

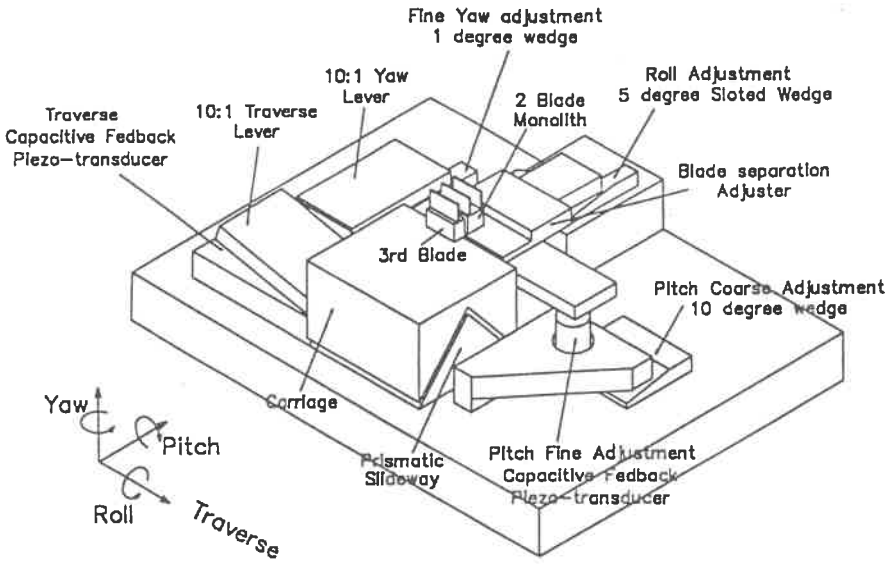

Figure 2: The super-precision kinematic slideway system [4].

assembly. A carriage block with a prismatic V cut from its underside rests on the slideway supported by five PTFE pads, three on one side of the prism and two on the other to form a kinematic arrangement with one degree of freedom. The carriage is driven by a piezoelectric actuator employing local capacitive feedback to provide linear motion at the nanometre level. This motion is then further reduced by a 10/1 reduction lever which pushes the carriage forward. The thrust-line of this lever is aligned closely along the carriage friction centre line. The carriage is pre-loaded against the driver by a simple helical spring, and its traverse is measured using a laser interferometer system, where a spot beam is bounced off a small mirror attached to the carriage. The stage was mounted on a granite table in a room temperature controlled to about ±1 K and held at approximately 40% relative humidity. The stage was enclosed by a Perspex cover to reduce air currents and thermal drift around the interferometer light paths. The input and output interferometer beams go through the clear plastic enclosure while all uncompensated (i.e. not common path) beams remain inside. The Hewlett Packard interferometer has an ideal resolution of 10 nm, estimated to be reduced to a useful resolution of 20 nm under these operating conditions.

The system includes a weight reduction mechanism for the moving carriage, figure 3. Supported by a metrology frame, a non-rotating-spindle micrometer holds a yoke suspending three soft springs which are attached to three spring posts on the moving carriage. Raising the micrometer stretches the suspension springs which then support a proportion of the carriage weight, the rest of which is balanced by the normal force on the contact bearings. This force can be reduced to very low values while ensuring that the slideway remains in proper kinematic contact. While unsuitable for most practical bearings, this geometry allows very soft springing that makes negligible any thermally related effects in the lifting system and ensures that there is no detectable change in the lift as the carriage travels over the range of motion here being used. The springs were selected such that an easily measured extension of 5 mm was required to completely lift the carriage while keeping well within their linear (Hooke's law) mode of behaviour. The micrometer adjustment then gave a load adjustment resolution much higher than required and overall linearity can be assumed based just on the reading of the micrometer. The experimental

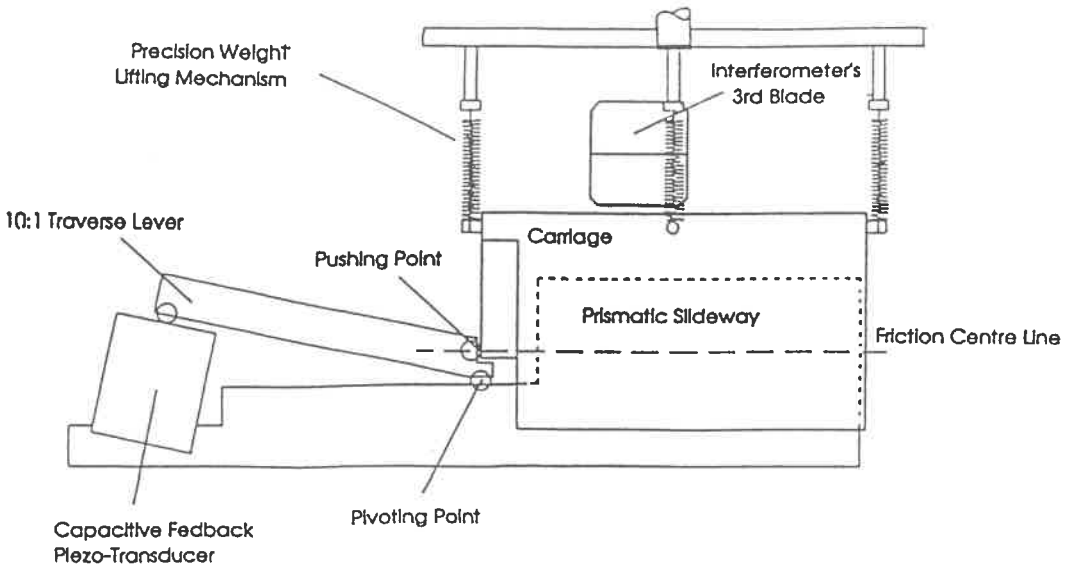

Figure 3: Details of the linear drive and weight reduction system.

investigation depends on the ability to change the load in known proportions, which is ensured by the linearity of the arrangement, and there is no special benefit in having a very precise knowledge of the load in absolute terms. Thus the force calibration consisted simply of weighing the carriage and then measuring the spring extension required to cause lift-off.

The carriage was driven back and forth through nominally ± 500 nm for two complete cycles while recording both the drive actuator displacement (from its internal capacitive gauge) and the resultant motion of the carriage (detected by the interferometer). The actuator control box was adjusted manually to give nominal positions and then the laser reading noted after a few seconds delay to ensure that the system had stabilized. This sequence was repeated for different settings of the micrometer head on the weight reduction mechanism, starting at a bearing load of around 0.5 N (9.5 mm at the head) and increasing it in steps of 0.5 N to 5.5 N (4.5 mm). Note that this procedure depends on the moderate stiffness of the coupling between drive and stage to relax sufficiently for the stage to follow the pads rather than the drive output.

Results and discussion. Figure 4 shows example cyclical plots using loads of 0.5 N and 5.5 N. Each cycle was performed twice to improve reliability and get a measure of the drift present in the interferometer system. The thermal drift over times of one or two minutes (attributable almost entirely to the interferometer) was roughly linear (experimental observation) and this first order effect can then be subtracted from the raw data (such as shown in figure 4) to obtain H. It was considered more practical to subtract modest drift from the measurements than to allow very long settling periods at each set-up. Observed drifts of up to half the width of the hysteresis loop in any measurement cycle were accepted for this procedure. The hysteresis is then the maximum separation of the higher and lower parts of each corrected cycle, which in practice always occurred at the mid-point of the cylce. It is plotted against the normal loading on the bearings in figure 5. The uncertainty in these readings is estimated to be around 20 nm standard deviation.

Experimentally, the load P is well represented by the displacement, d, of the micrometer supporting the weight-reduction springs. Taking the lowest micrometer reading at which the stage floats above the slideway with no normal loading as d_0, equation 6 can be re-written as

$$H = K_2(d - d_0)^{2/3} \qquad (7)$$

where K_2 is a constant incorporating K, μ and the combined stiffness of the three springs to the power of 2/3. This model can be compared to the data by estimating best-fit values for K_2 and d_0 but simple procedures for doing this are very sensitive to errors in d_0 at low loads. However there is little sensitivity to the offset at higher loads and so iterative procedures converge rapidly. By such an approach, values of $d_0 = 9.95$ mm and $K_2 = -73.4 \times 10^{-7}$ m$^{1/3}$ were found to be a good empirical fit to the data. The plot of the experimental data, figure 5, includes this theoretical fit and also shows the residual errors of the data from the line. The quality of the agreement strongly suggests that the hysteretic behaviour of the complex combination of materials in our bearings is not functionally different from the simple, single material case considered in [3] and above.

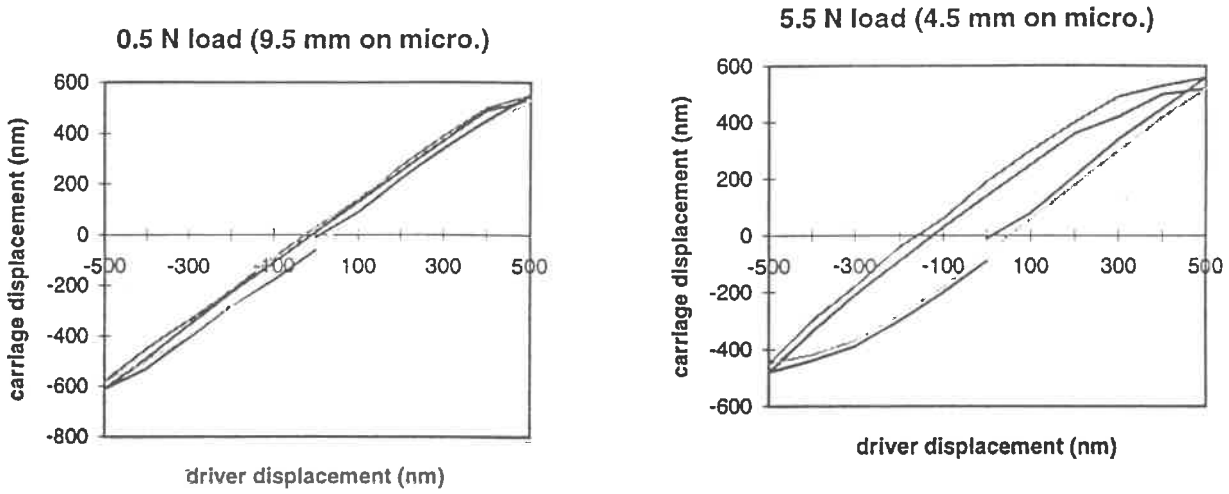

Figure 4: 'Raw' data of displacement resulting when drive is cycled at different bearing loads.

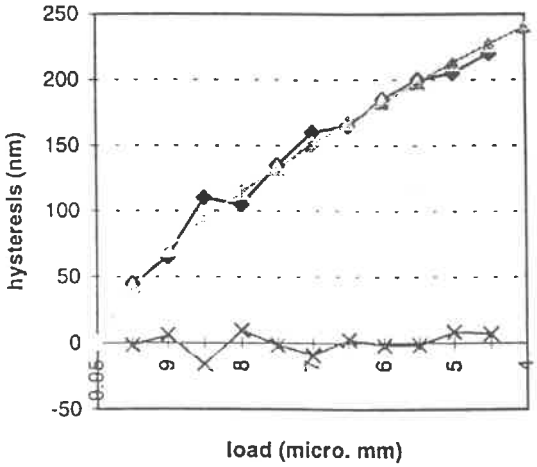

Figure 5: Measured hysteresis and best-fit form of equation (7), with residuals also plotted.

Parameter estimation. While the current experiments can readily show the general functional behaviour, they cannot provide values for the actual interface conditions, since the effects of several variables that cannot be directly determined are combined there. Nevertheless it is instructive to examine the data in the light of plausible assumptions about interface conditions. The combined spring constant of the suspension is about 1000 N m^{-1}. The friction coefficient for PTFE on glass is normally between 0.08 and 0.2. A relatively high value of 0.15 is used here because there is some evidence that the friction coefficient rises slightly at low loads and a very low traverse speed is being used (dynamic coefficient ≈ static coefficient). Given such considerations $K \approx 5\times10^{-7}\,N^{-2/3}m$ is the value obtained experimentally.

The model form is not very sensitive to small changes in the elastic moduli of the materials (cube-root relationships), so if we assume the shear modulus for the interface is that of bulk PTFE, G = 0.15 GPa, and that the pad has Young's modulus between 0.5 and 1.0 times that of glass, a 20 mm radius pad should show $K \approx 2.5\times10^{-5}\,N^{-2/3}$ m. Comparing this to the experimental value, the shear modulus of the interface needs to be increased by a factor of 50 to match our model. This gives G = 7.5 GPa, which is around one quarter of that for the substrate metal. This seems not unreasonable: since the PTFE film is very thin the stiffness of the interface is likely to be very different from that of bulk PTFE, but remains, of course, significantly lower than that of the uncoated metal.

Conclusions. Simple modifications to an approximate, analytic method of modelling transverse displacements of Hertzian contacts through microslip appear to be very effective at predicting the functional form of cyclic lost motion in a precision slideway driven by a position asserting system of finite stiffness. Load reduction is shown experimentally to be effective in reducing this loss. The model provides guidance on the relative effect on the lost motion of varying different design parameters.

References.

[1] Lindsey K., Smith S.T. and Robbie C J, 1988, Sub-nanometre surface texture and profile measurement with Nanosurf 2, *Ann. CIRP*, **37**, 519-22.

[2] Garratt J. D. and Bottomley S.C., 1990, Technology transfer in the development of a nanotopographic instrument, *Nanotechnology*, **1**, 38-43.

[3] Mindlin R.D. and Deresiewicz H., 1953, Elastic Spheres in contact Under Varying Oblique Forces, *Trans. ASME; J.Appl.Mech.*, **75**, *327-344*.

[4] Monteiro A.F., Smith S.T. and Chetwynd D.G., 1996, A super-precision linear slideway with angular correction in three axes, *Nanotechnology*, **7**, 27-36.

MICRO-DYNAMICS OF A SLIDE MECHANISM USING ROLLING ELEMENTS

Yuichi Okazaki*, Shun'ichi Sasaki**, Ryoji Murata**

* Mechanical Engineering Laboratory
Namiki 1-2, Tsukuba, Ibaraki, 305 JAPAN
**Science University of Tokyo
Yamazaki 2641, Noda, Chiba, 278 JAPAN

1. Introduction

Precision motion control of scanning stages is one of the key technologies for scanning probe profilers and beam scanning type lithographer for semiconductors aiming to expand the scanning area, as well as for precision NC machine tools. Rolling guides are most commonly used in linear scanning stages taking advantage of their smaller friction compared to sliding guides and their moderate guiding accuracy depending on the geometrical accuracy of the components. On the other hand its nonlinear friction force often disables the accurate motion control, so that the evaluation of the behavior of the mechanism in a small displacement region is important task for finer motion control. It was already found in 1950th that rolling mechanism shows elastic characteristics in a very small displacement region, i.e., that even a small driving force induces displacement, and that the displacement decreases as the force is removed, along a hysterisis curve [1]. Recently a couple of researches have been started focused on the characteristics of rolling mechanisms intending for ultraprecision motion control of mechanisms [2][3]. In most reports the characteristics were measured quasi-statically or based on simple frequency responses. Dynamic measurements and analysis of the nonlinear characteristics of mechanical slide comprising rolling elements have been done, and a coordination of results of static and dynamic tests concerning the behavior.

2. Experimental setup

The linear slide mechanism used is an ordinary designed stage comprising cross-roller guides driven by a direct mounted DC torque motor (Inland: T-1242-D) through a ball-screw of 14 mm diameter. The clearance of the screw is eliminated by preloading. The motor drive is a common velocity control using a tachogenarator. The displacement of the slide was measured by a laser interferometer with 2.5 nm resolution. The relationship between the velocity command, the displacement and the driving torque derived from the drive current of the motor were measured, while sinusoidal signals with variety of amplitude and frequency were applied as the velocity command.

3. Experimental results and discussion

(1) Frequency response

Fig. 1 shows the measured transfer function from velocity command to the displacement. The system behaves as an integrator for large amplitude commands, in the nature of a velocity control system. For a small amplitude command a resonance-like corner frequency was observed, beyond which the gain decay increases almost -60

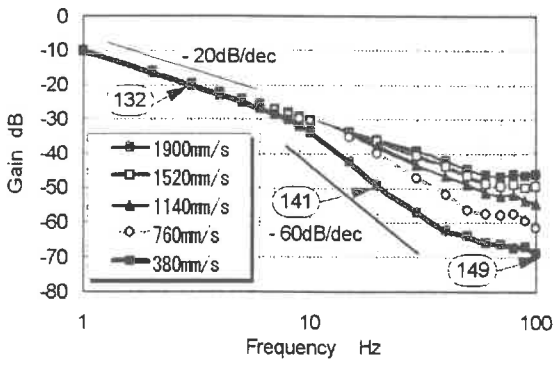

Fig. 1 Frequency response for various input amplitudes

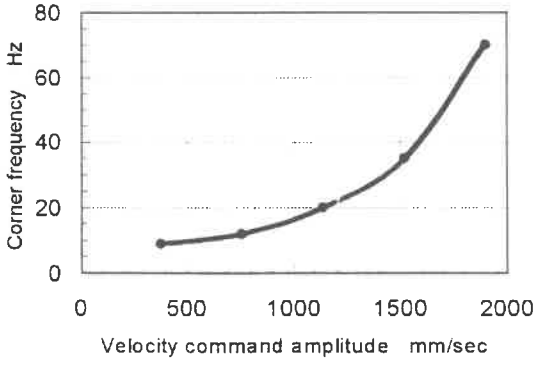

Fig. 2 Resonance-like corner frequency depends on the command amplitude

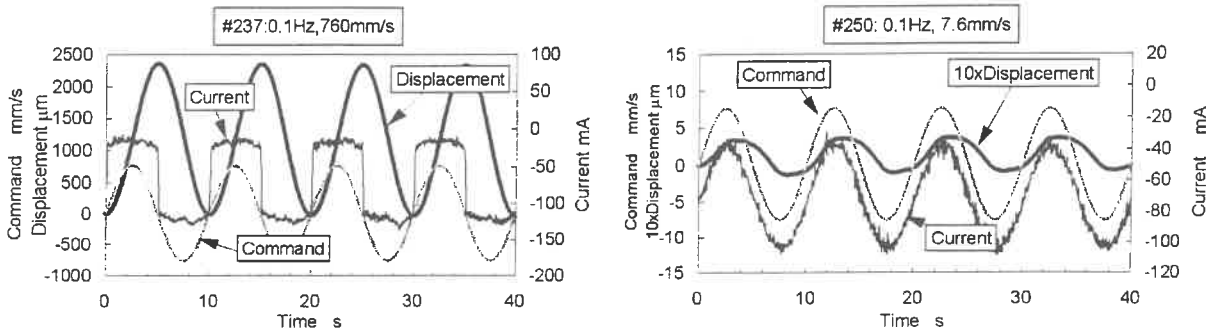

Fig. 3 Command, drive current and displacement.

db/decade. The gain decay is recovered over 60 Hz. The phase lag of the displacement response to the velocity command changes to be -100 degree, -135 degree and -100 degree at 30 Hz (#132), 20 Hz (#141) and 100 Hz (#149) respectively for the command single side amplitude of 380 mm/s. The location of the corner frequency depends on the command amplitude, increasing almost exponentially of command amplitude (**Fig. 2**). This result corresponds to a preceding report [3].

(2) Drive force and displacement

Fig. 3 shows some time series data of the velocity command, the armature current and the displacement. Under some conditions a the saturation of the drive current occurs, despite that both the command and the displacement change smoothly. Other plots of the current versus the displacement (**Fig. 4**) explain that as reported in [2] the curve is divided into three regions, i.e. region I: the stiff small displacement region, region II: the transient region, and region III: the large displacement region where the drive current is almost constant. The two boundaries lie around 100 nm and 5 to 10 μm, but the boundary between region II and III is not obvious. These results well correspond to the reported by quasi-static tests [2]. Furthermore, the result of #199 (**Fig. 4-c**) shows that this relationship is kept for a dynamic drive as well as for a quasi-static drive.

Fig. 5 summarizes the relationship between the phase difference of drive current and the displacement as a function of the command condition. Some data points in preceding figures are marked in the plot. A rough boundary line of the current saturation is also plotted in the figure. For a command of small amplitude and high frequency, the current and the displacement are in-phase, while for a large amplitude and low frequency the current leads the displacement by 90 degrees in phase. Note that a high frequency corresponds to a small displacement amplitude according to the frequency response.

3) Displacement amplitude, resonance-like corner frequency and drive current saturation

Fig. 6 is showing a mapping of the peak-to-peak displacement amplitude for various velocity commands. The command conditions which arises the resonance-like corner frequencies presented in **Fig. 2** are also plotted. The corner frequencies are located close to the line of the displacement amplitude = 10 μm. The actual displacement amplitudes at the corner frequencies lie among 9 and 17 μm.

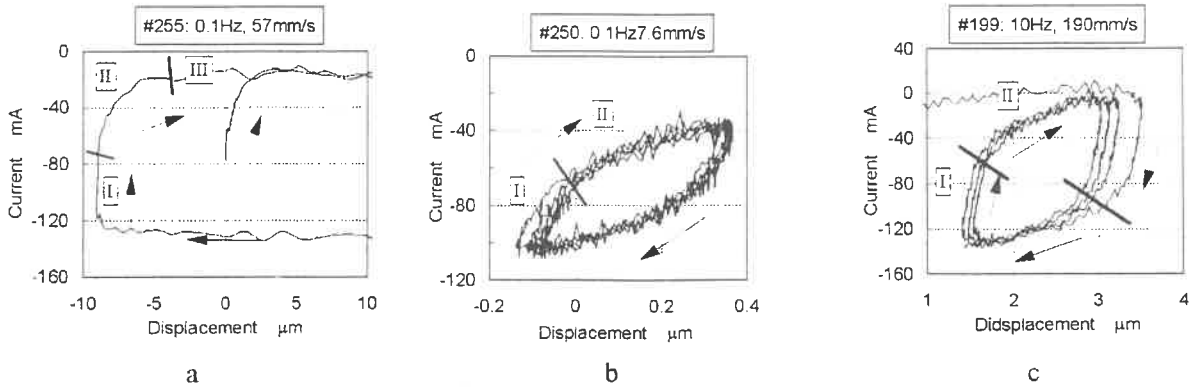

Fig. 4 Some plots of drive current vs. displacement

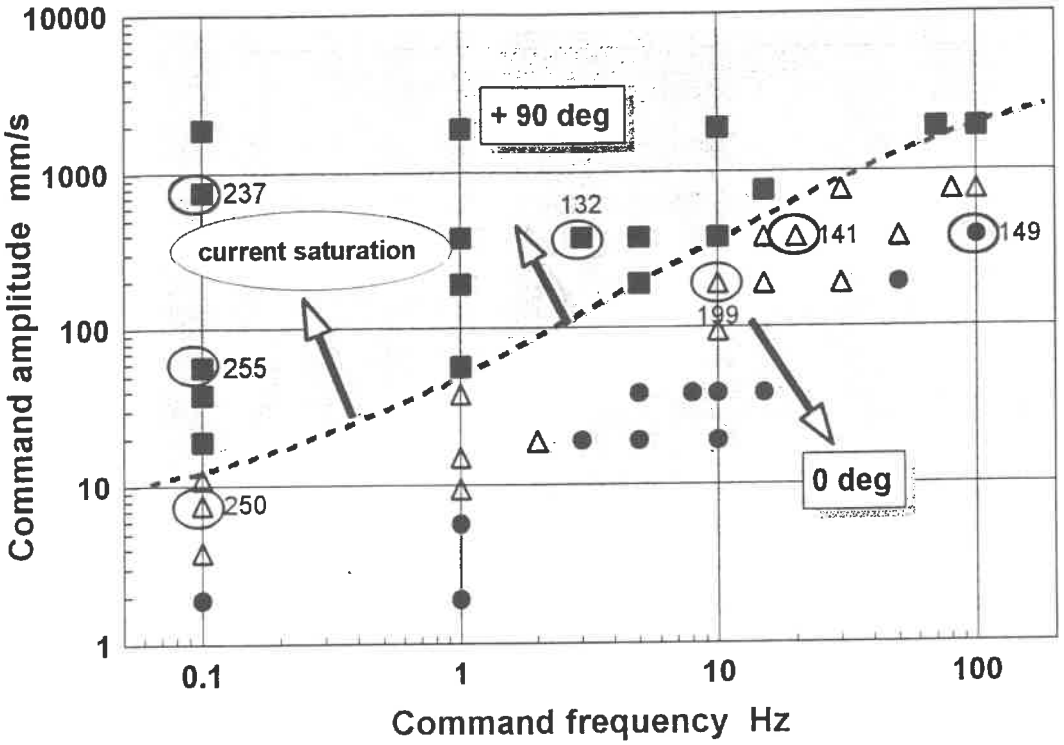

Fig. 5 Phase lead of the drive current to the displacement

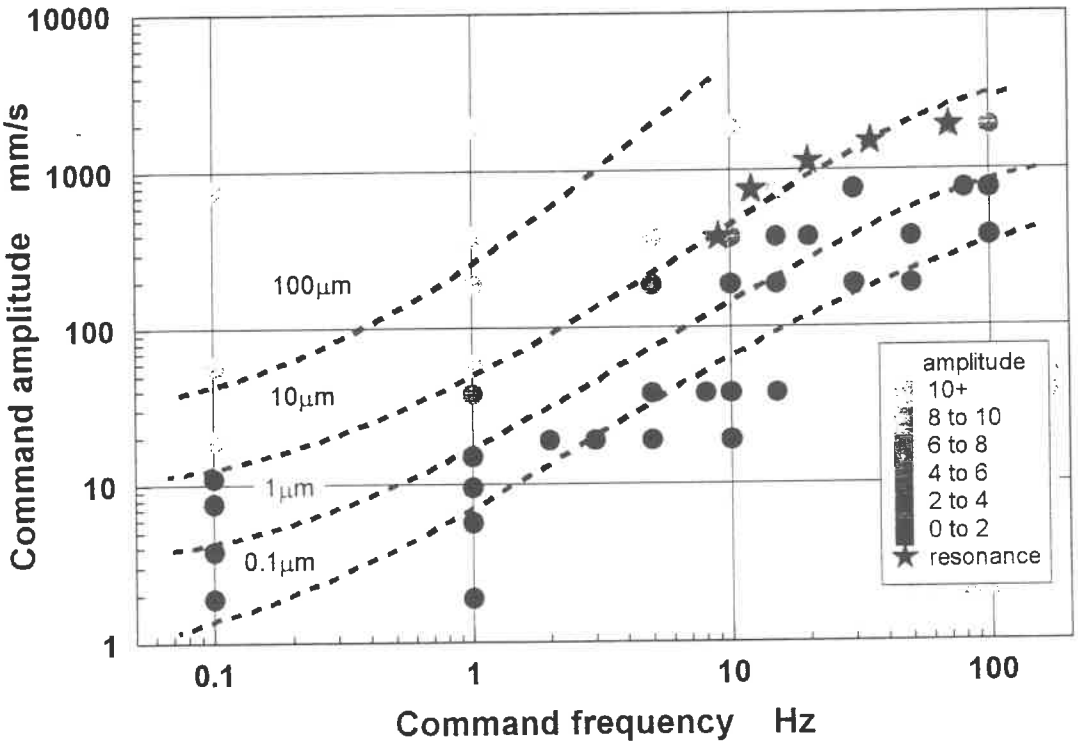

Fig. 6 Relationship between the displacement amplitude and the velocity commands

By comparing **Fig. 5** and **Fig. 6** the following features have been recognized: The current saturation occurs when the displacement amplitude is about 10 μm. The phase of the current leads that of the displacement by 90 degrees in the region of the displacement greater than 10 μm, and is in-phase when the displacement amplitude is smaller than 0.1 μm. The locations of resonance-like corner frequencies also roughly matche the conditions for a constant displacement amplitude of 10 μm. In the region I in **Fig. 4** the displacement amplitude is smaller than 0.1 μm. Because in this region the current and the displacement are in-phase, it proves the system is "elastic" there. In the same manner the model for the region III, i.e. that the system is "rolling" with a constant drive force, is also explained based on the phase difference.

By correcting the phase difference between the drive current and the displacement to zero, another features of current-displacement diagrams are revealed (**Fig. 7**): For almost all tests the correlation of them is virtually linear up to some points, and if the amplitude is large enough, the drive current saturates beyond the points. This saturation should correspond to the saturation in the leading discussion using **Fig. 4,** but is clearer. These curves composed of a straight line and two saturation lines mean that for small displacement amplitude without saturation, the waveforms of the drive current and the displacement are simmilar, despite that the plots for region I and II in **Fig. 4** are curved. The saturation means that the current waveform is distorted compared to the displacement waveform. The average gradient of the curve represents the ration of the drive current to the displacement. For a large displacement with saturation the ratio is smaller than a small displacement. This typical difference explains the gain decrease over the resonance-like corner frequency in the frequency response.

Note that in this diagram only the waveform is discussed, and that the displacement amplitude between the saturation points does not correspond to the actual displacement, and the gradient of the first straight line does not directly mean the effective stiffness of the elastic region I, because the phase relationship is lost.

Another understanding of **Fig. 7 b** is that it represents the drive force as a function of the velocity because the phase difference is about 90 degrees under the condition that current saturation occurs.

4. Conclusions

Through dynamic sinusoidal drive tests to observe micro-dynamics of rolling guideway system the following nonlinear characteristics of the mechanism have been revealed:

1) As already reported, in the diagram of the drive force vs. the displacement the curve is categorized into three regions by the gradient and weather the displacement is elastic or with rolling. This characteristic is also kept under a dynamic drive up to 100 Hz as well as a quasi-static drive qualitatively and quantitatively.
2) The resonance-like corner frequency in frequency response, the phase change and the burst of the displacement amplitude in drive current-displacement transfer characteristics can be associated with in terms of the drive current saturation around 10 μm of the displacement amplitude.
3) The models for the tree regions are proved by phase difference of the drive current and the displacement.

References

1) T. Hisada, Rolling friction and knife-edge resistance, Government Mechanical Laboratory Report 3(1950) (in Japanese)
2) S. Futami et. al., Nanometer positioning and its micro-dynamics, Nanotechnology 1 (1990)31
3) P. Ro et.al., Nonlinear micro-dynamic behavior of a ball-screw driven slide system, Prec. Eng. 14-4 (1992)229

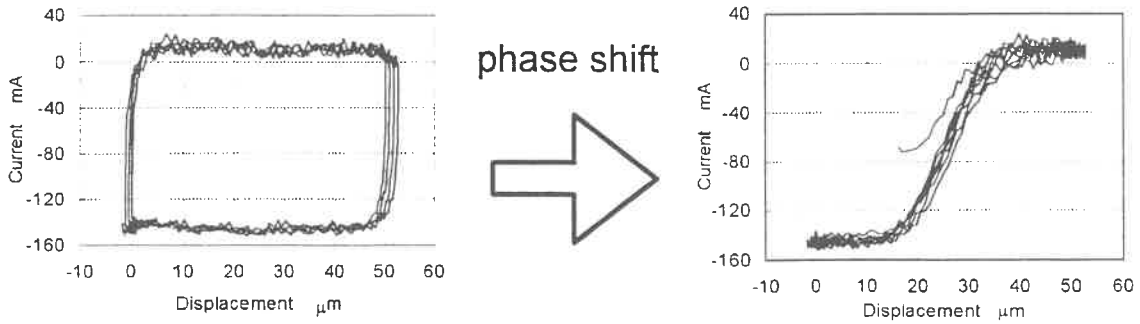

Fig. 7 Phase shift makes the current saturation clear

CHARACTERIZATION OF AN AIR BEARING FOR MIXING STUDIES OF BIOPROCESSES

J.M. Patiño[1], R. Vázquez[1], G. Ascanio[1], E. Galindo[2] and L. Serrano-Carreón[2].
[1] Centro de Instrumentos, UNAM, Apdo. Postal 70-186, México, DF 04510
[2] Instituto de Biotecnología, UNAM, Apdo. Postal 510-3, Cuernavaca, Mor. 62271

Abstract

A new air bearing used for mixing studies bioprocesses has been characterized. This bearing has been improved taking into account the possibility to carry out experiments with higher working volumes. The pneumatic bearing has been designed for using in dynamometer for the accurate measurement of power input and mixing applications in bench stirred reactors.
In this new design many changes have been carried out, such as 18 thrust nozzles distributed in three channels, which provide two resultants: radial and axial, allowing to work with high stability.
Results of characterization show a 106.926 kg maximum load when pressurized air at 5 x 10^5 Pa is introduced. For these conditions, a 2.8 x 10^{-5} m thrust clearence was found, and the static friction coefficient between air and the dynamic part was 3 x 10^{-6}.

Introduction

Power input is variable commonly used in chemical and bioprocess engineering. It is defined as the amount of energy necessary in a period of time, in order to generate the movement of the fluid within a container (e.g. biorreactor, mixing tank, chemical reactor, etc.) by means of mechanical or pneumatic agitation.

The costs associated with power input contribute to the overall costs of industrial plants. Therefore, it is desired that the mixing processes are performed efficiently and with a minimum of energy expenses required to achieve the objetive established *a prioi.*

The knowledge of the power input, in a specific stirred tank reactor, is necessary for scale-up and scale-down procedures, process characterization, modelling, mixing performance as well as transfer and fluid dynamic studies in a bioprocess. The success of a fermentation process depends strongly on the energy transmitted by the impellers to the liquid in the biorreactor tank, therefore the power input is an important factor in the determination of process costs.

Several methods are avalaible for the measurements of the power input in agitated vessels. On large scale, wattmeters and ammeters are suitable. On pilot scale dynamometers coupled to the shaft are commonly used. On bench scale, torquemeters and air bearings dynamometers have been used. In all scales torsion dynamometers and strain gauges can be used.

Dynamometers with bearing supporting a mixing vessel, have been used for the measurement of the power input in bench scale stirred tank reactors. In this case, the reaction torque due to rotation of the impeller in a specific fluid is determined. Nienow and Miles (1969) have developed an air bearing with a stable and trouble-free operations in which friction losses can be practically neglected.

Pneumatic bearings have several applications at industrial and laboratory levels, for example, as a part of dynamometers to measure the power input to a fluid in mixing processes. Considering its low friction coefficient, pneumatic bearings are suitable devices for this kind of equipments.

Description

A dynamometer has been developed for the accurate measurement of power input and mixing applications in bench stirred tank reactors. The dynamometer consists of a drive system, a transparent vessel and air bearing, which characterization is presented in this paper. The drive system consists of a direct current motor coupled to a belt-pulleys arrangement and an agitation shaft with one or two impellers, depending on the experiment. The impeller speed is controlled by an electrical potentiometer measured with a magnetic pick-up, a gear and a tachometer. The vessel consists of a cylinder and a water jacket for controlling the process temperature. In one side of the vessel, a rigid arm pushes against a load cell tip transducer placed at right angles to the arm. The torque transmitted by the impellers to the liquid can be measured when the vessel floats on the pneumatic bearing and tends to turn without restriction.
A diagram of torquemeter and ancillary equipment is shown in figure 1.

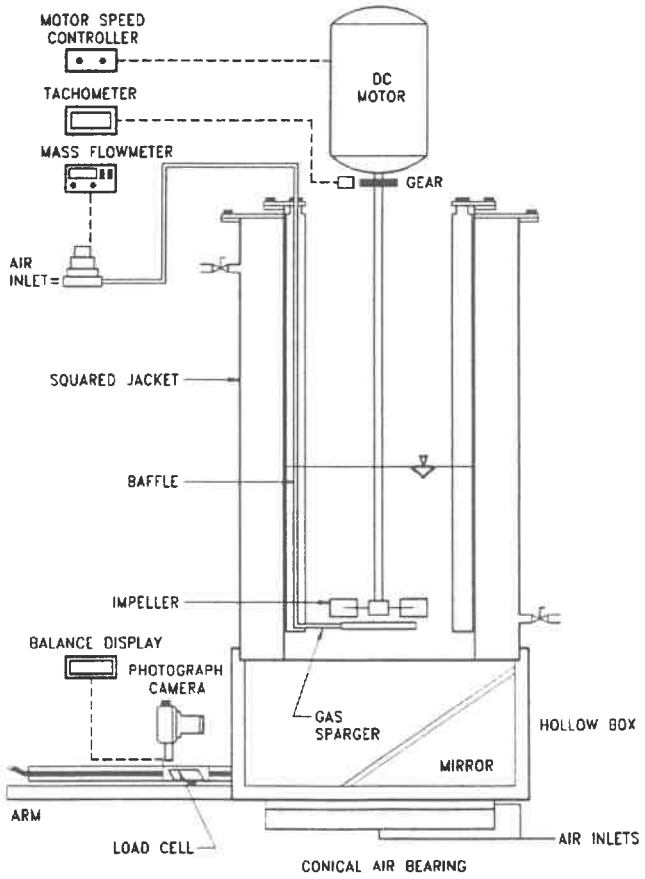

Fig. 1 Diagram of torquemeter with a pneumatic bearing

Design considerations were similar to those originally formulated by Reséndiz *et al* (1991).

The pneumatic bearing has two complementary elements: one static (lower) and the dynamic or floating (upper). The static element has a 40° conical cavity, whose function is to provide and axial and radial thrust component and a central component which provides just radial thrust component to the journal bearing. The pressurized air is introduced into the static element and distributed through the 18 thrust nozzles in three channels, which allows to operate with high stability due to a better air distribution. The dimensions are shown in figure 2.

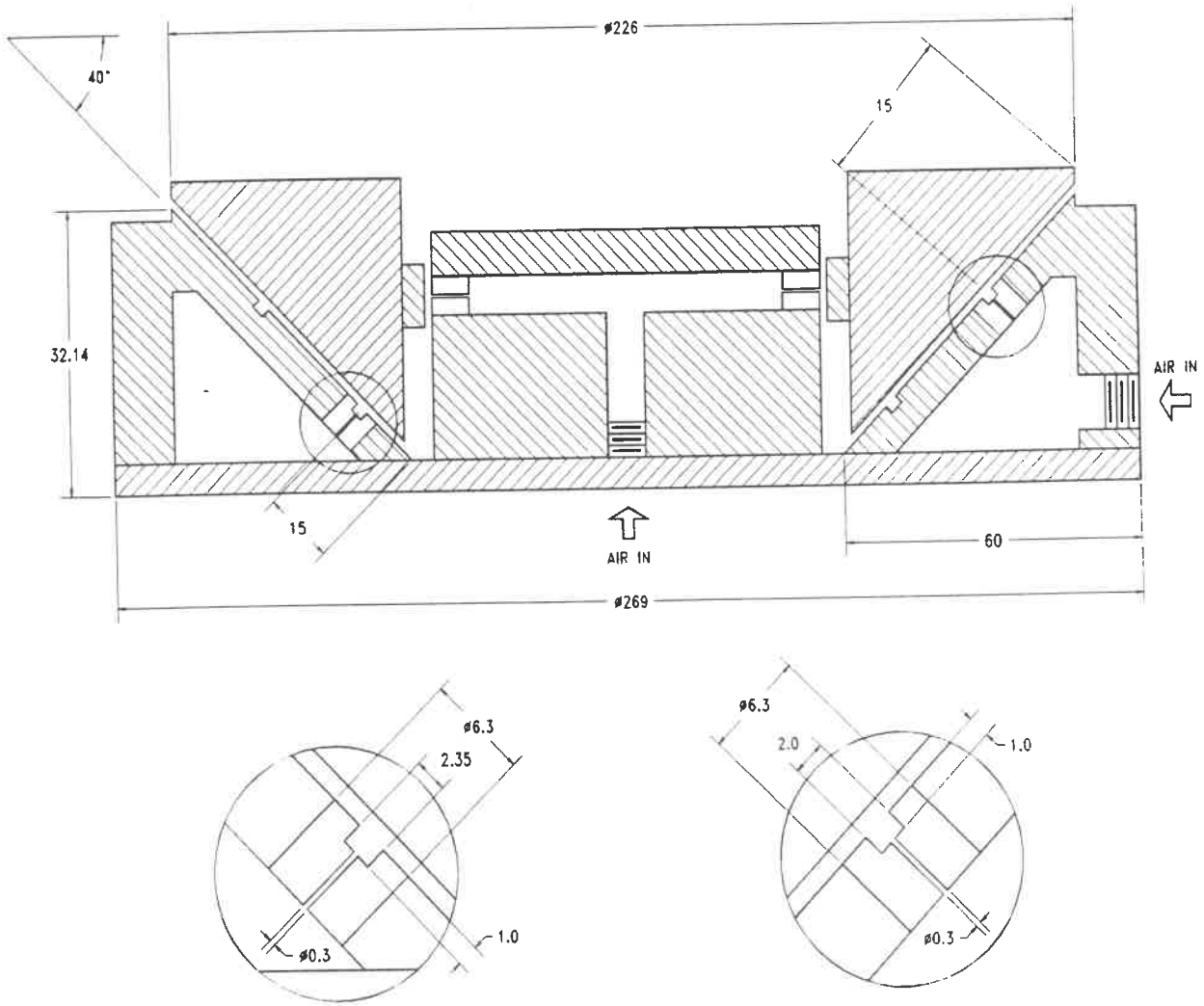

Fig. 2 Dimensions of the conical air bearing (in mm)

Characterization

Using a precision dial indicator, a 2.8 x 10^{-5} m thrust clearence was found, which is necessary for free rotation to occur between the static and dynamic part, when pressurized air is introduced into the pneumatic bearing.
The minimum torque required to rotate the floating vessel, named static friction torque is 4 x 10^{-4} Nm. Considering a very low static friction coefficient between the dynamic part and the air (3 x 10^{-6}) the pneumatic bearing can be considered practically frictionless.

Operating pressures to support masses of 25, 50 and 75 kg were found to be 1.17 x 10^5, 2.3 x 10^5 and 3.5 x 10^5 Pa, respectively. The maximum load that the pneumatic can support is 106.925 kg when pressurized air at 5 x 10^5 Pa is introduced into the bearing.

Conclusions

A pneumatic bearing used for bioprocesses aplications was developed and characterized. This new air bearing concept was carried out taking into account a previous desing of Resendiz *et-al* (1991). One of the fundamental differences to those originally formulated is the 40° conicity instead of 30°, as well as the18 thrust nozzles distributed in three channels, which provide a high stable and trouble-free operation, considering its static friction coefficient, which is of the order of 10^{-6}. The new pneumatic bearing allows to work with higher loads compared to the previous design.

References

1 Brown, D., *Chem. Ind. (N.Y.) 16* (1977) pp. 684-688.
2 Nienow, A.W. and Miles, D., *J.Sci.Instrum. 2* (1969) pp. 994-995
3 Reséndiz, R. et-al, *Chem. Eng. Technol. 14* (1991), pp. 105-108
4 Holman, J.P., *Experimental Methods for Engineers*, McGraw-Hill, Tokyo 1971.
5 Patiño, J.M., Vazquez, R., Bachelor thesis, National University of Mexico (1995).

Industrial inspection interferometer having a large equivalent wavelength

Peter de Groot and Carl Zanoni

Zygo Corporation, Laurel Brook Road, Middlefield, CT 06455

We have constructed an interferometer suitable for testing flat surfaces that are either too rough or deformed for conventional visible-wavelength interferometry.* The instrument uses a diffractive optical assembly to illuminate the test piece at two different incident angles, using visible wavelength light. The reflected beams recombine to generate an interference pattern with an equivalent wavelength twenty times larger than the actual wavelength of the illumination.[1,2] The slope tolerance and the acceptable surface roughness are correspondingly increased with respect to conventional interferometry.

The diffractive optical assembly is comprised of two linear diffraction gratings having a one-to-two frequency ratio (Fig.1). The beams make a double pass through the gratings, with a reflection from the object between the passes. The interference fringes have excellent contrast, because both of the interfering beams reflect off the object and the intensity balance is nearly independent of the surface reflectivity. The interference effect is achromatic, and conventional incandescent sources generate clear, colorless fringes.[3] The design is also compatible with inexpensive visible-wavelength laser diodes and LED's.

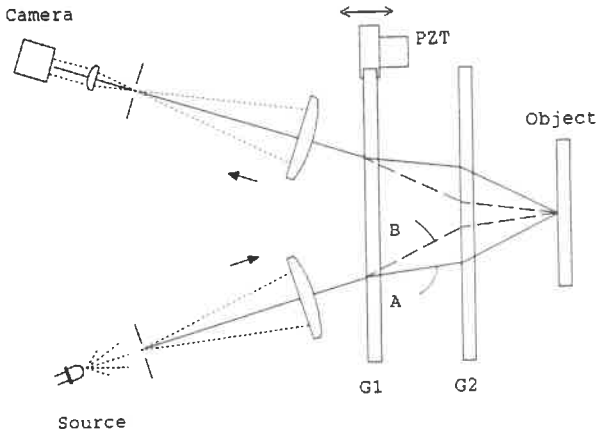

Figure 1: Grating interferometer for flatness testing. The equivalent wavelength is 12 μm.

* US Patent No.5,526,116 (1996). Additional US and Foreign Patents Pending.

A 100-mm aperture prototype instrument uses 100 X 150mm gratings and an equivalent wavelength of 12μm. The working distance is 60mm, which is far greater than that of grazing incidence interferometers. The maximum allowable surface roughness, as determined by measuring a sequence of machined metal parts, is 2.5μm Ra. This is significantly greater than the 0.3μm maximum roughness of the 1.55-μm laser diode interferometer reported at this meeting three years ago in Seattle.[4]

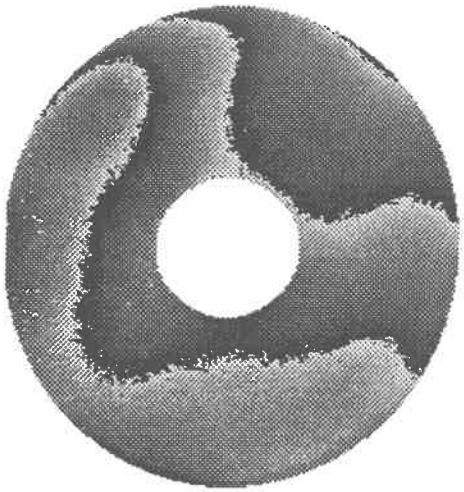

Figure 2: Wrapped phase data for a 95-mm diameter aluminum hard disk substrate. The sensitivity is 6mm of surface departure per fringe. The rms surface roughness is 0.4mm.

The maximum allowable peak-valley departure for a purely spherical distortion is 150μm over the 100-mm aperture. Phase-shifting techniques provide a single-measurement rms repeatability for smooth surfaces of .25nm and an accuracy of ±0.1μm. An additional benefit of the interferometer is the ability to separate the front and back surface reflections from transparent, plane-parallel objects.[5]

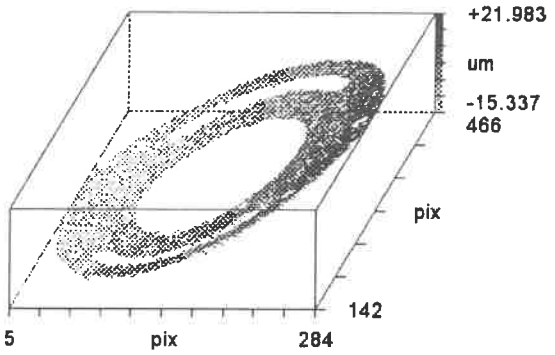

Figure 3: Oblique view of the machined surface of a 70-mm diameter mechanical pump component.

The 12-μm equivalent wavelength is a good compromise between measurement range and the increasing demands of precision metrology in manufacturing. The instrument is well suited to the metrology of manufactured items such as engine parts, components for magnetic storage devices, flat-panel displays, molded and textured plastic surfaces, and mechanical pump surfaces and seals (Fig,3). The common-path geometry is insensitive to vibration, and the large working distance will be advantageous for automated optical inspection. Additional information regarding this instrument is available in several publications.[5,6,7]

The Authors are pleased to acknowledge the contributions of C. Berg, J. Biegen, T. Connolly, L. Deck and D. Seniff to this work.

References

[1] K. Lewotsky, "Grating interferometer measures large departures," Laser Focus World, 40-41 (April 1996).

[2] P. Jacquot and P. M. Boone, "Deux methodes holographiques appliquées au controle de planéitié," Proceedings OPTO 88, 313-319 (ESI Publications, Paris, 1988).

[3] B. J. Chang, R. Alferness, and E. N. Leith, Appl. Opt. 14, 1592 (1975).

[4] P. de Groot and L. Deck, "Near-infrared phase-modulation interferometer for surface flatness measurement" Proc. ASPE, 33-36 (1993).

[5] P. de Groot, "Grating interferometer for metrology of transparent flats " *Optical Fabrication and Testing Workshop,* OSA 1996 Technical Digest Series, 7, 28-30 (Boston, 1996).

[6] P. de Groot, "Grating interferometer for flatness testing," Opt. Lett. 21(3) 228-230 (1996).

[7] P. de Groot, "Equivalent-wavelength interferometry using diffractive optics " Proc. SPIE 2782-48, Lasers, Optics, and Vision for Productivity in Manufacturing I (1996).

APPLICATION OF LIQUID CRYSTAL PANEL AS DIFFRACTION GRATING TO ZONE-PLATE INTERFEROMETER

Kazuhide Kamiya[1], Takashi Nomura[1], Hiroshi Miyashiro[1],
Kazuo Yoshikawa[2], Hatsuzo Tashiro[2]
1. Toyama Prefectural University, Kosugi-machi, Toyama, 939-03, Japan
2. Toyama University, Gofuku, Toyama, 930, Japan

Zone-plate interferometers[(1)] are used to measure an error in the shape of aspherical surfaces. It is not much influenced by vibrations and air turbulence compared with other interferometers, because it has a reference position on a surface under test and is a common path interferometer. A zone plate is a computer generated hologram and generates a diffracted wavefront whose shape is coincident with the design shape of a mirror surface. Therefore the manufacturing the zone plate is needed every time surface under test is changed. The manufacturing process has an exposure by laser, a development and a coating SiO_2[(2)]. As the process needs much time, the method of manufacturing zone plate in a short time is needed. Liquid crystal panels have a property of intensity modulators and change displayed patterns in video rate. We propose a zone-plate interferometer using the liquid crystal panel. As the phase of a interference fringe changes proportionally to the phase fraction of the zone plate displayed on liquid crystal panel[(3)], in the proposed interferometer the fringes is analyzed by the phase-shifting method[(4)].

Experiments are conducted using a liquid crystal panel from a projection type TV (Epson VPJ-2000) shown in Fig. 1. Specifications of the panel are shown Table 1. Resolution of the liquid crystal panel is high. As an aspect ratio of the panel is 1:1.14, the pattern of zone plate is compensated. A pattern of zone plate generated by computer is shown Fig. 2. The patterns have gray level from 0 to 255 and the

Table 1. Specifications of liquid crystal panel (Epson VPJ-2000 LC Projector).

Type	Twisted nematic, transmission TFT active matrix
Panel size	26.9mm(H) × 20.2mm(V)
Number of pixels	480(H) × 440(V)
Pixel pitch	56 μ m(H) × 46 μ m(V)

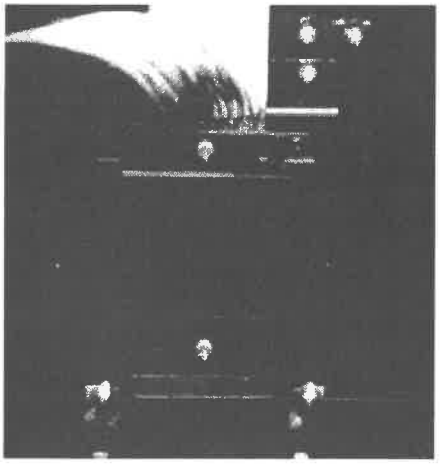

Fig. 1 Photograph of liquid crystal panel (Epson VPJ-2000).

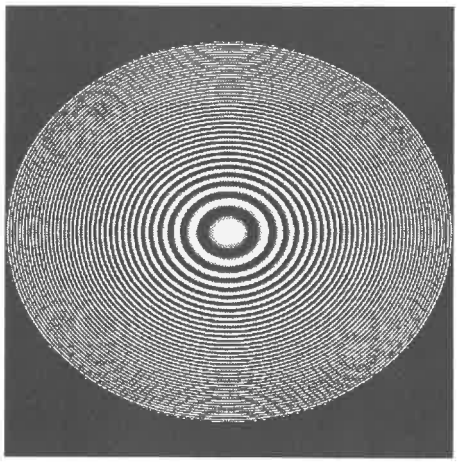

Fig. 2 Pattern of zone plate

aspect ratio of the pattern is compensated.

Flat Mirror is measured by using the liquid crystal panel zone plate. Figure 3 shows schematic diagram of the zone-plate interferometer using liquid crystal panel. Liquid crystal zone plate is illuminated by the parallel incident light. The light through the Liquid crystal zone plate is measurement light. And the diffracted light at liquid crystal zone plate is reference light. The measurement light reflected by the surface under test is distorted by error in the shape of surface under test and diffract at liquid crystal zone plate. The reference light passes through the liquid crystal zone plate. The both light is converged to a stigmatic point at aperture stop. The extraneous lights are removed almost completely by the aperture stop. The interference fringe is obtained on a charge coupled device camera. The photograph of the experimental setup is shown in Fig. 4. The interference fringe obtained by the proposed interferometer is shown Fig. 5. The

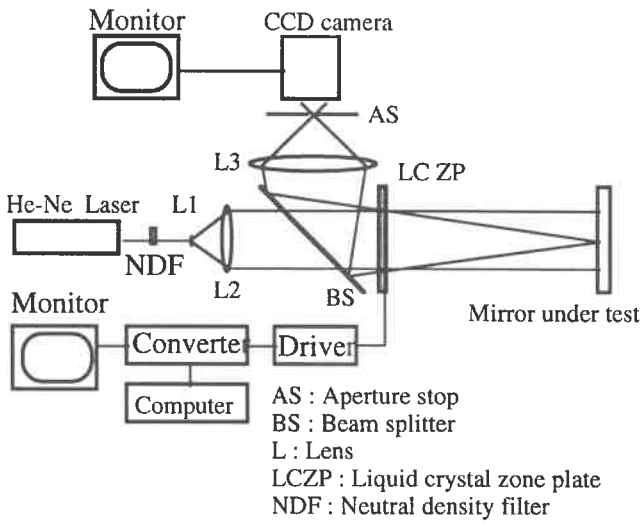

Fig. 3 Schematic diagram of a zone-plate interferometer using liqid crystal panel

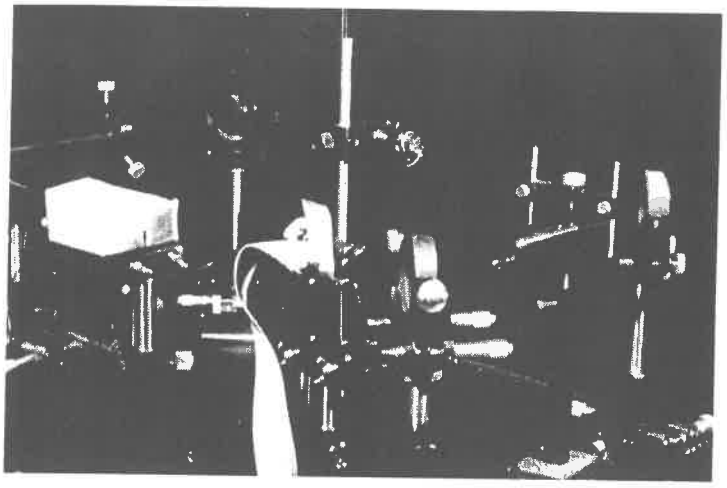

Fig. 4 Photograph of the experimental setup

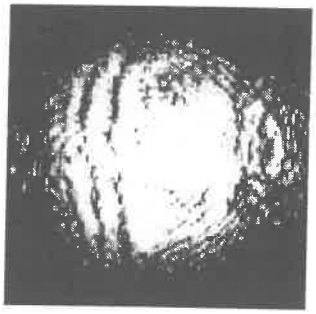

Fig. 5 Interferogram obtained by the zone-plate interferomete using liquid crystal panel.

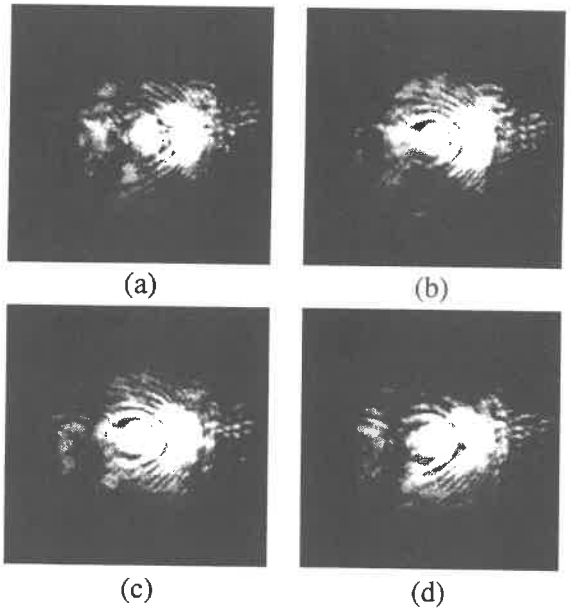

Fig. 6 Interference fringe obtained by the proposed interferometer. (a) Phase modulation of 0, (b) Phase modulation of $\pi/2$, (c) Phase modulation of π, and (d) Phase modulation of $3\pi/2$.

interference fringe is obscure because diffraction efficiency of the liquid crystal zone plate is low. However the interference fringe is stable when the interferometer receive vibrations and air turbulence.

The phase of a interference fringe varies in proportion as the phase fraction of the zone plate displayed on liquid crystal panel. When the initial phase of zone plate is changed to ϕ, the phase of the interference fringe is changed to 2ϕ. Therefore to obtain the fringe with the phase 0, $\pi/2$, π and $3\pi/2$, the initial phases of zone plate are 0, $\pi/4$, $\pi/2$ and $3\pi/4$. Figure 6 shows the fringes obtained by the proposed interferometer. The fringe obtained by the zone-plate interferometer is analyzed by the four step phase-shifting

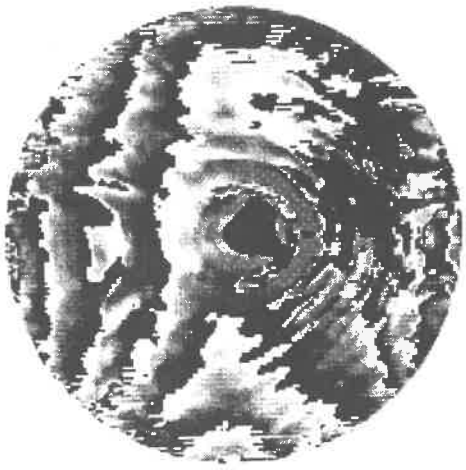

Fig. 7 Phase distribution analyzed by the proposed interferometer

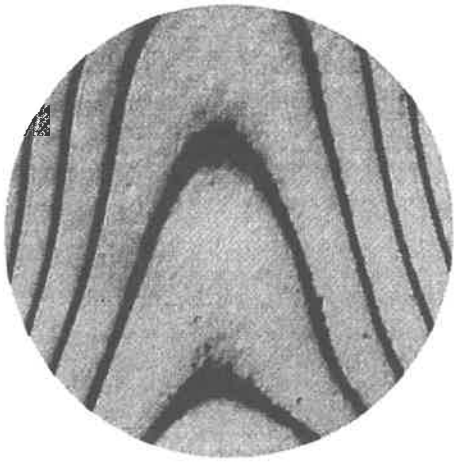

Fig. 8 Interference fringe obtained by Fizeau interferometer

method. The result of analysis from the four fringes obtained by zone-plate interferometer is shown in Fig.7. Figure 8 shows the fringe obtained by Fizeau interferometer to compare the result obtained by proposed method with the result obtained by Fizeau interferometer. The results agree well with the results obtained by Fizeau interferometer.

References

1. R.N.Smartt, "Zone Plate Interferometer," Appl.Opt., 13, 1093(1974).

2. Takashi Nomura, Kazuhide Kamiya, Hiroshi Miyashiro, Kazuo Yoshikawa, Hatsuzo Tashiro, Masane Suzuki, Shigeo Ozono, Fumio Kobayashi, and Masao Usuki, "An instrument for manufacturing zone plates by using a lathe," Prec.Eng., 16, 290(1994).

3. Takashi Nomura, Kazuhide Kamiya, Hiroshi Miyashiro, Kazuo Yoshikawa, Hatsuzo Tashiro, Shigeo Ozono, Masane Suzuki, "Application of a fringe scanning method to zone-plate interferometory," Proc.SPIE, 1720, 317(1992).

4. J. H. Bruning, D.R. Herriott, "Digital Wavefront Measuring Interferometer for Testing Optical Surfaces and Lenses," Appl. Opt. Vol.13, No.11, 2693-2703(1974).

KEYWORDS : zone-plate interferometer, shape measurement, liquid crystal panel, fringe scanning method

Wavelength-Shift Interferometry: Using a Dither to Improve Accuracy

Jack A. Stone, Alois Stejskal*, and Lowell Howard
National Institute of Standards and Technology, Gaithersburg, MD, 20899

*Permanent Address: Institute Of Scientific Instruments, AVCR, Brno, Czech Republic

Introduction: A dither (modulation) in path length can dramatically improve the accuracy of wavelength-shift methods used for absolute distance interferometry. Here we report how a dither improves the accuracy of absolute distance measurement by two orders of magnitude, reducing uncertainty from ~1 mm to ~10 μm (1 σ). Our results indicate that, when the path length is dithered, residual errors in fringe interpolation can be reduced to less than 0.6 nm after averaging.

"Absolute interferometry" refers to the use of interferometric techniques for determining the position of an object directly, without the necessity of measuring continuous displacements between points. In contrast to a standard interferometer, which measures a *displacement* by counting fringes as the length of the measurement arm is changed, an absolute interferometer directly measures the difference in *length* of its reference and measurement arms, with the length of the arms held constant. We have been investigating a wavelength shifting technique[1,2,3,4] for absolute interferometry. Using this technique, the position of a cube corner reflector in a single-pass interferometer is determined by observing the phase change at the interferometer output as wavelength of the laser is changed smoothly and continuously between two values. When the wavelength is changed, the relative phase change in light traversing the reference and measurement arms of the interferometer (or the number of fringes passing the detector) is proportional to the product of (1) the difference in length of the reference and measurement arms and (2) the amount by which the frequency of the laser source is shifted. If the frequency shift (or equivalently, the corresponding wavelength shift) is somehow determined, then the position of the cube corner can be inferred from the measured number of fringes passing the detector. In our experiment, the wavelength shift is not measured directly. Rather, the unknown length of the measurement arm (more precisely, the difference between this length and the fixed-length reference arm) is compared to the previously determined length of a "standard" interferometer, similar in construction to the interferometer of unknown length.[4] The ratio of the length of the unknown interferometer to that of the standard interferometer is simply equal to the ratio of the number of fringes passing in the two interferometers. The actual apparatus is shown schematically in Figure 1.

When using this technique for wavelength sweeping, it is necessary that the diode wavelength is tuned smoothly and continuously, without mode hops. Typically this is possible only over a

narrow tuning range. We obtained first results using a commercial laser for which the range of continuous tuning was only $\Delta\lambda/\lambda \approx 6x10^{-5}$. The number of fringes that are counted is then a factor ~$6x10^{-5}$ smaller than would be counted when measuring the distance by standard (displacement measurement) methods. Errors in fringe interpolation are magnified by the reciprocal of this same factor, or $1.7x10^{4}$, when computing the actual length.

Thus, in order to achieve an accuracy of a few micrometers when using this narrow sweep range, it is necessary to divide a fringe with sub-nanometer accuracy. Achieving sub-nanometer accuracy is difficult primarily because of errors that are periodic or quasi-periodic with wavelength, such as quantization errors, electronic interpolation errors, some forms of coherent scattering errors, and polarization mixing in heterodyne interferometers (not a problem with our geometry). Any of these error sources can be fatal to the wavelength sweeping technique unless appropriate measures are taken to reduce their influence. The effect of periodic errors can be greatly reduced by uniform averaging over all possible values of the phase at the start of the wavelength sweep. We dither this phase by modulating the path length; the cube corner in the reference arm of each interferometer is mounted on a simple loudspeaker and modulated with a triangular waveform with an amplitude of 5 to 25 μm.

Description of Experiment: We used a heterodyne method for fringe counting, with an acousto-optic modulator (AOM) that generates an 80 MHz frequency shift in one arm of each interferometer. The AOM frequency and ~80 MHz signals from the two interferometers are mixed down to ~2 MHz before processing. In the experiments described here, we processed the down-converted signals using commercial fringe-counting electronics modified so that the direction of counting can be switched synchronously with changes in the direction of the frequency sweep of our laser. As a consequence of the switching, counts that are accumulated when the laser is sweeping up in frequency run in the same direction as counts accumulated when sweeping down, and thus the total accumulated count reflects the average rate of counting for the two directions of frequency sweep.

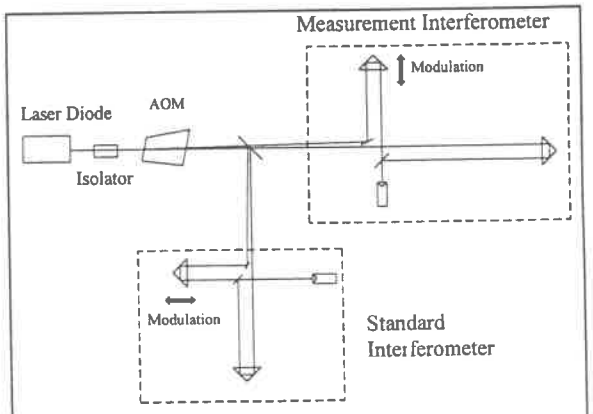

Figure 1: Absolute interferometer, heterodyne system.

In order to assess nonlinear errors in our absolute interferometer, we compared displacements, as determined from position measurements made with our system, to displacements measured using a commercial interferometer. Deviations from a linear relationship between the measurements of the two systems are shown in Figure 2. The data can be interpreted as follows: a linear least-squares fit is used to determine the optical length of our "standard" interferometer at ambient conditions, and the deviations shown (arising from nonlinearities or noise) are errors of our

absolute system excluding overall errors in determining the length of the "standard" interferometer. The uncertainty in the displacement measurement with the commercial interferometer is negligible relative to the errors shown here. This data was taken using a commercial 670 nm tunable laser source with a frequency sweep of 28 GHz ($\Delta\lambda/\lambda \approx 6\text{x}10^{-5}$). We were able to achieve 9 μm standard uncertainty (1 σ) over a range 0-1.5 m.

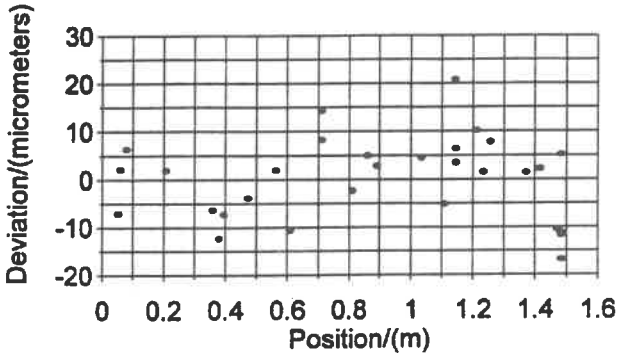

Figure 2: Deviations from linearity for absolute interferometer.

Discussion: In our system, the primary source of error is quantization error. We will discuss mainly this error source, although similar considerations apply to other quasi-periodic errors as well. Our electronics has a resolution of only λ/4. Without further measures, this will produce errors in length measurement on the order of $\lambda_{syn}/4$ in the unaveraged result, where λ_{syn} is the "synthetic wavelength"; for a wavelength sweep from initial wavelength λ_1 to final wavelength λ_2, the synthetic wavelength is $\lambda_{syn}=\lambda_1\lambda_2/\Delta\lambda$. Here λ_{syn} is a factor $1.7\text{x}10^4$ bigger than λ itself. More precisely, the expected 1 σ uncertainty of an unaveraged length reading for either the standard or measurement interferometer is $(\lambda_{syn}/4)/\sqrt{6}$. This result is a consequence of the fact that the 1 σ uncertainty arising from a quantization unit *r* is $r/\sqrt{12}$, (uniform rectangular uncertainty distribution)[5], and two independent phase measurements (at the two ends of the wavelength sweep) are required for 1 determination of the phase change. When both the standard and measurement interferometers are comparable in length, the expected uncertainty in the unknown length would be a factor $\sqrt{2}$ larger than this because it is derived from the ratio of two measured phase changes. An uncertainty of about 1.7 mm would be expected for the data shown here if averaging was not used. The observed uncertainty of 9 μm is almost 200x smaller, implying that the effect of quantization error has been correspondingly reduced. To achieve comparable results without averaging it would be necessary to reduce interpolation errors to less than 0.6 nm.

The reduction in quantization error is a consequence of modulation and averaging. We have modeled the measurement in a single interferometer (either the "measurement" or "standard" interferometer) and find the following results. The quantization error is very nearly periodic and averages to approximately zero over 1 unit of resolution (λ/4). (The error is more precisely periodic over the much longer distance $\lambda_{syn}/4$.) Uniform time averaging of results will give zero error if the length is modulated using a triangular waveform with peak-to-peak amplitude $n*(\lambda/4)$, where n is an integer. If n is not an integer, uniform time averaging will not produce a uniform average over all quantization errors and some residual error will remain. For a modulation with peak-to-peak amplitude $(n+\varepsilon)*(\lambda/4)$, the error has local maxima when $\varepsilon \approx 1/2$. The magnitude of these maxima is inversely proportional to the modulation amplitude. Because

the amplitude cannot be set exactly, it is advisable to use a sufficiently large value for n that the error will remain small even if $\varepsilon=1/2$. For $n>30$ it is possible to guarantee that the quantization error will be reduced by at least a factor of 100. However, a potential danger of using large-amplitude modulation is described below.

In fact, uniform time averaging is never achieved. Phases are measured only at the extremes of the frequency sweep. Thus the phase is sampled with a sampling rate equal to twice the frequency of the laser frequency modulation, and sampling may give rise to additional problems analogous to aliasing. Suppose, for example, that the length is modulated at a frequency that is exactly 1/10 the frequency of laser modulation, so that the phase is sampled at 10 equally spaced points in time as the length is modulated ½ cycle. The same 10 points will be sampled during the second half-cycle of length modulation and on all subsequent cycles. If the peak-to-peak amplitude of modulation is 5 resolution units ($5*\lambda/4$), then quantization errors will repeat on every other sample. All the phase-difference measurements, derived from pairs of phase measurements, will sample identical quantization errors, and averaging results with this modulation will not diminish the effects of quantization error over what occurs without modulation. This example is an extreme case, unrealistic because it assumes a precise amplitude that gives particularly bad results and because it requires that the ratio of the two frequencies be an exact integer, which would not occur unless the two modulation signals are somehow locked to each other. When the frequencies are not in an exact ratio of small integers, sampling effects will be minimal after long averaging times, but they may still degrade accuracy at shorter times.

If the peak-to-peak amplitude of modulation were reduced to $1*(\lambda/4)$ unit in the example above, then five distinct quantization errors are sampled when phase differences are measured, and the effect of modulation is essentially equivalent to increasing the resolution of the system by a factor of 5; errors will be 5x smaller than errors obtained without modulation, and the spatial period of the errors will also be reduced by a factor of 5.

Potential sampling problems are most easily avoided by setting the period of length modulation much longer than the period of laser frequency modulation, so that many samples occur during one modulation period. Alternately, if the periods of length and frequency modulation are not in a ratio of two small whole numbers, then the positions sampled will repeat only after a large number of cycles and once again sampling problems will be diminished.

The analysis above avoids the issue of noise. A small amount of noise is beneficial in reducing quantization errors in the same manner as the dither; Gaussian noise is in some respects superior to linear dither and has been used to improve electrical measurements[6]. Figure 3 shows results of a computer simulation of quantization errors under various circumstances, including the presence of noise. On both axes the units are $\lambda_{syn}/4$, the effective resolution of the device when the basic interferometer resolution is $\lambda/4$. Errors are shown for measurements of lengths over a range of about one wavelength , small relative to the synthetic wavelength. The lengths being measured in this example are nearly equal to $0.2*\lambda_{syn}/4$, and essentially the same pattern will be repeated at $(n+0.2)*\lambda_{syn}/4$ for any integer n. The basic quantization error in length measurement is shown by curve (a), a rectangular waveform varying between -0.2 and +0.8 units. Curve (b) in the figure shows the effects of adding random amplitude fluctuations--a Gaussian distribution

with 1 σ= 20 nm--to each phase measurement, and averaging over 6000 samples (60 s averages if the laser is modulated at 50 Hz). Here the noise reduces quantization errors by about a factor of 2. With both Gaussian noise and a modulation amplitude of 5.1 μm (30.5*λ/4), errors are reduced substantially [curve (c), with the errors multiplied by 10 for clarity.] When noise is eliminated and modulation is present, the errors decrease by more than a factor of 2 relative to curve (c), indicating that in this regime the noise is a hindrance rather than helpful in reducing errors.

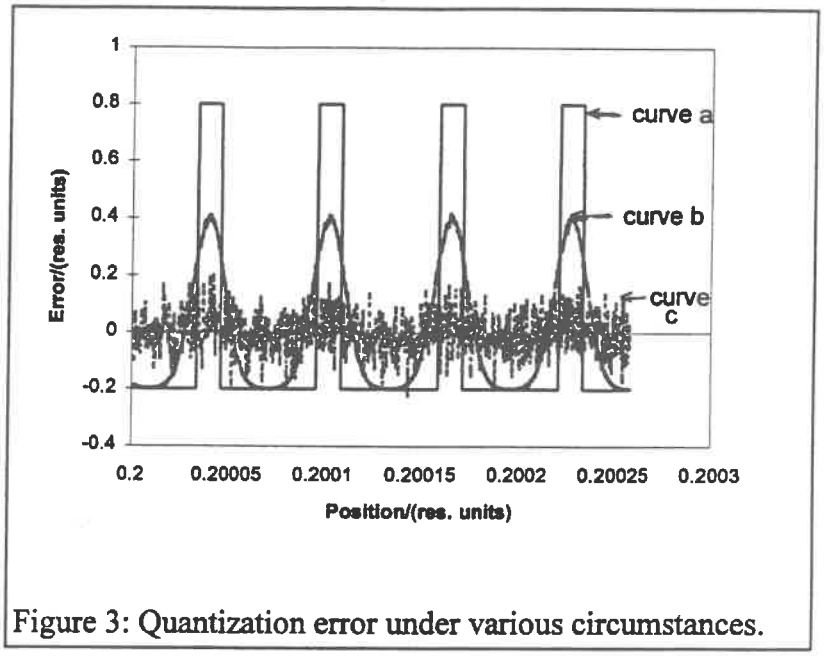

Figure 3: Quantization error under various circumstances.

Concluding Remarks: The computer simulations excluding noise suggest that the dither should reduce fringe interpolation errors somewhat more than observed. Remaining errors that dominate our result when the dither is present are presumably not periodic with fringe spacing. The sources of these errors have not been fully identified, although it is plausible that random vibrational motions of the interferometer reflectors are an important limitation on accuracy when results are averaged for less than 1 minute. In addition, signal processing delays were an important source of errors for short averaging times. We have now built new electronics to reduce these delays, and we have obtained a diode laser with much greater tuning range.[1] We still use modulation to improve our results, but with the larger tuning range the improvement in accuracy when using modulation is not quite so dramatic. The tuning range is now increased by a factor of 30 , the effect of periodic errors is 30x smaller, and other sources of error now dominate our results, which have been improved by about a factor of 6 relative to the results presented here.

It may seem disturbing that, although the dither provides averaged phase measurements with sub-nanometer fringe interpolation, the dither itself is thousands of nanometers in amplitude and may introduce drifts in the average length that are larger than the errors that are eliminated. This apparent problem is not so bad as it might appear at first glance. Although it may be true that the dither introduces small errors, these errors are not periodic with the period of wavelength sweeping and consequently can be reduced by averaging.

Our dithering technique of eliminating periodic errors may also be applicable to certain other measurements, such as measurement of linewidth. Using our absolute interferometer to measure a length of 1 meter with 10 μm accuracy is entirely equivalent, from the standpoint of the actual

phase measurements required, to a linewidth measurement that must determine a displacement of 60 μm with 0.6 nm accuracy . The change in optical phase is identical for these two measurements, although in one case the phase change results from tuning laser wavelength by $\Delta\lambda/\lambda=6x10^{-5}$ whereas in the other phase change results from motion of a cube corner reflector.

---

1 J. A. Stone, L.Howard, A. Stejskal, M. Stephens, C. Oates, and L. Hollberg, "Novel Methods for Length Measurement Employing Diode Lasers", Proc. 1996 NCSL Symposium, Monterey, 1996, p 667.
2 Hisao Kikuta, Koichi Iwata, and Ryo Nagata, "Distance measurement by wavelength shift of laser diode light", Appl. Opt. 25 (17), 1986, pp.976-980.
3 Hisao Kikuta and Ryo Nagata, "Absolute distance measurement by wavelength shift interferometry with a laser diode: some systematic error sources", Appl. Opt. **26** (9), 1987, pp.1654-1660.
4 J Thiel, T. Pfeifer, and C.Haas, "Absolute interferometric distance measurement with tunable laser diodes", VDI Berichte 1118, 3rd Int. IMEKO Symp. on Laser Metrology, Heidelberg, 1994, p.79.
5 Guide to the expression of uncertainty in measurement, International Organization for Standardization, Case postale 56, CH-1211 Geneve 20, Switzerland, 1995, p.13.
6 M.F. Wagdy, "Effects of various dither forms on quantization errors of ideal A/D converters", IEEE Trans. on Instr. and Meas., **38**, (4), 1989, p.850

ANGLE MEASUREMENT USING X-RAY MOIRÉ FRINGES

N. O. Krylova, D. G. Chetwynd and D. K. Bowen

Centre for Nanotechnology and Microengineering
Department of Engineering,
University of Warwick, Coventry CV4 7AL UK

Introduction and Principles. It is now established that x-ray interferometer (XRI) displacement fringes can provide practical, highly traceable displacements calibration in the nanometre to micrometre region [1-3], with resolution of a few picometres. The method is one used for basic calibration, not for direct application as an industrial gauge, since it is relatively slow and somewhat restricted by the need for x-ray safety enclosures. Nonetheless it is very attractive since the naturally occurring and extremely well characterized lattice parameters of pure single-crystal silicon, known and traceable to $3{:}10^8$ are used directly as secondary standards of length with a fundamental unit of a few tenths of a nanometre. For a review of X-ray interferometry and its applications see [4].

The monolithic XRI is machined from a high-purity single crystal of silicon and then etched to remove surface damaged layers. Three thin parallel 'blades' are left standing proud of the base, oriented so that suitable lattice planes of the crystal are normal to the surfaces and in identical orientation in the three blades. A collimated x-ray beam illuminates the first (splitter) blade at the Bragg angle and diffraction causes two transmitted beams to emerge from the blade at plus and minus this angle. These beams meet the second (mirror) blade where they are each split again; the diverging output beams are masked off and the converging ones meet and interfere inside the third (analyser) blade. Since this interference pattern and the lattice have similar wavelengths, they interfere further such that the phases of the two diffracted beams emerging from the third blade contain information about the lattice positions in all three blades. Displacing the blade in its plane (via a flexure mechanism machined into the monolith) modulates this output intensity to give displacement fringes; one sinusoidal cycle corresponds to a movement of one lattice spacing (around 0.2 or 0.3 nm for the most commonly used lattice orientations).

Very precise calibration of small (sub-microradian) angular displacements is needed in many fields such as precision optics, astronomy and space communications. Interest in XRI for this arises from its proven sensitivity and traceablity for linear applications. An angle measuring XRI has been produced by Windisch and Becker at PTB [5] which has sub-nanoradian sensitivity, but its traceability (absolute accuracy) depends directly on geometrical lengths in the monolith (not so easily determined) and its range is restricted by potential errors inherent to its x-ray optical configuration. Another approach is to exploit the moiré fringes generated if one XRI blade is twisted slightly with respect to the others - just as happens with optical diffraction gratings. These fringes have a pitch (wavelength) given by $\Lambda = d/\theta$ where d is the lattice parameter. Sensitivity to angle is thus very high (0.1 μrad twist gives fringes of the order of 1 mm) and the inverse relationship means that errors in fringe measurement are less critical at smaller angles, where fewer alternative methods are available. Traditionally, accidental generation of such fringes from parasitic rotations in a displacement interferometer has been viewed as a problem causing loss of contrast in the displacement fringes, although contrast variation has been used to monitor the angular parasitics of a mechanism [6]. Modern x-ray imaging allows relatively rapid and

cost-effective capture of moiré images and so of directly analysing the pattern for micro-angle measurement. We report on an experimental system to demonstrate the feasibility of this idea.

Measurement System. The system has four main parts: x-ray source, special monolith and associated drive, CCD camera system, and image processing and signal analysis computing. Figure 1 illustrates their arrangement in a set-up for calibrating an autocollimator. The source is a Mo K_α sealed tube with a 0.4 mm square focal spot in projection, operating typically at 45 kV and 45 mA. This is coupled to a brass collimator giving an output beam approximately 10 × 0.4 mm, expanded to 2 mm wide by asymmetric reflection from a monochromator crystal. The tube is 600 mm away from the monolith. A set of movable, and gauged, slits for image calibration is placed between the monolith and imager, which are 100 mm apart. The imager is a conventional low-light CCD camera (753 x 576 square pixels in standard 4:3 video format) fitted with a fibre optic (magnifying) faceplate that is coated with a gadolinium oxysulphide scintillation layer and then a metallic aluminium layer to exclude light. It has a window of 11 mm diagonal and a resolution of about 18 μm. Thresholded binary images are captured and averaged by a Matrox MVP500 image analysis board in a 486-based PC. The acquisition rate is only ~ 5% less than full frame rate because of data-transfer overheads: good quality images generally involve a 1000 frame average which takes around one minute to obtain, and weaker images rarely need more than 5000 frames.

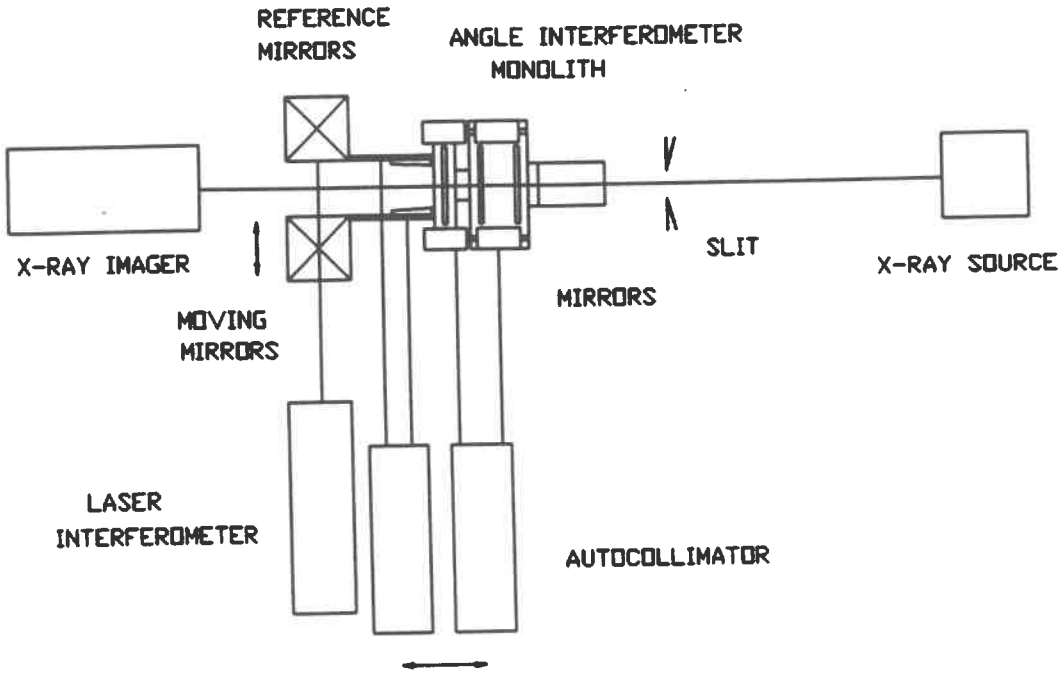

Figure 1: Schematic of an angular X-ray interferometer for testing autocollimators

The new monolith design, figure 2, is the heart of the system. The blades stand vertically on its top surface, each 35 x 30 x 1.6 mm and spaced 15 mm apart. These dimensions provide a 'thick-blade case' transmission interferometer. The crystal orientation gives (220) reflection planes parallel to both long edges of the blade. This is one of the strongest reflections, has the symmetry needed to align to both blade edges and has the added advantage of allowing alternative ranges of angle to be measured by using the (weaker) (440) or even (880) reflections. A problem could arise if the method showed significant sensitivity to displacement fringes superimposed on the moiré fringes since in practice it is

difficult to ensure that the centre of rotation is ideally sited. Our design provides for testing such sensitivity by deliberately placing the centre of rotation about 35 mm below the blade centre to give a considerable Abbe offset and allowing moirés to be taken from the vertical or horizontal crystal planes. The vertical lattice planes experience much larger normal translations than the horizontal ones for a given rotation (the ratio is closely half the radian angle of rotation), so measurements in both planes can detect effects due to displacement fringes. Rotation of the final blade is by applying small forces to the horizontal arm above a single notch hinge. This has nominally 5 mm radius, 10 mm depth and 3.5 mm central thickness, to give a design stiffness of around 1000 N.m rad^{-1}, dependent upon the Young's modulus in the particular crystal orientations used. The monolith incorporates provision for an asymmetric beam expander and monochromator, also adjustable on a notch hinge. Other cuts are for stress diversion, including regions where mirrors may be mounted to the block, to minimize lattice distortion in the blades.

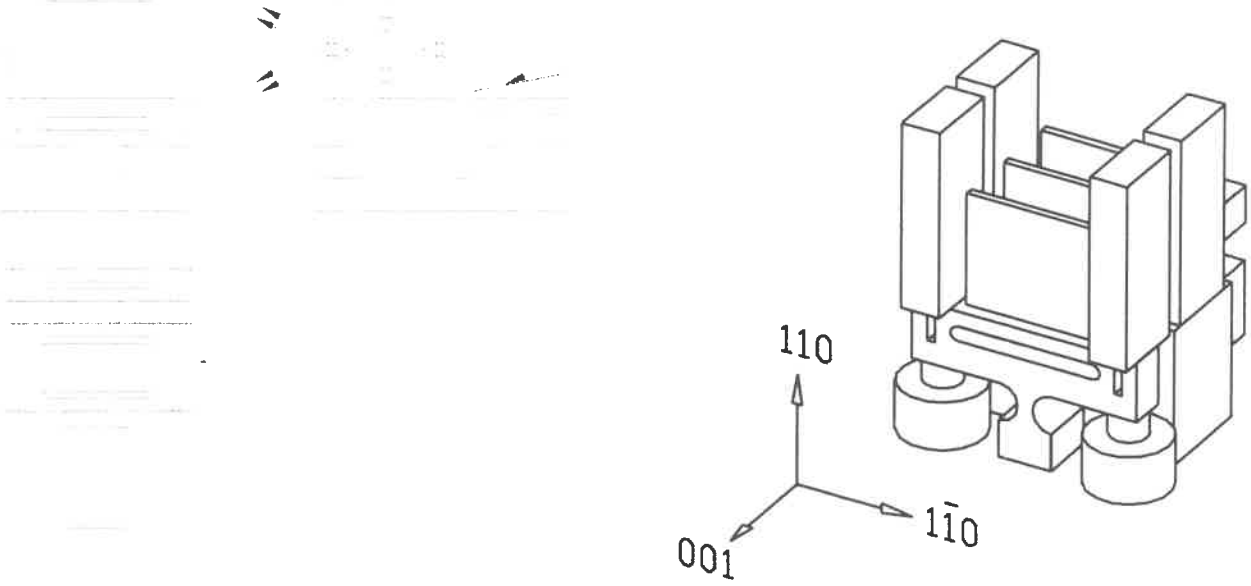

Figure 2: The new monolith, showing typical X-ray paths on the elevation and mirrors and drives on the isometric view.

Blade rotation is driven by small magnet-coil systems in which saturated permanent magnets are glued to the torque-arm of the monolith, surrounded by solenoid coils fixed to the same base-plate on which the monolith rests kinematically. Such actuators are very stable, capable of very high linear range to resolution and have very high compliance so that almost no vibration is transmitted through them [3]. General vibration isolation is provided by standing the whole of this system on a sandwich of thick plywood sheets separated by partly-inflated small pneumatic tyres, which rests on a heavy and actively air-suspended optical bench within a lead/plywood enclosure that provides both radiation and acoustic isolation.

The accurate determination of the spacing of the moiré fringes is of critical concern if the system is to be used for angle calibration. Provided that good fringe contrast is obtained there are several relevant image analysis techniques well known from optical interferometry that are useful under

different conditions. As this paper is concerned with the instrument design, no further discussion will be provided here. However, for any form of analysis the real image size must be accurately determined: the magnification from the final blade, where the fringes are true size, to the camera may not be exactly unity and there may be uncertainty on pixel size. Our approach is to place x-ray opaque artefacts very close to the blade and then to calibrate from their shadow images. For example, a steel sphere placed by the blade can check image distortion. Generally a slit with well-defined edges is kept close to the blade, see figure 1. One edge is fixed to one side of the field and the other is on a precision transverse slide, position monitored by laser interferometer (or inductive gauges in some cases). Fringe images taken with the moving edge in two positions of closely known separation give immediate data on the effective magnification. Linearity checks across the field may also be made. Often the slit spacing (which is always slightly less well defined than any one displacement) is sufficient alone for confirming that calibration is being maintained and the interferometer need not be used continuously.

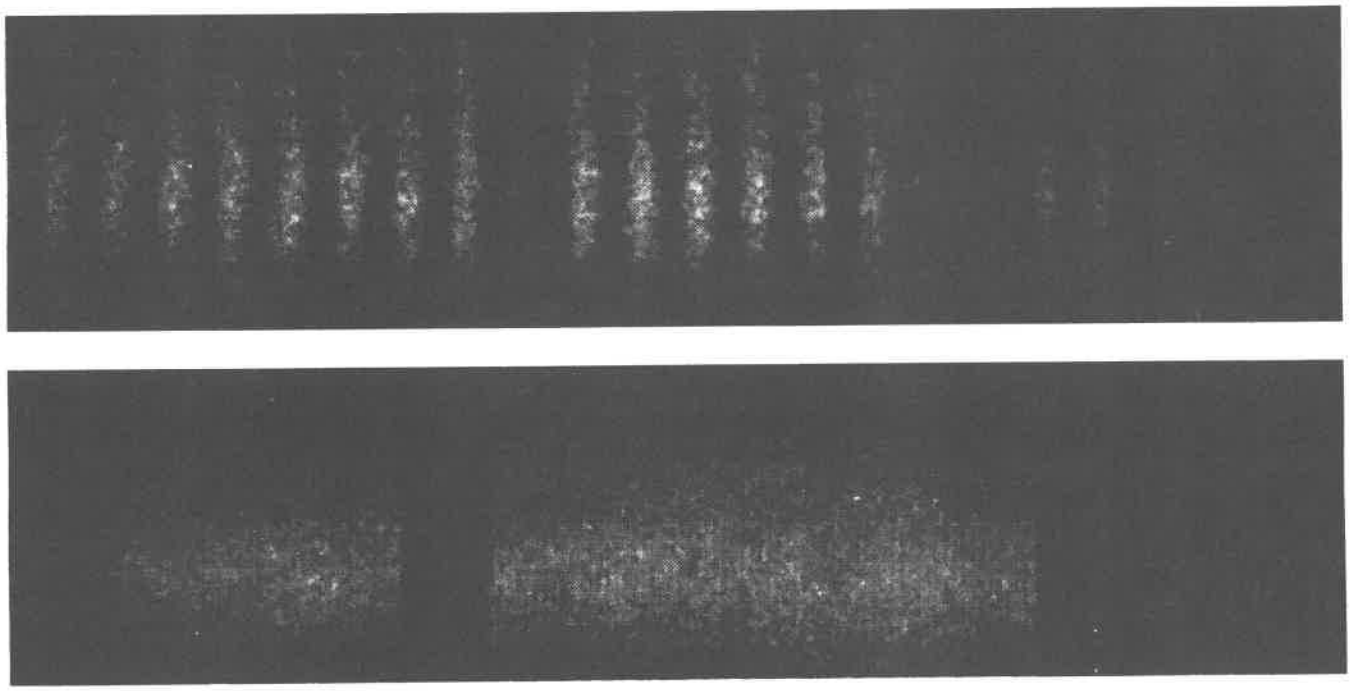

Figure 3: Fringe images at twists of about 0.4 and 2.2 μrad, with shadows of calibration wires.

Test Results. Figure 3 shows typical images captured by computer, including shadows of a pair of steel wires from a variant of the calibration system described above. In the present context the demonstration of stable, high-contrast fringes is sufficient to show that the system is in principle capable of acting as an angle calibrator. These images lose intensity towards their sides because some of the input beam conditioning has been removed for convenience during basic testing when regular major changes are being made to the system. Wider and more uniform images will be available with the full system, to the benefit of the fringe analysis statistics.

The smallest fringes yet resolved in practice have a pitch of around 60 μm, corresponding to an angle of 3.5 μrad (0.7 arcseconds). A similar camera having an 18 mm diagonal could detect fringes down to 90 μm (~2.2 μrad). Since fringe spacing is inversely proportional to angle, these limits give the maximum range of the configurations. They overlap usefully with the lower limits of more

conventional methods. Greater range can be obtained by means of either much more expensive cameras or (at a considerable cost of time) photographic films, where fringes as small as 5-10 μm can be readily detected and 1 μm is feasible (~200 μrad). Smaller angles give wider fringes, so resolution of angle rests with the image analysis technique. The field is about 6 mm wide and there are practical reasons for not much increasing this value, so if one complete fringe is needed within the field the resolution will be about 70 nrad (0.014 arcseconds). Many standard algorithms need several fringes in the field for good reliability, but some will work with sparse data and new developments involving phase stepping [1] should allow good estimation of the pitch even when only a small part of a fringe is in view. In this respect, carefully positioned phase plates can provide one image 'sheared' into three phase steps, figure 4, thus avoiding errors from thermal drift between sequential phase steps, each of which takes about 100 seconds.

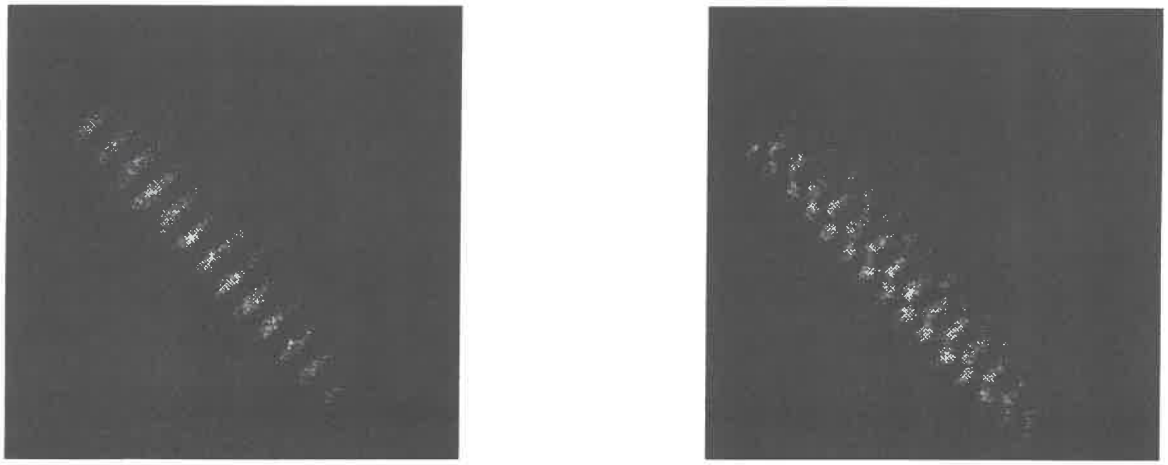

Figure 4: Moiré fringe image: original and simultaneous three-phased-stepped version.

Tests with the x-ray beam in both vertical and horizontal orientations detected no difference in the quality of the data. As contrast of the quality shown was maintained over the full test range in both cases, we conclude there are no practical problems in offsetting the flexure from its ideal (Abbe principle) position. This is advantageous in two respects. First it shows that simple, robust monoliths such as the present one may be used, with no need to introduce more complex mechanisms to project the rotation axis onto the centre of the blade. Second, with the vertical planes, displacement fringes from extremely small angular changes cause large phase shifts in the moiré fringes with virtually imperceptible change of their pitch and may be used for interpolation or for testing local sensitivity limits. Note that calibration of this phase shift depends on knowing the Abbe offset distance: for the present monolith 1 nrad rotation causes about 60° phase shift.

A 10 g laboratory weight placed on the monolith torque arm, directly above the position of one magnet, 30 mm from the centre caused fringes at the limit of image resolution. Thus this torque twists the blade about 3.6 μrad, indicating a hinge stiffness approaching 700 N.m rad^{-1}. Given heavy etching after machining to nominal size and the cube-law dependence of stiffness on the notch thickness, this is close enough to the design value of 1000 N.m rad^{-1} to provide further confidence that all system parameters are correctly cross-calibrated.

Discussion. We have demonstrated that a relatively simple silicon monolith can be used as an angular x-ray interferometer, with moiré patterns captured directly onto a full field imaging system. High contrast fringes are easily obtained and the relative twist between the blades determined from the spacing of the fringes. Attaching mirrors to the monolith for using it to assess autocollimators or other optical measurement systems is straightforward and there is no evidence of contrast reduction caused by their weight inducing strain in the monolith. It is particularly important that the angular interferometer provides a continuous measurement as the angle is changed, making it an ideal device for interpolation, not merely calibration at a few points. With the current device, the range and resolution depend on the pixel resolution and the field of view, which is largely a matter of cost. Various forms of signal processing can be used to obtain a 'best' estimate of the fringe spacing, some better in one region of spacings than others, but no one conventional method looks capable of delivering good results over the whole range of the device capability [7]. These issues will be explored further elsewhere: it appears that a technique based on phase-stepping may give considerable improvements over single image methods, especially at larger spacings. With such methods we expect that angle XRI will take its place alongside its linear brother as a valuable tool for top-level calibration.

Acknowledgment

We are grateful to the Paul Instrument Fund of the Royal Society for their support of this work.

References.

[1] D R Schwarzenberger, D G Chetwynd & D K Bowen 1989 Phase measurement x-ray interferometry. *J. X-ray Sci. Technol.* **1**, 134-142

[2] G Basile, P Becker, A Bergamin, G Cavagnero, A Franks, K Jackson, U Kütgens, G Mana, E W Palmer, M Stedman, J Stümpel & G Zosi 1993 COXI - a combined optical and x-ray interferoemter for high precision dimensional metrology. *International Progress in Precision Engineering* (eds. N Ikawa, S Shimada, T Moriwaki, P A McKeown & R C Spragg) Butterworth Heinemann, 248-259

[3] D G Chetwynd, N O Krylova & S T Smith 1996 Metrological x-ray interferometry in the micrometre region. *Nanotechnology* **7**, 1-12

[4] D K Bowen, Applications of X-ray interferometry, in *Dynamical X-ray diffraction theory and its applications* (eds A. Authier and B.K. Tanner), Plenum Press, 1996 in press.

[5] D Windisch & P Becker 1992 Angular measurements with x-ray interferometry. *J. Appl. Cryst.* **25**, 377-383

[6] D G Chetwynd, D R Schwarzenberger & D K Bowen 1990 Two-dimensional -ray interferometry. *Nanotechnology* **1**, 19-26.

[7] E Okuyama & D G Chetwynd 1995 Investigation of data processing algorithms for a micro-radian angular calibrator using an x-ray interferometer. *Control and Instrument Systems Centre Report #22*, Warwick University

Scanning Probe Microscopes for dimensional length measurements

K. Hasche, O. Jusko, L. Koenders, K. Thiele, G. Wilkening, X. Zhao (◆)

Physikalisch-Technische Bundesanstalt (PTB)
Braunschweig, Germany

1. INTRODUCTION

Scanning probe microscopes (SPM) can be used to obtain three-dimensional topographical data of surfaces with very high resolution. Most SPMs utilize piezoelectric (PZT) ceramic actuators to generate, and measure, the scan movement of the probe relative to the sample. Unfortunately PZTs are known to exhibit strong hysteresis, creep, and thermal drift. Although these measurement error sources can be reduced by software, precise measurements can only be obtained by controlling the scan accurately. This can be realized by coupling position sensors like capacitance transducers to the scanner. Their output signal is free of hysteresis and generally some orders of magnitude more linear than the PZTs. Most approaches use the output signal of the transducers as input to a closed feedback-loop, which controls the scan movement. The linearity of the scan then is determined by the inherent linearity of the capacitance transducers including the electronics. A residual nonlinearity of the order of 0.02% has been achieved [1,2]. In practice however, the linearity often is limited by misalignments, i.e. non-parallelism of the capacitor plates and guiding errors of the scanner [2]. Therefore the main advantage of a scanner with built-in capacitance transducers is the high reproducibility and thus the possibility to calibrate the instrument with low uncertainty. This may be performed by scanning a certified standard and analyzing the data [3]. Yet a lower uncertainty can be realized by calibrating the residual non-linearity of the capacitance transducers by an optical interferometer. Three different approaches for the realization of a measurement SPM - „3d-sample scan", "2d-sample scan" and „3d-probe scan" - have been pursued and are described in the following. These instruments are currently used for the traceable calibration of SPM standards and thickness standards, as well as tools for measurement tasks in nano- and micro technology.

2.„SAMPLE SCAN" SPM - APPROACH

The first microscope is a modified commercial metrological scanning sample AFM (VERITEKT 3 [4]) with a scan range (x,y,z) of 70 µm, 15 µm, 15 µm. The scan is generated by a 3d flexure hinge device with piezo actuators and integrated capacitance transducers acting in a closed feedback-loop. The resolution (x,y,z) is about 1.2 nm, 0.25 nm and 0.25 nm. The AFM has been equipped with three miniature laser interferometers verifying discrete calibration points in intervals of $\lambda/2$ in the entire measurement volume.

The principle arrangement of the laser interferometers in the AFM is given in fig.1. Primarily, the interferometers serve to calibrate the scales, not only referred to the axes x, y, z in the closer sense, but also for parallels of the axes within the entire measurement volume and to reduce the crosstalk of the three movement axes.

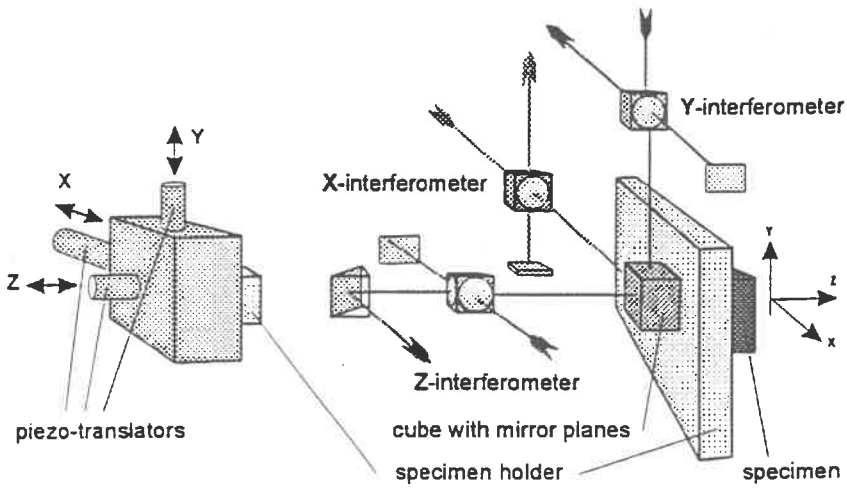

Fig.1 3d-"sample-scan" AFM; principle arrangement of the x-y-z-scanner and of the 3d plane-mirror laser interferometer system integrated in the AFM [4].

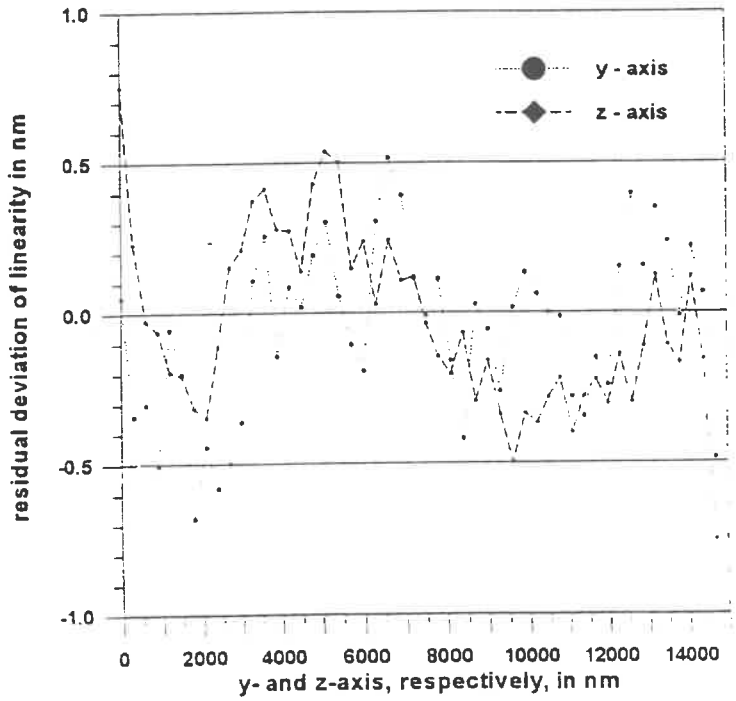

Fig.2 Residual linearity deviations for the x- and y-axis (after compensation)

The residual deviations of linearity for the y- and z-axis, after (on-line) compensation using the calibration data are illustrated in fig.2.

Fig.3 demonstrates the efficiency of the (on-line) crosstalk compensation. The given example refers to the most critical case of this AFM - the crosstalk from the z-axis to the x-axis caused by the non-orthogonality of the movement axes. The residual displacement in x-direction is plotted as a function of the position on the z-axis for nine representative positions of x and y, respectively. Abbe errors are caused in the AFM as a consequence of the distance of 23 mm between the cube mirror of the laser interferometers and the x-y-measurement plane. The resulting effects have been determined by angular measurements within the measurement volume and compensated by appropriate lateral displacements in the x-y-planes via the control software. The residual contribution to the uncertainty caused by uncompensated angular deviations is a displacement estimated to be not more than about 5 nm in the x- and y- direction, respectively. The expanded uncertainty of the measurement of any two points within the measurement volume is at present estimated to be

$u_{95;\,3\text{-dim}} = 5\text{nm} + 2 \times 10^{-4} \times d$, d = distance (nm).

If only one axis is used for the measurement the Abbe offset has no influence. The uncertainty of a step height measurement is estimated to be

$u_{95;\,1\text{-dim}} = 1.1\text{nm} + 2 \times 10^{-4} \times h$, h = height (nm).

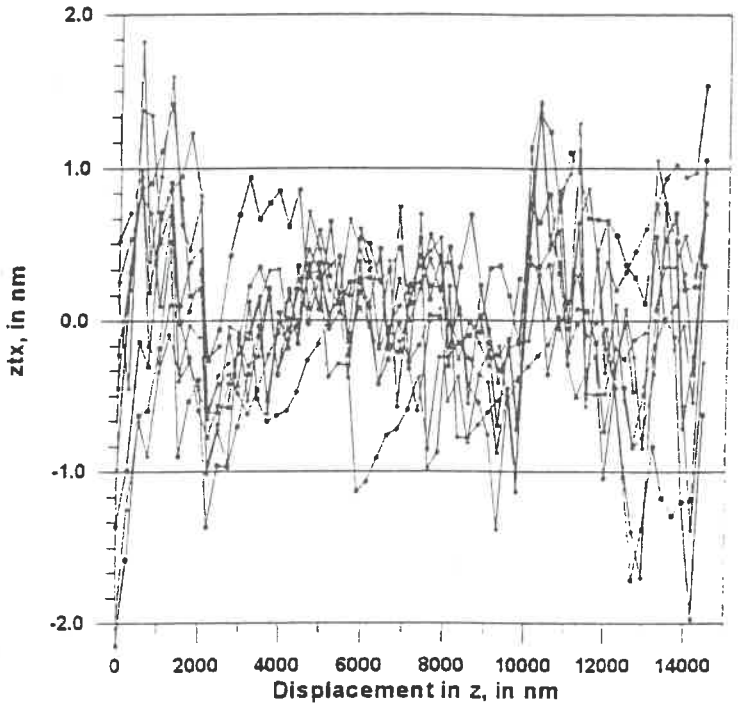

Fig.3 Residual crosstalk ztx from the z-axis to the x-axis for 9 significant positions of x and y.

The second microscope has been built up mostly from commercially available parts [5,6]. The scan range (x,y,z) is 120 µm, 120 µm, 15 µm. It is of the 2d-scanning sample type, consisting of a flexure hinge scanning x-y-table with integrated capacitance transducers and an interchangeable STM or AFM measuring head (see fig.4). The positioning of the x-y-table is controlled in a closed feedback-loop. The STM head consists of a z-piezo actuator with integrated capacitance transducer. The measurement uncertainty for measuring an arbitrary distance d within the measurement volume can be expressed by

$$u_{95;\,3\text{-dim}} = 10\ \text{nm} + 3 \times 10^{-4} \times d,$$

d = distance (nm).

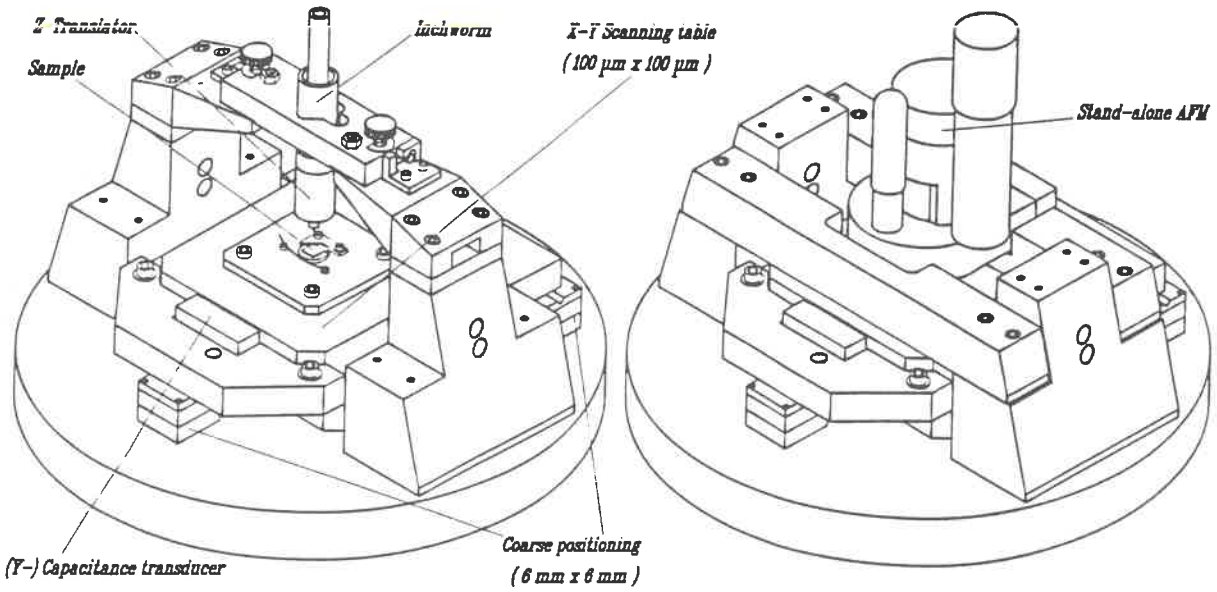

Fig.4 2d-"sample-scan" SPM; STM (left) and AFM version

The calibration is accomplished by using a laser interferometer. The x,y,z axes are calibrated successively by using a miniature prism mirror on the x-y table and a cube mirror replacing the tip as reflectors (see fig.5). This measuring STM has been used successfully for the calibration of standards [7]. However, for practical measurements AFMs are better suited. By replacing the z-scanner of the STM with a commercial stand-alone AFM head [8] the STM can be converted into an AFM-device with a laterally calibrated sample scanner. In fig.4 both possible setups, i.e STM and AFM-mode, are shown. This device may demonstrate that only

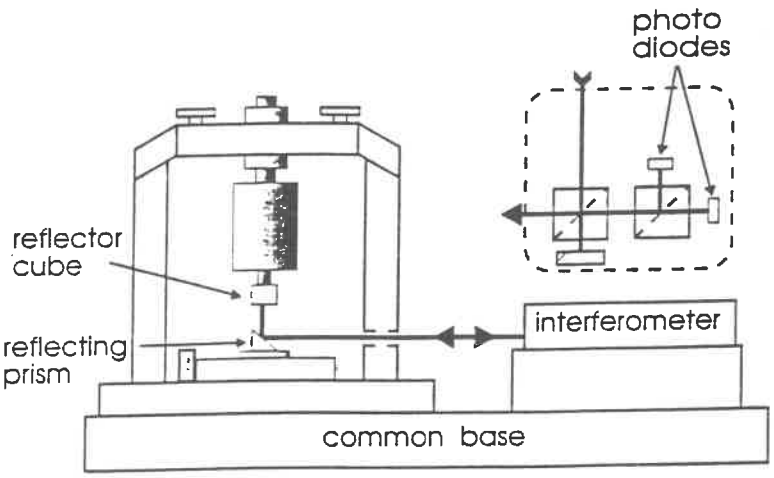

Fig.5 Calibration of the 2d-sample-scan STM; here, the calibration of the z-axis is shown; for x- and y-calibration, the vertical sides of the prism are used.

moderate effort is needed to extend a standard AFM to metrology specifications. In this case an uncertainty can only be given for a single axis measurement. For this case, The uncertainty has been estimated to be

$u_{95;\,1\text{-dim}} = 8\ \text{nm} + 4 \times 10^{-5} \times d$,

d = distance (nm).

Because the employed AFM lacks an independent gauge for the z-movement, it cannot be used to measure precisely in three dimensions, like for example it is needed for roughness measurements or for calibrating z-standards. Therefore it is necessary to replace the commercial AFM head with a (home-built) head with integrated z-gauging in the future.

3.„PROBE SCAN" SPM - APPROACH

Measuring SPMs have to be calibrated in the plane in which the actual measurement is carried out (surface of the sample under measurement). This is true for the calibration by standards as well as by interferometry. However, as the sample thicknesses are different in practice the actual measurement plane is likely to differ from the „plane of calibration". In the case of „sample scan" SPMs this fact may cause substantial systematic errors. Capacitance transducers, guiding elements of the x-y-table and the sample surface often are situated in different z-heights and the laser beam of the calibrating interferometer again travels in another plane. Such a setup causes a substantial calibration uncertainty by introducing serious Abbe-errors [3,9] in the case of angle errors of the motion of the x-y-table. This problem partly can be overcome by using „probe scan" SPMs. Here, the plane of calibration and the plane of measurement is always the same, provided that the tip position relative to the x,y,z-gauges stays the same under all circumstances (e.g. tip exchange). It has been shown that an STM working after this principle can be calibrated interferometrically by replacing the tip with a small cube mirror [1,10] and by using a special tip holder with a preadjusted tip [6].

The third microscope is a measuring „probe scan" SPM consisting of a scanning head with piezo actuators and capacitance transducers in all three axes. Fig.6 shows the design principle of this scanning head.

The x-y-motion is accomplished by means of a piezo bimorph frame. Two parallel bimorphs for each axis form a parallelogram („double leaf spring guidance"). The z-actuator consists of a double piezo plate arrangement. The x-y-actuators and capacitance transducers form a closed feedback-loop. The head is optimized for small Abbe-errors, because the actuators and the capacitors are in-plane, and the angle errors of the scan apparatus are minimized by compensation methods [1]. The scan range (x,y,z) is 30 µm, 30 µm, 6 µm. A calibration uncertainty for an arbitrary displacement measurement (3-dim) has been estimated to be

$u_{95;\,3\text{-dim}} = 8\ \text{nm} + 2 \times 10^{-5} \times d$, d = distance (nm).

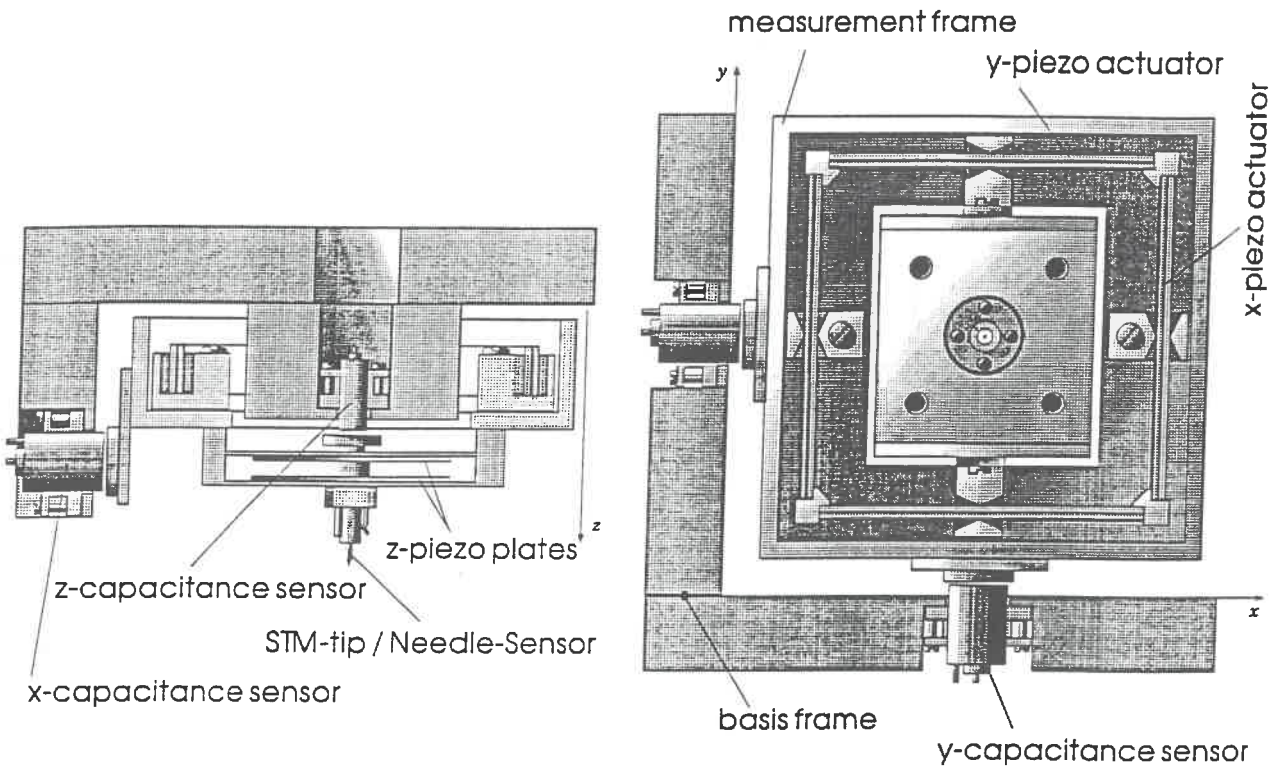

Fig.6 3d "probe scan" SPM head

The conversion of this measuring „probe scan" STM into an AFM is accomplished by the so-called „Needle Sensor" [11]. The Needle Sensor may be described as an AFM tip with integrated force sensing (in axial direction). As no external position detection (for force sensing purposes) is needed as it is the case with the conventional AFMs (e.g. triangulation, interferometry) the Needle Sensor is ideally suited for this SPM design. The needle-sensor fits into the already existing tip-holder. In this way STM and AFM operation is easily exchangeable.

4. Conclusions

Three different realizations of metrological SPMs have been shown. All of them use integrated capacitance transducers as position gauges. In all cases the calibration is accomplished by using laser interferometers. From the metrological point of view, the permanent installation of laser interferometers in the SPM for all three axes certainly is the best solution. The interferometers form a separate reference coordinate system and the three axes of the AFM can be investigted and calibrated simultaneously. With the other two SPMs, the axes can be calibrated only successively, and for investigations of the crosstalk and orthogonality, for instance, the built-in capacitance transducers have to be used. The attained uncertainties reflect the metrological (and financial) efforts.

The AFM with built-in laser interferometers rises the question why the interferometers are not used directly for positioning and measuring as they will assure direct traceability. There are mainly two reasons - firstly, the bandwidth of the capacitance transducers is larger than that of interferometers [2], - and secondly, the direct traceability is only true for $\lambda/2$ intervalls as interferometers show non-linearities in the sub-λ-range which are periodic with $\lambda/2$.

The reproducibility of the capacitance transducers in general does not effect the measurement uncertainty. The calibration of the "probe scan" SPM, for instance, showed no change within the stated mesurement uncertainty for a period of more than 1.5 years.

Concerning mechanical stability and vibration susceptibility the structures should be as small as possible. The necessity of large scan ranges, sufficient sample space and practical handling led to rather large structures with resonance frequencies of 500 Hz and below. Pneumatic optical tables proved to be sufficient for vibration damping.

The thermal stability is of great importance as due to the large scan ranges the measurement time often is rather long. The employment of material with a low thermal expansion coefficient - as is the case with No.1 AFM - , or high thermal conductivity together with a symmetrical design - as is the case with No.3 SPM - lead to reasonable results. The No.2 STM/AFM showed good results only in a well-stabilized thermal surrounding, as this instrumnet consists of a mixture of materials due to the fact that commercially available parts have been taken.

5. REFERENCES

[1] *X. Zhao*, Hochauflösende dreidimensionale Positionierungsbestimmung bei Rastersondenmikroskopen mittels kapazitiver Aufnehmer; Ph.d. thesis, PTB-Bericht F-20, Braunschweig (1995)

[2] *X.Zhao, G. Wilkening, and K. Horn*, High precision three dimensional tip position measurement in Scanning Tunneling Microscopes; Proc. 7th IPES, Kobe,Japan, 937 (1993)

[3] *R. Dürselen, U. Grunewald, and W. Preuß*, Präzisions-Piezoscanner für die Nanometrologie; Feinwerktechnik & Messtechnik, 483 (1995)

[4] "VERITEKT 3" is a product of Carl Zeiss Jena GmbH, Germany

[5] *O. Jusko, X. Zhao, and G. Wilkening*, A scanning tunneling microscope with high accuracy 3D position control; EOS Topical Meetings Digests Series: Vol 4,ISSN 1167-5357, 41-42 (1994)

[6] *O. Jusko, X. Zhao, H. Wolff, and G. Wilkening*, Design and three dimensional Calibration of a Measuring Scanning Tunneling Microscope for metrological Applications; Rev. Sci. Instr, 65 (8) 2514 (1994).

[7] *G. Barbato, K. Carneiro, J. Garnaes, G.Gori, G. Hughes, C.P. Petersen, J.F. Joergensen, O. Jusko, S. Livi, H. McQuoid, L. Nielsen, G.B. Picotto, G. Wilkening*; Scanning Tunneling Microscopy Methods for Roughness and Micro Hardness Measurements; Synthesis report on BCR project 3423/1/0/184/4/91-BCR-DK(30), 109 pages (1994)

[8] TopoMetrix TMX 2000 Explorer is a product of TopoMetrix, Inc., USA

[9] *J. Schneir, T.H. McWaid, J. Alexander, B.P. Wilfly*; Design of an atomic force microscope with interferometric position control; J. Vac. Sci. Technol. B12(6), 3561 (1994)

[10] *X. Zhao, G. Wilkening, H. Marth, K. Horn*; High-accuracy Capacitance Sensor for Positioning of Piezoelectric Displacement Actuator; ACTUATOR 94, June 15-17, Bremen (1994)

[11] *K. Bartzke, and T. Antrack*, Atomic Force Microscopic Sensor with Quartz Oscillator and Tip; Proc. UME 3 (International Conference on Ultra Precision in Manufacturing Engineering), ISBN 3-926832-11-8, Aachen, 63-67 (1994)

"Needle Sensor" is a product of Carl Zeiss Jena GmbH, Germany

(◆) *X. Zhao* now is with Physik Instrumente (PI) GmbH, Germany

Toward Accurate Measurements of Pitch, Height, and Width Artifacts with the NIST Calibrated Atomic Force Microscope

R. Dixson[1], T. V. Vorburger[1], P. J. Sullivan[1], V.W. Tsai[2], T. H. McWaid[1]*
[1] National Institute of Standards and Technology,Gaithersburg, MD 20899
[2] Dept. of Material Engineering, University of Maryland, College Park, MD 20742

Introduction

Atomic force microscope (AFM) measurements are being used increasingly for metrological applications such as semiconductor process development and control. Common types of measurements are those of feature spacing (pitch), feature height (or depth), and feature width (critical dimension). If high accuracy is required, the scales of an AFM should be calibrated. Presently available standards for this purpose are calibrated using stylus instruments and optical techniques. The effectiveness of this approach, however, is limited by the differences in the full ranges of the various techniques and by questions of methods divergence. As the repeatability of many commercial instruments continues to improve, the importance of accurate calibration standards will increase. In order to calibrate AFM standards using an AFM, we have designed and built a metrology atomic force microscope, called the calibrated AFM (C-AFM). This instrument has metrology traceable to the wavelength of light for all three axes. To realize this, a flexure translation stage, heterodyne laser interferometers, and a digital-signal-processor based closed-loop feedback system are used to control the x-y scan motion. The z-axis translation is accomplished using a piezoelectric actuator with an integrated capacitance sensor, which is calibrated using a heterodyne laser interferometer. Since the design of this instrument has been discussed in more detail elsewhere [1,2], we will focus here primarily on the results of performance testing of the C-AFM for pitch, height, and width measurements.

Performance Goals and Characterization

At present, our major goals for the C-AFM system are: (1) the capability of calibrating sub-micrometer pitch artifacts with an expanded uncertainty (2σ) of three nanometers [3]; (2) the capability of calibrating sub-micrometer height artifacts with an expanded uncertainty (2σ) of 0.3 nm plus 1% of the height; and (3) the measurement of the top width of sub-micrometer vertical features with an expanded uncertainty (2σ) of 20 nm. To characterize the current level of performance for these measurements, we have compared the C-AFM results with those obtained from other methods. The techniques and instruments used for this comparison include the NIST linescale interferometer [4,5] (used to calibrate standards for optical microscopes), a Talystep† stylus profiler (used to perform NIST's step height calibrations), and cross sectional transmission electron microscopy (TEM).

Pitch Measurements

We have characterized the performance of our system for pitch calibrations of artifacts with pitches ranging from 0.2 μm to 20 μm. This was accomplished by comparing the pitch as measured by the C-AFM with the value obtained by using other methods. Comparisons between the NIST linescale interferometer and the C-AFM were made using two samples: a prototype of NIST Standard Reference Material (SRM) 2800 [6], an optical microscope magnification standard, and a prototype of SRM 2090 [7], a scanning electron microscope magnification standard. Lines on these samples with pitches ranging from 4 μm to 20 μm were measured. We also measured, over approximately 50 intervals, the average pitch of an artifact produced by laser focussed atomic deposition [8]. The lines on this sample have a nominal pitch of 212.78 nm, which is traceable to the wavelength of the laser light used in fabrication.

A typical result for this series of experiments is given in figure 1, where results from the measurements of the 10 μm lines on SRM 2090 by both the C-AFM and the linescale interferometer are compared. The regions (1, 2, and 3) on the sample shown as the x-axis correspond to segments of the lines

that are one third of their length (roughly 15 μm) in the transverse direction (perpendicular the measured interval), and the C-AFM values are averages of line profile results over each of these regions. This procedure is necessary because the photodetector of the linescale interferometer averages over these portions of the lines. The error bars given are our estimates of the total measurement uncertainty (1σ) of the C-AFM. The uncertainty of the linescale interferometer measurements on this sample is currently being investigated, but it is estimated to be between 1 nm and 5 nm (1σ). It may be necessary to consider the potential methods' divergence between these two measurement techniques. Since the features on the sample have near-vertical sidewalls, the C-AFM is only sensitive to the edge locations near the top surface of the lines. The linescale interferometer, however, may detect light scattered from a different effective cross section of the feature. This could result in methods' divergence between the two measurements. Although this issue will require further consideration, the important observation is that the residual differences between the C-AFM values and either the nominal pitch or the pitch as measured by the linescale interferometer are consistent within our estimates of the expanded uncertainty (2σ) of the C-AFM measurement.

At the present, we estimate the uncertainty (1σ) for pitch measurements to be 7 nm for large pitch values, on the order of 10 μm. This is believed to be due mainly to motion between the AFM tip and the metrology frame, which realizes the coordinate system for the measurements. Such motion of the tip could result from cantilever flexing or tip deformation. For smaller pitch values, the uncertainty is approximately 3 nm, with the largest contribution being due to the Abbe´ offset uncertainty. Other sources of uncertainty are the digital resolution of the interferometer, polarization mixing in the interferometer.

Step Height Measurements

The C-AFM performance on height measurements has been characterized by measuring lithographically produced steps [9]† ranging in height from about 920 nm down to 18 nm and single-atom Si steps of about 0.3 nm [10]. As recent results of our single-atom step work are being presented elsewhere [11], we will focus here on our measurements of the lithographically produced step height samples.

Currently, the standard uncertainty (1σ) in step height measurements is approximately 1.9% and is limited by variability of the results under different measurement conditions. Some of our results are illustrated in figures 2 and 3 for a nominal 180 nm step. These variations were observed in both contact and intermittent-contact modes of operation. In addition to larger variations in intermittent-contact mode, an offset in the apparent step height of roughly 10 nm was observed between the two modes. Such an offset has not been observed on 18 nm steps. Several effects may be contributing to these observed variations. From other measurements, the calibration of the capacitance gauge itself is not a significant source of variation. Instead, we believe that the response of the force sensor to the upper and lower surfaces can be subject to variations. Cantilever flexing, especially in contact mode, and other cantilever-surface interactions, such as thermal or viscous damping, which are not localized at the tip, are possible explanations for this. In intermittent-contact mode, particularly for larger step heights, differential damping is likely to play an important role in the observed variations. We are continuing to investigate the variations in our measurements. Other possible sources of variation being considered are out-of-plane motions of the translation stage and changes in laboratory temperature and humidity. Smaller sources of uncertainty in the step height measurements also include variability and linearity of the capacitance gauge and Abbe´ offset. When we have improved the repeatability of our measurements, we will undertake a detailed intercomparison with measurements using the Talystep† stylus profiler which currently performs NIST's step height calibrations.

Linewidth Measurements

As with most commercial AFMs, feature width measurements with the C-AFM are dependent on the geometry of the probe. To obtain an accurate measurement, it is desirable to correct the apparent width of the feature for the width of the probe near its 'apex.' The development of methods and standards for tip characterization is crucial for width metrology, and there has been much recent work in this area [12]. If the geometry of the tip can be estimated, and it is reasonably stable during imaging, it can be deconvolved or eroded from an image to remove some of the probe dilation effects. We are exploring the use of various tip

characterizer samples to estimate the tip size and correct the apparent feature width for the broadening due to the probe. One type of characterizer sample is a cleaved mica surface with colloidal gold particles deposited on it. We have fabricated such samples, using gold particles ranging from 5 nm to 27 nm in diameter, and imaged them in the C-AFM to characterize the probe shape.

By imaging a tip characterizer sample before and after performing measurements on a linewidth sample it is possible to correct the apparent width of a feature for the size of the probe, within some uncertainty dependent upon the severity of the change in the tip from before to after. Figure 4 shows the results from an experiment in which we used this approach to measure the top linewidth (or top width) of preferentially etched lines on a silicon sample. This sample was fabricated by collaborators at the University of New Mexico [13]. After performing the C-AFM measurements, we had cross-sectional transmission electron microscopy (X-TEM) performed on the sample [14]†. Both the pitch of the lines and the linewidth were extracted from the TEM micrographs. We then scaled the TEM micrograph by equating the pitch from the TEM data to the pitch as measured by the C-AFM. The linewidths were then rescaled by this factor. Severe damage to the C-AFM tip during a width measurement could be readily identified by the extreme changes in the apparent width of the characterizer particles after the top width measurement. When such damage occurred, we typically found larger estimated uncertainties and significant discrepancies between the C-AFM width measurement and the TEM result. If severe damage did not occur, as for measurements 3 and 4, we found good agreement within our estimated uncertainties between the C-AFM width measurements and the TEM result. We have discussed elsewhere [15] more of the details of performing this type of measurement with the C-AFM system and the possible explanations for the variation in our measurements. Although there are some challenges that need to be addressed, we believe that the level of agreement achieved represents a significant step toward accurate linewidth measurements with the C-AFM.

At the present, we estimate that top width measurements of near vertical features using the C-AFM, provided that tip damage is not severe, have an uncertainty of about 15 nm (1σ). We plan to use other types of characterizers and tips to further quantify and reduce the uncertainty of these measurements. Although we believe it should be possible to achieve uncertainties of 10 nm (1σ) or better, we expect that width measurements will continue to be limited by our knowledge of the tip geometry and our ability to correct the apparent feature width for it.

Summary and Conclusions

We have completed a characterization of C-AFM performance for pitch, height, and width measurements, and we are continuing to work on reducing our uncertainties. At the present, we estimate the uncertainty (1σ) for pitch measurements to be 7 nm for large pitch values on the order of 10 μm and approximately 3 nm for smaller pitch values. The uncertainty (1σ) of our step height measurements of 18 nm and larger steps is approximately 1.9%. At the present, we estimate that top width measurements of near vertical features using the C-AFM, provided that tip damage is not severe, have an uncertainty of about 15 nm (1σ).

Plans for the near future include the testing of different tips and cantilevers to reduce anomalous probe sample interactions and the variations in our measurements. This could be particularly important in reducing our uncertainties in the step height measurements. We also plan to use other types of characterizers and tips to further improve the accuracy of C-AFM width measurements. Longer term goals include the development of a combined pitch/height or three-axis magnification standard for AFMs. We expect such a standard to play an important role in the continued development of AFMs into true metrology instruments.

---

*Present Address: Tencor Instruments, Santa Clara, CA 95054

†Certain commercial equipment is identified in this report in order to describe the experimental procedure adequately. Such identification does not imply recommendation or endorsement by NIST, nor does it imply that the equipment identified is necessarily the best available for the purpose.

Acknowledgments

This work was supported largely by the National Semiconductor Metrology Program (NSMP) at NIST. Step height samples were provided by J. Prochazka of VLSI Standards, Inc., and we also thank J. McClelland of NIST and S. H. Zaidi of the University of New Mexico for the provision of samples. Measurements using the NIST linescale interferometer were performed by J. S. Beers and W. B. Penzes. Finally, we give special thanks to C. J. Evans, R. S. Polvani, J. S. Villarrubia, and J. Dagata of NIST for many very helpful and informative discussions.

References

[1] J. Schneir, T. H. McWaid, R. Dixson, V. W. Tsai, J. S. Villarrubia, E. D. Williams, E. Fu, SPIE **2439**, 401 (1995).

[2] J. Schneir, T. H. McWaid, J. Alexander, and B. P. Wilfley, *J. Vac. Sci Technol. B*, **12**(6), 3561 (1994).

[3] B. N. Taylor and C. E. Kuyatt, *Guidelines for Evaluating and Expressing the Uncertainty of NIST Measurement Results*, NIST Tech. Note 1297 (1994).

[4] J. S. Beers, W. B. Penzes, NISTIR 92-4998 (1992).

[5] J. S. Beers, NBSIR 87-3625 (1987).

[6] J. E. Potzick, *Proceedings of SPIE Symposium on Microlithography and Metrology in Micromachining II*, Vol. **2880**-12 (1996).

[7] B. L. Newell, M. T. Postek, and J. P. van der Ziel, Proc. SPIE **2439**, 383 (1995).

[8] J. J. McClelland, R. E. Scholten, E. C. Palm and R. J. Celotta, Science, **262**, 877 (1993).

[9] Fabricated by VLSI Standards, Incorporated, San Jose, CA 95134-2006.

[10] E. D. Williams, R. J. Phaneuf, J. Wei, N. C. Bartelt, and T. L. Einstein, *Surf. Sci.*, **294**, 219 (1993).

[11] V. W. Tsai, T. V. Vorburger, R. Silver, R. Dixson, E. D. Williams, J. Schneir, to be presented at 1996 Annual ASPE meeting.

[12] J. S. Villarubia, Surface Science, **321**, 287 (1994).

[13] A. S. Chu, S. H. Zaidi, and S. R. J. Brueck, *Appl. Phys. Lett.*, **63**, 905 (1993).

[14] TEM analysis performed by R. Anderson of the IBM Analytical Services Group, Hopewell Junction, NY 12533.

[15] R. Dixson, J. Schneir, T. McWaid, N. Sullivan, V. W. Tsai, S. H. Zaidi, S. R. J. Brueck, SPIE Vol. **2725**, 589 (1996).

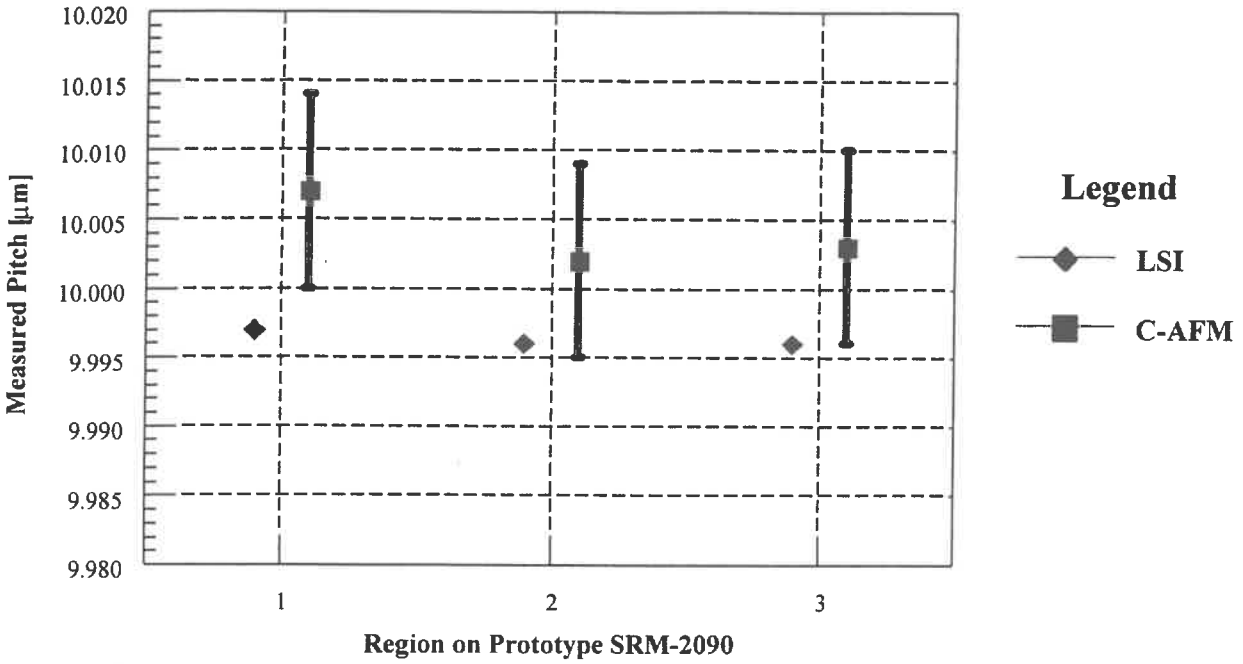

Figure 1. Comparison of C-AFM pitch measurements on prototype of SRM 2090 with results from the NIST linescale interferometer (LSI).

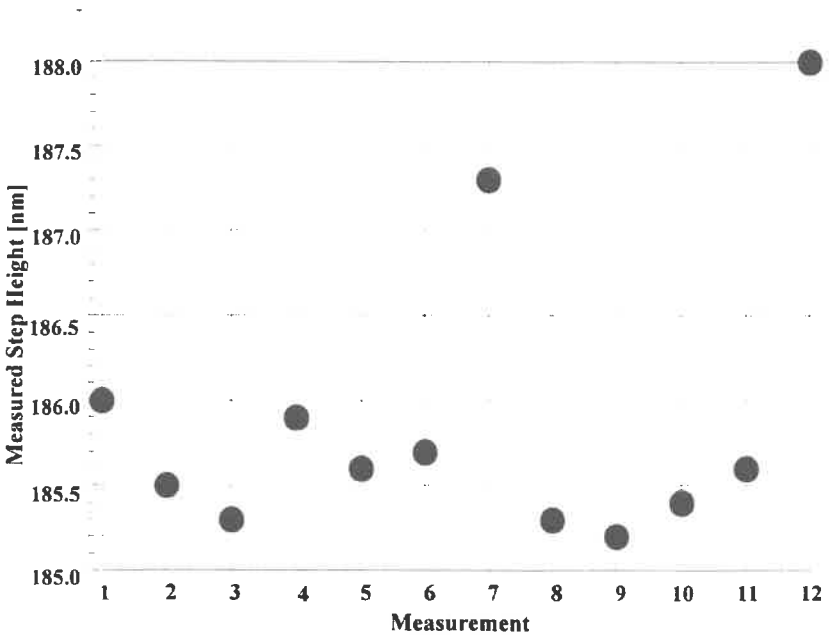

Figure 2. Contact mode measurements of a nominal 180 nm step. Each value represents the average of 10 measurements. The seventh and twelfth measurements were made with different step orientations relative to the fast scan direction.

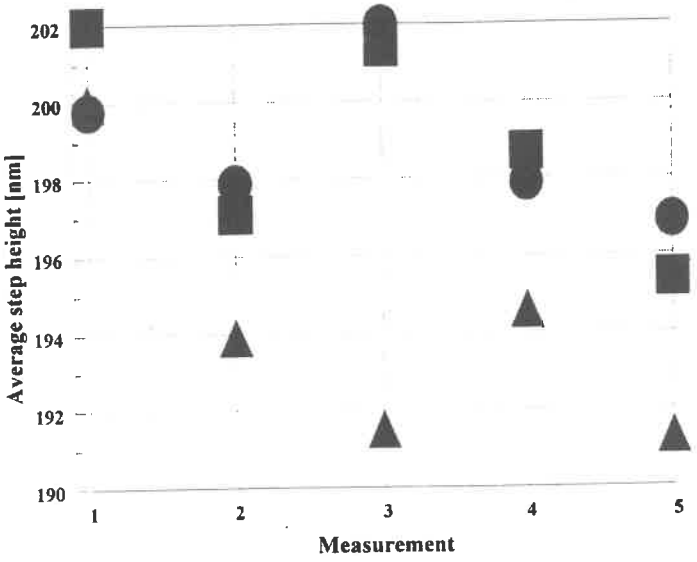

Figure 3. Intermittent contact mode measurements of a nominal 180 nm step. The set point of the z-axis feedback controller was toggled between three values, shown with three separate symbols. These set points correspond to the average cantilever osciallation maintained by the feedback. All data were obtained at the same location, and each value represents the average of 10 measurements.

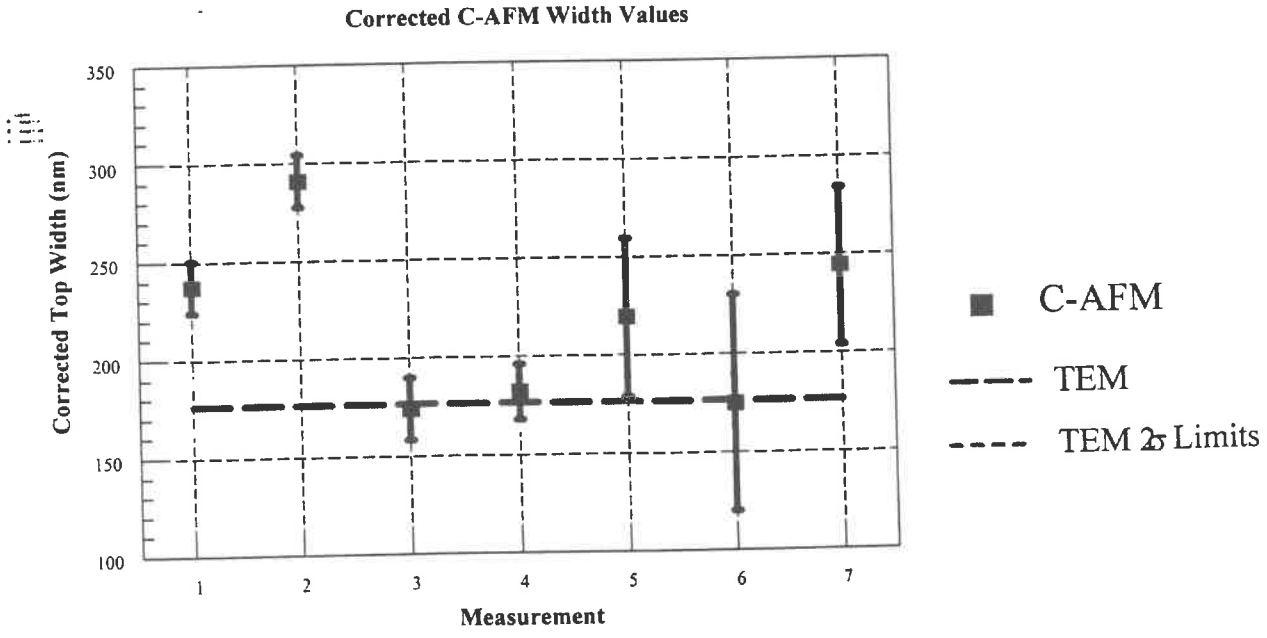

Figure 4. Comparison of C-AFM top width measurements (shown with 1σ error bars) with scale-corrected TEM results (and 2σ limits). When probe damage during the width measurement is not severe, good agreement is found with an estimated 15 nm (1σ) uncertainty.

MEASUREMENTS OF THE SURFACE ROUGHNESS OF GROUND SILICON WAFERS BY CROSS-SECTIONAL TEM

H. Murai, S. Kasaishi, Y. Yokota* and T. Kaneeda
P.O. Hahn**, M. Kerstan** and D. Helmreich**
*Natural Science Research Institute
Okayama University of Science, 1-1, Ridai-cho, Okayama 700, Japan
**Wacker Siltronic, Johannes-Hess-Strasse24,D-84479 Burghausen Germany

1.Introduction

The TTV (Total Thickness Variation) value of silicon wafer plays a important roll in the fabrication of the LSI (Large Scale Integrated circuits)[1]. As the integration of the LSI becomes large, the size of each element of the circuit becomes small, and the junction region of n- and p-type becomes shallow. The roughness of the wafer surface and the stacking faults which exist near the surface region (0～0.5μm depth) are directly affecting the efficiency of producing LSI. For 200mm wafer, the TTV value should be less than the 0.1μm.

The Si wafer surfaces, mechanically finished by several kinds of wheel grinding, were studied using the cross-sectional TEM (Transmission Electron Microscope) observation.

2.Experiment

The specimen Si wafers were used 200mm in diameter and of {100} orientation. Wafer surfaces were mechanically finished using VPG (Vertical type Precision surface Grinder) and HPG (Horizontal type Precision surface Grinder) with several kinds of wheel grinding[2]. The finished conditions were as follows,

1.Single point diamond turning
2.Resin bond wheel grinding #4000 (VPG)
3.Resin bond wheel grinding #3000 (HPG)

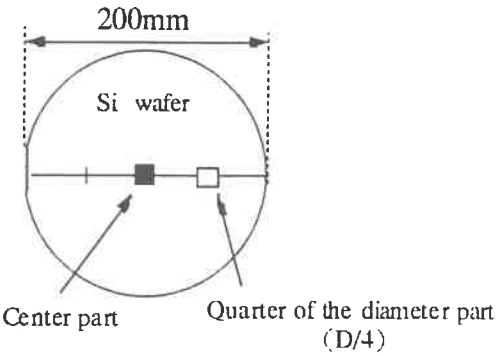

Figure 1. TEM Observation points of the wafer

These wafers were taken from process line of Wacker Siltronic GMBH[3]. TEM observation were carried out on a taken from the center part and the quarter of the diameter (D/4) part of the wafer (Figure.1) . The cross-sectional specimen were prepared by conventional methods [4].

3.Discrete Fourier Transformation (DFT)

For the characterization of the wafer surfaces, we applied the DFT (Discrete Fourier Transformation) calculation. The explanation of applying the DFT of wafer surface profile were in shown figure 2～4.

The figure 2 shows how to measure the wave heights. Tracing the surface shape, the amplitude f of eight points were measured for the same interval.

The equation (1) is the fourier transformation formula. Put f(t) values into the equation (1).

$$G(f) = \int_{-\infty}^{\infty} f(t)\ e^{-i2\pi ft}\ dt \qquad (1)$$

The exponential part of the fourier term was constructed of sine and cosine functions.

Figure 3 shows fourier analysis of the measured surface profile. The a_0, a_1, ..., a_4 values are the amplitude of sine part. The b_1, .., b_4 values are amplitude of cosine part.

$$c_n = \sqrt{a_n^2 + b_n^2} \qquad (2)$$

The c_n is the square root of power. The a_n and the b_n are the amplitude of sine and cosine part, respectively. Put each values of the a_n and the b_n into the equation (2).

The figure 4 shows the DFT result. X- and Y-axis are the amplitude c_n and spatial frequency, respectively.

The c_0 is average of the amplitude of measured surface. If the c_n values are small for all spatial frequency, the surface is flat. If the c_n values of the low frequency region are high, this means the amplitude of long period waviness is strong and the roughness is large.

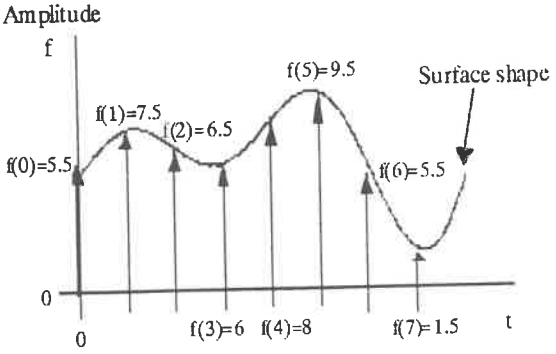

Figure 2. The measurement of the amplitude f

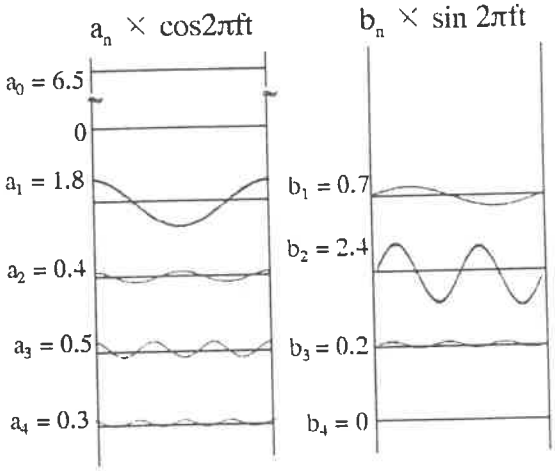

Figure 3. Fourier analysis of measured surface profile.

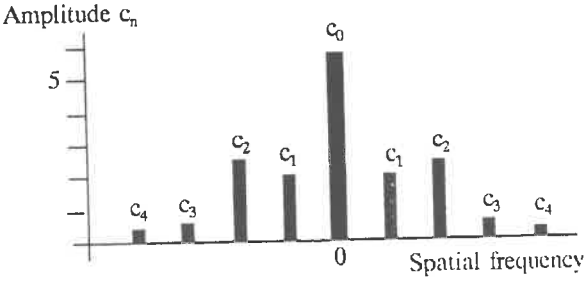

Figure 4. The DFT result of measured surface.

4.Results and Discussion

Figure 5 shows the cross-sectional TEM images at the center part of the wafer.

Figure 5 (A) shows the surface finished by diamond tool. The roughness value Rz (the ten point height) was 0.1μm. A dislocation depth reached 0.05μm from the surface.

Figure 5 (B) shows the ground surface for VPG #4000. The Rz was 0.02μm and the dislocation depth was 0.13μm. Figure 5 (C) shows the ground surface for HPG #3000. The Rz was 0.01μm and the dislocation depth was 0.20μm.

Table 1 shows the surface roughness and dislocation depth measured by TEM micrograph.

Comparing the center part and the D/4 part, the roughness value of D/4 part is larger than that of the center part. Comparing VPG and HPG, the latter has larger dislocation depth. Diamond turning is best among the three for both points.

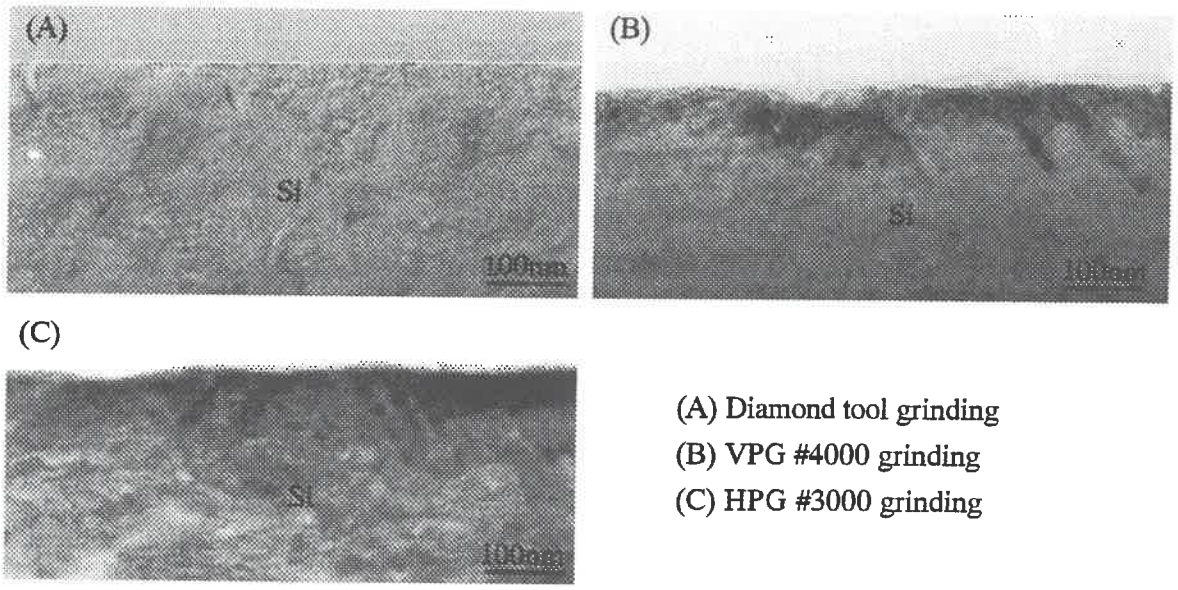

(A) Diamond tool grinding
(B) VPG #4000 grinding
(C) HPG #3000 grinding

Figure 5. The cross-sectional TEM images at the center part of the wafer

	Dislocation depth	Surface roughness
Diamond tool	0.05μm	0.01μm
VPG #4000	0.13μm	0.02μm
HPG #3000	0.20μm	0.01μm

The center part

	Dislocation depth	Surface roughness
Diamond tool	0.08μm	0.01μm
VPG #4000	0.16μm	0.03μm
HPG #3000	0.21μm	0.02μm

The D/4 part

Table 1. The surface roughness and dislocation depth measured by TEM micrograph

The graph 1 shows the DFT profiles of the surfaces at the center part of the wafer. The surface shapes were traced by cross-sectional images. 64 discrete points were measured for the same interval. Y-axis is the amplitude in log scale and X-axis is spatial frequency.

The profile of diamond tool lie in the lowest part for whole frequency region. This means the surface is flat. For VPG #4000, the amplitude of low frequency region is large. This means the amplitude of long period waviness is large and the roughness is large. This means we can measured the surface roughness and waviness by DFT profiles.

The graph 2 shows the DFT profiles of the surface at the D/4part of the wafer. The profile of diamond tool lie in the lowest part of the graph and the surface is flat. There was no difference between VPG grinding and HPG grinding. This means roughness value for HPG is as same value as for VPG.

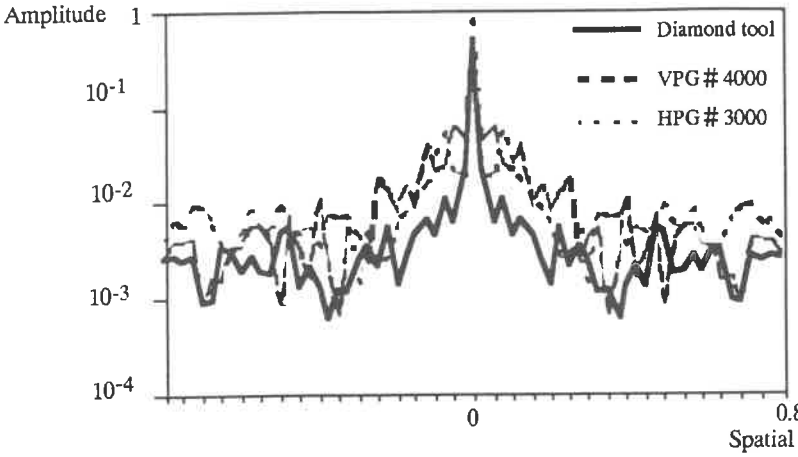

Graph 1. The DFT profiles at the center part of the wafer.

The profile of diamond tool lie in the lowest part for all frequency regons. This means the surface is flat.

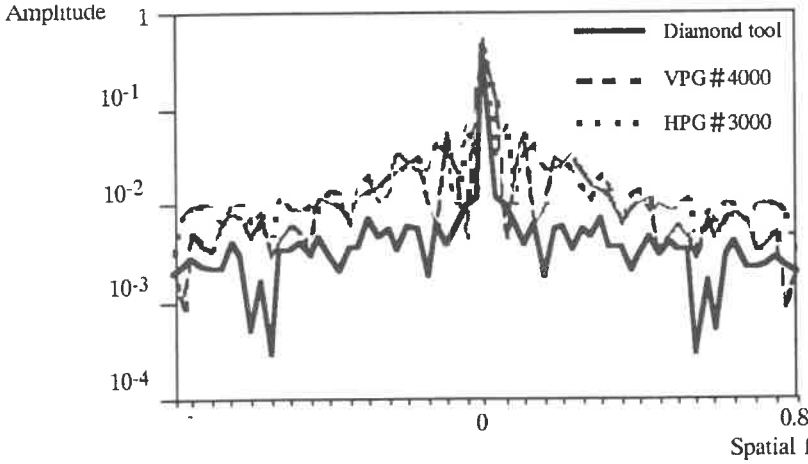

Graph 2. The DFT profiles at the D/4 part of the wafer.

There was no difference between VPG and HPG grinding. This means roughness value for HPG is as same value as for VPG

Summary

The roughness of the nm scale was measured by cross-sectional TEM and the surface shape and dislocation depth could measured. Comparing the center part and the D/4 part for all wafer, the latter has large both the roughness value and the dislocation depth.

The DFT profile give the information of not only the roughness but also waviness such as the number of the peak and trough.

Reference

1) J. Yoshioka, and F. Hashimoto, M. Miyashita, A. Kanai, T. Abo and M. Daito, "Ultraprecision grinding technology for brittle materials: Application to surface and centerless grinding process", *Grinding Symposium Proceeding, ASME, NY, 1985, p.205*

2) T. Abe, Y. Nakazato, M. Daito, A. Kanai and M. Miyashita, " The ductile mode grinding technology applied to silicon wafering process", Semiconductor silicon 1994, eds. H.R.huff et al (*Electrochem. Soc. Pennington 1994*)

3) H. Lundt, M. Kerstan, A. Huber and P.O. Hahn "Subsurface damage of abraded silicon wafers" Semiconductor silicon 1994, eds. H.R.huff et al (*Electron. Soc. Pennington 1994*)

4) Bravman, J.C. and Sinclair, R. : *J.Electron Microsc. Tech.*, 1,53 (1984)

Fabry-Perot Interferometers for Small Displacement Measurements

Lowell P. Howard, Fred Scire and Jack Stone
NIST Precision Engineering Division, Nano-Scale Metrology Group
Bldg. 220/Rm A-117, Gaithersburg, MD 20899

Introduction

Although both Michelson and Fabry-Perot interferometers are used in instruments designed to detect small displacements, it can be argued that Fabry-Perot interferometers (FPIs) offer some natural advantages due to their multipass nature and their ability to localize an extremely 'narrow' fringe. These perceived advantages are accompanied by a few caveats, however. Alignment is more problematic for multipass interferometers because each pass increases the effective path length and tightens the tolerance window for beam angles. Precise fringe localization in the FPI also means that there is no way to extract phase information from the interferometer cavity in the off-resonance condition because of the absence of a signal. In spite of these conditions, we feel that there are ample rewards to be gained, including traceable displacement measurements down to the atomic and subatomic level.

We are currently 18 months into a multiyear project to realize a compact Fabry-Perot interferometer system for scanned probe microscope z axis metrology and stylus profiler step height calibration. Given such goals, the useful range of our system is expected to be at least 1 μm with a resolution of approximately 1 pm and a displacement measurement combined standard uncertainty of 10 pm. For integration into calibration instruments the system must be located at the distal end of an optical fiber, have a built-in actuator and guiding mechanism and be no thicker than about 25 mm (see Fig. 1.)

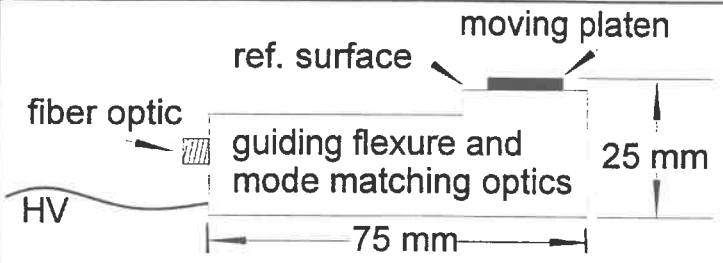

Figure 1. Fabry-Perot interferometer metrology cavity mechanical form factor design goal.

As the use of Fabry-Perot interferometers is somewhat novel amongst traditional metrology circles, a brief survey of some known FPI applications is useful for contrast and comparison. Laser spectroscopy is a traditional domain of the FPI. Using the FPI for metrology, however, requires access to the interferometer's scanning end mirror and some means to provide a reference plane for alignment purposes. Some workers in the field of x-ray interferometry[1] have used FPIs to make displacement measurements for silicon lattice parameter determinations used in Avagadro constant experiments. Such measurements are, in general, orders of magnitude slower than those used in scanned probe microscopy. Furthermore, FPI use in microscope metrology will not tolerate the gaps in data which are present when the FPI is not tuned to a resonant peak. Dilatometry[2] for thermal expansion coefficient of materials is another well known use of the FPI. Again, the rates of data acquisition in this application are orders of

magnitude slower than those needed for microscopy. Although the accepted mode of operation of the FPI in this instance, keeping a laser locked to a cavity resonance, avoids the problems associated with having no data in the off resonance condition, the available tracking range with a HeNe laser (≈1 GHz) limits the maximum continuously tracked displacement to some 300 nm or less. From even this brief survey, it can be seen that the task of making the FPI useful for microscope metrology will require technical approaches that are some departure from the established norms.

Simplified model of interferometer system

Our FPI system may be reduced to the model depicted in Fig. 2 for discussion purposes.

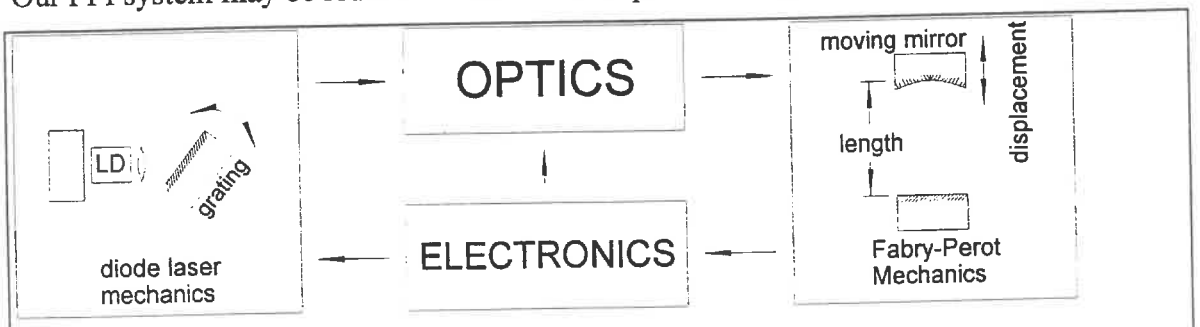

Figure 2. Greatly simplified diagram of Fabry-Perot interferometer system for small displacement measurements.

In operation, the optical and electronic systems keep the laser wavelength continuously locked to a fringe in the FPI. For the locked condition,

$$\Delta F = -\frac{F}{\ell}\Delta\ell, \quad \Delta\ell << \ell \qquad (1)$$

where ΔF is the change in the locked laser's frequency[3], F is the locking laser's nominal frequency, ℓ is the FPI's nominal cavity length and $\Delta\ell$ is the small displacement which is under scrutiny. Substituting in a few typical values for F (474 THz) and for cavity length (50 mm), we see the primary attraction of this method: a sensitivity of $\approx$-9.5 x 10^{15} Hz·m^{-1}. This high sensitivity means that with only moderate laser frequency control (≈10 kHz) we can measure displacements down to the picometer level with interferometric accuracy. Some of the significant limiting factors are: knowledge of the index of refraction inside the FPI cavity, parasitic motions of the FPI mirror, Abbe alignment effects and diffraction phase shifts. Diffraction phase shifts are often more problematic in FPIs than in Michelson interferometers because small (tens of micrometers) beam waists often exist inside spherical FPI cavities.

Referring once again to Fig. 2, we can explore some necessary and useful relationships between the laser cavity behavior and the FPI cavity. The tunable diode laser depicted in the figure contains a diffraction grating as a tuning element[4]; the exact configuration is not important here. What *is* important to realize is that the motions of the laser tuning mirror are servo locked to the motions of the FPI metrology cavity mirror and comprise essentially a mechanical follower mechanism. Having realized this, the following questions can be asked: what is the optimum relationship between the lengths of the two

cavities? Given this relationship, what role does vibration in the FPI cavity play and what can be said about the relationship of the FPI metrology cavity fundamental mechanical resonance to that of the laser? As to the question of optimum length relationship, we maintain that the laser cavity should be somewhat longer than the metrology FPI cavity based upon the following argument: limiting factors to resolution in both the FPI metrology cavity and the tunable laser will be electronic noise in the actuator drive system and environmental disturbances such as vibrations. Since we do not wish to have *both* the laser and the metrology cavity limited by essentially the same disturbances, we de-sensitize the laser somewhat by increasing the nominal length of its resonator cavity, referring back to eq. 1. In other words, the laser mirror is forced to move through a larger displacement than the FPI metrology cavity mirror. As to the question of vibration in the metrology cavity, we apply a simple first-order lumped-parameter model to the measured prototype interferometer fundamental resonance of 200 Hz. The resulting maximum environmental acceleration would then be $\approx 1.6 \times 10^{-6}$ m·s^{-2} or $\approx 1.6 \times 10^{-7}$ g (g = 9.8 m·s^{-2} is the acceleration due to gravity); this is representative of a very good environment indeed. Assume a cavity length relationship

$$\ell_{laser} = K\ell_{FPI} \quad (2)$$

where K is the mechanical 'gain factor' between the two cavity lengths. For a given time interval the laser tuning mirror must move K times as far as the FPI metrology cavity mirror. Therefore the laser mirror must also be moving K times as fast. In a purely mechanical system, the dynamic range-bandwidth product of the laser system must then be K times that of the FPI metrology cavity moving mirror. Given also the fact that the entire system is servo controlled, we must also strive to reduce phase lags in the response of the laser tuning mirror to the displacement of the FPI metrology cavity mirror. For a critically damped second order system, a prudent ratio of fundamental mechanical resonant frequencies might be somewhere around 2, where the laser fundamental mechanical resonance is always higher than that of the FPI metrology cavity. Fortunately, external cavity diode lasers can be electrically tuned small amounts by varying injection current. By using a 'woofer and tweeter' type control scheme where low frequency excursions are mechanically tracked and high frequencies are electrically tuned, phase lags inside the control loop can be kept to a minimum. This example does however, illustrate some of the difficulties encountered when attempting to solve the inverse problem of locking the FPI metrology cavity to a fixed laser source.

Prototype Interferometer

A full, detailed description of the prototype interferometer is beyond the scope of this abstract. The system can, however, be discussed in its block diagram form Fig. 3.

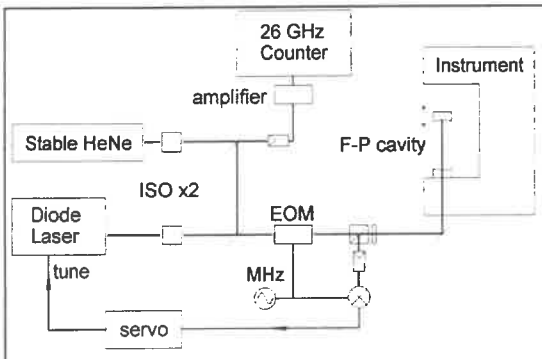

Figure 3. Block diagram of the Fabry-Perot prototype interferometer system.

The choice of laser wavelength influences many decisions and was complicated by the fact that 18 months ago, when we were picking technologies, 633 nm tunable diode lasers were an immature entity. This is only now being remedied with the introduction of commercially available products. We chose to remain at 633 nm primarily because of the enormous metrology infrastructure already in place with the HeNe laser, most notably the iodine stabilized frequency reference[5] and the accumulated knowledge of the refractive index of air[6] at 633 nm. While waiting for commercially produced products, we were ably assisted in our efforts to build a 633 nm diode laser by colleagues from NIST in Boulder, Co. They provided special antireflection coatings on the laser diodes and provided much needed advice on the construction of tunable diode lasers. Our internal effort to produce a laser light source that meets our specifications is depicted in Fig. 4.

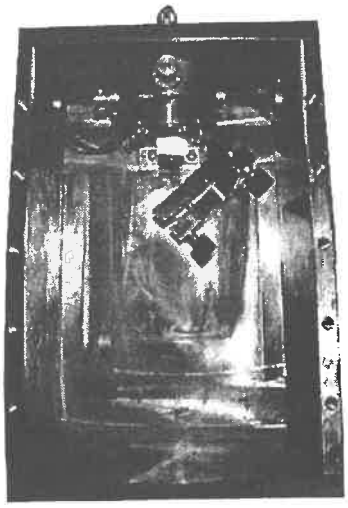

Figure 4. Tunable diode laser cavity on massive copper mounting plate.

The massive copper construction is for isothermal stability. Our laser diode sits upon a thermoelectrically cooled 5 degree-of-freedom mount made also of Cu or BeCu. Since the relationship of the diode facet with respect to the collimating lens was determined to be critical at the sub-micrometer level, a fine adjuster incorporating a demagnification mechanism consisting of a weak spring pushing against a stiff BeCu diaphragm was employed. This mechanism gives us 5.6 μm of laser travel for every 1 mm of micrometer screw travel. A prototype mount of lesser stability has already been used to produce heterodyne beat signals using a polarization stabilized HeNe laser as a frequency reference.

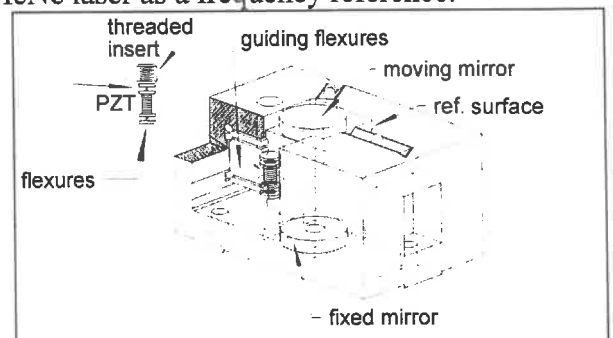

Figure 5. The metrology flexure mechanism for actuating and guiding the FPI mirrors.

The actuator and guiding mechanism for the Fabry-Perot mirrors (Fig. 5.) was constructed by electrical discharge machining (EDM) a solid monolith of invar, selected for thermal stability in an open, testing environment. Subsequent miniature versions of this flexure will be made of Cu or BeCu while attempting to increase the primary structural resonant

frequency, primarily through mass reduction. While invar is far from an ideal material for flexure mechanisms, the required travel of only a few micrometers for a flexure length of ≈20 mm make yield strength arguments moot. The scale of the flexure also helps reduce angular guiding errors, measured to be below 0.1" of arc using an autocollimator. The flexure is actuated by a low voltage PZT stack decoupled through hourglass flexures located at either end. The actuation point is approximately located at the centroid of the flexure blades for minimizing guiding errors. A reference surface is provided on the top of the invar block along with a set of vee grooves for kinematic mountings. Tungsten carbide inserts line the walls of the grooves for improved hardness and interface stiffness when used with mounting balls. During alignment, a CCD camera is placed on the kinematic mount to aid in making the Fabry-Perot cavity TEM_{00} mode collinear with the axis of flexure carriage travel to reduce Abbe offset.

The fringe locking servo control system functions in a similar fashion to those used for laser frequency stabilization[7]. The servo method, commonly referred to as a 'Pound Drever Hall lock' after some of its inventors, uses an electro-optic modulator (EOM) to introduce radio frequency sidebands to the light impinging upon the Fabry-Perot cavity. Reflected light from the cavity is collected using an optical circulator and processed using two phase sensitive detectors using the EOM driving signal as a reference. Theoretical lineshapes for our cavity conditions are shown in Fig. 6(a) with actual signals shown in Fig. 6(b). The quadrature signal is noteworthy in that a bipolar, linear signal is produced with a zero crossing exactly at the resonance condition. This linear portion of the signal makes an excellent discriminator for a control system scheme. The in-phase signal, with its bipolar spikes at the boundaries of the discriminator signal can be processed and used to validate that the laser is indeed locked to a fringe maximum. The fringe shapes of the prototype interferometer are distorted by at least two factors, both of which are currently being remedied. The extraneous signal present in Fig. 6(b) is presumably caused by nearly degenerate modes present in the current optical cavity configuration. New mirrors should fix this problem. The flattening at the fringe tops is caused by the phase detectors in the signal processing electronics being driven into nonlinear distortion, 'clipping' the signal tops. This too is being fixed and can be expected to yield a much higher fidelity representation of the theoretical signal in Fig. 6(a). Given the conditions of Fig. 6(b), the equivalent electrical noise level is some 3 pm rms for a 50 kHz bandwidth with a sensitivity ≈19 pm·V^{-1}.

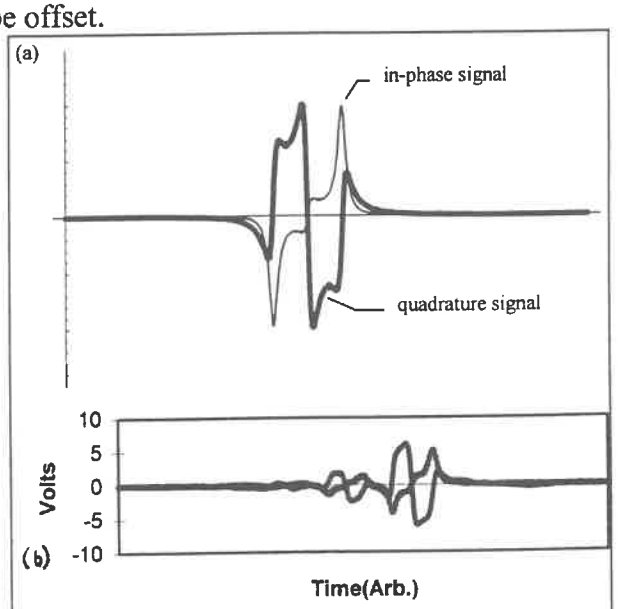

Figure 6. Theoretical (a) and actual (b) Fabry-Perot signals obtained using an RF reflection locking technique.

The project is currently in a state of final assembly. All the major components have been obtained. A significant portion of the systems had to be designed and fabricated in-house. The remaining task of locking our redesigned diode laser to our FPI metrology cavity and measuring the frequency shifts on our microwave frequency counter is not expected to be easy work, but should also hold few unpleasant surprises. Once initial testing is complete, fabrication of a miniature FPI metrology cavity will commence with an eye toward integrating the interferometer into stylus and scanned probe microscope calibrations.

Acknowledgments

The authors would like to thank Michelle Stephens and Leo Hollberg of the NIST Time and Frequency Division in Boulder, Co. for their contributions to the 633 nm external cavity diode laser.

---

[1] R.D. Deslattes, Applied Phy. Lett., **15**(11), p. 386, (1969).

[2] S.R. Patterson, *LLNL Report #UCRL-53787*, Feb. 19, 1988 (NTIS, US Dept. of Commerce, 5285 Port Royal Rd., Springfield, VA 22161).

[3] In this paper all frequency values are referenced to vacuum wavelength values using a nominal speed of light $c = 3 \times 10^8$ m·s^{-1}. In practice, knowledge of the speed of light in air is a significant limiting factor in the accuracy of any interferometer. Frequency and wavelength units are interchanged for convenience and readability.

[4] K. Liu and M. Littman, Optics Lett., **6**(3), 117, (1981).

[5] T.J. Quinn, "*Mise en Pratique...* ", Metrologia, **30**(5), 523, (1992).

[6] P. Ciddor, Applied Optics, **35**(9), 1566, (1996).

[7] R.W. Drever, J.L. Hall, F.V. Kowalski, J. Hough, G.M. Ford, A.J. Munley and H. Ward, Appl. Phys. B, **31**, 97, (1983).

A metrological three-axis translator and its application for constant force profilometry

V.G. BADAMI, S. T. SMITH, S.R. PATTERSON

Department of Mechanical Engineering and Engineering Science
University of North Carolina at Charlotte, Charlotte, NC 28223

Introduction

Stylus and constant force transducers form the basis of a broad range of instruments for metrological characterization of fine surface features.[1,2,3] Typically, stylus based instruments consist of a long range traverse mechanism for translation of the specimen relative to the probe, with the probe system mounted with its axis of measurement perpendicular to the traverse direction. In practice, it is the Abbe errors associated with the misalignment between the axis of the probe that interrogates the surface and the measurement axis of the transducer used to sense the displacement of the probe that dominate the achievable precision in profile height measurement. Currently, a force probe system is being developed to measure fine optical surfaces with an accuracy of 1 nm and a resolution of 0.1 nm for vertical surface profile deviations of up to 3 mm. The heart of this profiler consists of a constant force probe similar to that developed by Howard and Smith,[4,5] combined with a laser interferometer. Since the Abbe error is due to both the offset and the angle of tilt, control of either parameter can be used to minimize this error. The precision of alignment between the axis of the laser interferometer and the stylus probe is limited by manufacturing considerations. The strategy used to minimize this error is to control the angle of tilt. To this end a novel, three-axis flexure arrangement has been devised that allows for active control of two rotations over a range of 30 μrad while allowing a displacement of approximately 1.5μm.. The tilt control mechanism may also be exploited to obtain an estimate of the Abbe offset by monitoring the displacements as measured by the laser and the probe while rocking the probe head through a known angle.

Principle of Operation

A schematic diagram indicating the relationship between the various parts of the device is shown in Figure 1. The force probe is mounted to the target mirror assembly which, in turn serves as a plane mirror for a remote interferometer. The mirror assembly also functions as a target for capacitance gages. The PZT actuators can be controlled individually in combination to provide tilt and translation of the force probe relative to the top plate. Since tilt in two axes is required, a minimum of three actuators and three capacitance gages are required.

The force probe assembly used to interrogate the surface is shown in Figure 2. It consists of a stylus probe mounted on a glass cantilever. Electrodes deposited on the back of the cantilever and the top of the base form the plates of a capacitor. Deflections of the cantilever change the spacing between these plates, changing the capacitance, thus enabling the deflections of the cantilever to be monitored. This design is based on the work of Howard and Smith and is capable of sub-nanometer resolution over a 1 μm range.

In addition to providing tilt cancellation, the probe head also serves as a high-bandwidth actuator which is used to provide constant force stylus measurement. This is achieved by servo controlling the extension of the probe head to maintain constant cantilever deflection. The probe head in turn is mounted to a low-bandwidth, long-range vertical slide which provides the travel required by the large vertical profile deviations envisaged in current applications. For absolute measurements, the position and tilt of the force probe is measured relative to a metrology frame by interferometric methods. For this purpose, the rear surface of the probe is an optically flat reflector.

The force probe assembly is mounted to the probe head which consists of the actuators, flexures and capacitance displacement sensors. The flexure consists of two sets of three flexure elements (represented schematically in Figure 3 by the springs). The lower set of flexures provide the compliance for the PZT actuators to enable the required displacement and tilt. The upper set is used to adjust the preload on the actuators during assembly and allow for slight dimensional mismatch between the length of the flexure and that of the actuators. The adjustment

screws control the deflections of the more compliant upper flexures which in turn control the preload on the actuators due to the deflection of the lower flexures. Once the preload is set, the controlling stiffness is that of the lower flexures. The deflections of the individual PZT actuators are monitored by capacitance gages which can be used in combination to measure both displacement and tilt of the probe. Although the position of the force probe is monitored by a remote interferometer, the capacitance gages provide a more tightly coupled metrology loop that enhances the controllability of the entire system. In addition, the present design allows for the operation of the device as a stand alone device and facilitates bench testing.

Figure 4 shows an exploded view of the complete assembly. The two sets of flexures are part of a monolithic structure made out of aluminum which also includes slots for the PZT actuators. The flexures are equispaced around the circumference of a circle giving the monolithic flexure three-fold symmetry. Three PZT actuator segments are mounted on the top plate and pass through slots in the flexure. The actuators are made from a single piece of ceramic and exploit the Poisson effect to produce the desired fine motion. These actuators bear on the bottom plate via spherical contact surfaces that allow for the angular tilt. Capacitance gages mounted in the top plate monitor the displacement of each PZT with the bottom plate forming the target for the capacitance gages. The force probe is mounted to the bottom of the target mirror, which in turn is clamped to the lower surface of the bottom cap using a semi-kinematic clamping arrangement (not shown). Changes in length of the PZT actuators cause the bottom plate to tilt and translate relative to the top plate, the latter of which has a large aperture to allow the laser beams of a remote interferometer to pass through to the target mirror. While the aluminum structure of the probe head is susceptible to thermal changes, the force probe assembly and target mirror are constructed out of Zerodur™ and are directly referenced to the metrology frame through the interferometer, thus minimizing the thermal sensitivity of the main measurement loop. Monolithic construction has been employed to minimize joint losses and hysteresis and to obtain a compact, high stiffness structure.

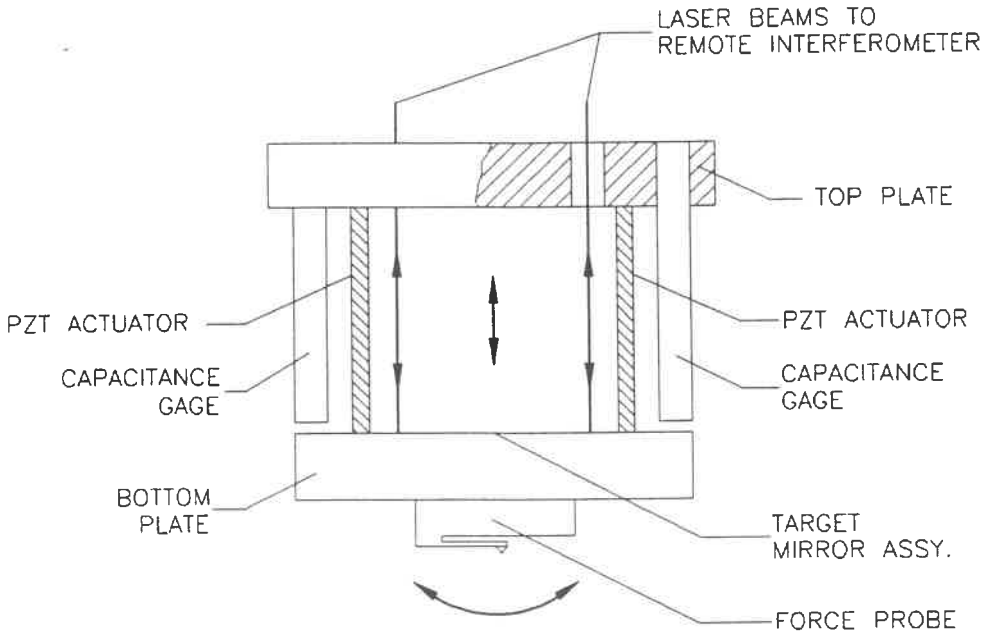

Figure 1: Relative dispositions of capacitance gages, interferometer and PZTs

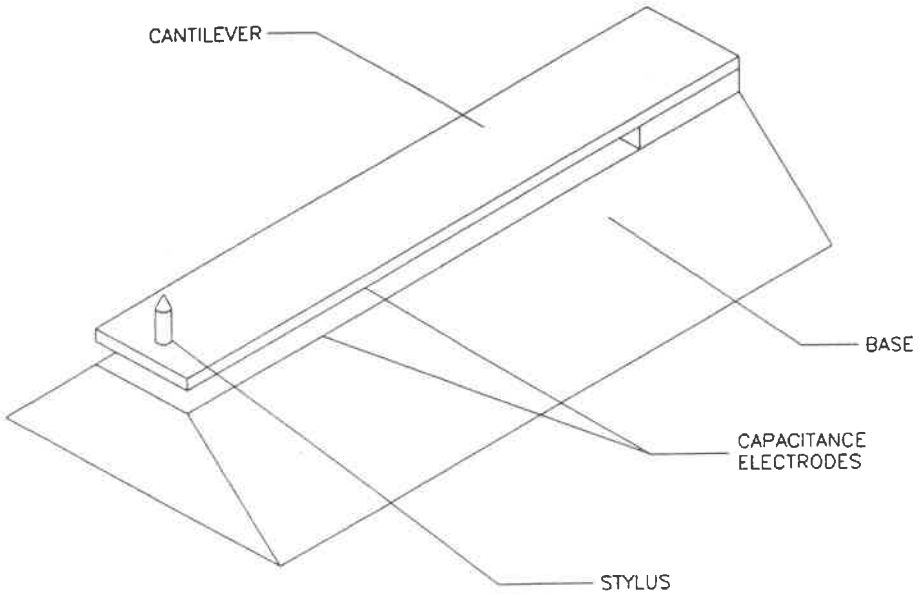

Figure 2: Schematic of force probe

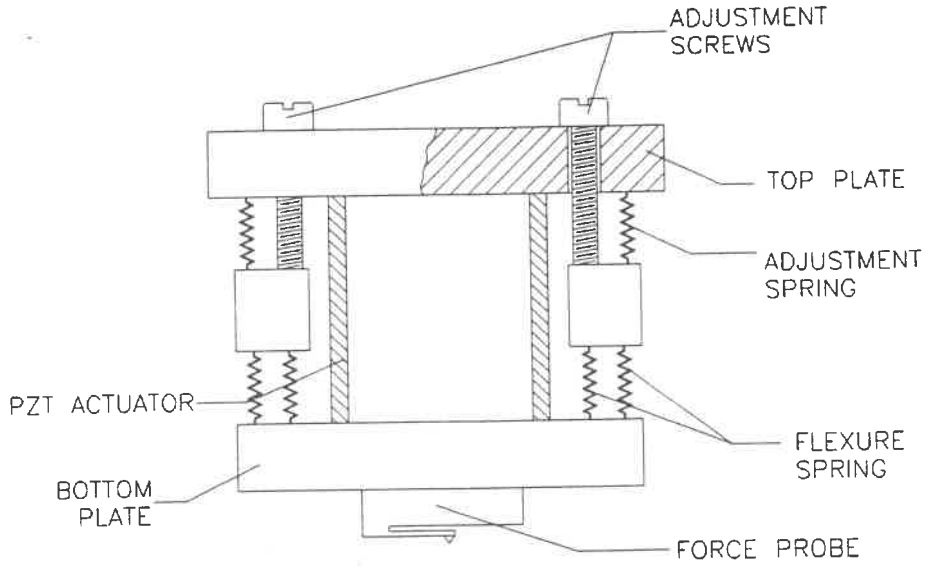

Figure 3: Schematic of flexure arrangement

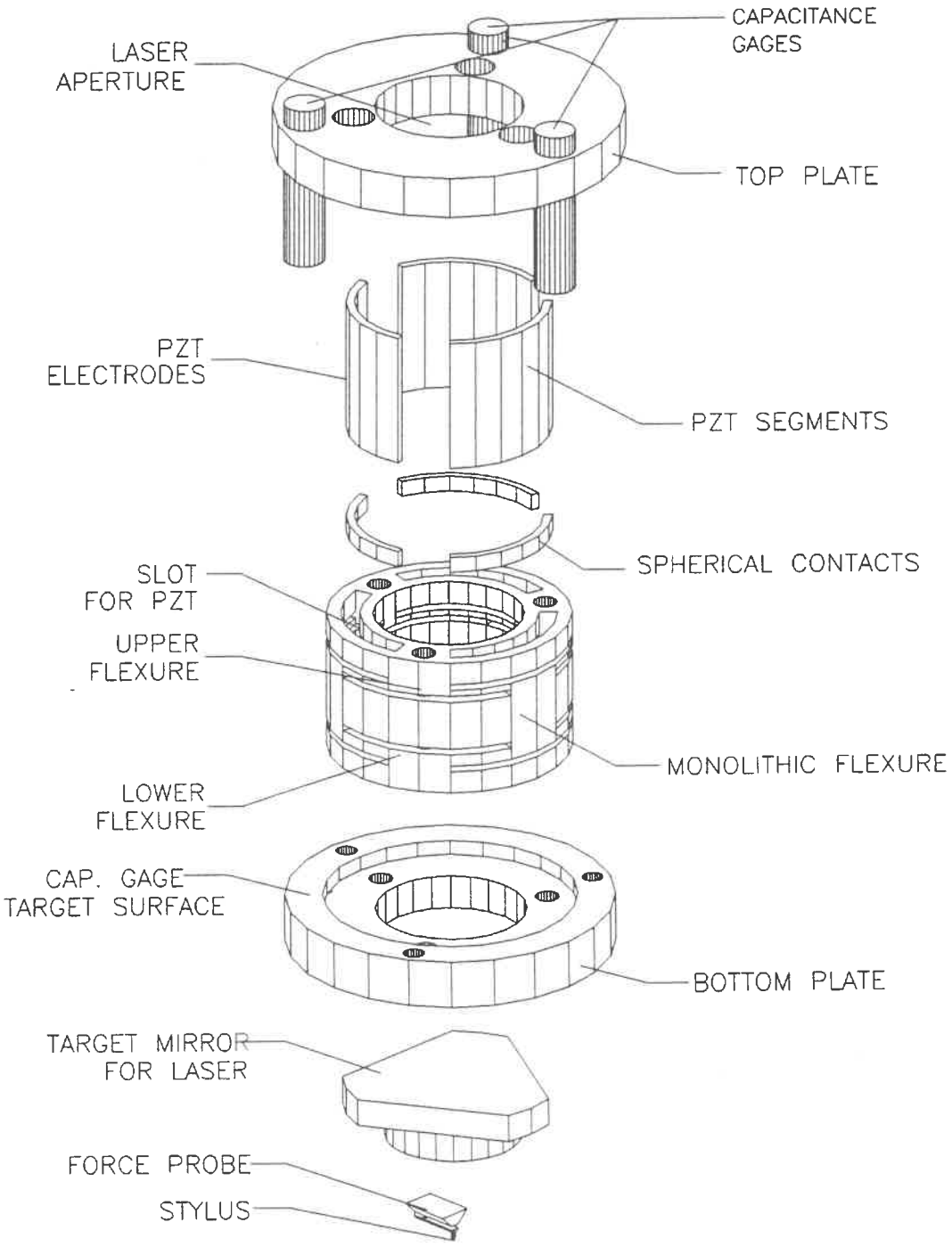

Figure 4: Exploded view of assembly

References

[1] Thomas, T. R., Rough Surfaces, Longman Press, London, 1982.

[2] Chetwynd, D. G., and Smith, S. T., "High precision surface profilometry: From stylus to STM,", *From Instruments to Nanotechnology*, ed. Gardner, J. W., and Hingle, H. T., Gordon and Breach, London, 1991, pp.273-300.

[3] Sarid, D., Scanning force microscopy: with applications to electric, magnetic and atomic forces, Oxford University Press, NY, 1994.

[4] Howard, L. P., and Smith, S. T., "A metrological constant force profiler," *Rev. Sci. Instrum.*, 65(4), 1994, pp. 892-902.

[5] Smith, S. T., and Howard, L. P., "A precision, low force balance and its application to atomic force probe characterization," *Rev. Sci. Instrum.*, 65(4), 1994, pp. 903-903

Modeling and Control of Hysteresis in a Piezoceramic Actuator

Ping Ge and M. Jouaneh
Department of Mechanical Engineering
University of Rhode Island, Kingston, RI 02881

Abstract

The hysteresis nonlinearity and output drift are two major limitations in open loop operation of piezoceramic actuators used in ultra-precision displacement applications. For tracking control applications, the hysteresis seriously affects the tracking performance even with the use of closed-loop feedback control. This paper presents a new approach for modeling the hysteresis nonlinearity of the actuator under non-cyclic input variations using a modified generalized Preisach model. Based on this model, a tracking control system for a piezoceramic actuator is developed by combining a PID feedback controller with a hysteresis linearizing scheme implemented in a feed-forward loop. Tracking control experiments of arbitrary input signals performed on a stacked piezoceramic actuator showed that a significant improvement of the tracking control accuracy can be obtained by using this tracking control scheme.

Generalized Preisach model for hysteresis

The classical Preisach model can be used to describe many physical phenomenons with nonlinear hysteresis behavior [1]. The hysteresis nonlinearity to be presented by this model must satisfy two important properties: the wiping-out property and the congruency property. Our experimental results show that the major hysteresis loop of a piezoceramic actuator is well shaped, and it does not depend on how the loop is approached [2]. This implies that any input extremum with small amplitude does not affect the future output values if the subsequent input value is larger than this input extremum. However, the hysteresis nonlinearity of a piezoceramic actuator does not satisfy the congruency property. This can be seen from Figure 1. When the input voltage starts from u_1, say $u_1 = 200$v, and monotonically increase to u_2, say $u_2 = 300$v, the output increments from different ascending loops are unequal, $\Delta_1 \neq \Delta_2$ in the figure. Such behavior also holds for the descending loop.

Consequently, when the hysteresis output runs on a minor loop (see Figure 2) as would be the case when tracking arbitrary input signals, a significant distortion will occur if we use the classical Preisach model to predict the hysteresis output of the actuator. To overcome this limitation, the generalized Preisach model needs to be developed for modeling the hysteresis output of a piezoceramic actuator for arbitrary types of input signals.

The generalized Preisach model can be mathematically expressed as

$$x(t) = \iint_{R_{u(t)}} \mu(\alpha,\beta,u(t))\gamma_{\alpha\beta}[u(t)]d\alpha d\beta + x^{+}_{u(t)} \qquad (1)$$

where, $\mu(\alpha,\beta,u(t))$ is a weight function of the Preisach model; $x^{+}_{u(t)}$ is the hysteresis output defined on the major ascending hysteresis loop; $\gamma_{\alpha\beta}[u(t)]$ is the hysteresis operator which has two output values, 0 and 1; α and β are the switching values of input, corresponding to the maximum value of input extremum and the minimum value of input extremum respectively; $R_{u(t)}$ is a rectangular region which can be subdivided into two sets, $S^{+}(t)$ and $S^{-}(t)$ (see Figure 3). In $S^{+}(t)$ the output value of the switching operator, $\gamma_{\alpha\beta}[u(t)]$ is equal to 1 while in $S^{-}(t)$, $\gamma_{\alpha\beta}[u(t)]$ is equal to 0. In the α-β diagram

of Figure 3, the horizontal interface link corresponds to an increment of the input on an ascending hysteresis loop, thus it always goes up, while the vertical link corresponds to a decrement of the input on a descending hysteresis loop, thus it always moves towards the left. Since $\gamma_{\alpha\beta}[u(t)]$ is equal to 0 in $S^-(t)$, the above Preisach model (1) can be simplified as

$$x(t)=\iint_{S^-(t)}\mu(\alpha,\beta,\mu(t))d\alpha d\beta + x^-_{u(t)} \qquad (2)$$

To obtain an expression for the weight function, we introduce a new function, $X(\alpha,\beta,u(t))$, which is defined as an output difference at a certain value of input, u(t), between a first-order reversal curve and a second-order reversal curve that is attached to the first-order reversal curve (see Figure 2), i.e.,

$$X(\alpha',\beta',u(t))=x_{\alpha' u}-x_{\alpha'\beta' u} \qquad (3)$$

Substituting for $x_{\alpha' u}$ and $x_{\alpha'\beta' u}$ in Equation (3) by using the facts shown in the Figure 4, gives

$$X(\alpha',\beta',u(t)=\iint_{R(\alpha',\beta',u)}\mu(\alpha,\beta,u(t)d\alpha d\beta=\int_{u}^{\alpha'}[\int_{\beta'}^{u}\mu(\alpha,\beta,u(t))d\beta]d\alpha \qquad (4)$$

From Equation (4), we can see that the double integral of the weight function over the rectangular region R can be evaluated from first and second order reversal curve output data. This fact is used in obtaining an explicit formula for the generalized Preisach model which can be written as:

$$x(t)=x^-_{u(t)}+\sum_{k=0}^{N}[X(\alpha'_{k-1},\beta_k u(t))-X(\alpha_k,\beta'_k u(t))] \qquad (5)$$

where, $x^-_{u(t)}$ is the hysteresis output value defined on the major descending loop and $X(\alpha_k,\beta_k,u(t))$ as defined in Equation (3). The details of the derivation of Equation (5) are given in reference [3].

Model-based tracking control scheme

Because of the existence of hysteresis in piezoceramic actuators, the traditional PID feedback controller is inadequate to obtain a good tracking control performance. Hence, we propose a tracking control scheme which consists of a PID feedback control loop augmented with a hysteresis model in a feed-forward loop. In the feed-forward loop, a model-based linearization of the nonlinear hysteresis is performed using the generalized Preisach model developed earlier.

Figure 5 shows the flow chart of the linearization algorithm. The linearizing algorithm involves the following steps: (i) The arbitrary reference signal is discretized and the initial control voltage is set to zero; (ii) the reference displacement is sampled and the hysteresis output of the actuator is computed by using the numerical generalized Preisach model. The calculated output is compared with the corresponding reference displacement, and the error between the reference and actual trajectories is used to compute the updated control voltage. This step is repeated iteratively until a specified accuracy of output displacement is obtained; (iii) The index *k* is increased and step (ii) is repeated for the next reference displacement value. Here, the new initial value of control voltage

is set to the last updated control voltage. It should be noted that in the linearization process, the control voltage extrema are determined from the reference displacement signal, i.e., when the reference displacement reaches a maximum (minimum) value, the control voltage also arrives at a maximum (minimum) value. This control voltage is, thereby, recorded as the previous input extremum and used in the Preisach model to determine the future hysteresis output.

The proposed tracking control system was designed by adding the above described feed-forward linearizing scheme to a PID feedback control loop. Figure 6 shows this control scheme. In the figure, the control voltage, $u_d(kT)$, is the linearizing term which is selected from a reference displacement/control voltage look-up table. The error signal, $\Delta u(kT)$, derived from the PID feedback controller, functions as the compensation term. As a result, the total control voltage sent to the piezoceramic actuator is the sum of these two signals, i.e.,

$$u(kT) = k_P e(kT) + k_I \Sigma e(kT) + k_D[e(kT)-e((k-1)T)] + u_d(kT) \qquad (6)$$

where, T is the sampling time of the control system.

Experimental results and conclusions

The experimental setup is shown in Figure 7. The control system performance was tested for tracking an arbitrary reference displacement signal. A comparison was made between an open loop control system, an open-loop feedforward linearizing control system, a PID feedback control system and a PID feedback control system augmented with a linearizing scheme in the feed-forward loop. Figure 8 shows the tracking control signals and their errors. The maximum error for the PID feedback controller augmented with a linearizing scheme in a feed-forward loop is about 1/4 of that of an open loop system and 1/2 of that of the regular PID feedback control system. The results show that after incorporating a model-based feed forward loop in a PID feedback control system, the tracking control error was significantly reduced.

References

[1] Mayergoyz, I., Mathematical Models of Hysteresis, Springer-Verlag, 1991.

[2] P. Ge and M. Jouaneh, "Modeling hysteresis in piezoceramic actuators", Precision Engineering, 1995, Vol. 17, pp. 211-221.

[3] P. Ge, "Modeling and control of hysteresis in piezoceramic actuators", Ph.D. dissertation, Dept. of Mechanical Engineering, University of Rhode Island, May 1996.

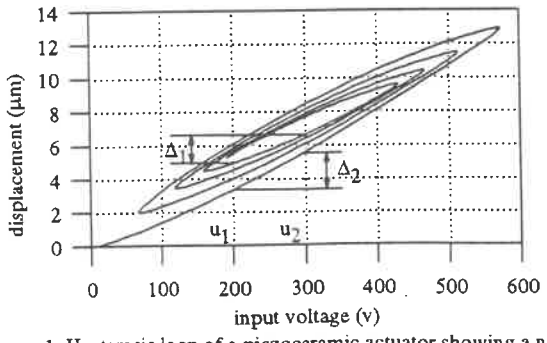

Figure 1. Hysteresis loop of a piezoceramic actuator showing a non-congruent behavior for the same change in input (from u_1 to u_2)

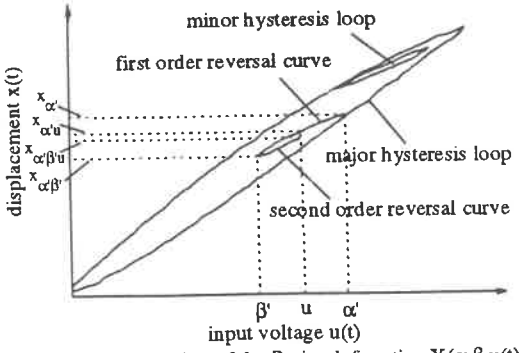

Figure 2. Illustration of the Preisach function $X(\alpha,\beta,u(t))$ defined on first-order and second-order reversal curves

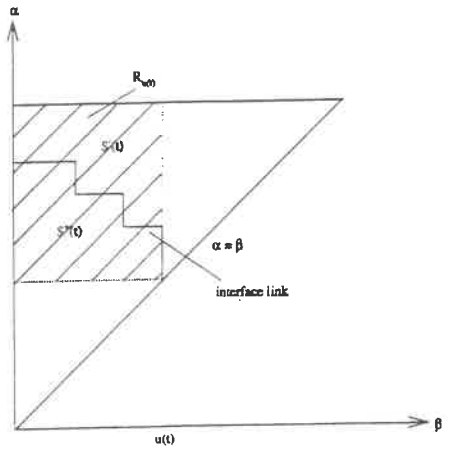

Figure 3. Geometrical interpretation of the generalized Preisach model

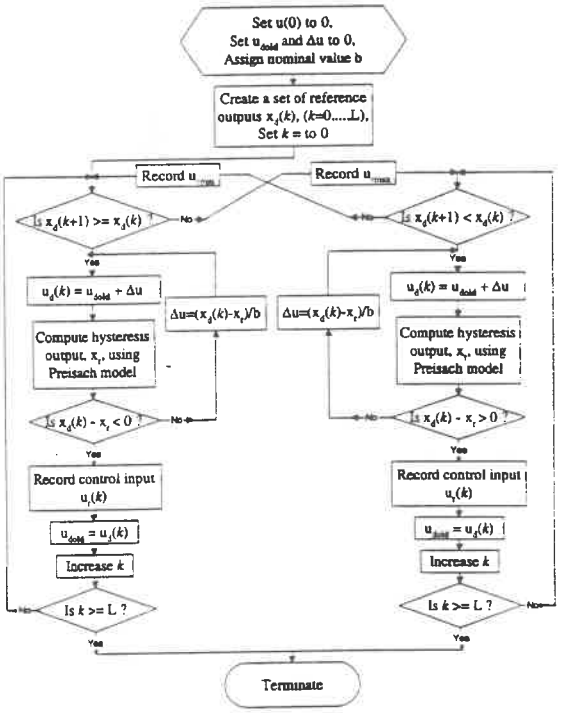

Figure 5. A Model-based linearizing control algorithm

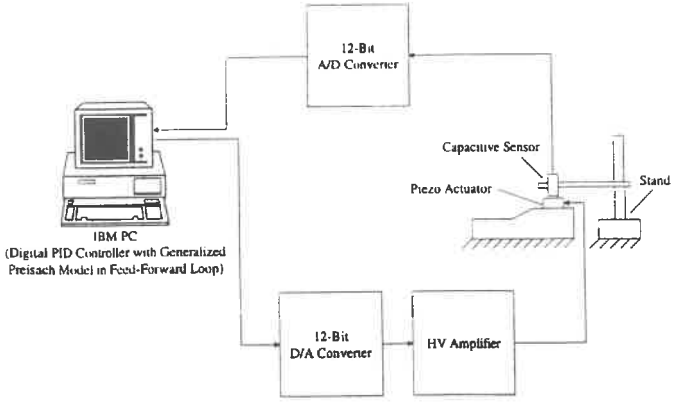

Figure 7. Experimental setup for the piezoceramic actuator control system

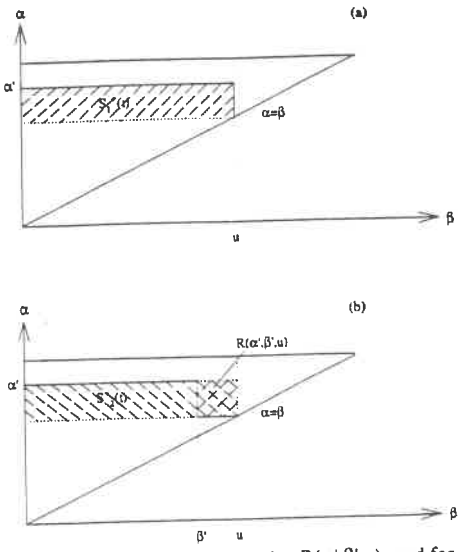

Figure 4. Illustration of the region R(α',β',u) used for computation of the function X(α',β',u)

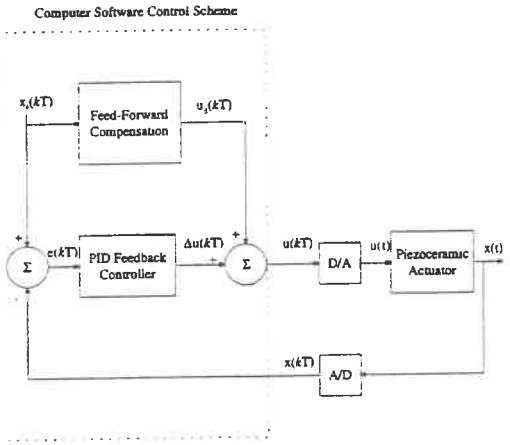

Figure 6. A block diagram of the tracking control system that is made up of a PID feedback controller augmented with a hysteresis linearizing scheme in a feed-forward loop

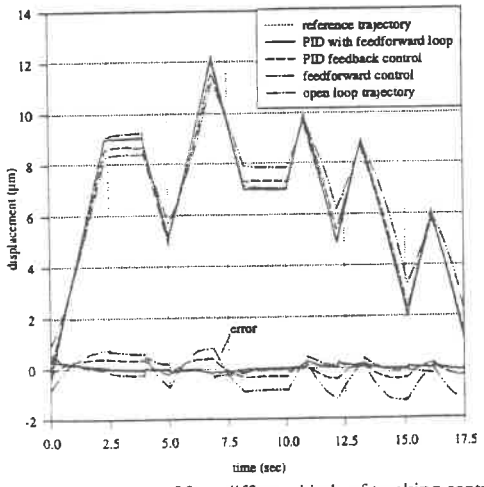

Figure 8. Comparison of four different kinds of tracking control schemes and their errors against the reference trajectory

Implementation of an Acoustic Emission Proximity Detector for Use in Generating Glass Optics*

Mark A. Piscotty, John S. Taylor, Kenneth L. Blaedel

Lawrence Livermore National Laboratory
L-537, P.O. Box 808
Livermore, CA 94551
510-422-2052 fax: 510-423-1460

Background and Motivation

The use acoustic emission (AE) sensing as a method to monitor proximity between a grinding wheel and a brittle material workpiece is being developed at Lawrence Livermore National Laboratory (LLNL) and the Center for Optics Manufacturing (COM) in Rochester, NY[1]. Significantly reducing the amount of expensive 'air-grinding' is one of the primary motivations behind this effort, along with lessening the chances of a crash which could damage the wheel, part and machine tool. AE sensing is well developed and routinely used in the metal working industry[2] for 'initial contact' sensing or tool breakage, for example, and in monitoring diamond turning and grinding processes[3]. However, using AE sensing to switch from a rapid to a final in-feed rate at the detection of initial-contact between the grinding wheel and a *brittle* material workpiece, such as an optical glass, is often unacceptable during fine grinding (less than 10 μm grit wheels) which produce surfaces with roughness values of 100 Å rms or less. In the approach taken here, we are sensing the AE *prior* to contact between the workpiece and the tool. The coolant between the workpiece and the grinding wheel is used as an AE medium to transfer AE signals generated by the relative motions of the coolant, workpiece and wheel. Capitalizing on the repeatability of the AE approach signal, we have developed a system to detect the proximity of the grinding wheel relative to the workpiece prior to initial contact.

Acoustic Emission System Design at LLNL

We have developed and installed an AE closed-loop feedback system on a spherical optics generator at LLNL. Two air bearing spindles are used on the grinder, one for the grinding wheel and the other for the glass workpiece. A through hole in the part spindle accommodates the AE sensor, AE transmission rod and preamplifier as shown in Figure 1. The transmission rod is a lightly spring-loaded, aluminum rod which is acoustically insulated from the machine tool to minimize machine induced noise in the AE signal. By lightly touching the back side of the workpiece, the transmission rod provides a practical method of coupling the AE sensor to the workpiece, thereby ensuring a desirable signal-to-noise ratio. A rotating union provides the means of connecting the amplified AE signal and preamp power lines between the rotating AE components within the grinding spindle and the outside stationary equipment.

Once the AE signal is transmitted through the rotating union, it is low-pass filtered, passed through an rms converting circuit, into a data acquisition system and finally to the CNC to provide the closed-loop feedback signal. The CNC can then utilize the feedback AE information to perform a variety of commands such as reducing the in-feed rate, changing spindle speeds, etc. Figure 2 is a schematic showing a possible scenario in which two AE thresholds are used to initiate CNC responses. In this scenario, the first threshold would trigger a routine with a set commanded lag time allowing a specified continuation of the fast in-feed (lag time) followed by a ramp down in the in-feed rate. This occurs in the *turbulence region* where the wheel is still not contacting the part and the AE is generated with and

* This work was performed under the auspices of the U. S. Dept. of Energy by LLNL under contract No. W-7405-Eng-48.

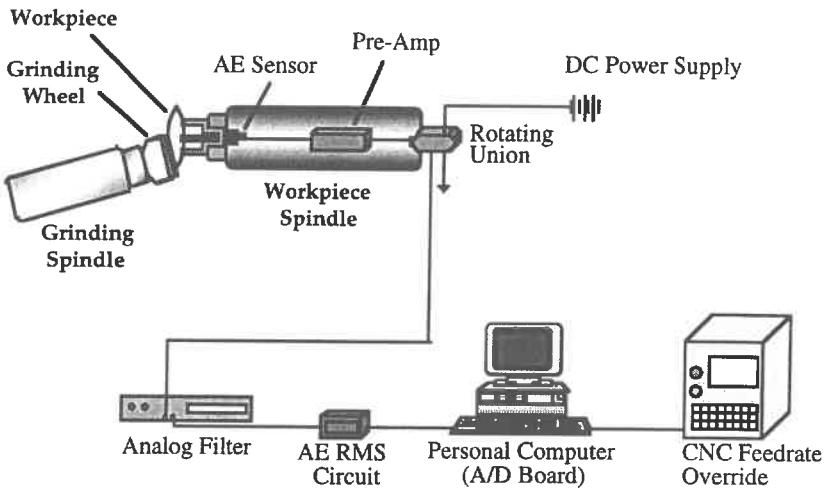

Figure 1. Schematic showing the AE closed loop system at LLNL.

transferred through the coolant layer between the wheel and the part. The next region is referred to as the *once-per-revolution region* in which the wheel is just beginning to make contact with the part due to axial error motions occurring every one revolution of the wheel. This region is noted by a sharp increase in the AE level and the second threshold located in this region could then be used to trigger a quick-change in the feed rate down to the final in-feed rate for the fine grit wheel. And lastly, the final region, *grinding*, is characterized by high, relatively constant AE levels. Repeatability of the AE approach signal is the key which allows exploitation of this process for use as a wheel-to-workpiece proximity sensor.

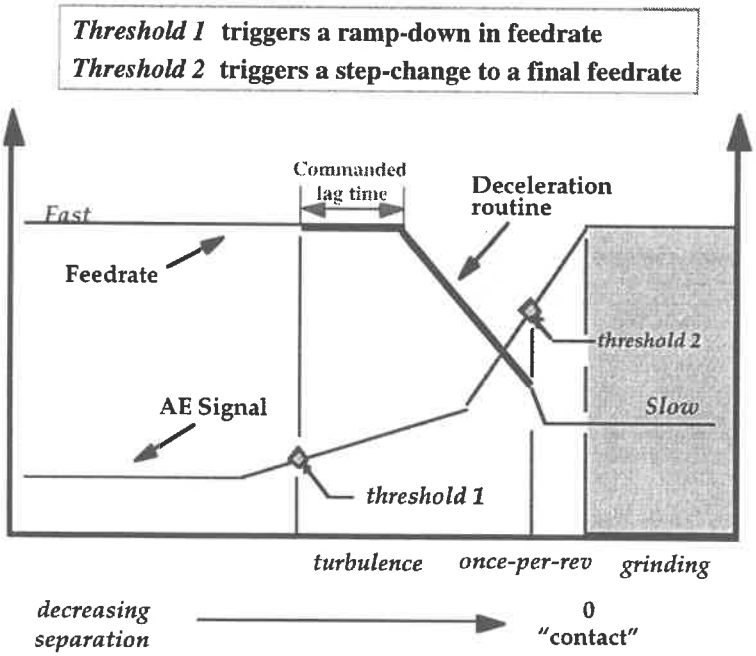

Figure 2. Using two distinct AE level thresholds is a possible implementation method of a closed-loop AE feedback system.

Acoustic Emission Data from LLNL's System

As might be expected with a system like this, it is sensitive to a number of operating parameters such as wheel speed, wheel configuration, coolant flow rate and approach angle of the grinding wheel. For example, Figures 3 a-c, show approach AE data for three grinding situations where the only process parameter change was wheel speed. The data acquisition process began with the approach of the grinding wheel toward the workpiece. Some approach data, such as Figure 3a will have a distinct ridge where the AE signal increases to a certain point and then decreases as the wheel gets closer to contacting the part. Other data will monotonically increase as the wheel-to-workpiece separation decreases, like Figure 3c. From left to right, Figures 3 a-c show approach data for three cases where the wheel speed is decreased. Focusing on only the approach portions of the data, it is evident that the AE levels during the approaches decrease with wheel speed until, in Figure 3c, the signal is almost unusable. The different AE magnitudes of the *contact* points is attributed to thermal growths of the wheel, workpiece and fixturing where a fraction of a micrometer may result in a significant change in the once-per-rev signal, where little material removal takes place. Although these signals may vary as process parameters are changed, when they are held constant, as they typically are during grinding, the AE approach signals are quite repeatable. It is this repeatability of the AE approach signal that allows sensing of the AE signals to be used as a proximity detector. Overcoming different AE approach characteristics as parameters are modified can be accomplished through a quick CNC calibration routine (i.e., recalibrate the system if parameters are changed).

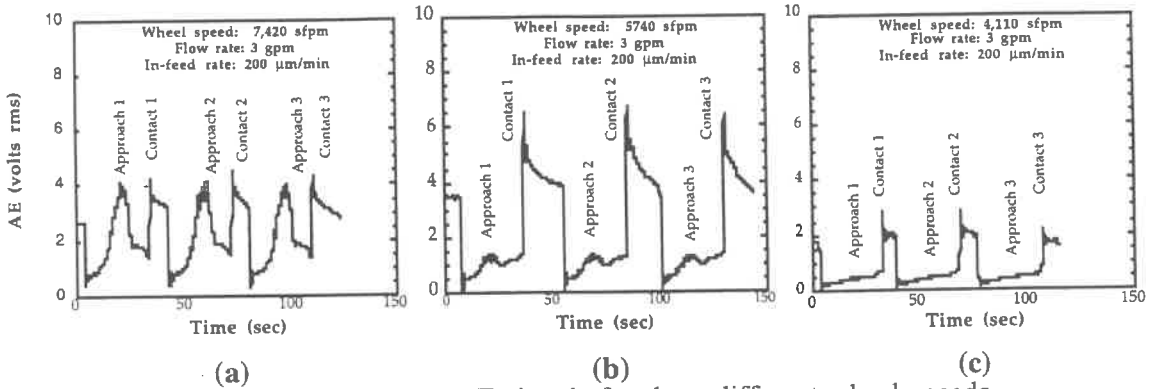

Figure 3. Approach AE signals for three different wheel speeds.

Since the repeatability of the AE system depends on the AE level threshold monitoring, tests were generally conducted using three different in-feed rates, from 50 to 200 µm/min. Figures 4 a and b, show repeatability data for two identical grinding conditions, but with two bronze bond, 2/4 µm diamond wheels with different body configurations. The tests consisted of initially grinding and dwelling on the part to establish the zero point. The wheel is then commanded off the part 100 µm, fed in towards the part until an AE threshold is reached. The CNC then commands the in-feed to stop and the separation distance is recorded.* This process is repeated 20 times to measure repeatability. Adjusting the threshold level will affect the separation stopping distance and can be dialed-in for a desired separation distance.

* Note that this separation is 'implied' from the axis position of the machine tool. Actual separation is sensitive to grinding zone thermal fluctuations which are not reflected in the axis position. This is one source of non-repeatability error in the test data.

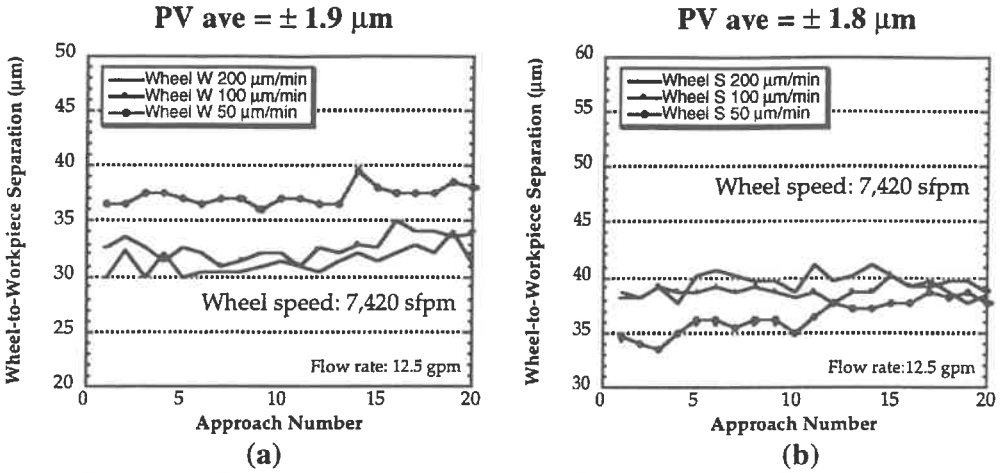

Figure 4. Repeatability data for two different body configurations of wheels.

Figures 5 a and b show repeatability data for two more grinding scenarios. Figure 5a uses the same parameter settings as in Figure 4b, except that the flow rate is reduced from 12.5 gpm to 3 gpm. The result was a more noisy signal which resulted in a greater PV variance. Figure 5b presents two identical repeatability runs, but in this case the wheel speed was 4950 sfpm and the flow rate was 7.5 gpm. This produced a relatively low AE approach level that resulted in a close stopping distance from the part (1 to 2 µm separation). The peak-to-valley variance of this case was by far the lowest of all the cases that corresponded to the approach signal also being the least noisy. The repeatability data for these cases is also a function of sampling strategy (filtering, rms calculation, time averaging) and balancing optimum repeatability and minimum response time is required for each grinding situation.

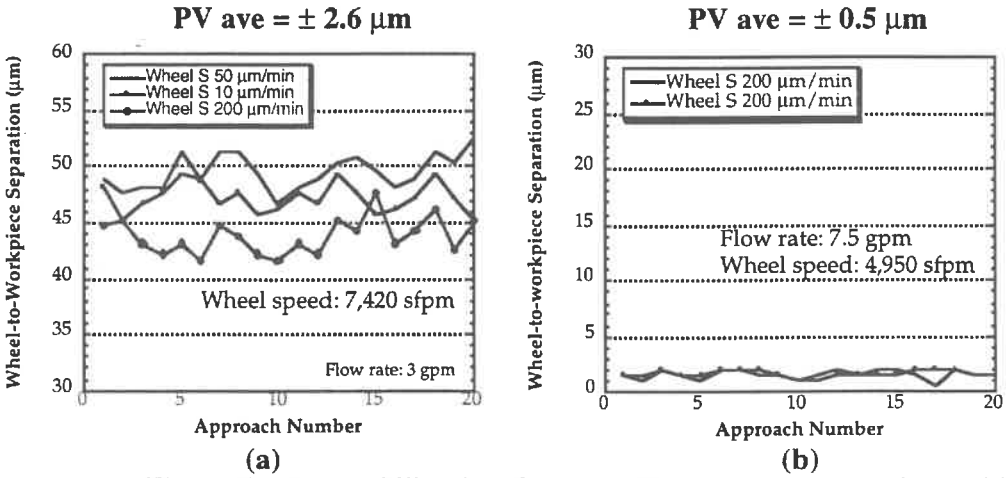

Figure 5. Repeatability data for two different parameter settings with the same wheel.

An additional benefit to the AE proximity system is that it allows real-time monitoring of the grinding process that can reveal such information as the need for the wheel to be dressed. Figure 6 shows an example of this. The upper left plot is of data acquired during a nominal grinding process. After an initial long term dwell, the wheel backs off the part, feeds in, grinds the part and dwells (sparks out) for 45 seconds. As seen in this first plot, the AE signal drops off quickly in the dwell region. The upper right plot is data from an identical run, but this time the wheel is in a loaded condition and needs to be dressed. Data in this plot contains much more noise and the dwell signals remain at relatively high levels. After dressing the wheel, another run is made and the bottom plot shows the resultant data with the return to nominal AE grinding characteristics.

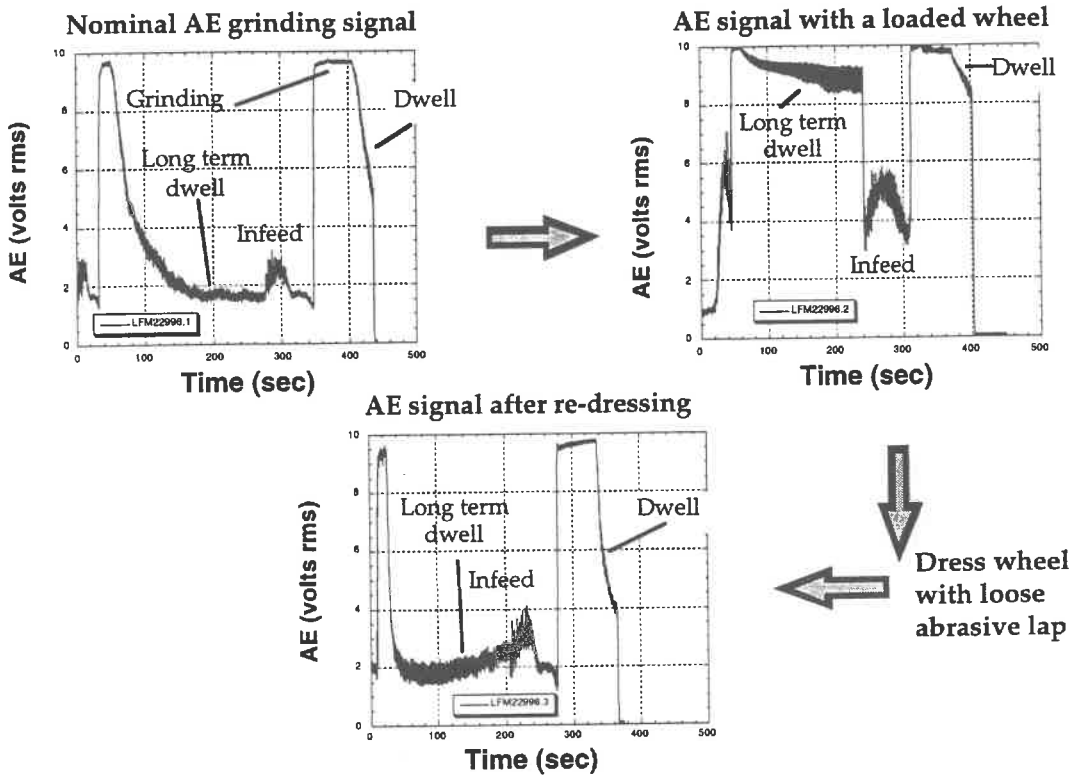

Figure 6. Using AE to monitor in-process grinding data reveals information such as the need to dress a wheel. Bronze bond, 2/4 μm diamond wheel, grinding BK7 glass.

Commercialization

An AE system similar to the one at LLNL is currently in the development and testing stages on commercially available spherical generator, the Micro SX from CNC Systems[4], and is located at the COM. The Micro SX has two vertically mounted spindles and can generate parts up to 25 mm in diameter. A significant difference between the LLNL generator and the Micro SX is that the Micro SX utilizes roller bearing spindles which tend to introduce more AE noise into the system. Sufficiently isolating the transmission rod from the workpiece spindle and filtering of the AE signals provides a useable AE signal.

Figure 8 is a close up view of the workpiece chucking mechanism, the transmission rod assembly and the AE sensor. The AE signal line exits the bottom end of the spindle and is connected to the preamp, which is also rotating with the spindle. The AE sensor is mounted on the lower end of the transmission rod and the sensor cable is fed through a center hole in the belt-driven spindle. The amplified AE signal is routed through a rotary union and is brought out to a data acquisition system and the Micro SX's CNC. Special programming of the CNC's programmable logic controller will provide the AE level threshold monitoring necessary for the closed-loop feedback implementation. Initial tests will be used to measure repeatability and robustness of the AE system as a wheel-to-workpiece proximity detector. An additional feature is that real-time in-process information will be available by monitoring the AE signal during grinding.

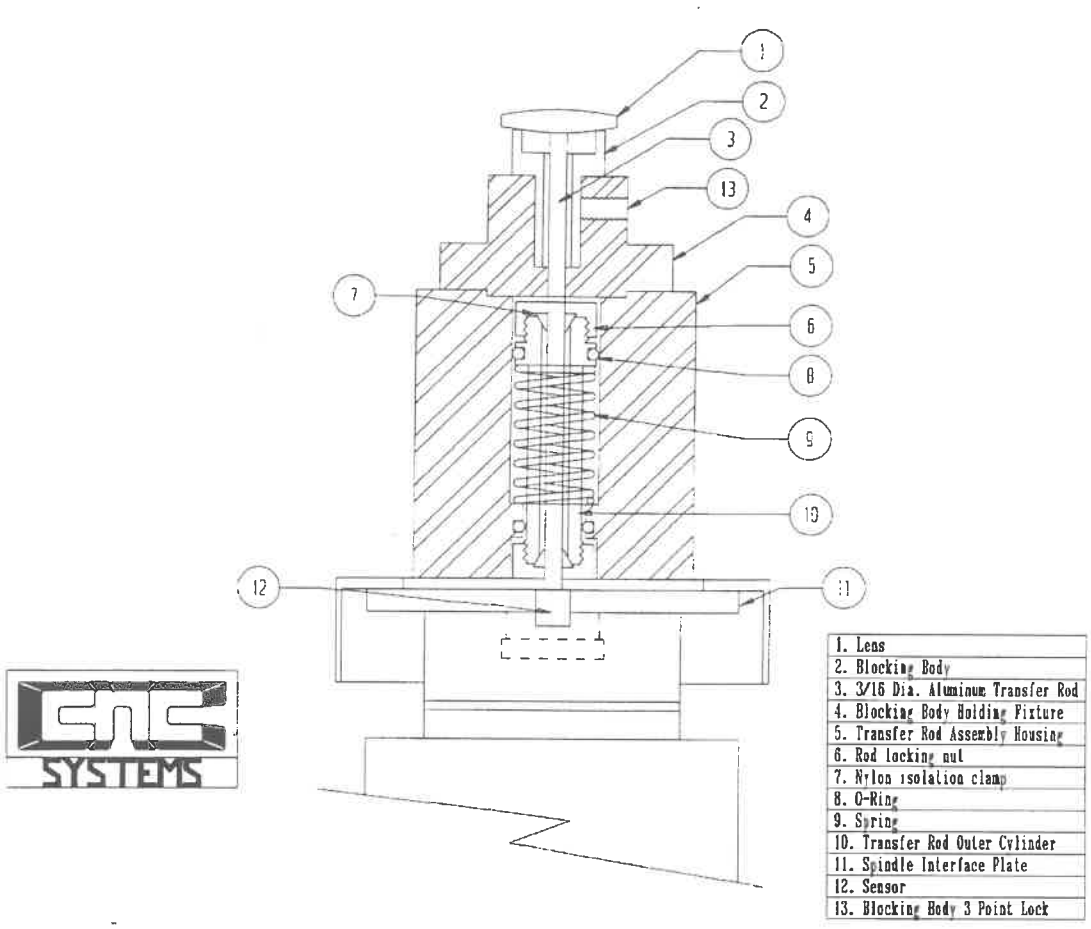

Figure 8. Detail of the acoustic emission sensor fixture for the OptiPro 100.

Summary and Conclusions

We are using the approach AE signal during a grinding operation to detect the proximity of the grinding wheel relative to a brittle material workpiece and are using this detection as a feed-back control signal in our CNC. The repeatability of the AE signal during the wheel approach is the key that allows AE to be used as a proximity detector and is demonstrated at LLNL to be about ±2 μm. We noted significant changes of the AE signal as process parameters are modified, but conclude that with a quick CNC calibration routine and holding the parameters constant during a given operation, the AE system can be successfully used to sense pre-contact wheel-to-workpiece separation. Additionally, the AE sensing system allows real-time monitoring during grinding to provide in-process information. The first prototype of an AE system on a commercially available generator is currently be tested at the Center for Optics Manufacturing.

---

[1] Taylor, J.T., Piscotty, M.A., Blaedel, K.L., Dornfeld, D.A., Weaver, L., "Investigation of Acoustic Emission for Use as a Wheel-to-Workpiece Proximity Sensor in Fixed Abrasive Grinding," ASPE Annual Meeting Proceedings, Volume 12, October, 1995.

[2] Dornfeld, D.A. "Acoustic Emission and metalworking - Survey of Potential and Examples of Applications," 8th NAMRC Conf., May 18-21, 1980, pp 207-213.

[3] Bifano, T.G. and Yi, Y. "Acoustic Emission as an Indicator of Material Removal Regime in Glass Micromachining," Journal of Precision Engineering, Vol. 14, No. 4, October 1992, pp 219-228

[4] CNC Systems, Inc., 369 Route 104, Ontario, NY 14519. Mike Bechtold, President.

Adaptive Pole-Zero Cancellation in Grinding Force Control

Hodge E. Jenkins[1]
Georgia Institute of Technology
The George W. Woodruff School
of Mechanical Engineering
Atlanta, GA 30332-0405

Thomas R. Kurfess
Georgia Institute of Technology
The George W. Woodruff School
of Mechanical Engineering
Atlanta, GA 30332-0405

Abstract

Previous work has demonstrated that grinding is a time-varying process, best modeled in real-time. Also it has been shown the integration of multiple sensor data can be used to achieve a superior estimation of a two-parameter grinding model, suitable for adaptive control of the normal grinding force. Building on these developments, this research investigates an adaptive force controller, using the real-time process model with multiple input estimation algorithms as a basis. An adaptive pole-zero cancellation technique is developed to overcome the grinding process variation. With the grinding model estimated in real-time, the adaptive controller provides inverse grinding process dynamics. This cancels the process effects on the controlled system. Real-time estimation and controller designs are implemented using parallel processors for higher speed control capability than is presently available in machine tool controllers. This approach to grinding force control has demonstrated the potential for increasing productivity with the reduction of tary time in plunge grinding, showing higher force regulation fidelity. Decreases in the normal force range and standard deviation is seen in comparisons to fixed-gain controllers. The implementation of this adaptive pole-zero cancellation approach in surface (traverse) grinding provides a superior surface following capability for fine finishing, as compared to fixed gain controllers.

Background

Grinding is a complex operation, seen as three separate and concurrent process actions: (1) cutting, (2) plowing, and (3) rubbing (Hahn and Lindsay 1971), occurring simultaneously in varying distributions depending on the grinding wheel, material, and operating conditions. This causes detailed process analysis, modeling and control to be difficult. Previous work has demonstrated that grinding is a time-varying process and should be modeled in real-time. The empirical grinding process model selected in this research is based on a combination of the grinding model developed by Hahn and Lindsay as well as the Preston model (Jenkins, et al, 1996). The selected, two-parameter grinding model is given in equation (1).

---

[1] Author is presently with Lucent Technologies, Bell Laboratories in Norcross, GA.

$$Q = K_P(F_N - F_{TH})V; \qquad F_N \geq F_{TH} \tag{1}$$

The material removal rate is defined as Q, while F_N is the applied normal force, and F_{TH} is the threshold normal force. V is the surface speed of the grinding wheel. The coefficient, K_P, and the threshold force, F_{TH}, are determined experimentally.

Although fixed-gain controllers (such as PID-type controllers) are preferred for industrial applications because of their simplicity in implementation and tuning. However, many processes or systems vary sufficiently to limit the usefulness or stability of fixed-gain controllers. Grinding has been shown to be a time varying process that can benefit from the application of such a controller.

The desired objective of this research is to provide a methodology for a stable force control in grinding to reduce cycle time and maintaining geometry in fine finishing, despite grinding process variation. The adaptive controller uses pole-zero cancellation and direct design methods to be self-tuning. The design approach and stability evaluation of the adaptive force controller, based on the previously described real-time process model, are presented.

Adaptive Process Control

To better control the normal grinding force for the system, adaptive control methods are applied building on the successful real-time grinding model with on-line parameter estimation. The approach taken in this adaptive force control effort for grinding is different from that of Tonshoff et al (1986). Tonshoff applied a fixed-gain controller to regulate the grinding force for an internal diameter grinder. Tonshoff used a separate off-line model estimation routine to determined the fixed-gains of the controller. In contrast the work undertaken here performs real-time estimation of the grinding process and uses a pole-zero cancellation approach to remove the process variation.

A block diagram of the overall system is depicted in Figure 1. The system model consists of several functional blocks: force controller, $G_{FC}(s)$, the position control loop, $G_{PC}(s)$, the tool-workpiece process interaction, $G_{TWP}(s)$, as well as the estimation and adaptation functions.

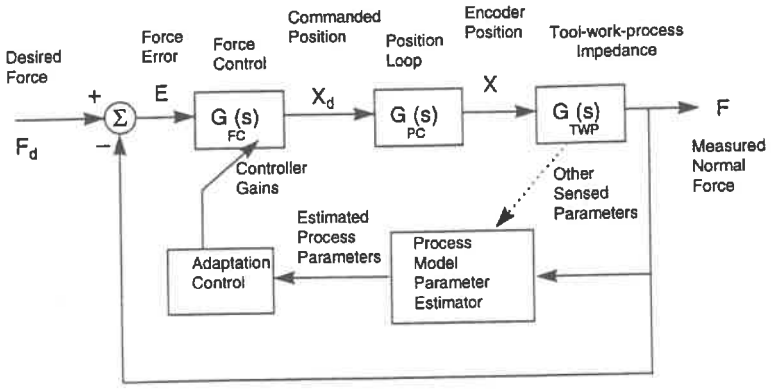

Figure 1. Plant and Controller Schematic for PMAC-based Force Control.

The development of the adaptive force controller for the grinding process can proceed directly from the plant model of Jenkins (1996).

$$G_{TPW}(s) = \frac{F_N(s)}{x_e(s)} = K_S\left(\frac{s}{s+\eta}\right) \tag{2}$$

where $\eta = K_P K_S V/A$

This is combined with a first order position servo model to yield the following continuous plant transfer function.

$$G_{PC}(s)G_{TWP}(s) = \frac{F_N(s)}{x_d(s)} = 203K_S\left(\frac{s}{s+\eta}\right)\frac{1}{(s+224)} \tag{3}$$

It has been shown that $\eta << 224$. Thus, variations in the process can dominate the system response. A fixed-gain controller can lead to poor performance as well as instabilities. An adaptive controller is desired to mitigate the effects of changing process dynamics and maintain a high MRR and a stable controller. From equation (3) it can be seen that the process dynamics can be eliminated by a pole-zero cancellation using a PI-type controller. The controlled system would then be of the form

$$G_{FC}(s)G_{PC}(s)G_{TWP}(s) = \frac{F_N(s)}{E_F(s)} = 203K_S\left(\frac{s}{s+\eta}\right)\frac{K_{PROP}(s+\alpha)}{s(s+224)} \tag{4}$$

In this scheme if the α (or K_I/K_{PROP}) of the PI controller in equation (4) is set to η, then the entire process grinding dynamics can be eliminated from the resulting equation. This reduces equation (4) to that of only a contact stiffness with a position loop (5).

$$G_{FC}(s)G_{PC}(s)G_{TWP}(s) = \frac{F_N(s)}{E_F(s)} = \frac{203K_S K_{PROP}}{(s+224)} \tag{5}$$

where $\alpha=\eta$. Since a discrete equivalent system is needed for the sampled plant in order to implement such a scheme on the digital controller, a ZOH equivalent discrete system is used.

$$G_{PC}G_{TWP}(z) = \frac{F_N(z)}{X_d(z)} = \left(\frac{z-1}{z}\right) Z\left(\mathcal{L}^{-1}\left[\frac{1}{s} 203K_S \left(\frac{s}{s+\eta}\right)\frac{1}{(s+224)}\right]\right) \tag{6}$$

denoting

$$C_o = e^{-224T}\ ;\ f(\eta) = e^{-\eta T}$$

$$f_2(\eta) = \frac{203K_S}{224-\eta}\left(f_1(\eta) - C_o\right) \tag{7}$$

$$G_{PC}G_{TWP}(z) = f_2(\eta)\left(\frac{z-1}{\left(z-f_1(\eta)\right)\left(z-C_o\right)}\right) \tag{8}$$

The discrete PI-type controller can be rewritten as follows

$$G_{FC}(z) = \frac{K_{PROP}}{1+\alpha}\left(\frac{z - 1/(1+\alpha)}{z-1}\right) \tag{9}$$

Thus if η varies sufficiently slowly or the controller is sufficiently fast, α can be chosen such that

$$\alpha = \frac{1}{f_1(\eta)} - 1 \tag{10}$$

then complete open-loop discrete transfer function is defined as

$$G_{FC}G_{PC}G_{TWP}(z) = \frac{K_{PROP}}{1+\alpha} f_2(\eta)\left(\frac{1}{z-C_o}\right) \tag{11}$$

Equations (7), (10), and (11) are used to determine the PI force controller gains in the controller design update of the self-tuning regulator. The effectiveness of the pole-zero cancellation is related to the process variation frequency spectrum and the gain update rate.

The implementation of this controller uses the windowed data handling scheme discussed by Jenkins (1996). The size of the data window is the key parameter to the success of this approach. The smaller the window the faster the gain update. However, as the sample window gets smaller the variance of the parameter estimation increases. This reduces the confidence of the estimate and ultimately the reduces the probability of an effective pole-zero cancellation.

A rigorous stability analysis in the sense of Lyapunov is complicated for STR systems, as the controllers are highly nonlinear. The relationship of the regulated force to the estimated parameter can be quite convoluted and is difficult to attain in many instances. A more tangible evaluation of stability can be performed, by a parametric examination of the effect of poor estimation and adaptive performance. The effect of poor performance can be seen by examining the combined open-loop, discrete plant and controller transfer functions given in equations (9) and (11).

$$G_{FC}G_{PC}G_{TWP}(z) = \frac{K_{PROP}f_2(\eta)}{1+\alpha}\left(\frac{z-\frac{1}{1+\alpha}}{(z-f_1(\eta))(z-C_o)}\right) \tag{13}$$

From equations (9) and (10) it can be seen that the poles of the open-loop system are all within the unit circle, so they are stable. The variable, α, is the ratio of the integral to the proportional gain and is always positive. Therefore the transfer function zero (4) is always positive and less than or equal to one and is at worst marginally stable.

$$z = \frac{1}{1+\alpha} \tag{4}$$

Another possibility for instability is in the calculation of the proportional gain. The overall gain is positive and is calculated in real-time to be stable, dependent on the estimated grinding model. However, α is positive and determined by the controller. Thus even if the pole-zero cancellation is not accurate the effects do not cause the system to go unstable; however, performance may suffer.

Results

Two benchmark experiments were conducted to evaluate the effectiveness of the adaptive pole-zero cancellation control and RLS-FF estimation technique. In the first experiment, plunge grinding, the adaptive force regulation successfully reduces the standard deviation and range of the controlled normal force, and yields a mean normal force closer to the 25 N reference. The second

benchmark experiment, a traverse grind over a flat surface, demonstrates better repeatability of the surface profile after grinding. The adaptive control and estimation technique appears to provide an improvement in surface following for fine finishing, compared to fixed-gain controllers The ratio of several surface profile characteristics is provided in Table 1

Table 1. Traverse Grind Surface Profile Statistic Ratios.

Material	O1	A2	4142
Ratio of Adaptive Control to Fixed-Gain Control			
Absolute Mean	35.7%	37.3%	70.2%
RMS mean	36.4%	40.9%	66.6%
Range	47.1%	54.7%	68.3%
Std. Deviation	36.4%	40.9%	66.6%

Conclusion Summary

A self-tuning regulator approach to adaptive control has been successfully developed for force control of a grinding system. The controller is based on a pole-zero cancellation of the estimated grinding process. The use of parallel processors is a key element in the combined servo control and process estimation functions. The final implementation of the adaptive controller and estimator yielded a superior grinding force controller. A higher fidelity force regulator with greater stability has been developed for plunge grinding. Similarly in traverse grinding, the surface profile following capability improves with the adaptive pole-zero cancellation technique, as contrasted to the fixed-gain controller. This approach to grinding force control has demonstrated the potential for increasing productivity with the reduction of tary time by use of the stable force control in plunge grinding, with higher fidelity in force regulation. The implementation of this approach in surface (traverse) grinding provides a superior surface following capability for fine finishing, as compared to fixed gain controllers. These conclusions are evident from the results of the benchmark experiments.

BIBLIOGRAPHY

Hahn, R. S. and Lindsay, R. P. "Principles of Grinding Part I Basic Relationships in Precision Machining," *Machinery*, July 1971, pp. 55-62.

Jenkins, H.E., Kurfess, T.R., and Ludwick, S.J., "Determination of a Dynamic Grinding Model," (accepted February 1996) *ASME Journal of Dynamic Systems, Measurement and Control.*

Landau, I. D., *Adaptive Control,* Dekker, New York, 1979.

Tonshoff, H. K., Zinngrebe, M., Kemmerling, M., "Optimization of Internal Grinding by Microcomputer-Based Force Control," *Annals of the CIRP*, Vol. 35, No. 1, 1986. pp. 293-296.

DIAMOND POINT TOOL FORCE MEASUREMENT IN A PRODUCTION ENVIRONMENT

J. Schaefer (Texas Instruments, Inc.), **C. Arcona** (IBM Corporation), T.A. Dow, G.M. Moorefield II (North Carolina State University), K. Falter (Rank Pneumo, Inc.), and R.L. Rhorer (National Institute of Standards and Technology)

INTRODUCTION

Diamond turning is used to produce optical surfaces in ductile and brittle workpieces. Materials of interest include aluminum, copper and electroless nickel for reflective optics and polycrystaline Germanium for transmissive infrared lenses. The geometry of the diamond tool plays an important role in the resulting surface finish and figure error for these optics. However, it is difficult to predict the change in geometry due to wear, the effect of wear on the surface and, most important, the appropriate time to change tools to optimize the cost and quality of the optics.

Tool force can be used to monitor the quality of the machined surface. Changes in force can forecast a change in surface finish due to a shift in the minimum chip thickness as well as a change in figure accuracy as the machine elastically deforms in response to increased tool forces. Although measuring tool forces during production has been considered a desirable goal, it has remained unimplemented because of (1) compliance typically introduced by including the force sensor in the structural loop and (2) the lack of availability of a user-friendly interface to assist the operator in making process and tool change decisions. To address this problem, a collaborative project has been undertaken by Los Alamos National Labs (LANL), Texas Instruments (TI) and North Carolina State University (NCSU). The objective of this project is to develop a tool force dynamometer and collect cutting force data in the background of normal part machining and display information about the process, tool condition, and tool life to the operator.

PRODUCTION FORCE ANALYSIS TOOL

The Production Force Analysis Tool (PFAT) was designed around a Kistler 9251A three-axis load cell which uses three pairs of quartz transducer rings to resolve forces in three orthogonal directions via the piezoelectric effect

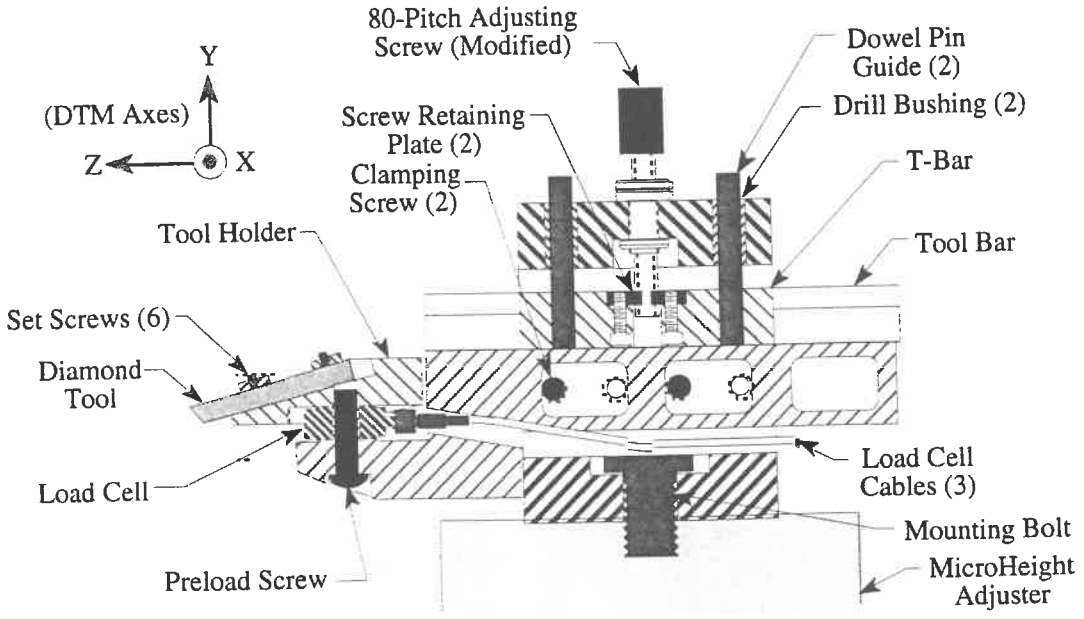

Figure 1: Cross-sectional view of the PFAT prototype.

(i.e., stresses in the quartz generate proportional charges). For reliable force measurement, the dynamometer must provide a rigid platform to which the load cell can be mounted, and a compact, yet robust, tool holder that can be attached to the load cell with the necessary preload. For this low-force application, a preload of approximately 8900 N was chosen. Because this preload force generates a 0.4 GPa tensile stress in the screw that clamps the load cell between the tool holder and the large cross-section tool bar, a heat treated alloy steel screw ($\sigma_{ut} \geq 1.17$ GPa) was selected.

To accommodate a wide range of workpiece thicknesses, this dynamometer design provides 40 mm of axial tool motion. The axial tool position is adjusted by first loosening the two clamping screws that constrain the moveable tool bar between the sides of the mounting structure, manually sliding the tool bar forward or backward, and then retightening the clamping screws to secure the tool bar in position. The dynamometer design also provides 12.7 mm of vertical tool positioning to allow coarse tool height alignment when tool changes are made. To adjust the tool height (see Figure 1), the two clamping screws are loosened to free the tool bar and the 80 pitch adjusting screw is used to vertically position the T-bar. To provide fine vertical tool positioning, the dynamometer is mounted on a MicroHeight Adjuster. The incorporation of the tool positioning mechanism in the dynamometer design eliminates the need for an Aloris tool post which is a weak link in the structural loop of the machine.

Tests were conducted to determine the static stiffnesses and the first resonant frequencies in the axial, horizontal, and vertical directions of a tool mounted in the PFAT. Supporting the tool with a stiff structure is necessary for the dynamometer to produce components with good figure and finish. High first resonances of the structure enable the load cell to operate with greater bandwidth, permitting the observation of high frequency force fluctuations. Table 1, which compares the experimental results with the design values, reveals excellent agreement between modeled and measured stiffness in all three directions.

The fact that all of the first resonant frequencies are in excess of 1000 Hz suggests that the cutting forces can be successfully monitored and correlated with the condition of the tool edge (i.e., the amount of tool wear). Furthermore, when FE models of the PFAT prototype and TI's production-proven tool holder are compared, the results indicate that the two structures possess nearly identical first resonant frequencies, despite the fact that the PFAT prototype includes the load cell while the TI device does not. The FE models indicate that the two structures have the same first vertical resonance (1700-1800 Hz) and the same first horizontal resonance (1800-1900 Hz). The experimental resonances of the PFAT prototype are lower than the predicted frequencies because the FE models did not include the tool post and microheight adjuster which reduce the natural frequencies.

PRODUCTION ENVIRONMENT

For the PFAT design to be beneficial in a production environment, the system must provide the following: (1) similar adjustments as the existing production tool holder, (2) static compliance that meets or exceeds that of the existing tool holder, (3) a data collection system that requires minimal operator interaction, (4) the data analysis software must be robust for accurate force data extrapolation, and (5) software that displays both real time, and historical tool force data to the operator for

	Stiffness (N/mm x 10-3)		Natural Frequency (Hz)	
Direction	**FEM Model**	**Measured**	**FEM Model**	**Measured**
Axial (Z)	27	28	-	2275
Horizontal (X)	3.7	3.3	1850	1275
Vertical (Y)	2.8	2.7	1750	1075

Table 1. Predicted and measured stiffness and resonance of the PFAT prototype

tool condition and process assessment.

There are multiple issues that naturally occur in a production environment that must be addressed in order for the tool force to be consistent, credible, and useful. Some of the issues that were considered when designing the tool force system and software included: (1) low run size, high part type mix, (2) multiple shift operation and operational variations, (3) influence of spray-mist coolant, (4) curvature of lenses, (5) process variation, and (6) different workpiece materials.

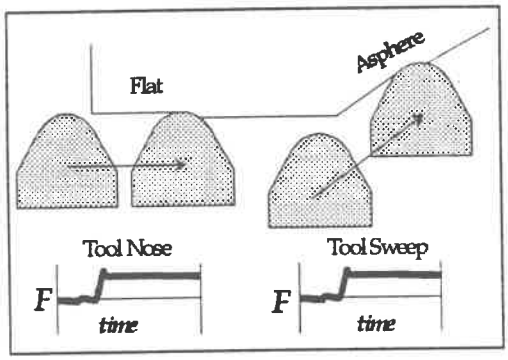

Figure 2. Tool edge condition assessment

Tool Condition Assessment Scheme

A fundamental limitation of a piezoelectric force transducer is that the force signal dissipates over time thus preventing continuous force monitoring of the entire finish pass. Most of the aspheric lenses machined at TI are concave with an outer locating flat. For this geometry, a method was devised to monitor the conditions of the nose and the outermost regions of the tool sweep for each finish pass. Tool force data recorded on the flat surface as shown in Figure 2 will register changes at the center of the tool while forces recorded as the tool enters the edge of the asphere will be influenced by tool changes at the other end of the tool sweep.

Data Collection and Software

To collect tool force data, a National Instruments data acquisition card was installed in a 486PC. The key to successful implementation of production tool force measurement lies in the software, and for this application, LabWindows CVI version 3.1, C language software was used. It was imperative that the data acquisition and software systems perform the work of a lab technician by extrapolating, validating, and presenting tool force information to the operator in an understandable format.

Because the tool forces are so small, it is a challenge for the software to detect and identify the force transition from an unloaded to a fully loaded tool. One source of confusion is the noise created when a the spraymist coolant is used. Several different software schemes have been evaluated to identify this transition zone including the change in the average force and the change in standard deviation of the thrust force from no cutting to cutting.

Data Analysis Figure 3 is an example of a tool force profile with coolant on a polycrystalline Ge workpiece using a 0.81 mm nose radii tool with a 1.25 µm depth of cut and a 1.25 µm feed per revolution. The depth of cut variation from initial tool contact to full depth causes the gradual transition slope. The data is averaged over a half-second interval before and after the transition to obtain the average cutting and thrust forces. A change in the resultant force angle between $F_{cutting}$ and F_{thrust} indicates tool edge wear. As the tool wears, F_{thrust} increases while $F_{cutting}$ remains nearly constant, thereby increasing the angle of the resultant force $\alpha_{resultant}$, where

$$\alpha_{resultant} = tan^{-1}\left(\frac{F_{thrust}}{F_{cutting}}\right) \qquad (1)$$

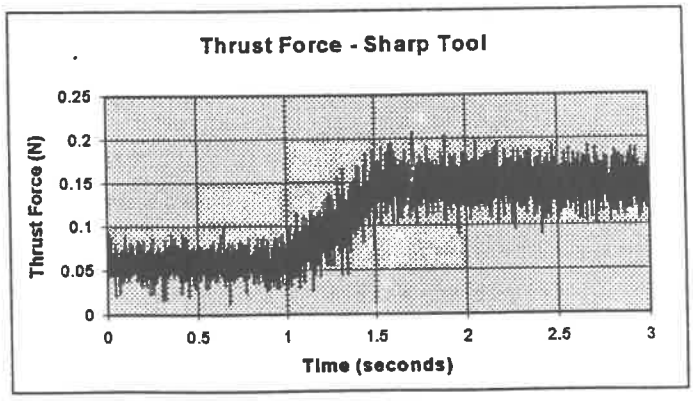

Figure 3. Thrust force data for Germanium

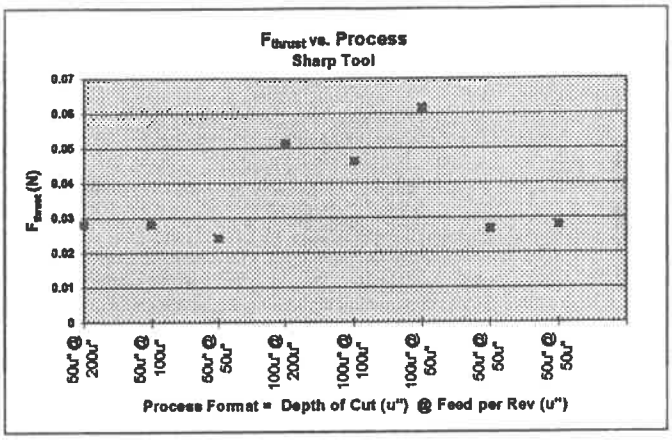

Figure 4. Thrust force for different conditions

Change in the standard deviation of the force signal from no cutting to cutting might also provide important information on the process such as the amount of material fracturing during machining. The chip area calculation is used to normalize cutting forces to account for process changes which affect the measured cutting forces and the chip volume calculation is used to track tool wear rates and tool change out thresholds.

RESULTS

The standard machining process for Germanium can be characterized using the measured tool force and chip structure. The typical process utilizes a negative 15 degree rake angle tool with a 0.76 mm nose radius, 1.25 µm depth of cut with a 1.25 µm feed per revolution produced by a feed rate of 1.9 mm per minute at a spindle speed of 1500 rpm. From Figure 4, it is clear that feed per revolution has little effect on the thrust force, whereas, doubling the depth of cut nearly doubles the thrust force. This is due to the proportional increase in the contact area of the tool as the depth of cut increases.

SEM micrographs of the Germanium chips confirm the ductile nature of this process. The tool used in this particular experiment had removed 75 µm of material from 12, 76.2 mm diameter Germanium lenses. The measured forces were $F_{cutting}$ = 0.069 N, F_{thrust} = 0.024 N. In Figure 5, the thickest portion of the chip is at the bottom of the picture and the chip is thinnest where it appears to form strands. These strands are actually hollow tubes similar to a rolled up piece of paper. The theoretical cross-sectional chip geometry is 0.075 µm thick by 40 µm wide. This correlates well with the scaled width in the micrograph.

SUMMARY AND DISCUSSION

Production diamond tool forces (~ 0.05 N) are smaller than conventional machining forces. This creates difficulty in extracting accurate cutting force data when small external disturbances generate variations in the measured values. For example, the standard spraymist application of coolant creates noise in the tool force data. Filtering the data and/or changing to a steady stream of coolant will be used to eliminate this difficulty. The thrust force on a sharp tool is nearly proportional to the depth of cut and is affected very little by a change in feed. Furthermore, changes in the standard deviation, σ, of the force signal is greater with a process creating fracture than a ductile process. The σ parameter could prove to be invaluable in process optimization. Another benefit of on-machine tool force measurement is the increased accuracy (< 20 nm) afforded the operator in registering the tool with the part surface. In conclusion, by providing proper hardware, software, and training to the operator, tool force measurement in a production diamond turning operation is viable and has proven to be an invaluable tool.

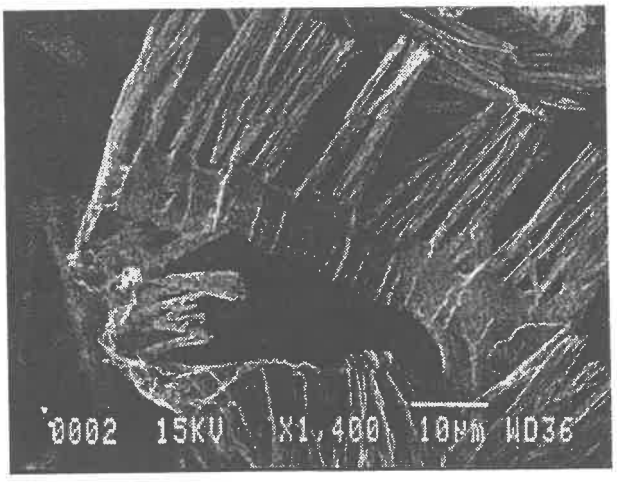

Figure 5. Germanium chip

Submicrometer Overshoot Control of Rapid and Precise Positioning

S. B. Chang

Precision Instrument Development Center, National Science Council

Hsinchu, Taiwan, R.O.C.

I. Introduction

Rapid and precise positioning is an important technique in micromachining such as in the machining and processing of semiconductors [1]~[3]. Also, small overshoot or submicrometer overshoot requirement is a main concern of controller design in many micromachining cases such as micro cutting, milling and turning. Therefore, to achieve submicrometer overshoot in a rapid and precise positioning is an important technique. The control algorithm proposed in this paper adopts the variable structure control method to provide a rapid, precise and submicrometer overshoot positioning. It is implemented on a linear motor drive stage guided by a rolling ball guide and with a 10 nm resolution laser interferometer as the displacement sensor to achieve an overshoot smaller than 0.2 um and rapid, precise positioning (1mm ~ 1cm positioning with steady state error smaller than 30 nanometer in 0.5 sec). The controllers in this algorithm are designed according to the corresponding dynamics and frictional effects of the stage during a long stroke positioning motion. It shows by combining mechanical design, system identification, lubrication and controller design techniques will lead to more successful results.

II. System Identification

The functional block diagram of our positioning system is shown in *Figure 1*. Similar to the experimental results in [2], we found the open loop frequency response of the plant varies with the magnitude of the input voltage. The dynamics and the corresponding transfer functions of the plant identified with different input voltages are summarized in *Table 1*.

III. Dynamics Transition During a Motion

In order to decide the dynamic condition of the plant during a motion, the following two definitions are proposed.

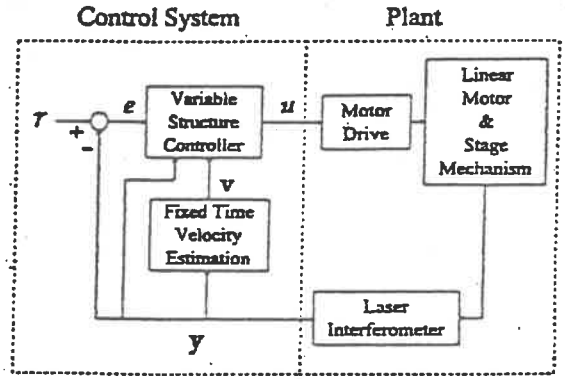

r : reference position
e : position error
u : input voltage
v : estimated velocity
y : output position

Figure 1. Functional block diagram of our positioning system.

Input voltage	0.05 V	0.2 V	0.5 V
dynamics	a hard spring element	a simple mass-damper-spring system	an ordinary 2nd order Type 1 system
corresponding transfer function	$\frac{55}{s^2+100s+6000}$	$\frac{55}{s^2+125s+700}$	$\frac{55}{s(s+1)}$

Table 1. Dynamics and corresponding transfer functions of the plant for different input voltages.

Definitions:

a. *Stick Point* :

When the input force of a stage is removed, the point where the stage naturally stops and sticks is called a '*stick point*'.

b. *Critical Speed* :

We define the speed below which the stage without input force will naturally stops and sticks within the distance of the maximum presliding displacement. According to the conservation of energy and neglecting the dissipative property of friction, we obtain the critical speed as follows

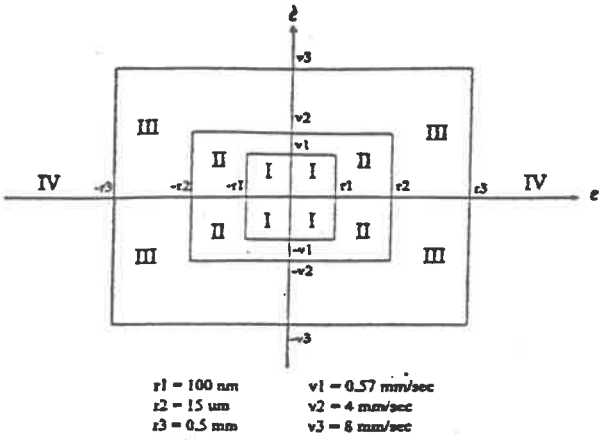

Figure 2. Regions division of the proposed variable structure control algorithm.

$$Vcr = \sqrt{\frac{2\int_0^{pd} f(x)\,dx}{M}} \quad \ldots (1)$$

where pd is the maximum presliding displacement, f is the friction under stick condition, M is the mass of the stage and x is the displacement.

The critical speed of the stage in our experiments is about 0.57 mm/sec. Then a dynamics transition condition is obtained as follows.

Dynamics Transition Condition

When the speed of a stage varies from a value larger than the critical speed to a value smaller than the critical speed, the dynamics of the stage varies from macrodynamics to microdynamics and a stick point occurs at that instant. In contrast, when the speed of a stage varies from a value lower than the critical speed to a value larger than the critical speed, the dynamics of the stage varies from microdynamics to macrodynamics and a stick point disappears at that instant.

In the precise positionings of long stroke, the stage must go through three different kinds of dynamics as described above. Moreover, the final precise positioning is fulfilled by using the presliding displacement of a stick point. Hence, in order to achieve a submicrometer overshoot, rapid and precise positioning, the following variable structure control algorithm is proposed.

IV. Proposed Control Algorithm

The control algorithm proposed in this paper divides the positioning range into 4 regions, as shown in Fig.2, according to the state of the stage.

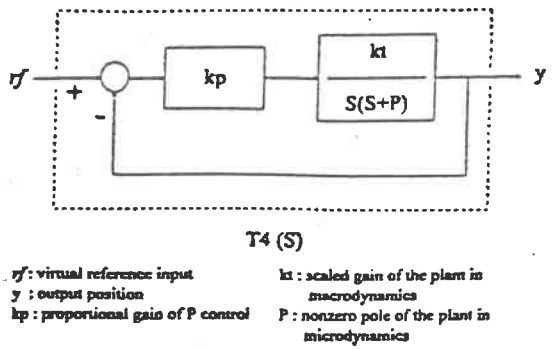

Figure 3. Block diagram of the virtual reference control in Region IV.

When the stage far from the reference position (position error > 0.5 mm or the moving speed > 8 mm/sec, Region IV), a novel and simple control method we called 'the virtual reference control' is proposed to let the stage move rapidly toward the destination position and decreases the speed near zero when it moves into the region III (position error ≦ 0.5 mm and speed ≦ 8 mm/sec). Then a constant speed control is adopted, which is proved that stick-slip will not occur and it can let the stage move into region II (position error ≦ 15 um and speed ≦ 4 mm/sec). In region II, pole assignment control with small integrator gain is adopted to achieve submicrometer overshoot. And finally, when the stage moves into region I (position error ≦ 100 nm and speed ≦ 0.57 mm/sec), pole assignment control with large integrator gain is adopted to shorten the settling time.

a. *Virtual Reference Control in Region IV*

The control configuration in Region IV is shown in *Figure.3*. If the destination position is denoted as r, we set the reference input rf to *T4(S)* as follows:

$$rf = \frac{r - sign(r)*r1}{1 + u * Mp} \quad \ldots (2)$$

where $r1$ is the width of Region I, u is the adjusting factor and Mp is the maximum overshoot of the system to a step response [4], $sign(r)=1$ if $r>0$, $sign(r)=-1$ if $r<0$.

By using above rf value as the reference input of *T4(S)* and the value of u is 1, then we can obtain the top displacement of the response is about $r - sign(r)*r1$. Therefore, this control algorithm can move the stage rapidly and smoothly into Region III.

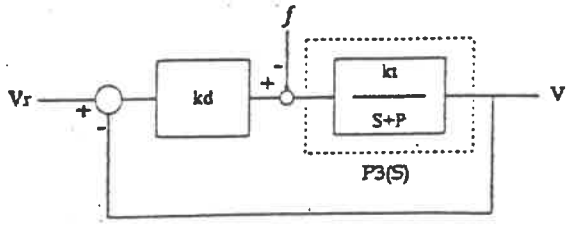

Vr : reference velocity
kd : proportional gain
f : slip friction
kt : scaled gain of the plant
P : pole of the plant
V : output velocity

Figure 4. Block diagram of the constant speed control in Region III.

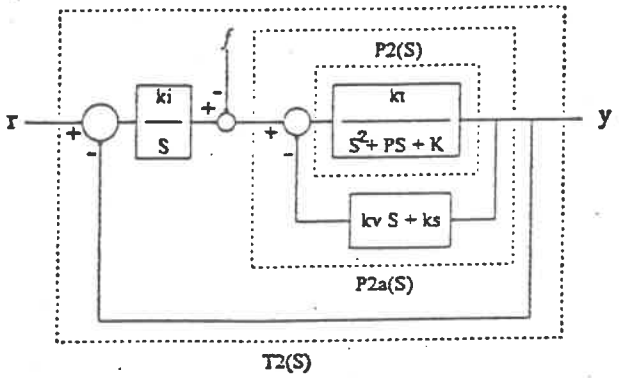

r : reference position
ki : gain of the integrator
f : slip friction
kt : scaled gain of the plant
P : scaled viscous coefficient of the plant
K : scaled stiffness coefficient of the plant
y : output position

Figure 5. Block diagram of the pole assignment control in Region II and Region I.

b. *Constant speed control in Region III*

To simply the analysis, we regard our speed servo system in Region III as an ordinary speed servo system suffering friction as shown in *Figure 4*. Where Vr is the reference speed, kd is the proportional gain and f is the scaled friction whose value is between $f_{\min}$ and $f_{\max}$. If the reference speed Vr is chosen to be large enough to avoid the occurrence of stick-slip, the velocity V presented in the time domain will be limited as follows:

$$V_{\min}(t) \geq V(t) \geq V_{\min}(t) \quad ...(3)$$

$$V_{\max}(t) = \left[(Vr - kt * f_{\min}/(P + kdkt)\right](1 - e^{-(P+kdkt)t})$$

$$V_{\min}(t) = \left[(Vr - kt * f_{\max}/(P + kdkt)\right](1 - e^{-(P+kdkt)t})$$

Therefore, by properly setting the parameters in Region III, the constant speed control can move the stage smoothly toward Region II without the occurrence of stick points near Region II. And it can limit the speed below $V_{\max}$ in Eq.(3) when the stage moving into Region II.

c. *Pole assignment control with small integrator gain in Region II*

In Region II the pole assignment control is adopted in order to achieve small overshoot requirement. Its control configuration is shown in Fig.5 and the overall transfer function can be expressed as follows,

$$T2(S) = \frac{a\,b\,c}{(S+a)(S+b)(S+c)} \quad ...(4)$$

Then according to the pole assignment control rule [4], we can arbitrarily assign the poles of $T2(S)$, i.e., -a,-b and -c, by choosing certain ki, ks and kv values.

Then the time response of the velocity $y'(t)$ in the final positioning can be simplified as follows:

$$y'(t) \approx C\,e^{-ct} \quad ...(5)$$

if positive real parts of $a, b >> c$

$$C = \frac{1}{(b-c)(c-a)}\left[c\,(a+b)\,y'(0) - a\,b\,c\,r\right]$$

The term e^{-ct} in Eq.(5) varies from 1 to 0 as time goes from 0 to infinity. Hence, to achieve no velocity reversal and no overshoot in the final positioning we have to let C in the Eq.(5) be positive. Moreover, in order to keep the stage in microdynamics and avoid stick-slip in the final positioning, we have to let C in the Eq.(5) smaller than the critical speed Vcr. Because the real parts of a and b are larger than c, $(b-c)(c-a)$ is negative. Therefore, to result in no overshoot and no stick-slip motion in Region II, the following equation must be satisfied.

$$\frac{(b-c)(c-a)\,Vcr + a\,b\,c\,r}{c\,(a+b)} < y'(0) < \frac{a\,b}{a+b}\cdot r \quad ...(6)$$

Therefore, if we can properly set the poles locations -a, -b and -c and limit the maximum value of $y'(0)$ by the constant speed control in Region III, a no overshoot positioning can be achieved theoretically.

d. *Pole assignment control with large integrator gain in Region I*

When stage moves from Region II into Region I, the position is near the destination position and the velocity is below the critical speed in Eq.(1). Therefore, in Region I the stage is in microdynamics and if we choose a properly large integrator gain ki,

TORSIONAL COMPLIANCE IN GRINDING CHATTER

Rodney D.Entwistle and Brian J.Stone
The University of Western Australia
Nedlands, Perth 6009
Australia

Introduction

Grinding is one of the important finish machining processes available for the manufacture of components requiring fine tolerances and/or fine surface finishes. However, the grinding machine tool is potentially subject to dynamic instability, known as chatter, which when present can reduce production rates, lead to a deterioration in surface finish, reduce the time between wheel dressings and cause aural discomfort for the machinist.

Research into chatter theory in general and grinding chatter in particular has been extensive, leading to a reasonably good understanding of the parameters involved. In the case of cylindrical grinding both the workpiece and the grinding wheel are rotating systems which will exhibit torsional responses. It appears that the grinding chatter models and simulations developed to date have assumed either explicitly or implicitly that torsional vibrations will not have any affect on the stability of the grinding process. This may seem reasonable when it is considered that torsional vibration of the workpiece will have an extremely small affect on the chip thickness. However, the cutting force models generally in use indicate that the tangential contact force in grinding is proportional to the workpiece surface speed and inversely proportional to the grinding wheel speed and hence there is a possibility of torsional oscillations influencing the cutting force in an oscillatory fashion. These oscillating tangential cutting also drive the transverse mode of the machine frame and thus will modify the chatter characteristics of the machine.

Model

To test the hypothesis a mathematical model has been constructed which allows the stability boundary to be determined under various conditions. The grinding force model utilised is that proposed by Chui and Malkin (1993). When sliding and ploughing are ignored the tangential grinding force can be described as:

$$P_t = \frac{u_c V_w b \delta}{V_g}. \qquad (1)$$

where V_w and V_g are the workpiece and grinding wheel surface speeds respectively, b is the width of cut (width of grinding wheel face) and δ is the feed per revolution of the workpiece. The constant u_c is termed the 'specific grinding energy'. A schematic of the model used is shown in Figure 1.

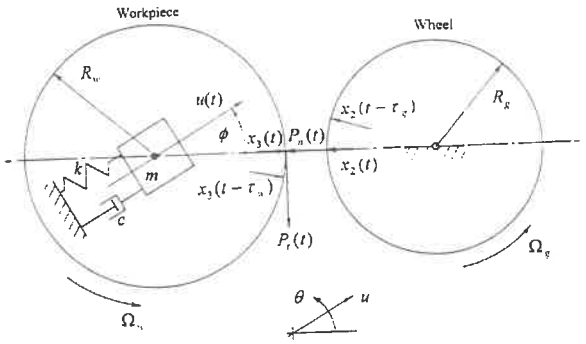

Figure 1 - System Schematic

The model contains three degrees of freedom which are coupled only via the grinding contact force. They are the transverse mode, u, which vibrates in the direction ϕ, and the uncoupled torsional modes of the workpiece and the grinding wheel. In each case they are modelled as spring-mass-viscous damper systems. Regeneration can occur on both the workpiece and the grinding wheel. The mutual wear rates are defined by the ratio of the volumetric material removal and is assigned the symbol G. Along with geometric constraints and the cutting force model of equation (1), these form the basis of the mathematical model.

The solution is progressed by assuming the system to be linear and that all degrees of freedom oscillate with an exponentially modulated sinusoid.

$$x_i(t) = X_i e^{st}, \text{ where } s = \sigma + j\omega. \qquad (2)$$

To locate the neutral stability condition which describes the stability boundary, the real part of the exponential is set to zero, thus imposing neither growth

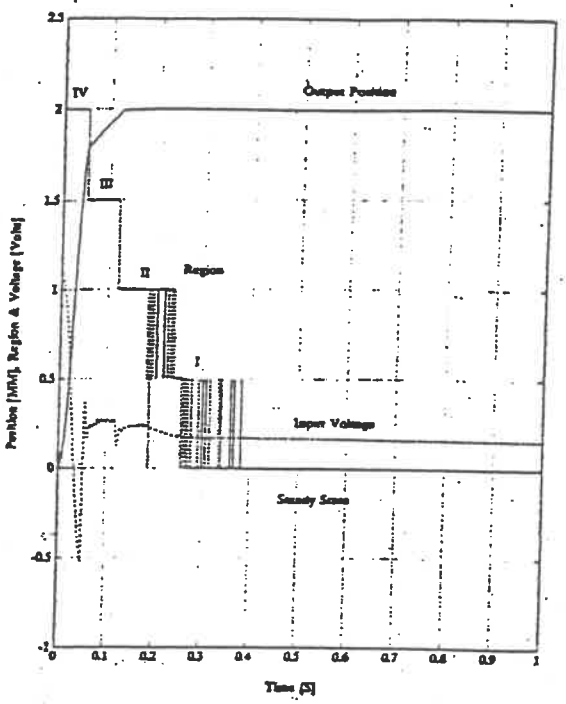

Figure 6. 2 mm positioning under proposed variable structure control algorithm.

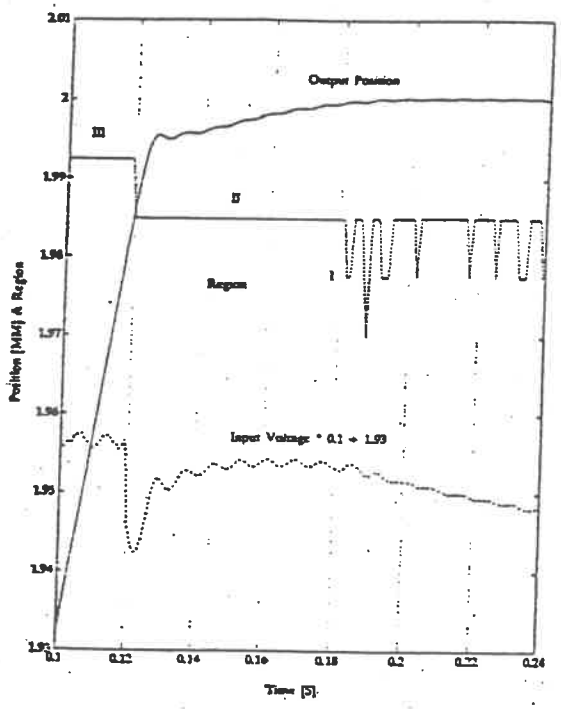

Figure 7. Final positioning condition of 2 mm positioning under proposed variable structure control algorithm.

we can move the stage into the default settling range(destination position $\pm$ 30 nm) rapidly. And its control structure is the same as in *Figure 5*.

V. Experimental Results, Discussions and Conclusions

An experimental result of a 2mm positioning is shown in *Figure 6* and *Figure 7*, it shows a rapid (settling time < 0.5 sec , almost about 0.4 sec), small overshoot (< 0.2 um) and precise (steady state error < 30 nm) positioning is fulfilled. The analysis in this paper and the experimental result show that by combining mechanism design, lubrication and controller design techniques to achieve more robust, rapid, smaller overshoot and precise positioning are expected.

VI. References

1. Brian Armstrong-Hélouvry, Pierre Dupont and Carlos Canudas De Wit, "A Survey of Models, Analysis Tools and Compensation Methods for the Control of Machines with Friction," *Automatica*, 1994, Vol.30, No.7, pp.1083-1138.
2. Shigeru Futami, Akihiro Furutani and Shoichiro Yoshida, "Nanometer Positioning and Its Micro-dynamics," *Nanotechnology*, 1990, 1 (1), pp.31-37.
3. P. I. Ro and P. I. Hubbel, "Model Reference Adaptive Control of Dual-Mode Micro/Macro Dynamics of Ball Screws for Nanometer Motion," *ASME Journal of Dynamic Systems, Measurement, and Control*, 1993, Vol.15, pp.103-108.
4. Ogata, *Modern Control Engineering*, Prentice-Hall International Editions, 1990.

not decay. Space does not allow a detailed solution to be presented here. Details can be found in Entwistle and Stone (1996). Some of the significant predictions of the model will be outlined here.

The major parameters of interest are the natural torsional frequencies of the workpiece and the grinding wheel relative to that of the transverse mode. These were varied over a large range and found to have a profound affect when in the vicinity of the transverse mode frequency. In what follows, the ratios of the natural frequencies of the torsional degrees of freedom to that of the transverse mode are labelled as F_w and F_g. Only plunge grinding will be considered here.

It is conventional to plot the stability boundary, characterised as the width of cut which gives neutral stability, against the workpiece rotational speed. While usually plotted on linear coordinates for turning and milling, the workpiece speed range for cylindrical grinding is very wide and therefore logarithmic axes are utilised in this work.

Simulations

In order to obtain a benchmark for comparison, the initial simulation is for the situation where both torsional degrees of freedom are inactive. Figure 2 shows the stability boundary predicted in this case.

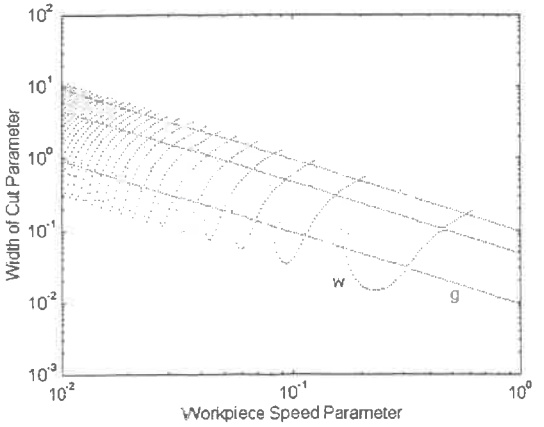

Figure 2 - Stability Plot Without Torsional Effects

Each dot on the plot represents a neutral stability condition, limited to frequencies which are up to twice the transverse natural frequency. The 'straight line' boundaries (labelled 'g') represent the situation where lobes wear on the grinding wheel while the 'U' shaped lobes (labelled 'w') is the situation where lobes wear on the workpiece. This plot is well known from previously published work.

The direction of the motion of the transverse mode can be modelled at any angle and clearly such motion will affect the surface speeds. Figure 3 shows the stability boundary for the same parameters as used for Figure 2 excepting that $\phi \neq 0$. At lower workpiece speeds the stability boundary is improved and furthermore, below some workpiece speed, the system is unconditionally stable.

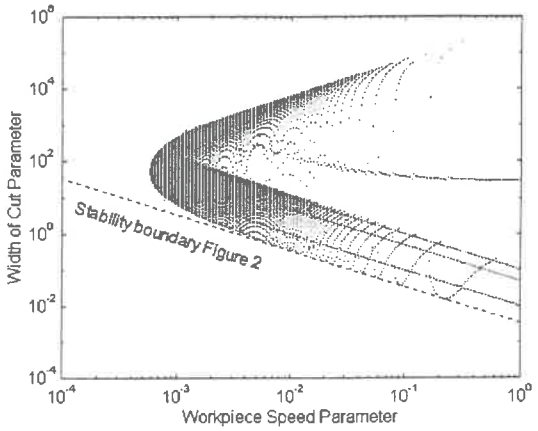

Figure 3 - Introduction of Transverse Mode Angle ϕ

The model is now modified to introduce torsional flexibility on the workpiece mounting and drive system. For illustration purposes the natural torsional frequency of the workpiece was chosen to be 90% of the transverse mode natural frequency ($F_w = 0.9$). Figure 4 is the stability chart for this situation.

It is seen that the introduction of a workpiece torsional flexibility has a similar affect as that due to the transverse mode angle excepting it is a much more dramatic modification. At low workpiece speeds, the model predicts unconditional stability while at higher speeds the boundary is improved. It is noted that the effect is a function of the feed rate; the higher the rate, the further the boundary moves to the right.

The next simulation removes the workpiece flexibility and imparts flexibility to the grinding wheel drive. For illustration purposes the natural torsional frequency of the grinding wheel was chosen to be 110% of the transverse mode natural frequency ($F_g = 1.1$). Figure 5 shows the result.

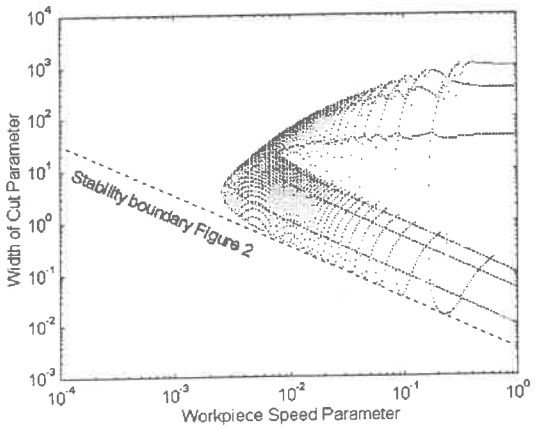

Figure 4 - Introduction of Workpiece Torsional Mode

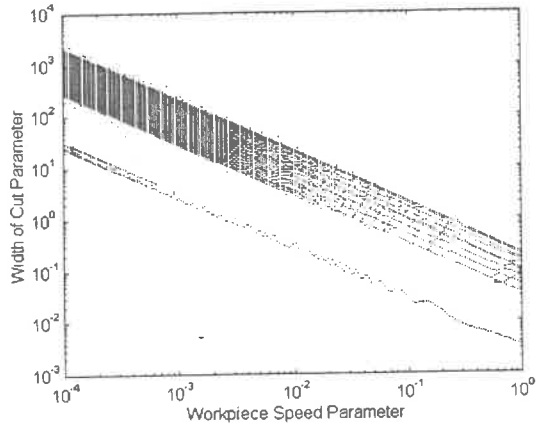

Figure 5 - Introduction of Wheel Torsional Mode

Clearly, if the natural frequency of the grinding wheel and its drive system is near to that of the transverse mode, the stability of the machine can be adversely affected.

The simultaneous application of both workpiece and grinding wheel torsional degrees of freedom results in the stability boundary shown in Figure 6.

The low speed unconditional stability 'cut-off' is reintroduced but above that speed the grinding wheel torsional mode dominates and lowers the stability boundary.

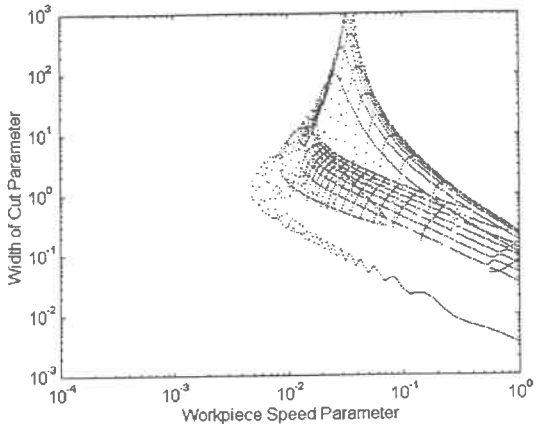

Figure 6 - Introduction of Workpiece and Wheel Torsional Modes

Growth Rates

Many grinding operations take place under unstable conditions but the growth rates can be sufficiently low to permit a considerable amount of useful grinding to be performed prior to the amplitude reaching unacceptable limits. Hence it is always useful to review the predicted growth rates in conjunction with the stability boundaries.

Figure 7 shows the growth rate parameter as a function of the width of cut parameter for the system parameters used to generate Figure 2. The rotational speed parameter chosen here is 0.03.

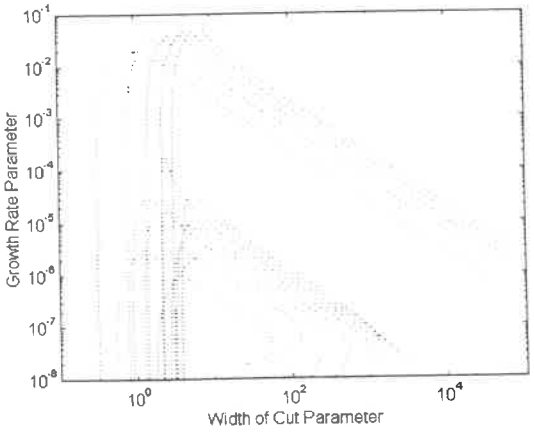

Figure 7 - Growth Rates Without Torsional Effects

The upper curves, which asymptote to zero at the higher workpiece speeds, represent the workpiece regenerative modes whereas the lower curves, at a

much lower growth rates, are associated with the grinding wheel modes which take long periods of time to develop.

In contrast, Figure 8 shows the equivalent plot for the conditions used to generate Figure 4.

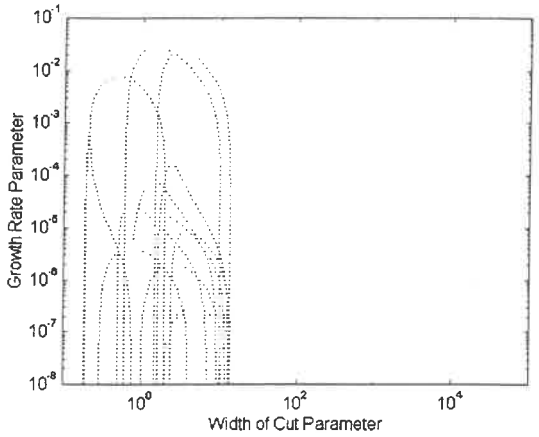

Figure 8 - Growth Rates With Torsional Effects

This last plot indicates that as the width of cut is increased the curves pass through zero growth again rather than asymptoting to zero. Another interpretation of this is that the curves in Figure 4 are closed and so the stability boundary forms a closed curve. Thus, according to the model, regions of stability exist both at low and high widths of cut, with the unstable region existing in between.

Conclusions

A mathematical model of a simplified grinding system has been presented and used to show that workpiece and grinding wheel torsional modes may affect the stability of cylindrical grinding machines. The work-wheel interactions in grinding are very complex and a very simple contact force model has been used. Also the transverse and rotational systems have been limited to single degrees of freedom. Cognisant of the simplifications made a study with the model has enabled the following broad conclusions to be drawn:

- A transverse mode with a component of its motion in the cutting velocity direction will result in increased stability and unconditional stability below some cutoff workpiece speed.
- The result of a workpiece torsional mode whose natural frequency is in the vicinity of the transverse mode natural frequency is increased stability and unconditional stability below some cutoff workpiece speed.
- When a grinding wheel torsional mode natural frequency is in the vicinity of the transverse mode natural frequency a grinding wheel torsional mode governs stability and is detrimental by lowering the stability boundary.
- If a grinding wheel torsional mode natural frequency is in the vicinity of the transverse mode natural frequency, its detrimental effect can be ameliorated by the introduction of a workpiece torsional mode whose natural frequency is in the vicinity of the transverse mode.
- The growth rates of developing chatter for widths of cut in excess of the stability boundary are modified and, in some cases, reduced to zero by the introduction, and tuning of, torsional degrees of freedom.

References

Chiu, N., and Malkin, S., 1993, "Computer Simulations for Cylindrical Plunge Grinding" *Annals of the CIRP*. Vol. 42 pp.383-387.

Entwistle, R.D., and Stone, B.J., 1996, "The Effect of Torsional Vibration on Chatter in Grinding". Submitted to *ASME Journal of Manufacturing Engineering and Science.*

CLOSED-LOOP CONTROL OF A MAGNETIC SERVO-LEVITATED FAST-TOOL SERVO SYSTEM

Hector M. Gutierrez
Department of Electrical and Computer Engineering

Paul I. Ro
Department of Mechanical and Aerospace Engineering

Precision Engineering Center
North Carolina State University
Raleigh, NC

INTRODUCTION

Magnetic Servo Levitation (MSL) [1,7] has been proposed as a method to drive fast-tool servo systems. It represents a promising but very challenging alternative to compensate for errors that can not be adequately handled by machine-tool positioning systems, and to increase the versatility of a given machining process (e.g. to achieve non-rotationally symmetric features in diamond turning).

While MSL could provide an adequate bandwidth within a range of motion twenty times larger than a piezoelectric-based fast-tool servo, there are a number of fundamental issues that make implementation difficult. A long-range MSL-based system is open loop unstable and highly nonlinear, and its dynamics can not be properly represented by simplified models. It is important to emphasize the need of both a highly accurate model and a robust control law if nanometer resolution is expected.

A novel parametric model of the electro-magneto-mechanical coupled system has been developed to describe the behavior of the system over a wide range of motion and frequency, as opposed to more conventional attractive force small perturbation models. It also provides a convenient way of devising a feedback linearizing control scheme that eliminates the need for high biasing currents present in most magnetic bearing systems. This paper presents a feedback-linearized controller coupled with a Kalman filter as a first approach to solve the problem. Good tracking performance has been found both in simulation and experiments.

ELECTROMAGNET DESIGN

The actuator had to be designed avoiding unnecessary mass that could reduce the natural frequency of the system, without sacrificing structural stiffness. Also, electromagnets can only exert attractive forces and therefore must be used in pairs. Fig. 1 depicts the design concept chosen by the authors.

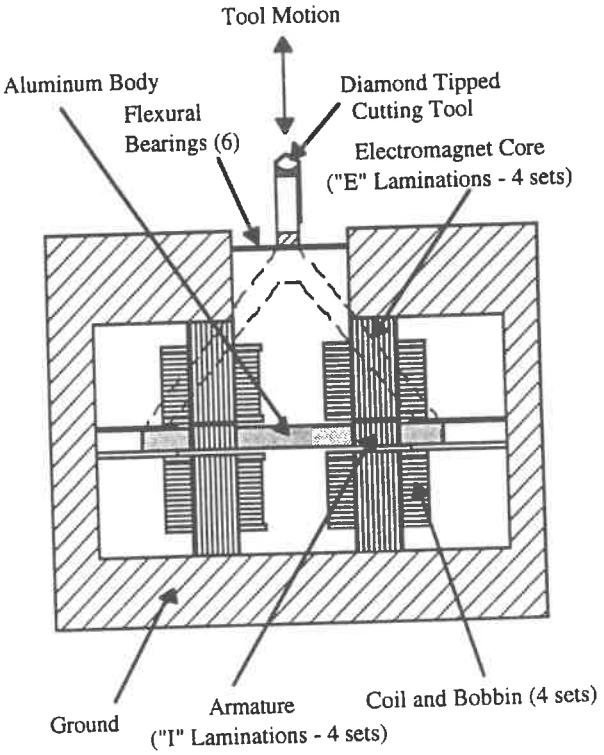

FIGURE 1: ACTUATOR SCHEMATIC

Flexures should be stiff enough to keep the natural frequency of the system above the desired bandwidth, but compliant enough to allow the electromagnets to pull against them and achieve the desired range of motion. This design allows for a tradeoff of bandwidth for range if necessary.

MATHEMATICAL MODELS OF MAGNETIC LEVITATION.

A long range of motion can not be properly described as small perturbations of a nominal trajectory. An adequate model must be accurate over a wide range of displacements and frequencies.

Eletromechanical systems driven by magnetic forces, such as magnetic bearings or micro-positioning stages [9], typically have very small range of motion (in the order of a few microns) and small bandwidth (in the order of a few Hertz). For this reason, simple mathematical models of the magnetic force seem to work reasonably well, for instance:

$$F_{mag} = K\frac{i^2}{g^2}$$

where i is coil current, g is air gap and K some constant to be determined. Furthermore, some of these systems operate at high bias current levels, thus allowing the use of Jacobian linearization. In the case of a magnetically levitated tool actuator, none of these assumptions hold true. This prompts for the development of a different modeling strategy.

A mathematical model can be formulated in such a way that input non-linearities are separable and additive:

$$a_1\frac{d^2x}{dt^2} + a_2\frac{dx}{dt} + a_3x = F_{mag2} - F_{mag1} \qquad (1)$$

where x is displacement, a_i are unknown parameters, and each magnetic force F_{mag} can be described as some polynomial of coil current (i) and the corresponding air gap. For instance:

$$F_{mag2} = \sum_{j=1}^{n}\left(K_{1j}\frac{i_2}{(x_o - x)^{0.5j}} + K_{2j}\frac{i_2^2}{(x_0 - x)^{0.5j}}\right) \quad (2)$$

In these equations, x (displacement) is measured from the equilibrium position, x_O is the nominal air gap, and K_{ij} are parameters to be determined. The problem is to find the unknown coefficients in Eqs. (1) and (2) such that experimental input-output sequences can be fitted in a minimum mean-square error sense. To use linear parametric techniques to find optimal fits for these parameters, each rational term in Eq. (2) can be considered a separate input to the system, in such a way that (1) can be written as:

$$\frac{d}{dt}\begin{bmatrix} x \\ \frac{dx}{dt} \end{bmatrix} = \begin{bmatrix} 0 & 1 \\ -\frac{a_3}{a_1} & -\frac{a_2}{a_1} \end{bmatrix}\begin{bmatrix} x \\ \frac{dx}{dt} \end{bmatrix} + \begin{bmatrix} 0 & 0 \ldots & 0 \\ K_{11} & K_{21} \ldots & K_{4n} \end{bmatrix}\begin{bmatrix} u_1 \\ u_2 \\ \ldots \\ u_{4n} \end{bmatrix} \qquad (3)$$

The techniques used to estimate the parameters involved are called prediction error methods [8], and are based on the minimization of a cost function which is the sum of the squared prediction errors. Previous knowledge or "reasonable guesses" of the parameters of the dynamic system (e.g. effective mass, estimated spring stiffness) significantly improves speed of convergence and minimizes the chance of hitting local minima since it provides initial estimates to the algorithm. These methods converge to a unique set of parameters and therefore model the system as time-invariant. More details and experimental results can be found in [10].

CONTROLLER DESIGN FOR MAGNETIC LEVITATION BASED ON FEEDBACK LINEARIZATION.

The model structure (Eqs. 2 and 3) is particularly well suited for feedback linearization as described on [2]. This is an approach to nonlinear controller design based on algebraically transforming a non-linear system into a linear one, so that linear control techniques can be applied. This differs entirely from conventional linearization (i.e., Jacobian linearization) in that feedback linearization is achieved by exact state transformations and feedback, rather than by linear approximations of the dynamics. For this reason, this technique is also known as "exact linearization" [3]. Feedback linearization does not require the system to operate around some nominal trajectory nor must the input signal be "small" compared to the input bias level. The MSL fast-tool servo can be feedback-linearized by the following input coordinate transformation:

$$\frac{dX}{dt} = AX + f(X, i_1, i_2) \quad \Leftrightarrow \quad \frac{dX}{dt} = AX + \begin{bmatrix} 0 & 0 \\ 1 & 1 \end{bmatrix}\begin{bmatrix} v_1 \\ v_2 \end{bmatrix} \qquad (4)$$

where $f(X,U)$ represents the input non-linearity described by Eq. (2). The problem becomes a standard linear controller design problem, and the performance is limited by the range of the input space $<v_1, v_2>$ over which the inverse map $i = f^{-1}(X, v)$ is well defined. To further clarify this point, consider again Eq. (1) and (2). Terms containing input currents can be factored as follows:

$$a_1\frac{d^2x}{dt^2} + a_2\frac{dx}{dt} + a_3x = K_1(x)i_1 + K_2(x)i_1^2 + K_3(x)i_2 + K_4(x)i_2^2 \qquad (5)$$

The following input coordinate transformation becomes obviously convenient:

$$v_1 = K_3(x)i_1 + K_4(x)i_1^2$$
$$v_2 = K_1(x)i_2 + K_2(x)i_2^2 \qquad (6)$$

which renders the system linear as in Eq. (4). This transformation is valid subject to the existence of the corresponding inverse maps, i.e.:

$$i_1 = \sqrt{\frac{1}{K_4(x)}\left(v_1 + \frac{K_3^2(x)}{4K_4(x)}\right)} - \frac{K_3(x)}{2K_4(x)}$$
$$i_2 = \sqrt{\frac{1}{K_2(x)}\left(v_2 + \frac{K_1^2(x)}{4K_2(x)}\right)} - \frac{K_1(x)}{2K_2(x)} \qquad (7)$$

Once the system is linearized, controller design is carried out based on a linear quadratic regulator (LQR), using a reduced-order Kalman filter to estimate the non-measurable states [4].

A singular value plot on the frequency domain shows that the system has inherently poor tracking capabilities. For this reason, the integral of the tracking error was added as an additional state to take advantage of the regulatory capabilities of the LQR design [5,6].

The feedback sensor used was an infrared optical probe. Tests were carried out on a smaller fixture, with a natural frequency of 190 Hz; in all plots, command signal is plotted in dashed line, measured response is shown in solid line.

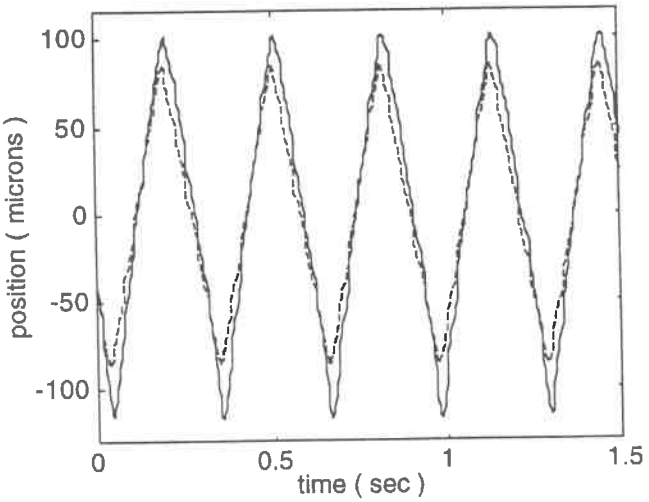

FIGURE 2. RESPONSE TO RAMP COMMAND

Figures 2 and 3 illustrate the tracking capabilities of the augmented LQR compensator. Tracking performance, however, degrades when either range or frequency bounds are exceeded. Since feedback linearization is sensitive to sampling rate, this deviation was primarily attributed to limitations in hardware used for these tests, in which closed-loop rate was limited to 2.5 kHz.

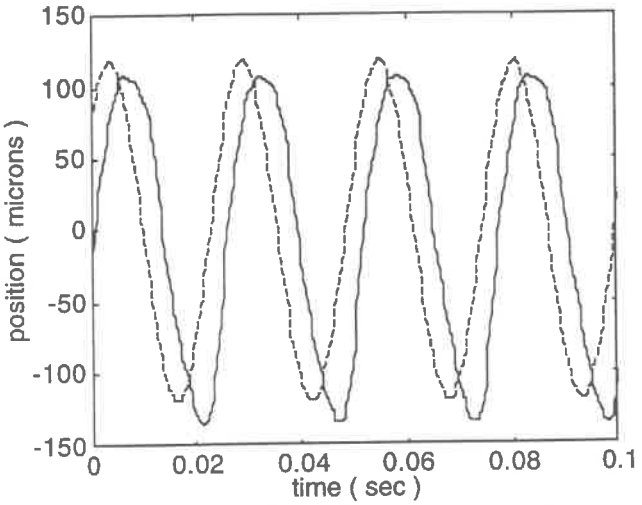

FIGURE 3. RESPONSE TO SINE WAVE COMMAND (40 Hz)

To further illustrate this, the closed loop system was simulated at a closed loop rate of 50 kHz, assuming a computational delay of 10 μsec (half the sampling period). Responses to a 400 micron step command are shown in Figure 4. This illustrates one key feature of exact linearization: the difference in response between actual plant and linearized system asymptotically decreases as the sampling time grows.

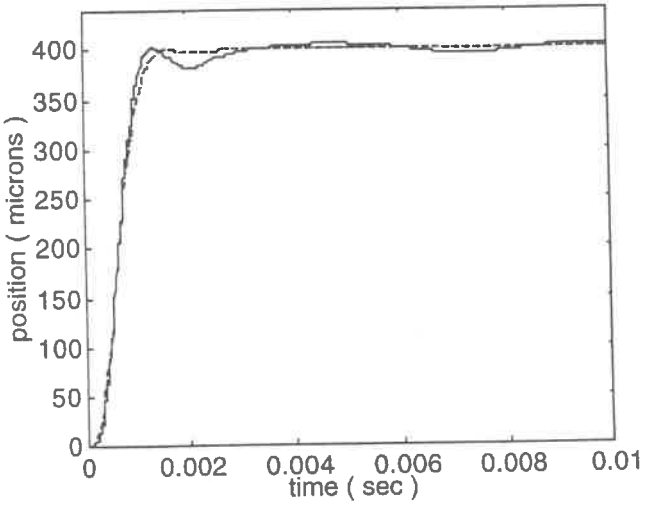

FIGURE 4. STEP RESPONSE AT 50 KHz (linearized model: dashed, nonlinear plant: solid)

At the current sampling rate both actual plant and nonlinear model fail to track the reference command beyond some range and frequency. To examine this assumption, input coil currents were recorded while operating the system in closed loop. Current coil data

was later sent through a simulation network corresponding to Eq. (1) and (2) in order to evaluate the model ability to reproduce the behavior of the nonlinear plant. Results showed good agreement between simulated and measured response.

Other plausible factors that degrade overall performance are inherent model limitations, amplifier bandwidth and sensor noise. Domain boundaries imposed by the inverse maps (Eq. 7) and amplifier bandwidth (frequency band over which the power amplifiers behave as ideal current sources) may also be affecting overall closed loop performance.

Experimental frequency response of the closed loop system is shown in Figure 5. Gain at frequencies below the resonance shows the range at which good tracking can be achieved with the current setup. This should significantly improve (get closer to 0 dB for frequencies below the resonance) at higher closed loop rates.

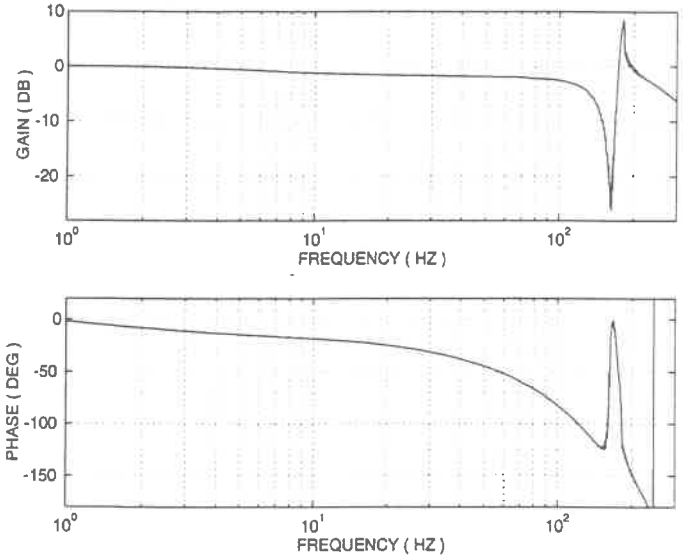

FIGURE 5. CLOSED-LOOP FREQUENCY RESPONSE

CONCLUSIONS

Magnetic Servo Levitation represents a promising alternative to long range tool actuation while keeping an adequate bandwith.

A novel mathematical model of magnetic levitation has been presented and used for controller design. The model has been experimentally tested both by simulating actual data and by closed loop tests. It is important to notice that an adequate model is essential to control an electromagnetic actuator since there is a highly nonlinear map between error signal and control action (coil currents).

The augmented LQR compensator has shown good tracking capabilities, although within a limited range and bandwidth. A substancial increase in closed loop rate may yield significant performance improvement.

Several other effects involved in the use of the magnetically levitated actuator are yet to be investigated. Inclusion of adaptive or learning schemes as a way of handling time varying effects and/or unmodelled dynamics represents an interesting path for future research.

ACKNOWLEDGEMENTS

Authors gratefully acknowlege David Trumper from MIT for his help on electromagnet design at an early stage of this project. This work was partially supported by ONR (Contract Number N00014-94-1-0235).

REFERENCES

[1] Tsuda, M. and T. Higuchi, "Design and Control of Magnetic Servo Levitation", *Report of the Institute of Industrial Science*, The University of Tokyo, March 1992, Vol. 37, No. 2, pp. 137-205.

[2] Slotine, J. J. and Li, W. : Applied Nonlinear Control. Prentice-Hall, Englewood Cliffs, NJ, 1987.

[3] Khalil, H. : Nonlinear Systems. Macmillan Publishing Company, New York, NY 1992.

[4]. Phillips, C. L. and Nagle, H. T. : Digital Control System Analysis and Design. Prentice-Hall, Englewood Cliffs, NJ, 1991.

[5] Franklin, G. F. and Powell, J. D. : Digital Control of Dynamic Systems. Addison-Wesley Publishing Company, Reading, MA, 1980.

[6] Dorato, P. , Abdallah, C. and Cerone, V. : Linear-Quadratic Control: An Introduction. Prentice-Hall, Englewood Cliffs, NJ, 1995.

[7] Higuchi,T., Tsuda,M. and Nakamura, Y.: "Design of Magnetic Servo Levitation for Robot Mechanisms". *Proc. of 20th Int. Symp on Industrial Robots*, 1989.

[8] Ljung,L.:System Identification:Theory for the User.Prentice-Hall,Englewood Cliffs,NJ, 1987.

[9] Trumper, D. L., Ludwick S.J. and Holmes, M.L.: "Design and Control of a 6-DOF Magnetic/Fluidic Motion Control Stage" Proceedings of the ASME Int'l Congress and Exposition, San Francisco, CA, 1995.

[10] Gutierrez, H. M. , Stancil, B. A. and Ro, P. I. : "Design and Modeling of a Magnetically Levitated Fast-Tool Servo System for Precision Turning". Proceedings of the ASME Int'l Congress and Exposition, San Francisco, CA, 1995.

Performance evaluator for open architecture NC boards

Minoru Hatakeyama, Shigeru Ueno

Technical Research Institute of
Japan Society for the Promotion of Machine Industry
1-1-12, Hachiman-cho Higashikurume-shi Tokyo, Japan

1. Introduction

The need for an open architecture for NC systems has increased[(1)(2)(3)], and many makers have begun to produce this type. The open architecture NC system has high flexibility and the ability to meet many sophisticated requirements such as adaptive control and intelligent prediction. Due to this advance, machine tool manufacturers today can choose and build the best matching NC system for their own products from various NC suppliers. However it is still difficult to select the best combination for the target machine from the many NC systems, servo amplifiers and other needed equipment because a method of evaluation for these has not yet been established. This research project is to develop a device that can evaluate many types of open architecture NC boards easily and consistently.

One of the major problems facing manufacturers is the need to assemble an NC system and

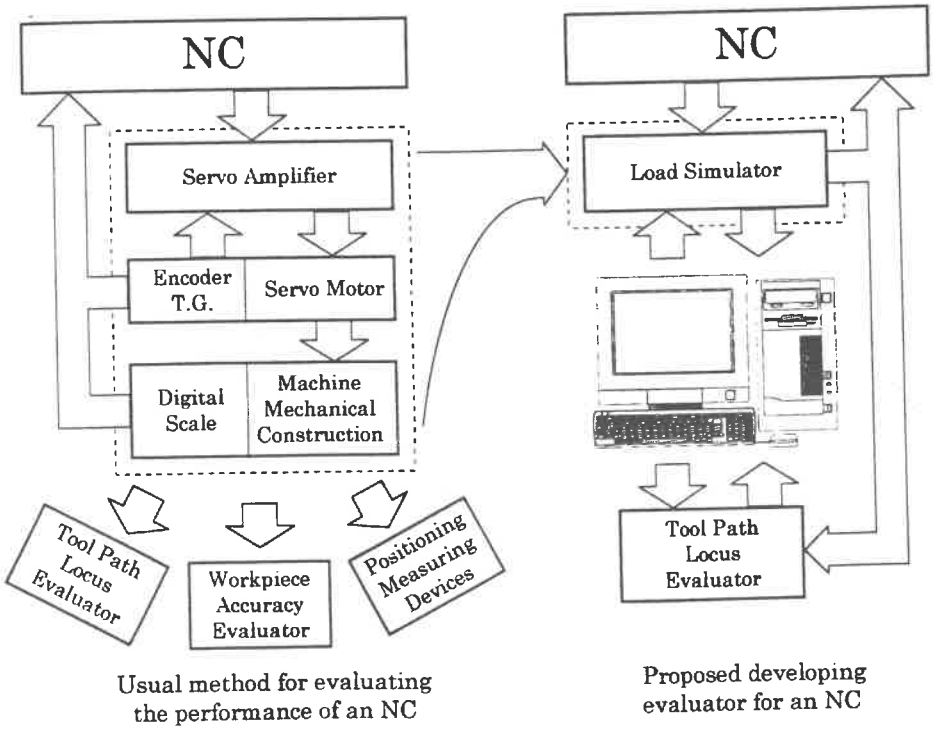

Figure 1 The examples of the method for evaluating a performance of NC

the servo amplifier on the target machine, and to activate it for evaluating the performance of the NC system.

However even this method's results are affected by the influence of the servo amplifier or the servomotor and therefore it is difficult to accurately evaluate the performance of the NC system itself. Also a standard system of evaluation has not yet been established.

2. Design Target and System Construction

An example comparing the present method for evaluating the performance of the NC system and the proposed performance evaluator for an NC system, are shown in Figure 1.

The proposed performance evaluator consists of a digital circuit that can simulate servo amplifiers and servomotors, and a load simulator that can simulate the target machine's mechanical characteristics. Due to the fully digital construction and software algorithm, the simulator can constantly evaluate performance according to each situation. With the digital circuit, the evaluator will be able to be set up various conditions from a personal computer. Information from the NC system is matched in the evaluator and converted to a digital signal. The converted signal is then sent to the various other simulator circuits.

As shown in Figure 2, the simulator consists primarily of four circuits. The first circuit is an IIR (Infinite Impulse Response) filter for linear responses. The second and third circuits are the simulators for nonlinear responses, i.e., the influences of friction that include stick slip motion, and mechanical backlash caused by changing one quadrant to another quadrant on Cartesian

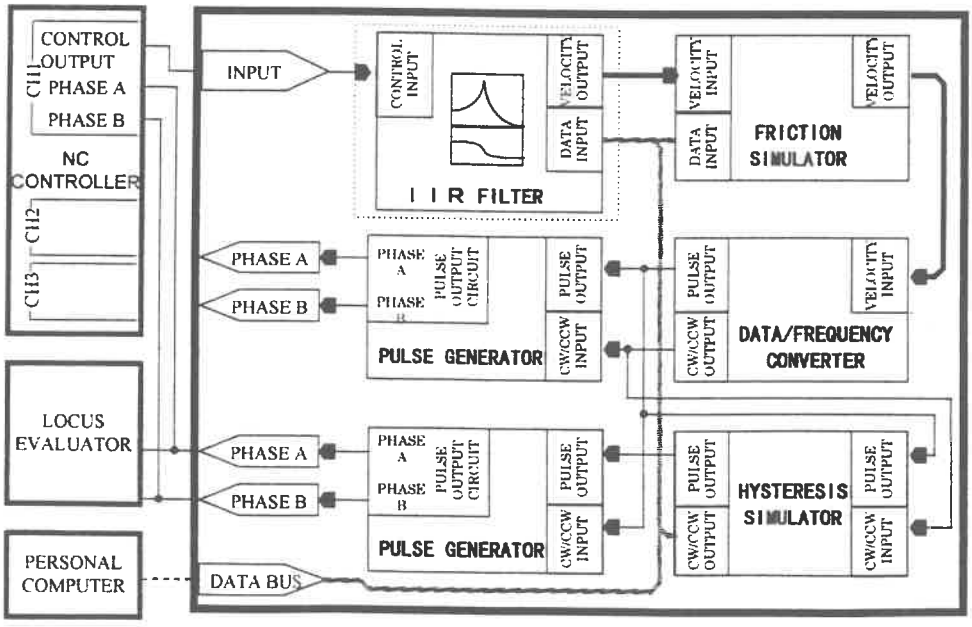

Figure 2 Outline of the Load Simulator

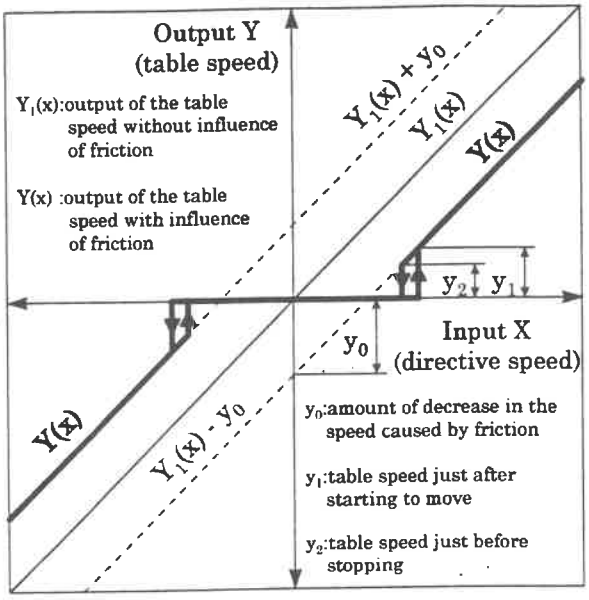

Figure 3 Output speed pattern considering the influence of friction

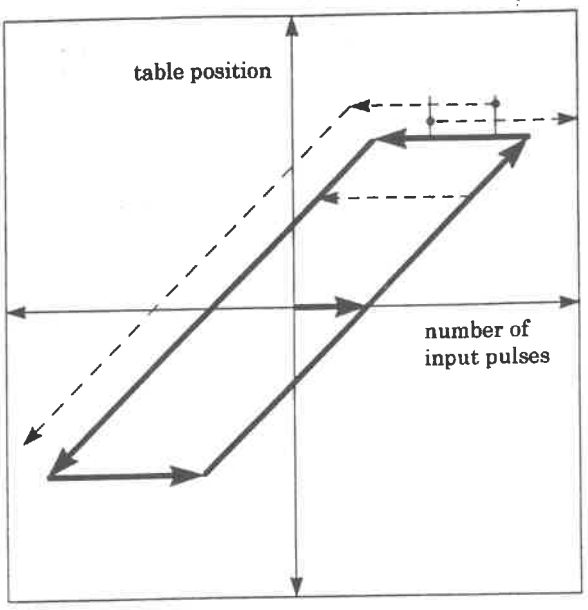

Figure 4 Behavior of the table considering the influence of mechanical backlash

coordinates. The last circuit is a pulse translator for feedback to the NC system. The system can accept AT bus NC boards that can export velocity analog outputs, and evaluation calculations are performed on two axes motions.

3. Kinematic models and its simulated device

One major focus of this study is the simulation of various kinematic behaviors. The mechanical and nonlinear behavior models, are shown in Figure 3 and Figure 4.

The behavior caused by the influence of friction, can become a simple model, so a digital circuit can simulate it in the friction simulator. In this circuit, the amount of decrease in the table speed by friction, the speed just after starting to move and the speed just before stopping can be set up independently. The combination of this circuit's effect and the delay response with the IIR filter in front of it, will be able to simulate the movement of stick and slip.

Figure 5 shows the outline of the circuit diagram. This circuit consists of comparators, data selectors and an adder. The adder computes the speed that is decreased by the friction. The comparators and the data selectors select the threshold value that is matched with the order of velocity. The hysteresis simulator circuit that simulates the influence of mechanical backlash, does not only cut the suitable pulses for it but traces the table position with a counter so it can prevent the table position from shifting in the backlash area.

After these procedures are performed, velocity output is calculated, and through the data/frequency converter and pulse generator, quadrate position pulses are generated as the

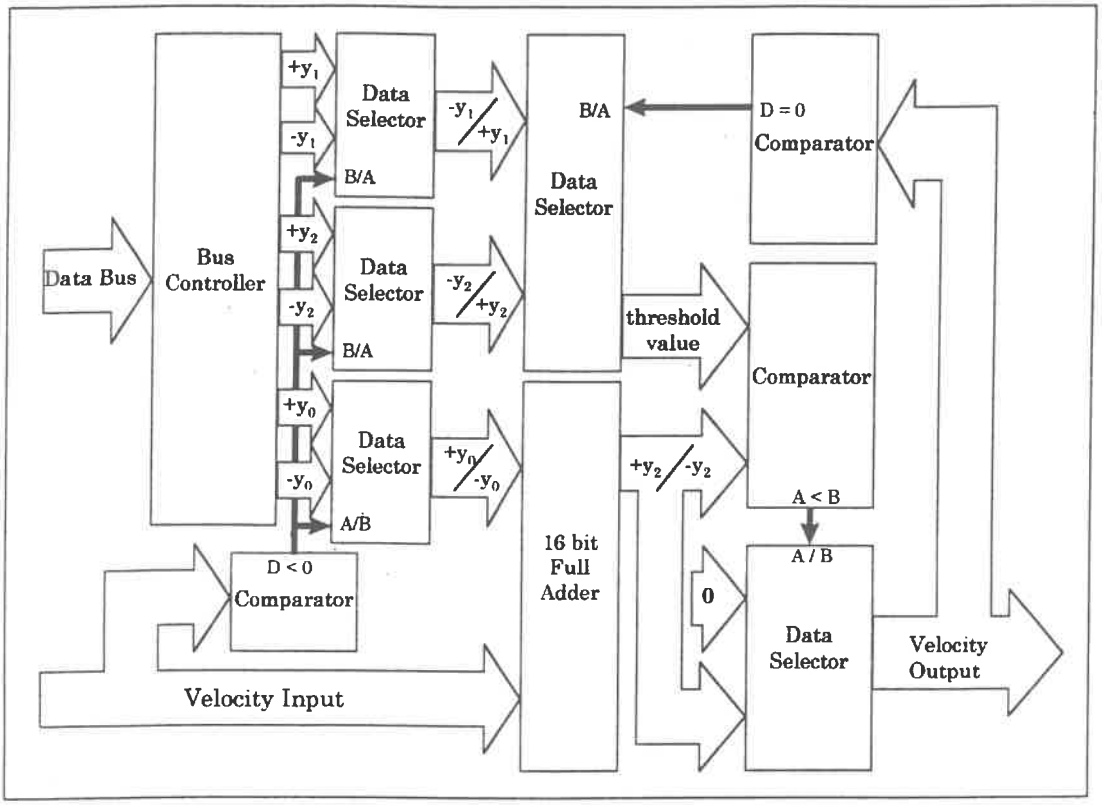

Figure 5 Friction Circuit

machine position. This information quality is evaluated by the digital locus evaluator that can calculate the difference between control position demands and simulated machine positions.

4. Future focus

The proposed system can evaluate various NC boards without actual machine hardware simulating the same specified conditions. The obtained output can used for the comparison of different NC boards' performance, and will also be useful for the improvement of NC boards.

5. Reference

(1)Requirements of Open, Modular Architecture Controllers for Applications in the Automotive Industry, Version 1.1, (1994), Chrysler, Ford, GM

(2)Open Architecture Controls for Precision Machine Tools, Bradley N. Damazo, Charles W. Yang, Robert J. Gavin, National Institute of Standards and Technology, the Proceedings of American Society for Precision Engineering Spring Topical Meeting on Mechanisms and Controls for Ultraprecision Motion, April 6-8, 1994, Tucson, AZ, pp. 26-31.

(3)OSEC Architecture Version 2.0 Pre-release, August 1996, OSE study members

Fabrication of Surface Perturbations on Inertial Confinement Fusion Targets

B. H. Jared, T. A. Dow, K. P. Garrard and G. M. Moorefield III
Precision Engineering Center, North Carolina State University, Raleigh, NC

C. Barnes, R. D. Day, D. J. Hatch, L. J. Salzer and G. Rivera
Los Alamos National Laboratory, Los Alamos, NM

Key Words: Inertial Confinement Fusion, diamond turning, fast tool servomechanism

Introduction

The production of inertial confinement fusion (ICF) targets for the National Ignition Facility is an important goal being pursued at Los Alamos National Laboratory (LANL). The geometry of ICF targets must be very well controlled as surface perturbations can create hydrodynamic instabilities when the targets are imploded during the fusion process. Targets with known surface features are currently being fabricated and tested in an attempt to better understand the impact of surface perturbations in ICF. Experimental data collected using targets with known surface features is also being compared with theoretical data generated by computer models.

Surface perturbations on flat target surfaces were initially produced by LANL using a standard diamond turning machine. Surface features have also been machined onto cylindrical ICF targets using both a precision fly-cutter mounted onto a diamond turning machine (DTM), and a piezoelectrically actuated tool which follows a reference surface on a rotating cam. Since each of these methods have limitations, an alternate target fabrication process has been developed at the Precision Engineering Center (PEC) which utilizes a fast tool servomechanism (FTS) mounted onto a diamond turning machine. The FTS system will give LANL the ability to produce more complex surface geometries with greater precision and a substantially reduced machining time than was previously possible.

Target Specifications

The manufacture of ICF targets requires a high degree of machining accuracy and precision. The cylindrical targets fabricated by LANL involve machining surface features around the circumference of 430 μm diameter cylindrical targets which are 430 μm in length. The current

fabrication techniques at LANL produce surface features which resemble a 0.5 μm amplitude sine wave pattern with a frequency of 10 waves per target revolution. Additional ICF tests specify the production of similar sized targets with up to 50 sine waves per revolution. LANL also has plans to produce spherical targets by machining 0.5 μm amplitude spherical harmonics on the outside diameter of 430 μm diameter hemispheres. Spherical targets cannot be produced using current LANL fabrication techniques, but should be machinable using a FTS. The desired figure accuracy of the surface perturbations on both the cylindrical and the spherical targets is 10 nm peak to peak.

FTS Design

The FTS built for LANL, as seen in Figures 1 and 2, uses the same basic concepts found in the FTS developed by Falter [1]. It was specifically designed, however, to meet the specifications required for the fabrication of ICF targets and for the DTM hardware utilized by LANL. The FTS uses an EDO E400P-0.5 piezoelectric actuator to provide 11.4 μm of tool motion. This tool motion is measured using a Lion Precision capacitance gage system with a PX405HC probe and a DMT10R probe driver. The Lion Precision system provides a measurement resolution of 1 nm at a bandwidth of 21 kHz. The moving components of the FTS were optimized such that their natural frequency approached 10 kHz. This was done by modeling the FTS in Pro/ENGINEER and then performing finite element analyses on the model using ANSYS. Since ICF targets are currently fabricated at LANL using a Moore M-18 Aspheric Generator, the FTS was also designed to mount to the side of the tool post of the M-18 so that the tip of its diamond tool could be easily positioned at the center of the rotary table in the horizontal plane and level with the spindle axis in the vertical plane.

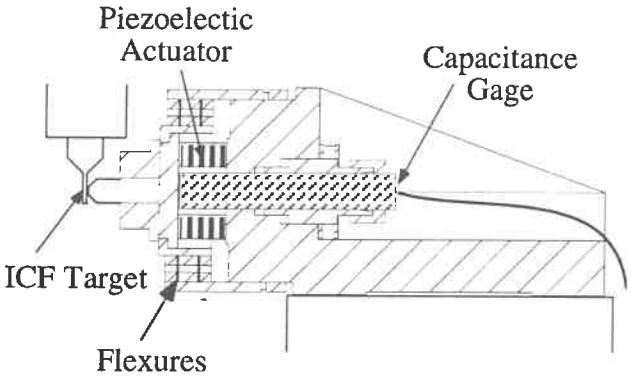

Figure 1: FTS Cross Section

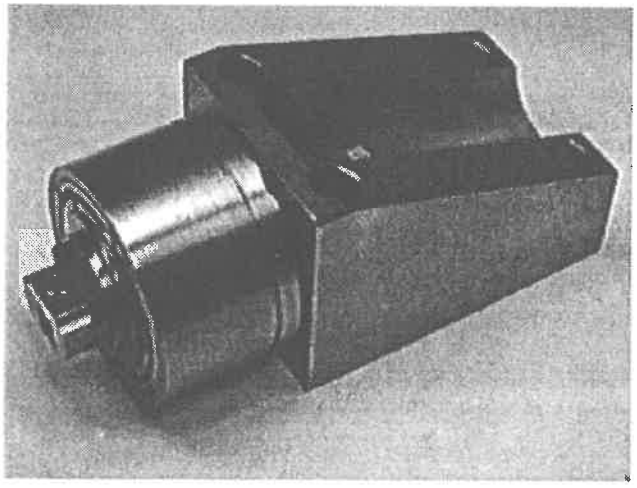

Figure 2: FTS

FTS Control

A FTS cannot generate the tool motions necessary to machine surface perturbations onto ICF targets while operating in an open loop mode due to hysteresis in the motion of the piezoelectric actuator and due to the necessity of coordinating the motion of the FTS with the motion of the spindle, axes and rotary table of the M-18. Since the M-18's Aerotech Unidex 31 (U31) controller does not provide the software and hardware configurations necessary to implement a FTS system, modifications were made to the U31 controller in the form of a separate control program for the FTS. The major hardware modifications to the U31 involved installing a Pentek 4284 DSP board and a Pentek 4242 Analog I/O board into its VME-bus. This allows the DSP board to perform the computations necessary to execute the FTS's PID control algorithm at an update rate of 30 kHz. Modifications were also made to the U31 program code to allow it and the FTS control program to operate concurrently.

The design of the control algorithm for the FTS involved optimizing the PID control gains using MATLAB simulations. An experimental gain plot of the FTS was obtained by measuring the response of the servo to a 50 V amplitude swept sine wave input with a maximum frequency of 15 kHz. A mathematical transfer function was fit to the experimental data and then utilized in the controller simulations. The PID control gains were varied through trial and error until the simulated response to a 1 μm step input was optimized, as seen in Figure 3. The simulation predicts that the FTS will exhibit a settling time of about 1 msec with zero overshoot and zero steady state error for a 1 μm step input.

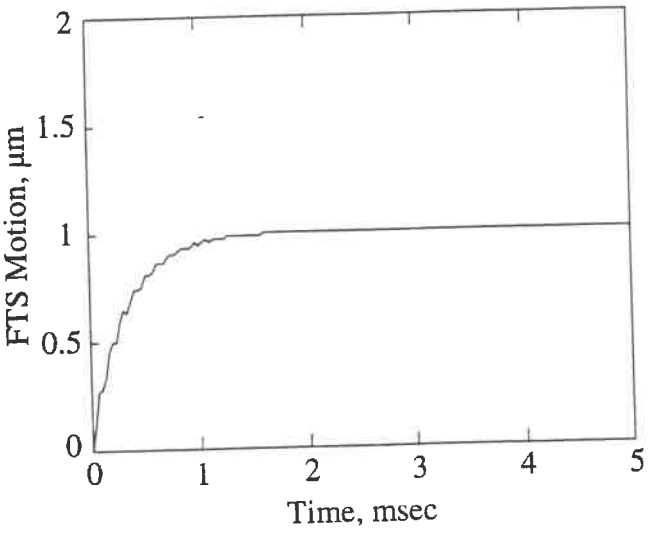

Figure 3: Simulated Step Response

FTS Testing

Once the PID control gains were obtained, initial tests were performed on the FTS to determine its response characteristics and to improve upon them. These tests were performed on a Rank Pneumo ASG 2500 located at the PEC. The ASG 2500 uses a controller designed at the PEC which only provides a 10 kHz sampling rate. This controller, however, has the hardware and

software necessary to implement a FTS system. Thus, initial testing of the FTS was performed with a minimal amount of controller modification. The FTS was commanded to follow a 1 μm square wave at 2 Hz to determine its response to a step input. Figure 4 shows the response of the FTS after the PID gains were optimized. It demonstrated a settling time of almost 4 msec with an overshoot of less than 0.6% and a steady state error of less than 0.1%. The FTS was also commanded to follow a 0.5 μm amplitude sine wave at 33 Hz. The FTS, as seen in Figure 5, demonstrated ±80 nm of following error. Much of this error, however, was associated with the phase response of the FTS as the error motion from a true sine wave geometry was only ±5 nm. Increasing the sampling rate of the controller to 30 kHz will greatly improve the phase response of the FTS and thus significantly reduce the following error.

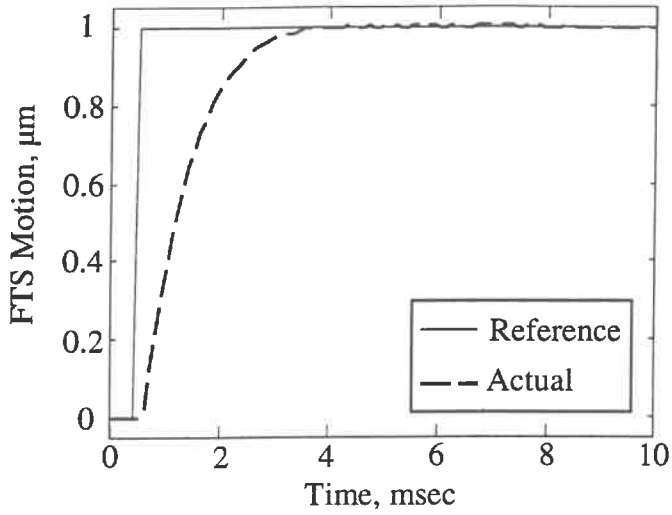

Figure 4: FTS Controlled Step Response

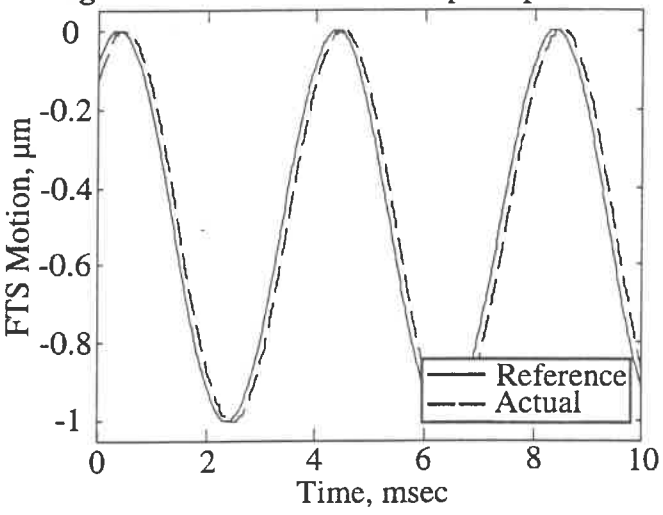

Figure 5: FTS Sine Wave Response

Conclusions

A FTS has been designed and built for LANL. Initial tests on the system indicate that it will generate surface perturbations which meet current ICF target specifications. The FTS, however, must still be interfaced with the Aerotech Unidex 31 controller. Once the FTS can be controlled by the U31 controller, it will be transferred to LANL as ICF targets will be machined with the M-18 to determine the response of the FTS system under machining conditions.

References

[1] Falter, Peter. "Diamond Turning of Nonrotationally Symmetric Surfaces," PhD Thesis. North Carolina State University. 1990.

AUTONOMOUS CUTTING PARAMETER REGULATION BY USING AN ADAPTIVE MODELING AND GENETIC ALGORITHMS

Tae Jo Ko, Hee Sool Kim
Department of Mechanical Engineering, Yeungnam University
Gyoungsan, Kyoungbuk 712-749 KOREA

ABSTRACT

In this research, a turning process was modeled adaptively by a back-propagation neural network with iterative learning method, and cutting parameters of the process model were optimized through a Genetic Algorithms(GAs). Some constraints were given to the input conditions and the process outputs for the desired surface integrity and to protect a machine tool. Such a constrained problem could be solved by introducing penalty values, which were included in the fitness evaluation of GAs. Experimental results show that the neural network could model the cutting process efficiently, and the cutting conditions such as spindle speed and feed rate were regulated for maximizing material removal rate through the GAs. Therefore the proposed approach can be well applied to the real machining process.

INTRODUCTION

In conventional machining systems, the cutting parameters such as cutting speed, feed rate and depth of cut are determined based on the operator's experience or empirical data hand book. Such systems can not be optimal in the sense of material removal rate since the cutting conditions are selected conservatively considering tool breakage or machine tool damage[1].

In this regard, the adaptive control system that can adjust the operating parameters on-line has been studied with interest. Adaptive control systems are classified into two types: adaptive control of constraints(ACC) and adaptive control with optimization(ACO)[5]. Although there have been considerable researches on the ACO systems[1-4], few of these systems are used in practice. The major problems with such systems have been the difficulties in modeling the cutting process. Although there are well known cutting process models, such models can not reflect the progress changes such as tool wear or any environmental effect. Adaptation of the cutting conditions to the new circumstances means better optimization in view of a greater utilization of the system's capabilities. Morcover, although there have been mathematical process model that can adapt the process changes, a calculus based optimization technique has a chance to give a local optimal value[10]. This is due to that the cutting process is rather complex and nonlinear with respect to materials, cutting conditions, cutting tools, etc.

In this paper, an adaptive optimization method of machining process using an adaptive modeling and GAs is introduced[6-8]. To this end, a multi-layered neural network is used to model the cutting process on-line.[9] The network learns the machining process iterativley using the errors between the sensor and the network outputs without supervisor. Therefore this model can adapts the process change such as the variations of tool wear or change of work-piece geometry. Then GAs are introduced to optimize the cutting parameters under the given constraints such as cutting force, motor current and machine tool vibrations. Consequently cutting parameters are continuously adjusted through the feedrate and spindle override function in NC machine tools. The result shows that a multi-layered neural network learns the process by machining two or three pieces of work-piece(total cutting length 50mm). The cutting parameters such as feed rate and spindle speed are adjusted autonomously to maximize the material removal rate without violation the given process constraints.

ADAPTIVE MODELING OF TURNING PROCESS

The optimization system consists of the engine for modeling the turning process adaptively and the one for optimizing the modeled process. As shown in Fig. 1, an error back-propagation multi-layered neural network is used for modeling, and GAs are introduced for optimization. In the modeling, the u_k of cutting parameters such

as cutting speed, feed rate, and depth of cut, which are initially given by the CAM software, is fed to the machine tool and the neural network simultaneously. The predicted outputs of a neural network may be wrong since the network never learned the process previously. The same cutting conditions given to the CNC machine tool also give the process output such as cutting force, machine tool vibration, and spindle motor current. Therefore there exists an error between the predicted value of network and the output of machining process, and the error is minimized by training the network recursively.

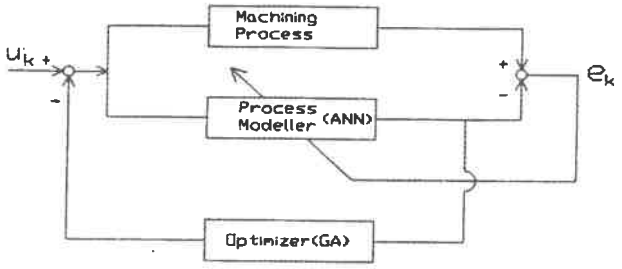

Fig. 1 The overall structure for the process optimizer

Therefore the optimized value determined from the GAs can not be optimum, and new input conditions are generated by feeding back the above value to the u_k of original inputs. The new cutting parameters are given to the network and the machine tool again, and the on-line learning process keeps on running until the error is within tolerance value. The neural network used in the research is multi-layered neural network which has three layered structures. that is input, hidden, and output layer.

OPTIMIZATION OF MACHINING PROCESS

The material removal rate can be represented by multiplying cutting speed, feed rate, and depth of cut as shown Eq. (1).

$$H = f \cdot d \cdot v \tag{1}$$

where f is feed rate, d is depth of cut, and v is cutting velocity. Feed rate and cutting speed are selected as the control parameters since the control technology uses the external input such as feed rate and spindle override function in NC. The change of depth of cut may be difficult in finish machining, therefore the control of depth of cut was omitted.

In Eq. (1), maximum material removal rate can be obtained by choosing maximum allowable values of three input parameters. However, some constraints should be given for assuring surface integrity and protecting a machine tool That is, the optimization problem of Eq. (1) has some constraints as follows;

Input constraints :

$$f_1 < f < f_2,\ s_1 < s < s_2 \tag{2}$$

Output constraints

$$F_c < F_{c\,max},\ I_s < I_{s\,max},\ A_s < A_{s\,max} \tag{3}$$

where $F_{c\,max}$, $I_{s\,max}$, and $A_{s\,max}$ represents the maximum constraint value of main cutting force, spindle motor current, and acceleration signal respectively. f_1, f_2, s_1, s_2 is the minimum and the maximum allowable value for the feed rate and spindle speed respectively.

The above constrained optimization problem can be transformed to unconstrained problem by penalty function technique as shown in Eq. (4). The above constrained optimization problem can be transformed to unconstrained problem by penalty function technique as shown in Equation (4).

$$H = f \cdot d \cdot v$$
$$- R_1(< f_1 - f >^2 + < s_1 - s >^2 + < f - f_2 >^2 + < s - s_2 >^2) \quad (4)$$
$$- R_2(< F_c - F_{\max} >^2 + < I_s - I >^2 + < A_s - A >^2)$$

where $< \bullet >$ represents <g>=g when $g \geq 0$, <g>=0 when g<0. R determines the relative penalty values imposed on the constrained conditions. These values play a role to reduce the fitness value in the application of GAs. The first term in Equation (4) is fundamental objective function, and the second one is the constraints to the input conditions. The other represents the maximum allowable output values to the cutting force, spindle current, and machine tool vibration. By applying GAs to the Equation (4), the globally optimized cutting conditions can be taken.

EXPERIMENTAL METHOD

Experimental Apparatus

A small CNC turning lathe was used for the experiment. Tool dynamometer, and accelerometer were used for measuring process output. Tool dynamometer(KISTLER 9272) for measuring cutting force signal was mounted on the fixture fixed on the gang type table as shown in Fig. 2. Instead of accelerometer for measuring vibration signal, piezo electric film(Pennwalt; sensitivity $10mV/g$) was attached under the tool holder. The reason is that we can fabricate it as a lower price to commercialize the system. The current signal was directly acquired from the spindle drive unit(A06B-6060-H003#H503), which is the line for the spindle load meter in operating console. Therefore we need not a current sensor or any other type of composition method for three phase current signals. The above signals were digitized through the A/D converter(PCL 812PG) and sampled to the PC. After optimizing the input cutting conditions, the cutting parameters were regulated through the feed rate and the spindle speed override function by a specially made I/O card. The work-piece used in the cutting was carbon steel(SM45C), and the cutting tool is tungsten carbide(TNMG 160412-B20).

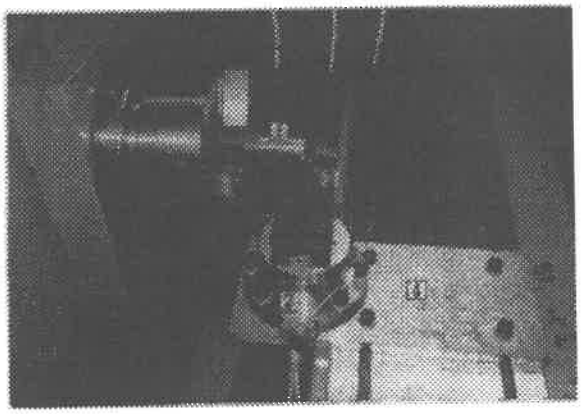

(1) Workpiece (2) Tool Dynamometer (3) Piezo Electric Film (4) Bracket
Fig. 2 The Experimental Set Up

Experimental Method

In the experiment, firstly, cutting force signals, vibration signals, and current signals are acquired through the sensors. Then the signals are used for training the neural network. Finally, the GAs optimizes the cutting parameters and new optimized cutting parameters are fed to the feed rate and the spindle speed override function in the CNC(FANUC 0T).

The override function in the CNC system are mainly consisted of feed rate and spindle speed, and which regulates the cutting parameters a little bit to the given initial values. For example, the feed rate uses four bits, and the combination of each bit has different values of override. Therefore, the override in feed rate has sixteen

step from 0% to 150% to the given initial value. On the other hand, the spindle override uses three bits, the range is from 50% to 120%. The functions on the operating console were switched by the control system through the PC.

EXPERIMENTAL RESULTS

Firstly the CNC turning center cut the work-piece without any information about the machining process. Of course, the machine has some constraints which were chosen from operator's experience. The main cutting force should be under $100N$, and the acceleration signal be under $2.5g$. The maximum current to the spindle motor is $15A$. The range of feed rate is from $0mm/rev$ to $0.75mm/rev$, and the spindle speed is from $500rpm$ to $1200rpm$. Two kinds of cutting experiments were carried out; one for the geometric change such as depth of cut, and the other for the progressive tool wear.

Cutting Parameter According to the Change of Depth of Cut

Fig. 3s show the optimized results to the depth of cut of $0.3mm$. The initial population in the GAs is 100, the crossover rate is 0.25, and the mutation rate is 0.01. Fig. 3(a) represents the maximum and averaged fitness value during the evolution of 1000 generations. Feed rate variation according to the evolution is Fig. 3(b), and Fig. 3(c) shows the change of spindle speed. As shown in the figures, the cutting parameters converged to the optimal value so fast in case of depth of cut of $0.3mm$. The neural network learns the machining process simultaneously as shown in Fig. 3(d), where the error tolerance is 0.01, learning rate is 0.5, and momentum rate is 0.5. The optimized cutting parameter of feed rate and cutting speed is $0.75mm/rev$ and $1200rpm$, respectively, which is the maximum value to the given constraints. Therefore, the maximum cutting conditions do not violate the given constraints to the small depth of cut.

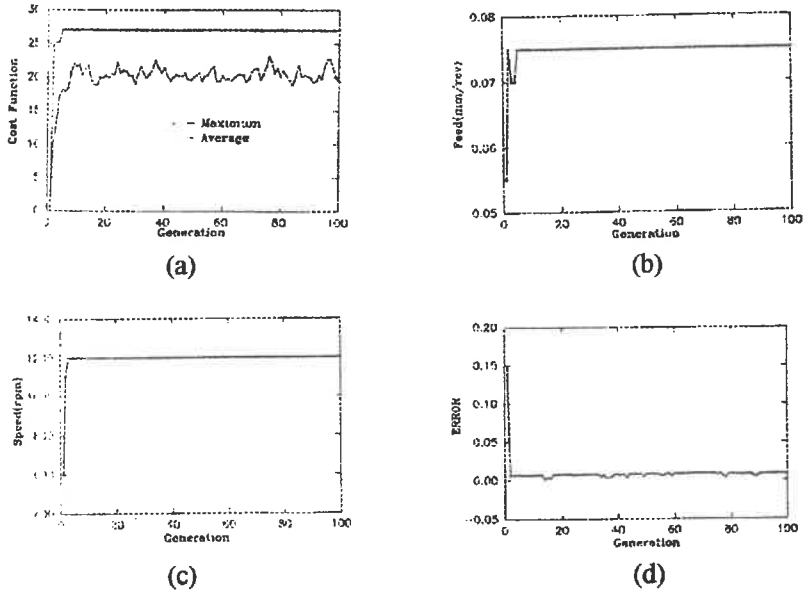

Fig. 3 Results of Genetic Algorithm according to the evolution; (a) Maximum and averaged values of evaluted costs, (b) Variation of feed rate, (c) Variation of cutting speed, (d) Learning errors of a neural network.

Fig. 4s show the optimization results by changing the depth of cut from $0.3mm$ to $0.6mm$. At this time, the neural network trained to the depth of cut of $0.3mm$ was used again. As shown in Fig. 4(a), there are big oscillation to find the optimum value initially since the network has wrong information about the process. As shown in Fig. 4(b) and 4(c), the system finds the optimal value by training the process simultaneously during 35 generation. After 35 generation, the error of the network is within the tolerance value, and the optimized value of

the cutting parameters converged steadily. The cutting speed did not change compared to the depth of cut of 0.3*mm*. However the feed rate was reduced to 0.055*mm/rev*. This means that main cutting force signal violates the given constraints by increasing the depth of cut. Therefore, the cutting speed should be increased or the feed rate be reduced. However, the spindle speed was constrained by maximum speed of 1200*rpm*, the feed rate was reduced. This is well coincident to the our intuition.

Fig. 5 shows the surface roughness of the machined work-piece. The surface is very random in the range of initial change of feed rate, on the other hand the surface roughness is constant in the range of 2.

From the above results, we can conclude the system can well learn the process and optimize the cutting parameter regardless of the geometric change such as depth of cut.

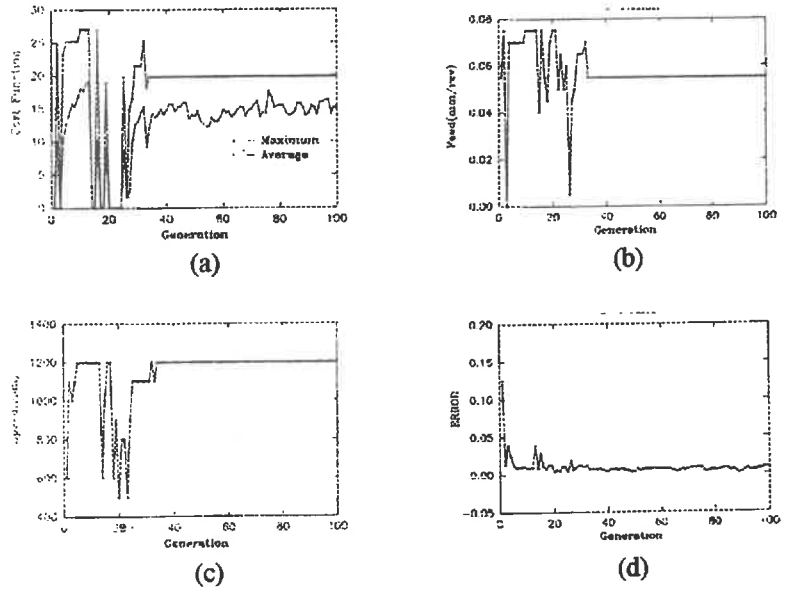

Fig. 4 Results of Genetic Algorithm according to the evolution; (a) Maximum and averaged values of evaluted costs, (b) Variation of feed rate, (c) Variation of cutting speed, (d) Learning errors of a neural network.

Cutting Parameters According to the Progressive Tool Wear

The applicability of the developed system to the progressive change such as tool wear was checked. The experiment was carried out to the new and worn tool. To compare the results, the depth of cut was fixed as 0.3*mm*.

The maximum and averaged fitness value of the GAs to the worn tool is shown in Fig. 6(a). In this case, the maximum removal rate was obtained as 19.8mm^3/min, which was 7 mm^3/min less than the new tool condition. The network learns the process during initial 30 generation. In this experiment, the tool was artificially ground to fake tool wear. However the optimization may be effective since the network does not learn immediately but progressively. In this case, the feed rate and the spindle speed is 0.055*mm/min* and 1200*rpm*, respectively as shown in Fig 6(b), 6(c).

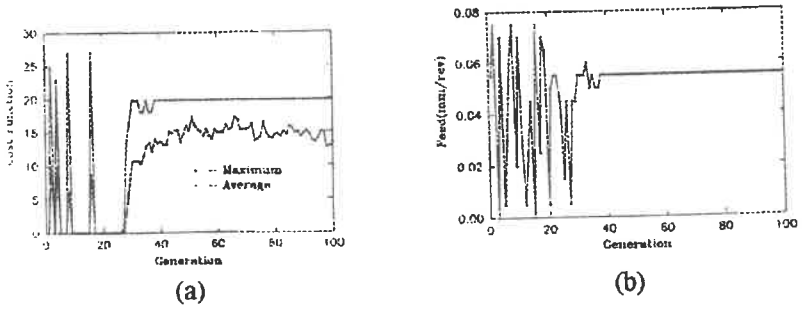

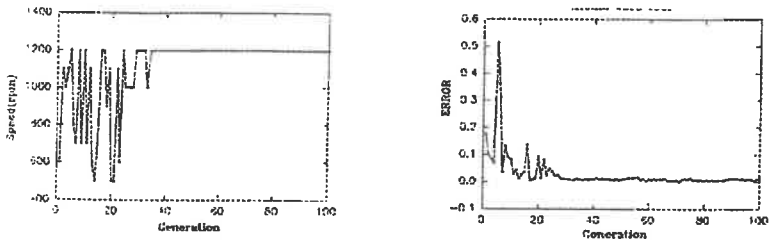

(c) (d)

Fig. 5 Results of Genetic Algorithm according to the evolution; (a) Maximum and averaged values of evaluted costs, (b) Variation of feed rate, (c) Variation of cutting speed, (d) Learning errors of a neural network.

CONCLUSIONS

In this research, the adaptive model for the CNC turning lathe was constructed by using an artificial neural network, and the cutting parameters were optimized through the GAs. The system could cut the work-piece optimally regardless of the geometric change such as the change of depth of cut and the progress of tool wear. From the experimental results, we can conclude that the system can well adapt the process change, and find the global optimum cutting parameters without violating the given constraints. The research will be expanded to the surface roughness and cutting temperature to improve the performance.

ACKNOWLEDGEMENT

This paper was supported by NON DIRECTED RESEARCH FUND, Korea Research Foundation. The authors would like to thank for the support.

REFERENCES

1. Rangwala, S. S., Dornfeld, D. A., "Learning and Optimization of Machining Operations using Computing Abilities of Neural Networks," IEEE Transactions on SMC, Vol. 19, No. 2, pp. 299-314, 1989.
2. Jang, D. Y., Seireg, A., "Machining Parameter Optimization for Specified Surface Roughness," ASME J. Engng. Ind., Vol. 114, pp. 254-257, 1992.
3. Matsumura, T., Obikawa, T., Usui, E, "Autonomous Turning Operation Planning with Predicting Tool Wear and Surface Roughness," Transactions of NAMRI/SME, Vol. 21, pp. 359-366, 1993.
4. Wu, S. M., Ermer, D. S., "Maximum Profit as the Criterion in the Determination of the Optimum Cutting Conditions," ASME J. Engng. Ind. Vol. 88, pp. 435-442, 1966.
5. Koren, Y., Computer Control of Manufacturing System, McGraw-Hill Book Company, pp. 249-251, 1983.
6. Buckles, B. P., Petry, F. E., Genetic Algorithms, IEEE Computer Society Press, 1992.
7. Michalewicz, Z., Genetic Algorithms + Data Structures = Evolution Programs, Springer-Verlag, 1994.
8. Goldberg, D. E., Genetic Algorithms in Search, Optimization & Machine Learning, Addison Wesley, 1989.
9. Pao, Y. H., Adaptive Pattern Recognition and Neural Networks, Addison-Wesley Publishing Company Inc., 1989.
10. Rao, S. S., Optimization Theory and Applications, 2nd edition, Wiley Estern Limited, 1984.

Development of a thin brittle filter insertion machine for optical WDM

Kazuki Kudo**, Fumikazu Ohira***, Kunio Koyabu***, Mitsushi Matsunaga***
and Yasuyuki Inoue****

** NTT Multimedia Business Department, Nippon Telegraph and Telephone Corporation,
2-2-2 Otemachi, Chiyoda-ku, Tokyo 100, Japan
NTT Opto-electronics Laboratories, Nippon Telegraph and Telephone Corporation,
*** 3-9-11 Midori-cho Musashino-shi, Tokyo 180, Japan
**** 162 Shirakata-Shirane Tokai-mura, Naka-gun, Ibaraki 319-11, Japan

Micrometer-order-accuracy insertion of a thin film into a narrow groove using image processing and improved stage accuracy, a method for distinguishing between sides of a curved film, and a precise insertion force control method are proposed and examined in this paper. Using these techniques, an automatic insertion machine has been developed.

To attain a highly-advanced network society that includes Fiber To The Home (FTTH), we will need optical devices such as wavelength division modules that use an optical waveguide or an optical fiber with a thin film filter inserted. Though an optical transceiver incorporating a wavelength division multiplexing (WDM) function is very useful for flexible subscriber access networks, a thin film filter-embedded multiplexer is not still cheap. Thus, an automatic insertion machine that can insert a thin film into a narrow groove reliably and at low cost will be required.

We assume that the filter will be a thin film filter 14-μm thick and that the narrow groove cut into the waveguide will be 18 to 22-μm wide. Such a filter is about 1.4 mm square and consists of a brittle multi-layer and a flexible resin sheet. Consequently, it has a warp of about 10 μm and exhibits both flexibility and brittleness.

Technological problems to be solved are:

- micrometer-order-accuracy insertion of a curved thin film filter into the narrow groove
- handling of the flexible and brittle thin film
- method of distinguishing the sides of the filter
- insertion without damaging the filter

To solve these problems, the following techniques have been newly proposed and examined.

(i) The relative position of the filter and groove are matched with a high degree of accuracy by

image processing observing from the upper side of the groove. Figure 1 shows a schematic configuration of this insertion method. The waveguide is placed on the 3-dimensional precise stage and its groove is observed from the upper side. Using an appropriate microscopic camera system, the observed image of the groove, as shown in Fig. 2, is clear enough for image processing to determine the position of the groove. This position is matched with the previously-measured position of the filter. The waveguide on the precise stage is transferred to just below the clamped filter. In this case, the repetitive accuracy of transfer movement is crucial. As shown in Fig. 3 , the repetitive accuracy of the transfer movement was highly improved to about 1μm.

(ii) The film is sucked by the vacuum clamp or clamped mechanically to correct the warp.

(iii) To distinguish the sides of the film, the film surfaces are scanned by a laser beam to measure their shape. Examples of scanned film profiles are shown in Fig.4, indicating that the sides of a filter can easily be distinguished.

(iv) To avoid damaging the filter during insertion, a weight cancellation function for the insertion mechanism by electromagnetic force is applied to control insertion force precisely. To optimize insertion force, the minimum force for insertion and the maximum force, above which the filter is damaged, are measured. The minimum force is 3 gf and the maximum force is 10 gf.

With all the techniques proposed above, a precise and reliable insertion is achieved. Moreover, an automated machine based on these techniques has been made. (Fig. 5) The machine picks up parts with its hand unit from the parts tray, inserts them and bonds them in place using adhesive and UV curing. UV adhesive is supplied by capillary action.

Using this machine, tolerance of the relative positioning error between centers of the filter and the groove for successful insertion is measured. The measured tolerance is about 25 μm. This width is several microns wider than that of the groove. This means that insertion is successful even when the filter touches the edge of groove. The average time for this machine to produce a module is about 1 minute. The module's light loss for the 1.5 μm wavelength reflected from the inserted filter is around 1.5 dB, which satisfies the requirements of less than 2 dB.

This machine should be capable of producing a large number of indispensable optical devices for the highly-advanced information society of the future at low cost.

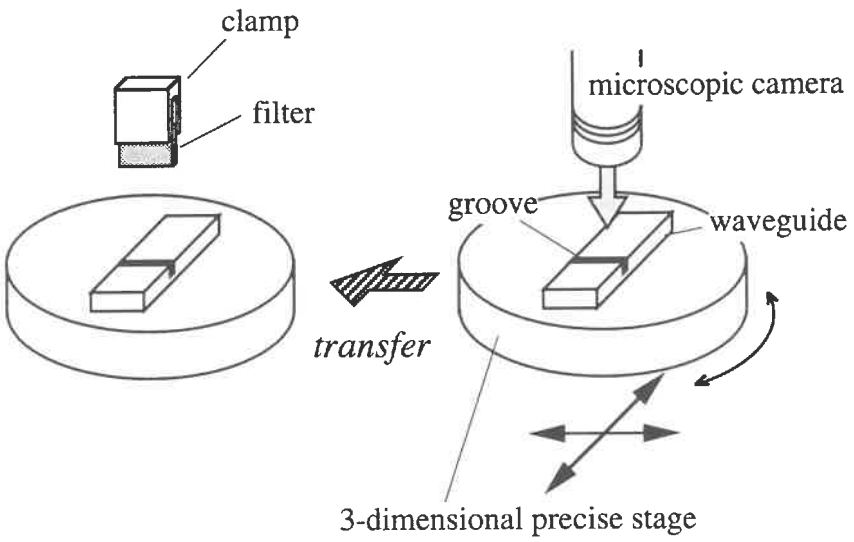

Fig. 1 schematic configuration of insertion method

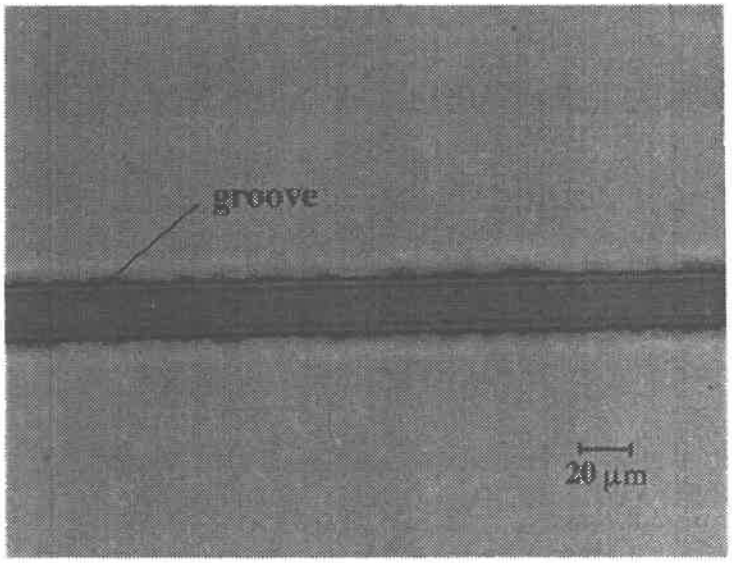

Fig. 2 image of a groove

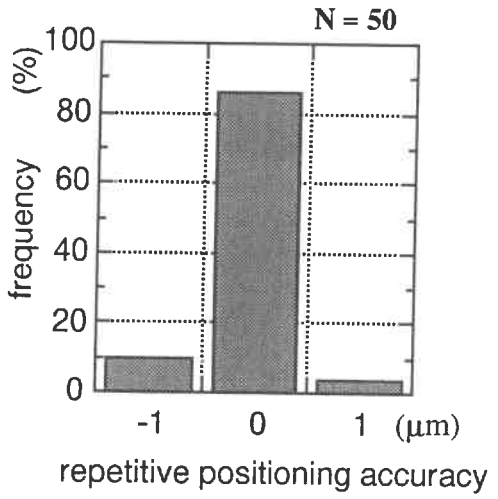

Fig. 3 repetitive positioning accuracy of transfer stage

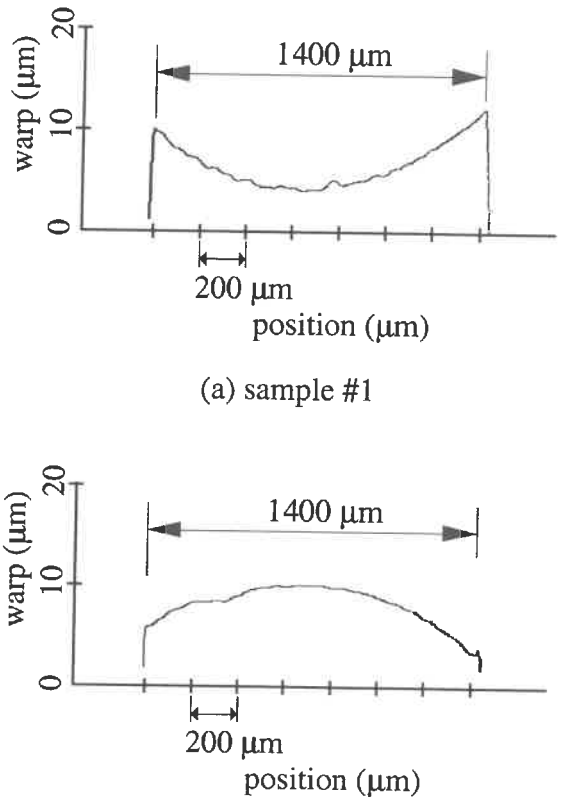

Fig. 4 scanned film profiles

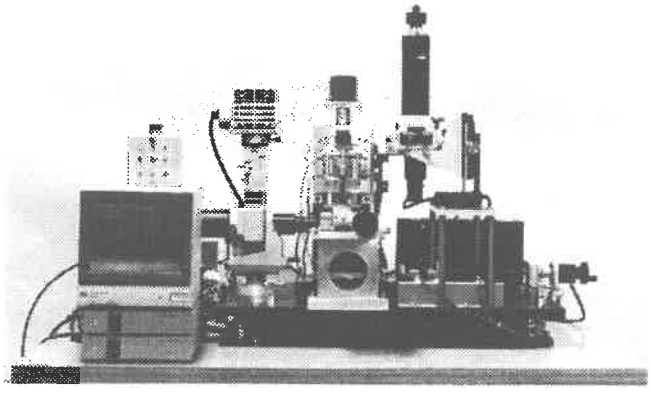

Fig. 5 photograph of developed filter insertion machine (prototype)

Autonomous acquisition of a shared, machining condition data-base in an open CNC environment

Mamoru MITSUISHI, Hideyuki OKABE, Makoto HASHIGUCHI, Katsuya TANAKA and Takaaki NAGAO

Department of Engineering Synthesis, Faculty of Engineering
The University of Tokyo
Hongo 7-3-1, Bunkyo-ku, Tokyo 113, Japan

1. Introduction

The authors have developed special functions that enable highly efficient adaptive control for high precision cutting with high cutting stability[1]. The system uses multi-axis force information that can be incorporated with control results and autonomously accumulated as a data-base in the form of a stability lobe diagram. The data-base is renewed in real-time and allows the optimization of the cutting conditions, including tool path, quasi-dynamically. Conventionally, each individual machine tool has its own data-base because the stability of the system depends on the stiffness and the damping factor of the machine. However, it is more efficient if the machining parameter data-base can be shared among multiple machines. This paper discusses a common data-base renewal method which considers the effects of the differences in mechanical properties among machine tools and of tool wear.

2. Related work

Many researchers have discussed the mechanism of chatter vibration and developed physical models[2, 3, 4]. In particular, Sato, et al. are discussing the multiple regenerative effect of chatter vibration[5]. [6] and [7] discussed a monitoring method of tool wear and breakage based on acoustic emission signals. A method for machining state detection and the modification of the conditions by adjusting the tool length was presented by Smith and Tlusty[8]. Some researchers are discussing open-architecture CNC machine tools [9, 10, 11]. In particular, Altintas, et al. realized an adaptive control on a machine tool equipped with an open-architecture CNC[10]. However, in his system the machine tool is not closely connected with CAD/CAM system. In our system CAD/CAM system and the machine tool are tightly connected[1]. In the system the optimization of cutting conditions is performed by changing the data-base dynamically during cutting. This paper describes a sharing method of data-base modification strategies depending on tool wear between two different machining centers.

3. System construction

3.1 Hardware system

A machining center which is controllable from an external, real-time computer, developed by the authors' group, was used. The machining center is equipped with a 6-axis force sensor to monitor the cutting state and a fail-safe table to prevent damage to the system in the case, for example, of an over-force condition. The rigidity, the natural frequency and the rated value of the 6-axis force sensing table developed by the authors' group are approximately 500N/μm, 2kHz and 2,000N for the spindle rotation direction and 1,000N for the orthogonal directions, respectively. The real-time controller, the data-base and the CAD system are connected and integrated with eachother through a computer network.

3.2 Software system

Fig.1 shows an overview of the software system. The system consists of a CAD system, a data-base and a real-time controller. One of the features of the system is that these processes are not static, but dynamic, communicating with eachother during the cutting sequence. More concretely, the contents of the data-base are dynamically revised by being sent the actual cutting conditions and cutting state from the real-time controller. Furthermore, the three-dimensional modeller in the CAD system can be accessed dynamically during cutting. Tool path and cutting conditions are regenerated depending on the revision of data-base and are sent to the real-time controller.

3.2.1 Data-base

The data-base consists of an "experimentally obtained stability lobe diagram," a "machining efficiency evaluation task" and a "machining condition determination task." The stability lobe diagram introduced by Merritt[2] and Tlusty is

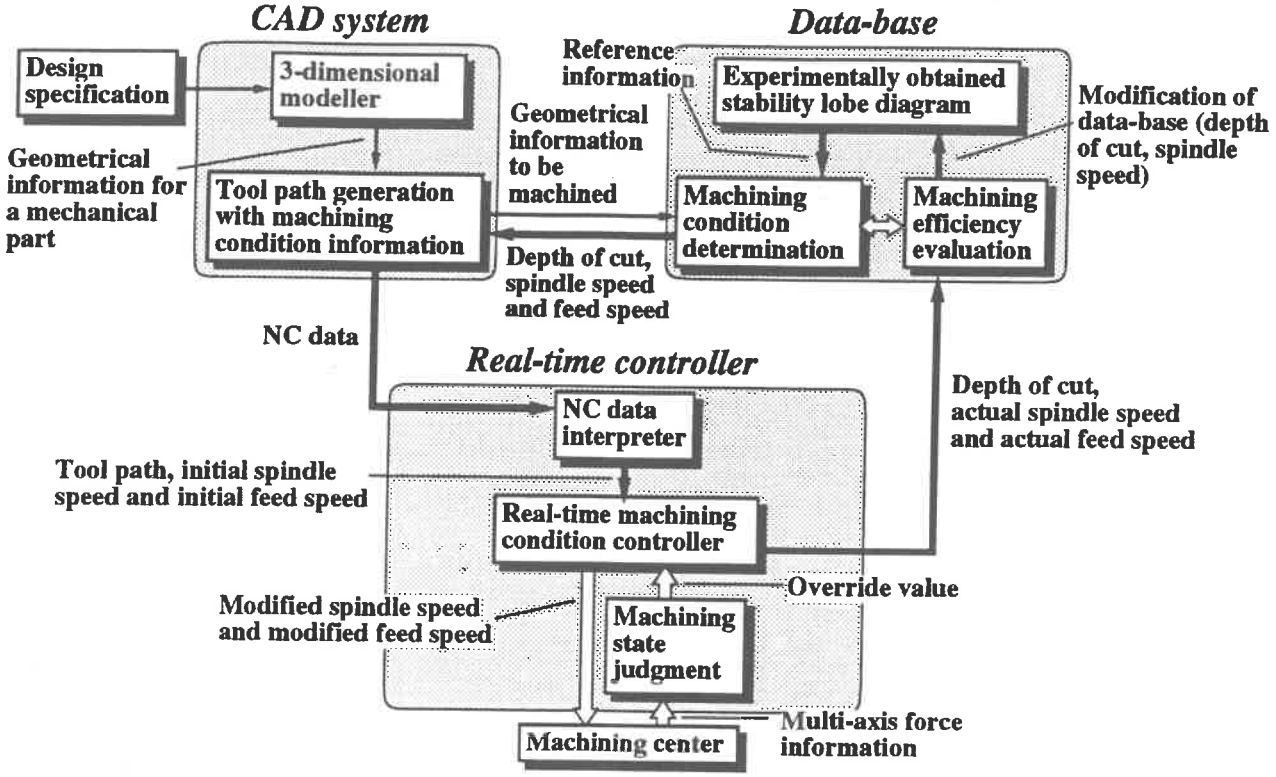
CAD system
Design specification
3-dimensional modeller
Geometrical information for a mechanical part
Tool path generation with machining condition information
Data-base
Reference information
Experimentally obtained stability lobe diagram
Modification of data-base (depth of cut, spindle speed)
Geometrical information to be machined
Machining condition determination
Machining efficiency evaluation
Depth of cut, spindle speed and feed speed
NC data
Real-time controller
NC data interpreter
Depth of cut, actual spindle speed and actual feed speed
Tool path, initial spindle speed and initial feed speed
Real-time machining condition controller
Override value
Modified spindle speed and modified feed speed
Machining state judgment
Multi-axis force information
Machining center

Fig.1 Software system configuration

experimentally obtained in the system described in this paper. Therefore, it is called an "experimentally obtained stability lobe diagram." Fig.2 shows an example of a stability lobe diagram.

The machining efficiency evaluation task and the machining condition determination task use the 3-dimensional modeller in the CAD system to determine efficient machining conditions and generate an appropriate tool path. Furthermore, the machining efficiency evaluation task modifies the stability lobe diagram as it varies during machining.

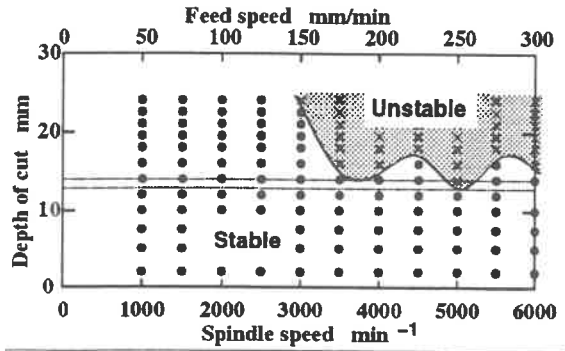

Tool : Square endmill
(helix angle = 40 deg., 2-edge, 15mm diameter)
Workpiece: Aluminum alloy, Feed per tooth: 0.025mm
Cutting type: Full immersion, Sampling rate: 5000 Hz
Coolant: wet

Fig.2 Stability lobe diagram

3.2.2 Real-time control

The "real-time machining condition controller" and the "real-time machining state judgment task" perform adaptive control by adjusting the override values for spindle speed and feed speed based on the previously determined machining conditions. Furthermore, the relationship between the machining conditions and the machining state is fed back to the data-base.

3.2.3 CAD system

In the CAD system, geometrical information for the component mechanical parts of a product is input to the 3-D modeller and the abstracted machining feature information is sent to the machining condition determination task in the data-base. The tool path generation task generates a 3-dimensional tool path appropriate to the received depth of cut and geometrical machining feature information. The most efficient set of spindle speed and depth of cut obtained from the machining condition determination task changes when the stability lobe diagram in the data-base is modified. Therefore, in the system described in this paper, the tool path generation task is invoked periodically during machining and the tool path and cutting conditions are quasi-dynamically modified to maintain maximum cutting efficiency. Typically, the tool path is regenerated after each cutting pass.

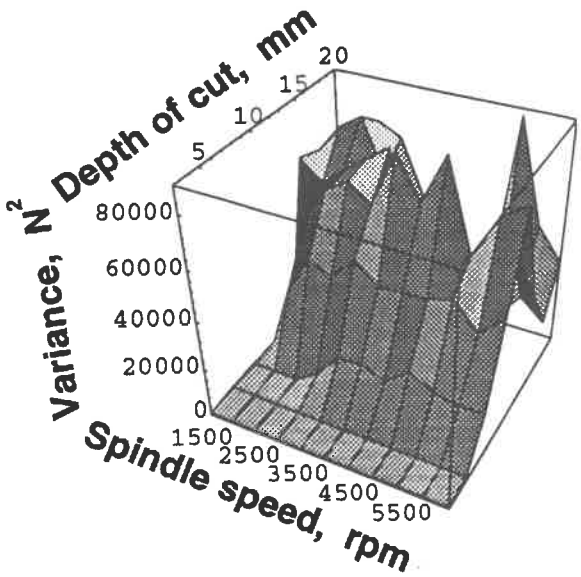

Fig.3 Variance of distance for M.C.-A (sharp tool)

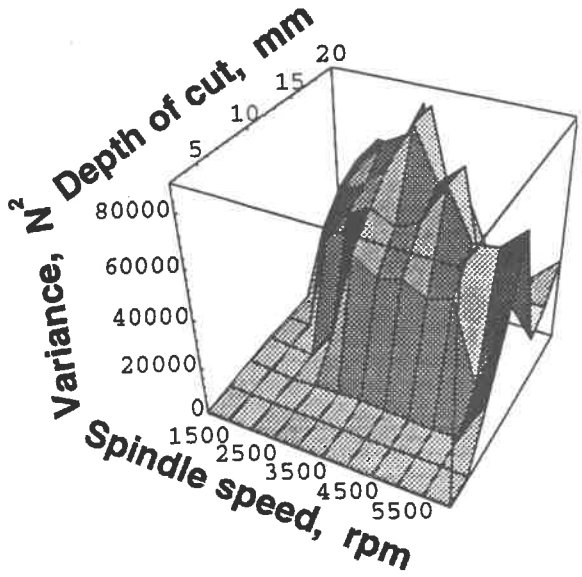

Fig.4 Variance of distance for M.C.-A (significant tool wear)

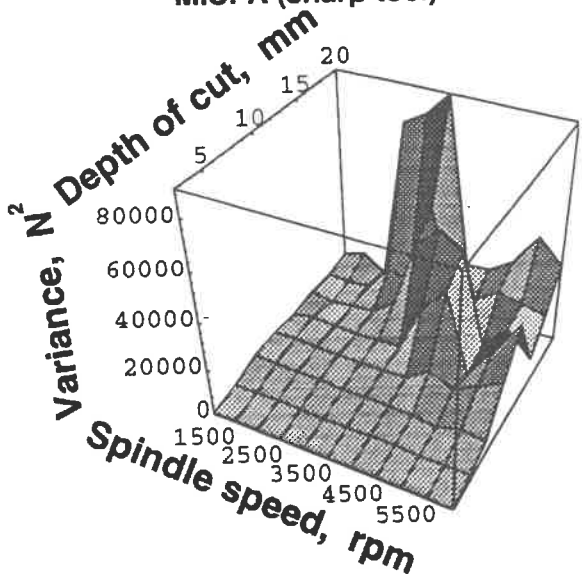

Fig.5 Variance of distance for M.C.-B (sharp tool)

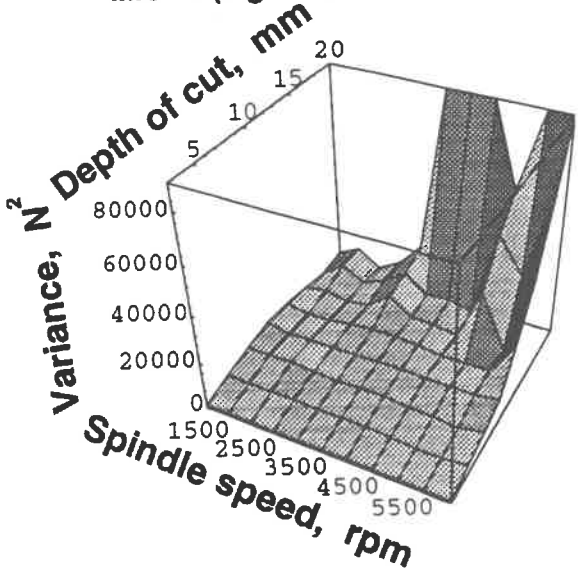

Fig.6 Variance of distance for M.C.-B (significant tool wear)

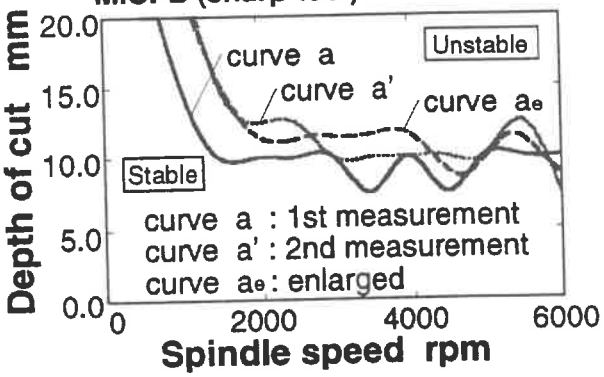

Fig.7 Modification of stability lobe diagram for M.C.-A

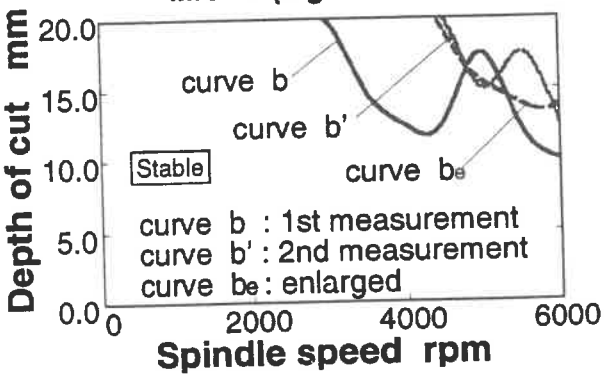

Fig.8 Modification of stability lobe diagram for M.C.-B

Table 1 Cutting conditions

Tool	square endmill (10 mm diameter, helix angle 40 deg., 2 teeth)
Workpiece	Aluminum alloy(A2017)
Feed per tooth	0.025mm/tooth
Cutting type	Full immersion
Sampling rate	5kHz
Coolant	Wet

4. Data-Base sharing

As cutting stability of a system depends on mechanical properties of machine tools such as shape of cutting tools, geometical shape of workpieces and machine tool structures. The stability lobe diagram is different for each machine tool. Therefore, it is required to obtain diagrams separately for various combinations of factors mentioned above. However, it is inefficient. One solution to solve this problem is to share database among multiple machine tools. According to [3], parameters which depend on tool wear are chip-thickness coefficient k_1 and penetration-rate coefficient K. k_1 transforms the diagram in the direction of depth of cut. Furthermore, it is known that K enlarges or shrinks the lobe in both the spindle speed and depth of cut directions. Therefore, the diagram after significant tool wear will be obtained by enlarging and shrinking the original one in the respective directions. Data-base renewal method is shared by considering that the magnification ratio presents the amount of the tool wear.

5. Experiment

Sharing of data-base renewal method between two machine tools was tried in the experiment. At first, the transition of stability lobe diagram caused by tool wear was measured on one machine tool. The tendency of lobe changes was used to estimate the other machine's lobe change after significant tool wear.

Fig.3 and Fig.4 were obained on machine tool A. Cutting conditions in the experiments are shown in Table1. The bases of the figures are composed of spindle speed and axial depth of cut, and the vertical axis represents a variance of distance in force vector locus which indicates the machining state. The cutting state is stable if variance of distance is small. Fig.3 and Fig.4 were obtained with a sharp tool and the same tool after significant tool wear, respectively. Fig.5 and Fig.6 show experimental results on machine tool B with the same condition as Fig.3 and Fig.4 . Fig.7 shows the cross sections of Fig.3 and Fig.4 at the hight of $20{,}000N^2$. Curve a_e was selected so as to minimize the area enclosed by curve a' and a curve obtained by magnifying curve a. In this experiment, the magnification ratio were 1.35 and 1.15 in the directions of spindle speed and axial depth of cut, respectively. Curve b and curve b' in Fig.8 are the stable-unstable boundaries in the cross sections of Fig.5 and Fig.6 at the hight of $20{,}000N^2$. Curve b_e was obtained by magnifying curve b at the same ratio as the case of Fig.7. Curve b_e can be regarded as the prediction of curve b. As is shown in Fig.7, stability lobe is well predicted. In particular, in the range of lower than 5,120 rpm, the predictedcurve fits exactly to the measured one.

6. Conclusions

The authors proposed a method for sharing machining data-bases among different machining centers whose rigidities and damping factors are different from one another. In the experiment, the proposed method was applied for the effect of tool wear. The experimental result shows the effectiveness of the proposed method.

References

[1] Mitsuishi,M., et al., "A Practical Machining Condition Determination Strategy Using Multi-Axis Force Information," *Annals of the CIRP*, 45/1, pp.373–376, 1996.

[2] Merritt,H.E., "Theory of Self-Excited Machine Tool Chatter," *ASME J. Eng. for Industry*, pp.447-454, Nov. 1965.

[3] Tobias,S.A., "Schwingungen an Werkzeugmaschinen," *Carl Hanser Verlag*, München, 1961.

[4] Minis,L., et al., "Analysis of Linear and Nonlinear Chatter in Milling," *Annals of the CIRP*, 39/1, pp.459-462, 1990.

[5] Kondo,Y., Kawano,O. and Sato,H., "Behavior of Self-Excited Chatter due to Multiple Regenerative Effect," *ASME, J. Eng. for Industry*, 103, 3, pp.324–329, Aug. 1981.

[6] Moriwaki,T., et al., "Application of Neural Network to AE Signal Processing for Automatic Detection of Cutting Tool Life," *Journal of JSPE*, vol.57, no.7, pp.1259-1264, 1991.

[7] Dornfeld,D.A. and Liu,J.J.B., "Abrasive Texturing and Burnishing Process Monitoring Using Acoustic Emission," *Annals of the CIRP*, 42/1, pp.397-400, 1993.

[8] Tlusty,J., et al., "Techniques for the Use of Long Slender End Mills in High-speed Milling," *Annals of the CIRP*, 45/1, pp.393–396, 1996.

[9] Pritschow,G., et al., "Open System Controllers – A Challenge for the Future of the Machine Tool Industry," *Annals of the CIRP*, 42/1, pp.449–452, 1993.

[10] Altintas,Y., et al., "A Hierarchical Open-Architecture CNC System for Machine Tools," *Annals of the CIRP*, 43/1, pp.349–354, 1994.

[11] Koren,Y., et al., "Real-Time Open Control Architectures and System Performance," *Annals of the CIRP*, 45/1, pp.377–380, 1996.

REVIEW OF DEVELOPMENTS IN SENSORS FOR UNTENDED MACHINING

A. Chukwujekwu Okafor and Anietie Ukpong
Laboratory for Industrial Automation and Flexible Manufacturing
Department of Mechanical and Aerospace Engineering and Engineering Mechanics
University of Missouri-Rolla
Rolla, MO 65409-0050

ABSTRACT

Traditional manual quality control based on detection after the facts — a post mortem process — are no longer adequate in the wake of increasing demand on manufacturing productivity forced by domestic and global competition. Costly and abrupt failures resulting from undetected tool wear, collision or breakage should be a thing of the past and moreover, the pressure of cost is increasingly forcing the service life of manufacturing equipment to be fully utilized, and tools are not to be changed or reground prematurely simply on the basis of experience or for safety reasons. Since the early 80s, when a comprehensive review of manufacturing sensors for unmanned machining was carried out by J. Tlusty and G. C. Andrews, numerous developments in sensors for unmanned machining have taken place. This review highlights these developments – past and present. The review appraises sensors for machining monitoring on the basis of specification and characteristics, reliability, precision, signal processing, speed and limitations. The extent to which these sensors are effective individually or in combination as a machining monitoring system are discussed.

1. INTRODUCTION

It has been established, that in order to increase the productivity of computer numerical control (CNC) machines, untended or minimally supervised operating conditions are desirable [1]. The emergence of unmanned machining centers and problems associated with adaptive control or untended machining in an operator's absence has continued to require attention. An untended machining situation thus warrants that operations provide for artificial intelligence necessary to mimic the qualitative judgement of operators and their instinctive reactions and, provide the expertise normally associted with human involvement. There have been numerous reviews on machining sensors and machine tool monitoring systems [1-3]. There has been however, a passive attitude towards the integration or incorporation of these technologies into our manufacturing endeavours, such that we are still currently faced with a situation of *backlog of unapplied technologies.* Moreover, there is still the reluctance of machine tool builders for changes in machine tool design configurations to incorporate the various "eyes" and "fingers" called sensors requisite for untended manufacturing. The review of these sensors are given in the following sections.

2.0 Types of commercially available sensors for untended machining

All the prerequisites for untended machining calls for operations such as automatic parts loading and unloading, in-process part gauging, adaptive control, monitoring for tool wear, collision, and breakage detection. Direct measurement techniques have been established to pose many problems for automation. Efforts therefore are directed toward indirect measurements of process variables that are closely correlated with tool and machining conditions.

2.1 Touch trigger probes

This device is used for workpiece monitoring and the information which is provided may be used to update tool offsets critical in an untended machining environment. First patented by Renishaw , the system consists of a very sensitive omnidirectional switch made up of a probe body and a stylus capable of detecting deflections in any direction. The probe body is available in two styles enabling machining center spindle-mounting and, machine tool table mounting for milling and drilling (figure 1.) For turning centers, the probe is mounted on the turret and programmed to confirm that the correct workpiece is loaded. Using results of probing and conditional part programming,

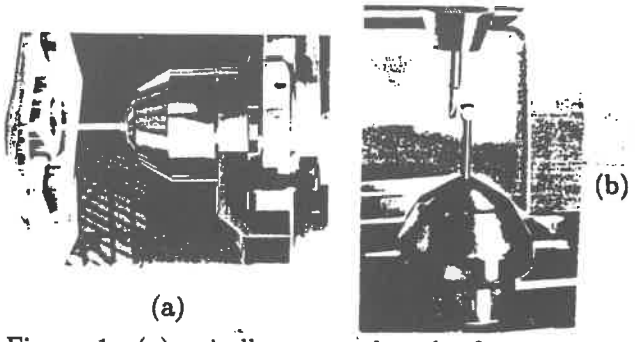

Figure 1: (a) spindle-mounted probe for machining center (b) tool-table mounted probe for drilling and milling

various workpieces can be accommodated, identified, and defined. Typical operations for CNC machine tools equiped with touch-trigger probes are stated to include: tool setting, initial job set-up, and sensing of tool wear and breakage. The probe can be used for nearly all tasks demanded for unmanned machining, however, the question of cost and efficiency, response time , and memory becomes critical and limits them to certain metal cutting operations [2].

2.2 Cutting force and torque sensors

There are many ways of measuring and infering cutting forces. However, most of the techniques are still limited to laboratories or their implementations are ad hoc. Commercially developed systems for unmanned machining over the years have tended to be force/torque - based or acoustic emission - based. Ways of measuring or infering cutting forces or torques for unmanned machining include:

- tool- holder and table-type dynamometer
- rotating cutting force dynamometer
- dynamometer built into spindle bearings
- 3-component piezoelectric measuring pin
- piezoelectric strain transducers
- force measuring bushings and bearings
- infering cutting force from spindle torque, electric current and power consumption of the main or feed spindle motors.

2.2.1 Dynamometers

Recent developments in piezoelectricity have produced numerous sensors with potential for use in tool monitoring. Kistler and Montronix are among the industrial leaders utilizing this technology in the development of a wide range of sensors by exploiting the piezoelectric effects that can be activated in quartz crystals.

(a) Tool holder dynamometers

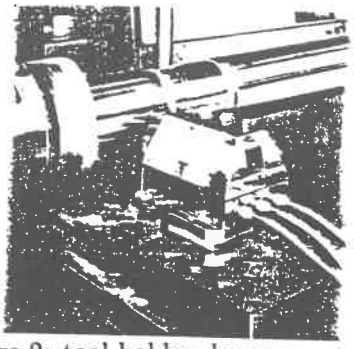

Figure 2: tool holder dynamometer

Figure 2 shows a tool holder dynamometer for typical force measurement with a 3-component dynamometer. As observed [2], these types of sensors are suitable for several tasks because of high sensitivity and high natural frequency, but they can not be used in turning centers with turret heads. Furthermore, being a specific laboratory tool, its bandwidth is still not large enough for high frequency force variation due to chip formation especially during high speed cutting. Other tool holder dynamometer based on strain gauge with small ring sensing element have been developed by WZL Aachen [2].

(b) Three component measuring pin

To circumvent problems associated with inadaptability of tool holder dynamometers for turret lathes, Kistler and Montronix have introduced a new 3-component measuring pin. It consists of a piezoelectric 3-component force measuring cell, and a double preloading wedge, figure 3 [5], enabling indirect measurement of three-force components orthogonal to each other. In principle, a three-component measuring pin of this kind measures the deformation caused in machine parts by external forces and torques. A typical Kistler's 9117A measuring cell is also shown in figure 3. The basic requirement for using this sensor is to ensure that the transducer is installed in the load path of the machine tool and in as close proximity as possible to the point of cut.

(c) Table - type dynamometers

Most of these are available as a measuring platform, which have an advantage that they permit a larger freedom of point of load application than would a single transducer [4]. Measuring platform 9257A for a 3-component force transducer from Kistler is shown in figure 4. On lathes, the platform is mounted on the slide and the tool is bolted onto the platform, whereas on milling machines, the workpiece is bolted onto the platform which is then afixed onto the machine table. It is conceivable that table - type dynamometers will

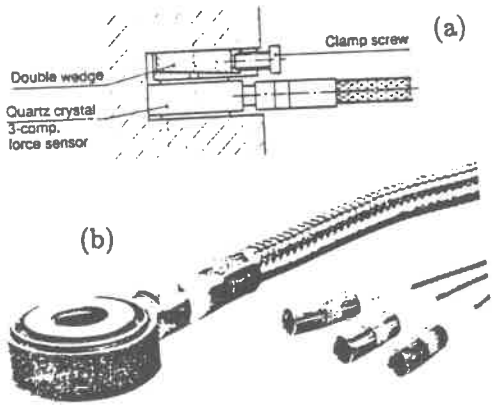

Figure 3: (a) measuring cell with preloading wedge, (b) Kistler's 9117A

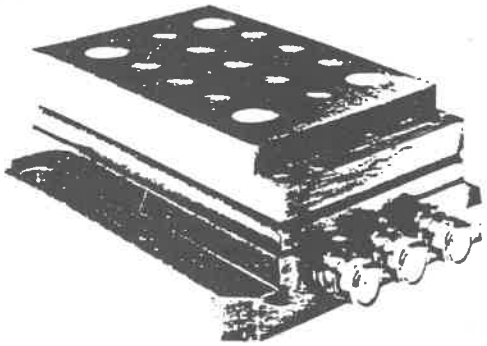

Figure 4: Kistler's 9257A measuring platform

be used for adaptive control in milling and for providing signals for tool wear and breakage detection simultaneously. However, for chatter research and testing of machining centers, special wide frequency band dynamometers are needed [2].

(d) Rotating cutting force dynamometers

The new rotating cutting force dynamometer (RCD) introduced by Kistler has the capability of measuring forces and moments on the rotating cutting edge , figure 5. Its high rigidity and compact design makes it adaptable to all machine tools and a large assortment of tools. The forces occuring (Fx, Fy, Fz) and moment (Mz) are measured with a piezoelectric sensor, featuring high rigidity, wide measuring range, and a minimum response threshold [6]. The measuring system has a facility for amplifying and transmitting the signal to a stationary receiver using pulse modulated telemetry. In milling, the RCD can be used for both exact precision and coarse processes by simply switching over measuring ranges. A force measuring system to determine tool-related cutting forces in 5-axis milling is shown in figure 6 [7]. The flange design of the tool holder enables tools most frequently used to be accommodated.

(e) Dynamometers built into spindle bearings

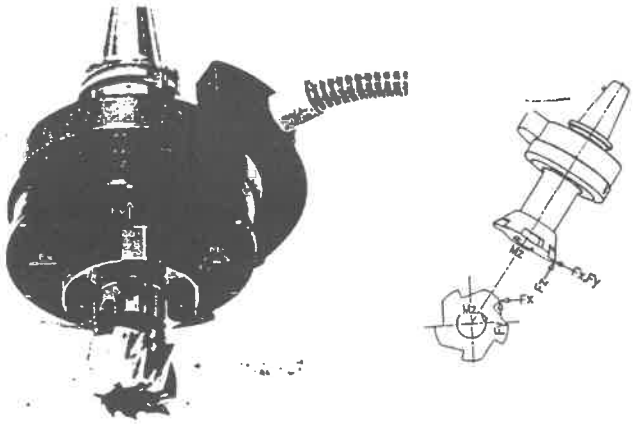

Figure 5: RCD and RCD coordinate system

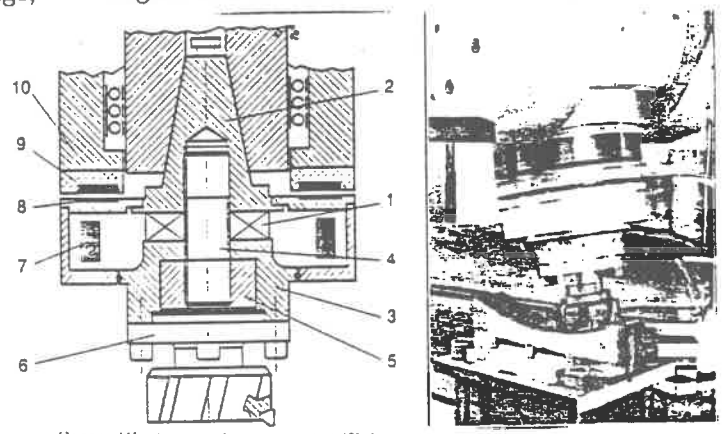

Sensor (1), steep angle taper socket (2), base ring (3), preloading bolt (4), ring nut (5), tool holder (6), charge amplifier (7), rotating antenna (8), fixed antenna (9), two-axis milling head (10)

Figure 6: RCD system for 5-axis milling

The first break through by PROMESS was to have spindle bearings communicate load information [8]. As shown in figure 7, when a roller bearing (tapered or ball) is loaded, load proportional strains are taken up by both inner and outer races of the bearing, leaving a major portion of the forces being transmitted in the hertz area. As load varies, this AC signal varies as a result of deformation variation to produce amplitude modulation, definable as axial or radial forces by strategic placement of the sensors. It is this change in amplitude that measures the forces. A major drawback of force measuring bearing, is the need to eliminate rolling noise frequencies by using a low pass filter, which consequently makes it impossible to detect rapid signal changes [3]. Further innovations for the measurement of fast signals include force-measuring bushings figure 7, and the fact that they require changes in the design of bearing arrangement make retrofitting almost always impossible. A major application area however, is in the axial force measurement on drilling machines. The cross-section of a typical assembly of the Z-axis feed force sensor built into spindle bearing to measure thrust force

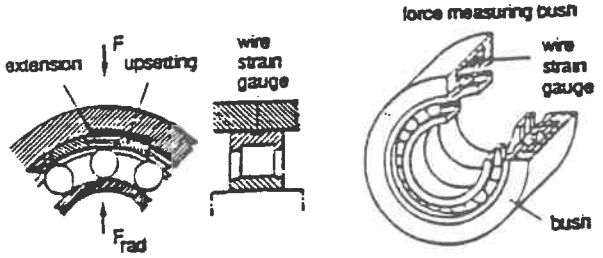

Figure 7: dynamometer built into spindle bearings and force measuring bushing

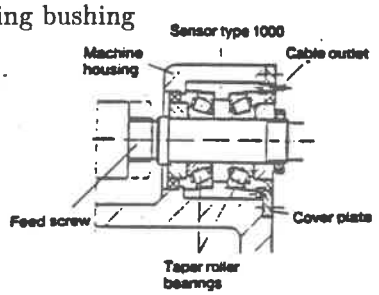

Figure 8: Z-axis feed force sensor

from Sandvik is shown in figure 8. This sensor can be used for the mounting of thrust bearings of a lead screw to monitor feed forces and to detect drill wear or any other effect which alters feed force, such as deterioration of the guideways [2]. The sensors are available in sizes from 25mm to 350mm and from 2 kN to 100 kN force ranges. Their compact design for machine tools ensures easier installation.

2.2.2 Infering cutting force from spindle torque, electric current and power consumption of the main or feed spindle motors

These indirect ways of measuring cutting forces and torques have been used in the development of many commercial applications, including the well documented Cincinatti Milacron's torque control monitor (TCM) [2,9]. It is easy to measure the motor current and voltage and thus evaluate the power being used and, by sensing the motor speed with current and voltage, it is possible to evaluate torque. Hence, with the diameter of the workpiece during turning or of the cutter in milling, the tangential component of the cutting force can be determined [2]. The problem with this approach is that the power required to overcome friction in the guideways usually far exceeds that needed for machining and the output signal usually has a low pass filtering characteristic due to inert masses. Moreover, tool wear monitoring is often difficult as spindle power is proportional to the resulting cutting force in the direction of primary motion, the least tool wear sensitive parameter. Despite these problems, such devices and techniques are employed commercially to detect tool collision, breakage, and wear if adequately large cross-sectional areas of cut are used [2].

2.3 Acoustic emission sensors

During metal cutting operations, acoustic emission (AE) results from the plastomechanical processes of crack formation, growth , chip removal, and from surface friction in the cut zone [3]. The exploitation of the AE signal for tool wear and breakage detection research is intensive [11]. Because of the propagation of waves through the whole machine structure, the point of attachment of an AE sensor is not very critical. However, multiple joints between the cutting position and the AE sensor result in increased attenuation of the AE signal on the order of 10db per interface, thus the sensor must be located as close as possible to cutting action [3]. Several AE sensors have been developed (figure 9). Digital Wave Corp. has introduced a new AE analysis technique based on waveform analysis using broadband transducer to capture wide range of frequencies within a given wave. The technique has unique merits over conventional AE analysis technique using resonant sensors [18].

A Piezotron AE sensor developed by Kistler, figure 10, has a built-in impedance converter for measuring AE above 50 KHz in machine structures. With its small size, it mounts easily near the source of emission and optimally captures the signal [12]. The power spectra of AE signal during normal cutting and at fracture is shown in figure 11 and it is obvious that the tool fracture signal releases high-powered oscillations in frequency range 300 KHz to 1 MHz, and it is distinguished from normal cutting bursts if passed through a high-pass filter with 300 KHz corner frequency. All other low frequency signals, such as those due to audible noise and mechanical vibrations would be filtered out at the same time. This is the basis of tool breakage detection by AE [2].

2.4 Dual-mode force/AE sensor

Recently, Kistler has introduced a dual-mode sensor that permits the simultaneous measurement of AE signals and one to three orthogonal forces, figure 12 [10]. Integrated in the middle of a force measuring ring, is an AE sensor with same properties as those of a Piezotron. The cutting force and AE signal recorded simultaneously during external diameter lathing is shown in figure 13. A dual-mode sensor was mounted under the turret housing and tool tip breakage signal with that recorded during turning over a hole are shown. The signals change due to interrupted cuts are easily recognized in the force signal

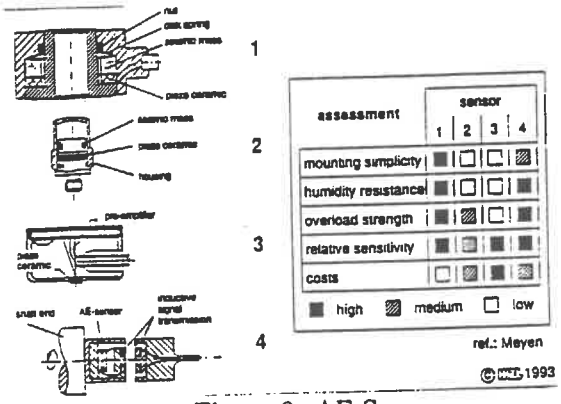

Figure 9: AE Sensors

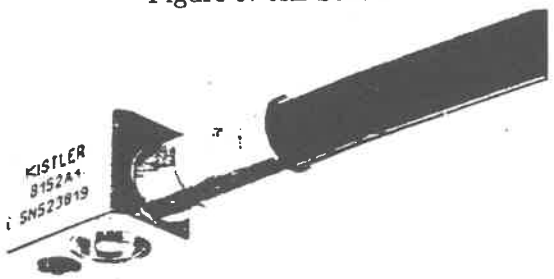

Figure 10: Kistler's Piezotron AE sensor

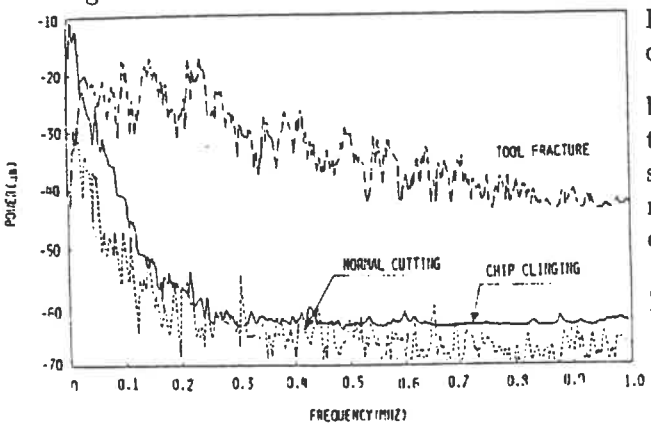

Figure 11: power spectra of AE signal

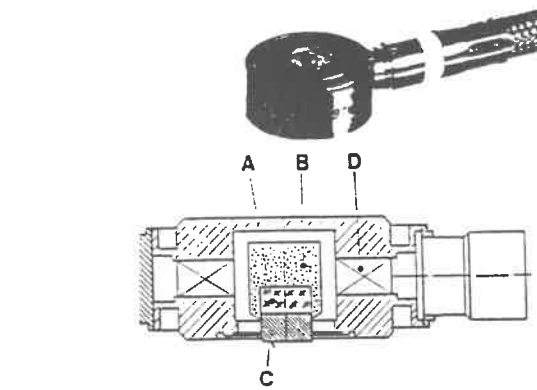

Dual-mode sensor. A is the piezoelectric element of the AE sensor C is the diaphragm, and D represents the quartz force sensor element B is the backing.

Figure 12: dual-mode AE sensor

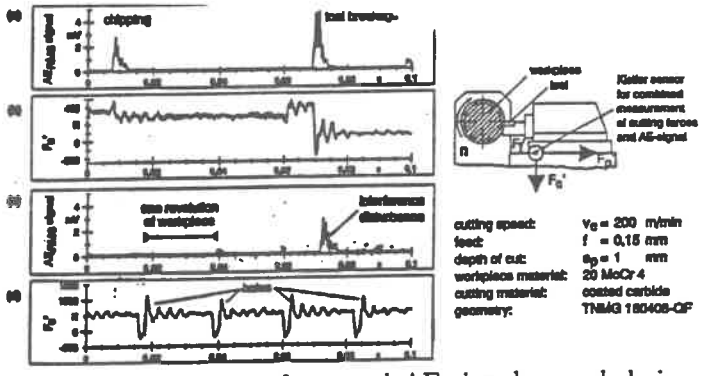

Figure 13: cutting force and AE signal recorded simultaneously

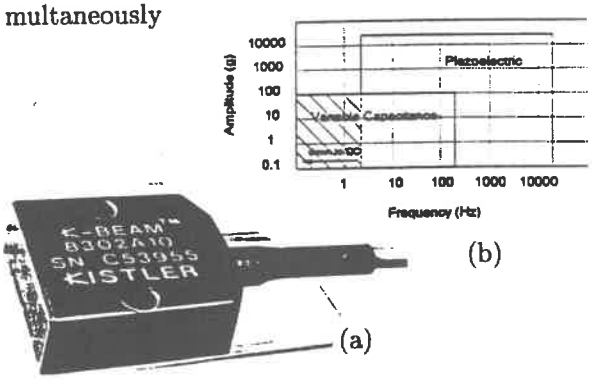

Figure 14: (a) K-BEAM variable capacitance accelerometer (b) Dynamic range comparison

but not in the AE. However, the pronounced peak in the AE signal caused by an interference is also not shown in the force signal. This example shows how multi-sensor signals allows a more reliable detection of the actual process disturbance – tool breakage.

2.5 Accelerometers

Kistler has recently introduced the K-BEAM silicon micromachined capacitive accelerometer for measuring low frequency, low level acceleration to zero Hertz. Figure 14 shows the variable capacitance accelerometer along with its dynamic range comparison with a piezo-electric type. They are available in +/- 2g, +/- 10g and +/- 20g ranges with high signal-to-noise ratio. Both types have unique merits [17].

3.0 SUMMARY

Many sensors and techniques have been studied and developed for tool wear or failure detection over the years. Most of these sensors and techniques can not by themselves suffice to provide the much needed unmanned machining and adaptive control edge. Different sensors are often sensitive to different process changes [14]. For instance, AE is less sensitive to cutting conditions such as depth of cut and feed, while force is less sensitive at reduced chip cross-sectional

area [3]. Hence the need for multiple sensors to take advantage of differing sensitivities of sensors to increase the range of applicability of sensing system. Pioneering efforts in this direction are well established [13-15]. Open issues must include not only the development of new sensors, but also the ability to use existing sensors in better ways to effectively understand the physics of chip formation [16] and tool conditions. We must also be able to combine outputs from such sensors into software architectures that more closely model the human machinist's ability to decide what to do next given the current state of the manufacturing process – A motivation for neuro-fuzzy tool monitoring systems.

4.0 ACKNOWLEDEMENT

The financial support of this work by the National Science Foundation, NSF grant No. GER-9355127 is gratefully acknowledged.

5.0 REFERENCES

1. Smith, Graham T., Advanced Machining – The Handbook of Cutting Technology, IFS Pub., pp. 80-107, 1989.

2. Tlusty, J. and Andrews, G. C., "A Critical Review of Sensors for Unmanned Machining", *Annals of the CIRP*, Vol. 32, pp. 563-572, 1983.

3. Dornfeld, D. A., Konig, W. and Ketteler, G., "Current State of Tool and Process Monitoring in Cutting, New Developments in Cutting Technology," *Proc. of CIRP/VDI Conf.*, Dusseldorf, Vol. 998, pp. 363-376, 1993.

4. Gautschi, G. H., "Cutting Forces in Machining and Their Routine Measurement with Multi-Component Piezo-electric Force Transducers," *Proc. of the 12th Int. Mach. Tool Design and Research Conf.*, Manchester, England, pp. 113-120, Sept. 1971.

5. Cavalloni, C., Engeler, P. and Schaffner, G., "Strain Measurement Inside Structures with Piezoelectric Sensors," *Sensors and Sensor Systems*, Expert Verlag, D-7044, Ehningen/Germany, pp. 132-143.

6. Cselle, T. and Stirnimann, J., "Cutting Force Measurements on Rotating Tools," Translated Paper, Carl Hanser Verlag, Munchen, 1993.

7. Spur, G., Al-Badrawy, S. J. and Stirnimann, J., "Measuring the Cutting Force in Five-Axis Milling," Translated paper, Carl Hanser, Munchen, Courtesy of Kistler Piezo-instrumentation, Sept. 1993.

8. Stockline, Larry E., "Tool and Machine monitoring Systems," *4th Biennial Int. Mach. Tool Tech. Conf.*, Vol. 10, pp. 158-165, Sept. 1988.

9. Burgam, P. M., "Two Tools for the Eighties: Machining Centers and Adaptive Control," *Manufacturing Engineering*, pp. 56-60, May 1984.

10. Claudio, Cavalloni and Kirchheim, Andreas, "New Acoustic Emission Sensors for In-Process Monitoring," *Presented at the 12th. Int. Acoustic Emission Symposium*, Sapporo, Japan, Oct. 17-20, 1994.

11. Dornfeld, D., "Acoustic Emission and Metal-Working Survey of Potential and Examples of Applications," *Proc. of the 8th NAMRC*, University of Missouri, Rolla, May 18-21, Dearborn, Michigan, pp. 207-213, 1980.

12. Kistler Instrument Corporation, "Piezotron," In-House Print, 1994.

13. Dornfeld, D. A., "Neural Network Sensor Fusion for Tool Condition Monitoring," *Annals of the CIRP*, Vol. 39, pp. 101-270, 1990.

14. Okafor, A. C., Marcus, M. and Tirpirneni, R., "Multiple Sensor Integration Via Neural Network for Estimating Surface Roughness and Bore Tolerance in Circular End Milling - Part 1: Time Domain," *Condition Monitoring and Diagnostic Tech. Journal*, Vol. 2, No. 2, pp. 49-57, 1991.

15. Mesina, O. S. and Langari, Reza, "A Neuro-Fuzzy System for Tool Condition Monitoring in Metal Cutting," *ASME Dynamic Systems and Control*, Vol. 2, pp. 931-938, 1994.

16. Wright, P. K. and Bourne, D. A., Manufacturing Intelligence, Addison-Weseley Pub. Co. Inc., 1988.

17. Berther, T., Kubler, J. M. and Cuhat, D., "A Lightweight Capacitive Accelerometer for Low Frequency Measurement," Kistler Piezo-Instrumentation, In-House Print, 1994.

18. Okafor, A. C., Chandrashekhara, k. and Jiang, Y. P., "Location of Impact in Composite Plates Using Waveform-based Acoustic Emission and Gaussian Cross-correlation Techniques," in *Smart Structures and Materials 1996: Smart Sensing, Processing and Instrumentation,*, Kent A. Murphy, Dryver, R. Huston, Eds., Proc. SPIE 2718, pp. 291-302.

Integrated Electrodynamic Multicoordinate Drives - Modern Components for Intelligent Motions

Dipl.-Ing. Chr. Schäffel; Dipl.-Ing. E. Saffert; Univ.-Prof.Dr.-Ing. habil. E. Kallenbach;
Technical University of Ilmenau, Faculty of Mechanical Engineering, Germany
e-mail: christoph.schaeffel@maschinenbau.tu-ilmenau.de

ABSTRACT

In the next decades the machine precision will permanently increase in both standard and precision as well as ultra-precision machines combined with an improvement in the dynamics. Most machines in high-technology areas require new drives for motion in several coordinates with positioning accuracy in the sub-micron area and fast dynamics. The paper presents a multi-coordinate drive developed at the Institute of Microsystems Technology, Mechatronics and Mechanics and illustrates the advantages of its new structure compared to conventional drive principles.

1 INTRODUCTION

In recent years many products appeared on the world market which have completely new properties and system parameters compared to traditional products. They are a result of the integration of electromechanics, microelectronics, hard- and software as well as optics.
Already in the early 70's the Japanese Ministry of Trade and Industry introduced the term "MECHATRONICS" for this particular field as a connection of *mechanics and electronics.* The multi-coordinate drive described below presents a typical mechatronic product.

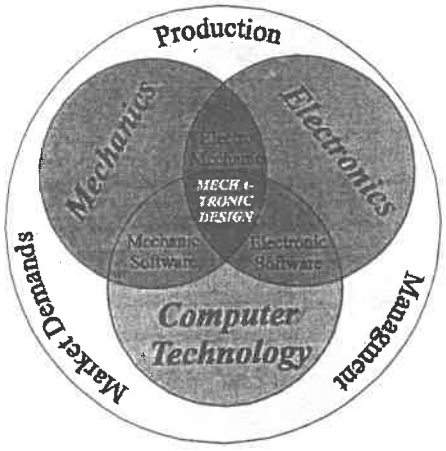

Fig. 1 Component integration of mechatronic Systems

2 STRUCTURES OF MULTI-COORDINATE DRIVE SYSTEMS

In most cases today's x-y-positioning systems generally consist of two serially coupled axes according to pick aback principle. The linear axes are usually fitted with a rotary motor (DC-servo motor, stepping motor) and a motion transmitter for generating the linear motion . In doing so (Fig. 2) the y-axis has to be carried by the x-axis. Beside the hiking loads created thereby the features of these multi-coordinate drives are determined by the clearance, the mechanical hysteresis and the elasticity of the essential motion transmitters.
These drives are limited in their positioning accuracy and speed not only because of the limited speed of motor spindle arrangements but also because of the high mass of coupling and guiding elements between the single axes.
The replacement of the motor-spindle arrangements by linear axes, however, gives only a small improvement. Substantial improvements can be obtained when the principle of functional integration in the area of mechanics and the principle of functional separation in the area of the automatic control is applied to the actuators of these so called multi-coordinate drives. The combination of

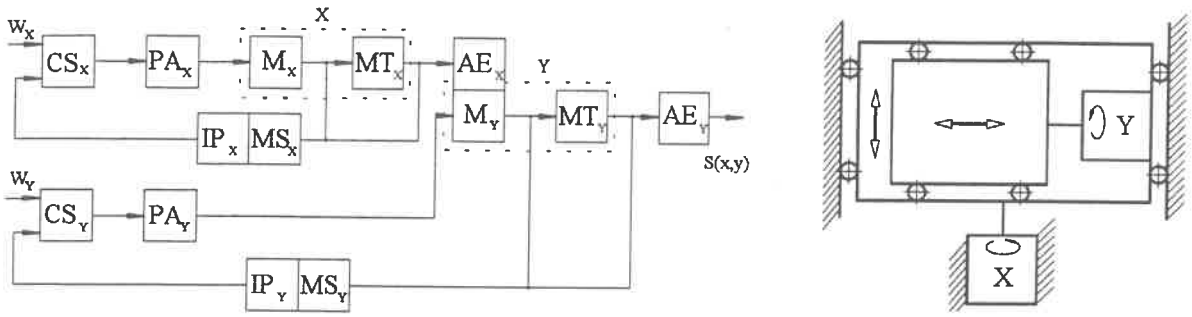

Fig. 2 Functional structure of multi-coordinate x-y-drives with serial arrangement of axes
CS control system, PA power amplifier, M motor, MT motion transmitter, AE acting element
MS measuring system, IP information processing

several single axis into *one integrated module* with a DOF of F>2 eliminates the disadvantages of conventional systems mentioned above. Functional structure and symbolic description of such a drive is shown in Fig. 3.

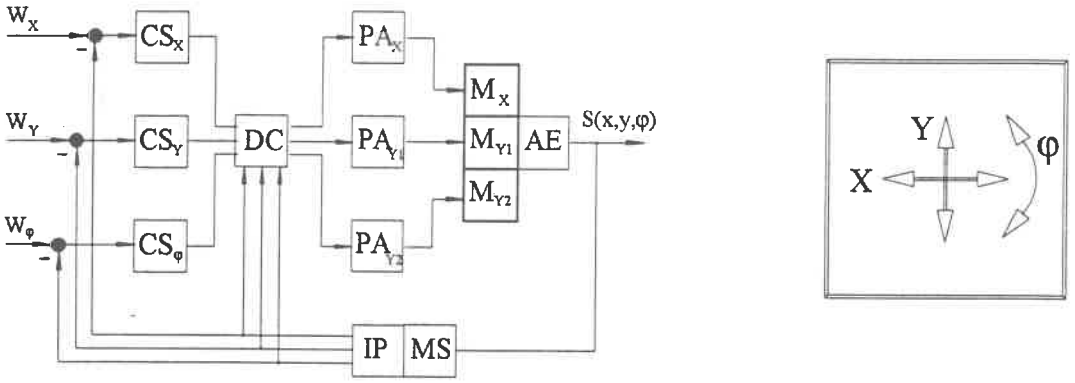

Fig. 3 Functional structure of multi-coordinate drives with integrated arrangement of axes
CS control system, PA power amplifier, M motor, MT motion transmitter, AE acting element
MS measuring system, IP information processing, DC decoupling controller

3 MEASURING SYSTEM

Integrated multi-coordinate drives can acquire extraordinary properties when if any mechanical rotary lock against the rotation of the actuator around the z-axis can be avoided. In this case the positioning accuracy in x-y-direction depends only on the quality of the measuring system applied. One possibility to eliminate the mechanical rotary lock is the guidance of the actuator in φ-direction also with electromagnetic forces. Then the drive has to be able to generate forces not only in the linear coordinates but also a torque around the vertical axis z (x-y-Δφ-motor). Furthermore a multi-coordinate measuring system has to be implemented which detects besides the linear

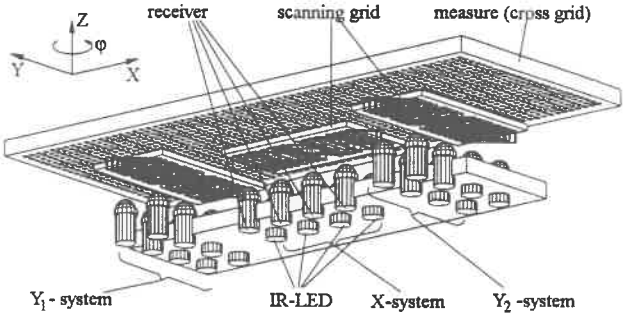

Fig. 4 x-y-Δφ-measuring system

coordinates (x, y) also the rotation of the actuator around the z-axis to a certain degree. The measuring systems for the linear coordinates (x, y), however, have to be insensitive to that rotation up to a certain degree. Fig. 4 shows a schematic representation of a suitable photoelectric x-y-Δφ-measuring system. It works according to the incident light technique. A cross grid serves as measure with a grid constant of g=40μm. The scanning plate carries groups of line grids, 4 for the x- and twice 4 for the y-coordinate. These line groups have the same grid constant and are shifted by g/4 each, similar to conventional linear incremental measuring systems.

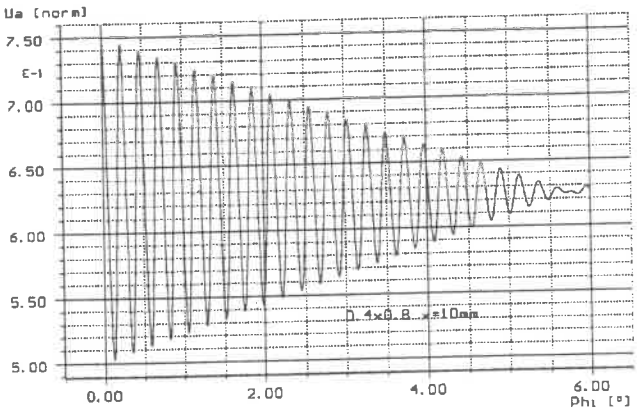

Fig. 5 Signal characteristic as function of angle φ

In general such measuring systems especially those having small grid constants are highly sensitive to the relative twist of the cross grid and the scanning grid. However, by modifying the size of the scanning window and changing the dimensions of the optical system, this sensitivity can be reduced considerably, and the actuator can turn up to several degrees. Fig. 5 shows the decrease of the amplitude of the primary signals from the measuring system as a function of the relative twist angle of the scanning grid.

The decreasing amplitude of the signals from the measuring system has to be compensated by a special interpolation method. At the same time, a correction of the dc level, the phase shift and the error caused by the harmonics of the primary signals can be achieved with software to a certain degree.

4 EXAMPLES FOR POSSIBLE MECHANICAL STRUCTURES

On principle there are two possibilities for the construction of a multi-coordinate electrodynamic drive - moving coils or moving magnets.

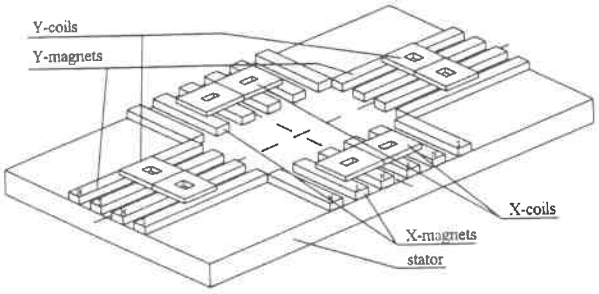

Fig. 6 Drive with moving coils

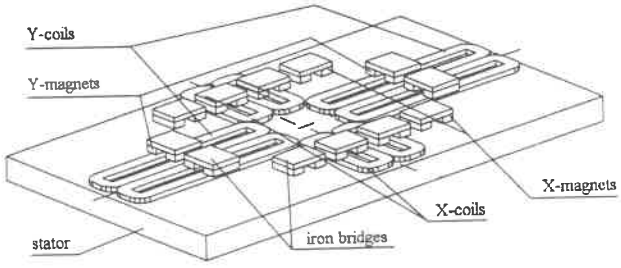

Fig. 7 Drive with moving magnets

Fig. 6 shows an integrated x-y-Δφ direct drive with moving coils. On a stator plate of iron flat permanent magnets are symmetrically arranged for both coordinates. The actuator carries a number of flat copper coils. The iron yokes which close the permanently excited magnetic circuits are not shown in the figure. Opposite coils generate the driving force (Lorentz force) along one coordinate. They are commutated according to the relative position of actuator and stator. In general

it will be advantageous for a highly dynamic drive to put the driving elements (coils or magnets) with the lower mass in the actuator. In case of moved coils this means short coils and long magnets. Fig. 7 shows the other way of generating an x-y-$\Delta\varphi$-motion with electrodynamic forces. On a stator plate pairs of long and flat copper coils are symmetrically arranged for each coordinate. 'Flying' magnets fixed in the actuator and closed to short circuits by iron yokes form the moving element. The guidance of the actuator in z-direction is favourably realised with air-bearings or magnetic levitation elements. Both demonstrated mechanical structures imply a number of advantages and disadvantages. Advantages of the second structure are

- a magnetic attraction between stator and actuator which permits an overhead operation of the drive and pre-loads the air bearings,
- a relatively small volume of the magnetic material needed,
- relatively light iron bridges and short magnetic flux ways,
- no disturbing forces on the actuator due to trailing cables for energy supply, and
- free accessibility of the actuator.

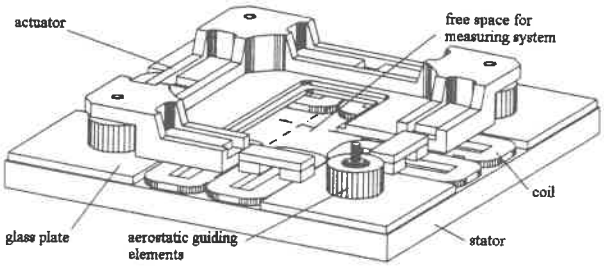

Fig. 8 CAD picture of realized drive

In order to create light actuators, a multiple array of driving elements for each coordinate is advisable. By doing so the moved iron volume for closing the magnetic circuits can be reduced to a minimum. By having a current flow through the opposite coils of one coordinate in different direction a torque can be generated, and the position of the actuator can be controlled to be $\Delta\varphi=0$.

Fig. 8 shows a newly designed drive system. Its structure corresponds to the system represented in Fig. 7. The actuator is guided on 4 air-bearings in the x-y-plane. The drive does not have any mechanical elements preventing the armature rotation around the z-axis.

The major advantage of this is, however, that the guidance system does not affect the accuracy of the three controlled axes anymore. The stage is guided electronically in those axes by the control system with the full accuracy of the measuring system. The mechanical guidance system takes only care of the so far uncontrolled z-axis and prevents rotation around the x- and y-axes.

The realised range of motion is 104x104mm^2. In the beginning of 1997 a drive with 208x208mm^2 will be available. In the centre of the actuator there is free space for mounting the measure of the measuring system. The scanning system (Fig. 4) is integrated in the stator.

5 Control of the drive

5.1 Control Hardware

The control of such a complex system requires a powerful hardware. Though control algorithms are inherently sequential the data acquisition and interpolation for the measuring system can be performed in parallel. Therefore, a transputer systems of seven processors and a PC as host is utilised (Fig. 9). Despite the parallel processing the limits of the system have been reached because of the comparatively small computing power of a single transputer processor. Therefore the system is currently being ported to a flexible DSP-hardware.

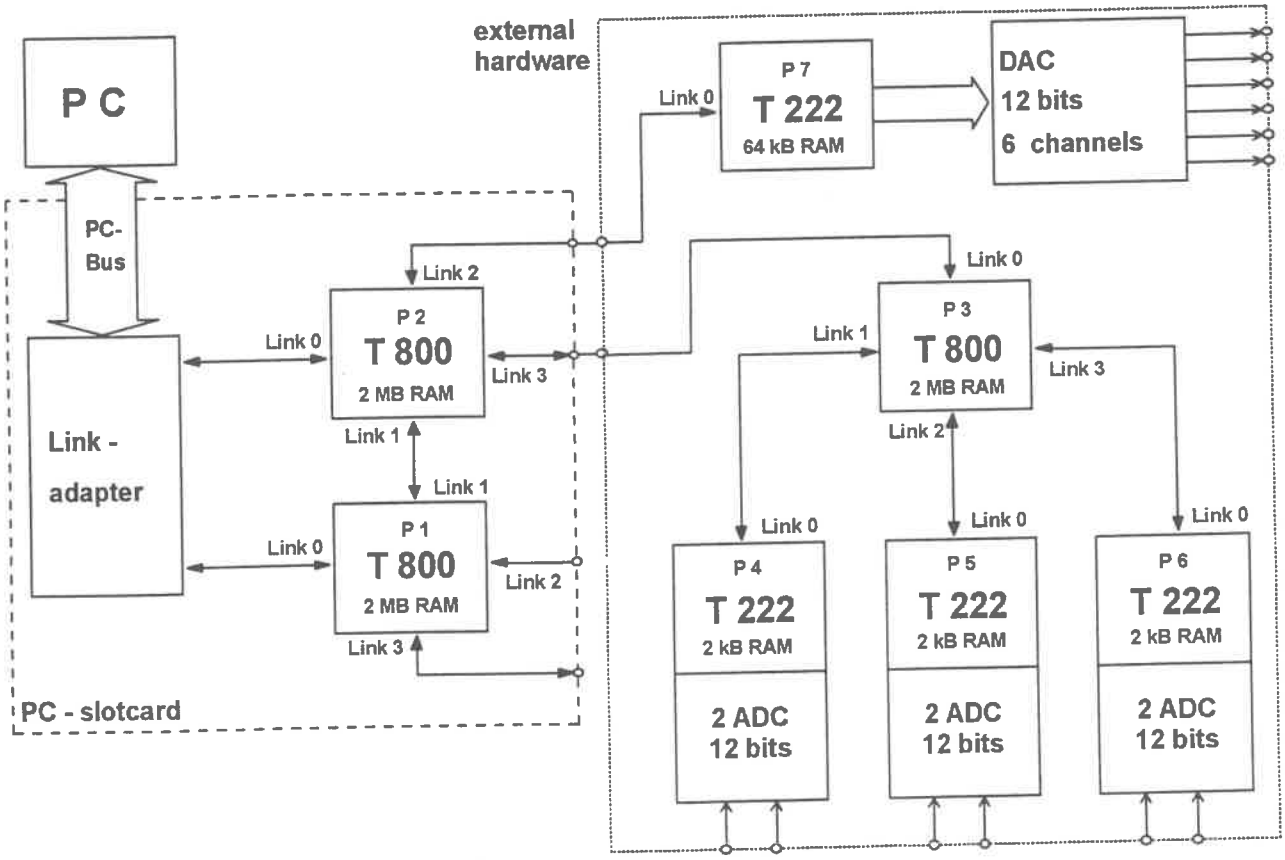

Fig. 9 Control system hardware

5.2 Control software

The software reflects the parallel processing concept. To fully exploit it the individual processes like data acquisition, interpolation and filtering, control algorithm and output are structured hierarchically and encapsulate a task specific functionality in an object-oriented way. Distributed on different processors they are running in parallel with different cycle times and communicating asynchronously with each other through a client-server interface, i.e. each communication consists of a software handshake with data request and successive data reception. On the other hand the incremental nature of the measuring system is completely hidden from the controller such that a change of it will require only minimal program changes.

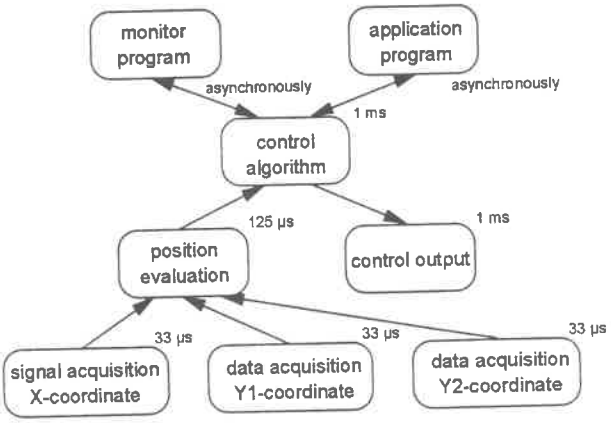

Fig. 10 Software structure

The distribution of the tasks (Fig. 11) onto the processors of the hardware is as follows:

- P1: monitor program, display (300 ms) and keyboard (asynchronous) drivers
- P2: control algorithm and data logging (1 ms), command interpreter (asynchronous)
- P3: interpolation, correction and filtering (140 µs) of position
- P4-6: data acquisition and processing (33 µs)

- P7: control output (1 ms)

5.3 Control Algorithm

A control concept called integral LQ-control with finite optimisation horizon is used [2]. It combines the advantages of state feedback control with the robustness and static disturbance cancellation properties of classical PID-control. Its structure is shown in Fig. 11.

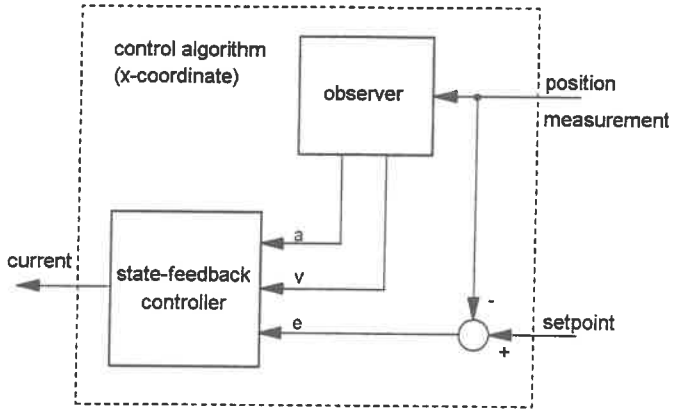

Fig. 11 Control structure

REFERENCES

[1] Schäffel, Chr., Schober, U., Kallenbach, E. *Measuring system for x-y-Drives without Mechanical Elements for Preventing the Armatures Rotation Round the z-Axis*, Proc. PCIM '94 Nürnberg, pp 173.

[2] Radtke, M. and Saffert, E. *Robust Adaptive LQG-Control under Consideration of the Identified Model Uncertainty (in German)*, Proc. 39th Int. Scient. Colloquium TU Ilmenau, Vol. 3, pp 723-730, 1994.

[3] Schäffel, Chr., Saffert, E. and Kallenbach, E. *A new integrated multi- coordinate drive with anti-rotation lock through field forces (in German)*, Proc. of the 40th Int. Scient. Colloquium TU Ilmenau, Vol. 4, pp 469-475, 1995.

[4] Saffert, E.; Schäffel, Chr.; Kallenbach, E. *Control of an Integrated Multi-coordinate Drive*, Proc. Mechatronics '96 conference, Portugal, 1996.

DESIGN OF A LONG RANGE FAST TOOL SERVO SYSTEM USING MAGNETIC SERVO LEVITATION

Brent A. Stancil
Harris Corporation
Government Communication Systems
Melbourne, FL 32902

Paul I. Ro
Precision Engineering Center
North Carolina State University
Raleigh, NC 27695-7918

1 INTRODUCTION

Magnetic Servo Levitation (MSL) [1] has been proposed as the basis of a Long Range Fast Tool Servo System (Figure 1). A system has been designed that is capable of a 1 mm range of travel, 300 Hz operating bandwidth, and nanometer resolution [2] (Figure 2). MSL utilizes the attractive forces of electromagnets to provide the actuating force for the system. Therefore, the system is open loop unstable and requires closed loop control to make any testing viable. Also, due to the large mass, long range, and decaying behavior of electromagnetic forces, the system was designed to have a natural frequency of 300 Hz, or the same as the desired bandwidth. Therefore, closed loop control will be necessary to provide the 300 Hz bandwidth. This abstract will attempt to show that the design is adequate and can be controlled.

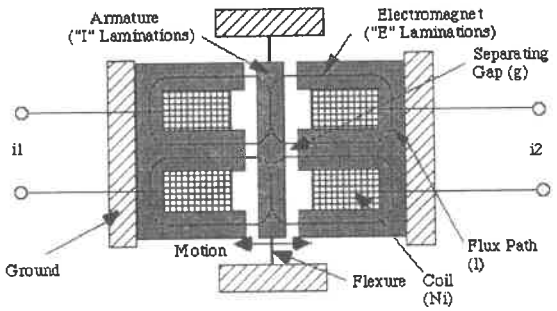

Figure 1: MSL Schematic

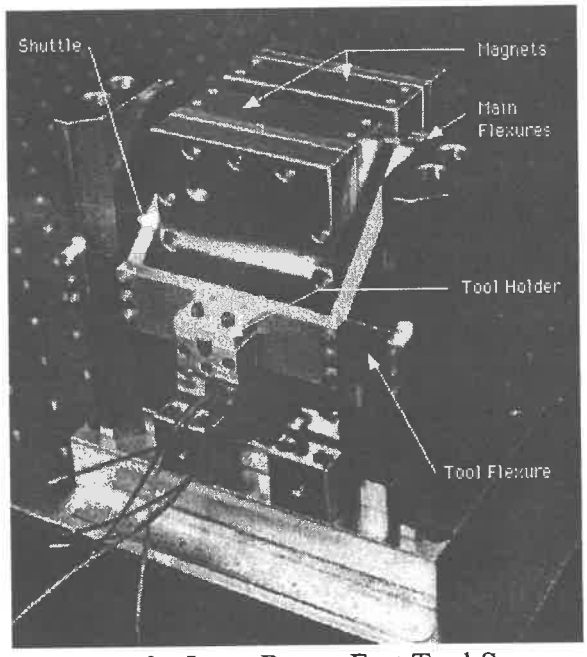

Figure 2: Long Range Fast Tool Servo

2 CONTROL

In order to provide closed loop control of nanometer resolution over a 1 mm range, a laser system had to be implemented into the final design. A Zygo ZMI-1000 system was chosen, because of its 2.47 nm resolution, capability of handling speeds up to 1 m/s, and its competitive cost of about $20,000. A version of a plane mirror interferometer was chosen that uses a focusing optic rather than a double pass configuration. This is required to accommodate the velocity requirement. A schematic of the system is show in Figure 3.

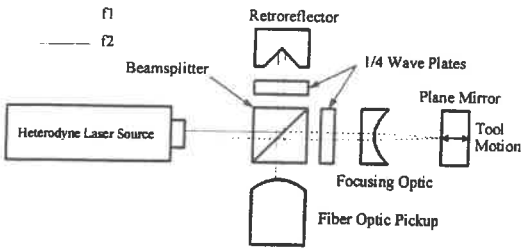

Figure 3: Laser Schematic

Two different control algorithms were used to show the effect of control on the open loop system. First, a robust time delay controller [3] was implemented. Its operating principle was that the input would be shaped in a way to cancel the dynamics of the system, or it add zeros to cancel the poles of the system. The controller, *D(z)*, has the form, in the digital domain,

$$D(z) = \frac{A_1 z^{k+1} + 1}{(A_1 + 1) z^{k+1}} \qquad (1)$$

where A_1 is found by

$$A_1 = \exp\left(\frac{\zeta\pi}{\sqrt{1-\zeta^2}}\right) \qquad (2)$$

and k is found by

$$k = \frac{T}{T_s} \qquad (3)$$

where T is the time delay found by

$$T = \frac{\pi}{\omega\sqrt{1-\zeta^2}} \qquad (4)$$

where ω is the natural frequency of the system, ζ is the damping ratio of the system, and T_s is the sampling rate of the controller.

The second control algorithm used was pole placement [4]. This algorithm operates on the principle of actually moving the system poles, and was investigated for the reason of extending the bandwidth.

3 TESTING

Testing was done on four different systems. First, testing was done open loop, only dividing the reference signal by the open loop gain. Secondly, the robust time delay controller was implemented. Thirdly, the pole placement routine was tested. Finally, the robust time delay was used to filter the reference signal to the pole placement controller. Bode plots of each of these are shown in Figures 4-7. Two time response tests were done for each configuration as well. Figures 8-11 depict the results for a 125 μm 20 Hz sine wave command and Figures 12-15 depict the response for a 200 nm 20 Hz square wave command. The 125 μm sine wave shows the ability of the system to achieve longer ranges than previous fast tool servo systems. This is also the limit of stability for the open loop case so that a comparison could be made with the controlled systems. The 200 nm sine wave shows the ability for the system to handle nanometer scale commands. These are typical amplitudes for error correction. The 20 Hz frequency corresponds to a once per revolution variation of the part being manufactured for a spindle speed of 1200 rpm.

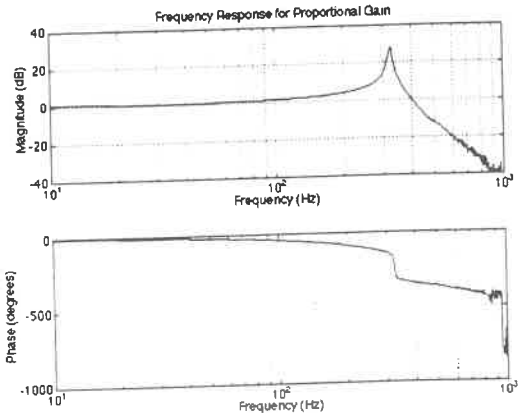

Figure 4: Open Loop Bode Plot

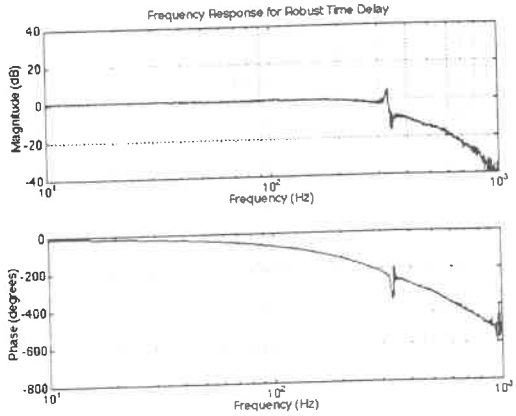

Figure 5: Robust Time Delay Bode Plot

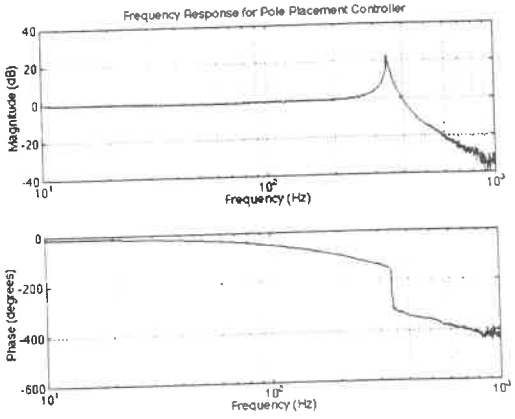

Figure 6: Pole Placement Bode Plot

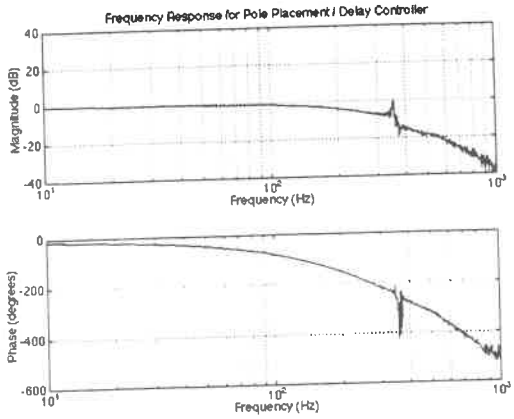

Figure 7: Combined Bode Plot

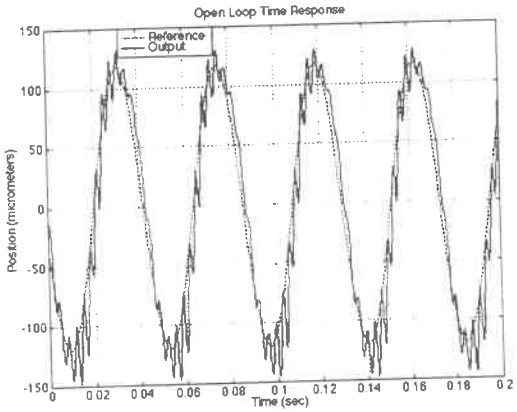

Figure 8: Open Loop
125 μm Sine Wave

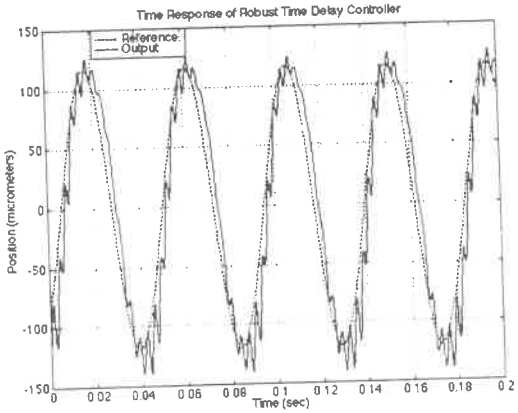

Figure 9: Robust Time Delay
125 μm Sine Wave

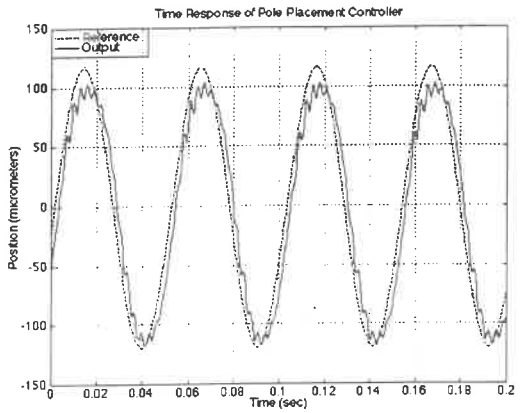

Figure 10: Pole Placement
125 μm Sine Wave

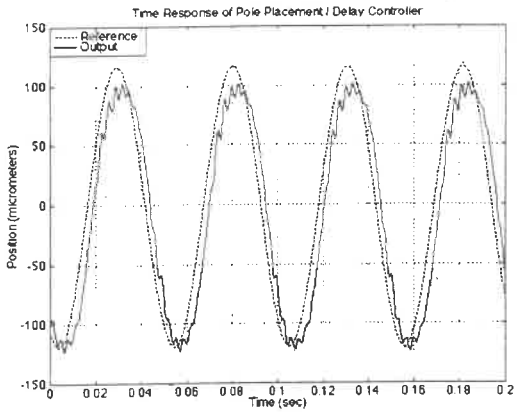

Figure 11: Pole Placement / Time Delay
125 μm Sine Wave

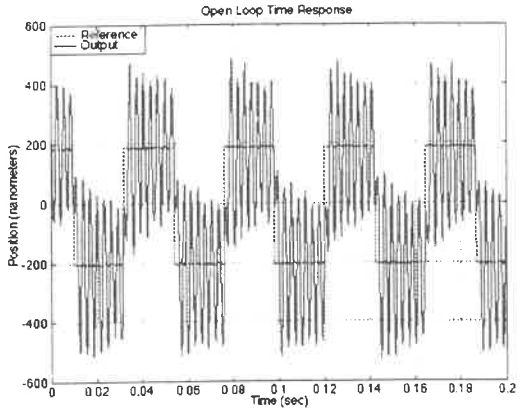

Figure 12: Open Loop
200 nm Square Wave

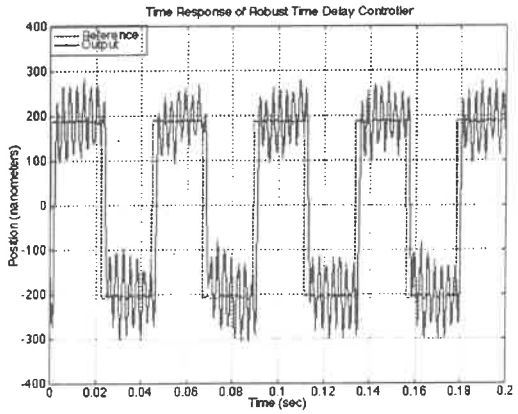

Figure 13: Robust Time Delay
200 nm Square Wave

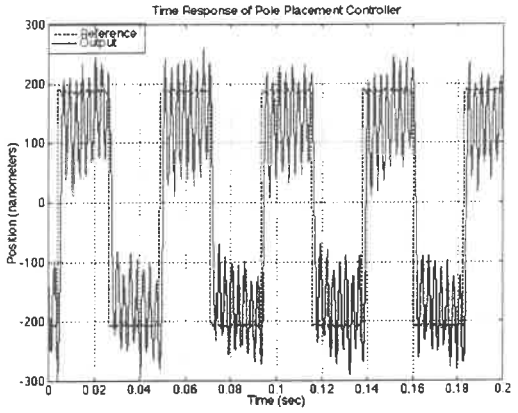

Figure 14: Pole Placement
200 nm Square Wave

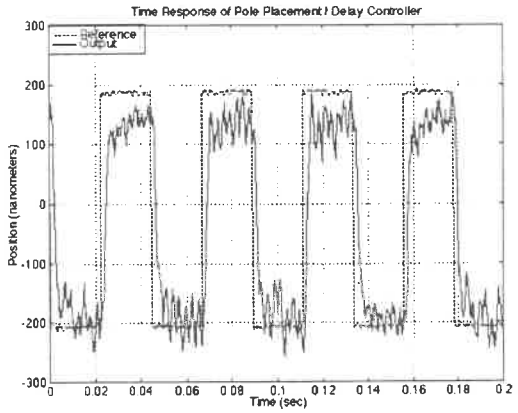

Figure 15: Pole Placement / Time Delay
200 nm Square Wave

The open loop bode plot (Figure 4) shows a mechanical resonance at about 325 Hz with about a 28 dB gain. The robust time delay (Figure 5) decreased this gain to about 5 dB. However, some phase was added to the system, which is expected since this is a time delay controller. The pole placement routine extended the bandwidth of the system by flattening the 0 dB region for a higher range of frequencies (Figure 6). However, some concern is raised since the resonant peak was not damped dramatically with the real poles that were designed for. This can be attributed to the nonlinearity of the system. The phase did not differ dramatically from the open loop system. The combination of the two controllers (Figure 7) provided a good frequency response. The resonant peak had been damped to 0 dB. However, the bandwidth was not quite as good as the time delay or pole placement. The phase was better than the case of the time delay by itself.

The open loop time response of the 125 μm sine wave (Figure 8) shows that the system is capable of tracking a command signal. However, there is an undesirable 325 Hz oscillation on top of the 20 Hz command signal. The magnitude of this oscillation is reduced somewhat by the robust time delay (Figure 9). Pole placement improves on this ringing to an even greater extent (Figure 10). The combination of the two controllers produces the cleanest signal (Figure 11).

Finally, the open loop time response of the 200 nm square wave was extremely noisy, with about 200 nm of unwanted oscillation (Figure 12). By adding the robust time delay, this oscillation was reduced to about 80 nm (Figure 13). However, the pole placement controller (Figure 14) was not as effective as it was with the 125 μm sine wave, and only reduced the oscillation to about 80 nm as well. However, the combination of the two controllers reduced this oscillation to about 40 nm (Figure 15).

CONCLUSIONS

By the addition of low order control algorithms to the Magnetic Servo Levitation based Fast Tool Servo System, bandwidth could be increased and the resonant peak could be damped considerably. However, there is some remaining effects of the resonant peak due to the nonlinearity of the system exciting this frequency. Higher order controllers should be able to help this system achieve the desired design goals.

REFERENCES

[1] Tsuda, M., and T. Higuchi. Design and control of magnetic servo levitation. *Report of the Institute of Industrial Science.* The University of Tokyo, March 1992, Vol. 37, No. 2, pp. 137-205.

[2] Stancil, B. A., H. M. Gutierrez, and P.I. Ro. Design of a Long Range Fast Tool Servo System Using Magnetic Servo Levitation. *Proceedings from ASPE 1995 Annual Meeting,* pp. 301-304.

[3] Singh, T. and S. R. Vadali. Robust Time-Delay Control. *Journal of Dynamic Systems, Measurement, and Control.* June 1993, Vol. 115, pp. 303-306.

[4] Phillips, Charles L. and H. Troy Nagle. *Digital Control System Analysis and Design, 3rd Edition.* Prentice-Hall, Inc., Englewood Cliffs, NJ, 1995.

A neural network-based real-time compensation technique for frequency output sensor arrays

G. Y. Tian Z. X. Zhao R.W.Baines

(School of Engineering, University of Derby , Kedleston Road, DE22 1GB, UK)

1. Introduction

Global and local networks have become the major computing platform for manufacturing systems. It becomes important to get the information from measurement sensors and to log them into computer based systems and/or networks. To do this sensors need to be compact, high-accuracy, safe, reliable and "smart and/or intelligent" enough to be integrated with different computing environments. To achieve this, smart and intelligent sensors have been researched and developed. Following this way, there is still a long way to go. Many techniques should be considered. They are as following:

A. New sensor theories, new materials and techniques based on high technology were adopted for developing sensors and their measurement and control system.
B. It is now widely accepted that new forms of sensors have improved performance over existing devices and are compatible with the extensive number of computer controlled system. With the development of the computer application, sensor compatibility with computer based system become emergency.

Due to the second opinion discussed above, a new approach to frequency output sensor arrays based on artificial neural network is proposed. The self-calibration/compensation technique including nonlinearity modelling recognition and coefficient evaluation/compensation, drift correcting readout during changing environmental conditions is discussed in the paper. There were three kinds of courses for self-calibration/compensation involved in the paper. One is for the non-linearity. The others are for stability relating to the change of temperature and humidity for both short and long term drift. The research work was taken into two steps.

Firstly, we designed and built a system linking frequency output sensors into PC. Based on the system, the data acquisition was provided. Different algorithms of neural networks were used for nonlinearity modelling recognition , coefficient estimation and compensation. Different sensors supported by different neural networks were discussed. The flexibility and accuracy of the self-calibration/compensation were validated.

Secondly, the self-compensation/compensation is imbedded in microprocessor-based sensor arrays. We used EEPROM instead of conventional ROM [1-2]. By using neural networks trained by a simple neural algorithm, the unknown coefficients of sensors can be estimated accurately and stored in EEPROM for real-time signal acquisition. When environmental conditions such as temperature and humidity are changed or sensors are to be renewed, the coefficients can be updated in real-time. From the coefficients of

compensation for long term drift, the quality information can be collected and the life time of sensors can be evaluated.

Finally as a conclusion, sensors with frequency output is an effective approach for resolving the "bottleneck" in computer application in measurement and control due to their the direct digital method and interface technique [3]. The approach presented in the paper will increase the intelligence of the sensors.

2. Frequency output sensor

Sensors transfer physical values into frequency especial digital pulse signal directly. This kind of sensors is called sensors with frequency output or frequency output sensors. The diagram of frequency output sensors was shown in Fig. 1. In this sense, many methods have been reported for the frequency converters [3]. We have designed electric oscillators for mechatronic sensors with frequency output. The stability of oscillators are the important factor for these sensors. The quartz oscillator is known for its dependence on temperature. Therefore, design quartz oscillators for different input quantities of sensors were used in our research.

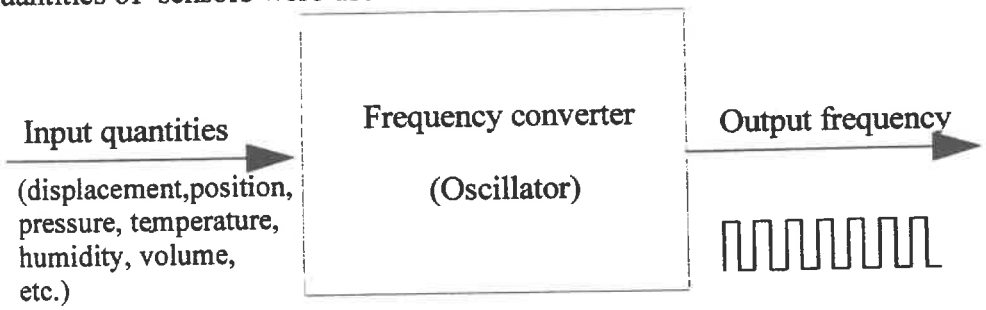

Fig. 1 Block diagram of the frequency output sensors

The advantages of research and development this kind of sensors are shown as following:

(1) sensors with frequency output transfer physical values into digital values directly. In this way, it is very easy to realise the interface from sensors and computer. Further, it can be reduced the design work for designer to design and adjust analogous circuit such as AC/DC amplifiers, filters. Therefore, using this kind of sensors do not require expensive A/D converter for computer interfaces.

(2) Since measuring frequency is a cumulative process such as output pulses are summed or integrated over a fixed period of time by numerical method using a microprocess or microcomputer or using IC unit, unwanted signal are inhibited. And the frequency output signals make the sensors insensitive to temperature and humidity change. So measuring frequency can achieve higher accurate. On the other hand, digital frequency signal have better anti-interference ability. It is operable in remote , hostile environment. Therefore, it can use for network or complicated measurement and control system especially under mal-condition environment.

(3) The sensors with frequency out can transfer analogue information into domain and can be digitised by a micro control directly. It can be helpful digitisation, integration and intelligence for sensors such as smart sensor and mechatrics devices. It can integrate

sensors and computer IC together, behaving functions about processing information, self-calibration, self-linearation, self-compensation, self-diagnositious and so on.
For example, an approach of intelligent system for frequency output sensors was shown in Fig.2. As we knew, sensor performances are generally decided by sensor drift including temperature drift and long term drift, non-linearity and resonant time. Resonant time will be discussed later. Relating to the stability and linearity of sensors, design high quality of the frequency converters is one resolved method, on the other hand, an intelligent system shown in Fig. 2 is transmitting the frequencies by the sensors to a microcomputer or embedding to a microprocessor system, via multi-cycle synchronous counter . Electrically Erasable Programmable Read only Memory (EEPROM) is used for saving programme code, data for compensation and non-linearity calibration and pattern recognition. Based on the intelligent system, numerical computation such as fuzzy logic, neural network and genetic algorithms could be integrated. The self-calibration, self-linearation and self-compensation for draft in the intelligent system are being studied in our research. By incorporating a single or multiple low-cost, uncalibrated frequency output sensor(s) into a software feedback loop, a self-normalised calibration/compensation table for each sensor can be generated and stored in EPROM for later use in real-time signal acquisition.

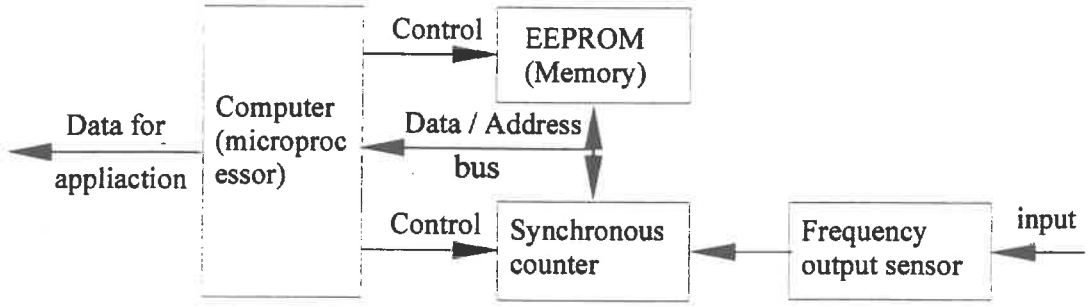

Fig. 2 Schematic diagram of an intelligent system for frequency output sensors

(4) This direct digit method is ideal for digital update of a lot of traditional dial gauges such as flow measurement and electricity measurement and further to design as a computer controlled network.
(5) Research and development this kind of sensors can simplify the sensor technology. Research only needs to pay attention how to design frequency output for sensors and interface for measuring frequencies.

3. Experimental test

An experimental test rig of an eddy current noncontact sensor with frequency output has developed at Derby university. The measured variable is displacement and the sensor output is digital frequency. The original relationship between the input and output quantity are shown as figure 3. In the experimental test, N stands for the test numbers for the same target at different positions with each other 10 mm. The output frequency can be got by a digital frequency meter. It is very clear that the nonlinearity is serious.

Based on the excellent long-term and temperature stability of the rig tested in the experiment, different compensation and calibration were taken. Using neural network software, Adaline and Madaline network and adaptive resonance theory networks have been used in the nonlinear compensation. The performances by the intelligent compensation are significant. Table 1 was shown the sensor performances compared with the traditional sensor.

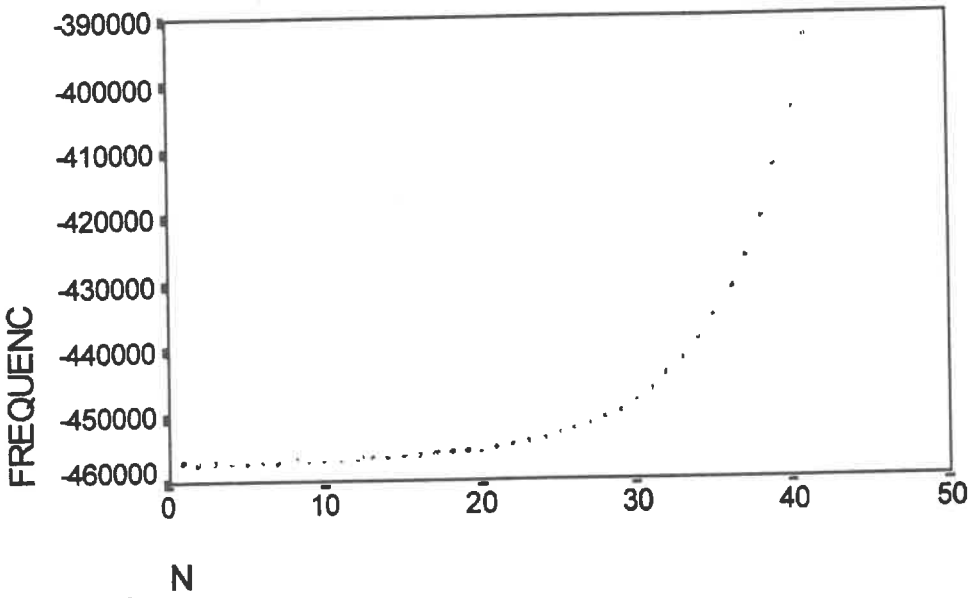

Figure 3 The frequency output for an eddy current sensor

Specification	New eddy current sensor	Conventional eddy current sensor
Range mm	0-2	0-2
Linearity %FS	0.1	0.25
Resolution μm	0.1	1
Temperature stability μm/°C	0.2	2

Table 1 - Comparison table for technical specifications of non-contact displacement eddy current sensors

4. Conclusion

With ever shrinking tolerances and reduction in manufacturing variability, pressure is increasing for the measuring and gauging industry to continually improve their own capabilities. The frequency output sensor approach can improve its stability and accuracy. The neural network-based real-time compensation technique has a potential future in the field of instrumentation and measurement. Not only can it improve system performance, but it is easily to be integrated into the existing quality assurance system such as manufacturing , monitoring and maintenance systems

5. References

[1] Jagdish Chandra Patra, Ganapati Panda, and Rameswar Baliarsingh, " Artificial Neural Network-Based Nonliearity Estimation of Pressure Sensors ", IEEE transactions on instrumentation and measurement, Vol. 43, No. 6. Dec. 1994.

[2] Paul T.Kolen, " Self-calibration/Compensation Technique for Microcontroller-Based Sensor Arrays ", IEEE transactions on instrumentation and measurement, Vol. 43, No. 4. Aug. 1994.

[3] Tian Guiyun, Yan Bin, " A New Fringe-field Capacitive Sensor ", The proceedings of 10th annual meeting for American Society for precision Engineering (1995 ASPE).

Development of NC Program Evaluator for Higher Machining Productivity

Xiren Yan, Keiichi Shirase, Masatoshi Hirao and Takeshi Yasui
Faculty of Technology, Kanazawa University
Kanazawa, Japan 920

1. Introduction

Numerical control machines, especially machining centers (MC), have been widely used in the precision and high speed cutting of complicated workpieces such as molds and dies. Their makers, as well as users, are focusing their attention on the machining productivity. Thus far, the productivity has been evaluated by the operational time and preparatory time generally. However, the productivity is greatly affected by NC programs used. Substantially, it should be evaluated by analyzing the NC programs, specifically the cutting conditions, tool paths, and cutting times in them. In other words, the NC programs should be analyzed internally. Thereby the quality of the NC programs will be evaluated clearly, and by employing the self-constructed expert system on cutting conditions based on the cutting know-how, the NC programs will be optimized.

Up to now, some controllers of machining centers and commercial software are available for part of the job. However, those only give the information on the cutting time, and far from evaluating and analyzing the productivity. Besides, due to the dependence of NC codes on controllers, and some optional codes added to NC code systems, no software for this purpose will apply for every kinds of NC code system. Moreover, as the cutting speeds and precision increase, a large number of tiny blocks, or the blocks where the moving distance is much shorter than that of the conventional case, appear in the NC programs, so that the actual feedrate is much lower than the commanded one. Consequently, the ideal cutting speeds and precision will not be obtained, and that will result in the calculations of cutting times based on command feedrates and moving distances far from actual ones. This causes the calculations much more difficult than imagined. In consideration of the above factors, an NC program evaluator has been developed for analyzing NC programs or evaluating cutting conditions, tool paths and operational times. With the evaluator, even before the actual cutting, the tool paths can be displayed and the times of feed motion and rapid motion, *etc*. can be calculated. Furthermore, the quality or productivity can be evaluated and expected to be improved. The overall block diagram evaluating and optimizing NC programs is shown in Fig.1[1].

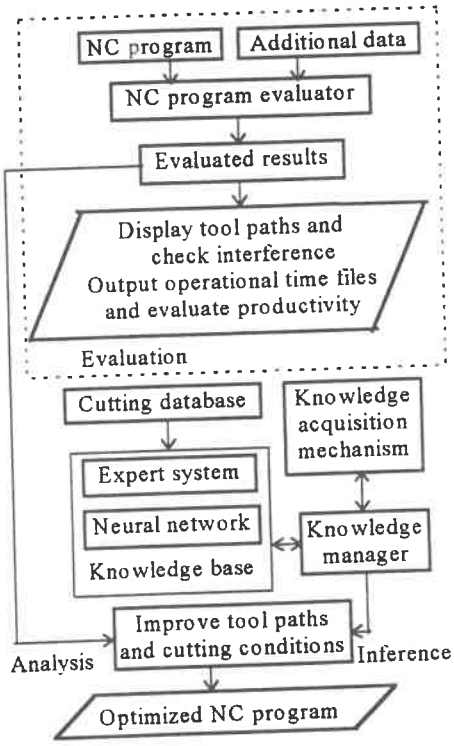

Fig.1 Overall block diagram of the system

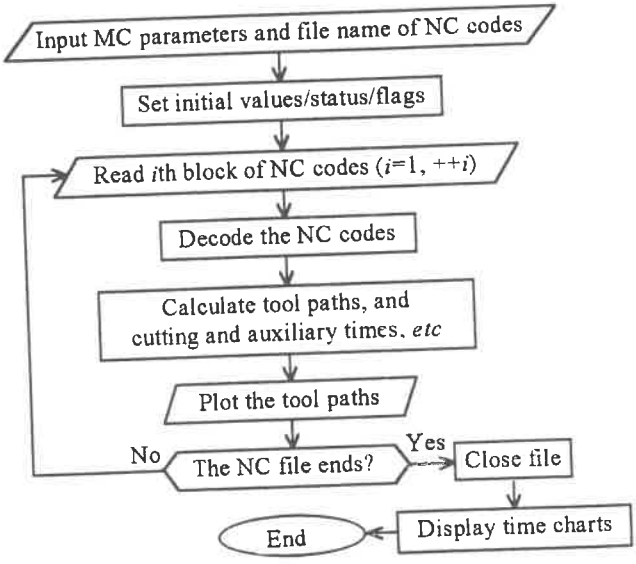
Input MC parameters and file name of NC codes
Set initial values/status/flags
Read ith block of NC codes (i=1, ++i)
Decode the NC codes
Calculate tool paths, and cutting and auxiliary times, etc
Plot the tool paths
No
The NC file ends?
Yes
Close file
End
Display time charts

Fig.2 General flow chart of the evaluator

2. NC Program Evaluator

The NC program evaluator works by decoding NC codes such as G and M in an NC program block by block, as shown in Fig.2. As decoding goes, the tool

paths are displayed and the feed times are calculated.

2.1 Tool paths

By decoding NC codes, the relevant coordinates of the tool are calculated and tool paths are drawn corresponding to G00, G01, G02, G03, *etc.* Furthermore, the quality of the tool paths can be evaluated.

2.1.1 Rapid feed (G00,G28,G29 and G30)

In the rapid feed, the tool path in one block is generally not a straight line but a broken line or sectional line, because the x, y, z axes in an MC are controlled separately. Therefore, in addition to the commanded dimensions (X, Y, Z *etc.*) , the coordinates of the midpoints where the tool traverses should be calculated. These can be obtained by comparison of the moving times in x, y, z axes. Figure 3 shows the calculation procedure of the midpoints M_1, M_2.

Letting S, D denote the start-point and destination point in the block respectively, then the positioning tool path is $S - M_1 - M_2 - D$.

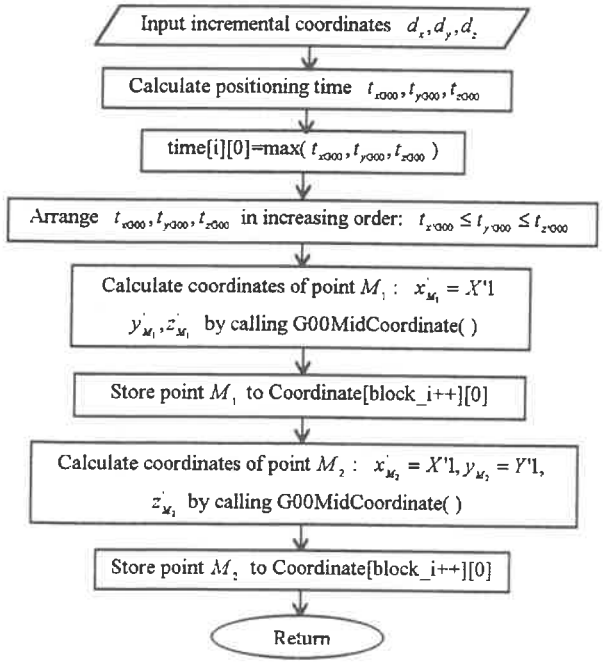
Input incremental coordinates d_x, d_y, d_z
Calculate positioning time $t_{x000}, t_{y000}, t_{z000}$
time[i][0]=max($t_{x000}, t_{y000}, t_{z000}$)
Arrange $t_{x000}, t_{y000}, t_{z000}$ in increasing order: $t_{x'000} \le t_{y'000} \le t_{z'000}$
Calculate coordinates of point M_1 : $x'_{M_1} = X'1$, y'_{M_1}, z'_{M_1} by calling G00MidCoordinate( )
Store point M_1 to Coordinate[block_i++][0]
Calculate coordinates of point M_2 : $x'_{M_2} = X'1, y'_{M_2} = Y'1$, z'_{M_2} by calling G00MidCoordinate( )
Store point M_2 to Coordinate[block_i++][0]
Return

Fig.3 Calculations of the midpoints in the rapid feed

2.1.2 Circular cutting (G02 and G03)

In the circular cutting, the center of the arc or vertices of its boundary rectangle should be calculated beforehand. Given the start-point $S(x_S, y_S)$ and the destination point $D(x_D, y_D)$, and the radius R, from the geometrical calculation, the coordinates of the center of the arc are obtained:

$$x_C = (x_S^2 - x_D^2 + y_S^2 - y_D^2 + 2(y_D - y_S)y_C) / 2(x_S - x_D)$$

$$y_C = (y_S + y_D)/2 \pm (x_S - x_D)\left(R^2 / ((x_D - x_S)^2 + (y_D - y_S)^2) - 1/4\right)^{1/2} \quad (1)$$

where + is for G02 and - is for G03.

2.2 Cutting times

The operational time for machining a workpiece includes the cutting (feed) time, positioning (rapid feed) time, and ac/deceleration time of the spindle, *etc.*

In the cutting feed motion, the cutting time will be much different from the actual one in some cases if it is calculated just based on the command feedrates (F code) and coordinates (X,Y,Z *etc.*) because the feedrates and accelerations are limited by some optional codes and accelerations. Besides, when the moving distance for each block is too short, the actual feedrate cannot reach to the command feedrate, especially in the high speed cutting. In the following sections, the calculations of the cutting time are derived for the feedrates of both the exponential and the linear functions.

2.2.1 Feedrate of exponential function

The instantaneous feedrate in an axis can be derived from the block diagram of the CNC controller. For example, the feedrate in x axis is expressed as

$$v_x(t) = \frac{v_{x0} - v_{x1}}{T_1 - T_2}(T_1 \exp(-\frac{t}{T_1}) - T_2 \exp(-\frac{t}{T_2})) + v_{x1} \quad (2)$$

Integrating Eq. (2) yields the moving distance:

$$x(t) = \frac{v_{x1} - v_{x0}}{T_1 - T_2}(T_1^2 \exp(-\frac{t}{T_1}) - T_2^2 \exp(-\frac{t}{T_2})) + v_{x0}(T_1 + T_2) + v_{x1}(t - T_1 - T_2) \quad (3)$$

where v_{x0}, v_{x1} are the components of the initial and commanded feedrates in x respectively; T_1, T_2 are the time constants of the ac/deceleration and positioning system respectively. T_2 is also called the reciprocal of the position loop gain. For FX-5 (Matsuura Machinery Corp.), $T_1 = 32\text{ms}$ and $T_2 = 33\text{ms}$.

With the approximation $\exp(x) \approx 1 + x (x << 1)$, and in consideration of the final feedrate of the current block or the initial feedrate of the next one, from Eq. (3) the cutting time can be estimated as

$$t = (d + (T_1 + T_2)(2f_0 - f_{0S} - f_{0D}))/f_0 \ (t >> T_1) \quad (4)$$

where d is the moving distance in the current block; f_0 is the command feedrate or its limit; f_{0S}, f_{0D} are the initial and final feedrates in the block respectively.

When $f_{0S} = f_{0D} = 0$, Eq.(4) becomes

$$t = d/f_0 + 2(T_1 + T_2) \quad (t >> T_1) \quad (5)$$

Equation(5) implies that the time calculated just by the commands F, and X,Y,Z *etc.* should be compensated by adding $2(T_1 + T_2)$ in this case.

Equation(4) can be used to calculate the cutting time

in the case of the exponential feedrate because t has a negligible error when $d > 4T_1 f_0$ and $T_1 \approx T_2$.

When $d \le 4T_1 f_0$, the approximation of t derived from Eq.(3) will be a transcendental function. Even though it can be fitted with $d = At^2$ based on some numerical analyses, here for simplicity, Eq.(4) is still used for this case and the absolute error can be neglected.

2.2.2 Feedrate of linear function

In the case of linear feedrates, the relations of feedrate and time can be divided into three cases from the moving distance, feedrates and accelerations. Suppose the feedrate at time t in the current block is denoted by $f(t)$ and the command feedrate in the next block by f_1. We will derive the formulas of the feed time corresponding to each of the cases. Note that the following formulas are relative to x axis, but the other axes are similar.

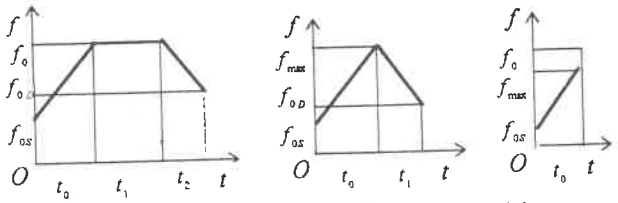

Fig.4 Feedrates in linear function

(1) Time estimation for the current block

Case 1: There exists time t where $f(t) = f_0$ (Fig.4(a))

When the following condition is satisfied

$$d_x' = |f_{0x}^2 - f_{0Sx}^2|/2a_{0x} + |f_{0x}^2 - f_{1x}^2|/2a_{1x} < d_x \qquad (6)$$

the maximum feedrate $f_{\max x}$ in x axis reaches to the x component of the command feedrate f_{0x} (refer to Fig.4(a)). In this case, $f_{0Dx} = f_{1x}$, and the feed time in x axis is calculated by

$$t_x = |f_{0x} - f_{0Sx}|/a_{0x} + |f_{0x} - f_{1x}|/a_{1x} + (d_x - d_x')/f_{0x} \qquad (7)$$

where f_{0x}, f_{1x} are the x components of the command feedrates of the current and next blocks respectively; a_{0x}, a_{1x} are the x components of the initial and final feed ac/deceleration of the current block respectively; f_{0Sx}, f_{0Dx} are the x components of the initial and final feedrates of the current block respectively; d_x is the commanded moving distance in x axis.

Case 2: There does not exist t where $f(t) = f_0$ but $f_{0D} = f_1$ exists (Fig.4(b))

When neither Eq.(6) nor the following equation is satisfied

$$f_{\max x} = \begin{cases} (f_{0Sx}^2 + 2\min(a_{0x}, a_{1x})d_x)^{1/2} < f_{1x} (f_{0Sx} \le f_{1x}) \\ (f_{0Sx}^2 - 2\min(a_{0x}, a_{1x})d_x)^{1/2} > f_{1x} (f_{0Sx} > f_{1x}) \end{cases} \qquad (8)$$

$f_{\max x}$ does not reach to f_{0x}, but f_{0Dx} reaches to f_{1x} of the next block, i.e., $f_{0Dx} = f_{1x}$ (Fig.4(b)). In this case,

$$f_{\max x} = ((f_{0Sx}^2 + f_{1x}^2 a_{0x}/a_{1x} \pm 2a_{0x}d_x)/(1 + a_{0x}/a_{1x}))^{1/2} \qquad (9)$$

where sign - is used when $f_{0Sx} > f_{0x}$ and the feed time

$$t_x = |f_{\max x} - f_{0Sx}|/a_{0x} + |f_{\max x} - f_{1x}|/a_{1x} \qquad (10)$$

Case 3: There does not exist t where $f(t) = f_0$ and $f_{0D} = f_1$ does not exist either (Fig.4(c))

When Eq.(6) is not satisfied but Eq.(8) is , we have $f_{0Dx} = f_{\max x}$, and the feed time

$$t_x = |f_{\max x} - f_{0Sx}|/\min(a_{0x}, a_{1x}) \qquad (11)$$

where $f_{\max x}$ is calculated by Eq.(8).

The feed time $t = \max(t_x, t_y, t_z)$.

(2) Time compensation for the last blocks

In the case of Fig.4(c), when the current block is the last of the consecutive moving blocks, i.e., $f_{1x} = 0$ and $f_{0Sx} > \sqrt{2a_{0x}d_x}$, letting the final feedrate of the current block $f_{0Dx} = f_{1x}$, then the initial feedrate f_{0Sx} is changed to $f_{0Sx}' = \sqrt{2a_{0x}d_x}$, and thus the variation of the initial feedrate $\Delta f_{0Sx} = f_{0Sx} - f_{0Sx}'$ is produced. Therefore, the feed time of the block should be compensated in corresponding to its feed cases. Differentiating Eqs. (7), (10) and (11) yields

$$dt_x = |(1 + f_{0Dx}/f_{0x})df_{0Dx}/a_{1x}| \text{ (Fig.4(a))} \qquad (12)$$

$$dt_x = |df_{0Dx}/a_{1x}| \text{ (Fig.4(b))} \qquad (13)$$

$$dt_x = |(1 - f_{0Dx}/f_{0Sx})df_{0Dx}/a_{0x}| \text{ (Fig.4(c))} \qquad (14)$$

Substituting df_{0Dx} in Eqs. (12)-(14) with Δf_{0Sx} yields the approximate value $\Delta t_x \approx dt_x$.

For the consecutive tiny blocks, the compensation should be for all the blocks. From Eq.(14) and $df_{0Sx} = f_{0Dx}df_{0Dx}/f_{0Sx}$, it is recurred and summed that

$$\Delta t_x = \sum dt_x = (1 - f_{0Dx}/f_{0firstx})df_{0Dx}/a_{0x} = f_{0Dx}/a_{0x} \qquad (15)$$

where $f_{0firstx}$ is the initial feedrate of the first block.

(3) Ac/deceleration of circular cutting

In the circular cutting, the resultant ac/deceleration is used instead of that of a particular axis. The resultant ac/deceleration $a_f = df/dt$ and satisfies for the cutting in xy plane (G17)

$$\begin{cases} |a_x| = |\mp a_t \sin\alpha - f^2 \cos\alpha / r| \le a_{\max x} \\ |a_y| = |\pm a_t \cos\alpha - f^2 \sin\alpha / r| \le a_{\max y} \end{cases} \quad (16)$$

where the upper sign is for G03 and the lower for G02. α is the angle between the radial direction and x axis; f is the instantaneous resultant feedrate; r is the radius of the arc; $a_{\max x}, a_{\max y}$ are the maximum feed accelerations in x and y respectively.

In most cases, an NC program used for cutting molds or dies is composed of a great number of consecutive tiny blocks, and thus the MC operates under command feedrates. Therefore, the feed time should be calculated after giving careful considerations to the accelerations.

2.3 NC program evaluator programming

The NC program evaluator was programmed in Visual C++ under Windows 95. It is object-oriented and has a friendly user's interface. The NC codes which can be analyzed by the evaluator, besides such basic codes as G00-G03, include M98 (sub-program), G65 and G66 (macro), and optional code G202 (high speed mode for specifying feed accelerations). From the viewpoint of evaluating NC programs, the evaluator can be executed in the modes of single or consecutive blocks. Besides, the plane, origin and scale, *etc.* for tool paths, can be chosen optionally. The tool paths will be drawn on the screen when each block is interpreted while at the same time the operational times are calculated and saved into data files.

2.4 Analyses of sample NC programs

The NC program evaluator has been applied to analyze some NC programs. Table 1 lists the operational times with the comparisons between the actual and analyzed times. From the table, we can see that the estimated error is no more than 4% and the average rate of the real cutting time to the total time for the practical NC programs is 93.8%. It is much higher than that of NC lathes which was 82.8%[2] .

In the analyzed NC programs, Conrod is used to cut a forging mold. Its NC program contains G202 code and has 40,240 blocks. End-mills were used and changed four times. In Fig. 5, (a) shows the tool paths and (b) shows the ratios of the operational times.

Furthermore, the quantitative effects of feed rates and /or accelerations on the productivity can be analyzed by changing their values. For Conrod, the cutting time will decrease by only 9.8% when the feedrates is doubled. In contrast, it will increase by 50.5% when they are reduced by half. This is because there are a large number of tiny blocks and the feedrates are limited by G202 code in the NC program. The result implies that only increasing feedrates is not an efficient way to raise the productivity for this kind of NC program but decreasing feedrates will cause rather low productivity.

Table 1 Analyzed results of NC programs (min)

Name	Rapid feed time	Cut. time	Total time	Actual total t.	Real cut. time rate
Conrod	1.63	71.2	73.1	75.2	97.3%
Iron	2.11	17.6	19.6	20.4	90.3%
Test	0.06	0.86	0.97	0.98	88.5%

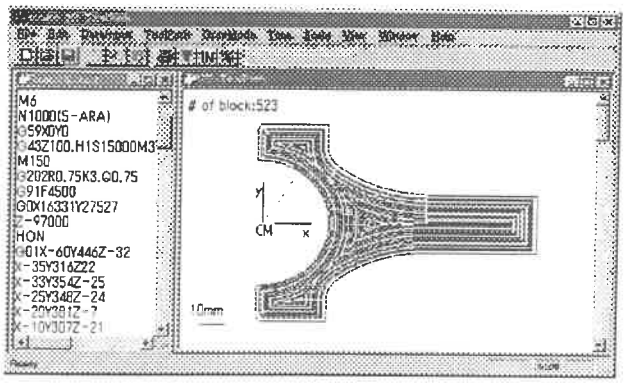

(a) Tool paths

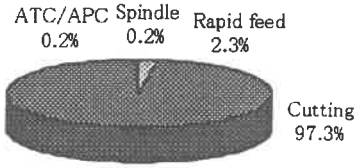

(b) Cutting time ratios

Fig.5 Analyzed results of Conrod NC program

3. Conclusion

The NC program evaluator used to analyze NC programs and evaluate their productivity has been developed. With the evaluator, (1) the tool paths can be drawn on a microcomputer, and their quality can be evaluated and even the faults such as the interference can be found, and (2) the operational times and the cutting conditions can be evaluated .

In conclusion, the productivity can be evaluated by analyzing NC programs and improved by modifying NC codes associated with the cutting conditions and the parameters associated with the MC.

References

1 Huang S.H. and Zhang H.C. On the Use of Knowledge-Based Connectionist Models in CAPP Systems. Manufact Sci & Engg, ASME, 1994,1, 65-74

2 Shirase K., Hirao M., Yasui T. *et al.* Improving Productivity in NC Lathe Turning Based on NC Program Diagnosis System (1st report). J Jap Soc Prec Engg, 1994,60(2),235-239 (in Japanese)

LOCAL LAPPING SYSTEM TO OBTAIN WIDE AND FLAT SURFACE WITH ACTIVELY CONTROLLED FORCE SENSOR

Kiyoshi MATSUMOTO, Masayuki NAKAO and Yotaro HATAMURA
Department of Engineering Synthesis, Faculty of Engineering, The University of Tokyo
7-3-1 Hongo Bunkyo-ku Tokyo 113, JAPAN

1.Introduction

Machining process to obtain a wide and flat surface in short time is highly required in many industrial fields. In the field of semi-conductor technology, enlargement of silicon wafers implies an increase in the number of chips available at one process, and results in a decrease in production cost. But obtaining large wafers of, for example, 12" diameter and 0.3um flatness by whole lapping is inefficient from view points of process time and material cost. The authors make an attempt on local lapping /grinding, which enables to lap or grind a surface locally to follow a prescribed trajectory.

2.Local lapping/grinding system with active force sensor

To achieve local lapping/grinding, the following problems need to be addressed. Because of the insufficient rigidity of the machining system, the mechanical elements such as the tool, the workpiece and the structural frame are deformed by lapping/ grinding reactive force. Fig.1 shows schematic of lapping/grinding process. If the tool is controlled so as to follow a prescribed trajectory in an open-loop fashion with no consideration on such deformation, the resulting surface does not retain the desired accuracy due to the deformation. Employment of a force sensor to detect lapping force is effective to monitor the deformation, but the presence of the sensor itself may cause a decrease in rigidity. The authors previously proposed a force sensor with actively controlled compliance.1) This sensor is actually equipped with an actuation capability of force or displacement as well as sensing capability in both. With this sensor, it becomes possible to control a tool position or lapping/grinding force while detecting the position and the force. A desired surface profile can be obtained in one pass by controlling this active tool with the force information and the knowledge about the rigidity of the lapping system. This operation consists of the following steps. First, the deformation of the sensor is compensated by actuating the device by the equal amount. Second, the deformation of the machining system can be canceled by detecting the reactive force and actuating the tool based on the knowledge about the rigidity.

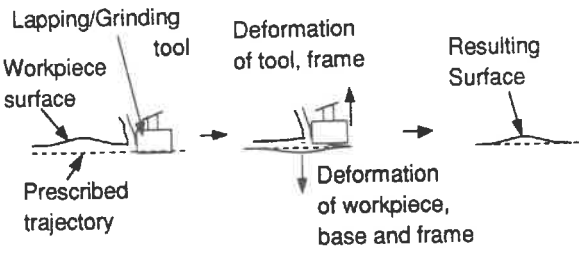

Fig.1 Schematic of lapping/grinding process

3.Development of a ring shape active force sensor

3.1 Basic structure

Active force sensor utilizes the parallel plate structure. Fig.2 shows the parallel plate structure and its applications. To detect force, the basic parallel plate structure shown in Fig.2 (a) is used. Two pillars are connected by

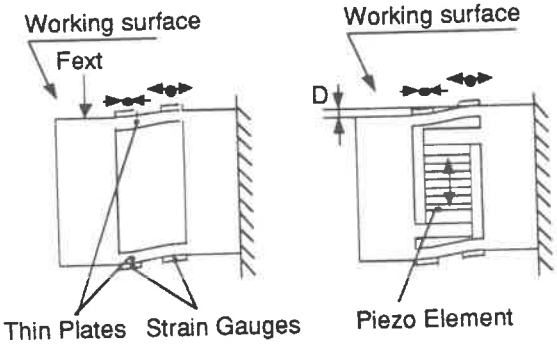

Fig.2 Two applications of parallel plate structure

a pair of parallel thin plates. One pillar is fixed to the rigid base, and another pillar is movable in one direction. The movable pillar has a working surface where external force or displacement is applied. On the surface of thin plates, strain gauges are glued. They detect deformation of the thin plates through surface strains, and thus applied external force or displacement can be detected. The structure shown in Fig.2 (b) is used for actuation. Between the pillars, a Piezo element is inserted. By elongation or contraction of the piezo element, displacement of the working surface is generated.

This Fig.3 shows the basic structure and the deformations of active force sensor.

A pillar is composed of upper/lower seats, and a piezo device which is glued between the seats. This pillar is movable and connected to a fixed pillar by a pair of parallel thin plates. The parallel thin plates limit movement of the movable pillar and movement of the piezo device in one direction. On the surface of the upper and lower thin plates, strain gauges are glued which detect their deformations respectively.

When the piezo element does not elongate, applied external force causes displacement of working surface D as shown in Fig3 (b). . Displacement D is detected by the upper and lower strain gauges and produce outputs Eu and El. When external force is not applied, elongation of the piezo element causes displacement of working surface D as shown in Fig (c) . Displacement D is detected by the strain gauges and produce outputs Eu and El similarly. The active force sensor uses superposition of these deformations. Assuming that the signs of Eu and El are positive as shown in the case of Fig.3 (c) . El-Eu is proportional to the applied external force, and is used to detect applied force. Eu is proportional to the displacement of the working surface, and is used to control actuation by the sensor.

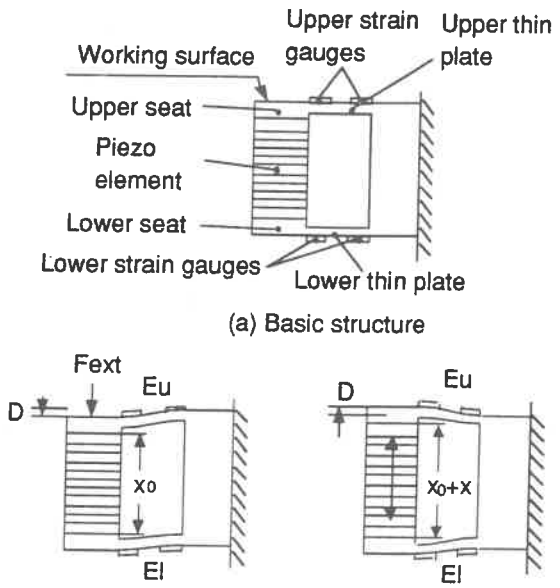

Eu : Displacement of working surface
El - Eu: Applied external force/displacement

Fig.3 Basic structure and deformations of active force sensor

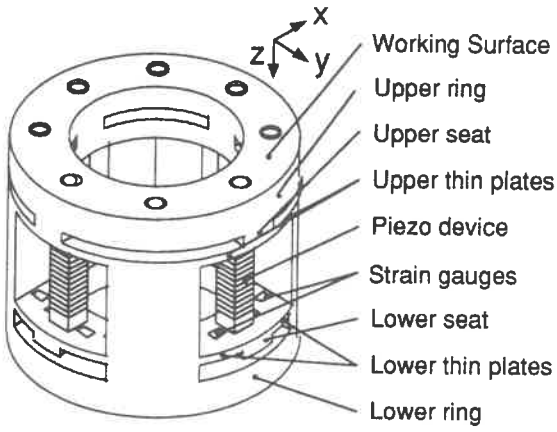

Fig.4 Ring shape active force sensor

3.2 Ring shape active force sensor

Fig.4 shows structure of ring shape active force sensor. Between upper and lower ring, 4 active sensing units are installed at every 90 degrees. Each unit can detect force and actuate independently. By calculation of the outputs from 4 units, force in the direction of z and moments around the axes x and y can be obtained. By actuation of the piezo elements in 4 units, displacement in the direction of z and inclinations around the axes x and y can be generated. The lower ring is fixed to frame or base, and machining tool is attached to the upper ring.

3.3 Sensing and actuating system

Fig.5 shows a block diagram of the sensing and actuating system. The output signals from 4 sensing units are expressed by suffix. Eui indicates displacement of the work-

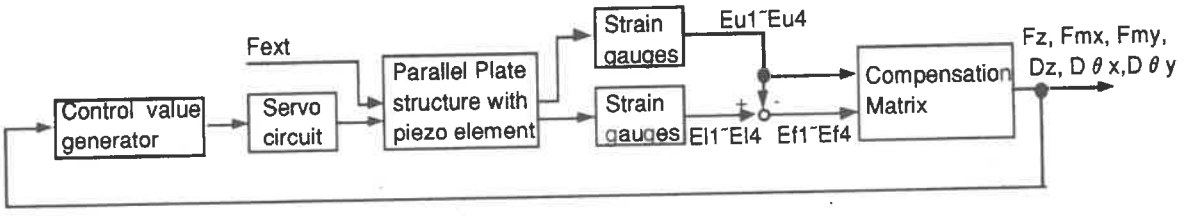

Fig.5 Block diagram of sensing and actuating system

ing surface detected by each unit. Efi produced by subtraction Eui from Eli indicates force detected by each unit. These signals have interferences from each other. Force and Displacement information is calculated by using compensation matrix to eliminate the interferences. As mentioned below, compensation matrix is obtained by calibration of the sensor.

Force and displacement information are fed back to control value generator. The control value is calculated so that the sensor acts as an spring which has arbitrary compliance. The control value drives piezo elements in sensing units through servo circuit.

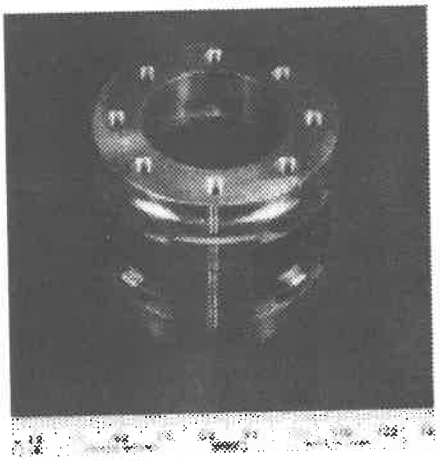

Fig.6 Photograph of sensor block

3.4 Characteristics of fabricated sensor

Fig.6 shows a photograph of an actually fabricated sensor block.

The rated value and the resolution of force in direction of z are 100N and 0.1N, respectively. The actuation range and the resolution are 10um and 0.01um, respectively. The parallel plate structures were designed so that the resonance frequency may be as high as possible and the output signal of strain gauges may be as much as possible. The thickness of the thin plates is 1.0 mm, the length is 8.5mm, and the width is 12 mm. Rigidity to the force in direction z is 17.3x106 N/m when piezo elements are not driven.

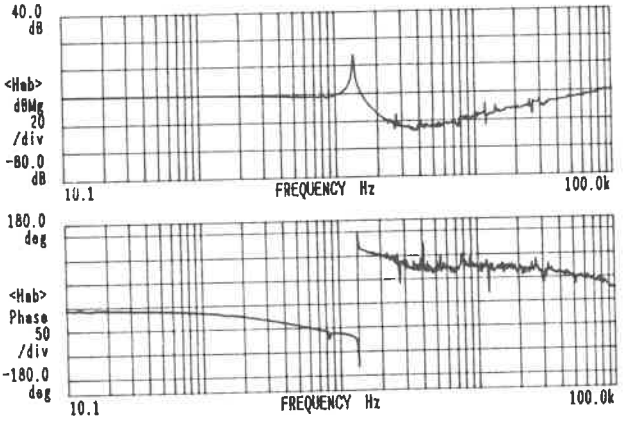

Fig.7 Transfer function

Fig. 7 shows measured transfer function from voltage supplied to piezo elements to outputs Eu, which is the response characteristics of the working surface. The natural frequency is about 1.2 KHz.

Fig.8 shows compensation equation to obtain force information from outputs Efi. The compensation matrix is obtained by calibration using weights.

$$\begin{pmatrix} Fz \\ Fmx \\ Fmy \end{pmatrix} = \begin{pmatrix} 2.00\times10^{4}, 2.00\times10^{4}, 2.10\times10^{4}, 2.00\times10^{4} \\ -9.43,\ 4.92\times10^{2};\ -7.52, -5.00\times10^{2} \\ -5.11\times10^{2}, -1.01\times10, 5.07\times10^{2}, -1.02\times10 \end{pmatrix} \cdot \begin{pmatrix} Ef1 \\ Ef2 \\ Ef3 \\ Ef4 \end{pmatrix}$$

Fig.8 Compensation equation for force detection

Fig.9 shows force detection output when external force in direction of z is applied. The output is expressed by units of u strain. It has good linearity. The sensitivity is 24.96 u strain/N.

Fig.10 shows the force detection output to external force in direction of z when displacement of the working surface is changed. Displacement change has little effect on

force detection output. On the other hand there are upper and lower limits of displacement as shown by dotted lines. These come from the existence of the working range of the piezo element, and vary in proportional to applied external force.

Fig.11 shows the displacement of the working surface to applied external force. The compliance can be changed within the working range of the piezo elements.

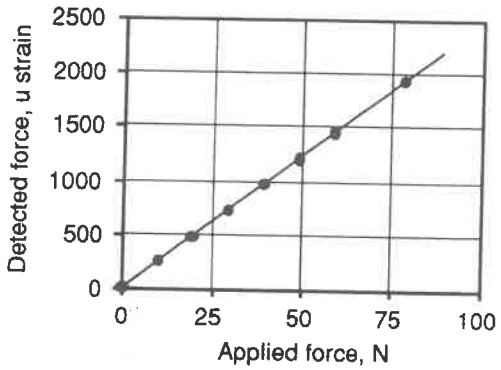

Fig.9 Force detection characteristics

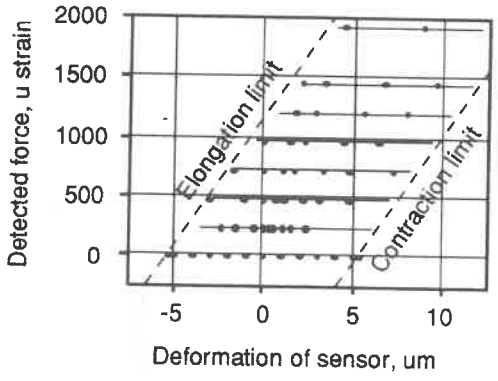

Fig.10 Force detection characteristics

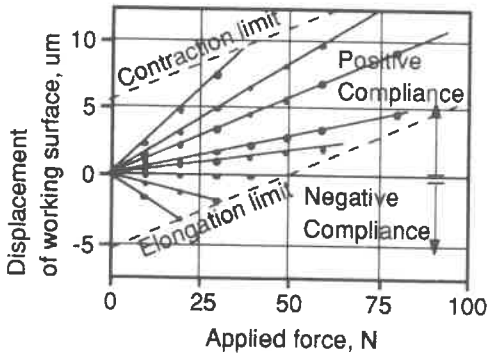

Fig.11 Compliance control operation

4. Experiment

4.1 Experimental system

Fig.12 shows the experimental system. A surface grinding machine is used as feed mechanism. Straight cup wheel is employed as grinding tool, and is rotated by a water driven turbine. The pressure of water fed to water inlet is about 3 MPa, and nominal rotation speed is 10000 r.p.m. Rotation shaft which connects the turbine and the grinding tool is suspended by a dynamic water pressure bearing. The ring shape active force sensor is installed between the turbine and the feed mechanism in z direction. An 8-inch silicon wafer is glued to the base by hot wax. The base is fed in x direction. The rigidity in direction z of this system without the sensor is measured to be 8.15x106 N/m, while that of the sensor is 17.3x106 N/m as mentioned before.

Fig.13 shows photograph of the experimental setup.

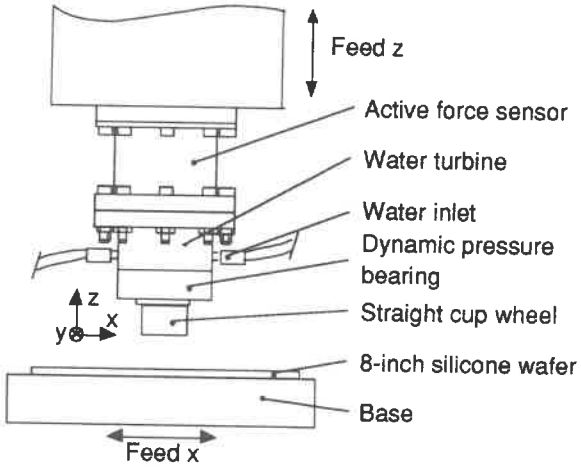

Fig.12 Experimental system

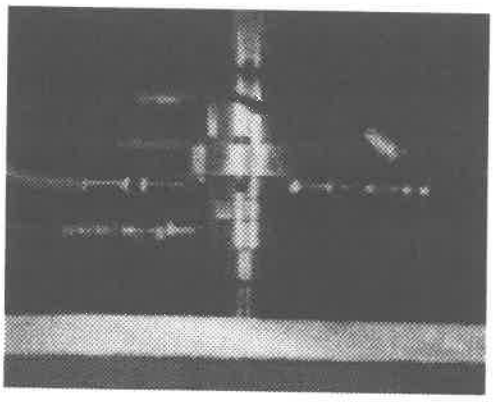

Fig.13 Photograph of experimental setup

4.2 Measurement of reactive force

Two straight cup wheels are used for experiment. The roughness numbers of abrasive grains on the wheels are 350 and 800. Feed rate is fixed at 200 mm/min. Reactive force of grinding measured is shown in Fig.14. Defining that the increase of the reactive force Fz to the depth of cut as dynamic rigidity Kd, Kd is 1.5x105~2.1x 105 N/m with the wheel of No.800. With the wheel of No.350, Kd is 8.5x104 N/m. Assuming that the rigidity of the grinding system as static rigidity Ks, Ks is 8.15x106 N/m as described in 4.1. Kd is 10~100 times lower than Ks.

Fig.15 shows distribution of the reactive force at the depth of cut 50um with the wheel of No.800. Regarding that the feed direction as 0 o'clock and the tool rotation as CW, maximum force arises at 3 o'clock. The center of reactive force calculated from Fz, Fmx and Fmy is around the inner cutting edge in direction of 4 o'clock. When the feed direction is opposite, the maximum force arises at 9 o'clock and the center is around the outer edge of 10 o'clock.

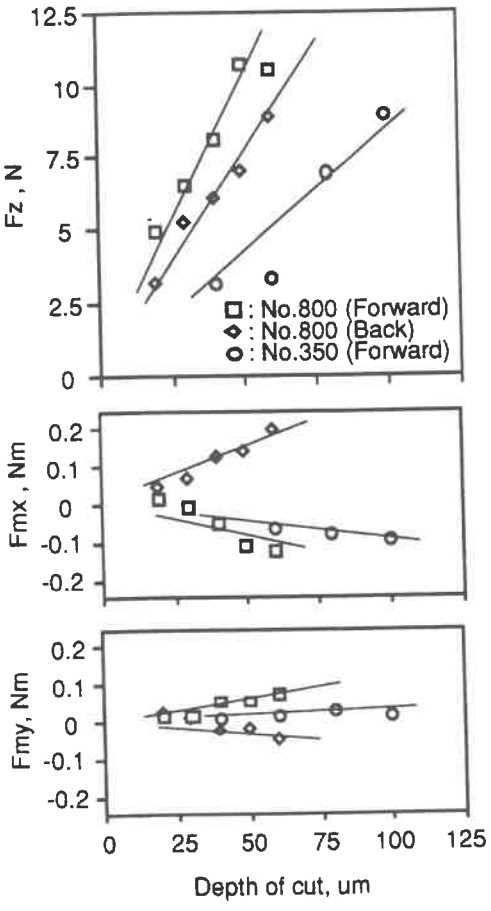

Fig.14 Reactive force of grinding

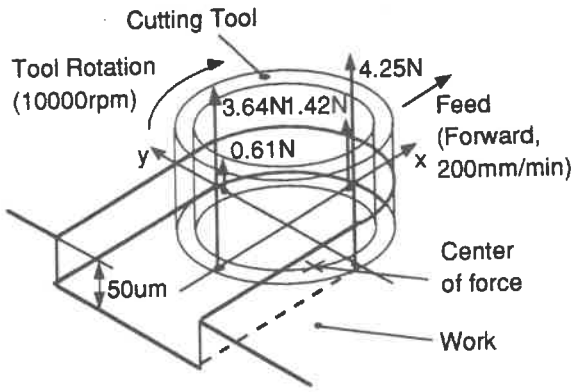

Fig.15 Distribution of reactive force

4.3 Grinding experiment with controlled compliance

In this experiment, reactive force was measured when grinding over a trapezoid shape of 100um, with variations of compliance of the sensor. The cup wheel is No. 350, and the feed rate is 200 mm/min. From the result of measurement in 4.2, the nominal reactive force is estimated to be about 8.5 N. Considering that the static rigidity of the grinding system Ks is 8.15x106 N/m, the total deformation including that of base, frame and tool is estimated to be about 1.04 um, which may remain as grinding error. Bandwidth of the servo system to control the compliance of the sensor is set at about 10 Hz. DC gain is about 60 dB.

Fig. 16 shows experimental results when the rigidity of the active sensor is set at -19x106 N/m. The sign minus means that the compliance is negative, and that the sensor actuates in opposite direction of applied force. The height of the trapezoid is measured to be 93um. The reactive force during grinding is about 11 N, and the sensor generates deformation of 0.5 um to cancel the relief of the work. The grinding error is measured to be 0.9 um.

Fig.17 shows grinding error to compliance of the sensor. Compliance is inverse from rigidity. When the compliance is 0 N/m, which means the rigidity of the sensor is infinite or there is no sensor installed, the grinding error is 1.2 um. Minimum grinding error 0.7 um is obtained when the compliance is set at -0.053 N/m. The grinding error is reduced to 60%. In the region where the compliance is

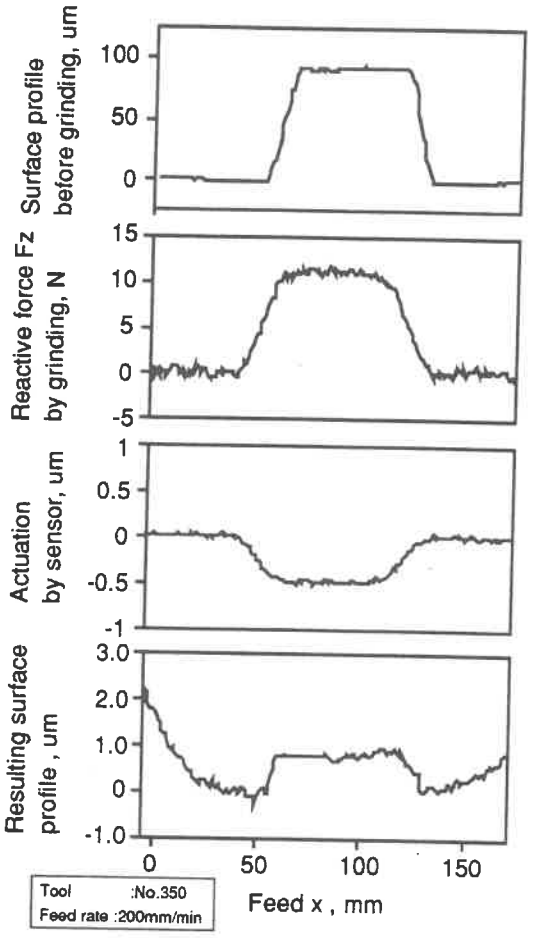
Surface profile before grinding, um
Reactive force Fz by grinding, N
Actuation by sensor, um
Resulting surface profile , um
Feed x , mm
Tool :No.350
Feed rate :200mm/min

Fig.16 Grinding experiment with negative compliance

less than -0.053 N/m, the servo goes unstable and the piezo elements elongate to their limits. The stability to the compliance has to be studied further.

5. Conclusions.

A local lapping / grinding system to obtain a wide and flat surface has been proposed. With this system, a significant decrease in process time and cost will be expected.

A ring shape active force sensor was developed which can change its compliance arbitrary.

The ring shape active force sensor was applied to surface grinding system with water driven turbine motor. In the experiment of grinding magnetic disk substrates, it was confirmed that grinding error was reduced to 60 %.

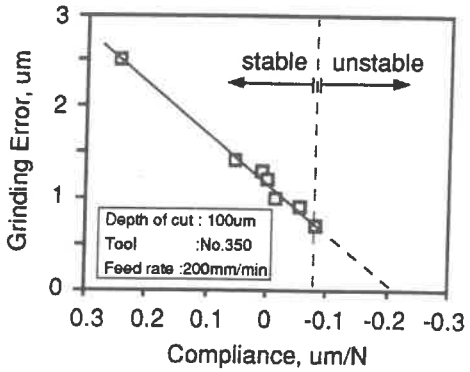

Fig.17 Grinding error to compliance

Acknowledgment

The authors would like to thank Mr. Masakazu Uesugi, Mr. Hiroyuki Ikeda and Mr. Katsutoshi Ohno of THK Co.Ltd. for discussion and supply of the water driven turbine motor and the dynamic water pressure bearing.

1) K. Matsumoto, et al., A Trial of Force Sensor with actively controlled Compliance, Proc. ASPE Spring Topical Meeting on Mechanisms and Controls for Ultraprecision Motion, ASPE, Tucson, USA, (1994)

Dynamic Friction Polishing of Diamond utilizing Sliding Wear by Rotating Metal Disc

K.Suzuki*, N.Yasunaga**, Y.Seki+, A.Ide*, N.Watanabe*, T.Uematsu++
(*Nippon Inst. of Tech., **Tokai Univ., +De Beers Japan, ++Toyama Pref. Univ.)

Summary: Dynamic Friction Polishing Method which enables highly efficient abrasive-free polishing of a diamond workpiece is proposed. In the method a diamond workpiece is pressed onto a metal disc rotating at a high speed and polished by utilizing dynamic friction between them. It has been found that a stainless steel(SUS304) disc gives especially high polishing efficiency and that, on a square pillar shaped single crystal diamond(0.6x0.6mm with (100)plane), polishing efficiency of as much as h'=2600μm/min(0.94mm^3/min) is attained under the conditions of sliding speed of Vs=4000m/min, stroke speed of Vw=200mm/min and pressing force of P=114MPa.

Key words; Dynamic Friction Polishing, Abrasive-free polishing, Grinding of diamond, Stainless steel disc

1. Introduction

In general, diamond tools or diamond thin films are polished with a diamond wheel or a lapping plate. But there are some problems in the process in terms of machining efficiency and wheel wear. As one of the measures to solve these problems, a method utilizing thermochemical reaction between a heated ferrous metal disc and a diamond workpiece placed in a vacuum or H_2 chamber was proposed and good results were reported[1,2]. The authors have investigated another method utilizing dynamic friction between a diamond workpiece and a metal disc rotating at a high speed in the air, leading to abrasive-free polishing on a simpler device.

2. Dynamic Friction Polishing

In the method proposed here, a diamond workpiece is polished without using abrasives but by being pressed at a predetermined pressure onto a special metal disc rotating at a high speed to generate dynamic friction. The authors named this "Dynamic Friction Polishing (*DFP*) Method". Compared with the existing method utilizing thermochemical reaction, the new method has a bigger potential for practical application as it doesn't require a vacuum chamber or/and an equipment to heat a disc.

3. Experimental Equipments

A schematic illustration of the polishing equipment and its external appearance are shown in **Fig.1** and **Fig.2**, respectively. A polishing tool was a metal disc with a diameter of 160mm (or 240mm in some cases) and was mounted on a spindle of a machining center(MC) with a tool holder. The lower surface of the metal disc was trued by cutting at a depth of cut of a=0.03mm using a tool set on the machine table to minimize run out of the disc. A sample prepared as a workpiece was a square pillar shaped single crystal diamond with (100) planes

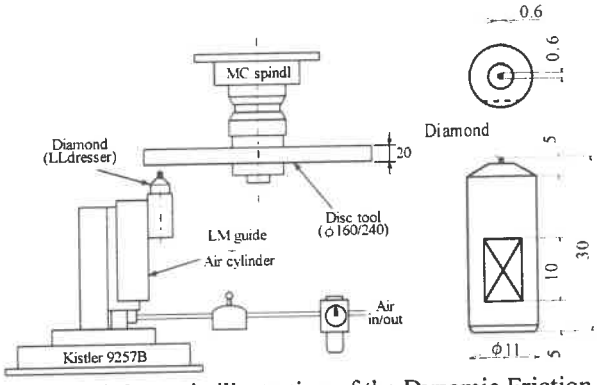

Fig.1 Schematic illustration of the Dynamic Friction Polishing and dimension of workpiece

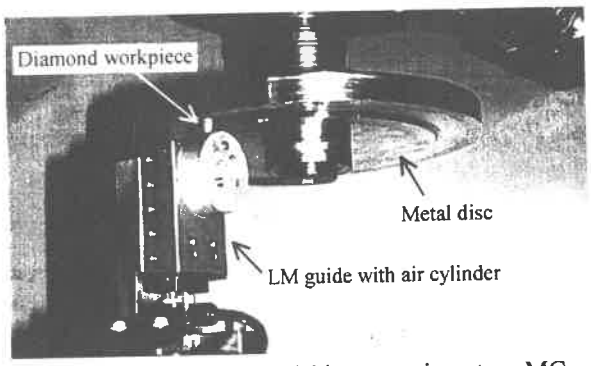

Fig.2 Abrasive free polishing experiment on MC

Table 1. Specifications of device and conditions

Device	Vertical MC, MT-V10(Mazak) + LM guide incorporated with an air cylinder
Disc	SUS304,S25C,S48C, ϕ160mm(ϕ240mm)
Cutting condition	Cutting edge: SNGG120408 V=96m/min,a=0.03mm,s=0.05,0.1 - 0.5mm/rev
Work-piece	Single crystal diamond Monodress(0.6x0.6x5mm, upper face:100), Holder:ϕ11mm(De Beers)
Polishing condition	Vs=1500,2000,2500,2750,4000m/min Vw=10,50,100,150,200,250,300mm/min, P=50,75,100,114,130MPa, L=10mm

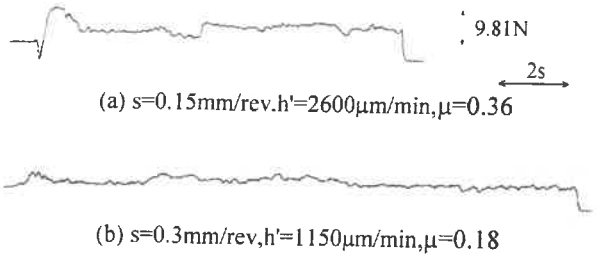

(a) s=0.15mm/rev.h'=2600μm/min,μ=0.36

(b) s=0.3mm/rev,h'=1150μm/min,μ=0.18

Fig.11 Change of tangential force at different disc surfaces
(SUS304 disc, Vs=4000m/min, Vw=200mm/min, L=10mm, P=114MPa)

significantly high removal rate was achieved in the range of Ra≒1.0~2.0μm is not clear enough, but it can be thought that the peak shape of the roughness curve in this region was sharp enough to give rise to the increase of surface pressure at contact points, giving improvement in polishing efficiency.

4.4 Condition of the polished surface

Fig.12(a) shows the condition of the polished surface of the diamond when relatively high polishing efficiency (h'=1300μm/min) was obtained. It is seen that SUS304 material is adhered on the polished surface. As can be seen from the roughness curve shown in Fig.12(b), the surface roughness obtained by Dynamic Friction Polishing is not good enough. Though the roughness value might be improved by varying the polishing conditions, another method was taken here, i.e. SiO_2 mixed solution (Compol 40 by Fujimi Inc.) was sprayed on the polishing disc surface and further polishing for 4 minutes was given on the diamond. The result was that the adhered material was cleanly removed and the peak to peak value of the surface roughness was improved from Rmax=0.6μm to Rmax=0.06μm (**Fig.13**a.b).

Material removing mechanism in the Dynamic Friction Polishing method has not been made clear yet. But from the facts that even an inclined surface can be easily polished (**Fig.14**) and that sparks fly during the process, it is suggested that it might be due to transformation or diffusion of diamond by thermochemical reaction.

5. Conclusion

Using a disc of SUS304 rotating at a high speed, abrasive-free polishing was carried out on single crystal diamond workpieces and, by optimizing the conditions, high polishing efficiency such as 2600μm/min (0.94mm^3/min) could be achieved.

Moreover, it is expected that this method can be used for flattening a wide area of surface and also for grooving by just mouting a stainless steel disc with a suitable thickness on a surface grinder in the same way as in ordinary surface grinding.

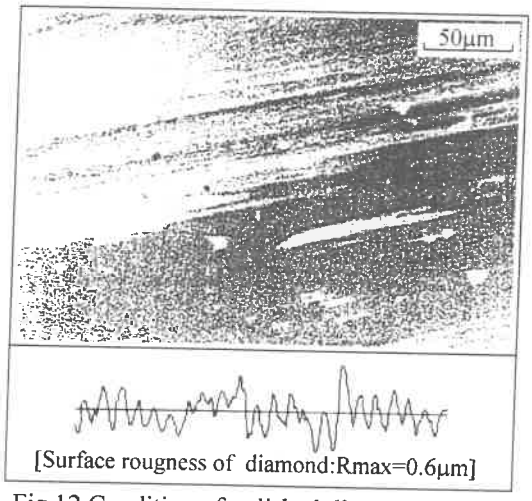

Fig.12 Condition of polished diamond surface by the Dynamic Friction Polishing method

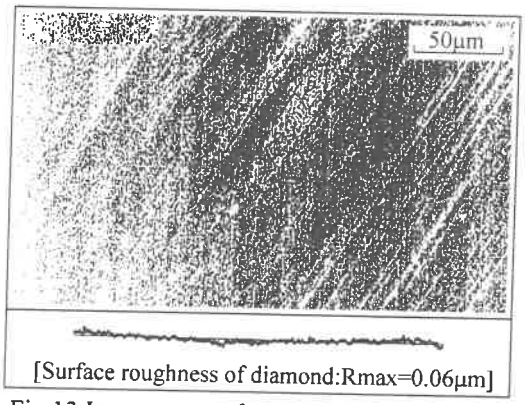

Fig.13 Imrovement of polished surface by coroidal silica

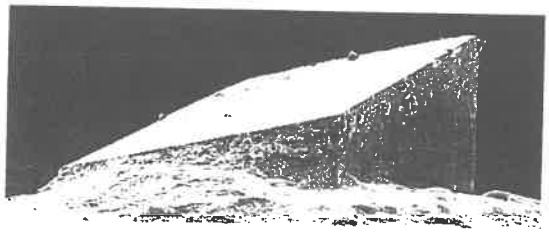

Fig.14 Slanted surface by the DFP method

In pursuing the study, the authors would like to express their heartfelt thanks to Noritake Diamond Co.Ltd., Ikegami Kanagata Kogyo K.K., Yamazaki Mazak Corp., Nisshin Seiko Co.Ltd., and Prof. S.Miyake of N.I.T. for their kind cooperation.

[References]
1)M.Yoshikawa et.al.:J.of JSPE 57-03(1991)106(in Japanese)
2)M.Yoshikawa et.al.:Proc. of JSDF's 8th Diamond Symposium (1994)16(in Japanese)
3)F.P. Bowden and H.G. Scott, Proc. of Royal Society, A248 (1958)368-378
4)N.Yasunaga et.al: J.of JSPE,38,4(1972)413(in Japanese)

Three-body Abrasive Wear Characteristics under Reciprocating Motion of CFRP in Vibrating Environment

Sadakazu TERAOKA *, Ken-ichi ISHIKAWA ** and Tatsuo NAKAGAWA **
* Kanazawa Technical College, ** Kanazawa Institute of Technology
* 2-270 Hisayasu Kanazawa Japan, ** Ohgigaoka Nonoich Kanazawa Japan

1. Introduction

Carbon fiber reinforced plastics (CFRP) has been widely used in industry because of their attractive mechanical characteristics.

Such CFRP parts are invariably subjected to three-body wear due to small indentations and machine vibrations.

In this study, the wear characteristics under the three-body condition and the abrasive wear of CFRP were investigated by using a vibrating environment and silicon carbide abrasive grains.

2. Experimental apparatus and method

The relation between the sliding direction and the lines of carbon fiber is defined as the rubbing direction. The L-direction is longitudinal and the T-direction is transverse, toward the lines of carbon fiber.

The abrasive wear apparatus is operated under the piston-reciprocated sliding friction based on the pin-on-plate method at as shown in Fig. 1.

The CFRP test piece (length 20mm x thickness 5mm x width 5mm) ① is fixed to the sliding table⑥ and it is rubbed on the plate(steel: S45C). The sliding table is moved by the crank⑧with the piston-reciprocated motion. The vibration action is created by using a mechanical oscillator④. The test piece is loaded by the weight of the sliding table⑥. The abrasive grain used for this

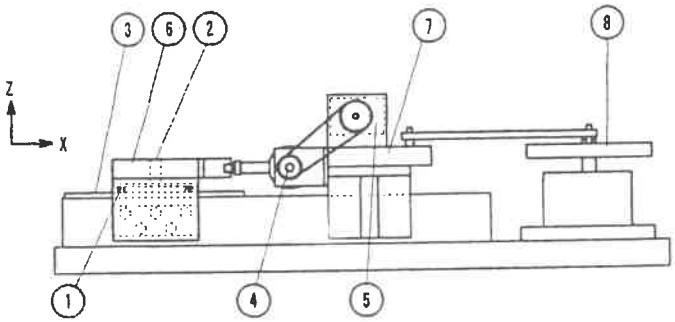

Fig. 1 Experimental apparatus

experiment is GC#600. A constant amount of the grain is supplied to the friction surface at hole②, and it was discharged from the side of sliding table.

The wear volume is detected by the decrease an amount of the test piece thickness using the micro-meter. The vibratory direction is parallel to the sliding direction. The X -directional vibration is the same as the sliding direction.

The sliding speed was considered as an average speed of the crank. The sliding distance, when the vibration acted, is not considered such as the moving length of the frictional surface, but is dealt with as a real sliding distance (Eq.(1)).

$$Lx = \dot{X}\left[1+\frac{2}{\pi}\left(\sqrt{V^2-1}-\cos^{-1}\frac{1}{V}\right)\right]\cdot t \quad \cdots (1)$$

where, t: friction time(s), ω :circular frequency(rad/s), a: amplitude (mm), V: velocity ratio($a\,\omega / \dot{X}$)

Table 1 Experimental conditions

Sliding speed	$\dot{X}$	13.3mm/s
Frequency	f	0-20Hz
Pressure	P	0.39MPa
Amplitude	a	0, 0.3, 0.5, 1.0, 1.95mm
Abrasive particles		GC#600

The velocity ratio(V) was defined as the maximum sliding speed ($a\omega$) of the test piece per sliding speed($\dot{X}$) of the plate. When vibration acts, the over-lapping ratio is defined by Eq.(2), then the calculated wear rate is defined by Eq. (3).

Over-lapping ratio:

$$Ov = \left(\overline{V_X} - \dot{X}\right) / \overline{V_X} \qquad \cdots \quad (2)$$

Wear rate:

$$W = Wn \cdot \left(1 - Ov\right) \qquad \cdots \quad (3)$$

where:

Wn: wear rate at non vibration(mm^2/m)

The experimental conditions are shown in Table 1.

3. Results and considerations

Fig.2 and Fig.3 show the relationship between the velocity ratio and the wear rate of CFRP and Epoxy resin. The doted line shows the calculated wear rate, considering wear volume under the non vibration and the over-lapping ratio(Eq.(3)).

When the velocity ratio is from 0 to 1, the wear rate is subjected to non-vibration effects, because the vibration velocity of the test piece is smaller than that of the frictional surface. When the velocity ratio is more than unity, the wear rate decreases. The wear rate of Epoxy resin is smaller than the CFRP. When a flexural strength of the fiber is low, it is broken briefly at the transverse force and therefore, the effect of fiber reinforcement does not exhibit with the three-body abrasive wear.

In the amplitude 0.3mm (Fig. 3 (a)), the experimental value is agreement with the calculated value. In the amplitude 0.5mm (Fig. 3 (b)), the experimental results agree well with the calculated value as far as the velocity ratio 1.9. In the amplitude 1.0mm (Fig. 3 (c)), the velocity ratio is 1.4, and in the amplitude 1.95mm(Fig. 3(d)), its ratio is 1.2.

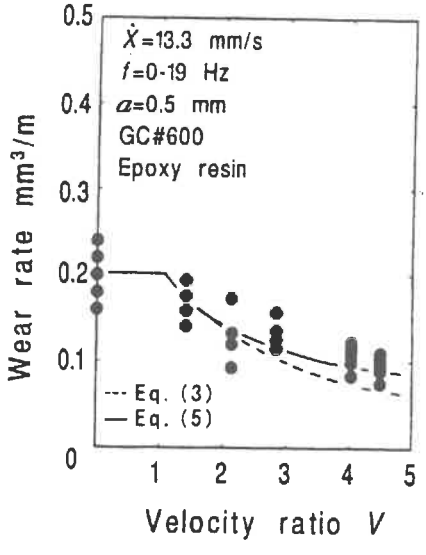

(a) a =0. 5mm

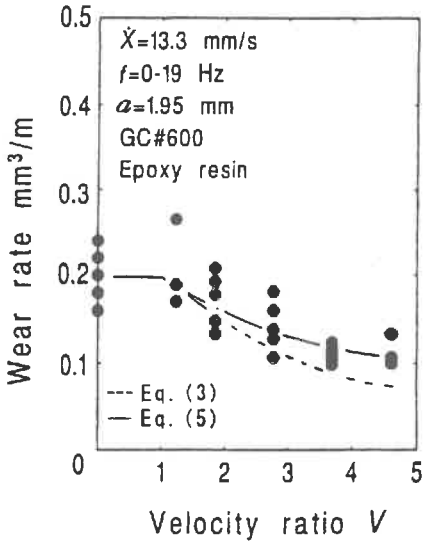

(b) a =1. 95mm

Fig. 2 Relationship between velocity ratio and wear rate (Epoxy resin)

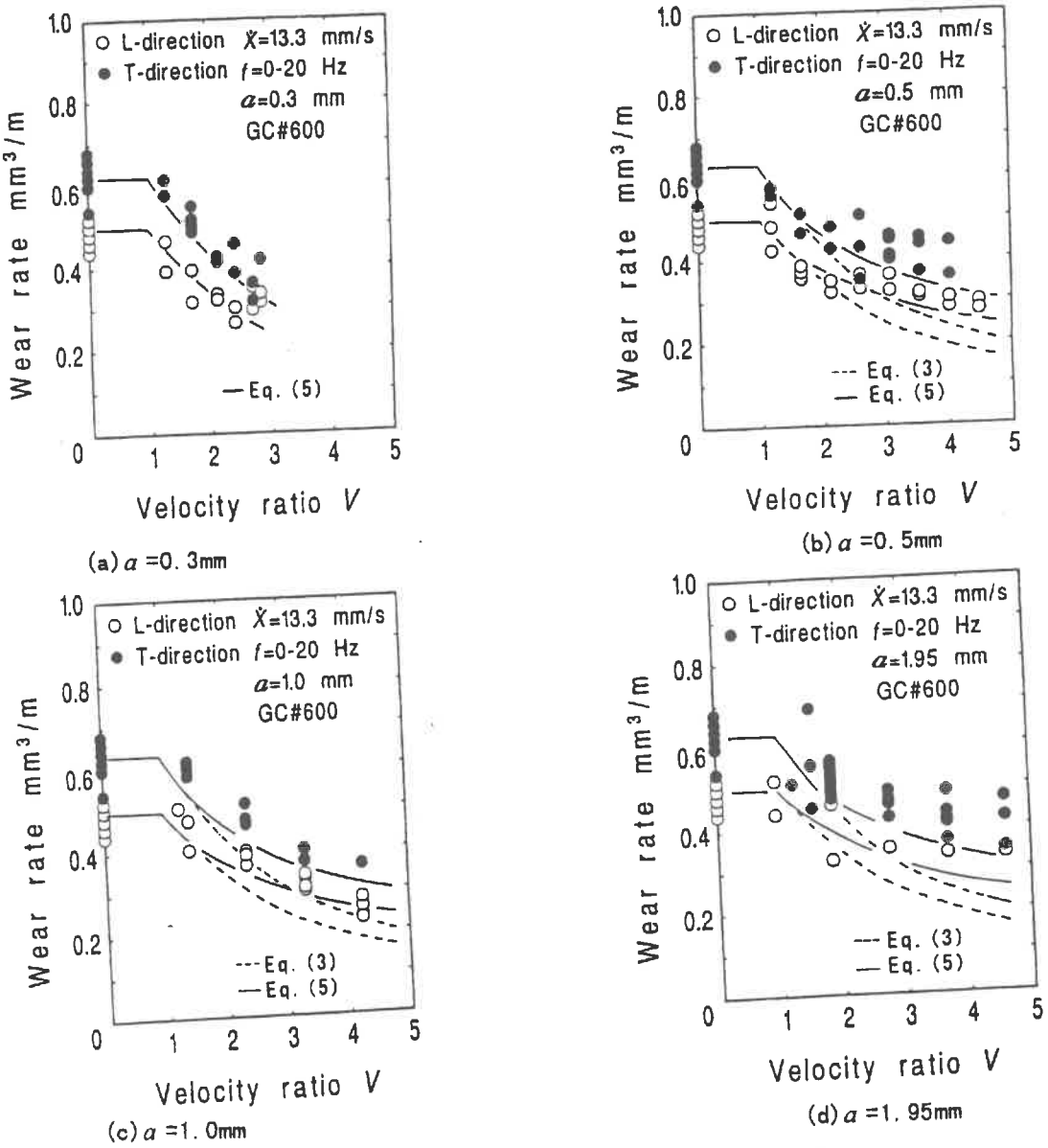

Fig. 3 Relationship between velocity ratio and wear rate (CFRP)

When the amplitude and the over-lapping distance increases, the motion of the abrasive grains become active rapidly. The over-lapping distance is defined by Eq. (4).

Over-lapping distance:

$$L_{OV} = 2 \cdot \left[a \left\{ \sin\left(\cos^{-1} \frac{1}{V} \right) \right\} - \frac{\dot{X}}{\omega} \cdot \left(\cos^{-1} \frac{1}{V} \right) \right] \quad \cdots\cdot(4)$$

Fig. 4 shows the velocity ratio and the over-lapping distance. In any amplitude, the over-lapping distance is 0.3mm, when the experimental value is not in comparison with calculate value.

The wear rate is calculated as follows:

1) In the velocity ratio from 0 to 1, the wear rate shows the same value at the non-vibration action.

2) In the over-lapping distance from 0 to 0.3mm, the wear rate was calculated by Eq.(4).

3) When the over-lapping distance is larger than 0.3mm, the place of the overlap is

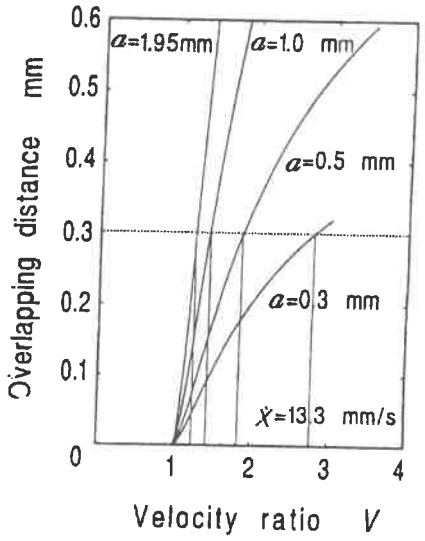

Fig. 4 Relationship between velocity ratio and over-lapping distance

influenced by the rolling and the scratching action of the abrasive grain. The value(*Rov*) is 30% mean frictional action. Then the wear rate is calculated by Eq. (5).

Wear rate:

$$Won = W + Wn\left\{2\left(Lov - 0.3\right) / \overline{Vx} / f\right\} Rov \cdots (5)$$

The calculated result is shown in Fig. 2 and Fig. 3 using a solid line. The experimental results agree well with the calculated value.

When the over-lapping distance is smaller than 0.3mm , the wear rate is not dependent upon the vibration. When the over-lapping distance is larger than 0.3mm, the wear rate depends on the vibration.

Fig. 5 shows observed results of CFRP by means of SEM. When the over-lapping distance is smaller than 0.3mm (Fig. 5 (a), (b)), the surface of CFRP showed a small indentation. As the over-lapping distance is larger than 0.3mm (Fig. 5 (c)), the breakage is sever.

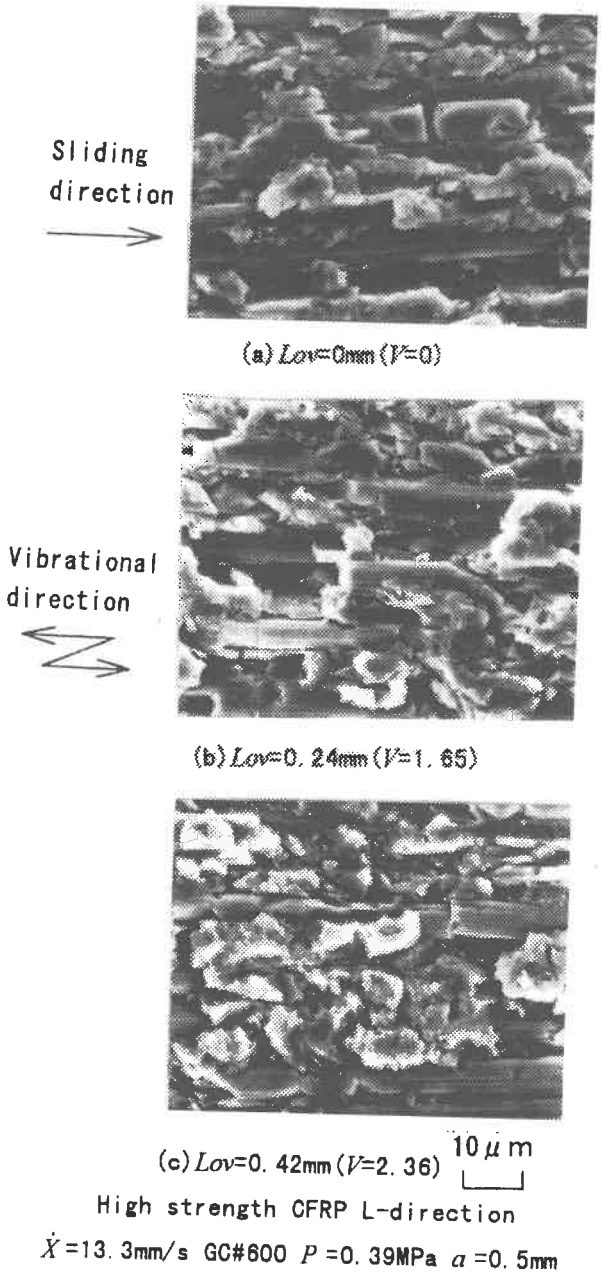

Fig. 5 Observation of CFRP

4. Conclusions

1) In the abrasive wear of CFRP, the effect of the fiber reinforcement is exhibited with the two-body abrasive wear. However, its effect was not exhibited with the three-body abrasive wear due to the rolling action of the grains.

2) In the vibration action when the over-lapping distance is smaller than 0.3mm, the wear rate does not depend on the vibration.

3) When the over-lapping distance is larger than 0.3mm, the wear rate dose not depend on the vibration.

SURFACE INTEGRITY OF POLISHED INFRA-RED OPTICS AND GLASS

Prof. V.C. Venkatesh*, W.K. Chee*, Dr. K.L. Pey**, K.H. Tan* & Dr. A. Trigg**
* School of Mechanical & Production Engineering, Nanyang Technological University, Singapore 639798
** Failure Analysis & Reliability Department, Institute of Microelectronics, Singapore 0511

ABSTRACT

Polished brittle materials, both hard (glass, Si, and Ge) and soft (ZnSe, ZnS, and GaAs) were examined by SEM and AFM for residual scratches; the AFM has a better resolution and pictures of these are compared with SEM. Preston's coefficient for ZnSe and glass (plano, convex and concave) were determined and their values were found to closely match each other and those obtained by other international research workers. Polishing was found to be easier when ductile streaks were present when the partial ductile mode grinding process was employed. Single grit diamond machining was carried out on hard brittle and soft brittle materials and a distinct difference in pile up was observed.

1.0 INTRODUCTION

Brittle materials like Si, Ge, and glass are hard and brittle whereas ZnSe, ZnS, and GaAs are soft and brittle. The hard materials are easy to grind and polish whereas the soft materials are difficult to polish and need non-toxic chemicals [1]. In association with opthalhmic and infra-red optics industries, the polishing process was investigated and Preston's coefficients were determined [2, 3]. Polishing was found to be easier when ductile streaks were present when the partial ductile mode grinding process was employed [4]. Studies were carried out on the polished surfaces by SEM (scanning electron microscopy) and AFM (atomic force microscopy) to determine the extent of scratches left behind. Finally, single grit grinding was done on polished surfaces to study lateral displacement (pile up).

2.0 PRESTON'S COEFFICIENT

Preston's equation is a rate equation which simply states that the velocity of the surface recession, *dT/dt*, is related to the relative velocity between part and lap, *ds/dt*, through elasticity. This model assumed that a population of uniform size spheres penetrate the ideal plane of the workpiece in elastic Hertzian fashion, and in shear, plough a groove whose cross section is proportional to that of the penetration [5]. Preston's equation is defined as $\frac{dT}{ds} = kp\frac{ds}{dt}$, where *dT/dt* is the layer removed per unit time, *k* Preston's coefficient, *p* the polishing pressure, and *ds/dt* is the relative speed between pad and substrate.

The results of polishing on glass and infra-optics are tabulated on Table 1. For ZnSe, Preston's coefficients are always the same order of 10^{-13} to 10^{-12} m^2/N (10^{-14} to 10^{-13} cm^2/dyne) [2]. Similarly, for glass, Preston's coefficients are of the order of 10^{-13} to 10^{-12} m^2/N (10^{-14} to 10^{-13} cm^2/dyne) [3]. These values coincide with the results of polished silicate and BK7 [5, 6]. Recent research has pointed out that Preston's coefficients for all kinds of standard glass polishing techniques are almost the same as long as a similar chemistry is applied [7]. The differences in material removal rate are merely due to different speeds and pressures.

Noting that Preston's equation describes the abrasive wear, the closeness of the results obtained seems to suggest that a similar set of abrasion phenomena underlay most polishing processes and that abrasion dominated the wear removal. However, it should be noted that only in gentle abrasion (which is the case for ZnSe and glass) plastic deformation dominates rather than hardness. The latter dominates in the more violent range of coarse abrasive removal [5]. At the same time, chemical influence cannot be ignored regardless of how minor the effect is. In fact, Brown, has indicated a strong chemical influence in the oxide abrasives CMP (chemical mechanical process) [5].

Table 1 Preston's coefficient for ZnSe and glass

Sample	Thickness removed during polishing, ΔT (μm)	Pressure, *p* (KPa)	Polishing time, *dt* (min)	Relative speed, *ds/dt* (m/s)	Preston coefficient, *k* (m^2/N)*
A (ZnSe)	78.4	137.9	240	0.1164	3.4×10^{-13}
B (ZnSe)	94	34.5	300	0.1164	1.3×10^{-12}
C (ZnSe)	41.3	13.4	300	0.1164	1.47×10^{-12}
D (ZnSe)	83.2	33.9	300	0.1164	1.17×10^{-12}
E (Plano Glass)	55	400	4	3.819	1.5×10^{-13}
F (Concave Glass)	161.5	400	1.75	3.496	11×10^{-13}
G (Convex Glass)	146	400	1.75	3.476	10×10^{-13}

* *multiply m^2/N by 1×10^{-1} to give cm^2 /dyne*

3.0 SCANNING AND ATOMIC FORCE MICROSCOPY

The polishing process however good it may be, leaves behind marks. Polished surfaces when viewed under SEM barely reveal any marks. However, under AFM, polishing marks are so evident as to cause concern. However, infra-red optics materials had a quality similar to that of glass optical flats as far as surface roughness and flatness are concerned. Polishing marks of infra-red optics and glass imaged under SEM and AFM were compared. (Figure 1 - 2). The images obtained clearly depict the superiority of AFM in imaging the polishing marks over SEM. Table 2 gives a summary of the capabilities of the two equipment [8].

Table 2 Characteristics of SEM and AFM [8]

	SEM	AFM
Sample operating environment	vacuum	ambient liquid vacuum
Depth of field	large	medium
Depth of focus	small	small
Resolution		
x, y	5 nm	0.1 – 1.0 nm
z	< 1 nm	0.01 nm
Magnification range	10X – 10^6X	5×10^2X – 10^8X
Sample preparation required	freeze drying, coating	none
Characteristics required of sample	surface must not build up charge and sample must be vacuum compatible	sample must not have excessive variations in surface height

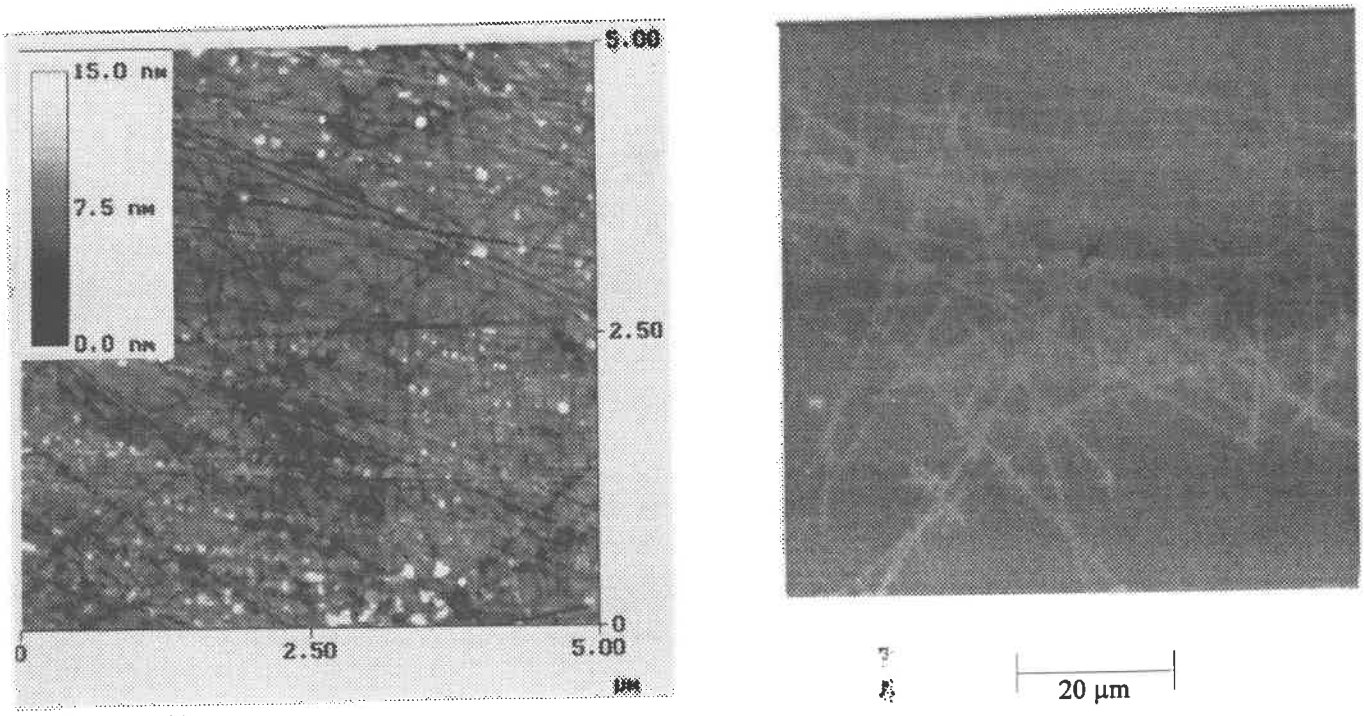

Figure 1 Surface topography of ZnSe imaged by AFM (left) and SEM (right)

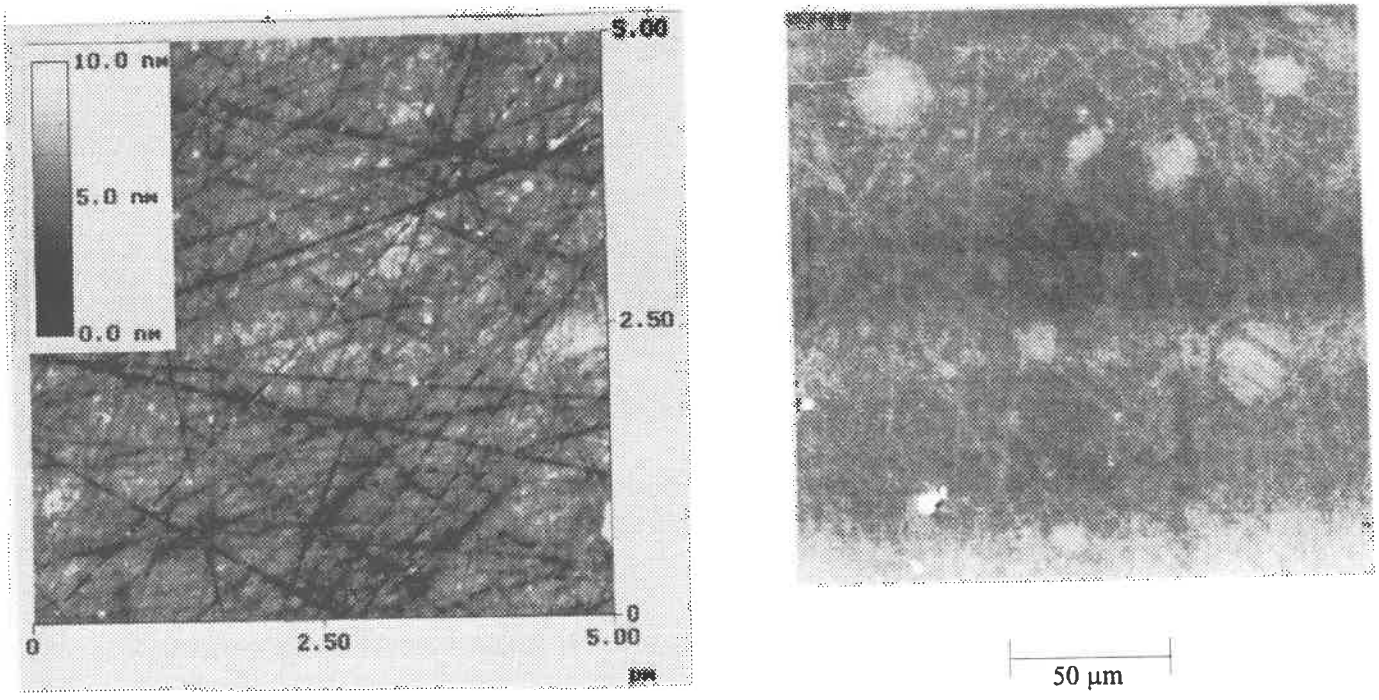

Figure 2 Surface topography of Ge imaged by AFM (left) and SEM (right)

4.0 SINGLE GRIT MACHINING

A coni-spherical diamond was used (Figure 3) for the single grit machining; given its accurate symmetry, the results of single and double pile up are due to material factors and not tool geometry. Single grit grinding was done on single crystal ZnSe (soft but brittle), Si, and glass (hard but brittle) using the Form Talysurf. It was observed that there is a distinct difference in the lateral displacement of the three materials. For ZnSe (Figure 4), equal pile up was observed, whereas only a single side pile up were observed on Si and glass (Figure 5-6). Reasons for this are still unclear and are being studied. The double pile up could be due to the softness and mono-crystalline nature of ZnSe. The single pile up could be due to the hardness and poly-crystalline nature of Si and glass.

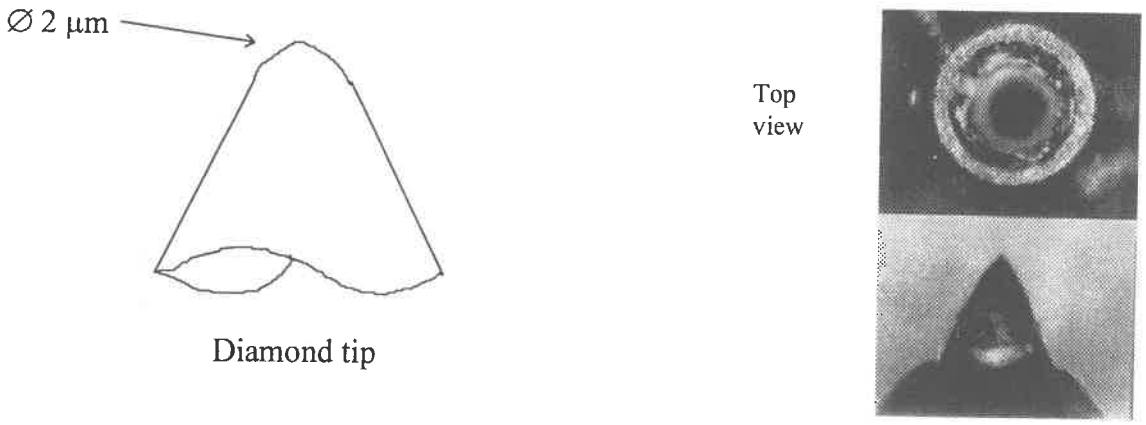

Figure 3 Coni-spherical diamond

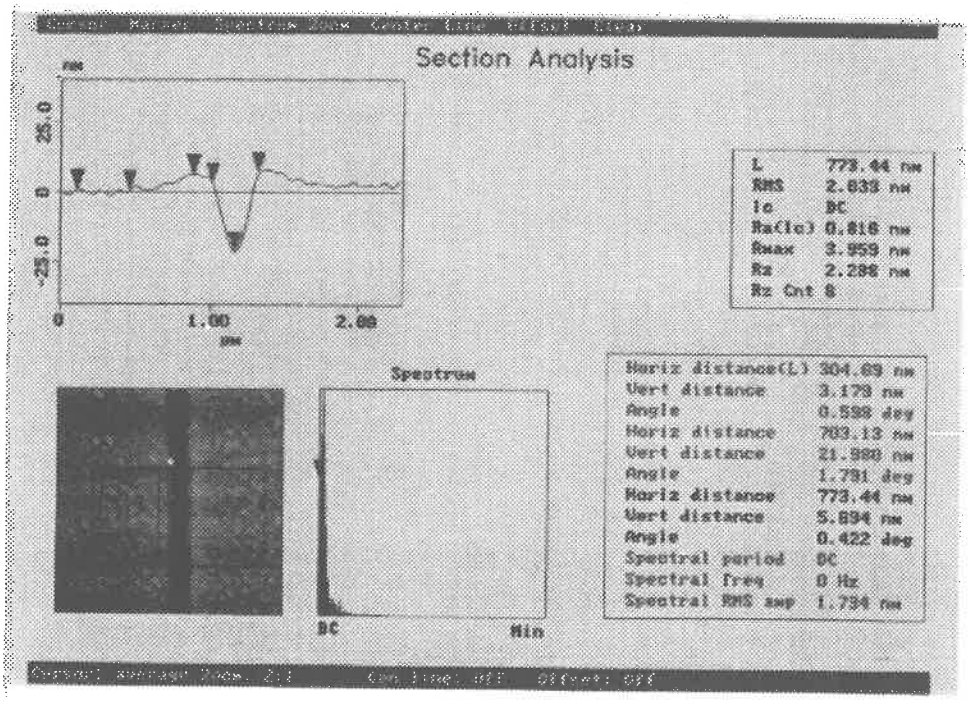

Figure 4 Ploughing action (without chip formation) causes equal pile up (ridges)on both sides for soft brittle mono-crystalline ZnSe

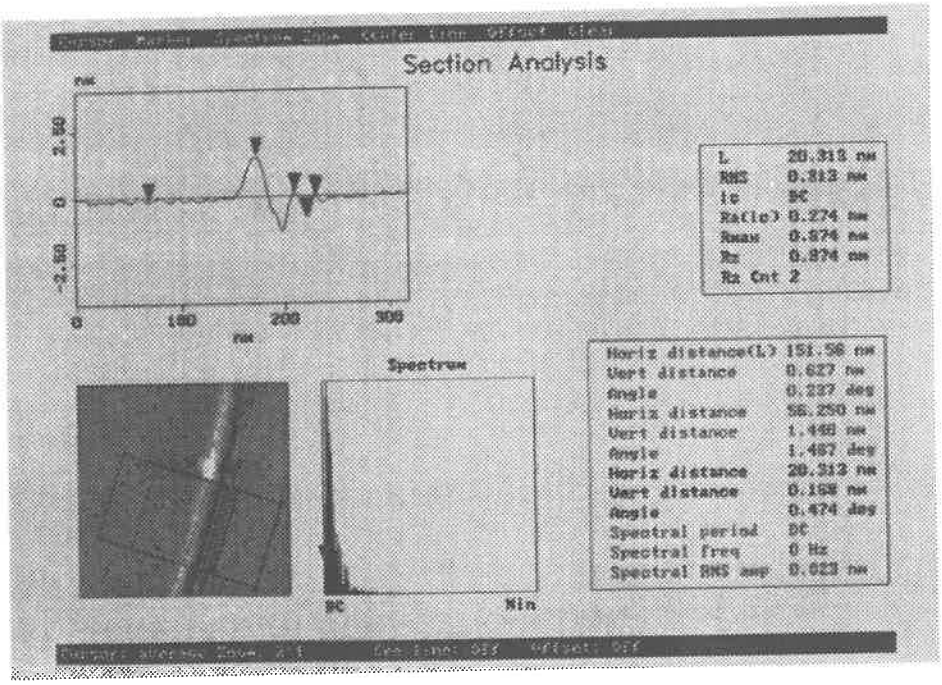

Figure 5 Pile up on only one side on hard brittle poly-crystalline Si

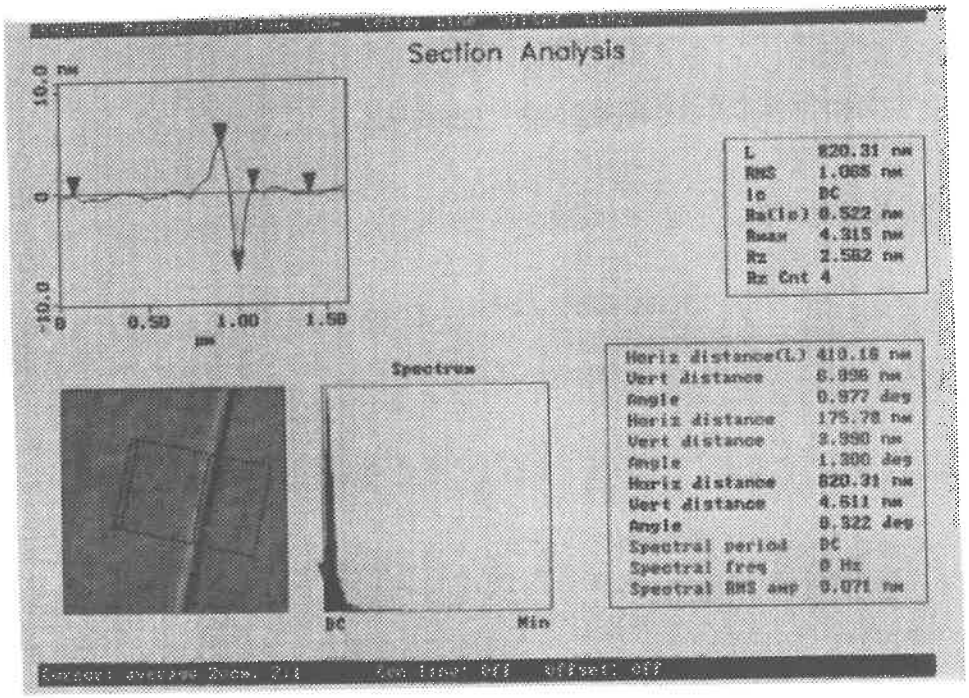

Figure 6 Pile up on only one side on hard brittle glass which is amorphous

5.0 CONCLUSIONS

1. The Preston's coefficient found for ZnSe and glass have the same order of magnitude (10^{-13} to 10^{-12} m^2/N). This suggests that a similar set of abrasion phenomena underlay most polishing process {Table 1).

2. The comparison of SEM and AFM shows the superiority of AFM in imaging fine polishing marks (Figure 1-2).

3. Double side pile up was observed on soft brittle ZnSe while single side pile up was observed on hard brittle glass and Si (Figure 4-6). Reasons for this are still unclear and are being studied. Possible reasons could be softness/hardness and mono/poly-crystalline nature of materials.

6.0 REFERENCES

1. Venkatesh, V.C., Inasaki, I., Toenshof, H.K., Nakagawa, T., and Marinescu, I.D. 1995. Observation on polishing and ultraprecision machining of semiconductor substrate materials. Annals of the CIRP 44/2: 611-618.

2. Chee, W.K. 1996. Surface integrity studies on hard and soft infra-red plano and spherical lenses. B.Eng. (Mech.) Thesis, Nanyang Technological University, Singapore.

3. Tan, K.H. 1996. A study of material removal during the polishing of precision spherical glass lenses. B.Eng. (Mech.) Thesis, Nanyang Technological University, Singapore.

4. Venkatesh, V.C., and Zhong, Z. 1995. Manufacture of spherical and aspheric surfaces on plastic, glass, and ceramics. Transactions of NAMRI/SME. Volume XXIII.: 669-174.

5. Brown, N.J. 1991. Lapping: polishing and shear mode grinding. Optical Society of America 3/1: 13-24.

6. Brown, N.J. 1987. Some speculations on the mechanisms of abrasive grinding and_polishing. Journal of Precision Engineering 9/3: 129-138.

7. Fiedler, K.H. 1995. Processing (Grinding and Polishing). From Neuroth, B. (ed.), The properties of optical glass. Berlin Heideiberg, Germany: Springer-Verlag. 247-264.

8. Strausser, Y.E., and Heaton, M.G. 1994. Scanning Probe Microscopy Technology And Recent Innovations. Santa Barbara, USA: American Laboratory: 1-2.

Burr and shape distortion in micro-grooving of optical components

Jung-Hwan Ahn*, Han-Seok Lim*, David A. Dornfeld**
* Pusan National University , Pusan, KOREA
** UC Berkeley, CA, U.S.A.

1. Introduction

Micro-groove, ranging in size from a few microns to several tens of micron, is the basic geometric shape of miniaturized/thinned optical components such as fresnel lens, lenticular lens, reflecter, etc. Requirements of high precision shape/surface quality for optical parts to function as designed need such a ultra-precision machining with a single point diamond tool. It has also a unique advantage that various grooves can be made only by changing the tool geometry or the machining program.

However, actual problems such as shape distortion and burr, which might be caused by high specific cutting force and ductile mold materials, is so undesirable because it absolutely degrade the performance of optical components. Many researches have been conducted about burr generation mechanism mostly in conventional machining[1,2]. Burr in a single groove, which swells up at both sides of a groove, was investigated.[3,4]

In this study, a simplied model of the burr/shape distortion in grooving multiple micro-grooves is proposed and the effects of cutting parameters such as depth of cut, groove angle, etc. are experimentally investigated.

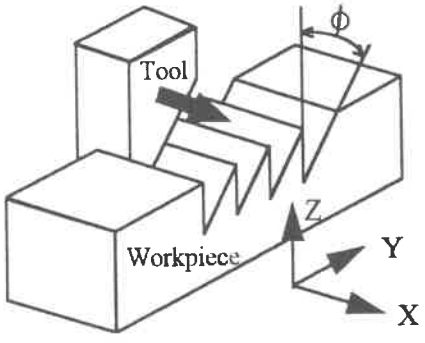

Fig.1 Array of micro-grooves and tool

2. Model of burr and shape distortion in micro-grooving

The term "burr", cited here, is limited to the burr which is generated at the summit of groove tooth, and, thus is equivalent to side burr in milling and grinding. Fig.1 shows the geometrical shape of an array of micro-grooves and a tool. Fig.2(a) shows a simplified model of burr generation and shape distortion and Fig.2(b) shows designations for burr height(Bh), burr thickness (Bt) and shape distortion(Dϕ).

When the tool begins cutting, the groove tooth is elastically/plastically deformed by the thrust force normal to groove surface during chip separation. The pre-generated burr hanged on the tooth edge rotates away the cutting edge so that only a part of burr is cut away by the tool. The rest of the burr remaines accumulated on the newly-generated burr. This is the formation process for burrs in multi-

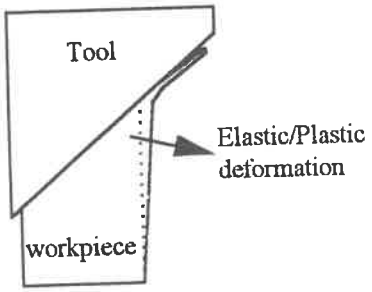

(a) Deformation of workpiece

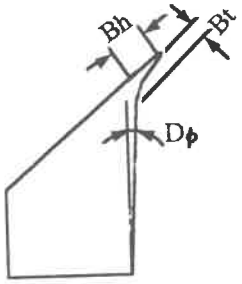

(b) Designation of burr/shape distortion

Fig.2 A model of burr/shape distortion in grooving

groove operations. That is, a combination of bending, shear and Poisson deformation due to both thrust force and the geometrically-weakened-tooth is assumed to cause the burr and shape distortion in multi- grooving.[5]

3. Experimental method

Fig.3 shows the schematic diagram of experimental setup. The self-developed machine has a microstepping motor driven z-axis with a resolution of 0.2 m and an AC servo motor driven XY table with a resolution of 1 m and is mounted on a granite plate with vibration-absorbed air springs. Cutting forces are measured with a tool dynamometer and recorded while grooving for afterward data analysis.

Cutting parameters to be investigated are depth of cut, groove angle, and workpiece material. Cutting speed, cutting edge radius, rake angle and tool setting angle are to be kept constant 5mm/s, 0.8μm, 0 deg and 0 deg respectively. The experiments were conducted in 2 ways. One is, for the convenience of measuring cutting force and burr shape, the orthogonal cutting with 0.5mm thick workpiece, so called single-grooving, and the other is multi-grooving to measure the shape distortion. Every experiment under a given condition is conducted repeatedly up to the total accumulated depth of 100μm and the total amount of burr and shape distortion is compared. Cutting condition is summarized as Table 1.

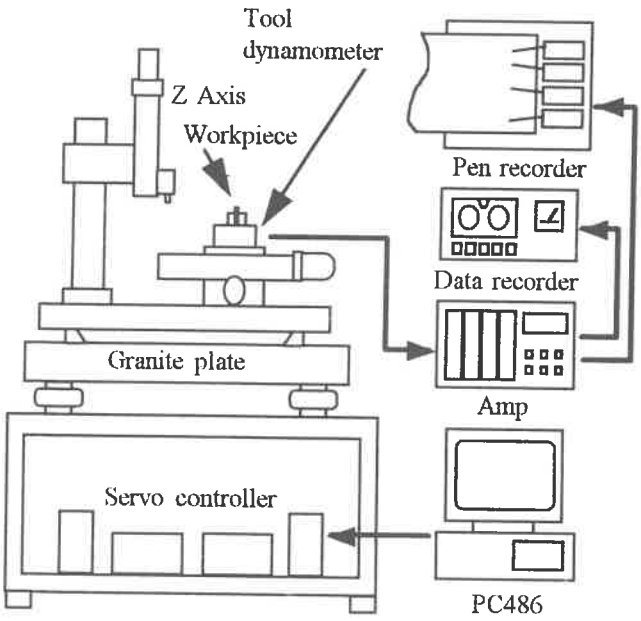

Fig.3 Schematic diagram of experimental setup

Table 1 Experimental cutting condition

scheme	speed	pitch	groove angle	depth of cut	work piece
single	5mm/s	-	20°-80°	1-12μm	brass Al7075 OFHC
multiple		50μm	50°	1-50μm	

4. Experimental results and discussion

4.1 Burr shape and shape distortion

Fig.4 shows (a)top view and (b)side view of a machined surface. Burr develops outwards at the sharper side of groove surface while nothing happens at the blunt side. This implies that burr of micro-grooving is generated in other way than in milling or grinding.

Fig.5 is a microscopic photograph showing cross-sectional view of distorted gooves. Grooves are deformed opposite to tool feeding direction, because the stiffness of groove tooth is not enough to sustain the thrust cutting force. Proper cutting condition, therefore, should be selected to keep burr/shape distortion within a tolerance level.

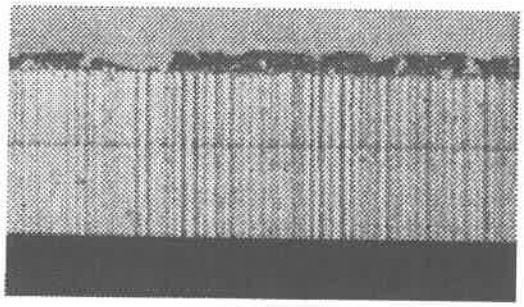

(a) Top view

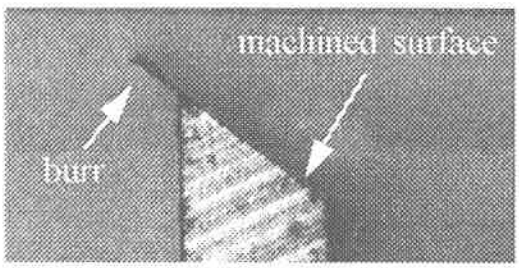

(b) Side view

Fig.4 Machined surface and burr

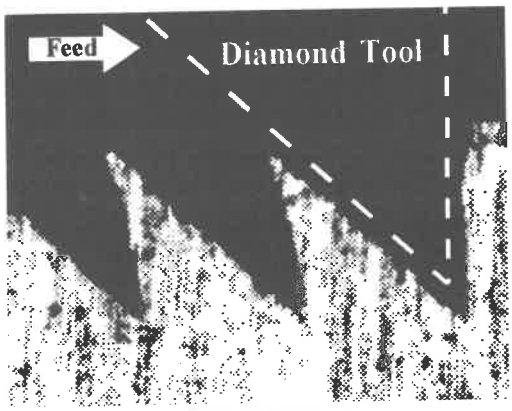

Fig.5 Shape-distorted groove

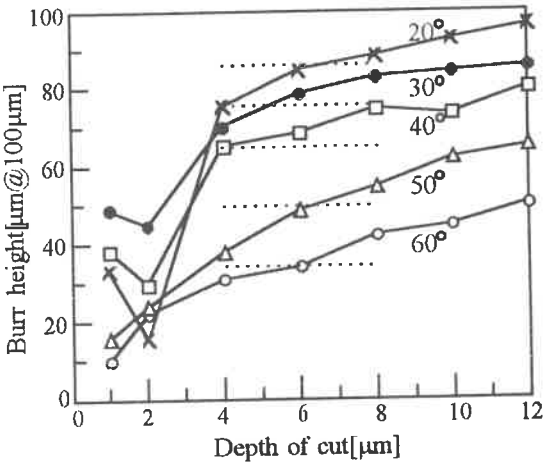

Fig.6 Accumulated burr height

4.2 Effects of depth of cut and groove angle

Fig.6 shows the accumulated burr height for 100μm depth-groove with depth of cut and groove angle varied. As depth of cut increases, burr gets thicker and larger. Burr height is nearly proportional to depth of cut.

As shown in Fig.7, in larger than 6μm of depth of cut, burr gets uniform. Meanwhie, in smaller depth of cut, burr becomes thinner and nonuniform with parts of burr torn out probably by the shear force and even small cracks in the boundary between burr and workpiece.

Smaller groove angle results in larger burr height. As the groove angle is getting smaller, the stiffness of tooth is getting lower and it causes the larger bending deformation which results in a larger burr. This demonstrates well the suggested model of burr in grooving.

As shown in Fig.6, for brass, 6μm may be a critical depth of cut where burr characteristics in view of uniformity and possibility of

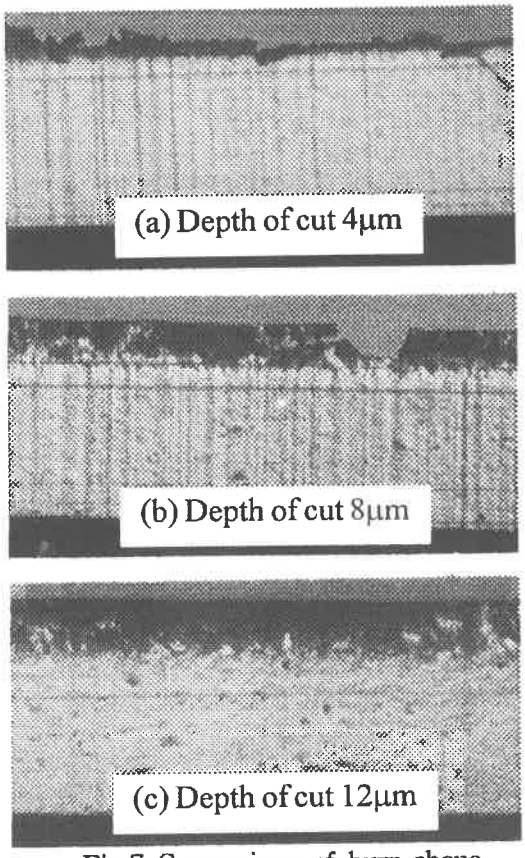

Fig.7 Comparison of burr shape

removal changes rapidly. The accumulated burr height at the depth of cut of 6μm is nearly equivalent to the projection(Bp) of the accumulated depth of 100μm on the machined surface. Dotted line indicates Bp for each groove angle. Cutting conditions to result in burr less than Bp would be recommended to help deburring following grooving.

Fig.8 shows cutting forces with depth of cut and groove angle varied. As depth of cut increases, both cutting forces increase almost linearly. As groove angle decreases, the thrust force increases largely whereas the principal force increses just a little. What is most important is that Fy, the y-directional component of thrust force, increases rapidly with groove angle decrease, as shown in Fig.8. It is considered due to the increase of elastic force reacted by the groove tooth which is largely elastically deformed. This also verifies why the burr is dominant at the sharp side in single- grooving.

4.3 Effects of workpiece material

Fig.9 shows the effect of workpiece

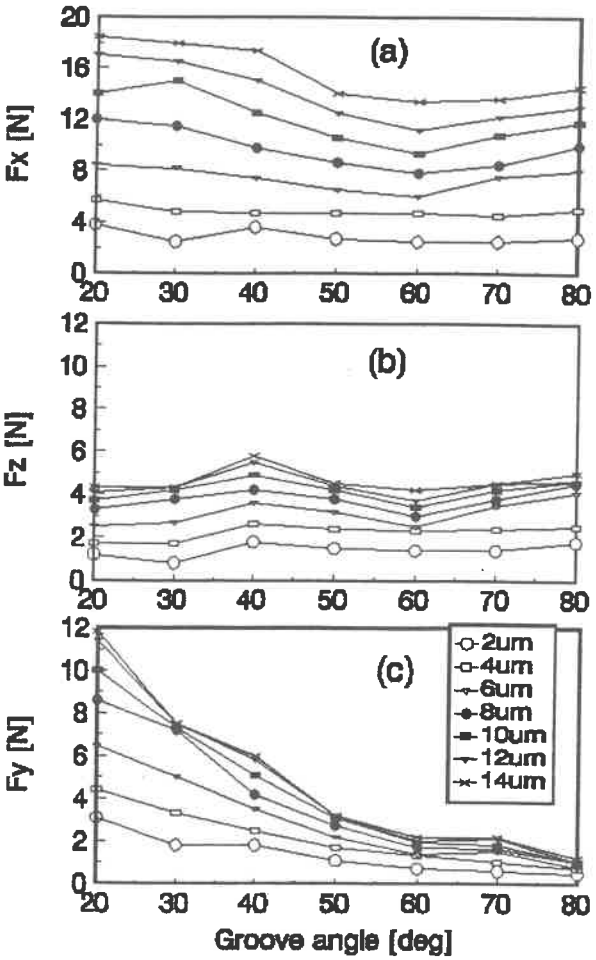

Fig.8 Variations of cutting forces
(a) principal force
(b) z-component of thrust force
(c) y-component of thrust force.

material to the burr height(a) and shape distortion(b) in multi-grooving. In Fig.9(a), the burr height increase with depth of cut like in Fig.6. Aluminium and copper seem to generate larger burr than brass because they are more ductile. As shown in Fig.9(b), shape distortion does not occur when depth of cut is less than 30μm because the strength of tooth can sustain the thrust force. Over 30μm shape distortion occurs nearly propotionally to depth of cut. Shape is less distored in brass than in the others because the strength of brass is higher.

Therefore shape distortion is less significant once depth of cut is selected referring to Bp.

5.Conclusion

1) The thrust force in micro-grooving plays a

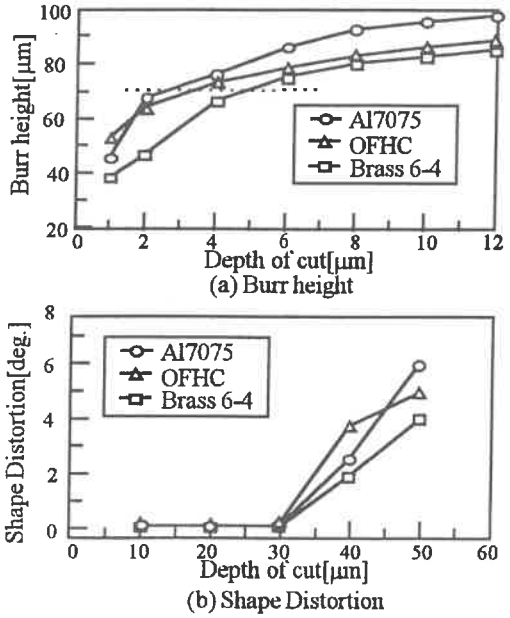

Fig.9 Accumulated Burr height and shape distortion of multi-grooving

significant role in burr generation and shape distortion.

2) Burr of micro-groove grows largely due to bending deformation caused by large groove angle and large depth of cut.

3) A critical depth of cut, where an accumulated burr height is less than the projection(Bp) of the accumulated depth of cut, is recommended for deburring after grooving.

4) Shape distortion is less significant when depth of cut is selected considering less burr.

References

[1] L.K. Gillespie, P.T. Blotter, The Formation and Propeties of Machining Burrs, J. of Eng. for Ind., Trans. of ASME, Feb., pp66-74, 1976

[2] Sung-Lim Ko, David A. Dornfeld, A sutdy on Burr Formation Mechanism, J. of Eng. Mat. and Tech., Trans. of ASME, Vol.113, Jan., pp75-87, 1991

[3]Ueda. K., Sumiya. M., Ultra High Precise Micro Grooving, J.of JSPE, Vo..52, No.12, pp. 22-25, 1986(in Japanese)

[4]Toshio Tamura, Noriyoshi Arakawa, Masami Masuda, Generation Phenomena of Burrs in Micro Grooving of Single Crystal Ferrite, J. of JSPE,Vol.57,No.5,pp.155-160,1991.(in Japanese)

[5]Kazuo Nakayame, Minoru Arai, Burr formation in metal cutting, Annals of the CIRP, vol.36, No.1, pp33-36, 1987

AN EMPIRICAL TOOL FORCE MODEL FOR PRECISION MACHINING

Christopher Arcona[1] and Thomas A. Dow[2]

INTRODUCTION

The components of the steady-state cutting forces in metal machining operations contain a wealth of information on the material removal process. Changes in these forces indicate changes in machining parameters, such as the depth of cut and tool sharpness. Thus, it should be possible to exploit tool force as a monitor of precision machining processes. The effective use of tool force in a feedback control scheme would require an understanding of the parameters that affect the force components and a model of the relationships between them. Unfortunately, an empirical model that would facilitate rapid data processing is not currently available for precision metal machining, although considerable effort has been expended in attempts to explain the cutting process [1-5].

A model of the machining process that is based on experimentally observed material flow is discussed in this paper. Chip formation is modeled as a process of shear where the angle of the shear zone is determined by the coefficient of friction between the chip and the tool. This proposed model also accounts for the contribution of elastic deformation of the workpiece to the total force on the tool and allows machining forces to be calculated from basic material parameters. Metals having dissimilar properties and grain structure (electroless nickel, electroplated copper, 6061-T6 and 5086 aluminum alloys) were studied. All machining experiments were carried out with a diamond tool having a 5.08 mm nose radius, 0° rake angle and 8° clearance angle.

TOOL FORCE MODEL

The chip structure of the four materials has been studied with the aid of a technique that produces high resolution images of the chip flow [6]. Consider the plated copper chip cross section in Figure 1. This chip was created with the freshly lapped diamond tool at a cutting speed of 25 mm/min. The morphology of this type of chip has been discussed elsewhere [6-8]. For this study, the important chip characteristic is the "shear angle,"or the angle that the thin, highly deformed zones make with the horizontal. For the plated copper chip shown in Figure 1, the shear angle, ϕ, is about 45°, as indicated in Figure 2. Figure 2 depicts the same cross section with the outline of the next segment overlayed. This segment would form if the tool could be replaced and moved about 500 nm to the right. The forces on this representative section are indicated in the diagram. The total force acting on the tool in the cutting direction is F_c. The force in this direction associated with elastic deflection of the workpiece, or material spring back, is $F_{celastic}$. The tool forces due to this elastic deformation of the workpiece have been shown to be significant in

1 Staff Engineer, International Business Machines Corp.; San Jose, CA 95193
2. Professor, Precision Engineering Center, North Carolina State University, Raleigh, NC 27695-7918

diamond turning, even for machining with a sharp tool [9]. The shear and normal forces on the shear zone inclined at the angle ϕ are F_s and F_n, respectively, while μ is the coefficient of friction between the tool and the chip. The equation for the total cutting force is obtained through a balance of forces in the horizontal direction. The total normal or thrust force, F_t, is provided by frictional forces on the tool rake face and the normal force associated with spring back ($F_{t_{elastic}}$). Thus, the force components are given by

$$F_c = F_s \cos\phi + F_n \sin\phi + F_{c_{elastic}} \tag{1}$$

$$F_t = \mu(F_c - F_{c_{elastic}}) + F_{t_{elastic}} \tag{2}$$

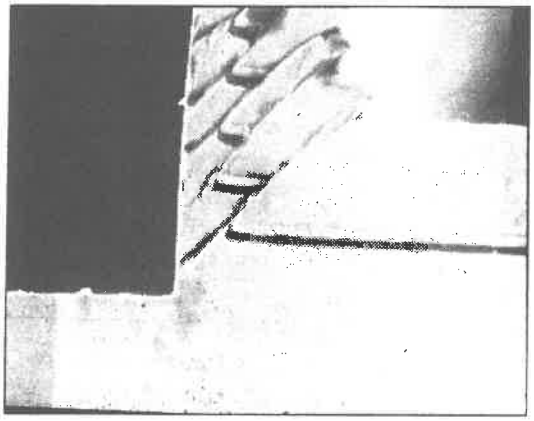

Figure 1. Cross section of plated copper chip.

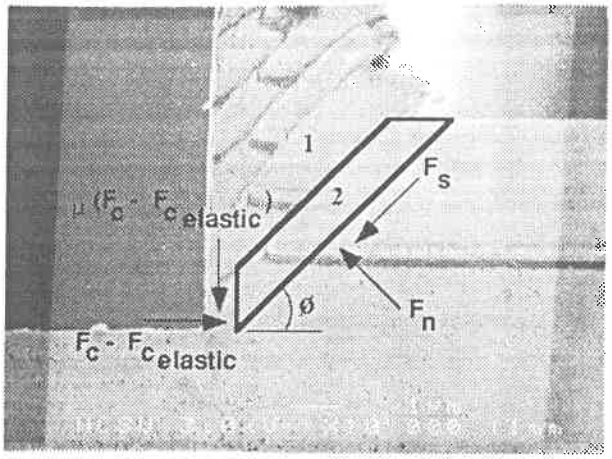

Figure 2. Chip cross section and free body diagram of chip segment.

Assumptions. Equations (1) and (2) contain several assumptions. The previously formed segment is regarded as exerting no shear force on the workpiece at the instant when a new segment forms. The material is regarded as elastic-perfectly plastic. The normal stress acting on the shear zone, σ_s, is taken as the uni-axial material flow stress, or one third the material hardness. Finally, a von Mises failure criterion is employed so that the shear stress, τ_s, is equal to $\sigma_s/\sqrt{3}$. These last two assumptions provide the maximum allowable normal and shear stresses in the cases of pure tension and pure shear, respectively. In a material that has a constant yield condition, and in which shear and normal stresses exist simultaneously, the magnitude of each component at yielding would be less than σ_s and τ_s as described in the preceding sentences.

Tool Force Equations. With these assumptions and the measured shear angle, ϕ, the coefficient of friction at the tool/chip interface, μ, can be calculated from a summation of forces in the vertical direction. The result of this operation yields

$$\mu = \frac{\cos\phi - \frac{\sin\phi}{\sqrt{3}}}{\frac{\cos\phi}{\sqrt{3}} + \sin\phi} \tag{3}$$

If the material hardness and either the shear angle or the coefficient of friction are known, the tool forces can be calculated. The development of models for material spring back and the associated contact stress between the tool flank and the workpiece is discussed by the authors elsewhere [9]. This work demonstrated that spring back in metal machining can be represented as a linear function of tool edge radius and the ratio of material hardness to elastic modulus. Thus, spring back is given by

$$s = k_1 r \frac{H}{E} \tag{4}$$

where s is the deflection of the machined surface or spring back, k_1 is a constant, r is the tool edge radius, H is the material hardness and E is the modulus of elasticity. For the 0° rake tool and the materials studied, $k_1 = 43$ provides good correlation between the measured and calculated values for spring back [9]. The contact stress due to this elastic spring back, σ_f, has been modeled as

$$\sigma_f = k_2 H \sqrt{\frac{H}{E}} \tag{5}$$

where k_2 is a constant ($k_2 = 4.1$ for best agreement with measured data [9]).

Knowledge of spring back allows the tool flank/workpiece contact area to be calculated. The product of this area and the interface stress yields the thrust force associated with elastic deformation of the workpiece. In terms of material data and cutting conditions, the complete tool force equations are then

$$F_c = \frac{H}{3\sqrt{3}} \frac{A_c}{\sin\phi} \cos\phi + \frac{H}{3} A_c + F_{c\,elastic} = \frac{HA_c}{3}\left(\frac{\cot\phi}{\sqrt{3}} + 1\right) + \mu_f A_f \left(4.1H\sqrt{\frac{H}{E}}\right) \tag{6}$$

$$F_t = \mu(F_c - F_{c\,elastic}) + F_{t\,elastic} = \mu\left[\frac{HA_c}{3}\left(\frac{\cot\phi}{\sqrt{3}} + 1\right)\right] + A_f\left(4.1H\sqrt{\frac{H}{E}}\right) \tag{7}$$

where A_c is the uncut chip area, A_f is the contact area between the tool flank and the workpiece and μ_f is the coefficient of friction between the tool flank and machined surface. Due to dissimilar conditions which exist along the nose region of the tool, the coefficient of friction between the tool flank and the workpiece is not required to be equal to the rake friction coefficient that is calculated from Equation (3) [10, 11].

EVALUATION OF THE MODEL

To verify the force model, the depth of cut, feed, tool nose radius, tool edge geometry, material properties (H, E) and either the shear angle or the coefficient of friction between the chip and tool rake must be known. Material data is provided in Table 1. The Vickers hardness of a diamond turned sample of each material was measured with a Zwick 3212 hardness tester. The elastic modulii were taken from a handbook [12]. In performing the calculations, the measured value for the coefficient of friction between the tool flank and the machined surface was used. For the four materials studied, this friction coefficient is about 0.2 [10]. Table 1 also contains shear angle data for the various materials and tool sharpnesses. The edge geometry of the diamond tool was varied by machining 6061-T6. The freshly lapped diamond tool had an edge radius of about 50 nm. The "worn tool" parameters (edge radius, flank wear land length) are also given in Table 1.

Material	Vickers Hardness (GPa)	Elastic Modulus (GPa)	Shear Angle (new tool)	Shear Angle (worn tool)
electroless nickel	5.3	200	22°	16° (300 nm, 2.4 μm)
plated copper	2.4	117	45°	33° (300 nm, 2.4 μm)
6061-T6	1.0	69	40°	30° (270 nm, 2.2 μm)
5086	1.0	71	30°	22° (270 nm, 2.2 μm)

Table 1. Material and machining data.

Comparisons of measured and calculated tool forces as a function of uncut chip area for electroless nickel cut with the 0° rake diamond tool in both its sharp and worn conditions are shown in Figures 3 - 6. The uncut chip area is the projection of the tool into the workpiece in the direction of cutting. The cutting speed for these tests was 25 mm/min. Figure 3 demonstrates excellent correlation between the measured and predicted forces in the cutting direction. The model accurately describes the tool forces for very large values of uncut chip area, A_c, as well as those typically encountered in diamond turning ($A_c < 400\ \mu m^2$). The model also provides a good estimate of the thrust force over a large range of uncut chip area, as shown by Figure 4. For the worn tool geometry, good correlation between the measured and predicted cutting forces was also obtained, as demonstrated by Figure 5. However, the thrust forces (Figure 6) are overestimated by an average of 50%. The high values of calculated thrust force in this case are due to the imperfect model for flank stress associated with spring back. As the tool sharpness decreases, the forces due to elastic deformation form a larger percentage of the total force[12]. Thus errors in the model for the flank stress (Equation (5)) become more significant with tool wear.

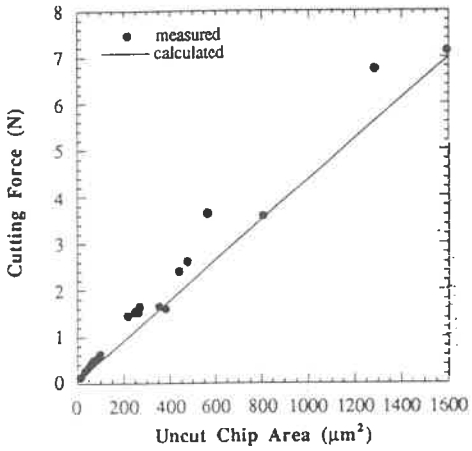

Figure 3. Measured and calculated cutting forces for electroless nickel (sharp tool).

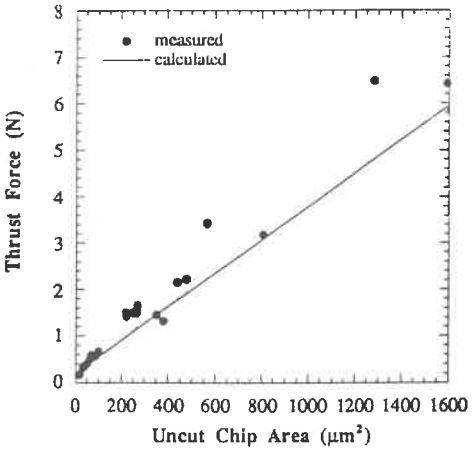

Figure 4. Measured and calculated thrust forces electroless nickel (sharp tool).

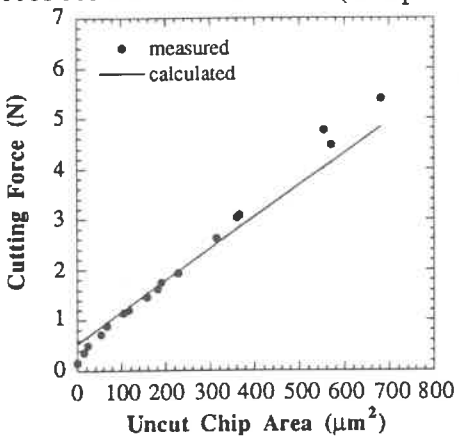

Figure 5. Cutting forces for electroless nickel (300 nm edge radius, 2.4 μm land).

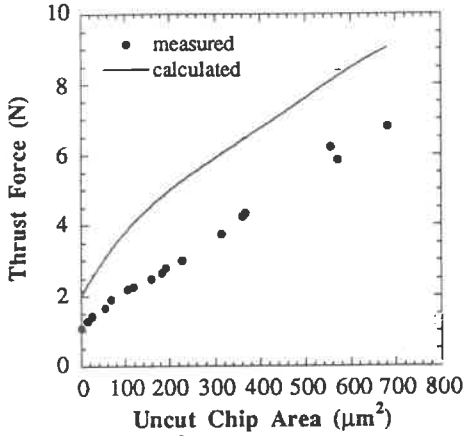

Figure 6. Thrust forces for electroless nickel (300 nm edge radius, 2.4 μm land).

Using the data in Table 1, the force model was evaluated for the three remaining materials and two tool conditions. The average variations between the measured and calculated forces in the cutting direction for chip areas less than 800 μm² are indicated in Table 2 (see Table 1 for worn tool data). Good correlation was also obtained for the thrust forces.

Material	Avg. Deviation from Measured Force (sharp tool)	Avg. Deviation from Measured Force (worn tool)
Plated Copper	25% (underpredicted)	30% (underpredicted)
6061-T6	30% (underpredicted)	20% (underpredicted)
5086	<10%	<10%

Table 2. Comparison of cutting force data.

CONCLUSION

A tool force model that is applicable in precision machining has been developed. This model accounts for chip formation as well as the elastic deformation of the workpiece that does not lead to material removal. The force components in the cutting and thrust (normal) directions are calculated

from the material hardness, elastic modulus, uncut chip area, tool geometry and shear angle for chip formation. The model was verified through the low speed machining of electroless nickel, electroplated copper and two aluminum alloys with a 0° rake angle diamond tool. These cutting tests were performed over a wide range in chip area and tool sharpness. The correlation between the measured and predicted force components is excellent for machining with a sharp tool. This agreement, however, generally degrades for cutting with a worn tool. The discrepancy between the measured and calculated forces for machining with a dull tool is primarily due to the increasing significance of elastic deformation of the workpiece with tool wear and inaccuracies in modeling the tool force caused by this elastic deflection. Despite this limitation, the predicted thrust forces vary by less than 50% from those measured for all the materials. The cutting forces are in better agreement, differing from the measured values by less than 40% for all materials and tool conditions. The relationships between cutting parameters and machining force that are incorporated in this model should help to establish tool force as a valuable process monitor in precision machining.

REFERENCES

1. Finnie, I. "Review of Metal Cutting Analyses of the Past Hundred Years." *Mechanical. Engineering*, v. 78, 1956: 715 - 721.

2. Ernst, H. and Merchant, M. E. "Chip Formation, Friction, and High Quality Machined Surfaces." Surface Treatment of Metals, ASM, 1941: 299 - 335.

3. Shaw, M.C.; Cook N.H. and Finnie, I. "The Shear-Angle Relationship in Metal Cutting." *Transactions of the ASME*, v. 75, 1953: 273 - 288.

4. Lee, E.H. and Shaffer, B.W. "The Theory of Plasticity Applied to a Problem of Machining." *J. of Applied Mechanics*, v. 18, 1951: 405 - 413.

5. Rowe, G.W. and Spick, P.T. "A New Approach to Determination of the Shear-Plane Angle in Machining." *J. of Engineering for Industry*, v. 89, 1967: 530 - 538.

6. Arcona, C. and Dow, T.A. "A New Technique for Studying the Chip Formation Process in Diamond Turning." *Precision Engineering*, v. 18, n. 2/3, 1996: 157 - 160.

7. Black, J.T. "Flow Stress Model in Metal Cutting." *J. of Engineering for Industry*, v. 101, 1979: 403- 415.

8. Ueda, K. and Manabe, K."Chip Formation Mechanism in Microcutting of an Amorphous Metal." *Annals of the CIRP*, v. 41, part 1, 1992: 129 - 132.

9. Arcona, C. and Dow, T.A. "Elastic Components of Deformation and Tool Force in Precision Machining." *Precision Engineering*, in press.

10. Arcona, C. "Tool Force, Chip Formation and Surface Finish in Diamond Turning." Ph.D. Dissertation, North Carolina State University, 1996.

11. Enahoro, H.E. and Oxley, P.L.B. "Flow Along Tool-Chip Interface in Orthogonal Metal Cutting." *J. of Mechanical Engineering Science*, v. 8, n. 1, 1966: 36 - 41.

12. Materials Engineering, Materials Selector 1989. Penton Publishing, Cleveland. OH, December, 1988.

Effect of Grain Orientation and Grain Boundaries on the Surface Topography of Diamond Turned OFHC Copper

E. Brinksmeier, W. Preuss, O. Riemer, J. Schmütz
LFM Labor für Mikrozerspanung, University of Bremen, Germany

1 Introduction

The microtopography of diamond turned polycrystalline metals depends on cutting parameters and on the crystallographic orientation of individual grains [1-4]. We are studying the influence of grain orientation on the microroughness of OFHC copper grains obtained in diamond cutting experiments. The aim of our work is to classify microtopographic features and to establish a relationship between grain orientation, cutting forces and surface topography.

2 Experimental setup

Inclined plunge-cut experiments with increasing depth of cut were performed in coarse-grained OFHC copper. The cutting experiments were carried out on a Moore M18 Aspheric Generator [2]. The diamond tools were mounted on the clamped spindle fixture. The copper specimen were slightly tilted (approx. 1 : 1000) and fixed on a piezo-electric force transducer. The relative motion between tool and specimen was obtained by moving the x-axis table at 10 mm/min and 100 mm/min, respectively. **Figure 1** shows the set-up of the inclined plunge-cut experiments.

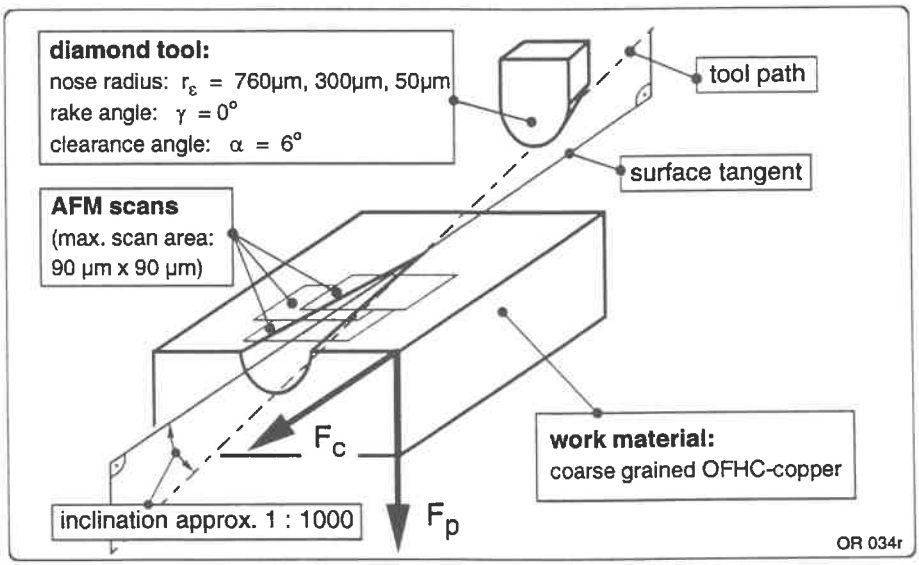

Fig. 1: Set-up of inclined plunge-cut experiments.

Each plunge-cut of the test series was repeated at least five times. The plunge-cut grooves were fully scanned and documented by Normarski microscope pictures.

Topographic details were studied with an atomic force microscope (AFM). Three different diamond tools with a nose radius of 760 µm, 300 µm to 50 µm were used. All tools had a 0° rake angle and a 6° clearance angle. The cutting edges radii of the tools, examined with a Nanoscope III atomic force microscope, were determined to be less than 30 nm.

3 Recrystallization of OFHC copper

Fine-grained OFHC copper commonly used for micromachining has an average grain size of approximately 80 µm. Single grains of this fine-grained polycrystalline material cannot be investigated by X-ray diffraction for determining crystal orientation, since the focus diameter is 0.1 mm or larger. Therefore, recrystallization was induced by cold rolling and annealing.

Since full recrystallization diagrams of copper do not exist, different samples made from commercially available OFHC copper were cold rolled with deformation ratios varying from 5 % to 15 %. Finally, a specimen was chosen which was cold rolled with a deformation ratio of 10 % followed by tempering at 830 °C for one hour in a nitrogen atmosphere. This process yielded a homogeneous grain size distribution with an average size of 330 µm. Though recrystallization should have no influence on the mechanical properties of the sample, the grain size does affect hardness testing. Therefore, the micro-hardness of the fine-grained samples (123 HV 0,05) was greater than the hardness after rolling and annealing (87 HV 0,05).

4 Experimental results

Analyzing the surface texture generated by plunge-cutting, different microtopographies were found depending on the depth of cut a_p. As long as $a_p < 2$ µm, all grooves exhibit a very smooth micro-topography (cf. picture on the left in **figure 3**) whatever the crystal orientation, and no extraordinary features were found at grain boundaries. A shallow waviness is observed along the cutting direction probably caused by the chip formation process. The average roughness R_a of these areas is less than 10 nm. The same observation is made with different diamond tools and cutting speeds. Moreover, plunge-cuts into fine-grained copper with $a_p < 2$ µm also show the same smooth surfaces whose topography seems to be characteristic for undisturbed machining.

If the depth of cut $a_p > 2$ µm, sections characterized by increased roughness and a markedly different microtopography appear in all grooves. These areas generally extend over a complete grain, but in some cases start out at a grain boundary and disappear before reaching the next boundary. **Figure 2** shows three adjacent plunge-cut grooves cut under identical experimental conditions, exhibiting both smooth areas and areas with increased roughness.

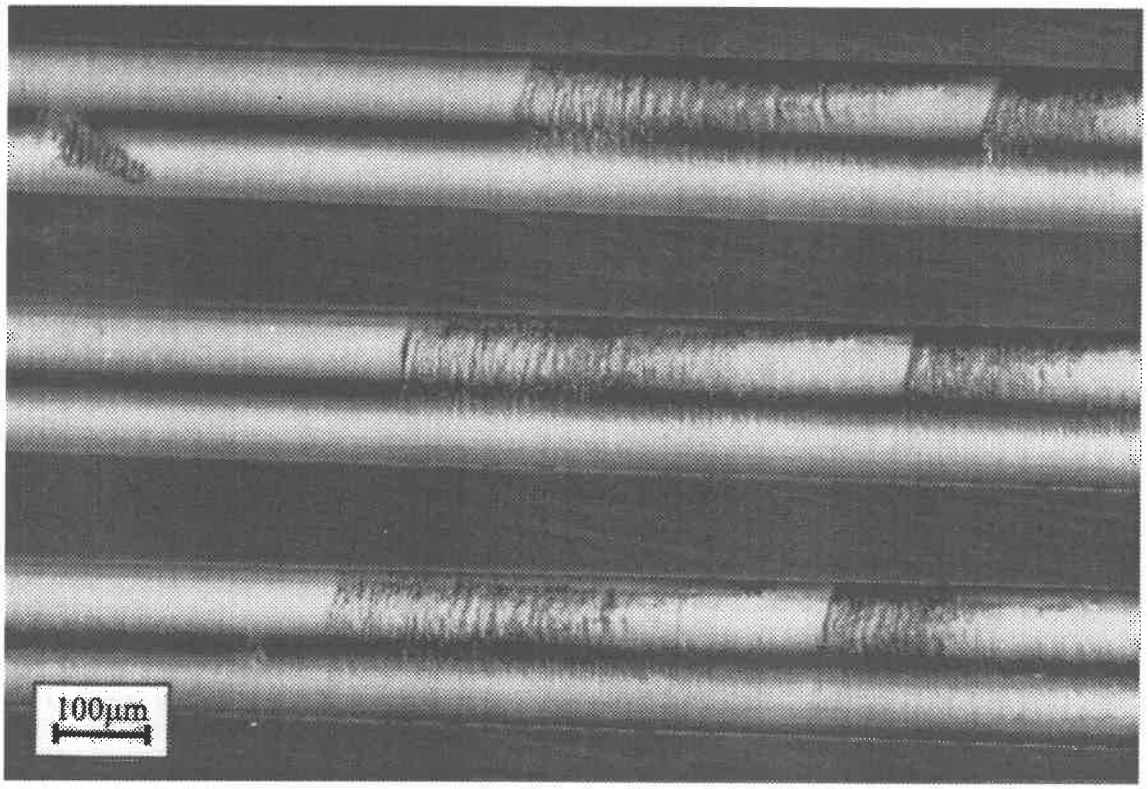

Fig. 2: Normarski photograph of three adjacent plunge-cut grooves.
Tool nose radius: r_ε = 300 µm, cutting speed: v_c = 10 mm/min,
cutting direction: left to right.

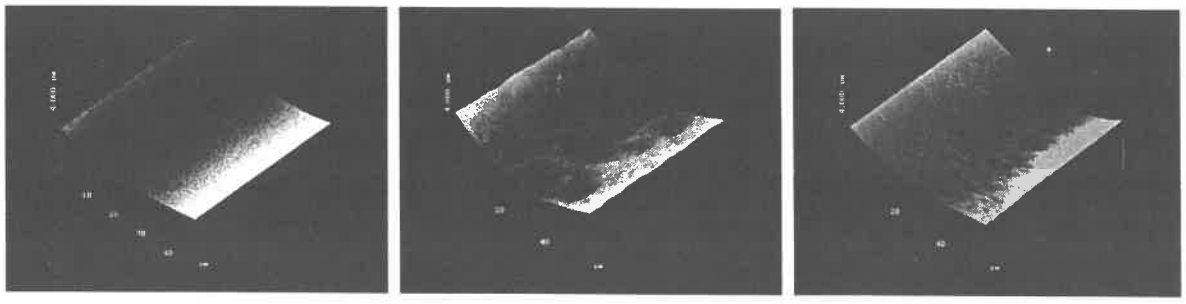

Fig. 3: Smooth, dented and rippled sections at the bottom of plunge-cut grooves.
Scale: 50 µm x 50 µm, lateral; 4 µm, vertical.
Tool nose radius: r_ε = 300 µm, cutting speed: v_c = 10 mm/min,
cutting direction: left to right.

We distinguish two types of areas with increased roughness, i. e. those with dented and others with rippled features. Examples of the different types of microtopography are shown in **figure 3** which can be characterized as follows:

- smooth sections: - $R_a < 10$ nm
  - always generated if depth of cut $a_p < 2$ µm
- dented sections: - 10 nm $< R_a <$ 100 nm
  - exhibiting small dents of approx. 10 µm in diameter
- rippled sections: - $R_a > 100$ nm
  - exhibiting ripples perpendicular to the cutting direction

All possible transitions between these three different types of surface topography can be found in the plunge-cut grooves. Thus, microtopography is correlated with individual grain orientation and is not exclusively depending on depth of cut.

If dented and rippled sections are regarded as a surface degradation, the ratio of degraded to total surface area is increasing rapidly with increasing depth of cut. Degradation up to 90 % can be found at larger depths of cut. Also, cutting force signals split into two or three different levels which can be correlated with microtopography. Areas with increased roughness show a considerably higher cutting force level than smooth sections. At grain boundaries abrupt changes between the force levels occur.

5 Conclusion

Inclined plunge-cut experiments with increasing depth of cut were performed in coarse-grained OFHC copper. Microtopographic features were divided into three distinct classes and correlated with cutting force measurements. It is assumed that the observed surface patterns depend on the number of gliding systems activated in the microcutting process. The analysis of X-ray diffraction patterns obtained from individual grains will provide a quantitative proof of this assumption.

6 References

[1] Brinksmeier, E. "Herstellung von Präzisionsbauteilen durch Mikrozerspanung". Industrie Diamanten Rundschau 4/1994: S. 210-217.

[2] Brinksmeier, E; W. Preuß; O. Riemer. „From Friction to Chip Removal. An Experimental Investigation of the Microcutting Process. Part I". Proc. 3rd Int. Conf. on Ultra Precision in Manufacturing Engineering; Hrsg: M. Weck, H. Kunzmann, Verlag Franz Rhiem, Duisburg, 1994: p. 393-400.

[3] Rentsch, R. „Molecular dynamics simulation for nanometer chip removal processes". Ph. D. thesis, Keio University, Japan, 1995.

[4] Spenrath, N. „Technologische Aspekte zum Feinstdrehen von Kupferspiegeln". Dissertation, RWTH-Aachen, 1991.

Design and Application of In-Process Acoustic Sensors for Maximum Sensitivity-Methods and an Example in Diamond Tooling

Jay Daniel, David Dornfeld, Laboratory for Manufacturing Automation, Department of Mechanical Engineering, University of California, Berkeley

Abstract: Acoustic sensors have been shown to be of value in precision manufacturing as near contact and contact sensors in a number of machining applications. Acoustic sensors have also shown promise in the detection and discrimination of various cutting parameters in cutting processes. Design methods that allow the sensitivity of these sensors to be maximized are not commonly available though, forcing users to adapt commercial acoustic emission equipment optimized to no particular situation. In particular, manufacturers are required to adapt existing sensors to the geometric constraints of their machining setup, and doing so can be difficult in many situations, restricting the utility of this sensing methodology. A quantitative design methodology that allows the manufacturer to consider tradeoffs in sensitivity and geometry for a unbacked bulk wave transducers is given. A design example for an acoustic sensor for diamond turning is considered.

INTRODUCTION

Acoustic sensors have been frequently investigated as in-process sensors for precision manufacturing processes.[1,2,3] They have been shown to be particularly robust in detecting changes in cutting condition.[4] Unfortunately, investigators seeking to incorporate acoustic emission sensors into process control schemes normally have had to work with the limits of commercially available acoustic emission transducers. These transducers can be limiting in terms of their size and cost.

In addition, maximizing sensitivity of acoustic receivers has not always driven design decisions for sensor manufacturers. With the approriate models at hand, the ability to "design in" a transducer into a manufacturing process allows the manufacturing engineer to maximize the utility of an acoustic sensor. This is particularly true in precision manufacturing applications, where exceedingly high sensitivity and signal to noise ratio is required for all process signals.

Previous authors have developed parameters ranking the sensitivity of acoustic receivers.[5,6] These models were not derived from first principles, and also did not incorporate the effects of the substrate through which the acoustic emission was propagating, or the parameters of the signal amplification. All of these parameters should be considered in designing an acoustic receiver for a particular machining application. The first step in considering piezoelectric acoustic receivers is the development of an appropriate model.

Following this, critical aspects of the model can be applied to given engineering situations to maximize sensor sensitivity. An example of this type of consideration is given for selecting a piezoelectric acoustic receiver for diamond tooling.

BULK WAVE MODEL FOR PIEZOELECTRIC RECEIVERS

Our goal is to develop an expression for the voltage generated by a piezoelectric receiver as it is acted upon by an acoustic wave propagating in from a substrate that it is mounted upon. Figure 1 shows the physical situation, and some of the terms used in the model.

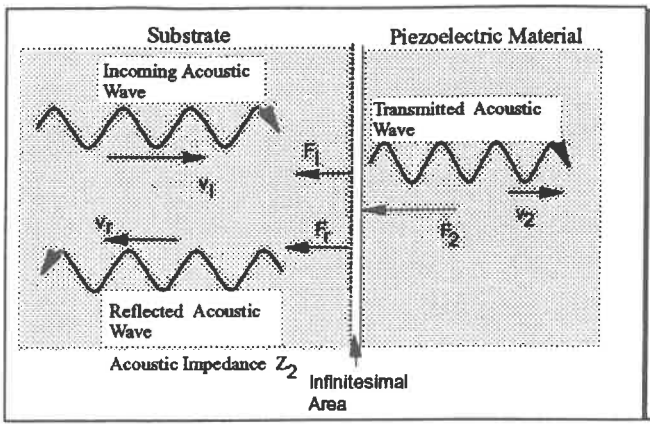

Figure 1: The physical model for an acoustic receiver showing the acoustic waves and traction and velocity vectors.

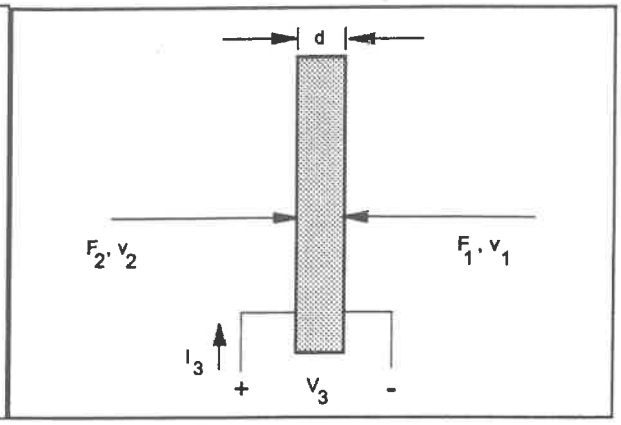

Figure 2: The three port model and terms used in the Mason model.

The transfer function we wish to obtain is the voltage generated by the piezoelectric material as generated by some aspect of the incoming acoustic wave. For our purposes, we choose particle displacement. Thus we want the transfer function V_3/u_i where V_3 is the voltage generated across the piezoelectric material.

To obtain this transfer function, we utilize the Mason model[7] for plane wave propagation in piezoelectric media along with relationships for plane wave reflection at an interface. The Mason model is

$$\begin{bmatrix} F_1 \\ F_2 \\ V_3 \end{bmatrix} = -i \begin{bmatrix} Z_o \cot(kd) & Z_o \csc(kd) & \frac{h}{\omega} \\ Z_o \csc(kd) & Z_o \cot(kd) & \frac{h}{\omega} \\ \frac{h}{\omega} & \frac{h}{\omega} & \frac{1}{\omega C_o} \end{bmatrix} \begin{Bmatrix} v_1 \\ v_2 \\ I_3 \end{Bmatrix} \tag{1}$$

and relates the forces and velocities at the front and back faces of the piezoelectric plate to physical parameters of the piezoelectric media and the voltage and current generated across the piezoelectric plate. Terms used in the model include the dynamic acoustic impedance(Z_o), the piezoelectric constant(h), the wave vector(k), the plate thickness(d), and the plate capacitance(C_o). Figure 2 shows the geometry of the model. For the excitation of an unbacked transducer from the substrate, we apply two boundary conditions to the Mason Model.

$$F_1 = 0 \tag{2}$$

and

$$V_3 = -Z_3 I_3 \tag{3}$$

The first boundary condition is used because the transducer is unbacked, and no force can be supported at the back of the plate. The second boundary condition applies to the electrical terminal. We assume that an impedance is placed across the electrical terminal across which the voltage generated by the piezoelectric plate is measured.

Finally, an expression needs to be developed that describes how much of an acoustic wave impinging on the piezoelectric plate from the substrate propagates into the piezoelectric plate, and how much reflects back into the substrate. First, we state the reflection coefficient of an interface, Γ, as a function of the impedances.[8] Z_{in} is the acoustic impedance looking into the piezoelectric plate from the substrate.

$$\Gamma = \frac{Z_{in} - Z_2}{Z_{in} + Z_2}. \tag{4}$$

Also, the traction vector at the boundary of the piezoelectric plate, F_2, is related to F_i and F_r by:

$$F_2 = F_i + F_r = F_i(1+\Gamma) = F_i \frac{2Z_{in}}{Z_{in} + Z_2} \tag{5}$$

Three other relationships need to be used to find V_3/u_i.

$$F_i = -\bar{Z}_2 v_i \tag{6}$$

$$Z_{in} = \frac{F_2}{v_2} \tag{7}$$

$$u_i = \int v_i dt = \int v_{io} e^{-i(kx-\omega t)} dt = \frac{v_{io}}{i\omega} e^{-i(kx-\omega t)} = \frac{v_i}{i\omega} \tag{8}$$

Using this system of equations, we can now solve for V_3/u_i.

$$\frac{V_3}{u_i} = \left[\frac{Z_3 Z_2}{\frac{Z_o}{h}\left(\cot(kd)+\csc(kd)\right)\left(iZ_3 + \frac{1}{\omega C_o}\right) - 2\left(\frac{h}{\omega^2}\right)} \right] \frac{2\left[\frac{2\left(\frac{h}{\omega}\right)^2}{\left(iZ_3 + \frac{1}{\omega C_o}\right)Z_o}\left(\sec(kd)-1\right) - \tan(kd) \right] Z_o i}{\left[\frac{2\left(\frac{h}{\omega}\right)^2}{\left(iZ_3 + \frac{1}{\omega C_o}\right)Z_o}\left(\sec(kd)-1\right) - \tan(kd) \right] Z_o i + Z_2} \tag{9}$$

Using this model, the effects of design parameters including the thickness and area of the piezoelectric material, the piezoelectric material and its properties, and the input impedance of the amplifier can be evaluated.

Assuming that Z_3, the input impedance of the amplifier used to amplify the signal from the piezoelectric receiver, is infinite, (9) reduces to[9]

$$\frac{V_3}{u_i} = \frac{-2hi}{\frac{Z_o}{Z_2}\left\{\cot(kd)+\csc(kd)\right\}\left\{1 + \frac{Z_2 i}{Z_o}\cot(kd)\right\}} \tag{10}$$

The figure of merit for various materials can be deduced from (10). The figure of merit(FOM) is the same well below and near resonance of the transducer, although the transducer acts as a surface velocity transducer well below resonance and a surface displacement transducer near resonance.[9] The figure of merit is

$$\text{FOM} = \frac{hZ_2}{Z_o}. \tag{11}$$

Table 1 lists a variety of piezoelectric materials by their figure of merit The substrate impedance, Z_2, isn't included in the FOM, as it isn't a transducer property. It does have tremendous importance in the sensitivity of an acoustic detection system, but often isn't controllable. Table 1 lists the relative permittivity of the piezoelectric material, the piezoelectric stress constant, the specific dynamic impedance, and the FOM. The piezoelectric parameter, h, is related to the relative permittivity, ε, and the piezoelectric stress constant, e, by

$$h = \frac{e}{\varepsilon} \tag{12}$$

Table 1 also includes a listing of whether the receivers are commonly used as thin film or macroscopic transducer materials.

A DESIGN EXAMPLE- DIAMOND TOOLING FOR A LATHE

Using these design guidelines, two sensor configurations were evaluated for an acoustic sensor mounted on a diamond tool used in a turning center. One configuration utilizes a macroscopic piece of PZT with a commercially available amplifier, while another utilizes a thin film zinc oxide sensor with a custom high frequency amplifier. Figure 3 demonstrates the locations of the sensors on the diamond tool.

MATERIAL	relative	piezo-stress	Spec. Dynamic	Figure of	Thin Film
	permitivity	const	Impedance	merit	Material?
	no units	C/m2	kg/(sec.m^2)	kg.C/(F.sec.m^5)	Y/N/both
SiO2	4.5	0.50	1.33E+07	982	N
AlN	8.5	2.12	3.40E+07	858	Y
Kynar	12	0.32	3.90E+06	792	Y
CdS	9.5	1.69	3.60E+07	580	Y
LiNbO3	39	6.56	3.42E+07	576	N
Keramos K83	150	8.90	2.56E+07	271	N
ZnO	8.8	0.70	3.60E+07	260	both
Murata SWM	240	13.44	3.74E+07	175	N
PZT-7A	235	9.5	3.65E+07	130	N*
PZT-2	260	9	3.35E+07	121	N
Na0.5K0.5NbO	306	9.8	3.09E+07	121	N
P3 BaTiO3	890	24.50	3.13E+07	103	both
P6 PZT	890	25.00	3.51E+07	94	N
P7 PZT	1000	27.57	3.60E+07	90	N
P5 PZT	850	19.25	3.16E+07	84	N
PZT-4	635	15.1	3.45E+07	81	N
PZT-8	580	13.2	3.48E+07	77	N
PZT-5A	830	15.8	3.37E+07	66	N
PZT-6B	386	7.1	3.64E+07	59	N
PZT-6A	730	12.5	3.40E+07	59	N
BaTiO3	1260	17.5	3.12E+07	52	both

Table 1: Ranking of piezoelectric materials as receivers. Data from references 8 and 10.

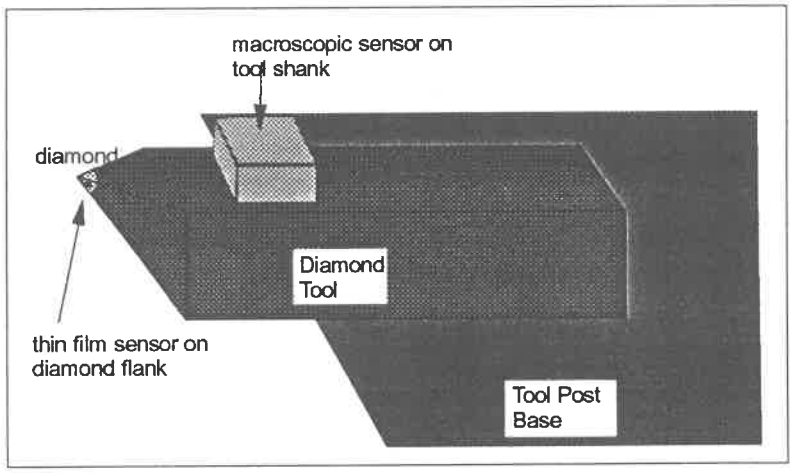

Figure 3: Locations of acoustic sensors on diamond tooling.

The considerations in maximizing sensitivity in this design example are the relative sensitivities of the acoustic sensors and the intensity of the acoustic waves at the two sensor locations. The sensitivities of the two sensor configurations can be calculated with (9) over the frequency range monitored. The ZnO sensor is significantly less sensitive than the PZT sensor, due to its operation well below the resonances of the sensor. The magnitude of the displacements generated by acoustic waves propagating as a result of time varying tractions imposed on the tool tip by the cutting process can be nominally estimated by FEM,[9] but the frequency capability of the FEM analysis is limited by element size in the FEM mesh. Results from the FEM analyses show that the macroscopic transducer configuration should be more sensitive overall, but the level of confidence in this result is not high due to the limits of the FEM analysis. The testing of these two sensor configurations is currently ongoing in our laboratory, and results will be published in the next year.

CONCLUSIONS

A model for the sensitivity of plane wave piezoelectric acoustic transducers has been developed. The figure of merit for various piezoelectric acoustic receivers has been extracted from the model. Estimates of sensitivity of two acoustic sensor configurations for an application in diamond tooling have been obtained, and experiments are being conducted to compare experimental results to the theoretical predictions.

[1] Taylor, J.S., et. al., Proceedings of the ASPE, Austin, TX, USA, Nov. 1995
[2] Osuri, R.H., et. al., Int. J. of Prod. Research, 29(7), 1991.
[3] Kamimura, Y., Tani, Y., Proc. 8th Int. Precision Eng. Sem., Compiegne, France May 1995.
[4] Dornfeld, D.A., JSME Int. Journal C, 34(4), 1994.
[5] Callerame, J., Tancrell, R.H., Wilson, D.T., 1979 IEEE Ultrasonics Symposium.
[6] Silk, M.G., *Ultrasonic Transducers for Non-Destructive Testing*, Adam Hilger Ltd., Bristol, 1984.
[7] Mason, W.P., *Pieoelectric Crystals and Their Application to Ultrasonics*, van Nostrand, New York, 1950.
[8] Auld, B., Acoustic Fields and Waves in Solids, 2nd ed., Robert E. Krieger Publishing Co., Malabar, Fl..
[9] Daniel, J.P. Ph.D. Thesis, University of California, Berkeley, 1996.
[10] Kino, G.S., Acoustic Waves. Devices, Imaging, & Analog Signal Processing, Prentice Hall, Englewood Cliffs, New Jersey, 1987.

Development of a Micro-Cutting/Testing System under Scanning Electron Microscope

Mamoru MITSUISHI, Naohiko SUGITA, Takaaki NAGAO and Yotaro HATAMURA
Department of Engineering Synthesis, Faculty of Engineering
The University of Tokyo
Hongo 7-3-1, Bunkyo-ku, Tokyo 113, Japan
mamoru@nml.t.u-tokyo.ac.jp
http://www.nml.t.u-tokyo.ac.jp/~mamoru

1. Introduction

Etching processes and the LIGA process are used conventionally to fabricate 3D micro-mechanical parts. It is also possible to manufacture 3D mechanical parts by cutting, using micro-tools. In this paper, a micro-machining system which works under an SEM was developed. The system incorporates 3-axis force sensing to measure and analyze cutting force. From the experiment it determined that as the cutting scale becomes smaller, the cutting force per unit increases. Therefore, a high stiffness micro tool is necessary for micro cutting.

2. Related work

An example of research on micro-machining and testing is micro-operation within an SEM [1]. The system includes a specimen stage and a 3 degree-of-freedom tool-handling robot, equipped with a single axis force sensor. It is driven by piezoelectric actuators and is installed in the vacuum chamber of the SEM. Johansson [2] has realized a system which can test the physical properties of a material, such as diffusion, at 500 degrees centigrade by holding a specimen in the SEM chamber. Takeuchi [3] has developed a lathe-type micro-milling machine. Brittle material such as glass was machined in the ductile mode. It was possible to obtain a glass mask of 1 mm in diameter with the surface roughness of 50 nm. Friedrich [4] has developed a micro-milling machine with milling tools with a diameter as small as 22 micrometers. The milling tools were made using FIB. Shimada[5] and Shimizu[6] are analyzing the micro cutting mechanism using the knowledge of molecular dynamics. Furthermore, Tokushige[7] is executing research concerning micro cutting in the vacuum environment.

3. Construction of a machine for micro-machining within an SEM

3.1 Construction of a micro-machining machine

Fig.1 shows the construction of a micro-machining machine (MMM) with three degrees

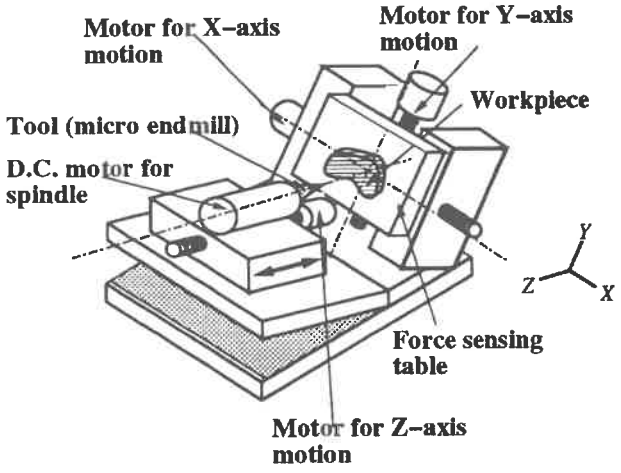

Fig.1 Construction of a micro-machining machine (MMM)

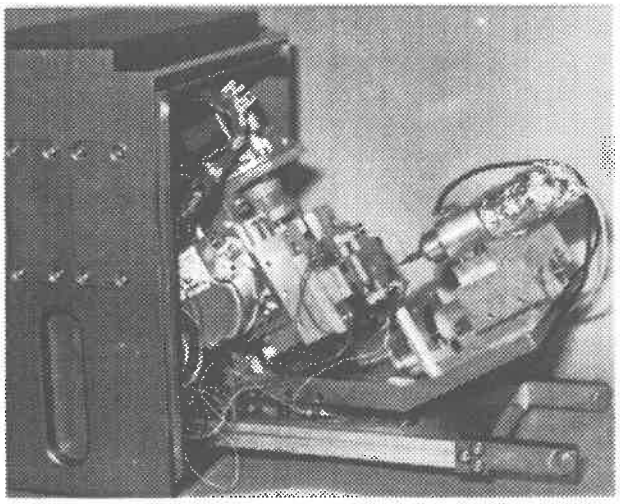

Fig.2 Overview of a micro-machining machine(MMM)

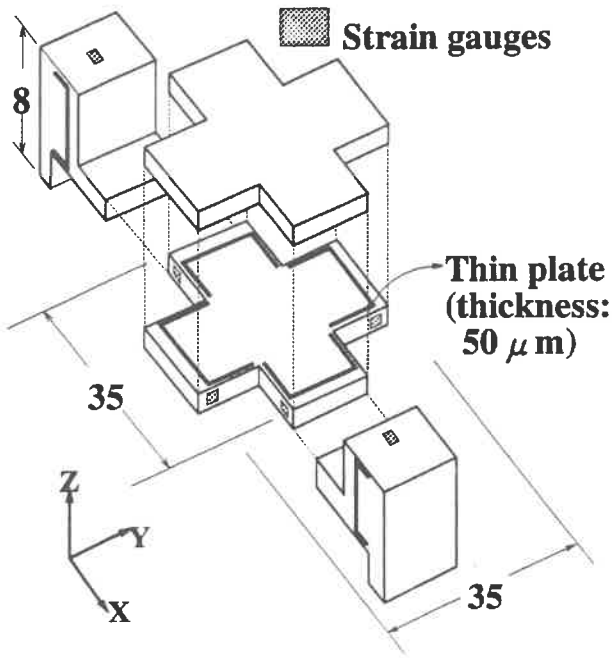

Fig.3 Structure of three-axis force sensing table

Table 1 Characteristics of the force sensing table

	Rated max. load value	Resolution	Natural frequency
X-axis	520mN	0.130mN	142Hz
Y-axis	752mN	0.188mN	104Hz
Z-axis	3528mN	0.882mN	324Hz

of freedom. The workpiece table translates in the X and Y directions and the tool moves in the Z direction. The translational mechanism uses ball screws and cross roller guides and is driven by ultrasonic motors with encoders. The working table is inclined at an angle of 60 degrees for optimal viewing under the SEM (Fig.2). The MMM has a rough positioning table to set the machining point at the center of the field of observation, with a three-axis force sensing table mounted on the XY-table (Fig.3). The sensing table is made of aluminum alloy and incorporates a parallel plate structure with strain gauge sensors. The thickness of the force sensing plate, which was produced using wire electrical discharge machining, is 50μm (length 4mm, width 3mm). Table 1 shows the characteristics of the developed force sensing table. For the MMM described in this paper, it is possible to fit a spindle motor on the Z-axis to rotate a small diameter end mill, which, when combined with Z-axis translation, produces a micro machining center. In our system, the shank portion of the

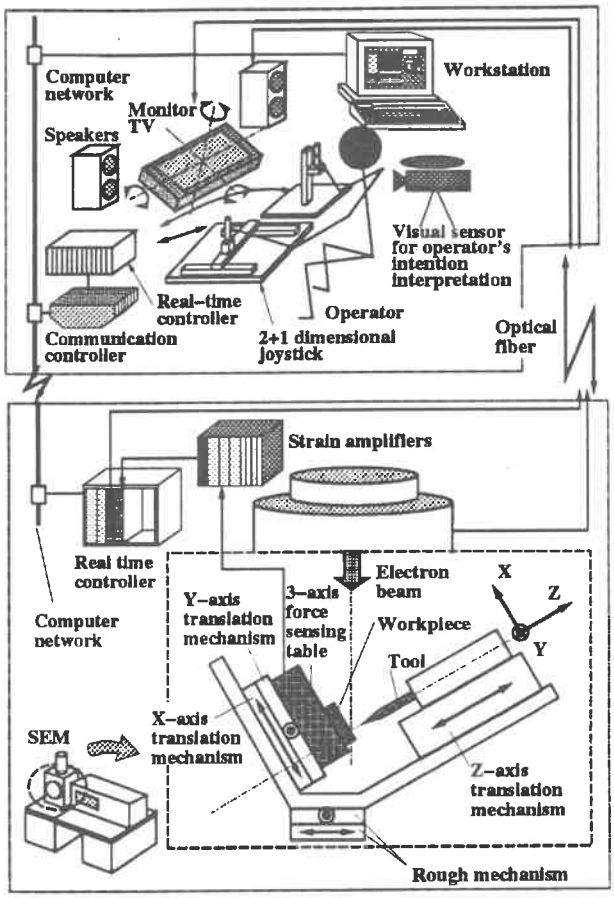

Fig.4 System configuration of a tele-micro machining system

endmill is directly supported by a bearing to reduce the deviation and the workpiece is fixed on the 3-axis force sensing table.

3.2 Tele-micro-machining system

The MMM is installed in the vacuum chamber of an SEM and micro machining is executed by controlling it with real-time controller which is connected to a computer network, such as the Internet (Fig.4). Visual information from the SEM and auditory information obtained the transformation of multi-axis force information into auditory information transformation method are sent through optical fiber to a remote operator. The remote operator controls the MMM, recognizing phenomena in the micro world by integrating the visual, auditory and tactile information. The control signal and force information are sent through a computer network, such as the Internet. For example, the MMM located at the University of Tokyo was operated from Karlsruhe University in Germany using ISDN as shown in Fig.5.

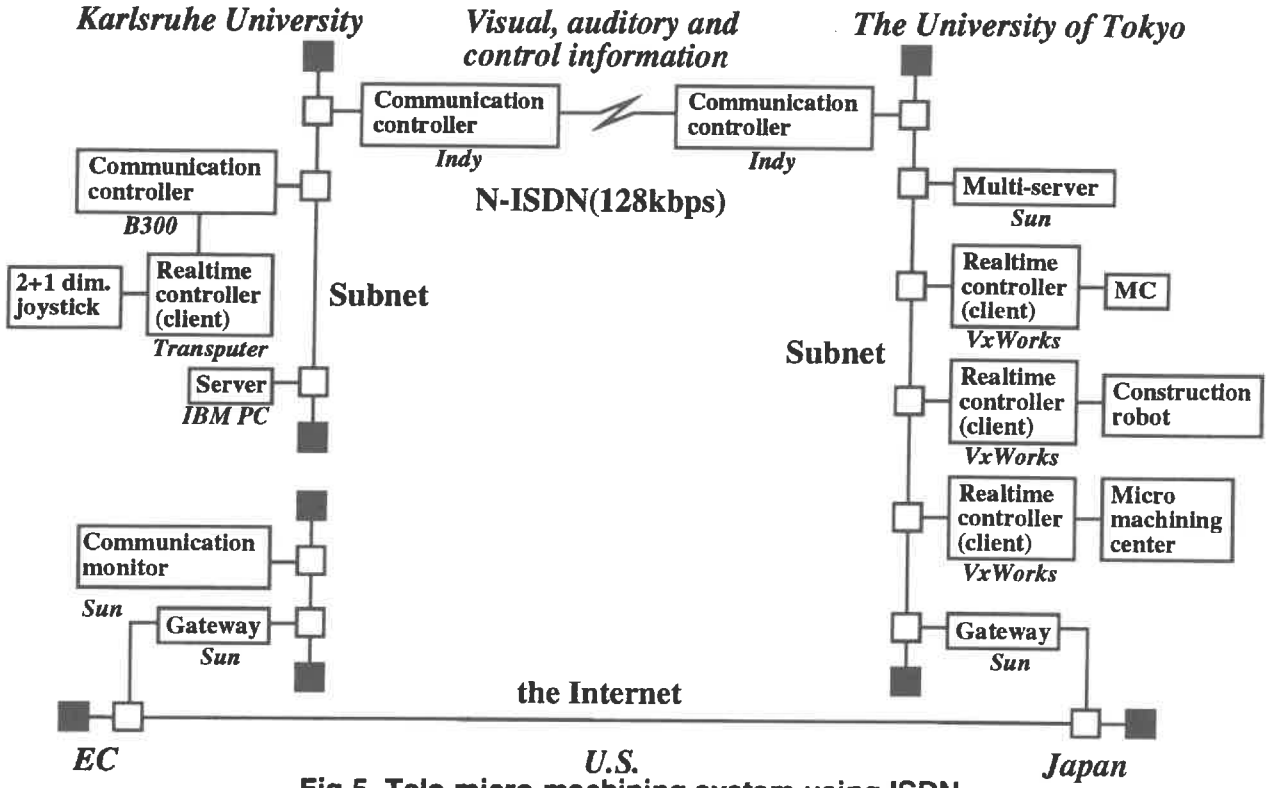

Fig.5 Tele-micro-machining system using ISDN

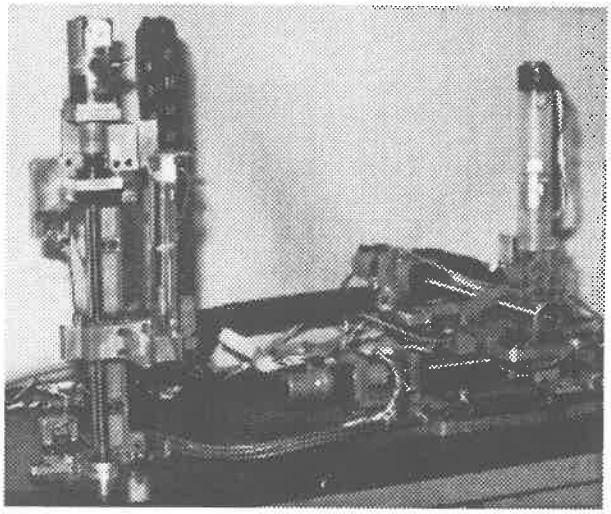

Fig.6 Overview of a 2+1 dimensional joystick

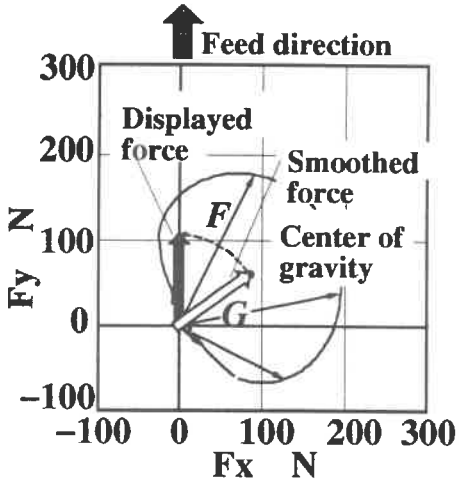

Fig.7 Cutting state index

3.3 Auditory information presentation of machining state

Because the MMM is located inside the chamber of an SEM, it is difficult to acquire the cutting sound which is, in general, effective in indicating the machining state to a human operator. Therefore, the cutting state is detected by a multi-axis force sensor and the sensed information is converted into auditory information. Generally, the output from a force sensor is presented as follows for each force direction:

$$f(t) = \sum_{i=1}^{\infty} a_i \sin(\omega_i t + \theta_i) \qquad (1)$$

where a_i, θ_i and ω_i are amplitude, phase and angular velocity, respectively. In the developed system the frequency of the sound ω_i was controlled to be proportional to the absolute value

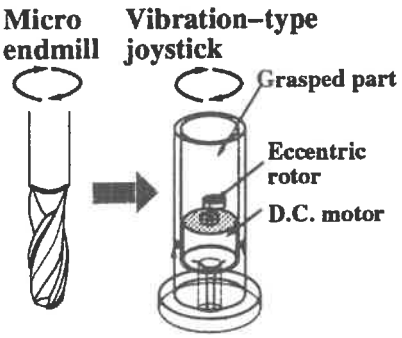

Fig.8 Vibration-type joystick

of the cutting force $||f(t)||$ while the amplitude A_i is constant.

$$\Phi(t) = A_i \sin((\alpha||f(t)|| + \beta)t + \theta_i) \qquad (2)$$

where α is a positive constant and β is defined as $2\pi \times 20$. The value 20 comes from the audible lower frequency limit of human hearing.

3.4 Tactile information presentation of machining state

In the implemented system, the machining state such as chatter vibration was presented as a vibration. To present the machining state the following value, named the "cutting state index" by the authors, is calculated in real-time and is sent from the micro-machining machine to the joystick controller:

$$\frac{V(|\mathbf{F} - \mathbf{G}|)}{|\mathbf{G}|^2}. \qquad (3)$$

where V, $\mathbf{F}$ and $\mathbf{G}$ represent the variance during one tool rotation, cutting force vector and the center of the gravity of cutting force during one tool rotation, respectively(Fig.7). The value $V(|\mathbf{F} - \mathbf{G}|)$ can be used to judge the machining state in real-time and the value becomes large when chatter vibration occurs [8]. However, the value changes depending on machining conditions such as feed per edge S_z even if the machining state is normal. Therefore, it is divided by $|\mathbf{G}|^2$ for the normalization. Fig.8 shows the grasp part of "2+1 dimensional joystick" with an eccentric weight and a motor at the operation room. The rotational speed of the motor is controlled as proportional to the value described in equation (3). The operator feels the vibration in case of chatter vibration.

4. Micro cutting experiments and discussions

Fig.9 shows one of the experimental results in micro machining. Fig.10 shows the plotted data

Table 2 Comparison of cutting force at macro and micro machining

	Micro cutting	Macro cutting	Magnification ratio
Tool diameter	0.2mm	10mm	$\alpha = 50$
Depth of cut	12.5μm	5.0mm	$\beta = 400$
Feed per tooth	0.75μm	25μm	$\gamma = 33.3$
Maximum cutting resistance	100mN	200N	$\delta_{exp.} = 2 \times 10^3$

in the plane perpendicular to the main axis of a micro endmill, as obtained from the experimental data in Fig.9. It is clear that in micro cutting, in some cases the cutting state is normal and in other cases chatter occurred.

Cutting force per unit was compared in both micro and macro cutting cases under the conditions shown in Table 2. According to the Kronenberg equation, cutting force F can be written as follows:

$$F = k_c A \qquad (4)$$

$$k_c = Ch^{-\varepsilon} \qquad (5)$$

$$h \simeq S_z \sin\phi \qquad (6)$$

where k_c, A, h and S_z represent cutting force per unit area of the cut, area of cut, undeformed chip thickness and feed per edge, respectively. C and ε are constants which depend on the workpiece material and on the shape of cutter. Based on the value $\varepsilon = 0.73$ obtained in macro cutting, the comparison ratio $\delta_{calc.}$ between macro and micro cutting can be calculated as follows, using variables shown in Table 2:

$$\delta_{calc.} = \alpha\beta\gamma^{-\varepsilon} = 1.55 \times 10^3. \qquad (7)$$

The value is the same order as the experimentally obtained comparison rate

$$\delta_{exp.} = 2.0 \times 10^3. \qquad (8)$$

Fig.11 shows the plotted data describing the relationship between cutting force per unit area of the cut and undeformed chip thickness. The inclination of the straight line in the figure shows $-\varepsilon$ which appears in an equation to calculate the cutting force. From Fig.11, it is easy to see that a stronger micro machine tool is necessary for micro cutting because the cutting force per unit increases as the scale becomes smaller. The experimental value obtained in micro cutting is approximately the same as the theoretical value 1.1×10^4 (MPa).

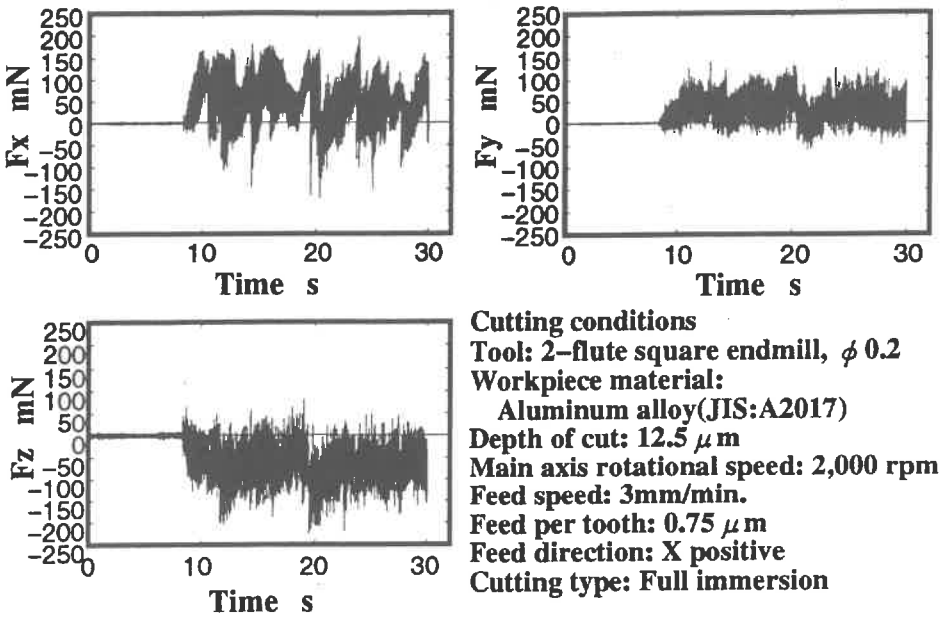

Fig.9 Experimental results using MMM

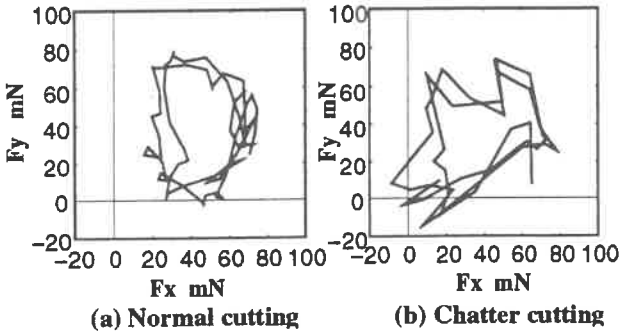

Fig.10 Force vector locus at micro cutting

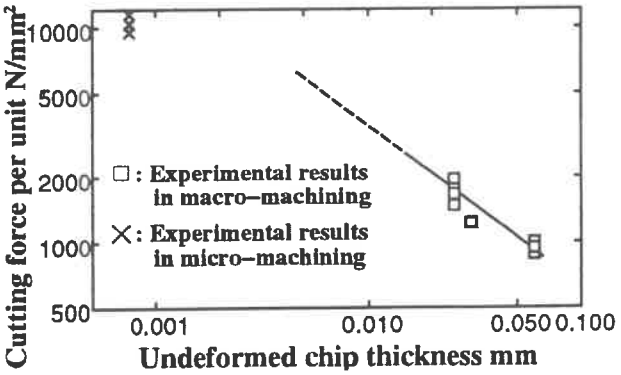
Cutting force per unit N/mm²
□: Experimental results in macro-machining
×: Experimental results in micro-machining
Undeformed chip thickness mm

Fig.11 Relation between undeformed chip thickness and cutting force per unit

5. Conclusions

A micro-machining machine inside an SEM, with 3-axis force sensing capability and which can be operated from the remote place was developed. From the experiment, it is clear that the cutting force per unit increases as the cutting scale becomes smaller. Therefore, a high stiffness micro tool is necessary for micro cutting.

References

[1] Hatamura,Y. et al., "Direct Coupling System Between Nanometer World and Human World," *Proc. IEEE Micro Electro Mechanical Systems*, pp.203–208, Napa Valley, California, 1990.

[2] Johansson,S., "Hybrid Techniques in Microrobotics," *Proc. IARP*, pp.72–83, Karlsruhe, 1993.

[3] Takeuchi,Y., et al., "Ultraprecision 3D Micromachining of Glass," *Annals of the CIRP*, Vol.45/1, pp.401–404, 1996.

[4] Friedrich,C., et al., "Mechanical Micromilling of PMMA," in *Proc. of the 10th Annual Meeting of the American Society for Precision Eng.*, pp.284–287, Austin, U.S.A., 1995.

[5] Shimada,S., et al., "Molecular Dynamics Modeling of Thermal Conduction in Microcutting of Metals," in *Proc. of the 10th Annual Meeting of the American Society for Precision Eng.*, pp.21-24, Austin, U.S.A., 1995.

[6] Shimizu,J. et al., "Research on Collision Mechanism of Atomic Cluster by Simulation," *Proc. Jap. Soc. Precision Eng. Spring Annu. Meeting*, pp.441–442, 1995 (in Japanese).

[7] Tokushige,N., et al., "Observation of Cutting Behavior under Scanning Electron Microscope," *Proc. Jap. Soc. Precision Eng. Spring Annu. Meeting*, pp.897–898, 1995 (in Japanese).

[8] Mitsuishi,M., et al., "Real-Time Machining State Detection Using Multiaxis Force Sensing," *Annals of the CIRP*, Vol.41/1, pp.505–508, 1992.

Ultraprecision Metal Cutting Process Monitoring Using Acoustic Emission -- Burr Formation

Jianshe Tang, Xuemei Chen and David Dornfeld
Department of Mechanical Engineering
University of California at Berkeley, Berkeley, CA 94720, USA

Abstract

The results of experimental studies of ultraprecision milling of aluminum are presented. The AE features correlated to burr formation in ultraprecision milling are discussed.

1. Introduction

Ultraprecision metal cutting (UPMC), in a contemporary sense, can be defined as a cutting technique which enables us to produce optical, mechanical and electronic components with micrometer or submicrometer form accuracy and a few tens nanometer surface roughness [Ikawa, 1991]. The accuracy of UPMC depends on the transfer characteristics of both machine tool motions and tool profiles into a workpiece. Submicrometer or even down to nanometer accuracies in machine tool motions and tool geometry are essential. Taking advantage of the development in advanced metrology, control technology and precision machine components, machine tools with motion accuracy at nanometric level and diamond tools with sharp cutting edge to as small as 20-45 nm were developed [Donaldson, 1986]. At present, ultraprecision metal cutting is extensively applied to the manufacturing of precision components, such as faceted optics used in laser systems, aluminum substrate drums in photo copying machine and aluminum substrates for computer hard disks.

There has been extensive investigations of UPMC in the area of chip formation and energy dissipation [Furukawa, 1988; Moriwaki, 1989; Ikawa, 1993; Lucca, 1994], where the cutting process is continuous and stable. Little research on the burr formation mechanisms and the in-process detection of burr formation in UPMC, where the cutting process is transient, has been done, even when the edge finishing is a critical specification for components such as polygon mirrors.

Acoustic emission is known to be sensitive to many process parameters and is evolving into an effective method for studying the process of material removal mechanisms and the condition of cutting tools in various metal cutting processes. The objective of this study is to investigate the connection between the burr formation and acoustic emission signal in ultraprecision milling.

2. Experimental approaches

2.1 Burr formation in face milling

During the milling operation, burrs are created where the milling cutter exits the machined part. Five different types of burrs can be formed with different combinations of milling conditions. It is generally accepted that both the height and thickness of burr are proportional to the undeformed chip thickness and usually are in the same order as the undeformed chip thickness [Nakayama, 1987; Chern and Dornfeld].

Figure 1 shows a diamond tool used in this test and the uncut chip geometry at two different depths of cut. The tool has a straight cutting edge and a circular cutting edge, with a transition edge between the straight and circular cutting edges. From the relationship between cutting parameters and tool geometry, it can be determined that when the depth of cut is smaller than 5 μm , see figure 1(a), work material will be removed only by the circular cutting edge of nose radius R=100mm. In this case, the maximum effective depth of cut can be calculated as $t_{max} = f(2d/R)^{1/2}$ and is in the range of several to several tens of nanometer for our test conditions. The exit burr generated should be in the same order and is negligible. Hence, a burr free surface can be expected. However when the depth of cut is larger than 5 μm, the straight cutting edge will be involved in cutting, and the maximum effective depth of cut can be calculated by $t_{max} = f\cos(\phi)$ and is on the same order as the feed rate. As feed rate is usually from 6μm/r to 40μm/r in our test setup, a surface with burrs with size in tens of micrometers is formed in this case. By monitoring and comparing the AE signals generated in these two cases, it is expected to see some AE features related to burr formation. The workpiece material in this experiment is as received 2024-T35 aluminum which is widely used for precision components like metal optics.

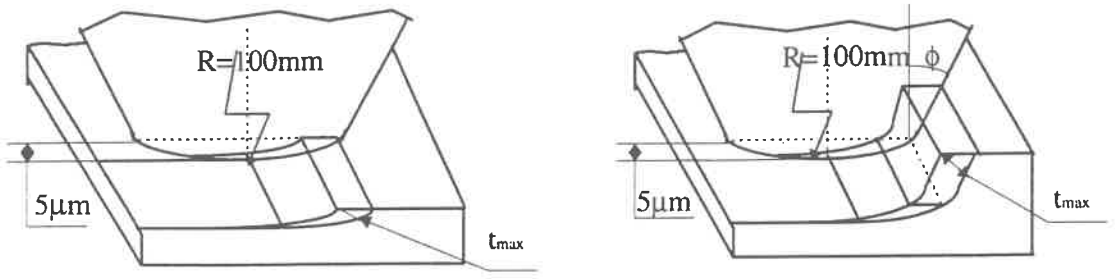

(a) When d<5 μm (b) When d>5 μm

Fig. 1 Schematics of a diamond tool and chip geometry

2.2 AE sources in burr formation and AE measurement setup

A burr formation process can be divided into three stages, namely initiation, development and final burr formation [Ko and Dornfeld, 1991; Hashimura and Dornfeld, 1995]. The AE sources in both continuous cutting and burr formation are shown in figure 2. In the burr formation process, in additional to the deformation in primary, secondly and tertiary shear zone which are the dominant AE sources in continuous cutting, a negative shear zone and a crack propagation process is evident [Hashimura and Dornfeld, 1995]. These additional sources will constitute AE. Therefore, the AE energy in a burr formation process should be higher than that in continuous cutting and the difference in magnitude could be used for an indication of burr formation. As these regions vary in contribution to the AE signal with time (with tool motion), this can also be a feature for burr detection.

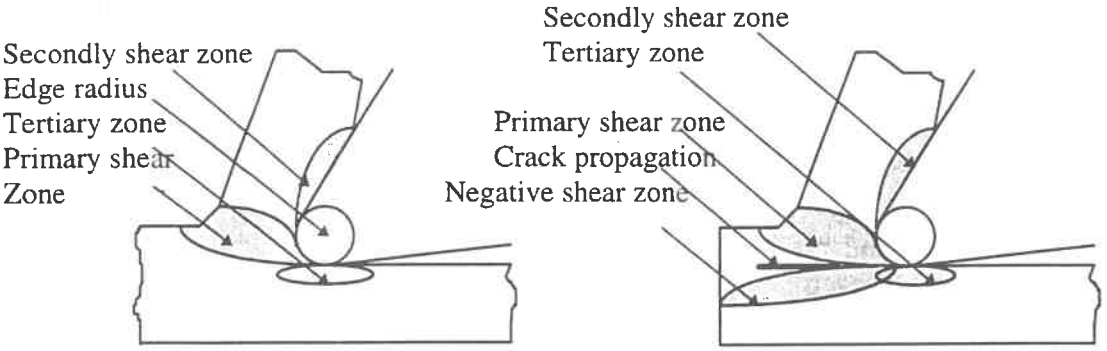

(a) Continuous cutting (b) Burr formation

Fig. 2 AE sources in continuous cutting and burr formation process

A special arrangement developed to measure the acoustic emission is schematically illustrated in Figure 3. The workpiece was attached to the work table and a Dunegan model D9201A wide-band (50 KHz to 1 MHz) piezoelectric transducer mounted underneath the workpiece was used to measure the acoustic emission signal. The raw AE signal was fed through a preamplifier with fixed 40dB gain and built-in high-pass filter with 50 KHz corner frequency. This output was further amplified by a Dunegan amplifier with 20 dB gain and fed to an AE rms meter with sampling time of 0.25 ms and then digitized on-line through an A/D channel of the data acquisition board with commercial software GageScope on an IBM PC-AT for further analysis.

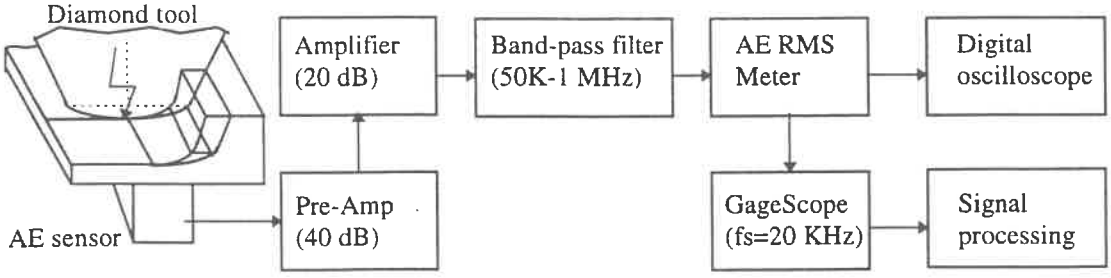

Fig. 3 Instrumentation for monitoring cutting process

3. Experimental results and discussions

Experiments were conducted on a Kuglar F380/1000 flycutting machine. The bed, guide block, X-slide and Z-column are manufactured from natural granite which gives excellent stiffness, thermal stability and good vibration damping of the machine structure. Machining spindle, X and Y axis slide tables, and work table are vacuum preloaded air-bearings. The infeed resolution in the vertical direction is 0.1 μm. Figure 4 shows two surfaces generated at feed rate f = 30μm/r, depth of cut d = 0.5 μm and 20 μm, that is t_{max} = 0.09 μm and 15 μm. As seen in the photos, surfaces with a burr and without a burr can be produced by changing the depth of cut d.

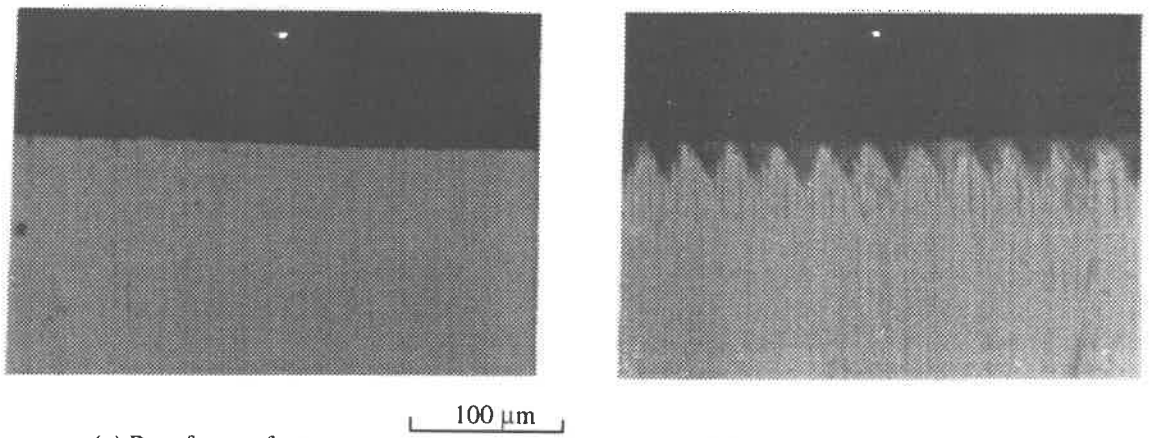

(a) Burr free surface (b) Surface with a burr

Fig. 4 Surfaces generated at different undeformed chip thickness

Figure 5 shows a chip generated at a depth of cut d=0.1 μm, and feed rate f=6 μm/r. This corresponds to a maximum uncut chip thickness t_{max} = 8.5 nm, and uncut chip width C_w=144 μm. It is clear from the photo that the machined chip width is about 50μm, which is only 1/3C_w. This is because the uncut chip thickness is not constant along the cutting edge. It takes a maximum value at the top of the uncut shoulder and gradually changes to 0 at the bottom of cutting. There is a transition value below which no chip will be generated. With the photos, it can be estimated that in this machining setup, the minimum uncut chip thickness in which chip can be generated is about 6nm. Fig. 6 is the corresponding AErms signal. The signal-to-noise ratio was on the order of 10^3, which shows the very high sensitivity of AErms to work-tool contact even in the range of nanometer chip dimensions.

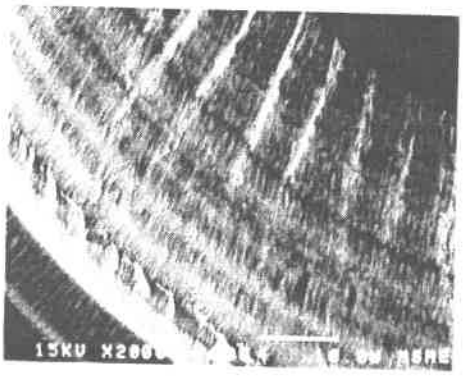

Fig. 5 A typical chip generated in UPMC

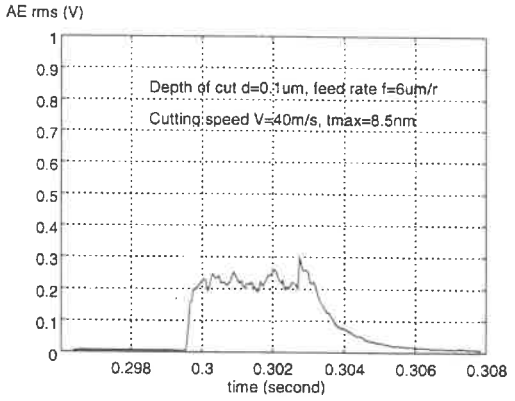

Fig. 6 Signal in burr free surface generation

Fig. 7 is the signal collected under the cutting conditions of d=40μm, f=6μm/r, that is, t_{max} = 3 μm. The average AErms is higher and the pattern is obviously different from that in Fig. 6. The peak in the exit point is an indication of a burr formation. This is, in fact, similar to the AE signal observed by Diei and Dornfeld [Diei and Dornfeld, 1987] in conventional flycutting milling tests. Fig. 8 shows the exit peak AErms variation with depth of cut d at several feed rates. It can be found that the exit peak AErms is sensitive to both depth of cut and feed rate, this implies that AE is also sensitive to burr size variation. The transition from a burr free surface to a surface with a burr at about 5μm can also be clearly identified from the figure.

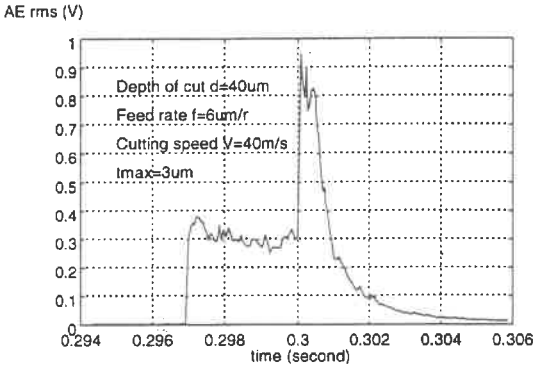

Fig. 7 Signal in burr formation

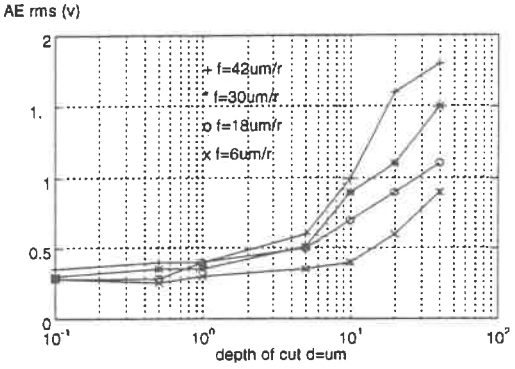

Fig. 8 AE rms peak value vs. cutting parameters

4. Conclusions

With a specially designed diamond tool, a burr free surface and a surface with burr can be generated by changing the depth of cut. The AE rms peak value at the exit point of cutting was found to be closely related to the burr formation from both AE source analysis and cutting tests. This AE feature could be used for in-process detection of burr formation.

References

1. Chern, G., et al., "Burr/breakout development and experimental verification", Trans. ASME, J. Eng. Mats. Tech., to appear.
2. Diei, E., et al., "Acoustic emission from the face milling process--the effects of process variables", Trans. ASME, Journal of Engineering for Industry, Vol. 109, 1987, pp92-99.
3. Donaldson, R., et al., "Design and performance of a small precision CNC turning machine", Annals of the CIRP, Vol. 36, No. 1, 1986, pp373
4. Furukawa, Y., et al., "Effect of material properties on ultraprecision cutting processes", Annals of the CIRP Vol. 37/1/1988, pp113-116.
5. Hashimura, M., et al., "Analysis of three dimensional burr formation in oblique cutting", Annals of the CIRP, Vol. 44/1/1995, pp23-26.
6 Ikawa, N., et al., "Ultraprecision metal cutting--The past, the present and the future", Annals of the CIRP, Vol. 40/2/1991, pp587-594.
7. Ikawa, N., et al., "Chip morphology and minimum thickness of cut in micromachining", . Journal of the Japan Society of Precision Engineering, Vol. 59, No. 4, 1993, pp141-147, (in Japanese).
8. Ko, S. and Dornfeld, D., "A study on burr formation mechanisms", Trans. ASME, J. Eng. Mats. Tech., Vol. 113, No. 1, pp 75-87.
9. Lucca, D., et al., "Aspect of surface generation in orthogonal ultraprecision machining", Annals of the CIRP Vol. 43/1/1994, pp43-46.
10. Moriwaki, K., et al., "Machinablity of copper in ultraprecision micro diamond cutting ", Annals of the CIRP Vol. 37/1/1989, pp115-118.
11. Nakayama, K., et al., "Burr formation in metal cutting", Annals of the CIRP, Vol. 36/1/1987, pp33-36.

Controlled Microcutting Tests on Single Crystal Silicon

B.V. Tanikella and R.O. Scattergood

Precision Engineering Center
Department of Materials Science and Engineering
North Carolina State University, Raleigh, NC 27695-7918

INTRODUCTION

Precision grinding [1] is accomplished by the cutting action of many sharp diamonds embedded in the wheel binder material. The fracture damage in the resulting part is dependent on the material properties and operating conditions. Considering grinding as a multi-scratch process, the response of a single cutting grain and the damage transitions produced by the cutting action as the load on the grain is varied, will be of primary interest. The microcutting action of a single cutter is important because it plays a key role in determining the subsurface fracture damage produced in processes such as polishing and grinding [1,2]. In recent studies with glass and amorphous SiC thin films, Tanikella and Scattergood [3,4,5] demonstrated a one-to-one correspondence between crack-initiation and depth-of-cut during microcutting. Extension of the results using statistical averaging effects will facilitate the prediction of the surface finish and subsurface fracture damage. The effect of crystallography is important for developing these models for crystalline materials. The purpose of the present work is to investigate the cracking thresholds, crystallography, and tool geometry effects for single crystal silicon. An understanding of the micromechanics of silicon would also enhance its utility as a high-precision, high-strength, high-reliability mechanical material, especially applicable in micro mechanical devices and components in conjunction with integrated electronics.

EXPERIMENTAL DETAILS

The material used in the present study was device grade single crystal p-type silicon with (100) and (111) surfaces. A freshly sharpened Vickers diamond pyramid indentor was used as the cutting tool for a series of tests and its condition was monitored frequently. All of the tests were conducted in controlled laboratory air at $20 \pm 0.05^{\circ}$ C and $40 \pm 10\%$ relative humidity. A field emission JOEL 6400 scanning electron microscope (SEM) was used for micrographic observations. Two different test systems [4,5,6] were used for conducting the microcutting tests and they adopt either force control or depth control.

In the force controlled setup [4], a 140 μm range piezo translator (PZT) was mounted to the moveable crosshead of an ATS benchtop load frame and the PZT amplifier was interfaced to a PC for closed-loop load control profiles during microcutting tests. A 10 N load cell and fixture to hold a Vickers diamond indentor were attached to the PZT. An x-y stage was mounted to the base of the load frame for sample positioning. One axis of the stage was driven by a motorized micrometer screw using an analog encoder-controller for speed control. An acoustic emission sensor with a frequency-detection window set between 100 KHz to 900 KHz (200 KHz resonance frequency) was used for the acoustic measurements. A nominal cutting speed of 5 μm/sec was used for all of the microcutting tests. The microcutting grooves for different maximum loads appear as shown in Figure 1a. The length of the entrance, exit and hold portion of each groove is constant because of the fixed cutting speed, but the groove widths change with maximum load as indicated. During a loading profile the acoustic pulses detected by the oscilloscope were transferred and stored in the PC (using Labview® software) for comparison with the load values.

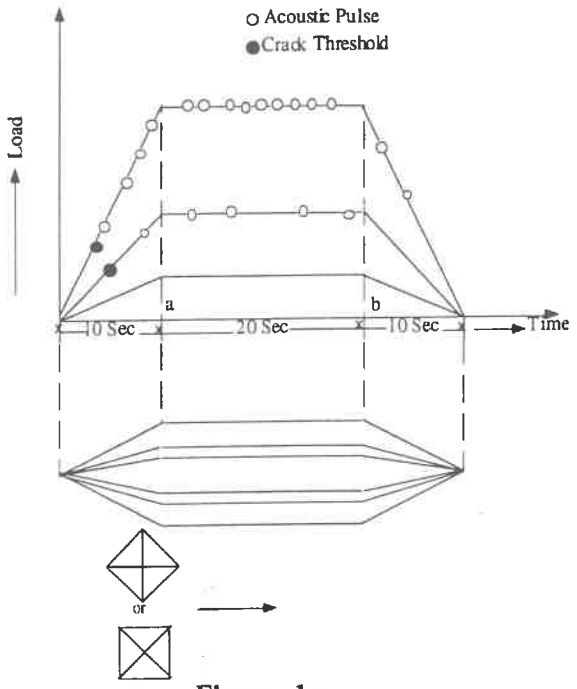

Figure 1a.
Test scheme during force control Tests

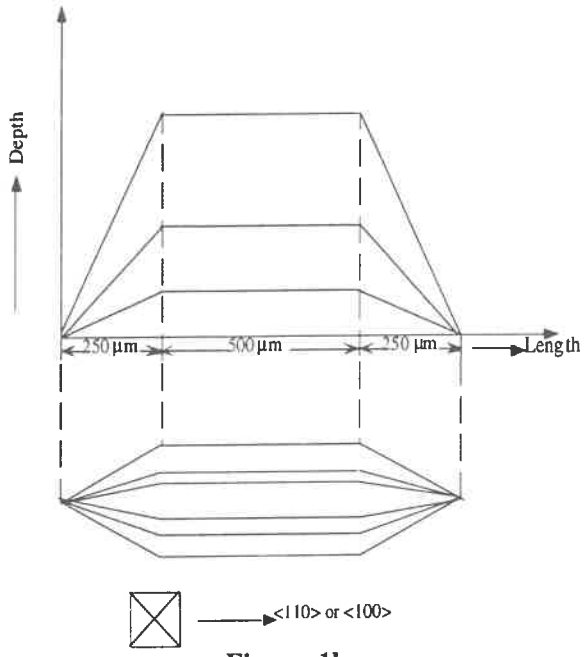

Figure 1b
Test scheme during depth control Tests

In the depth controlled setup [6], a Rank Pneumo ASG 2500 diamond turning machine (DTM) was used for conducting microcutting tests. This DTM features T-base configured hydrostatic bearing slides, an aerostatic bearing workpiece spindle, and laser interferometer feed back. The spindle of the diamond turning machine was locked mechanically and the vacuum chuck mounted on it was used to hold the sample. The sample was a 4 inch wafer and was mounted on the vacuum chuck of the DTM in as-received condition. <110> and <100> crystallographic directions of the wafer were adopted as two different cutting directions, and the direction was fixed before locking the spindle. A three-axis PZT load cell was used for recording the force data. The load cell and a specially fabricated fixture were mounted on a custom built dynamometer. Viscous grease was used between the interfaces and the assembly was held together with a torque of 11.3 N-m, to achieve a stiff setup. The slides of the DTM were programmed to perform the microcutting tests. A schematic of the test scheme is shown in Figure 1b. The x-slide of the DTM was programmed to give a nominal speed of 10 mm/min during all the microcutting tests. The side of the Vickers diamond is along the cutting direction. In earlier studies using the force controlled setup, it was found out that cutting along the side of the indentor produces less fracture damage compared to cutting along the diagonal for silicon. Performing constant depth-of-cut tests on single crystal silicon is complicated due to the nonflatness in silicon wafers due to residual stresses. A capacitance gage was used to determine the slope before conducting each microcutting test and the data thus obtained was applied in the part program assuming a linear slope. Thus, the resulting microcutting grooves would have the desired depth at a given position along the microcutting groove. The force data was acquired into a PC using Labview® software.

RESULTS AND DISCUSSION

Force Control

Microcutting tests as shown in Figure 1a were conducted in the load range of 0.03 to 3 N. The variables during microcutting were load, indentor orientation, cutting direction in relation to the crystal direction, and the normal to the crystal surface (i.e. (100) or (111)). The crack-initiation threshold, as manifest by the detection of an acoustic pulse during the load cycle in Figure 1a, was 0.04 to 0.4 N, depending upon test conditions. The threshold observed during the loading part of

the cycle varied significantly with the loading rate. Figure 2 shows the effect of loading rate while cutting along the diagonal on a (100) surface along one of the <110> directions. Similar loading rate effects were observed for various cutting direction combinations. Each data point in Figure 2 shows the first acoustic pulse observed during the load cycle, indicating that the crack-initiation threshold during loading can be increased with increasing loading rate. However, the amount of increase depended somewhat upon the direction of cutting and the crystal surface plane.

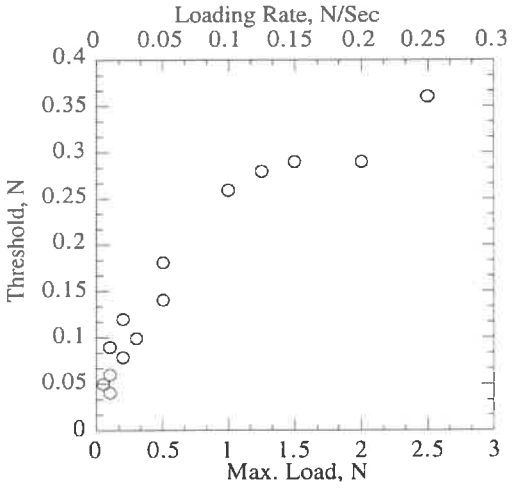

Figure 2
Plot showing the effect of loading rate

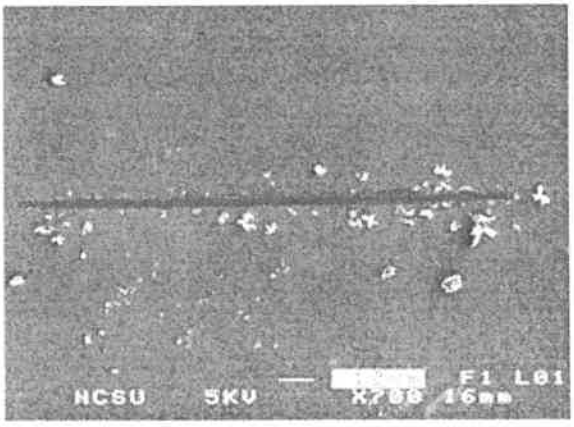

Figure 3a
Microcutting groove at a load of 0.04 N

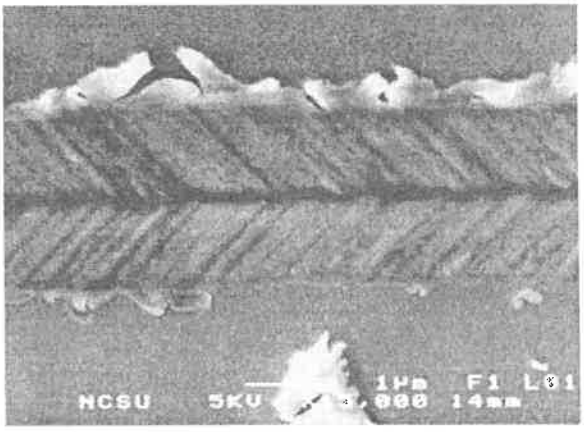

Figure 3b
A close-up look at the groove Figure 3a

The extent of fracture damage in the microcutting grooves depended strongly upon the cutting direction and the indentor orientation, in relation to the crystallographic orientation of the wafer. Figure 3a and 3b show a microcutting groove at the threshold 0.04 N. Detailed SEM observations showed that the groove is crack-free and is a ductile cut. Figure 4 shows a similar groove as in Figure 3b with the load just above the threshold, at 0.05 N. A tiny radial crack along the edge of the groove can be observed. This is the kind of cracking observed just above the threshold. Note that Figures 3b and 4 have opposite cutting directions. At the threshold, the cracking behavior was somewhat erratic and cracking events were not reproducible. As the load is increased the extent of damage increased, however, and it depended strongly upon the crystallography and the indentor

orientation in Figure 1a. The indentor oriented with its diagonal along the cutting direction produced more damage compared to the cutting grooves made with the indentor side along the cutting direction. This is in contrast to the observations with glassy amorphous materials such as borosilicate glass [4,5], wherein the extent of damage produced is less while cutting along the diagonal of the tool. Thus, in the case of single crystal silicon, a wedge-shaped tool produces more fracture damage compared to a flat-faced tool.

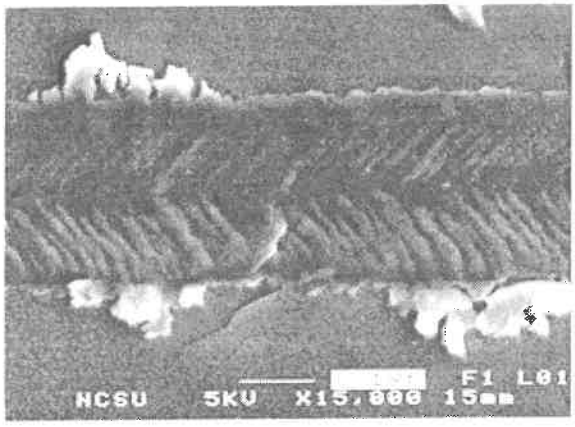

Figure 4
A close-up look at a 0.05 N microcutting groove

The effect of crystallography along with the indentor orientation provides an optimal direction for cutting. There were four different configurations when working with a (100) wafer. These constitute cutting along <110> and <100> directions, with two different indentor orientations. Cutting along <100> direction with the side of the indentor along the cutting direction is the optimal combination for minimal fracture damage in the microcutting grooves. Figures 5a and 5b show comparison of two microcutting grooves (with crystal surface (100)) at a load of 0.5 N, with differences in the indentor and crystallographic orientations. Figure 5a had the cutting direction along <100> with the indentor side oriented along the cutting direction, while Figure 5b had the cutting direction along <110> with the indentor diagonal oriented along the cutting direction. Figure 5a shows significant portions of ductile areas, while the groove in Figures 5b shows severe chipping damage. The crystallographic relations are in agreement with the observations in literature [7]. Similar crystallographic effects were observed in the case of (111) wafers [8].

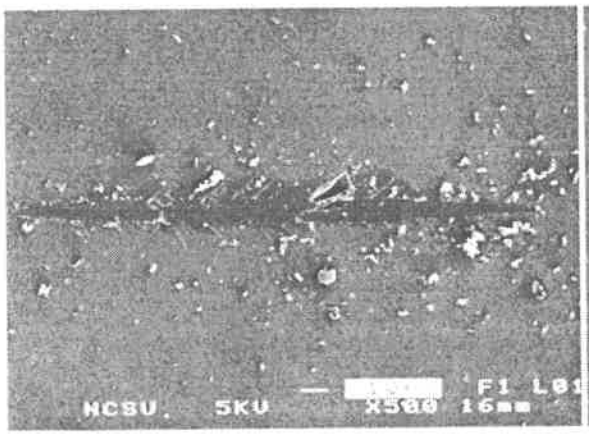

Figure 5a
Microcutting groove at 0.5 N along <100>
cut with the side of the Vickers indentor.

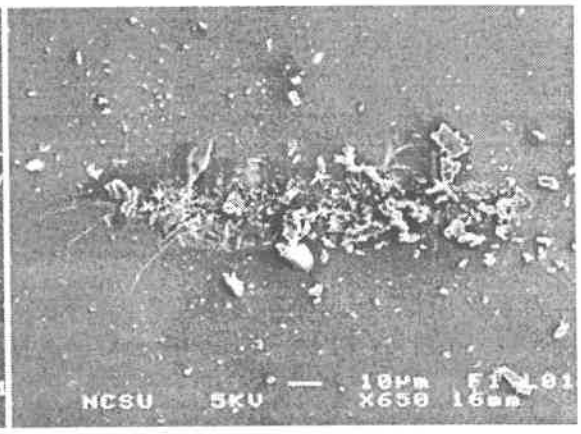

Figure 5b
Microcutting groove at 0.5 N along <110>
cut with the diagonal of the Vickers indentor.

Depth Control

Figure 6a shows a plot of normal force vs time for a microcutting groove at a depth-of-cut of 200 nm. Figure 6b shows an SEM micrograph corresponding to a portion of the groove in Figure 4, at the maximum cutting depth. Closer examination showed that the whole groove is crack-free and ductile. Also, the force is constant (above the noise level) at the maximum depth, indicating a uniform depth-of-cut. If the correction for the surface tilt of the wafer was inappropriate, the force profile would show a tilt of the force trace at the maximum depth-of-cut, indicating the deviation from a constant depth-of-cut.

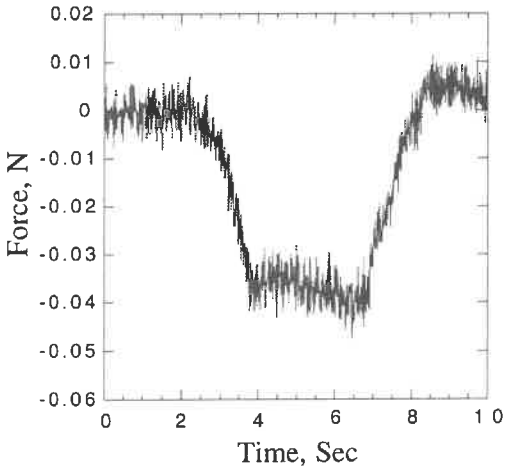

Figure 6a
Normal Force vs Time for a 200 nm depth-of-cut microcutting groove

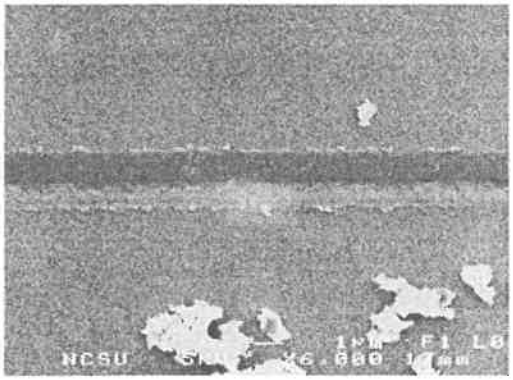

Figure 6b
SEM micrograph of the microcutting groove corresponding to Figure 6a at maximum depth

Above the cracking threshold, the force plots show significant deviation from Figure 6. Cracking thresholds are manifest as (unloading) pulses in the force traces. The threshold can be expressed in terms of a critical force or a critical depth-of-cut, since the tool geometry is known. As one would expect, results obtained from the depth-control tests match very well with the cracking thresholds obtained using the force control system. Figure 7a shows the force profile corresponding to a microcutting groove just above the threshold, at a depth-of-cut of 250 nm. In Figure 6a, the maximum normal force could be observed to be below the threshold, and the groove was of ductile nature. The maximum force in Figure 7a is about 0.06 N, and this is clearly above the threshold.

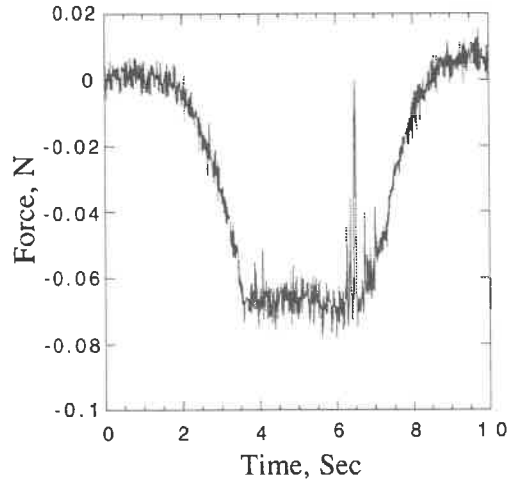

Figure 7a
Normal Force Profile for a 250 nm depth-of-cut micocutting groove

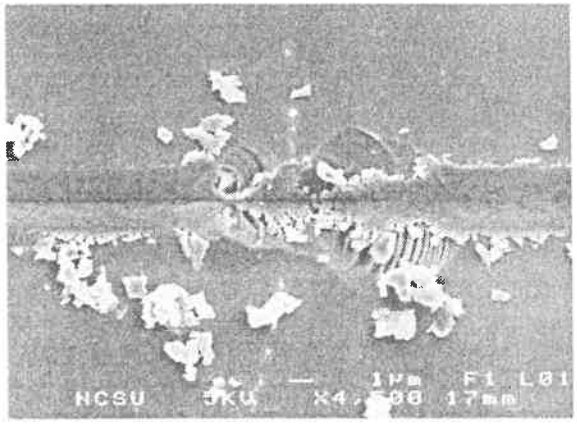

Figure 7b
SEM micrograph showing the fracture event associated with the large force pulse in Figure 7a

Detailed SEM observations showed a one-to-one correspondence between these force pulses in Figure 7a and a fracture event within the groove. The lateral chip in a portion of the microcutting groove shown in Figure 7b was associated with the largest force pulse in Figure 7a. This large force pulse indicates that the tool is unloaded to a large extent due to this large chip (or missing material ahead of the tool tip), and the force comes back to the normal position upon subsequent cutting to maintain the programmed depth. Similarly, the smaller force pulses corresponded to radial cracking and smaller scale chipping damage.

Figure 8a shows the normal and cutting force vs time respectively, for a microcutting groove at a programmed depth-of-cut of 1000 nm. It is evident that the depth-of-cut for this groove is well above the critical depth-of-cut. The initial force pulse during the load cycle occurs well above 0.045 N, indicating an increase in the cracking threshold as the loading rate goes up (loading rate increases with the depth-of-cut because the ramp distance in Figure 1b is fixed and the cutting speed is fixed). The initial pulse in Figure 8a occurs at a load close to 0.12 N. SEM observations showed no evidence of fracture in the microcutting groove before this initiation point. The loading rate effect clearly supports the results in Figure 2. The number of force pulses in Figure 8a far exceeds the number in Figure 7a. The cutting force profiles also showed a force pulse corresponding to each large pulse on the normal force profile. This indicates that there is also a significant force change in the cutting direction due to the chipping action. Detailed SEM observations of the microcutting groove corresponding to Figure 8a showed a one-to-one correspondence between the fracture events and the force pulses. Qualitatively, the magnitude of the force pulses were proportional to the extent of fracture. No attempts were made to provide quantitative measure of the extent of fracture. Figure 8a clearly shows that the tool is completely unloaded at the largest force pulse and this corresponded to the SEM micrograph shown in Figure 8b. There is a lateral chip ahead of the tool, and the tool is in a completely unloaded state for a short period due to the missing material, as indicated by the force information.

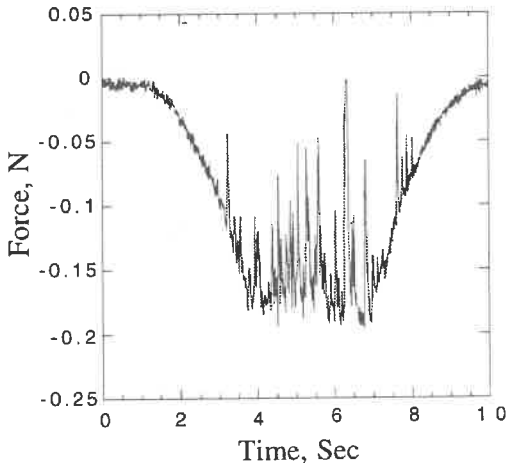

Figure 8a
Normal Force vs Time for a 1000 nm depth-of-cut microcutting groove

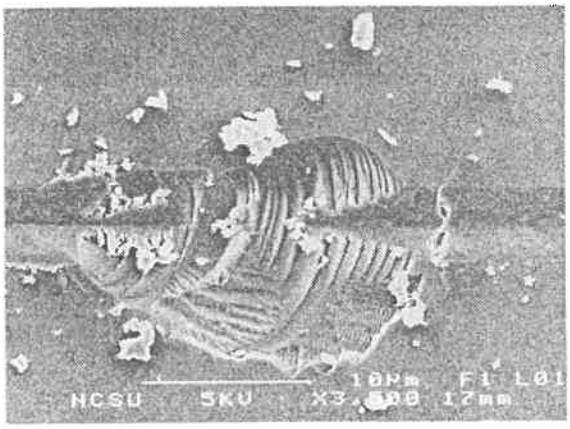

Figure 8b
SEM micrograph showing the fracture event associated with the large force pulse in Figure 8a

All the above results were obtained for cutting along the <110> direction on the (100) silicon wafers. Changing the cutting direction to <100> (by rotating the spindle by 45°), showed significant differences in the fracture morphologies of the microcutting grooves. Figure 9a shows the normal force corresponding to microcutting groove at a depth-of-cut of 1200 nm. This force curve doesn't show any force pulses similar to those in Figure 8a. The maximum normal force in this case is about 0.2 N, and is higher than that in Figure 8a. Even at such high force levels, there was no indication of large scale fracture associated with the present cutting groove. Detailed SEM

observations showed no lateral chips along the whole groove. However, the groove was observed to have radial cracks along both sides of the groove as shown in Figure 9b. This can be explained from consideration of the tool geometry, cleavage planes and directions. Indentation fracture [9] shows that the radial cracks originate from the corners of a Vickers indentor. When the cutting direction is along <100>, the radial cracks on {111} cleavage planes would initiate in the <110> directions. Since the <110> directions are the favorable directions for crack propagation, the radial cracks extend and show up along the edges of the cutting grooves. While cutting along <110>, the radial cracks could not propagate along the <100> directions and thus causing significant residual stress build-up. The residual stresses thus cause large scale chipping rather than radial cracking, for this geometry.

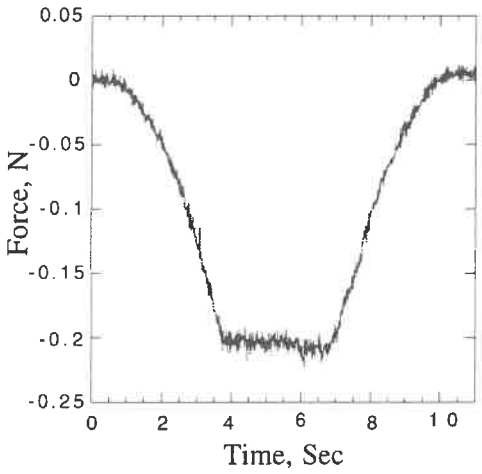

Figure 9a
Normal Force vs Time for a 1200 nm depth-of-cut microcutting groove, while cutting along <100>

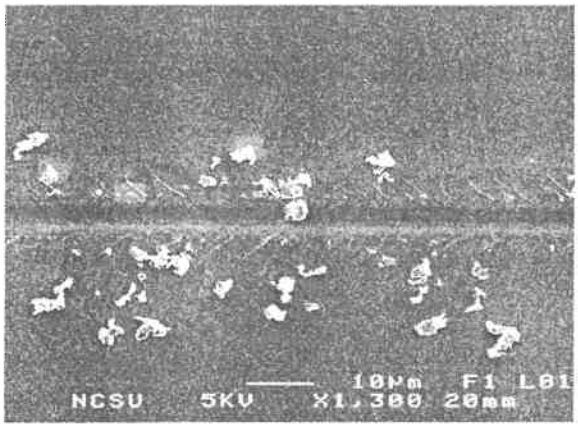

Figure 9b
SEM micrograph showing typical fracture morphology while cutting along <100> direction

Microplasticity

The features in the grooves and the debris around the microcutting grooves suggested pressure induced phase transformation during microcutting [10]. MicroRaman analysis confirmed the presence of amorphous Si phase within microcutting grooves and particle debris removed from the grooves. This can be attributed to the formation of the ß-tin metallic Si phase during the cutting process. Periodic features observed within the grooves (Figures 3b and 4) are consistent with an intemittent shear-type of chip formation process that will be facilitated by the formation of a ductile metallic phase. The MicroRaman scans also indicate the presence of large tensile residual stresses that are attributed to a mixture of amorphous and crystalline phases produced by microcutting. In situ recrystallization of the amorphous phase during microcutting has been suggested as a mechanism [10].

SUMMARY

Crack-initiation studies were conducted using two different test systems using force control and depth control respectively. Acoustic emission and force sensing were used as the tools for determining the cracking thresholds. An increase in the cracking threshold with loading rate was observed, and this would have important ramifications with respect to diamond turning and grinding. Cutting along the side of the Vickers indentor and <100> directions of the wafer were found to produce minimal fracture damage. Pressure induced phase transformation of silicon was understood to be the reason for periodic features in the grooves.

REFERENCES

1. T. Bifano, T. A. Dow, and R. O. Scattergood, "Ductile-Regime Grinding: A New Technology for Machining Brittle Materials", J. of Engr. for Ind., **113**, pp 184-189, 1991.

2. P. Blake et al., "Precision Machining of Brittle Materials", Ceramic Bulletin, **67** [6], (1988).

3. B.V. Tanikella and R.O. Scattergood, "Acoustic Emission during Indentation Fracture",J. Am. Ceram. Soc., **78** [6] pp 1698-702, 1995.

4. B.V. Tanikella and R.O. Scattergood, "Fracture damage in Borosilcate Glass During Microcutting Tests" Scripta Met., **34** [2], pp 207-213, 1996.

5. B.V. Tanikella, K.A. Gruss, R.F. Davis, and R.O. Scattergood, "Indentation and Microcutting Fracture Damage in a SiC coating on an Incoloy Substrate" surf. coat. tech., in press.

6. B.V. Tanikella and R.O. Scattergood, "Controlled Microcutting Tests on Semiconductor Silicon Crystals using a Diamond Turning Machine", Prec. Engg., to be submitted.

7. W.S. Blackley and R.O. Scattergood, "Crystal Orientation Dependence of Machining Damage-A Stress Model", J. Am. Ceram. Soc., **73** [10], pp 3113-15, 1990.

8. B.V. Tanikella, PhD thesis, North Carolina State University, in progress, 1996.

9. B.R. Lawn, "Fracture of Brittle Solids - second edition", Cambridge University Press, 1993.

10. B.V. Tanikella, A.H. Somasekhar, A.T. Sowers, R.J. Nemanich, and R.O. Scattergood, "Phase Transformation During Microcutting Tests on Silicon", Appl. Phys. Let., to be submitted.

Patterning Submicrometer Features Using Masked, Broad Beam Ion Machining

Helen E. Caggiano and Thomas G. Bifano
Boston University Precision Engineering Research Laboratory
Boston, MA

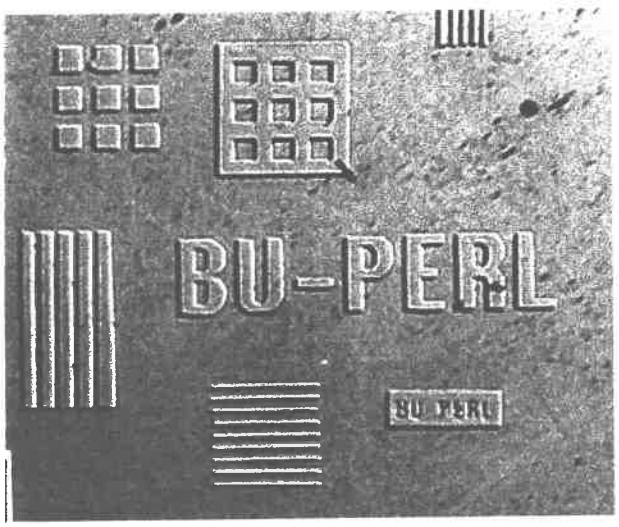

Broad beam ion machining is being investigated as a process for imprinting submicrometer features on advanced ceramic and glass materials. Ion machining has been used previously for final surface contour correction of mirrors [1 - 5]. This paper describes using broad, neutral ion beams to create patterns on the surface of a masked substrate. Photolithography techniques are used to mask the substrate with photoresist prior to ion machining. Portions of the substrate beneath the photoresist mask are shielded from the ion beam while the unmasked portions of the substrate are machined. While the substrate is being machined, the mask is also being machined.

To date, our research indicates that the achievable lateral resolution of this technique is limited only by the resolution of the photoresist (approximately 50 nm). Vertical precision is on the order of 10 nm. Several combinations of photoresist and substrate have been evaluated for various applications (i.e. diffraction gratings, video disc masters, compact disc masters, and magneto-optical storage devices). A calibration mask has been produced to evaluate achievable pattern resolution in the photoresist layer. After ion machining, the quality of feature transfer to the substrate has also been evaluated. It has been observed that when subjected to the intense energy of ion machining, the photoresist may flow and lose edge definition. Heat transfer in the ion machining process has been measured and numerically modeled. An ion machining system (IMS) has been designed and constructed to conduct broad beam ion machining experiments on large samples using a 110 mm diameter ion source. Submicrometer features have been produced in various ceramics (SiC, Al_2O_3, ZrO_2), glasses (fused silica, Corning 9600), metals (nickel, molybdenum), and semiconductors (silicon).

The IMS consists of an Ion Tech 110 mm ion source with a plasma bridge neutralizer (PBN). The source is mounted vertically in the IMS chamber. Samples are mounted directly beneath the source on a rotary stage.

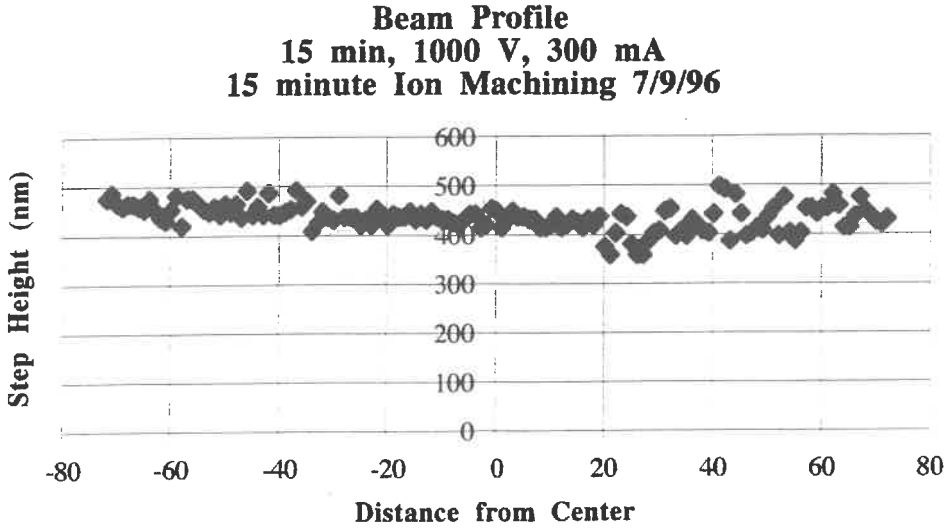

Figure 1. Beam profile of 110 mm ion source.

The ion source provides a nearly uniform beam over a 140 mm diameter. This allows large samples patterned with photoresist masks to be uniformly machined by the ion beam without introducing a rastering process.

As a result of this broad beam machining, the amount of heat energy directed toward the substrate is quite large. As a result, if the substrate temperature exceeds the melting temperature of the photoresist mask, the mask will flow, resulting in a loss of feature integrity. The heat transfer process has been investigated using silicon. An exposed junction thermocouple was placed under the substrate, using vacuum grease as a thermal conductor between the substrate and the thermocouple. The temperature of the substrate was measured for three different ion beam configurations as shown in Table 1.

Table 1. Ion source configurations for thermal testing.

Thermal Test	Beam Current (mA)	Beam Voltage (V)
1	300	1000
2	150	1000
3	140	500

Machining rate increases with increasing beam current and with increasing beam voltage. The measured temperature exhibit typical behavior of a first-order thermal system, as shown in Figure 2.

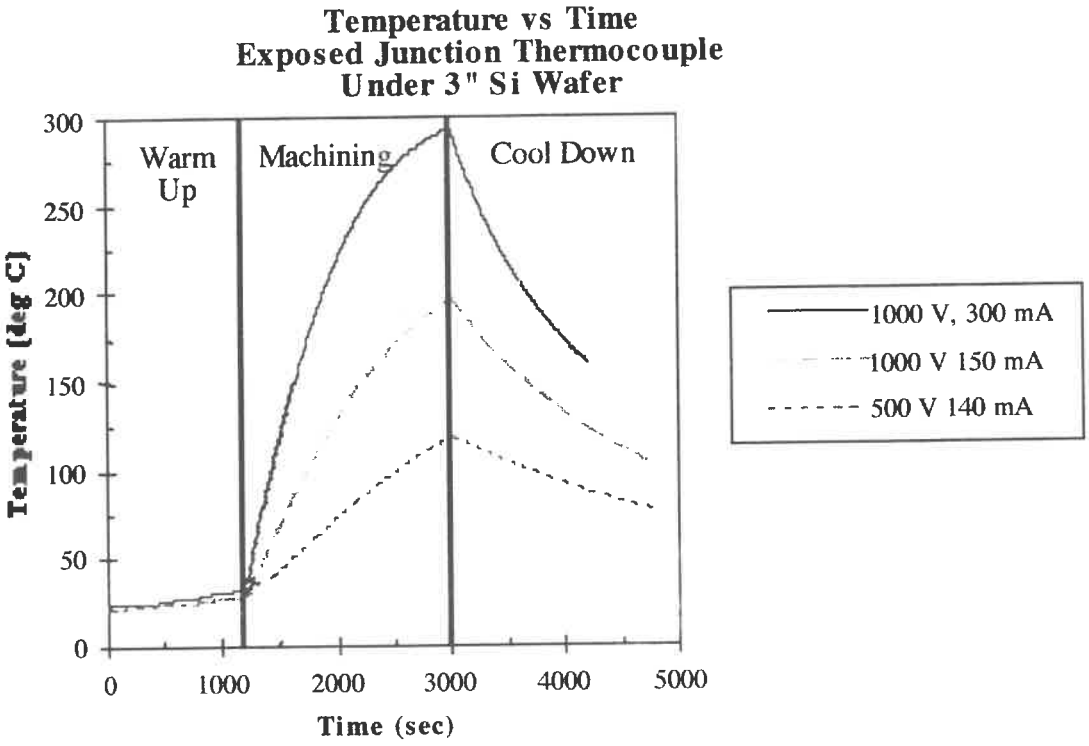

Figure 2. Measured temperature versus time for three machining conditions.

The curves in Figure 2 indicate the temperature measured during ion machining tests, during ion beam warm up, machining, and cooling. The first 1200 seconds (20 minutes) correspond to the warm up period during which the source is on (i.e. the ion source is generating an ionized plasma, but the ions are not being accelerated toward the substrate), and the plasma is stabilizing. The next 1800 seconds (30 minutes) correspond to machining, during which the ions are accelerated towards the substrate. The remaining 1200 seconds (20 minutes) indicates the cooling period, where the beam and source are shut down, and argon gas continues to flow. This cooling period is required to avoid oxidation of the source's tungsten filament as the chamber is vented to atmosphere. Argon continues to flow through both the source and the PBN until the chamber has cooled.

An analytical model of the heat transfer during these processes is under development. The model will be used to predict (and avoid) the onset of feature degradation during machining. The model can also be used to determine if auxiliary cooling systems are required and the amount of cooling needed during the machining process.

The machining rates for silicon were tested at each of these ion source configurations shown in Table 1, and the results are summarized in Table 2.

Table 2. Neutral ion machining rates for silicon using thermal testing configuration

Beam Voltage (V)	Beam Current (mA)	Silicon Material Removal Rate (Å/min)
1000	300	300
1000	150	150

Once the machining rate for silicon was determined, the samples were patterned using a photolithography mask. The patterns consisted of line widths from 0.3 μm to as much as 20 μm, with features similar to those needed for compact discs, diffraction gratings, and magneto-optical storage devices. Four different types of negative-tone photoresists were used in the ion machining study to determine which photoresist maintained the best feature integrity. The features were observed using the SEM prior to and following the machining process. The following SEM photographs show the pattern transfer from the photoresist mask to an ion machined silicon wafer.

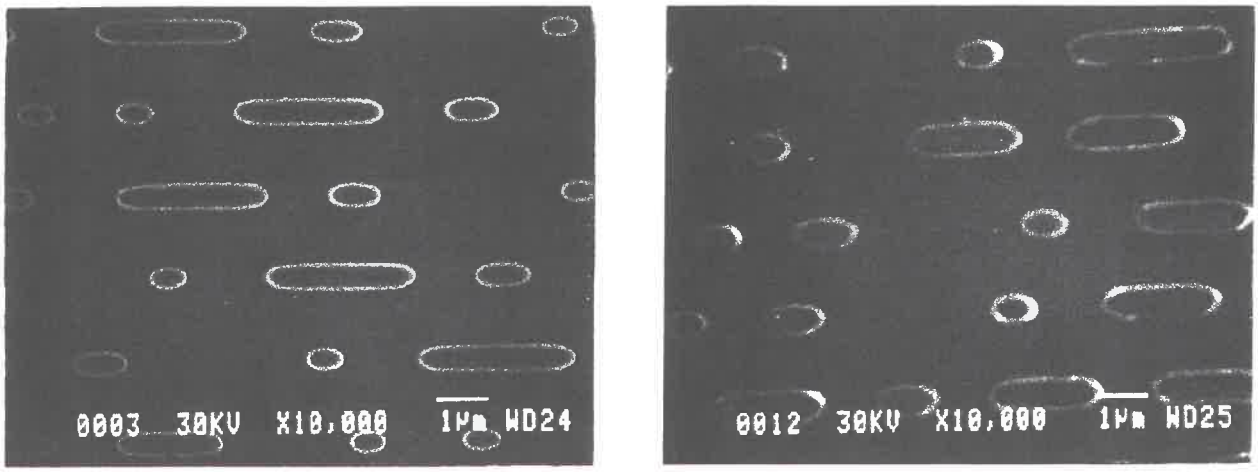

Figure 3. a. Photoresist mask on silicon wafer, prior to ion machining. **b.** Patterned silicon wafer after ion machining.

From the photographs in Figure 3, direct transfer from the exposure to the machining processes can be observed. Other substrate materials will be tested using similar conditions to those used with the silicon wafers. From these experiments, alternative substrates can be developed for potential use as stampers for compact disc and video disc replication and substrates for diffraction gratings and magneto-optical applications. Once alternative substrates are determined, their utility in these different applications can be verified.

References:

[1] Allen, Lynn N., Hannon, John J., and Wambach, Richard W., "Final surface error correction of an off-axis aspheric petal by ion figuring." *SPIE: Active and Adaptive Optical Components*, Vol. 1543, 1991, p. 190 - 200.

[2] Allen, Lynn N. and Keim, Robert E., "An ion figuring system for large optic fabrication." *SPIE: Current Developments in Optical Engineering and Commercial Optics*, Vol. 1168, 1989, p. 33 - 50.

[3] Allen, Lynn N., Keim, Robert E., and Lewis, Timothy S., "Surface error correction of a Keck 10 m telescope primary mirror segment by ion figuring" *SPIE: Advanced Optical Manufacturing and Testing II*, Vol. 1531, 1991, p. 195 - 204.

[4] Drueding, Thomas W., Bifano, Thomas G., and Fawcett, Steven C., "Contouring Algorithm for Ion Figuring." *Precision Engineering*, Vol. 17, 1995. p. 10 - 21.

[5] Fawcett, Steven C., Drueding, Thomas W., and Bifano, Thomas G., "Neutral ion figuring of chemical vapor deposited SiC." *Optical Engineering*, Vol. 33. No. 3. March 1994. p. 967 - 974.

Nanogrinding

Hans H. Gatzen and J. Chris Maetzig
Institute for Microtechnology (imt), Hanover University
Hanover, Germany

Abstract—Nanogrinding is an ultraprecision machining process that is based on a lapping kinematic and is very well suited for surface machining of advanced ceramics. While lapping uses loose grain, for nanogrinding the abrasive grain is completely embedded in a soft metallic plate which becomes the grinding tool. Therefore, nanogrinding is a two step process. The first step is to create the grinding plate, in a second step the work piece is machined. Nanogrinding requires a rough grinding plate, the roughness is created by conditioning the plate with pumice. During this process, pumice is embedded in the grinding plate and remains there throughout the process. Between pumice particles, the basic soft metalic plate material forms plateaus, in which diamond grain is embedded by a conditioning ring, which also aligns their summits coplanar to the plate surface. This arrangement allows to perform ductile machining, resulting in little material damage and excellent surface finish.

I. INTRODUCTION

The recording head industry is one of the dominant users of advanced ceramics, (like) as there are hot isostatic pressed (HIP) alumina-titanium carbide (70% Al_2O_3, 30% TiC), calcium titanate (Ca TiO_3), and, at an experimental level, silicon carbide (SiC). Furthermore, to a small extend, the semiconductor material silicon (Si) is utilized, which has machining properties similar to ceramics. One of the machining challenges when manufacturing recording heads for rigid disk drives is to generate surfaces that are plane (or very close to plane, with a crown of some hundred nanometers per mm work piece length) and smooth (with an average roughness in the 1 nm range) [1, 2]. Both conditions are essential for achieving good tribological behavior. Due to the fact that such a recording head is gliding on a diamond like carbon (DLC) coated disk for part of its operation, the called for excellent tribological behavior is mandatory.

The two dominant processes in machining flat surface planes are grinding and lapping [3, 4]. The atomic bond of ceramic materials is covalent, ionic, or a mix of both. This makes ceramic materials substantially more brittle than metals, which have a metallic bond where valence electrons are shared freely between the atoms of a structure. Therefore, while metals are typically machined in the ductile regime, i.e. a cutting based on plastic material deformation is performed, most commonly the machining of ceramics is done in the brittle regime. Brittle machining causes the material to form vertical cracks when a grinding or lapping grain is engaged and horizontal cracks when the load is removed. The formation of horizontal cracks causes surface chipping, which is the main mode of material removal, but due to the formation of the vertical cracks a substantial amount of subsurface damage is being inflicted. However, if a very small depth of cut is chosen, even very brittle materials may be machined in the ductile regime [5].

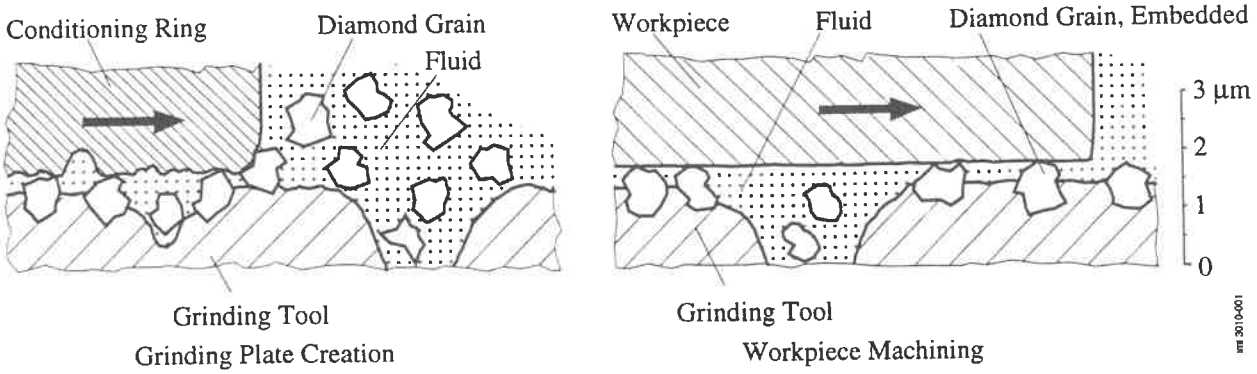

Fig.1. Nanogrinding process

Nanogrinding is a process based on a lapping kinematic [6]. While lapping uses loose abrasive grain, for nanogrinding the abrasive grain is completely embedded in a soft metallic plate which becomes a grinding tool. Therefore, nanogrinding is a two step process (Fig. 1). The first step is to prepare the grinding plate by embedding the abrasive grain in its surface. In a second step the workpiece is machined. To achieve a supersmooth surface finish, the machining parameters have to be chosen carefully to stay within the ductile regime.

II. Grinding Plate Creation

A. Grinding Plate Conditioning

The grinding plate has a diameter of 400 mm and consists of tin. Early experimental results indicated that nanogrinding cannot be performed successfully on a very smooth grinding plate. Therefore, the plate is conditioned at the beginning of each test cycle using pumice, that consists of alumina (Al_2O_3) and quartz (SiO_2); its grain size is scattering between 1 and 50 µm (Fig. 2a).

Before plate conditioning, the plate is cleaned with DI-water and is subsequently dried by blowing it off with air. To start the 30 minutes long plate conditioning cycle the plate is wetted with a slurry consisting of pumice powder and DI water, mixed at a ratio of 0.25 g/ml. Then the plate is rotated, while a cast iron conditioning ring positioned on the plate also rotates due to friction. The conditioning ring fulfills two functions: (1) it forces the plate's shape to conform to the negative of the envelope dictated by the conditioning ring, thus controlling the plate's macrotopography and (2) it causes the pumice to remove the plate's top layer and to roughen the plate's surface. During the course of the action, the pumice grain breaks down into small pieces, requiring to replenish the pumice slurry at a rate of 30 ml/min. The conditioning ring's hardness has a major influence on the breakdown velocity; by choosing cast iron, which is substantially softer than the pumice components, the pumice breakdown velocity is kept low. Ultimately, as we will find out, a substantial portion of pumice grain does remain in the plate. The amount of pumice embedded on the plate surface and the effect of its presence on the nanogrinding process will be discussed below. After the completion of the pumice plate treatment, the plate is subjected to the cleaning cycle outlined above, thus removing machining debris and loose pumice particles. At the end of the conditioning process the plate's surface roughness R_z is approximately 5µm.

Plate conditioning has to be done only occasionally to accomplish the desired plate roughness. In our case, a plate conditioning is done at the beginning of each test series to ensure equal starting conditions.

B. Diamond Impregnation

The key process to create a grinding plate is the diamond impregnation. For this step, a slurry consisting of 70% by volume DI-water, 20% ethylen glycol, and 10% ethanol, plus 17 carat/l diamond is distributed evenly over the plate surface. Depending on the application, the grain size is somewhere between 0.5 µm and 3 µm and either monocrystalline or polycrystalline diamond may be applied. Fig. 2b depicts an SEM micrograph of monocrystalline dia-

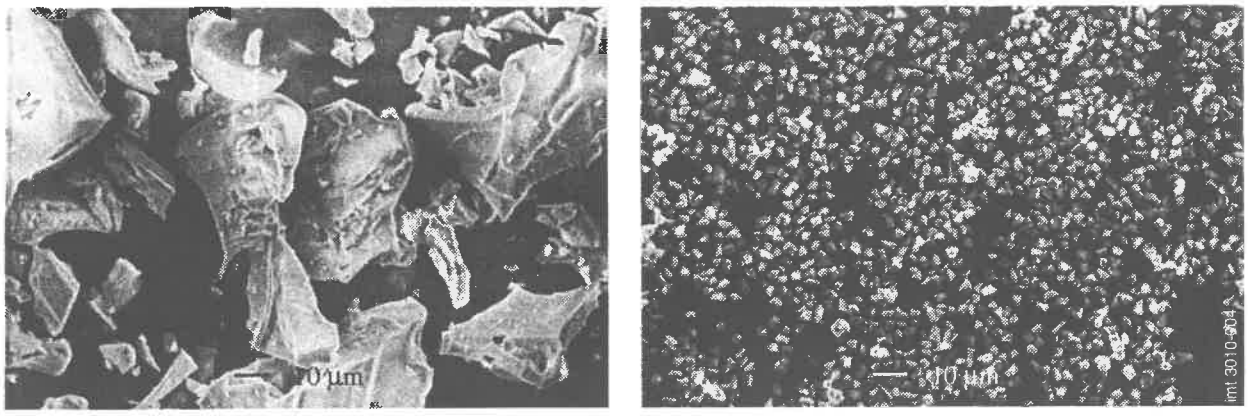

a) b)

Fig.2. Abrasives: a. Pumice grain for plate conditioning. b. 1.5-3 µm monocrystalline diamond grain.

mond with a grain size of 1.5-3 μm. The conditioning ring utilized for this process step has alumina pellets. The relative velocity between conditioning ring and grinding plate causes the conditioning ring not only to rotate, but also to float on a film of slurry fluid, holding the conditioning ring at a distance from the plate surface. The conditioning ring therefore not only embeds diamond grain in the plate, it also arranges the summits of the diamond grain in a plane coplanar to the conditioning ring envelope. A plate cleaning which removes contaminants and loose, as well as not sufficiently embedded diamond grains, concludes the grinding plate creation.

III. Workpiece Machining

After grinding plate creation, the actual workpiece machining takes place. As a first step, the plate surface is wetted with the same water based fluid used during diamond impregnation, but for this step the fluid does not contain diamond grain. During machining, fluid is added to the plate at a rate of 1 ml/min to maintain a fluid film of constant thickness. The workpieces are mounted on a disk which is placed inside the conditioning ring. The fluid film allows the workpiece to float on the grinding plate. The fluid film thickness depends on the fluid viscosity, as well as the relative velocity and pressure between plate and workpiece. The optimum working pressure was found to be 0.52 N/mm^2. It is achieved by adding weights to the disk. This pressure seems to create the proper amount of diamond protrusion to accomplish a machining in the ductile regime. Due to ductile machining, minimal damage is inflicted on the workpiece material's crystal structure at the boundary layer and a superb surface finish can be reached.

Best surface finish results are obtained when applying a two-phase machining process using a staggered diamond grain size. The first phase is a machining with 1.5-3 μm monochrystalline diamond on a grooved grinding plate, followed by a second phase with 0.5-1 μm polycrystalline diamonds on a non-grooved plate. The average surface roughness achieved with two-phase nanogrinding is R_a=1.14 nm for Al_2O_3-TiC and Ra=0.79 nm for SiC (measured by SFM). Fig. 3 depicts the nanoground SiC surface. The workpiece has a subnanometer average roughness, but the surface finish is slightly compromised by the presence of scratches. Further nanogrinding machining results are presented in [6].

IV. Plate Topography and Composition

To obtain a good understanding of the nanogrinding process, investigations regarding the grinding plate topography were performed, with the intention to shed some light on the actual machining and plate trueing mechanism. To analyze plate surface topography and composition after conditioning and plate generation, scanning electron microscopy (SEM), combined with energy dispersive spectroscopy (EDS) and scanning force microscopy (SFM) is utilized. Unfortunately, both SEM and EDS are limited to the analysis of a specimen size of below 100 mm which means, that the grinding plate would have to be dissected. For cost reasons, rather than to destroy a grinding plate by cutting it up, the experiment was performed with a tin probe small enough to fit into the SEM. This tin probe was put through a process closely resembling the one for the full size plate.

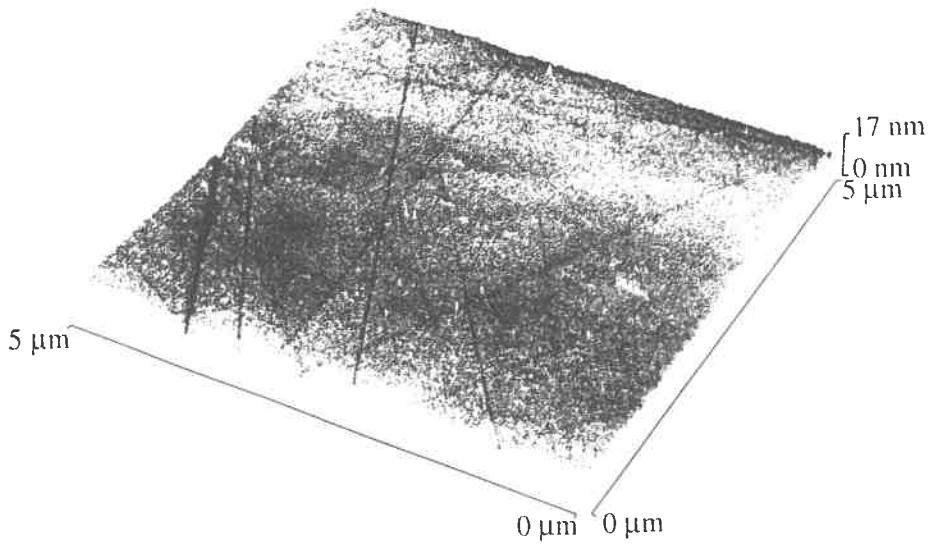

Fig.3. Surface topography of a nanoground SiC probe

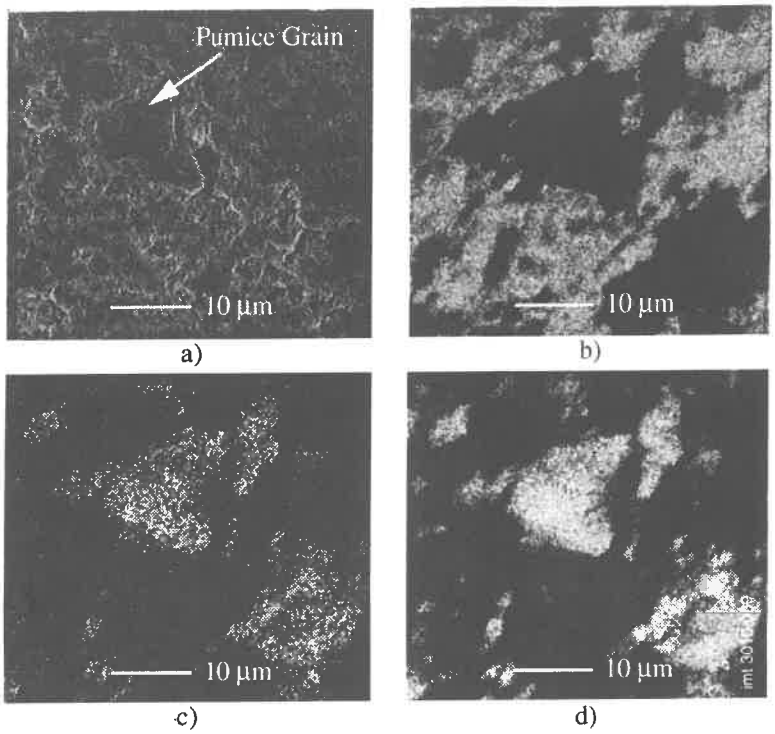

Above Fig.4. SEM/EDS micrograph of a tin probe simulating the grinding plate.
a. SEM micrograph. The arrow points at a pumice particle
b. tin.
c. aluminum.
d. silicon.

Below Fig. 5. SFM scan of the plate surface.
a. 3D plot.
b. Surface cross sections (line in a.).

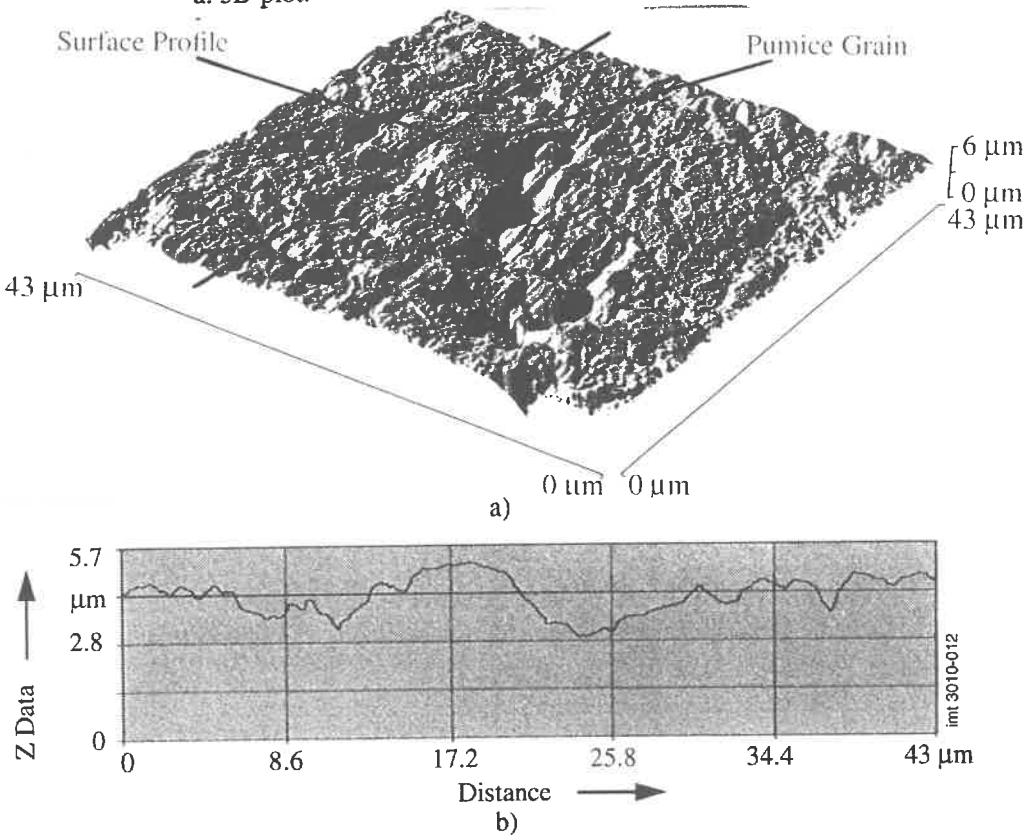

Fig. 4 b, c, and d the EDS scans for tin, aluminum, and silicon. As mentioned above, tin is the plate material, and aluminum and silicon are the elements present in pumice. Bright areas indicate a presence of the respective material, dark areas their absence. The micrographs show very clearly that a major portion of the plate surface consists either of tin or of pumice. Areas displaying the presence of aluminum and silicon are very similar in shape, which is to be expected since pumice, as mentioned above, consists of alumina and quartz. In the SEM micrograph, one of the crystal particles (s. arrow) is clearly noticable, the respective EDS micrographs characterizes the particle as pumice. All results indicate that a substantial amount of pumice remains embedded in the grinding plate. Fig. 5 depicts an SFM 3D-scan and a surface profile of the vicinity of the pumice grain found previously. The surface profile shows that the presence of the pumice particle substantially contributes to the plate's surface roughness. It also indicates that pumice protrudes above the tin level and that the tin more or less forms plateaus.

While the EDS micrographs provide clear evidence for the presence of pumice at the plate surface, only ambiguous data were obtained regarding the diamond distribution. This may be contributed mainly to the limitations of EDS: it is not capable to analyze elements below atom number 5 (bor) and has only limited capabilities between atom numbers 5 and 11, thus making it difficult to obtain good results on carbon (atom number 6).

Since there is a substantial amount of pumice on the grinding plate surface, the question arises, if pumice plays an active role in the machining process. To answer this question, the machining capabilities of a pumice conditioned plate without diamond impregnation is compared to a plate impregnated with diamond. The diamond used for the second part of this test has a grain size of 1.5-3 µm and is monocrystalline. The workpiece material is SiC, the tests are run over a machining time of one hour each. The removal rate for each test is determined every 10 minutes. Fig. 6 depicts the results, indicating distinctly that the material removal rate of pumice alone is negligible compared to the rate of a diamond charged plate. The decrease in the machining rate over time most dominantly observed in the regular nanogrinding process using a diamond charged plate may either be caused by diamond wear or, more likely, by a settling of the diamond grains in the plate surface due to the vertical machining load.

V. CONCLUSION

To perform nanogrinding successfully, a rough grinding plate is required. The surface roughness is achieved by conditioning the plate with pumice. Pumice particles embedded in the plate surface do contribute to the surface roughness. During the plate generation, the conditioning ring accomplishes three things: (1) it presses the pumice particles embedded during plate conditioning further into the soft metallic plate surface and arranges their summits in

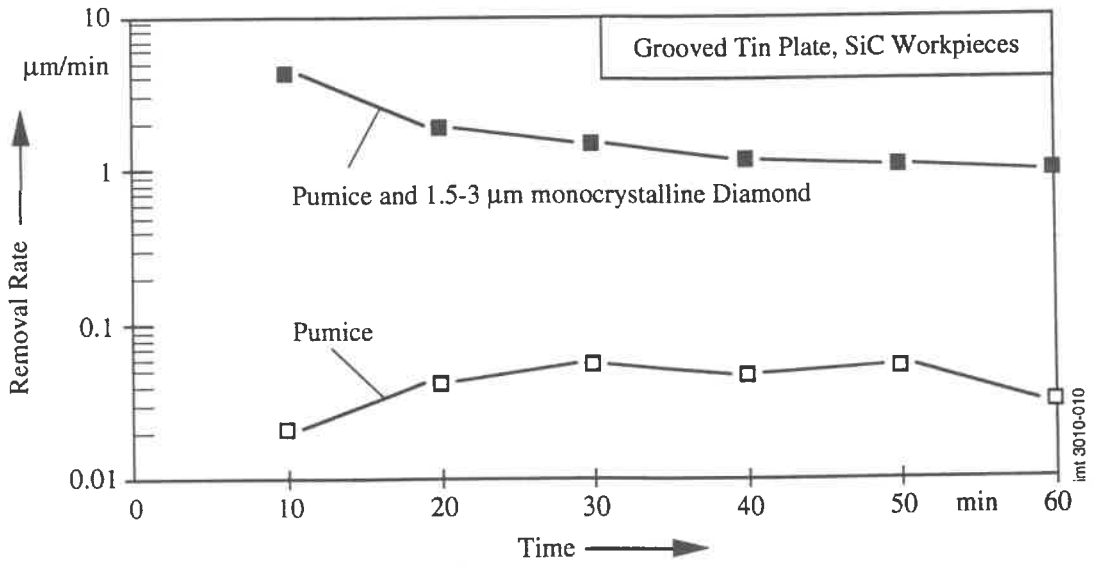

Fig. 6. SiC material removal rate for
a. Pumice.
b. Pumice plus diamond grain.

a plane; (2) it truncates the metal plate's summits in areas where no pumice is embedded, thus creating plateaus slightly below the plane formed by the pumice summits; (3) it embeds diamond grain in the tin plateaus and aligns their summits in a plane. The diamond grain causes a submicron depth of cut at the workpiece and therefore ductile machining. The pumice particles embedded don't contribute in the workpiece cutting worth mentioning, but may help to maintain the plates macroscopic shape required to achieve the required work piece flatness.

Future work will concentrate on a process optimization to eliminate surface scratches as well as investigations how nanogrinding may be applied to the coplanar machining of surfaces on the sandwich structure of materials with various hardnesses.

ACKNOWLEDGEMENTS

This research activity was in part sponsered by the DFG (German Research Foundation) and by Sumitomo Special Metals, Tokyo, Japan, who donated the ceramic materials. Furthermore, the authors would like to express their gratitude to the Hanover Laser Center in Hanover, Germany, for performing the EDS analyses, Topometrix, Santa Clara, California, for providing access to an SFM.

REFERENCES

[1] H.H. Gatzen, J.C. Maetzig and M.K. Schwabe, "Precision Machining of Rigid Disk Head Sliders", IEEE Trans. Mag. vol 32 (3), pp. 1843-1849, 1996

[2] H.H. Gatzen and L.P. Ruhbach, "Composite Tripad MIG Head for Proximity Recording", Proc., Idema '96, Santa Clara, California (accepted)

[3] G. Spur, "Keramikbearbeitung" (Ceramics Machining), Carl Hanser Verlag, Munich, Germany 1989

[4] C. Chen, S. Sakai, and I. Inasaki, "Lapping of Advanced Ceramics", Materials and Manufacturing Processes, vol. 6(2), pp. 211-226, 1991

[5] P. Shore, "Damage-free Grinding of Ceramics", British Ceramic Proc. vol. 46, 1990

[6] H.H. Gatzen and J.C. Maetzig, "Ultrapräzise Planbearbeitung hochfester Keramiken mittels Nanoschleifen (Ultraprecision surface machining of advanced ceramics using nanogrinding)". Schleifen, Honen, Läppen und Polieren, vol. 57, Vulkan-Verlag, Essen 1996 (accepted)

Effect of Vibration Using Ultrasonic and Low Frequency Vibrations on Grooving Process for Hard and Brittle Materials

Hitoshi SUWABE, Ken-ichi ISHIKAWA and Michio UNEDA
Kanazawa Institute of Technology
7-1 Ohgigaoka Nonoichi ISHIKAWA 921 Japan

1. Introduction

In many processing techniques for hard and brittle materials, the mechanical processing using grains is most generally used. Now, the processing methods using grains are classified into two types using free abrasive grains and fixed grains. The method using fixed grains generally uses diamond grains, and it has high machining efficiency as compared with the method using free abrasive grains. However, diamond grains on the tool bring about attritious wear, breaking down and thermal wear, and therefore it has some problems such as deteriorated grinding characteristics.

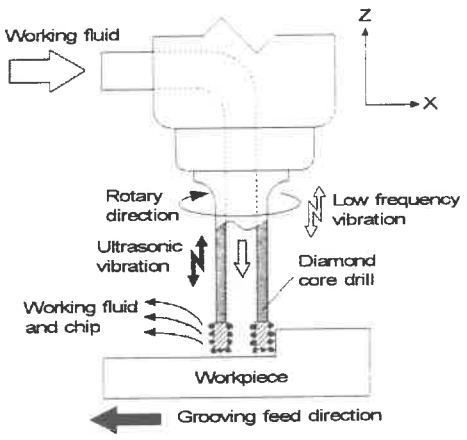

Fig.1 Model of combined vibration grooving

This study aims to develop a new grooving technique which has high efficiency and accuracy as compared with the conventional technique using a hollow cylinder drill fixed diamond grains (called such as diamond core drill) on the mechanical processing for hard and brittle materials. The new apparatus developed for grooving process is the combined vibration apparatus which can simultaneously supply a diamond tool with ultrasonic vibration and low frequency vibration as shown Figure 1. In the experiment, on the occasion of processing are carried out 4 type methods such as non-vibration, low frequency vibration, ultrasonic vibration and combined vibration (ultrasonic vibration and low frequency vibration) groovings. This paper describes about the effect of these methods as mentioned, the processing characteristics and accuracy.

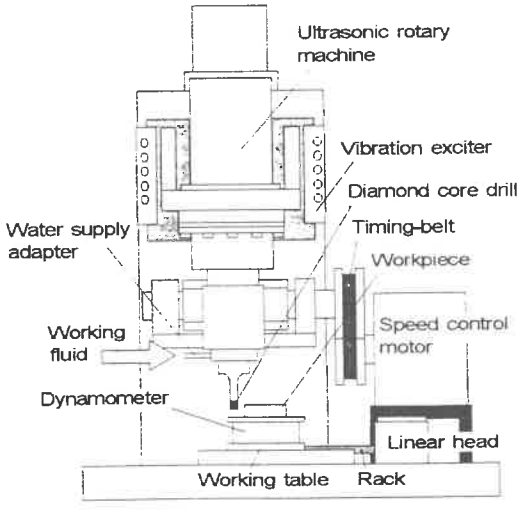

Fig.2 Apparatus of combined vibration processing

2. Experimental apparatus and methods

Figure 2 shows outline of experimental apparatus. In this experimental apparatus, the diamond core drill

is rotated at less than 5000 min^{-1} and is vibrated by ultrasonic vibration (frequency is 20 kHz, amplitudes are 0 ~ 10 μ m) and low frequency vibration (frequencies are 0 ~ 40 Hz, amplitudes are 0 ~ 160 μ m). The diamond core drill is vibrated by each vibrations, which have low frequency vibration and ultrasonic vibration individually, or combined vibrations in the processing. Tap water is used as the working fluid and the fluid is supplied into processing area through the tool inside. The experimental conditions are shown in Table 1.

Table 1 Main experimental conditions

Diamond core drill	Outer diameter		mm	ϕ6
	Inner diameter		mm	ϕ4
	Bond,Grain size			Metal-bond,SD#200
Ultrasonic vibration	Frequency	f_u	kHz	20
	Amplitude	a_u	μm	10
Low frequency vibration	Frequency	f	Hz	10 ~30
	Amplitude	a	μm	15 ~470
Number of revolution		N_0	min^{-1}	2000 ~5000
Feed speed of working table		V	mm/min	1 ~4
Workpiece	Material,Thickness		mm	Soda glass,10
Working fluid	Material			Water
	Pressure		kPa	29.4

3. Processing characteristics

Figure 3 shows the relationship between the applied amplitude and horizontal force. The horizontal force of the non-vibration grooving shows by symbol △ on Y axis, and another symbols △ are results of low frequency vibration. Symbol ● on Y axis is a result by grooved of ultrasonic frequency vibration and another symbols ● mean combined vibration grooving. As shown in experimental results, the horizontal forces of low frequency vibration and ultrasonic vibration and ultrasonic vibration grooving are less than one of non-vibration grooving. And, in the case of low frequency and combined vibration grooving, the horizontal force decreases with increase of the applied amplitude at low frequency.

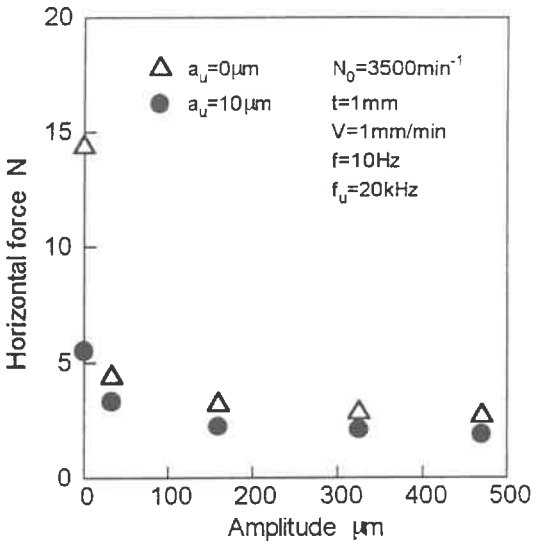

Fig. 3 Relationship between amplitude and horizontal force

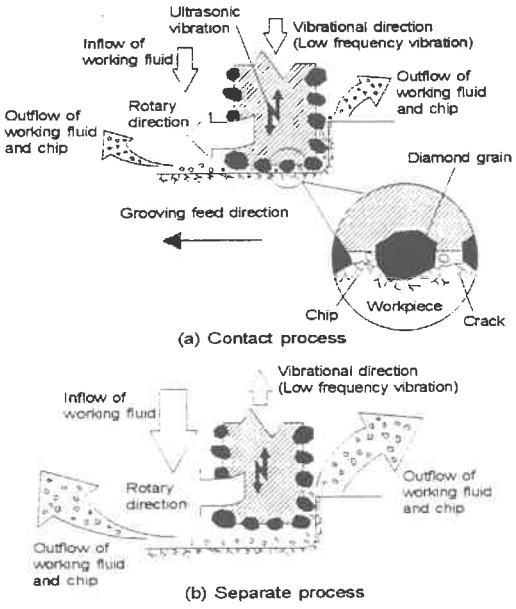

Fig. 4 Removal mechanism of chip in the case of combined vibration grooving

The vibration effect upon grooving is explained by a model of combined vibration in Figure 4. The vibration grooving brings about contact and separate phenomena between the tool and the workpiece in one vibration cycle. Therefore, in the separate time during one vibration cycle , the working fluid can be supplied

easily into processing parts and removal of chip is able to be improved. These phenomena are clear through measurement of flow rate of working fluid and observations of diamond grains on the tool surface.

Figure 5 shows the behavior of horizontal force obtained by continual grooving process without dressing. In this experiment, the last numbers of each grooving process show the numerical value when the horizontal force becomes 30 N. In the non-vibration grooving, the horizontal force increases rapidly with grooving number and the horizontal force reaches to 30 N at only 10 times of grooving number. The low frequency vibration grooving reaches to the last grooving number at 30 times, and the ultrasonic vibration grooving reaches to it at 70 times. On the other hand, in the combined vibration grooving, the horizontal force reaches to only 20 N over 100 times. Therefore, the tool life is improved in the order of non-vibration grooving and low frequency, ultrasonic, combined vibration groovings.

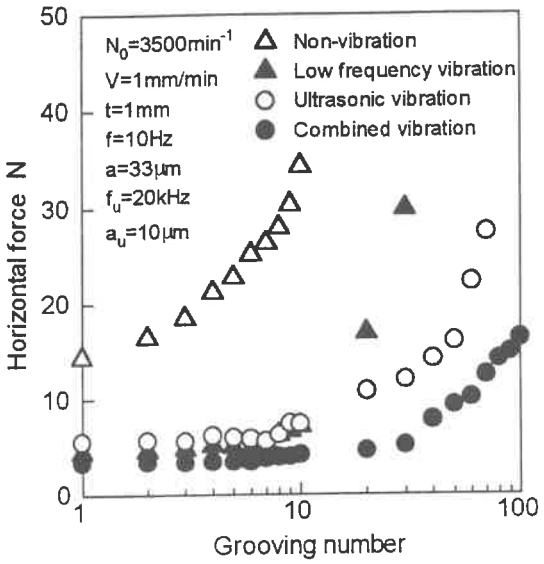

Fig. 5 Relationship between grooving number and horizontal force

4. Processing accuracy

Figure 6 shows the relationship between the amplitude of low frequency vibration and

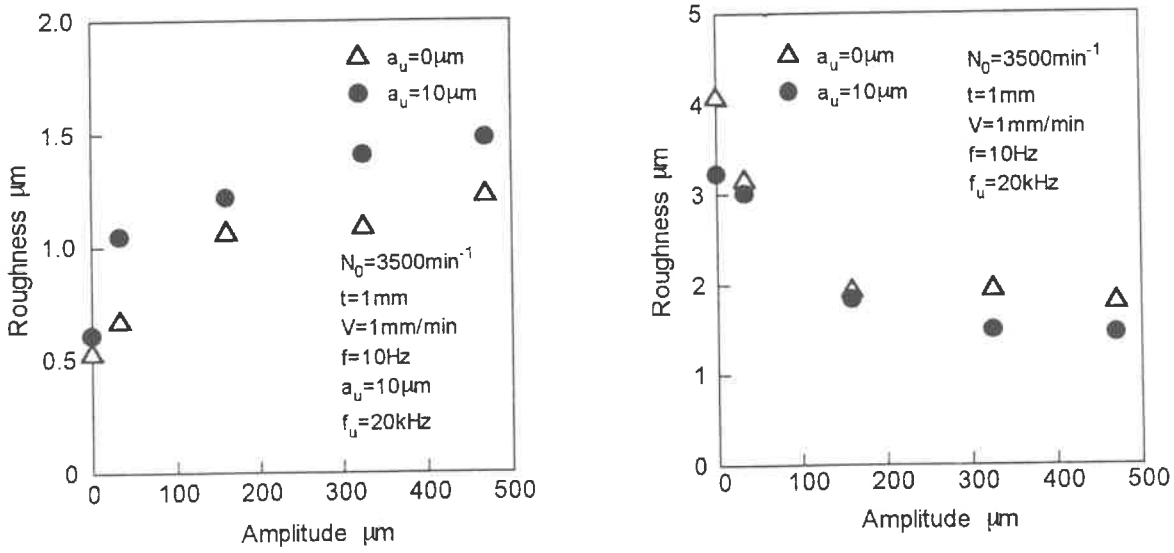

(a) Bottom surface of groove (b) Side surface of groove

Figure 6 Relationship between amplitude and roughness of groove

roughness of grooves. Figure 7 shows microscopic observations of grooved surface. In Figure 7, (a) is the bottom surface of grooves, and (b) is side surface of grooves. The low frequency vibration grooving and the ultrasonic vibration grooving increase roughness of bottom surface. When the amplitude of low frequency vibration increases, the surface roughness becomes still worse. The bottom surface is given continually an impact by diamond grains of the tool. Therefore, this continual impact of diamond grains brings about increase of surface roughness. On the other hand, roughness of the side surface is improved by low frequency vibration, ultrasonic vibration and combined vibration. And, when the amplitude of low frequency vibration increases, the surface roughness is improved. These things are clear from results of Figure 7-(b), especially. That is to say, the side surface of non-vibration grooving and ultrasonic vibration grooving show stripe marks. In the cases of low frequency vibration and combined vibration grooving, stripe marks on the side surface are not brought about.

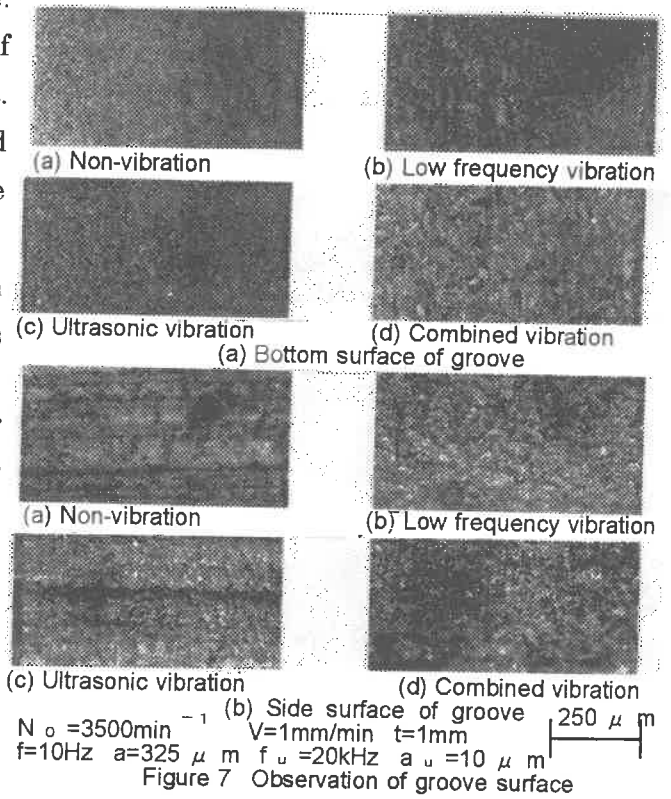
(a) Non-vibration
(b) Low frequency vibration
(c) Ultrasonic vibration
(d) Combined vibration
(a) Bottom surface of groove
(a) Non-vibration
(b) Low frequency vibration
(c) Ultrasonic vibration
(d) Combined vibration
(b) Side surface of groove
N o =3500min⁻¹ V=1mm/min t=1mm
f=10Hz a=325 μ m f u =20kHz a u =10 μ m
250 μ m

Figure 7 Observation of groove surface

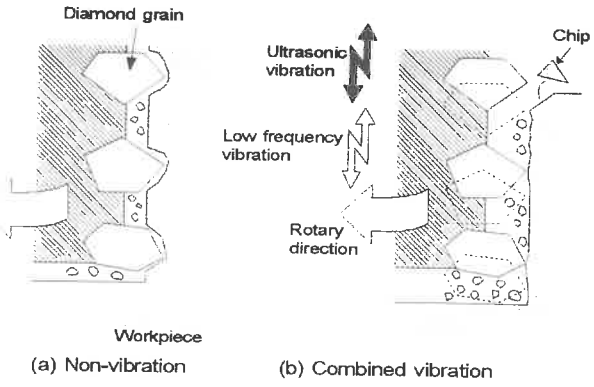

Fig.8 Model of grooving mechanism

Figure 8 shows a model of formation of stripe marks. In the case of very small amplitude, i.e. in non-vibration grooving and the ultrasonic vibration grooving, the stripe marks are formed by diamond grains on the side surface of tool. On the other hand, as the amplitude of low frequency vibration grooving and combined vibration grooving are larger than it of ultrasonic vibration grooving, the stripe marks of side surface are cut.

5. Conclusions

Through the obtained experimental results, the followings are clear.

(1) The horizontal force of vibration groovings are smaller than non-vibration grooving.
(2) In the combined vibration grooving, the tool life is as much as ten times as compared with non-vibration grooving.

Precision Trimming of Large GFRP Parts Using a Mobile Robot With Onboard Grinder

Yasuo Nasu*, Nobuhiro Kouda**, Kazuhisa Mitobe*,
Toshihiro Kuroda***, Keiichi Shibata*
*: Dept of Mechanical Systems Engineering, Yamagata University
Yonezawa, Yamagata 992, JAPAN
**: Hitachi Yonezawa Electronics Co.,Ltd
Yonezawa, Yamagata 992, JAPAN
***: Hitachi Chemical Co., Ltd
Shimodate, Ibaragi 308, JAPAN

1. Introduction

Edge trimming process of large GFRP parts is a remaining process to be automated in GFRP manufacturing because the work space of the trimming task for large GFRP parts exceeds the range of the work space of an articulated robot. We have developed a trimming method using a wheeled mobile robot (WMR) equipped with a handheld grinder[1]. In general, control of the motion of WMR is difficult because the existence of a smooth feedback control law, which regulate the motion to an arbitrary point, is not guaranteed[2]. However, in the edge trimming task, it is not necessary to control the position and orientation of the WMR simultaneously to an arbitrary point. The edge trimming task can be carried out by controlling the WMR to track the desired contour of the GFRP parts.

In this study, a precision curve edge trimming method using a wheeled mobile manipulator equipped with a handheld grinder is investigated. When the robot cuts off along a curve-line trajectory the grinding force due to the removal of GFRP may cause distortion of the grinding disk and slip of the tires. In order to obtain the required accuracy of the products and quality of the surface cut off, control of the grinding force is significantly important. The force control is based on the proper choice of the distance from the center of the disk to the contact point between the desired curve-line trajectory and the side surface of the grinding disk.

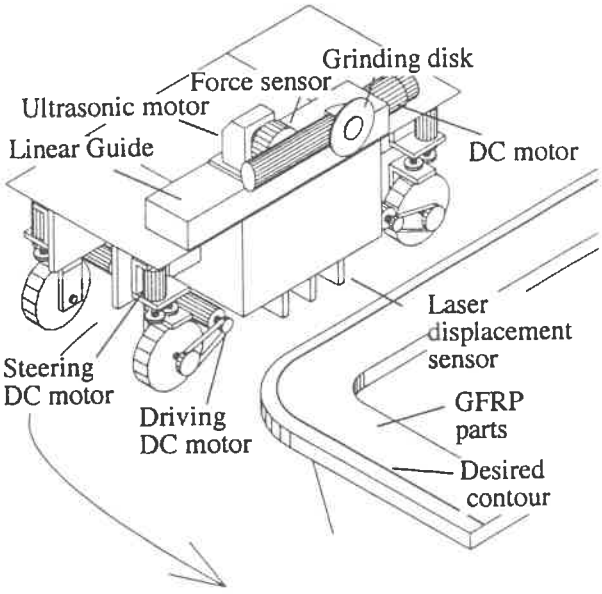

Fig.1 Wheeled mobile robot and GFRP parts.

2. Wheeled Mobile Manipulator System

Workpieces of GFRP, which measure over 2 by 4 m, are easily deformed under the external forces and hence the edge trimming process is necessary to guarantee the required accuracy: $\pm$5mm.

In the edge trimming, the wheeled mobile manipulator (WMM) is controlled to track a reference trajectory which is determined by the desired contour of the GFRP parts. The developed WMM system is shown in Fig.1. The WMM consists of the WMR and the 2D manipulator. The WMM is approximately 850mm in length, 500mm in width, and 300mm in height and 57kg in weight. In

order to determine the center of rotation of the WMR arbitrarily on the floor, a four-wheel-steering (4WS) system is adopted in the WMR. The WMR has also a four-wheel-driving (4WD) system and each wheel is steered and driven by two independent DC motors. The 2D manipulator consists of a prismatic joint and a revolute joint. The 2D manipulator is equipped with a handheld grinder. Specifications of the grinder are as follows: rotational speed is 10000rpm, type of the grinding disk is C80M-6, diameter of the grinding disk is 100mm. Vertical height of the grinding disk can be adjusted by the revolute joint. The prismatic joint moves the grinding disk along the direction of y axis of the WMR. The grinding force is measured by a force sensor which is attached between the prismatic joint and the revolute joint. The position and orientation of the WMR is detected by using three laser displacement sensors attached at the side wall of the WMR. that measure the distance from the guide path which is set on the floor. The guide path, which is set up along the desired contour of the GFRP with a curved plate, determines the reference trajectory of the WMR.

3. Distortion of the Grinding Disk

The elastic distortion of the grinding disk due to the grinding force in the lateral direction should be decreased because it causes the inclination of the finished surface.

Fig.2 illustrates the elastic distortion of the grinding disk. Point E is the contact point, where the grinding disk is in contact with the desired contour of the products as the WMR tracks the desired contour. Here V_{ex}, V_{ey} are velocities of the grinding disk and $\dot{\psi}$ is the angular velocity of the grinding disk. In order to reduce the distortion of the grinding disk. V_{ex} is taken to be zero. Since the lateral grinding force varies depending on the position of the contact point on the grinding disk, the inclination of the surface cut off can be reduced by the proper choice of the position of the contact point.

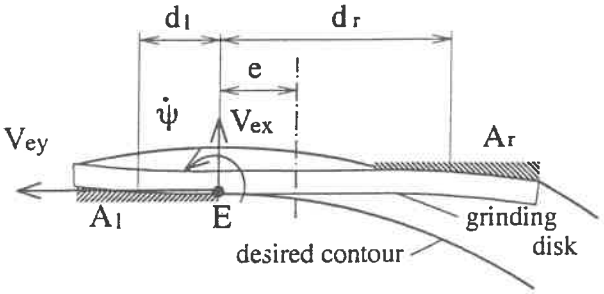

Fig.2 Elastic distortion of grinding disk.

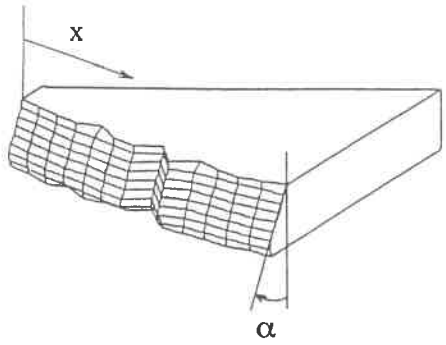

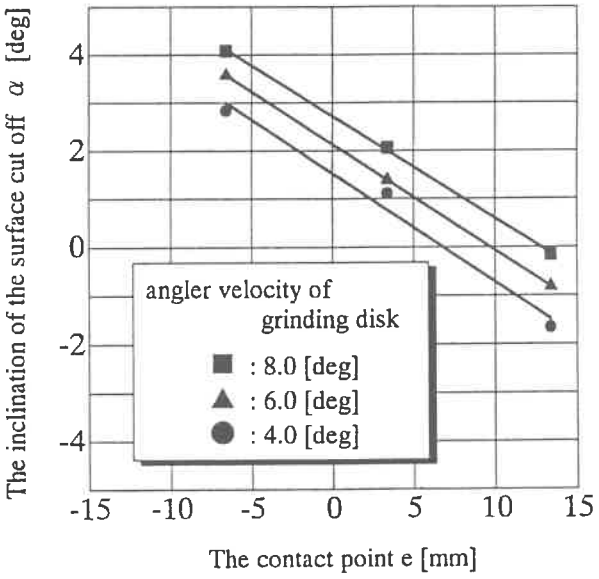

Fig.3 Relation between the inclination of surface cut off and the contact point.

Fig.3 shows the experimental results for the contact point e = -6.6, 3.4 and 10.4 mm, where e is the distance of the contact point from the center of the grinding disk. In the experiments, cutting speed of the grinder is 0.04 m/sec, thickness of the GFRP parts is 4

mm and the vertical height of the grinding disk from the surface of the GFRP is 40 mm. The result shows the existence of the optimum value of e and the value varies as the angular velocity of the WMR changes. From the experimental results the contact point is determined accordingly to the next equation so as to reduce the inclination of the surface cut off.

$$e = 0.8 + 1.5\dot{\psi} \qquad (1)$$

4. Contour Tracking Control

In this paper. we define a feedback law which locally stabilize the motion of the WMR to track the desired contour. For the simplicity of discussion. we assume that the reference trajectory for the WMR is given by a smooth curve formed by a constant curvature. The coordinate system is shown in Fig.4. ϕ_i and V_i (i = 1. .... 4) represent the steering angle and the translational velocity of each wheel. respectively. By fixing $V_{ex} = 0$. motion of the WMR is regarded as rotation about a point P. and hence. the velocity and steering angle of each wheel for given θ can be obtained. Defining a new coordinate system Σ_{tri} with its origin at the intersection of the reference trajectory and the line which goes through the contact point E (See Fig.2). the motion of the robot is given as

$$\begin{bmatrix} \dot{x} \\ \dot{\psi} \end{bmatrix} = \begin{bmatrix} -V_{ey}\sin\psi \\ \dot{\theta} - \dfrac{V_{ey}\cos\psi}{R+x} \end{bmatrix} \qquad (2)$$

Where x is the distance between the contact point and origin of Σ_{tri}. ψ is the orientation of the grinding disk with respect to axis y of the coordinate system Σ_{tri}. R is the curvature of the desired contour. Regarding θ as the control input system(2). a feedback control law is defined by linearizing the system(2) around $\psi = 0$. $x = 0$.

$$K = [K_r K_\psi] \qquad (3)$$

Where $\zeta = [x, \psi]^T$. $K_\psi < 0$. $K_r > -V_{ey}/R^2$. K_r and K_ψ are determined from simulation and experimental results.

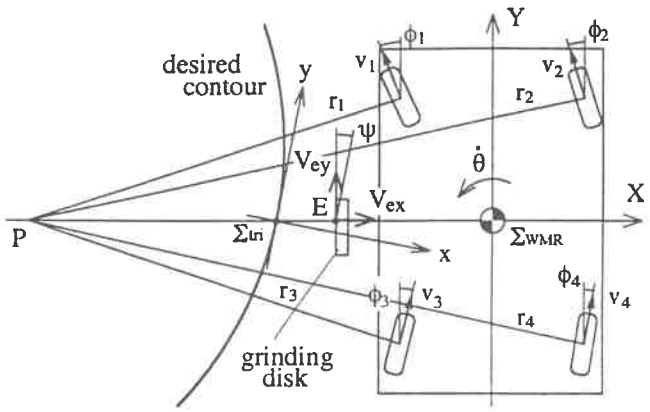

ϕ_i :Steering angle
v_i :Velocity of wheel
$\dot{\theta}$:Angular velocity of WMR
P :Center of rotation
E :Contacet point
Vey,Vex :Velocity of grinding disk
ψ :Angle with respect to desired counter
r_i :Distance between point P and each wheel

Fig.4 The coordinate systems.

5. Control Strategy for Trimming

Since the excessive grinding force may cause the slip of the wheels of the WMR. the force should be sufficiently small to maintain the tracking of the WMR to the desired contour of the GFRP parts. In the trimming system. the vertical force can be controlled by adjusting the driving velocity of the WMR because the grinding force is known to be proportional to the removal rate of the material and the removal rate is approximately proportional to the driving velocity of the WMR.

In order to maintain the acceptable tracking for the trimming task. we control the driving velocity of the WMR by using a PI controller. where the vertical grinding force is feed back to obtain the command value for the velocity. Fig.5 shows the block diagram of the trimming robot system. Note that in order to maintain the value of e given by equation (1). the prismatic joint moves the grinding disk along the y direction of the Σ_{WMR}. while the contact point E stays on the

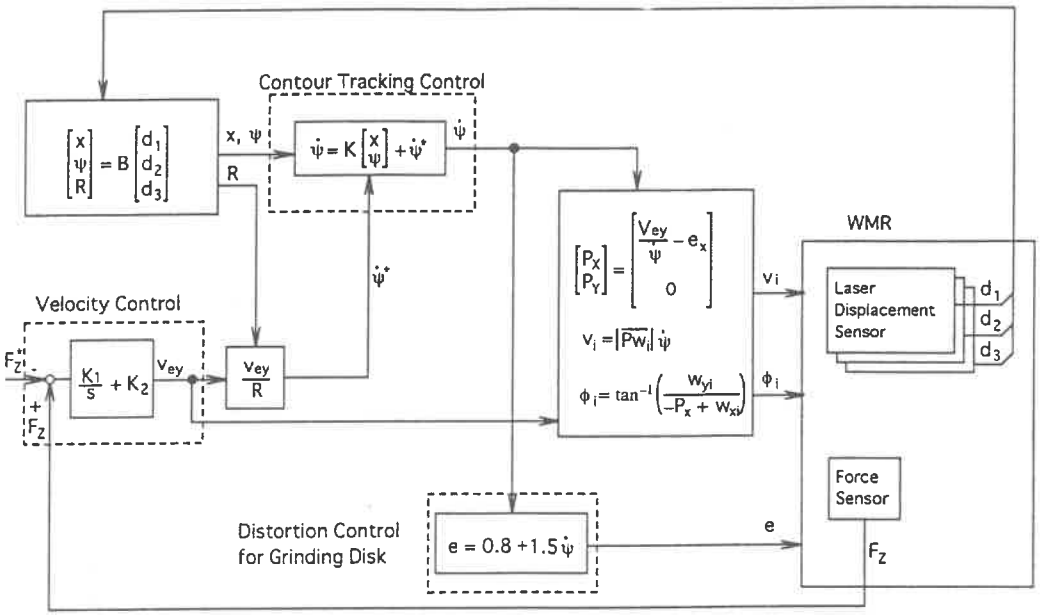

Fig.5 Block diagram of the trimming system.

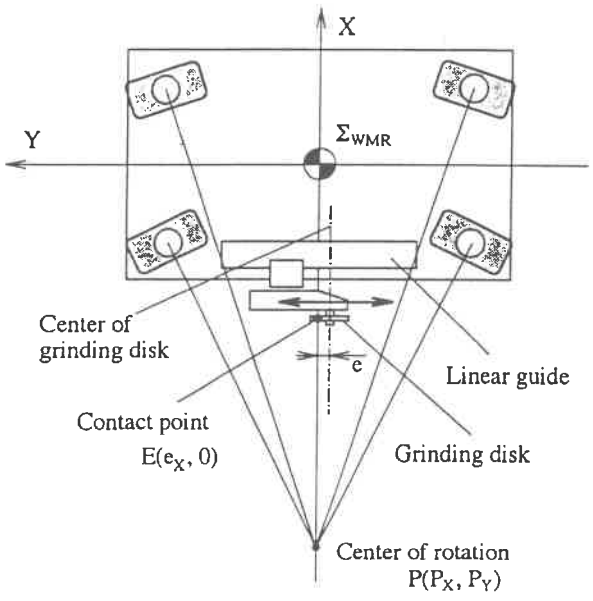

Fig.6 The linear guide to maneuver the contact point of the grinding disk.

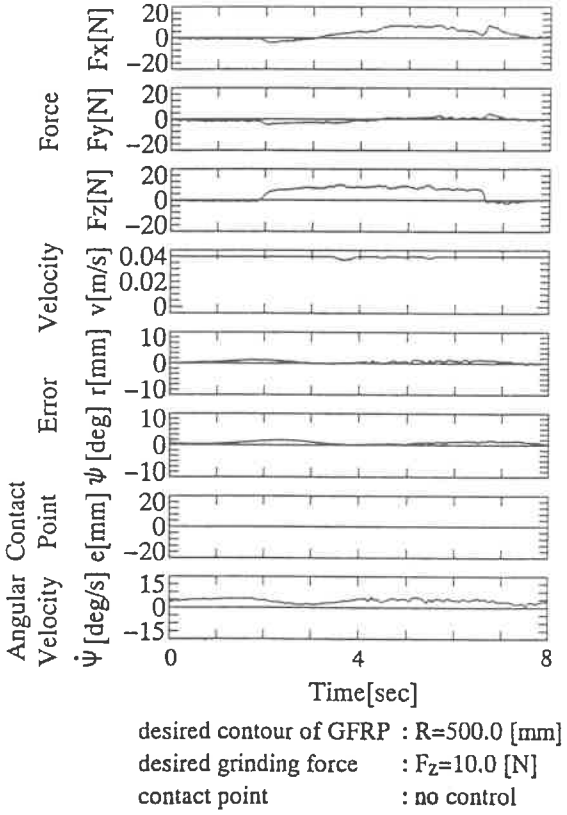

Fig.7 Experimental results without CPCM

straight line connecting the origin of the Σ_{WMR} and the center of the rotation P (See Fig.6).

6. Experimental Results

In order to examine the performance of the trimming system. experimental trimming tasks were carried out by using a GFRP plate with thickness of 4mm. The radius of the desired contour R_{cut} was chosen to be 500mm

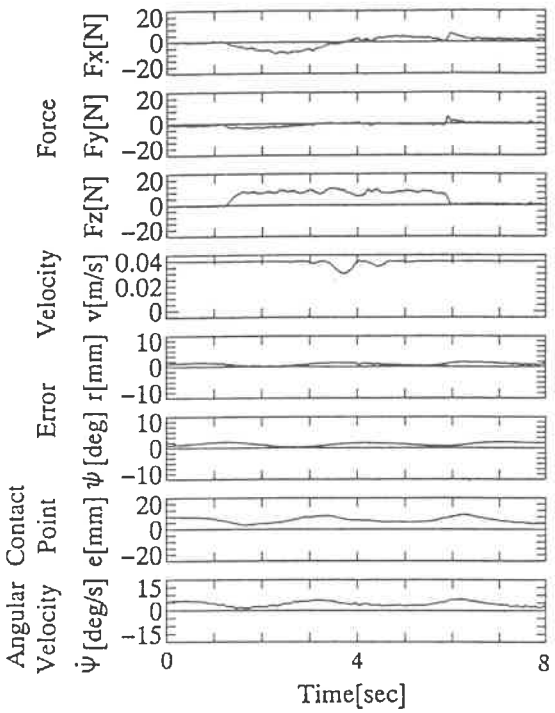

Fig.8 Experimental results with CPCM

and the guide path with the radius of 560mm. Fig.7 shows the experimental data without using the contact point control method (CPCM). In this case, the tracking error from the desired contour is 1.5mm～3.0mm. The average of the inclination of the surface cut off is +3～−1deg (Fig.9(a)). Fig.8 shows the experimental data with using the CPCM. The contact point distance from the center of the disk varied corresponding to the error of the position r and orientation ψ. The tracking error from the desired contour is 0.8mm～3.3mm. Fig.9(b) shows the average of the inclination of the surface cut off is ±1 deg.

7. Conclusion

In this study, an automated trimming system by using WMM is developed for the precision edge trimming of large GFRP parts. The inclination of the surface cut off due to the grinding force in the lateral direction of the grinding disk is experimentally analyzed.

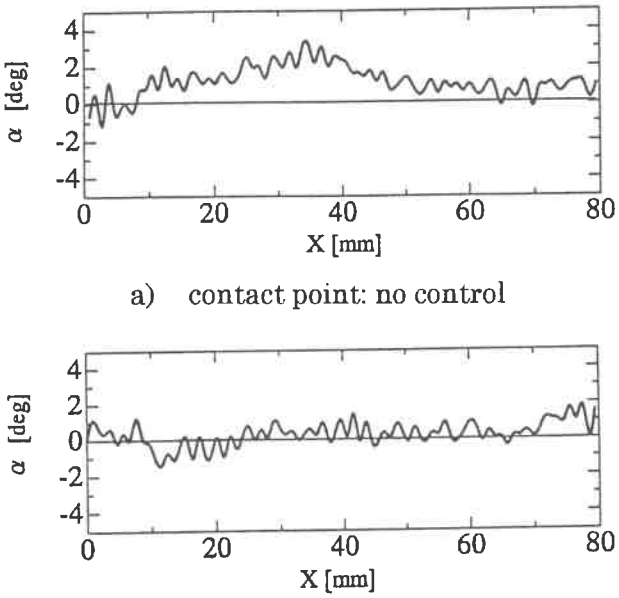

Fig.9 The inclination of the surface cut off.

In order to decrease the distortion of the grinding disk, the contact position between the grinding disk and the desired contour is controlled so as to minimize the lateral grinding force. On our experiments we achieved the required accuracy of ±5mm and a small inclination of the surface cut off ±1deg. Some experimental results of the trimming task are given to show the effectiveness of the developed system for automated edge trimming of large GFRP parts.

References

1) N. Kouda, Y. Nasu, K. Mitobe, K. Shibata: Development of a Trimming System of Large GFRP Parts Using a Mobile Robot, Proc. 2nd IABTEC Conference, 1995, p.489/494.

2) C. Canudas and O.J. Sordalen: Exponential Stabilization of Mobile Robots with Nonholonomic Constraints, IEEE Trans. Automat. Contr.,1992, Vol.37, p.1791/1797.

THERMAL CUTTING OF PLATE GLASS

K.Sadashivappa
Research Scholar

M.Singaperumal
Associate Professor

Mechanical Engineering Department
Indian Institute of Technology, Madras - 36
e-mail: mech2@iitm.ernet.in

C.S.Bhaskar Dixit
Lecturer, Mechanical Engineering Department
Bapuji Institute of Engineering and Technology, Davanagere-1

INTRODUCTION

Generally all optical instruments are expected to produce high precision results. Hence, it invites highest precision machining work. The heart of any optical instrument is the lens system. A lens is expected to produce an image which is an exact replica of a given object. The performance of any lens is limited by the presence of defects. Hence utmost care is taken in the fabrication of lenses.

The fabrication of lenses involves different stages which include blank preparation, grinding, polishing and centering and edging. Normally the optical glass is supplied in the form of thick slabs or thinner plates of required thickness. These are cut into squares to the approximate size of the lens required. The corners of the square plates are cut off with a glass cutter. These plates are then cemented on to a flat tool using pitch or a mixture of beeswax and resin. The tool along with the blank is held on a grinder and the grinding is done until the required lens diameter is obtained. An another alternative is to cut glass blanks with a trepanning tool in a standard drilling machine with adequate coolant flow. Then the plate is ground, polished and centered to get a lens of required curvature on the glass surfaces [1,2].

In the above conventional process of blank preparation, the number of operations involved are more and there is a possibility of developing internal flaws and small cracks, which reduce the performance of the lens. In the present paper a new method is proposed for cutting the lenses. The proposed method of thermal cutting of glass plates consists of propagation of a crack in glass, owing to thermal stream produced with the help of a moving hot air jet. A crack, if already present in the glass, can be extended. The movement of the jet governs the direction of propagation of the crack and thus it is possible to cut a glass plate accurately to any desired size and profile in a single step. Hence processes like chipping and grinding to size the blank can be avoided.

THERMAL CUTTING PROCESS

Any scratch or burr on the surface of a glass plate act as part of stress concentration. Hence the glass plate may break or fail easily under the influence of the residual stresses as well as thermal stresses caused by the external changes. This is known as static fatigue of glass which is used to cut glass by creating similar conditions.

Technique of thermal cutting

The hot air jet which is a main feature of this process can be produced by the flow of compressed air through a nozzle. The air is heated up by a heating coil. The crack should be initiated near the edge of the glass plate and can be propagated by moving hot air jet according to the required profile to be cut.

Material selection for the tube

The material of the tube should be such that it sustains the maximum temperature of 325°C required for producing hot air and should not create short circuit problem. Metallic tubes are not preferred owing to their conductivity and so a glass tube shall be of a good choice and being transparent material,glass tube provides a visual control on the performance of the heating element.

Control of air temperature

The voltage and current supply to the heating element governs the air jet temperature. By varying these with the help of a dimmerstat the temperature of air jet can be varied. The approximate value of current ranges between 3 Amps to 5 Amps and the temperature of jet ranges between 150°C to 280°C.

Other features

The compressed air enters at the top of the glass tube and rushes out of nozzle at the bottom in the form of a jet. There should not be any air leakage in order to maintain adequate flow of air. Leakage of air can possibly occur only at three openings (provided for applying voltage to the heating coil and for introducing a thermometer) and this leakage can be minimised with the help of hard rubber stopper coated with a layer of sealing compound. A hole is drilled along the axis of the stopper so that an aluminium electrode can be inserted. A thermometer is inserted to record the temperature of the hot compressed air to avoid over heating of the tube. The operating pressure is to be kept around 0.25 to 0.5 bar.

Parameters

The parameters which influence the thermal cutting process are:

1. Pressure (P), bar
2. Temperature (T),°C
3. Thickness of glass plate (t), mm
4. Type of glass plate
5. Nozzle diameter (d), mm
6. Stand-off distance (x), mm

Pressure and Temperature

The inlet pressure in the heating tube governs the air jet characteristics such as air pressure and air velocity. At higher pressures the force with which the air impinges on the glass plate is more and hence plates of larger thickness can be cut.

The normal temperature of air is around 200°C for obtaining the crack propagation. At higher operating temperatures the thermal stresses induced are more and hence crack propagation is faster. During operation care should be taken such that the heating element does not touch the walls of the glass tube.

Thickness of glass plate and type of glass plate

As the thickness of the glass plate to be cut increases the cutting speed decreases and the operating temperature has to be increased to increase the cutting speed.

Varieties of glasses also do affect this cutting process. Plate glass can be easily cut. Higher temperature is needed to cut tempered glasses.

Nozzle diameter and stand-off distance

A nozzle of diameter about 0.5 mm gives a fine air jet and hence it is possible to have a sharp cut edges. By increasing the nozzle diameter, the jet air will distribute over a larger area and hence the temperature is distributed over a larger area, making it difficult to cut sharp edges.

A very small stand-off distance will cause back pressure in the tube and hence the tube may break. If the stand-off distance is increased beyond a certain value, then the air jet diverges and hence the cutting becomes difficult. Hence an optimum stand-off distance should be maintained.

EXPERIMENTATION, RESULTS AND DISCUSSION

The thermal cutting setup consists of the following: A glass tube (Fig. 1) with a heating element of 1 kW capacity, a dimmerstat to vary the voltage applied to the heating element and hence the air-jet temperature, a mercury thermometer (0-400^{0}C) to measure the air-jet temperature, a x-y table to facilitate the straight line and a rotary table for circular cutting. Nozzles of different diameters are fixed to the tube using a hard rubber stopper. Stand-off distance between the jet and glass plate is varied by moving the glass tube vertically.

Types of cutting

(a) Straight line cutting

When the cut is to be made, an initial crack is obtained about 2 mm in length by a diamond cutter. It should be ensured that air jet is kept in fixed position by properly positioning the glass tube. Then compressed air is injected through the nozzle. A gap of about 2 mm is provided between the glass plate to be cut and the nozzle point. Then voltage is applied to the heating element. Temperature of the air jet can be controlled with the help of the dimmerstat. The hot air jet, first impinges on the area of the initial scratch. After about 10 seconds, the crack begins to propagate in a straight line, when the glass plate is moved in longitudinal direction with respect to the nozzle.

(b) Circular cutting

The glass plate is mounted on a rotary table using suitable fixtures and is fed against the nozzle to get a circular shape.

Experiments are conducted with glass plates of three different thicknesses (3,4 and 6 mm) and nozzles of two different diameters (1.3 and 2 mm) are used. A pressure of 0.25 bar is maintained. Straight line and circular cuts are made at different temperatures and the time taken for cutting a certain length is noted. Figs. 3 (a-d) show the results of the straight line cutting and Figs. 3 (e-h) show the results of the circular cutting.

Fig. 3 indicates that the cutting time increases with increase in the plate thickness at a particular temperature and stand-off distance. The time decreases with increase in air jet temperature and it is less when the nozzle diameter is 2 mm and also for the stand-off distance of 2 mm.

CONCLUSIONS

A new method for cutting glass plates is reported. Various experiments are conducted on the method and the results are presented. This method can be used for precise cutting of optical lenses and ortho dental photographic mirrors.

REFERENCES

1. Davidson A. (Ed.), Hand book of precision engineering, Vol. 3: Fabrication of non-metals, The Macmillan Press Ltd., London, 1971.

2. Elliott A. and Home Dickson, Laboratory Instruments - their design and applications, Chapman and Hall Ltd., London, 1959.

ACKNOWLEDGEMENTS

The authors are thankful to the following Sriyuths: Balaji Singh, Mallikarjuna Reddy, Siva Punna Rao and Venkateshwara Rao, Ex-scholars of B.I.E.T., Davanagere for their kind help during the experimentation and Karnataka State Council for Science and Technology, Bangalore for the financial assistance to carry out this work.

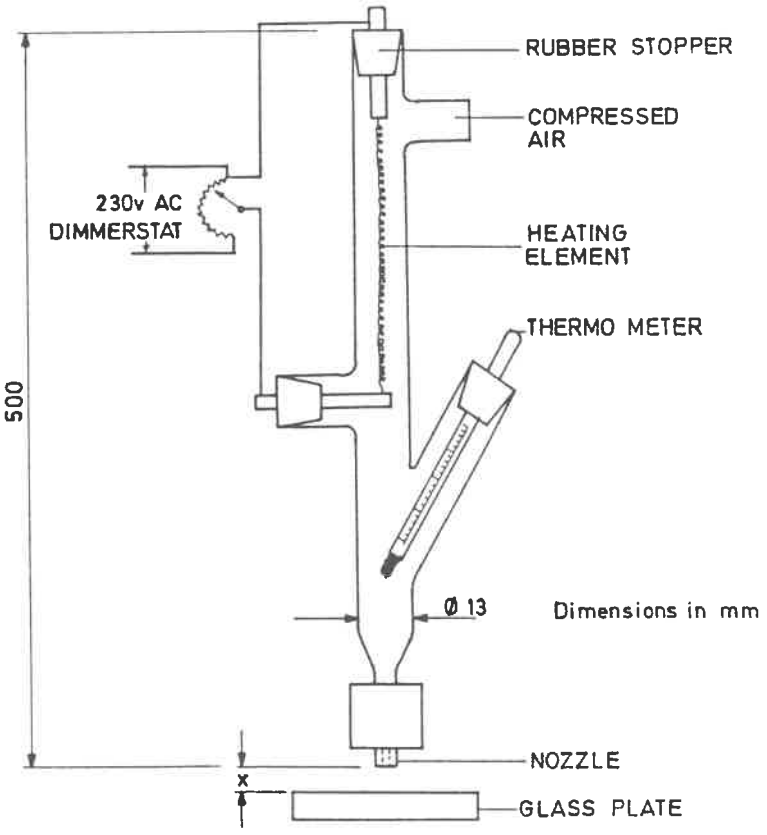

FIG.1 GLASS TUBE

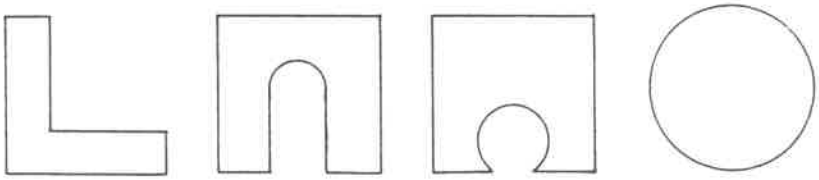

FIG.2 TYPICAL FORMS CUT

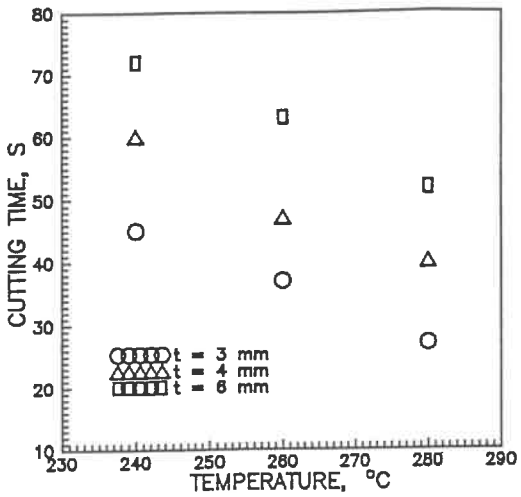

(a) d = 2 mm, x = 2 mm, l = 100 mm

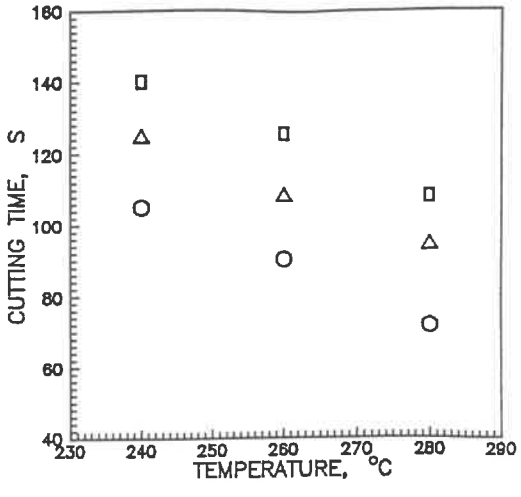

(b) d = 1.3 mm, x = 2 mm, l = 100 mm

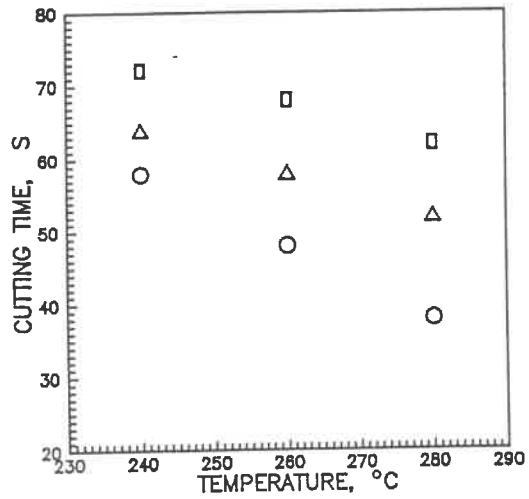

(c) d = 2 mm, x = 1.5 mm, l = 100 mm

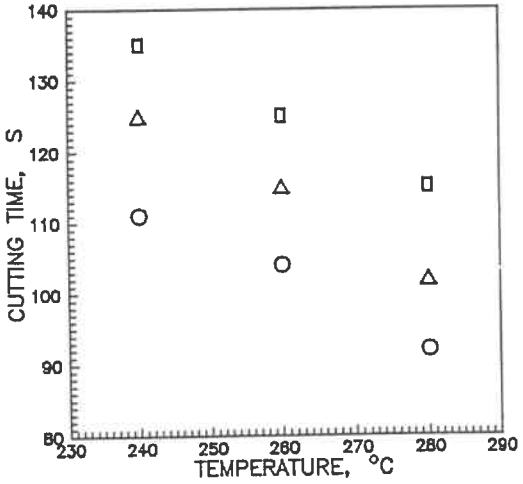

(d) d = 1.3 mm, x = 1.5 mm, l = 100 mm

Fig.3 Variation of cutting time with air-jet temperature
l = length of cut

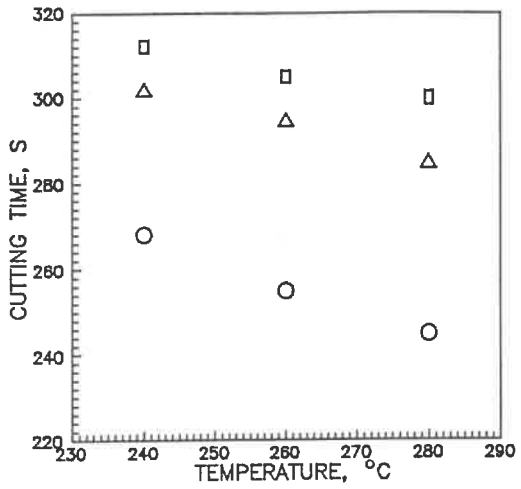

(e) d = 2 mm, x = 2 mm, dia = 150 mm

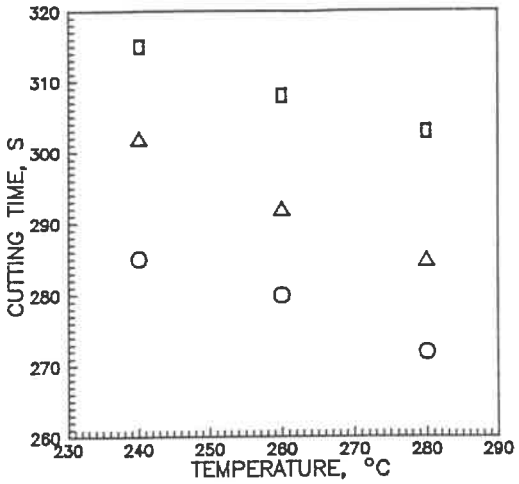

(f) d = 1.3 mm, x = 2 mm, dia = 130 mm

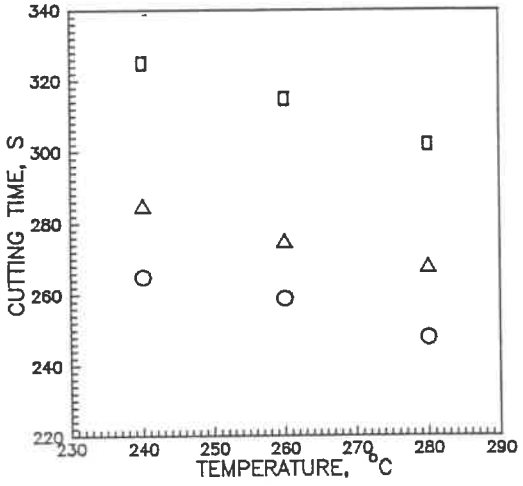

(g) d = 2 mm, x = 1.5 mm, dia = 130 mm

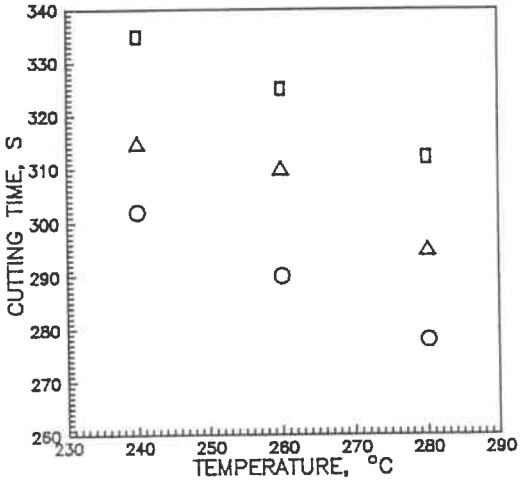

(h) d = 1.3 mm, x = 1 mm, dia = 130 mm

Fig.3 (Contd.) Variation of cutting time with air-jet temperature
dia = diameter of circle cut

Precision Polishing of Optical Fiber Connector

Hirofumi Suzuki, Tsunemoto Kuriyagawa and Katsuo Shoji
Faculty of Engineering, Tohoku University
Aramaki-Aoba, Aoba-ku, Sendai, Miyagi, 980-77, Japan

1. Introduction

Recently, advanced optical-fiber signal transmission equipment is being used extensively in various applications. As a result, greater demands are being placed on optical fiber connectors. This paper describes a high-speed precision polishing method for hemispherical surface optical fiber connecters.

The conventional method of machining physical contact (PC) connectors with hemispherical end faces is multi-step lapping using several abrasive lapping films. Use of this method has resulted in some problems in the areas of surface quality, shape accuracy and processing time, in turn causing a significant return.

The proposed machining process consists of three operations, it is composed of three operations. In the first operation, the end surface is ground by a resinoid bonded diamond wheel. In the second, the end surface is polished to hemispherical shape by diamond abrasive. In the final operation, the surface is hybrid-machined using diamond and silica. The new method reduces processing time to short, lowers step height, and reduces the depth of surface damage at the fiber ends.

2. The hemispherical surface optical fiber connector

The hemispherical surface optical fiber connector shown in Fig.1, reduces signal transmission loss but increases return loss in connecting systems. This is due to the fact that Fresnel reflection is eliminated by perfect physical contact (PC) made possible by elastic deformation at the fiber ends. Zirconia ceramic is effective as a connector ferrule because of its high stiffness. Table 1 shows the specifications of the ferrule/fiber end. The radius curvature of the end face should be 10 to 25 mm, the eccentricity of the convex end should be less than 50 μm, and fiber withdrawal from the ferrule end should be less than 0.05 μm through reliability testing under conditions of high temperature and humidity.

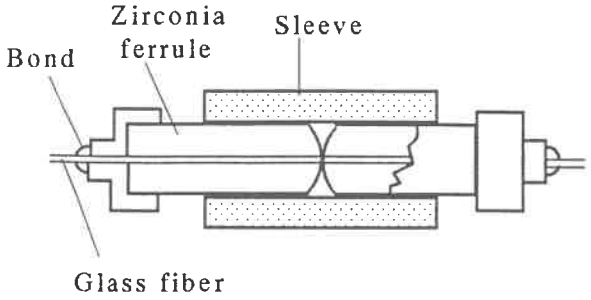

Fig.1 Hemispherical surface optical fiber connector

Table 1 Specifications of the PC connector

Radius of ferrule	10 ~ 25 mm
Step height	-0.1 ~ + 0.05 μm
Eccentricity	< 50 μm
Insertion loss	< 0.4 dB
Return loss	< -55 dB

3. Machining process

The conventional method of polishing optical fiber requires about 10 machining operations. First, the resinoid bond adhered to the zirconia ferrule end is removed using lapping film. Next, the ferrule end is ground with lapping film on a soft rubber plate to generate a rough hemispherical surface. After that, the end is ground using several grain sizes of diamond lapping film sequentially. Employing this method, processing time is long, and the return loss is significant, a damaged layer remains.

The proposed method requires only three operations shown in Fig.2. In the first operation, the end surfaces are ground flat by resinoid bonded diamond wheel. In the second operation, the end surfaces are lapped into hemispherical shape using diamond abrasives on a layer resine film over a rubber plate. In the final operation, the surfaces are polished with a hybrid abrasives of colloidal silica and diamond on a rubber plate. This hybrid machining is a characteristic operation of the proposed method.

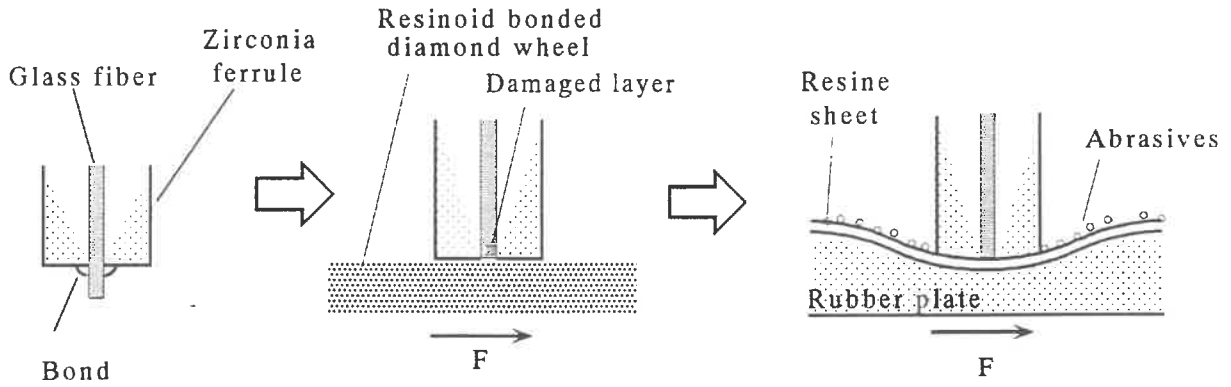

Fig.2 Proposed method of machining optical fiber

4. Grinding and polishing machine

Fig.3 shows a schematic illustration of the proposed grinding and polishing machine. Several dozens of fibers/ferrules are fixed in holes on a jig plate. Several jigs, weighted in the centers (Fig.4) are set on a grinding/polishing plate. Optical fibers are fixed in each jig. A grining/polishing disk and the workpiece jig rotate at the same rate and in the same direction.

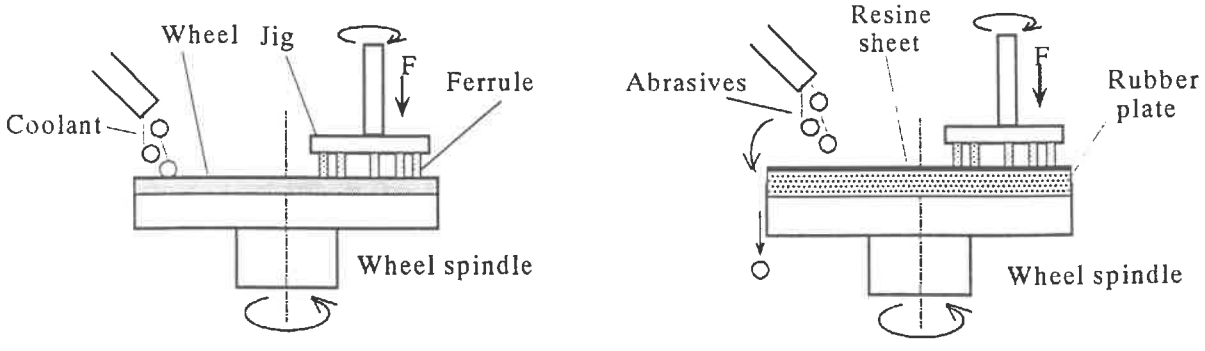

Fig.3 Schematic illustration of the proposed grinding/polishing machine

5. Experimental results

Table 2 shows the grinding/polishing conditions of the three operations. Resinoid bonded diamond wheel was used as the grinding wheel. A 5 mm thick silicon resin plate was used in the 2nd and 3rd operations as the rubber plate. The rotational rate of the grinding/polishing disk was 60 rpm. For the polishing abrasive, 1 um diamond slurry was used in the 2nd operation, and 80 nm colloidal silica and 1 μm diamond abrasive were used in the 3rd operation.

Fig.5 shows the relationship between the end radius and the polishing load, in the 2nd operation. The horizontal axis is the load applied to one ferrule. As the load becomes higher, the radius becomes smaller. From these results, the load is fixed at 1.90 N.

Fig.6 shows the height of the step between the glass core and the zirconia ferrule resulting from the use of various polishing abrasives in the 3rd operation. In case (a), the polishing abrasive was 1 μm diamond abrasive. In case (b), the polishing abrasive was 80 nm colloidal silica. In case (c), the polishing abrasive was 80 nm colloidal silica and 1 μm diamond abrasive. The step height was lowest in case (a) and within the specified 0.05 μm in case (c).

Table 2 Grinding/polishing conditions

Operation	1	2	3
Polisher/Wheel Abrasive size	Resinoid bonded diamond wheel #1200	Resine sheel –	Resin sheet –
Abrasive Abrasive size	Water –	Diamond slurry 1 μm	Colloidal silica 80 nm Diamond 1 μm
Load	1.9 N (0.194 kgf)	1.9 N (0.194 kgf)	1.9 N (0.194 kgf)
Rotational rate	60 rpm	60 rpm	60 rpm

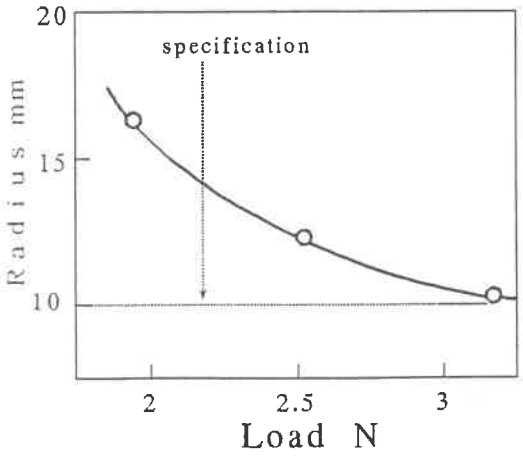

Fig.5 Variation of the end radius with the polishing load

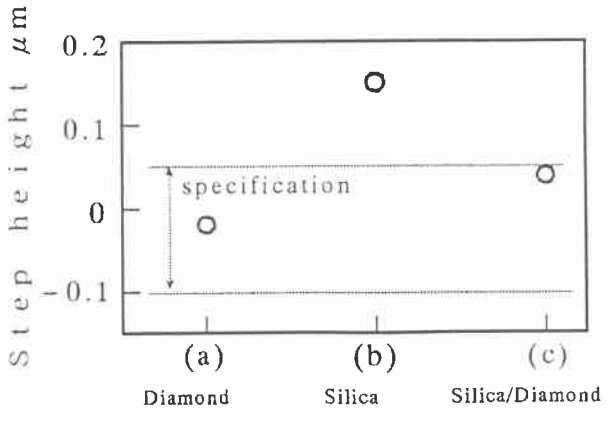

Fig.6 Step height resulting from the use of various abrasives

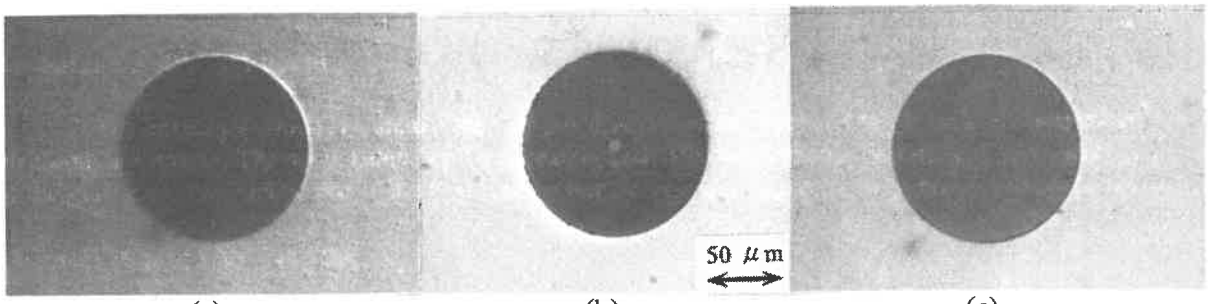

Fig.7 Nomarski photographs of the polished surfaces

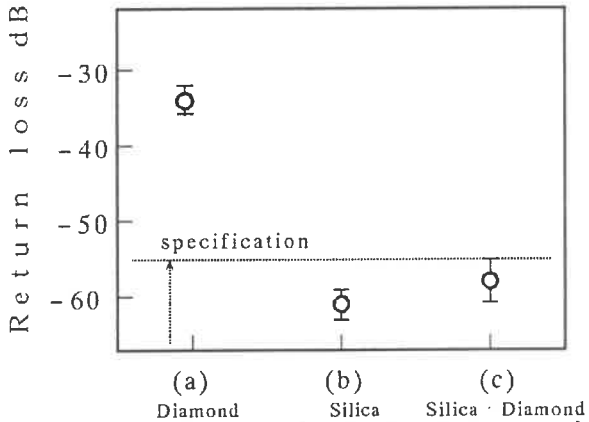

Fig.8 Return losses resulting from the use of abrasives

Fig.7 shows Nomarski photographs of the polished surfaces. Surface (b) is most clear. In (a), some runner cuts are visible. Fig.8 shows the return loss resulting from the use of various abrasives and polishers. In (b), the return loss is low because the layer of damage to the workpiece is thinnest. surface (c), resulting from the use of a hybrid polishing of diamond and silica, is smooth, and its step height is low. It seems that diamond abrasive makes the end shape precise and colloidal silica decreases a damaged layer.

6. Conclusion

In this report, a new method for precision hybrid polishing of optical fiber connectors was proposed. Then an experiment was performed, in which a physical contact-type fiber was polished using the proposed method. From the experiment, the following results were obtained:

(1) The radius curvature of the fibers was controlled to 15 ±3 mm, the step height between fiber and ferrule was less than 0.05 μm, and the eccentricity from the ferrule center axis was less than 30 μm.

(2) The insertion loss was less than 0.05 dB and the return loss was to be less than -55 dB.

(3) The total processing time was less than 15 seconds (per fiber end surface).

References

1) J.Watanabe and T.Saitoh, Proceedings of ASPE'89,(1989)133.
2) S.Matsui et al., Proceeding of ASPE'95,(1995)179.

In-Process Detection of the Ductile-Brittle Transition in High Speed Scratching of Glass-Theory & Experiment

Jay Daniel, David Dornfeld, Laboratory for Manufacturing Automation, Department of Mechanical Engineering, University of California, Berkeley

Abstract: In the machining of brittle materials, the transition from ductile mode to brittle mode material removal occurs as the material removal mechanism migrates from plasticity dominated mechanisms to mechanisms dominated by material fracture. In process differentiation of the material removal mechanism is an important factor in controlling the productivity and quality of the machining process. Passive acoustic monitoring is shown to yield a robust method of monitoring the ductile brittle transition. Transient acoustic waveforms in the machined material generated by representative ductile and brittle acoustic source functions are discussed. Surface displacements from these acoustic sources are calculated using a Green's function for an infinite plate. Trends in the displacement waveforms which will allow the in-process discrimination of ductile and brittle machining modes in a real machining process are discussed. A high speed transitional ductile-brittle scratching test is performed. Results show that signal peakedness is a strong indicator of the machining regime, per the prediction based on the theoretical waveforms.

INTRODUCTION

The problem of developing an in-process sensor to detect the amount of brittle damage occurring during the machining of brittle materials has interested many investigators. Such a sensor would have applicability in the control of processes involving fine grinding of brittle materials. The sensor most commonly used for these investigations has been the acoustic emission sensor.[1,2]

Previous work has established empirical relationships between the relative degree of brittle damage seen in the work and the frequency content, specific energy, and the event count rate of the acoustic emission.[3,1,2] These results, while promising, did not offer a final solution to the problem of developing an in-process sensor, because the relationships established were correlative in nature, and would need to be fitted for each process and setup. A more quantitative approach is warranted.

Fortunately, canonical forms for the transient surface displacements from various types of acoustic source functions exist, and computer programs have been developed to calculate these displacements.[4,5] In addition, investigators have considered acoustic source functions associated with both ductile and brittle machining.[6,7] An examination of the displacement wave forms that are generated by characteristic ductile versus brittle acoustic source functions show that fundamental differences in the generated waveforms exist.

TRANSIENT DISPLACEMENT WAVEFORMS FROM CHARACTERISTIC DUCTILE AND BRITTLE ACOUSTIC SOURCE FUNCTIONS

Considering the acoustic sources in grinding from the perspective of an acoustic receiver attached to the workpiece, one can list acoustic sources generated during ductile and brittle grinding that generate acoustic waves in the workpiece. Table 1 specifies these sources.

DUCTILE REGIME GRINDING	BRITTLE REGIME GRINDING
Moments from dislocations	Moments from dislocations
Tractions from grinding grits interacting with part surface + grits translating across surface + stick-slip events between grits and part + grit entrance/exit to/from part + tractions from grit fractures	Moments from fractures Tractions from grinding grits interacting with part surface + grits translating across surface + stick-slip events between grits and part + grit entrance/exit to/from part + tractions from grit fractures
Tractions from grinding wheel bond material interacting with part surface. + stick-slip events between bond and part + step function tractions from bond fractures	Tractions from grinding wheel bond material interacting with part surface. + stick-slip events between bond and part + step function tractions from bond fractures

Table 1: Acoustic Sources in Ductile and Brittle Regime Grinding

Examination of table 1 quickly shows that acoustic sources have been classified either as moments or tractions. This is because the mathematical description of transient surface displacement admits acoustic sources as either moments or tractions. The general expression for the calculation of transient surface motion in a medium resulting from an acoustic source in that medium is

$$u_n(x,t) = \int_0^\infty M_{kl}(\tau) G_{nk}(\tau - t; x)_{,l} - G_{ni}(\tau - t; x) T_i(\tau) d\tau \quad (1)$$

The normal indicial notation is used with u denoting displacement, M_{kl} denoting the moment acoustic source, G denoting the elastodynamic Green's function, ,l denoting the partial spatial derivative, $\frac{\partial}{\partial x_l}$, T_i denoting the traction acoustic source, and τ representing a variable of integration in time. $G_{ni}(\varepsilon, \tau - t; x)$ represents the Green's function for displacement in the nth direction at position x and time t in a body resulting from a delta function traction source occurring in the ith direction at time τ and position ε in a body. Assumptions in (1) include no body forces acting on the medium and all acoustic sources acting as point sources.

Although lack of space prevents a full treatment of all the acoustic sources listed in table 1, some statements about these sources can be made. First, dislocations in ductile regime grinding of brittle materials have been shown theoretically[8] and experimentally[9] to produce acoustic waves too small to detect in a typical machining setup. The other tractions associated with ductile regime machining either have frequency content too low to consider in acoustic emission monitoring, or can be treated as tractions with a step function temporal behavior. That is,

$$T_i(\tau) = T_i u(\tau) \quad (2)$$

where T_i is the ith component of the traction vector on a surface of the machined part imposed by the grinding wheel and u(t) is the step function.

Moment sources from fractures, specifically mode 1 surface breaking cracks, have been studied experimentally[7] and shown to be of the form,

$$M_{kl} = D \begin{bmatrix} 1 & 0 & 0 \\ 0 & 0.1 & 0 \\ 0 & 0 & 0 \end{bmatrix} \hat{S}(t) \quad (3)$$

when the normal to the crack surface points in the x direction and with D being

$$D \approx 20 A_f G_c \quad (4)$$

where D is the magnitude of the moment tensor, S(t) is the time dependence of the moment source, A_f the final crack area, and G_c the is the Griffith energy. S(t) can reasonably be assumed to be a step function over the frequency range

of interest.

Having identified the characteristic acoustic source functions for ductile and brittle machining modes, the transient surface displacement waveforms that these acoustic sources generate can be calculated. Figure 1a,b shows these displacements in an infinite plate for a sensor position of (50.8,0,0) mm given a source position of (0,0,0).

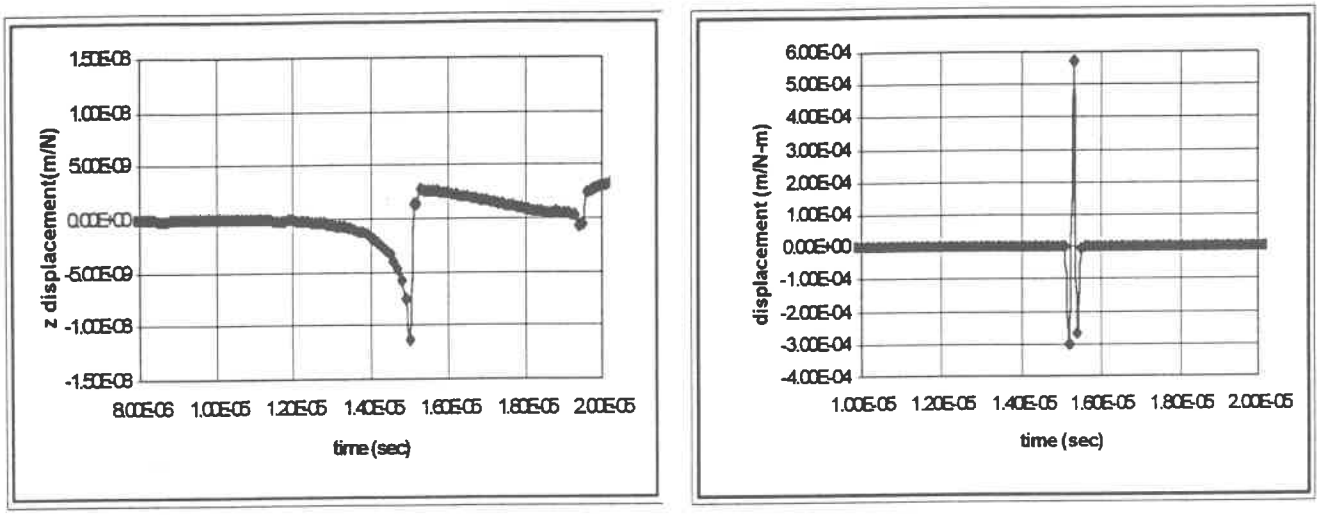

Figure 1a,b: The displacement waveforms in an alumina plate from characteristic ductile and brittle acoustic source functions.

Some characteristics of these signals are notable. First, they occur over very short time periods, requiring the use of a higher frequency acoustic receiver(1-3 Mhz) to monitor them. Monitoring at these higher frequencies also allows the examination of individual wave passages in more detail. For the purpose of discriminating ductile from brittle machining, a signal characteristic from these displacement waveforms is sought that is invariant to the signal energy and is easy to calculate in real time. The peakedness of these signals, relative to their energy, is such a characteristic.

EXPERIMENTAL-HIGH SPEED SCRATCHING

A high speed scratching experiment was devised with this in mind. Figure 2 is a diagram of the experimental setup.

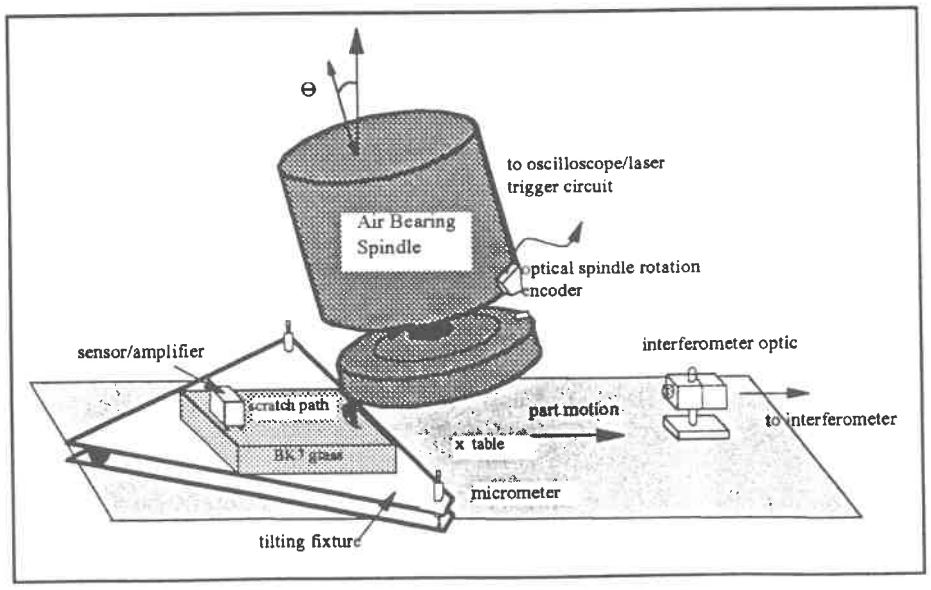

Figure 2: The experimental setup for acquiring acoustic emission from high speed scratching.

In the experiment, a Vicker's indentation tip with a 1x1 um flat on the tip was used to scratch a borosilicate glass(Schott BK7) at increasing depths of cut. Acoustic data was collected with a piezoelectric transducer, the Pinducer™, available from Valpey Fischer(Hopkinton, MA) incorporated into a custom amplifier. Data was sampled at 10 Mhz during the scratching. Each record consisted of 25000 points, representing 2.75 cm of scratch distance at the scratching speed of approximately 9.1 m/sec. The scratch tip position and acoustic data were correlated with a spindle position sensor. The position of the individual scratches on the workpiece and the acoustic file numbers were correlated with axis position data from a linear interferometer.

Scratching was conducted so that the scratch depth transitioned from ductile to brittle over a series of scratches according to the critical depth of cut parameter[10]. The scratch numbers were correlated with the acoustic files gathered. Axis position data and tip postion on the sample showed that the acoustic file number was related to the scratch number by

$$y = 0.4 * file\_number - 22.84 \tag{5}$$

with all positions in mm. Optical examination of the scratched workpiece with a Leitz optical microscope and a Zygo interferometer showed that the first scratch for which acoustic data was generated was scratch 75(corresponding to acoustic file #75). This scratch was approximately 5 nm deep. Scratches 76 and 77, along with scratch 75, were ductile in appearance. Scratch 78 was transitionally ductile-brittle. Scratches 79 and on showed largely brittle characteristics.

Because the acoustic sensor had been previously determined to be a surface velocity transducer, and the displacement record was of most interest, the raw signal(which is proportional to velocity) was numerically integrated. Also because previous examination of the acoustic waveform from indentation results showed that most of the significant signal characteristic of crack sources was at frequencies above 1.0 Mhz, the acoustic data files were processed through a high pass filter(9th order Chebyshev) at 1.0 Mhz

Then, a simple algorithm to characterize the peakedness of the scratch records was developed. The algorithm functioned as follows. For a given scratch record, a 15 sample(1.5 μsec of data) data window was interrogated starting with t=0. The difference between the highest and lowest values in that window was stored. The window was then incremented 0.1 μsec forward, and the maximum difference for that window was found and compared to the maximum difference from the first window. The largest value was retained. The window was incremented through the entire file, looking for the greatest dipole. This value(fig. 3b) was called the maximum dipole of the given scratch record. The integrated/high pass filtered voltage records(proportional to surface displacement) were interrogated in this way.

Next the RMS energy(fig. 3a) of the acoustic signal from the integrated, high pass filtered data files were calculated according to (6).

$$RMS = \left(\frac{1}{T} \sum_{i} \left(u_i^{\,2} \Delta t \right) \right)^{\frac{1}{2}} \tag{6}$$

where T is the total sample period, Δt is the time increment between samples, and u_i is the volt-sec value proportional to surface displacement. While a smaller window for the total T of the window could be chosen, for initial simplicity, each 2.5 millisecond record was examined separately.

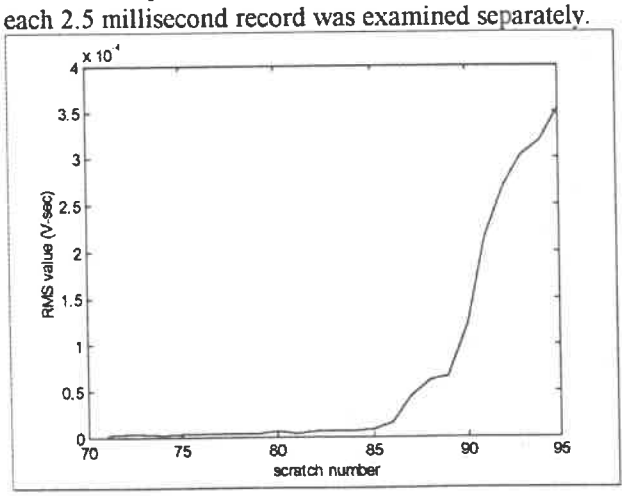

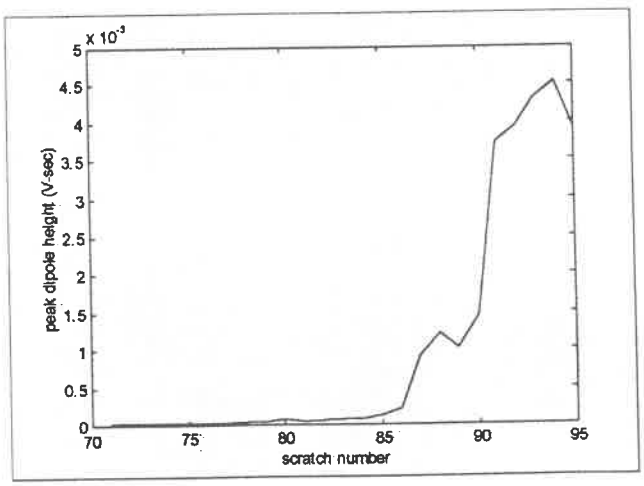

Figure 3a,b: RMS voltage and peak dipole values from the integrated, high pass filtered acoustic records. Records 71-74 are included to allow benchmarking vs. signal noise.

Finally, since it was desired to normalize the peak dipole value to the signal energy, the ratio of the peak dipole values to the rms voltage was taken(fig. 4).

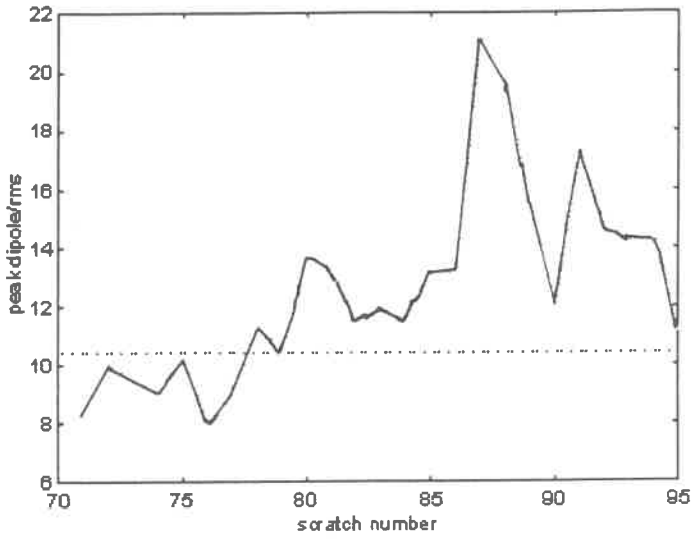

Figure 4: The ratio of peak dipole to rms voltage for scratches 71-95. Again, 71-74 indicate signal noise. Below the line scratches were ductile in appearance. Above the line, they appeared brittle.

This measure of signal peakedness showed a clear transition from ductile to brittle machining correlating exactly with physical observation of the scratches and model of critical depth of cut[10] for the ductile brittle transition. Furthermore, the peakedness of the records 71 through 77 was dominated by noise spikes from the motor driving the x axis. The ratios for records 71 through 77 would have been in the range of 5-7 had this noise source been excluded. The ratio for records 78-95 had no contribution to peakedness from motor noise. It is concluded, then, that an even stronger transition from ductile to brittle machining would have been seen with some modifications to the acoustic receiving system electronics to reduce noise.

CONCLUSIONS

A methodology for detection of the ductile-brittle transition in precision grinding has been developed from consideration of the surface displacement waveforms generated from characteristic ductile and brittle acoustic sources. A high speed transitional ductile brittle scratching experiment was conducted which confirmed that signal peakedness is a robust measure of the ductile brittle transition in high speed scratching. The methodology is invariant to the signal energy, and is motivated by the physics of acoustic propagation in the system.

REFERENCES

[1] Akbari, J., Saito, Y., Hanaoka, T., Enomoto, S., JSME International, Series C, **38**(1), 1995, pp. 175-180.
[2] Bifano, T.G., Yi, Y., **14**(4), Oct. 1992, pp. 219-228.
[3] Ichida, Y., Kishi, K., Hasuda, Y., JSPE, **58**(5), 1992, pp. 841-846.
[4] Johnson, L.R., Geophys. J. R. Soc. **37**, 1974, pp. 99-131.
[5] Hsu, N.N., NBSIR 85-3234. Available through NTIS, PB86-143956/AS (1985).
[6] Hsu, N.N., Simmons, J.A., Hardy, S.C., Mater. Eval., **35**, 1977, pp. 100-106
[7] Kim, K.P. Sachse, W., J. Appl. Phys. **59**(8), April 1986, pp. 2711-2715.
[8] Daniel, J.P. Ph.D. Thesis, University of California, Berkeley, 1996.
[9] Daniel, J.P. Engineering Systems Research Center Report No. 30, November 1994, Berkeley, CA.
[10] Bifano, T.G., Dow, T.A., Scattergood, R.O., ASME Trans., J. of Eng. for Ind., **113**, May 1991, pp. 184-189.

On-Line Measurement of Grinding Wheel Wear Using Acoustic Emission

W.P. Dong L. Annecchino J.A. Webster

Center for Grinding Research and Development
University of Connecticut
Storrs, CT 06269-5119
USA

Abstract

A new method based on an application of acoustic emission for on-line measurement of grinding wheel wear is proposed in this paper. The feasibility of the proposed method and the uncertainty of wheel wear measurement are studied with experiments.

1. Introduction

As grinding remains one of the most important precision manufacturing processes, feedback control for high efficiency, high quality and low cost production is of great interest to manufacturing industries[1-6]. In order to achieve reliable and cost effective feedback control, a critical issue is to realize on-line measurement of grinding wheel diameter which is affected by to wheel wear, wheel expansion and dressing operations. Diameter measurement of a grinding wheel can help to quantify wheel wear, to determine feedback compensation in dimensional control, and to decide dressing conditions. So far, however, there are no effective commercial methods available for on-line measurement of wheel wear or wheel diameter. Coolant and swarf in the grinding process forms a hostile environment for advanced measuring techniques, e.g. optical sensors[5,7]. The cost, the amount of retrofitting work to install a measuring system, the efficiency and the accuracy of such measurement are also big concerns before the system to be accepted by industry. Recently, Oliveira et al[8] has proposed a convenient method for dimensional measurement of grinding wheel using acoustic emission (AE). However, since a single point dresser was used in their method, the measuring accuracy is highly influenced by local geometry of the wheel, e.g. waviness, roughness and local cracks. In addition, low level AE caused by turbulence and elastic contact in the initial dresser/workpiece contact was very much the concern of their study, which would induce unstable AE detection. Bearing the above constraints in mind, a simple on-line wheel dimension or wheel wear measuring method is proposed in this paper. This method is based on utilizing the CNC controller and acoustic emission measurement. The principle of wheel wear measurement using acoustic emission and experimental approaches are introduced in this paper. The feasibility of the proposed method is experimentally verified and the uncertainty of wheel wear measurement is evaluated. It is expected that the proposed method will be cost effective, reliable, efficient and potentially applicable to manufacturing industry.

2. Description of Method

The proposed method is based on detection of an acoustic emission signal. As it is known , a grinding process produces high frequency (above 100KHz) AE waves due to plastic and elastic deformation of part and wheel materials. It has also been shown that AE is more sensitive than force, acceleration and power to reveal initial wheel/part contact in the grinding process[6]. Even if an initial contact is so weak that only a few active wheel grits rub against the part, the generated AE signal is still detectable with

sufficient signal to noise ratio for a high level of confidence[6]. Therefore, the AE measuring technique can serve as a touch trigger probe to be applied for wheel diameter measurement. The core principle of this method requires a reference surface located at an appropriate position on the grinding machine. Whenever dimensional measurement of the wheel is required, the wheel is touched on the reference surface and the corresponding AE signal produced triggers the positional capability of the CNC grinding machine, which compares the current value with the previous reading, to obtain the diameter change in the wheel surface position. This process is similar in operation to a coordinate measuring machine (CMM). The function of a mechanical touch trigger probe of a CMM is replaced by the AE sensor and the function of the CMM controller is replaced by the CNC controller. The accuracy of wheel wear measurement using this method will be influenced by several factors which will be discussed later.

3. Experiments

In order to verify the feasibility and accuracy of the proposed method, experiments were conducted on a CNC surface grinder. The experimental set-up is shown in Fig. 1. Since the controller's positional capability was not accessible during this experimental stage, a displacement sensor - LVDT instead of CNC controller was used to measure the wheel position. For obtaining quantitative wheel wear and its relationship with the measured results, wheel wear was simulated by a truing process, i.e. the amount of dimensional change of the wheel taken by a truing process is considered as the amount of wheel wear. The computer takes readings of two channels, AE and downward displacement of the wheel (LVDT), concurrently. When the wheel touches the reference surface and the root-mean-square (RMS) signal of AE exceeds a preset threshold, the computer records the instantaneous position of the wheel, which is compared with the data obtained in the last measurement and serves as the reference for next measurement. During each measurement, the reference surface was contacted (lightly ground) within a small local area, therefore the table should be moved a short distance horizontally to keep a fresh contact area for touching for next measurement. The experiments used an alumina oxide wheel, with an initial diameter of 420 mm and a width of 11 mm. The horizontal dimension of the reference surface was 100x20 mm, which was initially ground flat in-situ prior to the test.

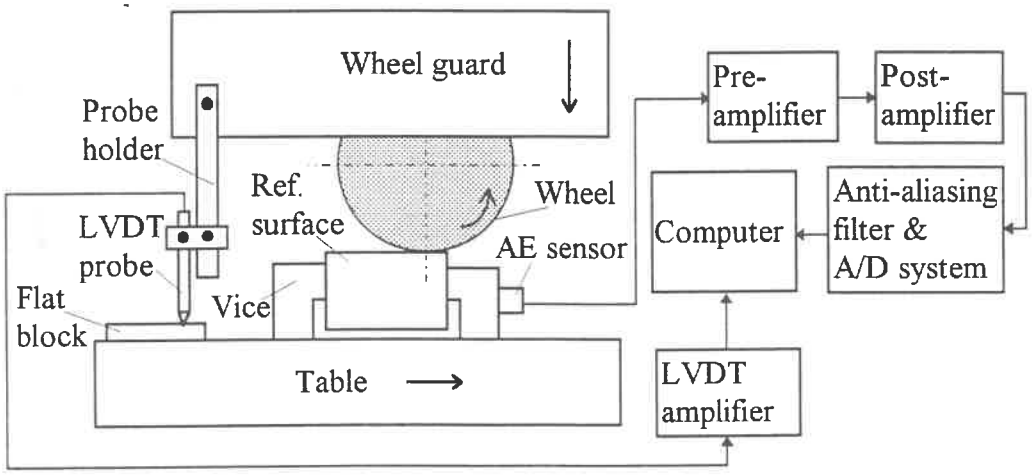

Fig. 1 Experimental setup of wheel measurement using acoustic emission.

With the described setup, two experiments were conducted. One was a repeatability test where the wheel touched the reference surface several times without grinding (except for the time of touching), therefore inducing no wheel wear. This test can help to determine measuring consistency since no wheel wear has occurred. The second experiment was a wheel wear test using the truing process to change the diameter of the wheel, instead of extensive grinding tests to generate natural wheel wear. Fig. 2 shows an example of AE RMS and LVDT signals where the horizontal broken lines are the threshold of AE and the circles represent the moment of AE trigging and corresponding displacement reading. The time constant of the AE RMS signal used was 12.8 ms. As can be seen in Fig. 2a, a larger threshold (20 dB) was set in the experiment. This is to avoid unstable touch trigging caused by a few protrude grits in initial wheel/part

contact and to maintain consistent touch trigging due to substantial wheel/part contact. The wheel or LVDT displacement shown in Fig. 2b has three distinctive zones after the LVDT touches the flat block, i.e. (i) the wheel approaches the reference surface with a fast speed where a linear LVDT displacement is observed (200-240 ms in Fig. 2b); (ii) the wheel approaches the reference surface with a reduced speed where a non-linear LVDT displacement is observed (240-600 ms in Fig. 2b); and (iii) the wheel stops where no further LVDT displacement is observed (flat response, after 600 ms in Fig. 2b). In the third zone, the differences of LVDT readings in consecutive wheel wear tests can reflect position accuracy (or truing compensation accuracy) of the wheel after truing.

4. Analysis of Experimental Results

The experimental results are presented in two phases, i.e. repeatability test and wheel wear test.

4.1 Repeatability of measurement

The repeatability test was conducted by touching the reference surface several times with the wheel rotating but without grinding (except for the moment of touching). After each measurement, the table was moved a few millimeters horizontally in order to offer a fresh reference area for the next measurement. As is seen from Figs. 2b, the wheel approached the reference surface fast and decelerated when it was close to the reference surface, where the wheel displacement is nonlinear due to the servo control. At the time when the displacement reading was taken, the plunge rate was approximately 300 μm/s. In Fig. 2b, readings were taken from two places. One was obtained from the circled place, which was AE trigging point, another was obtained from the flat response area (after 600 ms in Fig. 2b) where the wheel stopped downfeed and the reading represents the position of the wheel after truing, which should be directly related to the truing compensation value used.

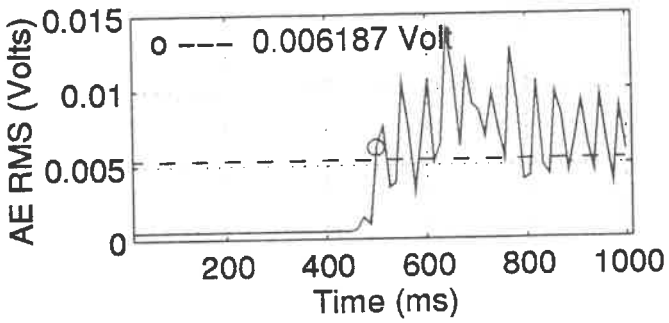

(a) AE RMS

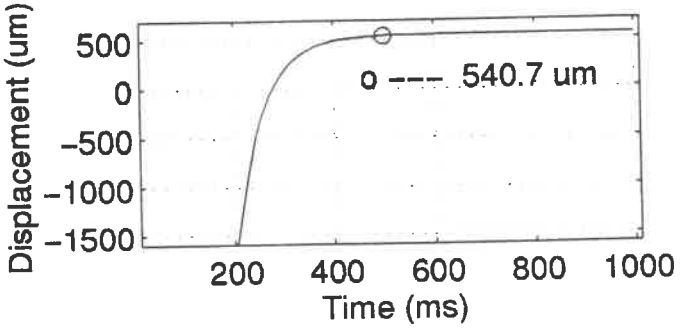

(b) Wheel (LVDT) displacement

Fig. 2 An example of AE RMS and displacement recorded concurrently.

The data obtained from seven consecutive measurements is presented in Table 1. The deviations of these consecutive measurements are shown in Fig. 3. The uncertainty of the repetitive tests trigged by AE is U_{r1}=1.9 μm; the uncertainty of the wheel repositioning is U_{r2}=2.07 μm. It appears that the proposed method was as accurate as wheel repositioning at a wheel approach rate of 300 μm/s.

4.2 Wheel wear test

As stated earlier, during the wheel wear test, wheel wear was simulated by the truing process. Between each pair of measurements, the wheel was trued by 25.4 μm (0.001 inch). The experimental results for the wheel wear test are given in Table 2 and Fig. 4. Fig. 4a shows the dimensional change of the wheel radius detected by the proposed technique versus the nominal accumulated truing depth; Fig. 4b is the deviations between them and Fig. 4c is the measured step increment after each truing cycle. The step increments are close to the nominal value which is 25.4 μm. The difference between the measured value

and the nominal value can be attributed to (i) error of the method; (ii) error of wheel reposition and (iii) error between the nominal truing depth and actual truing depth. The deviation of wheel reposition with respect to the nominal value after truing is shown in Fig. 4d. The uncertainty of wheel reposition, U_{w2}, is 1.29 μm. Surprisingly, the uncertainty of the measured accumulated wheel wear, U_{w1}, is 0.81 μm, which is smaller than U_{w2}. However, note that the deviations between the measured wheel wear and the accumulated truing depth (Fig. 4b) has a positive bias, which implies that the measured wheel wear is slightly larger than the nominal accumulated truing depth.

Table 1. Data of repeatability test (in μm)

	Measured value	Deviation with mean	Reposition	Deviation with mean
1	539.9	-1.13	551.6	1.82
2	542.3	1.27	549.7	-0.08
3	540.4	-0.63	548.6	-1.18
4	540.4	-0.63	548.1	-1.68
5	544.8	3.77	553.6	3.82
6	539.3	-1.73	548.4	-1.38
7	540.1	-0.93	548.5	-1.28
Mean	541.03	0	549.78	0
STD	1.9	1.9	2.07	2.07

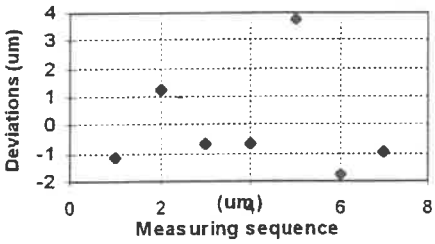

(a) Deviations obtained by AE triggering

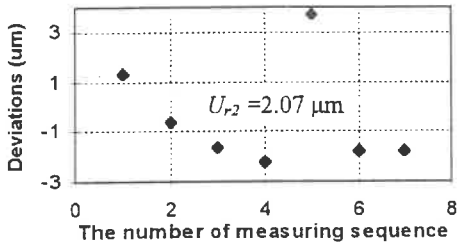

(b) Deviations of wheel reposition

Fig. 3 Deviations of repetitive measurements.

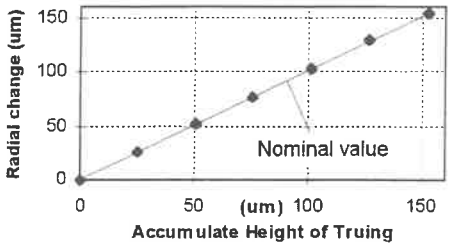

(a) Radial change of the wheel after truing

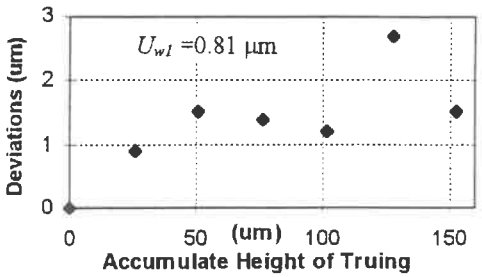

(b) Deviations between measured radial change and nominal accumulated truing depth

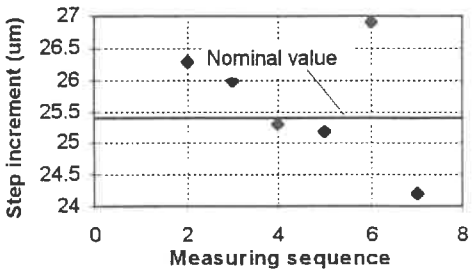

(c) Measured step increment after each truing cycle

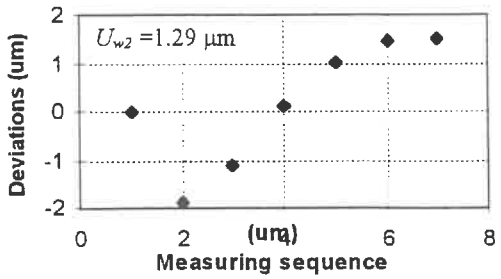

(d) Deviation of wheel reposition after truing

Fig. 4 Measurement of wheel wear.

Table 2. Data of wheel wear test (in μm)

	Nominal value	Measured value	Deviation with nominal value	Measured step increment	Reposition value	Deviation with nominal value	Step increment of reposition
1	0	0	0	N/A	0	0	N/A
2	25.4	26.3	0.9	26.3	23.54	-1.86	23.54
3	50.8	52.3	1.5	26	49.71	-1.09	26.17
4	76.2	77.6	1.4	25.3	76.32	0.12	26.61
5	101.6	102.8	1.2	25.2	102.63	1.03	26.31
6	127	129.7	2.7	26.9	128.47	1.47	25.84
7	152.4	153.9	1.5	24.2	153.92	1.52	25.45
Mean			1.31	25.65		0.17	25.653
STD			0.81	0.95		1.29	1.11

5. Discussions of the Accuracy of Wheel Wear Measurement

The accuracy of wheel wear measurement using the proposed method depends on the following factors: (i) the positional accuracy of the grinding machine; (ii) the flatness of the reference surface; (iii) the method to set threshold for AE; (iv) the rate of wheel approach to the reference surface and (v) the response characteristics of the CNC controller. Of these the method to set threshold for AE and the rate of wheel approach to the reference surface are considered the most important.

The application of AE for wheel wear measurement is different from contact detection for gap elimination since in the latter the threshold should be set as low as possible in order to be able to detect early contact of highest grits on the wheel. However, as the wheel consists of waviness, roughness and some protruding grits, the wheel wear measurement would be distorted if a reading was taken when only top or loose grits are in contact with the part surface. Ideally, the diameter reading should represent when the majority of grits are in contact with the surface. To achieve this the DC component of the AE RMS can be used. An example of a significant increase in this DC component is shown in Fig. 2a. Therefore, the threshold of diameter measurement should be set much higher than that for gap elimination. In this report, a threshold of 20 dB was used. Providing this threshold is consistent for two successive measurements, the error will be minimum.

The rate of wheel approach to the reference surface is also an important factor which influences accuracy. For example, assume the wheel approach rate is 1000 μm/s and the maximum variation of touching trigging is 10 ms, then a possible measurement error is 10 μm. Therefore, in order to reduce this kind of error source, the approach rate must not be too large. As from the experimental results, an uncertainty smaller than 2.1 μm was achieved with an approach rate of about 300 μm/s. Therefore it is assumed that a plunge rate smaller than 300 μm/s (i.e. 100 μm/s) would be suitable for practical applications. The slower approach rate need only be applied in close proximity to the reference surface, thus saving a considerable amount of measuring time.

6. Conclusions

Based on the experiments and above discussions, it may be concluded that

- the proposed method can be implemented in practice;
- the experimental results show that under the approach rate of about 300 μm/s, an uncertainty of smaller than 2.1 μm can be achieved in a large range of accumulated diameter change;

- the accuracy of diameter measurement using the proposed method can be as good as wheel reposition;
- the accuracy of diameter measurement using AE can further be improved by properly choosing approach rate and the method for setting the threshold.

In addition an algorithm of the CNC controller should be developed which uses the response of the AE triggering to access the encoder position at each moment of contact, therefore eliminating the need for the LVDT.

References

1. Blum, T. and Dornfeld, D.A., Grinding Process Feedback Using Acoustic Emission, Proceedings of 4th International Grinding Conference, 1990, MR90-525.
2. Konig, W. and Meyen, H.P., AE in Grinding and Dressing: Accuracy and Process Reliability, Proceedings of 4th International Grinding Conference, 1990, MR90-526.
3. Lezanski, P. and Rafalowicz, J., An intelligent monitoring system for cylindrical grinding, Annals of CIRP, Vol. 42/1/1993.
4. Kluft, W., Monitoring the Grinding and Dressing Operations Increases Output and Quality and Reduces Cost and Waste, Proceedings of 5th International Grinding Conference, 1993, MR93-371.
5. Tonshoff, H.K., Werner, F., Karpuschewski, B., Fast sensor systems for the diagnosis of grinding wheel and workpiece, Proceedings of 5th International Grinding Conference, 1993, MR93-369.
6. Webster, J.A., Dong, W.P. and Lindsay, R., Raw acoustic emission signal analysis of grinding process, Annals of the CIRP, Vol. 45/1/1996, 335-340.
7. Brinksmeier, E., and Werner, F., Monitoring of grinding wheel wear, Annals of the CIRP, Vol. 41/1/1992, 373-376.
8. Oliveira, J.F.G. and Dornfeld, D.A., Dimensional Characterization of Grinding Wheel Surface through Acoustic Emission, Annals of the CIRP, Vol. 43/1/1994, 291-294.

Development of Vibration Cutting using OD-Blade

Ken-ichi ISHIKAWA*, Hitoshi SUWABE* and Michio UNEDA**
*Kanazawa Institute of Technology **Graduate Student
7-1 Ohgigaoka Nonoichi-machi, Ishikawa 921 Japan

1. Introduction

This study aims to develop a new cutting method using OD-Blade [1] with high efficiency, high quality and a long tool life. In this method is applied a low frequency vibration on the workpiece side during the cutting. As shown Figure 1, the vibrational direction is parallel (X-axis) [2] and perpendicular (Z-axis) individually to the cutting feed (X-axis) direction. Figure 1 shows a model of the vibration cutting using OD-Blade to Z-axis vibration. In this paper, authors carried out a series of experiments utilizing the effect of vibration. From the results of investigation with regard to the behavior of grinding force, grinding ratio, waviness and chipping for cutting accuracy, this report made the vibration cutting characteristics using OD-Blade clear.

2. Experimental apparatus and method

Figure 2 shows the outline of experimental apparatus. This apparatus is a slicer using air static pressure bearing in the spindle. The cutting characteristics is evaluated by means of measuring of the grinding force using the octagonal ring dynamometer (natural frequency:325Hz). In the case of the vibration cutting, the vibration exciter for the workpiece as

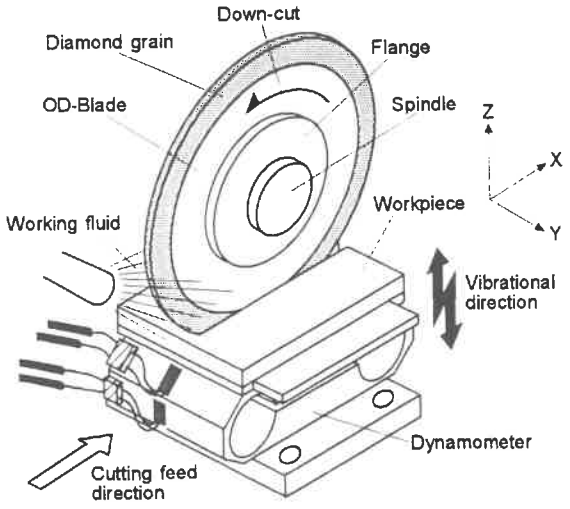

Figure 1 Model of vibration cutting

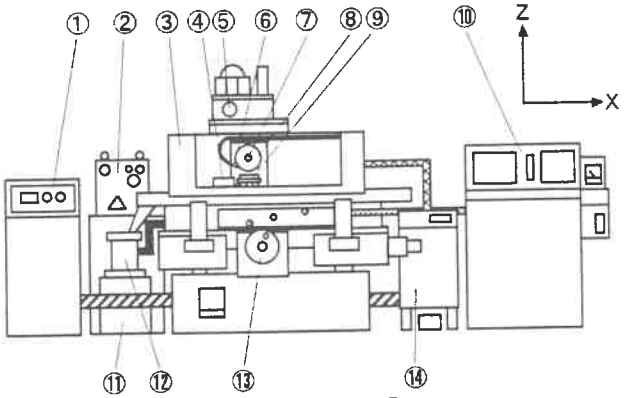

Figure 2 Outline of experimental apparatus

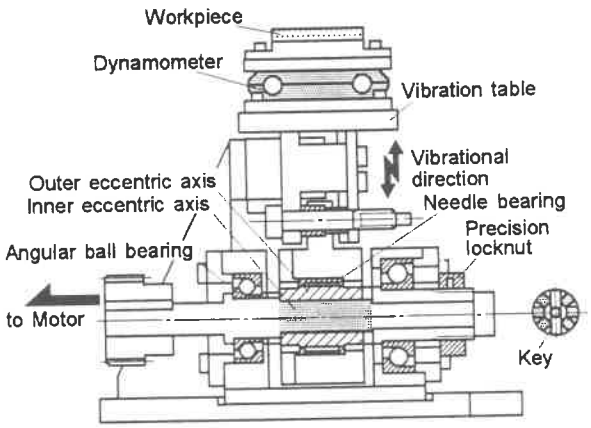

Figure 3 Outline of vibration exciter

Table 1 Experimental conditions

OD-Blade Size		ϕ125 × 1mm
Type		Metal-bond, SD#200
Blade speed		1963m/min
Cutting mode		Down-cut
Depth of cut	c	8.0, 11.0mm
Feed speed of workpiece	$\dot{X}$	20 ~80mm/min
Frequency	f	0 ~20Hz
Amplitude	a	0 ~315 μm
Workpiece, Size		Soda glass, 50 × 60 × 10mm
Grinding fluid type		Water soluble coolant (50:1)
Flow velocity V (Flow rate Q)		223m/min (5328g/min)
		358m/min (2203g/min)

shown Figure 3 is set on the working table in the apparatus and is vibrated under the experimental conditions. The double eccentric axes are used for the vibration exciter, and therefore, each amplitude can be operated at 8th stage from 15 ~ 315 μm by means of changing the combination of the inner eccentric axis and the outer eccentric axis using keys at the each axis side face. Also, the applied frequency can be generated from 0 ~ 20Hz by means of adjusting revolution of the speed control motor to the inner eccentric axis through the spur gear. The main experimental conditions are shown in Table 1.

3. Behavior of grinding force

Figure 4 shows the relationship between the applied amplitude and the normal grinding force. The symbols on the axis of ordinates show the conventional cutting and the other's symbols show the vibration cutting. From the experimental results, the normal grinding force in the vibration cutting to each feed speed of the workpiece (20 ~ 80mm/min) shows a decrease compared with one in the conventional cutting. And also, the normal grinding force tends to decrease with increasing the amplitude. It can be explained by a removal model of chip as shown in Figure 5. In the case of the vibration cutting, the processing becomes intermittent cutting owing to cutting and non-cutting phenomena (OD-Blade and the workpiece separate during cutting) in one vibration cycle. In the non-cutting process, inflow of working fluid for the

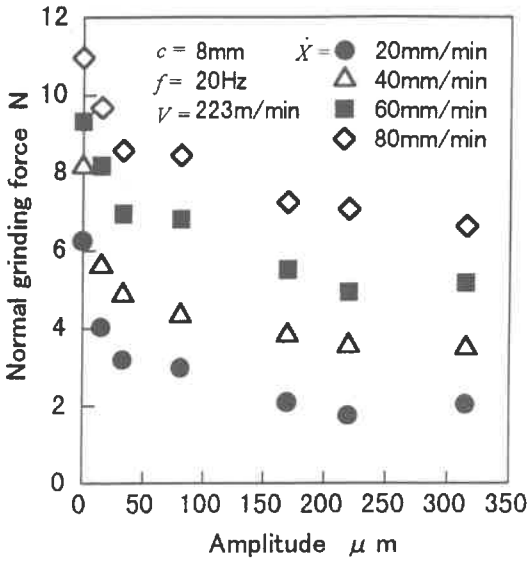

Figure 4 Relationship between amplitude and normal grinding force

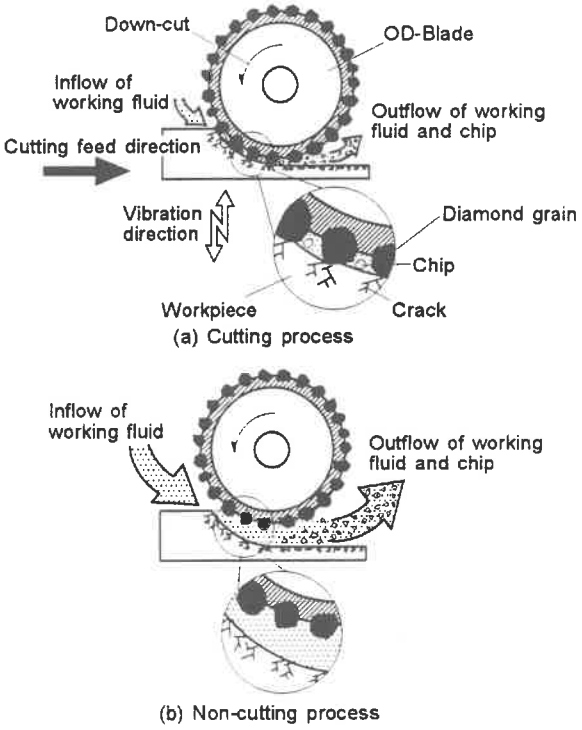

Figure 5 Removal model of chip

processing area is improved. Therefore, the effect of vibration cutting removes chips from the workpiece fully and restrains thermal wear of diamond grains. As a result, the cutting characteristics in the vibration cutting is improved to be compared with one in the

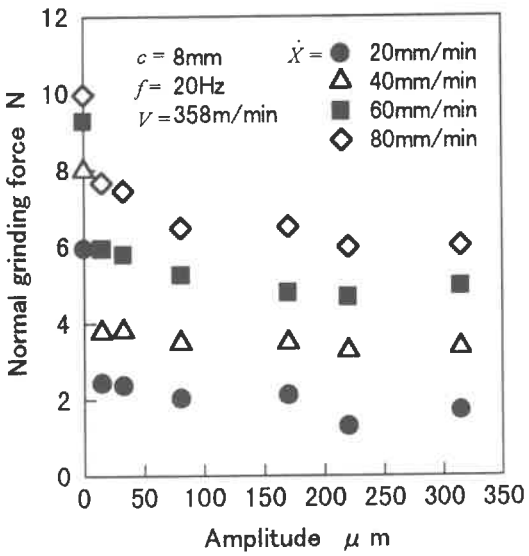

Figure 6 Relationship between amplitude and normal grinding force

conventional cutting, and then the normal grinding force shows a decrease. However, inflow effect of working fluid for the processing area in the case of the lower amplitude is difficult to improve, therefore, a decreasing effect of grinding force is a little. And then, if inflow effect of working fluid can be improved in the case of the lower amplitude, a decreasing effect of grinding force will produce remarkably. Therefore, authors tried an increasing of flow velocity using ϕ 2.8 pipe as the supplying procedure of working fluid. Figure 6 shows an experimental result in this case. From this result, in the case of the lower amplitude, a decreasing effect of grinding force becomes remarkably in comparison with Figure 4. As a result, it is considered that the cutting characteristics are influenced owing to the supplied method of working fluid in the cutting method using OD-Blade.

4. Dressing effect by vibration

Figure 7 shows the behavior of grinding force in the continuous vibration cutting by means of OD-Blade after non-vibration cutting. From experimental results, in order that a grain

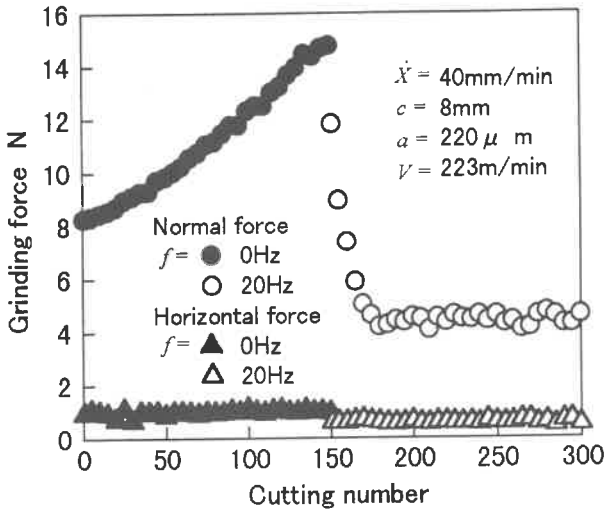

Figure 7 Dressing effect by vibration

is making progress with the attritious wear, loading of chip and breaking down gradually in the non-vibration cutting, the grinding force increases according to the cutting number. However, the grinding force decreases rapidly with vibration cutting within 30 times after the non-vibration cutting and maintains approximately constant value, even if the cutting is successive. Figure 8 shows the observed

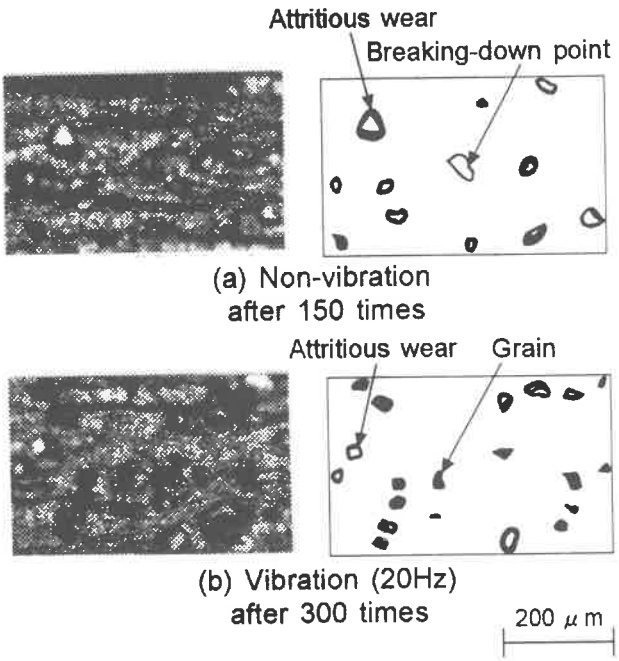

Figure 8 Observation of blade surface by optical microscope

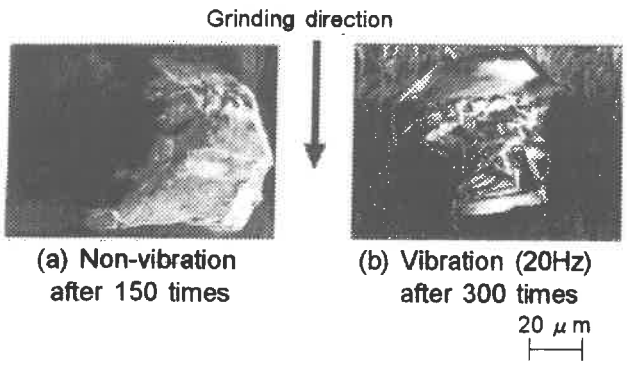

Figure 9 Observation of grain by scanning electron microscope (SEM)

result of OD-Blade surface by means of the optical microscope and Figure 9 shows a grain observed by means of the scanning electron microscope (SEM). In each photograph, (a) shows the non-vibration cutting (after 150 times) and (b) shows the vibration cutting (after 300 times). From these photographs, in the case of the non-vibration cutting, much attritious wear and many breaking down points of grains are observed, and a grain edge becomes roundish owing to attritious wear. However, in the case of the vibration cutting, attritious wear and breaking down points are a little, and much minute cracks have been observed. Therefore, the vibration cutting has the dressing effect of grains and recovers the cutting characteristics even if deteriorated OD-Blade is used.

5. Wear characteristics of OD-Blade

Figure 10 shows the relationship between the applied frequency and wear volume of OD-Blade (Diameter direction, Thickness direction) after 150 times of repetitive cutting. From an experimental result, all wear volume under each condition maintains constant value in the diameter direction. However, wear volume in the vibration cutting decreases as compared with the non-vibration cutting in the thickness direction. In the case of the non-vibration cutting, in general, the elastic deformation of OD-Blade occurrs during the cutting process. It is caused because of irregular volume of grains and shape of OD-Blade. As a result, the side surface of OD-Blade has been brought about attiritious wear because it is pushed against the workpiece during the cutting process due to restoring force of OD-Blade. On the other hand, the vibration cutting brings about the separate and contact phenomena between OD-Blade and the workpiece in one vibration cycle. The elastic

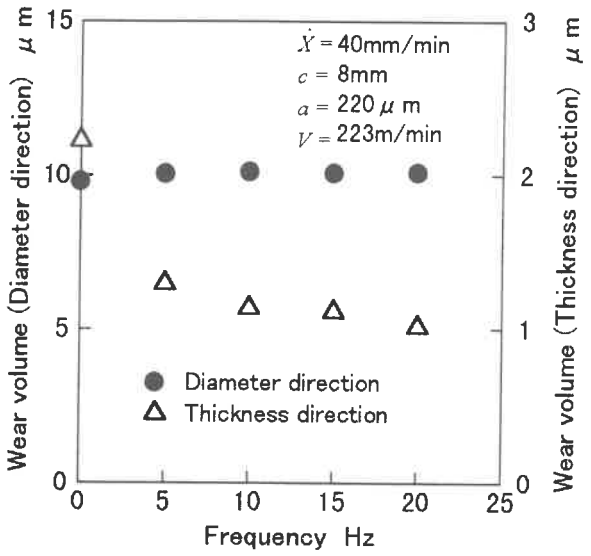

Figure 10 Relationship between frequency and wear volume of OD-Blade

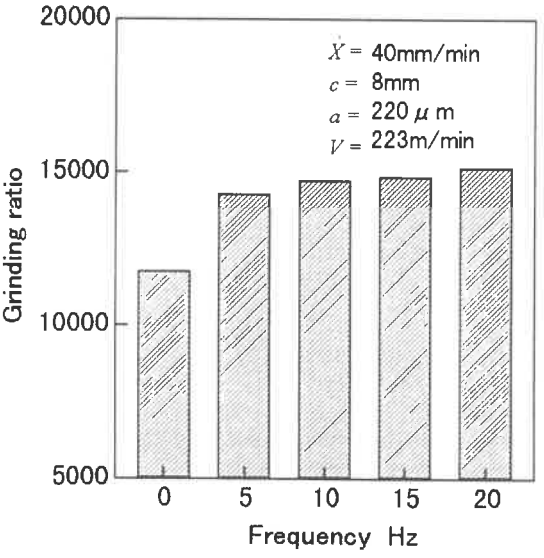

Figure 11 Relationship between frequency and grinding ratio

deformation of OD-Blade restores to the neutral position when the OD-Blade separates from the workpiece due to the elasticity of OD-Blade. Accordingly, the elastic deformation of OD-Blade is controlled in the vibration cutting and wear volume of the side surface of OD-Blade decreases in comparison with the non-vibration cutting. Also, Figure 11 shows the relationship between the applied frequency and the grinding ratio calculated from these results. As shown in the graph, it is clear that the grinding ratio in the vibration cutting increases in comparison with the non-vibration cutting, and the grinding ratio increases with increase of the applied frequency.

6. Cutting accuracy

Figure 12 shows the relationship between the applied frequency and waviness, and Figure 13 shows observed results of chipping formed in the cutting edge. The value Cp shows a quantity of chipping, and Cp is defined as shown in Figure 14. From the experimental results, it is clear that waviness in the vibration cutting is improved as compared with the non-vibration cutting. And also, chipping in the vibration cutting shows smaller than one in the non-vibration

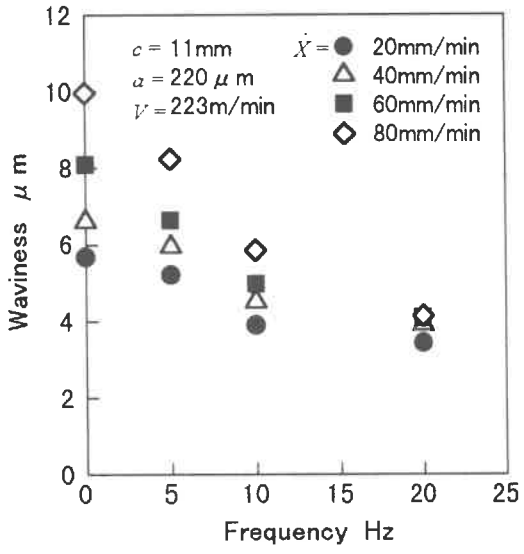

Figure 12 Relationship between frequency and waviness

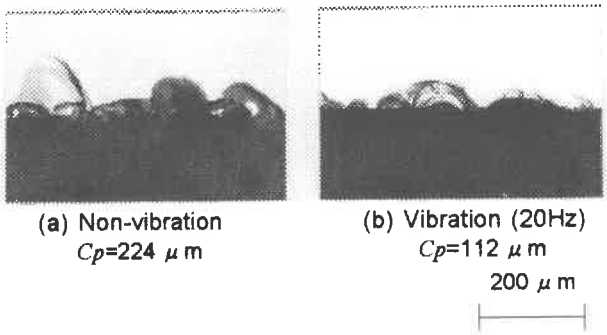

$\dot{X}$=40mm/min, c=8mm, V=223m/min
f=20Hz, a=33 μ m

Figure 13 Observation of chipping

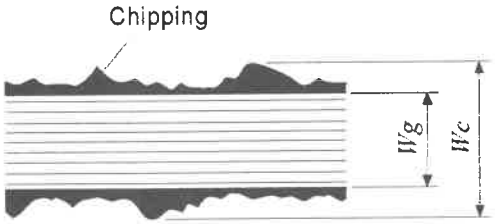

Wg : Width of cutting groove
Wc : Width of chipping
Cp : Chipping quantity determinal

$$Cp=\frac{Wc - Wg}{2}$$

Figure 14 Definition of quantitative chipping

cutting. These remarkable results are brought about by means of self corrective effect of OD-Blade during the separate process in one vibration cycle. As a result, in the case of the vibration cutting, the load oparated at the cutting edge decreases and chipping in the vibration cutting shows smaller than one in the non-vibration cutting. Also, this self corrective effect of OD-Blade increases according to increasing the applied frequency.

7. Conclusions

Through the experimental results obtained by means of the new cutting method applying low frequency vibration on the workpiece side when the vibrational direction is perpendicular (Z-axis) to the cutting feed (X-axis) direction, the

followings are clear.

(1)The grinding force in the vibration cutting decreases about 30 ~ 50% in comparison with the non-vibration cutting.

(2)The vibration cutting brings about a self dressing effect, and the grinding force in the vibration cutting maintains approximately constant value, even if the cutting process is done in succession.

(3)The grinding ratio in the vibration cutting increases as compared with the non-vibration cutting, and the tool life is improved.

(4)Waviness in the vibration cutting decreases in comparison with the non-vibration cutting, and chipping in the vibration cutting is smaller than one in the non-vibration cutting.

References

1)Ken-ichi ISHIKAWA : High Efficiency and Accuracy Slicing for Hard and Brittle Materials, IPC, (1995).

2)Ken-ishi ISHIKAWA, Hitoshi SUWABE, Kazuya MASUDA and Michio UNEDA : A Study on Vibration Cutting Characteristics Using OD-Blade, Journal of the Japan Society for Presicion Engineering, (1996), 62, 3, pp.438 ~ 442.

PROSPECTIVE OF FRACTAL APPLICATION IN GRINDING

X. M. Liu, G. Q. Cai, H. W. Zheng,
Mechanical Engineering Institute, Northeastern University P. R. China
D. L. Ma
Liaoning Industrial Art School P. R. China
Q. Y. Wen
Shenyang Donghang Mechanical &Electrical Technology Institute P. R. China

ABSTRACT

In this paper the concept of fractal which is a new mathematics branch developed in recent year is briefly introduced. Then, the dimension definitions and calculation methods are stated. At last, the prospective about fractal application in grinding is given.

KEY WORDS: Fractal Application Grinding

1. INTRODUCTION

Many phenomena in nature such as shape of cloud, rugged mountain and curve of coastline, etc., often show an irregular and altered state which can not be well described in Euclidean Space.

Mathematicians have developed geometrical concepts that transcend traditional geometrical concepts, but unfortunately, the concepts have failed in the past to gain acceptance in the natural sciences because of the rather abstract and "pedantic" presentation. Traditionally, the Euclidean lines, circles, spheres and tetrahedral have served as basis of the intuitive understanding of nature. Such shape-primitive representation function well in man-made carpentered environments. The problem, then, is how shall we describe the shape of a crumpled newspaper? a clump of leaves? a jagged mountain? When we attempt to describe the crumpled surface typical of natural objects, however, the result is usually complex. Such awkwardness makes these shape-primitive representations difficult to envisage as the basis for human performance level capabilities.

During the last 30 years, B. B. Mandelbrot has developed and popularized a relatively novel class of mathematical functions known as fractal. It has been proved that many phenomena and processes in nature have fractal structure.

The defining characteristic of a fractal is that it has a fractional dimension from which we get the word "fractal". Technically, a fractal is defined as a set for which the Hausdorff-Besicovich dimension is strictly larger then the Topological dimension. The point is that the definition although correct and precise, is too restrictive. Mandelbrot (1982) has retracted this tentative definition and proposes instead the following: A fractal is a shape made of parts similar to the whole in some way. A neat and complete characterization of fractal is still lacking (Mandelbrot, 1987).

The triadic Koch curve is an example which is used to illustrate that a curve may have a fractal dimension D > 1 shown in Fig. 1.

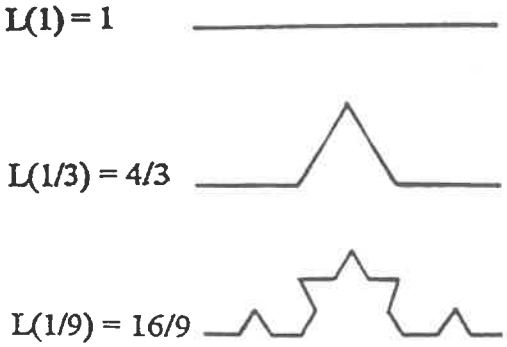

Fig. 1 Generation of Koch Curve

The picture illustrates an iterative or recursive procedure for constructing a fractal curve. A simple line segment is divided into thirds and the middle segments is replaced by two equal segments forming part of an equilateral triangle. At the next stage in the construction each of these 4 segments is replaced by 4 new segments with length 1/3 of their parent according to the original pattern. This procedure repeated over and over, will yield the beautiful Von Koch curve.

Shapes in world can be divided into two kinds:

(a) ones which have characteristic length and are smooth and differential;

(b) the others which have no characteristic length and are not smooth and differential.

Fractal geometry is mainly to deal with the later ones which include self-similar curves, positions and shapes, self-reverse irregular shapes, self-squaring transform, self-affinity transform and set. The essential characteristic of them is the scaling invariance. At present, the researches are mainly ranged in things which have self-similarity which can be popularly interpreted as the characteristic structure reappears at different scales, i.e.,multiplying any parts is statistically same as whole.

Fractal dimension is a kind of measurement. The larger the dimension is, the more complex the structure is, e.g., an object with dimension of $0 < D < 1$ describing an object with 0 length and ∞ points (Cantor Set), $1 < D < 2$ describing an object with 0 area and ∞ length (Serpinsky Gasket), $2 < D < 3$ describing an object with 0 volume and ∞ area (Serpinsky Sponge).

2. DIMENSION DEFINITION

At present there have not been a strict and overall definition for fractal dimension. The fractal concept is still in developing. Different definition determines different calculation method. Here the three commonly used fractal dimension are briefly introduced as below.

1) Box Dimension

How do we measure the "size" of a set S of points in space? A simple way to measure the length of curve, the area of surface or the volume of an object is to divide space into small cubes of side δ as an example illustrated in Fig. 2.

Fig. 2 Measuring the Size of a Curve

Here we may use small spheres of diameter δ instead. If we center a small sphere on a point in the set then all the points that are at a distance $r < 1/2\ \delta$ from the point at the center are covered by the sphere. By counting the number of spheres needed to cover the set of points we obtain a measure of the size of the set. So far, in order to give a measure of the size of a set of points in space we have taken a test function $h(\delta) = \gamma(d)\delta^{-d}$ - a line, square, disk, sphere or cube - and have covered the set to form the measure $M_d = \sum h(\delta)$. Here $\gamma(d)$ is geometrical factor. In general we find that as $\delta \to 0$, the measure M_d is either zero or infinite depending on the choice of d - the dimension of the measure. Then we call Md the d - measure of the set. If $N(\delta)$ is the numbers of the small spheres with diameter δ, then the Box Dimension Do can be defined as:

$$D_0 = - \lim_{\delta \to 0} \text{Ln } N(\delta) / \text{In } \delta \qquad (1)$$

Let us take coastline dimension as an example. On a map of coast, we could walk a divider with η an opening corresponding to δ km along the coastline on the map and count the numbers of steps $N(\delta)$ needed to move from one end of the map to the other. At beginning, we would choose such a large opening of the diameter that we would not have to bother about even the deepest fjord and estimate the length to be $L(\delta) = N(\delta)\delta$. Then, we would use a somewhat smaller opening δ and try again. This time the large fjords would contribute to the measured length. Every time we increased the resolution we find an increase in the measured length of the coastline. In fact, the measured length is nicely approximated by the formula $L(\delta) = a\delta^{1-D}$. Here, the a is constant and D is fractal dimension. So the coastline is fractal with a fractal dimension D. We may determine the fractal dimension of the coastline by finding the slope of Ln $N(\delta)$, plotted as function of Lnδ. The slope of the line in Ln-Ln plot is 1-D. The dimension determined from equation (1) by counting the number of spheres needed to cover the set as a function of the sphere size is now called the Box Dimension.

2) Information Dimension

In calculation of Box Dimension we count only the number of δ spheres and do not consider the cover points of each sphere. If it is considered the points density of δ spheres is different. Let P_i be the point density, then the $P_i \text{Ln} P_i$ shows the entropy of the systems, i.e., the information providing ability of the system. The information dimension D_1 can be defined by the formula:

$$D_1 = - \lim_{\delta \to 0} [\sum_{i=1}^{N} P_i \text{Ln}(1 / P_i)] / \text{Ln}\delta \qquad (2)$$

This expression is same as formula (1) when the point density of spheres is even. That is when $P_i = 1/N(\delta)$, the $D_1=D_0$. As stated above the expression shows the relationship between entropy of system to fractal dimension.

3) Relation Dimension

P. Grassberger and I. Procaccia gave the definition of relation dimension D_2 as below:

$$D_2 = -\lim_{\delta \to 0} LnC(\delta) / Ln\delta \qquad (3)$$

Where the $C(\delta)$ is a series of system results. If the δ is properly selected, there will be a scale range in which there is a relation $C(\delta) = \delta^D$. Here the D is approximate value of D_2. In calculation of relation dimension the value of δ must be selected in a proper range, because if δ is too big, then $C(\delta) = 1$ and $LnC(\delta) = 0$, thus the δ may not represent inner nature of system and if δ is too small then some accidental events may affect the real nature of system.

We briefly introduce the three fractal dimensions above, what is the relationship among D_0, D_1, D_2? It can be theoretically proved that there are unlimited kinds of dimensions, which can be stated as below:

$$D_q = 1 / (q-1) \lim_{\delta \to 0} (Ln\sum_i P_i^q) / Ln\delta \quad (q = 0,1,...., n) \qquad (4)$$

In this formula when q = 0,1, and 2 the D_q will be D_0, D_1 and D_2. They obey the rule $D_q > D_p$ (when $p > q$), i.e:, $D_T \le D_q \le ... \le D_2 \le D_1 \le D_0$ as shown in Fig.3.

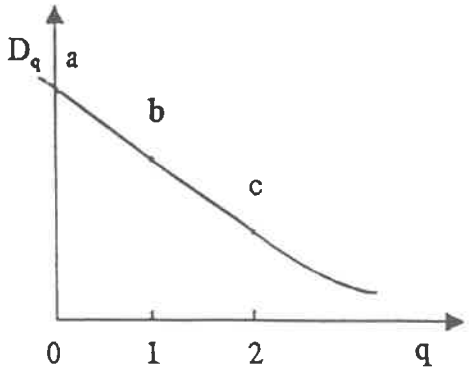

Fig.3 Relationship Curve between Dq and q

3. APPLICATION PROSPECTIVE IN GRINDING

Although the fractal geometry has been applied in many engineering, the authors until now have not found any application in grinding field. From the view of research object of fractal and characteristics of grinding, it is possible to find some applications of fractal in the field, which can be explained as below:

(a) Fracral is effective in dealing with objects which have irregular or scattered characteristics;

(b) Grinding is one of the process which have strong irregular and scattered characteristics.

First, considering from the grinding tools the grains which form surface of wheel, belt, etc., are irregular particles and so the surface of these tools are also rugged. The surface geometry of wheels, belts, and so on, which has great influence on grinding parameters has been an important research aspect in grinding for a long time. The researches in past have been strongly based on Plato Shape, this simplifying leads to inexact description and loosing many important information about the real nature. While the fractal geometry may be affective to deal with the problem for its characteristics.

Second, from the aspect of machining the process of tool wear and surface generation of workpiece has strong scattered characteristics especially in machining fragile materials such as ceramics, stone, and so on. The whole process consists of many small and random events. The irregular surface is affected by load and inner micro structure of materials. In this situation, micro fracture play an important role. There may be a number of cases in which microscopic fracture mechanism can create fractal characteristic in a certain range of scales.

From the view of mathematics the irregularity belong to nature of geometry and the fractal geometry may be found some usages in dealing with those such as the relationship between dimension and surface roughness of workpiece, etc.

Moreover, the fractal geometry can be used in computer technology to simulate and study irregular shape and roughness of workpiece, wear process, etc.

At present there have been some applications in rock crushing researches. The results are successful. Mandlebrot pointed that the rock surface and distribution of crushed pieces have unchanged scale or are fractal. Turcotto [3] proved that the crushed pieces of rock caused by explosion and impaction are fractal in structure, e.g., the particle distribution of rock crushed by lead hammer has fractal dimension of D = 1.44 [4]. The distribution of celestial body has also been proved to be fractal in structure.

In short, fractal is one kind of expression of nature . In order to know nature with fractal it is necessary to set up models and give analysis method. So that the essential relation between surface and true nature can be revealed. Because the fractal is a new branch of mathematics, it need to be more developed both from itself and application. Fractal is still at an early stage of development. But it is sure that with the development and completion of fractal geometry it will become one of powerful means to quantitatively know the objective world.

REFERENCE:

[1] B. B. Mamdelbrot, The Fractal Geometry of Nature, Freeman, San Francisco, 1983

[2] B. B. Mandelbrot, Stochastic Model for the Earth's Relief, the Shape and Fractal Dimension of the Coastline, Proc. Natl. Acad. Sci USA, 72,3825-3828, 1975

[3] T. L. Turcotto, A Fractal Model for Crustal Deformation, Tectonophys, 132,261-269, 1987

[4] M. A. Lange etal, Impact Gratering and Spall Failure of Gabbro, Icarus, 58, 383-395, 1984

[5] L. Z. Fong, Fractal of Large Scale Structure in the Universe, Modern Physics Letter A, 1,11,601-605, 1986

Grinding Characteristics of Plasma-Sprayed Ceramics

K. Narayanasamy
Associate Professor
Dept. of Mechanical Engineering
Indian Institute of Technology
Madras - 600 036, India.

S. Gowri
Senoir Lecturer
Dept. of Mechanical Engineering
Karnataka Regional Engineering College
Srinivasnagar - 574 157, India.

Rapid developments in ceramic materials and their processing techniques have widened the scope of applications either as monolithic or sprayed coatings. In any case, in order to meet the desired functions, one has to maintain the requisite surface finish, bearing area fraction and dimensional tolerance. These can be achieved by precision machining of ceramics by way of grinding, lapping and superfinishing. Since ceramics have low fracture/rupture strength, it is necessary to take utmost care during precision machining of ceramics, in order to avoid the occurrence of surface cracks and other associated defects. This paper presents an account on the grinding of Al_2O_3 and partially stabilized zirconia (PSZ) coatings.

Experimental:

Plasma sprayed Al_2O_3 and PSZ coatings were surface ground using diamond and CBN. Grinding performance was evaluated interms of grinding force and surface finish. Grinding force was measured using piezo electric type Kistler dynamometer. In order to assess the nature of grinding, Acoustic emission signals from the work piece were sensed using AET 5500 Acoustic emission recording system.

Parametric Influence on Cutting force

During grinding of plasma sprayed ceramics, the grinding force components were measured using piezoelectric dynamometer. Typical variations of normal force of grinding for Al_2O_3 and PSZ ceramics are shown in Fig.1. The grinding force is influenced by the cutting conditions, work material and the type of abrasives being used for grinding. It is seen that as the grinding speed increases, there is a reduction in grinding force in the case of diamond grinding, while raising trend can be seen in the case of grinding with CBN. Ploughing of diamond on the work surface with lower grinding velocity results in higher order F_N, while grinding performance at high speeds results in reduced order of grinding force. CBN grinds the ceramics with relatively higher order force. This can be attributed to the occurrence of grain-flattening. Both Al_2O_3 and PSZ exhibited certain phase transformation during grinding as illustrated in Table.1.

Table 1 Influence of grinding velocity on phase content of PSZ / Al_2O_3

Velocity m/s	PSZ m/t ratio Diamond	PSZ m/t ratio CBN	Al_2O_3 I_R ratio Diamond	Al_2O_3 I_R ratio CBN
5.7	0.153	0.150	0.202	0.200
11.5	0.166	0.159	0.164	0.153
15.7	0.194	0.159	0.140	0.142
31.5	0.194	0.162	0.138	0.141

Transformation of alpha to gamma Al_2O_3 during grinding reduces the hardness and consequently a reduction in the grinding force F_N. However, in the case of PSZ the t-->m transformation increases the toughness and hence results in higher order F_N. During grinding, PSZ ceramic experienced mechanical stress and rise in temperature. Depending up on the temperature or stress magnitude, it was possible that PSZ surface could undergo stress-induced t-->m transformation or with higher order temperature, it may experience t-->m-->t transformations [3]. At low speed range, due to mechanical plowing, the dominant mechanical stress might be resulting in t-->m transformation promoting transformation toughening of surface and hence the normal force increases.

Process status identification through AE parameters

Ceramics are brittle materials, known for the presence of isolated strength pockets over their matrix; hence during grinding of ceramics, depending upon the intensity of applied grinding stress and strength of the materials in the grinding zone, material removal would be associated with either deformation induced shear or clear rupture of the material [1]. When an abrasive enters the ceramic surface the material would be deformed resulting in flow of material around the intending abrasive. During indentation, the ceramic experiences median and lateral cracking in the material over the vicinity of the tip of the indenter as illustrated in Fig.2. In order to eliminate cracking, one has to limit the force of indentation. The permissible force of indentation without occurrence of cracking can be stated as [2]:

$$p = \frac{(K_{ic})^4 \cdot A\,(E/H)}{H^3}$$

K_{ic} = fracture toughness
H = hardness

Since the fracture toughness K_{ic} of ceramics is of lower magnitude, one has to control/limit the depth of grinding for defect free grinding. Limiting the depth of grinding produces ductile grinding of ceramics associated with deformation and shearing of ceramics and good surface texture.

During grinding of ceramics, the material can be removed by plastic deformation and shearing or instantaneous rupturing depending on the applied stress. The nature of material removal can be studied by sensing the AE signal emanating from the ceramics. AE signal parameters such as Event Duration (ED) and Ringdown Counts (RDC) were sensed during this study. Typical observations are presented in Fig.3. The steady reduction in the grinding force in the case of diamond grinding of Al_2O_3 has resulted in deformation and shearing of surface material as shown by the raising trend in ED and RDC. The relatively lower magnitude of ED and RDC in the case of CBN grinding is due to higher order grinding force F_N inducing rupturing of surface material. The near ductile regime of grinding due to lower order force exhibited by diamond grinding of ceramics results in production of better surface texture of ground ceramics.

Observation on Surface Finish

Typical observations on surface finish are presented in Fig.4. It is seen that with the grinding speed, there is an improvement in surface finish for both Al_2O_3 and PSZ ceramics. Referring to the figure, It can be seen that marginally rougher texture was observed in the case of CBN grinding. Apart from surface finish, the bearing area characteristic of the ground surfaces were also recorded as presented in Fig.5. Referring to the figure, there is a distinct difference in the bearing area characteristics of ceramics in the as-sprayed condition, especially the saturation tendency in the range of 80-100% t_p in the case of PSZ can be attributed to the occurrence of t-->m transformation of the material on striking the surface

associated with grain-flattening. During grinding, Al_2O_3 exhibits faster bearing area improvements, which can be attributed to the relatively higher hardness. Among the abrasives, CBN grinding results in a texture, exhibiting rapid bearing area development. The deformation of asperities over the ceramic surface due to grain-flattening of CBN abrasive may be the possible cause.

Conclusion

1. While grinding of ceramic coatings, grinding velocity, range of 11.5 to 16 m/s, and depth of grinding of 30 μm were evaluated to be critical.

2. Diamond wheel grinding, compared to that of CBN, gave better surface finish.

3. In case of Al_2O_3, the surface texture with faster bearing area improvement was observed.

4. PSZ ground by diamond showed higher t–>m phase transformation while it was limited in case of CBN grinding because of the relatively "cool" grinding of CBN.

5. AE parameters such as event duration and ring down count indicated good grinding associated with rupture of surface material when ground at 10-15 m/s speed; also indicated the occurrence of abrasive-dullness and consequent changes in the nature of grinding from perfect rupturing to one associated with deformation and shearing (ductile grinding).

Key words : plasma spraying, ceramics, grinding process, phase transformation, acoustic emission, surface finish.

References

1. Namba, Y., Yamada, Y. Tsuboi, A., Unno, K., and Nakao, H., "Structure of Mn-Zn ferrite single crystals ground by an Ultraprecision surface grinding with various diamond wheels", Annals of CIRP,1992, Vol.41, No.1, pp.347-351.

2. Krishnamurthy, R., Arunachalam, L.M., and Gokularathinam, C.V., Grinding of transformation-toughened Y-TZP ceramics", Annals of CIRP, 1991, Vol.40, No.1, pp.331-337.

3. Miller, R.A., Smilake, J.L., and Garlick, R.G., "Science and Technology of ZrO_2-Advances in ceramics", Journal of American Ceramic Society, 1981, pp.241-253.

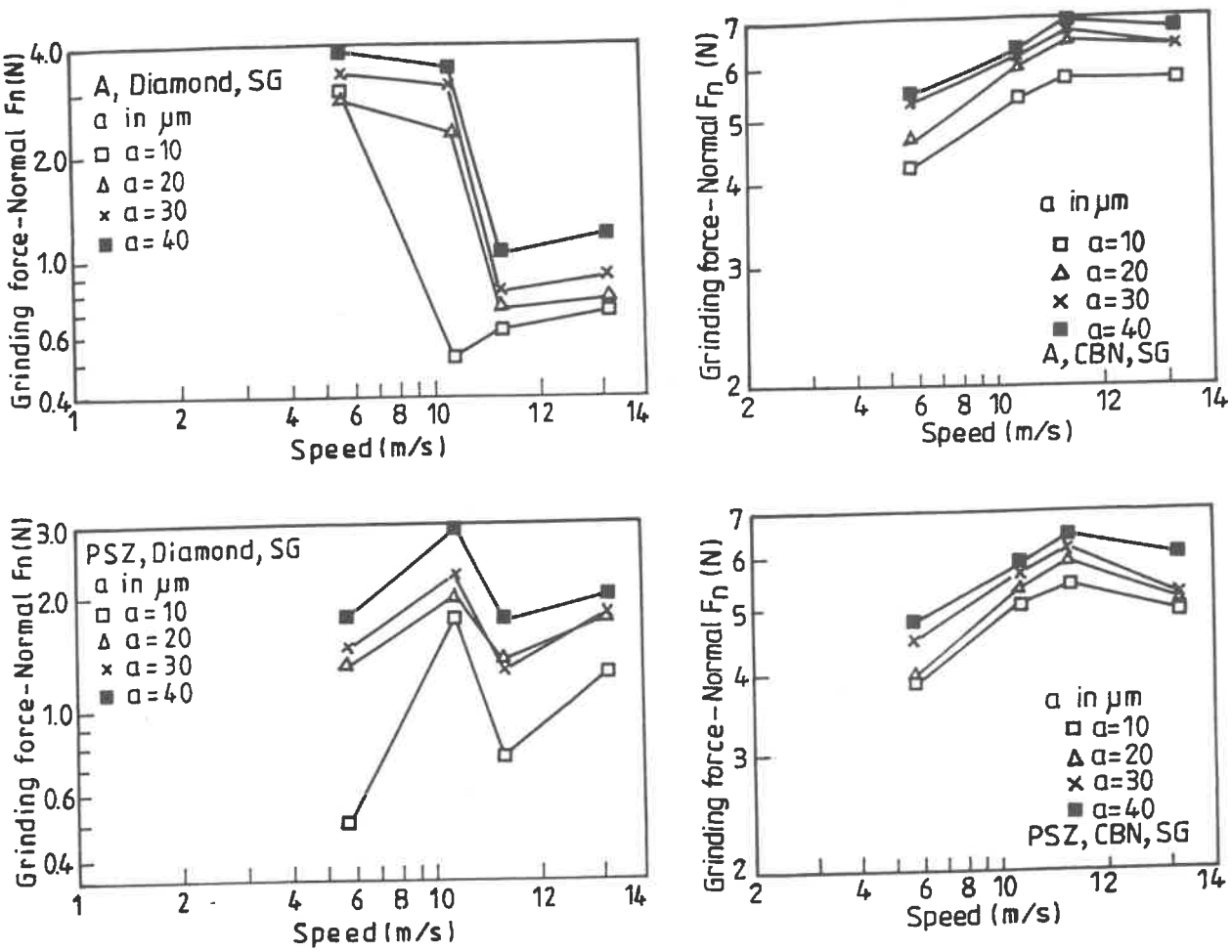

Fig.1

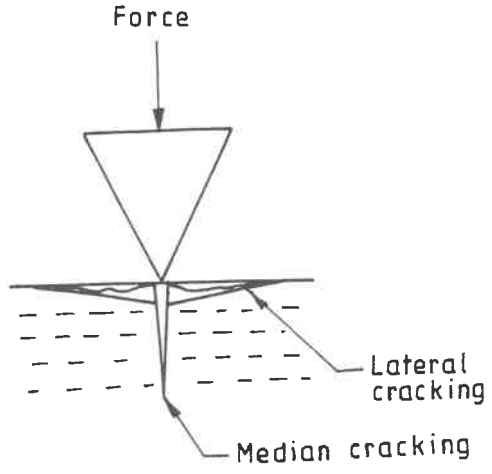

Fig.2

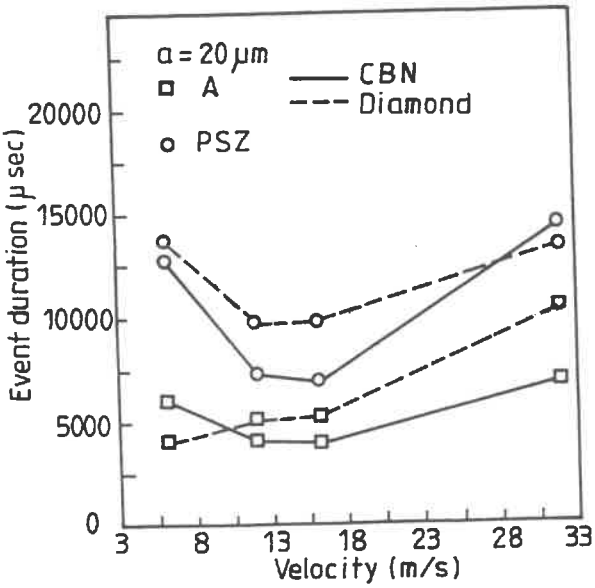

Fig. 3

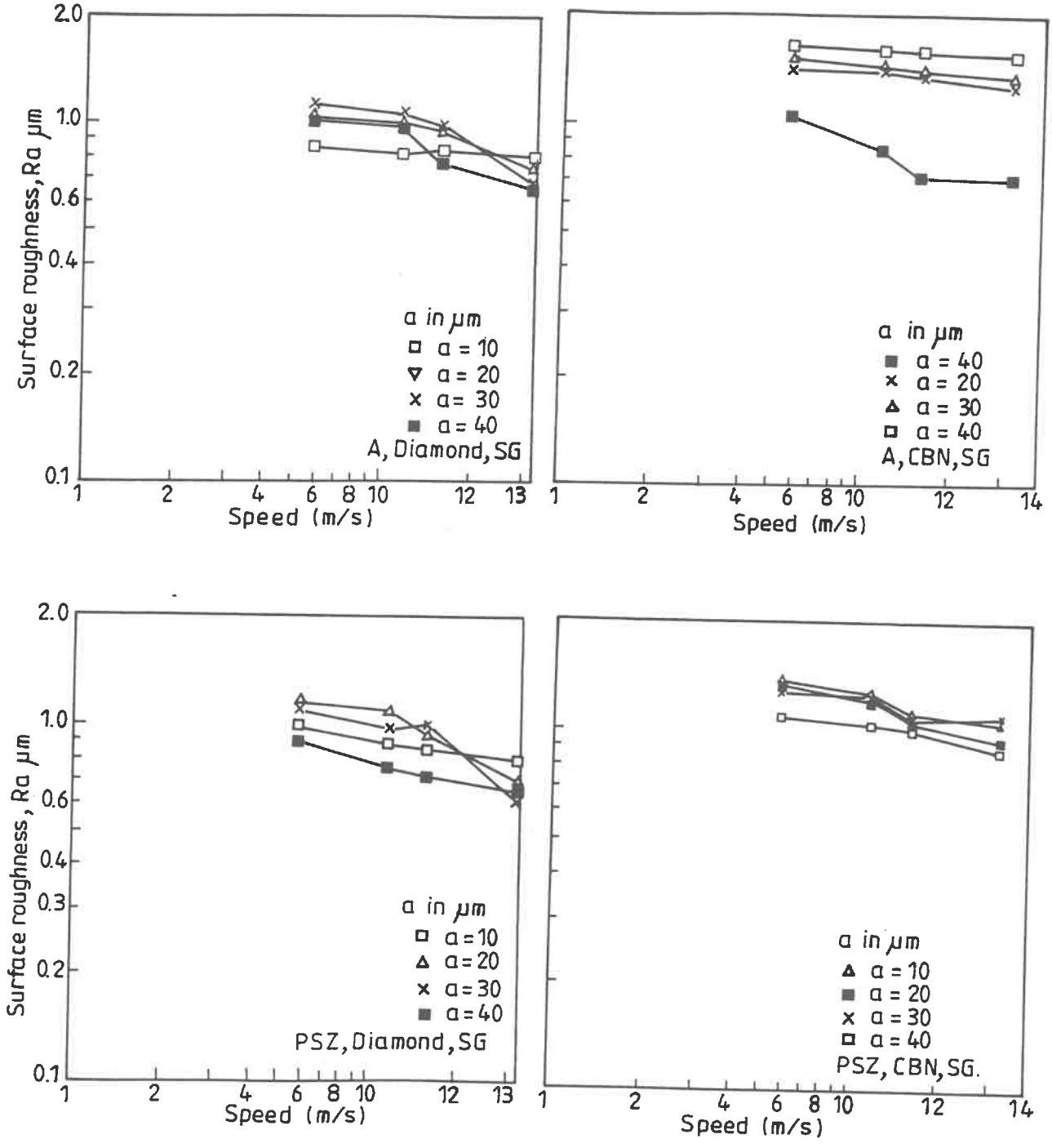
Surface roughness, Ra μm
2.0
1.0
0.6
0.4
0.2
0.1
1
2
4
6
8
10
12
13
14
Speed (m/s)
a in μm
a = 10
a = 20
a = 30
a = 40
A, Diamond, SG
A, CBN, SG
PSZ, Diamond, SG
PSZ, CBN, SG.
0.3

Fig. 4

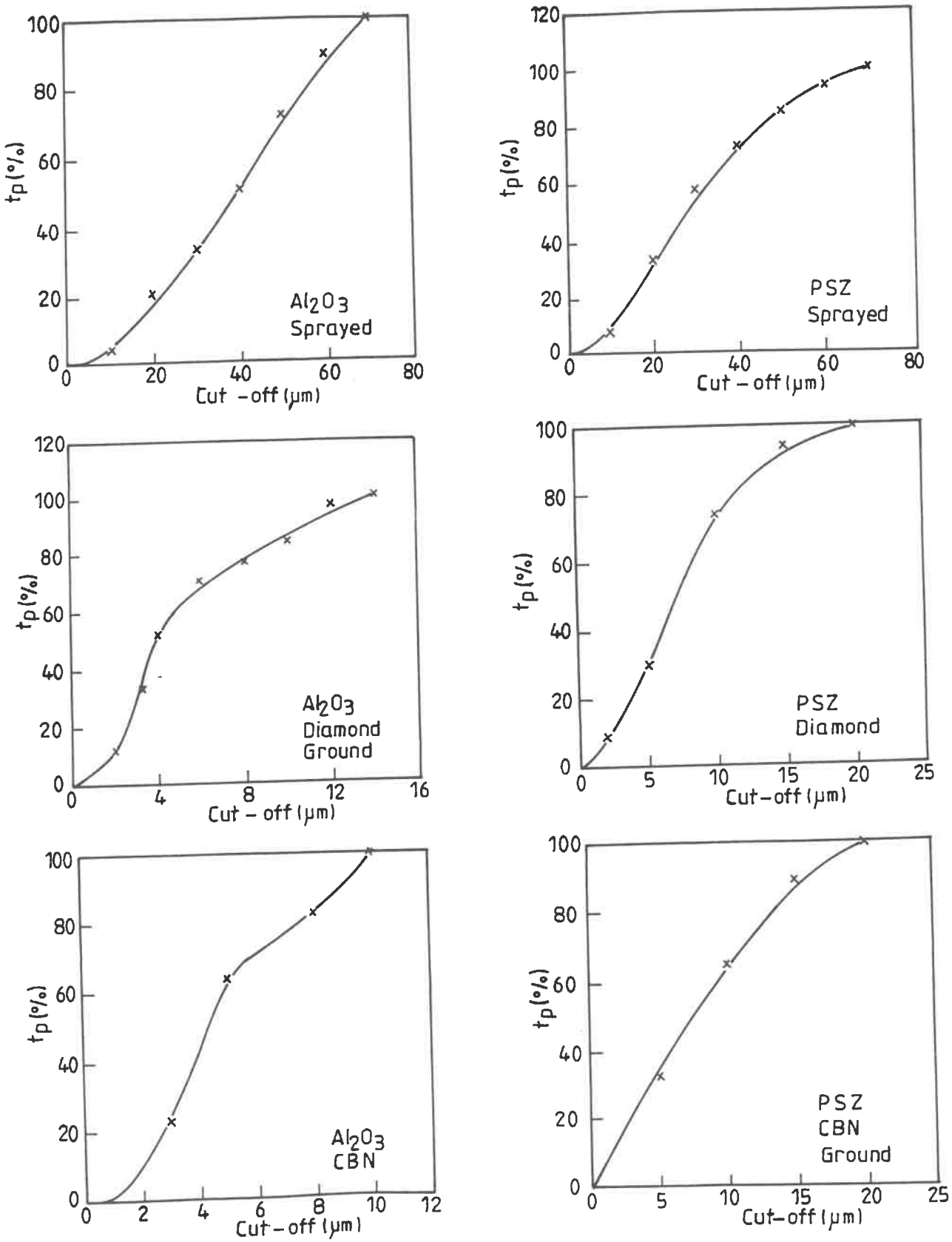
tp(%)
Cut -off (μm)
Al2O3
Sprayed
PSZ
Sprayed
Al2O3
Diamond
Ground
PSZ
Diamond
Al2O3
CBN
PSZ
CBN
Ground

Fig. 5

THE EFFECT OF WORKPIECE MODULATION ON GRINDING FORCE

Weimin Qu, Michele H. Miller
Department of ME-EM
Michigan Technological University
Houghton, MI

1 Introduction

High bandwidth actuators have made possible or improved performance in many precision engineering applications, such as high resolution microscopes and fine position control of structures. Another potential area of application is improvement of the machining process. Ultrasonic (>20,000 Hz) vibrations have been used to inhibit chatter in metal cutting [1] in addition to reducing fracture in the single point cutting [2] and grinding [3] of brittle materials. Surface roughness has been improved by modulating the workpiece transverse to the cutting direction at 1000 Hz [4]. The reasons for improvement are not well understood in all cases but are postulated to involve geometry effects, friction effects, and material behavior effects. Simulation has shown that geometric effects can adequately explain the improvement in surface roughness [4] but not the reduction of fracture [5] or inhibition of chatter. The present paper focuses on the effect of high frequency modulation on grinding force.

2 Theoretical Concept

One of the effects of high frequency relative motion between two materials is to reduce the effective friction force [6,7]. In machining, frictional forces arise due to relative motion between the chip and tool rake face and between the machined surface and tool flank face. A reduction in these frictional forces reduces the force components in the cutting and thrust directions. A lower cutting force is beneficial in that it reduces the power required while a lower thrust force reduces the possibility of chatter or fracture.

Moriwaki [2] achieved a seven times increase in critical depth of cut for single point machining of glass; however, the cutting speed was quite low--1.5 m/min. With the much higher cutting speed of grinding and the short time of each abrasive/work interaction, it is uncertain whether high frequency vibration would have any effect on abrasive/work friction and, consequently, performance.

3 Description of Experiments

Experiments were conducted to assess the effect of modulation on grinding forces. Figure 1 shows a schematic illustration of a surface grinder with a modulating workpiece holder attached to its feed table. The workpiece holder is driven in the crossfeed (or X) direction by a magnetostrictive actuator whose nominal maximum vibration frequency is 5000 Hz. A three axis dynamometer provides force measurement.

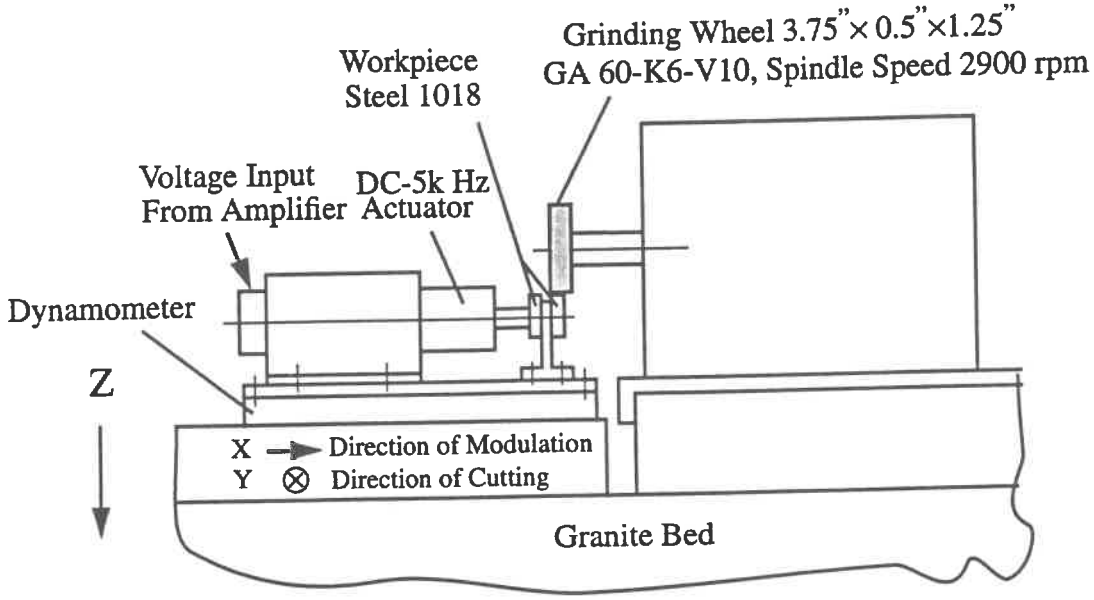

Figure 1: Schematic illustration of surface grinder equipped with actuator and force dynamometer

Cutting tests were performed at four modulation frequencies and with no modulation. The input amplitude of the sinusoidal voltage signal into the actuator amplifier was held constant at 125 mV for all frequencies. The output displacement amplitude was between 4 and 4.5 μm for three of the four frequencies and 9.5 μm for the resonant frequency (4000 Hz). Table 1 summarizes the output displacements. Significant coupling to the Y and Z directions occurs which may impact the force results. Experimental parameters common to all tests are listed in Table 2.

Frequency (Hz)	Input Signal Voltage (mV)	Output Displacement (μm)		
		X	Y	Z
1000	125	4	0	0
2500	125	4.5	0	2.1
3000	125	4.25	0	2.5
4000	125	9.5	2.12	3.6
4600	125	4.25	0	1.4

Table 1: Measurement of workpiece vibration

Figures 2(a) and (b) show examples of force measurements for the thrust direction (Z) without and with 1 kHz modulation. With modulation the thrust force decreases by 4.8% while the force in the cutting direction (not shown) decreases by 6.8%. The plotted forces have been averaged to remove the high frequency components. The raw force signal for the test with modulation included the inertial forces of the actuator system moving on top of the dynamometer. The inertial force occurs at the modulation frequency; its mean value is zero (which can be seen when not grinding). The inertial force is not apparent in Figures 2(a) and (b) due to the averaging.

Spindle Speed	2900 rpm
Cutting Speed	14.5 m/s
Feed Rate	19 mm/s
Depth of Cut	0.025 mm
Workpiece	1018 Low Carbon Steel

Table 2: Operating conditions for grinding experiments

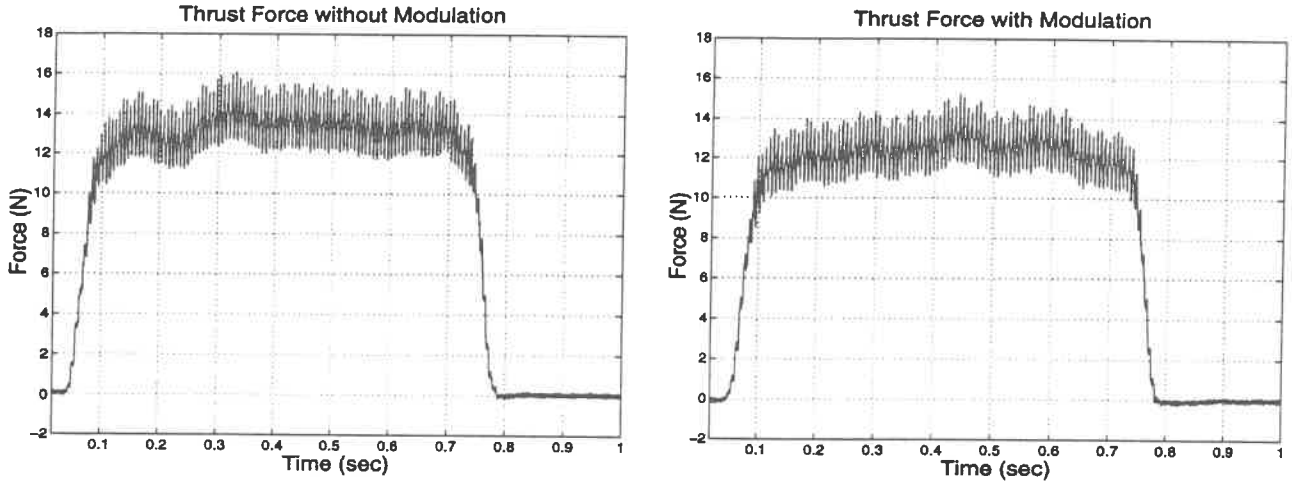

Figure 2: Grinding thrust force signals (a) without modulation and (b) with 1 kHz modulation. Data has been averaged to remove inertial force component.

Tests at higher frequencies exhibit a higher reduction in force as shown in Figures 3(a) and (b). Each data point in these figures represents the average of two tests. The highest reduction in force occurs at the resonant frequency. For this case, however, the vibration amplitude was significantly higher than for the other frequencies. Therefore, in addition to frequency, amplitude may have an important effect on the results and needs to be studied further.

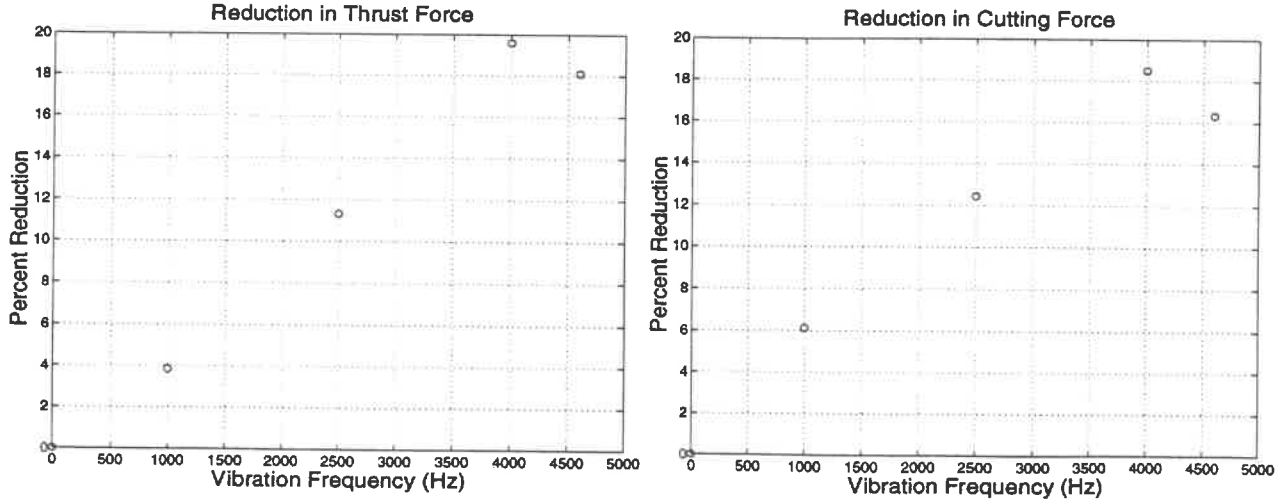

Figure 3: Reduction in (a) thrust and (b) cutting forces as a function of modulation frequency

4 Summary and Conclusions

Experimental studies of the modulation grinding of 1018 low carbon steel have demonstrated the following:

(1) High frequency modulation transverse to the cutting direction reduces the cutting and thrust forces in surface grinding.
(2) At the resonant frequency, the effect of modulation on forces is the biggest. The cutting force changes by 16.6% and the thrust force by 18.1%.
(3) An increase of the amplitude and frequency of modulation is beneficial to the reduction of the cutting and thrust force. Tests at even higher frequencies are required to find optimum values for amplitude and frequency.

Similar tests will be performed on brittle workpiece materials to determine if they also can be ground with less force and if the reduction in force reduces surface fracture.

References

[1] Shey, J. A., *Tribology in Metalworking: Friction, Lubrication, and Wear*, Amer. Soc. for Metals, Metal Park, OH, 1983.

[2] Moriwaki, T., Shamoto, E. and Inoue, K., "Ultraprecision Ductile Cutting of Glass by Applying Ultrasonic Vibration," *Annals of the CIRP*, Vol. 41, No. 1, pp. 141-144, 1992.

[3] Khanna, N., Pei, Z. J. and Ferreira, P. M., "An Experimental Investigation of Rotary Ultrasonic Grinding of Ceramic Disks," *Technical Papers of the North American Manufacturing Research Institution of SME*, pp. 67-72, 1995.

[4] Wang, Y., Moon, K. S. and Miller, M. H., "Micro-Actuation in Precision Grinding," *Proceedings of the 1996 ASME IMECE.*

[5] Miller, M. H. and Moon, K. S., "The Effect of Workpiece Modulation on Grinding Kinematics," *Proceedings of the ASPE Spring Topical Meeting on Precision Grinding of Brittle Materials*, pp. 70-75, 1996.

[6] Mohri, N., and Saito, N., "Some Effects of Ultrasonic Vibration on the Inserting Operation," *Int J Adv Manuf Technol*, Vol 9, pp. 225-230, 1994.

[7] Moriwaki, T. and Shamoto, E., "Ultrasonic Elliptical Vibration Cutting," *Annals of the CIRP*, Vol. 44, No. 1, pp. 31-34, 1995.

Acknowledgments

The authors wish to acknowledge the financial support provided by NSF Grant No. DMI9521494 and by the SME Education Foundation. The authors also thank the NSF/DARPA MT-AMRI for use of the magnetostrictive actuator.

DEVELOPMENT OF GRINDING MODELS FOR BRITTLE MATERIALS

Keith Sharp, Ronald O. Scattergood
Precision Engineering Center
North Carolina State University
Raleigh, NC

INTRODUCTION

The fracture mechanics used to predict subsurface damage during machining requires knowledge of the depth of cut of the tool. For brittle materials, analysis shows that there will be ductile response for cutting depths below a critical value and brittle response for depths above this value. Finding the depth of cut is relatively straightforward for single-point machining such as diamond turning, but much more difficult for the large number of randomly arranged grains involved in grinding. The aim of this research is to develop models for the statistical effects of multiple cutting grains. The key issue for the models is to derive the grain depth-of-cut for a distribution of cutting grains and specified operating conditions. In order to simplify the development work, plunge grinding (no cross feed) is being used for the prototype geometry.

Two different approaches have been taken to predict the grain depth-of-cut for given grinding parameters (grain size, shape, distribution, wheel radius, runout error, etc.). The first is an analytic model for steady-state grinding. The analytic model is based on the key assumption that there is no correlation between the surface profile generated and the profile of the active cutting grains on the grinding wheel. The workpiece surface position relative to the grinding wheel is then given only by its mean value and the surface profile itself is ignored. In the second approach, a computer simulation is used to generate the actual surface profile for steady-state grinding. The simulation takes correlation effects between the surface generated and the profile of the active cutting grains into account. The advantage of the analytic approach is its simplicity, the ease of application to a wide range of initial assumptions and the ability to provide closed form solutions. The computer simulation can predict representative surface features and can produce solutions for conditions which have surface correlation effects.

By combining this effort with previous work on chip geometry [1, 2] and microcutting tests for single cutting grains [3], a process model can be developed for grinding brittle materials. The intent is to either define the limits for eliminating subsurface damage (ductile-regime grinding) or to provide a rational basis with which to optimize the grinding parameters for control of subsurface damage in given grinding operations. The work summarized here represents results from the initial development of the analytic and computer simulation models.

ANALYTIC MODEL

A random distribution of spherical grains with radius R is assumed and the grinding wheel is assumed to be perfectly true (no runout error). The model is easily extended to arbitrary grain shapes and distributions as well as to runout error effects. The action of "average" cutting grains is shown in Fig. 1. The z axis projects downward from the wheel binder into the workpiece surface as shown. Since the actual surface profile is ignored, the position of the workpiece surface is given by its mean position $z_{surface}$. A_g is the projected area of the cut in the cutting direction and D_g is the mean diameter of the grain as measured in the workpiece surface. The maximum grain depth-of-cut relative to the workpiece surface is given by $d_m = z_m - z_{surface}$.

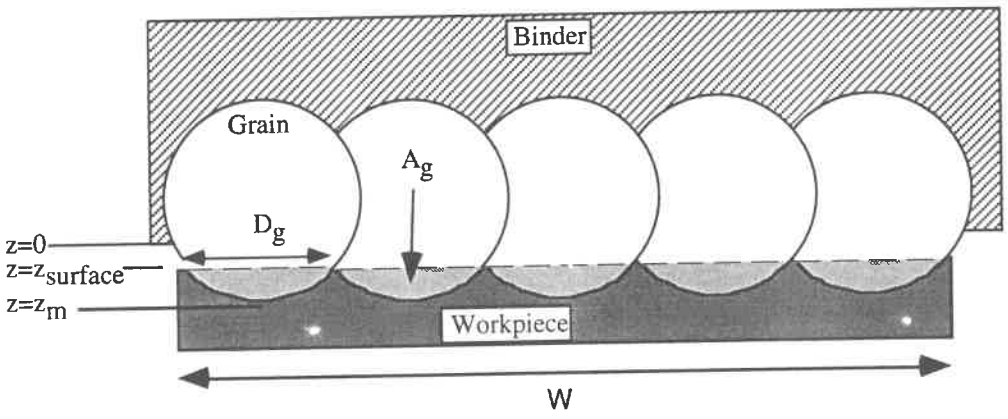

Figure 1 Schematic of plunge grinding.

The entire width W of the surface can be removed several times during a wheel revolution. The length of the grinding wheel that contains sufficient grains to remove one width W of the surface is called the characteristic length L and is a function of the surface position. The minimum number of cutting grains required to span one width of the surface, N_c , is given by W/D_g. The minimum length for L would contain only N_c grains. However a random distribution of grains is unlikely to be arranged so that the grains exactly span the width with no overlap, so a number of grains larger than N_c will be required to remove the width and L will be larger than the minimum value. The actual number of grains contained in a characteristic length, N_{tot} , is related to the number density ρ_{eff} of the cutting grains at $z = z_{surface}$. The total length of contact L_o of the grinding wheel is a function of the wheel circumference and the runout error. Assuming no runout error, L_o is just the circumference of the wheel ("continuous" grinding).

Under steady-state conditions for plunge grinding, the cross sectional area removed per wheel revolution by the cutting grains must be fW where f is the infeed per rev and W is the width of the cut. The cross section removed must then be equal to the number of times the surface width is removed, L_o/L, multiplied by the grain cutting area N_cA_g. In essence, the model treats continuous infeed of the grinding wheel as a succession of incremental motions where the duration for each increment is the characteristic length L. The relevant equations are

$$N_c = W/D_g$$

$$fW = \frac{L_0}{L} N_c A_g$$

$$N_{tot} = L W \rho_{eff}$$

$$f = L_0 \rho_{eff} A_g \frac{N_c}{N_{tot}}$$

In order to derive the relationship between d_m and f, i.e., the grain depth-of-cut relation, explicit expressions are needed for A_g and D_g in terms of d_m. Let $g(z)$ be the grain distribution function defined such that $g(z)dz$ is the total number of grains between z and $z+dz$. $A(z,z_{Surface})$ and $D(z,z_{surface})$ are geometrical functions giving the projected cutting area and grain diameter in the workpiece surface at given z, respectively. The relations for A_g and D_g then follow as

$$A_g = \frac{\int_{z_{surface}}^{z_m} A(z, z_{surface}) g(z) dz}{\int_{z_{surface}}^{z_m} g(z) dz} \qquad D_g = \frac{\int_{z_{surface}}^{z_m} D(z, z_{surface}) g(z) dz}{\int_{z_{surface}}^{z_m} g(z) dz}$$

These can be solved to obtain the desired relation between f and d_m. The solution gives the mean workpiece surface position $z = z_{surface}$, but not the actual form of the surface profile. The detailed expressions are rather lengthy and will not be reproduced here.

There is a limit for the domain in which the analytic model is valid. Physical requirements demand that a sufficient number of cutting grains exist to "span" the width W of the cross section, otherwise uncut gaps will be left in the surface. If the contact length L_o is less than the characteristic length L, there are too few grains to remove a surface width and the model is no longer valid. The lower limit for the validity of the analytic model is established when the contact length $L = L_o$ and L contains exactly $N_c = W/D_g$ active cutting grains. One expects that there will be some overlap of the cutting grains, hence $N_{tot} > N_c$ and the characteristic length L is greater than the minimum value. Defining a characteristic length that takes the overlap of random grains into account is a complex statistical function, the analysis of which is currently underway. All of the results presented were obtained for the lower limit of the analytic model, where L contains exactly N_c grains.

COMPUTER SIMULATION MODEL

The computer simulation model was developed by Miller [1]. This model has been adapted and modified for the work reported here. Basically, the simulation method unwraps the grinding wheel and treats the operation like an inclined cutting plane, the slope of which is determined by the infeed. A random distribution of spherical grains with radius R is again assumed. An initial reference surface profile is established by making one revolution of the grinding wheel (at the given infeed) with the workpiece surface initially set at the binder surface. One additional wheel revolution then determines the steady-state grain depth-of-cut d_m, as well as parameters such as A_g and D_g. In order to obtain proper statistical averaging, a number of identical runs must be made using different random seeds for the generation of the grain distributions.

Fig. 2 shows results obtained from the computer simulation and the analytic model for the same set of input parameters. As was noted by Miller [1], the computer simulation results show two regimes. At lower infeeds, the relation is $d_m = f$, which is the simulation data with the higher slope in Fig. 2. Above a transition infeed, the fitted relation becomes $d_m = constant\ f^{0.4}$ which is the simulation data with the lower slope. There is a transition between these two regimes, the transition infeed being identified by the intersection of linear fits to the data points for the two regimes in the log plot. The limit line shown for the analytic model marks the limit of the validity of the model, which is the case where exactly one characteristic length L has cut the surface during one revolution of the grinding wheel ($L = L_o$). The analytic model is physically meaningful only for infeeds that lie to the right of this limit line. As noted earlier, the solution for the analytic model is equivalent to the section width W being removed L_o/L times, i.e., the continuous infeed is treated as a sequence of incremental infeeds. The analytical model gives a closed-form solution for the d_m vs. f relation. The solution is rather cumbersome for spherical grains, but it can be closely approximated by the relationship $d_m = constant\ f^{0.4}$, which is the same form that is obtained from a fit to the computer simulation results. The analytic model solution also includes all of the grinding parameters (grain size, concentration, etc.) in the proportionality constant.

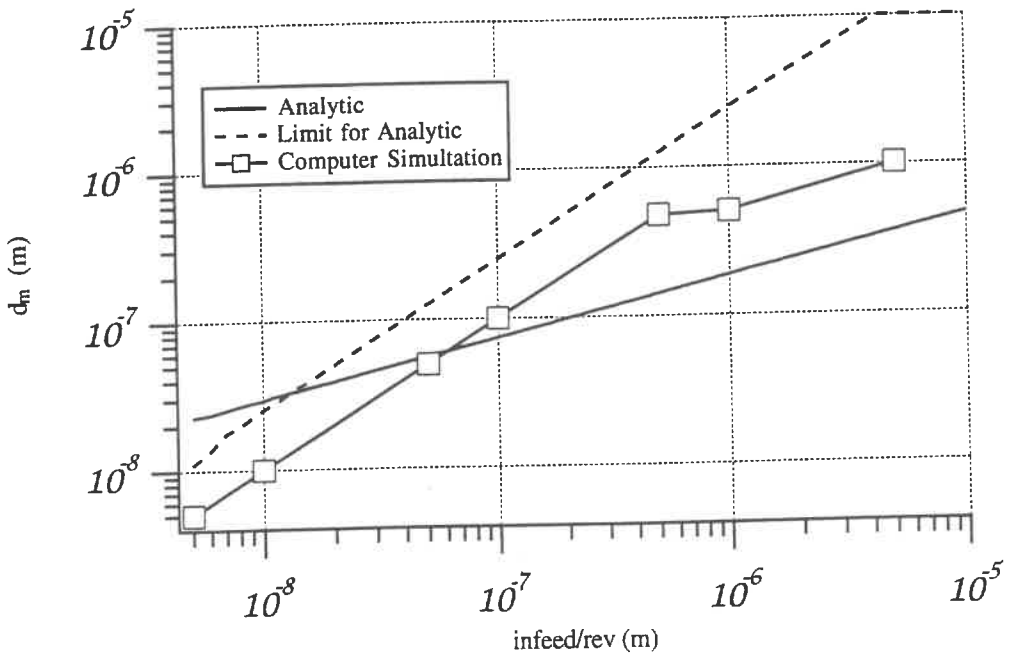

Figure 2 Model results for the maximum grain depth-of-cut vs infeed.

At lower infeeds, the simulation results give $d_m = f$. This is a result of the correlation between the surface profile and the active cutting grains on the grinding wheel. If the surface profile maintains a one-to-one correspondence with the cutting grains there is no grain intertaction such that following grains cut into grooves formed by lead grains. Hence, each grain cuts a depth equal to the infeed and $d_m = f$. At higher infeeds, the relationship changes and $d_m < f$ due to the action of multiple cutting grains and grain interactions. The analytic model and the computer simulation results can be described by similar power-law relations for the higher infeed regime, although there is a relative shift upward (Fig. 2) for the simulation results due to the larger proportionality constant in the power law relation. Apart from this scaling factor, it appears that the surface correlation effects can be ignored at higher infeeds where grain interaction occurs.

The actual profiles cut into the workpiece surface can be tracked from the computer simulation outputs. For the low infeed case, there is almost a perfect correlation between individual cutting grains and the peaks and valleys in the surface profile. This implies the relation $d_m = f$ as noted above. In contrast, at higher infeeds there is a large amount of grain interaction and the surface profiles generated at various stages during one revolution of the grinding wheel have markedly different peak-to-valley features. There is no longer a one-to-one correspondence between individual cutting grains and grinding grooves; the spatial region bounding each groove in the final peak-to-valley profile has been previously cut by many grains and only the last grain leaves a signature of the groove.

While the analytic model does not apply to the lower infeed regime where surface correlation effects dictate the grain depth of cut relation $d_m = f$, it is noteworthy that the limit line for the analytic model falls rather close to the $d_m = f$ line for the simulation results (Fig 2). The limit line for the analytic model is based on the condition that the characteristic length L is just equal to the contact length L_o. Since by definition the characteristic length is the minimum length for

which the active grinding grains can remove a cross section width W in one revolution of the wheel, it seems reasonable that this limit should also be related to the onset of surface correlation effects. That is, below this limit the surface profile must maintain a strong correlation with the active grinding grains in order for the cross section to be removed. It also follows that in the low infeed regime, where $L < L_o$, if one starts with a perfectly flat surface there will be a transient period such that many revolutions of the wheel (infeeds) are required before the steady-state surface profile is generated. This is confirmed in the computer simulation results where it was observed that the peak-to-valley roughness can be much larger than the infeed.

The results presented here using the analytical model were obtained by setting the characteristic length L to its minimum value. The minimum L corresponds to the length needed for exactly $N_c = W/D_g$ cutting grains, the minimum number needed to span the width W in Fig. 1. For a random distribution of grains, the value of L must be larger than the minimum because there will be overlap of the grains. The statistical problem is equivalent to determining the average number of randomly tossed pennies of diameter D_g needed to just "cover" a line of length W. Preliminary estimates show that this number is approximately 4-6 times the minimum number. If this estimate is incorporated into the analytic model, the line for the analytic results in Fig. 2 shifts upward such that the analytic model and computer simulation results for the higher infeed regime are in good agreement. Furthermore, the limit line for the analytic model shifts to the right so that it gives a better estimate of the onset of surface correlation effects.

CONCLUSIONS

Preliminary results have been presented for modeling the grain depth-of-cut in plunge grinding. The key relationship derived is the maximum grain depth-of-cut d_m vs. the infeed per rev f. At low infeeds, there is a one-to-one correspondence between cutting grains and grinding grooves in the surface and the relationship $d_m = f$ is obtained using a computer simulation model that accounts for correlation between the surface profile and the profile of the active cutting grains on the wheel. At higher infeeds, $d_m < f$ because of the increased number of cutting grains and interactions between grains. These interactions reduce the correlation effects and change the form of the d_m vs. f relationship. A power-law relation $d_m = constant\ f^{0.4}$ is obtained for the higher infeed regime. The same form of power-law relation is also obtained using an analytic model which does not account for correlations between the surface profile and the active cutting grains on the grinding wheel. The analytic and simulation models differ only by a scaling factor. A lower bound limit for the applicability of analytic model gives a good estimate of the point at which surface correlation effects become significant. Current work is in progress to further refine and extend the models, and to develop experimental techniques to verify the theoretical predictions.

REFERENCES

[1] Miller, M.H., "A Model for the Grinding of Brittle Materials", *PhD Dissertation,* N.C. State University, 1994, pp. 134-142.

[2] Storz, G.E., "Theoretical Modeling of Precision Contour Grinding Operations", *MS Thesis*, N.C. State University, 1994.

[3] Tanikella, B.V. and Scattergood, R.O., "Fracture Damage in Borosilicate Glass During Microcutting Tests", *Scripta Materialia*, Vol. 34, No. 2, pp. 207-213, 1996.

High-Efficiency Mirror Finishing Characteristics of Ceramics with Extremely Fine Grit Diamond Wheels

Xu-Jin Wang*, Katsuo Syoji** and Tsunemoto Kuriyagawa**

* *SpeedFam Co., Ltd., No. 2647 Hayakawa, Ayase-city, Kanagawa-pref., 252, Japan*

** *Tohoku University, Aramaki-Aoba, Aoba-ku, Sendai, 980-77, Japan*

1. INTRODUCTION

In order to solve the problems of the loose abrasive method. such as low finishing efficiency. etc., a new vertical type ultra-precision plane honing machine using an extremely fine grit diamond wheel was developed by the authors for mirror finishing of hard and brittle materials including ceramics as a bonded abrasive method. Using this machine, the high-efficiency mirror finishing of ceramics was carried out successfully[1)2)].

In this paper, the theoretical model and formulas of plane honing are presented along with the results of a few experiments for examining the high-efficiency mirror finishing characteristics of ceramics using extremely fine grit diamond wheels.

2. EXPERIMENTAL METHODS

Fig. 1 shows the main structure of the ultra-precision plane honing machine used in the experiments. In order to remove the effect of vibration, an air bearing was employed on the diamond wheel's spindle, and a hydrostatic bearing was also used on the workpieces' spindle in the machine. Moreover, for high-efficiency mirror finishing, the diamond

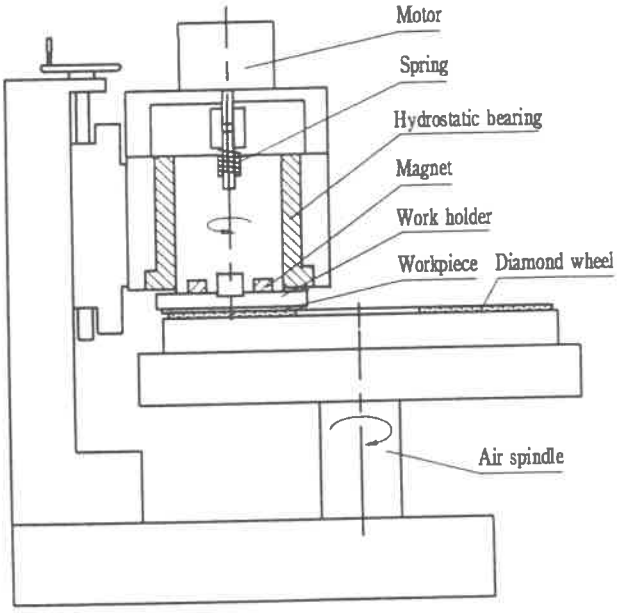

Fig. 1 Ultra-precision plane honing machine

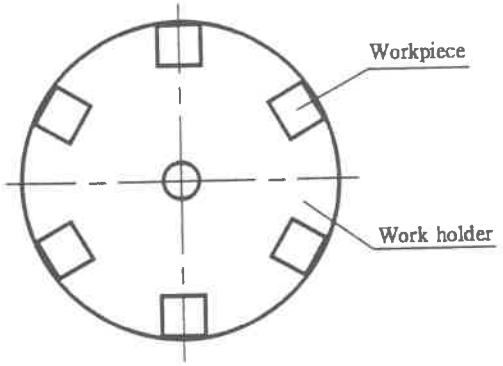

Fig. 2 Workpieces and work holder

wheel's spindle is a high-speed spindle which can be run up to 3000 rpm.

Fig. 2 shows the workpieces and holder. Prior to mirror finishing which uses extremely fine grit diamond wheels, the workpieces were lapped with diamond slurry. The workpieces were attached to the holder with glue in a concentric. The work holder was installed to the workpieces' spindle by magnets. The load was pushed down on the workpieces by a spring in the mirror finishing process.

To prevent the generation of hydro-planing force by the coolant, the plane type diamond wheels with a spiral groove was used in the process. Fig. 3 shows the diamond wheel. The truing and dressing of diamond wheels was performed by a cup type GC grinding wheel which was installed on the work holder.

3. EXPERIMENTAL CONDITIONS

In the experiments, a #1500 resinoid-bonded extremely fine grit diamond wheel and a #1500 metal-bonded extremely fine grit diamond wheel were used. Truing and dressing of these diamond wheels was carried out with a cup type #1500 GC grinding wheel.

The materials of the ceramic workpieces are zirconia (ZrO_2) and silicon nitride (Si_3N_4). The workpieces' roughness by lapping was R_{max} 1.5～1.7 μ m prior to mirror finishing.

The experimental conditions are described in Table 1.

Table 1 Experimental conditions

Grinding wheels	
Diamond wheels (ϕ 205mm)	① SD1500B100 ② SD1500M100
Truing wheel (ϕ 90mm)	GC1500H
Workpieces	
Materials	① Zirconia (ZrO_2) ② Silicon nitride (Si_3N_4)
Size	15mm × 15mm
Numbers of batch finishing	6 pieces (Work holder: ϕ 100mm)
Pre-machining method	Lapping (Rmax 1.5～1.7 μ m)
Finishing conditions	
Load	30 N
Workpiece speed	100 rpm
Diamond wheel speed	1000 rpm
Finishing time	5 min
Coolant	Water (15ml/min)
Truing and dressing conditions	
Load	30 N
GC wheel speed	300 rpm
Diamond wheel speed	300 rpm
Truing time	1 min

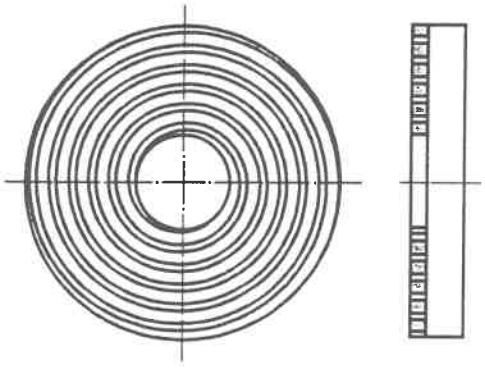

Fig. 3 Diamond wheel with spiral groove

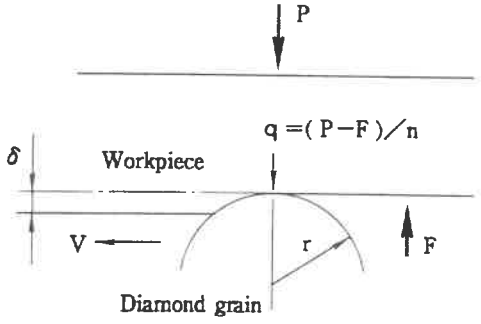

Fig. 4 Single point cutting model

4. THEORETICAL MODEL AND FORMULAS OF PLANE HONING

The single point cutting model of plane honing is shown in Fig. 4. The grain on the extremely fine grit diamond wheel is supposed as a ball

with radius r in the model. The symbols in fig. 4 are represented as following:

P: Finishing load

F: Hydro-planing force by coolant

n: Numbers of effective cutting grain in contact finishing area between workpieces and diamond wheel

q: Cutting force of single grain

v: Cutting speed

δ: Cutting depth of single grain

The cutting depth of single grain δ in Fig. 4 can be calculated using Equation (1). H_v is the micro-hardness in finishing surface of the workpiece in Equation (1).

$$\delta = \frac{0.3(P - F)}{nrH_v} \qquad (1)$$

The finishing rate h_w (the workpiece's removal depth per finishing time) can be calculated using Equation (2). A is the area of workpiece's finishing surface in Equation (2).

$$h_w = \frac{0.3V}{rA}\left(\frac{P - F}{H_v}\right)^{\frac{3}{2}} n^{-\frac{1}{2}} \qquad (2)$$

5. EXPERIMENTAL RESULTS AND DISCUSSION

Fig. 5 shows the changes in the stock removal depth and surface roughness R_{max} according to the length of finishing time. during the finishing of zirconia (ZrO_2) using both a resinoid-bonded diamond wheel (SD1500B100) and a metal-bonded diamond wheel (SD1500M100).

Fig. 6 shows the changes in the stock removal depth and surface roughness R_{max} according to the length of finishing time during the finishing of silicon nitride (Si_3N_4) using both a resinoid-bonded diamond wheel (SD1500B100) and a metal-bonded diamond wheel (SD1500M100).

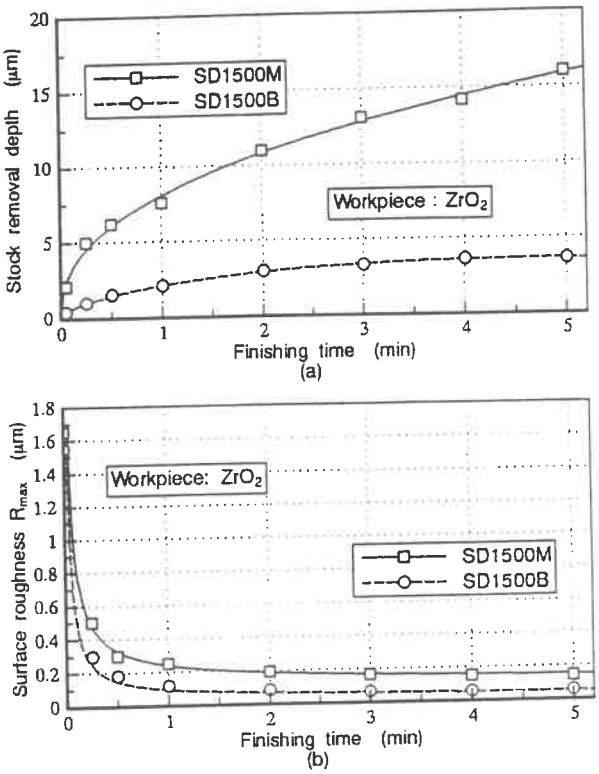

Fig. 5 Effects of diamond wheel's bonds (Workpiece: ZrO_2)

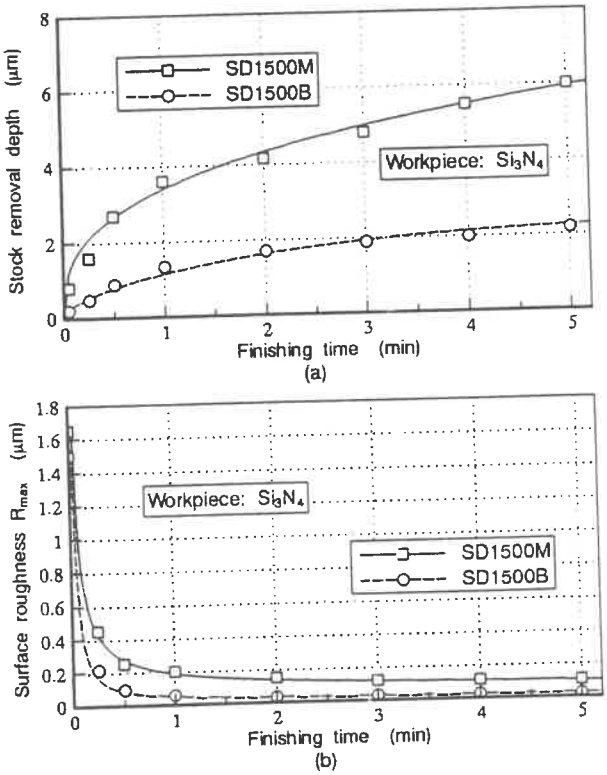

Fig. 6 Effects of diamond wheel's bonds (Workpiece: Si_3N_4)

We can understand that the finishing surface roughness using a resinoid-bonded diamond wheel is less than using a metal-bonded diamond wheel under the same mesh size and the same finishing conditions as stated in Fig. 5 and Fig. 6. The result is clear from Equation (1). Since the strength of the resinoid bond is less than that of the metal-bond, the numbers of effective cutting grain (n) on a resinoid-bonded diamond wheel is larger. As a result, the cutting depth of grains (δ) is less, so the surface roughness is less during the use of the resinoid-bonded diamond wheel.

However, Fig. 5 and Fig. 6 show that the finishing rate using a resinoid-bonded diamond wheel is less than that of using a metal-bonded diamond wheel . Using Equation (2) we can analyze the reasons. Since the strength of the resinoid-bond is less, the gap between the diamond wheel and the workpiece during the use of the resinoid-bond diamond wheel is less in the finishing process than during the use of the metal-bonded diamond wheel, so the hydro-planing force by coolant (F) is larger. Moreover, the numbers of effective cutting grain (n) on the resinoid-bonded diamond wheel is larger than that of the metal-bonded diamond wheel. For these reasons, the finishing rate (h_w) is less during the use of the resinoid-bonded diamond wheel.

Fig. 7 shows the comparative experiment's results of the final surface roughness R_{max} and average finishing rate during the finishing of zirconia (ZrO_2) and silicon nitride (Si_3N_4).

As shown by Equation (1) and Equation (2), the larger the hardness of the workpiece (H_v), the less the cutting depth of the grains (δ), and the less finishing rate (h_w). The results of the experiments shown in Fig. 7 agree with Equation

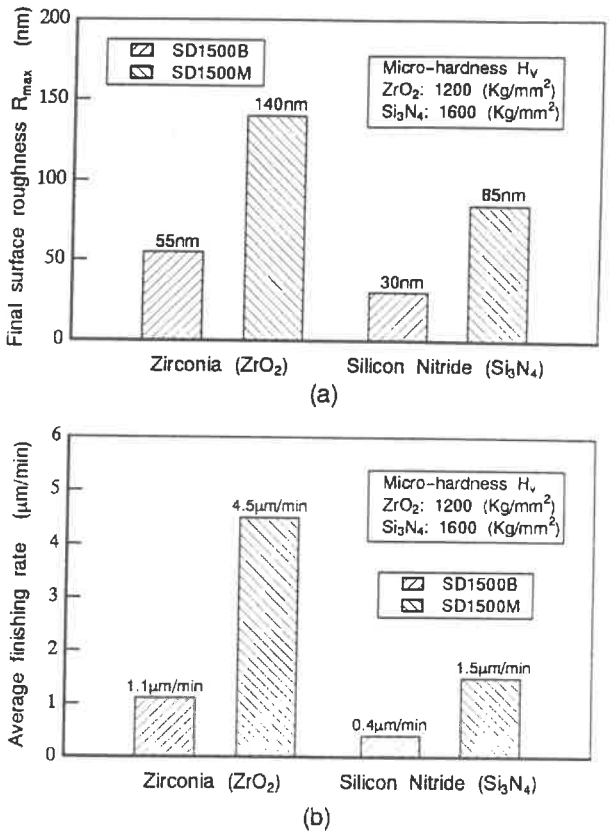

Fig. 7 Effects of workpiece's materials

(1) and Equation (2). Namely, the final surface roughness R_{max} and average finishing rate during finishing silicon nitride (Si_3N_4) are less than during finishing zirconia (ZrO_2) .

REFERENCES

1) X. J. Wang, K. Syoji and T. Kuriyagawa: "High-Efficiency Mirror Finishing of Ceramics with Diamond Wheels", Proceedings of ASPE 10th Annual Meeting (1995.10.).

2) X. J. Wang, K. Syoji and T. Kuriyagawa: "High-Efficiency Mirror Finishing of Ceramics with Plane Honing" , Proceedings of International Conference on Precision Engineering '95 (2nd ICMT) (1995.11.).

SHEAR-MODE GRINDING FORCE CRITERIA IN GRINDING SILICON WAFERS WITH CUP WHEELS

Y. Yoshida *, Pang Nan **, K. Imai***, S. Sekita°, I. Iida°,
N. Tsuda°°, H. Hashimoto***
*Tokyo Diamond Tool(2-3-5 Nakane Meguro-ku Tokyo Japan), ** North eastern Univ.,
*** Kanagawa Institute of Technology(1030 Shimo-ogino, Atsugi-shi 243-02 Japan),
°Okamoto-Shibayama Kikai, °°Tokai Univ.

1. Introduction

In recent years semiconductors have become more powerful and lower-priced, caused by an increase in the diameter of silicon wafers, with a tendency to grow from 12～16 inches in the near future. On the other hand, this has created a very serious problem in the manufacture of silicon wafers. In view of this fact, there are some trials to apply shear-mode (or ductile-mode) grinding for manufacturing of silicon wafers instead of lapping.

Previous papers [1) 2)] reported shear-mode grinding of various brittle materials using #3000 metal bond straight diamond wheels. In those experiments, it was shown that: (1) After a number of passes, the normal grinding force reached an approximate steady state; (2) during grinding, the wheel surface roughness and cutting performance were invariant; wheel truing and dressing were not carried out. From these experimental results, shear-mode grinding force criteria were defined as the steady, invariant grinding force which is a repeatable deterministic function of shear-mode grinding conditions including materials and grinding wheels. The criteria can usefully be applied to design high precision shear-mode grinding machines by determining their compliance.

We already tried to grind silicon wafers with #3000 metal bond diamond cup wheels. An approximate steady grinding force was found in grinding with serrated wheels with 1.0mm width. Normal grinding force over 25mm square test pieces was 10N at removal rate 10mm^3/min. Grinding force ratio of tangential to normal was 0.15. Further, subsurface damage was investigated by photo-conductivity transient technique. The depth of subsurface damage in the shear-mode grinding at a removal rate of 10mm^3/min was found to be 0.5-0.7 μ m[3)]. But there is an indication that heavy metals of metal bond stick to the surface of silicon wafers.

This paper describes experiments with resin bond diamond cup wheels which do not include any metals as fillers, and actually manufacture silicon wafers on the production machine.

2. Experimental methods and results

The grinding machine is a reconstructed surface grinding machine (OKAMOTO PSG-52DX) with PI motorized block head shown in Fig.1. 25mm square silicon wafers (100 surface) were ground with cup wheels under conditions shown in Table.1. Normal and tangential grinding forces were measured using a three-axis quartz piezoelectric instrument.

Two types of resin bond serrated wheels (ϕ 100-1.0w) were used in the experiment. One of these had a general resin bond type-A, the other had a characteristic that is consistent with high concentration cores and low concentration foundation (type-B). In the first stage, large changes are caused at the resin bond wheel surface, with every experiment carried out after dressing with resin bond GC (#3000) cup truer under the same conditions.

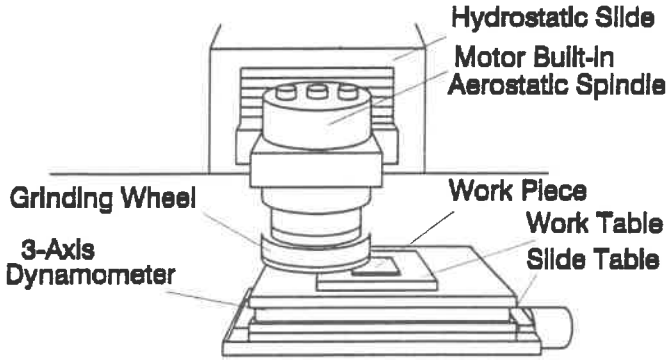

Fig.1 Schematic drawing of the grinding machine

Table.1 Grinding Condition

Workpiece	Silicon(w25-l25-t2.5)
Diamond Wheel 100-1.0w (slit-48-3mm)	Resin bond wheel SD2000N100(Type-A) SD2000N100(Type-B)
Wheel Speed	750,1000,1500,2000 rpm
Table Speed	50, 100, 150 mm/min
Depth of Cut	1, 2, 4, 6μm/pass
Coolant	AL-1 (Yushiro Co.)

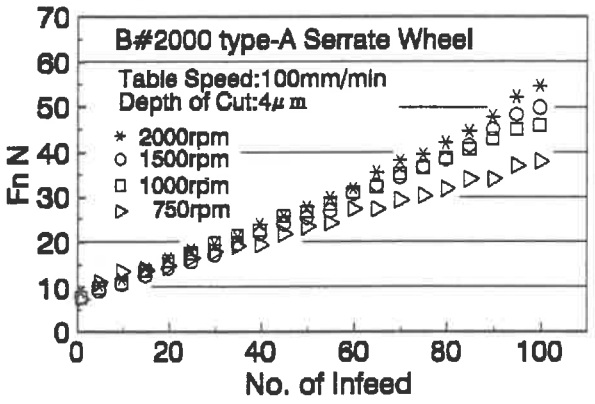

Fig.2 Normal Grinding Force of Type-A Wheel

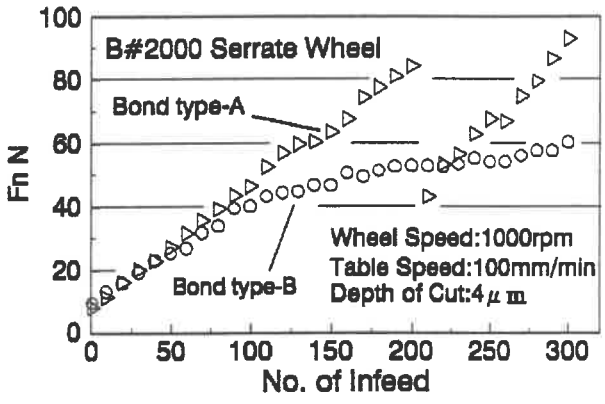

Fig.4 Comparsion of Normal Grinding Force of Type-A Wheel with Type-B Wheel

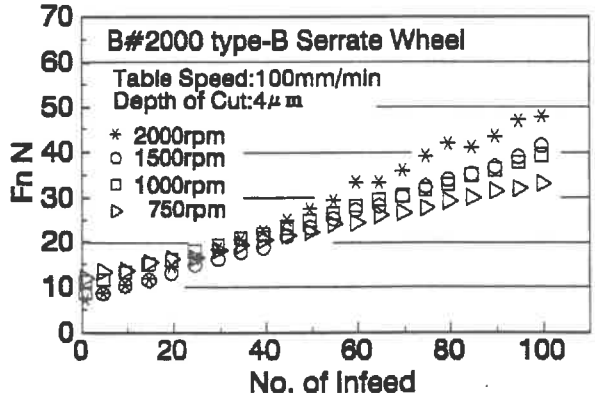

Fig.3 Normal Grinding force of Type-B Wheel

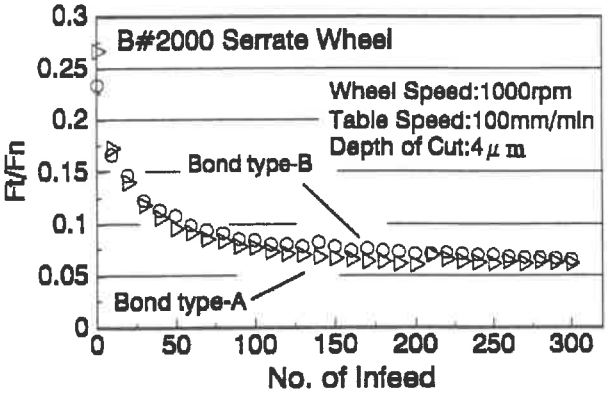

Fig.5 Comparsion of Grinding Force Ratio (Ft/Fn) of Type-A Wheel with Type-B Wheel

Fig.2 and Fig.3 show change of normal grinding force in variable wheel speed. Normal and tangential grinding force increased with increasing of passes at each wheel speed. Increasing rate of normal grinding force was larger than tangential grinding force. Consequently, the grinding force ratio Ft/Fn came down with increasing passes. In variable table speed and depth of cut, normal grinding force was increasing with increase of passes and grinding force ratio Ft/Fn decreased gradually and approximated steady state of each grinding condition.

Next, we tried 300 passes and compared change of the grinding forces between two types resin bond diamond wheels. The normal grinding force increased quickly and created unstable change in the resin bond type-A. But it showed a stable change at the resin bond type-B.

3. Manufacturing of Silicon Wafers

We carried out manufacture of silicon wafers on the production machine, it is possible to grind from 3" to 8" wafers. This machine is a vertical spindle rotary table type. Productivity and high accuracy on the part of the production machine is very important, accordingly the machine has two grinding stations, i.e. one is a rough grinding station with B#325 diamond wheel and another is a finish grinding station with B#2000 diamond wheel. And the machine has four vacuum chucks including stations for loading and unloading. To prevent micro cracks and dimples caused by contamination, the vacuum surface of the chuck is cleaned by de-ionized water and chuck cleaning devices. For example, the conditions of grinding for 8" silicon wafers is shown as follows: Diamond wheel: ϕ 250-3w-5x, SD#2000J75B, rotation of diamond wheel: 3000rpm, rotation of vacuum chuck: 50~20 μ m/min, feed rate: 25 μ m/min, stock removal of finish grinding: 20 μ m. It was possible to manufacture more than ten thousand 8" silicon wafers without any dressing. This fact shows the theory of the criteria has been applied to shear-mode grinding of 8" silicon wafers. Fig.6 shows a flatness of after grinding a 8" silicon wafer, realizing TTV=0.31 μ m.

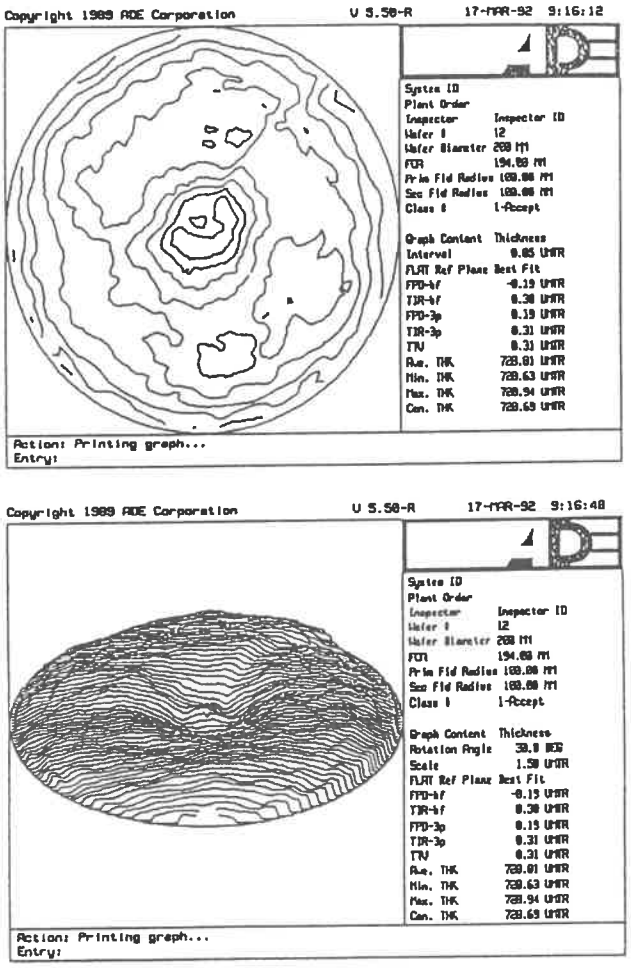

Fig.6 Flatness of ground 8" silicon wafer TTV=0.31μm

An illustration of image measured by AFM is shown in Fig.7. It shows an experimental specimen, with grinding conditions as follows: Rotation of diamond wheel: 1000rpm, table speed: 100mm/min, and depth of cut: 2 μ m/pass. It shows some grinding streaks, but can't find any fractures or pits on the surface, it shows the finished surface was ground by shear-mode.

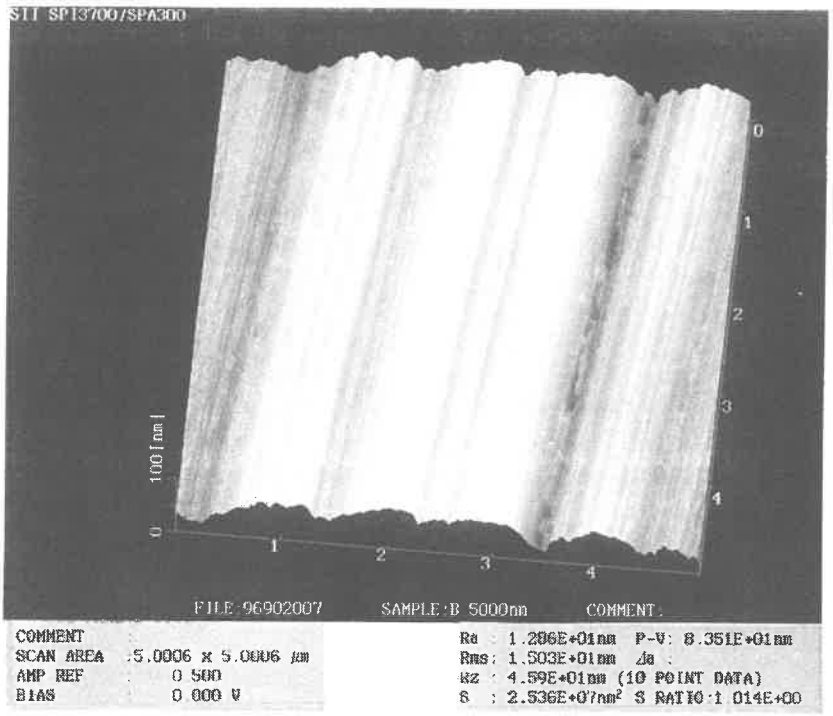

Fig.7 AFM image of ground with #2000 resin bond diamond wheel
Ra=12.8nm, P-V=83.5nm, Rms=15nm

4. Conclusions

1. An approximate steady grinding force like that of a metal bond wheel was not found with resin bond diamond wheels. But the grinding force ratio of tangential to normal was fixed under grinding conditions resulting in an increase of stock removal of close to 0.05-0.07.
2. Resin bond type-B with composite structure showed lower and stable normal grinding force in comparison with type-A.
3. It was found that more than ten thousand 8" silicon wafers can be ground without any dressing.

5. Reference

1) H.Hashimoto, J.Takeda, K.Imai, K.Blaedel: Shear-mode Grinding of Brittle Materials and Surface Characteristics, JSPE. 27,2(1993),95-99.
2) H.Hashimoto, K.Imai: Shear-mode Grinding Force Criteria in Grinding with Serrate Wheels, ASPE. (1995),171-174
3) Y.Ogita, H.Hashimoto, K.Imai, K.Yamamoto: The 42th Spring Meeting, 1995, The Japan

Cryogenic Grinding of Brittle Materials

Huadong YU, Shingo TERASHIMA, Noboru MORITA, Yoshitaro YOSHIDA
Chiba university, 1-33, Yayoi-cho, Inage-ku, Chiba-shi, Chiba 263, Japan

1.Introdution

It is well known that the strength of brittle materials such as glass depends on the loading rate and loading duration. Usually, glass, when loaded at a rapid rate or forced to support a given load for short time, is relatively strong. In reverse, it is relatively weak. Indentation techniques.which have long been used as a means of measuring hardness of materials, are usually used to understand behaviors of material removal, deformation and fracture during machining brittle materials.[1)-5)]

As the applied load gets higher, median crack, lateral crack, radial cracks appear around a residual impression formed by the indenter. Especially, it is thought that the cracks propagation depends on humidity of environment, and also depends on state of stress at the tip of the cracks.[6)] When a crack occured on the surface of the glass, a stress-dependent chemical reaction occurs between water vapor and the surface of glass. The stress corrosion promotes the crack propagation, and strongly depend on temperature of glass.[7)] So we think that the stress corrosion will decrease with decreasing temperature of glass, and that it is possible to restrain the crack generation and propagation during machining brittle materials at low temperature. In order to get the fundamental information on the cryogenic grinding of hard and brittle materials, the diamond indentation tests and the single point diamond scratching experiments have been carried out at a room temperature and cryogenic temperature using liquid nitrogen respectively.

2.Experimental procedure

The tests of diamond indentation were carried out by using of micro-Vickers hardness tester at a room temperature and liquid nitrogen temperature respectively. Material of test samples was soda-lome glass. The test specimen was kept on a special jig, which was full of liquid nitrogen and was placed on the table of the micro-Vickers hardness tester. The temperature of the indenter and the specimen were measured by thermocouple. When the specimen and the indenter had cooled down to liquid nitrogen temperature, the test indenter was loaded normally onto the surface of specimen with a dwell time of 30s. Indentations were for loads of 0.5 to 10 kgf. All observations were carried out at room temperature.

The single point diamond scratching tests were carried out at a room temperature and cryogenic temperature by using a grinding machine tool. In order to get continual depth of cutting, the test specimen was placed on the table of the machine tool with a small slope to the table. The scratching speed was determined by the feed of table of the machine tool.

3.Results and Discussion

3.1 Indentation

When the indenter indented into brittle materials such as glass, then above several kinds of crack usually occur. These cracks have also been observed in our experiments. Fig.1 shows dependence of radial crack length on indenting loads at room temperature and cryogenic temperature(77K) respectively. As shown in Fig.1, the crack length depends on indenting loads, and increases with increasing loads at both room temperature and cryogenic temperature. But the crack length occured at cryogenic temperature was markedly smaller than one occured at room temperature. Under an optical microscope, we observed that behaviors of deformation and cracking patterns at cryogenic temperature were different from those at a room temperature. At a room temperature, the boundary of

indentation (contact edges between the indenter and the surface of specimen) were very well defined, and some lateral cracks were found in subsurface by the reflections in addition to radial cracks. On the other hand, at cryogenic temperature, the contact edges were not clear, and the radial cracks decreased, but the ring crack occured around the indented impression. Moreover the size of indentations were much smaller than those at room temperature. It seems that hardness of glass at cryogenic temperature is higher than that at room temperature.

The dependence of Vickers hardness of soda-lime glass on temperature is shown in figure 2. All tests were carried out during the specimen temperature rising up to room temperature, and all measurements were carried out at room temperature. It is found that the hardness of soda-lime glass markedly increases with decreasing specimen temperature. The hardness of soda-lime glass at low temperature (77K) was as high as about 2.5 times of that at room temperture. It is well known that strength of a material is directly propotional to its hardness. So we believe that strength of soda-lime glass can become higher considerably, when cooled to liquid nitrogen temperature. Moreover, it is found that there is a point of inflection at about 180K. Why for the point of inflection to exist can not be explained clearly. We think that the point of inflection may be due to a changing in such as chemical structure of soda-lime glass at about 180K. Natrually it is necessary to verify this view.

The relationship between the radial crack and the specimen temperature is shown in Fig.3. It is found that the radial crack decrease with decreasing specimen temperature, and that there is a point of inflection at about 180K as well. It is thought that the phenomenon about reduction of crack length may results from follows: 1) increasing in the fracture strength with temperature of specimen down; 2) reducing in water activity at low temperature.

Fig.4 is relationship between radial crack length and area of indentation in soda-lime glass. It is found that the radial crack length increased with the area increasing at both room temperature and liquid nitrogen

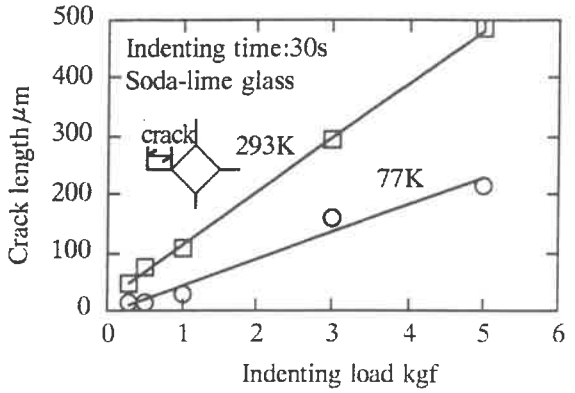

Fig.1 Dependence of radial crack length on indenting loads at room temperature and cryogenic temperature

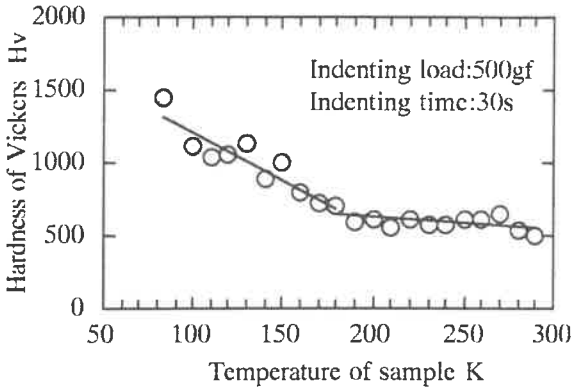

Fig.2 Dependence of hardness of soda-lime glass on temperature of specimen under room temperature

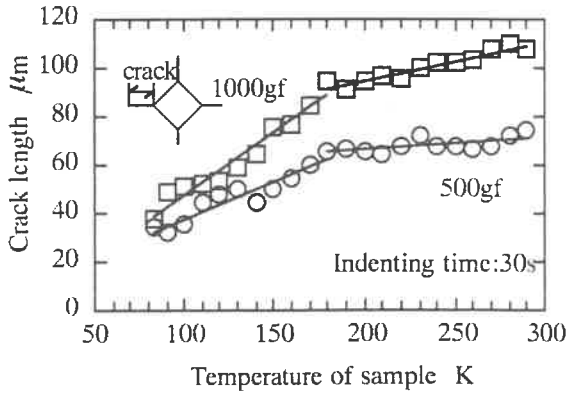

Fig.3 Relationship between radial crack length and specimen temperature under room temperature in soda-lime glass

temperature, but under just same area of indentation, the radial crack of the former is larger than the latter. In fact, because the indentation is deformed plastically and left on the surface of specimen by indenter, so the area of indentation amount to the volume of materials removed. It seems that the mechining at cryogenic temperature is favorable for restrainning cracking ,in the case of just same materials removed.

3.2 Single point diamond grinding

Experiment of single point diamond scratching is very useful method to understand the mechanism of machining brittle materials, as we can directly get fundamental informations on behavior of the interaction between a abrasive and a specimen.

It is well known that the brittle materials deform plastically when the depth of cutting is very small. Generally, The depth of cutting, when cutting mode changed from brittle mode to dutile mode, is defined to critical depth of Britlle-Ductile Transition(denoted by dc).

Fig.5 is dependence of critical cutting depth of BDT on the scraching speed. It is found that the critical cutting depth decreases with the scratching speed increasing, and depends on the specimen temperature. The dc at the cryogenic temperature is larger than one at room temperature. This corresponds with the result of the indentation. Photograph of scratching grooves which corresponded to Fig.5 is shown in Fig.6. From Fig.6, we can find that region of ductile mode of groove scratched at cryogenic temperature, is larger than one at room temperature as well. And also we can find that region of dcutile mode of groove depends on scratching speed and decreases with the scraching speed increasing. Morevoer under an optical microscope, we could observe that a lot of lateral cracks and chipping appeared beside the grooves at both room temperature and cryogenic temperature, but region of the lateral cracks or chipping beside the grooves at the latter were smaller that at the former. It is thought that this phenomenon result from changing in strength of glass and water activity as the case of the indentation.

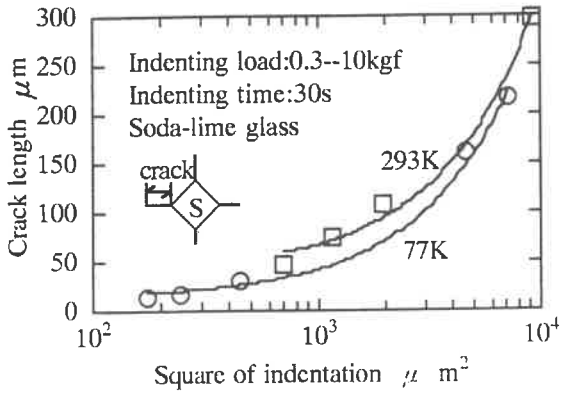

Fig.4 Relationship between crack length and area of indented impression

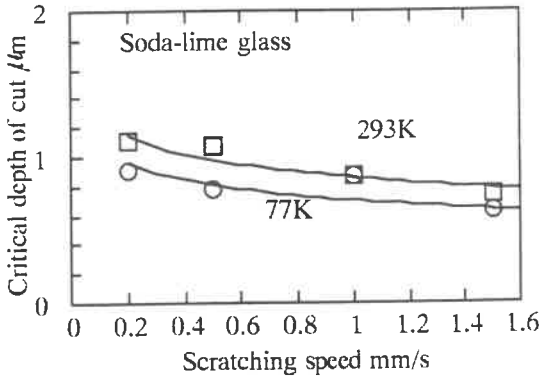

Fig.5 Relationship between critical depth of brittle-ductile transition and scratching speed

4.Conclusions

The experimental results of indentation tests indecat that ,when the temperature of specimen of soda-lime glass coolled down to cryogenic temperature(liquid nitrogen temperature), its Vickers hardness increases markedly, and that the radial crack due to indenter decreases. Moreover, the results of the single point scratching experiments indecate that ,at cryogenic temperature, the critical depth of cut without cracking is larger,and that the region of lateral cracks which occured within subsurface of glass (or chipping on the surface of glass) is smaller than those at room temperature. So we believe that it is possible to restrain crack generation and propagation during grinding brittle materials such as glass at cryogenic temperature.

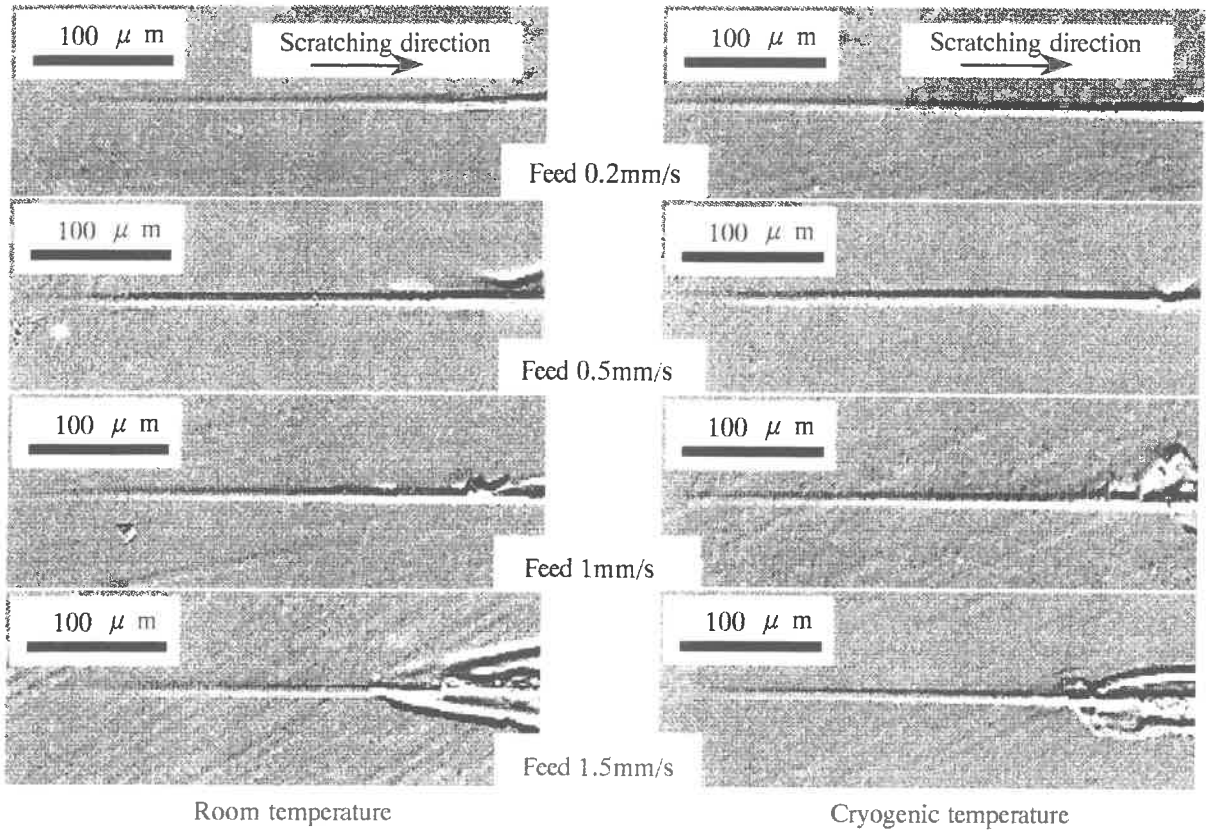

Fig.6 Optical photographs of scratched groove of soda-lime glass at room temperature and liquid nitrogen temperature respectively

5.Refrence

1)Maarten Buijs and Liesan A.A.G.Martens, Effect of Indentation Interaction on Cracking, J.Am.Ceram.Soc.,75[10]2809-14(1992)

2)K E Puttick, M A Shahid and M M Hosseini, Size effect in abrasion of brittle materials, J.Phys.D:Appl.Phys.,Vol.12,1979

3)M. ARAGAKI, J. SHIBATA, Collection of Freatises in Autumn Meeting '1994 of THE JAPAN SOCIETY OF PRECISION ENGINEERING, 173--174

4)C. L. Chao,C. M. Fang, C. L. Chen, S. M. Tsay and S. S. Kuo, Investigation of the Micro-Mechanical Properties of Various Brittle Materials Using Micro-Indentation Technique, The Second International Abrasive Technology Confrence, HsinChu, Taiwan, Nov.1995

5)N. MORITA, Y. YOSHIDA, Effect of Temperature and Load Rate on Brittle-Ductile Transition of Silicon Single Crystal, ASPE'1994

6) S. M. WIEDERHORN,Influence of Water Vapor on Crack Propagation in Soda-Lime Glass, J.Am.Ceram.Soc.,50[8]407-14(1967)

7)H. D. YU, N.MORITA, Y. YOSHIDA, Effect of Atmosphere on Crack Occurring and Extend during Indentation in Soda-Lime Glass, The Second International Abrasive Technology Confrence, HsinChu, Taiwan, Nov.1995

THE PLASTIC ZONE FORMATION IN ALUMINA ASSOCIATED WITH ULTRA PRECISION GRINDING

Irena Zarudi

Centre for Advanced Materials Technology, Department of Mechanical and Mechatronic Engineering, The University of Sydney, NSW 2006, Australia

1. Introduction

The ductile-regime grinding of alumina has been used in industry for several years, but still insufficient control of the process restricts its wide application. The problems arise from the fact that the mechanism of the ductile-regime grinding of alumina has not been fully revealed.

Recently it has been recognised [1] that a prominent plastic deformation is involved into the process and different slip and twin systems are initiated under the single-point ground groove. Furthermore, it has been concluded that the stress field in the vicinity of the cutting edge should be responsible for activation of these systems. Unfortunately, parameters of the stress field were not established and the mechanism formation of twin and slip systems hasn't been explored.

The present work is aimed at the computation of the stress field in the vicinity of the cutting edge as single-point grinding and computer simulation of the plastic zone formation during the process. Experimental data has been obtained as well and the theoretical results are compared with parameters of the real plastic zone formed while single point grinding of alumina in ductile mode.

2. Method

2.1 Theory. The model for calculation is based on the consideration of the plastic flow formation as a result of initiation and movement of dislocations and twins in the subsurface area. The crucial role in the calculation was the evaluation of the stress field (in particular, the shear stress distribution under the ground surface).

The shear stress evaluation. The shear stress component was computed in the plane perpendicular to the ground surface for 3-d elastic case and complex pyramid load distribution. The pyramid ramp distribution was worked out taking into account dimensions of a single-point groove (**Fig.1**). The base of the pyramid was approximated as an isosceles triangle with the side of the base equal to the width of the ground groove and the corresponding height equal to 0.5 of it's width. The volume of the pyramid was normalised by the applied load and then the height was evaluated. Ones the load distribution had been determined, the analysis was conducted by applying normal and tangential loads separately and load was evaluated in terms of three harmonic functions [2]. Dydo and Busby [3] solution for constant load distribution was used and the final solution was found by method of superposition.

Computation of dislocations motion. The movement of dislocations was estimated in the plane perpendicular to the ground surface. Basal and prism plane dislocations were computed as they were identified in the subsurface regions of the ground alumina [1]. The shear stress component along possible direction of dislocations motion was treated as a driving force for dislocation movement and activation of the dislocation sources considered in the regions adjacent to the ground surface (up to 0.1 μm under the surface). Assume further the lattice to be ideal without any defects and the only force opposing the dislocation movement the friction force of the lattice. The force exerted on dislocation was determined in accordance with method [4] taking into consideration the interaction

of the adjacent dislocations. The final equilibrium position of dislocations was then evaluated. Effective resolved shear stresses (ERSS) are as following: 17 GPa for basal slip system, 5 Gpa for prism plane slip system and 15 MPa for basal and rhombohedral twin systems.

2.2 Experiment. Two types of alumina with average diameter 1 μm and 25 μm were treated. Single point grinding experiments were conducted on a reciprocating sliding machine [1] to imitate the ductile regime mode of grinding. The diamond indenter with tip radius 100 μm and load 0.5 N was used. The microstructure of the subsurface was examined by transmission electron microscope [1]. The topography of the groove was investigated by means of atomic force microscope.

3. Results and Discussion

3.1 Shear stress. Results of the computation of the shear stress (**Fig.2**) revealed it's complex distribution with the absolute maximum in the middle of the groove and going sharply down along two symmetrical rims with deviation from the maximum point. The values of the shear stress along y axis follow the distribution of the shear stress along the groove width, distribution of the shear stress in z direction enables to establish stresses inside the material under the single-point ground groove. The contours corresponding to ERSS of the slip and twin systems initiated by the grinding process can be seen in **Fig.3**. Twin distribution was then approximated as an area with values of the shear stress exceeded 0.15 GPA (ERSS of twins). So twins can be expected under the whole width of the single-point groove and are spread to the depth of 19 μm.

3.2 Dislocations motion. Areas of possible dislocations motion (**Fig.4**) give the picture of the dislocation structure of the subsurface. Two zones can be easily explored. The first one with the width 3 μm and the depth 1.5 μm located in the middle of the groove where one can expect the possibility of the initiation of all 5 possible slip and twin systems. The second one covers the whole width of the groove (9 μm) and spreads to the depth of 4 μm. In the second area only 4 possible slip and twin systems can be expected. Van-Mises criterion can be satisfied only in the first area. The second one is dangerous from the point of view of the crack initiation.

3.3 Topography of the single-point ground grooves and structure of the plastic zones. The structure of the subsurface was explode before single-point grinding experiments to ensure that subsurface regions were dislocations free before tests. The depth of the grooves was measured to be 100 nm. The singe-point ground grooves occurred to be smooth and fracture free with Rms roughness of the surface equal to 60 Å that is comparable with the values of the roughness of the polished surface. The structure of the plastic zones was as following. Three zones could be easily distinguished in the subsurface regions of 25 μm grained alumina (**Fig.5a**). The first region is characterised by extremely high density of dislocations. It is spread to the depth 1.5-2 μm under the surface. The second region is located under the first an covers the depth 5-6 μm under the surface. The density of dislocations in this region is much lower and single dislocations are resolved easily, some cracks are detected. Only twins were found in the third region, they spread to the whole length of the grains (up to 20 μm) beneath the surface. No dislocations were observed under the second region. Cracks were seen at the sites of twin-twin intersection. In the case of 1 μm (**Fig.5b**) grained alumina only the first zone with the high density of dislocations is distinguished in the subsurface region, it covers the first row of grains. No dislocation were detected in the second row of grains. It indicates that the initiation of dislocations occurs immediately under the ground surface and movement of dislocations is terminated by grains boundaries.

It follows that the first zone in the model corresponds to subsurface area with high dislocation

density, 5 possible slip and twin systems can be initiated there and this zone should be cracks free, the second zone corresponds to the zone in subsurface with low dislocation density, it is dangerous from the point of view of cracks initiation, twins can be observed up to depth of 20 μm according to theoretical and experimental results.

4.Conclusions

(1) The new model for plastic zone formation is worked out. It gives good correlation with the structure and parameters of the plastic zones formed as single-point grinding of alumina in ductile mode.

(2) Real ductile mode can be achieved while single-point grinding of 1 μm grained alumina. The structure of the plastic zone in this case is characterised by high density of dislocations and twins in the first row of grains. Von-Mises criterion is satisfied by initiation of the sufficient number of twin and slip systems.

(3) For 25 μm grained alumina single-point grinding with small depth of cut (100 nm) forms three regions in subsurface zone. The first of them is spread to the depth of 1 μm under the groove bottom and is micro cracking free. The second and the third spread accordingly to the depth of 5 and 19 μm under the groove bottom and can be dangerous from the point of view of micro cracks initiation.

Acknowledgments

The support of the ARC large grant scheme is appreciated. The author would like to thank her supervisor L. Zhang for guidance of this work.

References

1. I. Zarudi and L.C. Zhang, "The dislocation structure in alumina associated with ultrapresicion grinding, Proceedings of the 10th ASPE Annual Meeting, 163(1995).

2 .K. L. Jonson, "Contact mechanics" (Cambridge University Press, New-York, 1985).

3. J. R. Dydo , H. R. Busby, " Complete 3-D elasticity solutions in the half-space for constant and linearly varying pressure loads", Proceedings of the international Conference on contact mechanics. 19-26 (1993).

4. C.M.Li, " Dislocation Modelling of Physical Systems", edited by C. S. Hartley, M. F. Ashby, R. Bullough and J. P. Hirth (Pergamon Press, Oxford, 1981).

5. T. G. Bifano, T. A. Dow, R. O. Scattergood, "Ductile-regime grinding: a new technology for machining brittle materials", Transactions of the ASME, **113,** 184(1991).

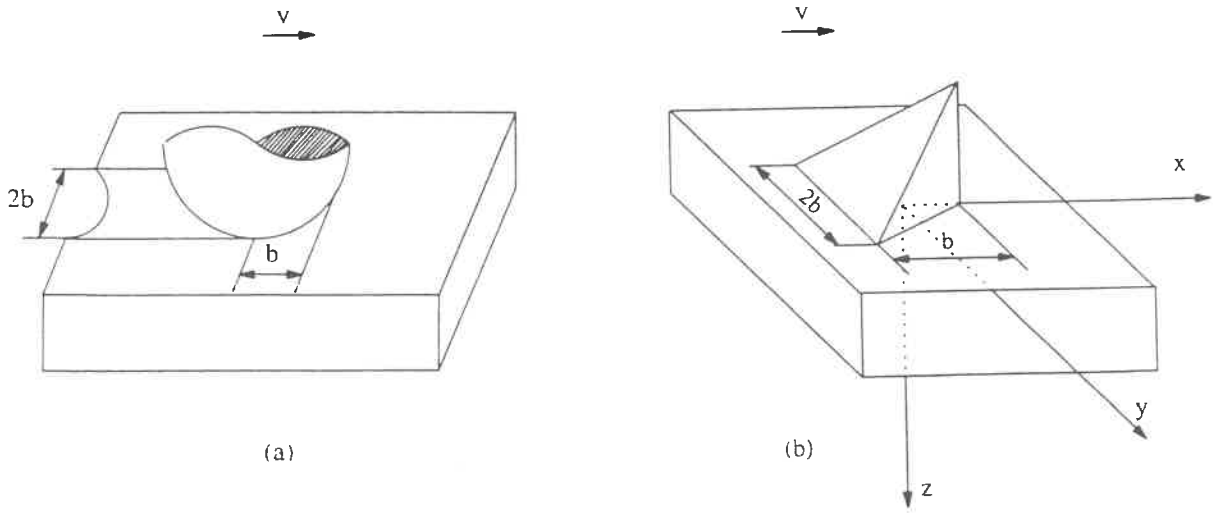

Fig.1 The model for shear stress calculation. (a) The single-point grinding. (b) The pyramid load distribution model.

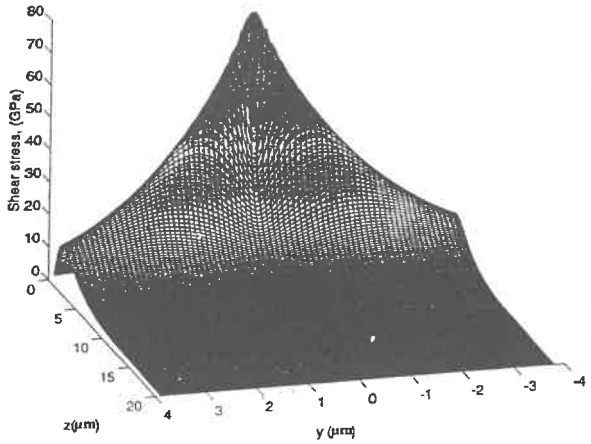

Fig.2 Shear stress distribution in yz plane.

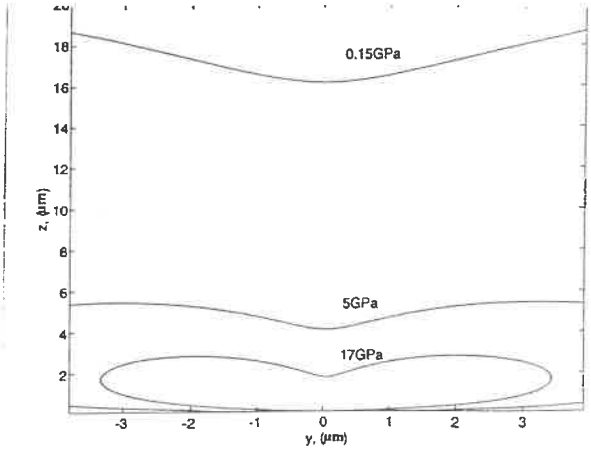

Fig.3 Contours of equal shear stress in yz plane.

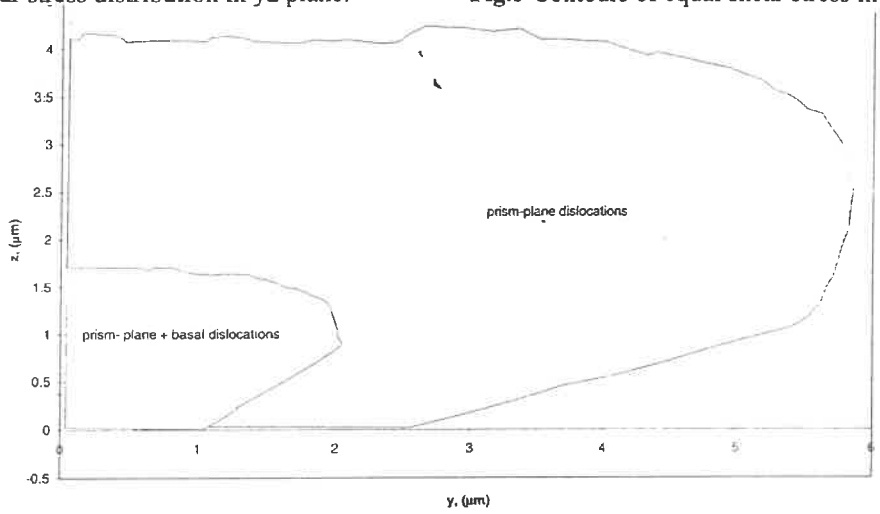

Fig.4 Areas of possible dislocations motion under the single-point ground groove.

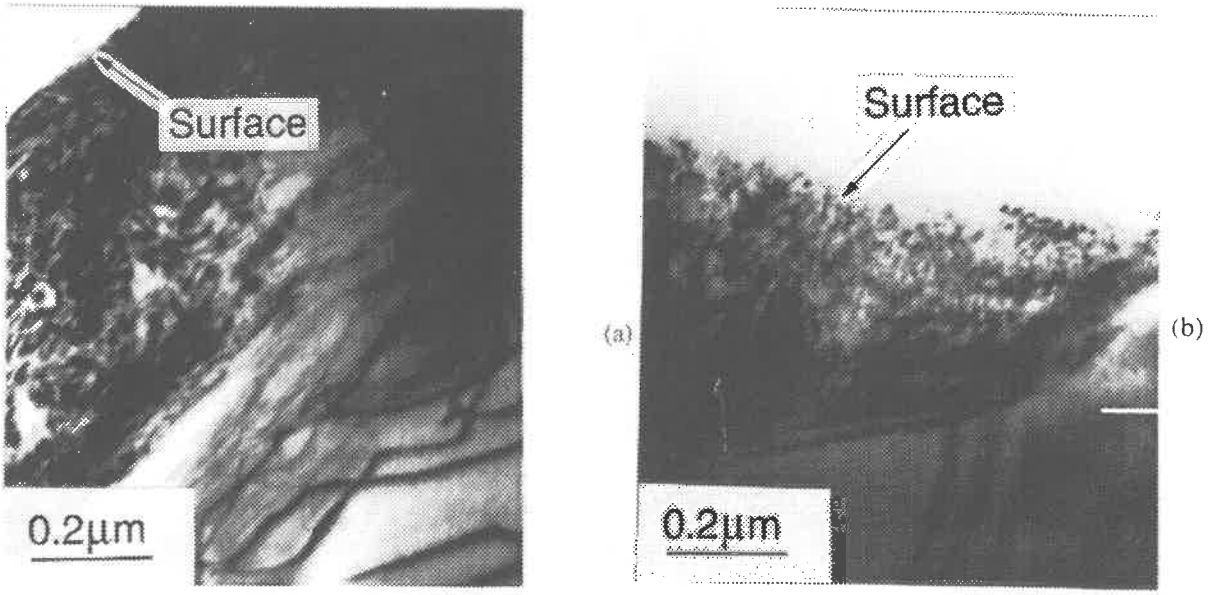

Fig.5 Subsurface damage in (a) 25 μm and (b) 1 μm alumina after single-point grinding tests.

Friction Characteristics of Linear Plain Bearing Guideway and Motion Controllability of Numerically Controlled Slide

A. Kanai, M. Miyashita, T. Hatai, M. Yoshida
Ashikaga Institute of Technology, 268 Omae, Asikaga, Tochigi 326, Japan

1. Introduction

Feed in NC machine tool is composed of summation of small stepwise feeds. Frictional load characteristics of plain bearing guideways for such stepwise feeds is expected to be different from it for continuouns feeds. In the present paper the frictional load characteristics for stepwise feeds of 1 nm/step, 10 nm/step, 100 nm/step and 1 μm/step at averaged feed rate of 0.05 μm/sec to 5 μm/sec in reciprocating slide feed is studied.

2. Test rig

Fig. 1 is the test rig. The slide is vertically supported by plain bearing guideways and horizontally by hydrostatic bearings. The slide positioning servo system is composed of force-operated hydraulic actuator and capacitive position sensor as feedback sensor. The slide is 450 mm × 300 mm in dimension and 150 kg in mass. The plain bearing guideways are two flats of 25 mm width × 450 mm length. Lubrication is applied with oilbath and ISO 22 oil is supplied as lubricant and power source. Piston of the hydraulic actuator is hydrostatically supported and pressure difference between the two cavities is perfectly transmitted to the slide as driving force. The driving load is the inertia of slide and the friction, and the inertia is negligible compared with the friction except at the transient. And the frictional load of the plain bearing guideways is derived from the pressure difference between the two cavities.

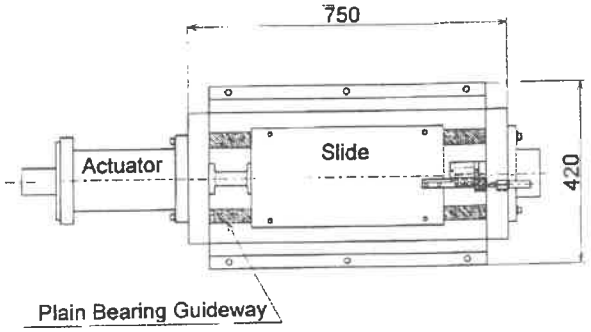

Fig. 1 Test rig

3. Motion and frictional load characteristics for continuous feeds and stepwise feeds of 1 nm/step and 10 nm/step

Fig. 2 shows the test results of slide displacements and frictional loads in time for the reciprocating feed of 2 μm at the feed rate of 0.5 μm/sec. By reversing feed direction the frictional load increases with the displacement to the stationary state. The region in which the frictional load increases with displacement after reversing is defined as the transient one and the region in which the frictional load arrives at the stationary state is defined as the stationary one.

Fig. 3 is arranged for explanation of the transient and stationary regions in detail. They are the test results of the slide displacements and the frictional loads for the continuous feeds in the reciprocating feed range of 16 μm at the feed rate of 0.5 μm/sec. (a) shows the frictional characteristics after reversing feed direction from backward to forward and (b) does the one after reversing from forward to backward. Both varying process

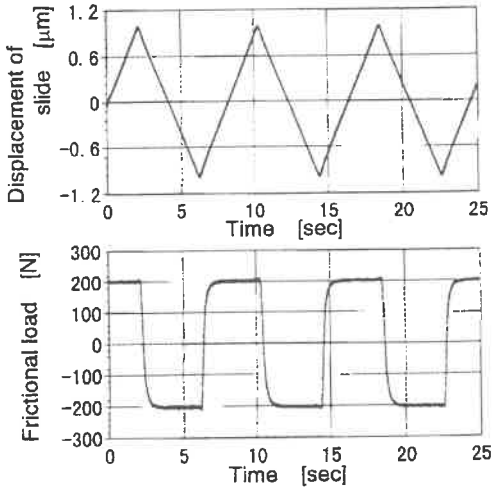

Fig. 2 Frictional Characteristic for Reciprocating Continuous Feed Motion (0.5 μm/sec)

of frictional load coincides very well. The 90 % of the slide displacement arriving at the stationary frictional load is assumed as a range of the transient region and it is about 0.2 μm.

Fig. 4 shows the test results of the slide displacement and the frictional load around reversing the feed direction for the stepwise feed of 10 nm/step at the feed rate of 0.5 μm/sec in the reciprocating feed range of 16 μm. The relationship between the slide displacement and the frictional load obtained for 10 nm/step slide feed is also just same as the one in Fig. 3. (a) shows the one from backward to forward and (b) does from forward to backward. The transient region is about 0.2 μm. Test results in Fig. 3 and 4 coincide respectively very well and the stationary frictional load is both about 170 N. Here, the relationship is defined as "displacement vs. frictional load characteristic curve".

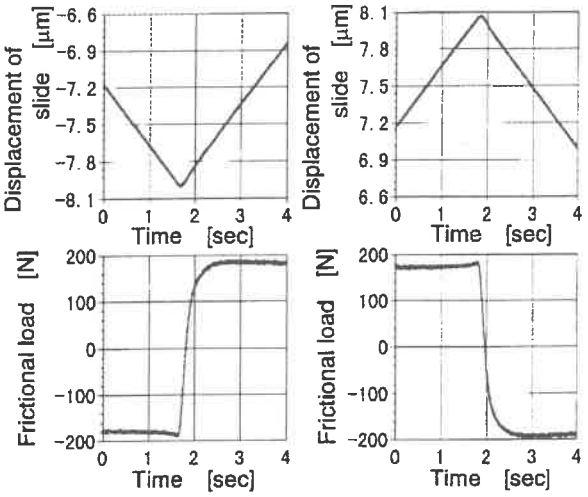

(a)Backward→Forward (b)Forward→Backward

Fig. 3 Transient Frictions at Reversing Point of Continuous Feed Motion (0.5 μm/sec)

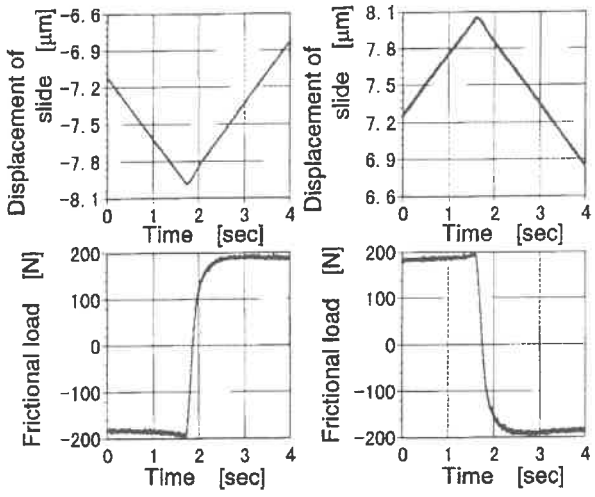

(a)Backward→Forward (b)Forward→Backward

Fig. 4 Frictional Characteristic for Reciprocating Stepwise Feed Motion (10 nm/step, 0.5 μm/sec)

Fig. 5 (a) shows the frictional loads in the stationary region for the continuous and stepwise feeds in the reciprocating slide feed at constant feed rate from 0.05 μm/sec to 5 μm/sec. Fig. 5 (b) shows the ranges of the transient region. The feed rates are 0.05, 0.10, 0.50, 1.0 and 5.0 μm/sec and the travel range is 16 μm. Difference of the frictional loads at the same feed rate between continuous and stepwise feeds is 8 % at most and the one at the different feed rates is 6 % in maximum. The frictional load tends a little bit to decrease with increase of the feed rate, and the range of transient region does similarly in the range of 0.25 μm to 0.16 μm.

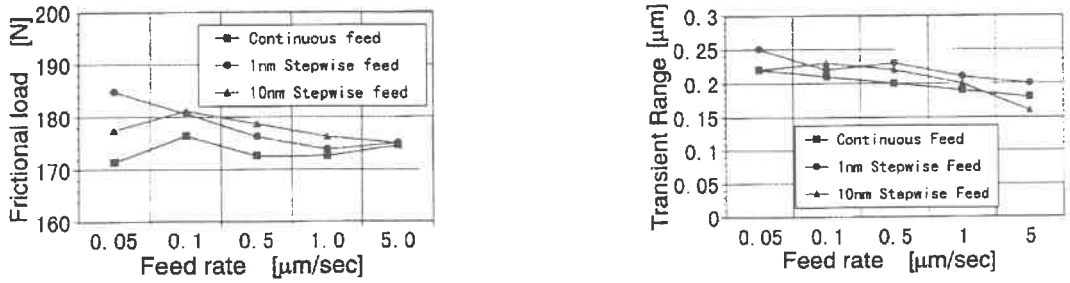

(a) Friction in Steady State Domein (b) Transient Range in Displacement

Fig. 5 Frictional Load in Steady State Domein and Transient Range in Displacement

4. Motion and frictional load characteristics for slide feed of 100 nm/step and 1 μm/step

Frictional load characteristics for stepwise slide feeds of 100 nm/step and 1 μm/step in the reciprocating feed

motion at constant feed rate is remarkably different from the one for stepwise feeds of 1 nm/step and 10 nm/step and continuous slide feed. Frictional load in the stationary region is measured small compared with the case of 1 to 10 nm per step and can be even negative. In the case of large slide stepwise feed, the transient slide motion, in particular, the overshoot is observed to dominate the frictional load in the stationary region.

Fig. 6 is an example of the measurements of the slide displacement and the frictional load around reversing feed direction for 100 nm/step slide feed in the reciprocating slide feed of 16 μm at the feed rate of 0.05 μm/sec. The frictional load after 4 steps from reversing becomes stationary to 80 N and is less than 170 N in Fig. 4.

Fig. 7 is an example in the case of 1 μm/step slide feed. The frictional load is negative and -50 N except the first step after reversing. In both case, it is remarkable that the peaks of frictional loads are almost constant to be +170 N or -170 N approximately.

The above mentioned phenomena in 100 nm/step and 1 μm/step slide feeds can be explained by application of the frictional load characteristics for continuous slide feed motion in Fig. 3 and the transient slide motion in Figs. 6 and 7. Fig. 8 is rearranged description of the displacement vs. frictional load characteristic curve in Fig. 3. Applying the 1 μm/step slide feed, one step of 1 μm exceeds the range of the transient region of 0.2 μm and then 1 μm slide feed covers the transient region up to the stationary region. The frictional load just before reversing feed is located at point A on the curve in Fig. 8 (a). After reversing the first 1 μm feed results the stationary frictional load of 170 N, but the overshoot of the slide motion is corrected along the curve in Fig. 8 (b). Amount of the overshoot is about 80 nm in Fig. 7 and the frictional load comes down along the curve by -80 nm in displacement to the point C of -50 N. The second 1 μm feed is positive and the point C is shifted to the point C′ on the curve in Fig. 8 (a) from which the frictional load increases to the stationary state and the overshoot of the slide motion results again as before. By reversing the slide motion for correcting the overshoot error the frictional load decreases along the curve in Fig.8 (b) to the point E corresponding to the overshoot error of 80 nm, which almost coincides with the point C because of the same amount of the overshoot. The first 1 μm slide feed results A→B→B′→C and the second feed C′→D→D′→E. The later process is repeated after the second stepwise feed, and the frictional load at the steady state becomes -50 N. And the peak loads are uniformly about +170 N or -170 N, which is just same as the frictional load in the stationary region in Fig. 3.

Similarly the behaviour shown in Fig. 6 for 100 nm/step slide feed can be explained. In viewpoint of the feedback control of the slide displacement, plain bearing guideways apply the spring-like load with very high stiffness of several Newton/nm to the servo control system in the transient region, and the stationary frictional load or the non spring-like load with zero stiffness in the stationary region. Therefore, there is a great difference in the step response motion between the control performances in the transient and stationary regions. In Fig. 6 the first and the second 100 nm slide feeds are within the transient region and then the step response motions do not show any overshoot due to the sprig-like load. However, in the stationary region there results the overshoot in the step response motion due to no spring-like load. In the case of large stepwise feed of 1 μm/step shown in Fig. 7, every stepwise feed ranges from the transient region to the stationary region and the stability of the servo system is decreased. And the step response motion of the slide becomes oscillatory repeating the motion in positive and negative, and also the frictional load varies complicatedly.

5. Conclusion

(1) From the experiments on reciprocating slide motions with constant feed rate composed of continuous feed and stepwise feeds of 1 nm/step and 10 nm/step displacement vs. frictional load characteristic curve is obtaind, which is characteristic of plain bearing guideway mechanism.

(2) Amount of stepwise slide feed exceeds the transient region to the stationary region and then overshoot in the step response displacement results. In such case, frictional load shows a peak and a steady force. The peak coincides with the displacement vs. frictional load characteristic curve. The steady force is less than the peak and can be negative.

(3) Experimental results shown in (2) can be explained analytically using the displacement vs. frictional load characteristic curve and the resulted amount of overshoot.

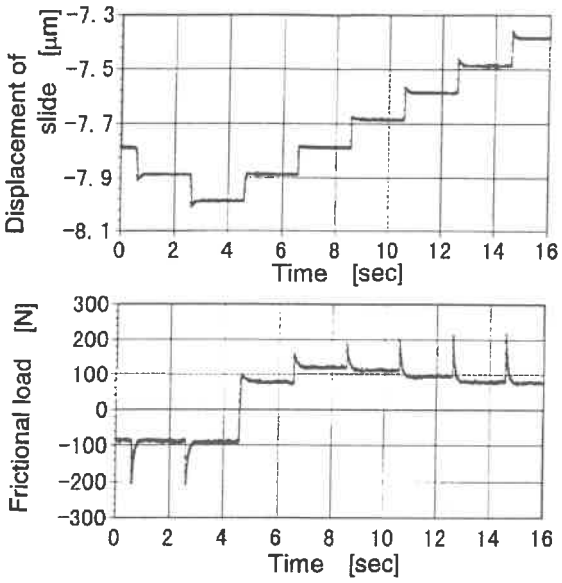

Fig. 6 Frictional characteristic for Stepwise Feed Motion (100 nm/step, 0.05 μm/sec)

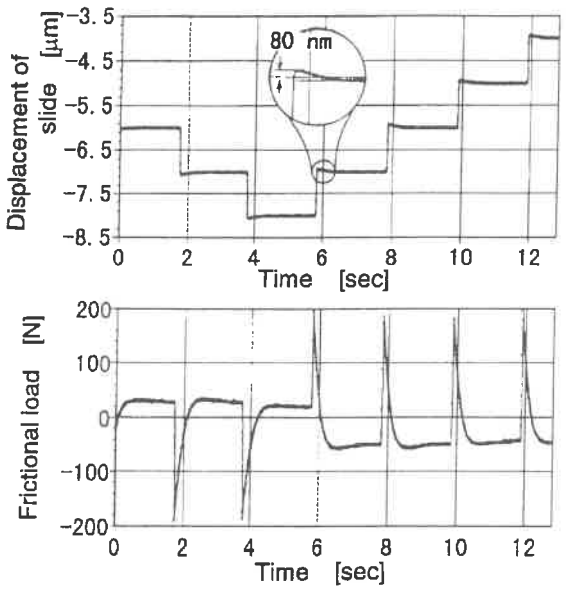

Fig. 7 Frictional characteristic for Stepwise Feed Motion (1 μm/step, 0.5 μm/sec)

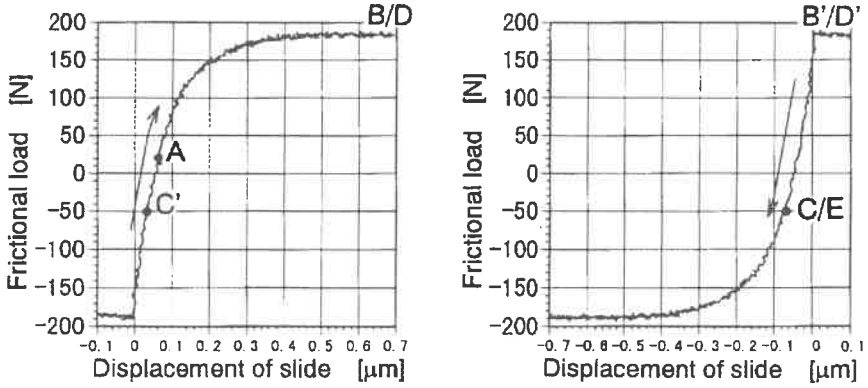

Fig. 8 Transient Friction characteristics at Reversing Point of Feed Motion

(4) In designing servo system for feeding slide on plain bearing guideways, strategies for overshoot problem in step response is to be considered taking account of the displacement vs. frictional load characteristic.

References

1. A. Kanai, I. Yosioka, M. Miyashita, Feed and Load Characteristics of Corriage on Plain Bearing Guideways in the Range of Nanometer Positioning, Proc. of 6 th Annual Meeting of ASPE, p. 80-84, Oct. 1991.
2. A. Kanai, M. Miyashita, H. Nishihara, A Study on Frictional Characteristics of Slide-way in Microdynamics, Proc. of 7 th Annual Meeting of ASPE, p.126-130,Oct. 1992.
3. A.Kanai, H.Sano, J.Yoshioka, M.Myashita, Presitioning of a 200 kg carriage on plain bearing guideways to nanometer accuracy with a foce operated linear actuator, Nanotechnology, vol. 2 (1991), p 43-51.

Tribology of Hard Bearing Coatings

A.P. Santavy and R.O. Scattergood

Precision Engineering Center
North Carolina State University, Raleigh, NC 27695-7918

INTRODUCTION

The performance of a linear sliding contact bearing is dictated by a frictional effect called stiction. Stiction exists when the static coefficient of friction is substantially higher than the dynamic coefficient. Stiction can cause chatter or jerky motion when attempting to move a slide at low speed. The force required to overcome static friction will cause deflection in the structure of the machine. If the dynamic coefficient is less than the static coefficient, when the slide breaks loose the friction force is suddenly reduced and there is an excess force on the slide and it is accelerated by this unbalanced force. As the slide moves relative to the rest of the structure the force due to the deflection of the structure is relieved. The inertia of the slide will carry it beyond the equilibrium point until the force on the slide is less than that required to overcome dynamic friction and the slide will stop. This process repeats. At high speeds, chatter does not occur because the velocity due to the suddenly unbalanced force at breakaway is small compared to the overall velocity so that the slide never comes to rest. For friction materials with a dynamic coefficient that is not less than static, stiction induced chatter does not occur because there is no excess force when the slide breaks away.

APPARATUS

The Vibratory Tribotester was designed to model a slideway system by sliding sample-on-sample at contact pressures less than 1MPa. This machine was developed because most friction data that is available for coatings has been obtained using pin-on-disc tests. The loading pressure is very high in these tests (greater than 0.5 GPa) and only a "continuous sliding" (dynamic) friction is measured. A sketch of the tribotester is shown in Figure 1. A vibration exciter, or shaker, oscillates the table on which the sled rests. The sled fits through a hole in the table and supplies the load to the test specimens. The sled has the specimen pad surfaces such that when it is placed on the table, they rest on the table mounted specimen pads. The shaker induces vibrational motion to the sled/table system at its resonance frequency. The amplitude of vibration is increased until the sled moves relative to the table, the condition of breakaway. The coefficients of friction are attained by simultaneously measuring the accelerations of the sled and table.

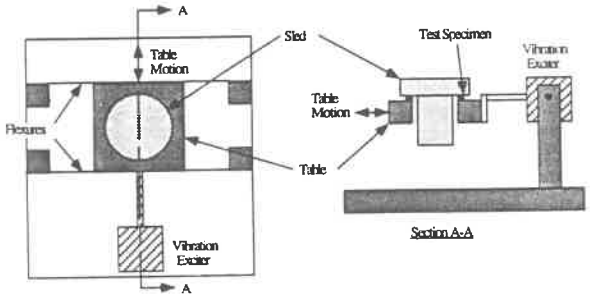

Figure 1: Vibrational Tribotester

It is important to note that the Vibrational Tribotester developed in this research measures the transient frictional behavior during breakaway and eventual coupling (sticking) of the sled and table system. In that regard, it is different from the conventional, steady state friction tests, for example pin-on-disc. Furthermore, the measurement method using accelerometers provides excellent time resolution. The system is designed to provide a unique characterization of breakaway friction behavior under conditions simulating machine tool bearing surfaces.

MODEL

A dynamic model of the sled/table system as a linear, forced single-degree-of-freedom system was developed. This configuration models the state of the system when the sled is coupled to the table (no breakaway). The equation of motion here is given by

$$M_{total}\ddot{x} + C\dot{x} + Kx = F(t)$$

where

$M_{total} = M_{table} + M_{sled}$
C = structural damping
K = total spring stiffness
$F(t)$ = forcing function of shaker

The amplitude of the sled/table is increased until the sled "breaks away"; that is, the inertia required to move the sled exceeds the maximum friction force developed at the specimen interface. This breakaway acceleration corresponds to the static coefficient of friction, μ_{static}. After breakaway, the sled is in a state of free sliding, with the only force acting being dynamic friction. The table, however, continues to be driven by the shaker. Its motion is described by

$$M_{table}\ddot{x} + C\dot{x} + Kx = F(t) \pm \mu_{dynamic} M_{sled} \cdot g$$

where

M_{table} = mass of table
C = structural damping
K = total spring stiffness
$F(t)$ = forcing function of shaker
M_{sled}= mass of sled
g = gravity

The sled continues to slide until the relative velocity between the sled and table is zero. The acceleration/deceleration profile of the sled describes the dynamic friction characteristics of the interface.

There are two cases for dynamic friction. The simplest is where, after breakaway, the acceleration of the sled "drops" to a constant value. This is classic static/dynamic friction. However, the other case is where $\mu_{dynamic}$ varies with respect to the relative sliding velocity. That is, $\mu_{dynamic}$ is velocity dependent. To characterize candidate bearing coatings, the dynamic friction coefficient was incorporated into the dynamic model by the empirical formula

$$\mu_{dynamic} = \mu_{static} \pm (\mu_{static} - \mu^{\infty}_{dynamic}) \bullet \left(1 - e^{-C \bullet |Z|}\right)$$

where

Z=relative velocity
C=constant
$\mu^{\infty}_{dynamic} = \underset{Z \to \infty}{Limit}\left(\mu_{dynamic}\right)$

The constant, C, is a factor that dictates the exponential rate of change of $\mu_{dynamic}$ with the relative velocity, Z, between the sled and the table. There are two types of velocity dependence The most common case is that where the friction coefficient decreases with increasing relative velocity. That is, the stiction situation where the static friction is greater than the sliding friction. Figure 2 shows the effect of C on the dynamic friction for the converse case where $\mu_{dynamic}$ increases with relative velocity. The values in Figure 2 for C are 0.5 (dotted), 5 (solid), and 50 (dashed). This is often observed for low friction bearing materials that show no stiction effect. In both cases, an increase in C causes the function to approach the $\mu_{dynamic}$ value more rapidly.

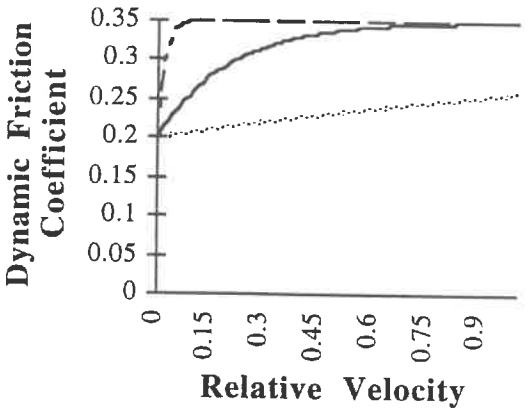

Figure 2: Exponential model for friction.

RESULTS

A FORTRAN simulation of the system dynamics was written to verify the friction measurements. A complete set of simulations

for the cases of constant dynamic friction and velocity dependent friction were developed. The values of μ_{static}=0.25 and $\mu_{dynamic}$=0.35 were used for the results of the simulated friction event in Figure 3.

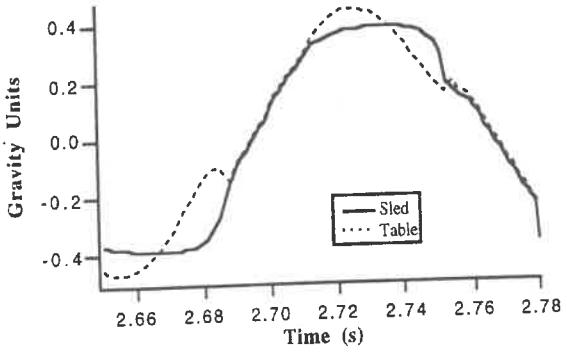

Figure 3: Simulated increasing velocity dependence.

This figure shows the acceleration measured during half of one cycle of motion where the sled (solid line) breaks away from the table (dotted line). Notice that near 2.69 seconds the curves become coincident indicating that the sled and table "stick" together as the acceleration (and therefore inertia) is reduced. As the acceleration increases again, the sled breaks away at about 2.71 seconds with a friction coefficient of approximately 0.25. This simulation uses a friction coefficient that increases with relative sliding speed (C=5).

Compare this trace with that in Figure 4 measured using a mating pair of steel specimens coated with a dry film lubricant (Hi-T-Lube) supplied by General Magnaplate. General Magnaplate suggests Hi-T-Lube-on-Magnaplate HMF™ for plain slideway bearings to reduce stiction.

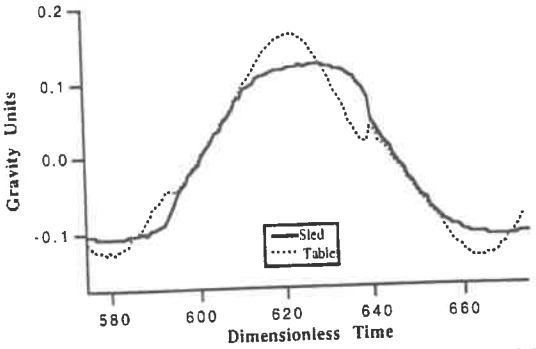

Figure 4: Measured Hi-T-Lube-on-Magnaplate HMF™ sled and table accelerations.

Figure 4 shows a friction event for this bearing counterface combination. The Magnaplate engineering data brochure claimed an elimination of stiction motion. If Figures 3 and 4 are compared, it can be seen that the simulation does model the system dynamics very well, and the Magnaplate bearing counterface does eliminate the effects of stiction. Also, Figure 3 demonstrates that the experimental results of Figure 4 can be duplicated by using an increasing velocity dependence for the dynamic friction.

Figure 5 shows the velocity dependence of the Magnaplate counterface. This curve was calculated from the acceleration data shown in Figure 4 by integrating the difference between the table and sled acceleration. The arrows on the curve indicate the integration path. The top part of the curve corresponds to the portion of Figure 4 where the table acceleration (dotted line) is increasing relative to the sled (solid line) just after breakaway.

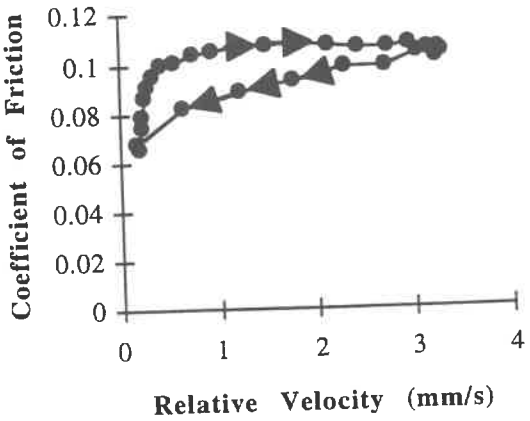

Figure 5: Range of dynamic friction.

This shows the dynamic friction increasing with respect to the relative velocity, much like in Figure 2. The maximum relative velocity between the sled and table occurs here at 3.5 mm/s, then the table decelerates relative to the sled. This corresponds to region of Figure 4 where the sled and table curve cross until they re-couple. The hysteresis in Figure 5 demonstrates that the frictional characteristics of an interface are dependent on whether the bodies are accelerating or decelerating relative to each other.

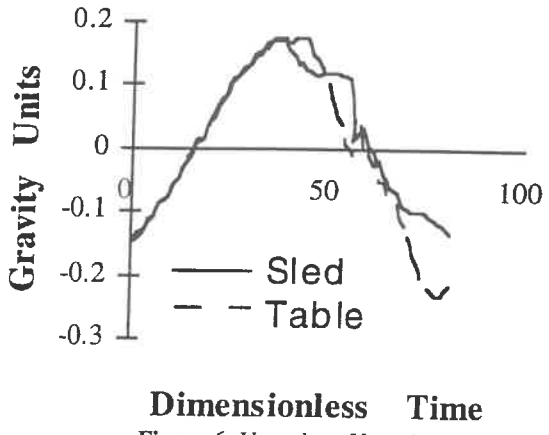

Figure 6: Vespel-on-Vespel

For comparison, the frictional properties of Dupont Vespel SP-211 were measured by sliding Vespel-on-Vespel. The friction event is shown in Figure 6. The sled acceleration curve has been overlaid on the table curve for comparison. The sled curve is a solid line and the dashed curve is the table. Initially, the curves are equal until the sled breaks free, at $\mu_{static} \cdot g$. The acceleration of the sled then drops to a virtually constant value $\mu_{dynamic} \cdot g$. A bearing material interface showing these characteristics can be described as a material with stiction. The values attained for this test yield μ_{static}=0.18 and $\mu_{dynamic}$=0.12 which agree well with the values given in the Vespel Properties Bulletin which are μ_{static}=0.20 and $\mu_{dynamic}$=0.12.

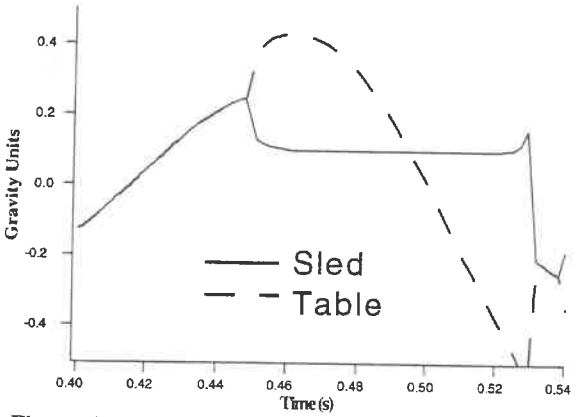

Figure 7: Simulated decreasing velocity dependence.

A calculated friction event with C = 5 is shown in Figure 7. The transition from breakaway friction to sliding friction is simulated as a decreasing function with relative velocity. This resembles the measured Vespel data of Figure 6 in that there is a distinct breakaway and a transition to constant sliding. The perturbation in the sled acceleration just as it stops sliding relative to the table is due to the assumption in the simulated dynamics that the breakaway friction is the same as the termination (of sliding) friction. The experimental results attained here indicate that this may not always be true.

Friction measurements were performed on a variety of interfaces, including traditional bearing interfaces (PTFE, disulfide), Diamond-Like Carbon (DLC), and common materials (steel, glass). The PTFE bearings, which are known to reduce stiction, were shown to have an increasing velocity dependence but the disulfide coatings had stiction. The DLC materials showed velocity dependence that varied with deposition parameters and composition.

SUMMARY

The scope of this study has been to measure and to characterize the frictional behavior of candidate bearing coatings. A unique tribotester was developed and modeled so that the frictional behavior of bearings surfaces could be characterized. It is important to note that the Vibrational Tribotester developed in this research measures the transient frictional behavior during breakaway and eventual coupling (sticking) of the sled and table system. In that regard, it is different from the conventional, steady state friction tests, for example pin-on-disc. The system is designed to provide a unique characterization of breakaway friction behavior under conditions simulating machine tool bearing surfaces. The measured acceleration(s) can be integrated to yield a profile of the velocity dependence of the interface. However, the accelerometer output must match for each time step to be completely accurate. In that regard, the integral of the acceleration up to steady-state, where the table acceleration curve crosses the sled curve, is the most reliable for interfaces with decreasing velocity dependence.

Non-Isotropy of Young's Modulus of Elasticity in Very Thin Metal Sheets

P.V.Pistecky
Delft University of Technology
Laboratory for Micro Engineering
2628 CD Delft, The Netherlands
email: p.v.pistecky@wbmt.tudelft.nl

Introduction

High precision devices used in research, development or production often require a very accurate spring action for their proper function. In many cases, very delicate thin metal foil springs must be applied to establish the necessary spring function. Very often these springs possess rather complicated shapes, usually as a result of space restrictions.

In the past three years, several types of thin foil springs have been implemented in devices and instruments designed by the Laboratory of Micro Engineering of Delft University of Technology. The NASA Gamma Ray Collimator[1] and the Ultra Sensitive Force Transducer for Biomedical Experiments[2] are two examples extensively using this type of springs. The typical thickness of the metal foils used in our devices ranges from 20 μm to 100 μm.

To design and calculate the characteristics of these types of thin springs, finite element analysis is often the only adequate tool to obtain sufficient accuracy. However, comparisons between calculated results and accurate laboratory measurements on real springs showed repeatedly considerable differences. After careful investigations it became obvious that the non-isotropy of Young's modulus of elasticity of applied thin metal sheets is most likely the reason for this mismatch.

For some practical reasons most of the springs used in our devices are made from stainless steel thin cold rolled sheets. Due to the cold rolled process and the need for high allowable stress of the spring material, the sheets apparently possess different material structure in the rolled direction and perpendicular to this direction. The material properties depend obviously very strongly on the length, orientation and number of crystals throughout the structure. The tensile strength of the thin stainless steel sheets (AISI 301) reaches a value of 2200 MPa for the thickness of 15 μm.

Material properties

Instrument designs very often require an accurate prediction of the component's behavior before the actual realization of the instrument itself. This is due to the fact that many scientific instruments are expensive, single piece, unique prototypes. For this reason, it is almost impossible to check the instrument properties by building a pre-prototype version of that instrument.

During the last five years our research group gained substantial experience in using the finite element method for an accurate prediction of mechanical properties of instrument parts, especially with respect to their mechanical stiffness. It is obvious that accurate calculations are only possible if all material properties are known with sufficient accuracy. If a material possesses a non-isotropic distribution. for example, of Young's modulus of elasticity, then this distribution is of great interest.

Measurement of the non-isotropy of Young's modulus of elasticity

As mentioned previously, the cold rolled metal sheets possess different material structure and therefore also different Young's modulus values in the rolled direction and in the direction perpendicular to the rolled direction. In the first approximation, it was reasonable to determine the Young's modulus values in only these two main directions.

For all measurement experiments it was necessary to have some suitable specimens. In most cases they were shaped as long narrow strips with a length axis along the rolled direction or perpendicular to it. All specimens used for our experiment were made by our precision metal etching technique. With this

manufacturing procedure it is possible to obtain shapes in the order of tens of millimeters with an accuracy within a few micrometers. Due to this dimensional accuracy, the tolerance of the specimen dimensions does not play any substantial role in the possible measurement errors. The etching technique has an important additional advantage of a stress-free manufacture.

To investigate the modulus values, different measurement methods had been used in the past two years. Initially, the measurements started with the strain gauge method, but this method failed for most of the thin foils due to the relatively large stiffness of the strain gauges.

The next method used in our investigations was the measurement of deflection of a cantilever spring tip loaded only with its own mass. Even with very simple means, it was possible to obtain rather accurate results that could be compared with the method of natural frequency described later. A discussion about the measurement results will be presented in an other paragraph.

Coil set of the rolled sheets

By using the method of cantilever beam deflection, it became obvious that the slight sheet curvature in the rolled direction, due to the coil set, can cause measurement errors. If the sheet curvature is perpendicular to the beam length axis, the moment of inertia of the beam cross section can reasonably be larger than that of a flat sheet. Therefore some calculations were made to establish the possible influence of this phenomenon. The only way to avoid this influence is by choosing the beam width which is small enough. Figure 1 gives some results of the ratio of the moments of inertia of curved and flat sheets. As the radii of the coil set in all cases were larger than 100 mm, a beam width of less than 1 mm will produce negligible measurement errors. The coil set problem applies also for the third method, the measurement of the first natural frequency.

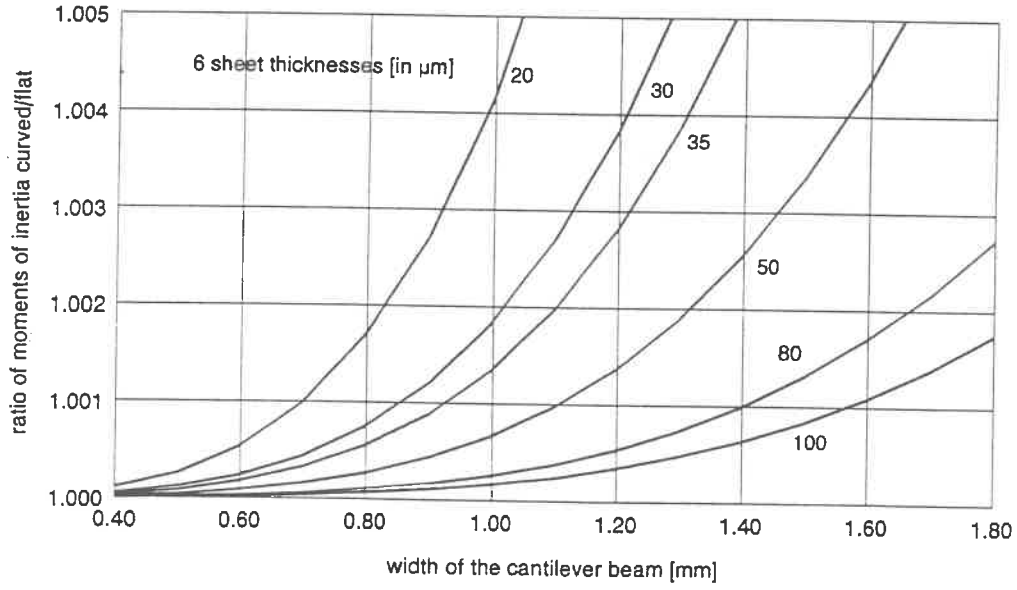

Fig. 1. Influence of the coil set of thin rolled sheets at the moment of inertia of cantilever beams. With a coil set of radius r ≥ 100 mm and beam width of ≤ 1 mm, the ratio of both moments is ≤ 1.004.

Measurement of the first natural frequency

The most promising method to determine the non-isotropy of Young's modulus of elasticity proved to be the measurement of the first natural frequency of long, specially designed cantilever springs (Figure 2). Their length axis was placed in the two main sheet directions, in the rolled direction and perpendicular.

The measurement of the first natural frequency of the cantilever springs has been performed for three different spring lengths and for six different foil thicknesses, all in both sheet directions. To obtain reliable results for each type of spring, five identical specimens were used for the measurement. For each specimen six successive values of natural frequency were recorded. A dynamic signal analyser along with electromagnetic initiation of the spring vibration has been used for these measurements.

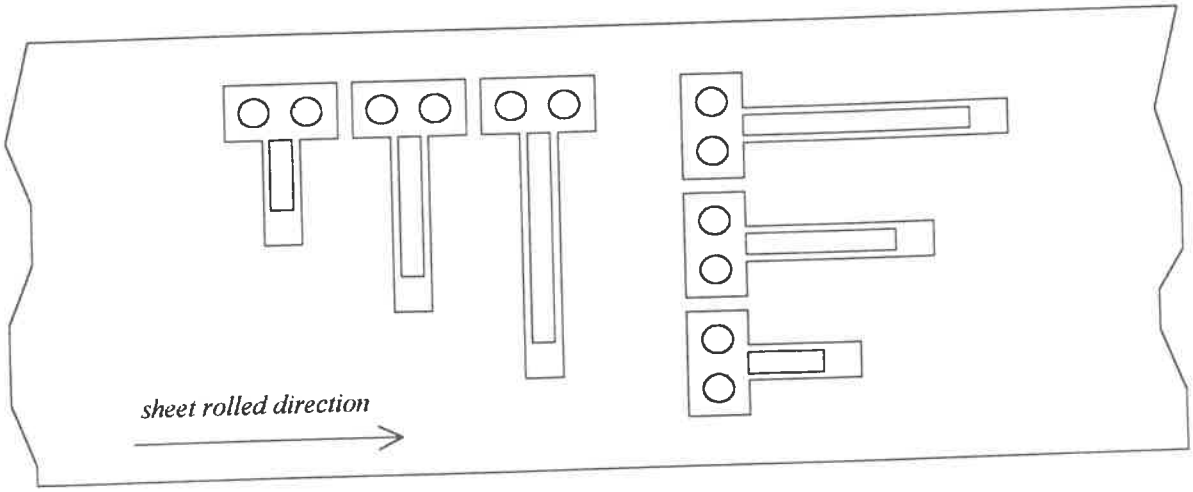

Fig.2. The actual size and orientation of the thin cantilever beam specimens used in the natural frequency measurement method.

Measurement results

The large amount of collected data was reduced by statistical methods to a small number of relevant values. The most reliable is the *ratio* of the two Young's moduli for the two main directions. These six values for each thickness are shown in Figure 3 along with the results of the previous method of bending deflection. With the latter method, three additional thicknesses were taken into consideration including a very thin sheet (15 μm) and a rather thick sheet (150 μm).

Examining the results, the overall trend is very obvious. The material structure following the cold rolled process shows a considerable non-isotropy of Young's modulus of elasticity. The value of the modulus in the direction perpendicular to the rolled direction is generally 1.2 times larger than the modulus value in the rolled direction. The thickness of the sheet plays an important role for the moduli ratio. The thinner the sheet the larger the difference of the Young's moduli is. There is also a remarkable correlation between the moduli ratio and the maximum tensile strength of the particular sheets. This correlation can clearly be seen in figure 3.

To help us understand Young's modulus non-isotropy, an extensive metallurgical analysis of the sheet specimens will be carried in the near future. The first investigations show very long (50 μm) and very thin (5 μm) crystals in the rolled direction. For the thin metal sheets it means that no more than ten crystals fill the entire sheet thickness.

Theoretical calculations

To support the investigations and to verify the measurement results, finite element modal analysis and two different theoretical calculations, effective dynamic mass method and transfer matrix analytical method, were performed to determine the first natural frequency.

These calculations are also necessary to determine the absolute value of Young's modulus of elasticity from the natural frequency measurements. The three calculation methods give slightly different results. The differences are up to 4%. However from our experience with ALGOR® finite element analysis

it is known that this method gives results with an accuracy on the average of 0.5%. Therefore these results are considered most reliable.

By using the finite element results, the average value of Young's modulus in the rolled direction is about 165 GPa and in the perpendicular direction 205 GPa.

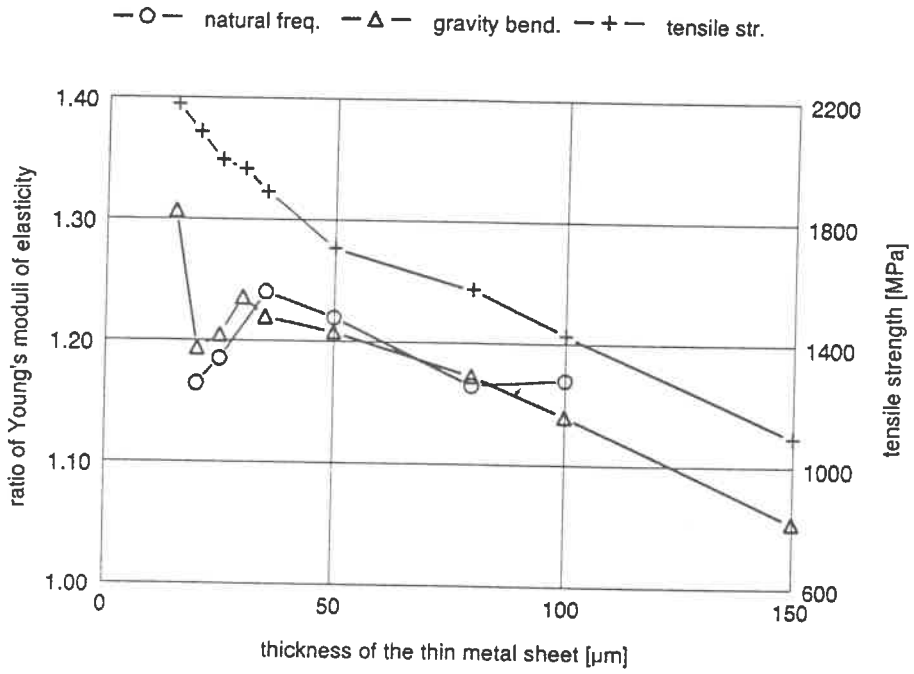

Fig.3. The results of the non isotropy measurements. Young's modulus in the direction perpendicular to the rolled direction is on the average of 1.2 times larger than in the rolled direction. The ratio of both moduli determined by the natural frequency method and the gravity bending method shows a strong similarity. There is a surprising correlation between Young's modulus ratio and the maximum tensile strength of the sheet material.

Conclusions

Accurate measurements of Young's modulus of elasticity of thin stainless steel sheets were performed using two different measurement methods. Differences in the modulus values up to 30% can be seen between the two main sheet directions, in the rolled direction and perpendicular to it. There is also a remarkable correlation between the moduli ratio and the maximum tensile strength of the sheet material.

References

[1] P.V. Pistecky, H.F. van Beek, H. van der Wulp: Development and Manufacture of Collimators for Gamma Ray Imaging, Precision Engineering Journal of the American Society for Precision Engineering, October 1994, Butterworth-Heinemann, Newton, MA, USA. ISSN 0141-6359.

[2] P.V. Pistecky, E. van Dop: Design of an Ultra Sensitive Force Transducer for Biomedical Experiments, Proceedings 9th Annual Meeting of the American Society of Precision Engineering, Oct. 2 - 8, 1994, Cincinnati, USA.

Acknowledgements

The author would like to thank Mr. Pavel Puchmajer from the Czech Technical University of Prague for his theoretical calculations and his stimulating discussion of the measurement results.

HIGH PRECISION X-Y-θ MICROPOSITIONING STAGE USING MONOLITHIC FLEXURE-PIVOTED LINKAGES

Jae-Wook Ryu, Dae-Gab Gweon
Dept. of Mechanical Eng., KAIST
Kusong-Dong, Yusung-Gu, Taejon, 305-701, Korea

A high precision X-Y-θ micropositioning stage has been developed as an aligner for optical reduction projection and electron beam exposure in lithography system. The micropositioning stage is designed to correct XY axes positioning errors and yaw error due to coarse positioning. In order to achieve large rotation about the θ-axis, the designed stage uses a special monolithic flexure pivoted mechanism. Three piezoelectric actuators with flexure-pivoted mechanical lever system amplifies the rotation range effectively. In addition, to improve immunity to temperature gradients, the micropositioning stage is designed rationally symmetric about the Z-axis. Open-loop characteristics of the micropositioning stage were measured by capacitance displacement transducers. Experimental results indicate that the micropositioning stage has 0.025 μm positioning accuracy over the total range of 38 μm and 30 μm along the X and Y axes, respectively. It also has 0.2 arcsec yaw accuracy over the total range of 350 arcsec about the θ-axis.

Introduction

Precise positioning is an essential technology for step and repeat lithography, particularly for optical reduction projection aligners and electron beam exposure systems. In such systems, a dual stage system consisting of a coarse and a fine table is used in order to achieve fast and accurate positioning.

Micropositioning stages utilizing piezo-driven flexure-pivoted linkages can have many advantages: negligible backlash and stickslip friction; smooth and continuous displacement; adequate for magnifying the output displacement of piezoelectric actuators; and inherently infinite resolution. Therefore, they are widely used in many different applications, such as scanning tunneling microscopes (STM)[1], step and repeat lithography[2], optical and electron microscopes[3], laser welding applications[4], *etc.* In this paper, a micropositioning stage is presented primarily designed for a fine table which moves precisely along the X, Y, and θ axes so as to correct positioning and rotation errors from a coarse table positioning. Particularly the yaw error from the coarse table is amplified as traveling along the XY axes, the proposed stage has large rotation capacity about the θ-axis.

In this paper, it is shown that the precision X-Y-θ micropositioning stage has a much larger rotation angle than parallel linkage type micropositioning stages[2]. In addition, some experimental results of the newly developed micropositioning stage are presented.

Micropositioning stage design

The stage design combines three piezoelectric actuators and monolithic flexure-pivoted linkages. To achieve a large rotation angle about the θ-axis, three input mechanism amplifies length change of a piezoelectric actuator by using flexure-pivoted mechanical lever system. Each one of the input mechanisms use a double compound flexure-pivoted lever system in order to minimize the lever length and maximize the mechanical displacement gain (Fig. 1). In addition, to improve immunity to temperature gradients, the stage is designed rationally symmetric about the Z-axis by placing each input mechanism 120 degrees apart

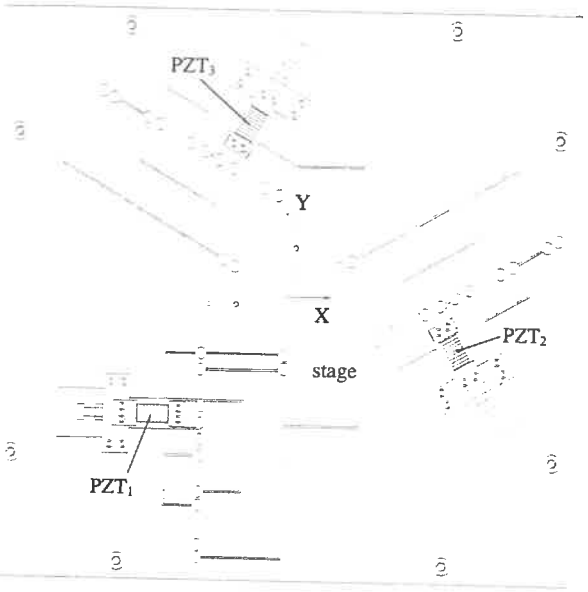

(a)

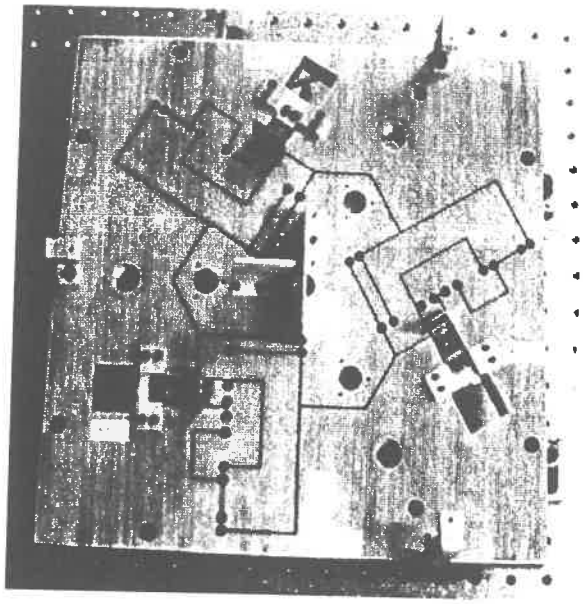

(b)

Fig.1 X-Y-θ micropositioning stage

about the Z-axis. The monolithic flexure-pivoted linkages are composed of typical notch flexure hinges which was machined from a $320\times320\times20$ mm metal blank. All flexure hinges have a hinge radius of 3.3 mm and a width of 20 mm. However, to maximize the rotation angle, minimum thicknesses of the hinge are varied from 0.5 mm to 2.9 mm while taking account of the allowable stress and the mechanical displacement gain of the input mechanism[5]. The stage was built from 7075-T6 aluminum alloy.

Each piezoelectric actuator is placed in a cutout actuator housing and preloaded with an axial force by pushing a bolt in order to be free from backlash. The piezoelectric actuator has dimensions of 10 by 10 by 18 mm and the rated maximum output displacement of 15μm/100V.

Experimental system configuration

Figure 2 shows the block diagram of the experimental system. The each command voltage from PC was converted to analog (0~10V) by a 12 bit D/A. And then the voltage was amplified approximately 10 times by using a power amplifier. Each piezoelectric actuator was driven independently. The open-loop displacement characteristics of the stage were measured with the use of six capacitance gages (Model 3890, ADE corp.) with 0.025 μm resolution. The relationship between input and output displacements for the stage was obtained by measuring the output displacements of the stage, translations along the X and Y-axis and rotation about the θ-axis, and the length changes of the piezoelectric actuators. Three gages, s_1, s_2, and s_3, were used in order to measure the output displacements of the stage. The other gages, s_4, s_5, and s_6, were used in order to measure the length changes of the piezoelectric actuators (Fig. 3).

Kinematic calibration

The relationship between input and output displacements for the stage should be known in order to move the stage to the desired position. From the some sets of measured input and output displacements, the relationship is obtained by using the following manner.

Suppose the relation is written in the form:

$$\boldsymbol{x}_i = \boldsymbol{T}_{io}\,\boldsymbol{x}_o \qquad (1)$$

where, $\boldsymbol{x}_i = [\ u_1,\ u_2,\ u_3\ ]^T$ are the length changes of the piezoelectric actuators, $\boldsymbol{x}_o = [\ X,\ Y,\ \theta\ ]^T$ are the output displacements of the stage, and $\boldsymbol{T}_{io}$ is the transformation matrix (3×3) from the output displacements to the input

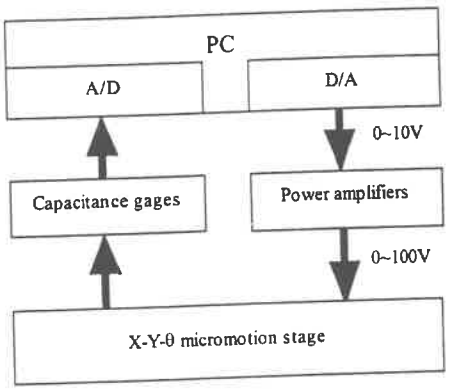

Fig.2 Block diagram of the stage system

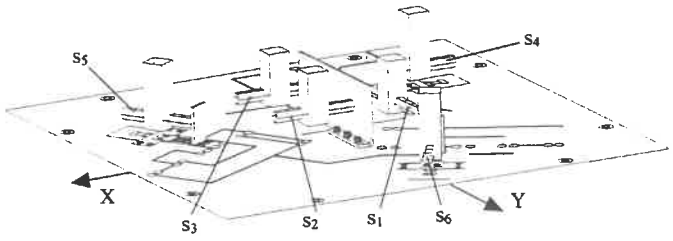

Fig.3 Schematic diagram of measurement system

displacements, respectively. From Eq. (1), the n sets of measured input and output displacements should satisfy the following relation:

$$\underset{(3\times n)}{X_i} = \underset{(3\times 3)}{T_{io}} \underset{(3\times n)}{X_o} \tag{2}$$

where, $X_i = [\, x_i^{\,1},\ x_i^{\,2}, \cdots,\ x_i^{\,n}\,]$
$X_o = [\, x_o^{\,1},\ x_o^{\,2}, \cdots,\ x_o^{\,n}\,]$

From Eq. (2), T_{io} can be found from the measured results of X_i and X_o experimentally.

$$T_{io} = X_i\, X_o^{\,T}\, (\, X_o\, X_o^{\,T}\,)^{-1} \tag{3}$$

From the obtained T_{io}, we can find the required length changes of the piezoelectric actuators to move the stage to the desired position.

In like manner, the transformation matrix from the input displacements to the command input voltages are obtained. That is,

$$T_{vi} = V\, X_i^{\,T}\, (\, X_i\, X_i^{\,T}\,)^{-1}$$
$$V = [\, v^1,\ v^2, \cdots,\ v^n\,] \tag{4}$$

where, $v = [\, v_1,\ v_2,\ v_3\,]^T$ are the command input voltages from PC to D/A.

Experimental results and discussions

Figure 4 shows the length changes of the piezoelectric actuators and the corresponding output displacements of the stage, when the command input voltages for driving piezoelectric actuators, PZT_1, PZT_2, and PZT_3, are all the same. At this driving condition, ideally, it is expected that the length changes of the piezoelectric actuators, u_1, u_2, and u_3, are all the same. Therefore, the stage will rotate about the θ-axis only. However, as can be seen from Fig. 4, experimental results indicate that the length changes of the piezoelectric actuators are somewhat different. Therefore, position errors, X and Y translations, are introduced. The different

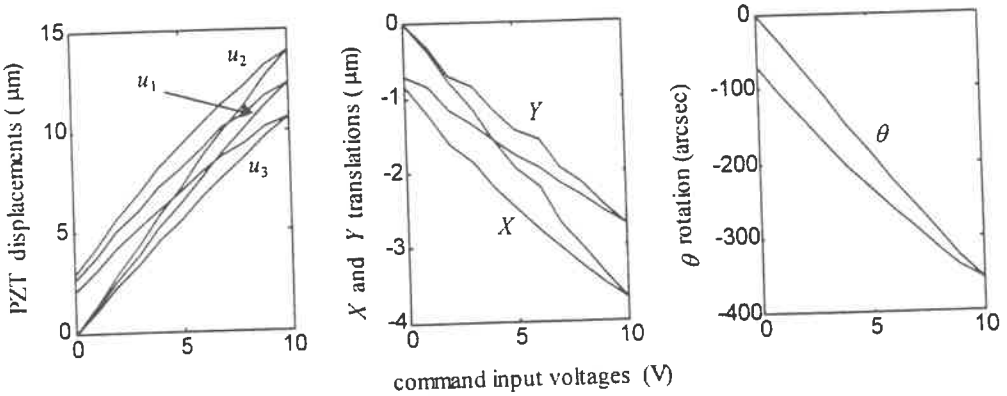

Fig.4 Length changes of the piezoelectric actuators and the output displacements of the stage, when the command input voltages for driving PZTs are all the same

length changes of the piezoelectric actuators are due to the manufacturing tolerance of the stage, the different preload and rated maximum output displacement of each piezoelectric actuator, and the different electrical gain of each power amplifier. The hysteresis of piezoelectric actuator is shown in Fig. 4.

The interference characteristics of each input are shown in Fig. 5. When PZT_1 is driven alone, small values of u_2 and u_3 are occurred in proportion to u_1. Because the stage is symmetric, similar results are obtained when PZT_2 and PZT_3 is driven alone, respectively. The interference ratio is below 5%. This means that each piezoelectric actuator is free from the other two piezoelectric actuators.

The open-loop step responses of the stage are shown in Fig. 6 and 7. If the desired output position of the stage is given, the command input voltages are calculated using T_{io} and T_{vi}, which had been found from Eqs. (3) and (4), respectively. Then, the calculated input voltages are commanded from PC, the stage will move to

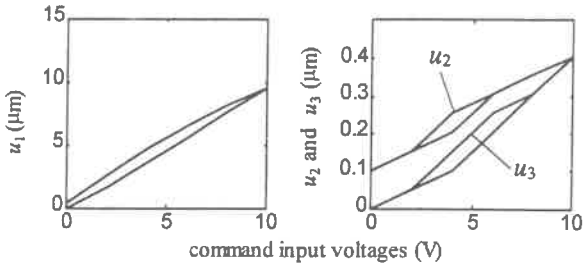

Fig.5 Input interference

the desired position with some open-loop errors. In order to verify the input-output relationship of the stage, step responses of the stage are experimented along the X, Y, and θ-axis, respectively. As can be seen from Fig. 6, the stage can be moved along the desired direction with small parasitic errors. Figure 7 shows open-loop step responses, when the desired step sizes are the resolution of 0.025 μm along the X and Y-axis and 0.2 arcsec about the θ-axis, respectively.

Table 1 shows the total ranges of output

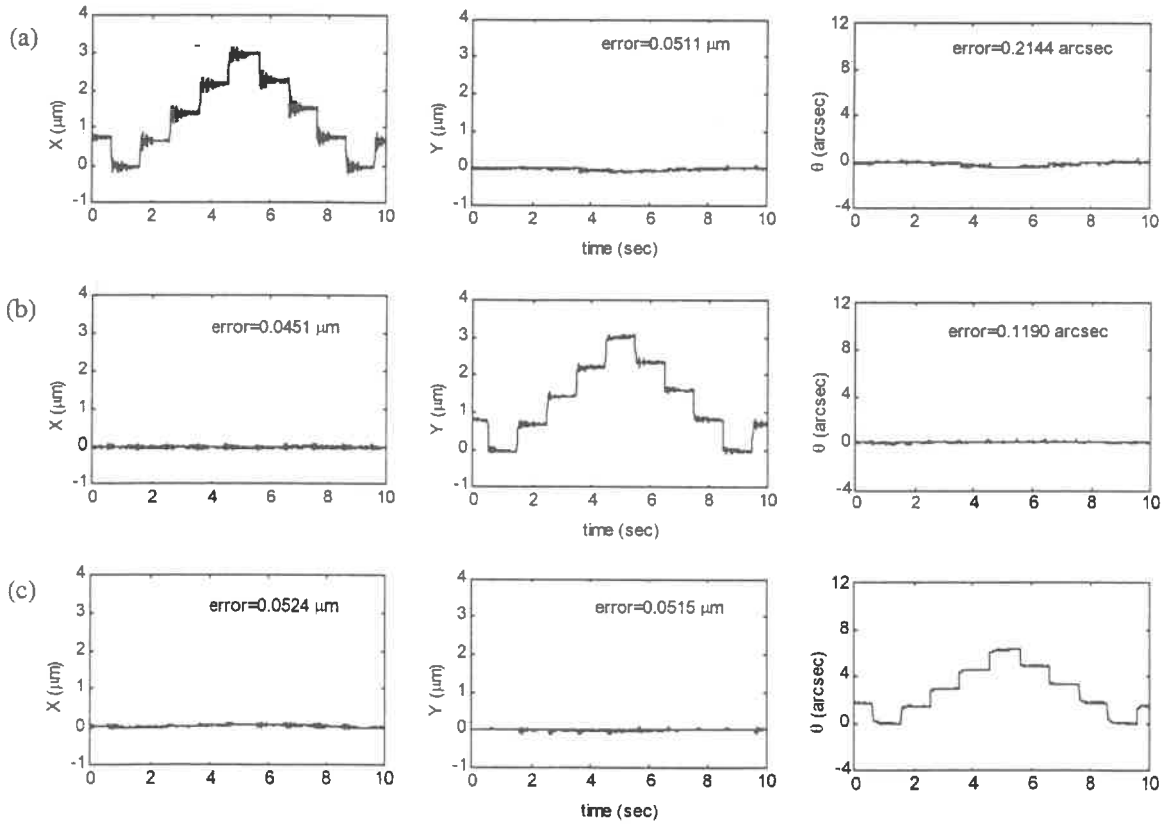

Fig.6 Step responses of the stage along (a) X, (b) Y, and (c) θ-axis (open-loop control)

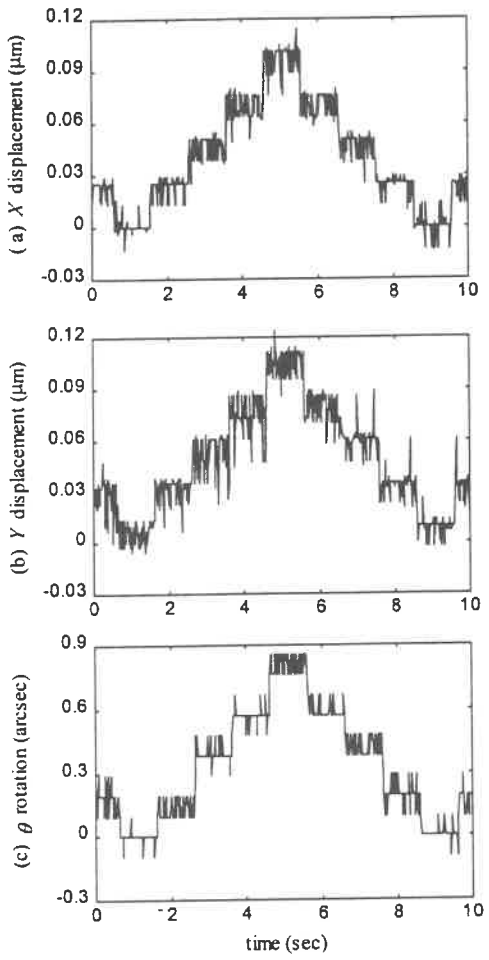

Fig.7 Resolution of the stage

displacements and the resolution along the X, Y, and θ-axis. The stage has 0.025 ㎛ positioning accuracy over the total range of 38 ㎛ and 30 ㎛ along the X and Y-axis, respectively, and 0.2 arcsec yaw accuracy over the total range of 350 arcsec about the θ-axis. Especially, the total range about the θ-axis is more than 10 times larger than parallel linkage type micropositioning stages[2].

Conclusions

In this study, a high precision X-Y-θ micropositioning stage has been developed for use of a fine table which corrects the XY axes positioning errors and the yaw error due to a coarse table and its open-loop characteristics have been experimented.

The developed micropositioning stage has 0.025 ㎛ positioning accuracy over the total range of 38 ㎛ and 30 ㎛ along the X and Y-axis, respectively. It also has 0.2 arcsec yaw accuracy over the total range of 350 arcsec about the θ-axis, which is about 10 times larger than that of the parallel type micropositioning stages.

Table 1 The total ranges of output displacements and the resolutions

		ranges	resolutions
X	(㎛)	38	0.025
Y	(㎛)	30	0.025
θ	(arcsec)	350	0.2

Acknowledgments

This work was funded by Korea Science Foundation (KOSEF) under grant 94-0200-09-01-3. The authors wish to thank KOSEF for their financial support.

References

1) E. Furukawa, M. Mizuno, and T. Hojo, "A Twin-Type Piezo-Driven Translation Mechanism", Int. J. Japan Soc. Prec. Eng., Vol. 28, No. 1, Mar. 1994, pp. 70-75.

2) S. Moriyama, T. Harada, and A. Takanashi, "Precision X-Y Stage with a Piezo-driven Fine-table", Bull. Japan Soc. of Prec. Engg., Vol. 22, No. 1, Mar. 1988, pp. 13-17.

3) F. E. Scire and E. C. Teague, "Piezodriven 50-㎛ range stage with subnanometer resolution", Rev. Sci. Instrum., Vol.49, No.12, Dec. 1978, pp. 1735-1740.

4) R. Yang, M. Jouaneh, and R. Schweizer, "Design and characterization of a low-profile micropositioning stage", Prec. Eng., Vol. 18, No. 1, Jan. 1996, pp. 20-29.

5) D. G. Gweon, *Development of Ultraprecision Positioning System Using PZT Actuators*, KOSEF research report, KAIST, 1996 (*in Korean*).

Innovations in the design and development of ultraprecision machines

Lightweight and ultrastiff single point diamond turning machine with submicron machining accuracy

J.P.M.B. Vermeulen, P.C.J.N. Rosielle, P.H.J. Schellekens
Precision Engineering Group
Department of Mechanical Engineering
Eindhoven University of Technology (the Netherlands)

Abstract

Main structural components of most existing single point diamond turning (SPDT) machines are made of granite, and conventionally, steel is applied in hydrostatic slideways. The structural design of moving parts of SPDT machines may be substantially improved, with regard to stiffness and dynamic behavior, using ceramic laminate materials with high specific stiffness (E/ρ). Applying readily-obtainable alumina ceramic tiles in a plate frame type SPDT machine - which is currently under construction - the slide's mass is reduced with a factor of three compared to an equal slide construction of steel or aluminum with the same stiffness.
A statically determinate and thermomechanically stable machine design significantly improves reproducibility. As a result, additional software compensation of residual errors, necessary to meet currently required submicron machining accuracy, is limited.
Based on existing compensation techniques, an infinitely stiff, reproducible aerostatic thrust bearing was developed. Direct drive systems are used for the slides and the main spindle, in order to eliminate a series of mechanical compliances as well as friction forces and hysteresis.
Innovations in this design are not confined to SPDT machines alone, but can readily be transferred to ultraprecision machines and instruments more generally.

Keywords: Ultraprecision machines, ceramic laminate materials, infinitely stiff aerostatic thrust bearings, direct drive systems

Introduction

In line with advances in precision manufacture, accuracies required in new industrial products continue to be demanding. Ultraprecision parts in particular, such as optical mirrors, molds for injection molding, and aerostatic bearings, are realized outstandingly through single point diamond turning (SPDT). In addition to non-ferrous metals and plastics, recently ferrous metals were machined with single point diamond tools, using an ultrasonic cutting device.

As a result of the need for extension of the ultra precision machining capacity in the Eindhoven University's Engineering and Design Facilities, an SPDT machine was designed by the

Eindhoven Precision Engineering Group [Vermeulen, 1994]. The machine, that is currently under construction, differs significantly from conventional SPDT machines.

Demands on slide constructions in high precision machines can be derived from the stated positioning accuracy. Single point diamond turning however, is more than a point-to-point positioning process. Each deviation from the diamond tool's desired movement, for example as a result of finite stiffness or thermal instability of the machine, will be directly depicted on the workpiece.

This paper briefly discusses three topics in our SPDT machine design, which highly determine its overall behavior. After a short description of the machine, the application of ceramic laminate materials, aerostratic thrust bearings and direct drive systems is highlighted.

SPDT machine design

Machining accuracy is closely related to predictability and especially reproducibility. The most cost-effective way to achieve this, is to create a statically determinate and thermomechanically stable machine design. In this way, minimum tolerances in the manufacture of the machine as well as minimum demands on conditioning of ambient temperature are required.
The objective was to attain accuracies in form and size of better than 0.1 μm over 100 mm, by a sound mechanical design. The effort to set up software compensation is significantly reduced, for a system with good inherent accuracy.

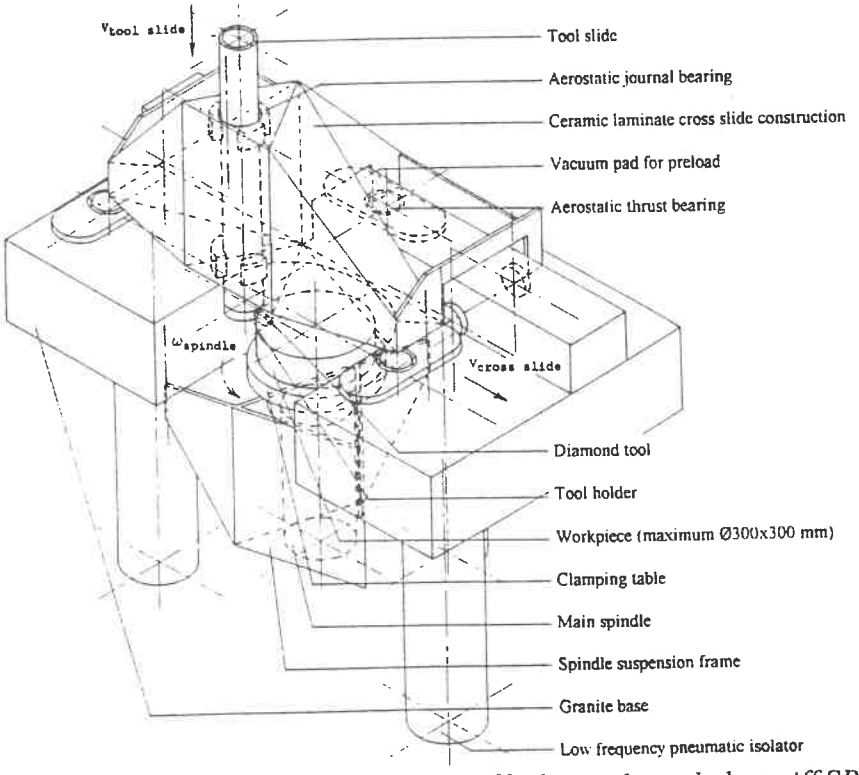

Figure 1. Schematic representation of lightweight and ultrastiff SPDT machine, currently under construction.

In figure 1, a schematic representation of the SPDT machine is shown. A turret configuration was chosen, since workpieces up to ∅300x300 mm cause an inadmissible deflection when mounted in a classical, horizontal set-up. The cross slide, that consists of a plate frame structure, runs on a granite guide way. Using a plate frame type slide construction, the utilization ratio of the applied material is optimized, giving a very favorable force transmission, and therefore, a lightweight and stiff design. Underneath the guide way, the main spindle is mounted in a triangular suspension frame. Thereby, the centerline of the workpiece remains stable, independent of room temperature fluctuations. The granite base is supported by three low-frequency pneumatic isolators (1 Hz) in order to eliminate disturbing vibrations. Automatic height-leveling systems are built in for varying load conditions (slide travel).

Ceramic laminate slide construction

When machining non-ferrous metals and plastics, diamond turning forces are very small [Oomen, 1992]. Therefore, in the design of an SPDT machine's slide construction, it is the material's modulus of elasticity (stiffness) rather than the admissible stress, on account of which a material should be selected.
A considerable mass of a slide construction causes high inertial forces as well as a substantial heat dissipation in the slide's driving system. Another reason to reduce the slide's mass is the increase of its natural frequency $\omega_e = \sqrt{(c/m)}$.
For plate frame type slide structures, both mass and stiffness are linear proportional to the sheet thickness. Therefore, optimizing the stiffness per kg (c/m) for a certain geometry constitutes to select a material with a high specific stiffness E/ρ [m^2/s^2]. In slide constructions of most existing ultra precision machines, conventional construction materials, like steel, aluminum and granite are applied. For the high specific stiffness of massive ceramics (factor 3.1 to 6.7 times E/ρ of steel, aluminum or granite), applying these might reduce the slides's mass significantly. The obtainability however, of standardized ceramic parts is limited. Only for Al_2O_3-ceramic, plates and sheets are standard obtainable and therefore priced reasonably.

Vibrations, caused by slide movements or coming from the environment, will influence the slide's position accuracy. Whilst the specific stiffness of massive ceramics is good, its vibration damping is bad. Therefore, in ceramic structures for precision engineering applications, a laminated build-up is highly preferable. The glued joints are barriers for vibrations, so that vibration damping is increased considerably.
Another advantage of a laminated build-up is the greater designer's freedom opposite to massive ceramic structures. Depending on the way of manufacturing, ceramic parts may have many internal defects. They also show a lot of shrinkage and deformation, in consequence of transformations at high temperature sintering. Therefore, in the design of massive ceramic parts, a uniform sheet thickness, relatively simple structures and the absence of sharp edges, and point or line forces are prescribed. For alumina ceramic plates with dimensions of typically 500x500 mm a minimum thickness of 25-50 mm is necessary. Complex ceramic plate frame structures with sharp included angles can therefore better be build out of prefabricated laminated plates. The Al_2O_3-ceramic laminate material has been patent applied for [Rosielle, 1996].

Experiments on a 5-layer Al_2O_3-ceramic laminate tensile strip, displayed an E/ρ factor of $75 \cdot 10^6$ m^2/s^2. That is a factor of 2.9 and 2.8 more than an aluminum or steel tensile strip respectively with equal mass.
In parts made of a homogeneous and isotropic material, the utilization ratio of the applied material μ [-] characterizes the stress distribution over the particular part [Hoek, vd, 1989]. If the stress is equal within the entire material, for example in a uniformly loaded massive tensile strip, μ=1, and for bending of a sheet of rectangular section by a constant moment, $\mu = {}^1/_3$.
From calculations on the ceramic laminate material, the number μ appeared to depend on the number of layers N. The in-plane stiffness of a multilayer ceramic laminate structure (N large), approaches the stiffness of the massive ceramic material [Vermeulen, 1996].
At present, the SPDT machine's cross slide construction is being build-up out of alumina ceramic laminates.

Aerostatic thrust bearings

Next to hydrostatic bearings, aerostatic bearings are commonly used in ultraprecision machines for their negligible friction and hysteresis. Until now, as air is highly compressible in comparison with oil, aerostatic bearings determine the overall obtainable machine stiffness.
In literature, a lot of investigation work on aerostatic bearings can be found. However, as different values of bearing parameters were chosen in different publications, it is very difficult to reserve a fair judgment about specific bearing features among different types.

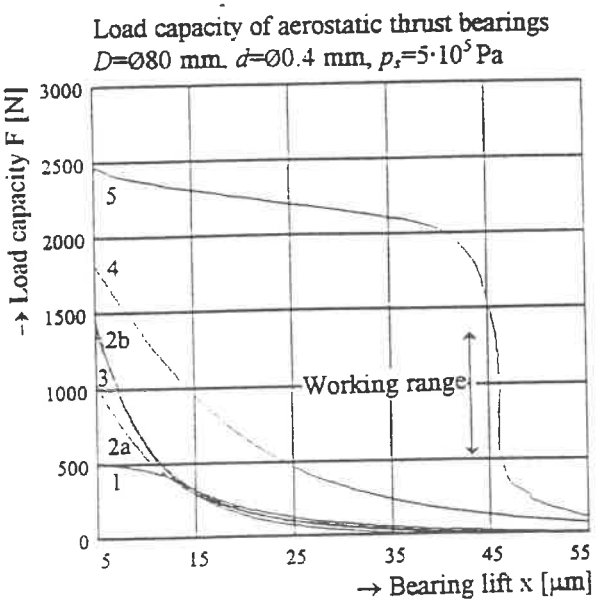

Figure 2a. Measured load capacity of aerostatic thrust bearings.

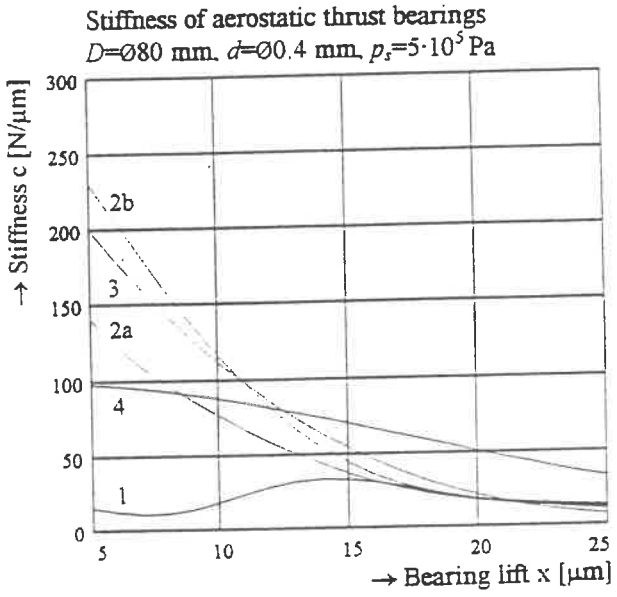

Figure 2b. Calculated stiffness of aerostatic thrust bearings.

1. Inherent parallel gap shape
2a. Conical gap shape, h_e/r=9.0µm/36mm
2b. Conical gap shape, h_e/r=27.6µm/36mm
3. Biconical gap shape, $h1_e/r1$=14.2µm/28mm, $h2_e/r2$=9.8µm/7.8mm
4. Porous
5. Compensated with centrally supported membrane

Therefore, five different aerostatic thrust bearings were made in-house, tested and mutually compared. The main proposal was to get a survey of stiffness and load capacity. Next to conventional parallel and conical gap shape bearings, biconical as well as porous bearings were investigated. The bearings all have an outer diameter D=80 mm, a central restrictor with d=0.4 mm (except for the porous bearing), and are supplied to an equal pressure $p_s=5\cdot10^5$ Pa.
A compensated aerostatic bearing with centrally supported membrane was made as well. Here, the bearing gap geometry is used as a controlling element. The convergence of the gap in the flow direction is forced to become an increasing function of the external load. Provided that the membrane deflection equals exactly the bearing displacement as a result of the compression of air in the bearing gap, an infinite bearing stiffness can be obtained [Blondeel, 1976], [Bryant, 1986], [Snoeys, 1987].
From the measured load capacity curves (about 500 data points), shown in figure 2a, the stiffness curves are calculated by means of a polynomial curve fit (see figure 2b). Results are conveyed in table 1. As the flatness of a guiding surface is typically of the order of 1 μm, a minimum air gap of 5 μm is used.

Bearing type D=Ø80 mm d=Ø0.4 mm $p_s=5\cdot10^5$ Pa	Remarks	Maximum stiffness [N/μm]	Air gap for maximum stiffness [μm]	Load capacity for maximum stiffness [kN]	Maximum load capacity [kN]
Inherent parallel gap shape		32	14	0.3	0.5
Conical gap shape	h_c/r=9.0μm/36mm	136	5	1.0	1.0
	h_c/r=27.6μm/36mm	230	5	1.5	1.5
Biconical gap shape	$h1_c/r1$=14.2μm/28mm $h2_c/r2$=9.8μm/7.8mm	200	5	1.4	1.4
Porous	Graphite UT6ST porosity 17%	99	5	1.8	1.8
Compensated with centrally supported membrane		∞	5-15	0.5-1.3	1.5

Table 1. Stiffness and load capacity of investigated aerostatic bearings.

For the infinite stiffness of the compensated bearing, a reproducible design was made and utilised in the SPDT machine.

Direct drive systems

In high precision machines, a wide range of drive systems is applied. Lead screw drives have considerable friction and hysteresis. As a result of the over determination, the accuracy of a lead screw drive is determined by a statistic mean of many contacts. Friction wheel drives in contrary, can have a prescribed level of preload at the wheel contacts, and therefore, its behavior is more predictable and reproducible.
Linear direct drive systems have no contacts and therefore no friction at all. A series of mechanical compliances is eliminated. The drive's stiffness is determined in the closed loop

servo system and depends directly on the resolution of the measurement system. As the application of linear direct drive systems in combination with linear optical encoders in SPDT machines is relatively new, its smoothness of motion was tested at different speed rates. Using sinusoidal software commutation and position feedback with 5 nm resolution zerodur scales, the slide's position error signal is restricted to about 0.1 μm. Heat dissipation in the applied linear motor is less than 1 W.
Next to the cross slide and the tool slide, a direct rotational drive system is applied for the main spindle. For its very small ripple torque as a result of the great number of turns, a disk armature coil motor is used. In order to eliminate the noise, originating from the motor's ball bearings, the latter were removed. Instead, the rotor is fixed directly to the spindle, which has an aerostatic bearing system.

Conclusions

Machining accuracy highly depends on stiffness, reproducibility and stability, keypoints in the development of a new, universal SPDT machine.
Applying alumina ceramic laminate materials, the slide's stiffness to mass ratio is increased with a factor of three, compared to conventional construction materials. Infinitely stiff aerostatic thrust bearings eliminate the determining compliance of the machine, and significantly reduce the slides' friction and hysteresis. The latter two are further reduced, using direct drive systems.
As a result, the amount of additional software compensation, necessary to meet submicron machining accuracy, is significantly reduced.

References

Blondeel, E., Snoeys, R., Devrieze, L., 1976, Aerostatic bearings with infinite stiffness, In: Annals of the CIRP, 25(1).

Bryant, M.R., Velinsky, S.A., Beachley, N.H., Fronczak, F.J., 1986, A design methodology for obtaining infinite stiffness in an aerostatic thrust bearing, In: Journal of mechanisms, transmissions, and automation in design, Transactions of the ASME, 86-DET-32.

Hoek, W. v.d., 1989, A mechanical designers case book, Philips CFT Report 59/85, translation of 'Des Duivels Pentenboek' (D.D.P.).

Oomen, J.M., Eisses, J., 1992, Wear of monocrystalline diamond tools during ultraprecision machining of nonferrous metals; In: Precision Engineering, 14(4), pp. 206-218.

Rosielle, P.C.J.N., Vermeulen, J.P.M.B., Reker, E.A.G., 1996, Laminaten, vervaardigd uit epoxy-verlijmde, dunne Al_2O_3-keramische tegels, geschikt voor sledeconstructies in precisietoepassingen (Laminates, made of epoxy glued, thin Al_2O_3-ceramic tiles, suitable for slide constructions in high precision applications), License request no. 1002369 (in Dutch).

Snoeys, R., Al-Bender, F., 1987, Development of improved externally pressurized gas bearings, KSME Journal, 1(1), pp. 81-88.

Vermeulen, J.P.M.B., 1994, Een ontwerp van een diamantdraaibank met submicron bewerkings-onnauwkeurigheid, (Design of a diamond turning machine with submicron machining inaccuracy), Masters thesis (in Dutch), Eindhoven University of Technology (the Netherlands).

Vermeulen, J.P.M.B., 1996, Development of a lightweight and ultrastiff single point diamond turning machine with submicron machining accuracy, Mechatronics post-masters design thesis, Eindhoven University of Technology (the Netherlands).

Straightness Errors of Rectangular Beams Caused by Ambient Air Temperature Gradients

Kevin L. Wasson[1]
Alexander H. Slocum[2]
John H. Lienhard V[3]

In a typical industrial building, vertical temperature gradients within the air may be 2°C per meter or greater, due to the tendency of air to stratify. Consequently, a beam with its length oriented horizontally will experience warping as its top becomes warmer than its bottom. The degree of warpage will depend upon the beam geometry, how it is fixtured, and its material properties. Our calculations show that this effect is important in applications such as coordinate measuring machines where micron-level precision is required, particularly when ceramic materials are used because they have very low thermal conductivities. Our work investigates the specific case of thermal straightness errors of rectangular beams caused by ambient air temperature gradients. Numerical simulations of heat conduction are used to evaluate the effect of beam geometry and material properties on beam warpage. These simulations are performed using experimentally-determined heat transfer coefficients applied to the beam surfaces and calculating the two-dimensional temperature field. Transient simulations are used to investigate beam sensitivity to changes in ambient temperature. Case studies are presented which illustrate the effect of beam material on thermal stability. Our results show that beams made of low-conductivity, low-expansivity ceramics can have considerably higher steady-state thermal deflections than similar beams made of high-conductivity, high-expansivity metals. Ceramic beams are less sensitive to fluctuations in ambient temperatures, however, because their thermal time constants are generally very high. The simulations are also used to investigate the potential advantages of using various insulating layers of materials to thermally isolate beams from their surroundings, and reduce thermal errors. A novel method is presented in which a layer of insulation followed by a thin layer of high-conductivity metal such as aluminum is used to reduce the thermal warpage by over an order of magnitude. Although this work presents only numerical simulations that have not been verified with experimentation, we believe that the work is valuable at least qualitatively because it improves our understanding of the thermal problems that are present in precision machines. In particular, the results representatively demonstrate that using materials with lower thermal expansivities does not always lead to lower thermal errors.

Key Words: thermal errors, thermal stability, ceramics

[1]Aesop, Inc. Bow, NH 03304.

[2]Alex & Britt d'Arbeloff Professor of Mechanical Engineering, M.I.T. Precision Engineering Research Group.

[3]Professor of Mechanical Engineering, Warren M. Rohsenow Heat and Mass Transfer Laboratory, M.I.T.

Using Chebyshev Norms for Estimating Machine Tool Error Parameters

Hooman Tajbakhsh, DOE Graduate Research Fellow
Zainul Abadin, Graduate Research Assistant
Placid M. Ferreira, Associate Professor *

University of Illinois, Department of Mechanical and Industrial Engineering, Urbana IL 61801

August 28, 1996

Abstract

Numerically controlled machine tools use their structure as a reference frame for monitoring and controlling the position of the cutting tool. The tool positioning accuracy and, eventually, the accuracy of parts machined (if other sources of errors are not overwhelming) are thus dependent on the accuracy of this reference. Manufacturing and assembly are known to leave behind substantial errors in this reference frame and quasistatic effects (thermal and flexural) can cause significant changes in these errors [10, 7, 3, 5, 12, 9, 8]. The problem of characterizing and compensating these errors is thus one of immediate importance.

A good deal of research has been reported on the modeling of these errors [4, 1, 11, 6, 8] and, given an adequately parameterized model, the production of compensated tool motion. Scant attention has been paid to the identification of model parameters and it would not be far from the truth to state that least squares has been the universally used criterion for identifying model parameters from observations. That is, parameters are identified for an error model so that the sum of squares of the difference between the actual machine errors and model predictions are minimized. Thus, for a machine using a model developed with such parameters and visiting a number of points in its workspace, nothing can be said of its accuracy at any one point. All that can be said is that if the sample of points visited represents an unbiased sample of the workspace, the mean squared errors of the machine at these points is minimized.

*Author for Correspondence

A part produced by an NC machine-tool will be evaluated, not on the basis of the average of all points on a machined feature, but on the basis of every point on a machined feature meeting a said tolerance criterion (refer to ANSI Y14.5). Similarly, the accuracy of an inspection task performed on a CMM does not depend on its average accuracy across the workspace but on its accuracy at the point at which it performs the task. Unfortunately, estimating model parameters by using the least squares criterion does nothing to minimize or bound the error or discrepancy between the model and observations at a single point. In fact, it might trade the discrepancy at a small subset of points to obtain a better average performance. The volumetric errors resulting from such compensation are thus unevenly distributed across the workspace and this effect is magnified in the event of the model being inadequate, resulting a in 'sweet spot' in the work volume where the model performs well and large errors outside this small region in the workspace.

One approach to overcome such problems is to choose a different criterion for identifying the model parameters. Estimating model parameters by minimizing the maximum difference between observed errors and those predicted by the model, the classical Chebychev or L_∞ norm [2], takes care of the problems mentioned above. Instead of trading off prediction errors at individual observation points to improve the mean square error, it reins in the large prediction errors, thus attempting to equalize the prediction error across the workspace. An end product of such approach is a tight bound on the maximum prediction error at all observation points and, assuming that the observation set properly characterizes the workspace, a close estimate of the worst case performance across the workspace. From a practical point of view, such a parameter estimation scheme would be important for a) compensation schemes on machines executing different and unpredictable work cycles (and hence using different parts of the workspace in no particular pattern) as those functioning in a FMS and b) acceptance testing of a machine tool, i.e., characterizing its best possible worst volumetric error.

Least squares criterion penalizes the larger errors more than the smaller ones because the error terms are squared. It is mathematically convenient, but it can still leave behind large prediction errors at some observation points if it finds a sufficient number of other observations points to offset this in a mean squared sense. The L_∞ norm also known as the Chebychev's norm is only concerned with the absolute value of the maximum error. While not as convenient in usage as least squares, it is particularly important in establishing worst-case behavior and could prove useful in (i) acceptance testing of machine tools, and (ii) software error compensation of general-purpose machine tools. Given an adequate sample of observation points, in machine tool applications, this criterion could guarantee that the maximum error across the workspace does not exceed some value.

The error model we use in this paper is one developed in this program of research and reported in [8, 10, 7]. The error model describes how the components of the error vector are related to structural errors of the links and transmission errors of the joints of the kinematic scheme of the machine. Using the link and joint transformation model for a serial mechanism, the kinematics of the machine-tool are modeled using a series of alternating fixed and moving co-ordinate frames. Next, each link transformation (which models the constant co-ordinate

transformation between the two joints connected by the link) is given six degrees of freedom to model the errors in the geometry of the represented link. The model contains 17 linearly independent parameters.

The performance of the parameter estimation techniques (least squares and Chebychev's linear program) are compared based on experimental results. Lacking an absolute means of measuring (a sufficiently accurate calibration artifact) errors in a machine tool's workspace, we use the measurements of an artifact in the 'cold state' of the machine as a reference. By taking the machine through a thermal cycle (exercising all its axes), we get the quasistatic effects to change the errors of the machine and observe the ability of our models to track these changes in (instead of the absolute) errors. An artifact with 27 optimally located points along with a 3 DOF probe is used to measure the errors in the x, y, and z directions. The probe has a resolution of 0.25 microns with 1 micron repeatability. A total of eight measurement sets were collected. Each of these measurement sets give rise to 78 independent observed errors at a particular thermal state of the machine. We then use these observations to study the model parameters using least squares and linear programming approach.

The Chebychev's fit shows that the model explains the errors in the workspace under the thermal conditions after 9.56 hrs of heating to within a maximum error of 0.000146 inches while the least squares fit has a maximum value of 0.000186 inches (The maximum observed errors were around 0.0027 inches). Both models perform well but the results reflect about a 25% improvement in terms of the maximum prediction error if the Chebychev's fit is used to estimate the parameters of the error model. It is seen, as expected, that the RMS error for the least squares estimates is better that the Chebychev, but is extremely small or even negligible for both.

In the next liner program, the entire eight set of experiments are used for the constraints of the linear program. The eight sets of experiments give rise to 1248 constraints. These results shows that there exists a set of parameters that optimizes for the entire work-cycle (or temperatures) to produce a maximum of 0.000776 inches compared to a 0.000952 inches for the least squares solution. It is again clear that the LP fit provides a better solution in terms of the maximum error than least squares. However, this performance (in terms of lower maximum error) might be inadequate for a compensation scheme.

When the operation of a machine involves repetitive work-cycles, it is possible (and useful) to identify a model with time varying model parameters. The time factor is incorporated into the system. This addition to the parameters (i.e., time dependent components) essentially allows the system increased degrees of freedom and therefore better solutions is expected. This system was also solved using all eight sets of measurements simultaneously, but ensuring that their time of collection was appropriately input into the model. A total elapsed time of 9.56 hours was used in the program with all the data from the experiments. The optimal solution provided a maximum error of 0.00027 inches for the entire work-cycle suggesting rather good performance across a 10 hour operating interval. If the work-cycles of the machine are not repetitive, and if jobs arrive randomly to the machine, the use of time dependencies will probably not provide an accurate characterization of the error variation. In such circumstances, it might be possible to substitute time dependency with temperature

dependency. This would require the identification of a few strategic locations on the machine structure where the temperatures are strongly correlated to the model parameter values. A methodology similar to the one described here can then be used to identify an adequate error model for compensation.

This research develops a new method for the estimation of the error model parameters of a machine tool using a Chebychev norm. This type of analysis forces strict bounds on the errors produced by the machine and can be used as a performance measure for the effectiveness of software compensation schemes on machine tools. As with any scheme, such a parameter estimation technique is not a universally superior technique. Its appropriateness for a particular situation is a matter of judgement. A few suggestions are relevant here. This technique must only be used when the maximum absolute error is the most relevant performance measure. Further, the maximum absolute error is very susceptible to outliers in the data. Therefore, such a technique must only be used when measurement errors are tightly bounded and measurement noise is low. Given proper experimental design and good instrumentation, such a technique can be gainfully utilized in machine tool metrology technologies and practice.

References

[1] Yuan J. X. Ni J. Chen, J. S. and S. M. Wu. Real-Time Compensation for Time-Variant Volumetric Errors on a Machining Center. *Journal of Engineering for Industry*, 115:472–479, 1993.

[2] Vasek Chvatal. *Linear Programming*. Freeman and Company, 1983.

[3] A. Donmez. *A General Methodology for Machine Tool Accuracy Enhancement-Theory, Application, and Implementation*. PhD thesis, Purdue University, West Lafayette, Indiana, 1985.

[4] R. J. Hocken. Three Dimensional Metrology. *CIRP Annals*, 26:403–408, 1977.

[5] R. J. Hocken and the Machine-Tool Task Force. Technology of Machine-tools, Vol. 5: Machine Tool Accuracy. Technical report, Lawrence Livermore Laboratory, University of California, Livermore, California, 1980.

[6] P. S. Huang and J. Ni. On-Line Error Compensation of Coordinate Measuring Machine. *International Journal of Machine-Tools and Manufacturing*, 35(5):725–738, 1995.

[7] V. S. B. Kiridena and P. M. Ferreira. Computational Approaches to Compensating Quasistatic Errors of Three-Axis Machining Centers. *International Journal of Machine-Tools and Manufacturing*, 34(1), 1994.

[8] V. S. B. Kiridena and P. M. Ferreira. Kinematic Modeling of Quasistatic Errors of Three-Axis Machining Centers. *International Journal of Machine-Tools and Manufacturing*, 34(1), 1994.

[9] V. S. B. Kiridena and P. M. Ferreira. Mapping the Effects of Positioning Errors on the Volumetric Accuracy of Five-axis CNC Machine Tools. *International Journal of Machine-Tools and Manufacturing*, 34(1), 1994.

[10] V. S. B. Kiridena and P. M. Ferreira. Parameter Estimation and Model Verification of 1st Order Quasistatic Error Models for Three-Axis Machining Centers. *International Journal of Machine-Tools and Manufacturing*, 34(1), 1994.

[11] Yuan J. Lo, C. H. and J. Ni. An Application of Real-Time Error Compensation on a Turning Center. *International Journal of Machine-Tools and Manufacturing*, 35(12):1669–1682, 1995.

[12] R. McClure, M. Weck, and G. Petuelli. Thermally Induced Error in Technology of Machine-tools. Technical report, Machine Tool Task Force, Vol. 5: Machine-tool Accuracy, Lawrence Livermore Laboratory, University of California, Livermore, California, 1980.

A 5-Degree-of-Freedom Laser System for Rapid Machine Volumetric Error Measurement and Compensation

Quanhe Ma, Xiaohua Chu, Kam Lau
Automated Precision, Inc.
Gaithersburg, MD 20879

Abstract

Due to increasing global competition, and the demand for improved product quality, the acceptable size and form tolerances for machined parts are continuously tightening. With the advancement of microprocessor control capabilities and software techniques, recent years have seen dramatic refinements in machine error characterization and compensation methods. In the production environment it is very important, sometimes even critical, to minimize measurement time on the machine, so that it is affordable for machine owners to conduct the measurements.

There are two conventional ways to measure volumetric errors on a multi-axis machining center. One method is using a laser interferometer. For a 3-axis machine, there are 21 independent error components: three linear errors and three rotational errors for each axis, and three squareness errors between the axes. The alignments for the measurements are very time consuming and tedious, because standard laser interferometer systems measure each error components separately. It normally takes a week to measure and characterize a 3-axis machine. The other approach employs distance measurement methods, such as diagonal measurements (via laser interferometer) or telescoping (LVDT- or laser-based) ballbars, to measure the volumetric errors. While faster, this method will provide data for overall volumetric errors, but cannot accurately identify the sources of the errors.

This paper introduces a new 5-degree of freedom (5-D) laser system. The 5-D laser system combines angular, straightness and linear displacement measurements in a single unit. Specifically, this unique device allows one to perform a dual-axis angle, dual-axis straightness and a linear displacement measurement in a single pass with a single set-up, eliminating the need for special and separate optics for straightness and angular measurements. The new 5-D laser dramatically reduces characterization time, e.g. to less than a day from over a week for a 3-axis CNC machining center.

The accuracy of the 5-D laser is analyzed and the test results comparing with a laser interferometer are presented in the paper.

The 5-D laser system has been used on many different CNC machining centers. Some measurement results are presented in the text, along with a volumetric model based upon measurements taken along the three orthogonal axes.

Key words: machine tool metrology, laser measuring system, machine error characterization and compensation

LASER MEASUREMENT INSTRUMENT FOR FAST CALIBRATION OF MACHINE TOOLS

P. S. Huang and Y. Li

Department of Mechanical Engineering
SUNY Stony Brook
Stony Brook, NY 11794-2300

1. Introduction

Calibration of machine tools is an essential operation in machine tool industry. It is routinely performed to keep machines in their peak performance and therefore to produce quality products. Some important purposes of calibration can be summarized as follows: 1) Error mapping of CNC machines for error compensation, 2) acceptance test of newly acquired machine tools, 3) periodic calibration for optimized performance of machine tools, 4) troubleshooting, and 5) demonstration of quality to potential customers.

One primary requirement for machine tool calibration is that the calibration must be performed as quickly as possible. Time-consuming calibration is costly due to the machine tool downtime as well as the expensive skillful labor required. Current industrial practice in machine tool calibration relies mostly on laser interferometers, such as HP5529A Dynamic Calibrator from Hewlett Packard and the laser calibration system from Renishaw. The latest models of these laser interferometers combine sophisticated optics and electronics with powerful software to simplify setup procedure and speed up data sampling and analysis. Relatively fast calibration have been achieved. However, the calibration speed is still limited because the basic measurement procedure did not change. With a single setup, still only one error component can be measured. Considering the fact that a multi-axis machine tool typically has tens of error components, the calibration is still a lengthy, time-consuming process.

To address the above problem, two multi-degree-of-freedom error measurement systems were developed to simultaneously measure up to five error components [Ni *et al.* 1992; Huang and Ni 1993], which significantly reduced the time of calibration. In another approach, the Telescoping Magnetic Ball Bar (TMBB) was developed [Bryan 1982] to quickly check the accuracy of a machine tool without measuring each individual error component. The capability of TMBB was further extended by the development of the Laser Ball Bar (LBB) [Ziegert and Mize 1993] which has much longer range of motion than TMBB. LBB can also provide the measurement of individual error components [Ziegert 1994], in addition to the quick check of machine tool accuracy.

In this research, we follow the first approach and propose a new laser instrument that measures 5-DOF error components simultaneously when used with either the HP or Renishaw laser calibration system. These error components include linear distance, horizontal straightness, vertical straightness, pitch and yaw errors. The instrument is designed as a compact device to be used as an accessory to the HP or Renishaw calibration system to provide the capability of fast calibration of machine tools. The measurement principle and experimental results of the instrument are presented in the following sections.

2. Principle of Measurement

Figure 1 shows the optical layout of the 5-DOF error measurement system. Here the linear distance error is measured by using HP5529A's standard linear distance optics which consists of the He-Ne laser head, a linear interferometer (LI) and two linear retroreflectors (RR1, RR2). The laser beam is split into two beams by the linear interferometer, one reflected from the stationary retroreflector RR1 as the reference beam and the other reflected from the moving retroreflector RR2 as the measurement beam. Two non-polarizing beam splitters BS1 and BS2 and an interference filter are inserted into this standard linear distance measurement optics. BS2 with a beam splitting ratio of approximately 1:1 is used to extract half of the beam reflected from RR2 for the measurement of the other four error components.

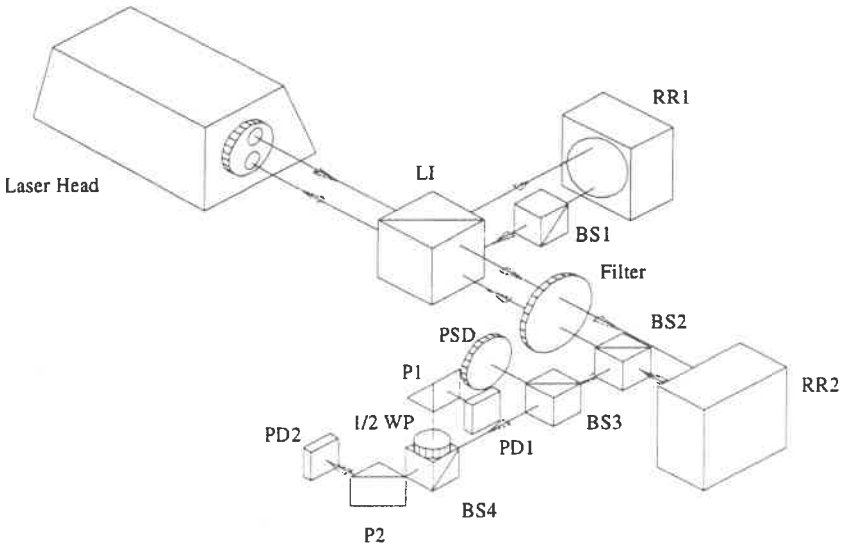

Figure 1 Optical layout of the instrument for 5-DOF error measurement.

BS1 is exactly the same type of beam splitter as BS2 and is inserted into the reference beam to balance the intensities of the reference and measurement beams for linear distance measurement. The band pass interference filter (peak wavelength 632.8 nm) is included to prevent the ambient light from reaching the photo sensors in the instrument and causing measurement errors.

The beam reflected from beam splitter BS2 is split again at beam splitter BS3. The reflected beam is directed to a two-dimensional position-sensing detector (PSD) for the measurement of horizontal (X axis) and vertical (Y axis) straightness errors. Following are the equations for calculating the straightness errors from the PSD signals:

$$S_x = K_1(x_1 - x_2)/(x_1 + x_2) \qquad (1)$$
$$S_y = K_2(y_1 - y_2)/(y_1 + y_2) \qquad (2)$$

where x_1, x_2, y_1, and y_2 are the four output signals of the PSD. Note (x_1+x_2) and (y_1+y_2) are both measures of the intensity of the incident laser beam.

The transmitted beam at BS3 is further split at BS4 into two beams, one for pitch measurement and the other for yaw measurement. Pitch and yaw measurements are done by using a new angle measurement principle which is a variation of the previously developed angle measurement principle based on the Internal-Reflection Effect [Huang *et al.* 1992, 1994] with a simplified one-prism optical design. The pitch measurement unit consists of a right-angle prism and photodiode pair P1 and PD1 and the yaw measurement unit consists of another right-angle prism and photodiode pair P2 and PD2. Following are the equations used to calculate pitch and yaw:

$$\theta_p = K_3(y_1 + y_2)/I_1 \qquad (3)$$
$$\theta_y = K_4(y_1 + y_2)/I_2 \qquad (4)$$

where I_1 and I_2 are the output signals of the photodiodes PD1 and PD2 respectively. Here pitch and yaw have been related to the inverse of the reflectance at right-angle prisms P1 and P2 respectively (note again that $y_1 + y_2$ is a measure of the intensity of the incident beam). We found that by so doing, the linearity is much improved in a certain angle range.

For the pitch measurement unit, a half-wavelength plate is also included to rotate the polarization of the laser beam so that the beam is reflected at P1 as a *p*-polarized beam, the same as that at P2 for the yaw measurement. Use of *p*-polarized beams is important in this application because the reflectance of a *p*-polarized beam is more sensitive to angular changes than that for an *s*-polarized beam.

Figure 2 shows the overall view of the measurement setup for simultaneous measurement of 5-DOF error components. All the optical components for measuring the additional straightness, pitch, and yaw errors are packaged into a small box, the 4-DOF Optical Head, that moves with the moving object. All the fixtures used in the setup are standard fixtures that come with the original laser calibration system.

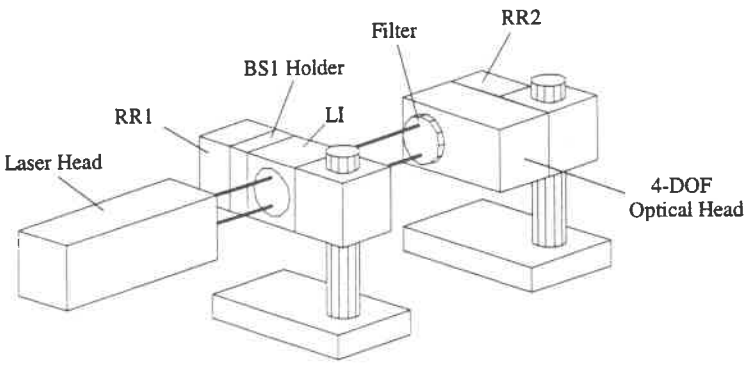

Figure 2 Overall view of the instrument for 5-DOF error measurement

3. Experiments

All the error measurement units except the linear distance measurement unit have to be carefully calibrated. In this research, we used a digital micrometer for the calibration of straightness error measurement and a precision angle measuring sensor [Huang and Xu 1995] for the calibration of pitch and yaw measurements.

Figure 3 shows the calibration result of the vertical straightness measurement unit. It is the average of six repeated calibrations. The calibration range is ±200 μm. From linear regression analysis, we found the maximum nonlinearity error to be approximately 1%. Better linearity can be obtained by using a better but usually more expensive PSD.

Figure 4 shows the calibration result for the yaw measurement unit. Again it is the average of six repeated calibrations. The angle range covered is ±100 arcsec. The maximum nonlinearity error of yaw measurement is approximately 1.3%. Calibration of horizontal straightness and pitch measurements showed similar results.

Figures 5 and 6 show the stability of the vertical straightness and yaw measurements in 20 minutes. The short term fluctuation of the vertical straightness measurement is small (< 0.5 μm), but there is a clear trend of drift. The problem could be caused by thermally induced errors. For yaw measurement, the short term variation is approximately 2 arcsec peak-to-peak. Investigations revealed that the instability of the yaw measurement was mostly caused by the noise in the $(y_1 + y_2)$ signal. Measures are being taken to remedy the problem. Stability tests of the horizontal straightness and pitch error measurements showed similar results.

The instrument is currently being modified and further evaluated. Once this is done, it will be used to

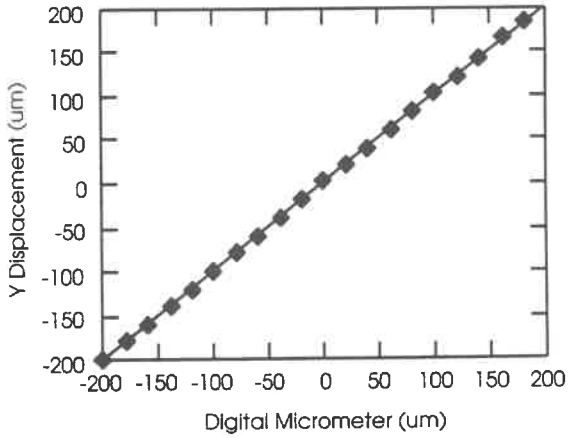

Figure 3 Calibration result for the vertical straightness measurement unit.

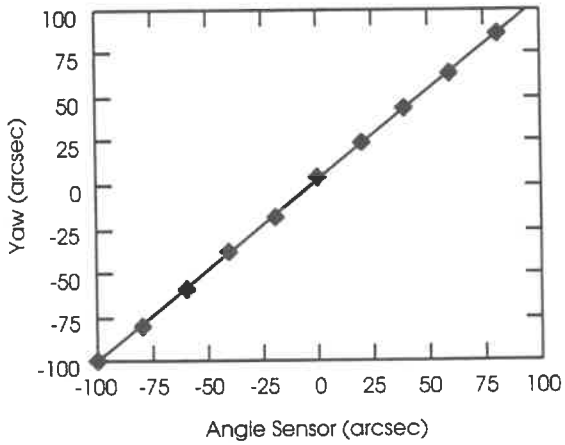

Figure 4 Calibration result for the yaw measurement unit.

calibrate the geometric errors of a CNC milling machine. The results will be reported shortly.

4. Summary

We have developed a new laser instrument for the simultaneous measurement of 5-DOF geometric errors of linear motion. The instrument has been designed as an accessory to the industry standard laser calibration system HP5529A from Hewlett-Packard. The instrument should also work with the Renishaw calibration system. When combined with the linear distance measurement optics of the above calibration systems, it provides the capability of simultaneous measurement of five error components, linear distance, horizontal straightness, vertical straightness, pitch, and yaw errors. The fast setup and measurement nature of the new instrument should significantly improve the efficiency of the machine tool calibration process.

References

[1] Bryan, J. B., "A Simple Method for Testing Measuring Machines and Machine Tools, Part I: Principles and Applications," *Prec. Eng.* 4(2), 61-69 (1982).

[2] Huang, P. S., Kiyono, S. and Kamada, O., "Angle measurement based on the internal-reflection: a new method," Applied Optics, 31, 6047-6055 (1992).

[3] Huang, P. S. and Ni, J., "Angle measurement based on the internal-reflection effect and its application in the measurement of geometric errors of machine tools." *Proc. ASPE Annual Meeting*, 350-353 (1993).

[4] Huang, P. S. and Xu, X., "Optical Probe for Surface Profiling of Aspherical Mirrors," *Proc. ASPE Annual meeting*, 112-115 (1995).

[5] Ni, J., Huang, P. S., and Wu, S. M., "A multi-degree-of-freedom measuring system for CMM geometric errors," ASME J. Eng. for Industry, 114, 362-369 (1992).

[6] Ziegert, John C. and Mize, Christopher D., "Design and Testing of a Laser Ball Bar for Rapid Machine Tool Metrology," *Proc. ASPE Annual Meeting*, 86-89 (1993).

[7] Ziegert, John C., "Measurement of Machine Tool Parametric Errors," *Proc. ASPE Annual Meeting*, 76-79 (1994).

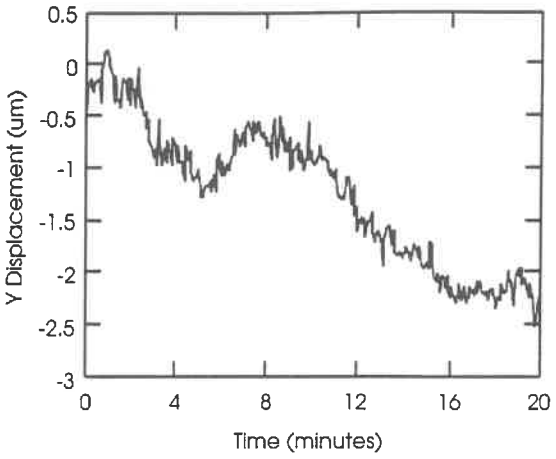

Figure 5 Stability of vertical straightness measurement.

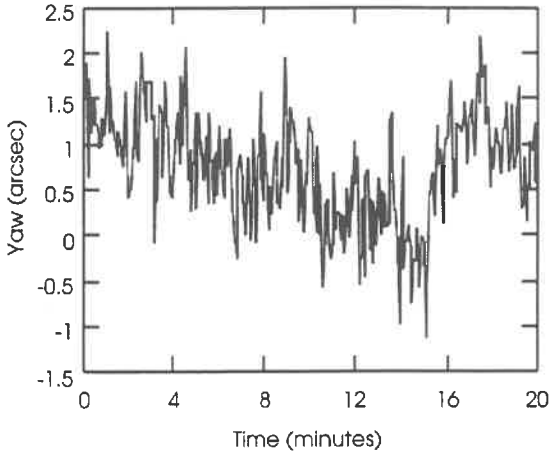

Figure 6 Stability of yaw measurement.

Practical Thermal Error Correction for CNC Machine Tools

J.P. Allen, S.R. Postlethwaite, D.G. Ford
The University of Huddersfield
Huddersfield, England.

Introduction

Internal heat generation and changes in environmental temperature inevitably produce changes in the temperature of machine tool structures. The resultant thermal distortion is widely recognised as a major cause of component inaccuracy. Design evolution has given improved thermal stability, through the development of more efficient spindle and axis drive systems and the use of cooling. Unfortunately the relentless drive for improved accuracy combined with increased cutting speeds and feed rates ensures that thermal errors remain a significant problem. Indeed it has been stated that in some cases thermal errors can account for up to 70% of the total machining error.

The aim of this research was to develop techniques for improving the thermal behaviour of general CNC machine tools beyond what is cost effectively achievable by good mechanical design. It was decided that compensation, where errors are corrected by adjusting the position of the tool or workpiece via existing machine axes, was the most promising basis for these general thermal error reduction techniques.

Thermal errors are dependent on the temperature distribution experienced by the machine tool structure. The operating conditions of most machine tools means that the heat generated internally varies significantly as the machine is used. This, combined with environmental temperature variation, can give rise to complex transient temperature distributions, making the resultant thermal errors difficult to quantify or predict. The principal problem facing the designer of a thermal error compensation system is determining how much correction is required at a particular instant.

The methods used by previous researchers to determine compensation values can be divided into two broad categories.

Direct Measurement: This usually takes the form of probing a reference face or an artefact mounted permanently on the machine. Systems based on direct measurement can give accurate results and the simpler ones are very effective at tracking and correcting slowly changing errors. Problems occur with more complex systems which require specialist hardware that must be specially tailored to fit individual machines and which can intrude on the working volume of the machine. Significant problems are also encountered when attempting to track rapidly changing errors, as each measurement operation requires a break in machining. Rapidly changing errors require frequent measurement operations and the result can be unacceptable time delays.

In-direct Measurement: Generally these systems calculate thermal errors from spot temperature measurements made on the surface of the structure. These systems can also give accurate results and have the advantage that errors can be tracked and corrected in the background. Additional hardware is fairly simple and does not intrude on the machine's working volume. The principle difficulty lies in determining the relationship between measured temperatures and compensation values. The majority of researchers have used large amounts of empirical data to train purely statistical models which relate temperature directly to error. They have not had access to a detailed picture of the temperature distribution produced by the machine and so they have tended to position temperature sensors intuitively. The result is that compensation can be very time consuming to implement. The models are also entirely statistical and so are not readily transferable even between machines of the same type.

Our Research Philosophy

This research project has attempted to address the weaknesses of previous research which have prevented thermal compensation being adopted widely. We have looked at developing techniques which can be implemented quickly, cost effectively and which are applicable to a wide range of machines.

Our research can be divided into two parts:

Part 1: The development of methods for the assessment of machine tool thermal behaviour.
Part 2: The development of general techniques for determining compensation values.

Methods for Assessing Machine Tool Thermal Behaviour (Part 1)

The purpose of this aspect of the research is to simplify the problem of applying compensation to a machine by identifying which aspects of its thermal behaviour produce the largest machining errors.

Machine Assessment Using Thermal Imaging: A machine tool can be considered as being made up of a number of discrete structural elements. Under normal operation some structural elements will undergo greater temperature changes and so are likely to produce greater thermal errors. A sequence of thermal images, recorded whilst the machine runs through a duty cycle, gives a detailed picture of temperature distribution and allows significant structural elements to be identified easily. An image of a Cincinatti vertical spindle NC milling machine is included here to illustrate the strength of thermal imaging in this application.

As expected the image shows a significant temperature rise of the headslide due to heat generated by the main spindle drive and bearings.

What is more interesting is a major, unexpected heat source within the column of the machine. Further investigation revealed that, because this is a relatively old machine, the spindle is driven via a gearbox mounted in the column. The thermal camera highlights the unexpected heat source immediately, giving not only its location but also the form of the temperature distribution it produces. It would be difficult to detect the presence of the gearbox using spot temperature measurements, let alone to obtain the same sort of detailed picture of temperature distribution. Without this knowledge it could be difficult to model the thermal behaviour of this machine.

Machine Assessment Using Measurement of Error: In addition to the thermal imaging tests equipment is set-up to measure thermal errors directly. These measurements are used in conjunction with the thermal images to assist with the machine analysis. The equipment we normally use is non-contact sensors and a spindle mounted mandrel for measuring drift and a laser interferometer for measuring positioning change.

Error measurements allow us to assess the relative magnitude of different thermal errors. We also use the measurements in conjunction with the thermal image sequence to attribute thermal errors to particular structural elements.

Assessing the Effect of Thermal Distortion on Workpiece Accuracy: The aim of this part of the work was to develop an understanding of the ways in which thermal deformation of the structure

affects workpiece accuracy. We were able to define two general categories of thermal error which has proved useful for further simplifying the problem and for helping to select the most suitable compensation technique. These two categories of thermal error are:

Position Independent Thermal Errors (PITE): A change in the machine offsets. PITE change with temperature but not with position.

The effect of PITE on component accuracy is strongly dependent on the rate of change of PITE relative to the time taken to produce a component. Even large changes in PITE may result in little error if there is no significant change during the time taken to machine a component.

Slowly changing PITE can, however, be particularly significant if the component is rotated as part of the manufacturing process and the distance between cuts made before and after rotation is critical. Any offset that exists between the tool and workpiece will be reproduced on the component and if the component is reversed then the total error will be double the offset. If the component is not moved then, although the offset will appear on all the machined surfaces, the distances between surfaces should be accurate.

Position Dependent Thermal Errors (PDTE): A change in the linear positioning of the machine. PDTE change with temperature and with position. PDTE will produce errors if the change in linear positioning of the machine does not match the change in linear positioning required by the thermal expansion of the component.

Thermal Error Compensation Techniques (Part 2)

This section outlines some of the compensation techniques we have developed. Each technique is illustrated by a case study.

Novel In-Direct Measurement Based Compensation: A 3-axis CNC machining centre was producing rapidly changing PITE in the Y direction. An initial investigation revealed that the errors were produced mainly by thermal distortion of the headslide, which is heated by the main spindle bearings. The errors were changing too rapidly to be tracked efficiently by direct measurement so a novel technique for determining compensation values from spot temperature measurements was implemented.

We have taken a more analytical approach to in-direct measurement based compensation than that taken by previous researchers. Rather than use a single statistical model to relate temperature measurements directly to error we use two distinct models, the temperature model and the distortion model, to calculate compensation values.

The temperature model calculates temperature distribution from spot temperature measurements. We have developed software which will analyse a sequence of thermal images to automatically choose optimum sensor locations and to optimise the calculation of temperature distribution. Normally separate models are built for each significant structural element. A simple heating-cooling test, with the camera focused on the structural element, recording images at intervals, normally provides enough data to build an accurate model.

The distortion model is used to calculate distortion from temperature distribution. It is usually analytically based but may feature some statistical tuning.

We have achieved success with this approach. Its main advantage over previous systems is that we are able to calculate thermal errors accurately using models built on data acquired during relatively short tests.

The graph below shows the results of compensation based on temperature measurements of the machine headslide. These results were obtained from a heating and cooling test that lasted approximately 3 hours.

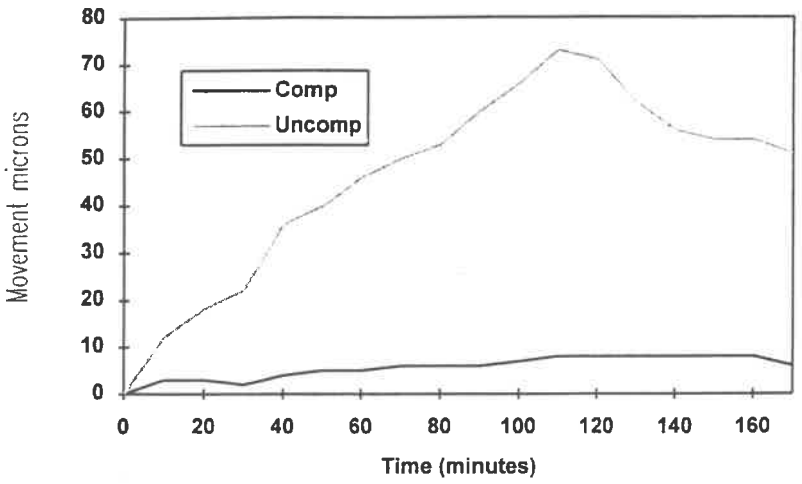

The system works well with the compensation holding errors within a ten μm band. The rate of change of error has been greatly reduced which should have a significant effect on workpiece accuracy. The models used are able to deal equally well with the temperature distributions produced by both heating and cooling.

Implementation of Intermittent Re-datuming on a CNC Planing Machine: A CNC planing machine was being used to produce symmetrical parts. During planing the parts were supported in vees on two ground diameters, produced in a previous operation. The parts were planed on one side, rotated through 180° and planed on the other side. The machine user was having difficulty achieving the tolerance for the spacing between the faces produced before and after rotation.

An initial survey was conducted which found that the main thermal effect was a slowly changing PITE in the Z direction, tool moving normal to the planed surface. Although the total change in PITE over an 8 hour period could be around 80μm the change over the time required to produce a single component would only have been around 10-15μm. Yet the user was experiencing errors of up to 100μm.

A detailed study of the manufacturing process pin-pointed the problem. The error was produced as a result of the way the machine was referenced to the workpiece. Although the machine was under CNC control the referencing process was still carried out manually. Referencing was achieved by bringing the tool to a point 25μm away from a ground diameter. Whilst this worked well it was only being carried out for the first workpiece in a batch, the user was relying on the stability of the machine for producing subsequent components. It may take several days to produce all the components in a batch during which time the machine could move significantly. As the workpiece is supported on a previously ground diameter any shift in the reference position produces an error in the workpiece. Reversing the component effectively doubles any error.

The PITE changes slowly and there is a single dominant direction of movement. Consequently it could be tracked by probing at quite large time intervals, which should not cause any significant machining delays. In this particular case probing was not available on the machine but we recommended that referencing be carried out for each new component and repeated immediately after the component was rotated. This has effectively solved the problem and the user has reported no problems achieving tolerances.

Although this is a fairly simple case it illustrates the strength of gaining a thorough understanding of the machine's behaviour and using this to decide on the best solution. In this case the solution was implemented at virtually no cost and resulted in reduced rework and scrap.

Use of a Thermally Stable Bar to Measure PDTE: Errors produced by change in linear positioning (PDTE) were experienced on a 3-axis CNC milling machine. An initial investigation on a single axis was carried out. The machine was fitted with rotary encoders mounted on the servo motors. The ballscrews were axially clamped at one end with the other end being free to slide. As a consequence the ballscrew itself is a major source of PDTE.

The first stage was to fit a linear scale to take the ballscrew out of the positioning loop. This reduced the PDTE from about 50μm change over the whole axis travel to 20μm, for similar duty cycles. In addition the reversal error in the axis was reduced to virtually zero. If free ended ballscrews are fitted to a machine then we would recommend linear scales as a prerequisite to achieving thermal stability.

The next stage was to track the remaining PDTE. To do this a thermally stable INVAR bar was mounted alongside the scale. The bar was clamped at one end and supported along its length on mounts that allowed axial movement. A displacement transducer measured relative movement between the free end of the bar and the scale. If we assume that the PDTE changes linearly then the thermally stable bar gives a direct measure of the expansion of the scale.

The graph below gives the results of a test. The data shows the change in positioning error over the whole axis length. The changes were produced by a combination of environmental temperature change and heat produced by cycling the axis at 2 m/min.

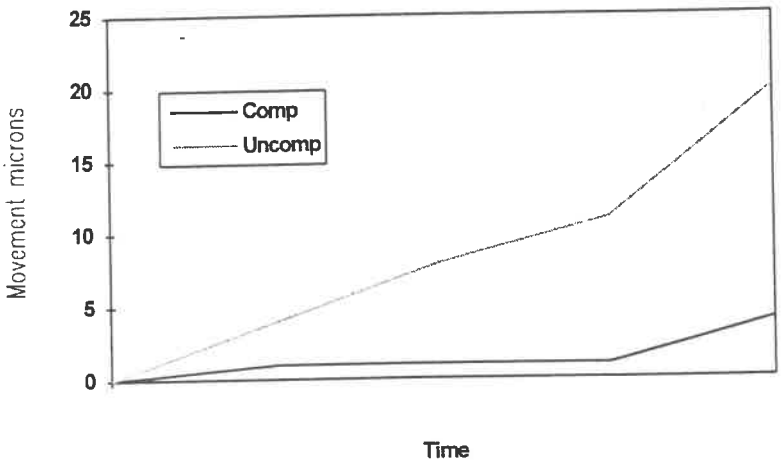

In this case the thermally stable bar gives a good measure of the error. Using a combination of a linear scale and the thermally stable bar allows the change in linear positioning to be reduced to less than 10% of its original value.

Direct Measurement Based Compensation Applied to a CNC Lathe: The final case concerns the thermal errors produced by a large CNC lathe. The initial investigation revealed rapidly changing PITE in the Z direction (along the spindle axis). These errors were produced by thermal expansion of the spindle shaft itself. The spindle had a low thermal mass and was heated directly by the main spindle bearings. As a consequence it heats and cools very rapidly. The spindle is supported in two sets of bearings. One provides axial location while the other is free, to prevent the bearings being overloaded by spindle shaft expansion. In this case the rear bearings were clamped causing the spindle to expand forwards out of the headslide, resulting in large machining errors.

Normally when faced with rapidly changing PITE we would use temperature sensor based compensation to track the errors. In this case the most significant structural element was the spindle

shaft. The rotation of the spindle made accurate temperature measurements difficult to obtain. Fortunately the initial investigation had given the information necessary to develop a simple direct measurement based solution. We mounted a non-contact displacement sensor on the machine to measure relative movement between the headstock and the back of the chuck. The signal from the sensor was used to provide a compensation signal for the Z axis drive.
The graph below shows the Z axis thermal error, with and without compensation, for a heating and cooling duty cycle.

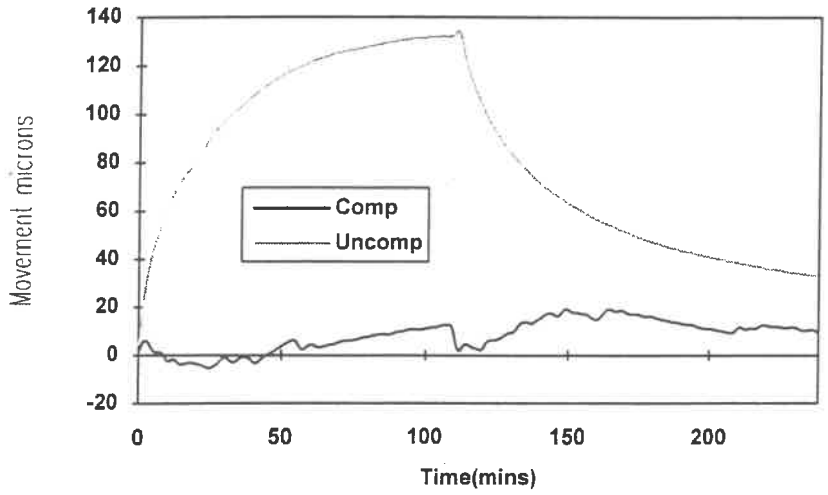

The system works well with the compensation holding errors within a 20μm band.
The technique will cope with errors produced by any relative movement between spindle and headstock.

Conclusions

- Techniques have been developed which use thermal imaging and error measurement to rapidly assess machine tool thermal error behaviour.
- A general philosophy of machine tool thermal error behaviour has been formulated. This can be used to help in the analysis and categorisation of individual machines.
- A range of practical techniques have been developed to address the specific thermal problems of individual machine tools.

Methodologies for the Evaluation of Systematic Form Deviations for Inside-Diameter Cylindrical Features and Their Relationship to Process Variables[1]

R. P. Henke, R. M. Cassou, K. D. Summerhays, University of San Francisco, San Francisco, CA; J. M. Baldwin, Sandia National Laboratories, Livermore, CA; and C. W. Brown, AlliedSignal Federal Manufacturing & Technologies, Kansas City, MO

ABSTRACT

The ever-increasing demands for precision machined parts has created a renewed emphasis on better understanding of the relationships between process control variables and deviations from perfect geometric form. To meet this demand, it is important to have high-precision, high-density metrology data on part features which (in some sense) span the range of variability in form for the process under study. Clearly the problem is a complex one involving the machine tool itself, materials, fixtures, cutters, feeds, speeds, and many other factors. In the work described here we introduce a methodology which can serve to identify key analytical deviations from form and their dependence on several of the factors enumerated above.

Artifact parts containing inside-diameter cylinders of various diameters and depths were produced in aluminum in statistically significant quantities on a flexible manufacturing system. Blind, counter and through holes were included. Manufacturing methods included drilling, boring, and reaming operations in various combinations. Nearly 1400 of these cylinders were measured on a high-precision coordinate measuring machine adapted for high-density sampling. Sample points (about 1000 per cylinder, taken on a uniform grid) were fitted by least-squares as a linear combination of analytic terms.

In most instances the systematic deviations from perfect geometric form could be conveniently modelled by treating the form deviations according to a Fourier series in the angular dimension and a simple polynomial in the axial dimension. A basis set of specific cross-terms in the resultant product function has served to represent what are often taken as the classic deviations from standard form, eg. taper, lobing, axial curvature, etc. One additional readily recognizable basis shape, not manifested in any *one* cross-term, but in a set of correlated terms, has been identified as a result of this work. The relative importance of the form deviation components in explaining the variance over a range of individual features has been assessed. In many cases the majority of the variance observed from ideal part geometry can be ascribed to fewer than a half-dozen such terms. The nature of these terms and their ranking in accounting for the variance is strongly influenced by the specific manufacturing method employed. The expression for the form deviations was further simplified by a principal component analysis of the shapes that result from a given manufacturing technique. This reduced the basis set to the minimum number of functions necessary to capture the resulting variability in the set of features manufactured by this technique.

In the characterization of cylinders produced by a succession of operations such a center-drill/drill/bore/ream, the importance of each step in the sequence is considered. Certain generalities have emerged which should aid in establishing the domain of process variable control.

METHODS

The deviation of a manufactured cylinder from perfect form must be expressed quantitatively and in a manner which is much more concise and abstract than the dense set of points used to measure the cylinder. For this reason the deviation has been expressed as a weighted sum (linear combination) of basis functions, each of which can be pictured as a shape over the cylinder which is to be multiplied by a coefficient and then added to the existing cylinder in a radial direction. One functional form used is the set consisting of all terms such as $T_n(z)$, $T_n(z)\cos(m\theta)$, or $T_n(z)\sin(m\theta)$. Here $T_n(z)$ is the Chebyshev polynomial of the first kind and order n, where $n \geq 0$ and the axial coordinate z has been normalized such that $-1 \leq z \leq 1$. The Fourier order $m > 0$ and θ is the polar angle. If the maximum order in θ is M and in z is N then we can define a basis function vector, $\mathbf{b}(z, \theta)$, which is to be evaluated at any point on the surface of the cylinder.

$$\mathbf{b}(z,\theta) = (T_0(z),\ T_0(z)\cos(\theta),\ T_0(z)\sin(\theta),\ T_0(z)\cos(2\theta),\ T_0(z)\sin(2\theta)\ \ldots\ T_0(z)\cos(M\theta),\ T_0(z)\sin(M\theta)\ \ldots$$
$$T_1(z),\ T_1(z)\cos(\theta),\ T_1(z)\sin(\theta),\ T_1(z)\cos(2\theta),\ T_1(z)\sin(2\theta)\ \ldots\ T_1(z)\cos(M\theta),\ T_1(z)\sin(M\theta)\ \ldots$$
$$\ldots$$
$$T_N(z),\ T_N(z)\cos(\theta),\ T_N(z)\sin(\theta),\ T_N(z)\cos(2\theta),\ T_N(z)\sin(2\theta)\ \ldots\ T_N(z)\cos(M\theta),\ T_N(z)\sin(M\theta))^t$$

As can be seen **b** is an (N+1)(2M+1) dimensional vector. Then the radius of the cylinder at the point z, θ is given by $r = R + \mathbf{b}^t\,\mathbf{a}$, where R is the average or perfect form radius of the cylinder, **a** is the vector of function coefficients, and $\mathbf{b}^t\,\mathbf{a}$ is the inner or "dot" product of the vectors **b** and **a**. In practice **a** is determined by a least squares fit to at least (N+1)(2M+1) measured points on the surface of the cylinder. The vector **a** represents the deviation from perfect form, so all of its components are assumed to be much smaller than R.

The representation given above is useful in several respects. 1) If we believe we have used orders in z and θ which are sufficiently high to represent the systematic component of the form error, we can determine **a** from relatively few points on the surface and then evaluate the radius of the actual "cylinder" at any point on its surface. How is it possible to know the required order in z and θ? Densely measuring and then least squares fitting a number of surfaces which are typical of those produced by a given manufacturing technique allows a determination of the z and θ orders of the terms which are statistically significant. 2) Once we have the functional form it is possible to use experimental design techniques[2] to find the optimal locations on the cylinder surface to provide the best determination of **a** from a minimum number of points. This determination has been one of the main thrusts of our research. 3) Knowing which terms are most significant (which components of **a** are large) provides a much better conceptual picture of the character of the form deviations than is provided by mere data sets alone. This is because certain terms in the above expansion can be identified with commonly known and named forms of error. Table I gives a list of the descriptions of some of the terms.

Table I

Term	Description
$T_0(z)$	Small change in radius
$T_0(z)\cos(\theta)$	Small change in x location
$T_0(z)\sin(\theta)$	Small change in y location
$T_0(z)\cos(n\theta)$, $T_0(z)\sin(n\theta)$	n lobes
$T_1(z)$	Taper
$T_1(z)\cos(\theta)$	Small change in direction cosine i
$T_1(z)\sin(\theta)$	Small change in direction cosine j
$T_2(z)$	Hourglass/barrel
$T_2(z)\cos(\theta)$, $T_2(z)\sin(\theta)$	Banana

One of the serious drawbacks of the Chebyshev/Fourier representation is that it is often necessary to go to a fairly high order in z and/or θ to represent the structure present in the data. When this happens it is reasonable to include all terms up to the maximum order in the polynomial. This results in a large number of terms, many of which are not statistically significant. Many points are required to determine all of the coefficients and much of weight of the data goes toward determining parameters which are not significant. A better approach is to capture just the right linear combinations of the Chebyshev/Fourier functions. These composite functions provide a basis set which can

best fit the structure present in a representative sample of cylinders. The technique used to find the proper basis set is principal component analysis. It is designed to represent the largest possible fraction of the variance present in the cylinder set with the minimum number of basis functions.

We now consider the error associated with the deviation from perfect form given over a cylinder by the function $\mathbf{b}^t(z,\theta)\ \mathbf{a}$. The goal of this procedure is to find the minimum number of basis functions that represent the variance over a large set of surfaces. The procedure is somewhat complicated so the reader may proceed to the next paragraph if he or she is willing to take the steps for granted. We choose a large number of analysis points, uniformly spaced over of the surface, and create one row of a matrix, **B**, for each point on the surface. This row will be $\mathbf{b}^t(z,\theta)$. The product **B a** is a column vector, each element of which is the deviation at one point on the surface. It is assumed at this point that the orders in z and θ are large enough to capture all of the systematic shapes contributing to the surface form deviations. (In practice we use 9th order for each of them, which leads to 190 basis shapes.) Now imagine a number of densely measured cylinders which represent all of the possible variation for the manufacturing method in question. Least squares fits of each of these results in a set of **a** vectors. We construct the matrix **A** by using each of the **a** vectors as a column of **A**. The product $\mathbf{S} = \mathbf{B}\ \mathbf{A}$ is a matrix whose columns are the vectors which give individual surfaces. The trace of $\mathbf{C} = \mathbf{S}\ \mathbf{S}^t$, divided by the number of points per generated cylinder surface and again divided by the number of surfaces, is the square of the rms error (the average variance) over all of the cylinders in the set. Our goal is to represent this average variance by as few basis set shapes as possible. Now $\mathbf{C} = \mathbf{S}\ \mathbf{S}^t = \mathbf{B}\ \mathbf{A}\ \mathbf{A}^t\ \mathbf{B}^t = \mathbf{B}\ \mathbf{E}\ \mathbf{V}'\ \mathbf{E}^t\ \mathbf{B}^t$. The last step is accomplished by realizing that the product $\mathbf{A}\ \mathbf{A}^t$ is the covariance matrix of the parameters in **a** times the number of cylinders in the set. We diagonalize this product using a standard single value decomposition. Since $\mathbf{A}\ \mathbf{A}^t$ is symmetric its decomposition is also symmetric and can be expressed as $\mathbf{E}\ \mathbf{V}'\ \mathbf{E}^t$, where **E** is a matrix whose columns are the eigen vectors and **V′** is a diagonal matrix with the eigenvalues along the diagonal. Next we replace **B E** with its product **F′**, which gives $\mathbf{C} = \mathbf{F}'\ \mathbf{V}'\ \mathbf{F}'^t$. Now to provide a normalized basis set (though not quite orthonormal), we normalize each of the columns of **F′** taken as a vector and multiply the corresponding diagonal element of **V′** by the square of its length. This leads to the normalized form $\mathbf{C} = \mathbf{F}''\ \mathbf{V}''\ \mathbf{F}''^t$. Finally we simultaneously rearrange both the position of the diagonal elements of **V″** and the columns of **F″** to place the elements along the diagonal in **V″** in descending order. With this last change we seek and we can write the modified expression as $\mathbf{C} = \mathbf{F}\ \mathbf{V}\ \mathbf{F}^t$. At this point we don't worry about the fact that **C** is multiplied by the number of points/surface times the number of cylinder surfaces because we will be expressing the variance associated with each of the eigensurfaces as a fraction of the total.

We now have the product $\mathbf{C} = \mathbf{F}\ \mathbf{V}\ \mathbf{F}^t$, which can be described as follows. The columns of **F** are the eigen normalized basis surfaces we seek, **V** is a diagonal matrix with descending size diagonal elements proportional to the variances associated with the corresponding column of **F**, and the trace of **V** is proportional (with the same proportionality constant) to the total variance over all of the surfaces. Hereafter we will assume that **V** is divided by its trace to make the diagonal elements the descending size fractional variances we seek.

RESULTS

Five different sequences of operations were employed in the manufacture of the 46 different cylindrical features on each of 30 nominally identical parts. The features included blind and through holes and counterbores with diameters ranging from 1/8" (3.2 mm) to 1" (25.4 mm) and lengths up to 0.997" (25.3 mm). Since our basis set as expressed in the vector **b** is normalized, it is possible to compare the form errors of cylinders of different diameters and lengths. The five different manufacturing sequences and their acronyms are: center drill/drill (CD), center drill/drill/ream (CDR), center drill/drill/bore/ream (CDBR), center drill/drill/plunge end mill (CDP), and center drill/drill/contour mill (CDM).

First we consider the fraction of the variance as explained by each of the Chebyshev/Fourier (polynomials) as a function of the manufacturing method. We are interested in knowing, as a function of the manufacturing sequence, which are important basis terms for expressing the form errors. All of the surfaces were least squares analyzed using the polynomial basis set. For each individual cylinder, taken over all 30 parts, the fractional variance explained by each of the basis functions was obtained. For all parts manufactured by a given sequence, the largest (worst) fractional error contributed by any of the holes was taken to be the significant requirement for inclusion of that term. Only cases where the fractional variance contribution was greater the 5% were registered to avoid overcomplicating

the result. The result of this study is shown in Fig. 1.

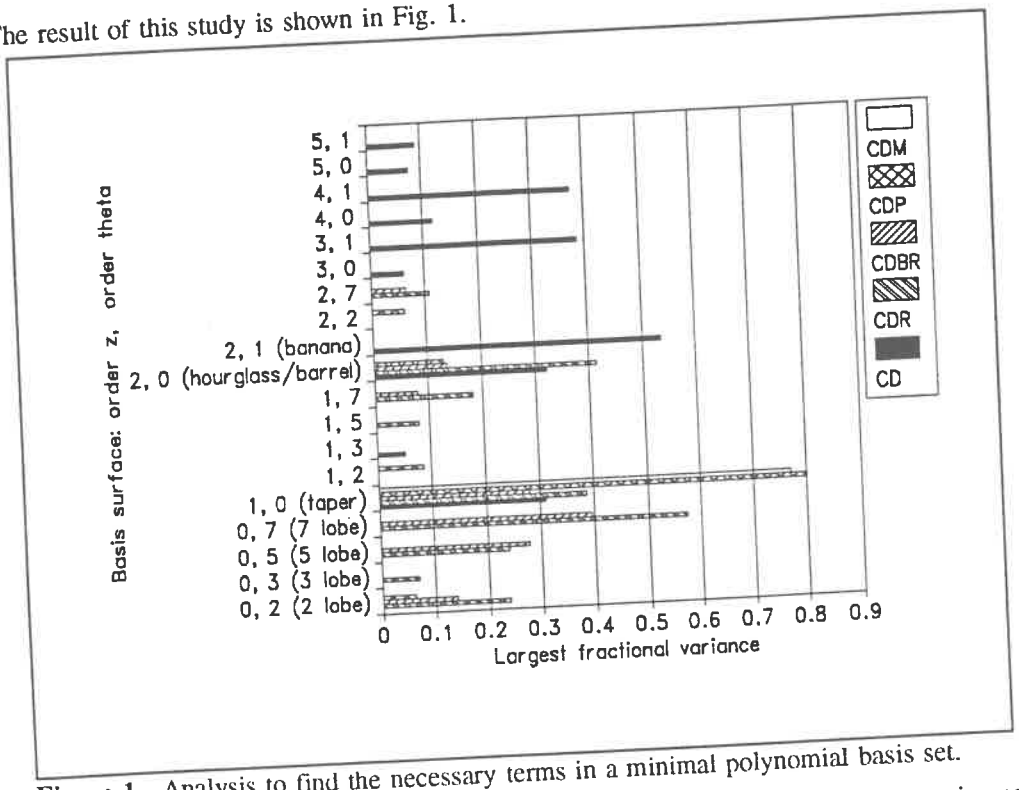

Figure 1. Analysis to find the necessary terms in a minimal polynomial basis set.

Next we consider the result of the principal component analysis. Each of the five manufacturing sequences was treated separately by including all cylinders made by that method. All terms through ninth order in both z and θ were allowed. The first result of this study is shown in Fig. 2. Presented is a comparison of the fraction of the variance which remains to be explained after n terms are included in the eigen basis set.

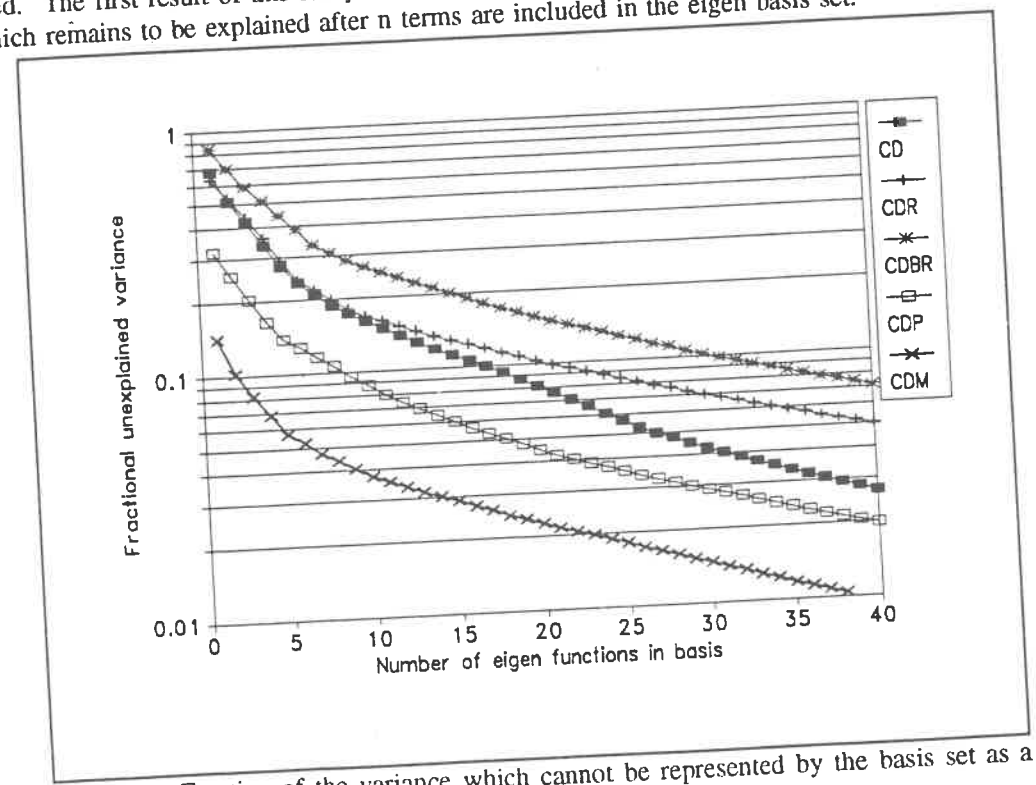

Figure 2. Fraction of the variance which cannot be represented by the basis set as a function of the number of eigen functions in the basis set.

Figs. 3-12 show two of the eigen shapes for each of the five manufacturing sequences employed. What is shown in each of these figures is six different views of the cylinder, each with a highly magnified rendition of the deviation from nominal form. The first four view are oblique side views. The arrow at the top of the cylinder indicates the direction of the origin in θ. The fifth view is a top view again with the arrow indicating where $\theta = 0$. The sixth view is a peeled out view of the inside of the cylinder (all of the cylinders were ID cylinders) with the cut being at the origin in θ. The near side is the top of the cylinder and the left side is $\theta = 0$.

DISCUSSION

Fig. 1 allows us to observe some generalities about the manufacture of ID cylinders. The most dominant behavior seen for all methods is taper. This is particularly true for holes generated with a final pass of a reamer. Another common error is hourglass. Both of these kinds of errors might be caused by lack of perfect concentricity of all of the elements of the machining operations. Reamed holes generated by an n-fluted reamer also show pronounced n-1 and n+1 lobed patterns. In Fig. 1 the CD method generates a number of predominant terms with both a higher order z and a θ dependence. It is not obvious, but can be seen from the eigen analysis, that these are mostly used to represent a spiral error structure.

The shapes shown in Figs. 3-12 may be said to be the essence of the errors from true form generated by the different manufacturing sequences. The dominant behavior for CD (Fig. 3) is a single-lobed right-handed spiral shape. It is designated as single-lobed because a cross section at any height is essentially a circle. Analysis of individual cylinders shows that the pitch of this spiral varies from about 1.3 to 4 times the pitch of the tool. CD eigen shape 2 is the other phase of the spiral and is not shown. The spiral shape was more predominant in smaller holes and was particularly pronounced in a 1/4" hole generated with a parabolic flute drill. It should be noted that the drills used have 2 flutes and produce a 1-lobe (n-1) pattern. The CD behavior that becomes more predominant for larger diameter holes is the eigen shape 3 shown in Fig. 4. It has a small banana shape combined with several different orders of z dependence.

The holes manufactured with the final pass being an n-flute reamer are dominated by n-1 and n+1 lobed patterns. They often also have a z dependence dominated by taper and/or hourglass. The CDR holes show both a nearly pure z dependence (Fig. 5), which is approximately an hourglass shape, and a lobed θ dependence (Fig. 6). The pattern shown in Fig. 6 is a 7-lobed pattern. The other phase of 7-lobe and both phases of a 5-lobe pattern also are present is the sequence of eigen shapes, but are not shown. Whereas the 7-lobe shape was more predominant in the CDR method, the CDBR method has a more predominant 5-lobe pattern (Fig. 7) but also has 7-lobe variation (Fig. 8). Notice that the CDBR holes are truer in the z direction than the CDR holes with the only z dependence in the first two eigen shapes being the slight taper in Fig. 7.

Holes generated by a final pass of an end mill are dominated by taper (Figs. 9, 11). They can also have very significant hourglass (Fig. 10). Fig. 10 also shows a 2-lobed spiral component. In the NC generated holes of the contour milling operation (Figs. 11, 12) the angles at which the tool entered and left the material are essentially the same from hole to hole. This can be seen as a slight hint in the shape dominated by taper (Fig. 11) and in a very conspicuous way in Fig. 12. The presence of this eigen shape 2 indicates this pattern varies from part to part.

Fig. 2 allows us to conclude that more complicated operations result in structures which vary from true form in a more complicated and detailed way. The operations which need few eigen shapes to explain the errors they generate can be said to have few degrees of freedom in the behavior of the tools as the holes are being generated. With each successive pass of a tool (which often is removing little material) the tool motion can couple with the existing pattern in the hole. That is, the previous pattern imprints itself on the following operation, which also produces its own contribution to the details of the shape of the hole. The holes generated by a mill, which is a reasonably rigid tool compared with either a drill or a reamer, essentially erase the effects of the preceding operation and might be considered to be a single-pass operation. This is particularly true of the contour milling operation, which removes much more material than the plunge milling operation. In the figure this is demonstrated by the fact that the milling operations require the fewest eigen shapes to explain the patterns they generate. The two-pass operation, CD, requires more shapes, the three-pass operation, CDR, requires even more, and the four-pass operation, CDBR, requires the most explanation.

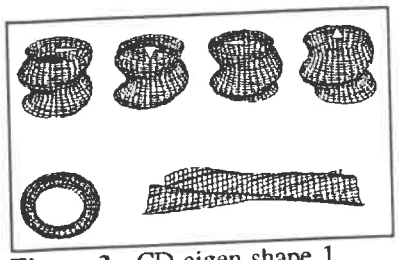

Figure 3. CD eigen shape 1.

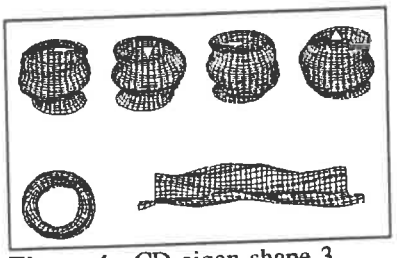

Figure 4. CD eigen shape 3.

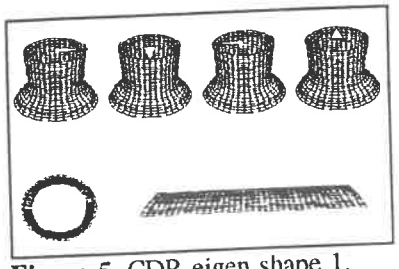

Figure 5. CDR eigen shape 1.

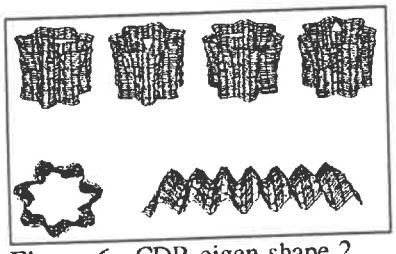

Figure 6. CDR eigen shape 2.

Figure 7. CDBR eigen shape 1.

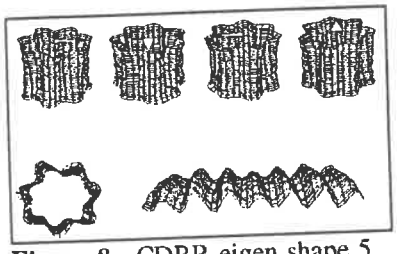

Figure 8. CDBR eigen shape 5.

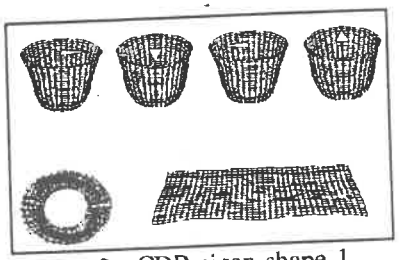

Figure 9. CDP eigen shape 1.

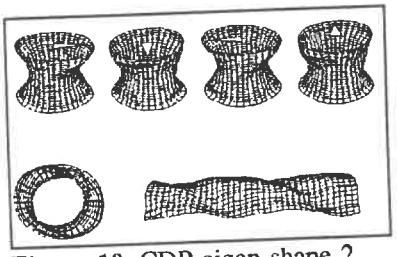

Figure 10. CDP eigen shape 2.

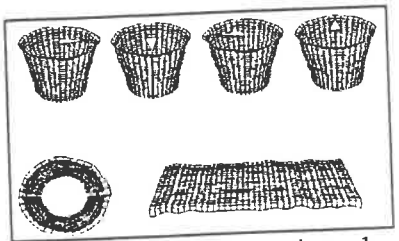

Figure 11. CDM eigen shape 1.

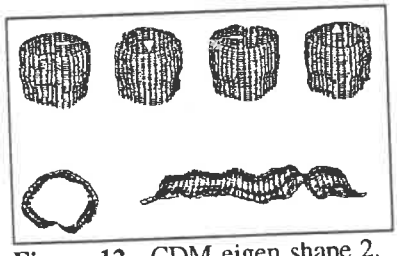

Figure 12. CDM eigen shape 2.

REFERENCES

[1]*Work supported in part by the Quality Assurance Program of the Institute for Manufacturing and Automation Research, Consortium for Advanced Manufacturing International, Bedford, Texas*

[2]K.D. Summerhays, R.P. Henke, R.M. Cassou, J.M. Baldwin, and C.W. Brown (1995), *New Algorithms for the Evaluation of Discrete Point Measurement Data and for Sample Point Selection on Surfaces with Systematic Form Deviations*, Proc. 10th Annual Meeting of the American Society for Precision Engineering, Austin, TX, 388-391.

BEST FIT TRANSFORMATION AND UNCERTAINTY ANALYSIS IN COMPUTATIONAL METROLOGY

Hong-Tzong Yau
Department of Mechanical Engineering
National Chung Cheng University
Chia-Yi, Taiwan

Introduction

In computational metrology, the key process for measurement and tolerance evaluation is the fitting of geometric elements [1], or sometimes referred to as the best fit. The goal of the best fit is to create substitute geometry from discrete measurement points. Traditionally, various fitting algorithms and criteria are used to fit data points to different geometric elements such as line, circle, plane, and cylinder. Due to the divergence of methods and criteria used, the best fit results tend to be different from case to case. Efforts have been made in the U.S. and Europe to develop software testing systems that will evaluate CMM software errors by comparing the results against some known reference algorithms.

In the author's previous work [2], a unified best fit algorithm was proposed as a reference algorithm for software testing based on least-squares criterion (which is adopted by most CMM vendors). The proposed algorithm does not rely on approximation or linearization to reduce complexity or enhance speed, therefore can produce "exact" answers opposed to approximate solutions. More importantly, the method points out that the best fit can be viewed as a coordinate transformation between measurement data and nominal geometry. Therefore, best fit for any geometric feature can be unified by minimizing the following cost function:

$$F = \sum_{i=1}^{m} \left| Q_i - TS_i \right|^2 \qquad (1)$$

where Q_i is a measured point, S_i is Q_i's projected point on the nominal surface, and T is the coordinate transformation matrix. The proposed algorithm has proven to be robust and can generate accurate solutions verified by simulations and experiments [2].

Uncertainty Analysis

Even with a perfect algorithm, true surface deviations plus measurement errors and limited sampling data can lead to uncertainties in the best fit result [3]. Assessment of uncertainty becomes important as it reveals reliability of the best fit result and can guide the inspector to determine a proper CMM sampling plan. Since the best fit can be viewed as a coordinate transformation, uncertainties of the best fit result can be modeled as the possible variations of the transformation parameters. In a 3D best fit, this would involve 3 rotation parameters (row, pitch,

and yaw) and 3 translation parameters (x, y, and z displacements). The variation of these parameters $\delta\tilde{t}$ can be related to surface form error $\tilde{\varepsilon}$ by a sensitivity matrix A [4].

$$\tilde{\varepsilon} = A\delta\tilde{t} \tag{2}$$

Assuming δt_i and ε_i are normally distributed random errors with zero means and let the sensitivity measure of δt_i to ε_i be defined as

$$S_{t_i} = \frac{\sigma_{t_i}}{s} \tag{3}$$

where σ_{t_i} and s are the standard deviations of δt_i and ε_i respectively, general sensitivity equation can be derived as [4]:

$$S_{t_i} = \sqrt{\sum_{j=1}^{m}\left[\left(A^T A\right)^{-1} A^T\right]_{i,j}^2} \tag{4}$$

This sensitivity measure relates uncertainties of the best fit transformation to surface form errors, measurement positions, and CMM sampling size.

The first attribute that affects the best fit uncertainties is the surface form error. Assuming sufficient measured points are sampled, based on equation (3), uncertainty is proportional to the standard deviation of the surface form error. In other words, the larger the form error, the more uncertain (and less reliable) the best fit result.

The second attribute considered is the sampling positions. Typically, given a part surface for measurement, uniform distribution is used to determine the sampling positions. In terms of reducing the uncertainty, "best" sampling positions (with a fixed number) can be obtained by minimizing the overall uncertainty values.

$$F = \sum_{i=1}^{6} S_{t_i} \tag{5}$$

Since the sensitivity matrix A is a function of the sampled point $\vec{N}_j$ and its normal vector $\vec{n}_j$, the cost function becomes

$$F = F(A(\vec{N}_j, \vec{n}_j)) \qquad j = 1,..,m \tag{6}$$

Yet, any surface can be parameterized as a function of the bivariate surface parameters (u, v). Therefore,

$$F = F(A(\vec{N}(u_j, v_j), \vec{n}(u_j, v_j))) \qquad j = 1,..,m \tag{7}$$

The minimization of this function is a nonlinear optimization problem with 2m variables. In this work, conjugate gradient method is adopted to search for the optimal sampling positions given a fixed number of measurement points. Uniform parameter distribution is used to initialize the iterative search. Figure 1 shows the method applied to a complex die surface for finding its best measurement positions. Figure 2 shows the convergence of the cost function. It appears the improvement in lowering the uncertainty is definite, but the gain is not much (compared to the sampling size effect discussed later). The result seems to indicate that as long as measurement

points are well distributed, fine tuning of the sampling positions does not reduce the best fit uncertainties much.

The third attribute considered is the CMM sampling size. It is known that increasing CMM sampling size would reduce uncertainties. But can this effect be measured and quantified? Using the previous die surface as an example, sensitivity measures (proportional to uncertainty values) for the transformation parameters were calculated and plotted against the CMM sampling size (Figure 3). The sensitivity measures exhibit exponentially decreasing patterns as the sampling size increases. Based on the 2D circle experience [4], it is speculated that the sensitivity measure (uncertainty value as well) is in general inversely proportional to the squared root of the sampling size. A theoretical curve $S = K / \sqrt{m}$, where K is a constant, is used to fit the curves in Figure 3. K can be calculated by

$$K = \frac{\sum_i S_i / \sqrt{m_i}}{\sum_i 1 / \sqrt{m_i}} \qquad (8)$$

Good matches were found between the theoretical curves and the original curves.

Once "calibrated", this curve can be used to characterize the relationship between uncertainty and CMM sampling size. For example, if the magnitude of the surface form error is increased by two, the CMM sampling size should increase by 4 to maintain the same uncertainty level.

The last but not the least important attribute is the geometric shape of the element. Consider a cone symmetric to the z-axis. The two parameters affecting the geometric shape are the height H and the radius R. If we vary H while holding R and plot the sensitivity measures of the x and y translation components, it results in interesting curves as in Figure 4. When R = H, uncertainty is at its lowest value, indicating when the cone angle is 90 degrees, the center position of the base circle is most certain. However, as H decreases, the uncertainty increases rapidly. On the other hand, when H is larger than R, the uncertainty value would increase somewhat and then saturates at a fixed value.

References

[1] T. Hopp, 1993, "Computational Metrology", Proceedings of the 1993 International Forum on Dimensional Tolerancing and Metrology, CRTD-Vol. 27.

[2] H.T. Yau, 1996, "A Unified Least-Squares Approach to the Evaluation of Geometric Errors Using Discrete Measurement Data", Int. J. of Machine Tools and Manufacture, in press.

[3] S.D. Phillips, B. Borchardt, and G. Caskey, 1993, "Measurement Uncertainty Considerations for Coordinate Measuring Machines", NIST report 5170.

[4] H.T. Yau, 1993, "Uncertainty Analysis of Circle and Arc Measurement Using Discrete Sample Points", Proceedings of the 1993 ASPE Annual Meeting.

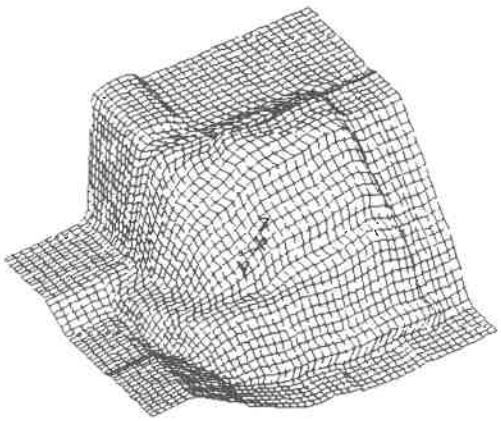

Figure 1. A complex die surface for uncertainty analysis.

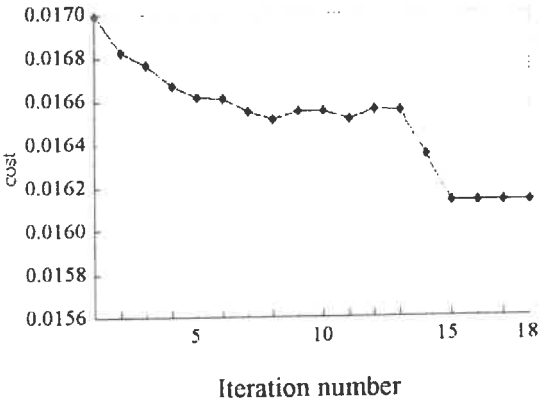

Figure 2. Convergence of the cost function.

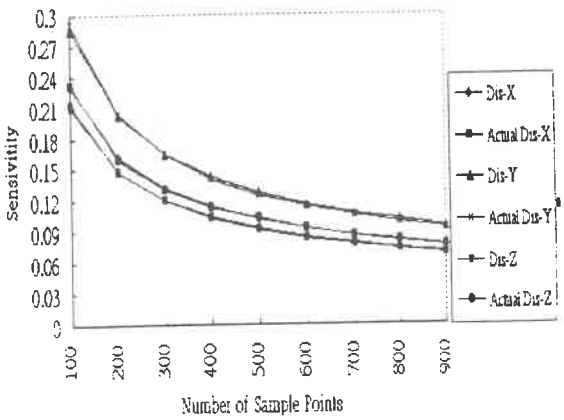

Figure 3. Theoretical and simulated sensitivity curves for the translation vector.

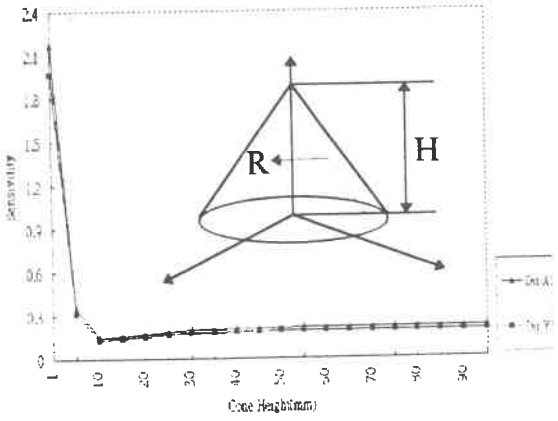

Figure 4. Illustration of geometric factor on the sensitivity curves.

Uncertainty of the Coordinate Measurement Process Due to Unwanted Asperities

James G. Salsbury *
The University of North Carolina at Charlotte; Charlotte, NC 28223

Introduction

In a variety of industries, coordinate measuring machines (CMMs) are becoming more commonly integrated into the manufacturing environment. Manufacturing process control requirements are driving CMMs towards increases in measurement flexibility, speed, automation, and ease of operation. In addition, there is an increasing desire to locate the measurement process as close as possible to the actual machining process. This often results in the placement of CMMs in relatively poor operating environments. Under these conditions, the quality of the measured part surface can be negatively effected by influences such as burrs, chips, coolants, cutting oils, and dirt. These factors can create unwanted asperities [1], or "spikes" or "flyers", in the measured data which can distort the dimensional results. The impact of unwanted asperities has most often been considered controllable or negligible by proper part handling and cleaning [2]; however, as the need for faster throughput and higher accuracy measurements continue to rise, the effect of the unwanted asperities are becoming more of a concern relative to the uncertainty of the CMM measurement results.

In this paper, an approach is presented to estimate the measurement error arising from the influence of an unwanted asperity. The analysis includes the development of the relationship between the sampling technique used to measure the part feature, including the number of discrete data points, and the magnitude of the surface irregularity. This approach is then incorporated into the CMM measurement uncertainty budget in order to determine acceptable limits for the magnitude of an unwanted asperity for a given measurement process. The approach presented in this paper is developed around the measurement of a circle diameter, though the method could be expanded to other geometric features using the same techniques.

Coordinate measuring machines, like a majority of today's modern dimensional metrology instruments, measure geometric features by sampling discrete points across surfaces and then utilize mathematical fitting algorithms to determine the "substitute geometry" of the feature. The measurement method of typical CMMs, using discrete sampling and the associated fitting algorithms, has prompted research efforts and a variety of publications over the past five to ten years (for example, see [3], [4], [5]). Those issues and discussions, however, are beyond the scope of this paper; instead, the measurement methods most widely used today on CMMs were considered. These more typical methods are based on least squares fitting algorithms, smaller point data sets, and no data elimination or filtering methods. However, since continuous scanning technology is becoming more readily available today, thus making larger data sets more feasible, this study also considers larger data sets.

Measurement Error in Circle Diameters

Figure 1 shows the typical results that may be seen when an unwanted asperity influences the measurement of a circular bore. In this particular example, the large inward deviation shown in (a) was determined to be due to the measuring probe stylus contacting a small spot of coolant that had dried on the bore surface. In (b), the bore has been recleaned and remeasured. Typically, when results such as these are discovered during part measurement, a decision to either accept the data or to remeasure the part must be made. What is missing is an understanding of how the unwanted asperity affects the measurement so that limits for the magnitude of the unwanted asperity can be established.

One alternative method of handling the unwanted asperity is to eliminate it. A number of CMM manufacturers offer some type of asperity or "data flyer" elimination in their software. Some typical approaches include the use of a set threshold value [6] or by basing the threshold relative to some

* Previously with Cummins Engine Company; Fuel Systems Business; Columbus, Indiana 47201

The standard uncertainty value can then be converted into a limiting value for the maximum change in the diameter, ΔD. It is assumed that the magnitude of the effect of the unwanted asperity is equally likely to be any value up to ± ΔD. This implies a rectangular or uniform distribution for the values. Using this model, the limiting value of ΔD can then be approximated from the standard uncertainty value as follows [9]:

$$u_a \cong \Delta D / (3)^{1/2} \quad (8)$$

$$\Delta D \cong (0.75) * (3)^{1/2} \cong 1.30\ \mu m \quad (9)$$

This maximum value of ΔD is then used in equation (4), which results in the following expression for the maximum allowable magnitude of an unwanted asperity, δ, for a given number of data points, *n*:

$$\delta = 0.65\, n \quad \mu m \quad (10)$$

Using equation (10), control limits for the magnitude of δ can be established to ensure that the uncertainty of the measurement process does not exceed acceptable limits due to larger unwanted asperities. Additionally, this equation can be used to help decide upon an optimal sampling density. For example, if ten inspection points are used for this circle, the control limit for δ is only 6.5 μm; however, if 50 points are taken, the control limit for δ increases to a fairly large 32.5 μm. The impact of this information can then be weighed against the time required to sample the additional points, the time and cost of measurement and potential remeasurements, the probability of probing unwanted asperities, and other factors influencing the sampling strategy for the particular feature.

Conclusions

Measurement can be a slow and costly operation. New CMM technology is allowing for higher data density sampling, particularly through the use of high-speed continuous scanning, which allows more of the part surface to be measured. With this trend, the occurrence of unwanted asperities in data sets may become more prevalent. Unless more intelligent methods are developed to sort out and eliminate unwanted asperities from the actual part surface data, CMM users will have to find methods to deal with the potential errors caused by the unwanted asperities. The cost of recleaning and remeasuring parts is often very high. This paper has shown that it is possible to quantitatively determine the effect of the unwanted asperities on the measurement results. The understanding of this relationship can then be used when developing an uncertainty budget for the CMM measurement process. The result is the definition of control limits for the unwanted asperities that will indicate to the CMM user when the data are questionable and when remeasurement of the part is recommended.

References

1. Term "unwanted asperity" was suggested by Mark Malburg, Cummins Engine Company, 1996.
2. Nilsson, J. T., "Application Considerations," Coordinate Measuring Machines and Systems, Bosch, J. A. (ed.), Marcel Dekker, New York, NY, 1995.
3. Hocken, R. J., Raja, J., and Babu, U., "Sampling Issues in Coordinate Metrology," *Manufacturing Review*, Vol. 6, No. 4, December 1993.
4. Hopp, T., "Computational Metrology," *Manufacturing Review*, Vol. 6, No. 4, December 1993.
5. Phillips, S. D., "Performance Evaluations," Coordinate Measuring Machines and Systems, Bosch, J. A. (ed.), Marcel Dekker, New York, NY, 1995.
6. CONCERTO User's Reference Manual, SIP, Geneva, Switzerland.
7. SCEPTRE Software Manual, Electronic Measuring Devices, Flanders, New Jersey.
8. Lin, S., Varghese, P., Zhang, C., and Wang, H. P. B., "A Comparative Analysis of CMM Form Fitting Algorithms," *Manufacturing Review*, Vol. 8, No. 1, March 1995.
9. International Organization for Standardization, *Guide to the Expression of Uncertainty in Measurement*, Geneva, Switzerland, 1995.
10. Salsbury, J. G., "A Simplified Methodology for the Uncertainty Analysis of CMM Measurements," Society of Manufacturing Engineers Technical Paper IQ95-155, 1995.

THREE-DIMENSIONAL METROLOGY FRAME FOR PRECISION APPLICATIONS

Maurice J. Prather, James F. Cuttino, and Dale E. Schinstock
Department of Mechanical Engineering
The University of Alabama

Abstract

A unique, three-dimensional, non-contacting metrology frame is presented. The metrology system uses information from three orthogonal XY stages to produce a six degree of freedom spatial representation of the object being measured. The forward and inverse kinematic solutions are presented and subsequently used to produce both a working envelope and an error budget for the metrology system.

Introduction

Complex, three-dimensional mechanical devices such as hexapod milling machines are faced with the challenge of measuring motion in six degrees of freedom. In the case of hexapods, encoders are often used on the motors of the actuators or linear sensors are mounted on the legs to measure the motion of the platform. This form of measurement directly couples the metrology system to the object being measured and subjects it to the same errors to which the device is subjected.

A three-dimensional, non-contacting metrology system (*3DMS*) is presented which provides position and orientation information while physically decoupling the metrology frame from the object being measured. By decoupling the metrology system from the mechanism, measurement errors are reduced and the design of the mechanism can be greatly simplified.

Conceptual Design

As shown in Figure 1, the 3DMS utilizes three orthogonal stages to produce the 6 degree of freedom (d.o.f.) representation of the object being measured. Three orthogonal laser diodes are mounted to the object and project their beams onto the orthogonal stages of the metrology system. Mounted on each XY stage is a four quadrant photo detector that measures the variance of the laser beam from the detector's center point. As the body being measured moves through space, the corresponding XY stages track the movement of the laser beams using the photo detector signals as feedback. In turn, the position of each XY stage is measured using plane mirror laser interferometers. This information is then used to provide a solution for the 3-D spatial representation of the object.

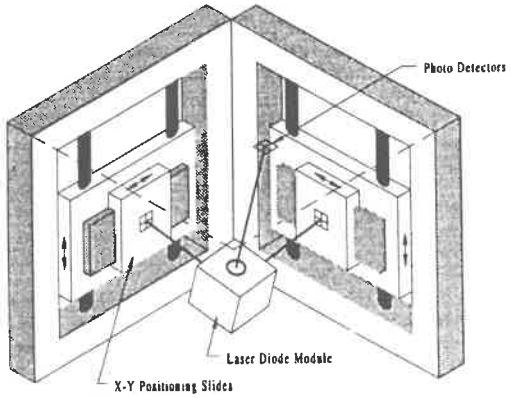

Figure 1: Metrology Frame (Top stage and interferometers removed for clarity)

Kinematic Solution

Both the forward and inverse kinematic solutions have been developed for the 3DMS. In the inverse kinematics it is assumed that the position and orientation of the body are known in the global coordinate system. Using this and known information about the construction of the system, the XY coordinates of each detector can be determined in its respective stage frame. In contrast, the forward kinematic solution assumes that the detector

coordinates are known in their respective stage frames. This information is used to determine spatial representation of the body in the global metrology frame.

The development of both kinematic solutions uses five coordinate frames. One frame is associated with each XY stage, one is attached to the body being measured, and one is a global coordinate system to which all other frames are referenced. The paths of the laser beams are nominally coincident with the axes of the body's reference frame and are referred to as the diode vectors.

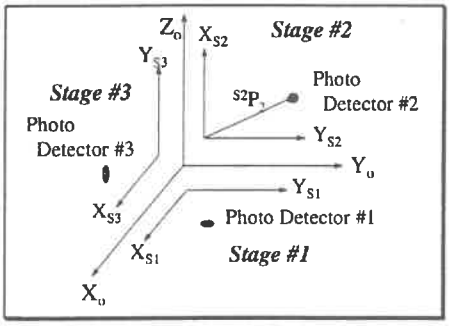

Figure 2: Axes definition

Inverse Kinematics

In the inverse kinematics the known position and orientation of the body (*b*) relative to the global origin (*o*) are represented by the homogeneous transformation matrix, ${}^{o}T_{b}$. The location of each detector with respect to its corresponding stage frame (s_1, s_2, *or* s_3) is given by,

$$ {}^{si}P_i = {}^{si}T_o \, {}^{o}T_b \, {}^{b}P_i \qquad (1) $$

where *i* represents both the stage and detector number as shown in Figure 2. The transformation matrices, ${}^{si}T_o$, are constructed using physical measurements of the metrology system. The position vector from the body to a corresponding photo detector, ${}^{b}P_i$, is unknown, but it can be separated into a known unit vector and an unknown magnitude,

$$ {}^{b}P_i = m_i \, {}^{b}\hat{p}_i . \qquad (2) $$

Substituting (2) into (1) results in three scalar equations that are linear in the magnitude and are represented by the vector equation

$$ {}^{si}P_i = \left({}^{si}R_o \, {}^{o}R_b \, {}^{b}\hat{p}_i\right) m_i + {}^{si}R_o \left({}^{o}P_b - {}^{o}P_{si}\right). \qquad (3) $$

Here, ${}^{si}R_o$ and ${}^{o}R_b$ are the rotation matrices from the stage frame to the global coordinate system and from the global coordinate system to the body, respectively.

The scalar equation in Equation 3 corresponding to the z component can be used to solve for m_i, since the z component of the detector is known in its stage frame. Substituting m_i back into the other two equations gives the XY coordinates of the detector, completing the inverse kinematics.

Forward Kinematics

The forward kinematic solution begins by equating the measured detector locations, ${}^{o}P_i$, to the unknown diode vectors through a transformation.

$$ {}^{o}P_i = {}^{o}T_b \, {}^{b}P_i \qquad (4) $$

This transforms the diode vector from the body reference frame to the global coordinate system. Subtracting any two of the three position vectors yields

$$ {}^{o}P_i - {}^{o}P_j = {}^{o}R_b \left[m_i \, {}^{b}\hat{p}_i - m_j \, {}^{b}\hat{p}_j \right] \qquad (5) $$

Equation (5) contains two unknown scalar values, m_i and m_j, and an unknown rotation matrix ${}^{o}R_b$. Using (5) and the fact that rotating a vector does not change its magnitude, the following equation can be written:

$$ \left| {}^{o}P_i - {}^{o}P_j \right|^2 = \left| m_i \, {}^{b}\hat{p}_i - m_j \, {}^{b}\hat{p}_j \right|^2 . \qquad (6) $$

Equation (6) represents a triangle drawn between the body and two of the detectors. Using the law of cosines and assuming that the two unit vectors are orthogonal, then

$$\left| m_i {}^b\hat{p}_i - m_j {}^b\hat{p}_j \right|^2 = m_i^2 + m_j^2 - 2 m_i m_j \cos(\theta_{ij}) \quad (7)$$

$$\left| {}^oP_i - {}^oP_j \right|^2 = m_i^2 + m_j^2 \quad (8)$$

Three combinations for i and j are used in (7) and (8) to obtain three equations. These equations are solved for the three magnitudes. The rotation matrix is then calculated by solving equation (5). Using the rotation matrix, the Euler angles describing the orientation are found. The position vector of the body is calculated using the equation

$$ {}^oP_b = {}^oP_i - {}^oR_b m_i {}^b\hat{p}_i . \quad (9)$$

This completes the forward kinematics solution with the assumption that the three laser diodes are orthogonal.

Error Budget

An error budget was developed for the 3DMS using the following procedure. First, the spatial position and orientation of the body are assumed. The error components (such as non-orthogonalities) are then introduced into the system, and the inverse kinematics are used to find the "actual" locations of the detectors. Since the metrology system will at this point be unaware of error motions, the predicted position and orientation of the body are calculated using the forward kinematics and assuming no kinematic errors. The final error budget is determined by the differences between the assumed and the predicted spatial representations.

Two errors are incorporated into the inverse kinematics, non-orthogonality of the stages and non-orthogonality of the laser beams. Two errors are incorporated after the inverse kinematics by modifying the detector coordinates obtained. These two errors are detector motion in the z direction of each stage and effects due to yaw. The z motion error of each stage is comprised of three components, pure z motion of the stage and error due to roll and pitch motions. Other error motions in the stages do not affect the error budget since they are measured by the interferometers.

The specific 3DMS being studied consists of air bearing stages with 4" travel. The vertical and angular error values were obtained from the stage manufacturer and are 0.5 μm and 3 arc-seconds (roll, pitch, and yaw), respectively. The non-orthogonalities of the laser beams and the XY stages were assumed to be 5 arc-seconds but will depend on the physical construction of the 3DMS.

Determining the error over the entire workspace of the 3DMS provides useful insight to the interaction between the stages and the body. The error budget in Figure 3 shows the position error when the object is translated with no rotation. The error was mapped across the horizontal workspace of the 3DMS at four equally spaced heights. The upper left graph is the minimum z position. In sequence from left to right, the height is increased to the maximum z position. The error magnitude increases as the body moves away from each of the stages.

Orientation error for the pure translation case is shown in Figure 4. The maximum orientation error is 8 arc-seconds and occurs when z is maximum. The non-symmetry is due to the fact that stage 2 is tilted towards stage 1 while stage 3 is tilted away from stage 1 in the x and y directions, respectively.

Figures 5 and 6 show the position errors and orientation errors for translations with 10^o rotations in the x, y, and z axes. The position error for both cases changes less than 30% with the additional rotations. As with the position error budgets, the orientation error magnitude in Figures 4 and 6 increases as the body's height is increased; however, the error magnitude plateaus toward the extreme corner of the 3DMS. This plateau is indicative of an increased angular resolution due to increased radial length of each laser beam.

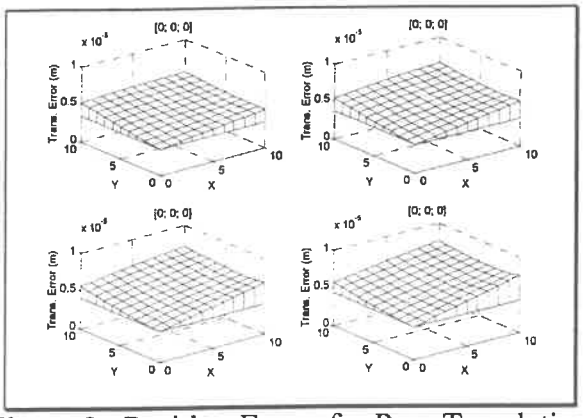

Figure 3: Position Errors for Pure Translation

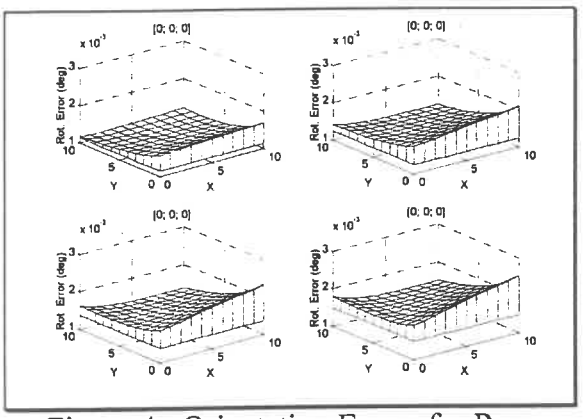

Figure 4: Orientation Errors for Pure Translation of the Object (no rotation)

Workspace Envelope

The inverse solution was used to calculate the working envelope of the 3DMS. A 2-dimensional grid representing a single XY stage was used to determine the maximum yaw angles that can measured. Figure 7 shows the relationship between the maximum yaw angle and the working envelope for the single stage.

Results and Conclusions

A unique, non-contacting metrology system, the 3DMS is introduced. The forward and inverse kinematic solutions for the 3DMS are presented. The process by which error motion values are incorporated into the overall solution is also described. The error budget for the 3DMS indicates position accuracy within 10 micrometers is easily obtainable. Rotational accuracy within 10 arc-seconds or less is possible depending upon the location of the body within the workspace.

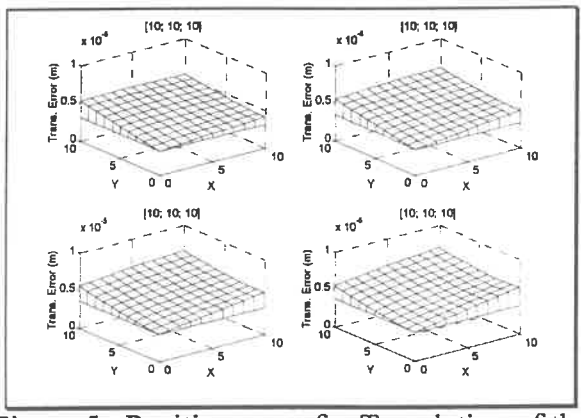

Figure 5: Position error for Translation of the Object and Rotations of θ, Φ, and Ψ = 10°

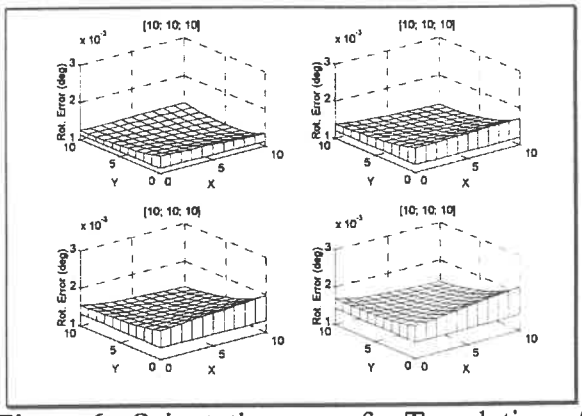

Figure 6: Orientation error for Translation of the Object and Rotations of θ, Φ, and Ψ = 10°

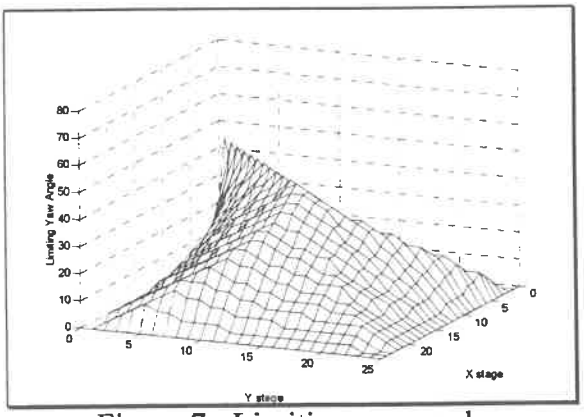

Figure 7: Limiting yaw angle

ASSESSMENT OF PLATEAU HONED SURFACE TEXTURE USING WAVELET TRANSFORM

Xiangyang Liu, Jay Raja and Harikrishna Sannareddy
Precision Engineering Laboratory
Department of Mechanical Engineering and Engineering Science
The University of North Carolina at Charlotte
Charlotte, NC 28223, USA

Introduction

Plateau honing is an important finishing technique used in the production of cylinder bores. Plateau honed surface is an "engineered surface" using two processes, namely rough and fine honing, in one setup. Monitoring and controlling the plateau honing process can be accomplished by characterizing these multiscale features comprehensively. The assessment and characterization of plateau honing and other multiprocess surface is difficult using traditional surface texture analysis. This paper briefly reviews the techniques used for characterizing honed surfaces and presents the application of wavelet transform to characterize plateau honed surface.

Analysis of plateau honed surfaces

Plateau honing is used to generate a particular type of surface structure that consists of deep groves for oil retention and fine plateaus for high bearing capability. The plateau honed surface is produced by first rough honing to generate deep scratches and the then fine honing to remove the peaks and obtain a plateau of fine machine marks. The resulting surface texture is a combination of the marks with various scales of amplitudes and wavelengths generated by the rough and fine honing process. A typical plateau honed profile is shown in the figure 1.

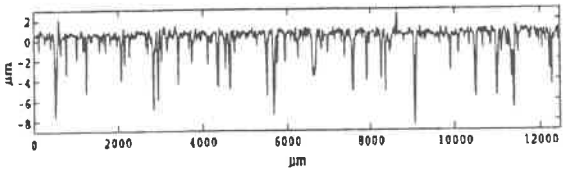

Figure 1 Plateau honed surface texture

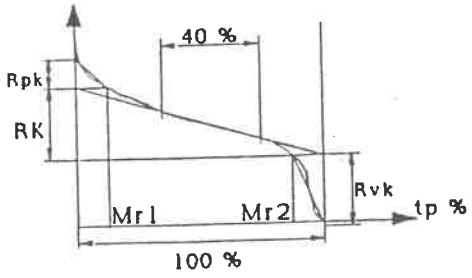

Figure 2 R_k parameters

A common method for characterizing plateau honed surface is using R_k parameters, which is specified according to DIN 4776 [1]. In this approach, the original plateau honed surface texture is divided three regions namely, extreme peaks, core and extreme valleys, shown as in figure 2. First, a minimum slope line is calculated

obtained within a 40% t_p window and the core of the profile is designated. Subsequent computation of parameters based on this line and the regions above and below it result in the following parameters such as kernel or core roughness depth R_k, reduced peak height R_{pk}, reduced valley depth R_{vk}, material ratio M_{r1} and M_{r2}. M_{r1} and M_{r2} establish a measure of the bearing ratio at the depth where the profile core meets the peaks or valleys respectively.

Another method for characterizing plateau honed surfaces is based on analyzing the cumulative distribution plot on a normal probability graph[2, 3]. A Gaussian distribution of each component of the plateau honed surface texture is appropriate since the abrasive grains within the honing stone are random in nature. Plateau honing can be modeled as two Gaussian processes. The plateau honing operation can be summarized by presenting the profiles, amplitude distributions and probability plots of the cumulative distribution as shown in figure 3. Figure 3a and 3b represent the individual stage of the plateau honing operation and figure 3c displays the truncation of the rough honed surface by the plateau surface. The slopes of these two lines represent the R_q values of the fine and rough texture. This information can be used to control the fine and rough honing processes.

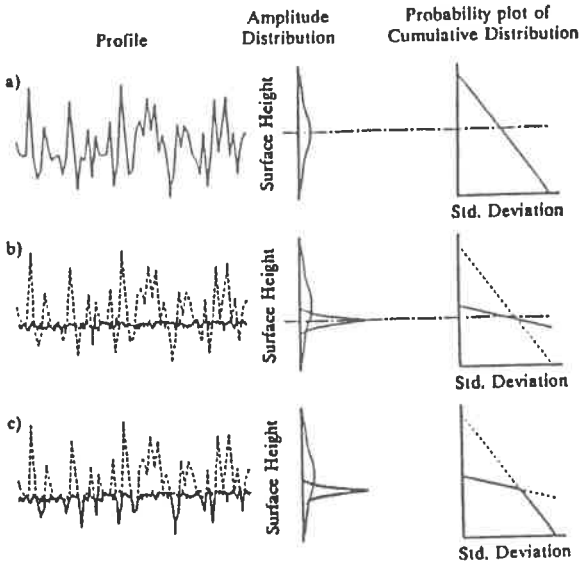

Figure 3 Characterization based on probability model

Wavelet transform for characterizing plateau honed surfaces

The wavelet analysis is performed using the basis family functions derived from the mother wavelet function by translation and dilation. The wavelet basis constructed this way has a flexible time-frequency window localized on time-frequency plane[4]. This provides a set of windows that change in proportion to the scale of the local event

observed and whose frequency bandwidth matches the frequency of the component studied. The fundamental idea behind wavelet transform is to analyze signal according to scale, i.e. process data at different scale or resolution, shown as in figure 4. Relatively large structures of a signal is looked at a low resolution and then smaller structures are added into the interpretation by increasing the resolution. This method appears to have the potential for analyzing the multiscale aspects involved in plateau honed surfaces. The property of good time-frequency localization with a flexible time-frequency resolution of wavelet transform is explored for characterizing honed surface. The Daubechies wavelet basis is used in this study.

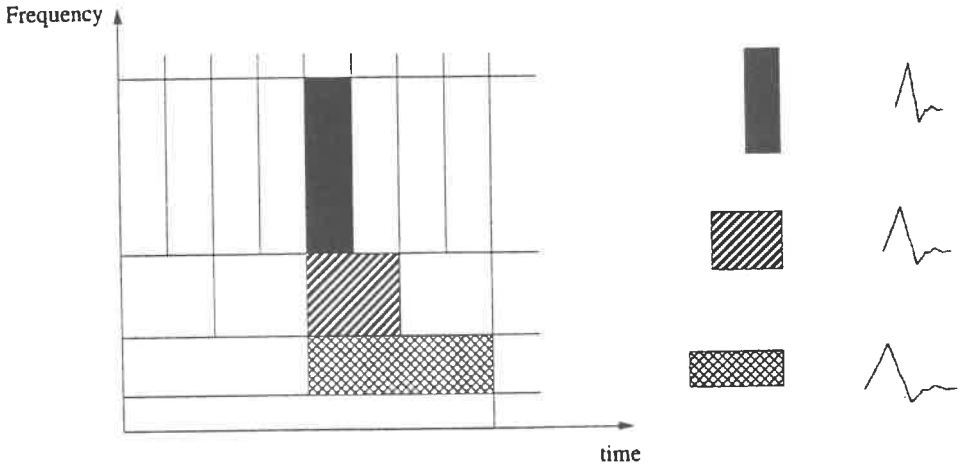

Figure 4 Flexible time-frequency resolutions of wavelet transform

In order to characterize the plateau honed surface texture, the wavelet coefficients are computed first and then the wavelet coefficients are divided into two groups based on the ratio of the valley energy to the total energy of the profile. The selection of this ratio will determine how well we separate the valley region and the plateau region. Generally, the key features of the texture are involved in the wavelet coefficients with larger magnitude and the reconstruction of the original texture is possible by using a few wavelet coefficients of larger magnitude. In plateau honed surface texture, these coefficients contain the details of the valley region since this region is the dominant than the plateau region. For constructing valley region, all coefficients larger than the threshold are kept with full accuracy while all smaller coefficients are set to zero. For constructing plateau region, all coefficients smaller than the threshold are kept with full accuracy while all greater coefficients are set to zero. By using inverse wavelet transform, the plateau region and the valley region of the plateau honed profile can be obtained separately. The two profiles obtained after separation can be characterized separately using the traditional surface texture parameters.

Figure 5 shows the separated plateau and valley portions of a plateau-honed profile using energy ratio R = 0.9. The separated plateau and the valley portions shown in this figure represent the corresponding portions of the original profile. Future work is in

progress to arrive at a quantitative basis for separating the rough and fine honed texture. The wavelet transform permits the analysis of surface texture in smaller bandwidths. These smaller bandwidths could be related to process parameters.

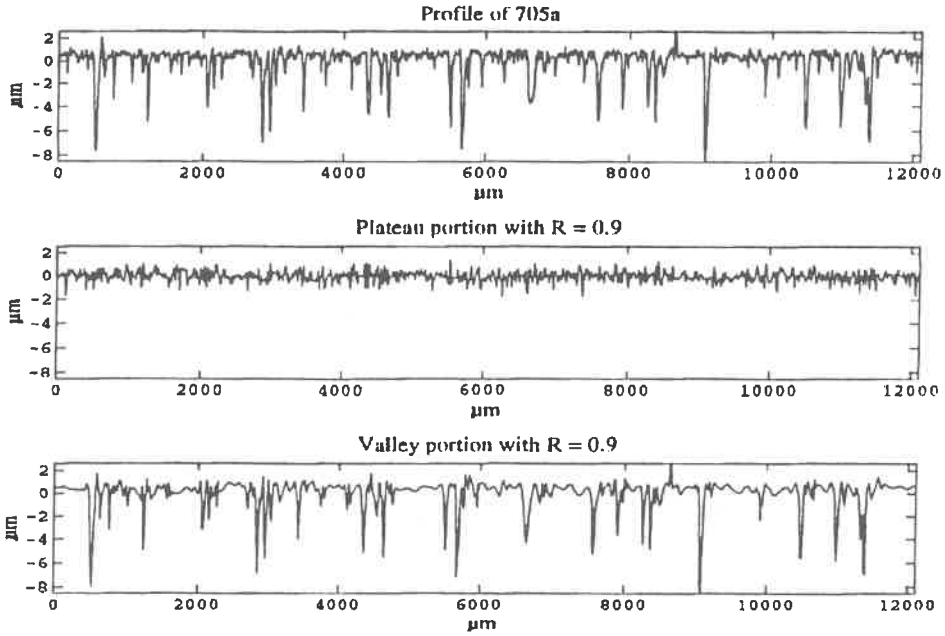

Figure.5 Separation of plateau honed surface texture by wavelet transform

References

1. DIN 4776, 1990, Measurement of surface roughness.
2. Mark, C. Malburg, Jay Raja, "Characterization of Surface Texture Generated by Plateau Honing Process", Annals of the CIRP Vol. 42/1/1993.
3. Mark. C. Malburg, 1989, The characterization of Surface Texture Generated by Multi-Process Manufacture, M. S. Thesis.
4. M. Vetterli and C. Herley, "Wavelets and Filter Banks: Theory and Design", IEEE Transactions on Signal Processing, Vol. 40, 1992.

Authors Index

Abackerli, Alvaro J. . . . 223
Abadin, Zainul . . . 638
Ahn, Hyeong-Joon . . . 328
Ahn, Jung-Hwan . . . 496
Aketagawa, Masato . . . 150
Allen, James P. . . . 648
Annecchino, L. . . . 566
Arcona, Christopher . . . 412, 500
Ascanio, Gabriel . . . 346
Atherton, Paul D. . . . 20
Badami, Vivek G. . . . 391
Baines, R. W. . . . 467
Baker, R. . . . 80
Baldwin, Jon M. . . . 654
Barnes, C. . . . 432
Bhaskar Dixit, C. S. . . . 551
Bibler, Jared E. . . . 62
Bierden, Paul . . . 69
Bifano, Thomas G. . . . 69, 532
Blaedel, Kenneth L. . . . 62, 400
Bowen, D. Keith . . . 363
Brinksmeier, Ekkard . . . 56, 506
Brown, C. W. . . . 654
Caggiano, Helen E. . . . 69, 532
Cai, Guang Qi . . . 578
Campos Rubio, J. C. . . . 294
Carlisle, Keith . . . 51
Cassou, R. M. . . . 654
Castle, Philip J. . . . 154
Chang, In-Bae . . . 328
Chang, S. B. . . . 416
Chee, W. K. . . . 490
Chen, Jenq-Shyong . . . 273
Chen, Jun . . . 132
Chen, Xuemei . . . 520
Chen, Y. . . . 51
Chetwynd, Derek G. . . . 141, 336, 363
Chu, Xiaohua . . . 642
Chun, Keyoung Jin . . . 300
Cook, Lee . . . 80
Cuttino, James F. . . . 310, 668
Daniel, Jay . . . 510, 561
Danyluk, Steven . . . 80
Darnold, Joel R. . . . 15
Davis, L. A. J. . . . 141
Day, Robert D. . . . 432
de Groot, Peter . . . 350
DeBra, Daniel B. . . . 114
Díaz, Rufino . . . 158
DiGiacomo, Benedito . . . 223
Dixson, Ronald . . . 212, 375
Dong, Weiping . . . 566
Dornfeld, David A. . . . 496, 510, 520, 561
Dow, Thomas A. . . . 412, 432, 500
Downs, Michael J. . . . 91
Duduch, Jaime G. . . . 294
Edgeworth, Robert . . . 229
Enami, Toshio . . . 86
Enke, Daniel . . . 306
Entwistle, Rodney D. . . . 420
Ertekin, Yalcin M. . . . 278
Falter, Karl J. . . . 412
Fang, Fengzhou . . . 95
Ferreira, Placid M. . . . 638
Finlayson, C. Jeffrey . . . 310
Fischer, S. . . . 51
Fon, Tien-Ron . . . 104
Ford, D. G. . . . 648
Frank, Thomas . . . 36
Fukada, Shigeo . . . 314
Furutani, Katsushi . . . 86
Galindo, E. . . . 346
Gao, Wei . . . 163, 186
Garrard, Kenneth P. . . . 432
Gatzen, Hans H. . . . 536
Ge, Ping . . . 396
Gee, Anthony E. . . . 190, 294
Gleason, Jr., Eugene A. . . . 167
Goto, Takayuki . . . 146
Gowri, S. . . . 583
Gutierrez, Hector M. . . . 424
Gweon, Dae-Gab . . . 626
Hahn, P. O. . . . 381
Han, Dong-Chul . . . 328
Harb, Salam M. . . . 41
Hasche, Klaus . . . 369
Hashiguchi, Makoto . . . 446
Hashimoto, Hiroshi . . . 602
Hatai, Tadaaki . . . 614
Hatakeyama, Minoru . . . 428
Hatamura, Yotaro . . . 74, 476, 515
Hatch, Douglas J. . . . 432
Hazra, Lakshman . . . 172
Helmreich, Dieter . . . 381
Henderson, David . . . 318
Henke, Richard P. . . . 654
Hicks, Thomas R. . . . 20
Higashi, Daisuke . . . 176
Hirao, Masatoshi . . . 472
Hocken, Robert J. . . . 322
Hogan, Shawn A. . . . 47
Holmes, Michael L. . . . 322

*Extended abstract not available at press time.

†Abstract not available at press time.

Holster, P. L. 51
Howard, Lowell P. 357, 385
Huang, Pei Sen 644
Ide, A. 482
Iida, I. 602
Ikawa, Naoya. 65
Imai, Kenichiro. 602
Inamura, Toyoshiro 65
Inoue, Yasuyuki 442
Ishikawa, Ken-ichi 486, 542, 572
Jablonski, Richard. 100
Jared, Bradley H. 432
Jenkins, Hodge E. 406
Jensen, Dana 318
Jokiel, Jr., Bernhard 233
Jordan, Jay D. 15
Jouaneh, Musa 396
Joung, Yoon 328
Jusko, O. 369
Kallenbach, Eberhard 456
Kamiya, Kazuhide 110, 353
Kanai, Akira 614
Kaneeda, Toshiaki. 176, 381
Kasaishi, S. 381
Kato, Hideo 172
Kato, Shigeo 332
Kawabe, Shigeru. 243
Kerstan, Michael 381
Khan-Malek, Chantal. 122
Kikuiri, N. 32
Kim, Hee Sool 436
Kim, Oui-Serg 328
Kim, Young Sam 284
Kiran, M. B. 180
Kiyono, Satoshi 163, 186
Ko, Tae Jo 436
Kobayashi, Keiko 150
Koenders, L. 369
Kothiyal, M. P. 217
Kouda, Nobuhiro 546
Koyabu, Kunio. 442
Krylova, N. O. 363
Kudo, Kazuki 442
Kurfess, Thomas R. 406
Kuriyagawa, Tsunemoto 557, 598
Kuroda, T. 546
Kuroda, Takaharu 172
Lau, Kam. 642
Lêdo, H. 294
Lee, Shuo-Jen. 104
Levert, Joseph. 80
Li, Y. 644
Lienhard, J. H. 637*
Lim, Han-Seok. 496
Liu Hongxiang 136
Liu, X-M. 578
Liu, Xiangyang. 672
Ma, De Long 578
Ma, Evan 122
Ma, Ping. . . . . +
Ma, Quanhe. 642
Maetzig, J. Chris 536
Masreliez, Karl G. 47
Matsumoto, Kiyoshi. 476
Matsunaga, Mitsushi 442
McCarthy, Michael B. 190
McConnell, Malachy 20
McWaid, Thomas H. 375
Mehrotra, Deepak 237
Mertens, B. M. 26
Mess, Francis 80
Miller, Michele H. 589
Mitobe, Kazuhisa. 546
Mitsui, Kimiyuki 146
Mitsuishi, Mamoru. 446, 515
Miyashiro, Hiroshi 110, 353
Miyashita Masakazu 614
Mizuhara, Kiyoshi 243
Mohri, Naotake 86
Monterio, A. F. 336
Moon, Joon Hee 284
Moon, Kee S. 263
Moon, Sungho. 247
Moorefield II, George M. 412, 432
Morita, Noboru. 606
Mostafavi, M. Taghi 196
Murai, Hisao 381
Murata, Ryoji 342
Nagao, Takaaki 446, 515
Nakagawa, Tatsuo. 486
Nakamura, Ryohei 172
Nakao, Masayuki. 74, 476
Nakayama, Yoshinori 150
Nan, Pang 602
Nanjyo, Toshiyasu 186
Narayanasamy, K. 583
Nasu, Yasuo 546
Natarajan, A. 122
Nava, Rigoberto 158, 202
Nishida, Jun. 32
Nomura, Takashi 110, 353
Ohira, Fumikazu 442
Okabe, Hideyuki 446
Okada, Hiroyuki. 110
Okafor, A. Chukwujekwu. 237, 278, 450
Okazaki, Yuichi 342
Onchi, Yoshiaki 65
Onnagawa, Hiroyoshi 110
Ozawa, Norimitsu 243
Padilla, Sergio 202

Pahk, Heui Jae 284
Patiño, Juan Manuel 346
Patterson, Steven R. 391
Peirce, Scott B. 114
Pereira, Paulo H. 223
Pey, K. L. 490
Piccirilli, Peter 318
Piscotty, Mark A. 400
Pistecky, Peter V. 622
Postlethwaite, Scott R. 648
Potzick, James 206
Pragalsingl, Satish. 196
Prather, Maurice J. 668
Preuss, Werner 56, 506
Qu, Weimin 589
Radhakrishnan, V. 180
Raja, Jay 672
Ramamoorthy, B. 180
Rehsteiner, F. 288
Rhorer, Richard L. 412
Riemer, O. 506
Rivera, G. 432
Ro, Paul I. 424, 462
Rosielle, P. C. J. N. 631
Ryu, Jae-Wook 626
Sadashivappa, K. 551
Saffert, E. 456
Sakuma, Itaru 172
Salant, Richard 80
Salsbury, James G. 664
Salzer, Leander J. 432
Sannareddy, Harikrishna. 672
Santavy, A. P. 618
Sasaki, Shigetoshi. 150
Sasaki, Shun'ichi 342
Sata, Toshio. 65
Satoh, Makoto 186
Scattergood, Ronald O. 55*, 524, 593, 618
Schaefer, John 412
Schäffel, Christoph 456
Schellekens, Piet H. J. 631
Schinstock, Dale E. 668
Schmitz, Tony 118
Schmütz, J. 506
Schneir, Jason. 212
Schwenke, Heinrich 167
Scire, Fred. 385
Seki, Y. 482
Sekita, S. 602
Serrano-Carreón, L. 346
Sharp, Keith W. 593
Shen, Yin-Lin. 247, 253
Shibata, Keiichi 546
Shimada, Soichi 65
Shin, Dae Young 300
Shirase, Keiichi 472
Shoji, Katsuo 557
Silver, R. 212
Singaperumal, M. 217, 551
Sirohi, R. S. 217
Slocum, Alexander H. 637*
Smith, Stuart T. 41, 391
Smith, Tony G. 15
Soltani, M. F. 267
Springer, Marlow E. 253
Stancil, Brent A. 462
Stejskal, Alois 357
Stenton, W. Conrad . . . . . +
Stone, Brian J. 420
Stone, Jack A. 357, 385
Sugawara, Takamitu 163
Sugita, Naohiko 515
Sullivan, Paul J. 212, 375
Summerhays, Kim D. 654
Sutherland, John W. 263
Suwabe, Hitoshi 542, 572
Suzuki, Hirofumi 557
Suzuki, Kiyoshi 482
Suzuki, Seiki 150
Syoji, Katsuo 598
Tajbakhsh, Hooman 638
Takada, Koji. 150
Takasu, N. 32
Takezawa, Nobuhiro 65
Tan, K. H. 490
Tanaka, Katsuya 446
Tang, Jianshe 520
Tanikella, B. V. 524
Tashiro, Hatsuzo 110, 353
Taylor, John S. 62, 400
Teraoka, Sadakazu 486
Terashima, Shingo 606
Thiele, K. 369
Tian, GuyYun. 467
Trigg, A. 490
Trumper, David L. 322
Tsai, Vincent W. 212, 375
Tsuchiya, Yoshihiro 172
Tsuda, N. 602
Uchida, N. 32
Udupa, Ganesha 217
Uematsu, Tetsuro 482
Ueno, Shigeru 428
Ukpong, Anietie 450
Uneda, Michio 542, 572
Valera, Benjamín 202
van Beek, H. Frank 26
van der Wulp, H. 26
Vázquez, R. 346
Venkatesh, Vellore C. 490

Vermeulen, J. P. M. B. 631
Vidic, Marina 41
Vieira Porto, Arthur J. 294
Vishwas, B. P. 259
Vorburger, Theodore V. 212, 375
Wang, Haibo 136
Wang, M. . . . . +
Wang, Wanjun 122
Wang, Xu-Jin 598
Wang, Yiding 263
Wasson, Kevin L. 637*
Watanabe, N. 482
Webster, John A. 566
Weck, Manfred 51, 267
Weikert, Sascha 288
Wen, Q. Y. 578
Wilhelm, Robert G. 229, 259
Wilkening, Günter 369
Williams, E. D. 212
Wronosky, John B. 15
Xu, Ying 20
Yamada, Kazutoshi 150
Yamazaki, Kazuo 126
Yan, Xiren 472
Yang, Ren 132
Yang, Yue 126
Yasui, Takeshi 472
Yasunaga, Nobuo 482
Yau, Hong-Tzong 273, 660
Yokomizo, Seiichi 176
Yokota, Yasuhiro 381
Yoshida, Masato 614
Yoshida, Y. 602
Yoshida, Yoshitaro 606
Yoshikawa, Kazuo 110, 353
You, Zheng 132
Yu, Huadong 606
Zanoni, Carl 350
Zarudi, Irena 610
Zhang, G. X. 95
Zhang, Y.Q. 95
Zhao, X. 369
Zhao, Z. X. 467
Zheng, Huan Wen 578
Zhu, Hongxi 136
Ziegert, John C. 118, 233